XRCF Phase 1 Testing: Analysis Results

Smithsonian Astrophysical Observatory

May 10, 2004

Contents

1 Introduction
- 1.1 The Facility and Experimental Setup . . . 1 – 1
- 1.2 The Measurements . . . 1 – 3

2 Summary

3 The HXDS Flow Proportional Counters
- 3.1 Introduction . . . 3 – 1
  - 3.1.1 Calibration Overview . . . 3 – 1
- 3.2 Apertures . . . 3 – 1
  - 3.2.1 Focal Plane Apertures . . . 3 – 1
  - 3.2.2 BND Apertures . . . 3 – 5
- 3.3 Spectral Response Function . . . 3 – 7
- 3.4 Gain Nonuniformity and Anode Aging . . . 3 – 12
- 3.5 Quantum Efficiency . . . 3 – 15
  - 3.5.1 Monochromator Results . . . 3 – 16
  - 3.5.2 Absolute Broad Band . . . 3 – 26
  - 3.5.3 Relative QEs from Flat Field Calibration . . . 3 – 28
  - 3.5.4 Relating Flat Field, HRMA, and BESSY measurements . . . 3 – 31
  - 3.5.5 Final Results: Standardized FPC QEs . . . 3 – 34
- 3.6 Future Work . . . 3 – 37

4 The HXDS Solid State Detectors
- 4.1 Introduction . . . 4 – 1
- 4.2 Calibration Overview . . . 4 – 1
- 4.3 Spectral Response Function, SRF . . . 4 – 2
  - 4.3.1 Components of the Response Function . . . 4 – 2
  - 4.3.2 Interpeak Pileup . . . 4 – 5
- 4.4 Results of Fitting Response Function Spectra . . . 4 – 7
- 4.5 Detector Efficiency vs. Energy Narrow Band . . . 4 – 20
- 4.6 Q. E. Broad Band: White light Calibration . . . 4 – 25
  - 4.6.1 The algorithm for calculating the synchrotron radiation spectrum . . . 4 – 25
  - 4.6.2 The SYNCH Model . . . 4 – 39
  - 4.6.3 Synchrotron Measurement Procedures . . . 4 – 39
  - 4.6.4 Results of the Fitting . . . 4 – 41

  - 4.6.5 Icing . . . 4 – 63
  - 4.6.6 Detector Uniformity . . . 4 – 63
- 4.7 Future Work . . . 4 – 63

5 Deadtime and Pileup Correction in the HXDS FPCs and SSDs
- 5.1 Introduction . . . 5 – 1
- 5.2 Deadtime and Pileup Time Windows . . . 5 – 2
- 5.3 Calibration Measurements . . . 5 – 3
- 5.4 Deadtime consistency testing . . . 5 – 3
  - 5.4.1 Experimental configuration . . . 5 – 3
  - 5.4.2 Data reduction . . . 5 – 4
  - 5.4.3 Correction equations . . . 5 – 5
  - 5.4.4 Results . . . 5 – 8
  - 5.4.5 Simplified and More General Method for Deadtime Determination . . . 5 – 8
  - 5.4.6 Estimated accuracy in analysis of AXAF calibration data . . . 5 – 9
- 5.5 Recommendations . . . 5 – 10
- 5.6 Appendices . . . 5 – 11

6 FPC Window Mesh Effect and its Correction
- 6.1 Introduction . . . 6 – 1
- 6.2 HRMA Image on FPC Mesh . . . 6 – 2
- 6.3 Mesh Transmission Model . . . 6 – 2
- 6.4 Mesh Scan . . . 6 – 2
- 6.5 Mesh Correction . . . 6 – 3
- 6.6 Conclusion . . . 6 – 4

7 High Speed Imager Calibration
- 7.1 Introduction . . . 7 – 1
- 7.2 Calibration Data Summary . . . 7 – 1
- 7.3 *HSI* Quantum Efficiency Measurements . . . 7 – 2
- 7.4 Count Rate Linearity . . . 7 – 2
- 7.5 Flat Fields . . . 7 – 10
- 7.6 Spatial Distortion . . . 7 – 20
- 7.7 Ion Shield Transmission . . . 7 – 22

8 HXDS Translation Stages and Related Calculations
- 8.1 Introduction . . . 8 – 1
- 8.2 Hardware Description: Focal Plane Stack . . . 8 – 1
- 8.3 Hardware Description: BND . . . 8 – 2
- 8.4 Hardware Description: Apertures for SSD and BND Detectors . . . 8 – 2
- 8.5 Stage Log File Formats . . . 8 – 3
- 8.6 Computations with the Stage Log information: fpc_x Detectors . . . 8 – 3
- 8.7 Computations with the Stage Log information: Other Detectors . . . 8 – 5
- 8.8 Known Shortcomings of this Method . . . 8 – 5

9 Spectral Fitting in HXDS Detector Data Analysis
9.1 Introduction . . . 9 – 1
9.2 Reduction of the Line Measurements . . . 9 – 1
9.3 A Sample Fit: Ti K–α . . . 9 – 4
9.4 A Higher Fidelity Method for Analysis of FPC Line Data . . . 9 – 5
9.5 Analysis of BESSY FPC Monochromator data . . . 9 – 8

10 Simulations
10.1 Introduction . . . 10 – 1
10.2 HRMA Model . . . 10 – 1
10.2.1 Optics' Figure . . . 10 – 1
10.2.2 Baffles and Support Structure . . . 10 – 3
10.2.3 Mirror Surface . . . 10 – 3

11 HRMA Effective Area: SSD C-continuum Measurements
11.1 Introduction . . . 11 – 1
11.2 SSD C-continuum Effective Area Measurements . . . 11 – 2
11.3 Pileup Correction . . . 11 – 2
11.4 SSD Flat Field Test . . . 11 – 22
11.5 SSD Energy Scale . . . 11 – 22
11.6 SSD Deadtime Correction . . . 11 – 27
11.7 Beam Uniformity Test . . . 11 – 34
11.8 SSD Relative Quantum Efficiency . . . 11 – 34
11.9 SSD Icing Effect . . . 11 – 39
11.10Background . . . 11 – 42
11.11Data Analysis and Reduction . . . 11 – 42
11.12Effective Area . . . 11 – 42
11.13Error Analysis . . . 11 – 49
11.14Comparing Measurements with the Raytrace Prediction . . . 11 – 49
11.15Calibrating the HRMA Effective Area . . . 11 – 54
11.16HRMA Effective Area Raytrace Predictions . . . 11 – 56
11.17XRCF HRMA Effective Area . . . 11 – 67
11.18On-orbit HRMA Effective Area Prediction . . . 11 – 77
11.19Conclusion . . . 11 – 87

12 HRMA Effective Area: Spectral Line Measurements
12.1 Introduction . . . 12 – 1
12.2 FPC Data Reduction . . . 12 – 1
12.3 Gain Nonuniformity in the open BND-H detectors . . . 12 – 2
12.4 FPC Beam Uniformity (BU) effects . . . 12 – 3
12.5 Relative Quantum Efficiencies (RQE) of the FPC detectors . . . 12 – 3
12.6 Corrected HRMA Entrance Flux: FPC detectors . . . 12 – 4
12.7 Effective Areas: FPC detectors . . . 12 – 5
12.8 Error Analysis: FPC detectors . . . 12 – 5
12.9 SSD Data Analysis . . . 12 – 10
12.10Monochromator/FPC Effective Area Measurements . . . 12 – 11

13 Fitting the HRMA Effective Area
13.1 Introduction . . . 13 – 1
13.2 Mirror Model . . . 13 – 1
13.3 Setup . . . 13 – 2
13.4 Fitting . . . 13 – 3
13.5 Resulting Fits . . . 13 – 35

14 Wing Scans: Data Reduction and Pinhole Effective Areas
14.1 Pinhole Effective Areas . . . 14 – 4
14.1.1 X-ray data reduction . . . 14 – 4
14.1.2 Raytrace simulations of the pinhole experiments . . . 14 – 5
14.2 The Experiment as Performed . . . 14 – 5
14.2.1 History of the Pitch Problem . . . 14 – 6
14.2.2 Yaw Reference Error . . . 14 – 8
14.2.3 Vignetting by Quadrant Shutters . . . 14 – 8
14.3 Pinhole Effective Areas: X-ray data *vs* Raytrace . . . 14 – 8
14.3.1 Single Quadrant Wing Scan Pinhole Data . . . 14 – 9
14.3.2 Transverse (out of plane) Wing Scan Pinhole Data . . . 14 – 55
14.3.3 Double Quadrant Wing Scan Pinhole Data . . . 14 – 58
14.4 Discussion and Outstanding Issues . . . 14 – 61
14.5 Raytrace and Data Reduction Versions . . . 14 – 61

15 Wing Scans: Analysis
15.1 PSD based on HDOS metrology . . . 15 – 1
15.2 Surface Brightness Profiles . . . 15 – 2
15.2.1 Shell 1 scans . . . 15 – 6
15.2.2 Shell 3 scans . . . 15 – 15
15.2.3 Shell 4 scans . . . 15 – 27
15.2.4 Shell 6 scans . . . 15 – 40
15.2.5 Double Quadrant Scans . . . 15 – 57
15.3 Out-of-Plane Scattering . . . 15 – 57
15.4 Comparison with Encircled Energy Data . . . 15 – 58
15.5 "$2W_1$" Profiles . . . 15 – 59
15.5.1 Shell 1 scans . . . 15 – 62
15.5.2 Shell 3 scans . . . 15 – 67
15.5.3 Shell 4 scans . . . 15 – 72
15.5.4 Shell 6 scans . . . 15 – 77
15.5.5 2 Quadrant Scans . . . 15 – 82
15.6 Outstanding Analysis Issues . . . 15 – 84
15.7 Implications for Scattering Models . . . 15 – 84

16 Encircled Energy
16.1 Comparison of Encircled Energy Measurements to Simulations . . . 16 – 2

17 Off Axis Effective Area

18 HRMA Ring Focus Measurements
18.1 Introduction . . . 18 – 1
18.2 Measurements and Data . . . 18 – 2
18.3 Data Analysis . . . 18 – 3
18.4 Results . . . 18 – 4
18.5 Ring Focus Models . . . 18 – 4
18.6 Comparison of Data with the Model . . . 18 – 7
18.7 Conclusion . . . 18 – 8

19 HRMA PSF

20 HRMA Ghost Image Properties
20.1 Ghost Images – Geometry . . . 20 – 1
20.2 Ghost Baffle Design . . . 20 – 3
20.2.1 Control of Single Reflection Ghosts . . . 20 – 5
20.3 HSI Images of Ghosts . . . 20 – 6
20.4 Determination of Off-axis Angle Using Ghosts . . . 20 – 7

21 Analysis of the "Mesh-Plane" HSI Image
21.1 Mesh-Plane HSI Image . . . 21 – 1
21.2 Raytrace Simulations . . . 21 – 2
21.3 Analysis of the Image . . . 21 – 3
21.3.1 Axial position of the image . . . 21 – 4
21.4 Updating the Tilts . . . 21 – 4
21.5 Mirror Distortions . . . 21 – 5

22 Off-Axis imaging: comparing HSI images to raytrace models
22.1 Off-axis HSI Images (Full HRMA) . . . 22 – 1
22.2 Off-axis HSI Images (Single Shell) . . . 22 – 13

23 Predictions of the On-orbit Performance

24 EIPS Beam Uniformity
24.1 Beam Uniformity Tests . . . 24 – 1
24.2 Beam Uniformity Analysis . . . 24 – 2
24.3 Future Directions . . . 24 – 9
24.4 Acknowledgments . . . 24 – 10

25 HRMA Ring Focus Shutter Test
25.1 Introduction . . . 25 – 1
25.2 Measurements . . . 25 – 1
25.3 Data Analysis . . . 25 – 1
25.4 Results . . . 25 – 2
25.5 Conclusion . . . 25 – 3

26 HRMA Focus Measurements and Raytrace Update
26.1 HRMA Focus Measurements at XRCF . . . 26 – 1
26.2 Update of SAO HRMA Raytrace Model from XRCF Focus Data . . . 26 – 4
26.3 Updated deformation and sum files . . . 26 – 10

27 Rigid-Body Misalignment Parameters
27.1 HATS Data . . . 27 – 1
27.1.1 November 1996 HATS ATP (Augmented) Data Set . . . 27 – 3
27.1.2 Conversion of HATS data to Rigid Body Coefficients . . . 27 – 5
27.2 Construction of the Mirror Rigid-Body Database . . . 27 – 5
27.3 Future Directions . . . 27 – 8

28 HRMA Tilts at XRCF
28.1 Coordinate Systems and tilt angles . . . 28 – 1
28.2 Tilt Measurements . . . 28 – 3
28.3 Comparison with models . . . 28 – 4
28.4 Future work . . . 28 – 4
28.5 Quad shutter tilt data from XRCF tests . . . 28 – 5
28.5.1 Shell 1 . . . 28 – 5
28.5.2 Shell 3 . . . 28 – 6
28.5.3 Shell 4 . . . 28 – 7
28.5.4 Shell 6 . . . 28 – 8

29 HRMA Off-Axis Focal Positions

30 Internal Tilt-Compensated Coma-Free Decenter of the AXAF mirrors
30.1 Quadrant Shutter Flux Balance . . . 30 – 1
30.2 Off-Axis X-ray Images . . . 30 – 2
30.3 Morphology of the Off-axis X-ray Images . . . 30 – 2
30.3.1 Off-Axis Images: Large Lobes . . . 30 – 6
30.3.2 Off-Axis Images: Pincushion Caustics . . . 30 – 7
30.4 Measuring the Tilt-Compensated Decenter . . . 30 – 10
30.5 Future Directions . . . 30 – 16

A Incidental Data Tables
A.1 Introduction . . . A – 1

B Coordinate Systems

C Quadrant Shutter Nomenclature

D Appendix: HRMA Pointing at XRCF
D.1 Introduction . . . D – 1
D.2 Sources of Information . . . D – 2
D.2.1 Test Order and Times . . . D – 2
D.2.2 Actuator Encoder Readouts . . . D – 2
D.3 Initial Actuator Position (IAP) . . . D – 3
D.4 Actuator Failures . . . D – 3
D.5 Data Processing . . . D – 5
D.6 Discrepant Tests . . . D – 6
D.6.1 Phase 1 . . . D – 6
D.6.2 Phase 2 . . . D – 6
D.7 The Pitch Problem and its Effect on Wing Scan Data . . . D – 7
D.7.1 History of the Pitch Problem . . . D – 7

D.7.2 Yaw Reference Error . . . . . D – 9

E HRMA Dimensional Data

E.1 HRMA Axial Datum Locations . . . . . E – 1
E.1.1 HRMA Baffle Plates . . . . . E – 4
E.1.2 P6 Ghost Baffle . . . . . E – 4
E.1.3 HRMA Structure Assembly (HSA) . . . . . E – 4
E.1.4 Forward HRMA Structure (FHS) . . . . . E – 4
E.1.5 Thermal Precollimator . . . . . E – 7
E.1.6 Aft HRMA Structure (AHS) . . . . . E – 7
E.2 HRMA Mirror Spacing . . . . . E – 10
E.3 HRMA Baffles and Obstructions . . . . . E – 16
E.3.1 Thermal Precollimator and Forward HRMA Structure Baffles . . . . . E – 18
E.3.2 Aft HRMA Structure Baffles . . . . . E – 20
E.3.3 CAP Ghost Baffles . . . . . E – 22
E.3.4 P6 Ghost Baffle . . . . . E – 22
E.3.5 Fiducial Transfer System Periscope . . . . . E – 22
E.4 Relation between HDOS and Raytrace Coordinates . . . . . E – 24
E.5 HRMA Optic Prescription . . . . . E – 26
E.6 HRMA Optic Clocking Angles . . . . . E – 26

Bibliography **Bib – 1**

List of Figures

1.1 Schematic of XRCF . . . 1 – 2
1.2 On-Axis Encircled Energy/Effective Area Measurements . . . 1 – 5
1.3 Wing Scan Measurements . . . 1 – 6
1.4 Mirror Ends Measurements . . . 1 – 7
1.5 2D Pinhole Scan Measurements . . . 1 – 7
1.6 PSF Outer Core Measurements . . . 1 – 8
1.7 HSI Image Measurements . . . 1 – 9

3.1 Relative size of 36-mm fpc_hn aperture . . . 3 – 8
3.2 Example spectra from BESSY SX700 monochromator . . . 3 – 9
3.3 BESSY KMC spectra–scan across Ar-K edge . . . 3 – 10
3.4 BESSY SX700 spectra–scan across Ar-L edge . . . 3 – 10
3.5 Ar-K edge work function . . . 3 – 11
3.6 Ar-L edge work function . . . 3 – 11
3.7 Counting rate linearity spectra . . . 3 – 13
3.8 Gain nonuniformity . . . 3 – 14
3.9 Model FPC QE . . . 3 – 16
3.10 Absolute QE for fpc_hn and fpc_x2 . . . 3 – 17
3.11 Relative QE for fpc_x2 from BESSY and XRCF . . . 3 – 19
3.12 Measured window transmissions . . . 3 – 20
3.13 QE vs. window transmission for fpc_x2 . . . 3 – 21
3.14 QE mapping of fpc_hn and fpc_x2 . . . 3 – 22
3.15 Measured window deflections . . . 3 – 23
3.16 Small-scale 2D QE mapping . . . 3 – 24
3.17 1D QE mapping scans of fpc_hn . . . 3 – 25
3.18 fpc_x2 QE at Ar-K edge . . . 3 – 26
3.19 White beam spectra . . . 3 – 27
3.20 Fitted absolute QE for fpc_hn and fpc_x2 . . . 3 – 39
3.21 Fitted absolute QE for fpc_ht and fpc_hb . . . 3 – 40
3.22 Fitted absolute QE for fpc_hs . . . 3 – 41
3.23 Fitted absolute QE for fpc_5 . . . 3 – 41

4.1 Components of the HYPERMET function. . . . 4 – 3
4.2 Response functions of ssd_5 on both sides of the Ge L_{III} edge. . . . 4 – 5
4.3 Response functions of ssd_x and ssd_5 at 4.1 keV. . . . 4 – 6

4.4 The pulse-height spectrum of radiation from an Fe target excited by a ^{244}Cm α-emitter. . . . 4 – 13
4.5 The difference between the monochromator energy setting and the fitted energy. . . . 4 – 15
4.6 Fitted low-energy (rising) tail parameters for ssd_5 and ssd_x. The upper panel shows the tail norm (counts in the tail), plotted as a fraction of the total number of counts in the main peak. The lower panel shows the corresponding values of the slope parameter. . . . 4 – 17
4.7 Fitted shelf norm (counts in the shelf) for ssd_5 and ssd_x, plotted as a fraction of the total number of counts in the main peak. . . . 4 – 18
4.8 Fitted escape and fluorescent line norms for ssd_5 (upper panel) and ssd_x (lower panel), plotted as a fraction of the total number of counts. . . . 4 – 19
4.9 Reduced chi-squared χ^2 values for the fitted regions of the spectra. . . . 4 – 20
4.10 Measured QE data from SX700 data and their corresponding fitted curves for ssd_5 and ssd_x. The upper panel emphasizes the Al-K edge fine structure, and the lower panel provides a detailed view of the QE near the O-K edge. . . . 4 – 22
4.11 The fitted QE curves extended to 10 keV. The upper plot shows the QE curve for ssd5 approaching a value of one at higher energies. The lower plot shows the ratio of QEs as a function of energy. . . . 4 – 26
4.12 ssd_x Synchrotron White Light Spectra . . . 4 – 40
4.13 Data and XSPEC fit at the white beam for ssd_5 with no Al filter . . . 4 – 42
4.14 Data and XSPEC fit at the white beam for ssd_x with no Al filter. . . . 4 – 45
4.15 Data and XSPEC fit for ssd_5 at the white beam with 27.4 μm Al filter. . . . 4 – 49
4.16 Data and XSPEC fit for ssd_x at the white beam with 27.4 μm Al filter. . . . 4 – 52
4.17 Data and XSPEC fit for ssd_5 at the white beam with 133.4 μm Al filter. . . . 4 – 56
4.18 Data and XSPEC fit for ssd_x at the white beam with 133.4 μm Al filter. . . . 4 – 59

5.1 Example SSD deadtime calibration ^{55}Fe spectrum . . . 5 – 5

6.1 HRMA HSI image with −9.7 mm defocus . . . 6 – 5
6.2 Shell 1 . . . 6 – 6
6.3 Shell 3 . . . 6 – 6
6.4 Shell 4 . . . 6 – 6
6.5 Shell 6 . . . 6 – 6
6.6 Al–Kα (1.49 keV) . . . 6 – 7
6.7 Ti–Kα (4.51 keV) . . . 6 – 7
6.8 Fe–Kα (6.40 keV) . . . 6 – 7
6.9 Zn–Kα (8.64 keV) . . . 6 – 7
6.10 Al–Kα. Shell 1. . . . 6 – 8
6.11 Al–Kα. Shell 3. . . . 6 – 8
6.12 Al–Kα. Shell 4. . . . 6 – 8
6.13 Al–Kα. Shell 6. . . . 6 – 8
6.14 Al–Kα. HRMA. . . . 6 – 9
6.15 Ti–Kα. HRMA. . . . 6 – 9
6.16 Fe–Kα. HRMA. . . . 6 – 9
6.17 Zn–Kα. HRMA. . . . 6 – 9
6.18 Al–Kα. HRMA. . . . 6 – 10

6.19 Ti–Kα. HRMA. . . . 6 – 10
6.20 Fe–Kα. HRMA. . . . 6 – 10
6.21 Zn–Kα. HRMA. . . . 6 – 10
6.22 Al–Kα. HRMA. . . . 6 – 11
6.23 Ti–Kα. HRMA. . . . 6 – 11
6.24 Fe–Kα. HRMA. . . . 6 – 11
6.25 Zn–Kα. HRMA. . . . 6 – 11
6.26 HXDS FPC-X2 Mesh Scan data fit to the model. Date: 96/12/21 . . . . 6 – 12
6.27 HXDS FPC-X2 Mesh Scan data fit to the model. Date: 96/12/24 . . . . 6 – 13
6.28 HXDS FPC-X2 Mesh Scan data fit to the model. Date: 97/01/15 . . . . 6 – 14
6.29 HXDS FPC-X2 Mesh Center Offset. . . . 6 – 15

7.1 Angular dependence of relative quantum efficiency. B-K and C-K. . . . 7 – 3
7.1 (continued) O-K and Fe-L. . . . 7 – 4
7.1 (continued) Cu-L and Mg-K. . . . 7 – 5
7.1 (continued) Al-K and Mo-L. . . . 7 – 6
7.1 (continued) Sn-L and Ti-K. . . . 7 – 7
7.1 (continued) Fe-K. . . . 7 – 8
7.2 HSI post-processing electronics fast discriminator count rate linearity . . . . 7 – 9
7.3 HSI post-processing electronics image count rate linearity . . . . 7 – 9
7.4 Sample flat field *FPC* scan pattern . . . . 7 – 11
7.5 *FPC* flat field profile scans. C-K and Fe-L. . . . 7 – 12
7.5 (continued) Al-K and Fe-K. . . . 7 – 13
7.6 *HSI* super flat field. . . . 7 – 14
7.7 Central *HSI* tile, showing region of degraded sensitivity . . . . 7 – 15
7.8 Horizontal cut across region shown in Figure 7.7. . . . 7 – 16
7.9 Low sensitivity region of *HSI* $(+Y, -Z)$ . . . . 7 – 17
7.10 Central 3×3 tile region of *HSI* flat field . . . . 7 – 18
7.11 $+Y, +Z$ region of *HSI* flat field, showing variable gap width . . . . 7 – 19
7.12 *HSI* super flat Z projection. . . . 7 – 20
7.13 *HSI* super flat Z projection (detail). . . . 7 – 21
7.14 *HSI* super flat Y projection. . . . 7 – 21
7.15 *HSI* super flat Y projection (detail). . . . 7 – 22

8.1 The HXDA translation stages and detectors . . . . 8 – 2

9.1 Sample `JMKmod` log file, obtained with the `show all` command in `XSPEC` . . . 9 – 6
9.2 Sample `JMKmod` spectral fit to Ti K–α spectrum. . . . 9 – 7
9.3 Line shape parameters for the `fpc_x2` as functions of energy. Top: Fano factor, and Bottom: Shelf norm . . . . 9 – 10
9.4 Line shape parameters for the `fpc_hn` as functions of energy. Top: Fano factor, and Bottom: Shelf norm . . . . 9 – 11

11.1 C-continuum SSX and SS5 spectra: Shell 1 . . . . 11 – 4
11.2 C-continuum SSX and SS5 spectra: Shell 3 . . . . 11 – 5
11.3 C-continuum SSX and SS5 spectra: Shell 4 . . . . 11 – 6
11.4 C-continuum SSX and SS5 spectra: Shell 6 . . . . 11 – 7
11.5 SSX and SS5 pulser spectra: Shell 1 . . . . 11 – 9
11.6 SSX and SS5 pulser spectra: Shell 3 . . . . 11 – 10

11.7 SSX and SS5 pulser spectra: Shell 4 . . . . 11 – 11
11.8 SSX and SS5 pulser spectra: Shell 6 . . . . 11 – 12
11.9 SSX spectrum and pileup correction: Shell 1 . . . . 11 – 14
11.10 SSX spectrum and pileup correction: Shell 3 . . . . 11 – 15
11.11 SSX spectrum and pileup correction: Shell 4 . . . . 11 – 16
11.12 SSX spectrum and pileup correction: Shell 6 . . . . 11 – 17
11.13 SS5 spectrum and pileup correction: Shell 1 . . . . 11 – 18
11.14 SS5 spectrum and pileup correction: Shell 3 . . . . 11 – 19
11.15 SS5 spectrum and pileup correction: Shell 4 . . . . 11 – 20
11.16 SS5 spectrum and pileup correction: Shell 6 . . . . 11 – 21
11.17 C-continuum flat field test SSX and SS5 spectra . . . . 11 – 23
11.18 SSX and SS5 energy scales for the flat field test (Phase-J) . . . . 11 – 24
11.19 SSX and SS5 energy scale linear fit residuals for the flat field test (Phase-J) . . . . 11 – 25
11.20 C-continuum flat field test SSX and SS5 spectra as functions of energy . . . . 11 – 26
11.21 SSX and SS5 energy scales for the C-continuum effective area measurements (Phase-E) . . . . 11 – 28
11.22 SSX and SS5 energy scale linear fit residuals for the C-continuum effective area measurements (Phase-E) . . . . 11 – 29
11.23 SSX and SS5 energy scales for the C-continuum effective area measurements (Phase-D) . . . . 11 – 30
11.24 SSX and SS5 energy scale linear fit residuals for the C-continuum effective area measurements (Phase-D) . . . . 11 – 31
11.25 C-continuum flat field test SSX and SS5 pulser spectra . . . . 11 – 33
11.26 C-continuum source beam uniformity test . . . . 11 – 35
11.27 C-continuum FPC-5 beam flux ratio . . . . 11 – 36
11.28 SS5/SSX quantum efficiency ratio . . . . 11 – 38
11.29 SSD 500 icing data . . . . 11 – 40
11.30 X-ray transmission of ice . . . . 11 – 41
11.31 SSX and SS5 spectra of background run . . . . 11 – 43
11.32 SSD C-continuum effective area measurement: Shell 1 . . . . 11 – 44
11.33 SSD C-continuum effective area measurement: Shell 3 . . . . 11 – 45
11.34 SSD C-continuum effective area measurement: Shell 4 . . . . 11 – 46
11.35 SSD C-continuum effective area measurement: Shell 6 . . . . 11 – 47
11.36 Calibration data vs. raytrace prediction: Shell 1 . . . . 11 – 50
11.37 Calibration data vs. raytrace prediction: Shell 3 . . . . 11 – 51
11.38 Calibration data vs. raytrace prediction: Shell 4 . . . . 11 – 52
11.39 Calibration data vs. raytrace prediction: Shell 6 . . . . 11 – 53
11.40 Calibration data vs. raytrace prediction: HRMA . . . . 11 – 55
11.41 Raytrace prediction of XRCF Shell 1 effective area and encircled energy . . . . 11 – 57
11.42 Raytrace prediction of XRCF Shell 3 effective area and encircled energy . . . . 11 – 58
11.43 Raytrace prediction of XRCF Shell 4 effective area and encircled energy . . . . 11 – 59
11.44 Raytrace prediction of XRCF Shell 6 effective area and encircled energy . . . . 11 – 60
11.45 Raytrace prediction of XRCF HRMA effective area and encircled energy . . . . 11 – 61
11.46 Raytrace prediction of on-orbit Shell 1 effective area and encircled energy . . . . 11 – 62
11.47 Raytrace prediction of on-orbit Shell 3 effective area and encircled energy . . . . 11 – 63
11.48 Raytrace prediction of on-orbit Shell 4 effective area and encircled energy . . . . 11 – 64
11.49 Raytrace prediction of on-orbit Shell 6 effective area and encircled energy . . . . 11 – 65

11.50 Raytrace prediction of on-orbit HRMA effective area and encircled energy . . 11 – 66
11.51 XRCF HRMA and four shells effective areas within 2 mm aperture . . . . . 11 – 68
11.52 XRCF HRMA and four shells effective areas within 35 mm aperture . . . . . 11 – 69
11.53 XRCF HRMA and four shells effective areas within 2π steradian . . . . . 11 – 70
11.54 On-orbit HRMA and four shells effective areas within 2 mm aperture . . . . . 11 – 78
11.55 On-orbit HRMA and four shells effective areas within 35 mm aperture . . . . 11 – 79
11.56 On-orbit HRMA and four shells effective areas within 2π steradian . . . . . 11 – 80

12.1 Shell 1 & 3 Effective Areas through 35 mm pinholes . . . . . 12 – 7
12.2 Shell 4 & 6 Effective Areas through 35 mm pinholes . . . . . 12 – 8
12.3 Full HRMA Effective Areas through 35 mm pinholes . . . . . 12 – 13
12.4 Shell 1 & 3 Effective Areas through 2 mm pinholes . . . . . 12 – 14
12.5 Shell 4 & 6 Effective Areas through 2 mm pinholes . . . . . 12 – 15
12.6 Full HRMA Effective Areas through 2 mm pinholes . . . . . 12 – 16
12.7 Full HRMA Effective Areas through 2 mm pinholes . . . . . 12 – 17

13.1 Multilayer mirror . . . . . 13 – 2
13.2 Shell 1 effective area and residuals through 2mm pinhole . . . . . 13 – 4
13.3 Shell 3 effective area and residuals through 2mm pinhole . . . . . 13 – 5
13.4 Shell 4 effective area and residuals through 2mm pinhole . . . . . 13 – 6
13.5 Shell 6 effective area and residuals through 2mm pinhole . . . . . 13 – 7
13.6 Shell 1 SSD continuum effective area *vs.* model, 2.01 – 2.4 keV . . . . . 13 – 9
13.7 Shell 1 SSD continuum effective area *vs.* model, 2.25 – 2.9 keV . . . . . 13 – 10
13.8 Shell 1 SSD continuum effective area *vs.* model, 2.8 – 4.0 keV . . . . . 13 – 11
13.9 Shell 1 SSD continuum effective area *vs.* model, 3.9 – 7.0 keV . . . . . 13 – 12
13.10 Shell 1 SSD continuum effective area *vs.* model, 5.0 – 8.5 keV . . . . . 13 – 13
13.11 Shell 1 SSD continuum effective area *vs.* model, 8.0 – 12.0 keV . . . . . 13 – 14
13.12 Shell 3 SSD continuum effective area *vs.* model, 2.01 – 2.4 keV . . . . . 13 – 15
13.13 Shell 3 SSD continuum effective area *vs.* model, 2.25 – 2.9 keV . . . . . 13 – 16
13.14 Shell 3 SSD continuum effective area *vs.* model, 2.8 – 4.0 keV . . . . . 13 – 17
13.15 Shell 3 SSD continuum effective area *vs.* model, 3.9 – 7.0 keV . . . . . 13 – 18
13.16 Shell 3 SSD continuum effective area *vs.* model, 5.0 – 8.5 keV . . . . . 13 – 19
13.17 Shell 3 SSD continuum effective area *vs.* model, 8.0 – 12.0 keV . . . . . 13 – 20
13.18 Shell 4 SSD continuum effective area *vs.* model, 2.01 – 2.4 keV . . . . . 13 – 21
13.19 Shell 4 SSD continuum effective area *vs.* model, 2.25 – 2.9 keV . . . . . 13 – 22
13.20 Shell 4 SSD continuum effective area *vs.* model, 2.25 – 2.9 keV . . . . . 13 – 23
13.21 Shell 4 SSD continuum effective area *vs.* model, 3.9 – 7.0 keV . . . . . 13 – 24
13.22 Shell 4 SSD continuum effective area *vs.* model, 5.0 – 8.5 keV . . . . . 13 – 25
13.23 Shell 4 SSD continuum effective area *vs.* model, 8.0 – 12.0 keV . . . . . 13 – 26
13.24 Shell 6 SSD continuum effective area *vs.* model, 2.01 – 2.4 keV . . . . . 13 – 28
13.25 Shell 6 SSD continuum effective area *vs.* model, 2.25 – 2.9 keV . . . . . 13 – 29
13.26 Shell 6 SSD continuum effective area *vs.* model, 2.8 – 4.0 keV . . . . . 13 – 30
13.27 Shell 6 SSD continuum effective area *vs.* model, 3.9 – 7.0 keV . . . . . 13 – 31
13.28 Shell 6 SSD continuum effective area *vs.* model, 5.0 – 8.5 keV . . . . . 13 – 32
13.29 Shell 6 SSD continuum effective area *vs.* model, 8.0 – 12.0 keV . . . . . 13 – 33

14.1 Effect of quadrant shutter vignetting: shell 3 *vs.* shell 4. . . . . 14 – 9
14.2 Effect of quadrant shutter vignetting. . . . . 14 – 10

14.3 Quadrant shutter vignetting: at the quadrant shutter plane. . . . . 14 – 11
14.4 Pinhole effective areas; Shell 1T at Al-Kα. . . . . 14 – 12
14.5 Pinhole effective areas; Shell 1N at Al-Kα. . . . . 14 – 13
14.6 Pinhole effective areas; Shell 1B at Al-Kα. . . . . 14 – 14
14.7 Pinhole effective areas; Shell 1S at Al-Kα. . . . . 14 – 15
14.8 Pinhole effective areas; Shell 1T at Ti-Kα. . . . . 14 – 16
14.9 Pinhole effective areas; Shell 1N at Ti-Kα. . . . . 14 – 17
14.10 Pinhole effective areas; Shell 1B at Ti-Kα. . . . . 14 – 18
14.11 Pinhole effective areas; Shell 1S at Ti-Kα. . . . . 14 – 19
14.12 Pinhole effective areas; Shell 3T at Al-Kα. . . . . 14 – 20
14.13 Pinhole effective areas; Shell 3N at Al-Kα. . . . . 14 – 21
14.14 Pinhole effective areas; Shell 3B at Al-Kα. . . . . 14 – 22
14.15 Pinhole effective areas; Shell 3S at Al-Kα. . . . . 14 – 23
14.16 Pinhole effective areas; Shell 3S at Ti-Kα. . . . . 14 – 24
14.17 Pinhole effective areas; Shell 3S at Cr-Kα. . . . . 14 – 25
14.18 Pinhole effective areas; Shell 3T at Fe-Kα. . . . . 14 – 26
14.19 Pinhole effective areas; Shell 3N at Fe-Kα. . . . . 14 – 27
14.20 Pinhole effective areas; Shell 3B at Fe-Kα. . . . . 14 – 28
14.21 Pinhole effective areas; Shell 3S at Fe-Kα. . . . . 14 – 29
14.22 Pinhole effective areas; Shell 4T at Al-Kα. . . . . 14 – 30
14.23 Pinhole effective areas; Shell 4N at Al-Kα. . . . . 14 – 31
14.24 Pinhole effective areas; Shell 4B at Al-Kα. . . . . 14 – 32
14.25 Pinhole effective areas; Shell 4S at Al-Kα. . . . . 14 – 33
14.26 Pinhole effective areas; Shell 4S at Ti-Kα. . . . . 14 – 34
14.27 Pinhole effective areas; Shell 4S at Cr-Kα. . . . . 14 – 35
14.28 Pinhole effective areas; Shell 4T at Fe-Kα. . . . . 14 – 36
14.29 Pinhole effective areas; Shell 4N at Fe-Kα. . . . . 14 – 37
14.30 Pinhole effective areas; Shell 4B at Fe-Kα. . . . . 14 – 38
14.31 Pinhole effective areas; Shell 4S at Fe-Kα. . . . . 14 – 39
14.32 Pinhole effective areas; Shell 4S at Cu-Kα. . . . . 14 – 40
14.33 Pinhole effective areas; Shell 6B at C-Kα. . . . . 14 – 41
14.34 Pinhole effective areas; Shell 6T at Al-Kα. . . . . 14 – 42
14.35 Pinhole effective areas; Shell 6N at Al-Kα. . . . . 14 – 43
14.36 Pinhole effective areas; Shell 6B at Al-Kα. . . . . 14 – 44
14.37 Pinhole effective areas; Shell 6S at Al-Kα. . . . . 14 – 45
14.38 Pinhole effective areas; Shell 6S at Ti-Kα. . . . . 14 – 46
14.39 Pinhole effective areas; Shell 6S at Cr-Kα. . . . . 14 – 47
14.40 Pinhole effective areas; Shell 6T at Fe-Kα. . . . . 14 – 48
14.41 Pinhole effective areas; Shell 6B at Fe-Kα. . . . . 14 – 49
14.42 Pinhole effective areas; Shell 6S at Fe-Kα. . . . . 14 – 50
14.43 Pinhole effective areas; Shell 6T at Cu-Kα. . . . . 14 – 51
14.44 Pinhole effective areas; Shell 6N at Cu-Kα. . . . . 14 – 52
14.45 Pinhole effective areas; Shell 6B at Cu-Kα. . . . . 14 – 53
14.46 Pinhole effective areas; Shell 6S at Cu-Kα. . . . . 14 – 54
14.47 Pinhole effective areas; Shell 6B at C-Kα (*transverse scans*). . . . . 14 – 56

14.48 Pinhole effective areas. Left: 1 mm pinhole scan, Shell 3B at Al-Kα. Right: 4 mm pinhole scan, Shell 3B at Al-Kα. These 3B Y–scans were performed in order to correct the in-plane 4N4S and 6N6S scans which were made with the 3B shutter stuck open. (*transverse scans*). . . . . 14 – 57
14.49 Pinhole effective areas; Shell 4NS at Al-Kα. . . . . 14 – 59
14.50 Pinhole effective areas; Shell 6NS at Al-Kα. . . . . 14 – 60

15.1 Shell 1T: Al-Kα surface brightness, towards and away from the optic . . . . . 15 – 7
15.2 Shell 1N: Al-Kα surface brightness, towards and away from the optic . . . . . 15 – 8
15.3 Shell 1B: Al-Kα surface brightness, towards and away from the optic . . . . . 15 – 9
15.4 Shell 1S: Al-Kα surface brightness, towards and away from the optic . . . . . 15 – 10
15.5 Shell 1T: Ti-Kα surface brightness, towards and away from the optic . . . . . 15 – 11
15.6 Shell 1N: Ti-Kα surface brightness, towards and away from the optic . . . . . 15 – 12
15.7 Shell 1B: Ti-Kα surface brightness, towards and away from th e optic . . . . 15 – 13
15.8 Shell 1S: Ti-Kα surface brightness, towards and away from the optic . . . . . 15 – 14
15.9 Shell 3T: Al-Kα surface brightness, towards and away from the optic . . . . . 15 – 17
15.10 Shell 3N: Al-Kα surface brightness, towards and away from the optic . . . . 15 – 18
15.11 Shell 3B: Al-Kα surface brightness, towards and away from the optic . . . . 15 – 19
15.12 Shell 3S: Al-Kα surface brightness, towards and away from the optic . . . . . 15 – 20
15.13 Shell 3S: Ti-Kα surface brightness, towards and away from the optic . . . . . 15 – 21
15.14 Shell 3S: Cr-Kα surface brightness, towards and away from the optic . . . . . 15 – 22
15.15 Shell 3T: Fe-Kα surface brightness, towards and away from the optic . . . . . 15 – 23
15.16 Shell 3N: Fe-Kα surface brightness, towards and away from the optic . . . . . 15 – 24
15.17 Shell 3B: Fe-Kα surface brightness, towards and away from the optic . . . . . 15 – 25
15.18 Shell 3S: Fe-Kα surface brightness, towards and away from the optic . . . . . 15 – 26
15.19 Shell 4T: Al-Kα surface brightness, towards and away from the optic . . . . . 15 – 29
15.20 Shell 4N: Al-Kα surface brightness, towards and away from the optic . . . . 15 – 30
15.21 Shell 4B: Al-Kα surface brightness, towards and away from the optic . . . . 15 – 31
15.22 Shell 4S: Al-Kα surface brightness, towards and away from the optic . . . . . 15 – 32
15.23 Shell 4S: Ti-Kα surface brightness, towards and away from the optic . . . . . 15 – 33
15.24 Shell 4S: Cr-Kα surface brightness, towards and away from the optic . . . . . 15 – 34
15.25 Shell 4T: Fe-Kα surface brightness, towards and away from the optic . . . . . 15 – 35
15.26 Shell 4N: Fe-Kα surface brightness, towards and away from the optic . . . . . 15 – 36
15.27 Shell 4B: Fe-Kα surface brightness, towards and away from the optic . . . . . 15 – 37
15.28 Shell 4S: Fe-Kα surface brightness, towards and away from the optic . . . . . 15 – 38
15.29 Shell 4S: Cu-Kα surface brightness, towards and away from the optic . . . . . 15 – 39
15.30 Shell 6B: C-Kα surface brightness, towards and away from the optic . . . . . 15 – 42
15.31 Shell 6T: Al-Kα surface brightness, towards and away from the optic . . . . . 15 – 43
15.32 Shell 6N: Al-Kα surface brightness, towards and away from the optic . . . . 15 – 44
15.33 Shell 6B: Al-Kα surface brightness, towards and away from the optic . . . . 15 – 45
15.34 Shell 6S: Al-Kα surface brightness, towards and away from the optic . . . . . 15 – 46
15.35 Shell 6S: Ti-Kα surface brightness, towards and away from the optic . . . . . 15 – 47
15.36 Shell 6S: Cr-Kα surface brightness, towards and away from the optic . . . . . 15 – 48
15.37 Shell 6T: Fe-Kα surface brightness, towards and away from the optic . . . . . 15 – 49
15.38 Shell 6N: Fe-Kα surface brightness, towards and away from the optic . . . . . 15 – 50
15.39 Shell 6B: Fe-Kα surface brightness, towards and away from the optic . . . . . 15 – 51
15.40 Shell 6S: Fe-Kα surface brightness, towards and away from the optic . . . . . 15 – 52
15.41 Shell 6T: Cu-Kα surface brightness, towards and away from the optic . . . . . 15 – 53

15.42 Shell 6N: Cu-Kα surface brightness, towards and away from the optic . . . . 15 – 54
15.43 Shell 6B: Cu-Kα surface brightness, towards and away from the optic . . . . . 15 – 55
15.44 Shell 6S: Cu-Kα surface brightness, towards and away from the optic . . . . . 15 – 56
15.45 Double quadrant wing scan surface brightness: Al-Kα. Top: Shell 4, N and S quadrant. Bottom: Shell 6, N and S quadrant. . . . . 15 – 58
15.46 Out-of-plane scans, compared to in-plane scans. Top left: 6B Y scan at C-Kα (out of plane). Top right: 6B Z scan at C-Kα (in plane, towards optic). Bottom left: 3B Y scan at Al-Kα (out of plane). Bottom right: 3B Z scan at Al-Kα (in plane). . . . . 15 – 59
15.47 Surface Brightness *vs.* Radius for Shell 1S at Ti K-α . . . . . 15 – 60
15.48 Shell 1T: $2W_1$ profiles, towards and away from the optic. XRCF data (*xrcf*) *vs.* raytrace data (*sim*). . . . . 15 – 63
15.49 Shell 1N: $2W_1$ profiles, towards and away from the optic. XRCF data (*xrcf*) *vs.* raytrace data (*sim*). . . . . 15 – 64
15.50 Shell 1B: $2W_1$ profiles, towards and away from the optic. XRCF data (*xrcf*) *vs.* raytrace data (*sim*). . . . . 15 – 65
15.51 Shell 1S: $2W_1$ profiles, towards and away from the optic. XRCF data (*xrcf*) *vs.* raytrace data (*sim*). . . . . 15 – 66
15.52 Shell 3T: $2W_1$ profiles, towards and away from the optic. XRCF data (*xrcf*) *vs.* raytrace data (*sim*). . . . . 15 – 68
15.53 Shell 3N: $2W_1$ profiles, towards and away from the optic. XRCF data (*xrcf*) *vs.* raytrace data (*sim*). . . . . 15 – 69
15.54 Shell 3B: $2W_1$ profiles, towards and away from the optic. XRCF data (*xrcf*) *vs.* raytrace data (*sim*). . . . . 15 – 70
15.55 Shell 3S: $2W_1$ profiles, towards and away from the optic. XRCF data (*xrcf*) *vs.* raytrace data (*sim*). . . . . 15 – 71
15.56 Shell 4T: $2W_1$ profiles, towards and away from the optic. XRCF data (*xrcf*) *vs.* raytrace data (*sim*). . . . . 15 – 73
15.57 Shell 4N: $2W_1$ profiles, towards and away from the optic. XRCF data (*xrcf*) *vs.* raytrace data (*sim*). . . . . 15 – 74
15.58 Shell 4B: $2W_1$ profiles, towards and away from the optic. XRCF data (*xrcf*) *vs.* raytrace data (*sim*). . . . . 15 – 75
15.59 Shell 4S: $2W_1$ profiles, towards and away from the optic. XRCF data (*xrcf*) *vs.* raytrace data (*sim*). . . . . 15 – 76
15.60 Shell 6T: $2W_1$ profiles, towards and away from the optic. XRCF data (*xrcf*) *vs.* raytrace data (*sim*). . . . . 15 – 78
15.61 Shell 6N: $2W_1$ profiles, towards and away from the optic. XRCF data (*xrcf*) *vs.* raytrace data (*sim*). . . . . 15 – 79
15.62 Shell 6B: $2W_1$ profiles, towards and away from the optic. XRCF data (*xrcf*) *vs.* raytrace data (*sim*). . . . . 15 – 80
15.63 Shell 6S: $2W_1$ profiles, towards and away from the optic. XRCF data (*xrcf*) *vs.* raytrace data (*sim*). . . . . 15 – 81
15.64 Double quadrant wing scans. Top: Shell 4 N and S quadrants: $2W_1$ profiles. Bottom: Shell 4 N and S quadrants: $2W_1$ profiles. XRCF data (*xrcf*) *vs.* raytrace data (*sim*). . . . . 15 – 83

16.1 On-axis Full-HRMA Cu L- and K-α and Cr K-α Encircled Energy . . . . . 16 – 2
16.2 On-axis Carbon and Aluminum K-α Encircled Energy . . . . . 16 – 3

16.3 On-axis Titanium and Iron K-α Encircled Energy . . . 16 – 4
16.4 Encircled Energy Fractions at 0.277 keV . . . 16 – 5
16.5 Encircled Energy Fractions at 1.486 keV . . . 16 – 6
16.6 Encircled Energy Fractions at 4.51 keV . . . 16 – 7
16.7 Encircled Energy Fractions at 6.4 keV . . . 16 – 8
16.8 HRMA Encircled Energy Fractions . . . 16 – 9

18.1 HRMA ring focus HSI image. Date: 1996/12/23 . . . 18 – 9
18.2 HRMA ring focus HSI image. Date: 1997/01/10 . . . 18 – 10
18.3 HRMA ring focus HSI image. Date: 1997/01/15 . . . 18 – 11
18.4 HRMA ring focus HSI image. Date: 1997/01/24 . . . 18 – 12
18.5 HRMA ring focus HSI image. Date: 1997/02/10 . . . 18 – 13
18.6 HRMA ring focus HRC image. Date: 1997/04/10 . . . 18 – 14
18.7 Radial profiles for ring 4. Date: 1997/01/24 . . . 18 – 15
18.8 Radial profiles for ring 4. Date: 1997/01/24 . . . 18 – 16
18.9 Radial profiles for ring 1. Date: 1997/01/24 . . . 18 – 17
18.10 Radial profiles for ring 1. Date: 1997/01/24 . . . 18 – 18
18.11 Ring width RMS for ring 1. Date: 1997/01/24 . . . 18 – 19
18.12 Ring width RMS for ring 3. Date: 1997/01/24 . . . 18 – 20
18.13 Ring width RMS for ring 4. Date: 1997/01/24 . . . 18 – 21
18.14 Ring width RMS for ring 6. Date: 1997/01/24 . . . 18 – 22
18.15 The Ring width RMS for ring 1, from all six ring focus measurements. . . . 18 – 23
18.16 The Ring width RMS for ring 3, from all six ring focus measurements. . . . 18 – 24
18.17 The Ring width RMS for ring 4, from all six ring focus measurements. . . . 18 – 25
18.18 The Ring width RMS for ring 6, from all six ring focus measurements. . . . 18 – 26
18.19 HRMA ring focus model with -0.5% epoxy strain . . . 18 – 27
18.20 HRMA ring focus model: Ring 1, Al-K source, no gravity, no epoxy strain. . 18 – 28
18.21 HRMA ring focus model: Ring 1, Al-K source, with gravity, no epoxy strain. 18 – 29
18.22 HRMA ring focus model: Ring 1, Al-K source, with gravity and epoxy strain change. . . . 18 – 30
18.23 The Ring width RMS for ring 1, from three ring focus measurements . . . 18 – 31
18.24 The Ring width RMS for ring 3, from three ring focus measurements . . . 18 – 32
18.25 The Ring width RMS for ring 4, from three ring focus measurements . . . 18 – 33
18.26 The Ring width RMS for ring 6, from three ring focus measurements . . . 18 – 34
18.27 HRMA ring focus Data: Ring 1, Al-K source, data of 1996/12/23 and 1997/02/10 . . . 18 – 35
18.28 HRMA ring focus Data: Ring 3, Al-K source, data of 1996/12/23 and 1997/02/10 . . . 18 – 36
18.29 HRMA ring focus Data: Ring 4, Al-K source, data of 1996/12/23 and 1997/02/10 . . . 18 – 37
18.30 HRMA ring focus Data: Ring 6, Al-K source, data of 1996/12/23 and 1997/02/10 . . . 18 – 38
18.31 HRMA ring focus Data: Ring 1, Al-K source, data of 1997/02/10 and 1997/04/10 . . . 18 – 39
18.32 HRMA ring focus Data: Ring 3, Al-K source, data of 1997/02/10 and 1997/04/10 . . . 18 – 40
18.33 HRMA ring focus Data: Ring 4, Al-K source, data of 1997/02/10 and 1997/04/10 . . . 18 – 41

18.34 HRMA ring focus Data: Ring 6, Al-K source, data of 1997/02/10 and 1997/04/10 . . . 18 – 42
18.35 HRMA ring focus model: Ring 1, Al-K source, epoxy strain with 0.0% and -0.3% moist and their difference. . . . 18 – 43

20.1 Schematic of single-reflection ghosts . . . 20 – 2
20.2 Schematic diagram of single-reflection ghosts. . . . 20 – 3
20.3 Ghost imaging . . . 20 – 4
20.4 Ghost baffles for Wolter type I optics. . . . 20 – 5
20.5 Ghost baffles for Wolter type I optics. . . . 20 – 6
20.6 Ghost baffles for Wolter type I optics. . . . 20 – 7
20.7 Off-axis image with ghosts . . . 20 – 8
20.8 HSI images of ghosts at 25′ off-axis . . . 20 – 9
20.9 Ghosts at 30′ off-axis . . . 20 – 10
20.10 Off-axis angle determination using ghosts. . . . 20 – 11
20.11 Off-axis angle determination . . . 20 – 12

21.1 The two “mesh plane” HSI images. . . . 21 – 2
21.2 Comparing the SAO and the EKC 1G mechanical models. . . . 21 – 6
21.3 Division of hsi111803i0 image into annuli. . . . 21 – 7
21.4 Raytraces for individual HRMA shells at the “mesh plane”. . . . 21 – 8
21.5 Ring radius for individual shells. . . . 21 – 9
21.6 Raytraces with varying Y-tilts compared to hsi111803 image. . . . 21 – 10
21.7 Raytraces with varying Z-tilts compared to hsi111803 image. . . . 21 – 11
21.8 Comparison of XRCF mesh plane HSI image and raytrace simulations . . . 21 – 12

22.1 Off-axis images: 5′ C-Kα, 5′ Ti-Kα. . . . 22 – 3
22.2 Off-axis images: 5′ Fe-Kα, 10′ C-Kα. . . . 22 – 4
22.3 Off-axis images: 10′ Ti-Kα, 10′ Fe-Kα. . . . 22 – 5
22.4 Off-axis images: 15′ C-Kα, 15′ Ti-Kα. . . . 22 – 6
22.5 Off-axis images: 15′ Fe-Kα, 20′ C-Kα. . . . 22 – 7
22.6 Off-axis images: 20′ Ti-Kα, 20′ Fe-Kα. . . . 22 – 8
22.7 Off-axis images: 25′ C-Kα, 25′ Ti-Kα. . . . 22 – 9
22.8 Off-axis images: 25′ Fe-Kα, 30′ C-Kα. . . . 22 – 10
22.9 Off-axis images: 30′ Ti-Kα, 30′ Fe-Kα. . . . 22 – 11
22.10 Off-axis images: 30′ Fe-Kα. . . . 22 – 12
22.11 Single shell off-axis images: 15′. . . . 22 – 14
22.12 Single shell off-axis images: 15′. . . . 22 – 15
22.13 Single shell off-axis images: 20′. . . . 22 – 16
22.14 Single shell off-axis images: 20′. . . . 22 – 17
22.15 Single shell off-axis images: 24′. . . . 22 – 18
22.16 Single shell off-axis images: 24′. . . . 22 – 19

24.1 fpc_hn Scan Pattern with a Polynomial Fit to Normalized Count Rates. . . . 24 – 2
24.2 fpc_5 Scan Pattern with Polynomial Fit to Normalized Count Rates. . . . 24 – 3
24.3 Variation in fit and data points as a function of azimuth for mirror Shell 1. . 24 – 4
24.4 Variation in fit and data points as a function of azimuth for mirror Shells 3 and 4. . . . 24 – 5
24.5 Variation in fit and data points as a function of azimuth for mirror Shell 6. . 24 – 5

25.1 D-IXH-RF-17.001, 108945, Shell 1 TB, 200 sec. . . . 25 – 4
25.2 D-IXH-RF-17.002, 108946, Shell 1 NS, 200 sec. . . . 25 – 4
25.3 D-IXH-RF-17.003, 108947, Shell 3 TB, 200 sec. . . . 25 – 4
25.4 D-IXH-RF-17.004, 108948, Shell 3 NS, 300 sec. . . . 25 – 4
25.5 D-IXH-RF-17.005, 108949, Shell 4 TB, 360 sec. . . . 25 – 5
25.6 D-IXH-RF-17.006, 108951, Shell 4 NS, 360 sec. . . . 25 – 5
25.7 D-IXH-RF-17.007, 108953, Shell 6 TB, 600 sec. . . . 25 – 5
25.8 D-IXH-RF-17.008, 108954, Shell 6 NS, 600 sec. . . . 25 – 5
25.9 108945 & 108946, Shell 1, 200 + 200 sec. . . . 25 – 6
25.10 108947 & 108948, Shell 3, 200 + 300 sec. . . . 25 – 6
25.11 108949 & 108951, Shell 4, 360 + 360 sec. . . . 25 – 6
25.12 108953 & 108954, Shell 6, 600 + 600 sec. . . . 25 – 6
25.13 The HRMA ring focus shutter test results. Shell 1 . . . 25 – 7
25.14 The HRMA ring focus shutter results. Shell 3 . . . 25 – 8
25.15 The HRMA ring focus shutter results. Shell 4 . . . 25 – 9
25.16 The HRMA ring focus shutter results. Shell 6 . . . 25 – 10

26.1 HRMA Focus Data . . . 26 – 2
26.2 HRMA Focus History . . . 26 – 3

27.1 Schematic diagram of HATS double-pass configurations. . . . 27 – 2

28.1 Schematic of coma circle (2θ) distortion . . . 28 – 2

29.1 Measured vs. Simulated Off-Axis Focus Data . . . 29 – 4

30.1 Off-axis images for individual shells; pitch = $-10.61'$, yaw = $10.61'$. . . . 30 – 3
30.2 pitch = $0'$, yaw = $-20'$. . . . 30 – 4
30.3 pitch = $16.42'$, yaw = $17.68'$ . . . 30 – 5
30.4 Variation of off-axis image with angle between source and decenter direction. Shell 3, pitch = $16.42'$, yaw = $17.68'$. . . . 30 – 8
30.5 Variation of off-axis image with angle between source and decenter direction. Shell 3, pitch = $16.42'$, yaw = $17.68'$. . . . 30 – 9
30.6 Schematic diagram of pincushion measurement. . . . 30 – 11
30.7 Off-axis images (Shell 1; pitch = $0'$, yaw = $-20'$). . . . 30 – 12
30.8 Off-axis images (Shell 1; pitch = $0'$, yaw = $-20'$). . . . 30 – 13
30.9 Core pincushions of off-axis images for individual shells; pitch = $0'$, yaw = $-20'$. . . . 30 – 14
30.10 Core pincushions of off-axis images for individual shells based on current SAO raytrace model; pitch = $0'$, yaw = $-20'$. . . . 30 – 15
30.11 Off-axis images for individual shells; pitch = $-10.61'$, yaw = $10.61'$. . . . 30 – 17
30.12 Off-axis images for individual shells; pitch = $0'$, yaw = $-20'$. . . . 30 – 18
30.13 Off-axis images for individual shells; pitch = $16.42'$, yaw = $17.68'$. . . . 30 – 19

B.1 Relations between HATS tower, XRCF, and `SAOsac` coordinates . . . B – 2
B.2 Schematic of XRCF coordinate and rotation conventions . . . B – 3

E.1 Schematic of relevant HRMA assemblies . . . E – 2
E.2 HRMA Axial Datum Locations . . . E – 3

E.3 Schematic of the P6 Ghost Baffle . . . E – 5
E.4 Schematic of the Forward HRMA Structure . . . E – 6
E.5 Schematic of the Thermal Precollimator . . . E – 8
E.6 Schematic of the Aft HRMA Structure . . . E – 9
E.7 Schematic of HRMA mirror positions. . . . E – 11
E.8 EKC Solid Model of Fiducial Transfer System Periscope. . . . E – 23
E.9 Clocking angle for the FTS Periscope . . . E – 23
E.10 EKC, SAOsac, and DPSAOsac optic clocking conventions. . . . E – 27

List of Tables

3.1 Summary of the FPC calibration program. . . . 3 – 2
3.2 Focal plane aperture sizes . . . 3 – 4
3.3 Blocking plate aperture sizes for reference detectors . . . 3 – 6
3.4 Differences among test environments. . . . 3 – 18
3.5 Relative QE for FPC detectors to fpc_hn . . . 3 – 29
3.6 Relative QE for FPCs to fpc_5 . . . 3 – 30
3.7 Relative QE for FPCs to fpc_x1 . . . 3 – 30
3.8 Relative QE for fpc_5 to fpc_hn . . . 3 – 30
3.9 QE Corrections for gas opacity effects . . . 3 – 32
3.10 Absolute QE for fpc_x2 and fpc_hn. . . . 3 – 36
3.10 Absolute QE for fpc_x2 and fpc_hn (continued) . . . 3 – 37
3.11 Absolute QE for fpc_ht, fpc_hb, and fpc_hs . . . 3 – 38
3.12 Absolute QE for fpc_5 . . . 3 – 38

4.1 Fitted energy, rising (low-energy) tail and shelf parameters for ssd_x. . . . 4 – 8
4.2 Fitted escape and fluorescent line parameters for ssd_x. . . . 4 – 9
4.3 Fitted energy, rising (low-energy) tail and shelf parameters for ssd_5. . . . 4 – 10
4.4 Fitted escape and fluorescent line parameters for ssd_5. . . . 4 – 11
4.5 Detector resolution parameters: Fano factor and electronic broadening. . . . 4 – 12
4.6 Energy scale parameters for each phase of SSD use. . . . 4 – 14
4.7 Measured and fitted QE values for ssd_5 from SX700 data. . . . 4 – 23
4.8 Measured and fitted QE values for ssd_x from SX700 data. . . . 4 – 24
4.9 Thickness of fitted window material for ssd_5 and ssd_x. . . . 4 – 25
4.10 Thicknesses of SSD Al filter material, measured at NSLS. . . . 4 – 41
4.11 Fitting parameters for ssd_5 white beam run, all energies, no Al filter. . . . 4 – 43
4.12 Fitting parameters for ssd_5 white beam run, only high energy, no Al filter. . 4 – 44
4.13 Fitting parameters for ssd_x white beam, all energies, no Al filter. . . . 4 – 47
4.14 Fitting parameters for ssd_x white beam, only high energies, no Al filter. . . . 4 – 48
4.15 Fitting parameters for ssd_5 white beam, all energies with 27.4 μm Al filter. . 4 – 50
4.16 Fitting parameters for ssd_5 white beam, Higher energies with 27.4 μm Al filter. . . . 4 – 51
4.17 Fitting parameters for ssd_x white beam, all energies with 27.4 μm Al filter. . 4 – 53

4.18 Fitting parameters for ssd_x white beam, higher energies with 27.4 μm Al filter. . . . 4 – 54
4.19 Fitting parameters for ssd_5 white beam, all energies with 133.4 μm Al filter. 4 – 57
4.20 Fitting parameters for ssd_5 white beam, higher energies with 133.4 μm Al filter. . . . 4 – 58
4.21 Fitting parameters for ssd_x white beam, all energies with 133.4 μm Al filter. 4 – 60
4.22 Fitting parameters for ssd_x white beam, higher energies with 133.4.4 μm Al filter. . . . 4 – 61
4.23 Summary of white beam normalization runs. See text for explanation. . . . 4 – 62
4.24 BESSY ssd_x uniformity scan . . . 4 – 63

6.1 HXDS FPC-X2 Mesh Scans . . . 6 – 3
6.2 HXDS FPC-X2 Mesh Center Positions . . . 6 – 3
6.3 XRCF HRMA Effective Area Measurements FPC Window Mesh Corrections 6 – 16
6.4 XRCF HRMA Effective Area Measurements FPC Window Mesh Corrections 6 – 17
6.5 XRCF HRMA Effective Area Measurements FPC Window Mesh Corrections 6 – 18
6.6 XRCF HRMA Effective Area Measurements FPC Window Mesh Corrections 6 – 19
6.7 XRCF HRMA Effective Area Measurements FPC Window Mesh Corrections 6 – 20

7.1 Image event rate dead-time percentages . . . 7 – 10

8.1 Sample stagelog entry . . . 8 – 3
8.2 Sample section from the FOA table . . . 8 – 4
8.3 Master table (left), and aperture size table (right) for the HXDA FPC detectors . . . 8 – 6
8.4 Master table (left) and aperture size table (center) for ssd_x, and aperture size table for ssd_5 (right) . . . 8 – 7
8.5 Master table for hsi . . . 8 – 7

9.1 Parameters for the JMKmod model, with recommended values. . . . 9 – 3

11.1 HRMA On-axis Effective Area Measurenents . . . 11 – 3
11.2 HRMA Off-axis Effective Area Measurenents . . . 11 – 8
11.3 X-ray Lines atop the C-continuum . . . 11 – 27
11.4 SSD Energy Scale . . . 11 – 32
11.5 SSD-500 Icing Data . . . 11 – 39
11.6 Effective Area Measurements SSD Pulser Deadtime Corrections . . . 11 – 48
11.7 XRCF HRMA Effective Area within 2 mm Aperture. Units: cm^2 . . . 11 – 71
11.7 XRCF HRMA Effective Area within 2 mm Aperture. Units: cm^2 (continued) 11 – 72
11.8 XRCF HRMA Effective Area within 35 mm Aperture. Units: cm^2 . . . 11 – 73
11.8 XRCF HRMA Effective Area within 35 mm Aperture. Units: cm^2 (continued) 11 – 74
11.9 XRCF HRMA Effective Area within 2π Steradian. Units: cm^2 . . . 11 – 75
11.9 XRCF HRMA Effective Area within 2π Steradian. Units: cm^2 (continued) . 11 – 76
11.10 On-orbit HRMA Effective Area within 2 mm Diameter. Units: cm^2 . . . 11 – 81
11.10 On-orbit HRMA Effective Area within 2 mm Diameter. Units: cm^2 (continued) 11 – 82
11.11 On-orbit HRMA Effective Area within 35 mm Diameter. Units: cm^2 . . . 11 – 83
11.11 On-orbit HRMA Effective Area within 35 mm Diameter. Units: cm^2 (continued) . . . 11 – 84
11.12 On-orbit HRMA Effective Area within 2π Steradian. Units: cm^2 . . . 11 – 85

11.12 On-orbit HRMA Effective Area within 2π Steradian. Units: cm^2 (continued) 11 – 86

12.1 Encircled Energy tests analyzed for the HRMA effective area . . . 12 – 2
12.2 Ancillary tests used in the effective area analysis. . . . 12 – 3
12.3 Effective Area results for 35 mm apertures . . . 12 – 6
12.4 Effective Area results for 2 mm apertures . . . 12 – 9

13.1 Shells 1, 3, 4, and 6 reduced χ^2 and σ . . . 13 – 8
13.2 Shell 1 reduced χ^2 and σ . . . 13 – 34
13.3 Shell 3 reduced χ^2 and σ . . . 13 – 34
13.4 Shell 4 reduced χ^2 and σ . . . 13 – 34
13.5 Shell 6 reduced χ^2 and σ . . . 13 – 34

14.1 XRCF Single Quadrant Wing Scan Measurements (by shell) . . . 14 – 2
14.2 XRCF Double Quadrant Wing Scan Measurements . . . 14 – 3
14.3 Single Quadrant Pitch/Yaw values . . . 14 – 3
14.4 Effect of Mesh on Wing Scans . . . 14 – 4

15.1 Wing scan shutter vignetting cutoffs . . . 15 – 4
15.2 Surface brightness fits (raytrace and XRCF data; Shell 1). . . . 15 – 6
15.3 Surface brightness fits (Raytrace, Shell 3). . . . 15 – 15
15.4 Surface brightness fits (XRCF data, Shell 3). . . . 15 – 16
15.5 Surface brightness fits (raytrace, Shell 4). . . . 15 – 27
15.6 Surface brightness fits (XRCF data, Shell 4). . . . 15 – 28
15.7 Surface brightness fits (raytrace, Shell 6). . . . 15 – 40
15.8 Surface brightness fits (XRCF data, Shell 6). . . . 15 – 41
15.9 Surface brightness fits (double quadrant scans, 4N4S. . . . 15 – 57
15.10 Surface brightness fits (double quadrant scans, 6N6S. . . . 15 – 57
15.11 Single quadrant wingscan $2W_1$ fits and mean square roughness (Raytrace simulation and XRCF data, Shell 1) . . . 15 – 62
15.12 Single quadrant wingscan $2W_1$ fits and mean square roughness (Raytrace simulation and XRCF data, Shell 3) . . . 15 – 67
15.13 Single quadrant wingscan $2W_1$ fits and mean square roughness (Raytrace simulation and XRCF data, Shell 4) . . . 15 – 72
15.14 Single quadrant wingscan $2W_1$ fits and mean square roughness (Raytrace simulation and XRCF data, Shell 6) . . . 15 – 77
15.15 Double quadrant wingscan $2W_1$ fits and mean square roughness (Raytrace simulation and XRCF data, Shell 4NS) . . . 15 – 82
15.16 Double quadrant wingscan $2W_1$ fits and mean square roughness (Raytrace simulation and XRCF data, Shell 6NS) . . . 15 – 82

18.1 HRMA Ring Focus Measurement data . . . 18 – 2

20.1 Phase 1 Off-Axis Images with P6 or H6 ghosts . . . 20 – 7

21.1 Mesh Plane HSI images . . . 21 – 2
21.2 Focus distance from CAP Datum –A– plane for EIPS Al-Kα source . . . 21 – 3
21.3 Vertical/Horizontal ratios for meshplane HSI image . . . 21 – 3

21.4 Parameters for the quasi-elliptical annuli used to split apart the hsi111803i0 image . . . 21 – 4
21.5 Ring radius parameters. . . . 21 – 4

22.1 Phase 1 Off-Axis Images (Full HRMA) . . . 22 – 2

24.1 Fit Results for all EIPS BU Tests. . . . 24 – 6

25.1 HRMA Ring Focus Shutter Test Data . . . 25 – 2

26.1 Best Estimate of XRCF Measured Focus of Shells, relative to Shell 3 . . . 26 – 2
26.2 Comparison of pre-XRCF Predictions of On-orbit and XRCF HRMA foci . . 26 – 4
26.3 As Measured Optic lengths and distances . . . 26 – 5
26.4 Final Mirror Focal Positions at XRCF and on orbit . . . 26 – 5
26.5 Test Data for HRMA Focus Tests: D-66 Series . . . 26 – 6
26.6 Test Data for HRMA Focus Tests: D-67 Series . . . 26 – 8
26.7 Test Data for HRMA Focus Tests: E-67 (Final) Series . . . 26 – 9

27.1 HATS Fourier Coefficients (ATP augmented data set) . . . 27 – 2
27.2 HATS ATP (Augmented) Data . . . 27 – 3
27.3 HATS Fourier Coefficients . . . 27 – 4
27.4 HATS Fourier Coefficients: r^2-weighted Q_0 removed . . . 27 – 4
27.5 Conversion to Lateral Parfocalization and Coma . . . 27 – 5
27.6 Summary: HRMA Lateral Parfocalization and On-Axis Coma (SAOsac coordinates) . . . 27 – 5
27.7 Conversion to Rigid Body Misalignment . . . 27 – 6
27.8 Body-center rigid body coefficients (*double-pass* coordinate system) . . . 27 – 6
27.9 Body-center rigid body coefficients (standard `SAOsac` coordinate system) . . . 27 – 7
27.10 `SAOsac` mirror parameters, baseline optic prescription . . . 27 – 7
27.11 `SAOsac` mirror parameters, decenters and tilts from ATP data; as-measured axial mirror positions . . . 27 – 8
27.12 Rigid-Body Mirror Parameters (EKCHDOS06) . . . 27 – 8
27.13 Fourier Coefficients: HATS *vs.* raytrace . . . 27 – 9

28.1 HRMA Tilt Angles . . . 28 – 3
28.2 Summary of HRMA Tilt Angles . . . 28 – 4

29.1 Offset from on-axis focus (mm), + towards HRMA . . . 29 – 1
29.2 HXDS FOA Values During Off-Axis Tests . . . 29 – 1
29.3 HSI PrimeX Values for Best On-Axis Focus . . . 29 – 2
29.4 Off-Axis Focus Test Data . . . 29 – 3

30.1 Phase 1 Off-Axis Images (Full HRMA) . . . 30 – 6
30.2 Phase 1 Off-Axis Images (Individual Shell) . . . 30 – 7
30.3 Measured Tilt-Compensated Decenters . . . 30 – 16

A.1 HXDS detector locations in XRCF testing phases . . . A – 1
A.2 BND aperture areas . . . A – 2
A.3 Source distances to HXDS and HRMA equipment . . . A – 2

B.1 Relations between coordinate systems . . . . . B – 3
B.2 Relations between coordinate systems . . . . . B – 4

C.1 Quadrant Shutter Nomenclature . . . . . C – 1

D.1 IAP table . . . . . D – 4

E.1 Baffle plate information . . . . . E – 4
E.2 FHS baffle plate axial positions . . . . . E – 7
E.3 FHP as-built axial position *vs.* design. . . . . E – 7
E.4 Precollimator baffle plate axial positions . . . . . E – 10
E.5 Precollimator as-built baffle plate axial positions *vs.* design. . . . . E – 12
E.6 AHS baffle plate axial information . . . . . E – 12
E.7 AHS baffle plate axial positions . . . . . E – 12
E.8 Aft HRMA Structure as-built baffle plate axial positions *vs.* design. . . . . E – 13
E.9 HRMA Mirrors: axial locations with respect to the CAP. . . . . E – 14
E.10 AXAF element interface data, Reid (1997) . . . . . E – 15
E.11 HRMA P Mirrors: key axial locations . . . . . E – 15
E.12 HRMA H Mirrors: key axial locations . . . . . E – 16
E.13 Baffle and Obstruction tables . . . . . E – 16
E.14 Raytrace and EKC baffle nomenclature . . . . . E – 17
E.15 Precollimator and Forward Hrma Structure Baffle Data; Shell 1. . . . . E – 18
E.16 Precollimator and Forward Hrma Structure Baffle Data; Shell 3. . . . . E – 18
E.17 Precollimator and Forward Hrma Structure Baffle Data; Shell 4. . . . . E – 19
E.18 Precollimator and Forward Hrma Structure Baffle Data; Shell 6. . . . . E – 19
E.19 Aft Hrma Structure Baffle Data; Shell 1. . . . . E – 20
E.20 Aft Hrma Structure Baffle Data; Shell 3. . . . . E – 20
E.21 Aft Hrma Structure Baffle Data; Shell 4. . . . . E – 21
E.22 Aft Hrma Structure Baffle Data; Shell 6. . . . . E – 21
E.23 CAP Ghost Baffle Data. . . . . E – 22
E.24 P6 Ghost Baffle Data. . . . . E – 22
E.25 FTS Periscope Data. . . . . E – 24
E.26 AXAF element axial data. . . . . E – 25
E.27 HRMA Optic Prescription (including end cut) for ideal optics. . . . . E – 26
E.28 Mirror clocking data. . . . . E – 27

Chapter 1

Introduction

This document is a report on the analysis of the data from Phase 1 of the calibration of the Advanced X-ray Astrophysics Facility (AXAF), which occurred between 1996 December 20 and 1997 February 11 at the X-Ray Calibration Facility (XRCF) at Marshall Space Flight Center (MSFC) in Huntsville, Alabama. The analysis of these data is still ongoing; this document is an update to Jerius (1997).

Because there isn't time in the lifetimes of the members of the team to completely calibrate or characterize every facet of the HRMA, the measurements are augmented by a highly detailed mechanical and optical ray-trace model of the HRMA. The XRCF measurements are used to refine and correct the *ab initio* and semi-empirical components which make it up. Chapter 10 provides more details.

During this test program, we ran a total of 1376 logical tests, each identified by an alphanumeric "TRW ID," assigned according to a scheme negotiated between the prime contractor, TRW, and the AXAF science community. Of these, 982 tests were done without transmission gratings, mostly for the calibration of the High Resolution Mirror Assembly (HRMA), or of the facility (such as background, beam uniformity, alignment to facility axis, etc.). The HRMA X-ray Detection System (HXDS) obtained a total of 5225 different run identifiers (runid's), which include 293,144 individual pulse-height spectra and 1486 High Speed Imager (HSI) images.

The HRMA-only tests will be described in some detail in this document. In Phase 2 of the XRCF test program, science instruments and their stand-ins were used at the focal point of the telescope. Those data are not presented here, though in many cases they bear on the same questions as the Phase 1 data.

TBR: Several puzzles remain to be solved. Most notable among these is the discrepancy in the effective area, discussed in Chapter **??**. Raytrace simulations predict an effective area significantly higher than that which is measured by two different techniques. In most cases this discrepancy amounts to $\sim 8-10\%$, though for mirror pair 1 near its high energy cutoff, the discrepancy is even larger.

1.1 The Facility and Experimental Setup

The test setup is described in detail elsewhere (for example, in SAO (1997)), but a brief description is in order here. A set of X-ray sources is available in Building 600. These include the Electron Impact Point Source (EIPS), a Penning source, and two monochrometers which select X-ray photons emitted by rotating anode sources. These are the Double Crystal Monochrometer

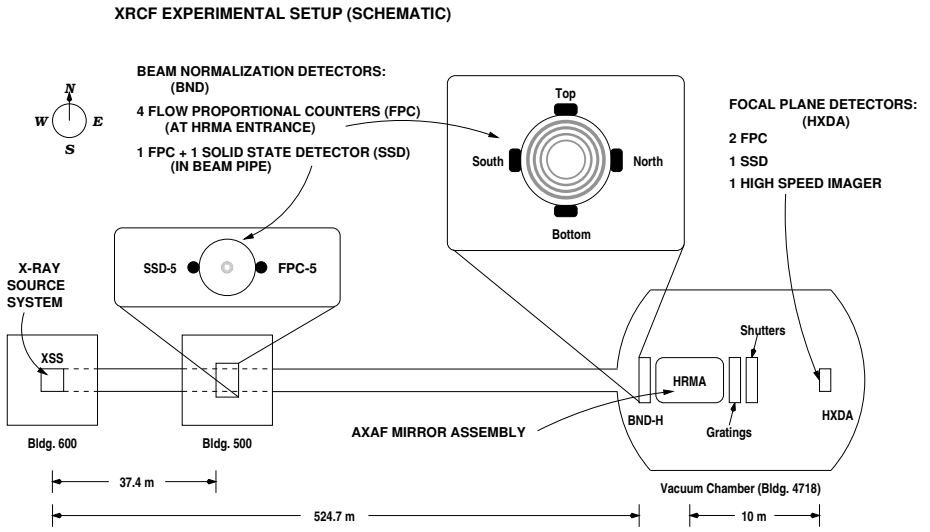

Figure 1.1: Schematic of XRCF

(DCM), and the High Resolution Erect Field Spectrometer (HIREFS).

Figure 1.1 shows the physical layout of the XRCF. Connecting Building 600 to the main instrument chamber in building 4718 at MSFC is an evacuated guide tube over 500 meters long. Approximately 38 meters down the guide tube in Building 500, but off to one side of the beam to avoid occulting it, are two beam normalization detectors (BNDs) known as the BND-500. These are a Flow Proportional Counter (FPC), fpc_5, and a solid state detector (SSD), ssd_5. The fpc_5 detector can be moved about in the beam by a pair of translation stage motors, to map the beam and test it for uniformity. The fpc_5 is closer to the source than the ssd_5. Both of the BND-500 detectors have selectable apertures.

The main instrument chamber contains a variety of equipment, including the HRMA, a set of BNDs surrounding the entrance to the HRMA, and the focal plane instrumentation, the HRMA X-ray Detector Assembly (HXDA). It also contains the flight Objective Transmission Gratings, a set of quadrant shutters (which allow each quadrant of each of the 4 constituent optic pairs of the HRMA to be exposed independently), the HRMA contamination covers, and various motors and other hardware to support operations.

The BND assembly at the HRMA entrance is known as the BND-H (Beam Normalization Detectors at the HRMA). It consists of four nearly identical flow proportional counters, whose nominal stations are adjacent to the north, bottom, south, and top quadrants of the outermost HRMA mirror shell. They are known, respectively, as fpc_hn, fpc_hb, fpc_hs, and fpc_ht. The fpc_hn detector can be moved around in front of the HRMA entrance to map the X-ray beam as it enters the HRMA. It is physically located a small distance closer to the source than the other three BND-H detectors. It can be used either with a 36 mm diameter circular aperture, in the open configuration.

The HXDA assembly at the HRMA focal point consists of two Flow Proportional Counters (FPC), one Solid State Detector (SSD), and a microchannel plate camera known as the High Speed

Imager (HSI). These detectors are known respectively as fpc_x1, fpc_x2, ssd_x, and HSI. The two FPCs are a redundant pair. Except for an early aliveness check, all of the FPC tests actually performed were done with fpc_x2.

All of the HXDA detectors are mounted on a stack of translation stages which allow them to be placed anywhere in three dimensions in the vicinity of the telescope focus, with an accuracy of about 2 μm. They also allow the apertures for the FPCs and SSD to be selected. FPC aperture sizes range from 3 μm to 35 mm diameters; apertures smaller than 7.5 μm were rarely used. Computations based on the positions of these stages are outlined in Chapter 8.

The BNDs are exposed simultaneously with the focal plane detectors. Focal plane count rates are normalized by the photon flux density at the BNDs, leading to *aperture–relative* effective areas, in units of cm^2. These are aperture–relative since the focal plane detectors have finite size. Chapter 9 and Chapter 12 go into more detail about the reduction efforts.

A great many facility physical dimensions are required to fully characterize the experiment for data reduction purposes. Chapter A lists a few of the most important dimensions, and the values they were assumed to have.

1.2 The Measurements

The objective of the test program is to validate a high-fidelity ray trace model of the HRMA, which includes a wide variety of information about the physical and engineering properties of the mirror assembly, including, for example, the effects of gravity, offloader stresses, epoxy shrinkage, surface deformations and roughness, rigid body position of the optical elements, etc. After the model is revised and validated by comparing its predictions to the XRCF data, it can then be used with considerable confidence to predict the performance of the mirrors on orbit.

Accordingly, the test program included a variety of experiments. These include measurements of encircled energy fractions *vs.* aperture size and measurements of effective area at various energies (see Figure 1.2 for a graphical summary of these tests); aperture scans of the wings of the point spread function (see Figure 1.3); measurements of the microroughness of the ends of the mirrors through encircled energy tests with the mirrors tilted to approximate the incident angles of photons from a point source at infinity (see Figure 1.4); 1- and 2-dimensional aperture scans of the point spread function (see Figure 1.5 and Chapter **??**); images of the point spread function (both the inner core of the image, and with that occulted, the outer core) and images taken to constrain the internal alignment of the HRMA optics (see Figures 1.6and1.7); images and aperture scans at the ring focus position; various attempts to detect molecular contamination (if any); measurements of the alignment of the mirror to the facility optical axis; shutter focus measurements; and various kinds of grating tests.

Brief descriptions of the measurements follow; many of them are described more fully, including the results and the analysis done to date, in the ensuing chapters.

Focus and Tilt
: The focal position and the intra-shell tilt of the mirrors can be determined by exposing, in turn, each quadrant of a mirror (or mirrors) with the quadrant shutters, and measuring the centroid of the resultant images. The offsets of the centroids allow calculation of the focus and tilts. With the HSI, this is an actual image, but with the FPC or SSD we make a 2 dimensional raster scan with a small pinhole. These measurements were typically made for each shell individually. (See Chapters 26 and 28).

Encircled Energy/Effective Area
: Each of a series of pinholes is carefully centered on the image centroid. The effective area as seen by each pinhole is given by

$$A_{eff,\mathrm{pinhole}} = A_{\mathrm{BND}} \times \frac{R_{\mathrm{pinhole}}}{R_{\mathrm{BND}}}$$

where A_{BND} is the open area of the BND. R_{pinhole} is the count rate through the pinhole, and R_{BND} is the count rate seen by the BND. The pinholes typically cover $0.1''$ to $6'$ radius around the image center. Effective area measurements are a special case of the encircled energy for the largest available pinhole. (See Chapters 16 and 12.)

Point Response Function
: The PRF of the mirrors was measured in two regimes. The inner core was sampled with one and two dimensional pinhole scans centered about the image centroid. The outer core was measured with the HSI by placing the inner core on specially designed masks. A one dimensional scan through the center gives the Full Width at Half Maximum measurement. Two dimensional scans can be deconvolved for ground effects to deduce the properties of the mirror in orbit. (See Chapters 19 and **??**.)

Wing Scan
: The far outer wings of the PRF are measured via a one-dimensional scan with a relatively large pinhole. These measurements are generally made using one quadrant of one mirror; the direction of the scan was in the plane of the incident and reflected ray at the midpoint of the quadrant. Typical scans are $20''$ to $35'$ from the image center. During many scans the HRMA was tilted so that the grazing angle of the photons from the XSS with respect to the mirror would be more similar to that on orbit. (See Chapters 14 and 15.)

Ring Focus
: The ring focus describes a position on the optical axis of the HRMA where spherical aberration due to a finite-distance source causes the rays from the front and back of the mirrors to cross, giving a minimum thickness ring which is ideal for analyzing 1g mechanical effects on the ground calibration. HSI images were taken at the ring focus position, which for the HRMA is 65.2 mm in front of the finite distance focal point. (See Chapter 18.)

Background
: Runs were made with the gate valve from the source chamber closed, so that there were no X-rays from the source. Setup of the detectors was identical to a subsequent series of measurements with a given X-ray source.

Beam Uniformity
: Two dimensional scans made with the BNDs at the HRMA and at at Bldg. 500. These scans approximated coverage of the region of space occupied by the HRMA, and by the fixed bnd detectors. (See Chapter 24.)

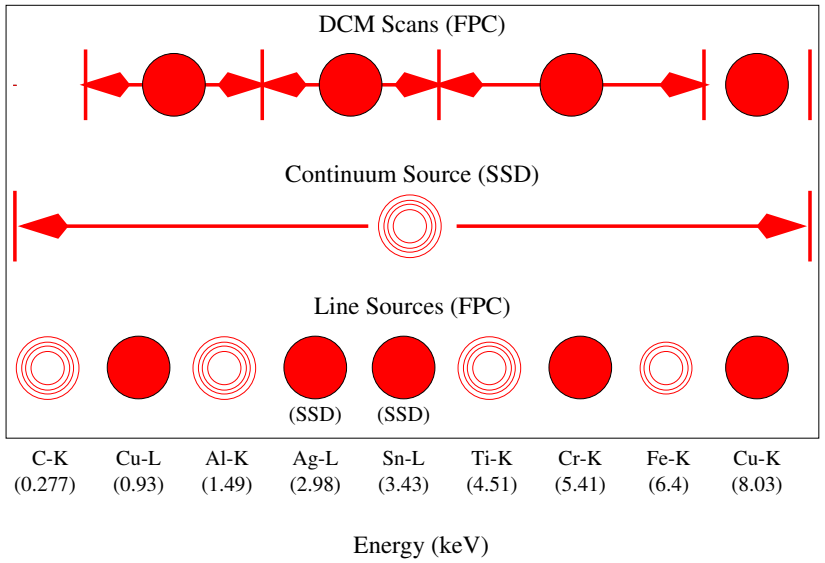

Figure 1.2: The on-axis encircled energy/effective area tests where performed using 3 complementary methods: 1) Line sources with the FPC (bottom row), a continuum source (i.e, the carbon anode run at a high voltage) with the SSD (middle row), and the DCM with the FPC (top row). Filled circles indicate tests that were done with the full HRMA, while open circles indicate tests that were done with single shells (e.g., 4 concentric circles indicate that the test was done for each shell separately).

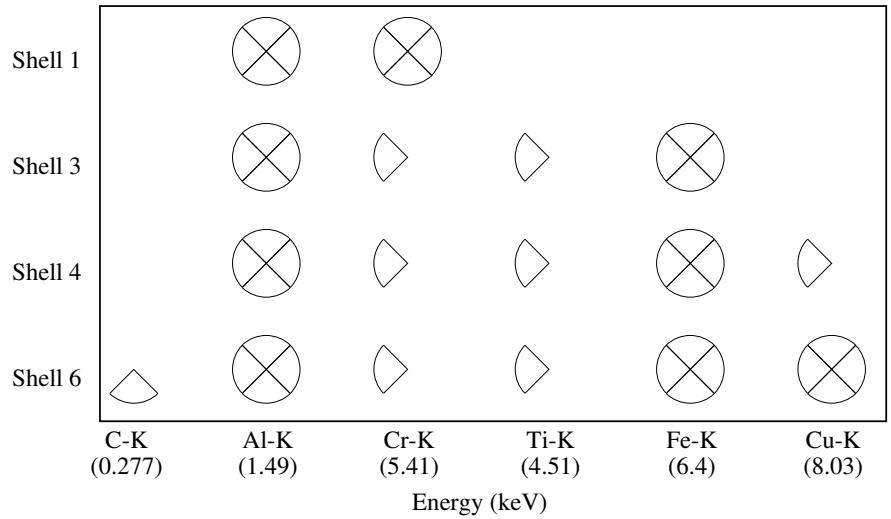

Figure 1.3: All wing scans were performed with only one quadrant of one shell open. This figure shows the wing scan measurements that were performed during Phase 1 as a function of energy, shell, and quadrant. The south quadrant is on the left and the north quadrant is on the right.

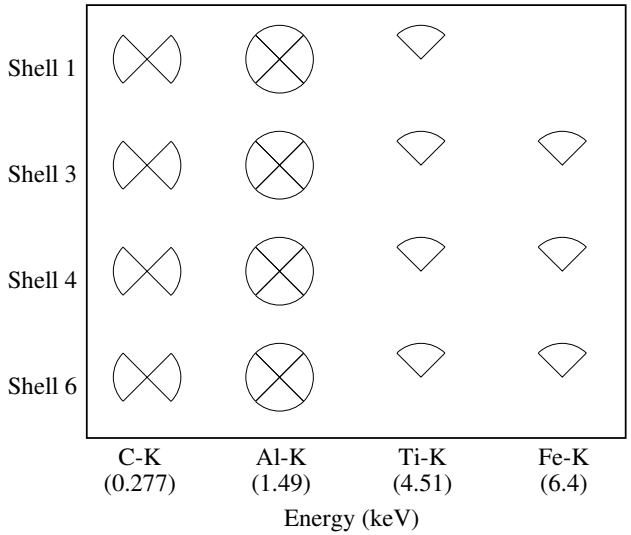

Figure 1.4: Mirror ends survey measurements completed during Phase 1 as a function energy, shell, and quadrant. The south quadrant is on the left and the north quadrant is on the right.

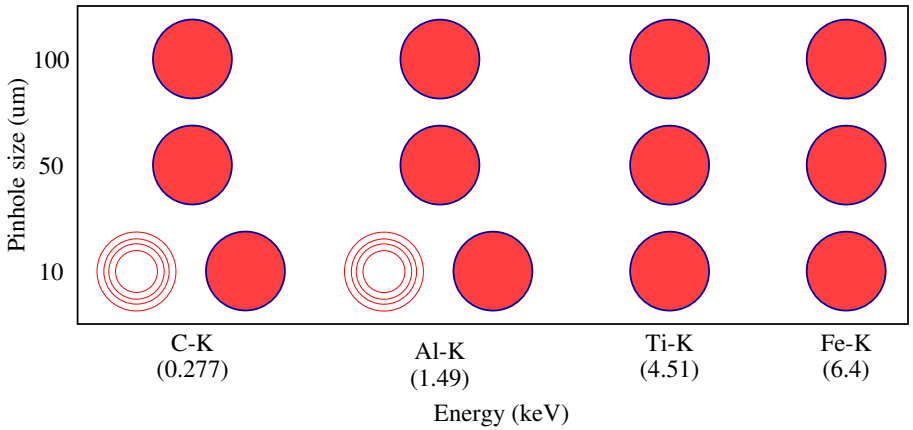

Figure 1.5: 2-D pinhole scans performed during Phase 1 as a function of energy and pinhole diameter. Filled circles indicate tests that were done with the full HRMA, while open circles indicate tests that were done with single shells.

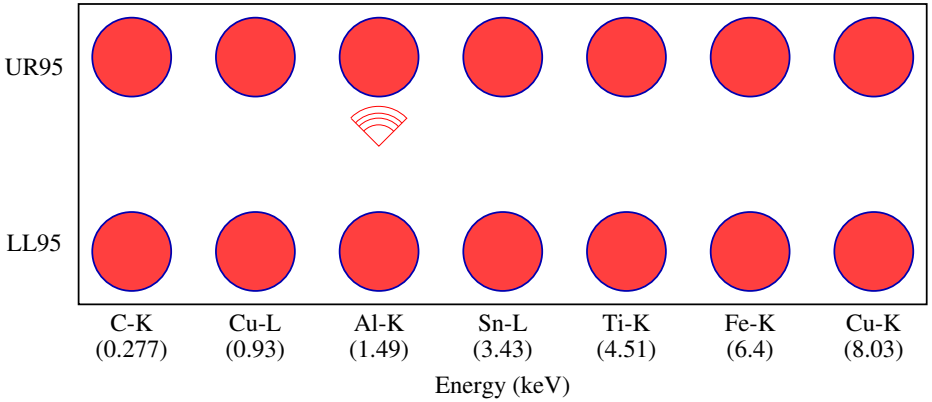

Figure 1.6: PSF Outer core measurements performed during Phase 1 with the HSI. The HSI has two cusps which can block out the centroid of the image. One is on the upper right of the detector (UR95) and one is on the lower left (LL95). The pie slice at Al-Ka indicates images that were obtained with only the top shutter open for individual shells.

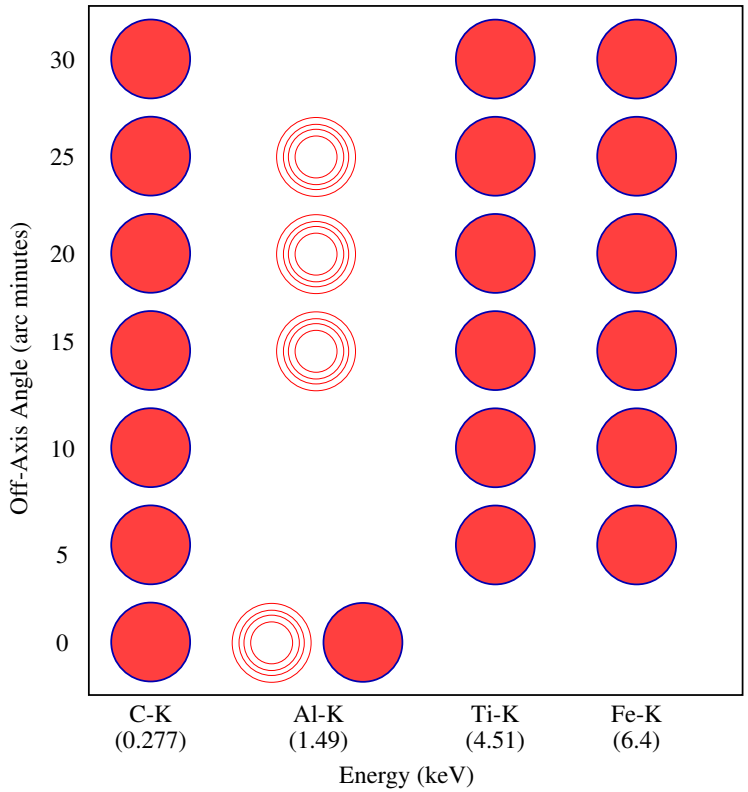

Figure 1.7: HSI images obtained during Phase 1 as a function of energy and angle off-axis. Filled circles indicate tests that were done with the full HRMA, while open circles indicate tests that were done with single shells.

Chapter 2

Summary

Chapter 3

The HXDS Flow Proportional Counters

Brad Wargelin and Richard J. Edgar

3.1 Introduction

In this chapter we discuss the calibration of the seven Flow Proportional Counters (FPCs) used during AXAF ground calibration. Five of the FPCs served as Beam Normalization Detectors (BNDs) throughout both phases of AXAF calibration, and one (with a backup) was used in the telescope focal plane in combination with a set of apertures to measure the point response functions and effective areas of the AXAF mirrors and transmission gratings during Phase 1 calibration. The BNDs also served as references for determining the effective areas of the several telescope/grating/flight-detector combinations.

An overview of the entire HXDS, along with a detailed discussion of the design and operation of the FPCs, may be found in Wargelin et al. (1997). In case of any discrepancies regarding distances and dimensions, this calibration report takes precedence.

3.1.1 Calibration Overview

The FPC calibration program was based on characterization of individual components (such as window transmission and aperture size) and the calibration of complete detector systems, particularly with regard to their relative and absolute quantum efficiencies. Calibration was conducted at SAO (primarily on the HXDS X-ray Pipe Facility), at MSFC (primarily during Phase I and J Flat Field testing at the XRCF in May and June 1997), and in collaboration with the Physikalisch-Technische Bundesanstalt (PTB) at the BESSY synchrotron in Berlin, Germany (December 1997 and January 1998). Theoretical modeling was also employed to quantify small effects that would be too difficult to measure directly. A summary of the calibration program is provided in Table 3.1.

3.2 Apertures

3.2.1 Focal Plane Apertures

Optical and X-ray Measurements

For apertures larger than about 100 μm, areas can be measured with sufficient accuracy using an optical microscope and two-dimensional translation stage. Although all apertures were measured

Characteristic	Measurement	Where
Focal plane aperture sizes	For smallest apertures, use electron microscope and/or measure relative sizes with uniform x-ray beam.	SAO BESSY white
	For larger apertures, use optical microscope with 2d stages.	SAO
BND aperture sizes	Optical microscope, with most accurate measurements for fpc_hn and fpcx2 blocking plates.	SAO
	Net collecting areas of other BNDs are normalized to fpc_hn by flat field relative QE measurements.	XRCF
Window support wire blockage	Calculate based on nominal wire diameter and do in/out x-ray measurements.	SAO
Gain nonuniformity	1d scan of several FPCs	SAO BESSY SX700
Anode aging	1d scan of fpc_x2 and fpc_hn	XRCF BESSY SX700
Spectral response function	Use monochromatic beam	BESSY SX700 KMC
QE: window transmission	In/out tests	BESSY SX700
QE: relative	Cross-calibrate all FPCs and SSDs during Phases I and J	XRCF
QE: absolute	Compare FPC rate with calibrated monochromator beam intensity, as part of Spectral Response Function msmts	BESSY SX700
QE: absolute broadband	Use synchrotron white beam with calibrated filters and compare FPC rate with calculated beam intensity	BESSY white
QE: gas opacity	Vary gas pressure at 1700 eV.	BESSY SX700
	Scan across Ar-K edge at 3206 eV.	BESSY KMC
QE: window bowing	Fine-scale scans at 330,500,930 eV	BESSY SX700
QE: window nonuniformity	XRCF relative QEs are for whole windows but BESSY beams are small. Sample QE at many points to relate XRCF to BESSY.	BESSY SX700
Deadtime consistency	Test rate reproducibility with SSD and ^{55}Fe, using many pulser rates, LLD settings, shaping times.	SAO lab
Counting rate linearity	Compare deadtime-corrected FPC relative counting rates with precisely known relative beam intensity	BESSY SX700 BESSY white
Misc. small effects	Model effects of temperature, pressure, effective gas and window absorption path lengths, anode wire absorption, aperture transparency at high energies, focussed x-rays hitting fpc_x2 support wires, window support wire reflectivity.	SAO

Table 3.1: Summary of the FPC calibration program.

before AXAF calibration, several of the most important were measured again with greater care in April 1998. Each of those apertures, between 100 and 500 μm in diameter, was measured twice along four diameters, with calibrated gauge blocks to correct for microscope stage errors (which were extremely small). The measurement resolution limit was 2.5 μm, and average diameters are quoted to the nearest 0.5 μm. Error estimates are equal to the larger of the resolution and the "sample standard deviation," defined as

$$\left(\frac{\sum_{i=1}^{N} (X_i - \langle X \rangle)^2}{N-1} \right)^{1/2}$$

where N is the number of diameters measured. (Strictly speaking, the sample standard deviation is not applicable here, but it provides a means of quantifying the uncertainty in the effective diameter of each aperture.) The two readings for each measurement were averaged and nearly always differed by ± 2.5 μm or less, so the average was treated as one value and $N = 4$. All the holes were quite circular except for the 300-μm, which had a sample standard deviation of 5.5 μm; because that hole is irregular and we may not have measured a sufficiently representative sample of diameters, we estimate the uncertainty in its average diameter as ± 4 μm.

Aperture sizes are listed in Table 3.2. Note that for the remeasured apertures, the original quoted uncertainties were sometimes too small. For the larger apertures (larger than 500 μm), the original uncertainties were ± 12.5 μm; the uncertainties listed in the table have been subjectively increased because only one or two diameters were measured, etc. Because the HRMA PRF is so peaked, however, errors in the sizes of these larger apertures cause negligible errors in Effective Area and Encircled Energy measurements.

For apertures smaller than 100 μm, sizes are most accurately measured with electron microscopes and calibrated references, or by measuring relative aperture areas by comparing counting rates when the apertures are exposed to a uniform x-ray beam. When using an electron microscope, measuring the size of the smallest apertures is complicated by the fact that the hole size becomes comparable to or smaller than the thickness of the gold foil in which it resides; the microscope can only "see" the entrance side of the tunnel, which is generally flared, and so it becomes problematic to assign a single number to describe the size of a hole that varies with depth, particularly when it is used with a focussed x-ray beam.

For these small apertures, therefore, we attempted to make measurements of relative size at the BESSY synchrotron, exposing the apertures to a nearly flat white beam and recording the observed x-ray signal with a photodiode. Because of alignment problems, however, some and perhaps all of the apertures were partially blocked from the beam, and so we must rely on the electron microscope results. (Future analysis of the BESSY results may provide useful results.) We were able, however, to confirm that the effective size of the nominal 5-μm-diameter aperture is much smaller than expected, as was observed during HMRA calibration at the XRCF.

Aperture Transparency

In order to minimize errors arising from the "tunnel" effect, apertures smaller than 25 μm were fabricated in thinner gold foil, i.e., 12.5 vs. 40-μm or thicker for larger apertures. (An exception is the 5-μm aperture, made from 40-μm foil. It replaced the original, too-small 5-μm aperture made from 12.5-μm foil during the calibration rehearsal phase.) At energies above about 6 keV the thin foil becomes increasingly transparent to x-rays (using the 1995 Henke tables and assuming a density of 18.85 g/cm^3, transmission equals 1.49e-6 at 5415 eV, 1.34e-4 at 6404 eV, 0.00307 at 7478 eV, 0.00831 at 8048 eV, 0.0184 at 8639 eV, and 0.0644 at 10 keV) and since the fraction of x-rays

Aperture	Shape	Nominal Size (μm)	Measured Size (μm)	Accuracy ($\pm\mu$m)
A	circle	35000 diam	35010	40
B	circle	20000 diam	20000	30
C	circle	10000 diam	10020	20
D	circle	4000 diam	4000	15
E	circle	2000 diam	1990	15
F	circle	1000 diam	980	15
G	circle	500 diam	500 498.0 (new)	2.5 2.5
H	circle	300 diam	300 285.5 (new)	2.5 4.0
I	circle	200 diam	200 195.5 (new)	2.5 2.5
J	circle	150 diam	150 149.5 (new)	2.5 2.5
K	circle	100 diam	101 99.0 (new)	2.5 2.5
L	circle	70 diam	70	4
M	circle	50 diam	49	3
N	circle	40 diam	40	3
O	circle	30 diam	30	2
P	circle	20 diam	20	2
Q	circle	15 diam	15	3
R	circle	10 diam	10	2
S	circle	7.5 diam	7.5	2
T	circle	5* diam	3	1
U	circle	3 diam	3	1
V	slit, vertical	5 × 100	5 × 100	2.5, 2.5
W	slit, vert−5°	5 × 100	5 × 100	2.5, 2.5
X	slit, vert+5°	5 × 100	6 × 100	2.5, 2.5
Y	slit, horiz−15°	5 × 100	6 × 98	2.5, 2.5
Z	slit, vert−15°	5 × 100	5 × 98	2.5, 2.5
AA	slit, vertical	10 × 200	10 × 198	2.5, 2.5
AB	slit, vert−5°	10 × 200	10 × 200	2.5, 2.5
AC	slit, vert+5°	10 × 200	10 × 198	2.5, 2.5
AD	slit, horizontal	10 × 200	10 × 198	2.5, 2.5
AE	slit, vertical	80 × 500	80 × 500	2.5, 2.5
AF	slit, vertical	500 × 10000	500 × 9990	2.5, 25
AG	slit, vert+5°	500 × 10000	506 × 10010	2.5, 25
AH	slit, vert−5°	500 × 10000	500 × 10020	2.5, 25

Table 3.2: Focal plane aperture sizes. Slit orientation: looking from the XSS, positive angles are clockwise. Circular apertures larger than 500 μm are made from 1/8"-thick stainless steel. The four largest slits and the 30-500 μm circles are laser-drilled in 40-μm gold foil. Smaller circles and slits are fabricated in 12.5-μm gold foil by ion beam milling. (*The 5-μm circle is made from 40-μm foil.)

focussed on the aperture hole is quite small at high energies because of scattering, a significant fraction of the detected x-rays may be transmitted through the foil out to a diameter of 2 mm, which is the size of the hole in the stainless steel "cupholder" which holds the foils. The measured Encircled Energy Fraction for an aperture of diameter D is then given by

$$EEF(D)_{meas} = EEF(D)_{true} + [EEF(2mm) - EEF(D)_{true}]\,T$$

where T is the transmission of the gold foil at the energy of the EE measurement (with the approximation that all the x-rays are at the line energy). The true EEF is then

$$EEF(D)_{true} = \frac{EEF(D)_{meas} - EEF(2mm)T}{1-T}.$$

As a worst case example, if the measured EE fraction for HRMA shell1 at Cu-Kα is 0.031 with the 10-μm aperture, and the EEF at 2 mm is 0.82, then $EE(10\mu m)_{meas}/EE(10\mu m)_{true}$ is $0.031/((0.031 - (0.82)(0.00831))/(1 - 0.00831) = 1.27$. At lower energies the corrections (for measurements actually conducted) are much less than 1%, which is completely negligible compared with other uncertainties.

Support Wire Blockage—the "Mesh" Effect

Another correction arises from the small fraction of focussed x-rays that hit the wires that support the FPC window. With a perfect mirror, the x-rays from each HRMA shell would intercept the FPC window in rings that fit between the window support wires (just over 1 mm in diameter for shell1, versus the wire pitch of 2 mm), but in the real HRMA, some x-rays are scattered to larger radii. A set of on-axis raytraces was run to quantify this effect and the results are described in great detail in Chapter 6. Corrections are largest for large apertures at high energies, with a value of just over 0.5% for the total HRMA at 8 keV, and 2% for shell 1 by itself. For off-axis sources and grating images, the image centroid will be slightly displaced, but much more important is the fact that the PRF is larger, especially for off-axis measurements. In the worst cases, corrections of a few percent may be needed, but accurate estimates require raytrace analysis.

3.2.2 BND Apertures

Blocking Plate Aperture Size

In order to determine the effective area of AXAF it is necessary to know the net collecting area of each of the BND FPCs, which is equal to the open area of the window times the effective QE. In practice, the only areas we need to measure are those of the blocking plate apertures for fpc_x2 and fpc_hn since all the other BND FPCs are normalized via the flat field relative QE measurements. For simplicity, and because the variation among them is negligible, the areas for all four rectangular BND-H apertures are defined to be the same, i.e., equal to the area of the full fpc_hn aperture.

Using an optical microscope with calibrated gauge blocks, the dimensions of the fpc_hn and fpc_x2 blocking plate apertures were measured to a resolution of 0.0001" (2.5 μm), with each measurement made twice (and the average of the two treated as one result). Results are shown in Table 3.3.

Error estimates for the measured values are equal to the sample standard deviation, as defined earlier, and the net area uncertainty is calculated using standard error propagation. The actual area uncertainties are somewhat different (larger if the samples were not representative, smaller if they were), but are essentially negligible if the quoted errors are any indication (0.06% for fpc_x2 and less than 0.03% for fpc_hn).

Detector/Aperture	Dimension	Number sampled	Value
fpc_hn/full	length	3	98.963 ± 0.016 mm
	width	5	36.441 ± 0.006 mm
	corner radius	2 in each corner	6.314 ± 0.038 mm
	area		3572.1 ± 0.9 mm^2
	net open area for all BND-H FPCs		**3224 ± 16 mm^2**
fpc_hn/36	area ratio vs. full aperture		0.2835 ± 0.0003
	net open area		**914 ± 5 mm^2**
fpc_x2	diameter	4	36.784 ± 0.010 mm
	area		1062.7 ± 0.6 mm^2
	net open area		**959 ± 5 mm^2**

Table 3.3: Blocking plate aperture sizes for reference detectors. The theoretical open area fraction (not blocked by support wires) is 90.26%, assuming 100-μm-diameter wires.

Support Wire Blockage

The major, though still small, source of uncertainty in the net geometric open area of the windows is the fraction blocked by the support wires. These wires are nominally 100-μm in diameter, with 2-mm pitch, so the calculated blocked area fraction per windowlet is equal to (area of 2 crossed wires - area of wire intersection)/(area of unit cell) = (2 x 2.0mm x 0.1mm - $(0.1\text{mm})^2$)/$(2.0\text{mm})^2$ = 0.0975. When accounting for fractional windowlets and curved edges of the blocking plate apertures, the blocked fraction is actually equal to 0.0974 for fpc_hn and fpc_x2. The number and length of the wires can be easily and accurately determined, so any uncertainty arises from knowing the average wire diameter. Measuring all the wires with a microscope is impractical, so one can either estimate the range of likely diameters (a 10% difference in the wire diameter makes a 0.9% difference in the open area fraction), or experimentally determine the open fraction with an in/out x-ray measurement.

Such measurements were conducted on the SAO Pipe in March 1998 for the fpc_hn and fpc_x2 windows. The fpc_hn (or fpc_x2) blocking plate was mounted on fpc_hb, which was held fixed in the x-ray beam, while the corresponding window was moved in and out in front of the detector. The measurements used Ti-K x-rays from a Manson source with 100-μm Ti filter, with normalization provided by a VETA monitor counter. The normalized ratio of the in/out counting rates is equal to the fraction of open area between the wires, after making small corrections for absorption by the polyimide/Al window material and the overlap of wires in the test and detector windows.

The statistical uncertainty for the fpc_hn measurement was ±0.12%, but there was a systematic uncertainty of 0.14% because we did not have time to align everything well enough to tell if one of the window support wires was included within the aperture or not. Splitting the difference and strictly adding the statistical and systematic uncertainties, and correcting for window absorption of 0.0056 ± 0.0006, the measured open area fraction was 89.77% of the total area of 3572.1 mm^2, or 3206.7 ± 8.6 mm^2 (0.27% uncertainty). This is 0.54% smaller than the model which assumes 100-μm diameter wires, and implies an average wire diameter of 105.2 μm. This is certainly within reason, but because of some small (∼1%) but poorly understood features in the lower channels of the Ti-K spectrum which seem to indicate a problem with the electrical connections to fpc_hb, we recommend using the theoretical model, which predicts an open area fraction of 90.26% for both fpc_hn and fpc_x2. The official open areas of the fpc_hn and fpc_x2 blocking plate apertures are therefore 3224.2 mm^2 and 959.2 mm^2, respectively, with somewhat subjective but conservatively

estimated uncertainties of 0.5%. Note, however, that the uncertainty in the *ratio* of the areas of the fpc_x2 and fpc_hn apertures is smaller (less than 0.1%), assuming that the average wire diameter (whatever it is) does not vary from one FPC to another by more than 1%.

The significance of x-rays reflecting off the window support wires and onto the window surface was also studied. Using reflectivity tables for gold, which coats the tungsten wires, a simple raytrace model showed that less than 0.01% of Ti-K x-rays hitting a wire will reflect from it, 0.08% for Al-K, 0.54% for C-K, and approximately 4% for Be-K. Since the wires block about 10% of the total window area, the net effect on the collecting area is less than 0.01% at energies above Al-K, 0.06% at C-K, and about 0.4% at Be-K. Since this effect is negligible except at extremely low energies where other terms dominate the uncertainty in QE, we have not applied any corrections for this effect.

Size of 36-mm fpc_hn Aperture

The BND-H mapper FPC, fpc_hn, has a 36-mm circular aperture that can be flipped in front of the full rectangular aperture. Because of the difficulty of aligning the mapper and its "flapper" aperture in situ, (particularly when the FPC was removed and reinstalled so many times, e.g., to use its aperture motor on the TMA shutter assembly), HXDS engineers noted that part of the circular aperture might fall outside the rectangular aperture, thus leading to a smaller than expected collecting area.

This hypothesis was tested during phase I and J flat field testing by exposing fpc_hn at many energies at the same location in the beam, and comparing the detected x-ray rate using the rectangular and circular apertures. The data were analyzed in two ways: assuming that the EIPS intensity was constant at each energy and, for comparison, using fpc_5 and ssd_5 for normalization. In order to minimize the effects of differences in effective window and gas transmission when using the two apertures, the average was computed using results from only those energies at which the FPC QE is greater than 75%. Results are plotted in Figure 3.1, and indicate a net open area ratio of 0.2835 ± 0.0003, which is 0.5% less than the nominal value of 0.2850. The net open area for the fpc_hn 36-mm aperture is thus 959 ± 5 mm^2.

3.3 Spectral Response Function

When fitting spectra with XSPEC, or any spectral fitting program, it is necessary to know what the output spectrum looks like when the detector is given a monochromatic input, that is, know the spectral response function, or SRF. Detailed results of FPC SRF calibration are presented in Chapter 9, but the main features are a main peak and a low-energy shelf. At energies above the Ar-K edge (at 3206 eV) there is also an escape peak that lies 2957 eV below the main peak. Background is generally a minor issue since its spectrum varies only slightly with energy and is quite stable and repeatable, although at very low energies and counting rates electrical noise may interfere with the x-ray peak. This noise is, however, essentially independent of the FPC voltage setting, and can be subtracted or modeled with little problem.

Spectral response functions were measured on fpc_x2 and fpc_hn between 70 and 1700 eV using the BESSY SX700 monochromator, which also provided QE calibration. Over 70 energies were sampled, with fine-step scans across the Ar-L, C-K, N-K, O-K, and Al-K absorption edges. Example spectra are shown in Figure 3.2. A noticeable trend is the increasing importance of the low-energy shelf as the x-ray energy is lowered. The SRF data were also used to obtain absolute QEs, since PTB has previously calibrated the SX700 beamline intensity. (FPC voltages were, of course, set to obtain the same gain vs. energy conditions as were used during AXAF calibration.)

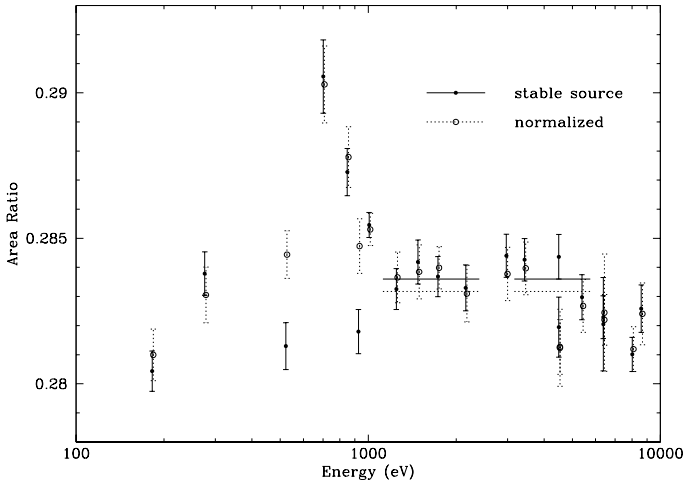

Figure 3.1: Area of fpc_hn 36-mm aperture, relative to rectangular aperture. Ratios were calculated assuming a stable source, and by normalizing to other detectors; points are slightly separated in energy for clarity. Using results from energies where QE > 75% (indicated by horizontal lines), the unnormalized average is 0.28360 ± 0.00027 and the normalized average is 0.28317 ± 0.00032. We take 0.2835 ± 0.0003 as the final answer, as listed in Table 3.3.

At higher energies, up to 5.9 keV, we used the double crystal KMC monochromator. The KMC beamline does not have absolute intensity calibration, and because of beam intensity instabilities arising from heat loading on the crystals and beamline apertures, it is difficult to obtain even relative QE information. By letting the beam stabilize and then making measurements over a relatively short period of time, however, we were able to quantify the P10 gas opacity by scanning across the Ar-K absorption edge at 3206 eV. Spectra from this scan are shown in Figure 3.3. Three features are readily observed in this series: the jump in the number of counts and the appearance of the escape peak as the x-ray energy is raised above the absorption edge threshold (thus providing precise energy calibration for the monochromator), and the nonlinearity of peak position versus x-ray energy.

This nonlinearity is caused by a discontinuity in the work function (average energy required to create a secondary electron) of the P10 gas at the Ar-K edge, as discussed in Jahoda and McCammon (1988). A similar discontinuity also occurs at the Ar-L edge, at 248 eV (see Figure 3.4); a sudden change in the fractional charge loss to the window may also be involved, since the average photon absorption depth jumps from about 2 mm to 0.2 mm as the photon energy crosses the edge. Plots of work function versus energy, normalized to 28 eV per secondary electron below the edges (the nominal value used in the `JMKmod` fitting program) are shown in Figure 3.5 (Ar-K) and Figure 3.6 (Ar-L). Although it is possible to modify `JMKmod` to include the energy dependence of the work function and/or charge loss, we have not done so since this phenomenon is only significant when trying to fit spectra in which continuum emission within the region of interest is significant so that details of energy/channel redistribution are important. Such a case may occur when analyzing white

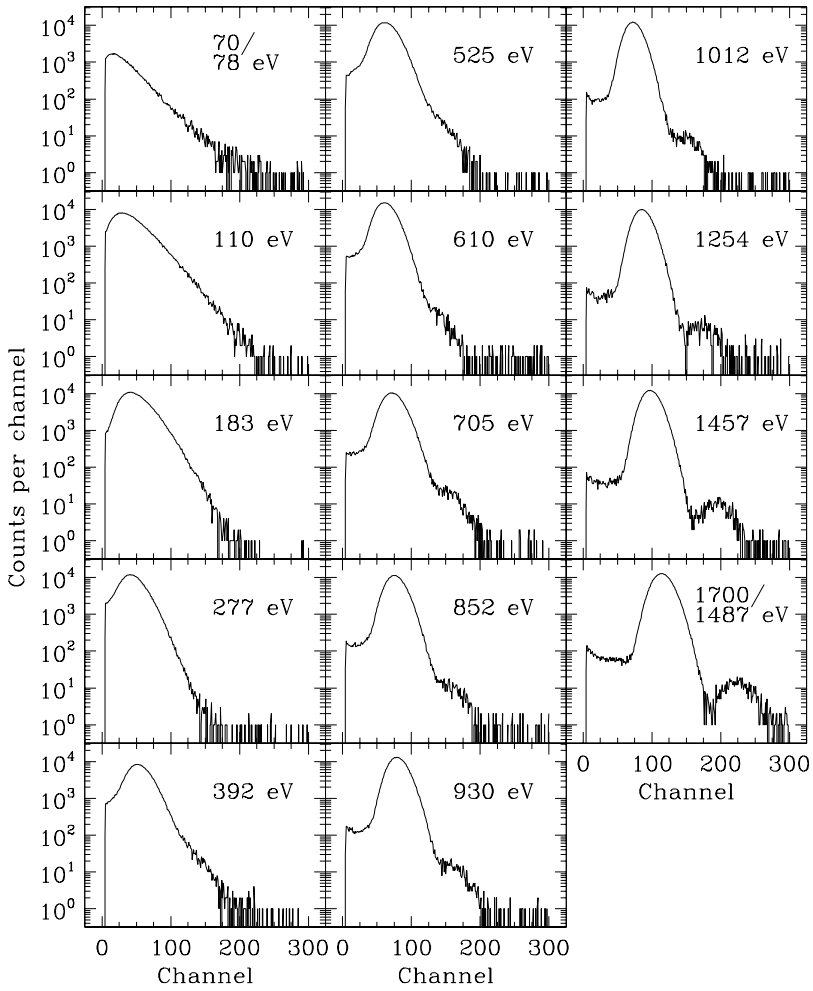

Figure 3.2: Sample spectra from the BESSY SX700 monochromator. Counting rates are generally around 4000 Hz, except for the 70-eV spectrum. Note the increasing contribution of the low-channel shelf at lower x-ray energies (see Chapter 9 for details). At higher energies, pileup and any second order diffraction are easily distinguished from the main peak.

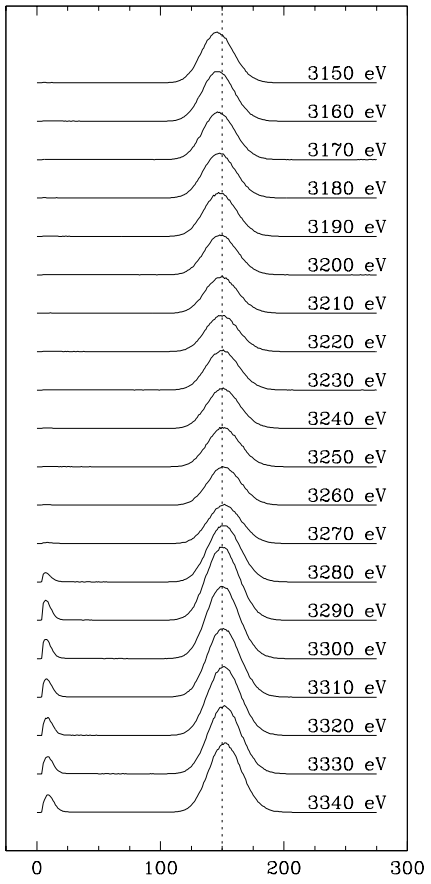

Figure 3.3: Ar-K edge scan with BESSY KMC monochromator. These data were used to measure the FPC gas opacity just below the edge. Listed energies are those requested; the true edge energy (indicated by the appearance of an escape peak and a jump in the strength of the main peak) is 3206 eV, thus calibrating the monochromator energy scale as approximately 75 eV too high. The dotted vertical line is merely to help discern relative peak positions.

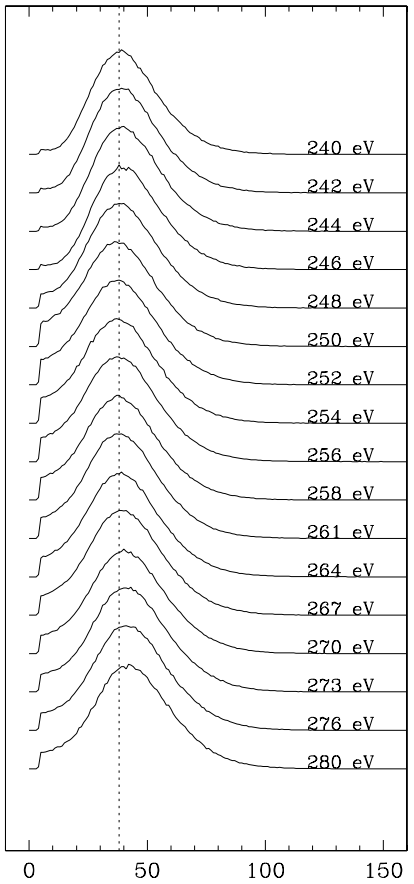

Figure 3.4: Ar-L edge scan with BESSY SX700 monochromator. Nominal L_{III} edge energy is 248.4 eV. Note that the main peak position does a little "backstep" as the beam energy crosses the edges (see the vertical dotted line for reference). This change in the average energy per effective secondary electron is plotted in Figure 3.6, and Figure 3.5 for the Ar-K edge. Charge diffusion losses may also be involved, particularly at the Ar-L edge.

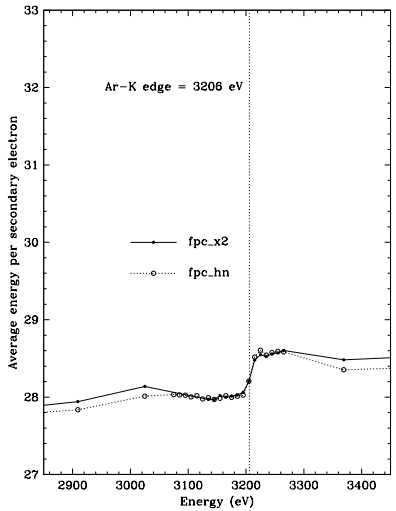

Figure 3.5: Ar-K edge work function, normalized to 28 eV below the edge. A 75-eV correction has been applied to the x-ray energies.

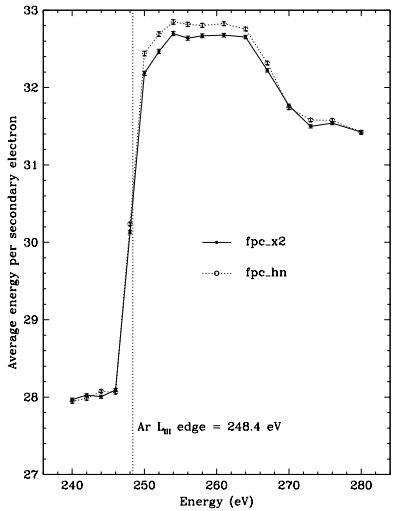

Figure 3.6: Ar-L edge work function, normalized to 28 eV below the edge. Part of the jump may arise from charge losses to the window.

beam spectra (see §3.5.2), when separating the main peak, pileup, and second order diffraction at energies between 124 and 248 eV, or perhaps when fitting C-K EIPS spectra (in which the above-edge and below-edge continua have different energy scales).

In addition to the Ar-K edge scan, about a dozen energies were sampled on the KMC beam, and measurements were often made over a wide range of energies at the same FPC voltage setting to characterize the energy linearity of the detector (although uncertainties in the energy scale of the monochromator have not yet been resolved). At energies above the Ar-K edge, spectra were often collected at several locations on the FPC—around the center, and near the short-side and long-side edges—to see how the fraction of counts in the escape peak varied. From preliminary analysis, the escape fraction appears to be fairly independent of energy (at about 8%) but slightly higher near the walls of the FPC (e.g., 8.1% vs. 7.7% in the center), as one would expect since it is more likely that an Ar-Kα fluorescence photon will escape when it is created near a wall. Characterization of the escape fraction as a function of energy allows one to calculate the contribution of continuum-escape events to the main peak. Although the relative contributions of these events to the focal plane FPC and the BND FPCs will be different (because of the HRMA reflectivity), the net contribution to the line flux is typically only of order 1% (assuming 8% escape from a slice of continuum which has roughly 1/10 the intensity of the main line that lies 3 keV below it). Future versions of `JMKmod` (or post-fit analysis routines) will include this correction.

At energies where the P10 gas is rather transparent, spectra were also collected with the x-ray beam directly above and a few mm to one side of the anode wire. As expected, the rate of events in the main spectrum peak was lower when x-rays hit the anode wire, since no charge amplification

occurred for those events. Such spectra showed a substantial increase in the relative intensity of the shelf below the main peak, and sometimes a weak peak appeared in the low channels, presumably from photons absorbed very close to the wire that did not undergo full electron-avalanche amplification. The small effects of anode wire absorption during AXAF calibration (always less than 1%) are discussed further in §3.5.4.

Typical FPC counting rates on both beamlines were around 4000 Hz, but at several energies, spectra were collected over a wide range of rates (from less than 1000 to more than 25000 Hz) in order to study the rate dependence of the SRF, collect counting rate linearity data, or separate the effects of pileup and higher order diffraction. Sample spectra at multiple rates are shown in Figure 3.7. These data have not yet been studied in detail, but preliminary analysis has reveal no surprises. As expected, peaks become slightly broader at high rates, but the XSPEC width parameter, which must always be allowed to float, simply adjusts to give an appropriate fit.

As mentioned in Chapter 9, small changes in channel offset or amplifier gain for each detector system have no significant effect on the quality of FPC spectral fitting results, but for completeness we note that on 97/02/25 (during phase F) the fpc_hb MCB was changed from serial number 205 to 204 (the former fpc_x2 MCB) because the ADC zero level would pop up to 1.8 volts during collects. This change was made just before runid 112370.

3.4 Gain Nonuniformity and Anode Aging

SRF measurements made at BESSY used a narrow x-ray beam; if gas gain varies across the detector, as it does with the HXDS FPCs, then the net spectrum collected from an FPC which is illuminated over a large area will be a composite SRF. Early tests of the FPCs at SAO showed that gain varies along the long axis of the detector, being fairly flat throughout the middle and rising toward the ends because of electric field end effects; there is no gain variation in the perpendicular direction. Tests with five FPCs showed that the gain curve was virtually identical for all of them, and independent of x-ray energy and FPC voltage (see Figure 3.8).

The impact of this position-dependent gain was reduced by shortening the length of the rectangular BND-H apertures from 5" to 4", to block the regions of highest gain. The remaining nonuniformity is well characterized in `JMKmod` fits by using a delta function plus "top hat" gain distribution curve for the BND-H FPCs, with fit parameters $gain_2 = 1.05 \times gain_1, dgain_2 = 0.1 \times dgain_1$, and $norm_2 = 0.724 \times norm_1$, as described in Chapter 9. (The top hat is not necessary for the focal plane or BND-500 FPCs, or when fpc_hn is used with its circular aperture.) Just to be sure that shortening the blocking plate apertures had no unexpected effects, the gain curve for fpc_hn was checked again at BESSY following AXAF calibration, and found to be unchanged, except that the high-gain ends were indeed excluded.

Another gain phenomenon is anode aging, in which nonconductive polymeric compounds formed during the electron avalanche process are deposited on areas of the FPC anode wire which collect the charge. The rate-dependent effect of such deposits is to reduce the gas gain and degrade energy resolution. Generally speaking, the amount of gunk deposited on the anode is proportional to the cumulative charge per unit area collected on the wire, and the rate of deposition can be reduced by using extremely high-purity gas and scrupulously clean hardware free of silicon and halogen compounds (Kadyk, 1991). Following these prescriptions, great care was taken when assembling the two gas supply systems, in Building 500 and the Instrument Chamber, and unnecessary exposure to x-rays was avoided during AXAF calibration.

The FPC most likely to suffer from anode aging was fpc_x2 because it collected the largest x-ray dose over the smallest area. During AXAF calibration, one aging diagnosis test was successfully

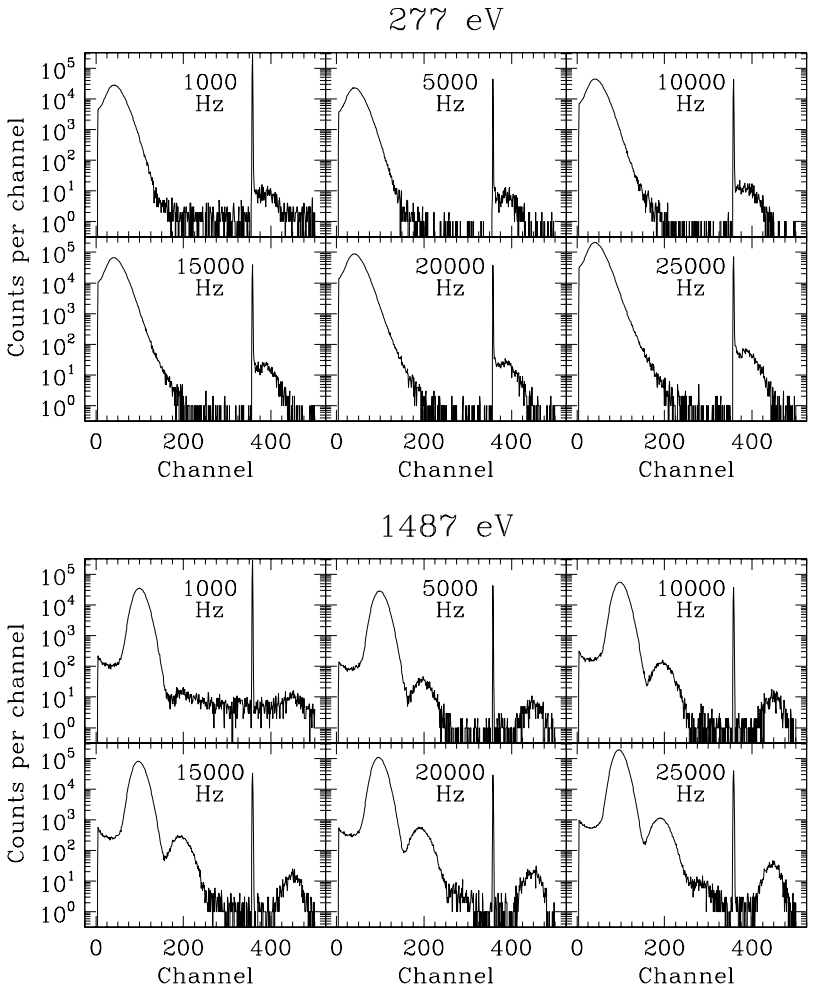

Figure 3.7: Sample spectra over a wide range of counting rate. These data can be used to measure the accuracy of deadtime-correction methods by comparing the detector counting rate with the synchrotron ring current, to study how the spectral response function varies as a function of rate, and to separate the effects of pileup and monochromator higher order contamination (since pileup is rate dependent but the fraction of higher order diffraction is not).

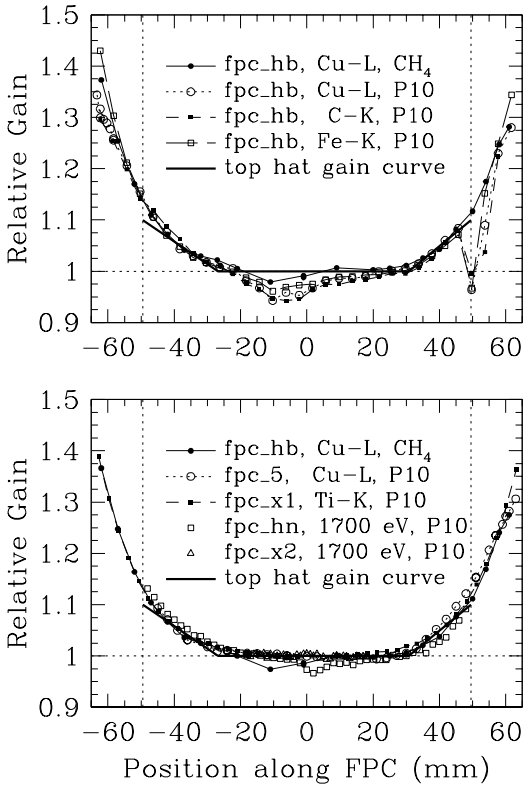

Figure 3.8: Gain scans for (top) a single FPC at several energies and with two kinds of gas, and (bottom) for several different FPCs. Vertical dotted lines mark the edges of the 99-mm blocking plates. In the top plot, the sharp dips in the P10 curves near one end are the result of an anode aging test conducted after the methane gain scan. The slight dips near the center are also from anode aging.

In the bottom plot, the curves for the five FPCs are nearly identical, and their characteristic shape (flat middle plus linearly rising ends) is well represented by the recommended `JMKmod` delta function plus "top hat" gain distribution model with $gain_2 = 1.05 \times gain_1, dgain_2 = 0.1 \times dgain_1$, and $norm_2 = 0.724 \times norm_1$. The fpc_hn curve has a slightly different shape, but the averaged-about-the-center gain curve is the same as for the other FPCs to better than 1%. The curve for fpc_x2, from -18 to +18 mm, is featureless and flat. The slight amount of anode aging seen in fpc_hn and fpc_hb only shows up because they were exposed to small, high-intensity beams; in normal flat-field operation the amount of gain depression, which roughly scales with x-ray intensity per unit length, is completely negligible.

completed (TRW-ID D-IXF-FA-4.013), which showed no detectable degradation in performance. A more thorough check was conducted at BESSY in December 1997, scanning in 1-mm steps along the anode wire to look for gain variations or degraded energy resolution, which confirmed that the gain curve was still perfectly flat. (The BESSY scans of fpc_x2 and fpc_hn are included in Figure 3.8). Surprisingly, a scan of fpc_hn did show a little gain depression near the center, presumably from early testing at SAO using methane, but that only appeared because of the small, high-intensity beam used to do the scan. In normal operation at the XRCF, the degree of gain depression, which roughly scales with x-ray intensity per unit length (see Algieri et al. (1994)), is completely negligible because incident x-rays are spread out over the entire BND aperture.

3.5 Quantum Efficiency

Probably the most important FPC characteristic to calibrate, and the most difficult and complex, is quantum efficiency. A large body of QE calibration data has been collected, both in flat field experiments at XRCF, and in the synchrotron at BESSY. The QE estimates provided here are much better than those provided previously, but may be refined at the percent level in the coming months.

A plot of FPC QE, approximated as the product of window transmission and gas opacity, is shown in Figure 3.9, along with a simple model of SSD QE for comparison. The true quantum efficiency of each FPC, which is defined to include the low-energy shelf and any escape peak, was determined in a variety of ways, depending primarily upon the x-ray energy. In general, absolute QEs for fpc_hn and fpc_x2 are derived using the BESSY SX700 monochromator between 80 and 1700 eV, with the primary sources of error being the calibration of the efficiency of the monochromator and the photodiode used to monitor the storage ring current. Net uncertainty is typically 1-2%, and somewhat worse below 200 eV; see Auerhammer et al. (1998) for details. The transmission of the fpc_x2 window was also measured on the SX700, and gas opacity at 1700 eV at several gas pressures was studied (unsuccessfully). The KMC beamline is not calibrated, but we did obtain some QE information by scanning across the Ar-K edge at 3206 eV.

Above 1700 eV, apart from the BESSY Ar-K edge data, we rely on calibration relative to the SSDs, using the flat field measurements at XRCF in November 1996 and during Phases I and J to provide the relative QE of all FPCs and SSDs (although errors accumulate relatively rapidly given the chain of beam maps and QE comparisons that are required to relate the BND-500 SSD to the BND-H and HXDA FPCs). The SSDs were themselves absolutely calibrated at high energies at BESSY using the white light beam and calibrated filters, and since their QE is nearly 100% above 1700 eV, the uncertainty in their QEs should be relatively small. (Note, however, that as of this writing the analysis of SSD calibration data is incomplete.) White light calibrations were also conducted for fpc_hn and fpc_x2, but the combination of broadband radiation, poor energy resolution, energy scale nonlinearities, and other factors greatly complicates analysis, so results are considered to be significantly less reliable than those obtained from comparisons with the SSDs. It should be possible, however, to extract reliable measurements of gas opacity (see §3.5.1) just below the Ar-K edge at 3206 eV from the Fe- and Cr-filtered spectra. Preliminary results from the white beam calibration and other BESSY measurements have been published by our PTB collaborators in Auerhammer et al. (1998).

As will be explained in more detail in §3.5.1:"Window Bowing and Nonuniformity" and §3.5.4, "Relating Flat Field, HRMA, and BESSY measurements", in order to apply QE calibration results to analysis of AXAF calibration data, one must take into account in how an FPC was used as it was being calibrated and how it was used for calibrating AXAF, since differences in gas temperature

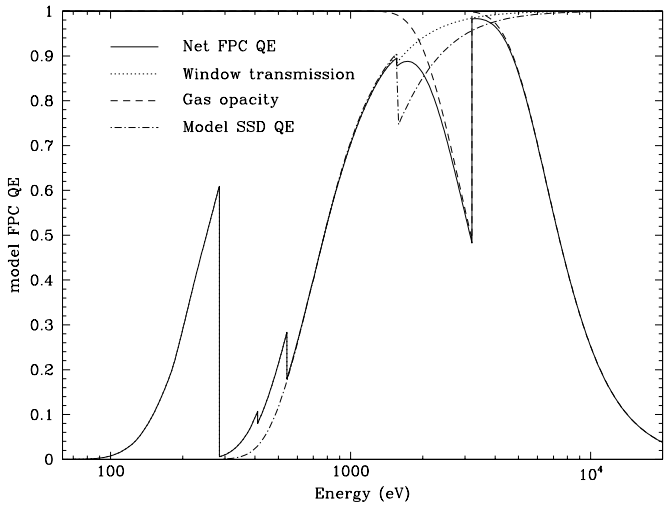

Figure 3.9: Model FPC QE. Net QE is the product of window transmission and gas opacity, assuming: 1.0 μm polyimide ($C_{22}H_{10}O_4N_2$) with a density of 1.3 g/cm^3, plus 200 Å of Al with a density of 2.6941 g/cm^3; 90.01% Ar plus 9.99% CH_4 at 400 torr and 10 °C, with an average gas depth of 55.93 mm. SSD QE was modelled as the transmission of 1.25 μm parylene (C_8H_8, density 1.10 g/cm^3) plus 2000 Å of Al. The 1995 Henke tables were used.

and the size and angle of incidence of the x-ray beam can lead to differences in effective QE of up to several percent, although the typical variation is much less. Table 3.4 summarizes the differences among the various test situations; keep them in mind while reading the rest of this section on Quantum Efficiency.

3.5.1 Monochromator Results

Absolute QEs from SX700

Between 80 and 1700 eV, the BESSY SX700 monochromator provides a well calibrated beam intensity with a beam size of approximately 600 by 300 μm FWHM, which neatly fits within the "sweet spot" of the central 2mm by 2mm windowlet. By monitoring the BESSY ring current, applying the monochromator efficiency calibration, and making deadtime and pileup corrections to the FPC spectra, the QEs of fpc_hn and fpc_x2 were measured from 80 to 1700 eV at over 70 energies, with fine-step scans across the Ar-L and C-, N-, O-, and Al-K edges. At the lower energies, the contributions of higher-order diffraction peaks and pileup (which are generally no more than a few percent) were removed by fitting a second peak fixed at twice the energy of the main peak. Net uncertainties are usually of order 1%, although worse at very low energies. As previously noted, these data were also analyzed to characterize the FPC spectral response functions, using the JMKmod fitting procedure with a single delta-function line, as described in §9.5.

We present in Figure 3.10 plots of the absolute quantum efficiency of the fpc_hn and fpc_x2 detectors over the range from 0.08 to 1.7 keV, when exposed to small beams in their central

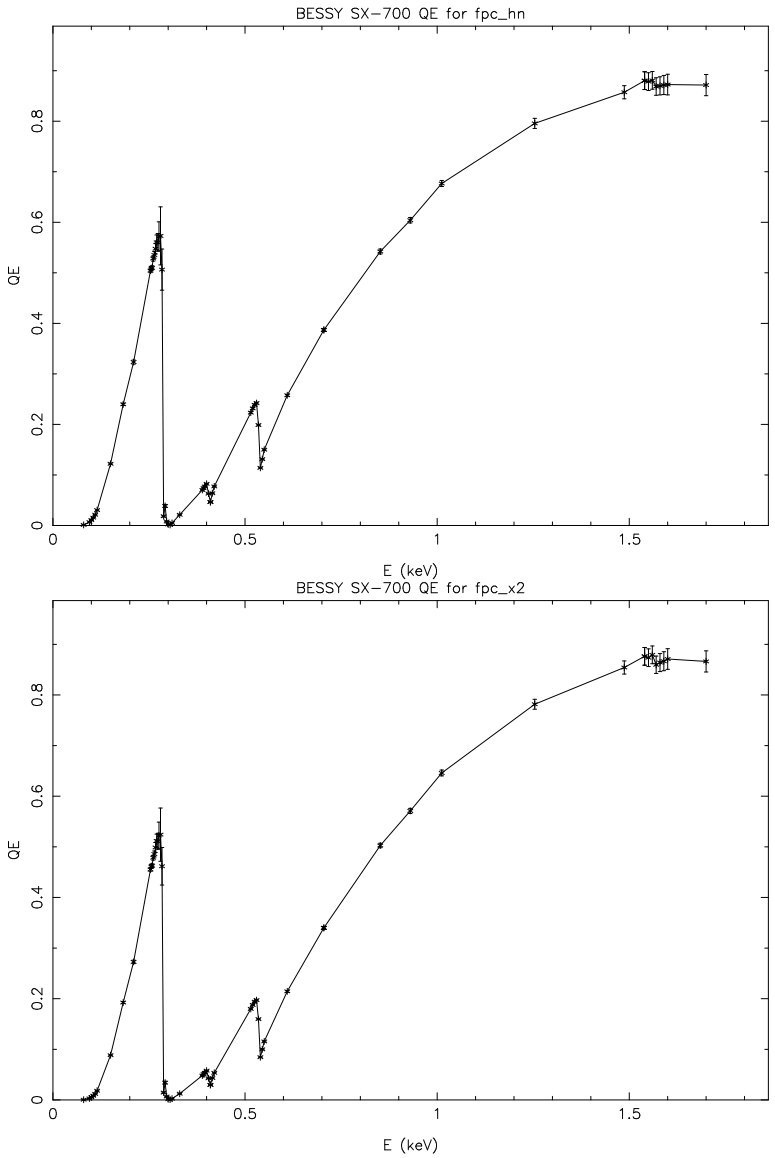

Figure 3.10: Absolute quantum efficiency for fpc_hn (top) and fpc_x2 from JMKmod fits to BESSY SX700 monochromator data

Test format	X-ray angle	Beam size	Approx. gas temp.
BESSY	normal incidence	smaller than windowlet	30°C (fpc_x2, fpc_hn)
Flat Field	normal incidence	blocking plate apertures for BND-H and fpc_x2, regular 4, 12, 36-mm aps for fpc_5	20°C for BNDs 30°C for fpc_x2
HRMA	normal for BNDs, up to ∼ 4° for fpc_x2	focussed beam, concentrated in rings on central windowlet; for off-axis or grating measurements, image may extend across more than one windowlet.	10°C for BND-H 20°C for fpc_5, fpc_x2

Table 3.4: Differences among test environments.

windowlets. Note that the error bars are relatively large near the C K edge (0.284 keV), due to SX700 facility effects (*e.g.* carbon contamination). Although two sets of measurements were made at 0.705 keV, only the results from one are shown; the second set is 4.5% higher for each FPC. Perhaps, although we hope and believe not, this indicates the irreducible error level of these measurements.

As another accuracy assessment, we divided the QE of fpc_x2 by that of fpc_hn to form a relative QE (RQE) for fpc_x2, as we did for the XRCF flat field experiments described later in §3.5.3. We plot in Figure 3.11 both of these curves, and the ratio of these two determinations. Although no adjustments have been made for window transmission nonuniformities (which will affect comparisons of BESSY vs. XRCF flat-field QEs at the ∼1% level), agreement is generally quite good, although it appears that there may be a systematic discrepancy in results derived from the two test locations.

Window Transmission

In addition to measuring the QE of assembled FPCs, we also measured the transmission of the central windowlets of the windows from fpc_x2 and fpc_5, along with a sample of unstretched (i.e., never mounted on an FPC or pressurized to 400 torr) window material. These in/out measurements were made at approximately 380 energies between 40 and 1700 eV, with 1-eV steps across absorption edges, using a calibrated photodiode. As one would expect, the transmission of the unstretched window was lower than that for either of the stretched windows, since the act of pressurizing windows permanently deforms them, although there is, of course, some relaxation between the pressurized and unpressurized states. Transmission curves are shown in Figure 3.12. The nominal uncertainty of these measurements is typically 2% (PTB has provided more detailed estimates of uncertainties as a function of energy), but at energies where transmission is substantially less than 10% the uncertainty may be quite a bit larger—see, for example, the wiggles around 110 and 350 eV.

One would expect that since window transmission is given by $\exp(-\mu\rho t)$, the ratio of the logarithms of two windows' transmissions should be equal to the ratio of their thicknesses (assuming that the composition and density of the two windows are the same), and indeed, we find that an energy-independent ratio of $t_{x2}/t_{unstretched} = 0.93$ fits the data very well. Similarly, if the net FPC QE is simply the product of window transmission and gas opacity, then window transmission and net QE should be the same below ∼1700 eV, since gas opacity is nearly 100%.

In Figure 3.13 we plot such a comparison for fpc_x2, and find that the QE is systematically lower than the window transmission. In the lower figure, we plot the shelf norm *vs.* the ratio of the

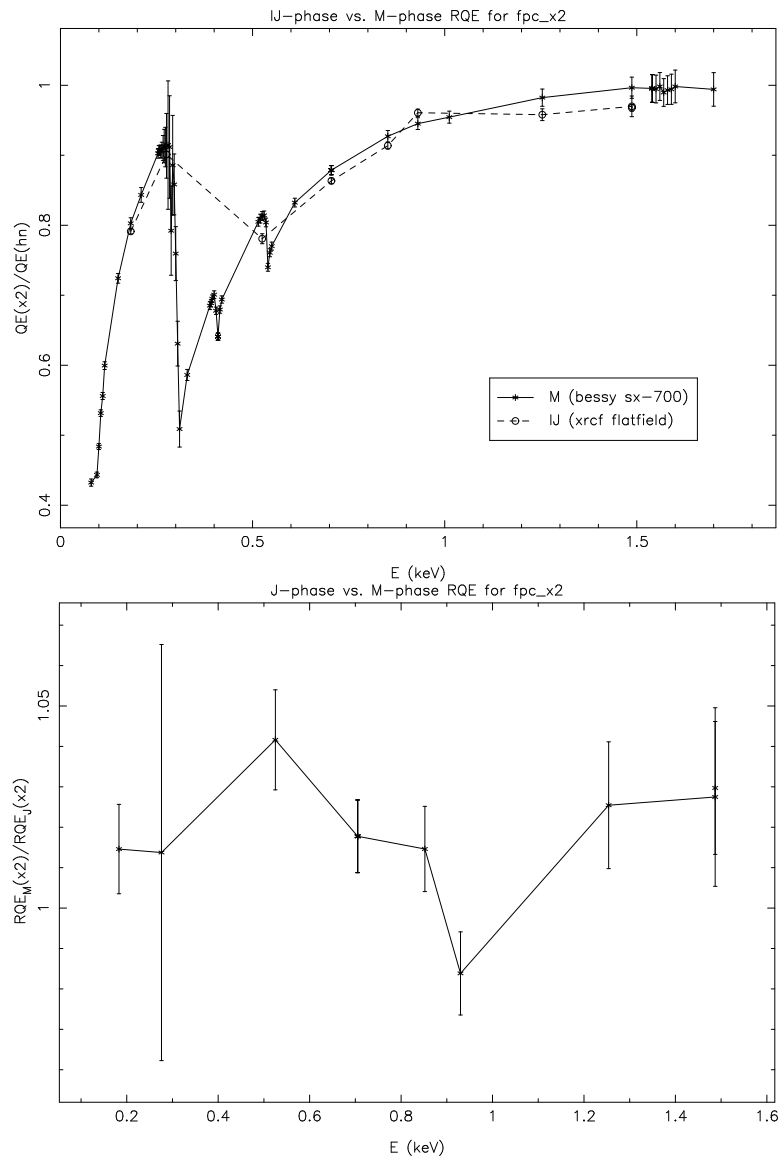

Figure 3.11: Relative quantum efficiency for fpc_x2 from BESSY (phase M) and XRCF (phases I & J) flat field measurements (top) and ratio (bottom)

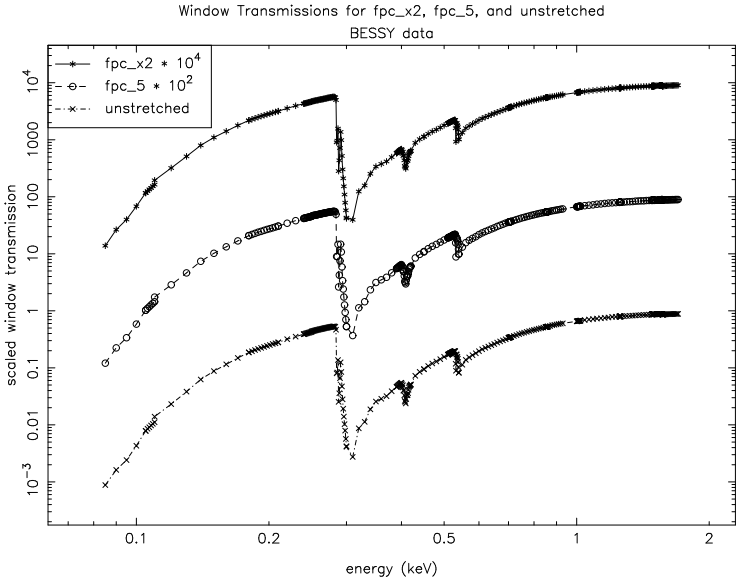

Figure 3.12: Transmission of 3 FPC windows as measured at BESSY. The windows are those of the fpc_x2, fpc_5, and an unstretched window. The first two curves are scaled for clarity.

detector QE to the window transmission. Except for spikes which may arise from fitting effects near the nitrogen and oxygen edges, the two quantities trend together. This suggests that the QE deficit may be an effect of charge loss to the window, which is also measured by the shelf normalization; we are consulting with outside experts regarding this idea.

Another possibility is that the window measurement was made in a different, lower-transmission windowlet than for the assembled-detector QE measurement; the windows barely fit inside the reflectometer chamber used for the measurements, and there were only a few mm of travel for alignment. Analysis of fpc_x2 window uniformity data will shed light on this matter.

Window Bowing and Uniformity Mapping

When applying any BESSY calibration data it is important to remember that analysis of HRMA calibration data requires that we know the QE of fpc_hn when exposed over its entire window, not just the center of the central windowlet, as with the BESSY measurements. We therefore measured the relative QE of fpc_hn (and fpc_x2) at the center of many windowlets in order to characterize large-scale window uniformity (see Figure 3.14). Strictly speaking, such a comparison is not necessary for fpc_x2 since we are ultimately interested in knowing its QE when exposed to x-rays focussed on the central windowlet, i.e., as used for HMRA calibration. Relating fpc_x2 QEs in BESSY and flat field tests, however, does provide a check on results for other FPCs that are derived from flat field comparisons with fpc_hn.

When applying BESSY calibration results to XRCF measurements, it is also necessary to con-

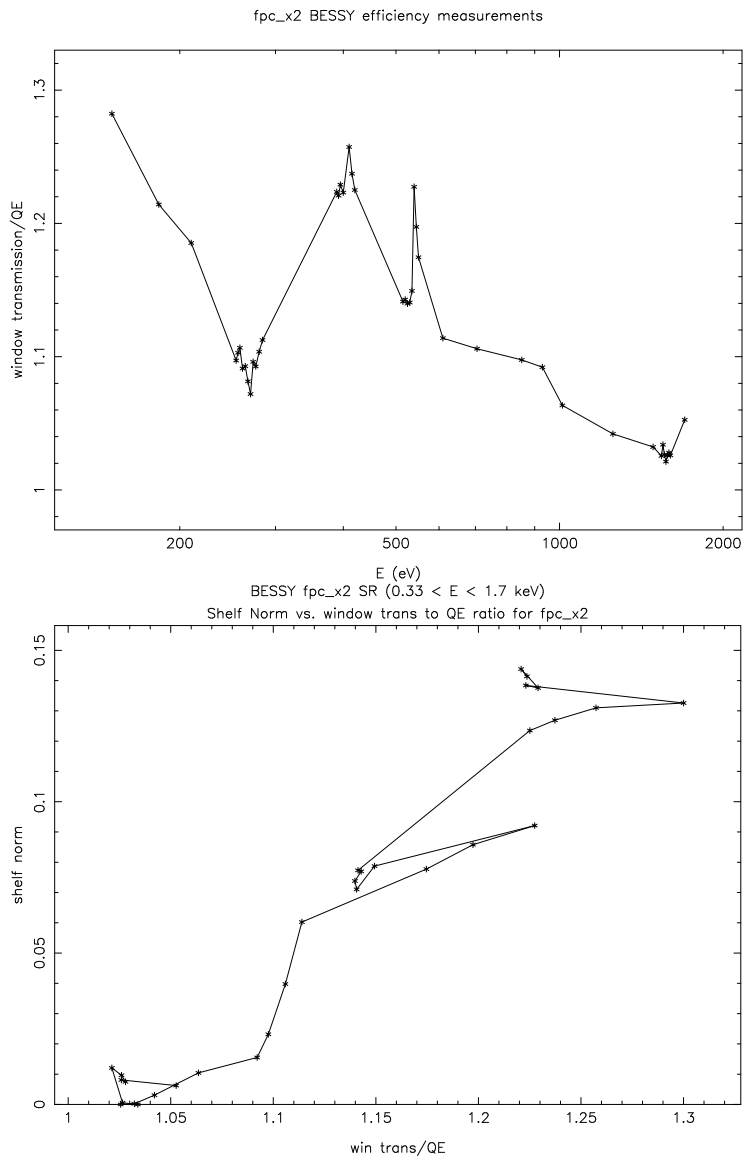

Figure 3.13: Ratio of fpc_x2 window transmission to QE *vs.* energy (top) and *vs.* shelf norm (bottom). This suggests the QE deficit may be due to charge loss to the window.

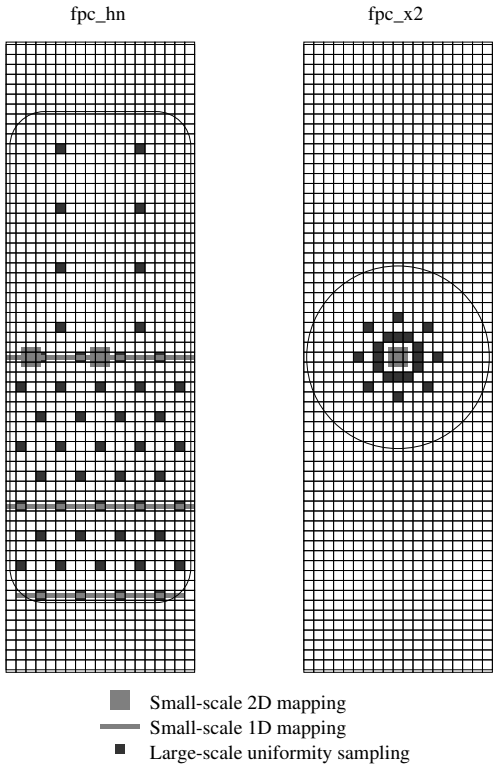

Figure 3.14: QE mapping of fpc_hn and fpc_x2. Drawings show full window assembly (1.5" by 5.0" with 2-mm wire spacing), with blocking plate apertures for fpc_hn and fpc_x2. Small-scale scans used five points per windowlet, in 350-μm steps. Most QE mapping was conducted at 330 eV; some scans were repeated at 500 and 930 eV. Mapping pattern for the two-dimensional small-scale scans is shown in Figure 3.16. SRF/absolute QE measurements were made in the center windowlets (or 2 mm to the side when using the higher-energy KMC beam, so that penetrating x-rays would not hit the anode wire running down the middle).

sider the effects of window bowing. In addition to a global deflection of the support wires of about 1.25 mm, the center of each 2-mm by 2-mm windowlet extends about 0.25 mm beyond its surrounding support wires (Goddard (1994)—see Figure 3.15), and the window surface is angled at approximately 15 °next to the wires (Cohen (1995)). The net QE of fpc_hn will therefore be lower at the XRCF than at BESSY because the average path length through the window for normally incident x-rays is longer. The effective thickness also depends on the angle of x-ray incidence, which can be several degrees from perpendicular for fpc_x2 at the XRCF. There are also true thickness variations in the polyimide caused by stretching between the wires.

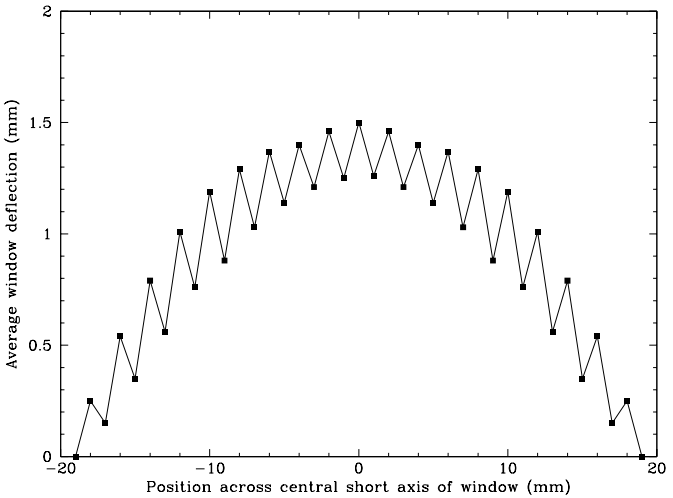

Figure 3.15: Measured deflection of the polyimide/Al window material across the central short axis. The average is shown from three windows, all measured at the standard operating pressure of 400 torr. Deflections were measured in the center of each windowlet and underneath the support wires. Variation between the two most different windows was typically 0.30 mm.

At low energies where window transmission is small, these differences in effective thickness can produce relatively large differences in QE. As an example, at O-K (525 eV) window transmission is approximately 0.250 at normal incidence, but only $(0.250)^{\sec 15^\circ} = 0.238$ at 15 °(near a support wire), a relative difference of 5%. At 95 eV, where window transmission is roughly 0.0040, the relative change is nearly 20%. Determining the effective QE of an FPC, particularly for grating measurements of intrinsically broad lines (which have the added complication of spanning a range of energies with a corresponding range of window transmissions), can therefore be a complicated enterprise.

To characterize the effects of bowing within a windowlet, we conducted fine-scale scans with the smallest possible beam (600 × 250 μm FWZI, as determined from beam profile scans across the edges of the fpc_x2 blocking plate aperture) around the central windowlets of fpc_hn and fpc_x2, and along three lines across the short axis of fpc_hn. The layout of these mapping measurements is shown in Figure 3.14 and Figure 3.16.

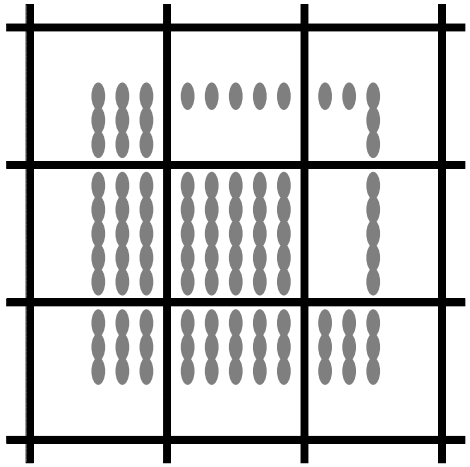

Figure 3.16: Small-scale 2D QE mapping. Data from these scans (conducted at the three window locations shown in Figure 3.14) will be used to characterize windowlet bowing and how it changes the effective QE of an FPC depending on the x-ray illumination pattern. Dark lines are the 100-μm-diameter support wires, 2 mm apart. The x-ray beam was approximately 600 μm × 250 μm full width at zero intensity, and FWHM was less than 300 μm × 200 μm. The beam size shown is 400 μm × 200 μm, with the short axis of the window lying horizontally.

Most of the large- and small-scale scans were conducted at 330 eV, but a few were made at 500 and 930 eV as double-checks. 330 eV was chosen because window transmission is very low there (about 2% for fpc_hn and 1% for fpc_x2), and so differences in window thickness will lead to relatively large differences in transmission, but the energy is still high enough to produce a well defined peak in the spectrum. An energy just above the C-K edge (at 284 eV) would have been better from that standpoint, but scattering from carbon contamination on the monochromator optics would introduce an unresolvable 277-eV component into the spectra.

Although these data have not yet been analyzed, plots of ROI-summed rates versus position are shown for the central short-axis scan of fpc_hn in Figure 3.17. Rates have not been corrected for beam decay, and each curve has been rescaled for plotting purposes, but it is clear that there can be significant variations in window thickness on fairly small scales; the roughly 25% peak-to-peak jump seen in the 330-eV center scan corresponds to approximately a 6% difference in window thickness. Rates for the 500-eV scan confirm that there is thickness nonuniformity, although the manifestation is much less pronounced because the window transmission at 500 eV is so much higher (20% vs 2%). The effect of bowing within each windowlet can also be seen in both sets of data.

Gas Opacity

At 1700 eV, the high end of the SX700 monochromator's energy range, we attempted to measure the opacity of the P10 gas in fpc_hn and fpc_x2 by comparing the detector counting rates at gas pressures of 400, 300, 200, and 100 torr. From those relative rates, and by estimating the small

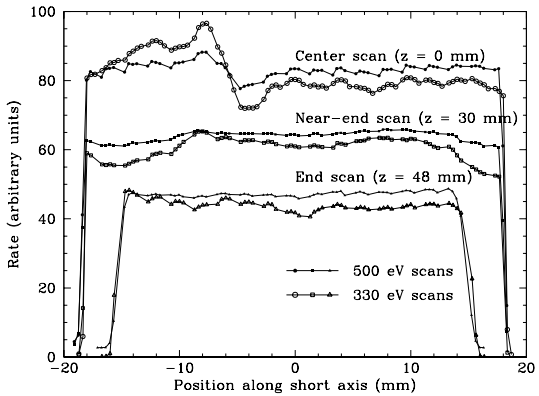

Figure 3.17: 1D QE mapping scans of fpc_hn. Rates are arbitrary and have been scaled to facilitate comparison of 330 and 500 eV results. Rates have not been corrected for beam decay, which is approximately 7% for the 330-eV data from left to right; beam decay is much less for the 500-eV scans. Note the sharp nonuniformity in the center scan and the reproducibility of results at different energies, after taking into account that variations in window transmission at 500 eV will be much smaller than at 330 eV.

opacity of the methane component (which composes 10% of the P10 partial pressure) and assuming that the Henke absorption coefficients are correct at all energies apart from a small scaling factor, the product of the gas depth and argon absorption coefficient at 1700 eV could be determined. From this, we could derive a scaling factor to use in our model of gas opacity, and then perhaps apply it at higher energies where we cannot directly obtain absolute QE calibration.

Unfortunately, the x-ray beam was centered on the central windowlet of the two FPCs, and as the gas pressure was reduced some of the x-rays penetrated the gas and hit the anode wire running down the middle of the FPC, producing a stronger shelf feature. Although this was a few-percent effect, it was enough to preclude the extraction of useful information from the measurement. (In future runs on the higher energy KMC beam, spectra were collected with the x-ray beam offset by 2 mm, so that anode wire absorption was not a problem.)

Despite the lack of beamline intensity calibration for the KMC monochromator, we were able to measure QE at a higher energy by scanning across the Ar-K absorption edge and recording the relative counting rates just below and above the edge. Because there is no intensity monitor on the KMC beamline, and intensity can vary with time because of thermal instabilities, we tried to let the beam stabilize so that relative rate comparisons would be valid. Analysis of data from the first energy scan, with fpc_hn, indicates that the beam was still unstable at the $\leq$10% level. The second scan, with fpc_x2, is believed to be valid at the one or two percent level based upon the amount of scatter in the counting rates at similar energies, but we have no way of knowing for sure. The fpc_x2 scan covered the range 3135 to 3265 eV (after applying a 75-eV energy correction) in 10-eV steps, as shown in Figure 3.18.

Taking the average of the 6 points between 3135 and 3185 eV (sample standard deviation 4.3% divided by $\sqrt{5} = \pm 1.9\%$) and the 5 points between 3225 and 3265 eV ($2.5\%/\sqrt{4} = \pm 1.2\%$), and adjusting for ring current decay (approximately 0.5% per minute) and the theoretical energy

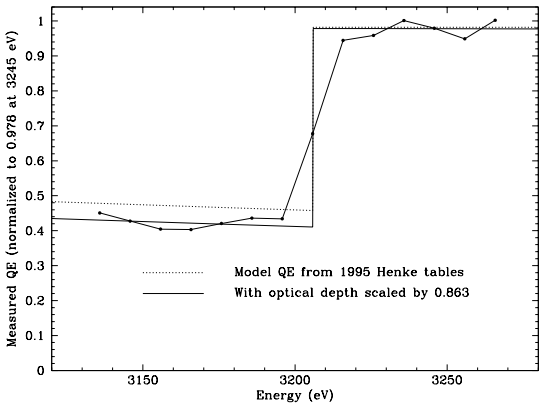

Figure 3.18: fpc_x2 QE at Ar-K edge. Relative QEs at 33.994 °C below and above the edge were derived from measured rates, after correcting for monochromator efficiency and beam decay. Assuming window transmission is 0.985, net QE at 10 °C is 0.9804 at 3245 eV and 0.4500 ± 0.0010 at 3160 eV.

dependence of the monochromator's output spectrum with silicon crystals (about a 9% difference between 3160 and 3245 eV) the QE as measured at 33.994 °C at 3160 eV is 0.4333 ± 0.0010 times that at 3245 eV.

If we then assume that net QE is equal to window transmission (which our model predicts is 0.985 at both energies) times gas opacity, without any other effects such as charge diffusion losses, and if we further assume that our theoretical models of window transmission and gas opacity are close to reality, apart from absorption coefficient scaling factors, we can determine the QE at both energies. We thus derive gas optical depths of 4.950 at 3245 eV and 0.5627 at 3160 eV, which are equal to 0.863 ± 0.026 times the values computed in our theoretical model, which assumes a net gas depth (with window deflection of 1.08 mm) of 56.10 mm, with 90.01% Ar and 9.99% methane, at 400 torr, using the 1995 Henke tables. The derived optical depth scaling factor is close to that derived from flat field normalization relative to the SSDs (see §3.5.3), but all the SSD-dervied results should be considered as somewhat preliminary at this time.

After adjusting for gas temperature, we finally obtain QEs at 10 °C of 0.9804 at 3245 eV and 0.4500 ± 0.0010 at 3160 eV. Note that the quoted uncertainty is purely statistical, and does not include systematic uncertainties in the values of KMC efficiency, beam intensity stability, or model FPC QE (such as from charge diffusion losses above the Ar-K edge). Any or all of these uncertainties, particularly the KMC efficiency, could reasonably be a few percent.

3.5.2 Absolute Broad Band

As with the SSDs (see Chapter 4), broadband QE was measured for fpc_hn and fpc_x2 on the BESSY white beam, which provides a pure synchrotron spectrum whose exact shape and intensity can be calculated from first principles based on precise knowledge of the ring energy, magnetic field, and the distance to and solid angle subtended by the detector aperture. In order to sample the detector QE over different energy regions, spectra were also collected with various thin filters—2.0-μm Be, 0.6-μm Fe, 1.5-μm Ti, and 2.0-μm Cr—placed into the beam (see Figure 3.19). The

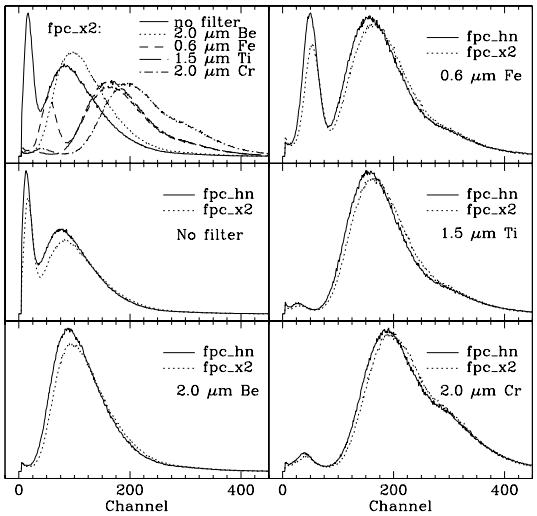

Figure 3.19: White beam spectra. Vertical scale is arbitrary, but the same for each curve within a given panel. Various filters were chosen to calibrate the absolute QE of the FPCs in different energy ranges. As already seen in the SX700 data, fpc_hn has higher QE than fpc_x2 at all energies. The difference in window thicknesses is, of course, most apparent at low energies, as seen in the spectra with the null and 0.6-μm Fe filters. Note that gains may be slightly different when comparing fpc_x2 and fpc_hn.

transmission of the Be, Fe, and Cr filters was measured at many energies up to 1900 eV during in/out tests with the PTB photodiode on the SX700 beamline, although the Be filter which was calibrated was not the same as the one used for the white beam QE measurements; the original broke after being calibrated, so a spare filter cut from the same foil was used on the white beam. Time constraints did not permit calibration of the Ti filter.

The transmission of each of these filters was measured during in/out tests with the PTB photodiode on the SX700 beamline, except that the Be filter which was calibrated was not the same as the one used for white beam testing; the original filter broke after being calibrated, so a spare filter cut from the same foil was used on the white beam. Also, time constraints did not permit calibration of the Ti filter.

A 1.5-mm aperture was fixed in front of a windowlet 2 mm off the center, so that anode absorption effects would not be present. Unfortunately, the alignment of the detector and beamline had to be adjusted while under vacuum in such a way that the entire detector chamber was slightly askew, with the result that the aperture was centered about 0.6 mm off-center from the 2-mm-square windowlet for both FPCs (as determined from x-ray scans). This makes data analysis more complicated, since the effects of wire blockage and window bowing must be considered. Because of these difficulties, the uncertainties in filter transmission calibration and the energy scale and linearity, and the general problem of interpreting a broadband spectrum with poor energy resolution, we have not yet analyzed the white beam data. A casual inspection, however, shows that the QE of fpc_hn is higher than that of fpc_x2 at all energies (as already determined from SX700 and flat

field measurements), and that the difference is more pronounced at low energies (see the Fe-filtered spectrum and compare the low and higher energy peaks). Despite the analysis problems mentioned above, it is likely that the Fe- and Cr-filtered spectra can be used to infer a fairly accurate optical depth for the P10 gas just above the Ar-K edge.

3.5.3 Relative QEs from Flat Field Calibration

During April and June of 1997, a series of flat field experiments were conducted at XRCF, after shipment of the HRMA to TRW. The first set, phase I, were conducted with the flight ACIS camera at the focal plane, the BND equipment in its usual places, with the exception that the fpc_x2 detector from phase 1 was put in place of the fpc_hs. The second set of tests, phase J, were conducted with all HXDS equipment in place, but with certain detectors swapped. The detector locations for the various phases are summarized in Table A.1.

During phase J, numerous experiments were done with the Electron Impact Point Source (EIPS) tuned to many of the energies used during the HRMA calibration. These runs were long enough to collect high signal-to-noise pulse-height spectra in each detector and thus allow a high precision cross-calibration of the various detectors. For most of the detectors, the combination of relative quantum efficiencies measured in phase J with absolute QEs from those few which were measured at BESSY, will be the only available absolute quantum efficiency numbers. Since there was no calibration of FPC QE above 1.7 keV at BESSY except for the indirect measurement at the Ar-K edge, the flat field data comparison between the FPC and SSD detectors at these higher energies is crucial for the understanding of this important quantity.

We present in Table 3.5 the results of these experiments.

Data for these tests were reduced as in §9.4, using double-`JMKmod` models in XSPEC. This accounts for the nonuniformity of the gain in the open fpc_h detectors. Single `JMKmod` models were used for the fpc_x2, since the smaller open area presents a nearly uniform gain to the incoming x-ray beam. Backgrounds were extracted from temporally nearby tests conducted during x-ray source system downtimes, modeled usually as a broad Gaussian plus a falling powerlaw, and then included in the fits with no free parameters. The C-statistic was used.

Using the distances listed in Table A.3, and aperture sizes listed in Table A.2, we then constructed fluxes for each detector, extrapolated to the source distance of the HRMA entrance. Beam uniformity factors were created for each iteration, (§12.4) and the position of the mapping detector with respect to the other detectors was noted. Selecting an iteration in which the mapping detector was in its home position, we then constructed relative quantum efficiencies, as discussed in §12.5.

We have then applied temperature corrections, to make the relative QE values in the table those appropriate to 10°C. This procedure is outlined in §3.5.4.

The two classes of experiments produce two different types of results. The BND-H beam uniformity maps allow us to compute the ratio of the QE of each of the fpc_h detectors and the fpc_x2 to one detector in this set, and fpc_hn was chosen to be that fiduciary detector. The Phase I tests, since the fpc_hs was not involved in the experiment, do not produce relative QE numbers for this detector.

The other type of experiment, BND-500 beam uniformity maps, allows computation of the relative QE of three detectors: the ones in the ssd_5, fpc_5 positions, and, when the gate valve was open exposing the BND-H detectors, the fpc_hb. Note that in phase J, these detectors were those otherwise known as ssd_x, fpc_x1, and fpc_hb. We have therefore computed the ratio of the QE of each of these detectors to that of the fpc_5 detector for that phase (*i.e.* fpc_5 for phase I and fpc_x1 for phase J). These data are presented in Tables 3.6 – 3.8.

E (keV)	Line	fpc_hs/fpc_hn		fpc_ht/fpc_hn		fpc_hb/fpc_hn		fpc_x2/fpc_hn	
0.183	B−Kα	0.94217	± 0.00321	0.80596	± 0.00279	0.84037	± 0.00291	0.79127	± 0.00365
0.277	C−Kα	0.95889	± 0.00210	0.92793	± 0.00203	0.92887	± 0.00254	0.90116	± 0.00420
0.277	C−Kα	0.95889	± 0.00210	0.92793	± 0.00203	0.92887	± 0.00254	0.90116	± 0.00420
0.524	O−Kα	...	± ...	0.76078	± 0.00255	0.86475	± 0.00290	0.78077	± 0.00705
0.705	Fe−Lα	0.97460	± 0.00307	0.84695	± 0.00241	0.88800	± 0.00252	0.86342	± 0.00404
0.852	Ni−Lα	0.98044	± 0.00293	0.89929	± 0.00270	0.93605	± 0.00281	0.91379	± 0.00485
0.929	Cu−Lα	0.98995	± 0.01601	0.94042	± 0.00241	0.96131	± 0.00247	0.96080	± 0.00525
1.254	Mg−Kα	0.99443	± 0.00978	0.98062	± 0.00950	0.98062	± 0.00952	0.95801	± 0.00843
1.486	Al−Kα	...	± ...	0.98271	± 0.01438	0.98350	± 0.01436	0.97405	± 0.01474
1.486	Al−Kα	0.99326	± 0.00396	0.98358	± 0.00380	0.98488	± 0.00378	0.96829	± 0.00476
1.739	Si−Kα	...	± ...	0.92961	± 0.00620	0.93868	± 0.00665	1.02899	± 0.00882
2.166	Nb−Lα	0.98655	± 0.00491	0.99937	± 0.00477	0.98863	± 0.00473	0.99318	± 0.00596
2.980	Ag−Lα	0.98689	± 0.00677	1.00136	± 0.00634	0.99062	± 0.00629	0.97519	± 0.00715
3.444	Sn−Lα	0.99592	± 0.00640	0.99713	± 0.00585	1.00344	± 0.00588	0.96486	± 0.00669
4.510	Ti−Kα	...	± ...	1.00306	± 0.00784	1.00241	± 0.00783	1.04596	± 0.00994
4.510	Ti−Kα	0.96891	± 0.00468	1.00925	± 0.00461	0.98500	± 0.00455	0.94846	± 0.00572
5.410	Cr−Kα	0.94797	± 0.00467	0.97872	± 0.00462	0.96246	± 0.00453	0.89659	± 0.00545
6.400	Fe−Kα	...	± ...	0.94574	± 0.04193	0.95654	± 0.04243	1.25165	± 0.04361
6.400	Fe−Kα	0.97052	± 0.00563	1.00101	± 0.00553	0.97457	± 0.00540	0.94306	± 0.00852
8.029	Cu−Kα	...	± ...	1.04459	± 0.03147	1.05810	± 0.03188	1.62196	± 0.03159
8.620	Zn−Kα	0.88706	± 0.00319	0.89029	± 0.00588	0.88850	± 0.00319	0.94848	± 0.00630

Table 3.5: Relative Quantum Efficiencies ($QE_{det}/QE_{\mathsf{fpc\_hn}}$) for the FPC detectors from Phases I & J XRCF flat field testing, corrected to 10° C

E (keV)	Line	fpc_hb/fpc_5		ssd_5/fpc_5	
0.524	O−Kα	1.46295	± 0.09260	...	± ...
1.486	Al−Kα	...	± ...	0.83396	± 0.00956
1.739	Si−Kα	1.01822	± 0.00582	0.92861	± 0.00473
2.166	Nb−Lα	...	± ...	0.97837	± 0.00652
4.510	Ti−Kα	...	± ...	0.99148	± 0.01325
6.400	Fe−Kα	...	± ...	1.65221	± 0.00772
8.029	Cu−Kα	...	± ...	2.46718	± 0.23668

Table 3.6: Relative Quantum Efficiencies ($QE_{det}/QE_{\mathsf{fpc\_5}}$) for the FPC detectors from Phase I XRCF flat field testing, corrected to 10° C

E (keV)	Line	fpc_hb/fpc_x1		ssd_x/fpc_x1	
0.852	Ni−Lα	...	± ...	0.28041	± 0.01517
1.254	Mg−Kα	0.99237	± 0.00830	0.72842	± 0.00342
1.486	Al−Kα	1.00035	± 0.00344	0.74572	± 0.00336
2.166	Nb−Lα	1.02267	± 0.00399	0.90712	± 0.00428
2.980	Ag−Lα	1.04323	± 0.00548	1.38284	± 0.00656
3.444	Sn−Lα	0.99431	± 0.00590	0.88771	± 0.00498
4.510	Ti−Kα	1.05040	± 0.00404	1.11598	± 0.00493
5.410	Cr−Kα	1.02044	± 0.00437	1.27460	± 0.00573
6.400	Fe−Kα	1.03022	± 0.00495	1.50606	± 0.00738
8.620	Zn−Kα	1.03440	± 0.00423	2.98828	± 0.01148

Table 3.7: Relative Quantum Efficiencies ($QE_{det}/QE_{\mathsf{fpc\_x1}}$) for the FPC detectors from Phase J XRCF flat field testing, corrected to 10° C

E (keV)	fpc_5/fpc_hn	
0.183	0.96346	± 0.01125
0.276	0.98315	± 0.01000
0.705	0.91775	± 0.03536
1.254	1.00441	± 0.01479
1.487	1.01667	± 0.00930
1.487	1.01290	± 0.00929
2.290	1.01626	± 0.01283
2.980	1.04801	± 0.01443
4.510	1.03286	± 0.00767
6.400	0.99712	± 0.01351
8.030	1.04397	± 0.01486

Table 3.8: Relative Quantum Efficiencies ($QE_{\mathsf{fpc\_5}}/QE_{\mathsf{fpc\_hn}}$) for the FPC detectors from Beam Uniformity tests in Phases D and E XRCF testing, corrected to 10° C

3.5.4 Relating Flat Field, HRMA, and BESSY measurements

As noted in the introduction to the section on Quantum Efficiency, because of differences in gas temperature and how the FPCs were illuminated, certain adjustments must be made when applying one set of detector QE calibration results to another situation. Table 3.4 listed the differences among these situations, and §3.5.1 explained how window bowing and nonuniformity data were collected for fpc_hn and fpc_x2. In the following subsections we discuss how QE corrections for various effects are calculated and applied.

Window Absorption Corrections

As explained earlier, measurements of fpc_hn QE made on the BESSY SX700 monochromator are not directly applicable to the XRCF because only the center of the central windowlet of the FPC was absolutely calibrated. Nonuniformities in window thickness over the entire blocking plate aperture, as well as the effects of variable effective path length within each windowlet, must be considered when assigning a net QE to fpc_hn as it was used during AXAF and flat field calibration. The same considerations apply for fpc_x2 when analyzing flat field data, or when computing the effective QE when a HRMA-focussed image extends over more than just the center of one windowlet.

It is our intention to analyze the large- and small-scale QE mapping data for fpc_hn and fpc_x2 and develop tables of energy-dependent correction factors for each FPC, along the lines of the Gas Absorption Correction table described in the next subsubsection. As part of our analysis, and to guide the construction of a theoretical model, we will also use the results of Lester Cohen's finite-element modeling of FPC window deflections (Cohen, 1995), which was based on Dick Goddard's experimental measurements Goddard (1994).

Gas Absorption Corrections

There are three effects related to absorption of x-rays in the FPC gas which modify the detector QE: effective absorption path length, absorption of x-rays by the anode wire, and gas density (which depends on pressure and temperature). QE modifications for each of these effects for all relevant combinations of detector, aperture, and HRMA shell and quadrant were calculated using the `qegas.f` FORTRAN program (which is extensively documented and includes definitive FPC dimensions, such as a distance of 9.12 mm from HXDA aperture plane to deflected FPC window, and a gas depth of 55.02 mm with undeflected window—see Appendices for URLs) and are listed in Table 3.9 at the energies of relevant absorption edges and selected Penning source and EIPS characteristic emission lines. In the table, QE modifications are listed as percentage differences; a more complete table with over 550 energies is available which lists QE correction *factors*.

At each energy, the `QEref` column lists the QE of a model reference FPC, defined as a BND-H FPC with full rectangular aperture, no anode wire, average gas depth 55.93 mm, P10 gas with 90.01% Ar and 9.99% methane at 400 torr and 10 °C, with a 1.0-μm-thick, 1.3-g/cm^3 polyimide ($C_{22}H_{10}O_4N_2$) window and a 200-Å coating of 2.694-g/cm^3 aluminum. Other column headings will be explained below. The table should be used to determine *relative* QE corrections, such as when correcting for temperature differences, or applying the measured flat-field QE of fpc_x2 (relative to fpc_hn) to analyze data acquired during AXAF calibration with a focussed x-ray beam. As is obvious from the table, at low energies, where the gas is opaque, differences in the optical depth of the gas have no impact on QE.

As seen in Figure 3.15, the wire support grid deflects by approximately 1.25 mm in the center of the window, and the polyimide/Al window material bulges out another 0.25 mm between the wires

Energy	OpDep	QEref	x2norm	1ns	1tb	3ns	3tb	4ns	4tb	6ns	6tb	bn36	hfull	f5-36	f5-12	f5-4	f5-1	bessy	per-dC
77.5	99.999	0.001	0.000	0.000	0.000	0.000	0.000	0.000	0.000	0.000	0.000	0.000	0.000	0.000	0.000	0.000	0.000	0.000	0.000
95.0	98.777	0.005	0.000	0.000	0.000	0.000	0.000	0.000	0.000	0.000	0.000	0.000	0.000	0.000	0.000	0.000	0.000	0.000	0.000
108.5	87.609	0.015	0.000	0.000	0.000	0.000	0.000	0.000	0.000	0.000	0.000	0.000	0.000	0.000	0.000	0.000	0.000	0.000	0.000
183.3	41.160	0.212	0.000	0.000	0.000	0.000	0.000	0.000	0.000	0.000	0.000	0.000	0.000	0.000	0.000	0.000	0.000	0.000	0.000
221.0	27.727	0.386	0.000	0.000	0.000	0.000	0.000	0.000	0.000	0.000	0.000	0.000	0.000	0.000	0.000	0.000	0.000	0.000	0.000
277.0	99.999	0.587	0.000	0.000	0.000	0.000	0.000	0.000	0.000	0.000	0.000	0.000	0.000	0.000	0.000	0.000	0.000	0.000	0.000
284.1	99.999	0.609	0.000	0.000	0.000	0.000	0.000	0.000	0.000	0.000	0.000	0.000	0.000	0.000	0.000	0.000	0.000	0.000	0.000
284.3	99.999	0.606	0.000	0.000	0.000	0.000	0.000	0.000	0.000	0.000	0.000	0.000	0.000	0.000	0.000	0.000	0.000	0.000	0.000
392.4	99.999	0.083	0.000	0.000	0.000	0.000	0.000	0.000	0.000	0.000	0.000	0.000	0.000	0.000	0.000	0.000	0.000	0.000	0.000
409.8	99.999	0.107	0.000	0.000	0.000	0.000	0.000	0.000	0.000	0.000	0.000	0.000	0.000	0.000	0.000	0.000	0.000	0.000	0.000
410.0	99.999	0.130	0.000	0.000	0.000	0.000	0.000	0.000	0.000	0.000	0.000	0.000	0.000	0.000	0.000	0.000	0.000	0.000	0.000
452.2	99.999	0.137	0.000	0.000	0.000	0.000	0.000	0.000	0.000	0.000	0.000	0.000	0.000	0.000	0.000	0.000	0.000	0.000	0.000
524.9	75.327	0.254	0.000	0.000	0.000	0.000	0.000	0.000	0.000	0.000	0.000	0.000	0.000	0.000	0.000	0.000	0.000	0.000	0.000
543.1	70.017	0.284	0.000	0.000	0.000	0.000	0.000	0.000	0.000	0.000	0.000	0.000	0.000	0.000	0.000	0.000	0.000	0.000	0.000
543.2	69.960	0.179	0.000	0.000	0.000	0.000	0.000	0.000	0.000	0.000	0.000	0.000	0.000	0.000	0.000	0.000	0.000	0.000	0.000
572.8	61.929	0.222	0.000	0.000	0.000	0.000	0.000	0.000	0.000	0.000	0.000	0.000	0.000	0.000	0.000	0.000	0.000	0.000	0.000
676.8	41.670	0.372	0.000	0.000	0.000	0.000	0.000	0.000	0.000	0.000	0.000	0.000	0.000	0.000	0.000	0.000	0.000	0.000	0.000
705.0	37.977	0.408	0.000	0.000	0.000	0.000	0.000	0.000	0.000	0.000	0.000	0.000	0.000	0.000	0.000	0.000	0.000	0.000	0.000
851.5	23.619	0.581	0.000	0.000	0.000	0.000	0.000	0.000	0.000	0.000	0.000	0.000	0.000	0.000	0.000	0.000	0.000	0.000	0.000
929.7	18.846	0.651	0.000	0.000	0.000	0.000	0.000	0.000	0.000	0.000	0.000	0.000	0.000	0.000	0.000	0.000	0.000	0.000	0.000
1011.7	15.113	0.711	0.000	0.000	0.000	0.000	0.000	0.000	0.000	0.000	−.001	0.000	0.000	0.000	0.000	0.000	0.000	0.000	0.000
1253.6	8.550	0.828	−.005	0.002	−.010	0.002	−.013	0.002	−.015	0.002	−.020	−.005	−.001	−.005	0.000	−.001	−.001	0.002	−.001
1486.7	5.385	0.886	−.021	0.030	−.034	0.028	−.050	0.028	−.061	0.027	−.093	−.021	−.007	−.021	−.003	−.013	−.017	0.025	−.009
1559.5	4.750	0.895	−.026	0.050	−.038	0.047	−.061	0.046	−.077	0.045	−.120	−.027	−.010	−.027	−.005	−.022	−.028	0.043	−.014
1559.7	4.749	0.877	−.026	0.050	−.038	0.047	−.061	0.046	−.077	0.045	−.120	−.027	−.010	−.027	−.005	−.022	−.028	0.043	−.014
1740.0	3.567	0.888	−.037	0.125	−.030	0.119	−.074	0.116	−.103	0.112	−.181	−.038	−.017	−.038	−.013	−.054	−.069	0.107	−.035
1775.0	3.385	0.887	−.038	0.143	−.026	0.136	−.074	0.133	−.105	0.129	−.191	−.040	−.019	−.040	−.015	−.062	−.079	0.123	−.041
2042.4	2.335	0.853	−.041	0.304	0.034	0.289	−.046	0.283	−.097	0.273	−.237	−.044	−.030	−.044	−.031	−.131	−.167	0.261	−.085
2165.9	1.996	0.823	−.039	0.382	0.072	0.363	−.022	0.355	−.082	0.343	−.243	−.042	−.034	−.042	−.039	−.164	−.209	0.328	−.107
2293.2	1.711	0.786	−.036	0.460	0.113	0.437	0.006	0.428	−.061	0.413	−.243	−.039	−.038	−.039	−.047	−.197	−.251	0.394	−.129
2984.3	0.827	0.552	−.010	0.788	0.309	0.748	0.154	0.732	0.059	0.707	−.196	−.014	−.052	−.014	−.081	−.334	−.427	0.675	−.219
3205.8	0.674	0.482	−.003	0.860	0.356	0.816	0.192	0.799	0.090	0.771	−.179	−.007	−.054	−.007	−.088	−.364	−.465	0.737	−.238
3206.0	6.363	0.983	−.014	0.013	−.025	0.012	−.035	0.012	−.041	0.012	−.060	−.014	−.004	−.014	−.001	−.006	−.007	0.011	−.004
3444.0	5.323	0.983	−.021	0.031	−.034	0.030	−.051	0.029	−.063	0.028	−.095	−.022	−.007	−.022	−.003	−.014	−.018	0.027	−.009
4510.8	2.644	0.924	−.042	0.245	0.009	0.233	−.060	0.228	−.105	0.220	−.226	−.044	−.026	−.044	−.025	−.106	−.135	0.210	−.069
5414.7	1.617	0.799	−.034	0.489	0.128	0.464	0.017	0.454	−.053	0.438	−.242	−.037	−.039	−.037	−.050	−.209	−.266	0.419	−.137
5898.8	1.279	0.720	−.026	0.603	0.194	0.573	0.066	0.560	−.015	0.541	−.230	−.030	−.044	−.030	−.062	−.257	−.328	0.517	−.168
6403.8	1.019	0.638	−.018	0.704	0.256	0.669	0.113	0.655	0.024	0.632	−.214	−.022	−.049	−.022	−.072	−.299	−.382	0.604	−.196
6930.3	0.818	0.558	−.010	0.792	0.312	0.752	0.156	0.736	0.060	0.710	−.195	−.014	−.052	−.014	−.081	−.336	−.429	0.679	−.220
7478.1	0.661	0.483	−.002	0.866	0.360	0.822	0.195	0.804	0.093	0.776	−.178	−.007	−.055	−.007	−.088	−.366	−.468	0.742	−.240
8047.8	0.538	0.416	0.004	0.927	0.401	0.880	0.228	0.861	0.121	0.831	−.161	0.000	−.057	0.000	−.095	−.392	−.500	0.794	−.257
8397.6	0.477	0.379	0.008	0.959	0.422	0.910	0.245	0.891	0.136	0.860	−.152	0.003	−.058	0.003	−.098	−.405	−.517	0.821	−.265
8638.9	0.440	0.356	0.010	0.978	0.435	0.929	0.256	0.909	0.145	0.877	−.146	0.005	−.058	0.005	−.100	−.413	−.527	0.838	−.271
9672.3	0.319	0.273	0.017	1.044	0.480	0.991	0.293	0.970	0.178	0.936	−.126	0.012	−.061	0.012	−.106	−.441	−.562	0.894	−.289

Table 3.9: QE Corrections for gas opacity effects. `QEref` is the QE of the reference detector, defined as fpc_hn with full aperture and no anode absorption at 400 torr and 10 °C, with average window deflection of 0.91 mm. All columns except the first two represent the percentage change in QE relative to the reference FPC. As an example, at Cu-K, `bessy` = 0.794 and `x2norm` = 0.004, so the QE of fpc_x2 as measured at BESSY (where the center of a slightly off-center windowlet—to avoid anode wire absorption—was exposed to normal incidence x-rays) is 0.790% higher than its effective QE during flat field testing (where the entire blocking plate aperture was exposed) because of differences in effective gas depth and anode wire absorption.

within each 2-mm-square windowlet. Because of this window deflection and the fact that HRMA-focussed x-rays intercept the focal plane FPC window at its point of maximum deflection, the gas depth is about 0.6 mm longer in fpc_x2 than the the average gas depth for the BND-H FPCs. Average deflections for window areas which are exposed to x-rays with various combinations of detector and aperture range from 0.54 mm (for fpc_5 with its 1-mm aperture) to 1.50 mm (for any FPC exposed in the center of its window). (Some refinement in window deflection values will occur once Lester Cohen's window deflection model has been studied.) QE adjustments for each of these x-ray exposure combinations are listed in Table 3.9, with the `x2norm` column referring to fpc_x2 with its 36.784-mm blocking plate aperture during flat-field normal-incidence calibration, `hfull` to BND-H FPCs with their rectangular apertures, `bessy` to fpc_hn or fpc_x2 at BESSY, `f5_36` to fpc_5 with its 36-mm aperture, and so on.

There are eight columns that apply to fpc_x2 when exposed to focussed beams, with North & South and Top & Bottom quadrants for each of the four HRMA shells. The breakdown by shell is needed because the effective gas depth along the focussed rays is increased by a factor of the secant of the angle of incidence, which adds another 0.1 mm for x-rays focussed by HRMA shell 1 (with cone half-angle equal to 3.3873°) and less for the other shells. At high energies where opacity approaches zero, this net ∼1.2% increase in gas depth (0.6 mm plus 0.1 mm out of about 56 mm) relative to the BND-H FPCs leads to a similar relative increase in QE, as shown in column `1ns`, for instance 0.8% at Ag-$L\alpha$ (just below the Ar-K edge), and 0.9% at Cu-$K\alpha$.

The further breakdown by quadrants is necessary because of anode absorption, which occurs when x-rays strike the anode wire running down the middle of the FPC. Instead of ionizing a gas atom which leads to an electron avalanche, the absorbed x-ray produces a very small electrical signal which may or may not appear as a weak feature at very low channels, and so that event is effectively lost.

Anode absorption occurs whenever the gas is not opaque and x-rays are directed toward the 50-μm-diameter anode wire. It *does not* occur, therefore, when the 1-, 4-, or 12-mm apertures are used with fpc_5 (since they are offset to one side of the window), or for x-rays collected by any of the North or South quadrants of the HRMA (since those x-rays are focussed into quarter-cones which intercept the vertically oriented fpc_x2 to either side of its anode wire). The largest quadrant-specific differences occur for shell 6, which has the smallest-diameter x-ray cone and therefore the largest fraction of x-rays aimed at the anode wire. At Cu-K, the relative difference in QE is 1.0%, from $QE_{6ns}/QE_{6tb} = (1 + 0.0083)/(1 - 0.0016) = 1.010$. When analyzing spectra acquired using a full shell, simply average the NS and TB columns. When analyzing spectra from more than one shell, use an effective-area-weighted average of the appropriate columns.

In most cases, the largest QE adjustments needed to relate one set of calibration results to another arise from differences in gas density, which is proportional to pressure and inversely proportional to temperature (in Kelvins). Because all the BND-H and focal plane FPCs were run off the same gas supply system, the pressure was virtually identical for all of them (and stable at 400 torr to within ∼0.1 torr). Temperature differences, however, of 10 or more degrees were not uncommon between different FPCs or calibration periods (see Table 3.4).

Percentage changes per degree Celsius (or Kelvin) are listed in the `per_dC` column and range up to nearly 0.3% per degree at 10 keV. Those correction terms, however, are strictly applicable only for small differences (a few degrees), and are shown merely for illustrative purposes. Proper corrections use the `OpDepth` column, which lists the optical depth of the gas at each energy, equal to $\sum \mu\rho l$, assuming 90.01% Ar and 9.99% methane at 10 °C and 400 torr. The ratio of QEs of a

single FPC at two different temperatures is then given by

$$\frac{QE(T_1)}{QE(T_2)} = \frac{1 - e^{-OpDepth(273.15+T_0)/(273.15+T_1)}}{1 - e^{-OpDepth(273.15+T_0)/(273.15+T_2)}}$$

where all the temperatures are in degrees Celsius and T_0 is the reference temperature of 10 °C.

(To date, none of these gas depth and anode absorption corrections have been applied to data analysis results because they are so small.)

Gas temperature corrections can be significant and have been applied to all flat field and (where necessary) BESSY data. The gas depth and anode absorption corrections, by comparison, are almost negligible, and have not been applied to any results. In the interest of thoroughness, however, the largest uncertainty in the gas depth/anode absorption corrections arises from the average window deflection, and the critical term there is the difference between the average fpc_x2 deflection and the central windowlet deflection. This is conservatively estimated this to be 0.42 ± 0.15 mm, resulting in an error of less than 0.22% at 10 keV.

Off-Axis and Grating Measurements

All the gas opacity corrections discussed thus far apply only to normal incidence or on-axis focussed x-rays. QE corrections for off-axis and grating measurements will be somewhat different for fpc_x2 because the images will in general extend across more than just the center of one windowlet (particularly for grating-dispersed intrinsically broad lines), but such correction factors will generally differ from the on-axis factors by no more than one percent, and so it should suffice to use rough approximations of the average angle of incidence and the image location with respect to the center of the central windowlet.

Corrections for variable window transmission and obscuration by window support wires will generally be larger and thus more difficult to estimate. As noted earlier, however, none of the window bowing and nonuniformity data have yet been analyzed.

3.5.5 Final Results: Standardized FPC QEs

This subsection describes the calculation of absolute quantum efficiencies for the BND-H detectors and the fpc_x2. We outline here the steps used in deriving these tables, and point out the possible systematic effects remaining in these data.

There are two energy regimes, $E < 1.700$ keV, and $E > 1.700$ keV.

For $E < 1.700$ keV, we have absolute calibrations for the fpc_hn and fpc_x2 from the SX700 beamline at BESSY. Details are in Auerhammer et al. (1998). The data were reduced as in §3.5.1, and combined with beam current files tabulated by J. Auerhammer.

For $E > 1.700$ keV, we have currently no absolute standard. We therefore have used a theoretical SSD QE curve, presuming the QE of an SSD is just the window transmission, using 2000 Angstroms of aluminum plus 1.25 microns of Parylene (C_8H_8, density 1.1 g cm^{-3}, and Henke tables from 1995. When results from the BESSY calibration of the SSD detectors are available, they will be incorporated.

Relative quantum efficiencies were measured in Phases I and J at XRCF, in two kinds of experiments: BND-500 maps and BND-H maps. These data and their reduction are described in §3.5.3.

The BND-500 maps exposed the fpc_5 at its home position, the ssd_5 position, and the projected position of the fpc_hb. When the shutters were open (all of phase J, and a few tests in phase I),

this allows relative QE to be computed for these 3 detectors, correcting for beam uniformity and temperature effects (for the FPCs).

The Phase I and J BND-H maps exposed the fpc_hn at its home position, the positions of the other fpc_h detectors, and the (projected) position of the fpc_x2. Relative QE's for these detectors were then computed at these energies, including BU and T corrections.

All QE's and relative QE's for FPC detectors are temperature corrected to 10°C.

We also have a code that allows us to fit a model of the form:

- a slab of Al
- a slab of polyimide ($C_{22}H_{10}O_4N_2$, density 1.33)
- a box of gas (P-10 = 90% Ar + 10% CH_4)
- an energy-independent geometrical factor

to a QE curve. We have done this with the BESSY SX700 data for fpc_hn and fpc_x2. We find recent Henke tables unable to adequately fit the data, so we fit them in energy slices, allowing different window thicknesses to make up for the inadequate Henke data. It may be the case that the stoichiometry of the plastic is slightly different from the above, or that older (or newer) Henke tables would do a better job of fitting these data.

To summarize, we obtain the QE of detectors in the following manner:

- For $E < 1700$ eV: interpolate the SX700 data with Henke fits for fpc_x2 and fpc_hn. Use RQE from phase I & J BND-H maps to get other fpc_h QEs at selected energies. Interpolate between these points to get QE(fpc_h*,E).

- For $E > 1700$ eV: Using the theoretical SSD QE curve, BND-500 maps allow computation of the QE of fpc_hb and fpc_5 (phase I),or fpc_x1, (phase J) at selected energies. Then the contemporary BND-H maps allow computation of other fpc_h QE from the fpc_hb numbers. We then interpolate between these points to get QE(fpc_h*,E).

To obtain fits for the other fpc_h detectors, we allow only the window thickness to vary, providing a single free parameter (the ratio of the detector's window thickness to the fitted value for fpc_hn). We require the same thickness ratio in all energy slices, despite the need for different thickness values for the fpc_hn fit for each energy slice.

The results of these procedures are illustrated in Figures 3.20through3.22. Note especially in the fpc_hn and fpc_x2 plots (Figure 3.20) how poorly the fit to the Henke tables approximates the data. Still, the fit falls within 3% of all the points except those near edges (which have been excluded from the fits), and so represents a reasonably good way to interpolate between the sparse points where data exist for the other detectors.

We list the measured QE values for the fpc_hn and fpc_x2 in Table 3.10. We include those for the other fpc_h detectors in Table 3.11.

The fpc_5 is a slightly different case. We have obtained relative QE numbers for this detector from beam uniformity tests in phases D and E of the XRCF testing, by comparing fluxes taken simultaneously by the two detectors during BND-H maps, and correcting for beam uniformity effects based on data from a nearly contemporaneous BND-500 map. These relative QE numbers, corrected to 10°C, are presented in Table 3.8. Using these numbers and the absolute QE curve for the fpc_hn presented above, we can obtain an absolute QE curve for the fpc_5. The resulting curve is in Figure 3.23. The absolute QE numbers for fpc_5 are presented in Table 3.12.

Table 3.10: Absolute QE for fpc_x2 and fpc_hn.

energy	QE(fpc_x2)	QE(fpc_hn)
0.095	0.00239 ± 0.00003	0.00553 ± 0.00006
0.100	0.00423 ± 0.00005	0.00896 ± 0.00009
0.105	0.00689 ± 0.00007	0.01325 ± 0.00014
0.110	0.01001 ± 0.00011	0.01837 ± 0.00019
0.115	0.01559 ± 0.00017	0.02649 ± 0.00028
0.150	0.08014 ± 0.00085	0.11185 ± 0.00116
0.183	0.17972 ± 0.00190	0.22559 ± 0.00236
0.210	0.25883 ± 0.00340	0.30902 ± 0.00402
0.254	0.44066 ± 0.00349	0.49017 ± 0.00385
0.256	0.44667 ± 0.00353	0.49463 ± 0.00389
0.258	0.44866 ± 0.00354	0.49640 ± 0.00389
0.261	0.46432 ± 0.00462	0.51457 ± 0.00510
0.264	0.47175 ± 0.00609	0.52187 ± 0.00671
0.267	0.48475 ± 0.00974	0.53432 ± 0.01069
0.270	0.49778 ± 0.01336	0.54700 ± 0.01463
0.273	0.49754 ± 0.01581	0.54752 ± 0.01734
0.276	0.50911 ± 0.02642	0.55915 ± 0.02892
0.280	0.50242 ± 0.05257	0.55213 ± 0.05748
0.284	0.43048 ± 0.03710	0.47595 ± 0.04069
0.288	0.01317 ± 0.00117	0.01680 ± 0.00147
0.292	0.03013 ± 0.00275	0.03451 ± 0.00311
0.296	0.00587 ± 0.00035	0.00697 ± 0.00041
0.300	0.00122 ± 0.00007	0.00165 ± 0.00010
0.305	0.00054 ± 0.00003	0.00088 ± 0.00005
0.310	0.00204 ± 0.00013	0.00410 ± 0.00025
0.330	0.01043 ± 0.00017	0.01817 ± 0.00028
0.389	0.04270 ± 0.00039	0.06323 ± 0.00057
0.392	0.04514 ± 0.00040	0.06648 ± 0.00057
0.395	0.04763 ± 0.00042	0.06949 ± 0.00060
0.400	0.05162 ± 0.00045	0.07466 ± 0.00064
0.405	0.03828 ± 0.00033	0.05722 ± 0.00049
0.410	0.02656 ± 0.00023	0.04201 ± 0.00036
0.415	0.03854 ± 0.00034	0.05751 ± 0.00049
0.420	0.04785 ± 0.00040	0.06991 ± 0.00058
0.515	0.16761 ± 0.00139	0.21002 ± 0.00172
0.520	0.17520 ± 0.00145	0.21823 ± 0.00178
0.525	0.18157 ± 0.00150	0.22510 ± 0.00184
0.530	0.18470 ± 0.00150	0.22869 ± 0.00184
0.535	0.14927 ± 0.00122	0.18719 ± 0.00151
0.540	0.07835 ± 0.00064	0.10683 ± 0.00086
0.545	0.09211 ± 0.00076	0.12222 ± 0.00099
0.550	0.10633 ± 0.00087	0.13939 ± 0.00114
0.610	0.20106 ± 0.00161	0.24339 ± 0.00195
0.705	0.32485 ± 0.00255	0.37165 ± 0.00289

Table 3.10: Absolute QE for fpc_x2 and fpc_hn (continued)

energy	QE(fpc_x2)		QE(fpc_hn)	
0.852	0.48896 ±	0.00449	0.52912 ±	0.00484
0.930	0.55858 ±	0.00509	0.59247 ±	0.00538
1.012	0.63479 ±	0.00578	0.66650 ±	0.00605
1.254	0.77416 ±	0.00978	0.78901 ±	0.00995
1.487	0.84923 ±	0.01298	0.85279 ±	0.01302
1.540	0.87167 ±	0.01749	0.87613 ±	0.01757
1.550	0.86902 ±	0.01744	0.87424 ±	0.01753
1.560	0.87456 ±	0.01755	0.87641 ±	0.01758
1.570	0.85495 ±	0.01716	0.86390 ±	0.01734
1.580	0.85931 ±	0.01782	0.86522 ±	0.01794
1.590	0.86201 ±	0.01877	0.86694 ±	0.01888
1.600	0.86649 ±	0.02043	0.86795 ±	0.02047
1.700	0.86248 ±	0.02086	0.86759 ±	0.02098
4.510	0.90130 ±	0.01285	0.92300 ±	0.00922
4.510	0.89122 ±	0.00875	0.93957 ±	0.00728
5.410	0.73849 ±	0.00806	0.82354 ±	0.00747
6.400	0.69454 ±	0.04425	0.69761 ±	0.00799
6.400	0.65795 ±	0.00960	0.71063 ±	0.03231
8.620	0.36862 ±	0.00659	0.38860 ±	0.00645

3.6 Future Work

Because so much FPC calibration data has only recently been acquired, a great deal of analysis remains to be finished. Substantial improvements can also be derived from the flat field calibration data, particularly at high energies, given more time. Below is a summary of work that remains.

General

- Spectral fitting accuracy can be improved by using the delta function plus top hat gain distribution for the BND-H FPCs (but not fpc_5, fpc_x2, or fpc_hn with its 36-mm aperture), letting the escape peak energy float a little (because of energy nonlinearities), using updated (and temperature-adjusted?) QE curves for each FPC, etc.
- The fraction of line counts arising from continuum escape is different between the BNDs and fpc_x2; corrections should be made, particularly for L-shell EIPS lines, which have relatively low line/continuum ratios.
- Corrections for gas temperature, window bowing, and focal plane image size should be automatically included in all analysis.
- Energy nonlinearity, particularly across the Ar-L edge, is not included in `JMKmod`. This may significantly affect the accuracy of low-energy fits, particularly for C-K where the below-edge and above-edge continua have different effective gains.
- None of the counting rate linearity data from BESSY have been analyzed. If there are significant errors at high rates, many measurements would be affected, particularly for fpc_x2 which was exposed to higher-intensity concentrated x-rays.

E (keV)	QE(fpc_hs)		QE(fpc_ht)		QE(fpc_hb)	
0.183	0.22589 ±	0.00082	0.19324 ±	0.00071	0.20149 ±	0.00074
0.277	0.54843 ±	0.00142	0.53072 ±	0.00137	0.53126 ±	0.00163
0.524	... ±	...	0.18166 ±	0.00065	0.20655 ±	0.00074
0.705	0.35661 ±	0.00124	0.32766 ±	0.00105	0.34354 ±	0.00110
0.705	0.37704 ±	0.00132	0.30991 ±	0.00100	0.32493 ±	0.00104
0.852	0.53155 ±	0.00179	0.48755 ±	0.00165	0.50749 ±	0.00171
0.929	0.59796 ±	0.00971	0.56805 ±	0.00167	0.58067 ±	0.00171
1.254	0.79132 ±	0.00791	0.78033 ±	0.00768	0.78034 ±	0.00770
1.486	... ±	...	0.84251 ±	0.01240	0.84319 ±	0.01239
1.486	0.85158 ±	0.00366	0.84329 ±	0.00353	0.84439 ±	0.00351
4.510	... ±	...	0.92708 ±	0.01175	0.92651 ±	0.00575
4.510	0.91135 ±	0.00831	0.94936 ±	0.00853	0.92651 ±	0.00575
5.410	0.78163 ±	0.00806	0.80703 ±	0.00825	0.79358 ±	0.00614
6.400	... ±	...	0.67276 ±	0.04272	0.68054 ±	0.00682
6.400	0.67771 ±	0.00870	0.69902 ±	0.00888	0.68054 ±	0.00682
8.620	0.34490 ±	0.00585	0.34616 ±	0.00618	0.34546 ±	0.00559

Table 3.11: Absolute Quantum Efficiencies for the fpc_ht, fpc_hb and fpc_hs detectors from XRCF flatfield measurements normalized to fpc_hn (up to 1.700 keV) and normalized to a theoretical SSD (above 1.700 keV), corrected to 10° C.

energy	QE(fpc_5)	
0.183	0.21735 ±	0.00341
0.276	0.54973 ±	0.02898
0.705	0.34108 ±	0.01341
1.254	0.79241 ±	0.01537
1.487	0.86579 ±	0.01542
1.487	0.86252 ±	0.01537
4.510	0.94466 ±	0.01179
6.400	0.67726 ±	0.01221

Table 3.12: Absolute Quantum Efficiencies for the fpc_5 detector from XRCF Phase D & E beam uniformity tests normalized to the fpc_hn, corrected to 10° C.

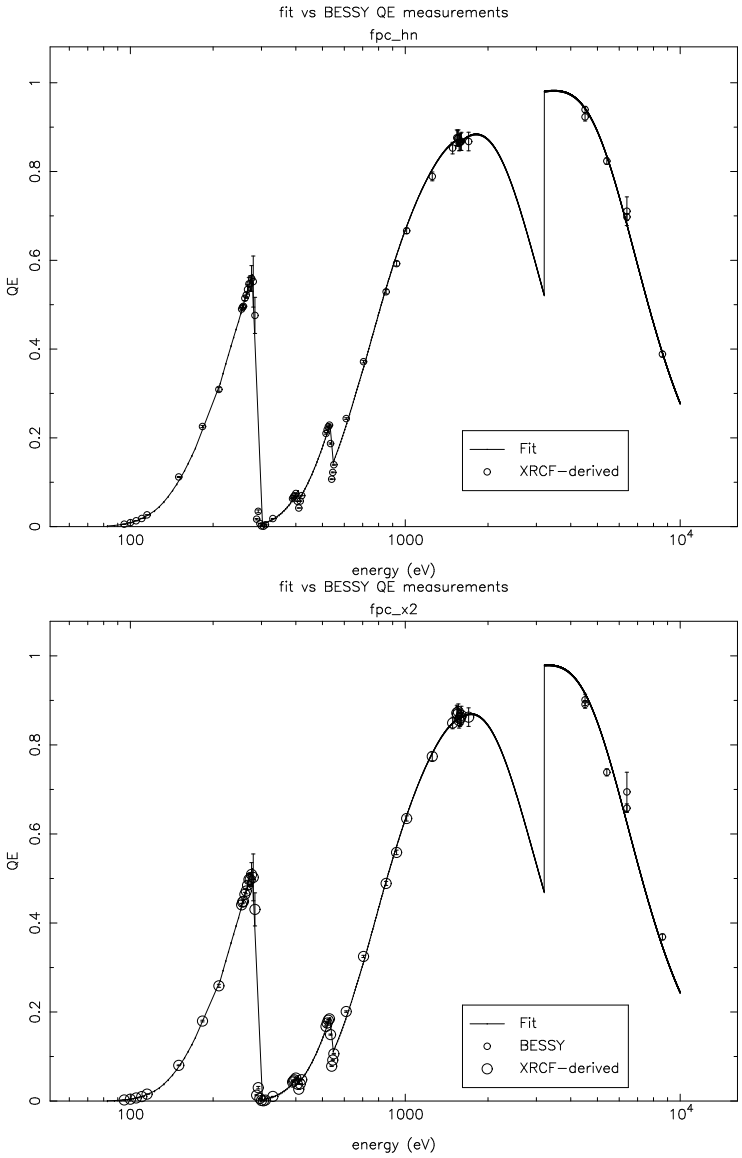

Figure 3.20: Absolute quantum efficiency for fpc_hn (top) and fpc_x2 from JMKmod fits to BESSY SX700 monochromator data ($E < 1.7$keV) and derived from a theoretical SSD curve and flatfield data ($E > 1.7$keV), with the fits described in the text.

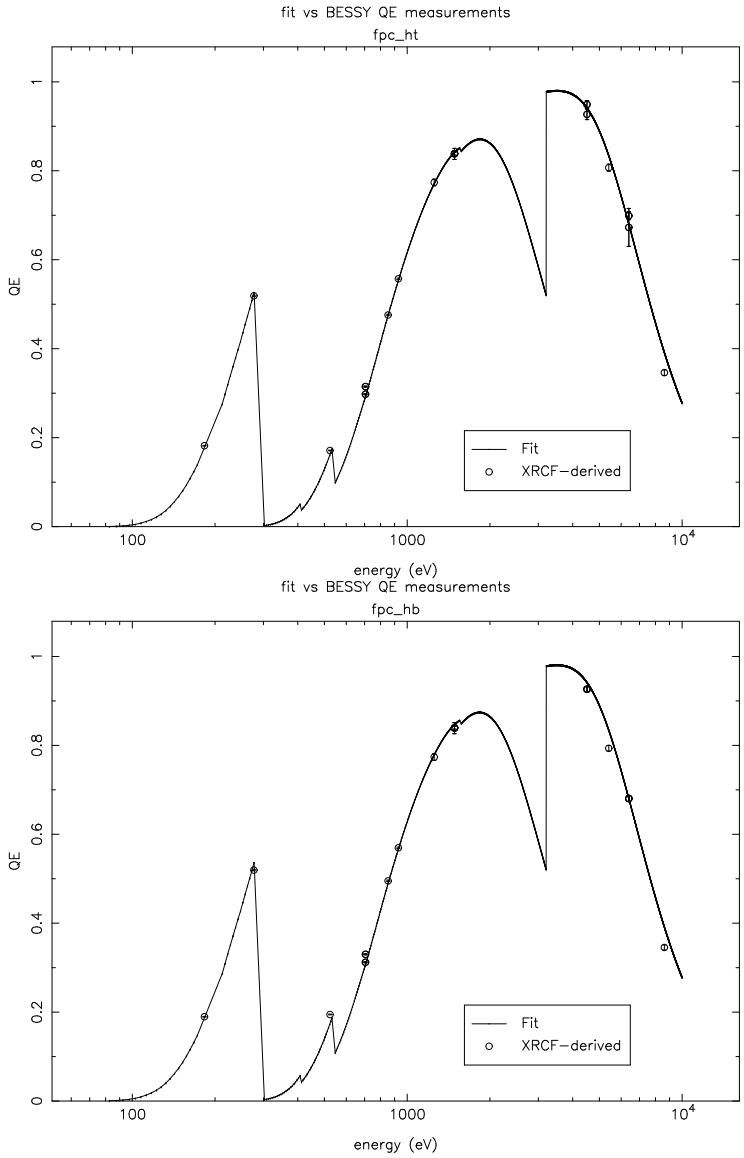

Figure 3.21: Absolute quantum efficiency for fpc_ht (top) and fpc_hb from flatfield data and the fpc_hn BESSY data ($E < 1.7$keV), and derived from a theoretical SSD curve and flatfield data ($E > 1.7$keV), with the fits described in the text.

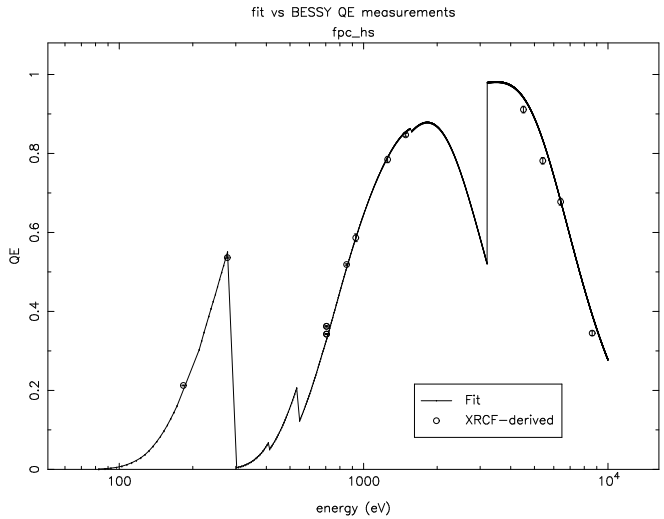

Figure 3.22: Absolute quantum efficiency for fpc_hs from flatfield data and the fpc_hn BESSY data ($E < 1.7$keV), and derived from a theoretical SSD curve and flatfield data ($E > 1.7$keV), with the fits described in the text.

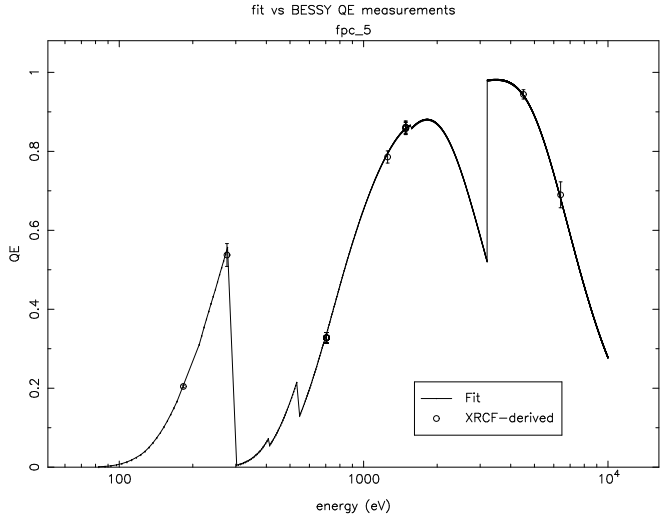

Figure 3.23: Absolute quantum efficiency for the fpc_5, derived from the fpc_hn curve and beam uniformity measurements in Phases D and E.

- Only half of the SSD deadtime consistency data (see Chapter 5) have been analyzed, and that was without applying the (small) corrections for incomplete pileup rejection that have been recently worked out.

Flat Field Calibrations

- None of the flat field data from November 1996 have been analyzed, apart from some preliminary FPC vs. HSI QE calibration. Good statistics were obtained with both SSDs (with ssd_x in the HXDA).
- Flat field data were collected at 19 energies (some of them during all three flat field calibration phases), but several of those energies have not yet been analyzed.
- Better statistics can be obtained for the beam uniformity maps by including more detectors for normalization, and by using *all* iterations at a given location.
- Much better statistics can be obtained for the relative counting rates of all BNDs by summing spectra from all the AXAF calibration runs at a given energy (as long as the source intensity and spectral shape are constant at the few percent level).
- Relatively less work has been done on the QE of fpc_5. Flat field data can also be used to calibrate the sizes of its four apertures.
- SSD data analysis is still relatively inaccurate at energies below 2 keV because of a lack of pileup rejection, but analysis tools to account for this are nearly ready. Improved FPC QEs can then be obtained at high energy via relative QE calibration.
- FPC spectral fitting accuracy can be checked by analyzing data taken at three energies with 2 and 4 mean-free-path source filters, and comparing the relative rates obtained with ssd_5 and the FPCs. The SSD analysis should be quite accurate because of its excellent energy resolution.

BESSY SX700 QEs

- Measured QEs are not always consistent (e.g., 705 eV), and there are sometimes jumps when the monochromator filter is changed.
- Why is the transmission of the fpc_x2 window so much higher than the net QE of the assembled detector? We are consulting with experts.
- Ring current logs must be edited to remove or correct occasional small (but sometimes extended) blips which can cause QE normalization errors. There may also be unexpected timestamp differences between BESSY and HXDS files.

BESSY window mapping

- None of these data have been analyzed.
- Results are needed to relate flat field and BESSY single-windowlet QEs, and to adjust the effective fpc_x2 QE when HRMA images are extended, as for off-axis and grating measurements.

BESSY white beam

- PTB has done some preliminary analysis, but results disagree with theoretical models by tens of percent below 1 keV.

- Analysis at low energies may be prohibitively difficult, but useful QE information can be derived for fpc_x2 and fpc_hn near the Ar-K edge for at least two of the filter combinations.

Chapter 4

The HXDS Solid State Detectors

Walter C. McDermott, Shaun Serej, and Edwin M. Kellogg

4.1 Introduction

This chapter describes the calibration of the HXDS Solid State Detectors (SSD) used during the ground calibration of AXAF. One SSD, ssd_5, was used as a Beam Normalization Detector in the Building 500 location, while the other, ssd_x, was used in the focal plane to measure the HRMA point response function and the HRMA effective area. This chapter is in a rather preliminary state, and all data contained in it should be accepted with caution.

4.2 Calibration Overview

The SSD's were calibrated using monochromatic and undispersed synchrotron radiation from the Physikalisch-Technische Bundesanstalt (PTB) beam lines, the SX700, a grating monochromator and the 12.20 or white beam line, an undispersed beam with no intervening optical elements between the beam source and the detector, and one BESSY beam line, the KMC or Krystall Monokromator, at the BESSY electron storage ring in Berlin, Germany. The calibration program is based on one designed earlier at PTB for use with lithium drifted silicon solid state detectors (Scholze and Ulm, 1994). First, we obtain pulse height distributions from the Ge detector at the SX700, from 0.4 to 1.7 keV, to derive the QE in narrow energy bands, as well as the pulse height distribution for a single energy (spectral response function, or SRF). The SX700 output beam is calibrated using the PTB electrical substitution cryogenic radiometer (Lederer et al., 1995), which is capable of 1% flux accuracy. The SX700 energy scale is calibrated to 2 eV, which also helps us to establish our SSD detectors' energy scales. This SX700 measurement is especially important below 1.6 keV because of the narrow absorption features and EXAFS in the SSD QE near the Al-K edge, 1.58 keV, Ge-L at 1.2 keV, and O-K at 0.54 keV.

At higher energies, the KMC was used to obtain the SRF, from 1.7 to 5.9 keV. It was not, however, possible to use the electrical substitution cryogenic radiometer with the KMC. In order to extend the QE calibration to higher energies, beyond the 1.7 keV upper limit of the SX700, we rely on the undispersed, or white, synchrotron beam, whose intensity can be calculated using PTB's measurements of the synchrotron ring current, beam energy, magnetic field, source-to-detector distance, beam emissivity, and detector aperture dimensions. The SRF measured with monochromatic

radiation is then convolved with the calculated synchrotron spectrum, and compared with the measured detector pulse height distribution. The comparison also accounts for the x-ray absorption taking place in the detector windows: the Al and parylene windows, and the inevitable layer of ice resulting from condensation of moisture on the cooled detector surface. The difference between predicted and observed pulse height distribution tells us the detector efficiency, since the intensity of the white beam from the synchrotron is calculated independently. While there is considerable room for uncertainty in this comparison at lower energies, where x-ray absorption in the detector windows is strong, at higher energies the windows are less important, and we are confronting the intrinsic absorption QE of the Ge detector crystal. We have always believed that this approaches 100%, but have set out to verify it for these detectors with the white beam calibration.

4.3 Spectral Response Function, SRF

The SRF is a description of how the detector redistributes a single-energy photon in pulse-height space. It was measured for the SSDs using monochromatic radiation from a double crystal monochromator on the BESSY KMC beam line at higher energies, and the PTB SX700 grating monochromator beam line at lower energies (Scholze and Ulm, 1994).

The KMC beam line was equipped with three selectable crystal sets: beryl, for the energy range between 800 eV and 1.7 keV, InSb for the energy range from 1.7 keV to 5.9 keV, and silicon for the range from 2.0 keV to 5.9 keV. Due to optics in the beam line and the characteristic operating conditions of the storage ring, the energies available from the KMC beam line were limited to less than or equal to 5.9 keV. The majority of the response function measurements were taken with the silicon crystal because the efficiency of the silicon monochromator over the needed energy range was relatively flat as opposed to the InSb crystal, whose efficiency is strongly dependent on energy. The InSb crystals were used mainly to bridge the gap between the beryl and Si crystals.

The SX700 beam line's energy range is from 70 eV to 1.7 keV. However, data were collected only down to 400 eV because the thermal noise in the SSD interferes with the x-ray peak below this energy. The SX700 had the added advantage that its absolute flux was calibrated using the electrical substitution cryogenic radiometer as a primary standard, and a set of photodiodes as transfer standards. This is discussed in the next section.

The SRF was generally measured in steps of 200 eV, but the step size was much finer through detector absorption features. This allows fitting the fine structure of these features.

4.3.1 Components of the Response Function

Some of the response function spectra have been fit using the XSPEC (Arnaud, 1996) model `JMKmod` (Tsiang, 1997). This model is a subroutine in XSPEC that contains a modified version of the HYPERMET function (Phillips and Marlow (1976), Scholze and Ulm (1994)). The HYPERMET function is an empirical model that is commonly used to fit solid state detector spectra. This function is a sum of terms that model certain portions of the recorded spectrum. The following four components are included in `JMKmod`.

$$G(E) = H_G \ \exp\left[-\frac{(E-E_0)^2}{2\sigma^2}\right] \tag{4.1}$$

$$T_L(E) = \frac{1}{2}H_{TL} \ \exp\left(\frac{E-E_0}{\beta_L}\right) \ \mathrm{erfc}\left(\frac{E-E_0}{\sqrt{2}\sigma} + \frac{\sqrt{2}\sigma}{2\beta_L}\right) \tag{4.2}$$

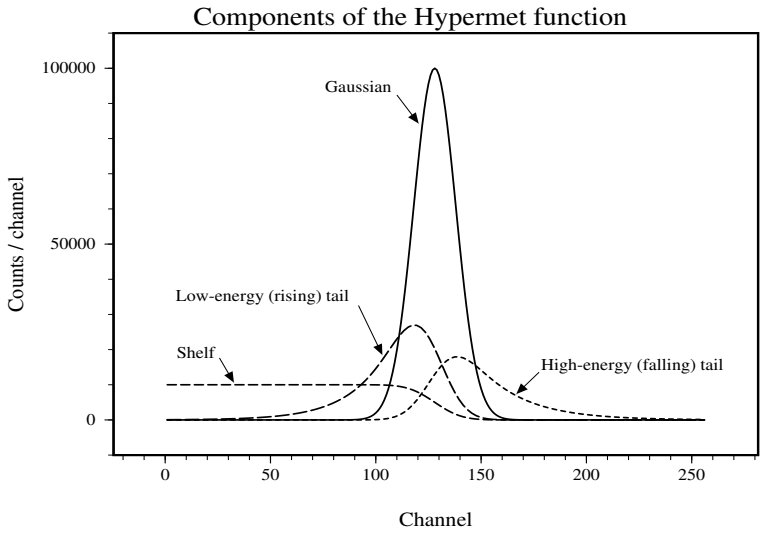

Figure 4.1: Components of the HYPERMET function.

$$T_P(E) = \frac{1}{2} H_{TP} \ \exp\left(\frac{E_0 - E}{\beta_P}\right) \ \text{erfc}\left(\frac{E_0 - E}{\sqrt{2}\sigma} + \frac{\sqrt{2}\sigma}{2\beta_P}\right) \tag{4.3}$$

$$S(E) = \frac{1}{2} H_S \ \text{erfc}\left(\frac{E - E_0}{\sqrt{2}\sigma}\right) \tag{4.4}$$

where G(E) is a Gaussian with H_G, σ, and E_0 as its amplitude, standard deviation, and center parameters, respectively, representing the main peak; T_L(E) is a low energy tail with amplitude and slope parameters of H_{TL} and β_L, respectively; T_P(E) is a high energy tail with H_{TP} and β_P as its amplitude and slope parameters; and S(E) is a stepwise flat shelf of amplitude H_S. A plot of the above four components is shown in Figure 4.1.

The Gaussian portion of the HYPERMET function is just the main line peak of the spectrum. This results from the conversion of all of the energy of a given photon into a pulse that is then recorded by the pulse-height analysis (PHA) chain. In an ideal detector, all of the photons from a monochromatic source would appear in the main peak. The width of this peak is influenced by the following factors: (1) the statistical spread in the number of electrons created by a given energy photon, and (2) fluctuations in the number of leakage current electrons across the detector diode, as well as (3) noise electrons in the FET preamp front end. The first contribution which is termed as the Fano broadening, σ_f, is expressed by

$$\sigma_f = (F \cdot E_0 \cdot W)^{1/2} \tag{4.5}$$

where W is the average energy required to create a free electron-hole pair in the detector material ($\approx$ 3 eV for germanium), E_0 is the photon energy (peak center), and F is the Fano factor which

accounts for constrained limits on the number of electron-hole pairs that can be created. The last two contributions make up the electronic broadening, σ_e, which is energy independent. The full width of the peak at one-half of the maximum height is

$$FWHM = 2.355 \ (\sigma_f{}^2 + \sigma_e{}^2)^{1/2}. \tag{4.6}$$

The low energy tail represents the contributions of three effects: (1) incomplete charge collection in the detector due to recombination of charges and impurities that act as traps, (2) the escape of photoelectrons from the sensitive region near the surface, and (3) pulse pileup resulting from an "undershoot" condition of the amplifier pulses in the PHA chain. Each of these is described by an exponentially decaying distribution below the peak. The contributions of the first and second effects are similar since both cause incomplete charge collection. However, since the energy distribution of the photoelectrons that escape the surface is wider than those that are trapped or recombined in the active region, the contribution due to the second effect decays slower than that for the first effect. The third effect is count-rate dependent and occurs when the amplifier is over-damped so that after a pulse is processed, the amplifier baseline quickly restores itself to a level less than zero. A subsequent pulse rides on the tail of the first pulse. The output of the second is then lowered by the amount of the undershoot. The pulse is then placed in a bin in the multichannel analyzer that is lower in pulse height. Because the likelihood of a second pulse arriving during the undershoot increases with x-ray rate, the fraction of total counts in such a feature would increase with rate.

The high energy tail represents the pulse pileup resulting from an "overshoot" condition of the amplifier pulses. The overshoot occurs when the pole-zero cancellation in the amplifier is overcompensated, and thus the pulses do not return to the base line but overshoot. Consequently, when two pulses are close in time, one sits on the overshooting tail of the other and registers an amplitude in the multichannel analyzer that has a higher value than the true amplitude. This tail is described by an exponentail function decaying above the peak (the so called "falling" tail).

The pulse pileup for both undershoot and overshoot conditions, which is also called "tail pileup," would tend to be suppressed by the action of pileup rejection circuitry, which was used in our apparatus. However, we discovered that the pileup rejection did not function properly below about 2 keV, so pulse pileup is significant at those low energies. But, since the pole-zero cancellation circuitry was disabled on the amplifiers in our apparatus, the overshoot condition was not expected to be present in our measurements.

The flat shelf is due to energy losses resulting from the transmission of primary (photo- and Auger) electrons in the detector dead layer, contacts, and any other filters outside the detector active area (Scholze and Ulm, 1994). The photo- and Auger electrons produced by the photon interactions within these layers lose energy or escape the detector as they travel towards the detector active region. The result is a pulse-height lower than would normally be expected. This shelf extends from the main peak down to zero pulse height, and is not rate-dependent.

In the`JMKmod` software(Tsiang, 1997), the HYPERMET model described above is formulated in the Fourier space, where the Gaussian distribution is represented by a moment generating function, and the tail and shelf components are generated by the convolution of this moment generating function with an exponential function.

Plots of some of the response functions are shown in Figures 4.2and4.3. The first figure is a plot of the change in the response function across the Ge L_{III} edge. As can be seen, the shelf increases as the energy goes above the absorption edge. This is because more photons are being absorbed relatively close to the surface of the crystal and do not have a chance for the full charge to migrate into the active region.

The plots in Figure 4.3 show the spectral response functions of `ssd_5` and `ssd_x` detectors at 4.1 keV. These spectra, in addition to the prominent features of the main peak (a Gaussian, a

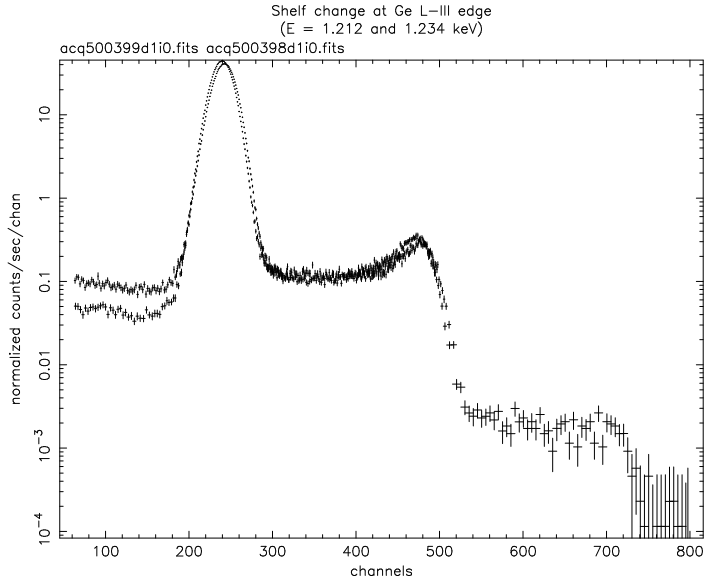

Figure 4.2: Response functions of ssd_5 on both sides of the Ge L_{III} edge.

low-energy tail, and shelf), display secondary features, such as, pileup, escape, and fluorescent peaks.

The escape peak is due to the escape of Ge-L x-rays from the detector. Ge-L and Al-K fluorescent peaks originate from the detector crystal material and the aluminum contact and filter material in the detector. The Si-K fluorescence is attributed to the Si crystals in the monochromator. The fluorescent peaks are located at fixed line energies in the spectrum, while the escape peak is always at a fixed separation below the main line peak energy.

Another aspect of the spectra is the smaller peak at twice the pulse height of the main peak. This peak can be a pileup peak, a second order photon peak from the monochromator, or a combination of both. When the energy for the monochromator is set above 2.9 keV, this smaller peak is all pileup because the optics in the beam line prohibit photons of energy beyond 5.9 keV from being introduced. The effects of pileup (rate-dependent) can also be separated from higher-order diffraction (rate-independent) by collecting spectra at different rates. Although the pileup rejection circuitry effectively eliminates pileup above 2 keV for count rates below 1000 Hz, it is unable to detect and reject the pileup events recorded at twice the pulse height of the main peak. Such pileup events involve pulses so close in time that cannot be detected by the pileup rejection circuit.

4.3.2 Interpeak Pileup

Another feature in the measured response function, as shown in Figure 4.3, is the events that occur between the main peak and the second order peak. These events arise from a pileup situation where the pileup rejection circuitry in the amplifier does not work correctly. We have called these events interpeak pileup.

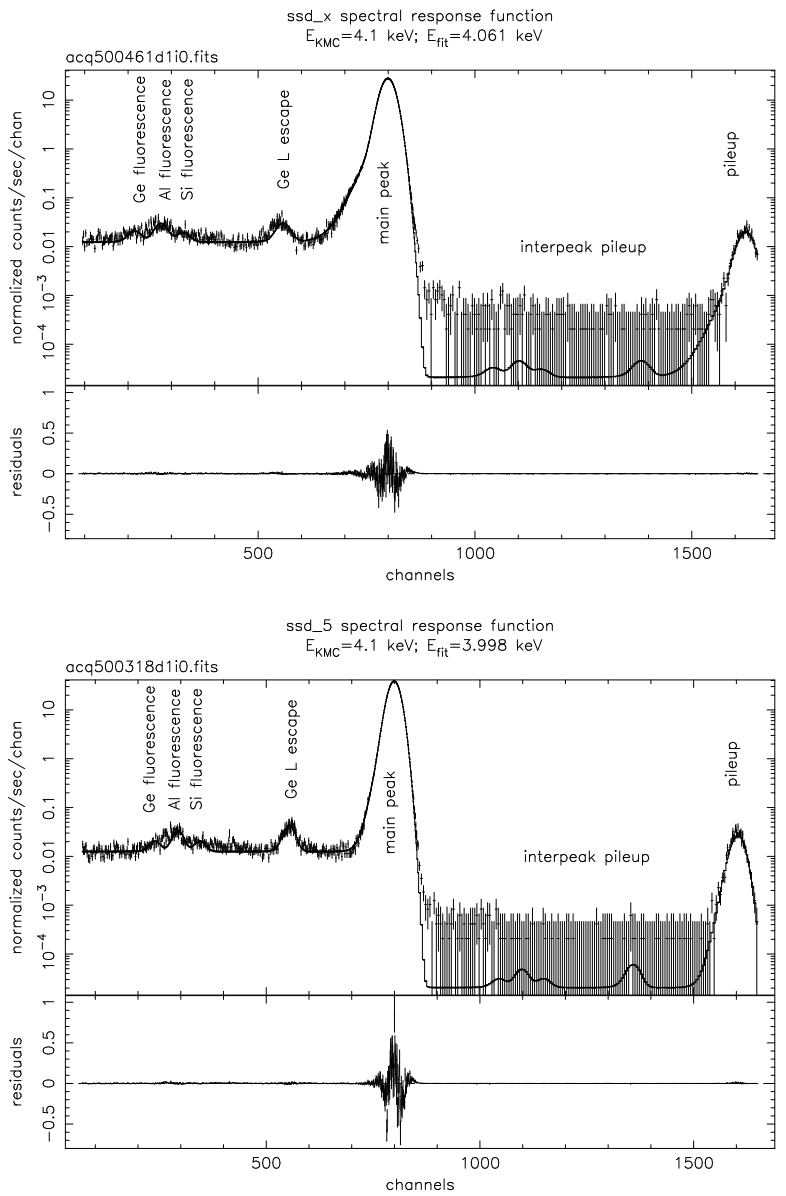

Figure 4.3: Response functions of ssd_x and ssd_5 at 4.1 keV.

The amplifier has two branches to it. The first is a fast discriminator circuit that determines whether there are piled up events. The second is the processing branch which amplifies and shapes the pulse from the pre-amplifier. The fast discriminator looks at the time difference between two pulses. If they are deemed to be too close in time such that the tail of one pulse might influence the height of another, this circuit sends a veto signal to the multichannel analyzer telling it not to count the forthcoming pulses. The method in which this circuit determines the temporal separation of two pulses is to use one pulse to turn on a clock, known as an inspection interval, and look for a second pulse to arrive while this clock is active. In order to activate the inspection interval, the pulse must be above a threshold voltage determined by the local amplifier noise. If the pulse is below this threshold, it can pass through the amplifier without triggering the inspection circuit. This allows pileup to occur. This pileup is not limited to the normal "twice-the-pulse-height" pileup that happens when the two pulses are so close in time that the rejection circuit cannot resolve them, but can fall anywhere from twice the pulse height down to the height of the largest pulse. For the HXDS SSDs, this situation occurs at energies below about 2 keV (40 mV preamplifier output). Analysis of such spectra is more complicated, and causes uncertainties.

4.4 Results of Fitting Response Function Spectra

The fitted response function includes a Gaussian, a low-energy tail, and a shelf component for the main line peak, as well as the same components for the escape and fluorescent lines. A sample of the XSPEC fits is shown in Figure 4.3. The high-energy tail component of the Hypermet function was not included in the fitted response function. Inclusion of such a tail improved the quality of the fits. However, the resulting values for the parameters of the tail suggested a tail pileup level as high as 20%, which is not possible for our 1000 Hz counting rate and 10 μs amplifier shaping time. Further, since the pole-zero cancellation circuit in our amplifiers was disabled, no significant overshoot condition for the amplifier pulse tails could be expected. (An amplifier without the pole-zero cancellation is usually over-damped, i.e., pulse tails undershoot.) The small amount of high energy tailing that can be seen in the pulse height spectra shown in Figure 4.3 is attributed to the interpeak pileup, which was not included in the fitted response function model. In our recorded spectra, the interpeak pileup was less than 0.2% for energies higher than 2 keV. However, for lower energies, it increased to values as high as 4% as the energy approached 0.4 keV and the pileup rejection circuitry became increasingly less effective.

The fitted response function parameters for both ssd_5 and ssd_x detectors in the energy range 0.4-5.9 keV are listed in Tables 4.1 – 4.4. The parameters for the energy range 0.4-1.7 keV are from fitting the spectra recorded at the SX700 beamline using a grating monochromator, and the parameters for the energy range 2.1-5.9 keV are from the spectra recorded at the KMC beamline using a silicon double crystal monochromator. Each row in the aforementioned tables shows the fitted parameters for a measured response function spectrum at a given x-ray energy, as identified by a "runid" and the monochromator energy setting E_{MC}. The listed parameters in these tables are: E_{fit}, the fitted line energy; t2norm, norm (area) of the low-energy tail; t2par, slope parameter of the low-energy tail; shelfnm, norm of the shelf; L2norm, norm of the Ge-L escape line; L3norm, norm of the Al-K fluorescent line; L4norm, norm of the Ge-L fluorescent line; and L5norm, norm of the Si-K fluorescent line. The tail and shelf norms are relative to the norm of the Gaussian component of the main line, and the escape and fluorescent line norms are relative to the norm of the main line (the sum of Gaussian, tail, and shelf norms).

The detector resolution parameters, the Fano factor and the electronic broadening (in channels), are shown in Table 4.5. As the value of these parameters show the ssd_5 has a better spectral

runid	E_{MC}	E_{fit} (keV)	t2norm	t2par	shelfnm
500504	0.400	0.404 ± 0.0000	4.0000 ± 0.0000	1.1400 ± 0.0000	0.0000 ± 0.0000
500508	0.450	0.454 ± 0.0000	4.0000 ± 0.0000	1.1040 ± 0.0000	0.0000 ± 0.0000
500510	0.500	0.505 ± 0.0000	4.0000 ± 0.0000	1.1230 ± 0.0044	0.0000 ± 0.0000
500505	0.538	0.538 ± 0.0000	4.0000 ± 0.0000	1.0940 ± 0.0026	0.0000 ± 0.0000
500507	0.548	0.555 ± 0.0000	4.0000 ± 0.0000	1.1060 ± 0.0016	0.0000 ± 0.0000
500509	0.600	0.610 ± 0.0000	4.0000 ± 0.0000	1.1020 ± 0.0009	0.0000 ± 0.0000
500511	0.700	0.705 ± 0.0000	1.0110 ± 0.1488	1.0940 ± 0.0035	0.0457 ± 0.0076
500512	0.800	0.803 ± 0.0000	0.4627 ± 0.0298	1.0780 ± 0.0018	0.0233 ± 0.0013
500513	0.900	0.902 ± 0.0000	0.3135 ± 0.0153	1.0710 ± 0.0013	0.0168 ± 0.0006
500524	1.000	1.000 ± 0.0000	0.2401 ± 0.0110	1.0670 ± 0.0012	0.0135 ± 0.0004
500523	1.100	1.100 ± 0.0000	0.1876 ± 0.0077	1.0610 ± 0.0010	0.0105 ± 0.0003
500522	1.200	1.200 ± 0.0000	0.1739 ± 0.0072	1.0610 ± 0.0010	0.0104 ± 0.0002
500521	1.212	1.212 ± 0.0000	0.1664 ± 0.0063	1.0580 ± 0.0009	0.0102 ± 0.0002
500520	1.234	1.231 ± 0.0000	0.7352 ± 0.0231	1.0600 ± 0.0005	0.0315 ± 0.0007
500519	1.300	1.300 ± 0.0000	2.5620 ± 0.1739	1.0570 ± 0.0003	0.1014 ± 0.0053
500518	1.400	1.400 ± 0.0000	1.9740 ± 0.0959	1.0520 ± 0.0003	0.0862 ± 0.0031
500514	1.500	1.503 ± 0.0000	1.9660 ± 0.0736	1.0480 ± 0.0002	0.0906 ± 0.0026
500545	1.555	1.555 ± 0.0000	1.7530 ± 0.0592	1.0480 ± 0.0002	0.0816 ± 0.0021
500548	1.560	1.559 ± 0.0000	1.6530 ± 0.0532	1.0480 ± 0.0002	0.0834 ± 0.0020
500541	1.570	1.571 ± 0.0000	1.9560 ± 0.0834	1.0480 ± 0.0002	0.1443 ± 0.0045
500540	1.575	1.575 ± 0.0000	1.7110 ± 0.0631	1.0480 ± 0.0002	0.1292 ± 0.0035
500539	1.580	1.581 ± 0.0000	1.8940 ± 0.0720	1.0480 ± 0.0002	0.1287 ± 0.0036
500537	1.590	1.590 ± 0.0000	1.6100 ± 0.0507	1.0480 ± 0.0002	0.1046 ± 0.0024
500533	1.600	1.602 ± 0.0000	1.8160 ± 0.0648	1.0480 ± 0.0002	0.1270 ± 0.0034
500534	1.605	1.606 ± 0.0000	1.6150 ± 0.0514	1.0470 ± 0.0002	0.1133 ± 0.0026
500535	1.610	1.610 ± 0.0000	1.5530 ± 0.0481	1.0470 ± 0.0002	0.1097 ± 0.0025
500536	1.630	1.629 ± 0.0000	1.4050 ± 0.0389	1.0460 ± 0.0002	0.0974 ± 0.0020
500544	1.650	1.648 ± 0.0000	1.3230 ± 0.0364	1.0460 ± 0.0002	0.0973 ± 0.0019
500530	1.700	1.698 ± 0.0000	1.1270 ± 0.0267	1.0440 ± 0.0002	0.0866 ± 0.0015
500231	2.100	2.132 ± 0.0000	0.6339 ± 0.0162	1.0390 ± 0.0002	0.0344 ± 0.0009
500233	2.300	2.323 ± 0.0000	0.5092 ± 0.0123	1.0390 ± 0.0002	0.0315 ± 0.0007
500239	2.500	2.516 ± 0.0000	0.3965 ± 0.0076	1.0370 ± 0.0002	0.0226 ± 0.0004
500235	2.700	2.708 ± 0.0000	0.3230 ± 0.0060	1.0360 ± 0.0002	0.0217 ± 0.0004
500238	2.900	2.902 ± 0.0000	0.2599 ± 0.0046	1.0340 ± 0.0002	0.0179 ± 0.0003
500240	3.100	3.095 ± 0.0000	0.2180 ± 0.0038	1.0330 ± 0.0002	0.0153 ± 0.0003
500241	3.300	3.289 ± 0.0000	0.1825 ± 0.0030	1.0320 ± 0.0002	0.0147 ± 0.0002
500242	3.500	3.483 ± 0.0000	0.1598 ± 0.0026	1.0310 ± 0.0002	0.0132 ± 0.0002
500243	3.700	3.676 ± 0.0000	0.1379 ± 0.0023	1.0300 ± 0.0002	0.0116 ± 0.0002
500244	3.900	3.869 ± 0.0000	0.1191 ± 0.0020	1.0290 ± 0.0002	0.0106 ± 0.0002
500245	4.100	4.063 ± 0.0000	0.1124 ± 0.0019	1.0290 ± 0.0002	0.0100 ± 0.0002
500247	4.300	4.256 ± 0.0000	0.0977 ± 0.0017	1.0280 ± 0.0002	0.0095 ± 0.0002
500249	4.700	4.640 ± 0.0000	0.0789 ± 0.0015	1.0280 ± 0.0002	0.0087 ± 0.0002
500250	5.100	5.026 ± 0.0000	0.0636 ± 0.0013	1.0270 ± 0.0003	0.0074 ± 0.0001
500251	5.500	5.410 ± 0.0000	0.0516 ± 0.0011	1.0260 ± 0.0003	0.0067 ± 0.0001
500252	5.900	5.786 ± 0.0000	0.0447 ± 0.0010	1.0260 ± 0.0003	0.0061 ± 0.0001

Table 4.1: Fitted energy, rising (low-energy) tail and shelf parameters for ssd_x.

runid	E_{MC}	L2norm	L3norm	L4norm	L5norm
500504	0.400	0.0000 ± 0.0000	0.0000 ± 0.0000	0.0000 ± 0.0000	0.0000 ± 0.0000
500508	0.450	0.0000 ± 0.0000	0.0000 ± 0.0000	0.0000 ± 0.0000	0.0000 ± 0.0000
500510	0.500	0.0000 ± 0.0000	0.0000 ± 0.0000	0.0000 ± 0.0000	0.0000 ± 0.0000
500505	0.538	0.0000 ± 0.0000	0.0000 ± 0.0000	0.0000 ± 0.0000	0.0000 ± 0.0000
500507	0.548	0.0000 ± 0.0000	0.0000 ± 0.0000	0.0000 ± 0.0000	0.0000 ± 0.0000
500509	0.600	0.0000 ± 0.0000	0.0000 ± 0.0000	0.0000 ± 0.0000	0.0000 ± 0.0000
500511	0.700	0.0000 ± 0.0000	0.0000 ± 0.0000	0.0000 ± 0.0000	0.0000 ± 0.0000
500512	0.800	0.0000 ± 0.0000	0.0000 ± 0.0000	0.0000 ± 0.0000	0.0000 ± 0.0000
500513	0.900	0.0000 ± 0.0000	0.0000 ± 0.0000	0.0000 ± 0.0000	0.0000 ± 0.0000
500524	1.000	0.0000 ± 0.0000	0.0000 ± 0.0000	0.0000 ± 0.0000	0.0000 ± 0.0000
500523	1.100	0.0000 ± 0.0000	0.0000 ± 0.0000	0.0000 ± 0.0000	0.0000 ± 0.0000
500522	1.200	0.0000 ± 0.0000	0.0000 ± 0.0000	0.0000 ± 0.0000	0.0000 ± 0.0000
500521	1.212	0.0000 ± 0.0000	0.0000 ± 0.0000	0.0000 ± 0.0000	0.0000 ± 0.0000
500520	1.234	0.0000 ± 0.0000	0.0000 ± 0.0000	0.0000 ± 0.0000	0.0000 ± 0.0000
500519	1.300	0.0000 ± 0.0000	0.0000 ± 0.0000	0.0000 ± 0.0000	0.0000 ± 0.0000
500518	1.400	0.0000 ± 0.0000	0.0000 ± 0.0000	0.0000 ± 0.0000	0.0000 ± 0.0000
500514	1.500	0.0062 ± 0.0022	0.0000 ± 0.0000	0.0000 ± 0.0000	0.0000 ± 0.0000
500545	1.555	0.0055 ± 0.0004	0.0000 ± 0.0000	0.0000 ± 0.0000	0.0000 ± 0.0000
500548	1.560	0.0053 ± 0.0004	0.0000 ± 0.0000	0.0000 ± 0.0000	0.0000 ± 0.0000
500541	1.570	0.0055 ± 0.0005	0.0000 ± 0.0000	0.0000 ± 0.0000	0.0000 ± 0.0000
500540	1.575	0.0045 ± 0.0005	0.0000 ± 0.0000	0.0000 ± 0.0000	0.0000 ± 0.0000
500539	1.580	0.0043 ± 0.0004	0.0000 ± 0.0000	0.0000 ± 0.0000	0.0000 ± 0.0000
500537	1.590	0.0039 ± 0.0004	0.0000 ± 0.0000	0.0000 ± 0.0000	0.0000 ± 0.0000
500533	1.600	0.0038 ± 0.0003	0.0000 ± 0.0000	0.0000 ± 0.0000	0.0000 ± 0.0000
500534	1.605	0.0039 ± 0.0003	0.0000 ± 0.0000	0.0000 ± 0.0000	0.0000 ± 0.0000
500535	1.610	0.0039 ± 0.0003	0.0000 ± 0.0000	0.0000 ± 0.0000	0.0000 ± 0.0000
500536	1.630	0.0038 ± 0.0002	0.0000 ± 0.0000	0.0000 ± 0.0000	0.0000 ± 0.0000
500544	1.650	0.0035 ± 0.0002	0.0000 ± 0.0000	0.0000 ± 0.0000	0.0000 ± 0.0000
500530	1.700	0.0030 ± 0.0002	0.0000 ± 0.0000	0.0000 ± 0.0000	0.0000 ± 0.0000
500231	2.100	0.0030 ± 0.0002	0.0014 ± 0.0002	0.0020 ± 0.0002	0.0000 ± 0.0000
500233	2.300	0.0027 ± 0.0002	0.0004 ± 0.0003	0.0015 ± 0.0001	0.0000 ± 0.0000
500239	2.500	0.0027 ± 0.0001	0.0005 ± 0.0001	0.0011 ± 0.0001	0.0003 ± 0.0001
500235	2.700	0.0020 ± 0.0004	0.0003 ± 0.0001	0.0011 ± 0.0002	0.0000 ± 0.0000
500238	2.900	0.0017 ± 0.0001	0.0003 ± 0.0001	0.0009 ± 0.0001	0.0000 ± 0.0000
500240	3.100	0.0011 ± 0.0001	0.0004 ± 0.0001	0.0006 ± 0.0001	0.0005 ± 0.0001
500241	3.300	0.0010 ± 0.0001	0.0004 ± 0.0001	0.0006 ± 0.0001	0.0000 ± 0.0000
500242	3.500	0.0009 ± 0.0001	0.0004 ± 0.0001	0.0007 ± 0.0001	0.0000 ± 0.0000
500243	3.700	0.0008 ± 0.0001	0.0003 ± 0.0001	0.0006 ± 0.0001	0.0003 ± 0.0001
500244	3.900	0.0007 ± 0.0001	0.0003 ± 0.0001	0.0006 ± 0.0001	0.0003 ± 0.0001
500245	4.100	0.0006 ± 0.0001	0.0003 ± 0.0001	0.0006 ± 0.0001	0.0002 ± 0.0001
500247	4.300	0.0005 ± 0.0001	0.0003 ± 0.0001	0.0005 ± 0.0001	0.0003 ± 0.0001
500249	4.700	0.0004 ± 0.0001	0.0002 ± 0.0001	0.0004 ± 0.0001	0.0002 ± 0.0001
500250	5.100	0.0003 ± 0.0001	0.0001 ± 0.0000	0.0004 ± 0.0001	0.0003 ± 0.0000
500251	5.500	0.0002 ± 0.0000	0.0001 ± 0.0000	0.0005 ± 0.0001	0.0005 ± 0.0001
500252	5.900	0.0002 ± 0.0000	0.0001 ± 0.0000	0.0004 ± 0.0000	0.0004 ± 0.0000

Table 4.2: Fitted escape and fluorescent line parameters for ssd_x.

runid	E_{MC}	E_{fit} (keV)	t2norm	t2par	shelfnm
500379	0.400	0.398 ± 0.0000	0.0000 ± 0.0000	1.0020 ± 0.0000	0.0000 ± 0.0000
500354	0.450	0.446 ± 0.0000	0.0000 ± 0.0000	1.0020 ± 0.0000	0.0000 ± 0.0000
500357	0.500	0.498 ± 0.0000	0.0000 ± 0.0000	1.0020 ± 0.0000	0.0000 ± 0.0000
500394	0.548	0.547 ± 0.0000	0.0308 ± 0.0000	1.0020 ± 0.0000	0.0000 ± 0.0000
500358	0.600	0.599 ± 0.0000	0.0254 ± 0.0006	1.0120 ± 0.0031	0.0000 ± 0.0000
500362	0.700	0.699 ± 0.0000	0.0205 ± 0.0056	1.0180 ± 0.0083	0.0000 ± 0.0188
500363	0.800	0.801 ± 0.0000	0.0105 ± 0.0009	1.0270 ± 0.0061	0.0097 ± 0.0014
500396	0.900	0.902 ± 0.0000	0.0153 ± 0.0030	1.0600 ± 0.0070	0.0110 ± 0.0003
500366	1.000	1.002 ± 0.0000	0.0233 ± 0.0034	1.0640 ± 0.0050	0.0091 ± 0.0002
500368	1.100	1.103 ± 0.0000	0.0276 ± 0.0034	1.0630 ± 0.0040	0.0080 ± 0.0002
500401	1.200	1.204 ± 0.0000	0.0335 ± 0.0030	1.0600 ± 0.0026	0.0075 ± 0.0002
500399	1.212	1.216 ± 0.0000	0.0347 ± 0.0031	1.0620 ± 0.0026	0.0074 ± 0.0001
500398	1.234	1.233 ± 0.0000	0.2224 ± 0.0121	1.0880 ± 0.0018	0.0195 ± 0.0003
500397	1.400	1.398 ± 0.0000	0.5291 ± 0.0220	1.0840 ± 0.0010	0.0391 ± 0.0007
500395	1.500	1.497 ± 0.0000	0.4726 ± 0.0169	1.0740 ± 0.0008	0.0397 ± 0.0006
500393	1.555	1.556 ± 0.0000	0.7628 ± 0.0370	1.0870 ± 0.0009	0.0441 ± 0.0011
500391	1.560	1.561 ± 0.0000	0.7812 ± 0.0413	1.0880 ± 0.0010	0.0469 ± 0.0012
500390	1.570	1.574 ± 0.0000	1.0610 ± 0.0679	1.0880 ± 0.0010	0.0838 ± 0.0030
500389	1.575	1.579 ± 0.0000	0.9983 ± 0.0557	1.0850 ± 0.0009	0.0774 ± 0.0023
500388	1.580	1.583 ± 0.0000	0.9487 ± 0.0531	1.0860 ± 0.0009	0.0724 ± 0.0022
500387	1.590	1.592 ± 0.0000	0.8038 ± 0.0415	1.0850 ± 0.0009	0.0590 ± 0.0015
500386	1.600	1.603 ± 0.0000	0.7713 ± 0.0358	1.0810 ± 0.0009	0.0626 ± 0.0015
500385	1.605	1.608 ± 0.0000	0.8068 ± 0.0405	1.0830 ± 0.0009	0.0630 ± 0.0016
500384	1.610	1.613 ± 0.0000	0.7666 ± 0.0375	1.0810 ± 0.0009	0.0610 ± 0.0015
500383	1.630	1.632 ± 0.0000	0.6993 ± 0.0318	1.0790 ± 0.0009	0.0567 ± 0.0013
500382	1.650	1.652 ± 0.0000	0.6415 ± 0.0221	1.0750 ± 0.0007	0.0551 ± 0.0009
500381	1.700	1.700 ± 0.0000	0.4257 ± 0.0118	1.0650 ± 0.0006	0.0462 ± 0.0006
500331	2.100	2.103 ± 0.0000	1.0120 ± 0.0926	1.0780 ± 0.0007	0.0333 ± 0.0017
500330	2.300	2.290 ± 0.0000	0.7967 ± 0.0572	1.0750 ± 0.0007	0.0257 ± 0.0009
500329	2.500	2.478 ± 0.0000	0.5816 ± 0.0334	1.0730 ± 0.0007	0.0199 ± 0.0005
500328	2.700	2.667 ± 0.0000	0.5074 ± 0.0287	1.0710 ± 0.0007	0.0184 ± 0.0005
500327	2.900	2.857 ± 0.0000	0.4370 ± 0.0231	1.0700 ± 0.0008	0.0167 ± 0.0004
500324	3.100	3.047 ± 0.0000	0.3696 ± 0.0176	1.0680 ± 0.0007	0.0146 ± 0.0003
500323	3.300	3.238 ± 0.0000	0.2731 ± 0.0131	1.0650 ± 0.0008	0.0123 ± 0.0002
500322	3.500	3.428 ± 0.0000	0.2867 ± 0.0136	1.0650 ± 0.0008	0.0121 ± 0.0002
500318	4.100	3.998 ± 0.0000	0.1998 ± 0.0086	1.0630 ± 0.0007	0.0092 ± 0.0001
500316	4.300	4.188 ± 0.0000	0.2104 ± 0.0104	1.0650 ± 0.0009	0.0090 ± 0.0002
500315	4.500	4.377 ± 0.0000	0.1725 ± 0.0092	1.0630 ± 0.0010	0.0077 ± 0.0001
500314	4.700	4.566 ± 0.0000	0.1433 ± 0.0071	1.0610 ± 0.0009	0.0074 ± 0.0001
500313	4.900	4.756 ± 0.0000	0.1472 ± 0.0077	1.0610 ± 0.0010	0.0075 ± 0.0001
500311	5.300	5.134 ± 0.0000	0.1346 ± 0.0079	1.0630 ± 0.0011	0.0066 ± 0.0001
500310	5.500	5.322 ± 0.0000	0.1279 ± 0.0076	1.0610 ± 0.0011	0.0062 ± 0.0001
500309	5.700	5.509 ± 0.0000	0.1157 ± 0.0072	1.0600 ± 0.0012	0.0053 ± 0.0001
500308	5.900	5.697 ± 0.0000	0.1013 ± 0.0063	1.0590 ± 0.0012	0.0055 ± 0.0001

Table 4.3: Fitted energy, rising (low-energy) tail and shelf parameters for ssd_5.

runid	E_{MC}	L2norm	L3norm	L4norm	L5norm
500379	0.400	0.0000 ± 0.0000	0.0000 ± 0.0000	0.0000 ± 0.0000	0.0000 ± 0.0000
500354	0.450	0.0000 ± 0.0000	0.0000 ± 0.0000	0.0000 ± 0.0000	0.0000 ± 0.0000
500357	0.500	0.0000 ± 0.0000	0.0000 ± 0.0000	0.0000 ± 0.0000	0.0000 ± 0.0000
500394	0.548	0.0000 ± 0.0000	0.0000 ± 0.0000	0.0000 ± 0.0000	0.0000 ± 0.0000
500358	0.600	0.0000 ± 0.0000	0.0000 ± 0.0000	0.0000 ± 0.0000	0.0000 ± 0.0000
500362	0.700	0.0000 ± 0.0000	0.0000 ± 0.0000	0.0000 ± 0.0000	0.0000 ± 0.0000
500363	0.800	0.0000 ± 0.0000	0.0000 ± 0.0000	0.0000 ± 0.0000	0.0000 ± 0.0000
500396	0.900	0.0000 ± 0.0000	0.0000 ± 0.0000	0.0000 ± 0.0000	0.0000 ± 0.0000
500366	1.000	0.0000 ± 0.0000	0.0000 ± 0.0000	0.0000 ± 0.0000	0.0000 ± 0.0000
500368	1.100	0.0000 ± 0.0000	0.0000 ± 0.0000	0.0000 ± 0.0000	0.0000 ± 0.0000
500401	1.200	0.0000 ± 0.0000	0.0000 ± 0.0000	0.0000 ± 0.0000	0.0000 ± 0.0000
500399	1.212	0.0000 ± 0.0000	0.0000 ± 0.0000	0.0000 ± 0.0000	0.0000 ± 0.0000
500398	1.234	0.0000 ± 0.0000	0.0000 ± 0.0000	0.0000 ± 0.0000	0.0000 ± 0.0000
500397	1.400	0.0000 ± 0.0000	0.0000 ± 0.0000	0.0000 ± 0.0000	0.0000 ± 0.0000
500395	1.500	0.0039 ± 0.0007	0.0000 ± 0.0000	0.0000 ± 0.0000	0.0000 ± 0.0000
500393	1.555	0.0033 ± 0.0003	0.0000 ± 0.0000	0.0000 ± 0.0000	0.0000 ± 0.0000
500391	1.560	0.0033 ± 0.0003	0.0000 ± 0.0000	0.0000 ± 0.0000	0.0000 ± 0.0000
500390	1.570	0.0032 ± 0.0003	0.0000 ± 0.0000	0.0000 ± 0.0000	0.0000 ± 0.0000
500389	1.575	0.0032 ± 0.0003	0.0000 ± 0.0000	0.0000 ± 0.0000	0.0000 ± 0.0000
500388	1.580	0.0033 ± 0.0003	0.0000 ± 0.0000	0.0000 ± 0.0000	0.0000 ± 0.0000
500387	1.590	0.0029 ± 0.0002	0.0000 ± 0.0000	0.0000 ± 0.0000	0.0000 ± 0.0000
500386	1.600	0.0030 ± 0.0002	0.0000 ± 0.0000	0.0000 ± 0.0000	0.0000 ± 0.0000
500385	1.605	0.0029 ± 0.0002	0.0000 ± 0.0000	0.0000 ± 0.0000	0.0000 ± 0.0000
500384	1.610	0.0027 ± 0.0002	0.0000 ± 0.0000	0.0000 ± 0.0000	0.0000 ± 0.0000
500383	1.630	0.0026 ± 0.0002	0.0000 ± 0.0000	0.0000 ± 0.0000	0.0000 ± 0.0000
500382	1.650	0.0028 ± 0.0002	0.0000 ± 0.0000	0.0000 ± 0.0000	0.0000 ± 0.0000
500381	1.700	0.0023 ± 0.0002	0.0000 ± 0.0000	0.0000 ± 0.0000	0.0000 ± 0.0000
500331	2.100	0.0028 ± 0.0001	0.0011 ± 0.0001	0.0022 ± 0.0001	0.0000 ± 0.0000
500330	2.300	0.0020 ± 0.0002	0.0009 ± 0.0001	0.0018 ± 0.0001	0.0002 ± 0.0001
500329	2.500	0.0024 ± 0.0001	0.0002 ± 0.0001	0.0016 ± 0.0001	0.0004 ± 0.0001
500328	2.700	0.0017 ± 0.0001	0.0001 ± 0.0001	0.0012 ± 0.0000	0.0004 ± 0.0001
500327	2.900	0.0015 ± 0.0001	0.0002 ± 0.0001	0.0009 ± 0.0001	0.0003 ± 0.0001
500324	3.100	0.0014 ± 0.0001	0.0002 ± 0.0001	0.0008 ± 0.0001	0.0002 ± 0.0001
500323	3.300	0.0011 ± 0.0001	0.0002 ± 0.0001	0.0006 ± 0.0001	0.0000 ± 0.0000
500322	3.500	0.0011 ± 0.0001	0.0002 ± 0.0001	0.0006 ± 0.0001	0.0000 ± 0.0000
500318	4.100	0.0007 ± 0.0001	0.0002 ± 0.0000	0.0005 ± 0.0001	0.0002 ± 0.0000
500316	4.300	0.0006 ± 0.0001	0.0002 ± 0.0000	0.0005 ± 0.0001	0.0002 ± 0.0000
500315	4.500	0.0006 ± 0.0001	0.0001 ± 0.0000	0.0004 ± 0.0001	0.0002 ± 0.0000
500314	4.700	0.0005 ± 0.0001	0.0001 ± 0.0000	0.0004 ± 0.0000	0.0002 ± 0.0000
500313	4.900	0.0004 ± 0.0001	0.0001 ± 0.0000	0.0003 ± 0.0000	0.0002 ± 0.0000
500311	5.300	0.0003 ± 0.0000	0.0001 ± 0.0000	0.0003 ± 0.0000	0.0001 ± 0.0000
500310	5.500	0.0004 ± 0.0000	0.0001 ± 0.0000	0.0002 ± 0.0000	0.0002 ± 0.0000
500309	5.700	0.0003 ± 0.0000	0.0000 ± 0.0000	0.0002 ± 0.0000	0.0001 ± 0.0000
500308	5.900	0.0003 ± 0.0000	0.0000 ± 0.0000	0.0002 ± 0.0000	0.0001 ± 0.0000

Table 4.4: Fitted escape and fluorescent line parameters for ssd_5.

phase	detector	fano	broad (chan)
sx700	ssd_5	0.1140	11.87
sx700	ssd_x	0.1450	14.20
kmc	ssd_5	0.1140	10.92
kmc	ssd_x	0.1450	13.23

Table 4.5: Detector resolution parameters: Fano factor and electronic broadening.

resolution than ssd_x, i.e., a narrower electronic broadening and smaller Fano factor. The higher values of electronic broadening for ssd_x are most likely due to a higher leakage current on the crystal surface for this detector, as it was subjected to possible surface contamination while undergoing several repairs. The Fano factor of 0.114 for ssd_5 is consistent with values reported by Knoll (1989) for germanium. The Fano factor for ssd_x, 0.145, is a little larger than expected. This is surprising considering the two crystals were presumably cut from the same boule and should have similar bulk properties. However, the result is undeniable: ssd_x has poorer energy resolution than ssd_5.

Determination of the Fano and the electronic broadening values was one of the most challenging part of the fitting procedure. We initially fit the spectra recorded at the KMC beamline for x-ray energies higher than 3 keV, where the peak pileup located at twice the main-peak pulse-height is a purely pileup peak, free of higher order photon peaks from the monochromator. The width of these pileup peaks is a sum in quadrature of two Fano broadening, σ_f, terms and one electronic broadening, σ_e, term. Whereas, the width of the main line peak is the quadratic sum of only one Fano broadening term and one electronic broadening term. This difference in width made it possible to get good starting values for the Fano factor and the electronic broadening. Then, using these starting values and keeping the Fano factor fixed, all the KMC spectra (in the energy range 2.1-5.9 keV) for each detector were fitted while the electronic broadening parameter was allowed to float. Once the series of spectra were fitted, the trend of the electronic broadening parameter could be plotted as a function of energy. If the Fano factor and the electronic broadening were correct, there would be no energy dependence on the broad parameter. If there were an energy dependence on the broad parameter, then a subsequent change in the Fano factor could be estimated. After several iterations, the Fano factor could be determined. The value of the Fano factor determined by this procedure was then used as a known value for fitting the spectra recorded at the SX700 beamline (in the energy range 0.4-1.7 keV). The electronic broadening values listed in Table 4.5 are the average values for each set of measurements, calculated from the energy-independent values (from the final iteration that showed no energy dependence trend for the electronic broadening).

The energy scale for the ssd_5 detector was obtained from a built-in radioactive source, consisting of an Fe target excited by a ^{244}Cm α-emitter, which was located on the aperture wheel. The pulse height spectra of radiation from this source were recorded at different times during the course of data recording at the KMC, X700, and 12-20 beamlines for energy calibration as well as for monitoring the possible build-up of ice on the detector surface (as the detector crystal is cooled down to liquid nitrogen temperature, it acts as a cold trap). Figure 4.4 shows the pulse-height spectrum of the radiation from this built-in source. The peak positions of the following lines were fitted to determine the energy scale parameters: Fe Lα and Lβ lines (at 0.7050 and 0.7185 keV), Al Kα lines (1.4866 keV), Ge escape lines at 4.392 and 4.423 keV, Cr Kα lines (at 5.4055 and 5.4147 keV), Fe Kα lines (at 6.3908 and 6.4038 keV), Fe Kβ lines (at 7.05798 keV), Ge escape lines at 8.407 and 8.438 keV, Pu Lα lines (at 14.2786 and 14.0842 keV), and Pu Lβ_2 line (at 17.2553 keV). The following intensity-ratio constraints were used to facilitate the fitting: $FeL\beta/FeL\alpha = 0.225$,

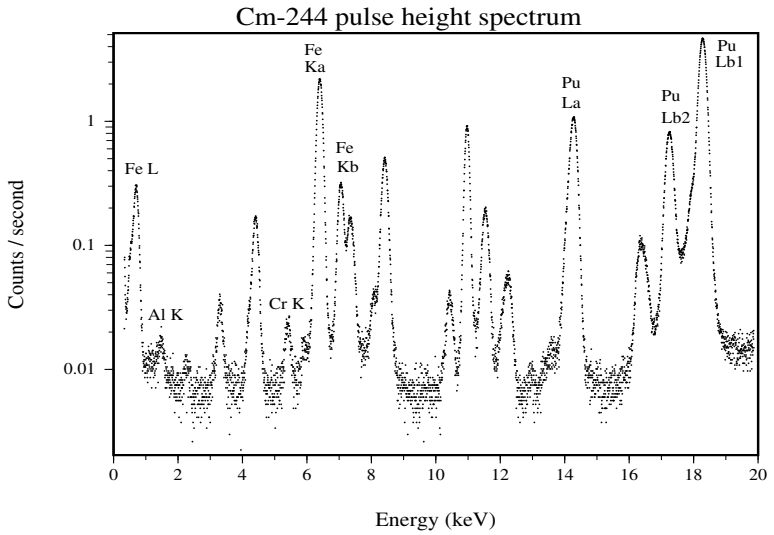

Figure 4.4: The pulse-height spectrum of radiation from an Fe target excited by a ^{244}Cm α-emitter.

$CrK\alpha_2/CrK\alpha_1 = 0.500$, $FeK\alpha_2/FeK\alpha_1 = 0.500$, and $PuL\alpha_2/PuL\alpha_1 = 0.100$. These ratios include the effects of 2 micron of ice, 2 micron of Parylene, and 0.3 micron of aluminum filters.

Determination of the energy scale parameters for the ssd_x proved to be more challenging since there was no built-in radioactive source in this detector. The energy scale for the specra recorded at the KMC beamline were determined from the known spectral features such as Ge escape and fluorescence, Al fluorescence, and the peak pileup. Since the peak pileup is at twice the pulse height (but not necessarily twice the channel number) of the main line, it was possible to determine the channel offset (zero point of the energy scale) from the channel locations of the main peak and the pileup peak. The peak locations of the escape and fluorescent lines helped in determining the gain parameter of the scale. For the spectra recorded at the SX700 beamline, the spectral features mentioned above could not be used to determine the energy scale. In this case, those features were either much weaker or overlapping with other features in the spectra. However, since the energy scale of the SX700 grating monochromator was calibrated by PTB to within ± 2 eV), we used the energy settings of this monochromator as the energy standards in our fits.

The fitted energy scale parameters, gain and channel offset (choff) for both detectors are summarized in Table 4.6. The channel offset values in this table are the average values of the fitted values for each set of measurement. The channel offset is nearly constant for each set. The energy scales for the ssd_5 are valid for the entire energy range of the white light spectra. The estimated energy uncertainty for this energy range (i.e. 0.4-10 keV) is ± 5 eV. This uncertainty is mostly due to the the uncertainty in the energy offset which is more influenced by the low-energy peaks in the ^{244}Cm spectra. The uncertainty in the energy gain is much smaller. For the ssd_x detector, however, the given energy scales have an uncertainty of ± 8 eV for the energy range 0.4-1.7 keV.

phase	dates	detector	gain (chan/pair)	choff (chan)
D	961230−970126	ssd_5	0.5914	−12.02
D	961230−970126	ssd_x	0.6039	−12.92
E	970128−970211	ssd_5	0.5905	−10.31
E	970128−970211	ssd_x	0.6119	−12.78
J	970618−970626	ssd_5	0.5965	−10.84
J	970618−970626	ssd_x	0.6211	−12.84
kmc	971013−971017	ssd_5	0.6052	−8.19
kmc	971013−971017	ssd_x	0.6100	−27.85
sx700	971020−971026	ssd_5	0.6048	−7.09
sx700	971020−971026	ssd_x	0.6161	−26.13
12-20	971020−971026	ssd_5	0.6050	−6.65

Table 4.6: Energy scale parameters for each phase of SSD use.

The uncertainty for higher energies are much higher and increases with energy. This is due to the fact that for this detector, as stated above, there were no energy calibration standards for energies higher than 1.7 keV, and it was, further, not possible to get a unique set of values for the gain and channel offset parameters in the 0.4-1.7 KeV range, where the energy settings of the SX700 grating monochromator were used as calibration standards. The difference between monochromator energy settings and the corresponding fitted energy values for the main line for both detectors are shown in Figure 4.5. The upper panel is for the measurements with the SX700 grating monochromator, and the lower panel is for measurements with the KMC Si double crystal monochromator, which has much less accurate energy scale than the grating monochromator.

Plots of the response function parameters for the low-energy tail and shelf as well as the escape and fluorescent lines as a function of energy for both detectors are shown in Figures 4.6–4.8. The upper panel in Figure 4.6 shows the tail norm (counts in the tail) relative to the total number of counts in the main peak, and the lower panel shows the tail slope parameter. As can be seen in this figure, for energies higher than 2 keV, the ssd_5 detector has a slightly larger, but faster decaying (sharper), tail contribution than ssd_x. The energy dependence of the tails for both detectors in this energy range agree qualitatively with the energy dependence of Ge atomic photo-absorption cross section. However, at lower energies the the energy dependence of the tail for ssd_5 is drastically different from that of ssd_x. Both tails drop sharply at the Ge-L edge. Below the Ge edge, the ssd_x tail rises in agreement with the Ge absorption cross section, but the ssd_5 tail decreases to even lower values. Both tails have structures at the Al-K edge, showing the contribution of the Al layers on the detector crystal and the radiation shield. There is a sharp drop in the tail norm for ssd_5 in the energy range 1.75-1.85 KeV, located in the energy region separating the KMC measurements (with the Si crystal) from the SX700 measurements. This feature is not present in the ssd_x tail. Since both detectors have identical filters and contact material, we first suspected this feature to be due to a change in the detector electronics, when switching from the KMC beamline to the SX700 beamline. However, by inspecting the width of the pulser peak in all the spectra recorded at both beamlines, we have ruled out such a possibility. Further, the analysis of another set of measurements, in the energy range 1.7-5.1 keV, which were taken prior to the measurements with the Si monochromator, produced the same tail behavior. The four data points in the energy range 1.7-2.1 keV for the ssd_5 detector in Figure 4.6 are from the data taken by the InSb monochromator.

The low-energy tails for both detectors have some small tail-pileup contributions. This was

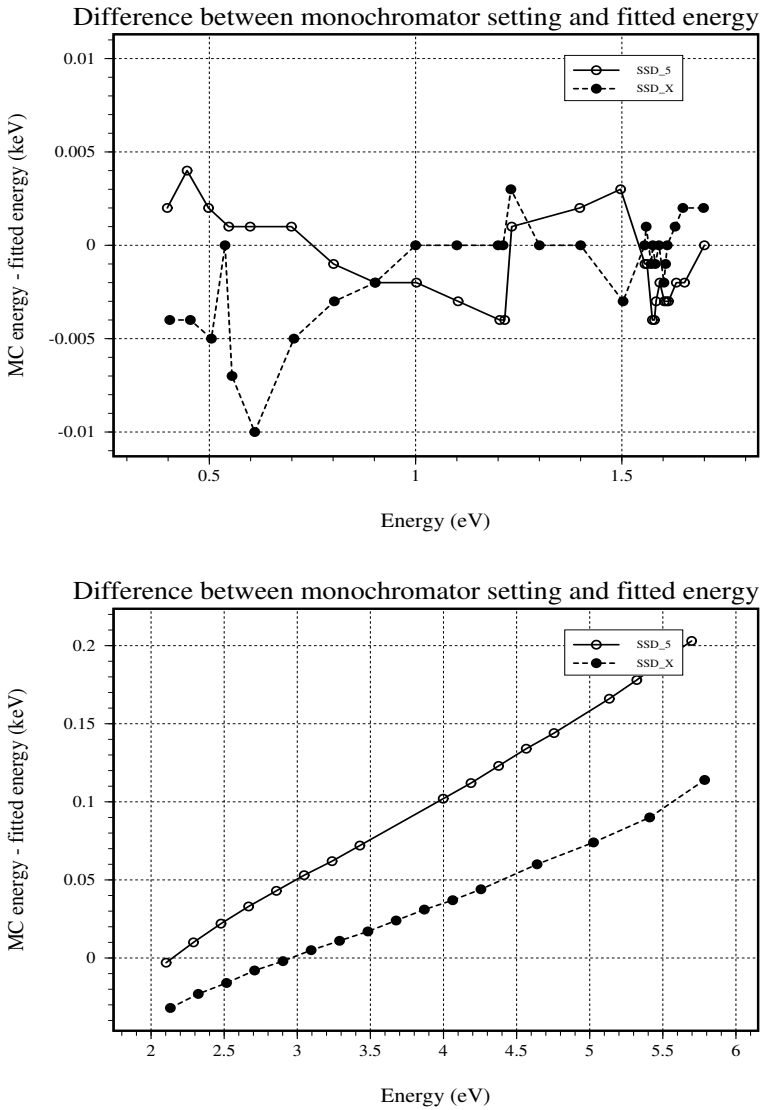

Figure 4.5: The difference between the monochromator energy setting and the fitted energy.

discovered by checking the pulser peak in the spectra. The pulser peak in all the spectra, except for ssd_5 spectra taken at SX700, show some low-energy tailing. This kind of tailing in the pulser peak is an indication of the presence of tail pileup.

Figure 4.7 shows the shelf norm (counts in the shelf) relative to the total number of counts in the main peak for both detectors. As is seen in this figure, for energies above 0.8 keV, both detectors have the same general trend for the energy dependence of the shelf. This trend is in agreement with the model calculation of Kraft et al. (1997), which is based on the calculation of energy losses for the transmission of photo- and Auger electrons through the detector dead layer and contact material. For energies below 0.8 keV, the shelf for the ssd_5 detector decreases, while the shelf for ssd_x increases in agreement with the calculation of Kraft et al. (1997). The disagreement between the two detectors at lower energies in this case, as well as in the case for the low-energy tail, as discussed above, might be related to the fact that at these low energies the detector noise partially masks the tail and shelf features in this part of the pulse-height spectra, and consequently the response-function model does not fit the data well. This can be seen in Figure 4.9, where the chi-squared of the fits for spectra at lower energies have very high values, specially those for the ssd_5 detector.

The secondary features of the response function: Ge-L escape, Al-K and Ge-L fluorescent lines, are shown in Figure 4.8, where the norm for each line, relative to the total number of counts in the corresponding spectrum, has been plotted as as a function of energy. The Si-K fluorescent line shown in this figure is not part of the detector response function, since it originated from the Si double crystal monochromator, not the detector. As can be seen in the figure, these lines are very weak, and the most dominant line, Ge-L escape, has values less than 0.6% of the total counts recorded by the detector.

In Chapter 11, SSD carbon continuum spectra from various phases of XRCF testing for both SSD are described. By fitting the energy scale to the known energies and observed pulse heights of impurity lines, energy scale constants can be derived. The parameters are given in Table 4.6. The fitting formula used there is:

$$Energy = a + b \times channel. \tag{4.7}$$

In the JMKmod software, the relationship between energy and channel is:

$$channel = Energy \times gain/i\_pot + ch\_off + gain + 1, \tag{4.8}$$

where i_pot is the ionization energy (0.003 keV per ion pair). It follows that

$$gain = i\_pot/b, \tag{4.9}$$

and

$$ch\_off = -(gain + 1) - (gain/i\_pot) \times a. \tag{4.10}$$

We have taken the fitting results presented above, and produced an XSPEC-compatible response matrix for each of the two SSD detectors. Since the energy scale of each detector is different in each phase of the testing (because of slightly different noise environments or amplifier settings), a separate matrix is required for use with the data from each phase of the testing. Because of limits on the number of non-zero response matrix elements, we elected to create 1024×1024 matrices, which necessitates the binning of the raw data into 4-channel bins. The input parameters were linearly interpolated between those presented above.

A response matrix R_{ij} is a set of response functions, one for each of a number of energy bins E_j. Given that a photon of energy E_j is detected, the element R_{ij} is the probability that the

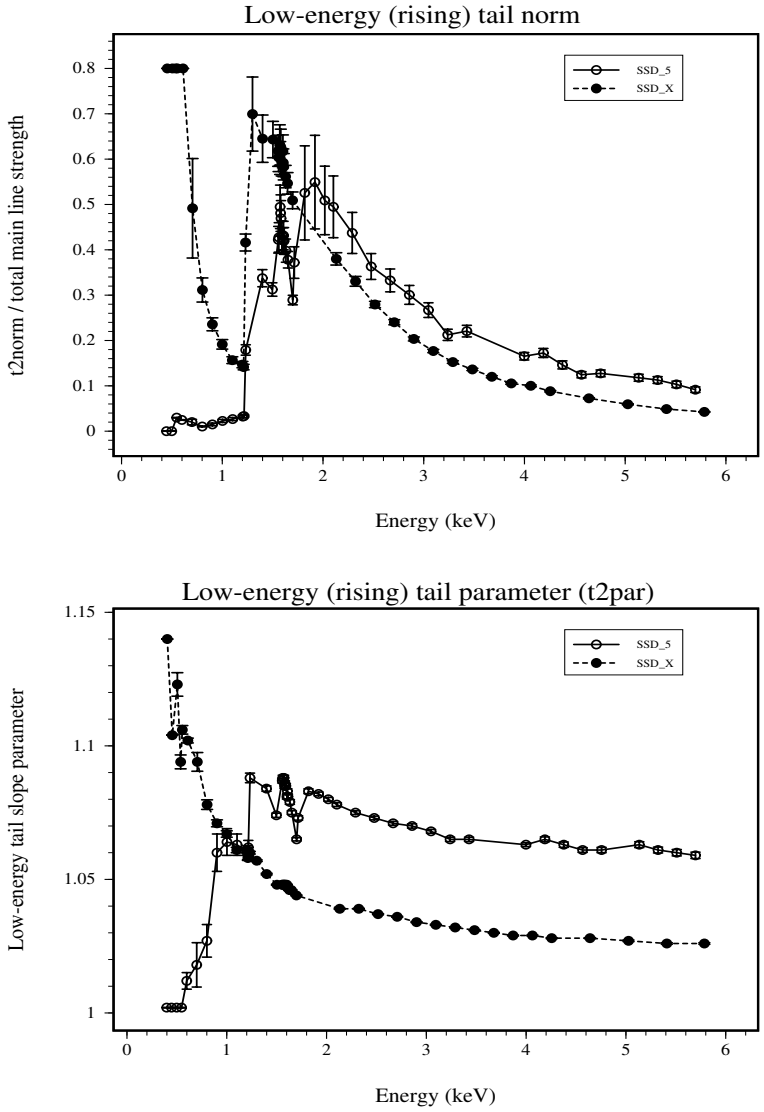

Figure 4.6: Fitted low-energy (rising) tail parameters for ssd_5 and ssd_x. The upper panel shows the tail norm (counts in the tail), plotted as a fraction of the total number of counts in the main peak. The lower panel shows the corresponding values of the slope parameter.

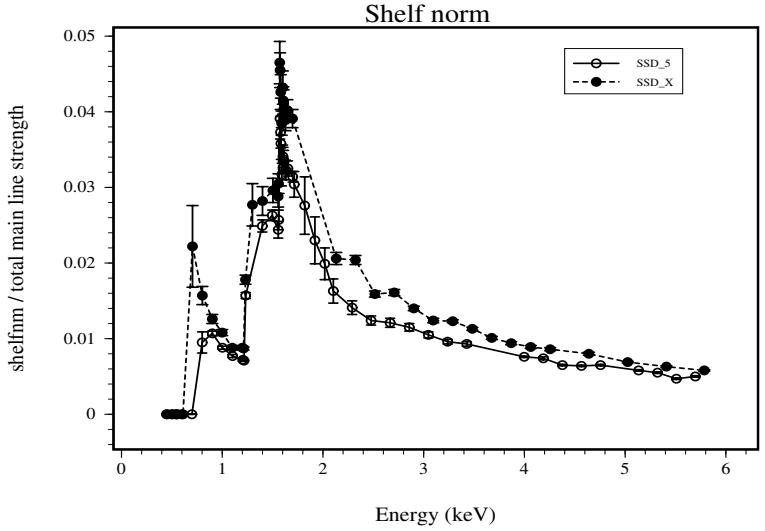

Figure 4.7: Fitted shelf norm (counts in the shelf) for ssd_5 and ssd_x, plotted as a fraction of the total number of counts in the main peak.

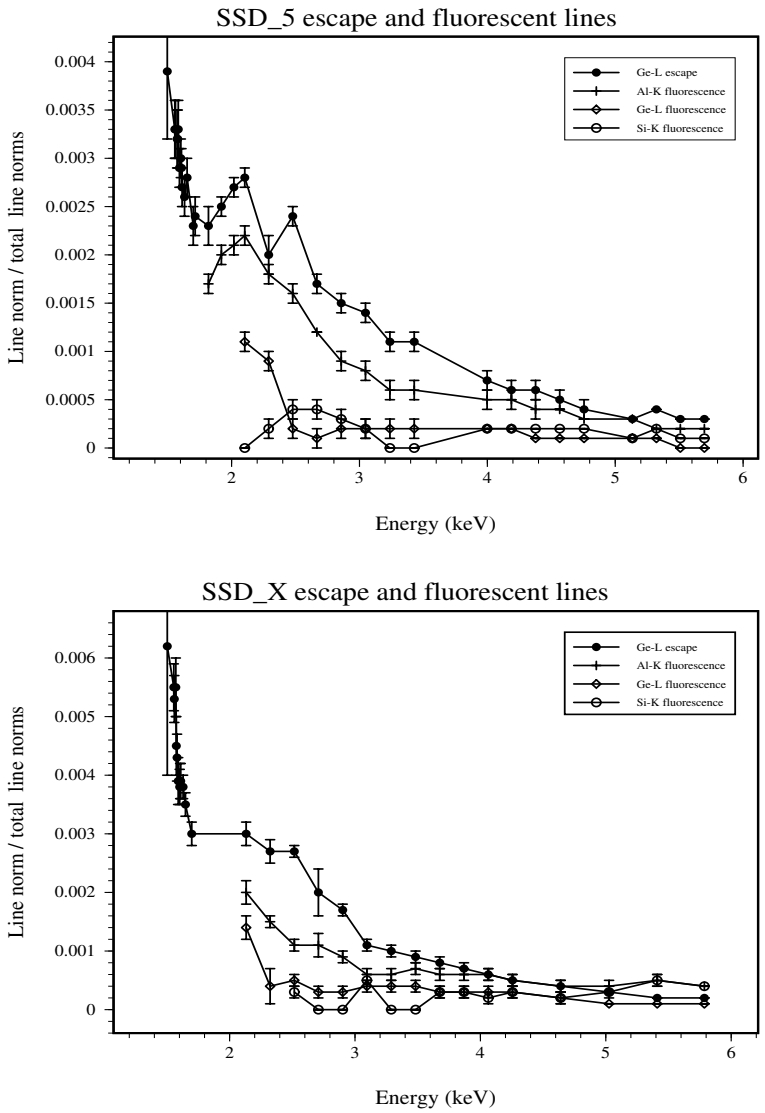

Figure 4.8: Fitted escape and fluorescent line norms for ssd_5 (upper panel) and ssd_x (lower panel), plotted as a fraction of the total number of counts.

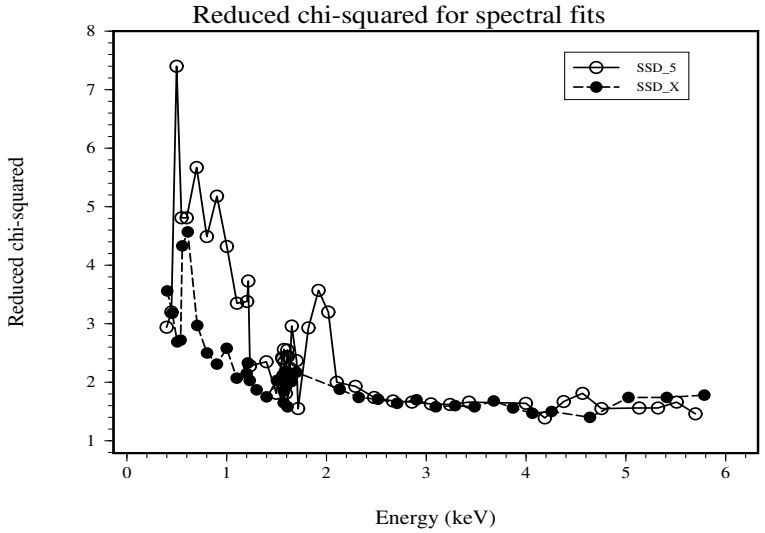

Figure 4.9: Reduced chi-squared χ^2 values for the fitted regions of the spectra.

detector emits a pulse of pulse height E_i. Thus each column of the matrix is just the (normalized) detector response function for monoenergetic photons of a given energy. Energy dependent quantum efficiency effects are accounted for in a separate computer file, known as an Ancillary Response Function (ARF). See the next section for the derivation of the SSD quantum efficiency.

4.5 Detector Efficiency vs. Energy Narrow Band

The detector efficiency as a function of energy over the range from 400 eV to 1.7 keV was measured on the SX700 Grating monochromator beam line. These data also provided a measure of the response function of the detector from 400 eV to 1.7 keV which include some energies that were not reachable by the KMC beam line. The flux recorded by the detector on this beam line can be compared to the transfer standard calibrated photodiode (traceable to the cryogenic electrical substitution radiometer) in the beam line to measure the detector efficiency over this energy range.

In the calibration, we scanned the monochromator from 400 eV to 1.7 keV with carefully selected steps taken around the O–K, Ge–L and Al–K absorption edges to capture fine structure such as EXAFS. The oxygen is from the ice, the Ge is from any possible dead layer on the front of the detector face, and the aluminum is from the IR shield and the Aluminum contact on the detector surface. We fitted the main peak, including the rising tail and shelf to determine the counts in this part of the spectrum. The counts under the germanium escape peak as well as the counts under the aluminum and germanium fluorescent peaks were added to the main-peak counts. Then these counts were corrected for pileup effects. The interpeak, peak, and pulser pileup events were determined by inspecting each individual spectrum, setting regions of interest containing these

events, and summing the counts in the corresponding regions of interest. Special care was taken to exclude counts due to the monochromator higher order lines. The interpeak and peak pileup counts are actually two events registered as one and thus were multiplied by two. However, the pulser-pileup events were not counted twice since each of these events involves one pulse from the pulser and one pulse from the detector. since the count rate for all of the recorded spectra were around 1000 counts/second, the effect of higher order pileups involving more than two pulses was negligible and was not considered.

$$\begin{aligned} \textit{Total Recorded Counts} = \textit{Main Peak} + \textit{Escape Peak} + \textit{Fluorescent Peaks} + \\ 2(\textit{Interpeak} + \textit{Peak Pileup}) + \textit{Pulser Pileup} \end{aligned} \tag{4.11}$$

Next the total counts were corrected for dead time by summing the counts in the pulser and pulser-pileup peaks and dividing by the number of injected pulser pulses. This gives the live time which is divided into the total recorded counts. The result is the measured flux incident on the detector crystal. This value was compared with the flux as measured by the PTB photodiode to determine the detector efficiency for the given energies.

The QE results from the SX700 are shown in Figure 4.10, and the numbers for the measured and fitted quantum efficiencies are in Tables 4.7 and 4.8.

We fitted the QE data for both detectors to a model consisting of the x-ray transmission of the detector windows, which included parylene-N (C_8H_8) coated with aluminum and ice which builds up on the detector. The Gullikson 1995 version of the optical data (update of Henke et al. (1993)) were used in the model, which was upgraded with data from Tikkanen (1997)) to include the extended x-ray absorption fine structures (EXAFS) above the oxygen and aluminum K edges.

The resulting fitted curves are shown in Figure 4.10. The corresponding fitted thicknesses for the window materials are summarized in Table 4.9. These thicknesses were obtained assuming a density of 2.70 g cm^{-3} for aluminum, a density of 1.10 g cm^{-3} for parylene, and 0.917 g cm^{-3} for ice.

The fitted parylene thickness value for ssd_5, 1.41 μm, is close to the expected nominal value of 1.2 μm (1 μm vacuum barrier window plus a 0.2 μm IR shield). However, the value for ssd_x, 2.07 μm, is much thicker than this nominal value. The fitted aluminum values for both detectors are almost identical but are thicker than the nominal value of 0.2 μm that is expected form the aluminum contact on the detector and the IR shield. The fitted ice value is 1.58 μm for the ssd_5 and 2.37 μm for ssd_x. The value for ssd_x is comparable to the 3 μm value found at XRCF from the ^{244}Cm source data (§11.9). For the ssd_5, a somewhat thinner layer of ice than for ssd_x is reasonable, because we know that it was dehydrated better during its manufacture, and it may have been de-iced more recently before the BESSY measurements.

It is interesting to note that we have not included the possible Ge dead layer as a window material in our fits. Inclusion of such a layer (180 $\AA$ for ssd_5 and 65 $\AA$ for ssd_x) improves the fits in the region just below the aluminum edge, where the model does not fit the data well. However, the lack of any structure in the data around the Ge–L edge for both detectors clearly does not justify the inclusion of a Ge dead layer. (The edge structure due to the above Ge thicknesses is as much as five times larger than the error in the data.)

The ice thickness on the ssd_x seems to be essentially time-independent during the SX-700 QE measurement run. We know this because of the following exercise: We presumed that the discrepancy between the measured QE and the best-fit parylene/aluminum (ice-free) window transmission was entirely due to ice. This assumption allows one to compute a thickness of ice as a function of runid (and hence energy and time). We find that, at least in the energy range between the oxygen

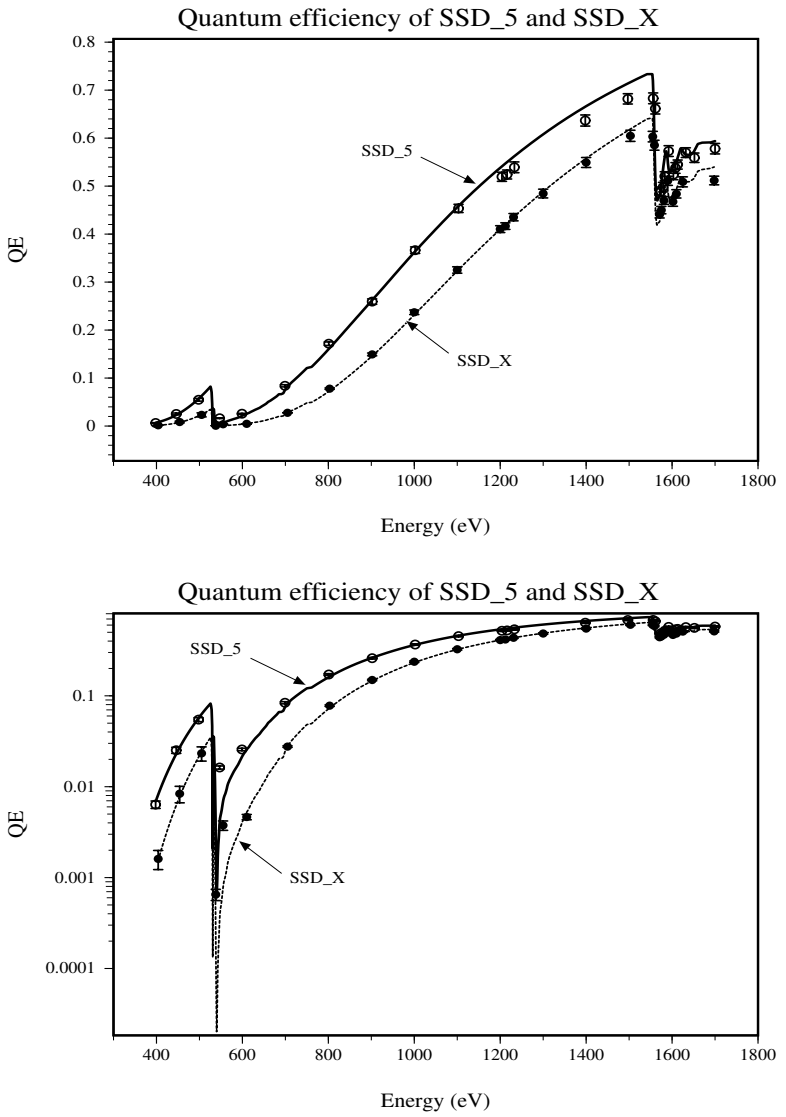

Figure 4.10: Measured QE data from SX700 data and their corresponding fitted curves for ssd_5 and ssd_x. The upper panel emphasizes the Al-K edge fine structure, and the lower panel provides a detailed view of the QE near the O-K edge.

Energy (keV)	QE	fit
0.398	0.00636 ± 0.00060	0.00690
0.446	0.02518 ± 0.00195	0.02300
0.498	0.05473 ± 0.00277	0.05692
0.547	0.01627 ± 0.00065	0.00400
0.599	0.02570 ± 0.00081	0.02096
0.699	0.08384 ± 0.00228	0.07412
0.801	0.17159 ± 0.00371	0.15924
0.902	0.25936 ± 0.00563	0.26074
1.002	0.36650 ± 0.00680	0.36229
1.103	0.45353 ± 0.00858	0.45699
1.204	0.51946 ± 0.00948	0.53953
1.216	0.52419 ± 0.00934	0.54851
1.233	0.53920 ± 0.01123	0.56090
1.398	0.63670 ± 0.01157	0.66417
1.497	0.68184 ± 0.01070	0.71269
1.556	0.68295 ± 0.01124	0.70708
1.561	0.66156 ± 0.01123	0.51650
1.574	0.48880 ± 0.00931	0.49843
1.579	0.49781 ± 0.00991	0.53437
1.583	0.52049 ± 0.00943	0.56143
1.592	0.57303 ± 0.01116	0.53505
1.603	0.52386 ± 0.01041	0.54102
1.608	0.53781 ± 0.01110	0.54792
1.613	0.54493 ± 0.00944	0.55920
1.632	0.56975 ± 0.01012	0.56579
1.652	0.55915 ± 0.00982	0.57405
1.700	0.57799 ± 0.01090	0.59389

Table 4.7: Measured and fitted QE values for ssd_5 from SX700 data.

Energy (keV)	QE	fit
0.404	0.00161 ± 0.00038	0.00155
0.454	0.00837 ± 0.00173	0.00778
0.505	0.02328 ± 0.00415	0.02417
0.538	0.00065 ± 0.00009	0.00021
0.555	0.00376 ± 0.00044	0.00077
0.610	0.00464 ± 0.00031	0.00525
0.705	0.02761 ± 0.00054	0.02866
0.803	0.07788 ± 0.00153	0.07348
0.902	0.14929 ± 0.00290	0.14606
1.000	0.23707 ± 0.00473	0.23195
1.100	0.32521 ± 0.00666	0.32318
1.200	0.41038 ± 0.00708	0.40993
1.212	0.41669 ± 0.00687	0.41992
1.231	0.43522 ± 0.00759	0.43528
1.300	0.48453 ± 0.00911	0.48857
1.400	0.54923 ± 0.01037	0.55785
1.503	0.60485 ± 0.01162	0.61898
1.555	0.60316 ± 0.01098	0.63593
1.559	0.58525 ± 0.01034	0.52220
1.571	0.44097 ± 0.00733	0.42642
1.575	0.44998 ± 0.00764	0.44986
1.581	0.47009 ± 0.00811	0.48823
1.590	0.51108 ± 0.00949	0.49078
1.602	0.46755 ± 0.00950	0.48286
1.610	0.48388 ± 0.00867	0.49335
1.625	0.50890 ± 0.01045	0.51415
1.698	0.51172 ± 0.00902	0.53989

Table 4.8: Measured and fitted QE values for ssd_x from SX700 data.

Detector	Al (μm)	Parylene (μm)	Ice (μm)
ssd_5	0.34 ± 0.01	1.41 ± 0.02	1.58 ± 0.05
ssd_x	0.33 ± 0.01	2.07 ± 0.04	2.37 ± 0.06

Table 4.9: Thickness of fitted window material for ssd_5 and ssd_x.

and aluminum K edge regions where the Henke tables are a good representation of reality, the ice thickness is independent of runid (and hence of energy and time).

As expected, the fitted QE curves for both detectors approach a value of one at higher energies, where the window material becomes transparent to the higher energy photons. This has been shown in Figure 4.11, where the upper plot shows the QE for ssd_5 reaching a value of one around 10 keV. The lower plot shows the ratio of ssd5 QE to the QE of ssd_x. This plot clearly shows that, although the QE of ssdx is lower than the QE for ssd5 at energies lower that 9 keV, both QEs approach the expected value of one near 10 keV.

4.6 Q. E. Broad Band: White light Calibration

The broad band QE of the detectors was measured at the PTB 12.20 beam line. This beam line does not contain any optical components and "sees" the raw undispersed synchrotron radiation.

4.6.1 The algorithm for calculating the synchrotron radiation spectrum

For the white beam, the calibration is done by calculating the intensity of the synchrotron x-ray emission from first principles, and comparing with the observed counting rate in the detector. We are in the process of doing these comparisons. One important step is the calculation of the beam intensity. The following is a derivation of the predicted flux, given the known operating parameters of the storage ring. We begin with the treatment by J. D. Jackson Jackson (1962) for the power radiated by a single electron.

Using Mathcad, we express the photon spectrum of x-rays emerging from the storage ring tangent point as a function of the ring parameters - electron energy, circulating storage ring current, magnetic field, distance from tangent point to detector, diameter of the circular detector aperture, and the angular displacement of the detector from the orbit plane. We discuss evaluation of the required Bessel functions. In order to calculate the spectrum, we derive expressions for the electron gyroradius, and perform the 2D integration of the flux distribution over the circular detector aperture. We calculate the flux at a set of energies, and we do an integration over all x-ray energies from the detector LLD at 308 eV to a high enough energy to include essentially all the flux.

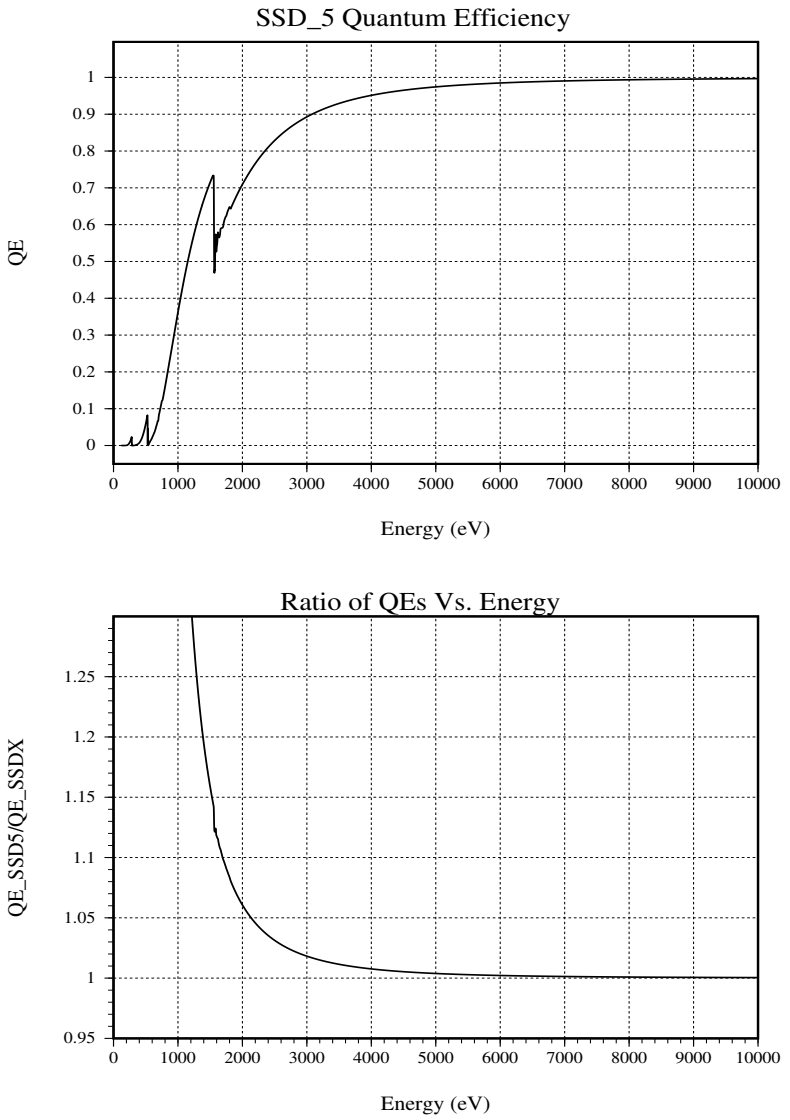

Figure 4.11: The fitted QE curves extended to 10 keV. The upper plot shows the QE curve for ssd5 approaching a value of one at higher energies. The lower plot shows the ratio of QEs as a function of energy.

In section 14, Jackson, uses $K_\nu(x)$, the modified Bessel function of the second kind. We call that BesseK(x,n) following Kostrun's series expansion (Vaclav O. Kostrun, 1980 N..I.M. 172 371, SCHWINGER program from Thornagel at PTB; also SAOLIB, fn. called kbess.f, maintained by Leon Van Speybroeck, or in mathematica, BesselK[n,x]. PTB's algorithm (Thornagel,private communication) is used here:

Epsilon := $1 \cdot 10^{-6}$ Step := .0625

BesseK(x,ν) :=
- 0. if x>88.
- otherwise
  - Summand ← $\frac{\exp(-x)}{2.}$
  - Help ← Summand
  - h ← Step
  - while $\left[\left(\frac{\text{Help}}{\text{Summand}}\right) > \text{Epsilon}\right]$
    - Help ← $\exp(-x \cdot \cosh(h)) \cdot \cosh(\nu \cdot h)$
    - Summand ← Summand + Help
    - h ← h + Step
  - Summand·Step

$K_{13}(x) := \text{BesseK}\left(x, \frac{1}{3}\right)$ $K_{23}(x) := \text{BesseK}\left(x, \frac{2}{3}\right)$

If we used Mathematica, we could use their built-in routines for K_n directly. Below, we show that the differences between the two evaluations are < 10^{-6} .

$K_{23}(.1) = 4.7529605281$ Mathematica gives 4.75296268

$\text{del} := \frac{K_{23}(.1) - 4.75296268}{4.75296268}$ $\text{del} = -4.5275294 \cdot 10^{-7}$

$\text{del2} := \frac{K_{23}(3.) - .0370570745}{.0370570745}$ $\text{del2} = -5.7495124 \cdot 10^{-7}$

Flux through HXDS detector Aperture

Now we calculate how much of the emerging spectrum passes through the circular aperture of our detector. In order to do this calculation, we need the expression for the angular distribution of the radiation, and we need to integrate it over the aperture.

We define

α too be the angle between the detector normal and the orbit plane, assuming the detector normal is always parallel to the ring plane, but the detector can be translated out of the ring plane, so α measures how far out of plane the detector is translated.

r to be the radius of the circular detector aperture.

d to be the distance from the ring tangent point to the detector aperture.

θ to be the angle between the orbit plane and the view angle

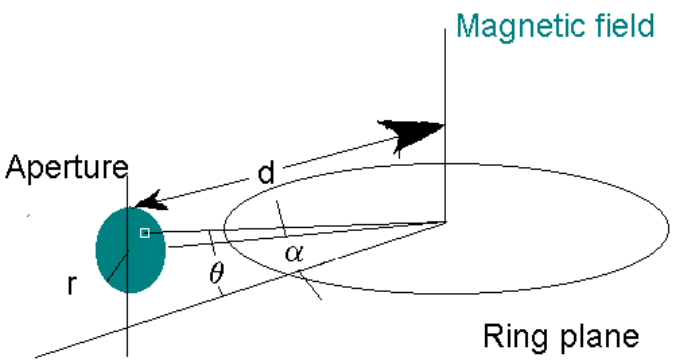

The storage ring electrons have γ_0 as follows where E_0 is their total energy:

$$\gamma_0(E_0) = \frac{E_0}{m \cdot c^2} \qquad m \cdot c^2 = 0.5109991 \cdot \text{MeV} \qquad \gamma_0(E_0) := \frac{E_0}{0.5109991 \cdot \text{MeV}}$$

and a typical BESSY value might be: $\gamma_0(797.6 \cdot \text{MeV}) = 1560.86$

Gyration radius of the electrons

In a field H, to find the gyroradius, consider an electron of energy E_0 and relativistic factor $\gamma_0(E_0)$ moving in a circle whose plane is perpendicular to the magnetic field. In one turn, the time is the inverse of the gyration frequency ν. The distance travelled in one orbit is 2πρ. The distance is also velocity times time or velocity divided by orbit frequency = βc/ν. Solving for ρ,

$$2 \cdot \pi \cdot \rho_{gy}(\gamma, H) = \frac{\beta(\gamma) \cdot c}{\nu_{gy}(H, \gamma)} \qquad \beta(\gamma) = \sqrt{1 - \frac{1}{\gamma^2}}$$

From Jackson, op cit eq. 7.99, adding relativistic mass:

$$\omega_{gy}(B, \gamma) = 2 \cdot \pi \cdot \nu_{gy}(B, \gamma) = \frac{e}{(\gamma \cdot m) \cdot c} \cdot B$$ and since in gaussian units, μ_0 = 1, H=B.

$$\rho_{gy}(\gamma, H) = \frac{\sqrt{1 - \frac{1}{\gamma^2}} \cdot c}{2 \cdot \pi \cdot \left(\frac{e}{2 \cdot \pi \cdot m \cdot c} \cdot \frac{H}{\gamma} \right)} \qquad \rho_{gy}(\gamma, H) = \sqrt{\gamma^2 - 1} \cdot \frac{m \cdot c^2}{e \cdot H}$$

Or expressing as a function of E_0,

$$\rho_{gy}(E_0, H) = \sqrt{\gamma_0(E_0)^2 - 1} \cdot \frac{m \cdot c^2}{e \cdot H} = \frac{E_0}{e \cdot H} \cdot \sqrt{1 - \left(\frac{m \cdot c^2}{E_0} \right)^2}$$

If we make a series expansion of the radical:

$$\rho_{gy}(E_0,H) = \frac{E_0}{e\cdot H}\cdot\left[1-\frac{1}{2}\cdot\left(\frac{m\cdot c^2}{E_0}\right)^2-\left[\frac{1}{8}\cdot\left[\left(\frac{m\cdot c^2}{E_0}\right)^2\right]^2\right]-\ldots\right]$$

and $$\left(\frac{m\cdot c^2}{797.6\cdot MeV}\right)^2 = 4.1\cdot 10^{-7}$$

we see that even the first order term contributes < 10^{-6} at our energy, so

$$\rho_{gy}(E_0,H) := \frac{E_0}{e\cdot H}$$

The differential photon spectrum

Using Jackson' s eqn 14.80, we first define the parameter ξ, where ε is the x-ray energy:

$$\xi(\varepsilon,H,E_0,\theta) = \frac{2\cdot\pi\cdot\varepsilon\cdot\rho_{gy}(E_0,H)}{3\cdot h\cdot c}\cdot\left(\frac{1}{\gamma_0(E_0)^2}+\theta^2\right)^{\frac{3}{2}} = \frac{2\cdot\pi\cdot\varepsilon\cdot E_0}{3\cdot h\cdot c\cdot e\cdot H}\cdot\left(\frac{1}{\gamma_0(E_0)^2}+\theta^2\right)^{\frac{3}{2}}$$

$$\frac{2\cdot\pi}{3\cdot h\cdot c\cdot e} = 5.6348049\cdot 10^6\cdot\frac{tesla}{MeV\cdot keV}$$

$$\xi(\varepsilon,H,E_0,\theta) := 5.6348049\cdot 10^6\cdot\frac{\varepsilon\cdot E_0}{H}\cdot\left(\frac{1}{\gamma_0(E_0)^2}+\theta^2\right)^{\frac{3}{2}}\cdot\frac{tesla}{keV\cdot MeV}$$

$$\xi(keV,1.5\cdot tesla,797.6\cdot MeV,0) = 0.787912$$

Then, to get the differential photon spectrum, we use Jackson' s eqn 14.83 for the energy radiated per unit frequency interval dω from a single particle into a solid angle dΩ from a single pass of an electron :

$$dI(\omega,\gamma,\theta,\xi) = \frac{e^2}{3\cdot\pi^2\cdot c}\cdot(\omega\cdot\rho_{gy})^2\cdot\left(\frac{1}{\gamma^2}+\theta^2\right)^2\cdot\left[K_{23}(\xi)^2+\left[\frac{1}{1+\frac{1}{(\gamma\cdot\theta)^2}}\right]\cdot K_{13}(\xi)^2\right]\cdot d\Omega\cdot d\omega$$

Now for the radiated power from a number of electrons passing per unit time,

$$\frac{d}{dt}\varepsilon = dI\cdot(number\_of\_electrons\_passing\_per\_unit\_time) = dI\cdot\frac{amps}{e}$$

Also, $d\omega = \frac{2\cdot\pi}{h}\cdot d\varepsilon$ which gives

$$\frac{d}{dt}\varepsilon\left(amps,\varepsilon,H,E_0,\theta\right)=\frac{2\cdot\pi\cdot amps\cdot e\cdot\left(2\cdot\pi\cdot\frac{\varepsilon}{h}\cdot\rho_{gy}\left(E_0,H\right)\right)^2}{3\cdot\pi^2\cdot c^3\cdot h}\cdot\left(\frac{1}{\gamma\left(E_0\right)^2}+\theta^2\right)^2$$

$$X\left[K_{23}(\xi)^2+\left[\frac{1}{1+\frac{1}{(\gamma\cdot\theta)^2}}\right]\cdot K_{13}(\xi)^2\right]\cdot d\Omega\cdot d\varepsilon$$

Now since $d\Omega=\cos(\theta)\cdot d\theta\cdot d\phi$

and θ is very small, < 0.15 mrad, and r/d and α/d are also very small, we integrate over the circular aperture and divide by ε to get the expression for a photon spectrum. If we define dphperkeV=factor1*factor2, with:

$$factor1\left(amps,E_0,H,\varepsilon\right)=\frac{\left[(16\cdot\pi\cdot e\cdot amps)\left(\rho_{gy}\left(E_0,H\right)\right)^2\right]\varepsilon}{3\cdot(h\cdot c)^3}$$

then the photon spectrum is

$$dphperkeV\left(amps,\varepsilon,H,E_0,\alpha,r,d\right)=factor1\left(amps,E_0,H,\varepsilon\right)\cdot factor2\left(\alpha,r,d,E_0,\varepsilon,H\right)$$

Now to substitute expressions, evaluate the constants and establish units,

$$\frac{16\cdot\pi\cdot e\cdot amps\cdot\rho_{gy}\left(E_0,H\right)^2\cdot\varepsilon}{3\cdot(h\cdot c)^3}=\frac{16\cdot\pi\cdot amps\cdot E_0{}^2\cdot\varepsilon}{3\cdot e\cdot(h\cdot c)^3\cdot H^2}$$

$$\frac{16\cdot\pi}{3\cdot e\cdot(h\cdot c)^3}=8.7915208\cdot10^{29}\cdot\frac{Hz}{keV}\cdot\frac{tesla^2}{amp\cdot MeV^2\cdot keV}$$

giving the formula for factor1, in which arguments are substituted in with physical units and are evaluated with units. Note: from this point on, Mathcad notation is used. Wherever you see ":=" , that is an active declaration used in subsequent calculations. Also, Mathcad has some specific nomenclature for indicating a quantity to a power. For example f(x) to the second power is written $f(x)^2$ in Mathcad notation.

$$factor1\left(amps,\varepsilon,E_0,H\right):=(8.7915208\cdot10^{29})\cdot\left(\frac{Hz}{keV}\cdot\frac{tesla^2}{amp\cdot MeV^2\cdot keV}\right)\cdot amps\cdot\varepsilon\cdot\left(\frac{E_0}{H}\right)^2$$

$$factor3\left(\varepsilon,H,E_0,\theta\right):=\left[\left(K_{23}\left(\xi\left(\varepsilon,H,E_0,\theta\right)\right)\right)^2\ ...\right.$$
$$\left.+\left[\frac{\theta^2}{\theta^2+\frac{1}{\gamma_0\left(E_0\right)^2}}\right]\cdot\left(K_{13}\left(\xi\left(\varepsilon,H,E_0,\theta\right)\right)\right)^2\right]$$

$$\text{factor2}(\alpha, r, d, E_0, \varepsilon, H) := \int_{\alpha - \frac{r}{d}}^{\alpha + \frac{r}{d}} \sqrt{\left(\frac{r}{d}\right)^2 - (\theta - \alpha)^2} \cdot \left(\frac{1}{\gamma_0 (E_0)^2 \ldots + \theta^2}\right)^2 \cdot \text{factor3}(\varepsilon, H, E_0, \theta)\, d\theta$$

$$\text{dphperkeV}(\text{amps}, \varepsilon, H, E_0, \alpha, r, d) := \text{factor1}(\text{amps}, \varepsilon, E_0, H) \cdot \text{factor2}(\alpha, r, d, E_0, \varepsilon, H)$$

Next, we evaluate dphperkeV for a set of energies ε_l, and for 5 electrons in the ring, and a particular set of H_1, E_1, θ (=0), r=2.5 and d_1, corresponding to run #500480d1i0 of the ssd_x on the PTB white beam line at BESSY.

$E_1 := 798.191 \cdot \text{MeV}$ $i_1 := (5) \cdot 7.6 \cdot 10^{-13} \cdot \text{amp}$, $H_1 := 1.490797 \cdot \text{tesla}$,

$d_1 := 16169.48$

$l := 0 .. 11$

$\varepsilon_l :=$

.1
.3
.5
.7
1
2
3
4
5
6
7
10

Now we form the quantity p_l, which must be dimensionless for plotting purposes:

$$p_l := \text{dphperkeV}\left(i_1, \varepsilon_l \cdot \text{keV}, H_1, E_1, 0., 2.5, d_1\right) \cdot \frac{\text{keV}}{\text{Hz}}$$

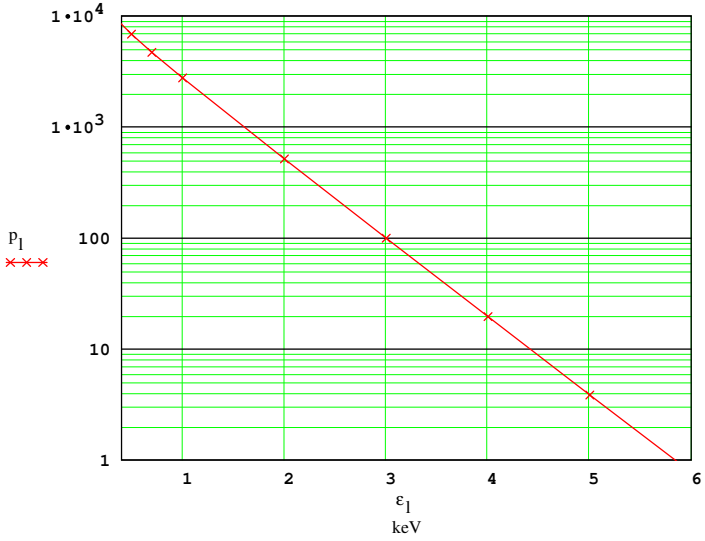

Differential photon spectrum from BESSY

Notice that the spectrum is very steep. If the energy of the electrons in the storage ring were higher, the spectrum would be flatter. For our measurements, this means that to detect photons above ~ 2 keV, we must get rid of great many low energy photons if we are to avoid clogging up our detector with them.

Variation of flux through aperture with detector displacement

As the detector is moved in the vertical direction, out of the storage ring plane, the intensity of the synchrotron x-radiation varies as shown below. This means that the detector must be carefully aligned so that the aperture is centered on the ring plane.

$m := 0..3$

$ds_m :=$

.0005
.1
.2
.3

$$norm_l := dphperkeV\left(i_1, \varepsilon_l \cdot keV, H_1, E_1, \frac{ds_0}{d_1}, 2.5, d_1\right)$$

$$q_{m,l} := \frac{dphperkeV\left(i_1, \varepsilon_l \cdot keV, H_1, E_1, \frac{ds_m}{d_1}, 2.5, d_1\right)}{norm_l}$$

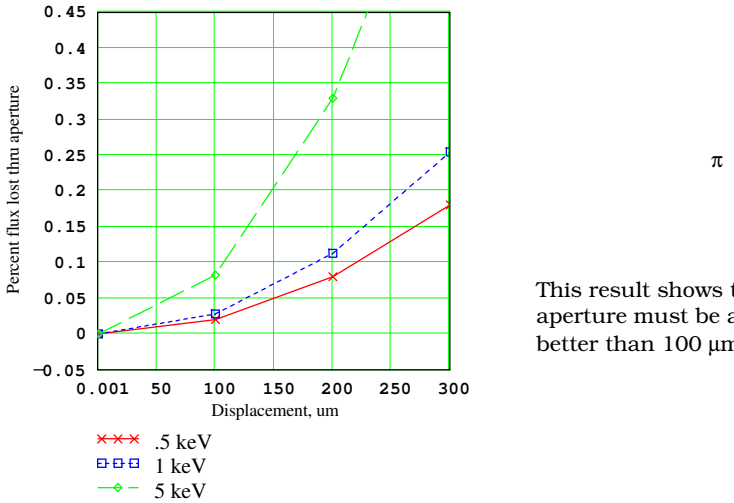

π

This result shows that the aperture must be aligned to better than 100 μm.

Numerical integration of photons incident on crystal:

Computational detail: the numerical integral ends up with an extremely small imaginary part, of order 10^{-40}, so we take the real part:

$$ssdInt\left(amps, H, E_0, \alpha, r, d\right) := \int_{0.30789 \cdot keV}^{10 \cdot keV} Re\left(dphperkeV\left(amps, \varepsilon, H, E_0, \alpha, r, d\right)\right) d\varepsilon$$

$ssdInt\left(i_1, H_1, E_1, 0, 2.5, d_1\right) = \circ Hz$

This number represents the total photons incident on the detector. Many of them will be absorbed in the detector windows. That will be accounted for in the SYNCH model, which calculates the photoelectric absorption from the windows using Henke tables.

Reference:C:\WINMCAD\Units.mcd

See http://hea-www.harvard.edu/MST/hxds/topics/units.ps

The above derivation needs to be checked against the PTB calculation. The algorithm was coded into FORTRAN for use in fitting white beam BESSY pulse height spectra from the SSD and FPC detectors.

4.6.2 The SYNCH Model

The synchrotron algorithm derived in §4.6.1 was coded in FORTRAN as an XSPEC local model, named SYNCH. This model calculates the photon flux output from a synchrotron over a circular aperture, including the damping effect of six filters, and passes the resulting spectrum to XSPEC to be folded with the detector response matix. Since the filter calculations are done by calling the JMKMOD subroutine "source," the SYNCH model is limited to only 1024 channels (maximum array dimensions within subroutine source), and a response matrix of size 1024 x 1024. The model has provisions for adding Gaussian lines to the spectrum and also for pileup calculations. The pileup calculation at present is based on a very simple algorithm that piles up every channel in the synchrotron spectrum with all the other channels in the spectrum. A more realistic algorithm is needed for a better analysis of the pileup features. The input parameters of the model are self-explanatory and are well documented within the code. One, however, should note that the ring current is either provided directly by the "current" parameter (when number of electrons = 0) or calculated from the number of electrons (when number of electrons is nonzero).

4.6.3 Synchrotron Measurement Procedures

The procedure for measuring the undispersed synchrotron radiation involved injecting the storage ring with approximately 2 mAmps of current and allowing 2 hours for the beam to stabilize. After this waiting time, an RF signal was injected perpendicular to the electron beam. This RF wave as scanned in frequency until a resonance with the electrons in the storage ring was obtained. This could be observed by measuring a sharp decrease in the ring current as the excitation caused the electrons to depart from their orbit and collide with the walls of the storage ring.

Reaching this resonance meant that the resonant frequency, and therefore the energy, of the electrons had been reached. Once the energy of the electrons was measured and the orbit of the electrons in the storage ring had become stable, a polarizing crystal was inserted in the beam line. This crystal was scanned in the vertical direction until a peak in counting rate was reached. This provided information on exactly where the electron beam was in the storage ring. Knowing this, it then possible to scan the detector in the vertical plane so as to make it lie in the same plane as the electron orbit.

Next the ring current was reduced by slowly inserting a baffle into the storage ring which ejected some fraction of the electrons on each orbit until the desired ring current was reached. During this reduction of current, the current was measured using a calibrated photodiode in the SX700 beam line. Once the ring current got below 1000 electrons it was possible to see the quantum jumps in the ring current as single electrons were removed from the storage ring.

The spectral output from BESSY is peaked at low energy. With the Aluminum IR shield in place, the peak corresponds to about 1 keV. As a consequence, the usable photon flux tends to tail out around 4-5 keV. In order to achieve significant counting statistics at the higher energies desired (up to 10 keV), Aluminum filters were placed into the aperture that could suppress the lower energy photons, allowing a higher ring current and therefore a higher rate of high-energy photons. The two filters used were a 27.4 μm and a 133.4 μm Al filter. The 27.4 μm filter effectively shifted the peak energy synchrotron source spectrum to 4 keV, while the 133.4 μm filter shifted it even farther to 6 keV. As can be seen in Figure 4.12, there is now sufficient flux at 10 keV to be useful in fitting.

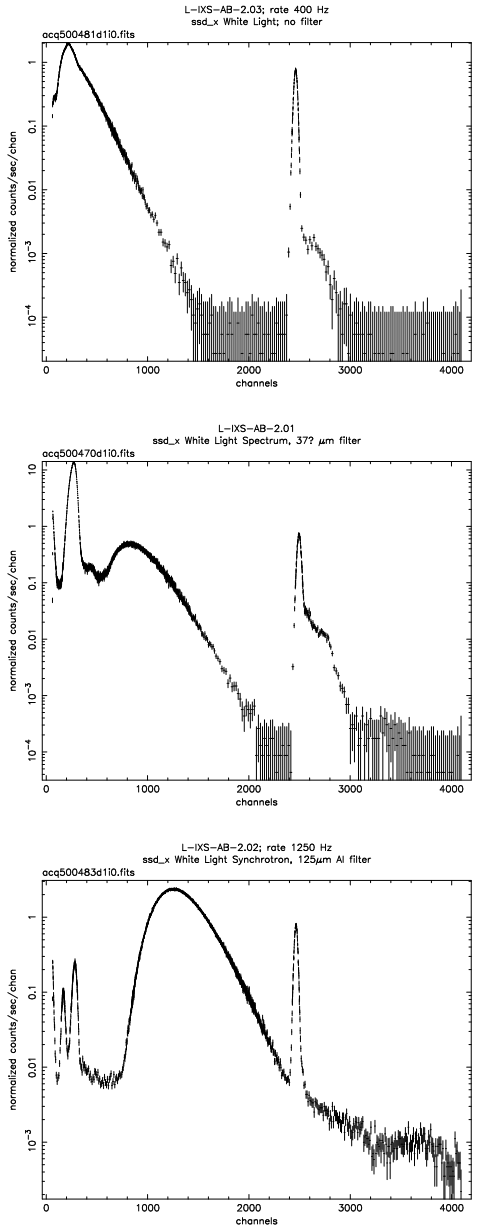

Figure 4.12: ssd_x Synchrotron White Light Spectra

Energy (keV)	Transmission	Al thickness μmm
2.5	9.11×10^5	27.0
3.	3.41×10^3	27.0
4.	7.48×10^2	27.4
5.	2.49×10^1	27.6
6.	4.28×10^1	27.7
7.	5.94×10^1	27.4
4.5	1.23×10^4	132.5
5.	1.29×10^3	132.3
5.5	6.02×10^3	133.6
6.	1.90×10^2	133.2
6.5	4.24×10^2	134.
7.	7.77×10^2	134.4

Table 4.10: Thicknesses of SSD Al filter material, measured at NSLS.

This technique was regarded as somewhat speculative, because the great attenuation of the thick Al filters would have to be corrected to a fraction of 1% in order to make the measurement useful. However, we did a careful measurement of the x-ray absorption of this thick Al filter material at the BNL synchrotron, in order to aid the measurement. The net result was an equivalent thicknesses of 27.4 ± 0.3 μm and 133.4 ± 0.8 μm. See Table 4.10 for the complete set of BNL measurements.

The development in §4.6.1 was coded into FORTRAN, and implemented as the XSPEC model subroutine SYNCH. Using the response matrices derived above (from the BESSY monochromator spectral response function tests), we can then fit the spectra. If all goes well, the normalization factor should be unity; i.e. the absolute intensity of the synchrotron light beam should be computed correctly and require no renormalization in order to match the data.

4.6.4 Results of the Fitting

The first case is shown in Figure 4.13. Here, we see the results of fitting to the data from the ssd_5.

The upper panel shows the fit to the entire pulse height spectrum, from 0.4–6.5 keV. The fit is good at energies above 2 keV. It is not too bad qualitatively down to about 0.8 keV, but the residuals show considerable structure. The SYNCH model in XSPEC used here contains the synchrotron continuum and a Henke model of absorption by the filters. This has the limitation that the fine structure from EXAFS at the O–K, Ge–L and Al–K edges known to exist are not in the Henke data. The correct way to do this is to include a .arf auxiliary response file in the XSPEC fit, with the .arf file containing the QE vs. E information discussed in §4.5. Since we have not yet finalized those QE values, this remains to be done. Therefore, to obtain the best present value of the broadband QE, we restrict ourselves to data at higher energy, where the window absorption is less important.

The parameters for this fit are listed in Table 4.11. The lower panel in Figure 4.13 shows the fit including the energy range 3.5–6.6 keV only. The parameters for this fit are listed in Table 4.12. The overall normalization, parameter 'norm' is consistent with 1.00, indicating that the high energy QE is 100%.

The second case is shown in Figure 4.14. Here, we see the results of fitting to the data from the ssd_x. The upper panel shows the fit to the entire pulse height spectrum. Structure in the

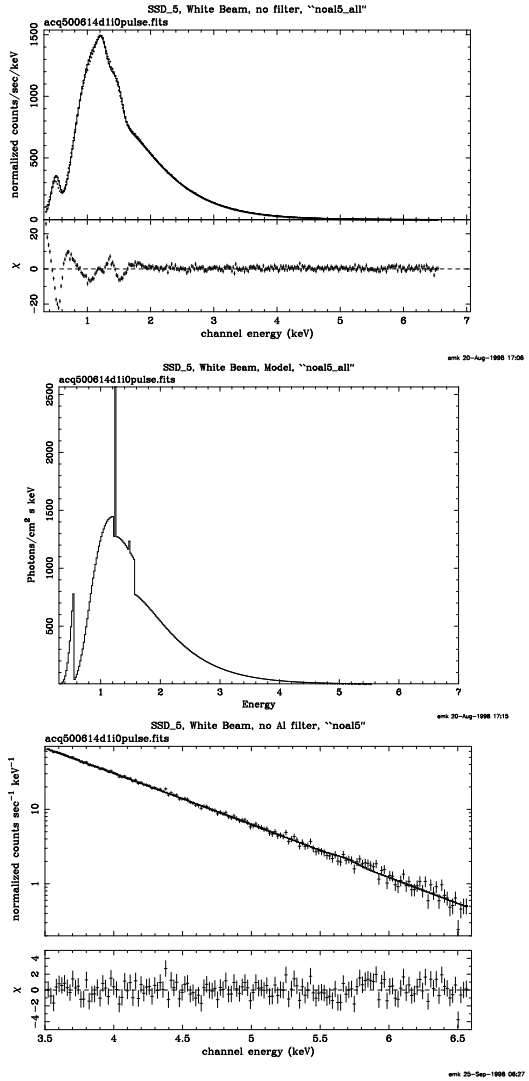

Figure 4.13: Data and XSPEC fit at the white beam for ssd_5 with no Al filter, with input synchrotron model folded through XSPEC . The upper panel shows the entire pulse height distribution and the XSPEC calculation, with residuals, from the lower level discriminator cutoff at 0.4–.5 keV. The center panel shows just the input synchrotron+window absorption model, SYNCH, from 0.4–6.5 keV. The lower panel shows the pulse height distribution and the folded model with residuals, for 3.5–6.6 keV only.

Parameter	Value	Status
alpha	0.	frozen
radius	2.500	frozen
distance	1.6242E+04	frozen
E_electr	798.2	frozen
H	1.491	frozen
e_to_cur	7.6970E−13	frozen
N_electr	8.000	frozen
current	3.800	frozen
pileup	0.	frozen
filter1	2.000	frozen
thcknss1	3.1241E−05	frozen
filter2	6.000	frozen
thcknss2	5.7040E−05	frozen
filter3	32.00	frozen
thcknss3	3.5067E−06	frozen
filter4	48.00	frozen
thcknss4	2.9854E−04	frozen
filter5	19.00	frozen
thcknss5	0.	frozen
filter6	45.00	frozen
thcknss6	0.	frozen
lineE1	1.239	frozen
sigma1	1.9814E−03	frozen
norm1	237.3	frozen
lineE2	1.486	frozen
sigma2	4.3000E−04	frozen
norm2	0.3809	frozen
lineE3	1.557	frozen
sigma3	8.0000E−03	frozen
norm3	3.5012E−07	frozen
norm	0.9719	0.2041E−02

Table 4.11: Fitting parameters for ssd_5 white beam run, all energies, no Al filter. Runid 500614, channels = 141 – 299, nbins = 159, reduced $\chi^2 = 0.9954577$

Parameter	Value	Status
alpha	0.	frozen
radius	2.500	frozen
distance	1.6242E+04	frozen
E_electr	798.2	frozen
H	1.491	frozen
e_to_cur	7.6970E−13	frozen
N_electr	8.000	frozen
current	3.800	frozen
pileup	0.	frozen
filter1	2.000	frozen
thcknss1	5.3860E−05	0.1252E−04
filter2	6.000	frozen
thcknss2	5.7279E−05	frozen
filter3	32.00	frozen
thcknss3	3.0000E−06	frozen
filter4	48.00	frozen
thcknss4	2.9745E−04	frozen
filter5	19.00	frozen
thcknss5	0.	frozen
filter6	45.00	frozen
thcknss6	0.	frozen
lineE1	1.240	frozen
sigma1	1.0000E−03	frozen
norm1	20.00	frozen
norm	1.019	0.1270E−01

Table 4.12: Fitting parameters for ssd_5 white beam run, only high energy, no Al filter. Runid 500614, channels 176–329, nbins=154, reduced $\chi^2 = 0.9547486$

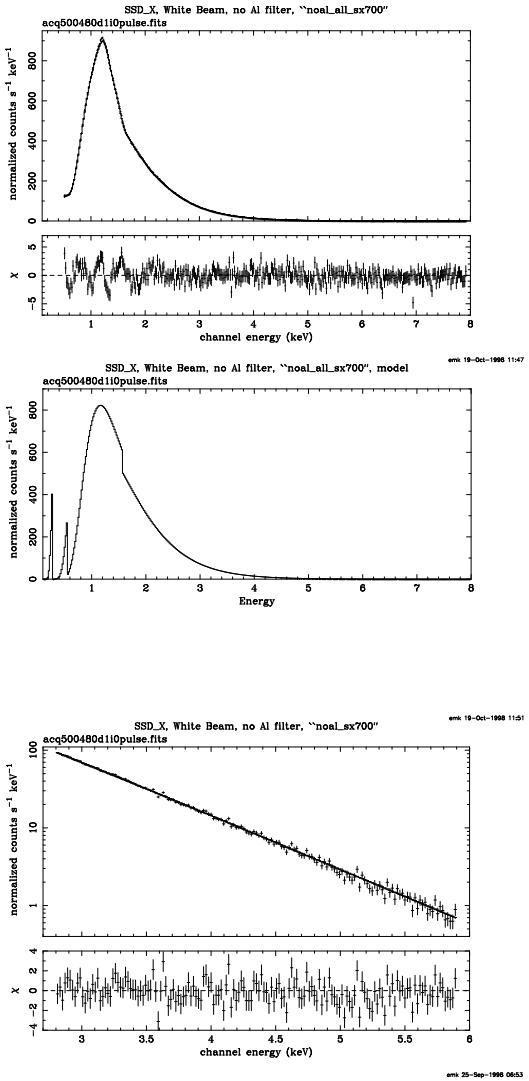

Figure 4.14: Data and XSPEC fit at the white beam for ssd_x with no Al filter. The upper panel shows 0.4–7.9 keV, with input SYNCH model folded through XSPEC, and residuals. The center panel shows the input synchrotron+window absorption SYNCH model. The lower panel shows just 2.8–5.9 keV, with folded model.

fit is very similar to that for Figure 4.13 for the same reasons. The parameters for this fit are listed in Table 4.13. The middle panel shows the input model before being folded through the detector response by XSPEC. The absorption edges from C–K at 0.28 keV, O–K at 0.54 keV and Al–K at 1.58 keV are seen, as well as the general absorption that causes the smooth synchrotron spectrum to turn over at energies below 1.5 keV. The lower panel again shows the fit to the higher energies, with residuals showing no structure or energy dependence. The parameters for this fit are listed in Table 4.14. The absence of structure or energy dependence is significant because the overall normalization for the ssd_x is not consistent with 1.00, rather being about 27% low. Lack of structure in the residuals means that whatever is affecting the normalization is independent of energy, so must be some sort of beam blocking, rather than an error in the energy scale or in the energy-dependent part of the prediction calculation.

Whatever is causing this discrepancy for ssd_x is not a function of energy. Other comparisons of ssd_x and ssd_5 do not show this discrepancy. See Zhao et al. (1998). Also compare the narrow band QE measurements discussed in §4.5. Therefore, our present conclusion is that the ssd_5 QE normalization is 100%, and that we do not have a corresponding number for ssd_x from the white beam calibrations.

Figure 4.15 shows the response of ssd_5 to the white beam, with a 27.4 μm filter. In the upper panel, we see a large peak at 1.5 keV. This is the synchrotron continuum being transmitted through the Al filter just below its Al–K edge. In the upper panel, at energies below $\sim$ 0.8keV, we see the shelf discussed previously. Here, the calculated shelf is far less intense than the observed one. In the region from 1.8–2.5 keV we see interpeak events from electronic pileup, as discussed previously. From $\sim$ 2.8–3.1 keV, we see an apparent pileup peak. The observed peak is not at the same pulse height as the calculated one. We think we know the defect in the algorithm that causes this, but have not fixed it yet. At E $>$ 3.3 keV, the fit is rather good. The parameters for this fit are listed in Table 4.15. The overall normalization, our main interest here, is not very reliable in this fit; see next fit.

The lower panel in Figure 4.15 shows the fit restricted to 3.5–6.5 keV. The residuals show little structure. There is a feature in the folded model curve at 5.7 keV that causes a peak in the residuals. This is probably in the response matrix, where the upper boundary of the measured response curve meets the extrapolation of the matrix to higher energies, where we have no measurements on which to base the matrix. The overall normalization for this fit, listed as 'norm' in Table 4.16, is far from 1.00. We do not understand why this is so, but we realize from Table 4.10 that the attenuation in this filter at 4 keV is about a factor of 13.5. One possible cause of discrepancy is that the thickness derived from the NSLS x-ray transmission measurements was measured just on one spot in the Al foil, used later to fabricate the filters by cutting out small circular disks for each detector. Therefore, if there was any thickness variation in the foil sheet, the actual sample use in the detector could have a different thickness. However, when we allowed the thickness of the Al foil to vary as a free parameter in the XSPEC fits, the result was consistent with the nominal value from NSLS.

Figure 4.16 shows the response of ssd_x to the white beam, with a 27.4 μm filter. In the upper panel, the energy range is 0.8–5.9 keV. We again see a large peak at 1.5 keV, from the Al–K absorption edge. The residuals in the vicinity of the energy of that peak are qualitatively different from those for ssd_5 (Figure 4.15), and that may be due to differences in the faithfulness of the energy scale, which is based on the ^{244}Cm source for the ssd_5, but for the ssd_x must rely on less direct means. The interpeak pileup between 1.6–3.0 keV is also different. The lower panel shows the fit for the higher energy range, 3.2–9.8 keV. There is some structure in the residuals. This may indicate an inability to fit the shape of the Al photoelectric absorption vs. energy. That in turn could be due to limitations in our rather simple pileup correction model. The value for 'norm', the last entry in Table 4.18, is far from 1.00, as it was for the ssd_5 with the 27.4 μm Al filter.

Parameter	Value	Status
alpha	0.	frozen
radius	2.500	frozen
distance	1.6242E+04	frozen
E_electr	798.7	frozen
H	1.491	frozen
e_to_cur	7.6970E−13	frozen
N_electr	5.000	frozen
current	3.800	frozen
pileup	0.	frozen
filter1	2.000	frozen
thcknss1	1.7730E−05	0.9757E−06
filter2	6.000	frozen
thcknss2	8.6098E−05	0.1066E−05
filter3	32.00	frozen
thcknss3	0.	frozen
filter4	48.00	frozen
thcknss4	2.5155E−04	0.5297E−01
filter5	19.00	frozen
thcknss5	0.	frozen
filter6	45.00	frozen
thcknss6	0.	frozen
lineE1	0.6148	0.1370
sigma1	0.3954	0.5217E−01
norm1	17.53	7.100
lineE2	0.9653	0.6952
sigma2	0.9194	0.2023
norm2	3.389	2.873
norm	0.7178	0.6949E−02

Table 4.13: Fitting parameters for ssd_x white beam, all energies, no Al filter. Runid 500480, channels 20–400, nbins=381, reduced $\chi^2 = 1.648170$

Parameter	Value	Status
alpha	0.	frozen
radius	2.500	frozen
distance	1.6242E+04	frozen
E_electr	798.7	frozen
H	1.491	frozen
e_to_cur	7.6970E−13	frozen
N_electr	5.000	frozen
current	3.800	frozen
pileup	0.	frozen
filter1	2.000	frozen
thcknss1	1.9764E−05	frozen
filter2	6.000	frozen
thcknss2	2.0924E−05	frozen
filter3	32.00	frozen
thcknss3	0.	frozen
filter4	48.00	frozen
thcknss4	6.3292E−05	0.8126E−04
filter5	19.00	frozen
thcknss5	3.6279E−05	frozen
filter6	45.00	frozen
thcknss6	0.	frozen
lineE1	1.225	frozen
sigma1	2.9965E−02	frozen
norm1	1.219	frozen
lineE2	1.109	frozen
sigma2	0.2560	frozen
norm2	2.343	frozen
norm	0.7329	0.6280E−02

Table 4.14: Fitting parameters for ssd_x white beam, only high energies, no Al filter. Runid 500480, channels 138–296, nbins=159, reduced $\chi^2 = 1.205958$

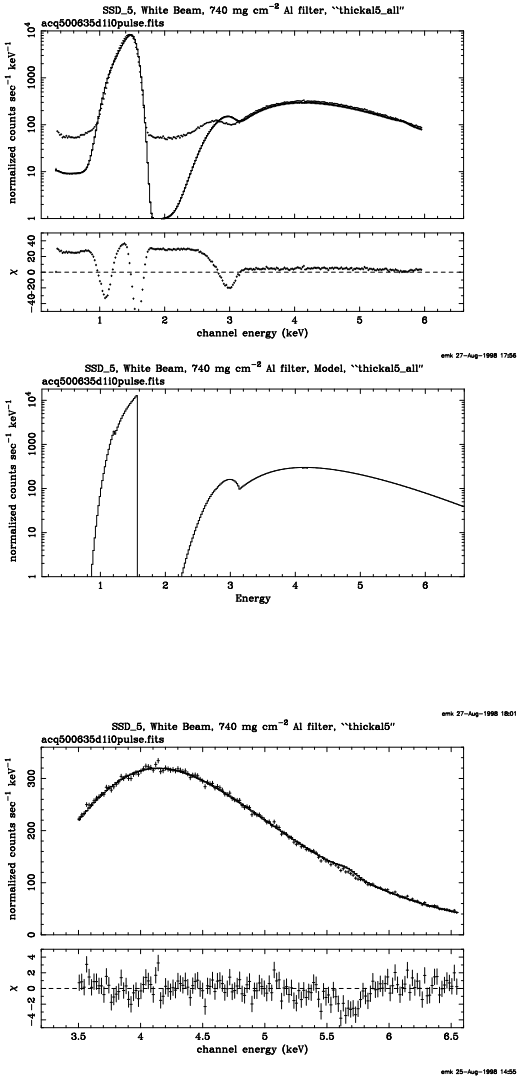

Figure 4.15: Data and XSPEC fit for ssd_5 at the white beam with 27.4 μm Al filter. The upper panel shows the entire pulse height distribution, 0.4–6.0 keV, with SYNCH/XSPEC model. The center panel shows the input SYNCH model, 0.4–6.0 keV. The lower panel shows 3.5–6.5 keV, with folded model.

Parameter	Value	Status
alpha	0.	frozen
radius	2.500	frozen
distance	1.6242E+04	frozen
E_electr	798.2	frozen
H	1.491	frozen
e_to_cur	7.6970E−13	frozen
N_electr	0.	frozen
current	1403.	frozen
pileup	2.2067E−02	0.1473E−03
filter1	2.000	frozen
thcknss1	2.7400E−03	frozen
filter2	6.000	frozen
thcknss2	0.	frozen
filter3	32.00	frozen
thcknss3	9.7414E−06	0.5422E−07
filter4	48.00	frozen
thcknss4	0.	frozen
filter5	19.00	frozen
thcknss5	0.	frozen
filter6	45.00	frozen
thcknss6	0.	frozen
norm	0.5531	0.8266E−03

Table 4.15: Fitting parameters for ssd_5 white beam, all energies with 27.4 μm Al filter. Runid 500635, channels 16-299, nbins=284, reduced $\chi^2 = 353.4951$

Parameter	Value	Status
alpha	0.	frozen
radius	2.500	frozen
distance	1.6242E+04	frozen
E_electr	798.2	frozen
H	1.491	frozen
e_to_cur	7.6970E−13	frozen
N_electr	0.	frozen
current	1403.	frozen
pileup	2.4664E−02	0.3252E−01
filter1	2.000	frozen
thcknss1	2.7400E−03	frozen
filter2	6.000	frozen
thcknss2	5.6046E−11	0.2073
filter3	32.00	frozen
thcknss3	1.4657E−05	0.5497E−03
filter4	48.00	frozen
thcknss4	7.9732E−07	0.2386
filter5	19.00	frozen
thcknss5	7.5167E−10	0.3916
filter6	45.00	frozen
thcknss6	0.	frozen
norm	0.5984	0.1145E−01

Table 4.16: Fitting parameters for ssd_5 white beam, Higher energies with 27.4 μm Al filter. Runid 500635, channels 176-329, nbins=154, reduced $\chi^2 = 1.577946$

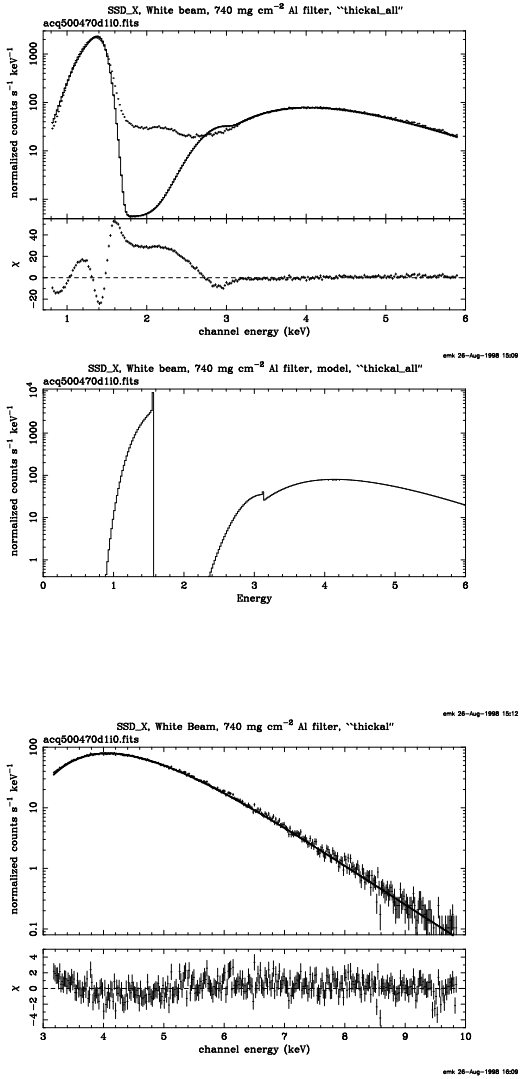

Figure 4.16: Data and XSPEC fit for ssd_x at the white beam with 27.4 μm Al filter. The upper panel shows 0.4–6.0 keV, with SYNCH/XSPEC folded model. The parameters for this fit are listed in Table 4.17. The center panel shows the input SYNCH model, 0.4–6.0 keV. The lower panel shows 3.5–6.6 keV, with folded model.

Parameter	Value	Status
alpha	0.	frozen
radius	2.500	frozen
distance	1.6242E+04	frozen
E_electr	798.7	frozen
H	1.491	frozen
e_to_cur	7.6970E−13	frozen
N_electr	438.0	frozen
current	3.800	frozen
pileup	9.2580E−03	frozen
filter1	2.000	frozen
thcknss1	2.7400E−03	frozen
filter2	6.000	frozen
thcknss2	0.	frozen
filter3	32.00	frozen
thcknss3	0.	frozen
filter4	48.00	frozen
thcknss4	2.7472E−04	frozen
filter5	19.00	frozen
thcknss5	4.8176E−09	frozen
filter6	45.00	frozen
thcknss6	0.	frozen
lineE2	1.560	0.2529E−02
sigma2	8.0000E−03	frozen
norm2	60.99	0.4718
norm	0.6060	0.9617E−03

Table 4.17: Fitting parameters for ssd_x white beam, all energies with 27.4 μm Al filter. Runid 500470, channels 41-299, nbins=259, reduced $\chi^2 = 236.7270$

Parameter	Value	Status
alpha	0.	frozen
radius	2.500	frozen
distance	1.6242E+04	frozen
E_electr	798.7	frozen
H	1.491	frozen
e_to_cur	7.6970E−13	frozen
N_electr	438.0	frozen
current	3.800	frozen
pileup	3.3334E−04	frozen
filter1	2.000	frozen
thcknss1	2.7400E−03	frozen
filter2	6.000	frozen
thcknss2	0.	frozen
filter3	32.00	frozen
thcknss3	0.	frozen
filter4	48.00	frozen
thcknss4	2.1681E−03	0.1004E−03
filter5	19.00	frozen
thcknss5	1.2500E−04	frozen
filter6	45.00	frozen
thcknss6	0.	frozen
lineE2	1.560	frozen
sigma2	8.0000E−03	frozen
norm2	60.99	frozen
norm	0.6769	0.3091E−02

Table 4.18: Fitting parameters for ssd_x white beam, higher energies with 27.4 μm Al filter. Runid 500470, channels 161-500, nbins=340, reduced $\chi^2 = 1.304896$

Figure 4.17 shows the result of the run taken by exposing ssd_5 to the white beam, using the 133.4 μm Al filter. In the upper panel, we see the entire energy range from 0.4–10.8 keV. The broad peak at ~ 5 keV is from the synchrotron continuum. It falls off to higher energy because of the falling xynchrotron spectrum. It also falls off below 5 keV because of absorption in this very thick Al filter. The shelf from $\sim 0.4 - -3.7$ keV is caused by incomplete charge collection events from the main peak. There is a peak in the data at about 1.5 keV. This comes from the continuum spectrum being very intense at that energy, and being transmitted partially through the Al filter below its K edge. We were not able to get even a qualitatively satisfactory fit without adding two lines, lineE1 and lineE2 in Table 4.19. From Table 4.10 we see that at 6 keV, this filter attenuates by about a factor of fifty. Also, using the Henke tables, Henke et al. (1993), we find an attenuation factor of 3.15×10^5 just below the Al–K edge. With such a large factor, we perhaps cannot expect to get an accurate fit across the edge; the discontinuity in the photoelectric cross section of Al may not be well enough known for that. There is also some possibility that some fluorescence Al–K_α radiation is generated within the filter and escapes out its back, into our detector. The calculation also shows a peak at about 1.2 keV. This comes from the response matrix used for the fits, and is meant to account for Ge–L fluorescence from the detector crystal. As a result of observing this, we need to correct the response matrix.

In the lower panel, we show the fit over the 4.8–10.9 keV range. Here, the only peculiarity is the bump in the calculated response at ~ 5.65keV from the joining of measured to extrapolated response matrix. This region was ignored in the fits that gave the parameters in Table 4.20.

The parameters for the fits in Figure 4.17 are given in Table 4.19 and Table 4.20. The overall normalization, 'norm', is far from 1.00. This is perhaps not too surprising, since the attenuation in this very thick Al filter is very large, about a factor of 50 at 6 keV, and we just may not be able to calculate it and correct for it to sufficient accuracy. What are the possible sources of error? First, if we make a small error in the energy scale, since the absorption cross section is varying with the 8/3 power of energy, there is a larger error in absorption. For example, a 20 eV 0.3% change in energy gives a 3.5% change in x-ray transmission at 6 keV for this filter. This is not nearly large enough to explain the difference.

Figure 4.18 shows the result of the run taken by exposing ssd_x to the white beam, using the 133.4 μm Al filter. In the upper panel, we see the entire energy range from 0.4–11.6 keV. In addition to the main broad peak at 6 keV from the synchrotron continuum plus absorption in the vbery thick Al filter, we see peaks at lower energy. The peak at 1.5 keV is from continuum x-rays penetrating the Al filter just below the Al–K edge. We were not able to get a good fit without adding two lines at 1.486 and 1.550 keV to the model. As in the similar case for ssd_5, the model was unable to match the data across the Al–K edge. There is another line in the data, at 0.89 keV. We are not able to identify its source at the present time. The parameters of the fit are given in Table 4.21. The normalization is far from 1.00, but we would use this normalization because of the uncertainties introduced by attempting to fit the low energies.

The lower panel shows the fit over the 3.8–10.6 keV energy range. Here, the low energy features are ignored, and we concentrate on the main peak. The residuals show some structure, which we cannot explain. The parameters of the fit are given in Table 4.22. The normalization is far from 1.00.

The results of all the absolute calibration runs analyzed are shown in Table 4.23. The first column identifies the detector. The second gives a reference to the filename in `/data/axaf/emk/xspec/logs/white` for the XSPEC output files, or indicates a MEAN between two runs. The third column gives the unique HXDS RUNID. The fourth column gives the energy range analyzed. The fifth column gives the "rawQE" derived from the 'norm' parameter in the XSPEC output for the run. This has been corrected for dead time by modifying the integration

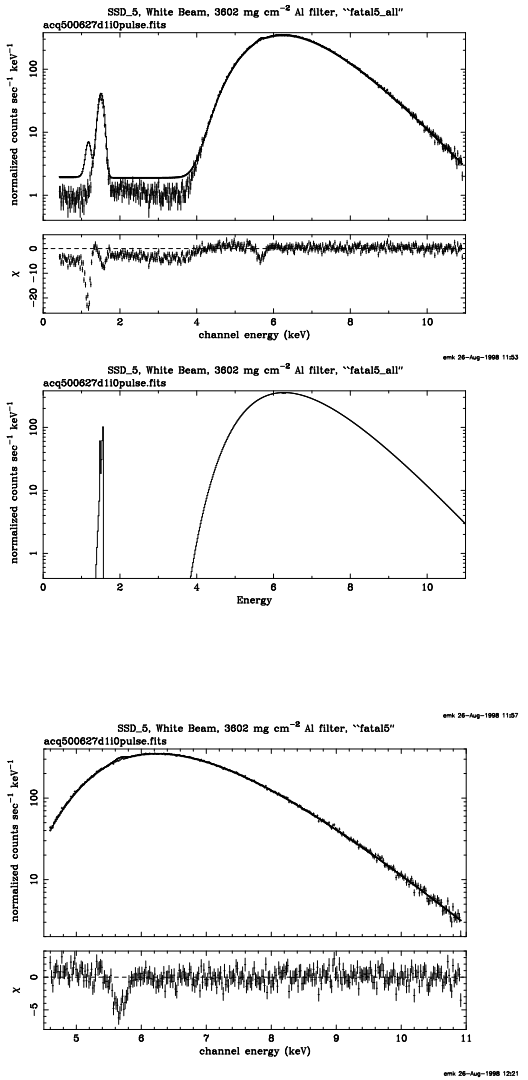

Figure 4.17: Data and XSPEC fit for ssd_5 at the white beam with 133.4 μm Al filter. The upper panel shows the entire pulse height distribution from the lower level discriminator cutoff at 0.4–10.8 keV, with folded SYNCH/XSPEC model. The center panel shows the input SYNCH model, 0.4–10.8 keV. The lower panel shows 4.8–10.9 keV, with folded model.

Parameter	Value	Status
alpha	0.	frozen
radius	2.500	frozen
distance	1.6242E+04	frozen
E_electr	798.2	frozen
H	1.491	frozen
e_to_cur	7.6970E−13	frozen
N_electr	0.	frozen
current	1.2901E+05	frozen
pileup	9.0914E−05	frozen
filter1	2.000	frozen
thcknss1	1.3340E−02	frozen
filter2	6.000	frozen
thcknss2	4.6609E−06	frozen
filter3	32.00	frozen
thcknss3	0.	frozen
filter4	48.00	frozen
thcknss4	6.8707E−05	frozen
filter5	19.00	frozen
thcknss5	1.0000E−05	frozen
filter6	45.00	frozen
thcknss6	0.	frozen
lineE1	1.550	0.8236E−01
sigma1	8.0000E−03	frozen
norm1	8864.	0.1054E+06
lineE2	1.486	0.4013E−01
sigma2	4.3000E−04	frozen
norm2	3.5642E+05	0.5932E+05
norm	0.6893	0.7891E−03

Table 4.19: Fitting parameters for ssd_5 white beam, all energies with 133.4 μm Al filter. Runid 500627, channels 21-549, nbins=529, reduced $\chi^2 = 12.19044$

Parameter	Value	Status
alpha	0.	frozen
radius	2.500	frozen
distance	1.6242E+04	frozen
E_electr	798.2	frozen
H	1.491	frozen
e_to_cur	7.6970E−13	frozen
N_electr	0.	frozen
current	1.2901E+05	frozen
pileup	4.1963E−06	0.2438E−02
filter1	2.000	frozen
thcknss1	1.3340E−02	frozen
filter2	6.000	frozen
thcknss2	2.3189E−07	0.1104
filter3	32.00	frozen
thcknss3	0.	frozen
filter4	48.00	frozen
thcknss4	1.3648E−07	0.8630E−01
filter5	19.00	frozen
thcknss5	7.4147E−07	0.2029
filter6	45.00	frozen
thcknss6	0.	frozen
lineE1	1.550	frozen
sigma1	8.0000E−03	frozen
norm1	8864.	frozen
lineE2	1.486	frozen
sigma2	4.3000E−04	frozen
norm2	3.5642E+05	frozen
norm	0.7496	0.7787E−02

Table 4.20: Fitting parameters for ssd_5 white beam, higher energies with 133.4 μm Al filter. Runid 500627, channels 231–269 and 301–549, nbins=288, reduced $\chi^2 = 1.164951$

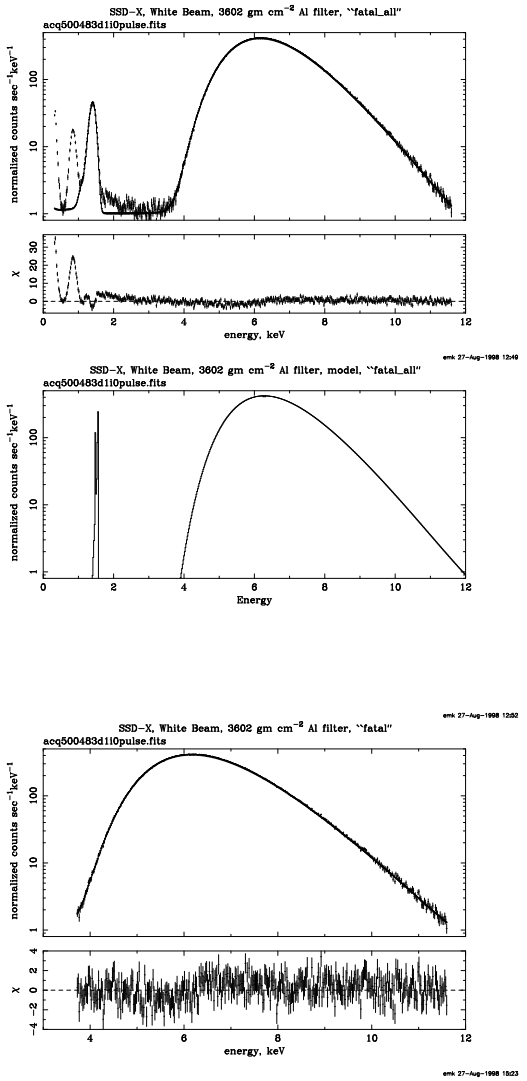

Figure 4.18: Data and XSPEC fit for ssd_x at the white beam with 133.4 μm Al filter. The upper panel shows the entire pulse height distribution from the lower level discriminator cutoff at 0.4–11.6 keV, with input synchrotron model folded through XSPEC. The center panel shows the input SYNCH model, 0.4–11.6 keV.The lower panel shows just 3.8–10.6 keV, with folded model.

Parameter	Value	Status
alpha	0.	frozen
radius	2.500	frozen
distance	1.6242E+04	frozen
E_electr	798.2	frozen
H	1.491	frozen
e_to_cur	7.6970E−13	frozen
N_electr	0.	frozen
current	1.2901E+05	frozen
pileup	9.0914E−05	frozen
filter1	2.000	frozen
thcknss1	1.3340E−02	frozen
filter2	6.000	frozen
thcknss2	4.6609E−06	frozen
filter3	32.00	frozen
thcknss3	0.	frozen
filter4	48.00	frozen
thcknss4	6.8707E−05	frozen
filter5	19.00	frozen
thcknss5	1.0000E−05	frozen
filter6	45.00	frozen
thcknss6	0.	frozen
lineE1	1.550	−1.000
sigma1	8.0000E−03	frozen
norm1	8864.	−1.000
lineE2	1.486	−1.000
sigma2	4.3000E−04	frozen
norm2	3.5642E+05	0.5631E+05
norm	0.7449	0.8526E−03

Table 4.21: Fitting parameters for ssd_x white beam, all energies with 133.4 μm Al filter. Runid 500627, channels = 21–49, 64–279, and 301-549, nbins = 494 reduced $\chi^2 = 5.836680$

Parameter	Value	Status
alpha	0.	frozen
radius	2.500	frozen
distance	1.6242E+04	frozen
E_electr	798.7	frozen
H	1.491	frozen
e_to_cur	7.6970E−13	frozen
N_electr	0.	frozen
current	1.7721E+05	frozen
pileup	3.9025E−04	0.6484E−03
filter1	2.000	frozen
thcknss1	1.3340E−02	frozen
filter2	6.000	frozen
thcknss2	0.	frozen
filter3	32.00	frozen
thcknss3	4.0312E−05	0.3247E−05
filter4	48.00	frozen
thcknss4	1.2267E−06	0.2486
filter5	19.00	frozen
thcknss5	1.2500E−04	frozen
filter6	45.00	frozen
thcknss6	0.	frozen
lineE1	1.488	frozen
sigma1	4.3000E−04	frozen
norm1	8.3373E+07	frozen
lineE2	1.552	frozen
sigma2	8.0000E−03	frozen
norm2	8.3937E+04	frozen
norm	0.6670	0.8215E−01

Table 4.22: Fitting parameters for ssd_x white beam, higher energies with 133.4.4 μm Al filter. Runid 500483, channels = 189–589, nbins = 401 reduced $\chi^2 = 1.232058$

Det.	File	ID 500+	keV	raw QE%	Pileup Corr'd%	σ %	lost Hz	e	Rate Hz	ROIrate Hz
ssd_5	noal5.log	614	3.5–6.6	101.9	102.2	1.3	4.66	8	1782.83	45.6616
	noal5_2.log	615	3.5–6.6	98.2	98.3	0.6	0.695	5	1112.03	28.3543
	MEAN		3.5–6.6	98.99	**99.1**	**0.6**				
	thickal5.log	635	3.5–6.5	59.8		1.1				
	fatal5.log:	627	4.8–10.9	75.0		0.8				
ssd_x	noal_sx700.log	480	2.8–5.9	73.3	73.4	0.6	1.442	5	984.231	20.38
	noal_2_sx700.log	481	2.8–5.9	72.9	72.9	1.0	0.387	2	405.229	8.00589
	MEAN		2.8–5.9	73.17	**73.3**	**0.5**				
	thickal.log	470	3.2–9.8	67.7		0.3	15.28			
	fatal.log	483	3.8–10.6	66.7		8.2	2.153			
ssd_5	noal5_all.log	614	0.4–6.5	97.19		0.2				
	noal5_all_2.log	615	0.4–6.5	99.62		0.1				
	thickal5_all.log	635	0.4–6.0	55.31		0.1				
	fatal5_all.log	627	0.4–10.8	68.93		0.1				
ssd_x	noal_all_sx700.log	480	0.4–7.9	71.80		0.7				
	noal_all_2.log	481	0.4–7.9	83.33		0.2				
	thickal_all.log	470	0.8–5.9	60.60		0.1				
	fatal_all.log	483	0.4–11.6	74.49		0.04				

Table 4.23: Summary of white beam normalization runs. See text for explanation.

time in the input data file to correct for dead time by counting the pulser pulses in the pulser peak appearing in the pulse height spectrum and dividing by the recorded total number of pulses from the pulser. The sixth column gives the QE corrected for pulser pileup, which is not accounted for in our XSPEC/SYNCH model. This is a very small correction done by adding back the pulses that have piled up with the pulser pulses. These appear in the pulse height spectrum at channels just above the pulser peak. They are recorded in column eight. Column seven gives the estimated 1 σ error in "Pileup Corr'd." Column nine gives the number of electrons in the storage ring for that run. Column ten gives the raw counting rate obtained by summing over all channels in the pulse height spectrum, and column ten gives the rate recorded in the ROI by the HXDS. This is just for the purpose of a sanity check for the four runs shown with no Al filter. It demonstrates that the rates are closely proportional to the number of electrons in the storage ring for runs 500614 and 500615, and also for runs 500480 and 500481. This seems to eliminate the possibility that the anomalous value of the QE for ssd_x could be a result of some gross error in the reduction and analysis of the pulse height data, because the raw rates show the same effect.

The rows with the entry MEAN give our best estimate of the overall QE and its σ for the two detectors. For ssd_5 the result is consistent with 1.00. For ssd_x it is not. This discrepancy between the two detectors is not seen in the SX700 QE measurements For example, in Tables 4.7 and 4.8 we see that the measured and predicted QE's are in very good agreement with a model that just includes low energy absorption from the known windows in the detector. There is no overall discrepancy of 27% as there is in the white beam measurements for ssd_x. This agreement is also seen in the flat field calibration done at XRCF Zhao et al. (1998). We must therefore assume that the white beam calibration of ssd_x is flawed, and is to be disregarded. However, we are continuing to investigate this problem to see if we can identify what caused the problem, such as a misalignment or some other thing that may have blocked some of the beam from entering the

	-400	-200	0	200	400
400	...	44.44	43.58	40.63	...
200	40.49	46.05	43.10	43.79	41.67
0	44.31	42.08	44.49	41.88	44.77
-200	43.23	44.77	42.50	43.12	41.78
-400	...	41.79	41.92	43.41	...

Table 4.24: BESSY ssd_x uniformity scan; unprocessed sum file data Rates are in counts per second; coordinates are in μm.

detector aperture.

4.6.5 Icing

Description of the detector and modeling of ice build up (we hope).
Trends of ice build up as a function of time
Nice plots again, etc.

4.6.6 Detector Uniformity

A uniformity scan of the SSD's was done at BESSY as well as XRCF. The scan at BESSY was done on the white light beam line with a movable 140 μm aperture. The aperture was scanned in a 5x5 raster pattern on 200 μm spacing. This gave a coverage of an area of about 1 mm x 1 mm. A similar scan was done at XRCF on the ssd_x detector using the focused HRMA beam.

The results from the BESSY ssd_x uniformity scan are shown in Table 4.24. These are unprocessed results based on the region of interest sums recorded in the sum files. No corrections for pileup, deadtime, or any other postprocessing effects have been made. The mean of these 21 measurements is 43.04 and the standard deviation is 1.43, or 3.3% of the mean. The number of counts in each measurement should be displayed, to see if these results are consistent with poisson fluctuations.

4.7 Future Work

- Continue to try to figure out why so many of the white beam runs give a low QE by 20–30%.
- Include recent fit with the new response matrices just built.
- More careful analysis of uniformity scans.
- Need to add more complete error propagation to BESSY results, to include effect of errors in measuring storage ring parameters.

Chapter 5

Deadtime and Pileup Correction in the HXDS FPCs and SSDs

Brad Wargelin

5.1 Introduction

The Ortec 671 shaping amplifiers and 921 multi-channel buffers (MCBs) used with the HXDS FPCs and SSDs provide automatic deadtime-correction estimates using built-in circuitry and algorithms that follow the Gedcke-Hale formalism. In most cases, this provides excellent deadtime estimates, particularly for work above several keV using solid state detectors. Our soft x-ray work, however, involves relatively weak signal amplitudes much smaller than such circuitry was designed to work with. In the SSDs, a 2 keV x-ray produces a preamplifier output signal of only 4 mV. The goal with the SSDs was to use them as low as 500 eV, which requires turning down the lower level discriminator (LLD) setting on the MCB to a very low level. At such a low level, the LLD effectively blocks sub-LLD events from appearing in the MCB spectrum, but the cutoff for the electronics processing isn't perfectly sharp and extends to a lower level, where there is a significant amount of steeply rising electronic noise. This hidden noise contamination becomes more severe as the LLD is lowered, and is impossible to avoid at energies below several keV in the SSD. The same problem applies to the FPCs, although less severely because the FPC preamp output signals are about 40 times larger.

The net effect is that sub-LLD, hidden-noise events contribute to the electronic deadtime but are not completely corrected for by the Gedcke-Hale (or any other) built-in deadtime correction circuitry. The alternative is to use the pulser method, in which artificial pulses are injected into the detector preamplifier to mimic real x-ray events. Since the pulses are processed just like x-rays, and subject to the same interactions with hidden noise events, preamplifier reset pulses, etc., the fraction of pulses that appear in the output spectrum is, to a good approximation, equal to the system livetime. Some care must be taken, however, to make the pulses look something like x-ray signals, avoid under- or over-shoot, and to select a rate as low as possible but high enough to provide adequate statistics.

A pulser cannot perfectly mimic real x-rays because the output pulses are not randomly distributed in time. Most pulsers emit regularly spaced pulses; some are designed to be more random, triggering off electronic noise, but the trigger threshold is continuously adjusted to keep the average pulser rate near the set point, which leads to a pulse distribution which is somewhere between

regular and random. For many applications this is good enough, but not for our system.

A more truly random pulser can be constructed using radioactive decay to trigger a pulse, but there is still a limit to how close together the pulser can emit pulses. Such systems are also more complicated—typically consisting of a radioactive source, a detector, preamplifier, amplifier, single- or multi-channel analyzer, and the pulser which is triggered by a TTL signal from the analyzer—and we didn't have enough rack space or electronic units to use in the 5 pulser systems at XRCF. The XRCF safety officers would also be unenthusiastic about having 5 radioactive sources floating around. We therefore settled on using the regular pulser method, and developed models to correct for the nonrandomness of the pulses.

Historical note: During AXAF calibration at the XRCF, electronic noise was extremely low and we probably could have gotten away with the built-in deadtime estimates for the FPCs. The pulser method, however, was necessary for other work, particularly early on. The HXDS lab originally had a great deal of electronic noise, MCB deadtime errors were very apparent, and something had to be done. Noise was also often a problem when calibrating the detectors at the BESSY synchrotron. Lastly, because of their greater intrinsic noise, the SSDs required pulsers even at XRCF.

5.2 Deadtime and Pileup Time Windows

The time intervals of relevance to our signal processing model are:

T_{shape}	the shaping amplifier time constant
T_{pile}	pileup time window
T_{peak}	time for the shaping amplifier output signal to reach its peak, roughly 2 x T_{shape}
T_{width}	full width of the shaping amp output signal, roughly 8 x T_{shape}
t	time between one event and the next event.

Treatment of each pulse depends on how closely it is followed by the next pulse:

$0 < t < T_{pile}$	The pileup rejection (PUR) circuitry cannot distinguish between the two events and they are treated as one valid event, with an amplitude equal to the sum of the two.
$T_{pile} < t < T_{peak}$	PUR is activated, and both events are thrown out because the amplitude of neither can be determined
$T_{peak} < t < T_{width}$	PUR is activated, and the second event is discarded
$T_{width} < t$	Both events are processed as valid

The two time windows that really matter are T_{pile} and T_{dead}. $T_{dead} = T_{peak} + T_{width}$ ($-T_{pile}$ if you want to be picky). Notice that T_{peak} is effectively counted twice in T_{dead} (since it is contained within T_{width}), because if the two events occur within that time they are both discarded. Typical times for the shaping time constants we use are:

T_{shape} (μs)	T_{pile} (μs)	T_{dead} (μs)	Detector
0.5	0.6	5.8	(all FPCs used 0.5 μs)
2	0.6	18	(a very few SSD runs used this at XRCF)
10	0.6	75	(almost all the SSD measurements used this)

The table below illustrates the contributions of deadtime and pileup:

T_{shape} (μs)	X-ray rate (cts/s)	Deadtime (%)	Pileup (%)
0.5	10000	5.64	0.60
0.5	1000	0.58	0.06
10	1000	7.23	0.06
10	100	0.75	0.01

The exact values of T_{dead} and T_{pile} depend on the particular shaping amplifier used (and to a much lesser extent the MCB and preamp). The pileup time, in particular, shows the most relative variation from one unit to another—0.3 to 1.0 μs. When the pileup rejection is working, pileup events only occur when the two signals peak nearly simultaneously (within T_{pile}), so there is a single pileup peak (assuming a monochromatic input spectrum). When PUR is not working, the second event can ride on the tail of the first, and the MCB will record an event any time a local maximum in the (summed) signal is detected, thus causing lots of "interpeak" events in the spectrum. As was discovered after XRCF, and discussed in Chapter 4, because the SSD preamp signals are so small at low x-ray energies, the pileup rejection starts to fail at about 2 keV. Below that, there is either a partial or complete lack of pileup rejection and deadtime. Approximate corrections for the lack of PUR below 2 keV are explained in Chapter 11.

5.3 Calibration Measurements

Two kinds of measurements were made to calibrate the pulser method: 1) deadtime consistency (DTC) tests, looking at a fixed intensity source with a stable-QE detector under a variety of operational parameters, and comparing the regular pulser method with the radioactively triggered random pulser method, and 2) counting rate linearity (CRL) measurements at the BESSY synchrotron, in which relative incident x-ray rates are known with high precision.

The BESSY CRL measurements were conducted on both SSDs and two FPCs in late 1997 and early 1998, but the data have not yet been analyzed. Relative beam intensity uncertainties are $\pm$0.6% on the SX700 monochromator beamline and $\pm$0.2% on the white beam. For the FPCs, the range of calibrated counting rates was 1000-25000 Hz, with x-ray and pulser statistics of $\pm$0.1%. Analysis of the BESSY CRL data may be complicated by the non-random nature of the synchrotron emission—only about half of the ring "buckets" are filled, contiguously.

The DTC testing was conducted in the HXDS lab using a strong radioactive source (^{55}Fe, emitting Mn Kα photons at 5.9 keV) and an SSD (ssd_5). FPCs could not be tested with the desired accuracy because their QE is very sensitive to temperature and gas density fluctuations at that energy (we wanted to make measurements to 0.1% accuracy), and because a suitable test chamber was not available in time. FPC testing was also deemed unnecessary because the SSDs and FPCs use identical pulse height analysis electronics chains.

5.4 Deadtime consistency testing

5.4.1 Experimental configuration

DTC tests were conducted Jan. 4–5 1996 and Sept. 18–23 1997 by Brad Wargelin and Mike McDermott. The 1997 data have not been analyzed, but all data were collected in the same way. In the 1996 testing, three types of pulser were used:

- a regular pulser with a fixed rate,
- a (pseudo)random pulser with varying time intervals between pulses and a roughly fixed average rate (triggered by noise),

- and a random pulser which was triggered by radioactive decays,

along with many different combinations of:

- shaping amp time constant (2 or 10 μs–also 0.5 for the 1997 runs)
- multi-channel buffer lower level discriminator (LLD) setting (20 or 45)
- pulser rate (100 to 500 Hz—30 to 500 Hz for 1997 runs).

Spectra were collected with the x-ray source at two distances from the detector, at x-ray rates of approximately 2900 and 8800 Hz (the highest rate achievable). The 8800-Hz measurements only used a shaping time constant of 2 μs because the deadtime fraction using the 10-μs setting would be much too large. Two "random" and two "regular" spectra were collected at the higher x-ray rate, and five random and eight regular spectra at the lower rate. Data using the pseudorandom pulser were problematic to analyze because of the not-regular yet not-really-random nature of the pulses. The results were poor and are not discussed further. Information for the 1996 measurements is tabulated below.

RunID	Approx. R_{x-ray} (cts/s)	LLD	Approx. R_{pulser} (cts/s)	T_{shape} (μs)	Mode	MCB deadtime MCBdead	T_{real} (s)	X-ray counts
80208	8800	20	500	2	random	18.17	300	2210106
80213	8800	20	100	2	random	16.97	1000	7491697
80212	8800	20	500	2	regular	18.39	300	2234150
80217	8800	20	100	2	regular	17.02	1000	7488795
80229	2900	20	100	10	random	21.56	1000	2303596
80230	2900	20	100	2	random	8.50	1000	2765301
80231	2900	20	500	2	random	10.19	1000	2752915
80243	2900	45	200	2	random	4.95	1000	2766311
80244	2900	45	200	10	random	20.73	1000	2318810
80223	2900	20	100	10	regular	21.51	1000	2304904
80224	2900	20	100	2	regular	8.46	1000	2770243
80235	2900	20	500	2	regular	10.05	1000	2749523
80236	2900	20	500	10	regular	24.39	1000	2243354
80237	2900	45	500	10	regular	22.33	1000	2274635
80238	2900	45	500	2	regular	5.41	1000	2758089
80239	2900	45	100	2	regular	4.79	1000	2771131
80240	2900	45	100	10	regular	20.19	1000	2339508

5.4.2 Data reduction

Each spectrum was analyzed by first determining the number of counts in various features:

- N_x – the main x-ray peak (down to 2.5 keV to include the bulk of the shelf)
- N_{xx}^{pile} – the x-ray/x-ray pileup peak
- N_p – the pulser peak
- N_{xp}^{pile} – the x-ray/pulser pileup peak.

The number of injected pulses (N_{pin}) and the total exposure time (T_{real}) were also recorded for each measurement.

Note that it was not necessary to fit the x-ray peaks, since we were only interested in whether or not we got the same rate when looking at the same signal. Regions of interest (ROIs) were fine to

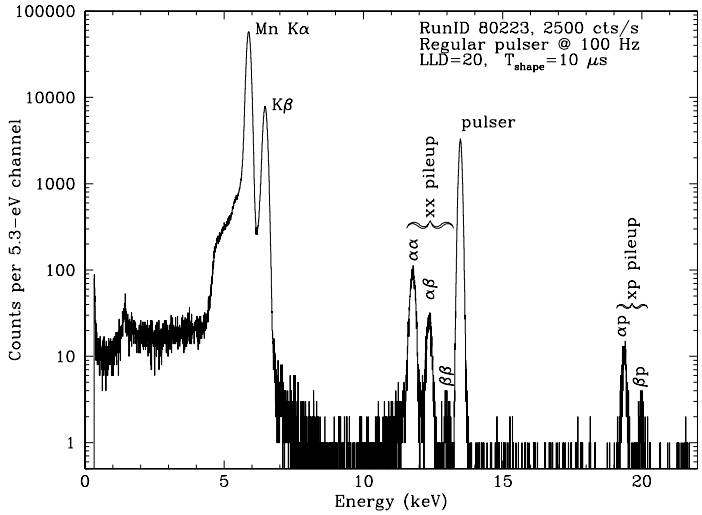

Figure 5.1: Example ^{55}Fe spectrum used in CRL calibration. X-ray and pulser peaks, and resulting pileup, are marked. True x-ray input rate was determined to be 2937.3 ± 5.1 cts/s, with a deadtime of 21.14% and pileup fraction of 0.23%.

use (in fact, more accurate than fitting peaks) because the ^{55}Fe spectrum was so clean, with well-defined features (see Figure 5.1). For consistency, ROIs were adjusted slightly to account for slightly differing energy scales when using different shaping time constants. Errors in N_x determinations are estimated to be less than 0.02%.

Background spectra were also collected for each combination of shaping time constant and LLD setting. Even when nothing appeared in the spectra but the pulser peak (not even electronic noise), the deadtime sometimes exceeded 0.2%. In order to reach our goal of 0.1% measurement accuracy, we therefore assigned a rate of "hidden" events (from sub-LLD noise, discussed above) for each shaping time/LLD combination. The rates R_{hid} were determined from *livetime fraction* $= N_p/N_{pin} = e^{-(R_{hid}+R_{pin})T_{dead}}$ using equations derived in §5.4.3 and are listed below.

T_{shape} (μs)	LLD	R_{hid} (cts/s)
2	20	150
2	45	20
10	20	10
10	45	0

5.4.3 Correction equations

Corrections were then made to reconstruct what the spectra would look like if 1) pulser events were perfectly random and 2) if there were no pileup. Our corrections are extensions of those described by Bolotin, Strauss, and McClure (NIM 83, 1-12 [1970]). The objective is to derive corrected values for N_x and N_p. T_{dead} and T_{pile} are also determined during the analysis. Once corrected,

pileup and x-ray events experience the same deadtime, and the ratios of corrected detected and input x-ray and pulser events must be same. The input rate of x-ray events is then given by

$$R_{xin} = (N'_x/T_{real})(N'_p/N_{pin}), \tag{5.1}$$

where the prime ($'$) denotes corrected values.

By definition, the system livetime fraction is

$$\begin{aligned} N'_p/N_{pin} &= \textit{Probability of 0 events within } T_{dead} \\ &= e^{-(\textit{input rate of all events})T_{dead}} \\ &= e^{-(R_{xin}+R_{hid}+R_{pin})T_{dead}}, \end{aligned} \tag{5.2}$$

where we have also used Poissonian statistics, in which the probability of N events occurring within a time interval T when the average rate of the events is R is given by

$$P(R \mid N,T) = \frac{(RT)^N}{N!}e^{-RT}. \tag{5.3}$$

The value of T_{dead} can thus be determined from

$$T_{dead} = -\ln\left(\frac{N'_p}{N_{pin}}\right)/(R_{xin}+R_{hid}+R_{pin}). \tag{5.4}$$

Likewise the x-ray/x-ray pileup fraction is given by

$$\begin{aligned} N^{pile}_{xx}/N_x &= \textit{Probability of 1 } x-\textit{ray event within } T_{pile} \\ &= R_{xin}T_{pile}e^{-R_{xin}T_{pile}}. \end{aligned} \tag{5.5}$$

The exponential term is nearly 1, and T_{pile} can be adequately approximated as

$$T_{pile} = (N^{pile}_{xx}/N_x)/R_{xin}. \tag{5.6}$$

T_{dead} is used extensively in the equations that follow; T_{pile} is only needed when analyzing non-monochromatic spectra, in which case the number of pileup events, N_{xx} and N_{xp}, usually can not be measured directly and must be estimated.

To correct for pileup, the number of main peak x-ray counts is increased by $2\times$ *number of xx pileup counts* plus $1\times$ *number of xp pileup counts*, and the number of main pileup peak counts is increased by $1\times$ *number of xp pileup counts*. The equations are

$$N'_x = N_x + 2N^{pile}_{xx} + N^{pile}_{xp} \tag{5.7}$$

and

$$N'_p = N_p + N^{pile}_{xp}, \tag{5.8}$$

where the prime ($'$) refers to the corrected number of x-ray or pulser counts (in the absence of pileup).

The nonrandomness corrections are somewhat more complicated, and based on the fact that pulser events cannot interact with themselves the same way they would if they occurred randomly in time. There are therefore fewer (or no) deadtime losses or pileup events, which means that more pulser counts appear in the spectrum than should. Likewise, those "extra" pulser events can interact with x-ray events and lead to the loss of some x-ray counts.

For the regular pulser, pulser events can never cause deadtime for another pulser event because the pulses are too far apart. For the random pulser, pulser events can occur as close together as 2.5 μs (limited by the amplifier used to trigger the pulser), which is nearly random but still a non-negligible interval of time. Treatment of the two sets of data is therefore slightly different. Specifically, Eqs. 5.9 and 5.10 are correct only for the regular pulser; the first two occurrences (of three) of "T_{dead}" within each must be replaced by "2.5 μs $-T_{pile}$" when the random pulser is used.

Referring to Eq. 5.3, the number of pulser-pulser deadtime events that did not occur, but would have occurred if the pulser were perfectly random is

$$\begin{aligned} N_{pp} &= (\textit{Number of input pulses}) \\ &\quad \times (\textit{Probability that another pulser event occurs within the deadtime time window}) \\ &\quad \times (\textit{Probability that no other non} - \textit{pulser} (x - \textit{ray or hidden}) \textit{ events occur during } T_{dead}) \\ &= (N_{pin})(R_{pin}T_{dead}e^{-R_{pin}T_{dead}})(e^{-(R_{xin}+R_{hid})T_{dead}}). \end{aligned} \tag{5.9}$$

Likewise, the number of pulser-pulser-pulser deadtime events that did not occur, but would have appeared in the spectrum if the pulser were perfectly random is

$$\begin{aligned} N_{ppp} &= (\textit{Number of input pulses}) \\ &\quad \times (\textit{Prob that 2 pulser events occur within the deadtime window}) \\ &\quad \times (\textit{Prob that no other non} - \textit{pulser events occur during } T_{dead}) \\ &= (N_{pin})(\frac{(R_{pin}T_{dead})^2}{2!}e^{-R_{pin}T_{dead}})(e^{-(R_{xin}+R_{hid})T_{dead}}). \end{aligned} \tag{5.10}$$

The total number of extra pulser events floating around and able to interfere with non-pulser events is then (excluding negligible higher-order terms)

$$N_{p\,extra} = N_{pp} + 2N_{ppp}. \tag{5.11}$$

Of those extra events, a fraction (about equal to the system livetime) end up in the pulser peak, and the rest (the deadtime fraction) follow an x-ray or hidden noise event within the T_{dead} time window and are discarded. Likewise, some of the extra pulser events create deadtime and cause some x-ray events that should have been recorded to instead be discarded. The number of pulser and x-ray counts must therefore be adjusted as follows:

$$\text{Pulser counts to subtract} = N_{p\,extra}e^{-(R_{xin}+R_{hid})T_{dead}} \tag{5.12}$$

$$\text{X} - \text{ray counts to add} = N_{p\,extra}(1 - e^{-R_{xin}T_{dead}}) \tag{5.13}$$

There are higher-order corrections such as the absence of pulser-pulser pileup, and other subtleties such as SSD preamp resets, but they are all negligible and in some cases difficult to accurately quantify, and are not discussed further. The final equations for the pileup- and nonrandomness-corrected numbers of x-ray and pulser counts are therefore

$$N'_p = N_p + N^{pile}_{xp} - (N_{pp} + 2N_{ppp})e^{-(R_{xin}+R_{hid})T_{dead}} \tag{5.14}$$

and

$$N'_x = N_x + 2N^{pile}_{xx} + N^{pile}_{xp} + (N_{pp} + 2N_{ppp})e^{-R_{xin}T_{dead}}. \tag{5.15}$$

Eqs. 1, 4, 9, 10, 14, and 15 are then solved iteratively, using improved values for R_{xin} and T_{dead} until convergence.

Analysis of spectra using the random pulser (which, as noted above, is not completely random since pulses cannot be injected less than 2.5 μs apart) is more reliable then when using the regular pulser because the corrections for nonrandomness are smaller. We therefore assume that the x-ray rates derived from the corrected random pulser data are the true rates. The 2.7-year half-life of the ^{55}Fe source was accounted for, leading to rate adjustments of up to 0.07%.

The statistical accuracy of the pulser livetime determination is set by the number of pulses that are lost to deadtime. The fractional error is given by

$$\frac{\sigma_{LT}}{LT} = \frac{[(N_{pin} - N_p)^{0.5}/N_{pin}]}{[N_p/N_{pin}]}. \tag{5.16}$$

Net error is given by quadrature summing of the relative statistical errors in the deadtime and number of x-ray counts.

5.4.4 Results

Using the corrections described above, the following results were obtained:

random:		
average of 5 tests	2942.8	Hz
average statistical uncertainty (+/-)	3.2	(0.11%)
variance	3.3	(0.11%)
regular:		
average of 8 tests	2940.2	
average statistical uncertainty (+/-)	3.2	(0.11%)
variance	4.4	(0.15%)
difference from average random result	-2.6	(-0.09%)
random:		
average of 2 tests	8787.4	
average statistical uncertainty (+/-)	11.4	(0.13%)
variance	4.2	(0.05%)
regular:		
average of 2 tests	8740.4	
average statistical uncertainty (+/-)	10.9	(0.13%)
variance	1.7	(0.02%)
difference from average random result	-46.6	(-0.53%)

As can be seen, agreement between the regular- and random-pulser results for the 2900-Hz measurements is excellent. For comparison, the built-in MCB livetime differed from the pulser-method value in some cases by more than 4%. Agreement among the 8800-Hz measurements is not quite as good, but those measurements were made under extreme conditions, far more difficult than any encountered during AXAF calibration. The actual conditions at XRCF (LLD/noise level, pulser rate, and x-ray rate) were much less challenging than in any of our testing.

5.4.5 Simplified and More General Method for Deadtime Determination

The above results were derived for the case of a nearly pure monochromatic source, in which pileup peaks can be easily discerned. For the vast majority of AXAF calibration data, however, it

is difficult to distinguish pileup peaks from continuum spectra, and so a second deadtime-correction program was also written with the intention that it be applied to any spectrum in which one x-ray energy was quasi-dominant, such as in EIPS spectra. That program does not require the number of pileup counts to be determined; those were calculated based simply on the number of (fitted) counts in the x-ray peak, the estimated value of T_{pile}, and the number of pulser peak counts (plus other quantities that are simply read in from the data file header such as integration time T_{real} (`trueTime_sec`) and the number of injected pulses N_{pin} (`autoDeadTime_pulses`).

As a test of its accuracy, this program was used to analyze the regular pulser data described above. Using a fixed value of 0.78 μs for T_{pile} (which must be independently determined for each shaping amplifier) the results were:

average of 8 tests	2940.2	Hz
average statistical uncertainty (+/-)	3.2	(0.11%)
variance	4.9	(0.17%)
difference from average random result	-2.6	(-0.09%)
average of 2 tests	8761.7	
average statistical uncertainty (+/-)	11.0	(0.13%)
variance	0.0	(0.00%)
difference from average random result	-25.7	(-0.29%)

At the lower rate, the results were statistically identical. At the higher rate, agreement with the random pulser results improved from 0.5% to 0.3%. This fortuitous improvement was mostly because of a discrepancy in the number of x-ray/pulser pileup counts; the number of observed counts is about 20% larger than predicted. At this time (Mar 1998) the cause of this discrepancy is not known for certain. In any case, the second deadtime correction method works at least as well and is easier.

5.4.6 Estimated accuracy in analysis of AXAF calibration data

The SSD calibration data were taken under more challenging conditions (with respect to deadtime correction accuracy) than for virtually all AXAF calibration data. In particular, the deadtime caused by the pulser (which scales as the product of the shaping time constant and pulser rate) was much higher than used during AXAF calibration, resulting in larger correction terms and therefore larger uncertainties in the final deadtime calculation.

A comparison of the magnitude of deadtime corrections—for the deadtime calibration measurements described above vs. AXAF calibration measurements—was made using model SSD and FPC spectra as inputs, with pulser rates and shaping time constants set to the values actually used during AXAF calibration, specifically:

SSD shaping time constant	= 10 μs	pulser rate =	27 Hz
FPC shaping time constant	= 0.5 μs	pulser rate =	300 Hz

The two contributions to deadtime correction (pileup and pulser nonrandomness) were calculated, along with the net deadtime correction which may differ slightly from the sum of the two estimated contributions because of the iterative process involved and because the two effects are not entirely independent. In the table of results below, "Raw rate" refers to the x-ray rate derived from uncorrected pulser counts, or

$$\textit{Raw rate} = (N_x/T_{real})(N_p/N_{pin}). \tag{5.17}$$

Raw rate(Hz)	Pileup (%)	Pileup corr(%)	Nonrandom corr(%)	Net corr(%)	Final rate
SSD CRL calibration data					
8694.14	1.177	0.076	0.723	0.778	8761.74
8747.94	1.183	0.014	0.151	0.158	8761.72
2919.57	0.361	0.016	0.652	0.668	2939.08
2938.60	0.434	0.016	0.180	0.188	2944.14
2913.85	0.431	0.078	0.791	0.909	2940.34
2848.27	0.352	0.080	3.210	3.404	2945.22
2840.16	0.357	0.080	3.027	3.233	2931.97
2917.14	0.432	0.078	0.795	0.916	2943.87
2928.77	0.434	0.016	0.174	0.181	2934.09
2924.24	0.367	0.015	0.611	0.626	2942.55
Model SSD data					
100.00	0.015	0.004	0.153	0.188	100.19
500.00	0.075	0.004	0.190	0.199	501.00
900.00	0.131	0.004	0.191	0.196	901.78
1200.00	0.170	0.004	0.189	0.193	1202.30
1500.00	0.208	0.004	0.187	0.191	1502.86
Model FPC data					
1000.00	0.155	0.047	0.132	0.172	1001.72
5000.00	0.763	0.046	0.158	0.170	5008.52
10000.00	1.493	0.043	0.158	0.167	10016.70
15000.00	2.191	0.039	0.153	0.161	15024.20
20000.00	2.857	0.034	0.145	0.151	20030.27

Note that the net pileup correction is quite small. This is because the fractions of pileup events added to the main x-ray and pulser peaks are nearly the same (both scaling nearly linearly with x-ray rate), and so the corrections to each roughly cancel out. Also note that the net corrections to the x-ray rates are nearly constant regardless of the rate.

5.5 Recommendations

For SSD spectra at energies above 2 keV, the pulser method must be used since the MCB deadtime estimate can be off by several percent. For the FPCs, the pulser method can always be used, but the MCB deadtime estimate is probably good enough that it can be used *if* pileup corrections are made.

When using the pulser method, whether for SSDs or FPCs:

1. Fit the number of x-ray line counts in the main peak
2. Determine the number of pulser counts (excluding any piled-up counts)
3. $R_{xin} = 1.0018(N_x/T_{real})(N_p/N_{pin})$.

The resulting number, with appropriate statistical uncertainty estimates, should have systematic errors of less than +/-0.10% for rates up to 2500 Hz. For higher rates with the FPCs, systematic errors are estimated to be less than 0.25% at 10000 Hz and 0.50% at 20000 Hz. Note that corrections for pileup are automatically included.

For the FPCs, if you don't want to bother finding the number of counts in the pulser peak, it's probably good enough to use the MCB deadtime. You must correct for x-ray/x-ray pileup,

however, by adding twice the rate of pileup counts back in to the main x-ray peak. Rather than try to fit the pileup peak (which is quite broad in the FPCs, and sits on top of continuum), it's much easier to simply estimate the rate of pileup counts as $R_{pile} = R_{xin} \times T_{pile}$ where T_{pile} is about 0.6 μs. (T_{pile} can be off by +/- 0.2 μs or so, but that's only a 0.4% error in the x-ray rate at 10000 Hz. Eventually we will analyze selected data from each FPC and SSD to determine T_{pile} for each shaping amp.)

To make sure you handle the pileup correction correctly, with the proper deadtime, use this equation:

$$R_{xin} = N_x/T_{live}[1 + 2T_{pile}N_x/T_{live}] \tag{5.18}$$

where T_{live} is the MCB livetime listed in the *.pha file header (`liveTime_sec`).

5.6 Appendices

Two FORTRAN programs were used to derive the results presented above. `do98_12.f` is for analyzing the SSD deadtime consistency data. `test.data` is the input file and `do98_12.out` is the output file. `correct4.f` can be used to analyze the results from any spectrum, and calculates the expected xx and xp pileup so that those peaks don't have to be fitted in the spectrum. Sample input and output files are also listed. Files are located at `http://hea-www.harvard.edu/MST/hxds/topics/` under "Deadtime and Pileup Correction in the HXDS FPCs and SSDs."

Chapter 6

FPC Window Mesh Effect and its Correction

Ping Zhao

6.1 Introduction

During the HRMA calibration, the HXDA Flow Proportional Counters (FPC) were filled with P10 gas (90% Ar + 10% CH_4) with a constant pressure of 400 torr and operating temperature of approximately 20°C. The FPC windows were made of 1 μm polyimide ($C_{22}H_{10}O_4N_2$) with 0.02 μm aluminum coating. A wire mesh was used to support this very thin window membrane under vacuum. The wires were made of 0.1 mm diameter gold-plated tungsten with 2 mm pitch.

As the wires are opaque within the energy range of the calibration X-rays, the mesh changes the FPC window transmission. For BND counters, assuming a uniform distribution of the X-rays, the transmission is decreased by a factor of

$$\frac{(2mm - 0.1mm)^2}{(2mm)^2} = 0.9025 \tag{6.1}$$

(see also §3.2.2). For the focal plane FPC, the transmission decrease due to the mesh is much more complicated. During the VETA-I calibration, the FPC mesh was made with 50.8 μm diameter wire, an average pitch of 529.17 μm, and located 25 mm behind the focal plane. The X-ray transmission varied from 75% to 92%, depending on the phase of the mesh grid relative to the single photon ring on the mesh.(Zhao et al., 1992)

For the HRMA calibration, improvements have been made to reduce the mesh effect: the mesh pitch was increased to 2 mm and the distance between the aperture plate and center of the mesh window was reduced to 9.1±0.2 mm.[1] Thus the four photon rings from the four HRMA shells should be inside one mesh grid cell if the mesh is well centered. The mesh wires should not block any of the focused photons. However, in case the mesh were not centered, its effect can be very severe. Theoretically, it can decrease the transmission by more than 40% in some cases (e.g. when mesh wire block X-rays from one side of the ring 6). Even the mesh were well centered, the mesh wires could still block scattered photons. Therefore, the mesh effect needs to be carefully evaluated and its corrections needs to be calculated in order to obtain the correct calibration results.

This Chapter discusses the mesh effect and its corrections for the on-axis encircled energy measurements.

[1] During the calibration, this was thought to be 9.7 mm based on the then available data. It was remeasured after the calibration to be 9.1±0.2 mm.

6.2 HRMA Image on FPC Mesh

Since the FPC mesh window is located about 9.1 mm behind the aperture plate, when the aperture plate was positioned in the HRMA focal plane, the focused X-rays diverge behind the aperture and form four ring patterns entering the mesh window. The diameters of the four rings are 1.06 mm, 0.85 mm, 0.75 mm, and 0.56 mm, respectively. X-rays that fall on the mesh wire will not enter the FPC and therefore will not be counted. (For high energy X-ray photons hit the edge of the wire, some of them may go through. But this effect is very small and completely negligible for our data analysis.)

Figure 6.1 is a HSI image with −9.7 mm defocus with an Al-Kα source. (This was thought to be the FPC mesh position during the calibration. The actual mesh position was measured after the calibration to be −9.1±0.2 mm defocus.) The horizontal line underneath the figure indicates 1 mm. Four rings are clearly shown in the image, as well as the effect due to the gravity and epoxy strain (see Chapter 18). Ring 6 is tilted to the lower left as is known.

6.3 Mesh Transmission Model

Raytracing simulations were made to model the mesh transmission. Figures 6.2–6.5 are simulated images of four individual shells at the mesh window plane (−9.1 mm defocus), with an Al-Kα source. Each figure is 2×2 mm^2 – the size of a mesh grid cell. For shell 1 the mesh cell has to be centered within 300 μm laterally with respect to the focus in order to avoid the mesh wire. For other shells, this tolerance is larger as the rings are smaller. Figures 6.6–6.9 are simulated images of the full HRMA with four different energies when they enter the mesh window.

The mesh transmission can be modeled by moving a blocking mesh grid with respect to the photon images generated by raytrace. Here the transmission is the ratio of with mesh in place versus without mesh.

Figures 6.10–6.13 show the mesh transmission as a function of Y and Z offset for four individual shells with an Al-Kα source. The plateau in the center of each figure indicates where the mesh is centered well enough so that the transmission is near 100%. For shell 1, the transmission plateau is the smallest because its tolerance is the smallest as mentioned above. For other shells, the plateau becomes larger as their tolerance increases.

Figures 6.14–6.25 show the mesh transmission as a function of Y and Z offset for the full HRMA with four different energies (1.49 keV, 4.51 keV, 6.40 keV, and 8.64 keV) and three aperture sizes (0.01 mm, 1 mm, and 35 mm). The center transmission plateau is smaller for lower energies as most of the X-rays are reflected by shell 1. For higher energies, as less X-rays reflected from outer shells and more X-rays reflected from inner shells, the tolerance of mesh centering becomes larger and so is the plateau. For the 0.01 mm aperture, the transmission plateau is not a square because the aperture cuts off some of the focused photons.

6.4 Mesh Scan

In order to check the exact location of the FPC window mesh with respect to the focus, mesh scan tests were needed in which an aperture was fixed at the focus while the FPC counter scans behind the aperture. During the calibration, three such mesh scans were made. With the 1 mm aperture fixed, FPC-X2 counter (the focal plane FPC detector) were scanned in both Y and Z directions to measure the variations in the counting rate. The scans went from −1.2 mm to 1.2 mm with respect to the current counter location. Table 6.1 lists these three mesh scans.

Table 6.1: HXDS FPC-X2 Mesh Scans

Date (GMT)	Run ID	TRW ID	Source	Aperture	Y-offset	Z-offset
961221	106785	C-IXF-FM-3.001	Al-Kα	1.0 mm	-0.4176 mm	-0.0827 mm
961224	106926	C-IXF-FM-61.001	Al-Kα	1.0 mm	-0.3978 mm	-0.0221 mm
970115	108922	D-IXF-FM-3.002	C-Kα	1.0 mm	$+0.0188$ mm	-0.1449 mm

By fitting the mesh scan data to the mesh transmission model, the exact mesh positions can be located. Figures 6.26–6.28 show these three pairs of mesh scan data and their fit to the mesh transmission model. It is obvious that the first two scans reveal the mesh was offset in the Y direction by about 400 μm.

After the first mesh scan was made on 1996/12/21, it was known that the mesh center was off. But no corrections were made as that was at the very beginning of the calibration. Three days later, after the second mesh scan was made, a correction was made to bring the mesh center aligned with the aperture center, using a quick look analysis. When the third mesh scans were made on 1997/01/15, the mesh was still reasonably well centered. According to the scan data, it was only off very little in the Z-axis. This could be due to the counter was drifting off slowly, or the original centering was not perfect. On 1997/01/16, a mesh center correction of $+95\mu$m in the Z-direction was made based on a quick look analysis of mesh scan data on 1997/01/15.

Therefore, there were four mesh center positions during the calibration, based on the mesh scan data and subsequent corrections. Table 6.2 lists these mesh positions. We do not know the exact location between the mesh scan measurements. It might have drifted a little, but that should not be too much. Figure 6.29 shows these mesh center positions during the calibration.

Table 6.2: HXDS FPC-X2 Mesh Center Positions

Position	Dates (GMT)	Run IDs	Y-offset	Z-offset
1	1996/12/20 – 1996/12/21	106697 – 106785	-0.4176 mm	-0.0827 mm
2	1996/12/21 – 1996/12/24	106786 – 106926	-0.3978 mm	-0.0221 mm
3	1996/12/24 – 1997/01/16	106927 – 109015	$+0.0188$ mm	-0.1449 mm
4	1997/01/16 – 1997/02/11	109016 – 111906	$+0.0188$ mm	-0.0499 mm

As all the HRMA on-axis encircled energy measurements were made during the phase D and E of the calibration, i.e. period of 1996/12/31 – 1997/02/11, only mesh position 3 and 4 are relevant for calculating the mesh effect corrections.

6.5 Mesh Correction

Using the mesh center offset at positions 3 and 4, the mesh transmission can be calculated using the raytrace simulation. Mesh correction is the reciprocal of the calculated mesh transmission.

Tables 6.3 – 6.7 give the mesh effect correction factors for Shell 1, Shell 3, Shell 4, Shell 6, and HRMA, respectively. Aperture diameters and the X-ray energies are the ones actually used for the calibration. At the inter section of Aperture and Energy, the Tables give the corresponding mesh correction factor. For example, for Shell 1, Zn-K source (8.6389 keV), 35 mm aperture, and

on 1997/01/20, the on-axis FPC encircled energy result needs a mesh correction of 1.0284 (this actually is the largest mesh correction factor in all five tables). Because the HXDS system was properly designed and the mesh was well centered during the encircled energy measurements, the mesh effect was very small. Except for Shell 1 and large aperture, higher energies, most of the correction factors are less than 1%. No corrections are needed for apertures less or equal to 0.5 mm diameter.

6.6 Conclusion

Based on the mesh scan data taken during the HRMA calibration and raytracing simulations, the HXDS FPC window mesh effects were studied and its correction factors were calculated. For the on-axis encircled energy measurements,[2] the mesh effect was very small. Except for Shell 1 and large aperture, higher energies, most of the correction factors are less than 1%. The mesh effect corrections are listed in five tables at the end of this Chapter.

[2]For the off-axis encircled energy measurements, the mesh effects are much more severe and complicated (depends on the off-axis angle and direction), which is beyond the scope of this Chapter.

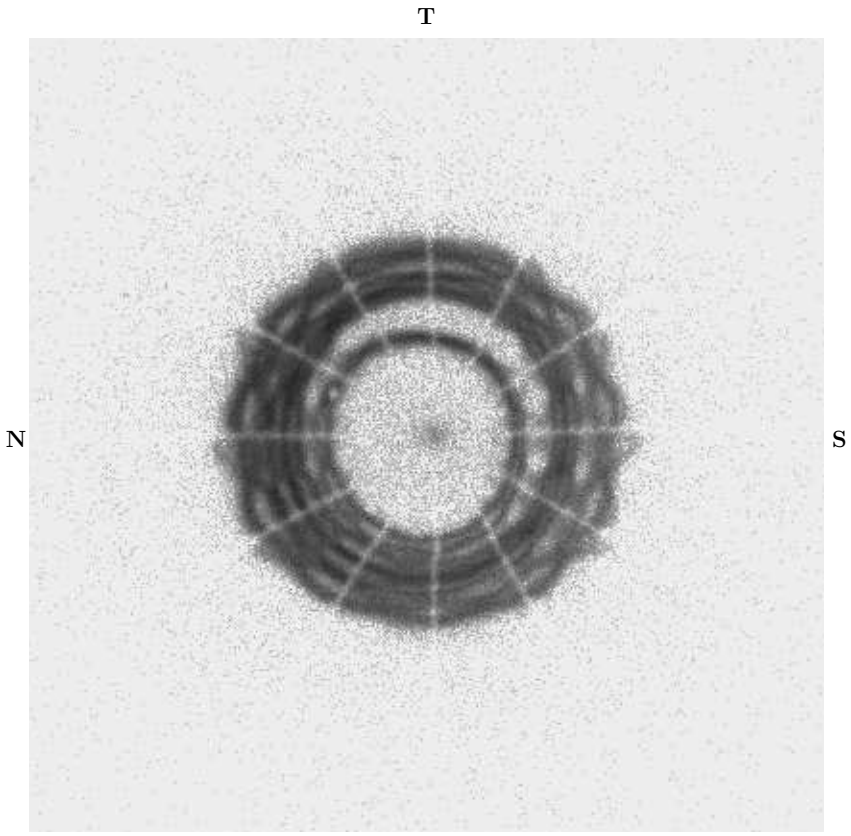

Figure 6.1: The HRMA HSI image with −9.7 mm defocus. (This was thought to be the FPC mesh position during the calibration. The actual mesh position was measured after the calibration to be −9.1±0.2 mm defocus.) Date: 97/01/15; TRW ID: E-IXH-RF-18.002; Run ID: 111803; Source: Al-Kα; Defocus: −9.7 mm; Integration time: 1000 seconds.

Simulated XRCF HRMA Images on FPC Window Mesh
Four Shells Source: Al–Kα (1.49 keV) −9.1 mm Defocus

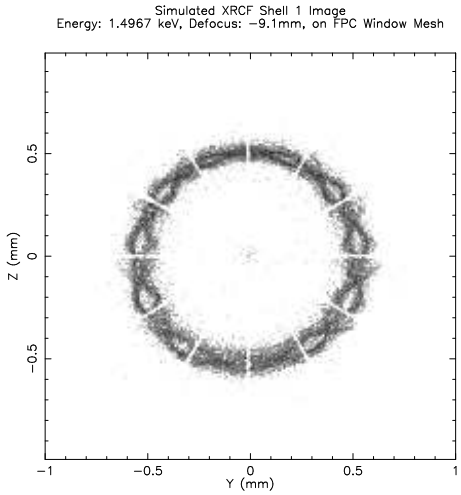

Figure 6.2: Shell 1

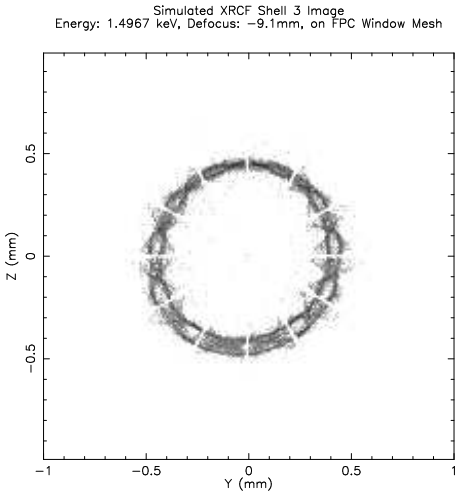

Figure 6.3: Shell 3

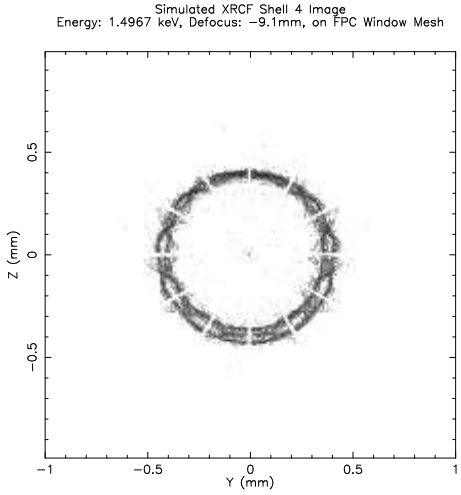

Figure 6.4: Shell 4

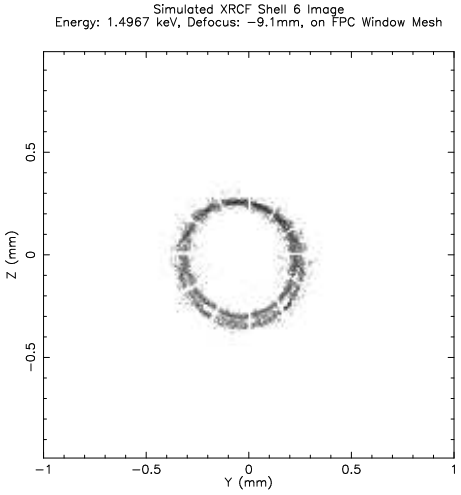

Figure 6.5: Shell 6

Simulated XRCF HRMA Images on FPC Window Mesh
Full HRMA Four Energies −9.1 mm Defocus

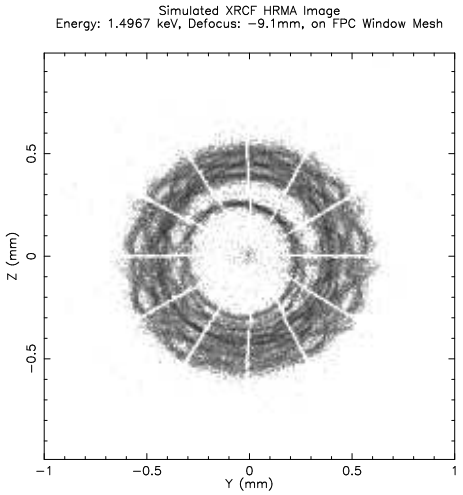

Figure 6.6: Al–Kα (1.49 keV)

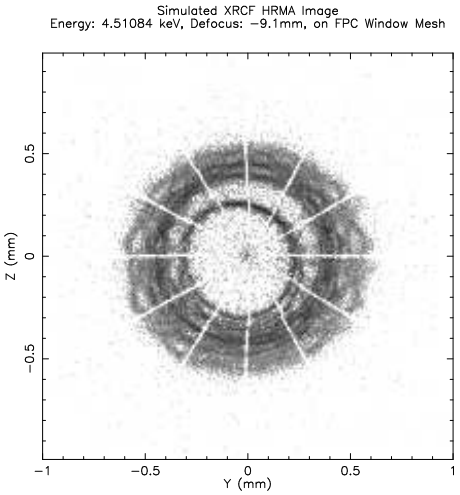

Figure 6.7: Ti–Kα (4.51 keV)

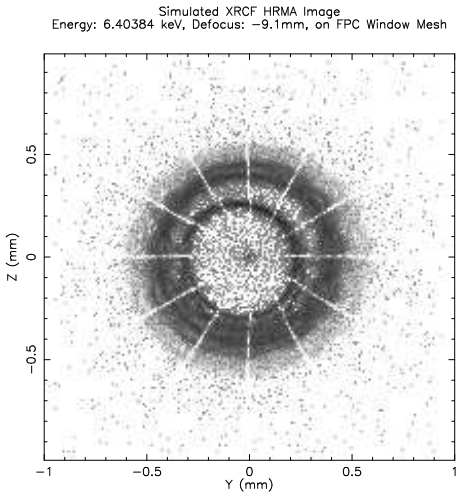

Figure 6.8: Fe–Kα (6.40 keV)

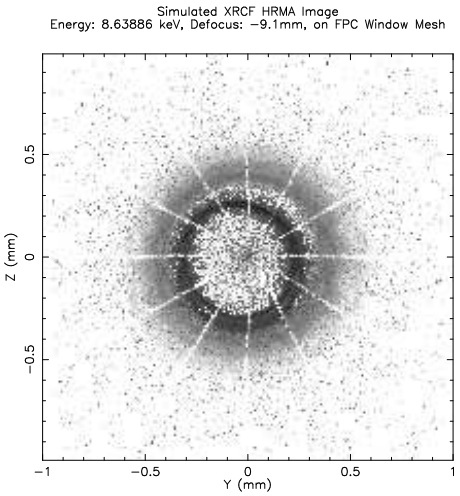

Figure 6.9: Zn–Kα (8.64 keV)

Mesh Window Transmission Model
Four Shells Source: Al–Kα (1.49 keV) 1.0 mm Aperture

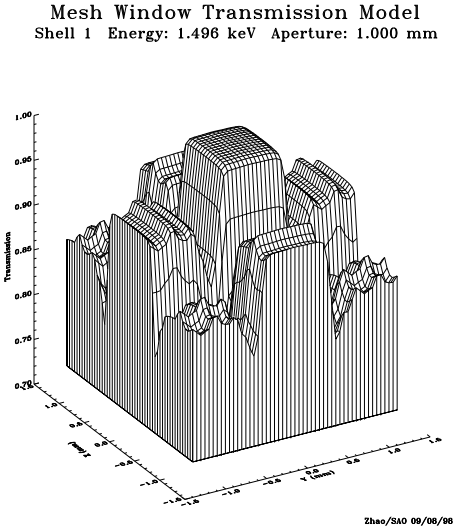

Figure 6.10: Al–Kα. Shell 1.

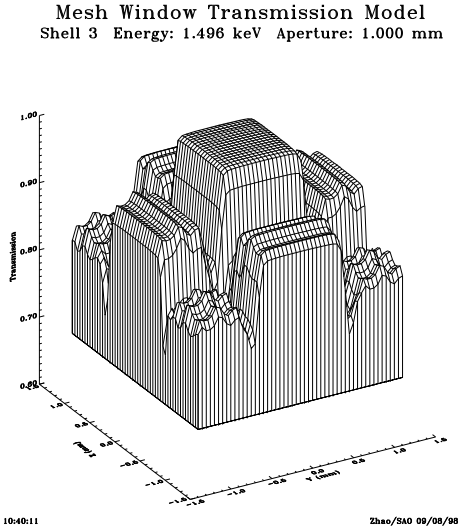

Figure 6.11: Al–Kα. Shell 3.

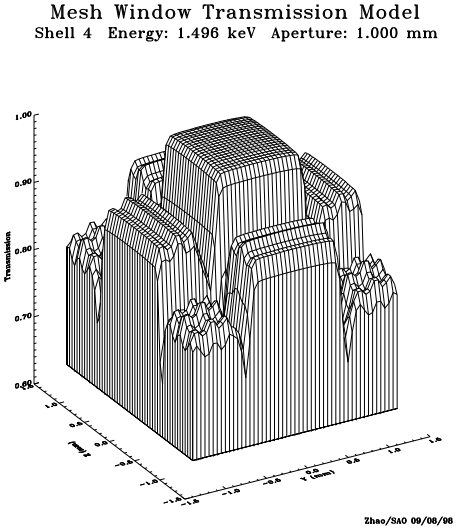

Figure 6.12: Al–Kα. Shell 4.

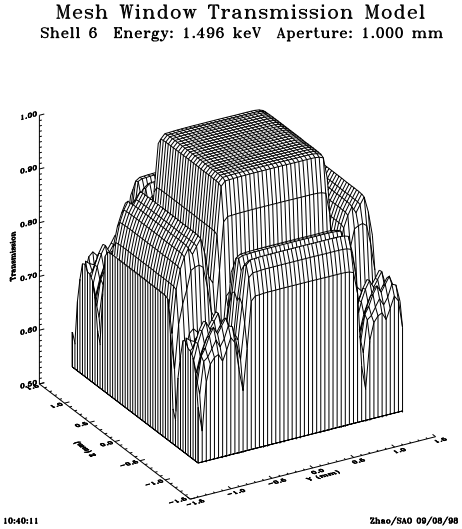

Figure 6.13: Al–Kα. Shell 6.

Mesh Window Transmission Model
Full HRMA Four Energies 0.01 mm Aperture

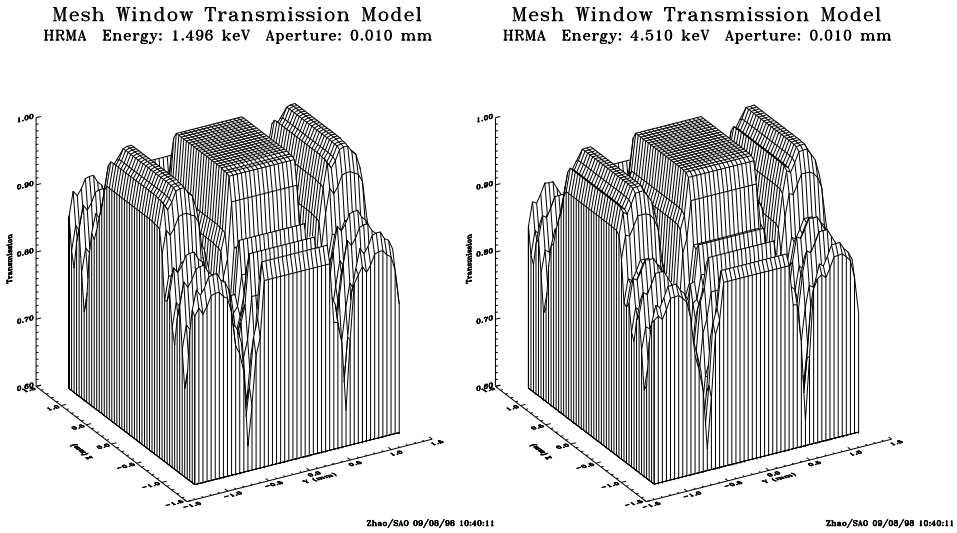

Figure 6.14: Al–Kα. HRMA.

Figure 6.15: Ti–Kα. HRMA.

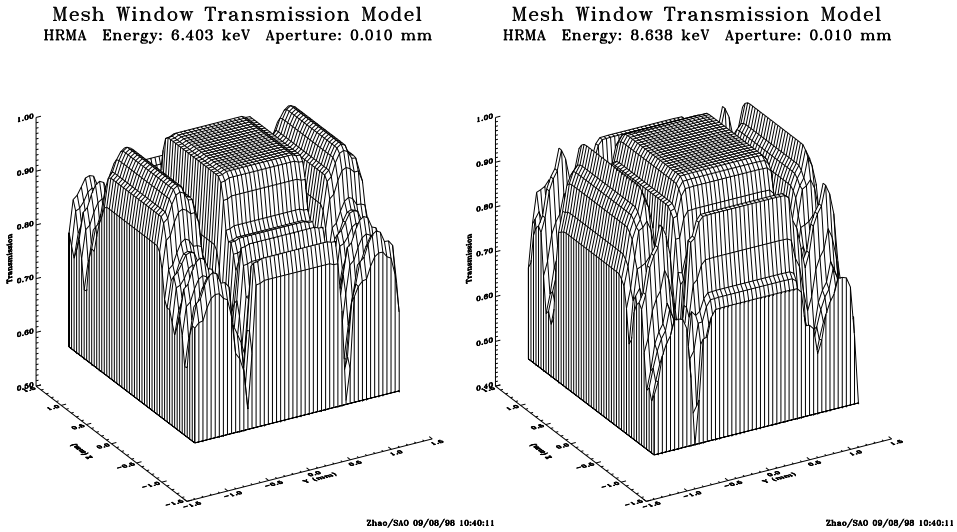

Figure 6.16: Fe–Kα. HRMA.

Figure 6.17: Zn–Kα. HRMA.

Mesh Window Transmission Model
Full HRMA Four Energies 1.0 mm Aperture

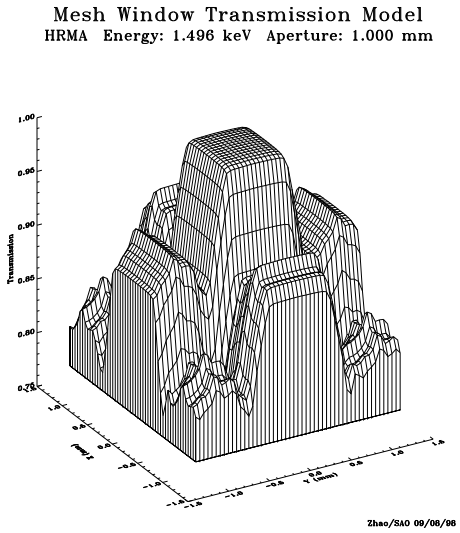

Figure 6.18: Al–Kα. HRMA.

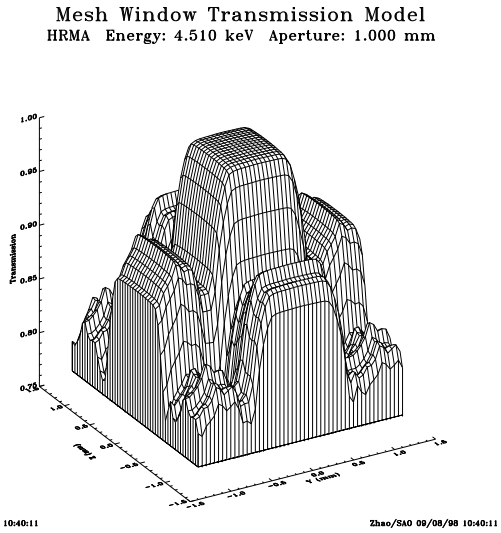

Figure 6.19: Ti–Kα. HRMA.

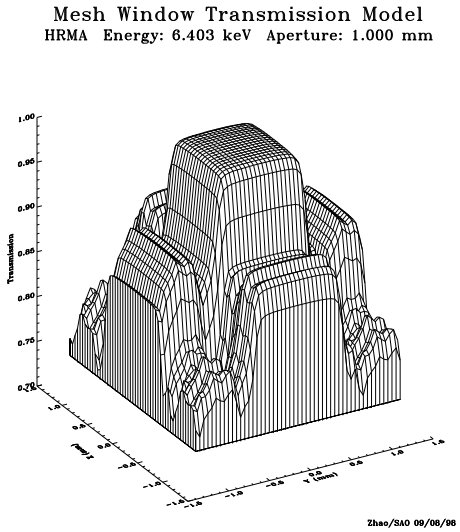

Figure 6.20: Fe–Kα. HRMA.

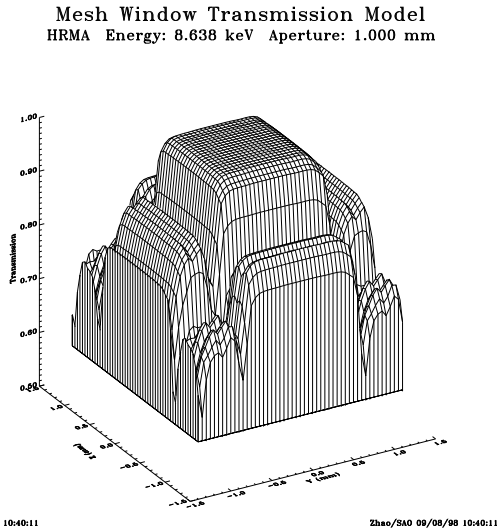

Figure 6.21: Zn–Kα. HRMA.

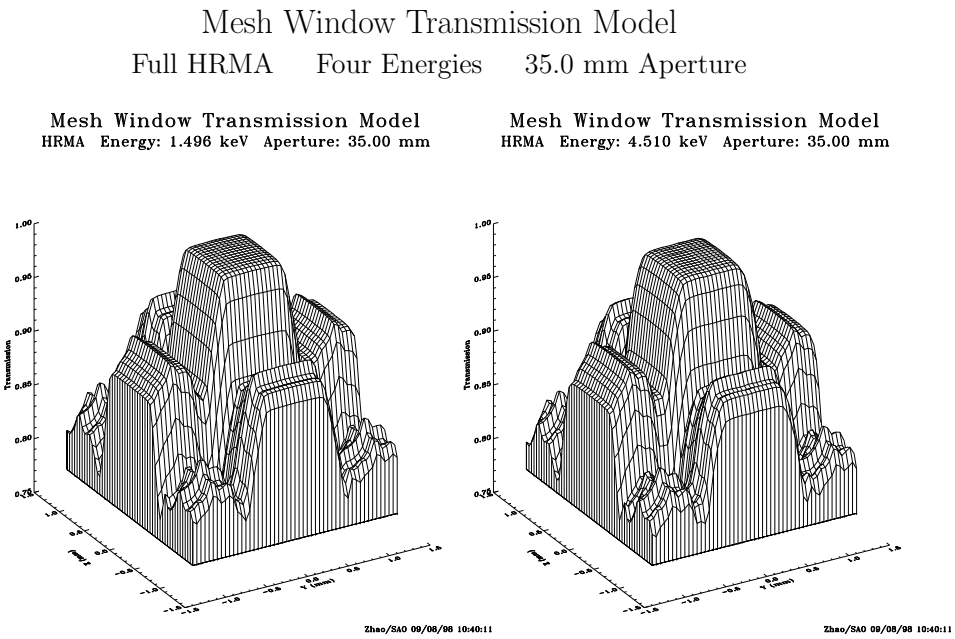

Figure 6.22: Al–Kα. HRMA.

Figure 6.23: Ti–Kα. HRMA.

Figure 6.24: Fe–Kα. HRMA.

Figure 6.25: Zn–Kα. HRMA.

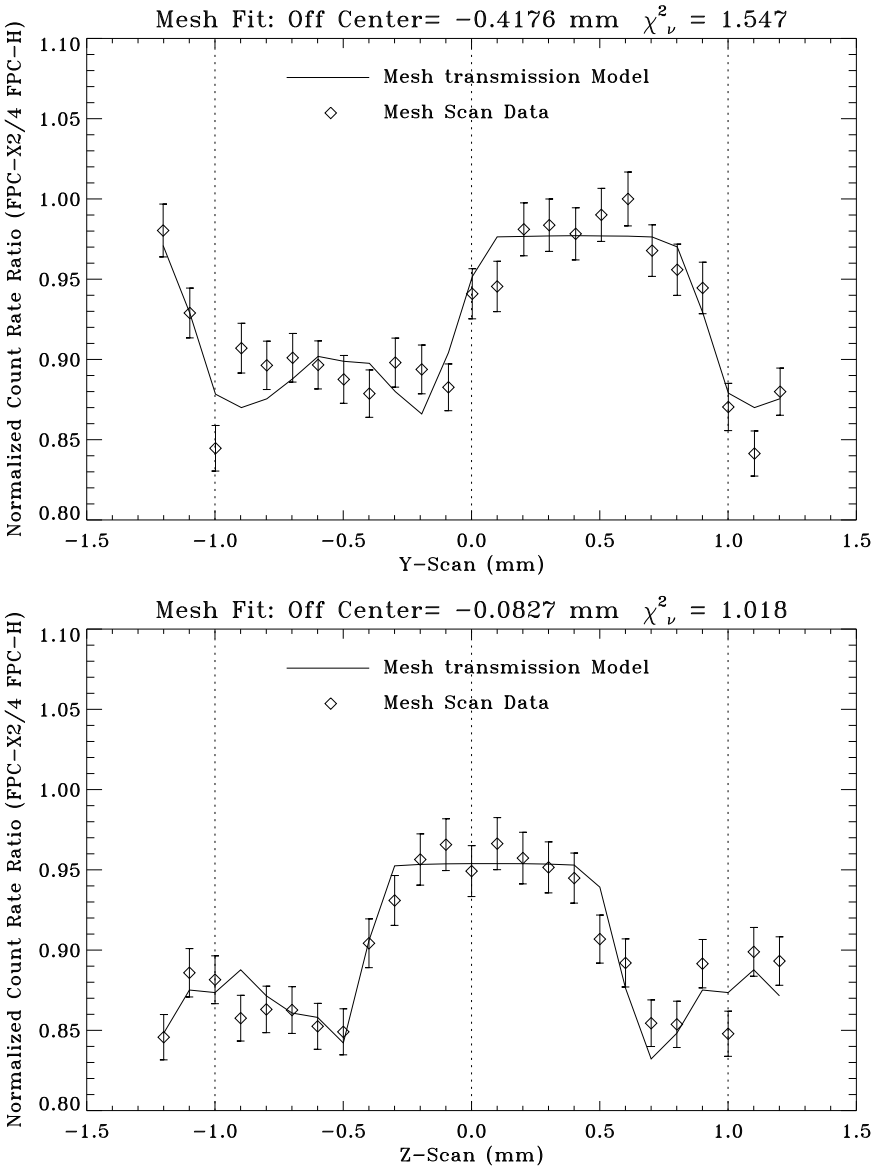

Figure 6.26: HXDS FPC-X2 Mesh Scan data fit to the model. Date: 96/12/21; TRW ID: C-IXF-FM-3.001; Run ID: 106785; Source: Al–Kα.

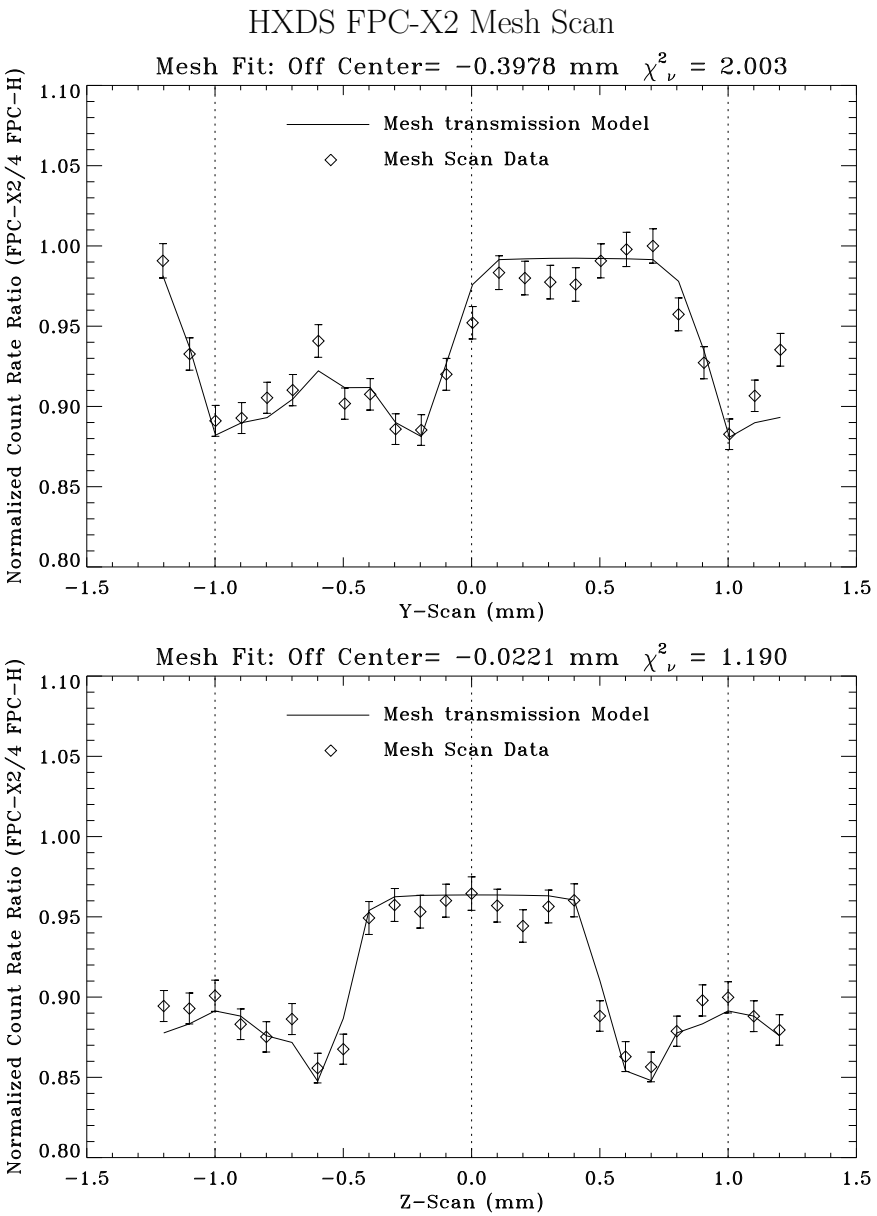

Figure 6.27: HXDS FPC-X2 Mesh Scan data fit to the model. Date: 96/12/24; TRW ID: C-IXF-FM-61.001; Run ID: 106926; Source: Al–Kα.

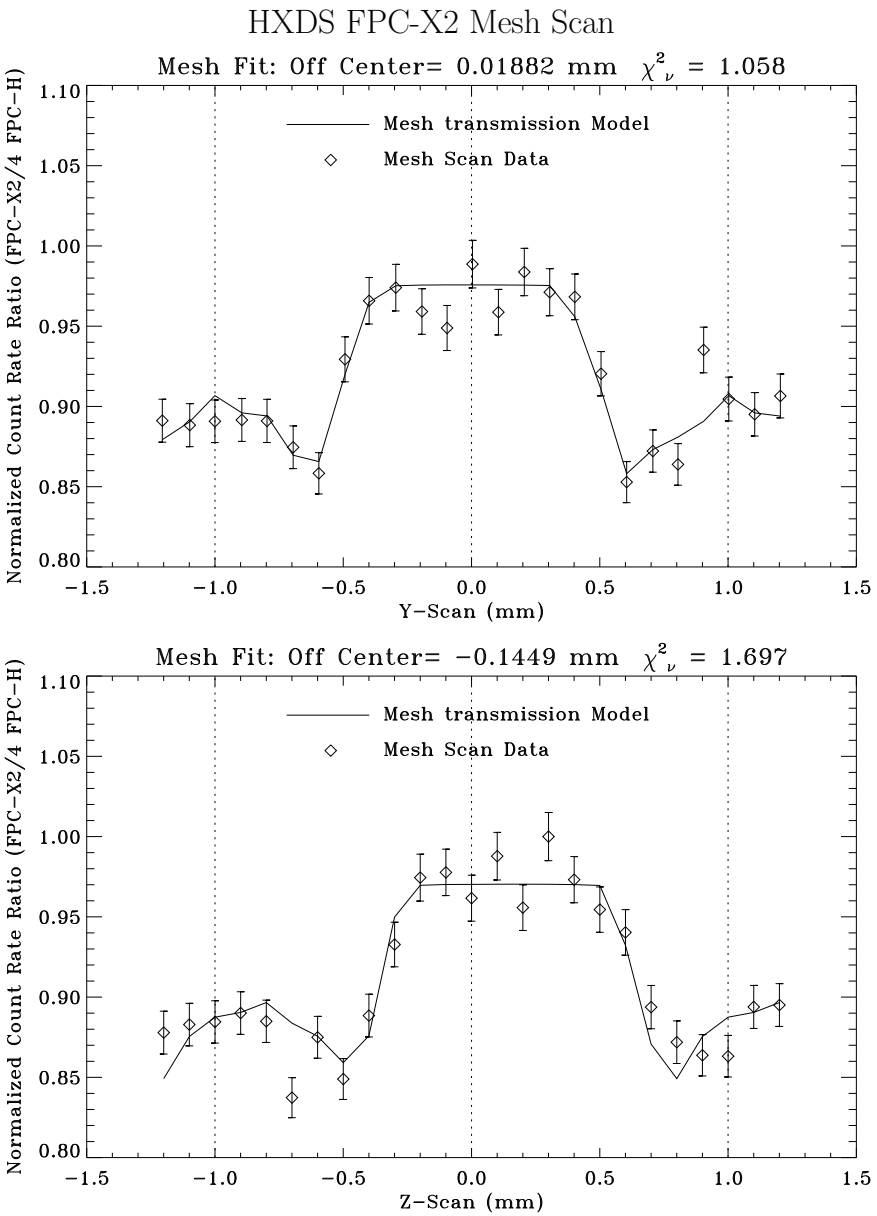

Figure 6.28: HXDS FPC-X2 Mesh Scan data fit to the model. Date: 97/01/15; TRW ID: D-IXF-FM-3.002; Run ID: 108922; Source: C–Kα.

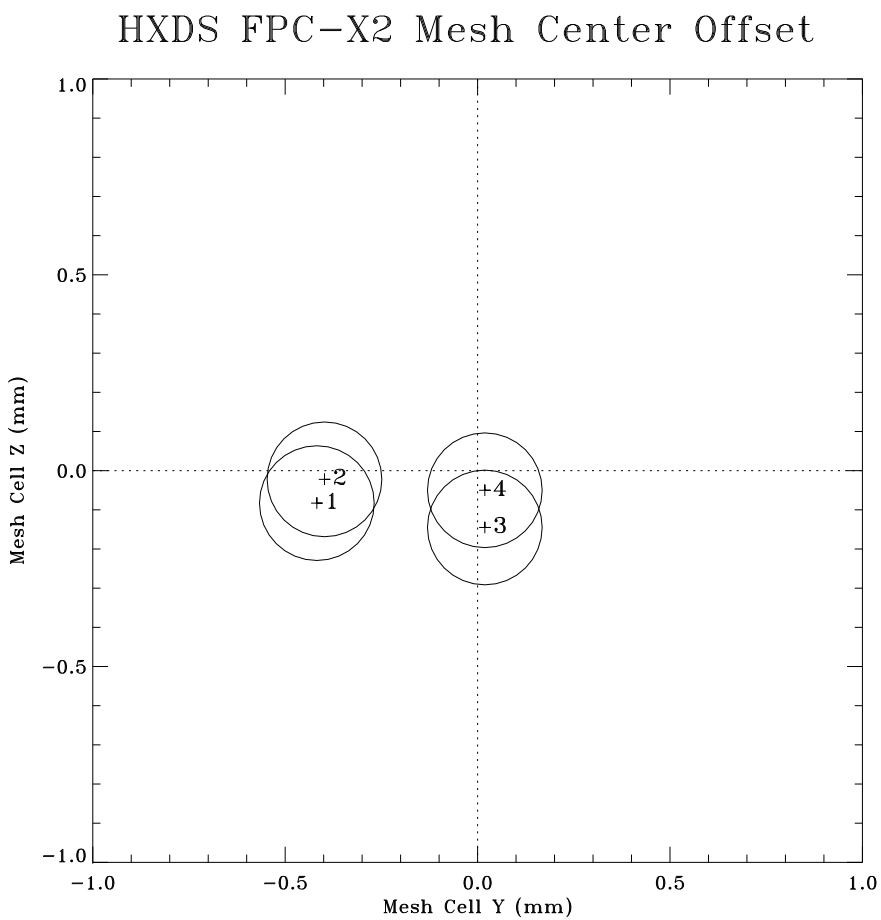

Mesh position	Dates	Y−offset(mm)	Z−offset(mm)
1	96/12/20−96/12/21	−0.4176	−0.0827
2	96/12/21−96/12/24	−0.3978	−0.0221
3	96/12/24−97/01/16	0.01882	−0.1449
4	97/01/16−97/02/11	0.01882	−0.0499

Figure 6.29: HXDS FPC-X2 Mesh Center Offset.

Table 6.3: XRCF HRMA Effective Area Measurements FPC Window Mesh Corrections

Shell 1

Date: 1996/12/24 – 1997/01/16 Mesh offset: Y = 0.0188 mm, Z = −0.1449 mm

Aperture (mm)	Energy (keV)												
	0.1085	0.1833	0.2770	0.5230	0.9297	1.4967	2.0424	2.9843	3.4440	4.5108	5.4147	6.4038	8.0478	8.6389
≤0.50	1.0000	1.0000	1.0000	1.0000	1.0000	1.0000	1.0000	1.0000	1.0000	1.0000	1.0000	1.0000	1.0000	1.0000
1.00	1.0001	1.0001	1.0003	1.0006	1.0007	1.0006	1.0008	1.0008	1.0008	1.0012	1.0016	1.0016	1.0031	1.0031
2.00	1.0001	1.0003	1.0006	1.0010	1.0015	1.0017	1.0017	1.0025	1.0024	1.0033	1.0043	1.0059	1.0103	1.0102
4.00	1.0002	1.0004	1.0008	1.0013	1.0020	1.0021	1.0023	1.0035	1.0038	1.0061	1.0082	1.0108	1.0155	1.0169
10.0	1.0003	1.0005	1.0008	1.0014	1.0024	1.0027	1.0035	1.0050	1.0063	1.0091	1.0119	1.0150	1.0215	1.0229
20.0	1.0003	1.0005	1.0009	1.0016	1.0027	1.0031	1.0041	1.0061	1.0073	1.0105	1.0137	1.0172	1.0246	1.0261
35.0	1.0003	1.0005	1.0009	1.0017	1.0029	1.0033	1.0043	1.0070	1.0080	1.0114	1.0147	1.0191	1.0264	1.0283

Date: 1997/01/16 – 1997/02/11 Mesh offset: Y = 0.0188 mm, Z = −0.0499 mm

Aperture (mm)	Energy (keV)												
	0.1085	0.1833	0.2770	0.5230	0.9297	1.4967	2.0424	2.9843	3.4440	4.5108	5.4147	6.4038	8.0478	8.6389
≤0.50	1.0000	1.0000	1.0000	1.0000	1.0000	1.0000	1.0000	1.0000	1.0000	1.0000	1.0000	1.0000	1.0000	1.0000
1.00	1.0000	1.0002	1.0001	1.0002	1.0006	1.0004	1.0006	1.0005	1.0005	1.0009	1.0017	1.0019	1.0022	1.0028
2.00	1.0001	1.0003	1.0003	1.0008	1.0013	1.0014	1.0016	1.0020	1.0021	1.0028	1.0045	1.0058	1.0090	1.0103
4.00	1.0002	1.0004	1.0005	1.0012	1.0017	1.0020	1.0022	1.0031	1.0037	1.0058	1.0085	1.0101	1.0143	1.0172
10.0	1.0003	1.0005	1.0006	1.0012	1.0023	1.0024	1.0033	1.0052	1.0060	1.0089	1.0122	1.0137	1.0199	1.0232
20.0	1.0003	1.0006	1.0006	1.0013	1.0026	1.0028	1.0038	1.0062	1.0069	1.0103	1.0140	1.0162	1.0229	1.0264
35.0	1.0004	1.0006	1.0006	1.0014	1.0028	1.0030	1.0040	1.0069	1.0077	1.0110	1.0152	1.0175	1.0243	1.0284

Table 6.4: XRCF HRMA Effective Area Measurements FPC Window Mesh Corrections

Shell 3

Date: 1996/12/24 – 1997/01/16 Mesh offset: Y = 0.0188 mm, Z = −0.1449 mm

Aperture	Energy (keV)													
(mm)	0.1085	0.1833	0.2770	0.5230	0.9297	1.4967	2.0424	2.9843	3.4440	4.5108	5.4147	6.4038	8.0478	8.6389
≤0.50	1.0000	1.0000	1.0000	1.0000	1.0000	1.0000	1.0000	1.0000	1.0000	1.0000	1.0000	1.0000	1.0000	1.0000
1.00	1.0000	1.0001	1.0000	1.0003	1.0001	1.0002	1.0001	1.0000	1.0000	1.0001	1.0002	1.0003	1.0006	1.0006
2.00	1.0001	1.0001	1.0002	1.0003	1.0002	1.0004	1.0004	1.0004	1.0008	1.0010	1.0010	1.0012	1.0023	1.0025
4.00	1.0001	1.0001	1.0002	1.0003	1.0003	1.0004	1.0005	1.0006	1.0009	1.0016	1.0017	1.0028	1.0046	1.0047
10.0	1.0001	1.0001	1.0003	1.0003	1.0004	1.0005	1.0005	1.0011	1.0011	1.0026	1.0025	1.0039	1.0057	1.0059
20.0	1.0001	1.0001	1.0003	1.0003	1.0004	1.0005	1.0006	1.0014	1.0014	1.0030	1.0027	1.0045	1.0063	1.0064
35.0	1.0001	1.0001	1.0003	1.0003	1.0004	1.0006	1.0007	1.0014	1.0016	1.0031	1.0029	1.0046	1.0067	1.0069

Date: 1997/01/16 – 1997/02/11 Mesh offset: Y = 0.0188 mm, Z = −0.0499 mm

Aperture	Energy (keV)													
(mm)	0.1085	0.1833	0.2770	0.5230	0.9297	1.4967	2.0424	2.9843	3.4440	4.5108	5.4147	6.4038	8.0478	8.6389
≤0.50	1.0000	1.0000	1.0000	1.0000	1.0000	1.0000	1.0000	1.0000	1.0000	1.0000	1.0000	1.0000	1.0000	1.0000
1.00	1.0000	1.0000	1.0000	1.0000	1.0000	1.0000	1.0000	1.0001	1.0000	1.0000	1.0000	1.0000	1.0000	1.0001
2.00	1.0001	1.0000	1.0001	1.0001	1.0001	1.0002	1.0003	1.0006	1.0007	1.0008	1.0009	1.0010	1.0023	1.0024
4.00	1.0001	1.0000	1.0001	1.0001	1.0003	1.0003	1.0003	1.0007	1.0009	1.0015	1.0019	1.0025	1.0045	1.0046
10.0	1.0001	1.0000	1.0002	1.0002	1.0003	1.0003	1.0004	1.0014	1.0012	1.0024	1.0029	1.0037	1.0056	1.0058
20.0	1.0001	1.0000	1.0002	1.0002	1.0003	1.0003	1.0005	1.0015	1.0014	1.0030	1.0032	1.0043	1.0062	1.0062
35.0	1.0001	1.0000	1.0002	1.0002	1.0003	1.0004	1.0005	1.0015	1.0014	1.0030	1.0035	1.0044	1.0068	1.0069

Table 6.5: XRCF HRMA Effective Area Measurements FPC Window Mesh Corrections

Shell 4

Date: 1996/12/24 – 1997/01/16 Mesh offset: Y = 0.0188 mm, Z = −0.1449 mm

Aperture	Energy (keV)													
(mm)	0.1085	0.1833	0.2770	0.5230	0.9297	1.4967	2.0424	2.9843	3.4440	4.5108	5.4147	6.4038	8.0478	8.6389
≤0.50	1.0000	1.0000	1.0000	1.0000	1.0000	1.0000	1.0000	1.0000	1.0000	1.0000	1.0000	1.0000	1.0000	1.0000
1.00	1.0000	1.0000	1.0001	1.0001	1.0001	1.0000	1.0001	1.0002	1.0000	1.0000	1.0003	1.0004	1.0002	1.0001
2.00	1.0000	1.0001	1.0002	1.0006	1.0004	1.0008	1.0008	1.0008	1.0006	1.0009	1.0010	1.0015	1.0023	1.0029
4.00	1.0000	1.0001	1.0003	1.0009	1.0007	1.0011	1.0016	1.0014	1.0012	1.0017	1.0024	1.0033	1.0051	1.0052
10.0	1.0000	1.0001	1.0004	1.0009	1.0008	1.0012	1.0017	1.0017	1.0019	1.0024	1.0031	1.0042	1.0063	1.0069
20.0	1.0000	1.0001	1.0004	1.0010	1.0008	1.0013	1.0019	1.0020	1.0021	1.0027	1.0033	1.0049	1.0072	1.0075
35.0	1.0000	1.0001	1.0004	1.0010	1.0008	1.0015	1.0020	1.0021	1.0022	1.0029	1.0035	1.0053	1.0077	1.0079

Date: 1997/01/16 – 1997/02/11 Mesh offset: Y = 0.0188 mm, Z = −0.0499 mm

Aperture	Energy (keV)													
(mm)	0.1085	0.1833	0.2770	0.5230	0.9297	1.4967	2.0424	2.9843	3.4440	4.5108	5.4147	6.4038	8.0478	8.6389
≤0.50	1.0000	1.0000	1.0000	1.0000	1.0000	1.0000	1.0000	1.0000	1.0000	1.0000	1.0000	1.0000	1.0000	1.0000
1.00	1.0000	1.0000	1.0000	1.0000	1.0000	1.0000	1.0000	1.0000	1.0000	1.0000	1.0000	1.0000	1.0000	1.0000
2.00	1.0001	1.0001	1.0002	1.0006	1.0004	1.0009	1.0008	1.0007	1.0005	1.0008	1.0012	1.0011	1.0024	1.0030
4.00	1.0001	1.0001	1.0004	1.0008	1.0004	1.0012	1.0012	1.0014	1.0009	1.0018	1.0026	1.0030	1.0044	1.0052
10.0	1.0001	1.0001	1.0004	1.0009	1.0005	1.0013	1.0014	1.0016	1.0017	1.0026	1.0034	1.0039	1.0058	1.0067
20.0	1.0001	1.0001	1.0004	1.0009	1.0006	1.0014	1.0015	1.0018	1.0020	1.0029	1.0039	1.0044	1.0064	1.0080
35.0	1.0001	1.0001	1.0004	1.0009	1.0006	1.0015	1.0016	1.0019	1.0022	1.0031	1.0042	1.0048	1.0068	1.0082

Table 6.6: XRCF HRMA Effective Area Measurements FPC Window Mesh Corrections

Shell 6

Date: 1996/12/24 – 1997/01/16 Mesh offset: Y = 0.0188 mm, Z = −0.1449 mm

Aperture	Energy (keV)													
(mm)	0.1085	0.1833	0.2770	0.5230	0.9297	1.4967	2.0424	2.9843	3.4440	4.5108	5.4147	6.4038	8.0478	8.6389
≤0.50	1.0000	1.0000	1.0000	1.0000	1.0000	1.0000	1.0000	1.0000	1.0000	1.0000	1.0000	1.0000	1.0000	1.0000
1.00	1.0000	1.0000	1.0000	1.0000	1.0000	1.0000	1.0000	1.0000	1.0000	1.0000	1.0000	1.0000	1.0000	1.0000
2.00	1.0001	1.0000	1.0001	1.0004	1.0004	1.0006	1.0009	1.0009	1.0010	1.0010	1.0007	1.0008	1.0013	1.0012
4.00	1.0001	1.0000	1.0001	1.0009	1.0007	1.0008	1.0011	1.0014	1.0018	1.0019	1.0015	1.0018	1.0027	1.0034
10.0	1.0001	1.0004	1.0002	1.0009	1.0009	1.0008	1.0012	1.0018	1.0022	1.0024	1.0026	1.0025	1.0040	1.0052
20.0	1.0001	1.0004	1.0002	1.0009	1.0010	1.0009	1.0013	1.0020	1.0024	1.0026	1.0032	1.0027	1.0046	1.0061
35.0	1.0001	1.0004	1.0002	1.0010	1.0010	1.0009	1.0015	1.0021	1.0024	1.0027	1.0033	1.0032	1.0047	1.0066

Date: 1997/01/16 – 1997/02/11 Mesh offset: Y = 0.0188 mm, Z = −0.0499 mm

Aperture	Energy (keV)													
(mm)	0.1085	0.1833	0.2770	0.5230	0.9297	1.4967	2.0424	2.9843	3.4440	4.5108	5.4147	6.4038	8.0478	8.6389
≤0.50	1.0000	1.0000	1.0000	1.0000	1.0000	1.0000	1.0000	1.0000	1.0000	1.0000	1.0000	1.0000	1.0000	1.0000
1.00	1.0000	1.0000	1.0000	1.0000	1.0000	1.0000	1.0000	1.0000	1.0000	1.0000	1.0000	1.0000	1.0000	1.0000
2.00	1.0000	1.0000	1.0001	1.0001	1.0006	1.0005	1.0008	1.0007	1.0006	1.0009	1.0008	1.0013	1.0011	1.0008
4.00	1.0000	1.0000	1.0001	1.0007	1.0008	1.0008	1.0011	1.0014	1.0016	1.0019	1.0018	1.0021	1.0026	1.0031
10.0	1.0000	1.0004	1.0002	1.0007	1.0010	1.0009	1.0012	1.0016	1.0020	1.0022	1.0029	1.0033	1.0037	1.0048
20.0	1.0000	1.0004	1.0002	1.0007	1.0011	1.0010	1.0013	1.0017	1.0023	1.0024	1.0033	1.0039	1.0041	1.0058
35.0	1.0000	1.0004	1.0002	1.0008	1.0011	1.0010	1.0013	1.0017	1.0023	1.0026	1.0034	1.0043	1.0043	1.0061

Table 6.7: XRCF HRMA Effective Area Measurements FPC Window Mesh Corrections

HRMA

Date: 1996/12/24 – 1997/01/16 Mesh offset: Y = 0.0188 mm, Z = −0.1449 mm

Aperture	Energy (keV)													
(mm)	0.1085	0.1833	0.2770	0.5230	0.9297	1.4967	2.0424	2.9843	3.4440	4.5108	5.4147	6.4038	8.0478	8.6389
≤0.50	1.0000	1.0000	1.0000	1.0000	1.0000	1.0000	1.0000	1.0000	1.0000	1.0000	1.0000	1.0000	1.0000	1.0000
1.00	1.0000	1.0001	1.0002	1.0003	1.0003	1.0003	1.0004	1.0003	1.0003	1.0004	1.0004	1.0003	1.0001	1.0000
2.00	1.0001	1.0002	1.0003	1.0006	1.0008	1.0010	1.0010	1.0012	1.0013	1.0016	1.0014	1.0013	1.0015	1.0014
4.00	1.0001	1.0002	1.0004	1.0009	1.0011	1.0013	1.0015	1.0018	1.0020	1.0029	1.0028	1.0029	1.0032	1.0036
10.0	1.0002	1.0003	1.0005	1.0010	1.0013	1.0015	1.0020	1.0026	1.0031	1.0043	1.0041	1.0038	1.0046	1.0054
20.0	1.0002	1.0003	1.0005	1.0010	1.0015	1.0017	1.0023	1.0032	1.0037	1.0050	1.0046	1.0044	1.0052	1.0062
35.0	1.0002	1.0003	1.0005	1.0011	1.0016	1.0019	1.0024	1.0035	1.0040	1.0054	1.0050	1.0047	1.0054	1.0067

Date: 1997/01/16 – 1997/02/11 Mesh offset: Y = 0.0188 mm, Z = −0.0499 mm

Aperture	Energy (keV)													
(mm)	0.1085	0.1833	0.2770	0.5230	0.9297	1.4967	2.0424	2.9843	3.4440	4.5108	5.4147	6.4038	8.0478	8.6389
≤0.50	1.0000	1.0000	1.0000	1.0000	1.0000	1.0000	1.0000	1.0000	1.0000	1.0000	1.0000	1.0000	1.0000	1.0000
1.00	1.0000	1.0001	1.0001	1.0001	1.0002	1.0002	1.0002	1.0002	1.0002	1.0003	1.0002	1.0000	1.0000	1.0000
2.00	1.0001	1.0002	1.0002	1.0005	1.0007	1.0009	1.0009	1.0011	1.0011	1.0014	1.0015	1.0012	1.0014	1.0009
4.00	1.0001	1.0002	1.0003	1.0007	1.0009	1.0012	1.0013	1.0018	1.0019	1.0028	1.0031	1.0027	1.0030	1.0033
10.0	1.0002	1.0003	1.0004	1.0008	1.0012	1.0014	1.0018	1.0027	1.0030	1.0043	1.0044	1.0039	1.0042	1.0049
20.0	1.0002	1.0003	1.0004	1.0008	1.0013	1.0016	1.0020	1.0032	1.0034	1.0050	1.0051	1.0045	1.0046	1.0060
35.0	1.0002	1.0003	1.0004	1.0009	1.0014	1.0018	1.0021	1.0034	1.0038	1.0053	1.0055	1.0048	1.0049	1.0062

Chapter 7

High Speed Imager Calibration

Ian Evans

7.1 Introduction

The current status of the calibration of the High Speed Imager (*HSI*) microchannel-plate based x-ray imaging detector (Evans et al., 1997) is reported. The *HSI* imager is part of the *HRMA* X-ray Detection System (*HXDS*) that was used during Phase 1 of the *AXAF* calibrations at the *MSFC* X-Ray Calibration Facility (Weisskopf and O'Dell, 1997).

Immediately prior to the beginning of Phase 1 calibrations at the *XRCF*, the *HSI* microchannel-plate assembly was replaced. Therefore, no valid pre-Phase 1 calibration data exist for the *HSI*. Calibration of the *HSI* was performed, primarily at the *SAO* X-ray Pipe Facility (*XPF*), during October and November, 1997.

At the time of writing, all the calibration data have been inspected and qualitative studies of the data have been performed. However, detailed quantitative analyses have not yet been completed. Therefore, we present here a description of the *HSI* calibration data, and a discussion of calibration features significant to scientists who are analyzing *HRMA* calibration data obtained using the *HSI*.

7.2 Calibration Data Summary

The following calibration data were obtained at the *SAO XPF*:

- Quantum efficiency measurements at several energies and for several angles of incidence,
- Electronics count rate linearity/dead-time measurements,
- Flat fields at several energies for normal incidence,
- A pinhole mask image at one energy, to measure spatial distortion.

Additionally, the x-ray transmission of the ion shield across the principal element edges was measured at the *BESSY* facility.

Detailed descriptions of the calibration data obtained, and relevant features identified in the calibration data, are presented below.

7.3 *HSI* Quantum Efficiency Measurements

The area-averaged mean quantum efficiency (*QE*) of the *HSI* was measured by exposing the *HSI* to a nominally uniform x-ray flat field generated using an Manson electron impact source. The *HSI* count rate is determined from the secondary science fast event discriminator event counter. Without changing the x-ray source, the *HSI* is removed from the beam and a *HXDS* flow proportional counter (*fpc_hb*) (Wargelin et al., 1997) is inserted into the beam at the same location. Comparison of the *HSI* count rate with the *FPC* dead-time corrected count rate provides a *QE* calibration relative to the (TBD) *fpc_hb* counter efficiency. During the measurements, a second flow proportional counter was used to monitor and correct for temporal variations of the x-ray beam intensity.

These measurements were obtained at the following 11 energies: B-Kα, C-Kα, O-Kα, Fe-Lα, Cu-Lα, Mg-Kα, Al-Kα, Mo-Lα, Sn-Lα, Ti-Kα, and Fe-Kα (Figure 7.1). Because the *HSI* has essentially no energy discrimination, the Manson source high voltage was restricted to twice the line energy for these measurements. An approximately one mean-free-path (*mfp*) thickness source filter made of either the same material, or $Z-1$, was used to further supress the high energy continuum.

For these calibrations, a target value of 40,000 counts in the *HSI* was used to provide $\sim$0.5% statistical errors.

To calibrate the variation of *QE* as a function of x-ray incident angle, data were obtained with the *HSI* rotated at several angles around the Z axis. Such rotation alters the angle between the incident x-ray photons and the microchannel-plate pore axis. The latter is nominally rotated 6° around the *HSI* Z axis from normal incidence, with the front of the pores being offset in the $+Y$ direction. In practice, ring focus images obtained during Phase 1 *HMRA* calibrations at the *XRCF* suggest that the rotation axis is offset by about $\sim$10–12′ from the Z axis, so that the front of the microchannel-plate pores is offset slightly in the $-Z$ direction in addition to the $+Y$ direction.

Data were obtained for incident angles corresponding to Z axis rotations of $-8.0°$ to $+8.0°$ in 0.5° increments ($+6.0°$ corresponds to the *nominal* pore axis angle). For Z axis rotations $|\theta| > \sim 6.0°$ the microchannel-plates were only partly illuminated because of obscuration by the *HSI* gate valve structure. For these incident angle data, the measured count rates must be corrected for the fractional microchannel-plate area illuminated by the x-ray beam. However, this has not been done in the data presented in the figures.

7.4 Count Rate Linearity

The *HSI* counting rate response is modified by the dead-time inherent in the post-processing electronics. For compact sources, local pore-saturation effects in the microchannel-plates also reduces the detected count rate.

The *HSI* post-processing electronics detects an event when the summed $(Y+Z)$ output signal from the cross-grid charge detector exceeds a programmable threshold. Once an event is detected, the position of the event must be determined, and the event is processed by veto logic that determines whether the event is "valid" or not. In configuration used at the *XRCF*, to be valid an event must be detected in both Y and Z (so that its position can be localized), and must occur sufficiently after the previous event that the analog electronics (preamplifiers, sample and hold detectors) have returned to normal operations, and the digital electronics have completed the event processing cycle.

Because the event processing time is relatively long, imaging event processing saturates at a relatively low count rate, of order 2,500 Hz. Therefore, the *HSI* incorporates a secondary science

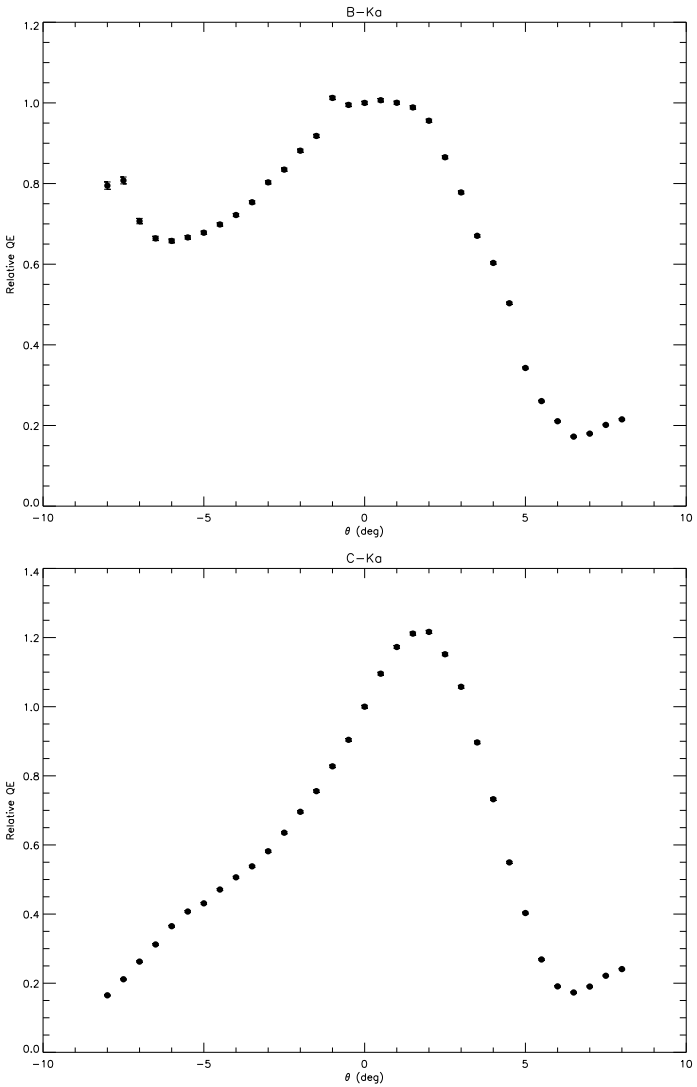

Figure 7.1: Angular dependence of relative quantum efficiency. θ is the angle to the normal of the MCP face, around the Z axis. $(\theta - 6)$ is the angle of the beam relative to the pore axis. Points marked with open circles are not corrected for known vignetting, and therefore represent a lower limit to the relative quantum efficiency. B-K and C-K.

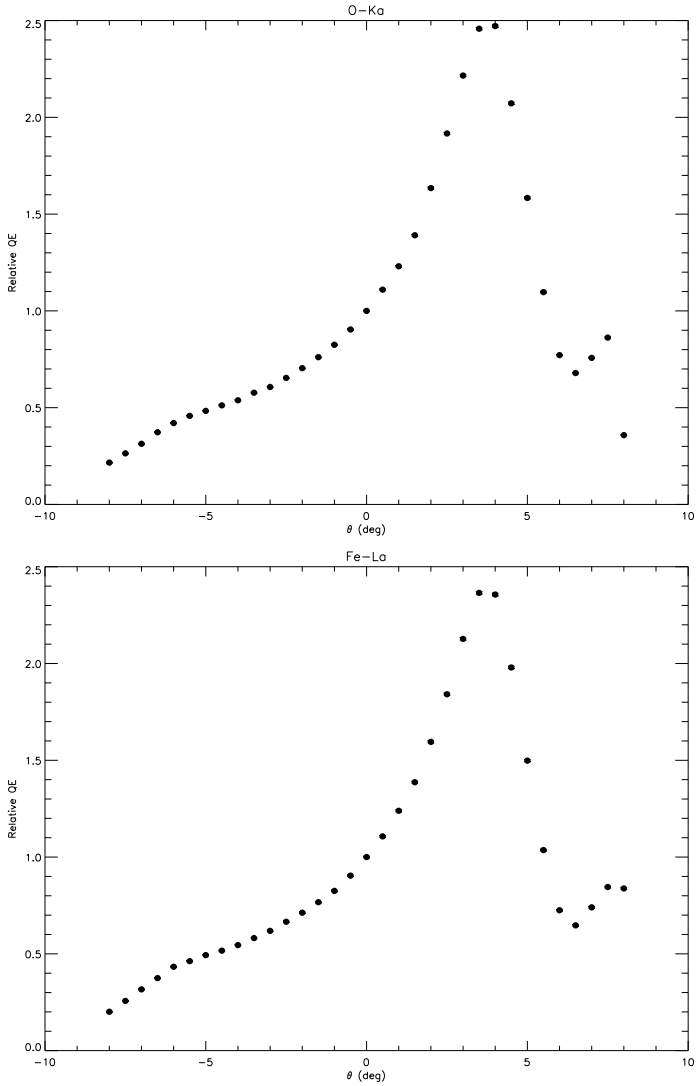

Figure 7.1: (continued) O-K and Fe-L.

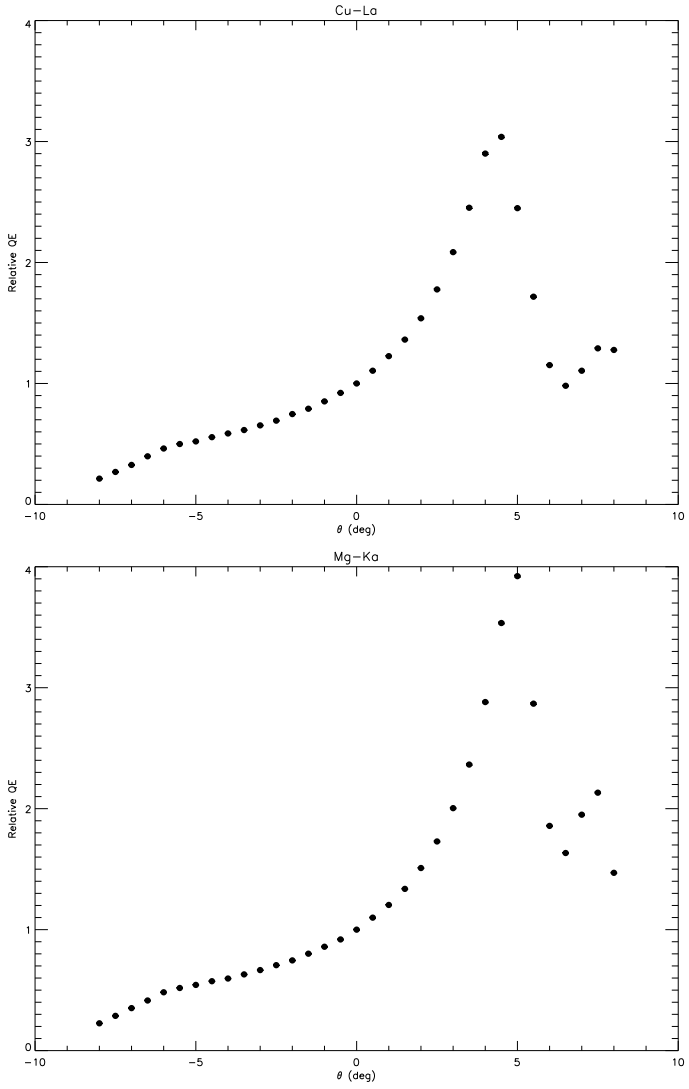

Figure 7.1: (continued) Cu-L and Mg-K.

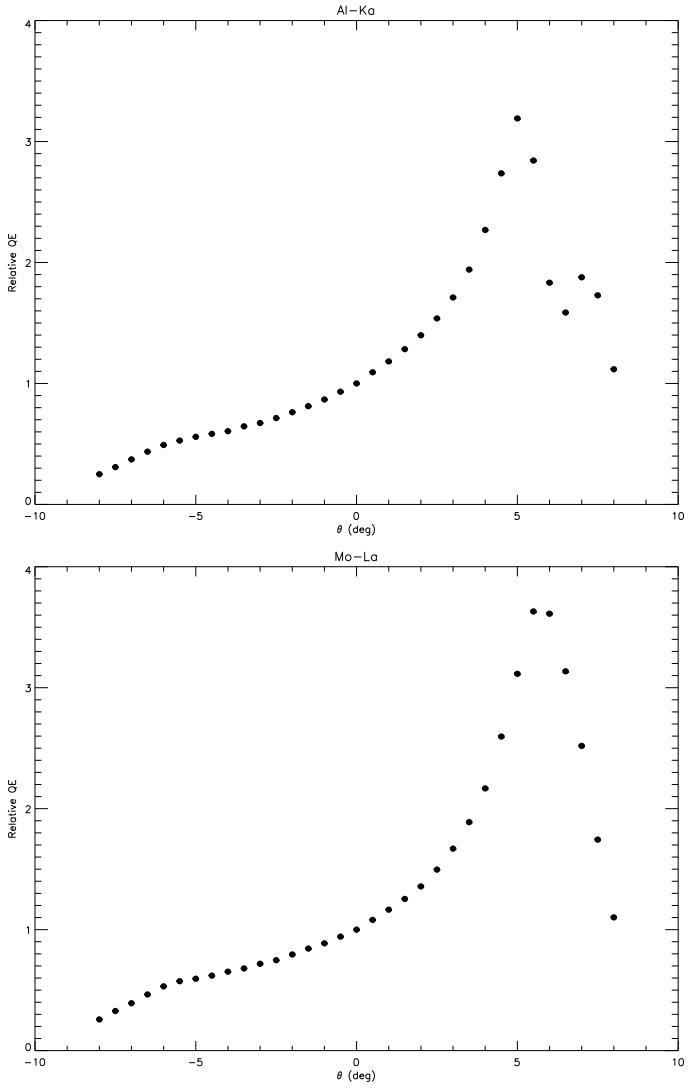

Figure 7.1: (continued) Al-K and Mo-L.

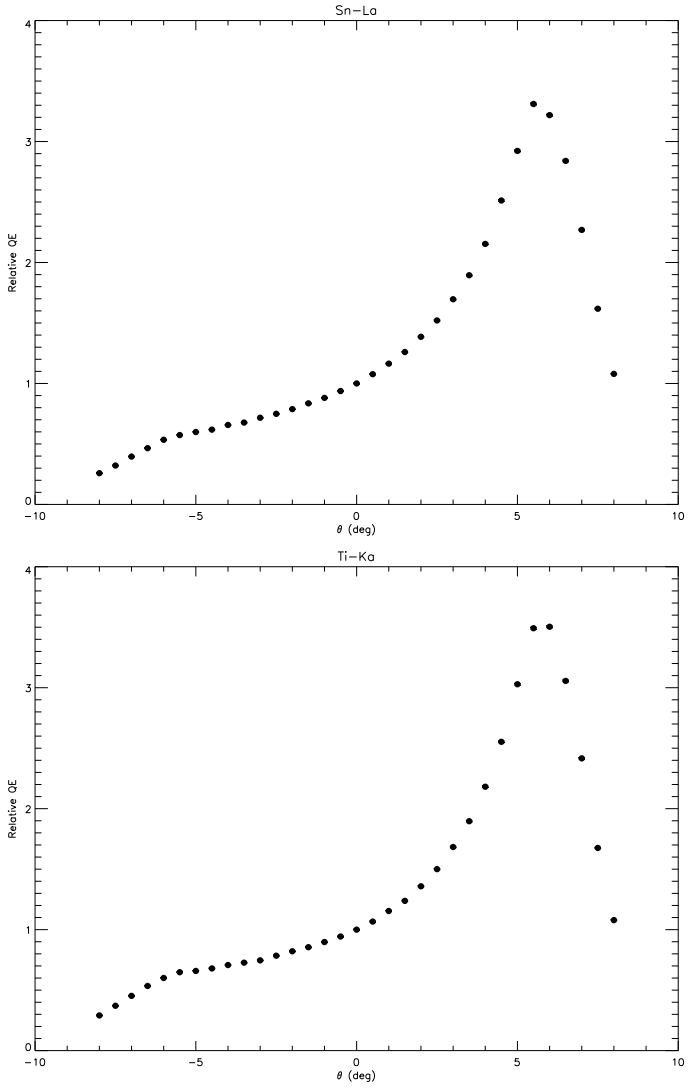

Figure 7.1: (continued) Sn-L and Ti-K.

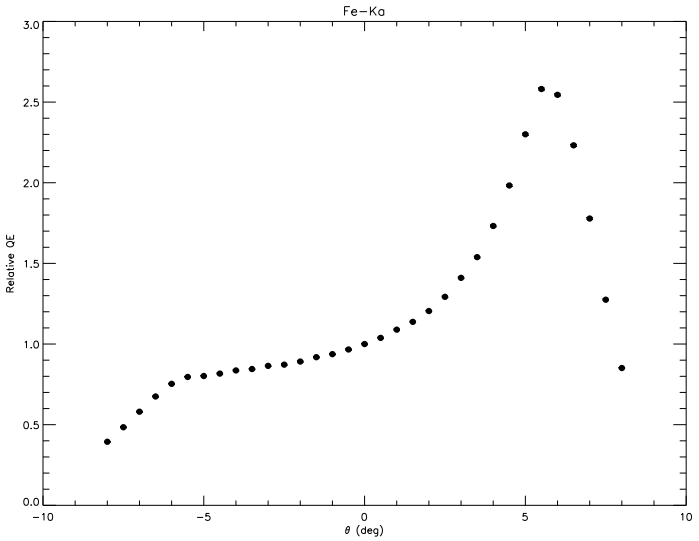

Figure 7.1: (continued) Fe-K.

fast discriminator that simply counts detected events for which the summed $Y + Z$ signal exceeds the threshold. The dead-time of this fast discriminator is a few μs, which is completely negligible for image event rates less than 2,000 Hz (the CEI spec (SAO, 1998) maximum count rate requirement). The fast discriminator event counter is recorded in the FITS file header with the keyword `FASTEVNT`. (Note that the secondary science counters do not accumulate counts for exactly the same time as the imager; therefore, when the most precise knowledge of the fast event rate is required, the fast event counter time must be derived from the number of event counter major frames recorded in the FITS file header with the keyword `NUMCTRMF`.)

The post-processing electronics count rate linearity was measured using an Al-Kα flat field and range of *HSI* event rates from $\sim$15 Hz to $\sim$2,200 Hz. The observed *HSI* count rate were referenced to the rate observed in a monitor flow proportional counter. For the figures presented here, the variation of the monitor *FPC* dead-time with rate is assumed to be accurately represented by the internal Gedke-Hale circuitry over the range of count rates considered here. Error due to counting statistics is $\sim$0.5%.

The data demonstrate that the *HSI* fast event discriminator has no significant dead-time correction for event rates up to at least 2,200 Hz (Figure 7.2). However, the image event rate, together with the total and valid event rates stored in secondary science counters, have significant dead-time corrections for count rates in excess of a few hundred Hz (Figure 7.3; Table 7.1).

Pore saturation effects cannot be quantified using the present calibration data since a compact ($\lesssim$ 20 μm diameter), high intensity x-ray source was not available. Measurements obtained at the *XRCF* using the *Technology Mirror Assembly* (*TMA*) suggest that pore saturation effects are insignificant for integrated *TMA* point response function profile count rates < 85 Hz, and are a few percent at $\sim$100 Hz. These measurements were made with the *HSI* using a set of microchannel-plates of identical design to those used during the Phase 1 *HRMA* calibrations. The response of

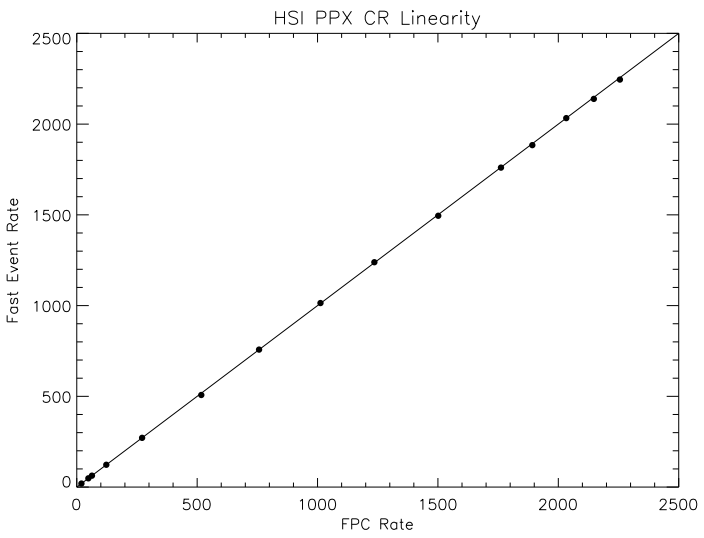

Figure 7.2: HSI post-processing electronics fast discriminator count rate linearity

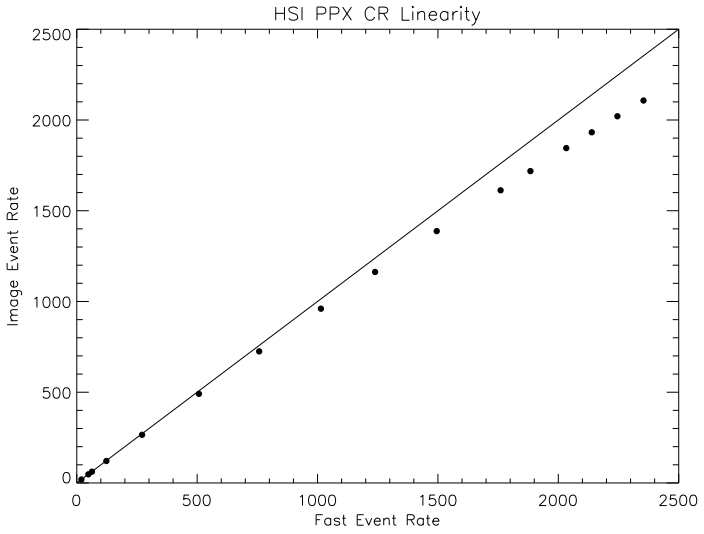

Figure 7.3: HSI post-processing electronics image count rate linearity

Fast Event Rate	Dead-Time
500 Hz	2.9%
1000 Hz	4.7%
1500 Hz	7.0%
2000 Hz	9.1%

Table 7.1: Image event rate dead-time percentages

the *HSI* in the current configuration is expected to be similar.

7.5 Flat Fields

HSI flat fields were obtained at normal incidence using an experimental setup similar to that used for the *QE* measurements. These flat fields were obtained at the following 9 line energies: C-Kα, Fe-Lα, Cu-Lα, Mg-Kα, Al-Kα, Mo-Lα, Sn-Lα, Ti-Kα, and Fe-Kα. In order to maintain an acceptable count rate, the Manson source high voltage generally was set between 3 and 4 times the line energy. These settings enhanced the high energy continuum more than is desirable, but with the high voltage limited to twice the line energy the exposure times would have been much longer than practicable.

The goal of each flat field was to obtain 4×10^7 total counts, which yields $\sim$5% statistics in a $1'' \times 1''$ area for uniform illumination.

The large scale uniformity of the x-ray beam was investigated using a *FPC* with a 2 mm diameter aperture mounted on a two axis translation stage to map the area of the beam that illuminated the *HSI*. This mapping was performed using a 69 point *listscan* (SAO, 1997) to step across the illuminated area in a raster scan with a 2 mm step size (Figure 7.4). At each point in the scan, $\sim 40,000$ counts were obtained. Thus, the statistical accuracy of the flat fields is limited on scales larger than $\sim 500\mu$m by the accuracy of the beam map. This is considered acceptable, since those features studied during Phase 1 *HRMA* calibrations that require the highest flat field accuracy have smaller scales.

Although beam uniformity measurements indicate that the *XPF* beam is very uniform within a $\sim$18 mm diameter area for most energies, this is not always true (Figure 7.5). In some cases (e.g., Sn-Lα) this non-uniformity can be traced to physical defects on the source target, while in others there is not any identifiable reason for the beam to be non-uniform. Regardless of the reason for the beam non-uniformity, an appropriate correction to the flat field data must be applied during the final calibrations.

The cosmetics of the *HSI* flat field were investigated by summing all of the flat fields obtained at individual energies to form a total summed or "super" flat field. The super flat field has approximately 3.6×10^8 overall counts, corresponding to a mean of ~ 67 counts per pixel over the illuminated area (Figure 7.6).

Immediately obvious from the super flat field is an approximately circular region of decreased sensitivity in the center of the detector (Figure 7.7). The sensitivity within a circle $\sim 150\,\mu$m diameter in the center of the detector is degraded to $\sim$75% of the surrounding uniform flat field level, and is surrounded by a annulus $\sim$250 μm wide where the sensitivity ramps up to the normal value (Figure 7.8). This is the region of the detector that was exposed to the greatest number of counts at the *XRCF*, so presumably the low sensitivity in this area is due to gain degradation caused by charge depletion in the pores of the microchannel-plates. If this is the case, it should

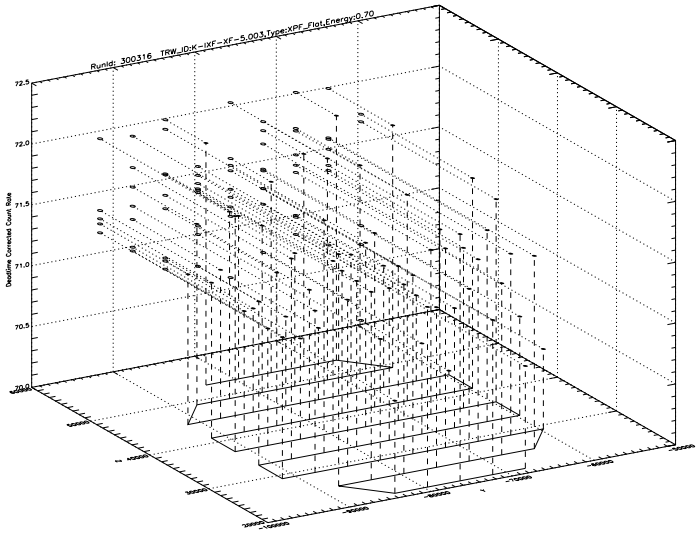

Figure 7.4: Sample flat field *FPC* scan pattern

be possible to develop a statistical correction to the observed count rate by interpolating from the total *HSI* dose maps maintained by the *AXAF Science Center* calibration group.

A few other mm scale regions of slightly degraded or enhanced sensitivity are visible in the super flat field. However, these regions are not located in areas of the detector that were used at the *XRCF* during Phase 1 calibrations (e.g., Figure 7.9).

There are several small scale cosmetic defects with much reduced sensitivity visible in the super flat field image. One of these is located ~ 1 mm from the center of the *HSI* field in the $-Y, +Z$ direction (Figure 7.10). Some small defects *may* be associated with foreign material that has settled on the ion shield, as there is evidence in some cases for correlations between defect positions and visible dust particles on the shield.

Also evident from the super flat field is variability of the width of an individual gap as a function of position along the gap (Figure 7.11). Current degapping algorithms allow for differences between the widths of individual gaps, but, because they apply on a tap by tap basis, cannot correctly degap images with gaps whose width varies along the gap. Prior flat field data had insufficient counting statistics to identify this problem. An extension of the current degapping technique that works on a tile by tile basis (rather than tap by tap) in each axis should provide adequate degapping.

Forming Y and Z projections of the super flat field reveals additional image features. The Z projection demonstrates an apparent medium spatial scale sensitivity variation in which a band in the center of each tile appears to be more sensitive than the regions of the tiles near the gaps, with a maximum peak-to-peak variation in apparent sensitivity is $\sim 9\%$ (Figures 7.12and7.13). Similar structure is visible in Y, but at much reduced amplitude. However, it is not clear whether this structure is actually caused by a spatial sensitity variation, or whether it is due to significant non-linearity of the spatial scale. Unfortunately, the available spatial distortion calibration data do not have a sufficiently fine grid to identify distortions on a scale that is significantly smaller than

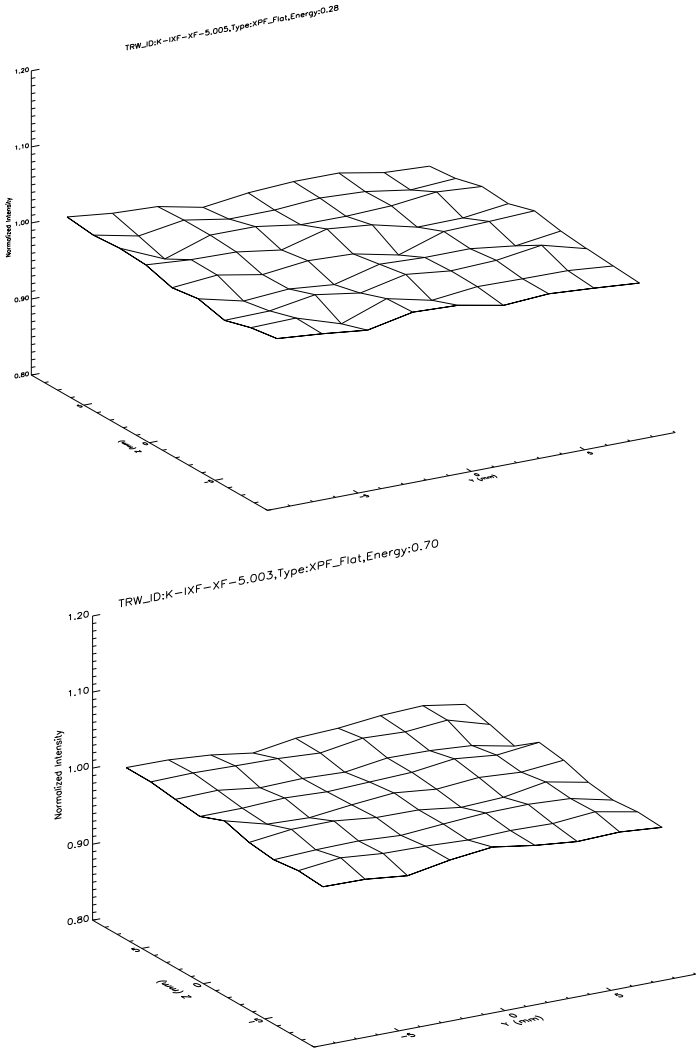

Figure 7.5: *FPC* flat field profile scans. C-K and Fe-L.

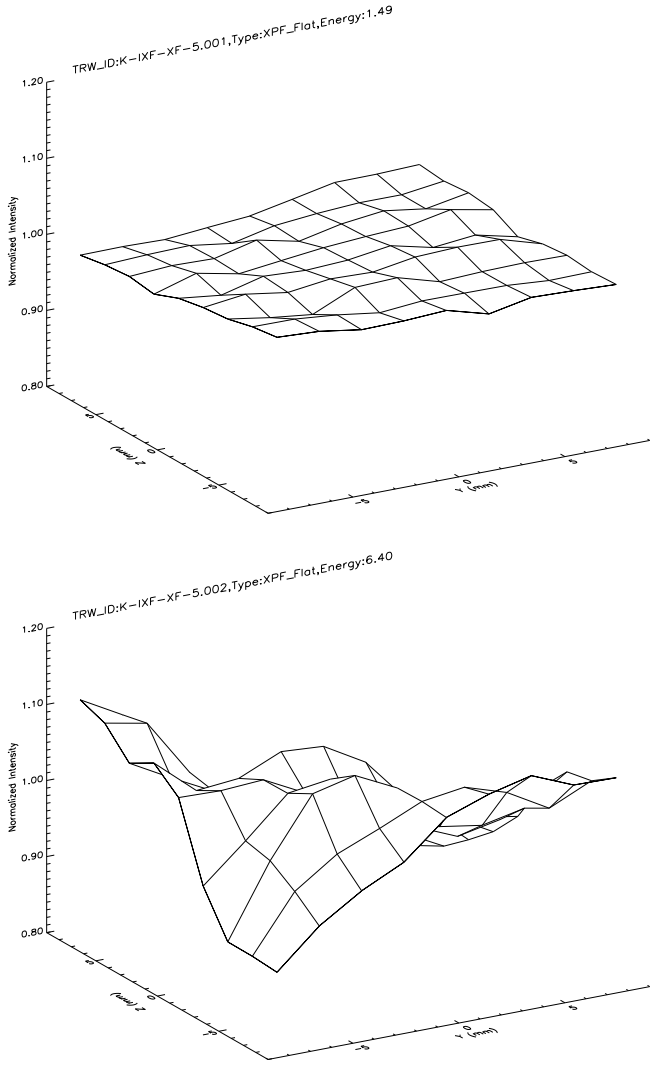

Figure 7.5: (continued) Al-K and Fe-K.

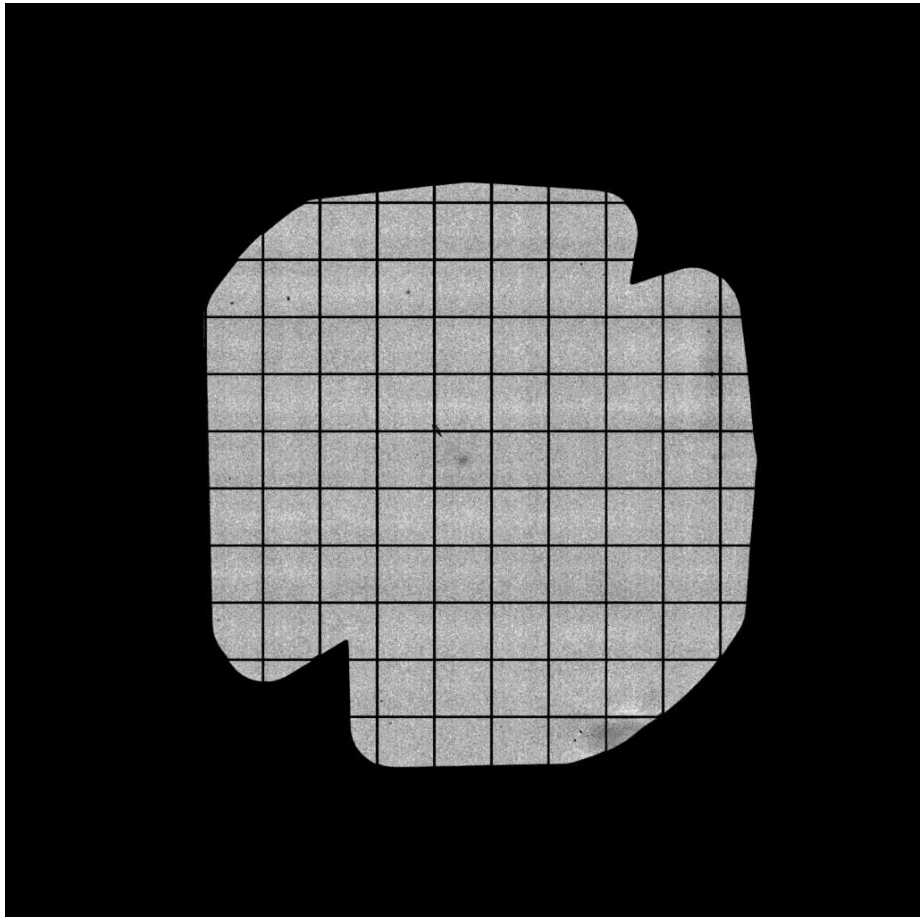

Figure 7.6: *HSI* super flat field (Y is positive to the right, Z is positive towards the top of the page). The *HSI* scale is $\sim$1.645 mm per tap.

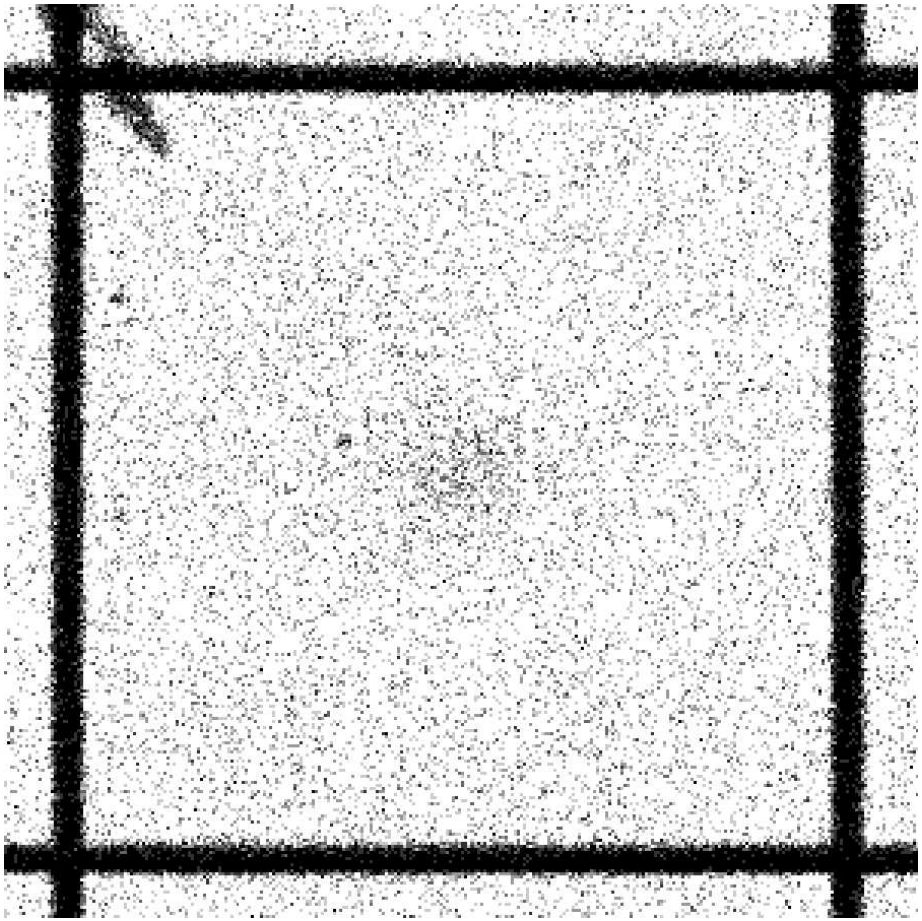

Figure 7.7: Central *HSI* tile, showing region of degraded sensitivity

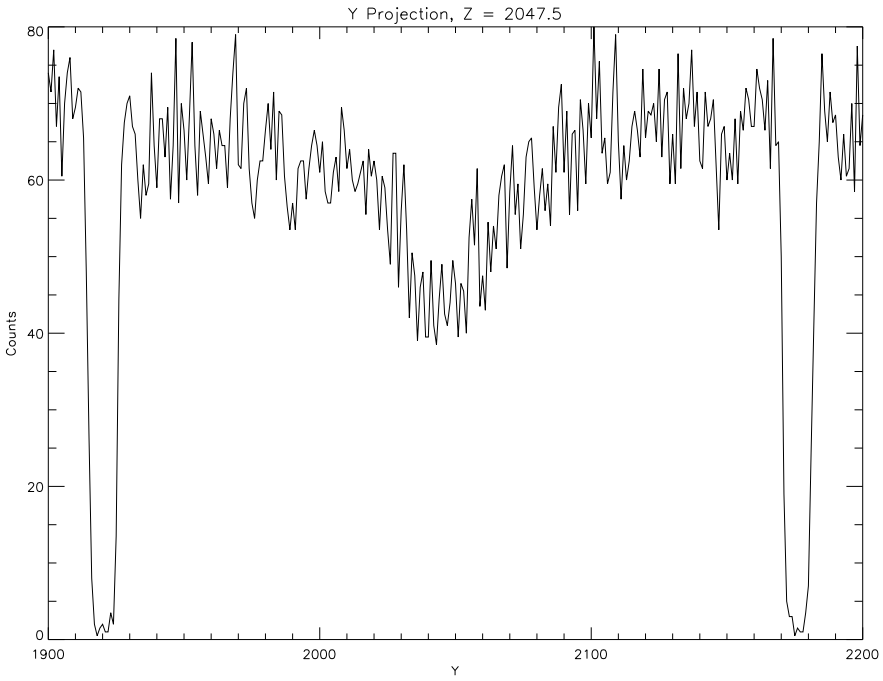

Figure 7.8: Horizontal cut across region shown in Figure 7.7. The ordinate is Y pixel number. One pixel is $\sim 6.428 \mu$m wide.

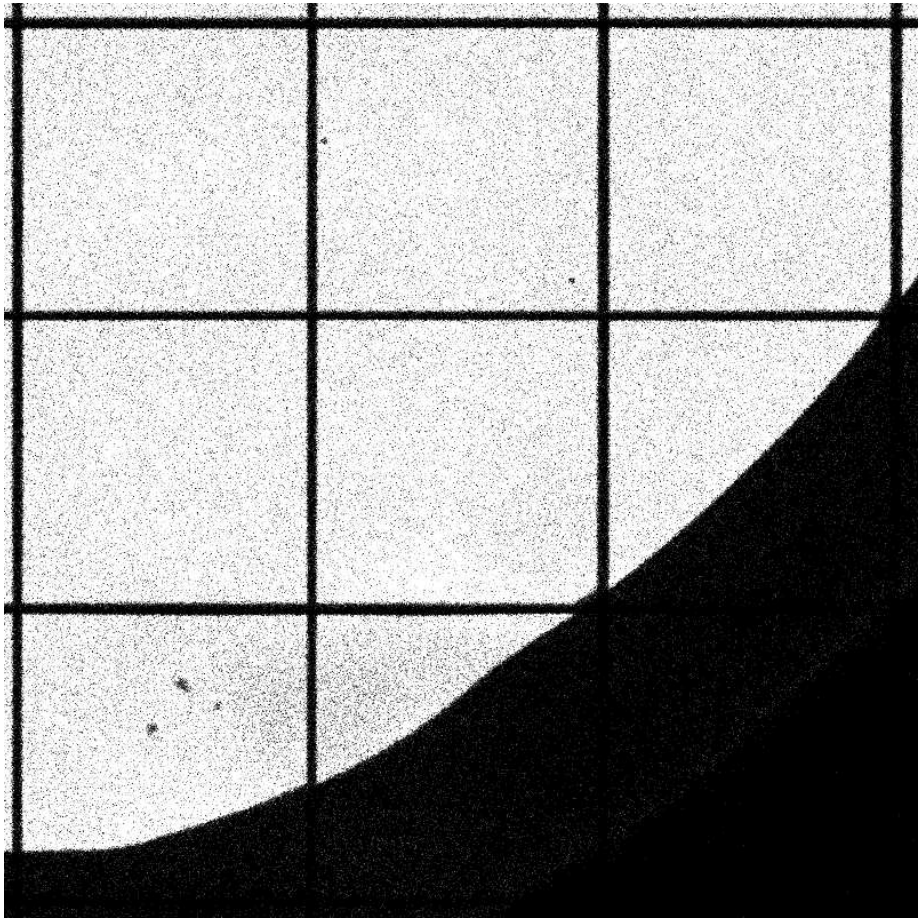

Figure 7.9: Low sensitivity region of *HSI* $(+Y, -Z)$

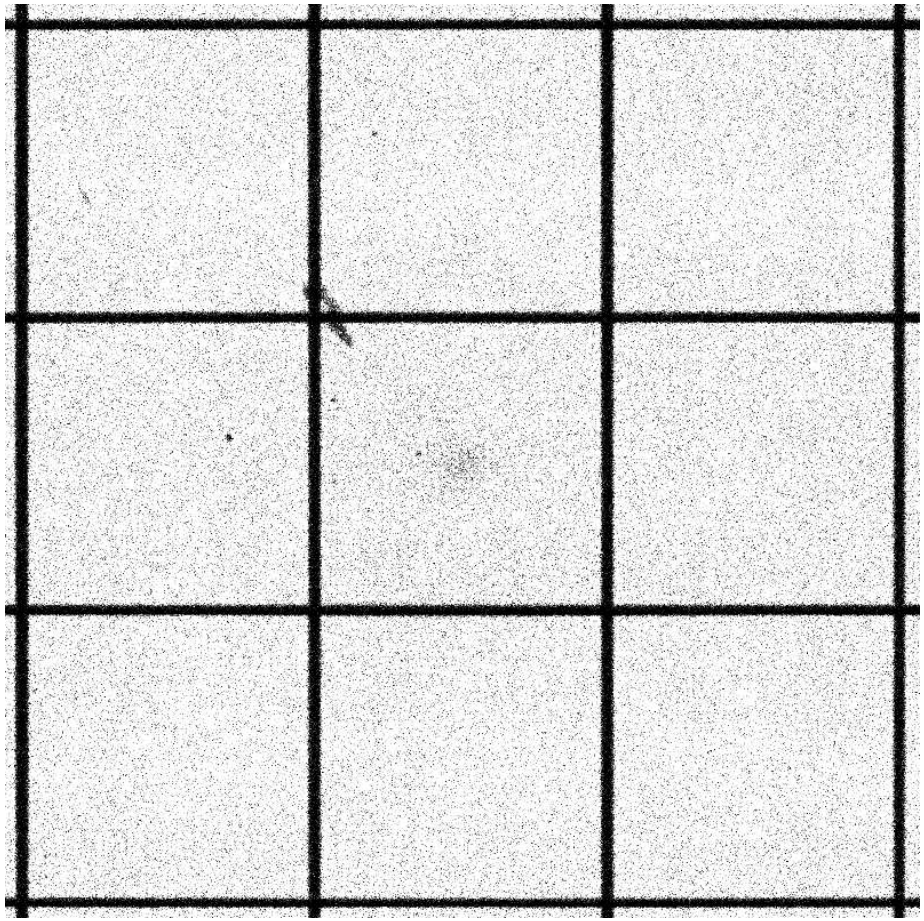

Figure 7.10: Central 3×3 tile region of *HSI* flat field

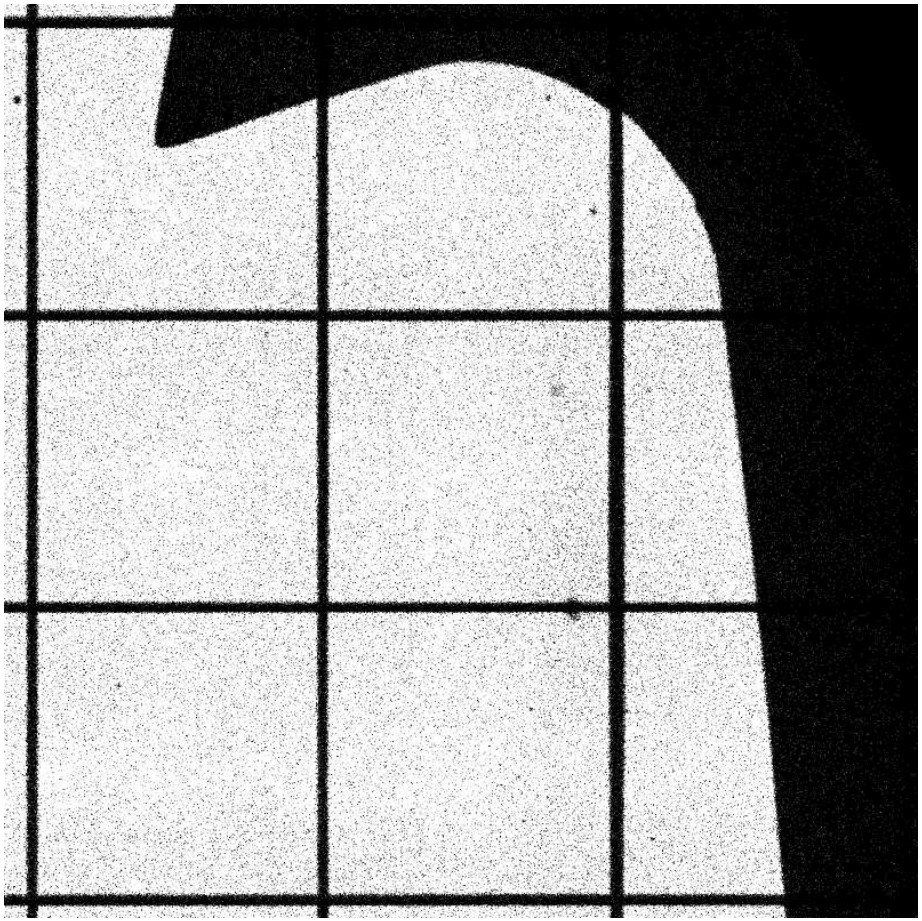

Figure 7.11: $+Y, +Z$ region of *HSI* flat field, showing variable gap width

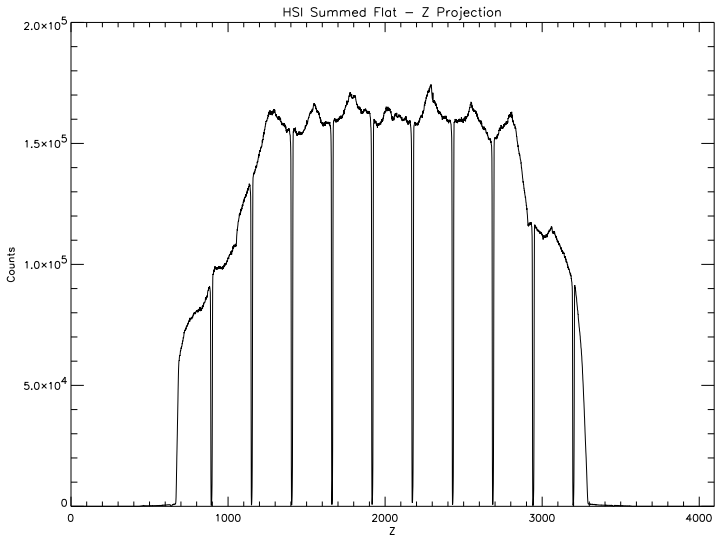

Figure 7.12: *HSI* super flat Z projection. Ordinate is Z pixel number.

one tile in size. Alternative methods of resolving this question need to be persued.

In the Y projection the dominant feature is an approximately sinusoidal apparent sensitivity variation with a maximum peak-to-peak amplitude of $\sim 5\%$ and 8 periods per tile (Figures 7.14and7.15). The peaks of the sinusoid appear to correspond to the positions of the individual cross-grid charge detector wires. These features do not appear to be evident in the Z projection. Once again, it is not clear whether spatial sensitivity variation or spatial scale distortion is responsible for these features.

7.6 Spatial Distortion

The large scale spatial distortion of the *HSI* was measured by replacing the permanent mask/ion shield assembly with a pinhole mask mounted in proximity focus to the front microchannel-plate and exposing the detector to Al-Kα x-rays. The pinhole mask consists of a rectangular grid of $50\,\mu$m diameter pinholes on $500\,\mu$m spacing. At the time of writing, the exact physical locations of the pinhole positions has not been determined through metrology. However, the manufacturer's specification states that the deviation between the actual and nominal hole positions do not exceed $2\,\mu$m. Approximately 1600 pinholes are imaged onto the *HSI* active area, and the spatial distortion corrections will be determined by mapping the centroids of pinhole images to physical pinhole locations.

Obviously, the derived spatial distortion map will be dependent on the degapping used. Because a revised degapping algorithm has not yet been tested, a spatial distortion map for the current *HSI* configuration has not yet been constructed. However, a spatial distortion map exists for a previous *HSI* configuration using similar microchannel-plates to those employed during Phase 1

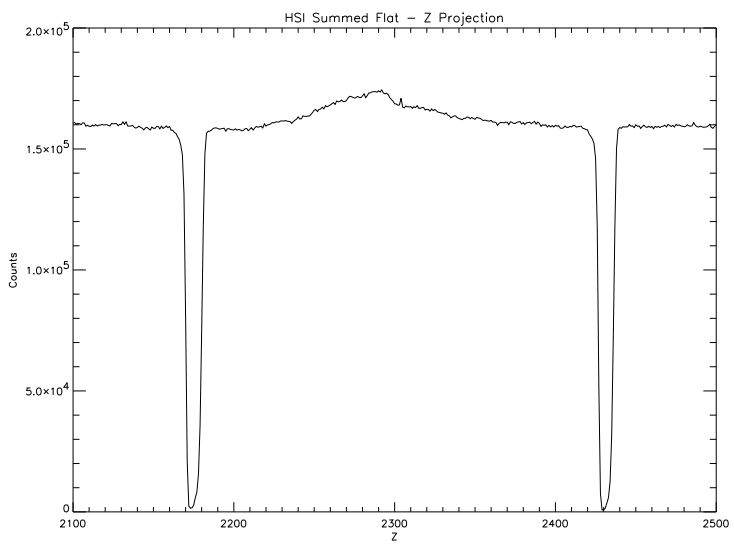

Figure 7.13: *HSI* super flat Z projection (detail). Ordinate is Z pixel number.

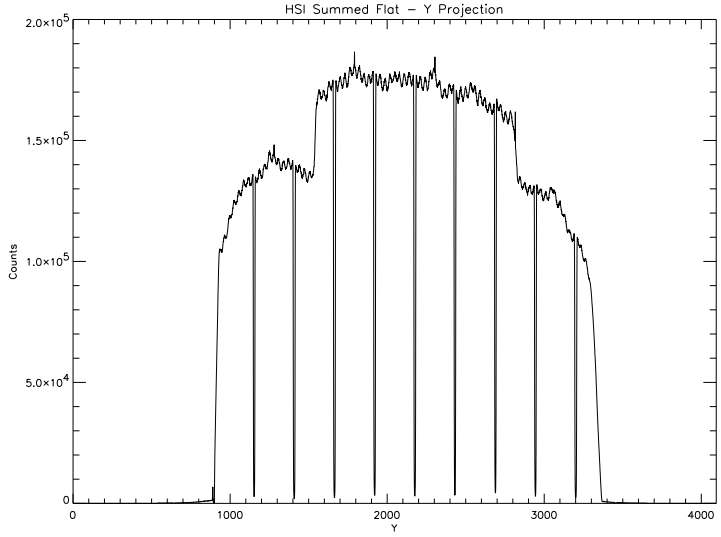

Figure 7.14: *HSI* super flat Y projection. Ordinate is Y pixel number.

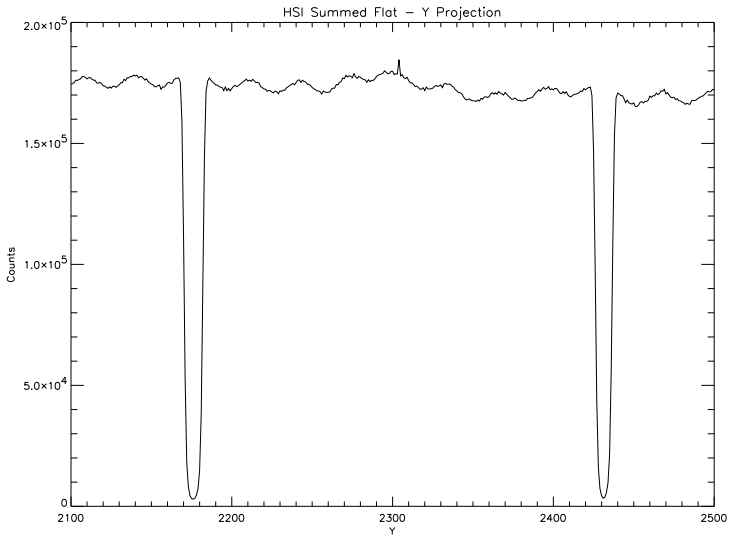

Figure 7.15: *HSI* super flat Y projection (detail). Ordinate is Y pixel number.

calibrations at the *XRCF*. That spatial distortion map revealed that measured random spatial distortions of order $10\,\mu$m were typical over most of the detector area, with some localized areas of the detector showing larger and organized distortion patterns. There was no clear evidence for any correlation between measured distortion vectors and position within tiles, *suggesting* that the apparent sensitivity variations observed in the super flat field projections are not due to spatial scale nonlinearities. If we reasonably assume that most of the spatial distortions arise due to imperfections in the construction of the cross-grid charge detector, then we would expect that the spatial distortions inherent in the current *HSI* configuration should be similar in nature to those measured for the earlier configuration.

7.7 Ion Shield Transmission

The x-ray transmission of the *HSI* ion shield used during Phase 1 *HRMA* calibration at the *XRCF* (serial number 011) was measured at the *BESSY* facility using the *SX700* monochromator beamline. The x-ray transmission was measured at three positions near the center of the ion shield at energies just above and below C, O, and Al absorption edges. The ion shield consists of a substrate of $\sim$1000 Å Lexan (H, C, and O) coated with $\sim$250 Å thickness Al.

Chapter 8

HXDS Translation Stages and Related Calculations

Richard J. Edgar

8.1 Introduction

This chapter describes the HXDS translation stage equipment, what each stage moves, and how to compute useful information from the raw numbers given in the stage log files.

8.2 Hardware Description: Focal Plane Stack

In Figure 8.1 we diagram the logical structure of the focal plane HXDS equipment and translation stages. The entire HXDS detector set at the focal point (the HRMA X-Ray Detector Assembly, or HXDA) is mounted on a pair of translation stages, which move in the x and y directions. These stages are known, respectively, as `primex` and `primey`.

On top of this moving platform, there are two stacks of equipment. The first consists of the `hsiz` stage, which moves in z and supports both the `hsi` and `ssd_x` detectors.

The second stack of equipment on the platform is the `fpc_x1`, the `fpc_x2` and their supporting translation stages. The two detectors can be moved in y and z with the `pcy` and `pcz` stages. This set of equipment in turn sits on another pair of translation stages, the `pcay` and `pcaz`, which also support the aperture screen for the two `fpc_x` detectors. Each z stage stits upon the corresponding y stage.

In order to position the `hsi` or `ssd_x` at a desired position in space, one uses the `primex`, `primey`, and `hsiz` stages. Aperture selection for the `ssd_x` is by way of the `ssda` stage, described below.

The motion of the two `fpc_x` detectors is more complex. Their aperture screen is a flat screen roughly 30 ×60 cm, with apertures placed in a diamond pattern spaced approximately 5 cm apart. To select an aperture, one uses the `pcy` and `pcz` stages to move the desired detector into position behind the selected aperture. Then the whole assembly can be put into position in space using the `primex`, `primey` or `pcay`, and `pcaz` stages. Since the accuracy specifications are more stringent for the `primey` stage than the `pcay`, standard procedure calls for using the `primey` for precise positioning.

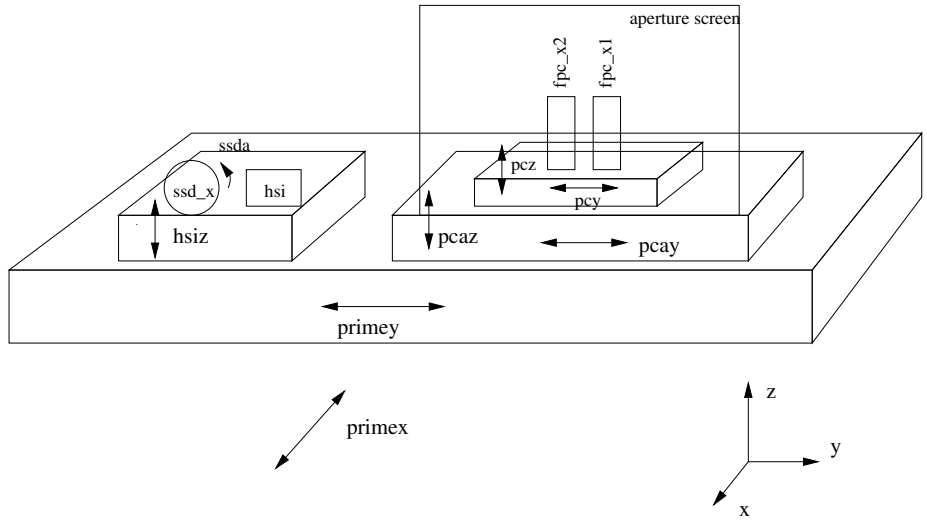

Figure 8.1: A diagram of the focal plane HXDA translation stages and detectors. Coordinates are XRCF coordinates; the HRMA is in the $+x$ direction from the detectors. Top refers to the $+z$ direction, and South to the $+y$ direction.

8.3 Hardware Description: BND

The `fpc_hn` detector can be moved about in two dimensions in a plane just in front of the HRMA entrance. This is accomplished with the `hy` and `hz` stages. In a similar way, the `fpc_5` detector can be moved in two dimensions in building 500, roughly 38 meters from the x-ray source. This motion is by way of the `5y` and `5z` stages. These two pairs of translation stages were used primarily for making beam maps, during tests known as Beam Uniformity tests.

8.4 Hardware Description: Apertures for SSD and BND Detectors

The two `ssd_` detectors each had an integral aperture wheel, operated by a rotary stage motor. These two stages are known as the `ssda` and `5ssda`, for the `ssd_x` and `ssd_5` respectively.

The `fpc_5` apertures are on a sliding plate, which could be put into place by moving the `5fpca` stage. This detector also has a blocking plate with a 36 mm diameter circular hole in it. Only one aperture at a time can be placed in front of the hole.

The `fpc_hn` has a circular aperture which can be moved in front of the detector using the `ha` stage, or it can be left open, exposing the full detector area. This stage, unlike the others mentioned in this chapter, has no encoder on it, and so cannot be read back to determine the status of this aperture. Standard procedure calls for running the stage until it trips limit switches, and counting steps. The resulting number in the `stglog` files thus varies somewhat from instance to instance, but it seems to be the case that `ha` values less than -2000 indicate the 35 mm aperture was in place,

irig	runid	caller	hsiz	ssda	primex	primey	pcaz
015193056000	108975	collect	−3411.75	144124.00	−46652.34	431655.41	−38280.75

pcz	pcay	pcy	hy	hz	ha	5y	5z
35431.00	−17297.00	−21031.00	−72563.87	−83537.02	0.00	120600.45	−89341.00

5fpca	5ssda
19999.50	32997.00

Table 8.1: Sample stage log entry, split into several lines for the reader's convenience

while those greater than -2000 indicate an open detector collecting area.

8.5 Stage Log File Formats

Entries in the stage logs were recorded by the HXDS computers for each "test," *e.g.* commanded stage motion, data collection etc. These logs, split into short files by time, are rdb tables (tab delimited ASCII files with headers identifying the columns). They contain three identifying columns plus the readouts of all HXDS stages. The columns are the irig time (in format DDDHHMMSSsss; a 3 digit day, 2 digits each of hours, minutes, and seconds, plus 3 digits of decimal seconds. Then follows the HXDS runid, a unique identifier which increments with each test, and a field called "caller" which identifies what operation was in progress following the move. Examples of this include "collect" (*i.e.* collecting x-rays; a single exposure), "beamcen" (finding the beam in the $y-z$ plane), and "acis_collect," a procedure for taking numerous short exposures for later coadding. The remaining columns are the values from the translation stage readouts, in units of microns. A sample entry (split into several lines to facilitate reading by humans) is presented in Table 8.1.

8.6 Computations with the Stage Log information: fpc_x Detectors

The basic maneuver with the HXDA equipment is a `focusmove` command. This causes the selected aperture to be put into the position of the last known best focus for a given mirror combination. The software must rely on a number of tables of information in order to accomplish this. These tables are as follows:

- The facility optical axis (FOA) table `foa.rdb`, which contains the 3-dimensional position of the best focus for each supported mirror combination (each shell, the full HRMA, and the outer and inner pairs of shells). The best focus is actually the stage readings of the fpc_x2 `P` aperture (*i.e.* the 20 μm diameter aperture). The mirror identifier, and the irig time at which the focus was updated are also included in this table. A sample of this table is shown in Table 8.2.
- The master table for the focal point instrument in question. This contains the hardware coordinates for the necessary stages to move each of this instrument's apertures to the focal point. It stores the geometry of the aperture screen or wheel. In the case of the `hsi`, various aim-points on the chip were established as pseudo-apertures, and these are listed with their

irig	mirror	primex	primey	pcaz
015132723000	all	−32882	−307149	10650
015132724000	1	−33115	−307149	10650
015132724000	3	−32764	−307149	10650
015132725000	4	−32495	−307149	10650
015132726000	6	−32867	−307149	10650
015132727000	13	−32968	−307149	10650
015132728000	46	−32634	−307149	10650
015132728000	leg	−32882	−307149	10650
015132729000	meg	−32968	−307149	10650
015132730000	heg	−32634	−307149	10650

Table 8.2: Sample section from the FOA table

  hardware coordinates in the `master.hsi` file. These tables were updated from time to time as the geometry became better understood, and so the final version of the table is to be used in each case.

- A table of aperture sizes. Each aperture has a name, which is what is given in the master table. To convert the name into a size (diameter in microns, if a circular aperture, or dimensions in microns with a tilt for rotated slit apertures), this table is used. The master tables and aperture sizes for the detectors are listed in Tables 8.3 – 8.5.

These tables are found in the `$DB` directory at XRCF. A copy of this directory as it existed at the end of Phase E of the calibration was made at SAO and is the default location for these tables. As of this writing, it is kept in `/proj/axaf/simul/databases/hxds`.

What follows is an English description of the computation of the aperture in use, and its position, which is implemented in the perl script known as `calcstage4`.

- Read the FOA table and the master table for the fpc_x2. Compare the numbers from the last FOA table entry prior to the measurement for the mirrors used, to the entry in the fpc_x2 master table for aperture P. Differences in the 3 coordinates ($FOA - master$) are the offset between the original and the contemporary facility optical axis ("FOA offsets").
- Search the master table for the fpc_x for `pcy` and `pcz` values that match those from the stage log, within a given tolerance (5000 μm works well). This identifies the aperture in use.
- Look up the aperture size in the aperture size table.
- Compute the location of the aperture center:

$$X = stglog_{\texttt{primex}} - master_{\texttt{primex}} \quad (8.1)$$

$$Y = stglog_{\texttt{primey}} - master_{\texttt{primey}} + stglog_{\texttt{pcay}} - master_{\texttt{pcay}} \quad (8.2)$$

$$Z = stglog_{\texttt{pcaz}} - master_{\texttt{pcaz}} \quad (8.3)$$

- Subtract the FOA offsets from all 3 coordinates.

8.7 Computations with the Stage Log information: Other Detectors

The computations with ssd_x and hsi detectors are not very different from the above, except for the method for obtaining the aperture in use. For the ssd_x, one compares the entries in the master table for the ssd_x to the stage log ssda stage, within tolerance, to obtain the aperture ID. For the hsi, which has no native apertures, the name of the pseudo-aperture (*i.e.* aim point on the chip) is obtained from a parameter (*i.e.* supplied by the user). In this case the aperture size is not applicable.

The Y and Z position computations are also slightly different, since the ssd_x and hsi detectors are not sitting on the pcay and pcaz stages:

$$Y = stglog_{\texttt{primey}} - master_{\texttt{primey}} \quad (8.4)$$

$$Z = stglog_{\texttt{hsiz}} - master_{\texttt{hsiz}} \quad (8.5)$$

The remainder of the computation proceeds as above for the fpc_x detectors.

8.8 Known Shortcomings of this Method

During Phase E of the XRCF testing, tests were performed with nonzero values of the HRMA pitch. Because of a stuck actuator, the HRMA was rotated not about its node, but about a line through the stuck actuator. This results in a motion of the focal point by approximately -317.7 μm for each arcminute of pitch. This offset was made manually by the HXDS operators for each test, and not in general incorporated into the FOA table. Thus the calcstage4 script outlined above cannot include this offset, and the offset must be applied after the fact to the results of the calculation. Details are in §14.2.

Brad Wargelin's Analysis of the focus tests with the hsi and the fpc_x2 shows a systematic offset along the facility axis direction (x), in the sense that the hsi is 2744 μm from the fpc_x2 in the x direction, which is 291 μm less than the the assumed value of 2975 μm. This could be fixed for analysis purposes by adjusting the primex values in the hsi master table.

It also appears, from Brad Wargelin's analysis of the non-zero-order grating focus check tests, that the primey stage is rotated slightly about its vertical axis, so that primex (along the FOA) changes slightly as primey is varied. The amount of rotation is approximately 0.0058 ± 0.0004 radians (1/3 of one degree) in the sense that the focal plane detector moves slightly away from the HRMA ($-x$) as primey is increased ($+y$, to the south).

Details for these last two effects may be found, for now, on the web at

http://hea-www.harvard.edu/MST/simul/xrcf/HRMA/focus/hsi_offset.

Another shortcoming has come to our attention: The FOA table was often not updated to reflect beam centering tests. Often prior to a test the beamcen procedure was run with a small aperture to find the beam for the subsequent test. The test was then run not at the recorded FOA position but at the location of the beam found by the beamcen. We are therefore analyzing the sum files from the beamcen runs, and will produce an FOA table which can be read by the calcstage script which will reflect their results.

aper	primex	primey	pcaz	pcz	pcay	pcy
A	−43381	−325402	7244	11600	50614	−86871
B	−43440	−325402	11932	6912	10357	−48614
C	−43500	−325402	7939	10905	−29140	−9117
D	−43501	−325402	−40573	59417	−82683	44426
E	−43461	−325402	−40284	59128	−56716	18459
F	−43461	−325402	−40471	59315	−30373	−7884
G	−43430	−325402	−40411	59255	−3775	−34482
H	−43361	−325402	−21405	40249	19880	−58137
I	−43470	−325402	−16635	35479	−17284	−20973
J	−43469	−325402	−16681	35525	−43485	5228
K	−43499	−325402	−16756	35600	−69645	31388
L	−43510	−325402	7804	11040	−82766	44509
M	−43480	−325402	7835	11009	−56570	18313
N	−43450	−325402	32554	−13710	−17292	−20965
O	−43500	−325402	32466	−13622	−43505	5248
P	−43500	−325402	32416	−13572	−69634	31377
Q	−43530	−325402	56229	−37385	−82746	44489
R	−43531	−325402	56292	−37448	−56528	18271
S	−43500	−325402	56326	−37482	−30399	−7858
T	−43440	−325402	56412	−37568	−3793	−34464
U	−43440	−325402	44511	−25667	19898	−58155
V	−43502	−325402	80136	−61292	−69678	31421
W	−43500	−325402	80152	−61308	−43468	5211
X	−43461	−325402	80188	−61344	−17304	−20953
Y	−43499	−325402	80234	−61390	8950	−47207
Z	−43441	−325402	80239	−61395	35134	−73391
AA	−43500	−325402	−65107	83951	−69621	31364
AB	−43450	−325402	−65171	84015	−43531	5274
AC	−43350	−325402	−65105	83949	−17212	−21045
AD	−43301	−325402	−69843	88687	9015	−47272
AE	−43251	−325402	−48294	67138	23489	−61746
AF	−43170	−325402	−64957	83801	50642	−86899
AG	−43301	−325402	−32714	51558	50574	−86831
AH	−43300	−325402	49043	−30199	50530	−86787

aper	size
A	35000
B	20000
C	10000
D	4000
E	2000
F	1000
G	500
H	300
I	200
J	150
K	100
L	70
M	50
N	40
O	30
P	20
Q	15
R	10
S	7.5
T	5_40
U	3
V	5x100v
W	5x100v−5
X	5x100v+5
Y	5x100h−15
Z	5x100v−15
AA	10x200v
AB	10x200v−5
AC	10x200v+5
AD	10x200h
AE	80x500v
AF	500x10v
AG	500x10v+5
AH	500x10v−5

Table 8.3: Master table (left), and aperture size table (right) for the HXDA FPC detectors

aper	primex	primey	hsiz
ap1	−57039	413484	18482
ap2	−57039	413464	18380
ap3	−57039	413464	18380
ap4	−57039	413464	18380
ap5	−57039	413296	18410
ap6	−57039	413354	18408
ap7	−57039	413384	18387
ap8	−57039	413372	18393
ap9	−57039	413395	18407
ap10	−57039	413478	18426
ap11	−57039	413481	18428
ap12	−57039	413596	18472
ap13	−57039	413405	18453
ap14	−57039	413331	18534
ap15	−57039	413584	18540
ap16	−57039	413498	18546
ap18	−57039	413609	18529
ap17	−57039	413484	18482
ap19	−57039	413484	18482
ap20	−57039	413484	18482

aper	size
ap4	5000al25
ap3	5000al125
ap2	5000
ap5	2000
ap6	500
ap7	200
ap8	100
ap9	70
ap10	50
ap11	40
ap12	30
ap13	20
ap14	15
ap15	10
ap16	7
ap18	5_40
ap1	Fe_LK
ap17	5_12
ap20	200x2v+5
ap19	200x2v−5

aper	size
ssd5_12	5_12
ssd5_40	5_40
ssd7	7
ssd10	10
ssd15	15
ssd20	20
ssd30	30
ssd40	40
ssd50	50
ssd70	70
ssd100	100
ssd200	200
ssd500	500
ssd2000	2000
ssd5000	5000
ssd5000al25	5000al25
ssd5000al125	5000al125
ssd2spos	2spos
ssd2sneg	2sneg
ssd244cm	244cm

Table 8.4: Master table (left) and aperture size table (center) for ssd_x, and aperture size table for ssd_5 (right)

aper	primex	primey	hsiz
CEN	−46475	64863	17134
CA1	−46475	64958	17894
CA2	−46475	64547	17898
CA3	−46475	64136	17902
CA4	−46475	64954	17483
CA5	−46475	64543	17487
CA6	−46475	64132	17491
CA7	−46475	64950	17072
CA8	−46475	64539	17076
CA9	−46475	64128	17080
CAL1	−46475	68188	22291
CAL2	−46475	67398	22729
LL90	−46475	68018	22879
LL95	−46475	68039	22919
LL99	−46475	68210	23227
CAR1	−46475	59451	12749
CAR2	−46475	60104	12238
UR90	−46475	59521	12291
UR95	−46475	59493	12264
UR99	−46475	59236	11997

Table 8.5: Master table for hsi

Chapter 9

Spectral Fitting in HXDS Detector Data Analysis

Richard J. Edgar

9.1 Introduction

This chapter discusses the use of spectral fitting and the `JMKmod` software in the analysis of AXAF calibration data. What is described here is the standard reduction of the data. A somewhat more sophisticated use of `JMKmod` which produces higher fidelity results, but at a significant cost in attention and labor, is described in §9.4.

9.2 Reduction of the Line Measurements

The outputs of the HXDS (HRMA X-ray Detector System; the assemblage of detectors described in the introduction) equipment, for spectral detectors, consists of a pulse-height spectrum for each of the detectors (focal plane plus BNDs), and various derived products based on region-of-interest sums over spectral channels. These are converted into FITS files compatible with the XSPEC X-ray spectral analysis program.

The resulting FITS files are fit to a model which includes the source properties (spectral lines plus a Kramer continuum model, of the form $(E_{max} - E)/E$), the X-ray filter properties, and the detector properties. This model, known as `JMKmod` (Tsiang et al., 1997) is based on the discussion by Jahoda and McCammon (1988) of proportional counter physics, generalized to include solid state detectors. We use a unit diagonal response matrix in XSPEC with this software, allowing us to control all the features of the detector model within our own software, and to adjust detector parameters as well as source parameters to fit the observed spectra. Further details and discussion of the model can be found in Edgar et al. (1997) and Tsiang et al. (1997).

There are in excess of 50 parameters to be set in this model, but the vast majority of them can be set from values obtained from the facility data or experiment design. We then fit the remaining 3 to 6 parameters interactively, once for each type of detector for each source setup. The interesting parameters here are the ones that describe the flux in the spectral line in question (including escape peaks, partial charge-collection "shelf" features in the spectrum, pileup, and other detector effects). Also allowed to float freely in most fits is the relative flux of the continuum and the line.

For a typical fit, all parameters but a few are fixed to theoretical values. The floating parameters typically include either the fano factor or the Polya h parameter (which have nearly identical effects on the line width and shape, and so should never be allowed to vary freely at the same time); the shelf norm (which models partial charge collection); the continuum norm (for EIPS spectra which have a continuum); the overall `JMKmod` norm (*i.e.* the intensity); and escape line energies and norms (if $E > 3$ keV). For SSD spectra, the `broad` (electronic line broadening) can also be allowed to float freely. The energy of the escape peak should be allowed some freedom because of energy nonlinearities such as that shown in Figure 3.6, which shows a discontinuity in the effective ionization energy of the gas across the Ar L-edge.

Some energy/channel nonlinearity is expected in any proportional counter, and it is likely that each detector system has its own small channel offset, but this does not significantly affect our results because the fitting process (and particularly the energy scale determination) is dominated by the main peak. Likewise, slight rate-dependent variations in peak width are automatically accounted for during the fitting process.

As explained in Chapter 5, for SSD spectra above 2 keV, the pileup parameter should be frozen at $1 - 0.6\mu s \times Rate$, if one is using the Gedcke-Hale deadtime estimates from the file headers. Pileup should not be included in the fits if the pulser peak is used to determine the deadtime fraction. Below 2 keV, the incomplete pileup rejection greatly complicates matters.

We show in Table 9.1 a list of the parameters in the `JMKmod` XSPEC model, with their default values, and recommended values for fitting FPC and SSD spectra.

There are numerous effects to be accounted for in such a procedure. Here is a list of those we have done only approximately, with an estimated bias or error at the few percent level for each. They are discussed one by one below.

- Most fits are done by minimizing the χ^2 statistic.
- Backgrounds were modeled rather than subtracted.
- No correction is made for the mesh in the focal plane FPC window.
- Deadtime is estimated by the detector pulse-processing electronics, and we use this estimate.

In cases where there are few counts per channel, the χ^2 statistic, with its built-in assumptions of Gaussian distributed errors, is both inappropriate and biased (Bevington and Robinson, 1992). A more appropriate statistic, the C–statistic, based on maximum likelihood arguments and the Poisson distribution is discussed by Cash (1979), and Nousek and Shue (1989). This statistic is implemented within XSPEC, and we have used it in such cases as wing scans, and some BND fits, which have weak signals. We have verified that in cases with many counts per channel this C–statistic produces comparable results to the conventional χ^2 method.

For the Encircled Energy experiments, the count rates are orders of magnitude above background in every case. Therefore, for these cases, background subtraction or modeling will not be a significant effect. For wing scan spectra, however, this will be important. In those cases, because of poor statistics in the background spectra, we elected to fit a function (often a power law plus broad Gaussian combination) to the background spectrum, and then use this function (with no free parameters) as a component in fitting the X-Ray spectra. This decision was driven in part by a feature of XSPEC which makes use of the C–statistic (see previous paragraph) incompatible with background subtraction. It also eliminates the need to deal with channels which, due to statistical fluctuations, would have a negative count rate if background subtraction were done.

Table 9.1: Parameters for the `JMKmod` model, with recommended values.

#	Name	Default	FPC	SSD	Remarks
1	fano	0.2	0.2	0.2	Fano factor; line width
2	polyah	1.2	1.2	ignored	Polya H param; line width for FPC
3	E_offset	0.0	0.0	0.0	zero−point offset in E scale (keV)
4	i_pot	2.8e−2	2.8e−2	3.0e−3	energy per ion pair, keV
5	gain	4.0	.5−−4.0	0.6	gain in channels/ion pair
6	ch_off	0.0	0.0	0.0	zero−point offset in channel scale
7	broad	0.0	0.0	10.0	electronic Gaussian broadening (chans)
8	d_gain	0.0	0.0	0.0	width of top hat gain distribution
9	nchan	512.	512.	4096.	number of channels
10	sestype	1.	1.	1.	1=FPC 2=SSD 3=FPC w/distrib gain
11	contin	1.	1.	1.	1=yes 0=no continuum
12	econt	10.	10.	10.	high energy cutoff of continuum (keV)
13	contnorm	1.	.1	.1	norm of continuum, rel to line
14	E_max	10.	10.	10.	max energy for contin; set = param 12
15	E_min	0.01	0.01	0.01	min energy for contin (keV)
16	E_char	2.	2.	2.	characteristic energy for Gaussian continuum
17	E_width	0.1	0.1	0.1	width of Gaussian continuum (keV)
18	nInt	512.	512.	512.	number of points in contin integral
19	temper	15.	15.	ignored	FPC temp (C) for QE only
20	pressure	400.	400.	ignored	FPC pressure (torr) for QE only
21	argrat	0.9	0.9	ignored	proportion of Argon; rest is CH4
22	shelfsw	0.	0.	0.	1=yes; 0=no low energy shelf
23	t1norm	0.	0.	0.	falling tail norm
24	t1par	0.999	0.999	0.999	falling tail scale length
25	t2norm	0.	0.	0.	rising tail norm
26	t2par	1.001	1.001	1.001	rising tail scale length
27	shelfnm	0.	0.	0.	flat shelf norm
28	pulser	0	0	0	1=yes 0=no pulser peak fit
29	pulsepos	100.	100.	100.	position of Gaussian pulser (chans)
30	pulsesig	1.	1.	1.	sigma of Gaussian pulser peak (chans)
31	pulsenrm	1.	1.	1.	norm of Gaussian pulser peak
32	numcomp	2.	2.	2.	Number of lines *DO NOT CHANGE*
33	numfil	6.	6.	6.	Number of "filters" *DO NOT CHANGE*
34	pileup	0	0	0	1=yes 0=no pileup
35	pilepar	1.	0.999	0.999	pileup parameter
36	bfield	1.45e4	1.45e4	1.45e4	B(gauss) for synchrotron model
37	current	1.	1.	1.	beam current (amps) for synch mod
38	incline	0.	0.	0.	inclination (deg) for synch mod
39	abswitch	0.	0.	0.	1=yes 0=no absolute norm for synch mod
40	phi	135.40	135.40	135.40	azimuth angle (deg) for A_eff filt
41	theta	40.20	40.20	40.20	off−axis angle (deg) for A_eff
42	shell	12.	12.	12.	mirror combo for A_eff
43	E_line1	1.49	1.49	1.49	Energy of line 1 (keV)

Table 9.1: (continued)

#	Name	Default	FPC	SSD	Remarks
44	E_line2	1.56	1.56	1.56	Energy of line 2 (keV)
45	E_norm1	1.	1.	1.	norm of line 1 (set to 1)
46	E_norm2	1.	1.	1.	norm of line 2 rel to line 1
47	src1	35.	35.	35.	src/filter 1 (kramer continuum)
48	src2	6.	6.	6.	src/filter 2 (carbon XSS filter)
49	src3	2.	2.	2.	src/filter 3 (Al in window)
50	src4	19.	19.	19.	src/filter 4 (polyimide in window)
51	src5	38.	38.	37.	src/filter 5 (FPC or SSD body QE)
52	src6	45.	45.	45.	src/filter 6 (unused)
53	srcthk1	0.	0.	0.	thickness of flt 1 (unused)
54	srcthk2	2.5e−4	2.5e−4	2.5e−4	thickness of flt 2 (cm)
55	srcthk3	2.e−6	2.e−6	2.e−6	thickness of flt 3 (cm)
56	srcthk4	1.065e−4	1.065e−4	1.065e−4	thickness of flt 4 (cm)
57	srcthk5	5.36	5.686	0.5	thickness of flt 5 (cm)
58	srcthk6	0.	0.	0.	thickness of flt 6 (cm)
59	norm	1.	?	?	overall norm (counts/sec)

The FPC detectors have a mesh of 100 μm diameter wires on 2 mm centers to support their plastic windows against the pressure differential. For the BND detectors, which are uniformly illuminated, we have reduced the working area by the fraction of the geometrical area obscured by this mesh. For the focal plane detector, a focused, on-axis image will fit within a single mesh cell, and an effort was made to place the focused image at the center of such a mesh cell. Mesh obscuration is extremely small in on-axis cases without gratings. Proper accounting for this effect is done by a ray trace simulation of the mirrors and FPCs. This effect is discussed in further detail in Chapter 6.

Note that the fitted counting rates are in *counts* s^{-1}. To get photons per second, the detector quantum efficiency must be divided into the counting rate. In many cases of phase 1 measurements, we can use relative quantum efficiencies, which in some cases are better known than the absolute ones.

Detector dead time is estimated by the detector operating software using a Gedcke-Hale technique, and we adopt this estimate (which is recorded in each raw spectral file header). An electronic pulser input was included in nearly all spectra, and a comparison of pulses injected to pulses detected will allow a more accurate dead time correction. While work remains to be done on the accuracy of this estimate, The Gedke-Hale deadtime matches that determined from the pulser peak to much better than 1% for FPC spectra. For SSD measurements, the pulser peak is used to determine the deadtime. This is further complicated by incomplete pileup rejection below 2 keV (see Chapter 4).

9.3 A Sample Fit: Ti K–α

In this section we discuss a sample `JMKmod` fit. The data in question are an `fpc_5` spectrum of the EIPS, with a Ti anode and the source high voltage set to about 15 kV, with a Ti filter which is about 2 mean free paths thick at Ti K–α. This results in a spectrum which contains the Ti K–α and K–β lines, and a bremsstrahlung continuum. Much of the continuum just hardward of the

lines is absorbed by the filter.

We fit a spectral model using the `JMKmod` software, with parameters as shown in Figure 9.1. The model consists of four δ-function lines: Ti K–α (4.51 keV), Ti K–β (4.93 keV), and the Ar K–α escape lines of these two, at the above energies minus 2.9577 keV. There is also a Kramer continuum of the form $(E_{max} - E)/E$, with E_{max} in keV set numerically equal to the source high voltage in kV.

We allowed the following parameters to float freely: the detector gain, the continuum norm (ratio of continuum counts to the K–α line counts), and the overall norm (total counting rate).

Note that the residual, while nearly flat, has a systematic wiggle in it which indicates that our model is not an entirely adequate description of the actual pulse height spectrum. We adjust the gain, line shape parameters, etc. to minimize this wiggle, and in cases where it cannot be eliminated, we make the (eyeball) integral of the residual near zero, so that the error in the line countrate is a small fraction of the amplitude of the wiggle, which in turn is a small fraction of the amplitude of the line. In this case, we obtain $\chi^2_\nu = 0.9888$, though in many cases the reduced χ^2 value exceeds unity.

We plot the results in Figure 9.2.

9.4 A Higher Fidelity Method for Analysis of FPC Line Data

The data were processed in much the same way as the generic XRCF FPC data, as described in §9.2. In order to improve the fidelity of the analysis, however, certain systematic effects need to be accounted for, which necessitates additional care in some aspects of the data reduction.

One such effect is to include the (rough) shape of the HRMA effective area curve in the analysis. This changes not the counting rate at the line, but rather the shape of the continuum. Fitting the continuum well allows one to confidently separate continuum photons that fall in the region of the line from line photons, and to quote a counting rate due to line photons only, despite the poor intrinsic resolution of the FPC detectors.

Many of the tests covered here are encircled energy (EE) tests, which have many iterations using different sizes of pinhole apertures on the focal plane detector. After verifying that the counting rates measured by the BND-H detectors are time-independent, the data from all these iterations (or those where a given detector was functioning, if it went offline for some of them) were co-added, to improve the signal to noise ratio for further analysis.

Unlike the `fpc_5` and focal plane FPC detectors, the BND-H detectors have a substantial amount of open area, approximately 3.6 × 9.9 cm. The response of these single-wire flow proportional counters has been found to be quite uniform across the wire (in the Y direction at XRCF), but the gain is significantly higher near the ends of the detectors. Prior to the calibration, the blocking plate apertures were reworked, giving a somewhat smaller open area and masking the ends of the counters where the gain was largest. However, there is still enough variation of gain along the wire that it must be taken into account in order to obtain acceptable fits to the spectra.

The `fpc_hn` detector could be used either open, or with a 35 mm circular aperture. When used with the 35 mm aperture, the gain nonuniformity effect is negligible.

As shown in §3.4, the gain distribution for the various counters is nearly the same, and they are quite flat for the central ∼ 6 cm of each counter. Then, to good approximation, the gain increases nearly linearly to the ends of the active part of the counter. Thus the gain distribution can be approximated as a delta function plus a top-hat function extending from the center-section gain value to some larger value. Fortunately, both delta function and top-hat function (*i.e.* constant between two given values of x, and zero elsewhere) gain distributions are available within the


```
XSPEC> show all
  15:53:03 16-Sep-98
Auto-saving is done after every command.
Fit statistic in use is Chi-Squared
Minimization technique is Lev-Marq
  Convergence criterion =   1.000000000000D-02
Querying enabled
Prefit-renorming enabled
Solar abundance table is angr

Information for file   1
  belonging to plot group   1, data group   1
telescope = HXDS , instrument = fpc_5 , channel type = PHA
Current data file: acq111140d310.fits
No current background
No current correction
Response (RMF) file    : /home/edgar/diag512.rmf
Auxiliary (ARF) file   : none
Weighting method is standard
  Noticed channels      9 to   469
  File integration time     11.14
    and effective area      1.000
  File observed count rate    2384.   +/- 14.650    cts/s
  Model predicted rate :      2347.

mo = jmkmod4[1]
------------------------------------------------------------------------
mo = jmkmod4[1]
Model Fit Model Component  Parameter  Unit     Value
par  par comp
  1    1   1   jmkmod4    fano       null     0.1432       frozen
  2    2   1   jmkmod4    polyab     null     1.215        frozen
  3    3   1   jmkmod4    E_offset   keV      0.           frozen
  4    4   1   jmkmod4    i_pot      null     2.8000E-02   frozen
  5    5   1   jmkmod4    gain       chan/pai 1.197        +/- 0.6200E-03
  6    6   1   jmkmod4    ch_off     chan     0.           frozen
  7    7   1   jmkmod4    broad      null     0.           frozen
  8    8   1   jmkmod4    d_gain     null     0.           frozen
  9    9   1   jmkmod4    nchan      null     512.0        frozen
 10   10   1   jmkmod4    sestype    null     1.000        frozen
 11   11   1   jmkmod4    contin     null     1.000        frozen
 12   12   1   jmkmod4    econt      keV      15.30        frozen
 13   13   1   jmkmod4    continorm  null     6.2624E-02   +/- 0.6074E-02
 14   12   1   jmkmod4    E_max      keV      15.30        = par  12
 15   14   1   jmkmod4    E_min      null     1.000E-02    frozen
 16   15   1   jmkmod4    E_char     null     0.1000       frozen
 17   16   1   jmkmod4    E_width    null     2.000        frozen
 18   17   1   jmkmod4    temper     C        15.00        frozen
 19   18   1   jmkmod4    pressure   torr     400.0        frozen
 20   19   1   jmkmod4    argrat     null     0.9000       frozen
 21   20   1   jmkmod4    shelfrw    null     1.000        frozen
 22   21   1   jmkmod4    shelfsw    null     0.           frozen
 23   22   1   jmkmod4    t1norm     null     0.           frozen
 24   23   1   jmkmod4    t1por      null     0.990        frozen
 25   24   1   jmkmod4    t2norm     null     0.           frozen
 26   25   1   jmkmod4    t2par      null     1.001        frozen
 27   26   1   jmkmod4    shelfnm    null     1.0000E-02   frozen
 28   27   1   jmkmod4    pulser     null     0.           frozen
 29   28   1   jmkmod4    pulsepos   null     100.0        frozen
 30   29   1   jmkmod4    pulsesig   null     1.000        frozen
 31   30   1   jmkmod4    pulsenrm   null     1.000        frozen
 32   31   1   jmkmod4    numcomp    null     4.000        frozen
 33   32   1   jmkmod4    numfil     null     6.000        frozen
 34   33   1   jmkmod4    pileup     null     0.           frozen
 35   34   1   jmkmod4    pilepar    null     1.000        frozen
 36   35   1   jmkmod4    bfield     gauss    1.4500E+04   frozen
 37   36   1   jmkmod4    current    mA       1.000        frozen
 38   37   1   jmkmod4    incline    rad      0.           frozen
 39   38   1   jmkmod4    absvitch   null     0.           frozen
 40   39   1   jmkmod4    phi        deg      135.4        frozen
 41   40   1   jmkmod4    theta      arcmin   40.20        frozen
 42   41   1   jmkmod4    optconst   null     0.           frozen
 43   42   1   jmkmod4    E_line1    keV      4.510        frozen
 44   43   1   jmkmod4    E_line2    null     1.520        frozen
 45   44   1   jmkmod4    E_line3    null     4.932        frozen
 46   45   1   jmkmod4    E_line4    null     1.934        frozen
 47   46   1   jmkmod4    E_norm1    null     1.000        frozen
 48   47   1   jmkmod4    E_norm2    null     6.7203E-02   frozen
 49   48   1   jmkmod4    E_norm3    null     0.           frozen
 50   49   1   jmkmod4    E_norm4    null     1.2443E-02   frozen
 51   50   1   jmkmod4    src1       null     35.00        frozen
 52   51   1   jmkmod4    src2       null     14.00        frozen
 53   52   1   jmkmod4    src3       null     2.000        frozen
 54   53   1   jmkmod4    src4       null     19.00        frozen
 55   54   1   jmkmod4    src5       null     38.00        frozen
 56   55   1   jmkmod4    src6       null     45.00        frozen
 57   56   1   jmkmod4    srchk1     cm       0.           frozen
 58   57   1   jmkmod4    srchk2     null     4.3850E-03   frozen
 59   58   1   jmkmod4    srchk3     null     2.0000E-06   frozen
 60   59   1   jmkmod4    srchk4     null     1.0650E-04   frozen
 61   60   1   jmkmod4    srchk5     null     5.360        frozen
 62   61   1   jmkmod4    srchk6     null     0.           frozen
 63   62   1   jmkmod4    norm                2065.        +/-  15.07
 ------------------------------------------------------------------------
 ------------------------------------------------------------------------
Chi-Squared =          460.6877      using    461 PHA bins.
Reduced chi-squared = 1.005868       for    458 degrees of freedom
Null hypothesis probability = 0.456
XSPEC> ipl
XSPEC> ipl
XSPEC> quit
Do you really want to exit (y)y
XSPEC: quit
```

Figure 9.1: Sample `JMKmod` log file, obtained with the `show all` command in `XSPEC`

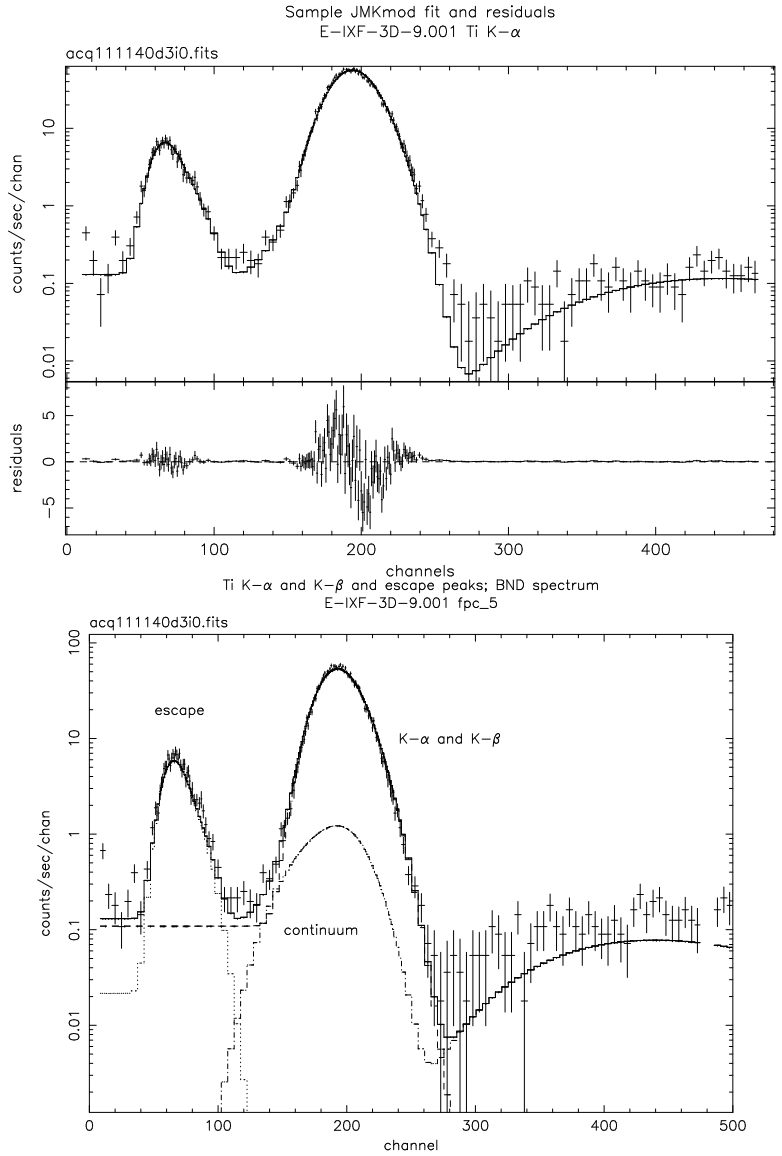

Figure 9.2: Sample `JMKmod` spectral fit to Ti K–α spectrum. Upper panel: data (+ signs), model (solid curve) and residuals in the same units as the upper plot. Lower panel: data and three model components. This shows that the continuum contributes $\sim 1\%$ to the counting rate in the main bump.

`JMKmod` version 7.0 software as it was released in December 1996.

We thus use not a single `JMKmod` component as a model, but two `JMKmod` components, with nearly all their parameters linked together (*i.e.* constrained to have the same value for both models). The exceptions are the `gain` (central section gain for model 1 and the middle of the top-hat function for model 2), `dgain` (the half-width of the top-hat function for model 2), and the normalizations of the two models. This permits excellent fits with small residuals and reduced χ^2 values. The line count rate is then the sum of the line norms for constituent lines of the complex (for example, K–α and K–β and their escape peaks), times the sum of the overall norms for the two `JMKmod` model components.

The recommended parameters for this type of model are these:

- $gain_1$ is the gain of the delta function center-section model.
- $gain_2 = gain_1 \times 1.05$. This is the central gain of the top-hat function gain distribution.
- $dgain_2 = gain_1 \times 0.1$. This is the full width of the top-hat function gain distribution.
- $norm_2 = norm_1 \times 0.7241$. This represents the relative wire length involved in each of the two gain distributions (delta function and top-hat).
- $sestype_1 = 1$ (delta-function gain distribution), and $sestype_2 = 3$ (top-hat gain distribution function).

9.5 Analysis of BESSY FPC Monochromator data

During the periods December 4–7, 1997 and January 20–23, 1998, two of the FPC detectors were calibrated at BESSY. During this time, a number of runs were done at various energies with the SX-700 monochromator, in the energy range from 0.08 to 1.7 keV. This monochromator beamline is well calibrated, and ring currents and x-ray intensities in photons per second per unit ring current are known to 0.5% at most energies.

We have analyzed these data using the `JMKmod` fit procedure outlined in §9.2, using as a model a delta-function line convolved with the `JMKmod` FPC response. In addition, it was necessary over the energy range from the carbon edge at 0.284 keV to about 0.300 keV to introduce a continuum to the fit, peaked sharply about 1 keV, due to a low level of leakage of photons near 1 keV through the monochromator. These are normally down 5 or more orders of magnitude relative to the main line, but in this particular energy range, the quantum efficiency of the detector at the main line is $\sim 10^{-5}$ or less, while around 1 keV the QE is ~ 0.7. In practice, we found it sufficient to model this extra component with another spectral line with energy near 1 keV and floating, and floating normalization relative to the main line.

The counter high voltage was set to correspond to a central energy for each scan, and then the monochromator was scanned through a number of energy settings, with the FPC at the same setting. We adjusted the gain parameter of the detector model in accordance with the standard FPC tuning practice, namely $gain \propto E_{target}^{-1/2}$ with a gain of 1 channel per ion pair (one ion pair is fixed at 28 eV in these fits) at about 4.5 keV. This was then allowed to float over a narrow range to compensate for possible temperature effects on the gain. The counting rate and these parameters are then fit.

We also allowed a few of the line shape parameters (Fano factor, and shelf norm) to vary. The Polya h parameter is set to its default value of 1.2. In practice the Fano factor and h have nearly indistinguishable effects on the line width and shape, and so only one of these two parameters was

allowed to vary. The resulting fitted Fano factor may not be physically reasonable, but the fits to the data closely match the observed line shape nonetheless.

Also freely varying was the pileup parameter, which is the fraction of the counts not involved in x-ray/x-ray pileup collisions. The line count rate is then divided by this parameter to reconstruct the total detected counting rate, including pileup effects. The pulser peak and higher pulse height channels were ignored, as were the first 8 channels, below the lower level discriminator. This analysis of the data produces results in general within 1% of the counting rates obtained by PTB from region of interest analysis of the pulse height spectra.

We present in Figure 9.3 and Figure 9.4 plots of the line shape parameters as functions of energy. Note the jump in the shelf norm occurs at the Ar L edge at 248 eV. This happens since the gas becomes much more opaque just hardward of this edge, and so the x-rays are converted to charge clouds closer to the window, resulting in more charge loss to the window than for softer photons.

Note also that the shelf is not well constrained by the data at very low energies (below about 0.2 keV) since the peak is at such low pulse height that most of the shelf is moved below the lower level discriminator.

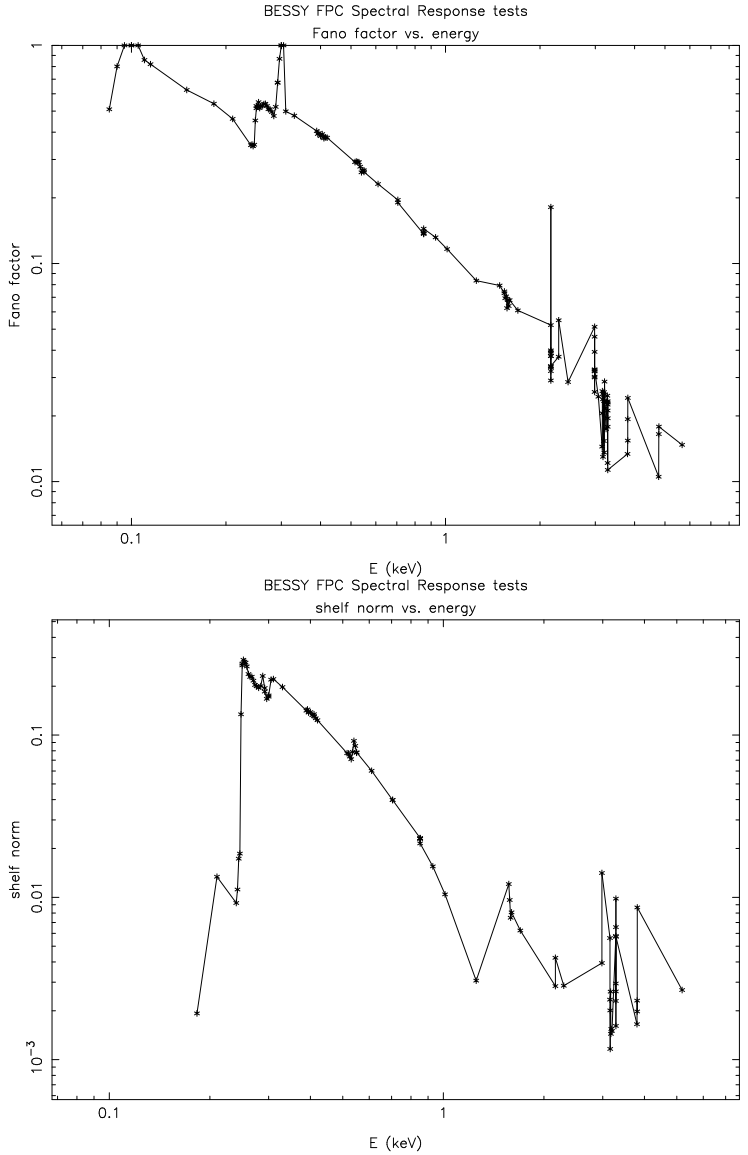

Figure 9.3: Line shape parameters for the fpc_x2 as functions of energy. Top: Fano factor, and Bottom: Shelf norm

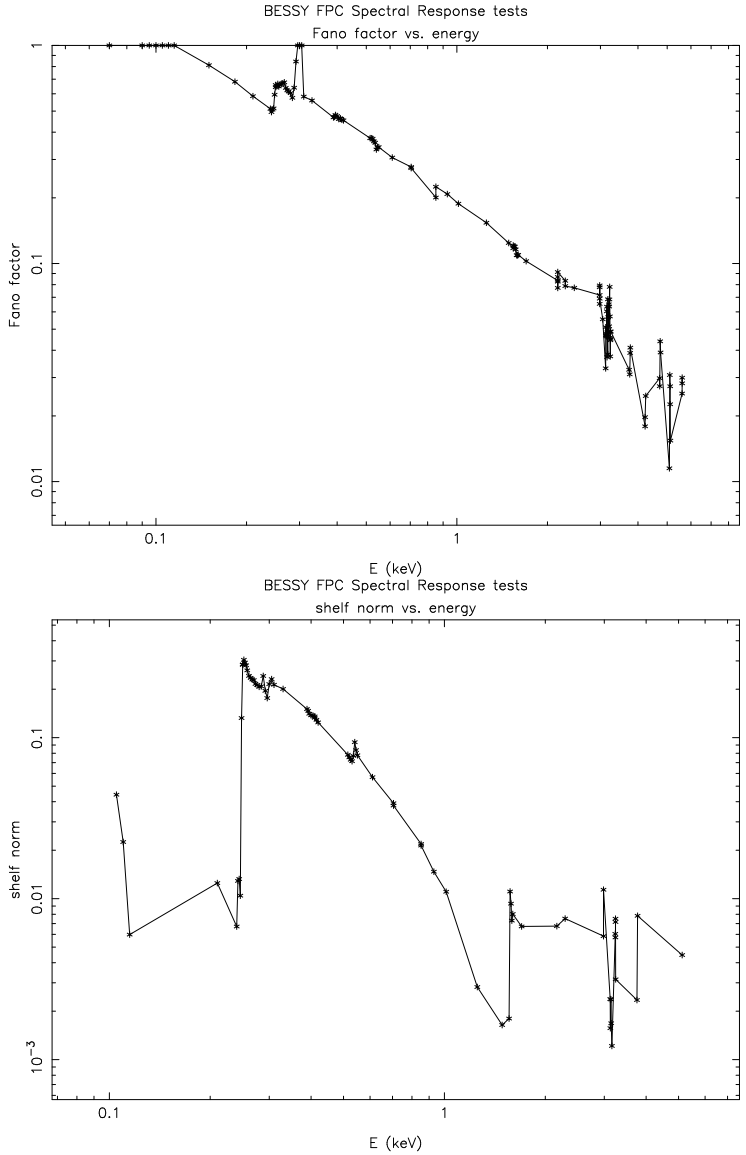

Figure 9.4: Line shape parameters for the fpc_hn as functions of energy. Top: Fano factor, and Bottom: Shelf norm

Chapter 10

Simulations

Diab Jerius

10.1 Introduction

Simulations of the HRMA are done by coupling raytraces of the optics with models of the support structure and detectors. The simulations are based as much as possible upon following individual rays from the source, through the HRMA, and to the detectors. In order to minimize the computational burden of these calculations, we model the probabilistic reflection of photons from the mirrors by assigning each photon a unit weight at the entrance aperture and multiplying it by the photon's reflection probability at each surface. Only the weights are used in the analysis of the simulations.

10.2 HRMA Model

The HRMA is composed of several components which are are not entirely separable. We have nonetheless attempted to do so, modelling it according to the following characteristics or systems:

- the geometric properties of the optics (i.e., their figure)
- the surface properties of the optics
- the HRMA baffles and support structure

10.2.1 Optics' Figure

The model of the optics can be thought of as comprising two basic elements: geometric prescriptions for the shape and positions of the optics, and the deviations from those prescriptions. Deviations from the ideal geometry can arise from a host of manufacturing errors (e.g., from current technical limitations in aligning or polishing optical elements) or can be the result of an operational configuration (the XRCF testing environment). Clearly the key to making a high fidelity model of the HRMA lies in accurately modeling the effect of these deviations on X-ray performance. To this end we have identified several classes of deviations:

1. Those which are actually measured and which result in exact geometric distortions of the imaging performance. Examples of such deviations include misalignments measured during the assembly process at EKC and maps of the low spatial frequency manufacturing errors of the optical surfaces from HDOS.
2. Deviations which are measured but which result in probabilistic distortions to the imaging performance. The main example here is the data from HDOS on high spatial frequency manufacturing errors in the form of the power spectral density (PSD) of irregularities on the optical surfaces. For this we use a statistical treatment of scattering from rough surfaces developed by L. Van Speybroeck.
3. Modeled deviations of essentially deterministic effects which result in exact geometric distortions of the imaging performance. Examples include finite element models (FEM) of thermally or gravitationally induced deviations of the optical surfaces.
4. Modeled deviations of non-deterministic effects which result in exact geometric distortions of the imaging performance. Examples include the FEM of manufacturing errors (essentially low frequency) induced on the optical surfaces during assembly of the HRMA in the alignment tower at EKC. These are non-deterministic since they arise from unmeasureable variations of otherwise controlled quantities. It is not clear at the present time how these will be included in the final HRMA model. In general it is expected, based on the error budgets, that these effects result in only modest performance degradations and thus it may be possible to include them, in the ensemble, as a small intrinsic Gaussian broadening of the image core.

Item 2 illustrates that descriptions of the optics' figure contain elements of the surface properties (i.e. roughness), and are thus not quite separable. We discuss the latter more completely in §10.2.3. The components which go into the description of the optics' geometric shape are:

- Geometric prescriptions of the optics, taking into account the actual end-cuts. These are derived from the "EK05lvs" prescription (Van Speybroeck, 1989a).
- HDOS surface deviation maps. These maps are spline fits to the low frequency deviations from the optics' geometric prescriptions, as measured by HDOS.
- Positions and orientations of the optics as determined from measurements in the HRMA Alignment Test System (HATS) during assembly, as well as measurements made at the XRCF (see Chapters 26, 27 and 30).
- Estimates of the second and third order Fourier-Legendre distortions from HATS data.
- Epoxy cure shrinkage effects for two weeks after pump-down.
- Distortions due to the HRMA's horizontal orientation in gravity, including the effects of the off-loading ground support equipment (GSE). These distortions are modelled via a high precision FEM of the optics and the HRMA support structure (HSS), with the optics in their nominal position and orientation. In a consistent treatment, the FEM would include the measured positions and orientations; we have assumed that the deviations from nominal are small enough to be treated as perturbations to the FEM.
- Modifications to the optics' cone-angles to give correct focal positions as determined from XRCF measurements (see Chapter 26).

10.2.2 Baffles and Support Structure

The HRMA support structures include the Central Aperture Plate (CAP) and the Mirror Support Sleeves (MSS), to which the optics are attached via flexures. The CAP, MSS, and flexures impart distortions to the optics, due to assembly strains and gravitational loading. These effects are modelled via the FEM described in §10.2.1. The CAP also serves as an optical obstruction due to its 12 struts. We model this separately, as thick, 100% opaque rectangular struts superimposed upon four open annuli. We do not separately model the CAP scrapers or cut-outs.

There are additional baffles in the system: the forward thermal pre-collimator, the P6 ghost baffle, and the aft thermal post-collimator. We treat these as obstructions; they are not included in the FEM model. These are modeled as a series of 100% opaque plates of zero thickness.

10.2.3 Mirror Surface

We divide our description of the optics' surface characteristics into the two components of reflection and scattering. Again, these are not perfectly separable.

Reflectivity

To confuse matters, this report contains results from simulations with two different models for the surface reflectivity. The simpler model describes the surface as a semi-infinite slab of iridium. The second, more realistic model, treats the surface as a multilayer consisting of layers of iridium and chromium on a semi-infinite base of Zerodur. In both cases we use iridium optical constants derived from the Henke data (Henke et al., 1993) below 2 keV, and from the data released by the MST Synchrotron group on 23 December 1996 for the 065 P6 witness coupon. Optical constants for the chromium and Zerodur are derived from Henke et al. (1993). In both approaches we have assumed a uniform, 100% bulk density of 22.39 $\mathrm{gm \cdot cm^{-3}}$ for iridium.

The multilayer treatment is similar to the approach layed out by Elsner and O'Dell (1991), but with a few wrinkles.

Surface Scattering

As mentioned above, we use a statistical description for the scattering of rays off of the optics due to surface microroughness. In the formulation we employ (outlined in some detail by Van Speybroeck (1989b)), an in-surface spatial wavelength $1/f$ diffracts (or scatters) light of a given wavelength λ through an angle θ according to the grating equation

$$\theta = f\,\frac{\lambda}{\sin\alpha}, \tag{10.1}$$

with α as the mean grazing angle of the surface. It is possible to relate (Beckmann & Spizzichino 1963) the normalized surface brightness $\psi(\theta)$ at scattering angle θ to the power spectral density (PSD) of surface irregularities $W_1(f)$ through

$$\psi(\theta) = \frac{16\pi W_1(f)}{f}\left(\frac{\sin\alpha}{\lambda}\right)^4. \tag{10.2}$$

We assume a particular form for the surface PSD and construct a look-up table which relates the amount of incident energy which is scattered to all angles in the focal plane. In general, this table would need to be two-dimensional, i.e., parameterized in terms of both the mean incident graze angle and wavelength of the radiation. However, Eqs. 10.1 and 10.2 reveal that the functional

dependence is one-dimensional, i.e., it depends only on the ratio of the sine of the grazing angle to the photon wavelength. We utilize this feature in our implementation of X-ray scatter since it has greatly reduced the complexity associated with building and interpolating the table in the raytrace software. The radii corresponding to 1% increments in the fractional encircled energy distribution are stored for each value of $\sin\alpha/\lambda$ in the table. A power-law extrapolation in the point spread function is used for radii beyond the 99% encircled energy value. During each invocation of a scattering event, a random number between 0 and 1 is selected and used to determine the appropriate radii for the 2 bracketing values of $\sin\alpha/\lambda$ from the table. The final scattering angle is obtained by interpolation between the bracketed values.

Surface micro-roughness scattering derived from high order HDOS surface map data (20 February 1997 distillation). **NOT REALLY! ??**

- a monochromatic point source at the XRCF distance of 527279 mm to the front side of the CAP.

One major deficiency of this model is that the X-ray source is modeled as a point source, rather than as an extended object. Since the source varied in size (up to $\sim 0.2''$), the simulations are uniformly "peakier" in the core than the measurements.

In comparisons to the measurements we make no attempt to model the detectors; instead we rely upon the spectral analysis to determine effective areas free of detector artifacts. All simulation results described in this document are derived from this model, unless otherwise noted.

The MST simulation is composed of the following components (which describe model `xrcf_SAO1G+HDOS_HDOS-scat-970220_03`):

- a monochromatic point source at the XRCF distance of 527279 mm to the front side of the CAP.
- Iridium optical constants derived from the Henke data (Henke et al., 1993) below 2 keV, and from the data released by the MST Synchrotron group on 23 December 1996 for the P6 flat.
- Rigid-body Optic positions and tilts as discussed in Chapters 26, 27 and 30.
- Mirror deformations:
  - Low order surface map data from HDOS.
  - Estimates of the 2nd and 3rd order distortions from HATS data.
  - Epoxy cure shrinkage effects for 2 weeks after pump-down.
  - Distortion due to horizontal orientation in 1g.
  - Modifications to cone-angle to give correct focal positions as determined from XRCF measurements (see Chapter 26).
- Surface micro-roughness scattering derived from high order HDOS surface map data (20 February 1997 distillation)
- Apertures, Collimators, Baffles (Central Aperture Plate (CAP), fore and aft structures, and P6 Ghost baffle) modeled as annuli with rectangular obstructing struts (where appropriate). All plates are 100% opaque, and are of zero thickness, except for the CAP, which is given the as-measured thickness

One major deficiency of this model is that the X-ray source is modeled as a point source, rather than as an extended object. Since the source varied in size (up to $\sim 0.2''$), the simulations are uniformly "peakier" in the core than the measurements.

In comparisons to the measurements we make no attempt to model the detectors; instead we rely upon the spectral analysis to determine effective areas free of detector artifacts. All simulation results described in this document are derived from this model, unless otherwise noted.

Chapter 11

HRMA Effective Area: SSD C-continuum Measurements

Ping Zhao

11.1 Introduction

During the calibration, the HRMA on-axis effective area was measured in two different ways in terms of the X-ray source characteristics: the discrete line measurements and the carbon-continuum (C-continuum) measurements. The former uses characteristic X-ray lines generated by an Electron Impact Point Source (EIPS) with various anodes. The latter uses continuum X-ray radiation generated by EIPS with a carbon anode at 15 kV and using a beryllium (Be) filter to attenuate the lowest energies including the C-Kα line (0.277 keV). A preliminary result of this measurement was reported in SPIE '98 (Kolodziejczak et al., 1997).

For the X-ray line measurements, both Flow Proportional Counter (FPC) and Solid State Detector (SSD) were used. For the FPC, 4 energy lines (C-Kα: 0.277 keV; Al-Kα: 1.486 keV; Ti-Kα: 4.51 keV; Fe-Kα: 6.40 keV) were used for four individual shells effective area measurements, and 3 energy lines (Cu-Lα: 0.9297 keV; Cr-Kα: 5.41 keV; Cu-Kα: 8.03 keV) were used for the HRMA (all four shells open) effective area measurements. Several other energy lines were used for the HRMA or MEG (Shells 1 and 3 open) or HEG (Shells 4 and 6 open) configurations and with 1 mm and 0.5 mm apertures only. For the SSD, 3 energy lines (Nb-Lα: 2.16 keV; Ag-Lα: 2.98 keV; Sn-Lα: 3.44 keV) were used for the HRMA (all four shells open) effective area measurements. Four energy lines (Al-Kα: 1.486 keV; Ag-Lα: 2.98 keV; Fe-Kα: 6.40 keV; Cu-Kα: 8.03 keV) were used for the MEG and HEG configurations and with 0.5 mm aperture only. No SSD measurements were made for the effective area of individual shells.

For the continuum measurements, only SSD was used, and only the effective area of each individual shell were measured. The effective area was measured for each individual mirror shell by comparing the spectrum detected by ssd_x (SSD at the HRMA focal plane) with the spectrum detected simultaneously by ssd_5 (SSD in Building 500 of the XRCF, to one side of the X-ray beam). The continuum measurements have the advantage of providing the effective area data for nearly the entire AXAF energy band, but the data analysis and results evaluation need careful attention. Factors such as SSD response, pileup correction, energy scale, deadtime correction, quantum efficiency, background, icing effect, *etc.*, need to be carefully evaluated.

This Chapter discusses the data analysis and HRMA effective area measured using the C-continuum source and solid state detectors. The results are compared with the X-ray line measurements and with the HRMA raytracing models. The comparison are used to make an on-orbit HRMA effective area prediction.

11.2 SSD C-continuum Effective Area Measurements

The effective area measurements with the C-continuum Source were made with two nearly identical high-purity-germanium solid state detectors: one (ssd_5) is a beam-normalization-detector (BND) located at 38.199 meters from the source in Building 500, another one (ssd_x) is the focal plane detector located at the HRMA focus, 537.778 meters from the source. An aperture wheel was mounted in front of each SSD. The HRMA effective area was measured with a 2 mm diameter aperture in front of the ssd_5 and apertures with various sizes in front of the ssd_x.

Table 11.1 lists all the on-axis effective area measurements with the C-continuum source and SSD detectors. The measurements were made for each of the four HRMA shells. No measurement was made when all four shells were open. Apertures ranging from 0.015 mm to 2 mm diameters were used in front of the ssd_x for the measurements. In several measurements of shell 3 (runids 108447–108456), the ssd_5 was inadvertently turned off. For one measurement of shell 4 (runid 108478), the ssd_x was tripped off. Most of the measurements were made in Phase-D on 970112-970113 (Date notation for 12-13 Jan 1997), with various apertures on ssd_x and 300-second integrations. One set of measurements was made in Phase-E on 970130 with only the 2 mm aperture on ssd_x and 1000-second integrations.

Table 11.2 lists all the off-axis effective area measurements with C-continuum source and SSD detectors. These measurements were made in Phase-E on 970131 with apertures ranging from 0.04 mm to 2 mm diameters, 300-second integrations, and off-axis angles of $5'$, $10'$, $15'$, $20'$, $25'$, and $30'$.

For the on-axis effective area, measurements with the TRW IDs E-IXS-MC-15.001,2,3,4 (Run ID: 110539, 110540, 110541, 110542) had the longest integration time and the largest apertures. In this Chapter we use this set of data to demonstrate the data reduction and to make the HRMA effective area predictions from this result. All other sets of data can be processed the same way.

Figures 11.1–11.4 show the ssd_x and ssd_5 spectra of this set of measurements. The profiles show the C-continuum spectra with several spectral peaks on top. The largest Gaussian-like peak at around channels 2400–2500 is the injected pulser spectrum to be used for the pileup and deadtime corrections (see §11.3 and §11.6). Other peaks are characteristic X-ray lines due to contaminations to the carbon anode. These peaks will be used to determine the energy scale (see §11.5).

The are many factors need to be considered during the data analysis process, such as the pileup correction, deadtime correction, X-ray beam uniformity, SSD quantum efficiency, SSD energy scale, SSD background, SSD icing effect, etc. We will explain each of these effect in the following sections while we go through the data processing procedure.

11.3 Pileup Correction

Before analyzing the SSD spectra, the first thing to do is to make the pileup correction. Pileups are when more than one photon enter the detector within a small time window (a few μsec). Instead of recording each photon event, the detector registers only one event with the summed energy of all photons. The pileup can also occur for a real photon with a pulser event. The SSD has pileup rejection electronics to reduce the pileup. However, the rejection does not work well if one of the

Table 11.1: HRMA On-axis Effective Area Measurenents
Source: C-continuum Detector: SSD

TRW ID	Run ID	Date	Shell	Aper (μm)	Int (sec)	Note
D−IXS−EE−1.001	108425	970112	1	500	300	
D−IXS−EE−1.001	108426	970112	1	2000	300	
D−IXS−EE−1.001	108428	970112	1	70	300	
D−IXS−EE−1.001	108430	970112	1	50	300	
D−IXS−EE−1.001	108432	970112	1	40	300	
D−IXS−EE−1.001	108434	970112	1	30	300	
D−IXS−EE−1.001	108438	970112	1	20	300	
D−IXS−EE−1.001	108441	970112	1	15	300	
D−IXS−EE−1.002	108444	970113	3	100	300	
D−IXS−EE−1.002	108447	970113	3	200	300	SSD-500 off
D−IXS−EE−1.002	108449	970113	3	500	300	SSD-500 off
D−IXS−EE−1.002	108450	970113	3	2000	300	SSD-500 off
D−IXS−EE−1.002	108452	970113	3	70	300	SSD-500 off
D−IXS−EE−1.002	108454	970113	3	50	10	SSD-500 off
D−IXS−EE−1.002	108455	970113	3	50	10	SSD-500 off
D−IXS−EE−1.002	108456	970113	3	50	10	SSD-500 off
D−IXS−EE−1.002	108457	970113	3	50	1500	
D−IXS−EE−1.002	108460	970113	3	50	300	
D−IXS−EE−1.002	108462	970113	3	40	300	
D−IXS−EE−1.002	108464	970113	3	30	300	
D−IXS−EE−1.002	108467	970113	3	20	300	
D−IXS−EE−1.003	108473	970113	4	100	300	
D−IXS−EE−1.003	108475	970113	4	200	300	
D−IXS−EE−1.003	108478	970113	4	500	300	SSD-X off
D−IXS−EE−1.003	108484	970113	4	2000	300	
D−IXS−EE−1.003	108486	970113	4	70	300	
D−IXS−EE−1.003	108488	970113	4	50	300	
D−IXS−EE−1.003	108490	970113	4	40	300	
D−IXS−EE−1.003	108492	970113	4	30	300	
D−IXS−EE−1.003	108494	970113	4	20	300	
D−IXS−EE−1.004	108496	970113	6	100	300	
D−IXS−EE−1.004	108498	970113	6	200	300	
D−IXS−EE−1.004	108499	970113	6	500	300	
D−IXS−EE−1.004	108500	970113	6	2000	300	
D−IXS−EE−1.004	108502	970113	6	70	300	
D−IXS−EE−1.004	108504	970113	6	50	300	
D−IXS−EE−1.004	108506	970113	6	40	300	
D−IXS−EE−1.004	108508	970113	6	30	300	
E−IXS−MC−15.001	110539	970130	1	2000	1000	
E−IXS−MC−15.002	110540	970130	3	2000	1000	
E−IXS−MC−15.003	110541	970130	4	2000	1000	
E−IXS−MC−15.004	110542	970130	6	2000	1000	

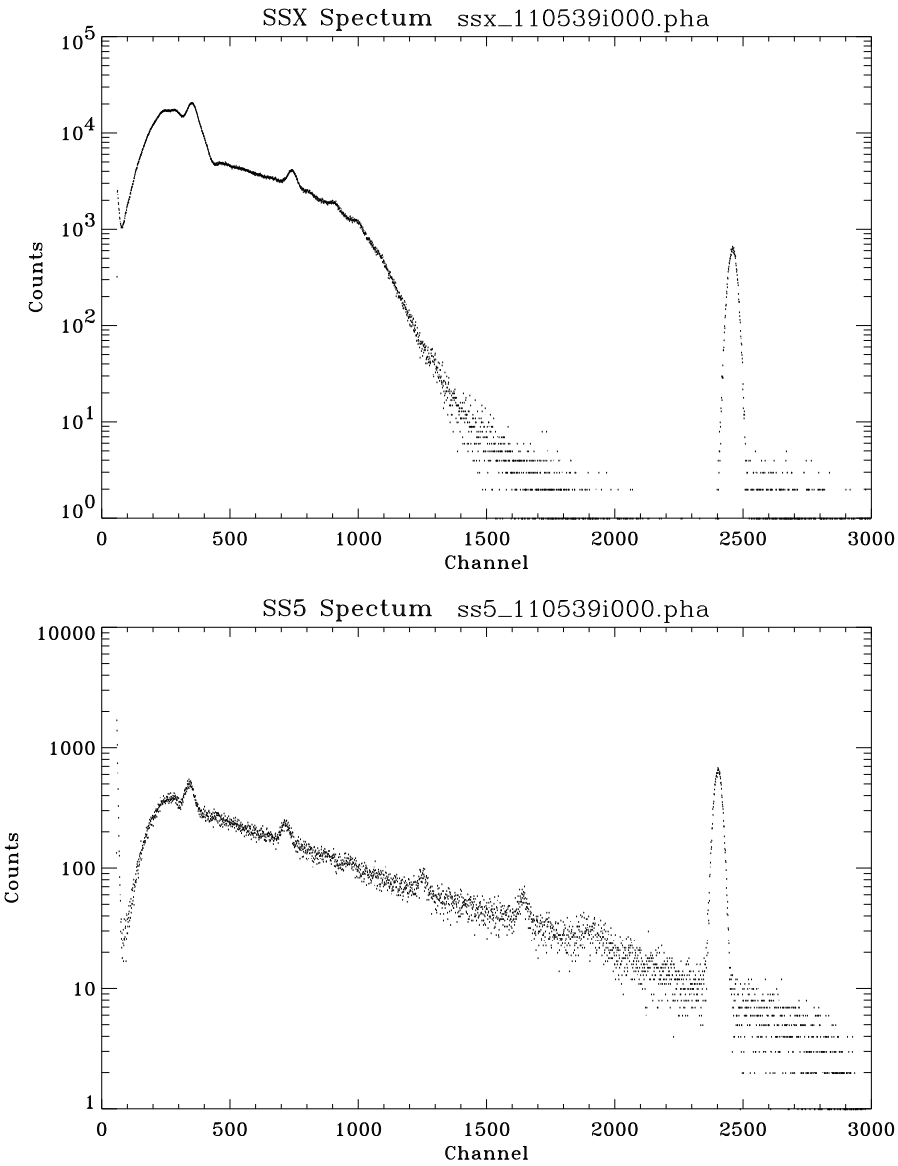

Figure 11.1: C-continuum SSX (focal plane) and SS5 (beam normalization) spectra: Shell 1; Date: 970130; TRW ID: E−IXS−MC−15.001; Run ID: 110539; Aperture: 2 mm; Integration time: 1000 seconds. The Gaussian-like peak at around channels 2400–2500 is due to the electronic pulser.

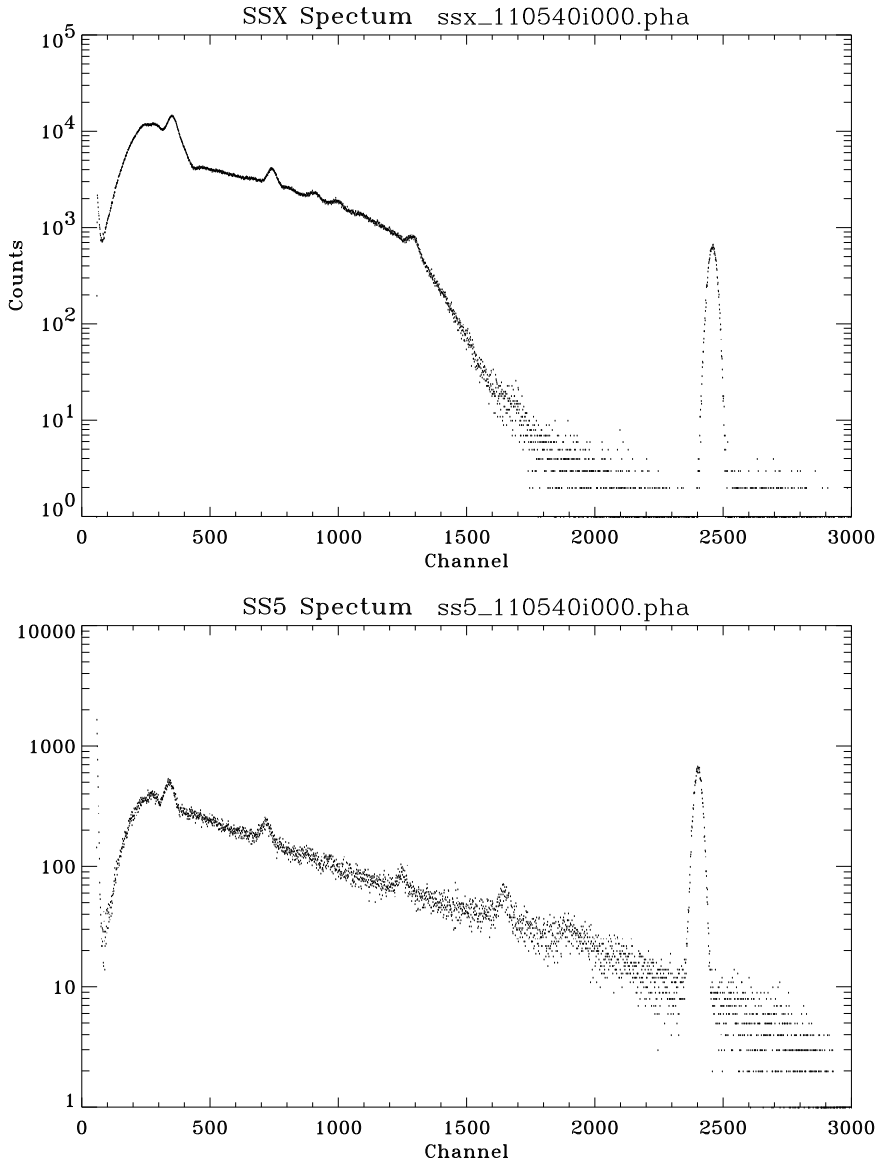

Figure 11.2: C-continuum SSX and SS5 spectra: Shell 3; Date: 970130; TRW ID: E−IXS−MC−15.002; Run ID: 110540; Aperture: 2 mm; Integration time: 1000 seconds.

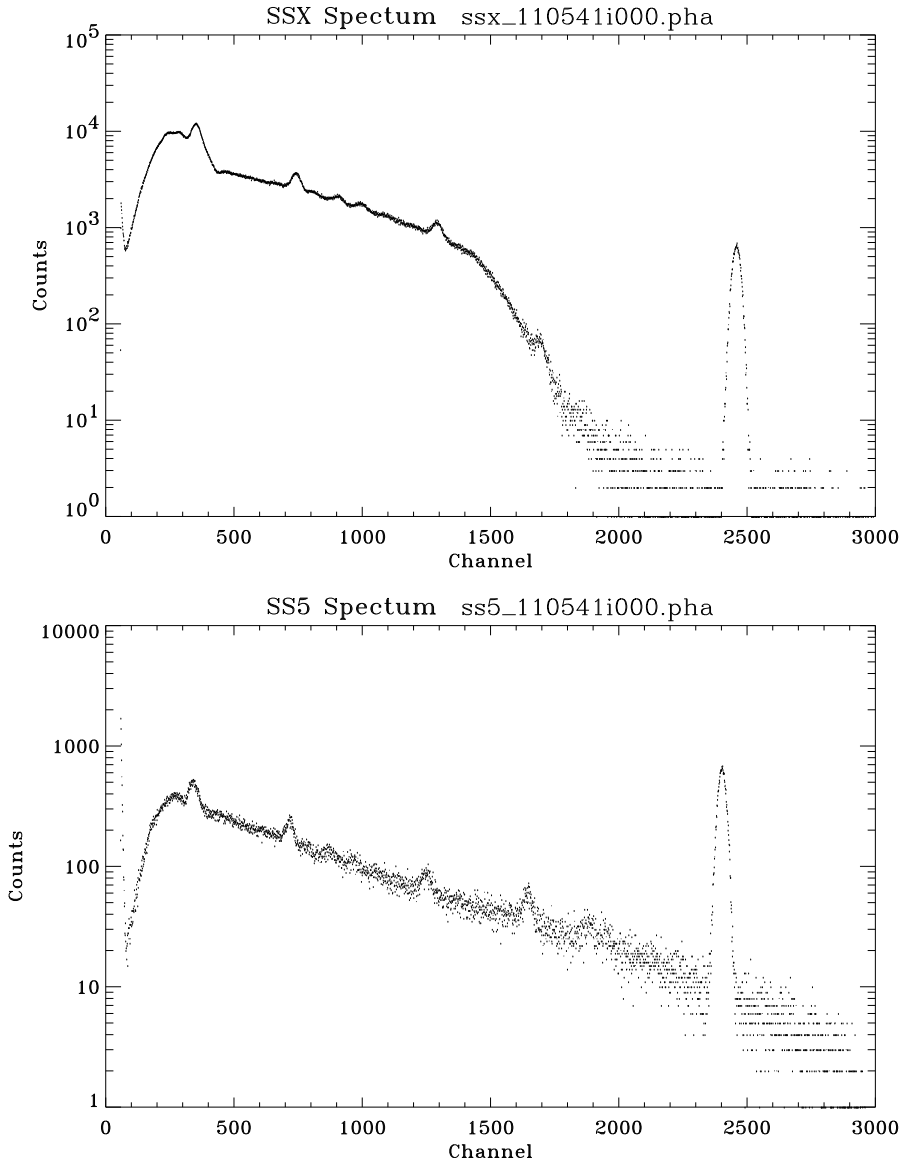

Figure 11.3: C-continuum SSX and SS5 spectra: Shell 4; Date: 970130; TRW ID: E−IXS−MC−15.003; Run ID: 110541; Aperture: 2 mm; Integration time: 1000 seconds.

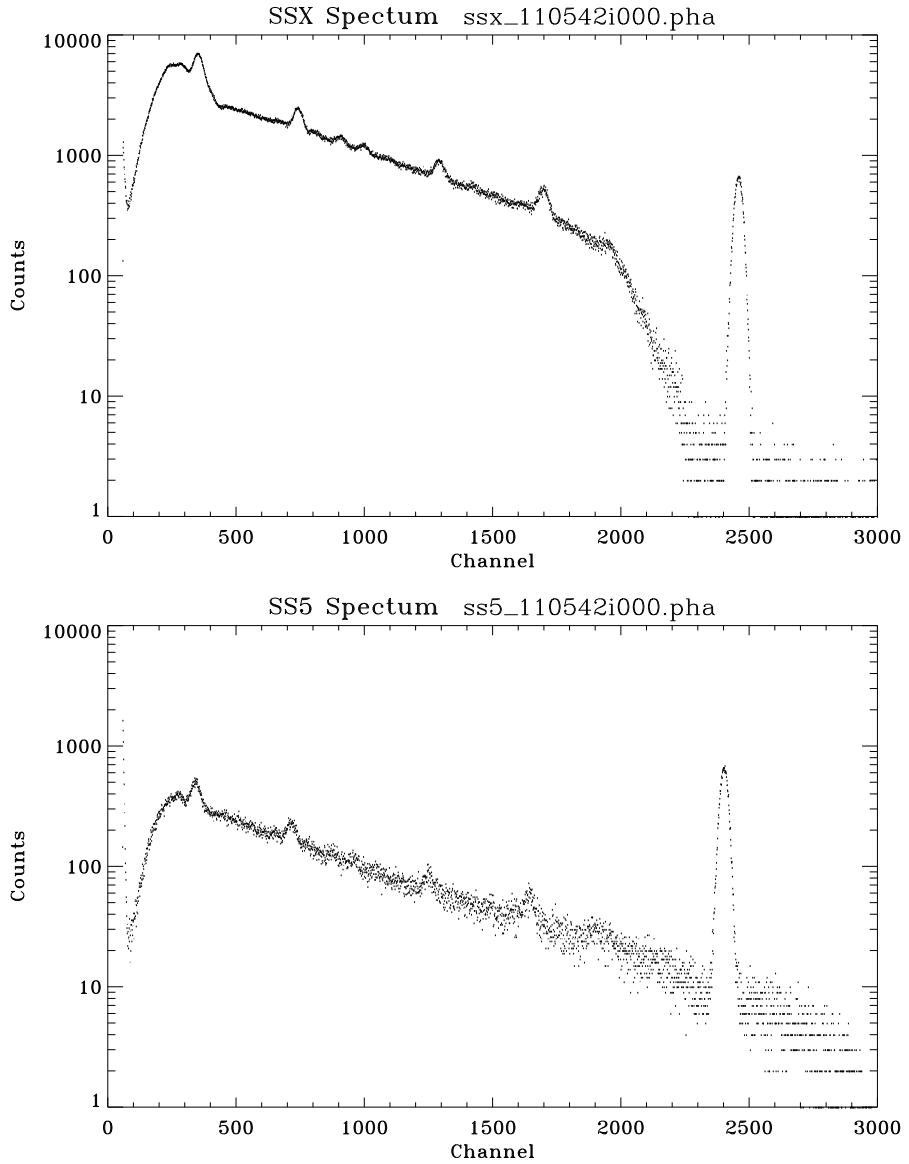

Figure 11.4: C-continuum SSX and SS5 spectra: Shell 6; Date: 970130; TRW ID: E−IXS−MC−15.004; Run ID: 110542; Aperture: 2 mm; Integration time: 1000 seconds.

Table 11.2: HRMA Off-axis Effective Area Measurenents
Date: 970131 Source: C-continuum Detector: SSD

TRW ID	Run ID	Shell	Aper (μm)	Int (sec)	Pitch (arcmin)	Yaw (arcmin)	Off-axis (arcmin)
E−IXS−EE−5.001	110718	HRMA	200	300	−3.53553	3.53553	5
E−IXS−EE−5.001	110719	HRMA	500	300	−3.53553	3.53553	5
E−IXS−EE−5.001	110720	HRMA	500	300	−3.53553	3.53553	5
E−IXS−EE−5.001	110721	HRMA	2000	300	−3.53553	3.53553	5
E−IXS−EE−5.001	110723	HRMA	100	300	−3.53553	3.53553	5
E−IXS−EE−5.001	110725	HRMA	70	300	−3.53553	3.53553	5
E−IXS−EE−5.001	110727	HRMA	50	300	−3.53553	3.53553	5
E−IXS−EE−5.001	110732	HRMA	40	300	−3.53553	3.53553	5
E−IXS−EE−5.004	110733	HRMA	500	300	0	−10	10
E−IXS−EE−5.004	110734	HRMA	2000	300	0	−10	10
E−IXS−EE−5.004	110736	HRMA	200	300	0	−10	10
E−IXS−EE−5.004	110738	HRMA	100	300	0	−10	10
E−IXS−EE−5.004	110740	HRMA	70	300	0	−10	10
E−IXS−EE−5.004	110742	HRMA	50	300	0	−10	10
E−IXS−EE−5.004	110745	HRMA	40	300	0	−10	10
E−IXS−EE−5.005	110749	HRMA	2000	300	−10.6066	10.6066	15
E−IXS−EE−5.005	110751	HRMA	500	300	−10.6066	10.6066	15
E−IXS−EE−5.005	110754	HRMA	200	300	−10.6066	10.6066	15
E−IXS−EE−5.005	110756	HRMA	100	300	−10.6066	10.6066	15
E−IXS−EE−5.005	110759	HRMA	70	300	−10.6066	10.6066	15
E−IXS−EE−5.007	110760	HRMA	2000	300	−14.1421	14.1421	20
E−IXS−EE−5.007	110761	HRMA	500	300	−14.1421	14.1421	20
E−IXS−EE−5.007	110764	HRMA	200	300	−14.1421	14.1421	20
E−IXS−EE−5.009	110766	HRMA	2000	300	−17.6777	17.6777	25
E−IXS−EE−5.010	110768	HRMA	2000	300	−21.2132	21.2132	30

photons has energy below 2 keV, corresponding to a pre-amplifier output signal of 4 mV. Thus each spectrum needs to be corrected for pileups of any photon with a low energy ($<$ 2 keV) photon. Since three or more photon pileups are extremely rare events and their effect is negligible, we only consider two photon pileups.

Figures 11.5–11.8 show the pulser spectra of both ssd_x (top panels) and ssd_5 (bottom panels) for the four measurements. In the ssd_x pulser spectra for shell 1 and 3 (Figures 11.5and11.6), the pulser pileups are clearly shown to the right of the pulser peak. In the ssd_x pulser spectra for shell 4 and 6 (Figures 11.7and11.8), the pulser pileups are mixed with the continuum pileups to the right of the pulser peak. There is no direct continuum spectrum above channel ∼2240 (∼11 keV) in ssd_x since the HRMA has null reflectivity above ∼11 keV. In the ssd_5 pulser spectra, the continuum dominates the right side of the pulser peak; the pileup effects are very small since they are proportional to the counting rate. The total continuum counting rates in ssd_5 are 1–2 orders of magnitude lower than that of ssd_x (see Figures 11.1–11.4).

We use the ssd_x pulser spectra for shell 1 and 3 (Run ID 110539 and 110540), where the pulser

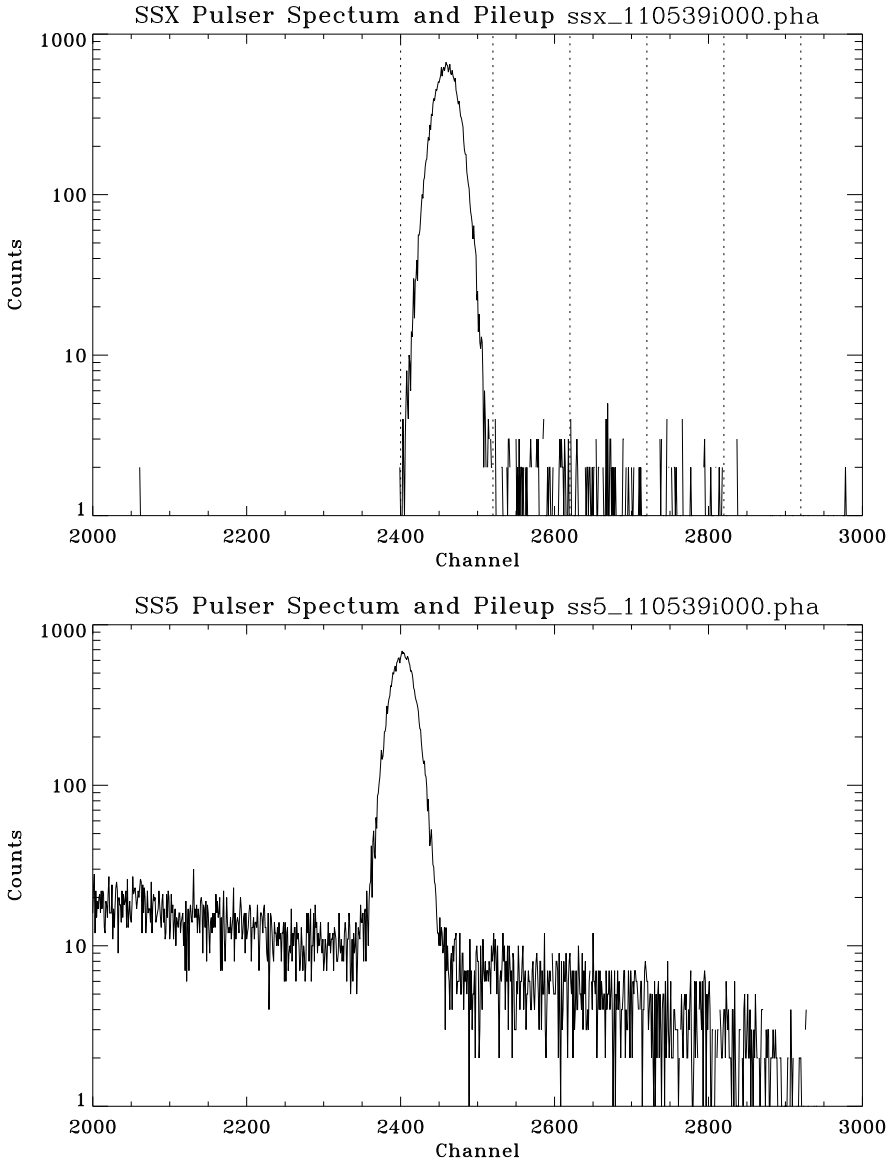

Figure 11.5: SSX and SS5 pulser spectra: Shell 1; Run ID: 110539. Counts to the right of the SSX pulser peak are the pileups from the pulser and low energy photons. Dotted vertical lines in the upper panel indicate the pulser region and four pileup bands.

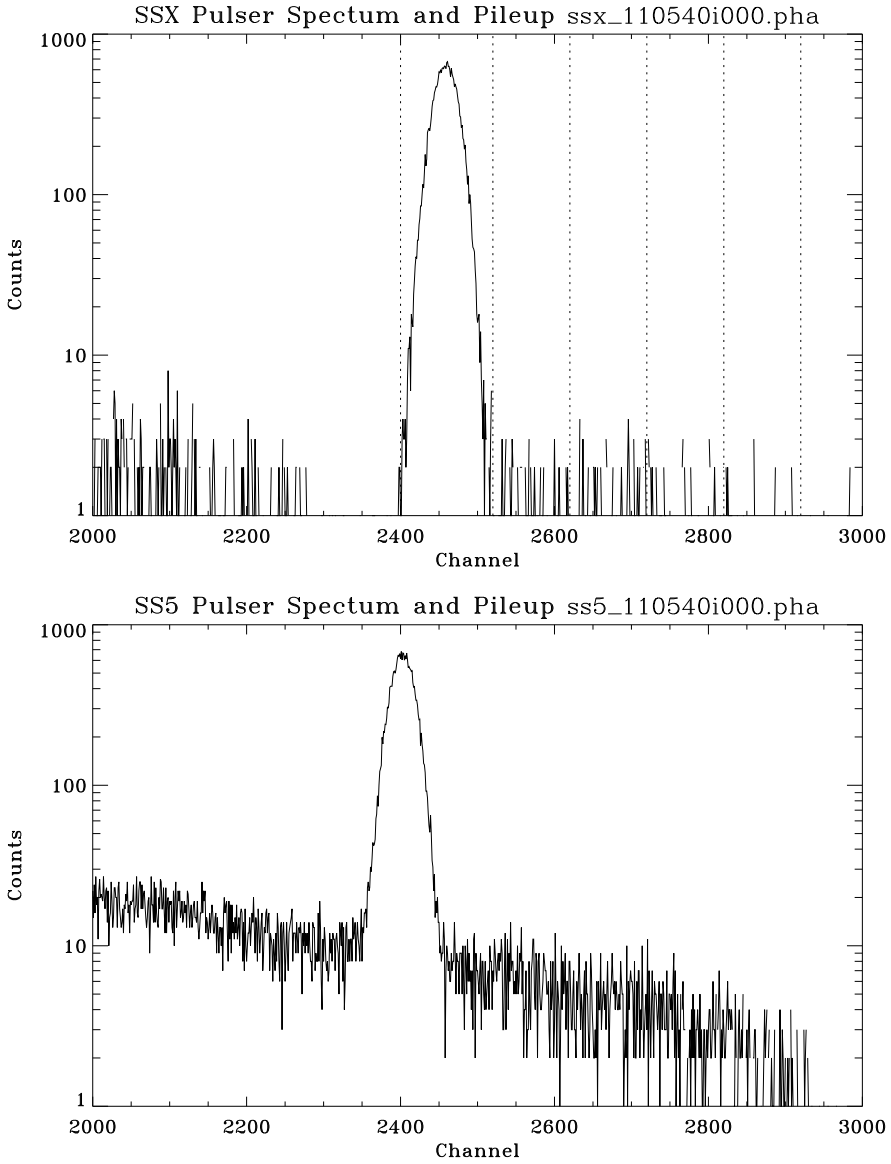

Figure 11.6: SSX and SS5 pulser spectra: Shell 3; Run ID: 110540. Counts to the right of the SSX pulser peak are the pileups from the pulser and low energy photons. Dotted vertical lines in the upper panel indicate the pulser region and four pileup bands.

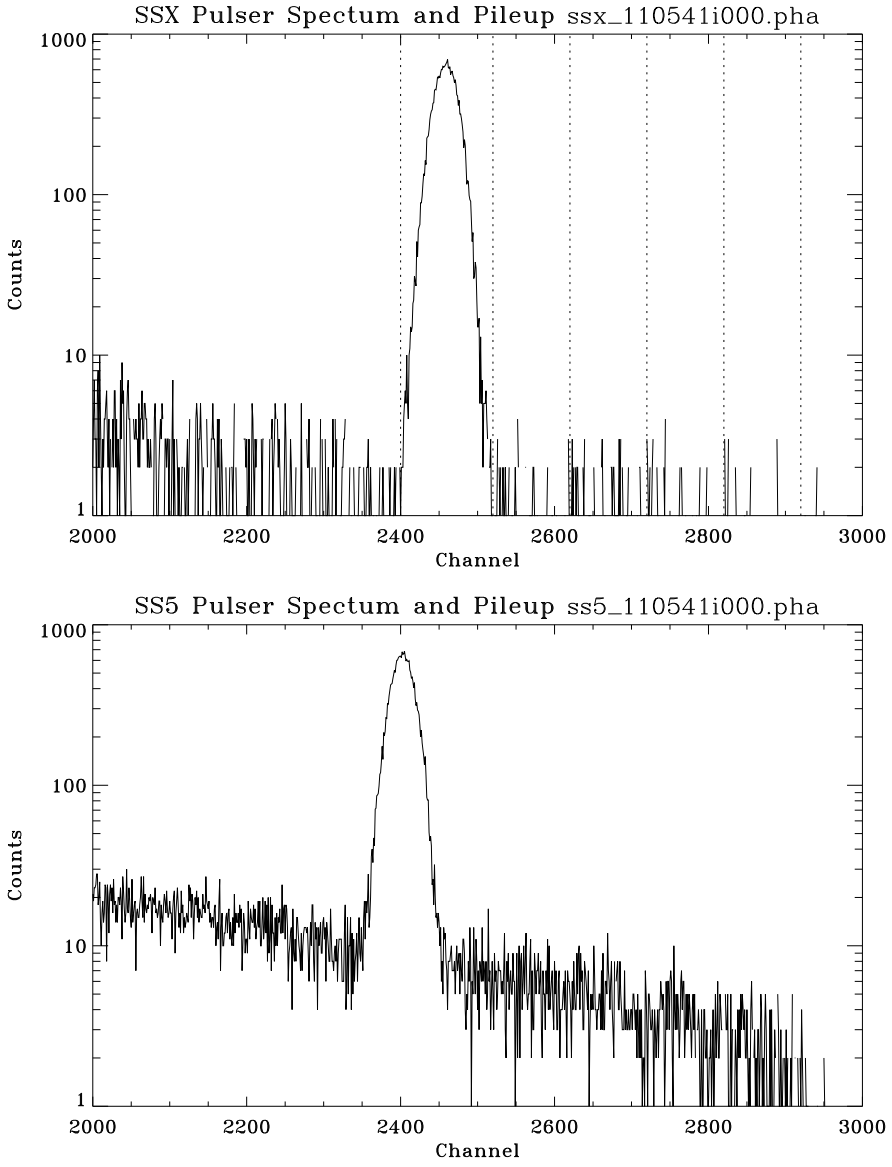

Figure 11.7: SSX and SS5 pulser spectra: Shell 4; Run ID: 110541. Counts to the right of the SSX pulser peak are mainly due to pileups from the pulser, a small amount are due to pileups from the continuum.

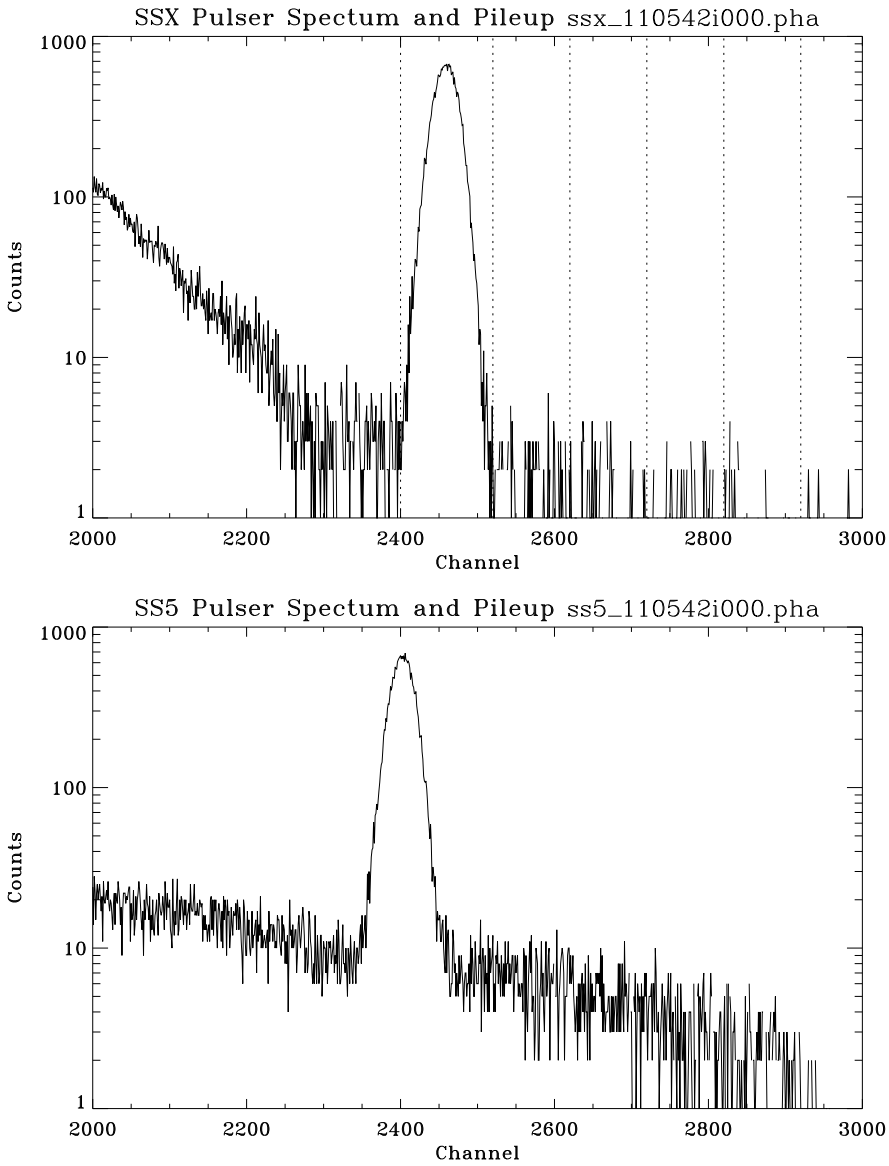

Figure 11.8: SSX and SS5 pulser spectra: Shell 6; Run ID: 110542. Counts to the right of the SSX pulser peak are mixtures of the pulser pileups and the continuum pileups.

pileup effects are clear and not mixed with the continuum pileups, to establish an empirical model for the pileup correction. In ssd_x pulser spectra shown in Figures 11.5–11.8, there are six vertical dotted lines dividing the spectra into 5 bands. The first one on the left covers the pulser peak. The other four bands, with 100 channels per band, cover the pileup region. Since 2 keV $\approx$ 400 channels, counts in these regions are pileups of low energy photons ($<$ 2 keV) with the pulser. Since the pileups are proportional to counting rate of photons $<$ 2 keV, we define a pileup rate as the pulser pileup fraction (pulser pileup counts divided by the total pulser counts) divided by the counting rate within channels 0–400. Both ssd_x spectra give, as it should be, about the same results: for the four 100-channel windows after the pulser, the pileup rates are 1.2×10^{-6} sec/count in channels 1–100, 1.0×10^{-6} sec/count in channels 101–200, 0.7×10^{-6} sec/count in channels 201–300, and 0.3×10^{-6} sec/count in channels 301-400. Notice that here the unit for pileup rate is "second/count". When calculating the pileup fraction, we need to multiply these pileup rates by the counting rate within channels 0–400. For example, for ssd_x spectrum 110539, CR(0–400) = 4448 counts/second, pileup fractions are 0.005337, 0.004448, 0.003114, 0.001334 in the four windows; for ssd_x spectrum 110542, CR(0–400) = 1415 counts/second, pileup fractions are 0.001698, 0.001415, 0.000990, 0.000424. Meantime, for all the ssd_5 spectra, CR(0–400) = 100, so the pileup fractions are 0.000120, 0.000100, 0.000070, 0.000030, which are negligible.

In each channel of the raw spectra, there are real events at that energy plus some pileup events which come from lower channels. Meanwhile, some of the real events at that energy were piled up to higher channels following the above empirical model. To make the pileup correction, we need to subtract pileup fractions from each channel and put them back where they belong, and remember each pileup photon came from two lower energy photons. These were done as follows: first multiply the CR(0-400) by the pileup rates given above to obtain the pileup fractions for that spectrum; for each channel N, we add the pileup fractions of channel N back to channel N, subtract one percent of pileup fractions of channel N from each channel N + X (X = 1–400), and also add the same number to channel X; then just step along for the entire spectrum.

Figures 11.9–11.12 show the ssd_x pileup corrections. In the top panels, the dots are the raw data, the solid line show the pileup corrected data. It is seen that when the spectra have sharp declines, the pileup corrections make the spectra even lower. The bottom panels show the ratio of the pileup corrected data vs. the raw data.

Figures 11.13–11.16 show the ssd_5 pileup corrections. Since the counting rates are very low, the pileup effects are negligible. The ratios between the pileup corrected data vs. the raw data are nearly unity between channel 400 and the pulser peak (notice the vertical scale difference comparing to the bottom panels of Figures 11.9–11.12).

The dashed vertical lines in the top panels of Figures 11.9–11.16 indicate the position of six selected X-ray characteristic lines to be used to determine the energy scale of the spectra (see §11.5 and §11.11).

After the pileup correction and before reducing the effective area, we need to know the relative quantum efficiency of the two SSD detectors.

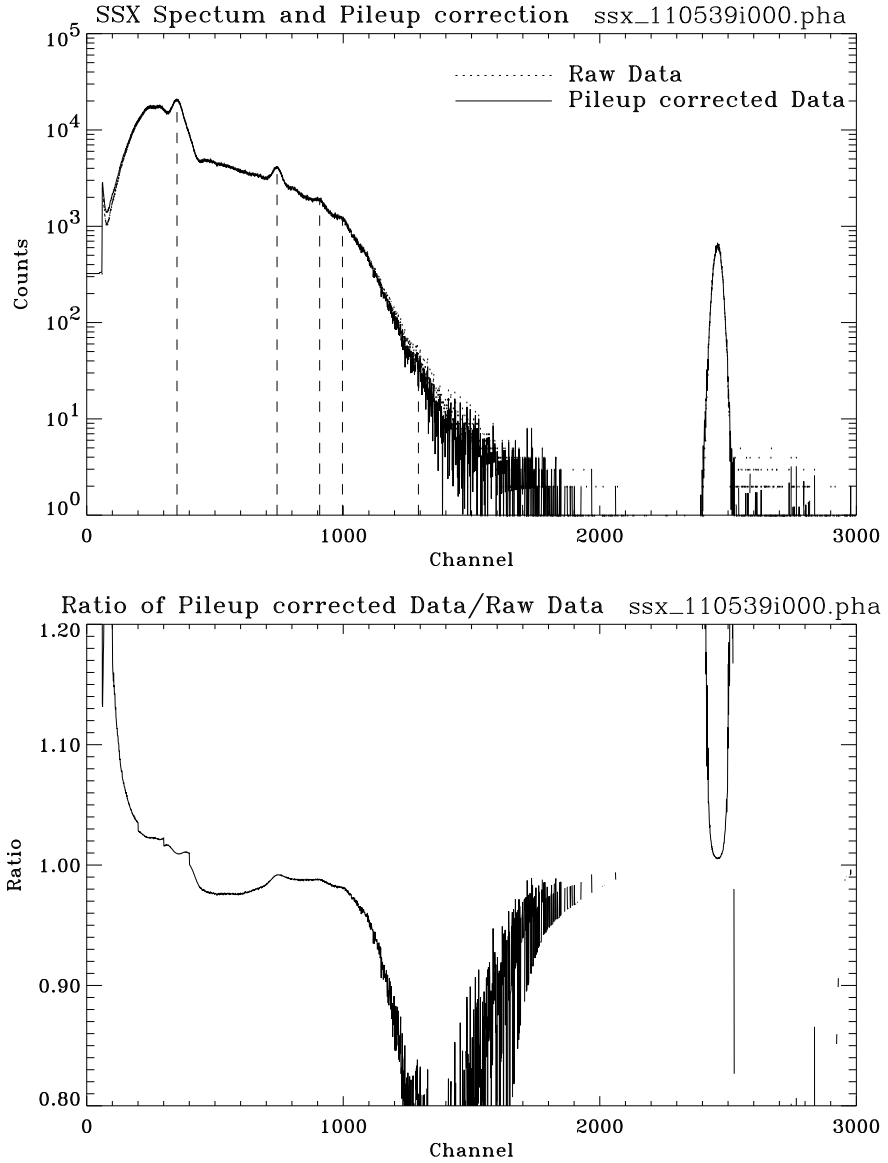

Figure 11.9: SSX spectrum and pileup correction: Shell 1; Run ID: 110539. Upper panel shows the raw data and pileup corrected data. Dashed vertical lines indicate the X-ray lines to be used to calibrate the energy scale. Lower panel shows the ratio of pileup corrected data to the raw data.

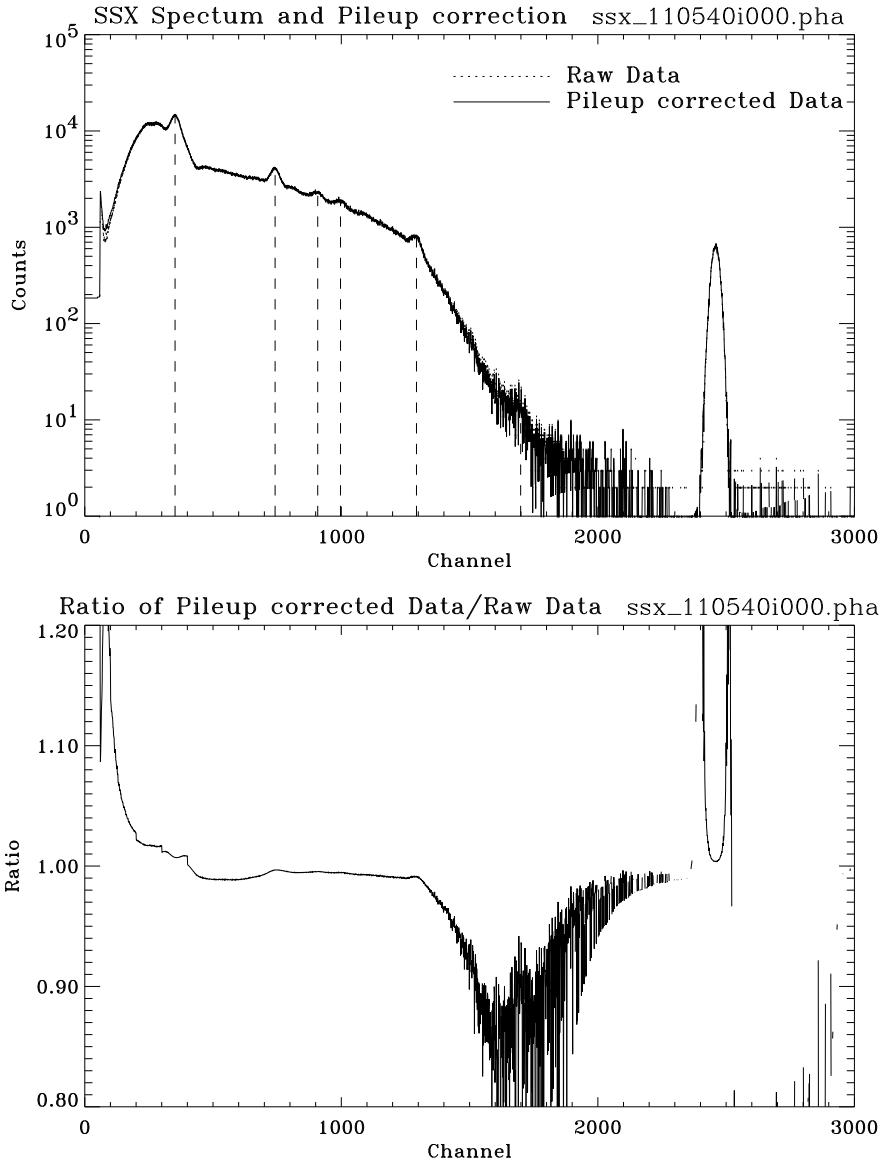

Figure 11.10: SSX spectrum and pileup correction: Shell 3; Run ID: 110540. Upper panel shows the raw data and pileup corrected data. Dashed vertical lines indicate the X-ray lines to be used to calibrate the energy scale. Lower panel shows the ratio of pileup corrected data to the raw data.

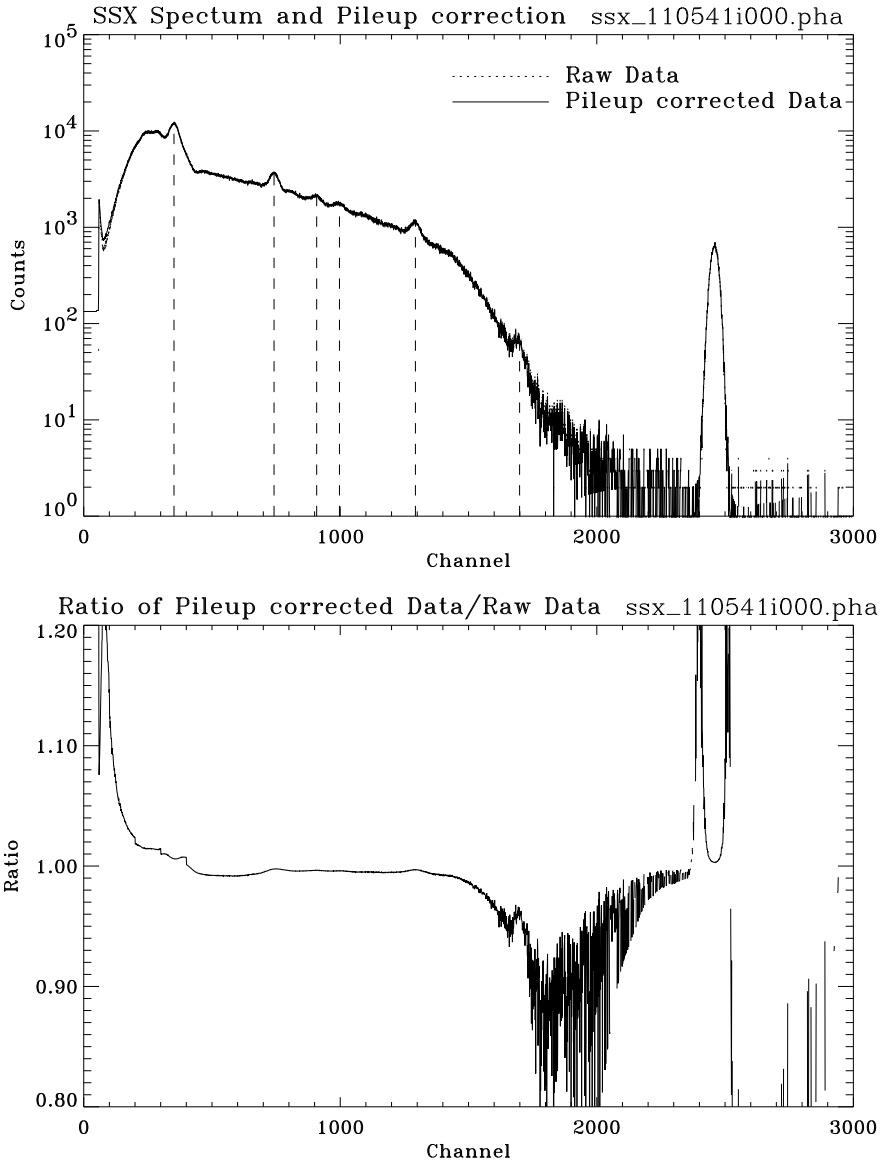

Figure 11.11: SSX spectrum and pileup correction: Shell 4; Run ID: 110541. Upper panel shows the raw data and pileup corrected data. Dashed vertical lines indicate the X-ray lines to be used to calibrate the energy scale. Lower panel shows the ratio of pileup corrected data to the raw data.

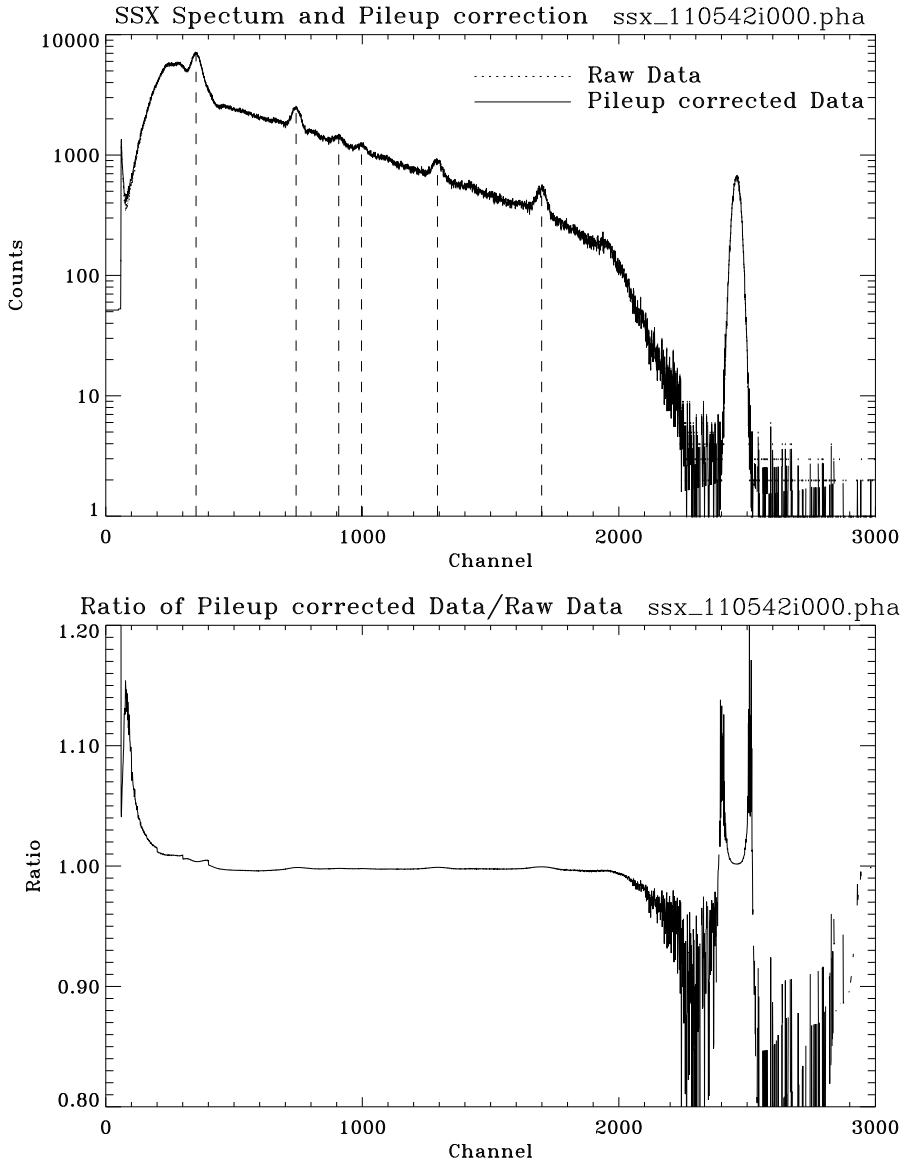

Figure 11.12: SSX spectrum and pileup correction: Shell 6; Run ID: 110542. Upper panel shows the raw data and pileup corrected data. Dashed vertical lines indicate the X-ray lines to be used to calibrate the energy scale. Lower panel shows the ratio of pileup corrected data to the raw data.

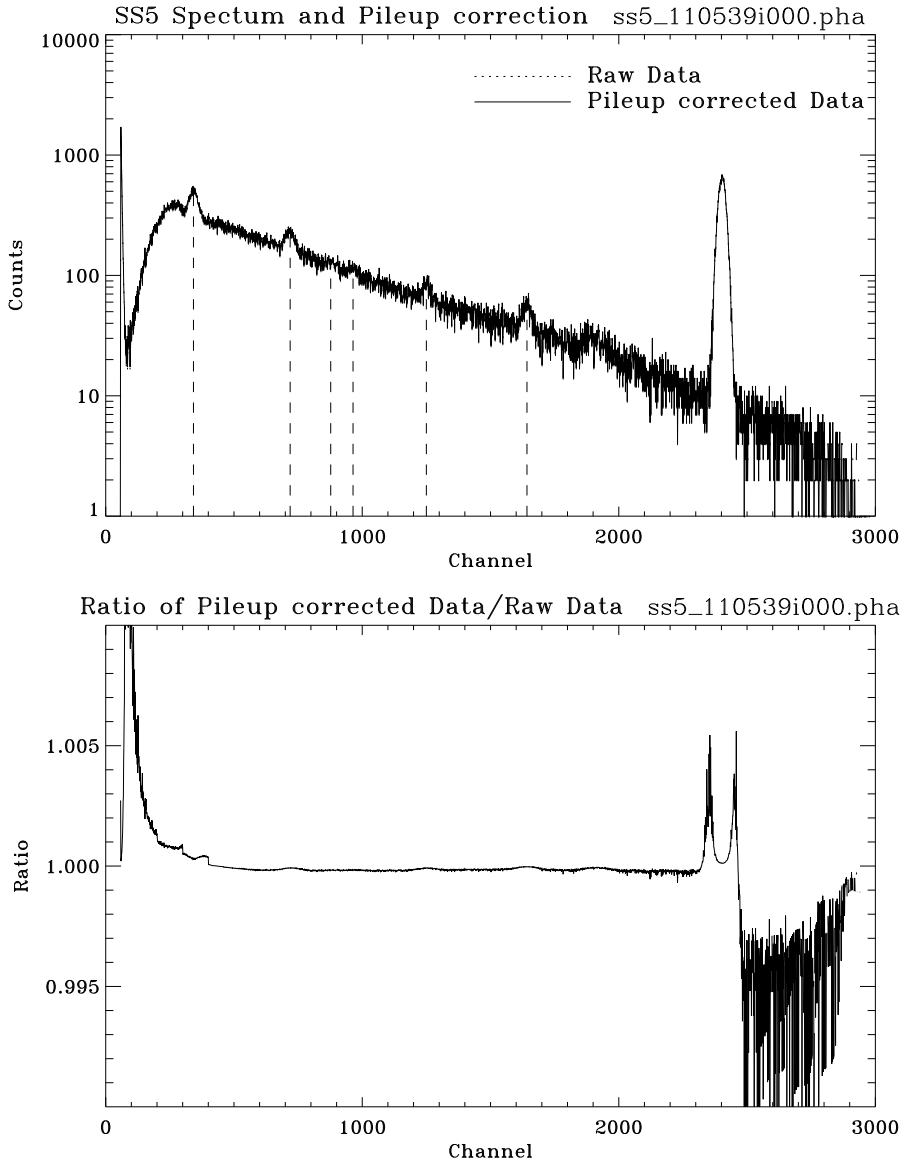

Figure 11.13: SS5 spectrum and pileup correction: Shell 1; Run ID: 110539. Upper panel shows the raw data and pileup corrected data. Dashed vertical lines indicate the X-ray lines to be used to calibrate the energy scale. Lower panel shows the ratio of pileup corrected data to the raw data.

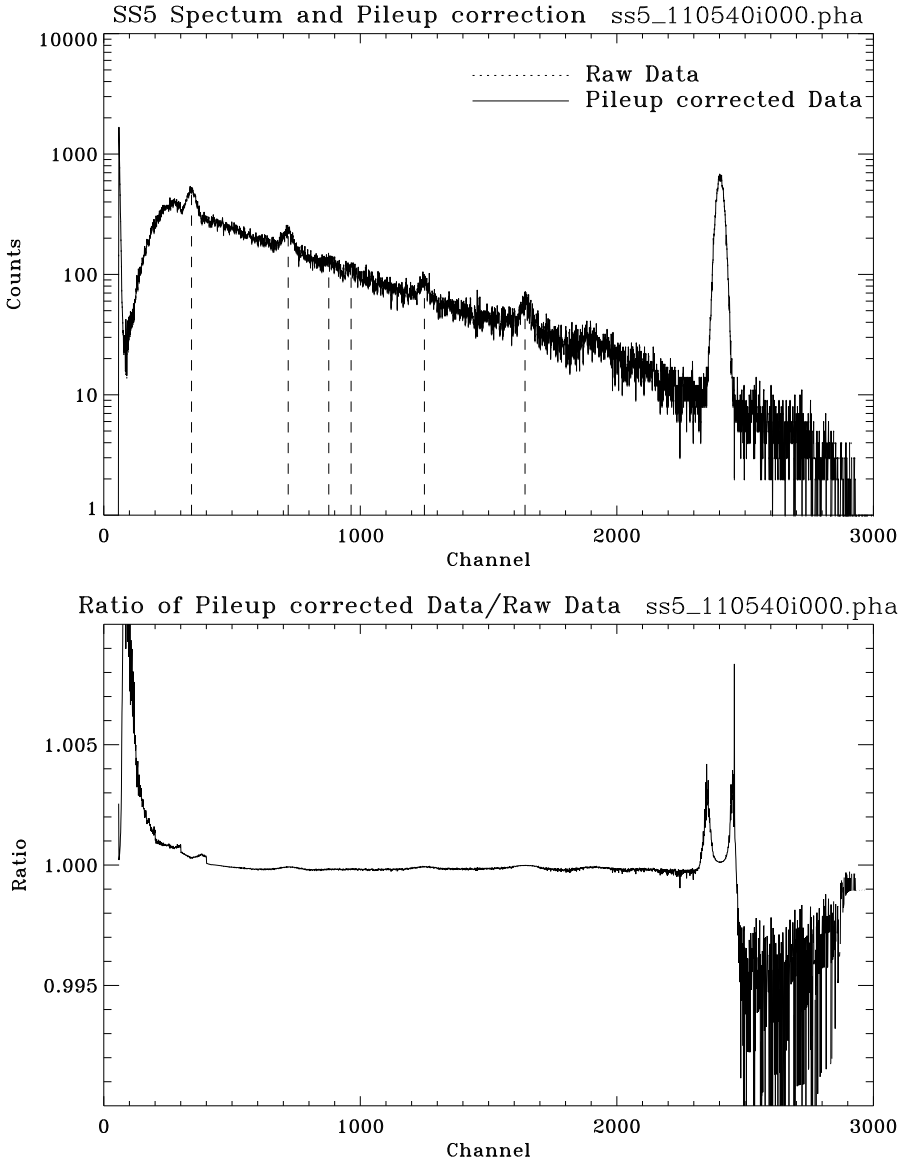

Figure 11.14: SS5 spectrum and pileup correction: Shell 3; Run ID: 110540. Upper panel shows the raw data and pileup corrected data. Dashed vertical lines indicate the X-ray lines to be used to calibrate the energy scale. Lower panel shows the ratio of pileup corrected data to the raw data.

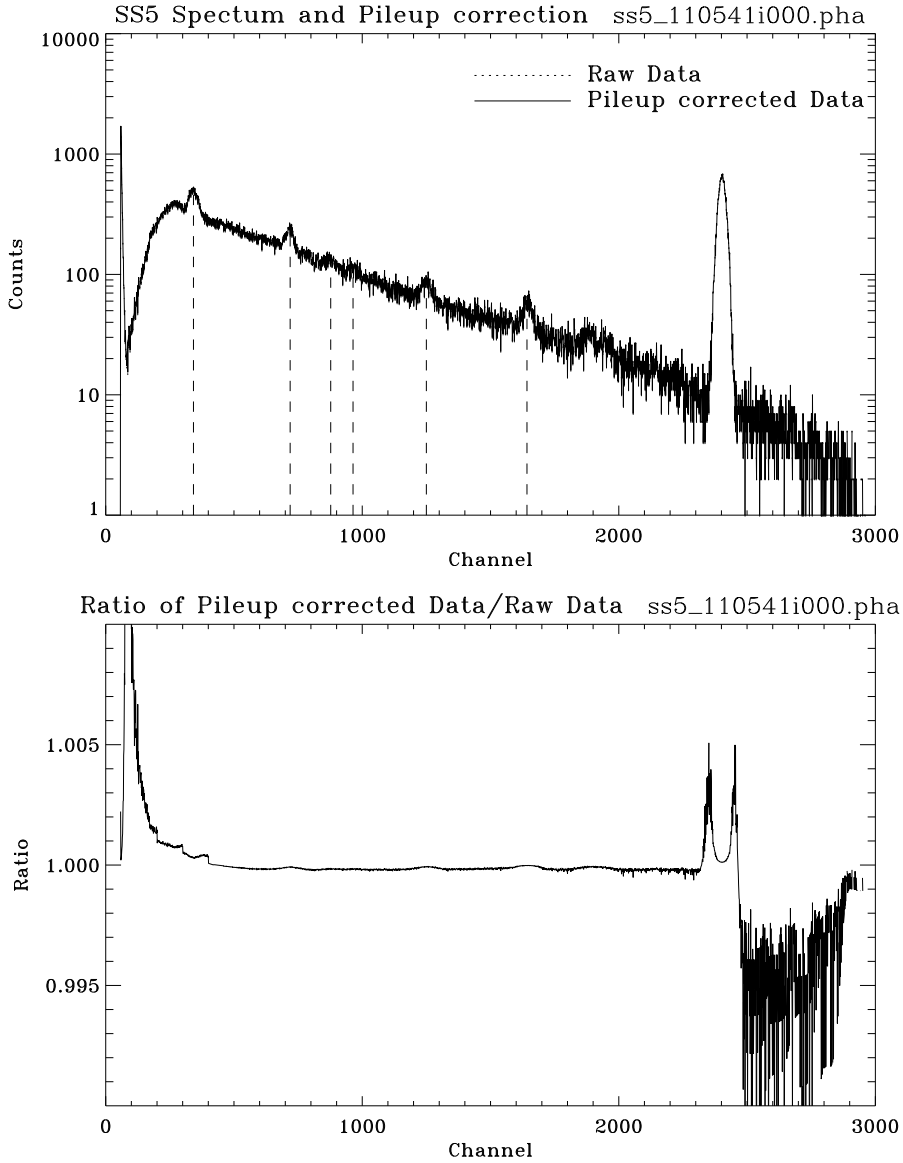

Figure 11.15: SS5 spectrum and pileup correction: Shell 4; Run ID: 110541. Upper panel shows the raw data and pileup corrected data. Dashed vertical lines indicate the X-ray lines to be used to calibrate the energy scale. Lower panel shows the ratio of pileup corrected data to the raw data.

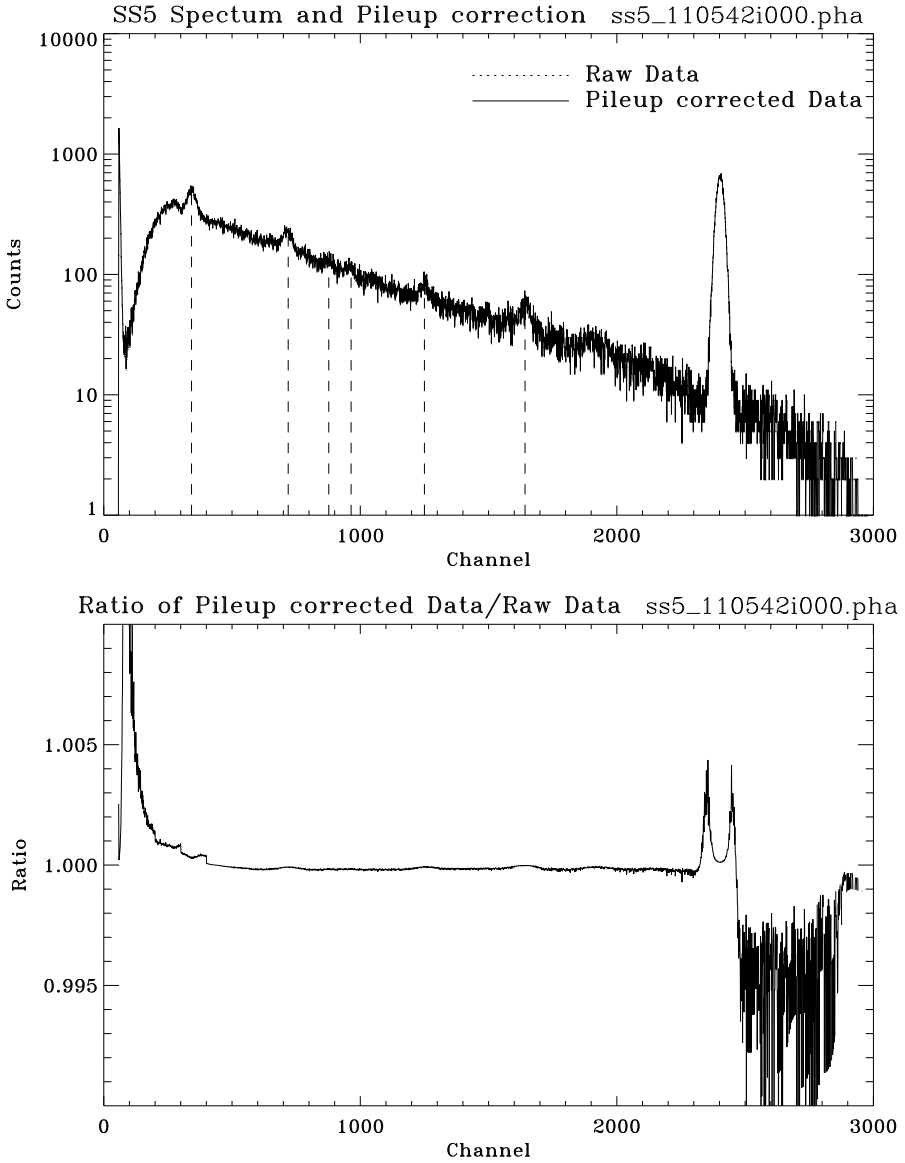

Figure 11.16: SS5 spectrum and pileup correction: Shell 6; Run ID: 110542. Upper panel shows the raw data and pileup corrected data. Dashed vertical lines indicate the X-ray lines to be used to calibrate the energy scale. Lower panel shows the ratio of pileup corrected data to the raw data.

11.4 SSD Flat Field Test

In order to obtain the effective area by dividing the spectra of ssd_x and ssd_5, we need to know the relative Quantum Efficiency (QE) of the two SSDs as a function of energy. The SSD QE was measured as part of the HRMA calibration at both the XRCF and BESSY. This section discusses the SSD QE measurement made at the XRCF, i.e. the SSD C-continuum flat field test.

The C-continuum flat field test was done in June 1997, when the HRMA had been removed from the testing chamber and shipped to TRW. The two SSDs were swapped, ssd_x was placed at the ssd_5 location in building 500 and ssd_5 was placed at the focal plane.

If the X-ray beam were uniform (this is not exactly the case – see §11.7), the X-ray flux at the two SSDs should be proportional to inverse square of their distance to the source. The distance from the source to ssd_x was 38.199 m and to ssd_5 was 537.778 m. The 2 mm aperture was used for the ssd_x and 5 mm aperture was used for the ssd_5 for the flat field test.

Figure 11.17 shows the spectra, with counting rate as a function of spectral channel, obtained with the two SSDs.[1] There are several spectral peaks atop the continuum. The largest peak to the right of each spectrum is the pulser peak, which is used to estimate the pileup correction, as discussed in the previous section, and to calculate the deadtime correction (see §11.6). Other peaks are characteristic X-ray lines due to contaminations to the carbon anode (also seen in Figures 11.1–11.4).

As the counting rates for the flat field test were very low (the ssd_x counting rate for the flat field test was about the same as the ssd_5 counting rate during the effective area measurements, see previous Section. The ssd_5 counting rate was 200 times lower than that of the ssd_x during the flat field test.), so the pileup effect is negligible.

11.5 SSD Energy Scale

Using the characteristic X-ray lines atop the continuum spectra, the SSD energy scale can be determined. As shown in Figure 11.17, six strong and single peaked lines were selected to determine the energy scale. Table 11.3 lists these six lines, from left to right.

To determine the line centers, a Gaussian profile with a quadratic function base was fitted to each peak. The centers of fitted Gaussian are shown in Figure 11.17 as dashed vertical lines with the peaks. Each SSD energy scale is determined by fitting a linear least square fit of the line energies as a function of line centers:

$$Energy = a + b \cdot Channel \tag{11.1}$$

Figure 11.18 shows the energy to channel linear fit for the two SSDs during the flat field test, i.e. Calibration Phase-J. The fitted energy scale parameters, a and b, are listed in the Figure. The fits are extremely good, as shown in Figure 11.19, which plots the residuals of the fits.

Using the above energy scales, the SSD spectra are converted from functions of channel to functions of energy and re-binned into equal energy bins. Figure 11.20 shows the C-continuum ssd_x and ssd_5 spectra as functions of energy, in units of counts per second per keV, where all the spectral lines are aligned up.

Since the operating conditions were different during the calibration, the energy scales were not the same in different phases of the calibration. For the SSD effective area measurements in Phase-E, we use the same method to obtain the energy scale.

[1] Notice that the data file for ssd_x starts as 'ss5' and vice versa, because the two SSDs were swapped and the data files were named after the location of the detector.

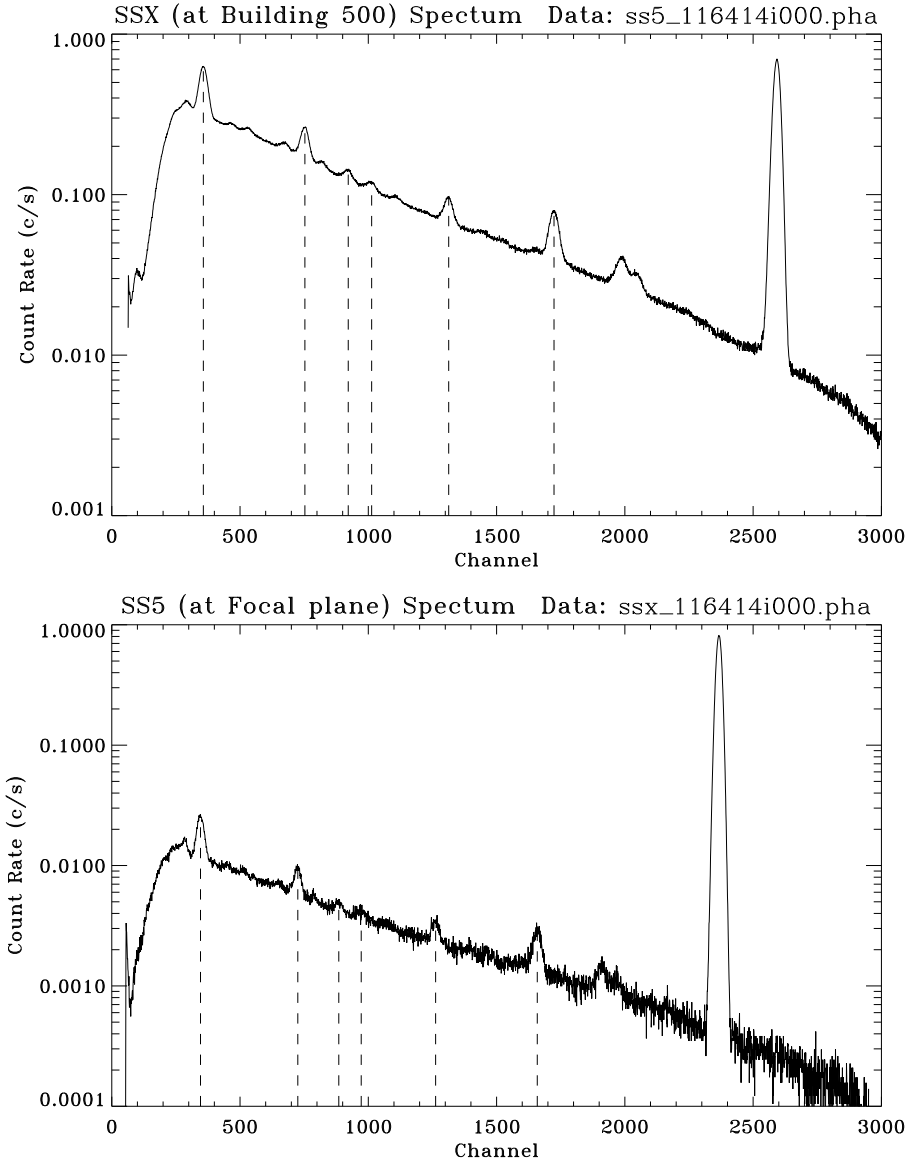

Figure 11.17: C-continuum flat field test SSX and SS5 spectra: Date: 970625; TRW ID: J−BND−BU−2.137; Run ID: 116414; Integration time: 57600 seconds. Dashed vertical lines indicate fitted centers of X-ray characteristic lines atop of the C-continuum spectrum.

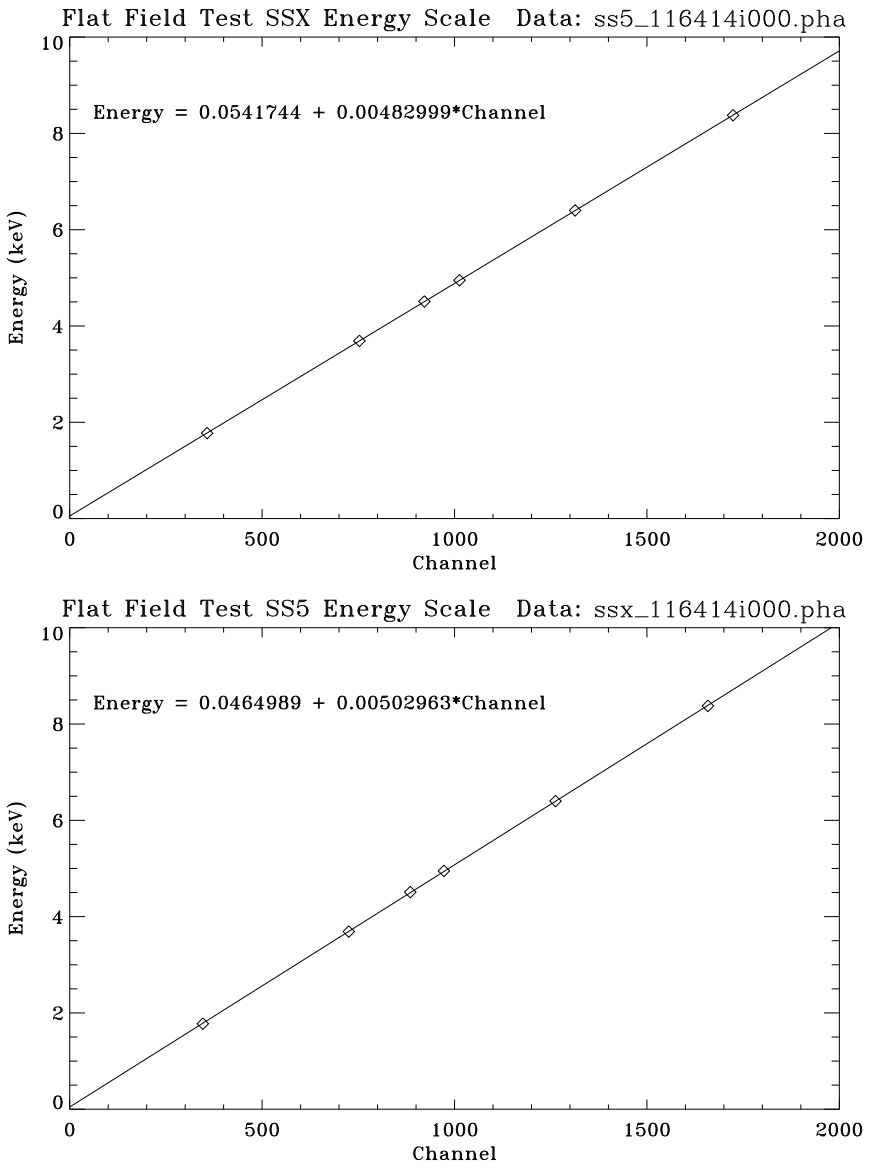

Figure 11.18: SSX and SS5 energy scales for the flat field test (Phase-J), fitted with six X-ray line energies.

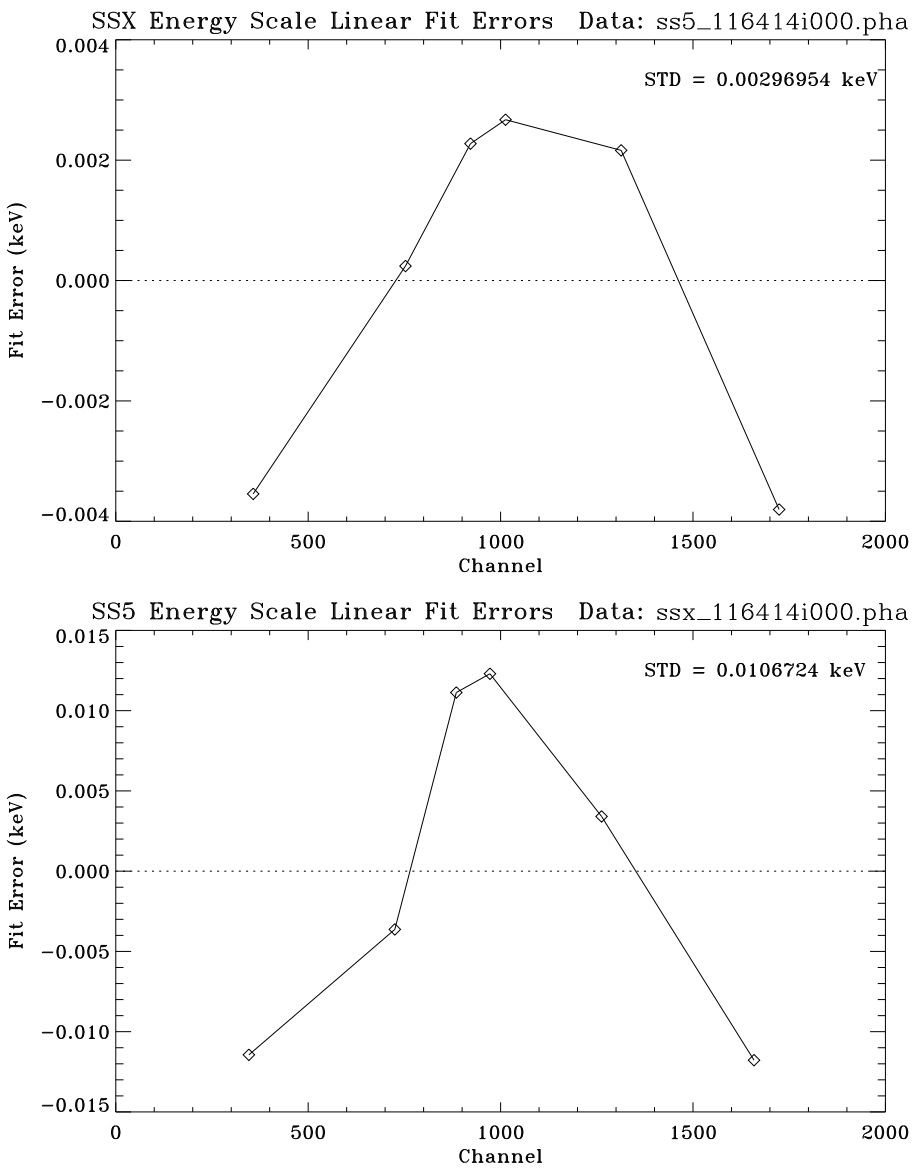

Figure 11.19: SSX and SS5 energy scale linear fit residuals for the flat field test (Phase-J).

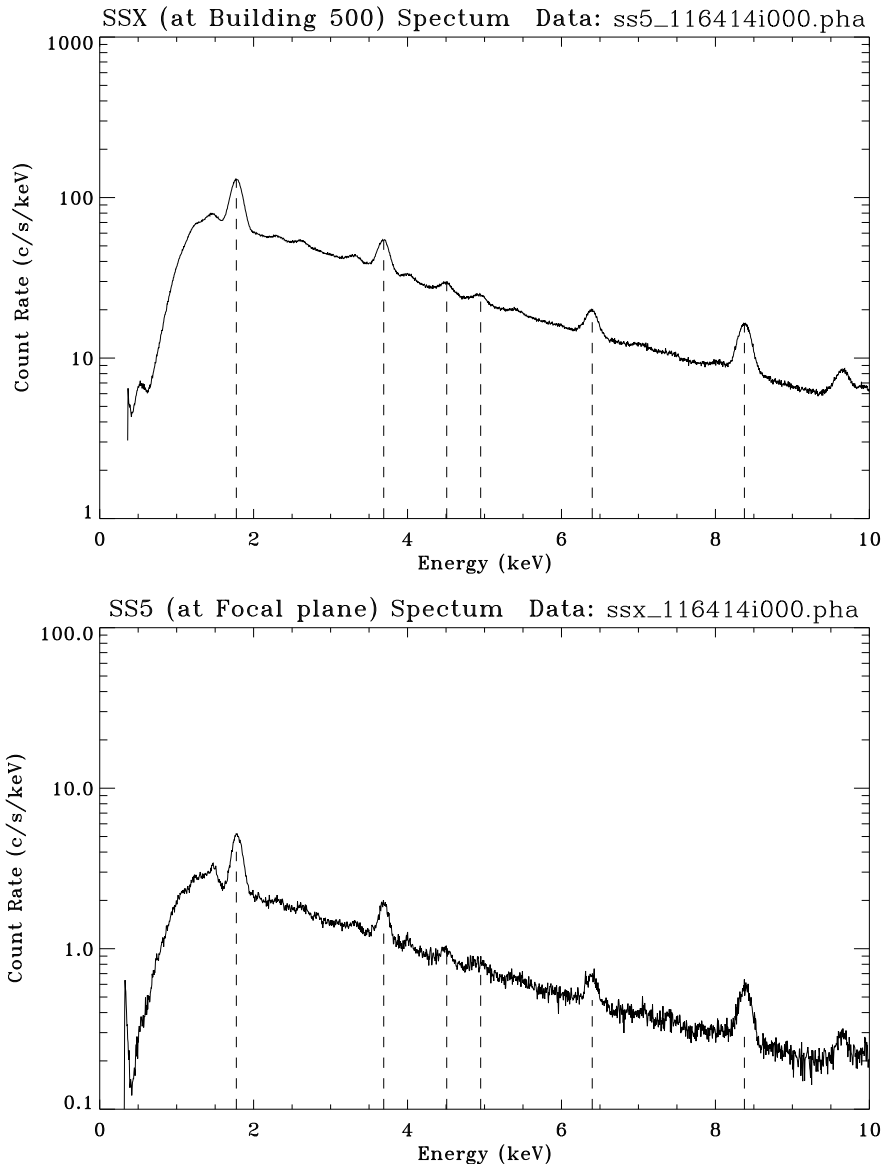

Figure 11.20: C-continuum flat field test SSX and SS5 spectra as functions of energy, using energy scales from Figure 11.18.

Table 11.3: X-ray Lines atop the C-continuum

X-ray Line	Energy
Si-Kα, W-Mα and W-Mβ	1.77525 keV *
Ca-Kα	3.69048 keV
Ti-Kα	4.50885 keV
V-Kα **	4.94968 keV
Fe-Kα	6.39951 keV
W-Lα	8.37680 keV

* The line center for Si-Kα, W-Mα and W-Mβ multiplet is weighted by line strength according to the HEG spectrum.
** Another choice for this line is Ti-Kβ (4.93181 keV). We chose V-Kα because this line has almost the same intensity as the Ti-Kα line, while in the same spectrum all the β lines are about an order of magnitude weaker than their α counterparts. Also V-Kα gives a slightly better linear fit to the energy scale. Had Ti-Kβ been chosen, the result is to lower the energy offset (parameter a in Eq. 11.1) by 0.003 keV, i.e. to decrease parameter a in Table 11.4 by 0.003.

We use the pileup corrected ssd_x and ssd_5 spectra (see §11.3) to obtain the energy scale. In Figures 11.9–11.16, the upper panels show the pileup corrected ssd_x and ssd_5 spectra. The SSD energy scale was determined using the six characteristic X-ray lines atop the continuum spectra, indicated by dashed vertical lines and as listed in Table 11.3. First a Gaussian profile with quadratic function was fitted to each peak to determine the line center. The fitted centers for the same line in different spectra of the same SSD differ only by a couple of channels, which is well within the fitted errors. So an averaged center for each line from the four measurements was used to obtain the energy scale. The energy scales of ssd_x and ssd_5 are determined by doing a linear least square fit of the averaged line centers to the line energies.

Figure 11.21 shows the energy to channel linear fit for the two SSDs in Phase-E. The fits are also extremely good, as shown in Figure 11.22, which plots the residuals of the fits.

Same practice was also used to obtain the SSD energy scale in Phase-D. We choose the effective area C-continuum measurements with run IDs 108426, 108450, 108484, and 108500 (TRW IDs D-IXS-EE-1.001,2,3,4), which had integration time of 300 sec and 2 mm apertures. Figure 11.23 shows the energy to channel linear fit for the two SSDs in Phase-D. Figure 11.24 show the residuals of the fits.

Table 11.4 lists the fitted energy scale parameters for the two SSDs in Phase D, E, and J. Notice that the energy scales are slightly different between Phase D and E and quite different for Phase J of the calibration.

Now it seems that we can obtain the relative QE by simply dividing the two spectra and considering the distance and aperture factors. But this can not be done before the deadtime and beam uniformity corrections are carefully evaluated.

11.6 SSD Deadtime Correction

In the raw data, the deadtime correction was automatically estimated, using a built-in circuitry and algorithms that follow the Gedcke-Hale formalism (Jenkins et al., 1981), and entered in the pha file header for each spectrum. However, for the SSDs, Gedcke-Hale formalism does not provide an

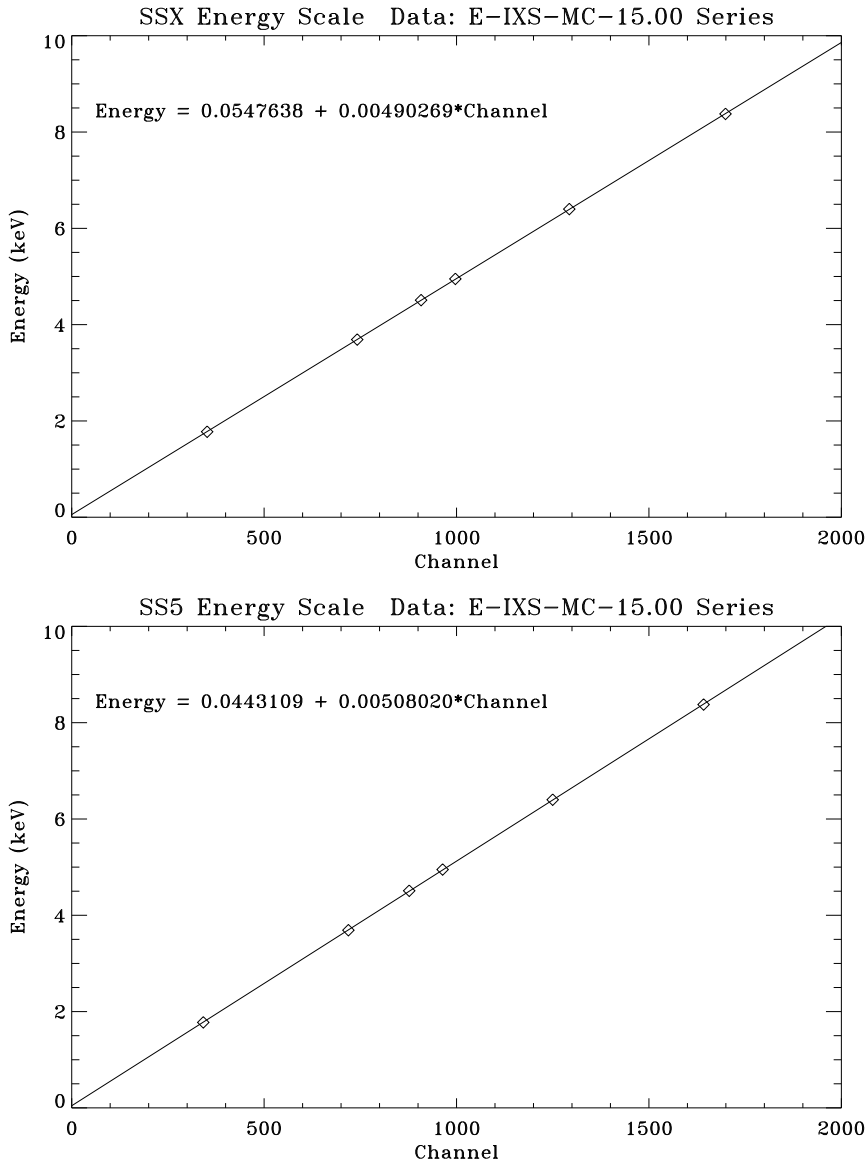

Figure 11.21: SSX and SS5 energy scales for the C-continuum effective area measurements (Phase-E), fitted with six X-ray line energies, averaged over four spectra (Run IDs 110539–110542).

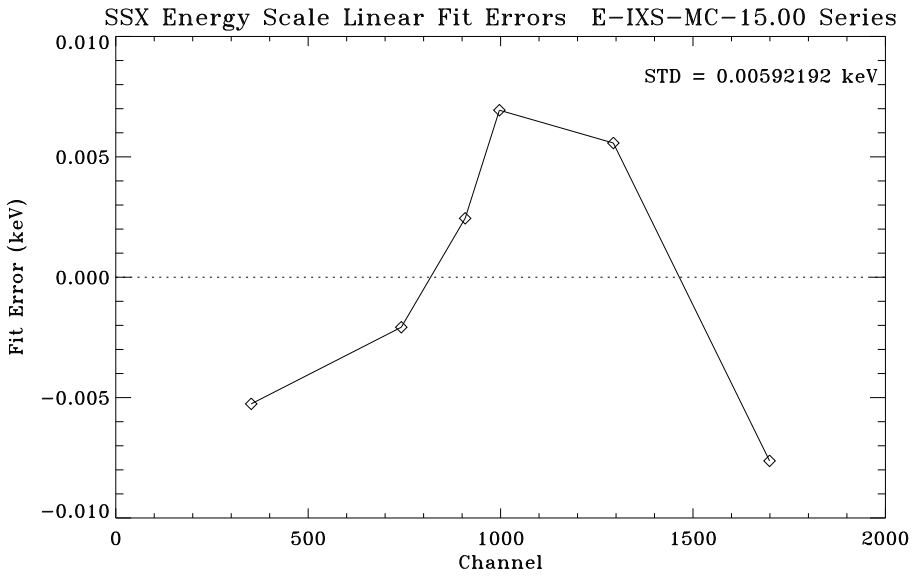

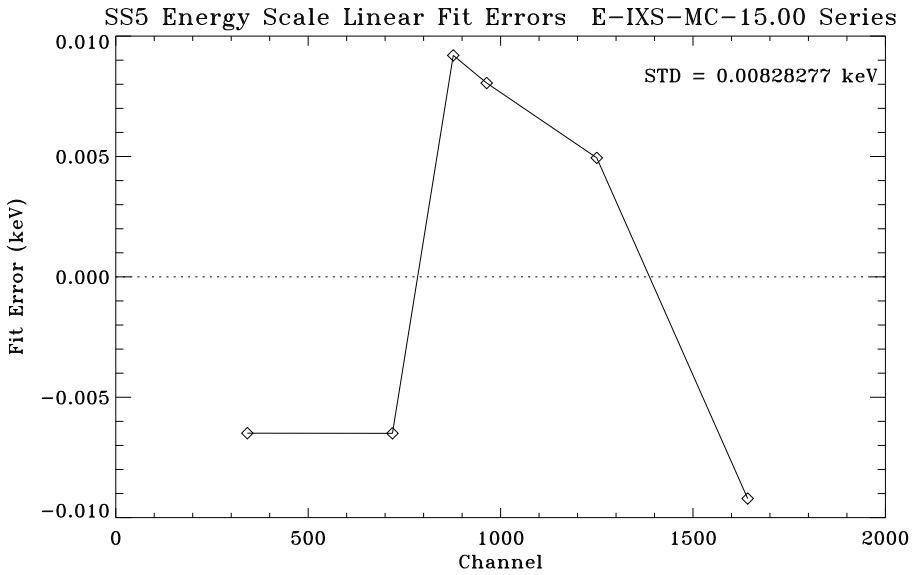

Figure 11.22: SSX and SS5 energy scale linear fit residuals for the C-continuum effective area measurements (Phase-E).

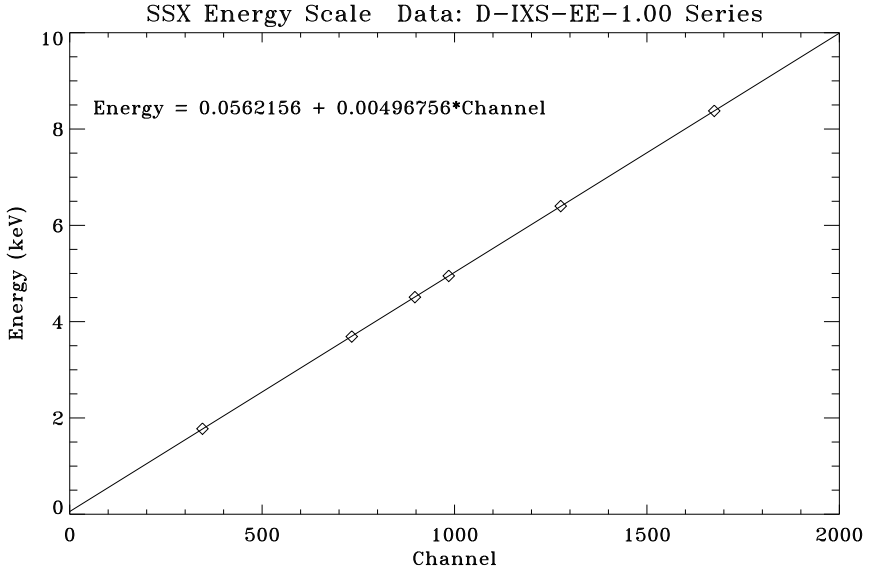

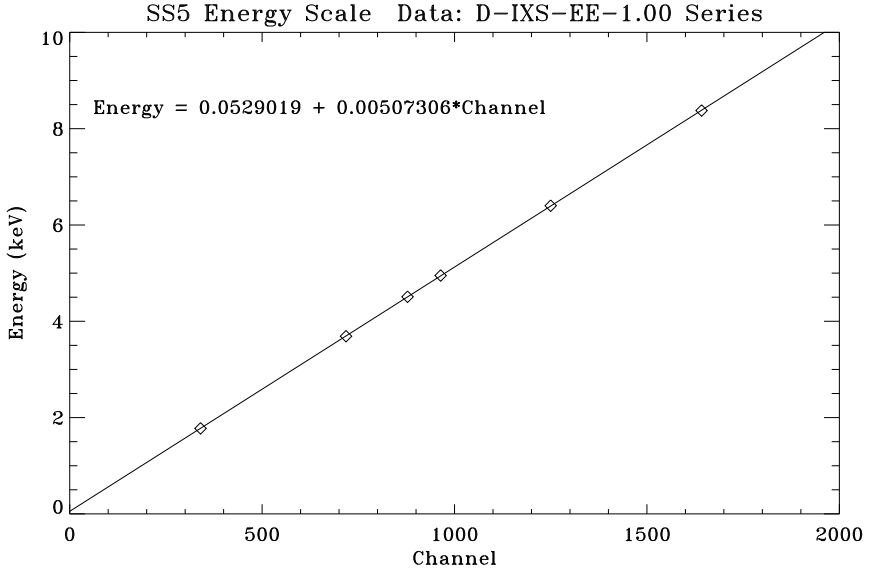

Figure 11.23: SSX and SS5 energy scales for the C-continuum effective area measurements (Phase-D), fitted with six X-ray line energies, averaged over four spectra (Run IDs: 108426, 108450, 108484, 108500).

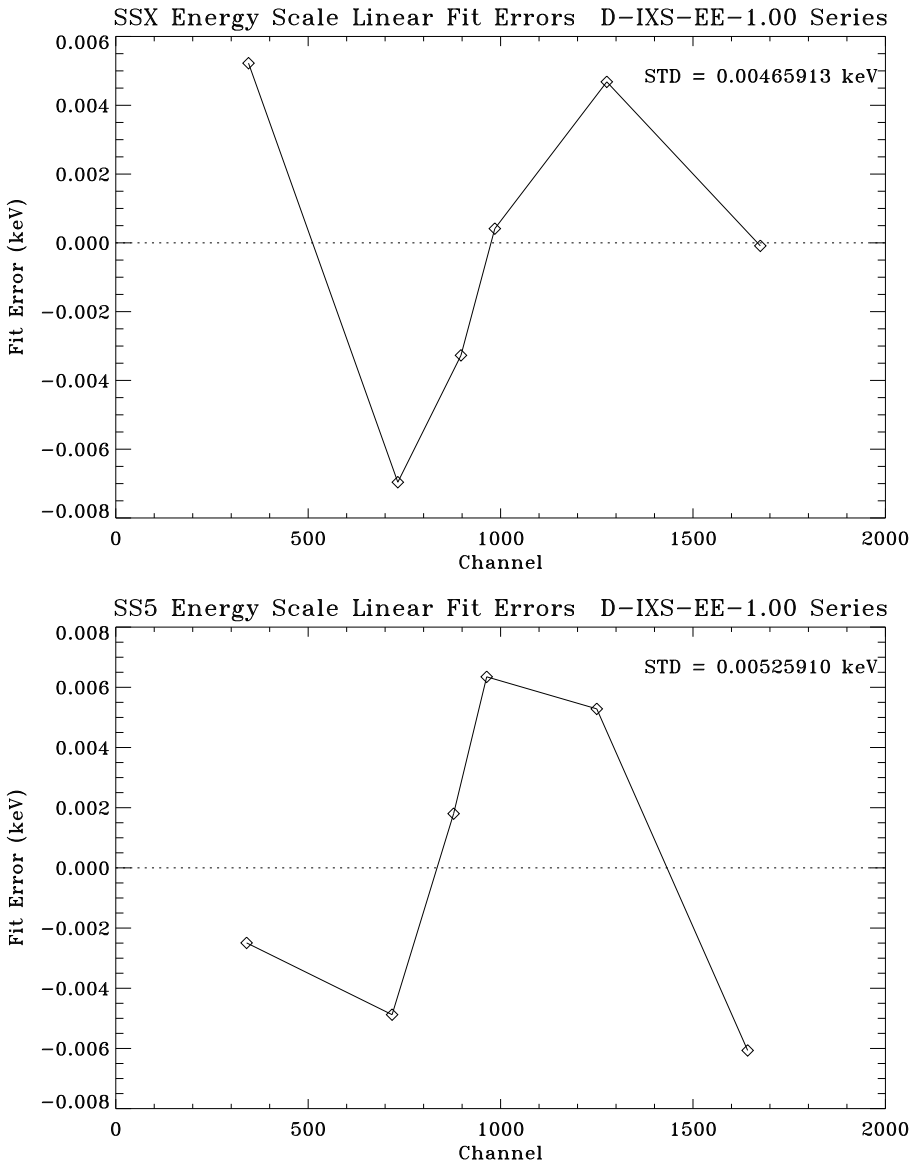

Figure 11.24: SSX and SS5 energy scale linear fit residuals for the C-continuum effective area measurements (Phase-D).

Table 11.4: SSD Energy Scale

Phase & Test	Detector	Spectral data	a	b
Phase-D	ssd_x	ssx_108426,450,484,500i000.pha	0.0562156	0.00496756
(EA Measurements)	ssd_5	ss5_108426,450,484,500i000.pha	0.0529019	0.00507306
Phase-E	ssd_x	ssx_110539,540,541,542i000.pha	0.0547638	0.00490269
(EA Measurements)	ssd_5	ss5_110539,540,541,542i000.pha	0.0443109	0.00508020
Phase-J	ssd_x	ss5_116414i000.pha	0.0541744	0.00482999
(Flat Field Test)	ssd_5	ssx_116414i000.pha	0.0464989	0.00502963

accurate estimation because of low-level noise; the lower level discriminators were set very low to extend the SSDs' energy coverage as low as possible. (For more details on this topic, see Chapter 5.)

A more accurate way to calculate the deadtime correction is to use the pulser method, in which artificial pulses are injected into the detector preamplifier to mimic real x-ray events. Since the pulses are processed just like X-rays – subject to interaction with hidden noise events, preamplifier reset pulses, *etc.* – fraction of pulses that appear in the output spectrum is, to a good approximation, equal to the system livetime fraction. The formula applying the deadtime correction to SSD spectra using the pulser method is:

$$Actual\ counts = Measured\ counts \cdot \frac{Input\ pulser\ counts}{Measured\ pulser\ counts} \tag{11.2}$$

where the *Measured counts* and *Measured pulser counts* are from pileup corrected spectra.[2]

Figure 11.25 illustrates how to determine the measured pulser counts. The top panel shows the ssd_x pulser spectrum from the SSD flat field test (see Figure 11.17). The bottom panel shows the ssd_5 pulser spectrum. Two vertical dotted lines surround the pulser peak indicate the pulser region. A power law is fitted to the spectrum outside the pulser region (100 channels below the left vertical line plus 100 channels above the right vertical line). The measured pulser counts equal the total counts under the pulser spectrum within the pulser region minus the total counts under the fitted power law spectrum within the pulser region. Since the counting rates are very low for the flat field test, the pileup effects are negligible. Later when we use the same method to do the deadtime corrections for the effective area measurements, we apply it to the pileup corrected data only.

For X-ray counting rate calculated using the pulser deadtime correction, the formula is:

$$Actual\ rate = \frac{Measured\ counts}{TrueTime} \cdot Pulser\ deadtime\ correction \tag{11.3}$$

$$= \frac{Measured\ counts}{TrueTime} \cdot \frac{Input\ pulser\ counts}{Measured\ Pulser\ counts} \tag{11.4}$$

where $TrueTime$ is the full integration time which is listed in the pha file header as $\#trueTime\_sec$.

[2] In Eq. 11.2, had the raw spectra (without pileup corrections) been used for the *Measured counts* and *Measured pulser counts*, there should be an additional factor of 1.0018 on the right hand side of the equation. This factor accounts for the non-randomness of the pulser events, which can not pileup or cause deadtime lossed among themselves, in the case of a 27-Hz pulser rate and 10-μsec amplifier shaping time constant. For more details, see Chapter 5.

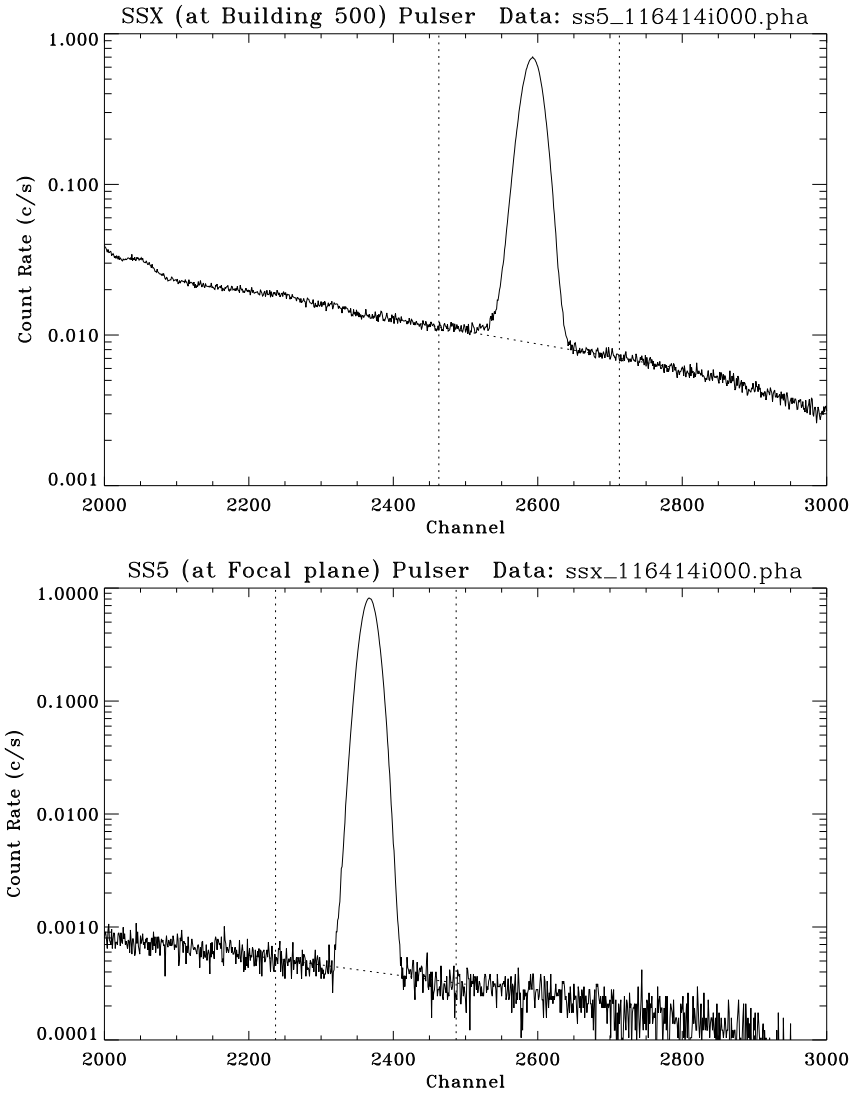

Figure 11.25: C-continuum flat field test SSX and SS5 pulser spectra. Two vertical dotted lines indicate the pulser region. A dotted line under the peak is the power law fit to the continuum. The pulser spectrum counts equal to the total counts under the pulser spectrum within the pulser region minus the total counts under the fitted power law spectrum within the pulser region.

For the effective area, $A_{eff}(E)$, calculated using the ssd_x counts, $C_{\text{ssd\_x}}(E)$, divided by ssd_5 counting rate, $C_{\text{ssd\_5}}(E)$, the pulser deadtime correction is:

$$A_{eff} = A_{eff}(w/o\ deadtime\ correction) \cdot \frac{\text{ssd\_x } Pulser\ deadtime\ correction}{\text{ssd\_5 } Pulser\ deadtime\ correction} \quad (11.5)$$

$$= A_{eff}(w/o\ deadtime\ correction) \cdot \frac{\left(\frac{\text{ssd\_x } Input\ pulser\ counts}{\text{ssd\_x } Measured\ pulser\ counts}\right)}{\left(\frac{\text{ssd\_5 } Input\ pulser\ counts}{\text{ssd\_5 } Measured\ pulser\ counts}\right)} \quad (11.6)$$

11.7 Beam Uniformity Test

We can obtain the relative quantum efficiency by dividing the two SSD spectra directly only if the X-ray beam intensities were exactly the same toward the directions of the two SSDs. But was the beam from the C-continuum source really uniform? To answer this question, a C-continuum beam uniformity test was made immediately after the C-continuum flatfield test (the flatfield test run ID is 116414, the beam uniformity test run ID is 116415).

During the beam uniformity test, the C-continuum source was operated in the same condition as for the flat field test, and the FPC-5 (i.e. the FPC detector in the Building 500) was scanned from the FPC-5 home position to the center (optical axis towards the HRMA), and to the SSD-5 home position, and then it scanned back in a reversed path. Two spectra were taken at each position. Figure 11.26 shows the six spectra taken during the C-continuum beam uniformity test. The small tick-marks on the horizontal axis are channels. The large tick-marks are the energies in unit of keV, based on the FPC-5 energy scale. The top two panels are the spectra at the FPC-5 home position, the middle two panels are the spectra at the optical axis, the bottom two panels are the spectra at the SSD-5 home position. Those six spectra look very similar. Taking the two spectra taken at the SSD-5 home position and dividing by the average of the two spectra taken on the optical axis, we obtain the relative flux ratio at those two positions as a function of energy (with low spectral resolution). Figure 11.27 show the relative flux ratio. It is seen that the beam is close to but not exactly uniform. It varies between 1.00 and 1.02. The solid curve in Figure 11.27 is a quadratic fit to the data. This is purely an empirical model which fits the data very well. The reduced χ^2 is 1.01652. So the beam uniformity as a function of energy can be well represented using this quadratic function, with a relative error of 0.0034:

$$FR = 1.01341 - 0.00512E + 0.000567E^2 \quad (11.7)$$

where FR is the flux ratio of at ssd_5 position vs. on the optical axis, and E is the X-ray energy in unit of keV.

11.8 SSD Relative Quantum Efficiency

With all above considerations, we now finally can obtain the relative quantum efficiency of the two SSDs. The ssd_5/ssd_x quantum efficiency ratio, $R(E)$, is:

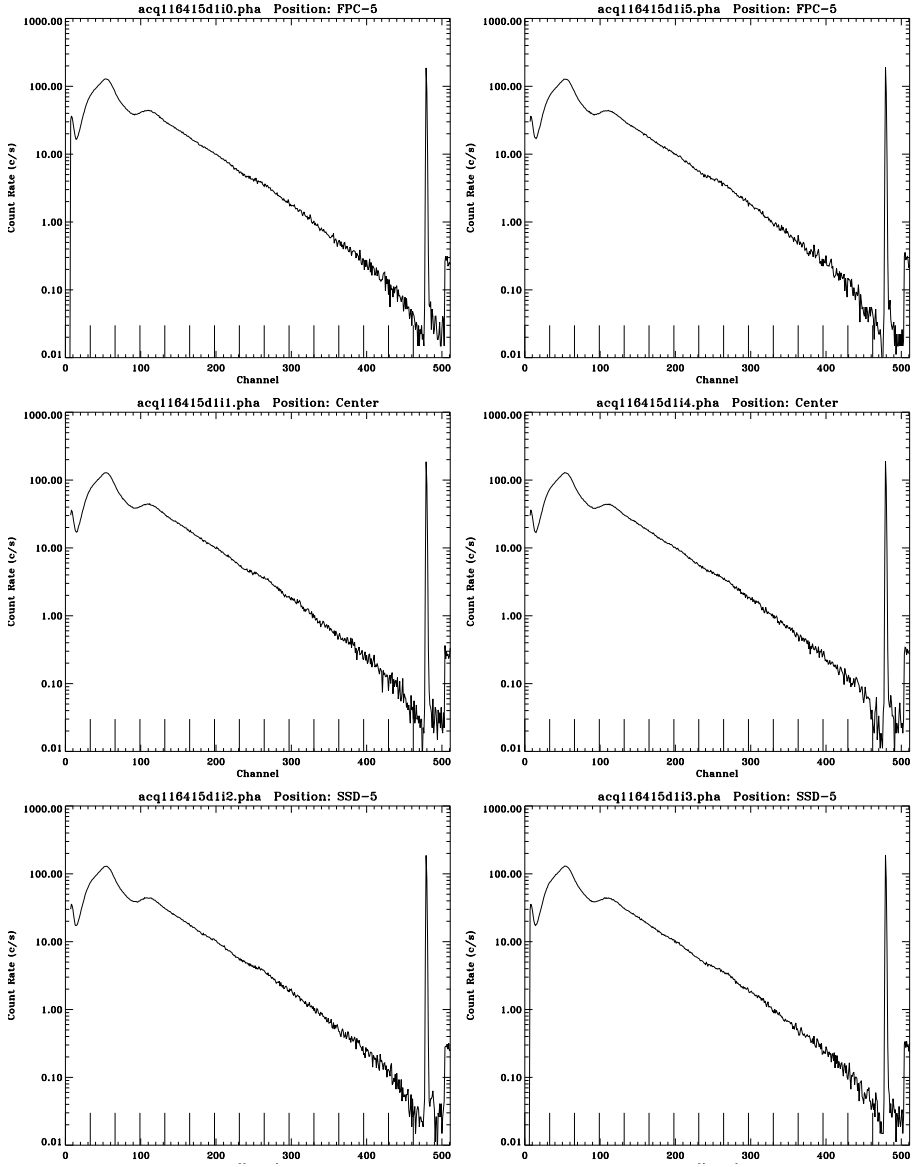

Figure 11.26: C-continuum source beam uniformity test. Scanned FPC-5 spectra at FPC-5 home, center or optical axis, and SSD-5 positions. The small tick-marks on the horizontal axis are channels. The large tick-marks are the energies in unit of keV, based on the FPC-5 energy scale.

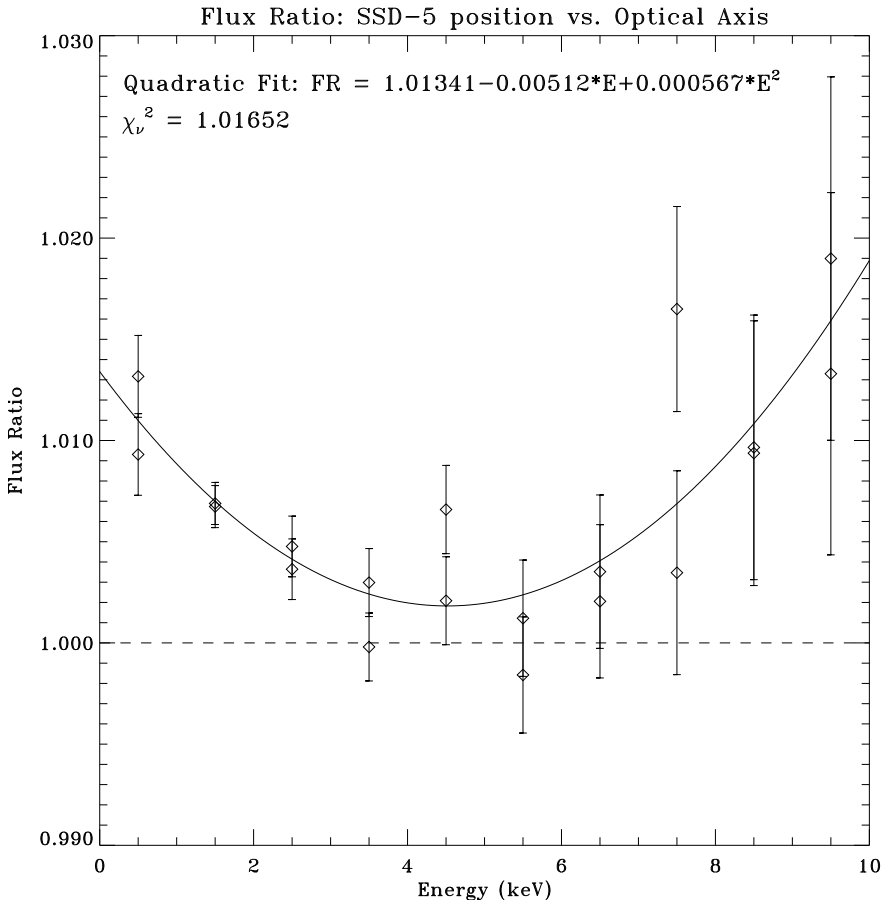

Figure 11.27: C-continuum FPC-5 beam flux ratio – SSD-5 position vs. optical axis – as a function of energy. Data are fit to a quadratic function.

$$R(E) = \frac{C_{\mathsf{ssd\_5}\ flatfield}(E)}{C_{\mathsf{ssd\_x}\ flatfield}(E)} \cdot \frac{\mathsf{ssd\_5}\ pulser\ deadtime\ correction}{\mathsf{ssd\_x}\ pulser\ deadtime\ correction} \cdot \frac{(\mathsf{ssd\_5}\ to\ source\ distance)^2}{(\mathsf{ssd\_x}\ to\ source\ distance)^2} \cdot \frac{\mathsf{ssd\_x}\ aperture\ area}{\mathsf{ssd\_5}\ aperture\ area} \cdot (Beam\ flux\ ratio\ between\ \mathsf{ssd\_5}\ position\ and\ optical\ axis) \quad (11.8)$$

where

- $C_{\mathsf{ssd\_5}\ flatfield}(E)$ and $C_{\mathsf{ssd\_x}\ flatfield}(E)$ are counts as functions of energy for the two SSDs from the flatfield test (see Figure 11.20).
- Using the method discussed in §11.6, the pulser deadtime corrections are calculated to be 1.0092 and 1.0569 for ssd_5 and ssd_x, respectively.
- The source to SSD distances are 537.778 m and 38.199 m for ssd_5 and ssd_x, respectively. Errors on the distance measurements are negligible for this calculation.
- For the flat field test, the apertures used were 2 mm (actual diameter = 1.9990 ± 0.0073 mm) for ssd_x. and 5 mm (actual diameter = 4.9962 ± 0.0073 mm) for ssd_5. The combined relative error due to the two aperture area uncertainties is 0.0079.
- For the beam flux ratio, measured with FPC-5, we use Eq. 11.7.

So ssd_5/ssd_x Quantum Efficiency ratio is:

$$R(E) = \frac{C_{\mathsf{ssd\_5}\ flatfield}(E)}{C_{\mathsf{ssd\_x}\ flatfield}(E)} \cdot \frac{1.0092}{1.0569} \cdot \frac{537.778^2}{38.199^2} \cdot \frac{1.9990^2}{4.9962^2} \cdot FR(E) \quad (11.9)$$

$$= \frac{C_{\mathsf{ssd\_5}\ flatfield}(E)}{C_{\mathsf{ssd\_x}\ flatfield}(E)} \cdot 30.2964 \cdot (1.01341 - 0.00512E + 0.000567E^2) \quad (11.10)$$

Figure 11.28 shows the ssd_5/ssd_x QE ratio, $R(E)$, as a function of energy. The top panel show the QE ratio calculated using formula (Eq. 11.9). $R(E)$ is near unity for energies above 2 keV as expected. $R(E)$ varies drastically for energies below 2 keV, because of the icing effect (see the following section). In this case, there was more ice on the ssd_x therefore there was much higher transmission for ssd_5. A wiggle around line 1.775 keV indicates that the two SSDs have slightly different spectral resolution.

This $R(E)$ curve is rather noisy. In the bottom panel, the data were binned into 0.3 keV bins and fitted to a flat ratio for energies above 3 keV (since at energies between 2 and 3 keV, the ratio was still slightly effected by the icing). The fit is very good, with a ratio of 1.0141 ± 0.0021 and $\chi^2_\nu = 1.0897$. Here the error, 0.0021, is only the standard deviation of the mean of the binned flat field data in the 3–10 keV band. The total error for the quantum efficiency ratio also includes the beam uniformity error (0.0034) and the aperture size error (0.0079). Adding them in quadrature, the total relative error is 0.0088.

Because of the icing effect, the flat field test can only provide us with this ratio within 3–10 keV band. Since this ratio is reasonably energy independent, we assume, for the entire 0–10 keV energy band, the ssd_5/ssd_x quantum efficiency ratio is

$$R(E) = 1.0141 \pm 0.0089 \quad (11.11)$$

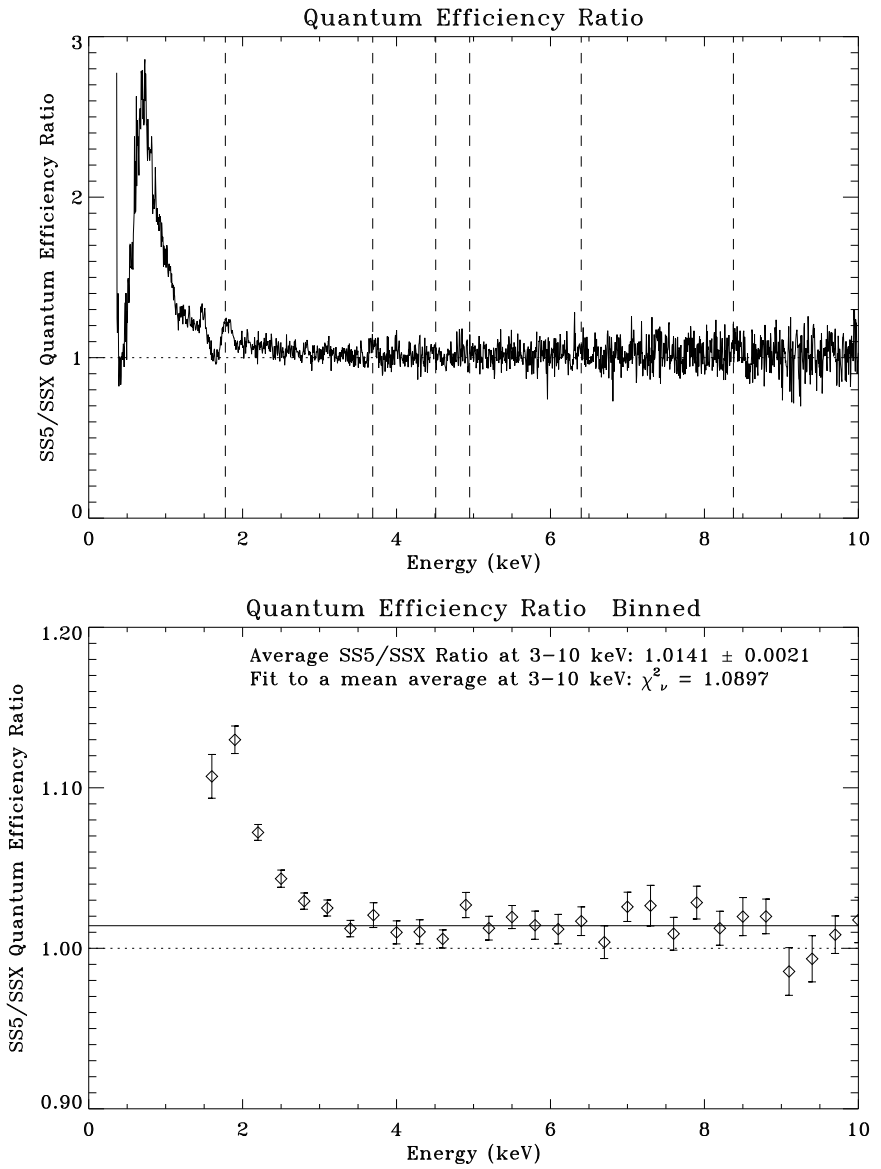

Figure 11.28: SS5/SSX quantum efficiency ratio. In the top panel, the large ratio below 2 keV is mainly due to the different ice build up on the two detectors. The bottom panel shows the ratio curve binned and fitted to a constant ratio. The solid line is the average ratio at 3–10 keV.

In the following we will use this QE ratio to calculate the HRMA effective area.[3]

11.9 SSD Icing Effect

In this section we discuss the so called SSD icing effect which we encountered in the previous section. Because SSD was cooled to liquid nitrogen temperature, even in its vacuum container, there was still a small amount of trapped water which condensed on the surface of the SSD to form a very thin layer of ice. This thin ice layer decreases the transmission of low energy X-rays.

In order to monitor the ice build up, a radioactive isotope $^{244}_{96}$Cm excited Fe source was placed on the aperture wheel and rotated in front of the ssd_5 from time to time. The Figure 11.29 shows the Fe-Lα (0.705 keV) and Fe-Kα (6.40 keV) line intensity with error bars measured with ssd_5 as a function of time from 960824 to 970521 (JD 2450320 – 2450590). The SSD C-continuum measurements were made in the middle of that period on 970113 and 970130. In the top panel, the Fe-Lα intensity has two peaks, on 961031 and 970223, followed by declines. These two peaks indicate the time when the ssd_5 was warmed up and we assume there was no ice then. The declines indicate the ice build up, reducing the transmission of Fe-Lα into the ssd_5. In the bottom panel, the fluctuations of Fe-Kα intensity could be due to icing, source aging and other temporal variations. To obtain the icing information, we only need to focus on the intensity ratio of Fe-Lα/Fe-Kα. Data from Figure 11.29 are listed in Table 11.5:

Table 11.5: SSD-500 Icing Data

Icing Period		Fe-Lα Intensity	Fe-Kα Intensity	Intensity ratio
First Period	Begin	34.2	90.8	0.3767
961031 – 970129	End	24.5	87.9	0.2787
End/Begin Ratio				74.00 %
Second Period	Begin	32.0	87.1	0.3673
970223 – 970514	End	23.5	86.5	0.2717
End/Begin Ratio				73.97 %

At the end of each ice build up period, the Fe-Lα/Fe-Kα transmission ratio is 74% of its initial value. This result can be used to obtain the ice thickness.

Figure 11.30 shows the X-ray transmission of ice. The solid line is a fit with Fe-Lα (0.705 keV) line transmission being 74% of Fe-Kα (6.40 keV) line transmission. The result is a 0.3 μm ice layer. For reference, a transmission curve of a 1μm ice layer is plotted as a dotted line. According to this fit, during the calibration, the thickest ice build up on ssd_5 was 0.3 μm, at around 970129 and 970514. At other times, the ice was thinner. The ssd_x did not have a $^{244}_{96}$Cm source, so we do not have any data about the icing on the ssd_x.

Figure 11.30 tells us that icing has less than 0.7% effect for energies over 3 keV. At 2 keV, it can decrease the X-ray transmission by up to 2%. At the same time, icing has very severe effect for

[3]Because this ratio is energy independent, a large portion of the offset from unity is probably due to the combined aperture size error (0.0079). Because the aperture wheels were built into the SSD system, the apertures moved with the SSDs when the two SSDs were swapped during the flat field test. The measured ssd_5/ssd_x quantum efficiency ratio reflects a combination of real QE ratio of the SSDs and the aperture area ratio. In any case, the result of $R = 1.0141 \pm 0.0089$ provides the correct QE ratio for the effective area measurements. To measure the 2 mm and 5 mm aperture areas more accurately will reduce the QE ratio error.

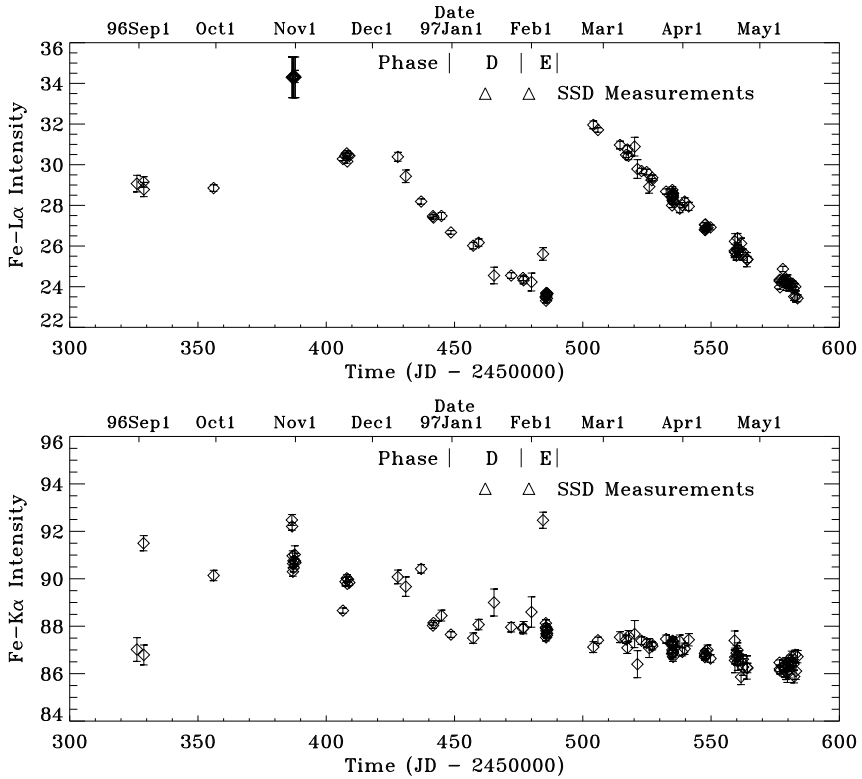

Figure 11.29: SSD 500 icing data (courtesy: Allyn Tennant). In order to monitor the ice build up, a radioactive isotope $^{244}_{96}$Cm excited Fe source was placed on the aperture wheel and rotated to front of the SS5 from time to time. The Figure shows the Fe-Lα (0.705 keV) and Fe-Kα (6.40 keV) line intensity with error bars measured with SS5 as a function of time from 960824 to 970521 (JD 2450320 – 2450590). Upper portions of each panel show the Phase D and E of the HRMA calibration and the dates of the SSD C-continuum measurements. In the top panel, the Fe-Lα intensity has two peaks, on 961031 and 970223, followed by declines. These two peaks indicate the time when the SS5 was warmed up and assuming there was no ice then. The declines indicate the ice build up and therefore reducing the transmission of Fe-Lα into the SS5. In the bottom panel, the fluctuations of Fe-Kα intensity could be due to icing, source aging and other temporal variations. To obtain the icing information, we only need to focus on the intensity ratio of Fe-Lα/Fe-Kα. At the end of each ice build up period, the Fe-Lα/Fe-Kα transmission ratio is 74% of its value at the beginning. This result is used to obtain the ice thickness.

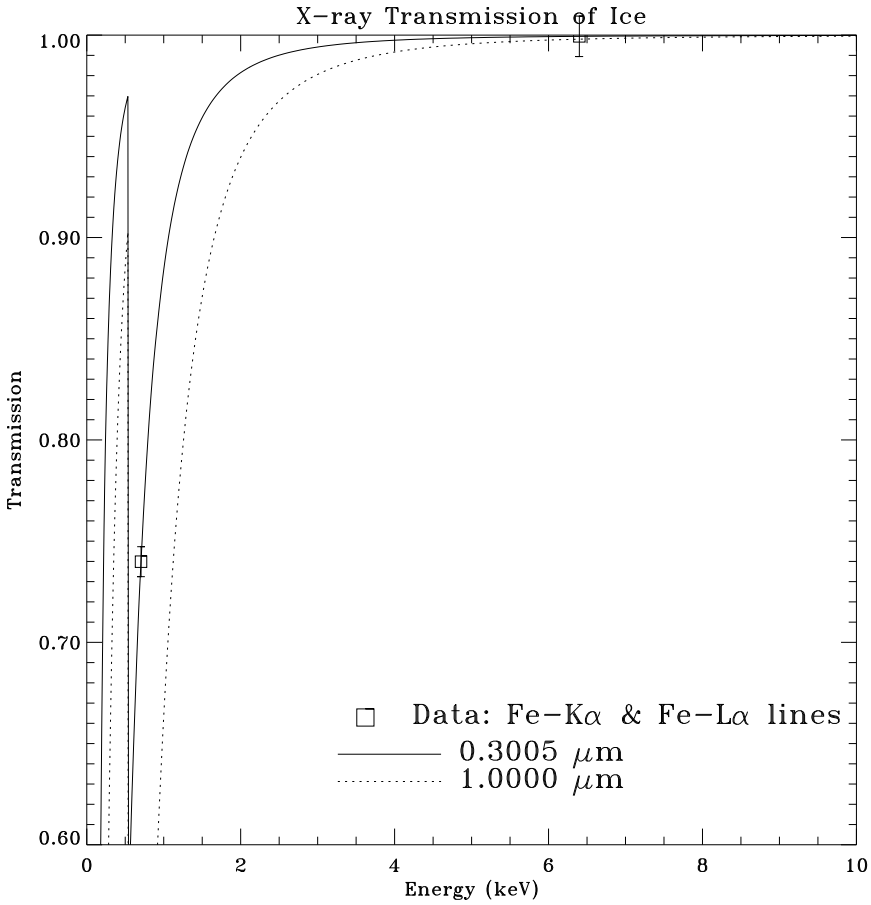

Figure 11.30: X-ray transmission of ice. The solid line is a fit with Fe-Lα (0.705 keV) line transmission being 74% of Fe-Kα (6.40 keV) line transmission. The result is a 0.3 μm ice layer. According to this fit, during the calibration, the thickest ice build up on SS5 was 0.3 μm, at around 970129 and 970514. This layer would have caused <2% decrease in transmission for X-rays above 2 keV, but a much larger attenuation below 2 keV. For reference, the transmission curve of a 1μm ice layer is plotted as a dotted line.

energies below 2 keV. Because the ice build up is a function of time and the build up on two SSDs could be different, the SSD data below 2 keV are not reliable. We have seen an indication of that in the previous section (see Figure 11.28). So in the flat field data analysis and in the following effective are data, we will not use the SSD spectra at low energies.

11.10 Background

During the HRMA calibration, background runs were taken almost every day when the source valve was closed and all the detectors were turned on. To evaluate the effect of the background on the SSD C-continuum measurements, we examined all the SSD background spectra and found that the background is extremely low.

Figure 11.31 shows a pair of typical SSD background spectra. It was take on 970124, with TRW ID D-IXF-BG-1.021, run ID 110036 and integration time of 2100 seconds. They are summed spectra of seven background runs of 300 seconds each. It is seen that, other than the pulser peak near channel 2400 and some electronic noise at near channel 60, the spectra are very clean in the region to be used to reduce the HRMA effective area (channels 100–2000). The average counts per channel per second are 0.000046 and 0.000024 for ssd_x and ssd_5, respectively. For all the background spectra, the average counting rate in channels 100–2000 ranges from 0.000019 to 0.000098 c/s/ch. This level of background is negligible in our data analysis.

11.11 Data Analysis and Reduction

With all the above considerations, we can now obtain the HRMA effective area. In this section we use the C-continuum SSD on-axis effective area measurements in Phase-E to demonstrate the data reduction process. All other measurements listed in Tables 11.1 and 11.2 can be reduced the same way.

The four Phase-E SSD effective area measurements for the four shells have TRW IDs of E-IXS-MC-15.001,2,3,4 and run IDs 110539, 110540, 110541, and 110542. The "MC" in TRW ID stands for molecular contamination measurements, but they also serve as on-axis effective area C-continuum measurements. They have longer integration time, 1000 seconds, and the largest ssd_x aperture, 2 mm, used for this kind of measurements.

We start with the pileup corrected ssd_x and ssd_5 spectra (see §11.3). In Figures 11.9–11.16, the upper panels show the pileup corrected ssd_x and ssd_5 spectra. The SSD energy scale was determined in §11.5.

Using the linear fit parameters listed in Table 11.4, each of the eight SSD spectra was scaled as a function of energy. Then they were binned into equal energy bins by dividing the spectra by the fitting parameter b in Table 11.4. The pulser deadtime corrections are also applied to the spectra the same way as to the flat field data. The results are four pairs of ssd_x and ssd_5 spectra as functions of energy and in units of counts/second/keV. They are shown in the top and middle panels of Figures 11.32–11.35. The dashed vertical lines indicate the six X-ray lines used for energy scaling.

11.12 Effective Area

The HRMA effective area at the XRCF is defined to be the photon collecting area in the plane of the HRMA pre-collimater entrance, which is 1491.64 mm forward from CAP Datum-A (the front

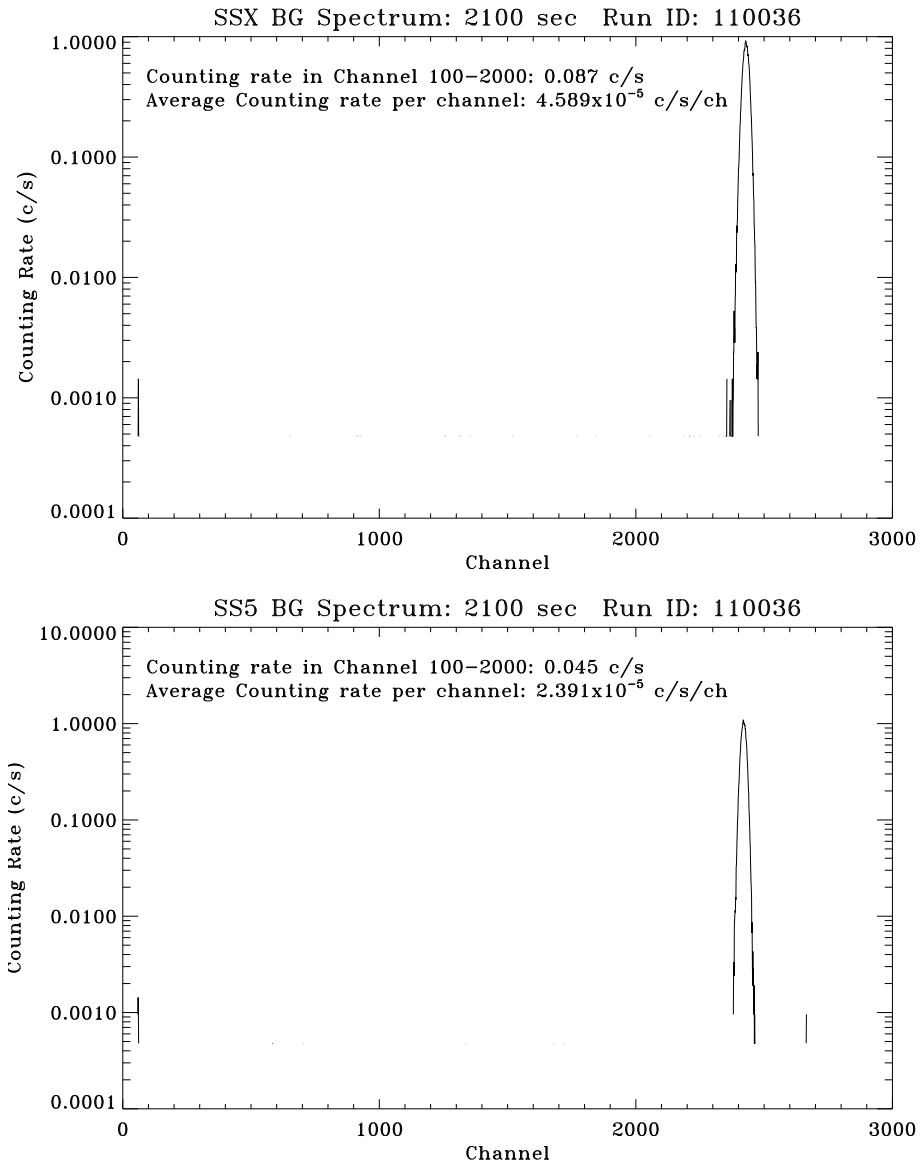

Figure 11.31: SSX and SS5 spectra of background run. Date: 970124; TRW ID: E−IXS−BG−1.021; Run ID: 110036; Integration time: 2100 seconds. The average counts per channel per seconds are 0.000046 and 0.000024 for SSX and SS5, respectively.

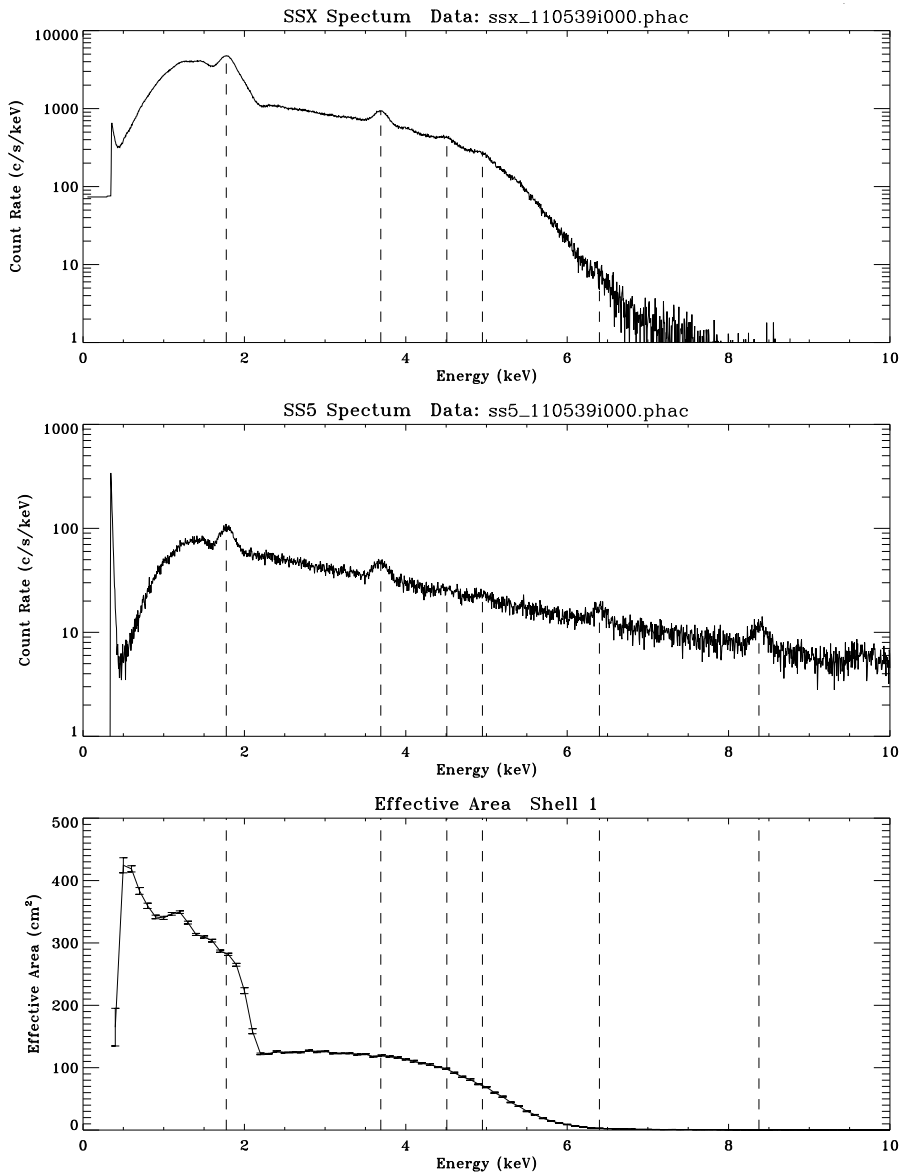

Figure 11.32: SSD C-continuum effective area measurement: Shell 1; 2 mm aperture; Run ID: 110539. Top panel is the SSX spectrum. Middle panel is the SS5 spectrum. Bottom panel is the measured effective area.

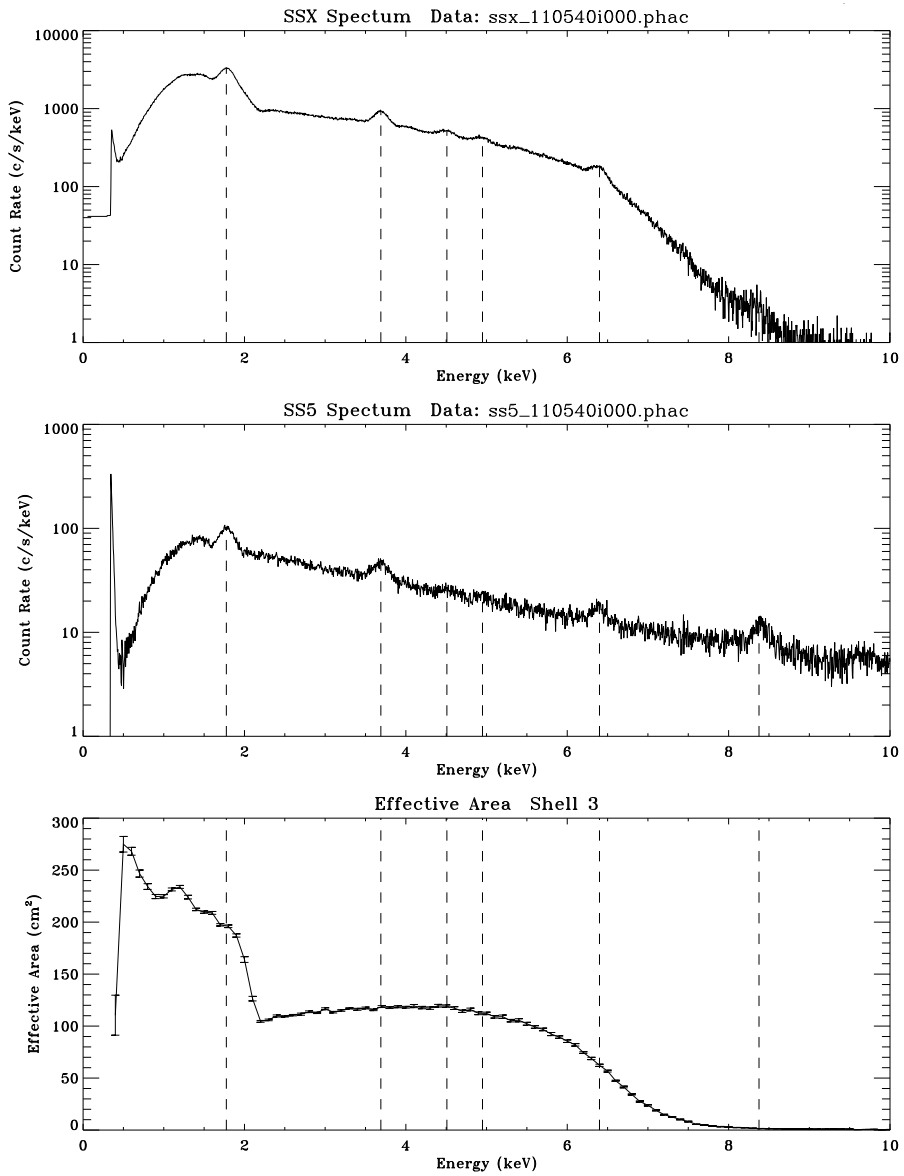

Figure 11.33: SSD C-continuum effective area measurement: Shell 3; 2 mm aperture; Run ID: 110540. Top panel is the SSX spectrum. Middle panel is the SS5 spectrum. Bottom panel is the measured effective area.

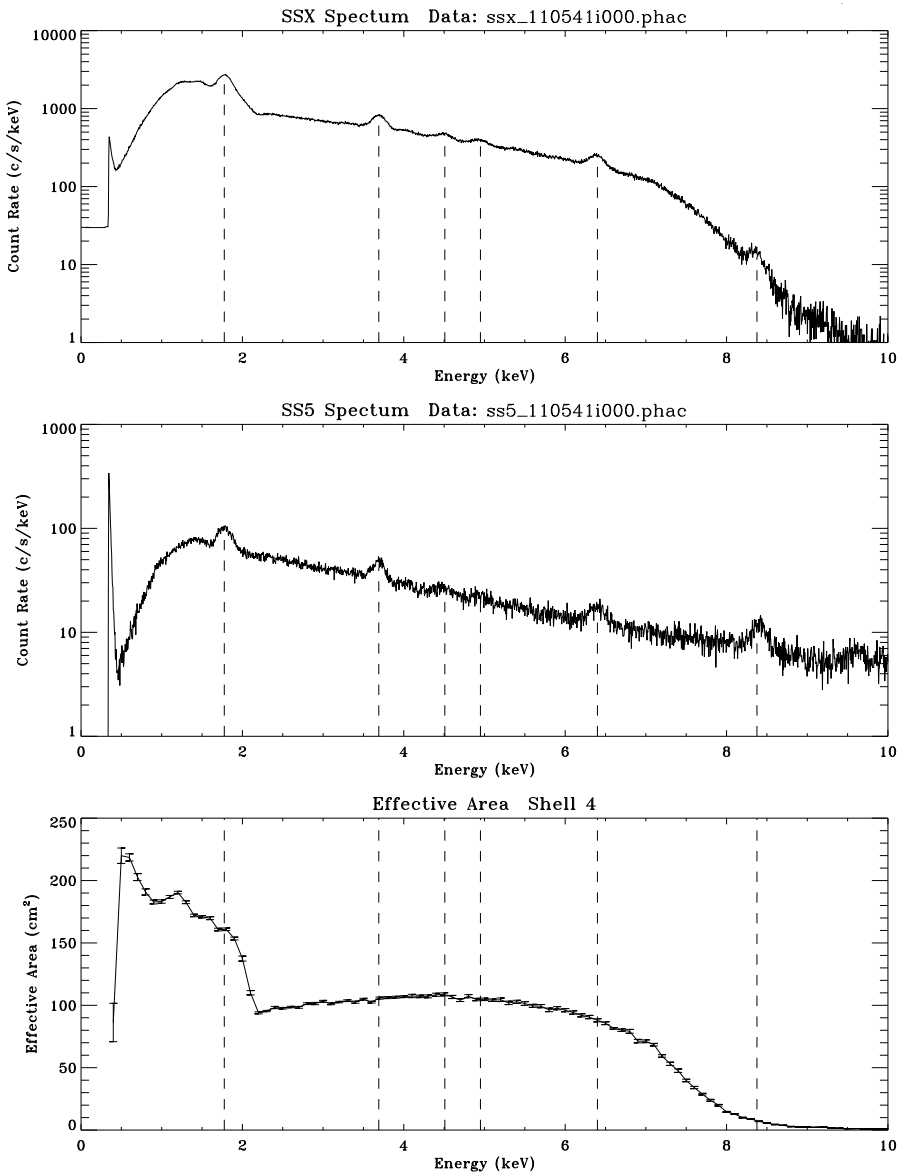

Figure 11.34: SSD C-continuum effective area measurement: Shell 4; 2 mm aperture; Run ID: 110541. Top panel is the SSX spectrum. Middle panel is the SS5 spectrum. Bottom panel is the measured effective area.

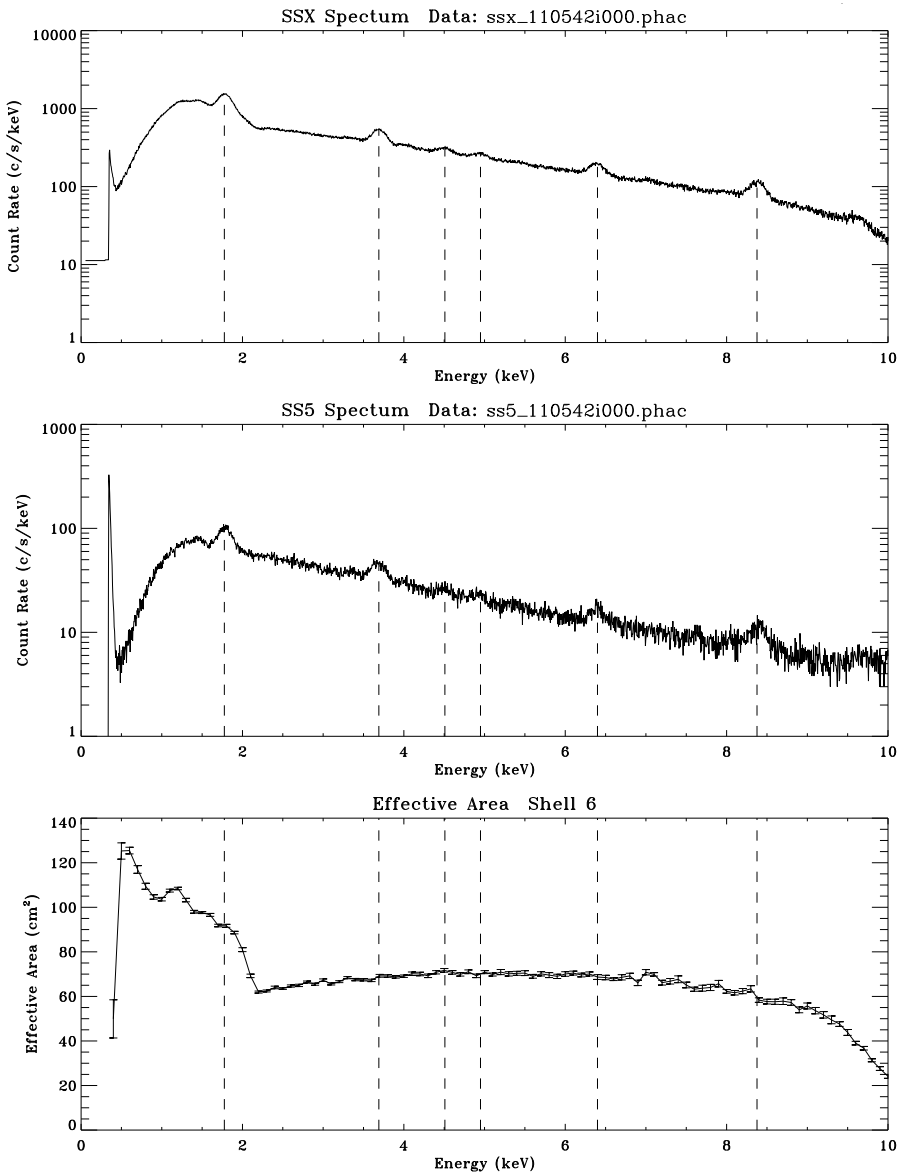

Figure 11.35: SSD C-continuum effective area measurement: Shell 6; 2 mm aperture; Run ID: 110542. Top panel is the SSX spectrum. Middle panel is the SS5 spectrum. Bottom panel is the measured effective area.

surface of the Central Aperture Plate), i.e. 526.01236 meters from the source.[4]

For the C-continuum SSD measurements, the HRMA mirror effective area, $A_{\mathit{eff}}(E)$, is:

$$A_{\mathit{eff}}(E) = \frac{C_{ssx}(E)}{C_{ss5}(E)} \cdot \frac{PDC_{ssx}}{PDC_{ss5}} \cdot \frac{D_{hrma}^2}{D_{ss5}^2} \cdot A_{ss5} \cdot R(E) \tag{11.12}$$

where

- $C_{ssx}(E)$ and $C_{ss5}(E)$ are the ssd_x and ssd_5 spectra with the correct energy scale and equal energy bins (in units of counts/second/keV).
- PDC_{ssx} and PDC_{ss5} are the pulser deadtime corrections for the ssd_x and ssd_5.
- $D_{hrma} = 526.01236$ meter is the distance from the source to the HRMA pre-collimater entrance, where the effective area is defined.
- $D_{ss5} = 38.199$ meters is the distance from the source to ssd_5.
- A_{ss5} is the ssd_5 aperture area. A 2 mm aperture was used for all the measurements. Its actual equivalent diameter is 1.9990 ± 0.0073 mm. So $A_{ss5} = 0.031385 \pm 0.00023$ cm^2
- R(E) $= 1.0141 \pm 0.0089$ is the relative ssd_5/ssd_x quantum efficiency from the flat field test.

Because each of the ssd_5 spectra are rather noisy, four ssd_5 spectra are averaged to make $C_{ss5}(E)$, which has the noise reduced by a factor of two. The source intensity was stable enough during these four measurements so the temporal fluctuation is negligible.

The $C_{ssx}(E)$ and $C_{ss5}(E)$ are obtained using the method discussed in the previous Section. The PDC_{ssx} and PDC_{ss5} are obtained using the method discussed in §11.6 and listed in Table 11.6.

Table 11.6: Effective Area Measurements SSD Pulser Deadtime Corrections

Run ID	PDC$_{ssx}$	PDC$_{average\ ss5}$	PDC$_{ssx}$/PDC$_{average\ ss5}$
110539	1.11827	1.01651	1.10011
110540	1.10408	1.01651	1.08615
110541	1.09579	1.01651	1.07799
110542	1.07069	1.01651	1.05330

So the effective area of each HRMA shell measured with the C-continuum and SSD is:

$$\begin{aligned} A_{\mathit{eff}}(E) &= \frac{C_{ssx}(E)}{C_{average\ ss5}(E)} \cdot \frac{PDC_{ssx}}{PDC_{average\ ss5}} \cdot \frac{526.01236^2}{38.199^2} \cdot 0.031385 \cdot 1.0141 \qquad (cm^2) \\ &= 6.03519 \cdot \frac{C_{ssx}(E)}{C_{average\ ss5}(E)} \cdot \frac{PDC_{ssx}}{PDC_{average\ ss5}} \qquad (cm^2) \end{aligned} \tag{11.13}$$

The bottom panels of Figures 11.32–11.35 show the effective area results according to Eq. 11.13. The six vertical dashed lines are the six energy lines used to determine the energy scale. Each

[4]This definition is necessary because of the diverging X-ray beam at the XRCF. It is not necessary for on-orbit case as the X-rays are parallel and the effective area is the same in any plane.

effective area curve was binned into 0.1 keV energy bins. According to the SSD energy scale, there are 20 channels in each energy bin. The plotted error bars are the standard deviation of the mean in the energy bins. Systematic errors such as the ssd_5 aperture area uncertainly (0.0073) and the SSD quantum efficiency ratio error (0.0088) are not included in these four plots but will be included later in the final results.

11.13 Error Analysis

The error of the HRMA effective area is:

$$\sigma_{ea} = (\sigma_{e-bin}^2 + \sigma_{2mm-ap}^2 + \sigma_{qe}^2)^{1/2} \tag{11.14}$$

where

σ_{e-bin}	Standard deviation of the mean in each 0.1 keV bin of the SSD spectra	∼1–4%
σ_{2mm-ap}	Uncertainty of the ssd_5 2 mm aperture area (0.031385 ± 0.00023 cm^2)	0.73%
σ_{qe}	Error of the SSD quantum efficiency ratio (1.0141 ± 0.0089)	0.88%
σ_{ea}	Effective area error	∼1.3–4%

where the error of the SSD quantum efficiency ratio is from the flat field test data reduction:

$$\sigma_{qe} = (\sigma_{std}^2 + \sigma_{bu}^2 + \sigma_{ap}^2)^{1/2} \tag{11.15}$$

where

σ_{std}	Standard deviation of the mean of QE ratio flatfield data in 3–10 keV band	0.21%
σ_{bu}	Error of beam uniformity	0.34%
σ_{ap}	Uncertainty of the 2 mm and 5 mm aperture areas	0.79%
σ_{qe}	Total quantum efficiency ratio error	0.88%

For the effective area of the entire HRMA, the absolute errors are the quadrature sum of the absolute errors from the four shells. Therefore its relative errors are reduced accordingly, to ∼0.7–3.6%.

11.14 Comparing Measurements with the Raytrace Prediction

Figures 11.36–11.39 compare the measured effective area with the raytrace prediction within a 2 mm aperture for each mirror shells. In the top panels, the solid lines are the raytrace predictions, the dotted lines are the SSD measured effective area with the C-continuum source, which is the same as plotted in the bottom panel of Figures 11.32–11.35. As mentioned before, the SSD data below 2 keV (most parts are higher than the raytrace prediction) should be ignored due to the icing effect. The FPC spectral line data are also plotted in the figures for comparison.

For energies above 2 keV, the data are significantly below the prediction, especially for shell 1. The bottom panels of Figures 11.36–11.39 show the effective area ratio of data/raytrace. It is seen that for shell 1, the data is about ∼10–15% less than the prediction at 2–4 keV and ∼15–30% less than the prediction for shell 1 at 4–6 keV. For other shells the discrepancies are less than 15%.

Figure 11.40 shows the full HRMA effective area data with the raytrace prediction within a 2 mm aperture. The SSD C-continuum data and four of the seven FPC line spectral data (0.277 keV, 1.49 keV, 4.51 keV and 6.40keV) are the sums of data from the four shells. The SSD line spectral

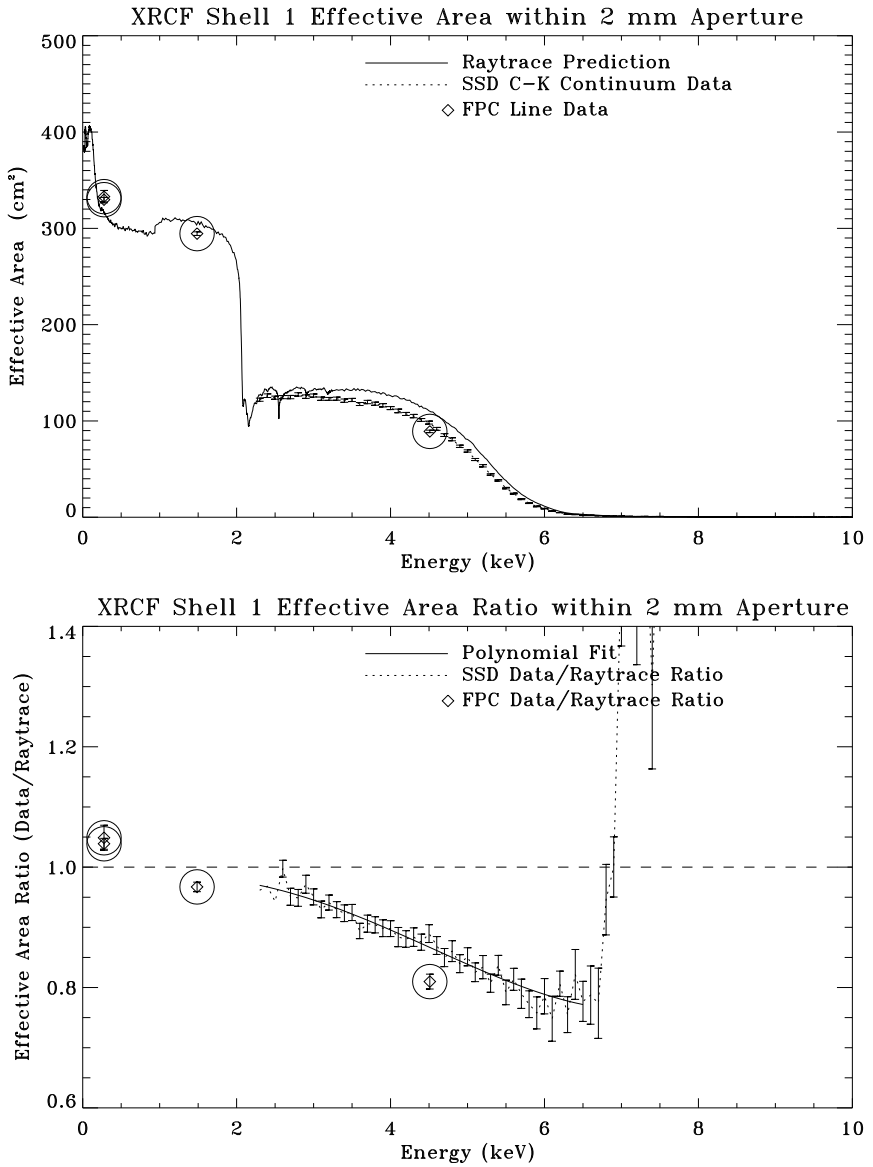

Figure 11.36: Calibration data vs. raytrace prediction. Top panel shows the XRCF Shell 1 effective area within 2 mm aperture. Bottom panel shows the effective area ratio of data/raytrace.

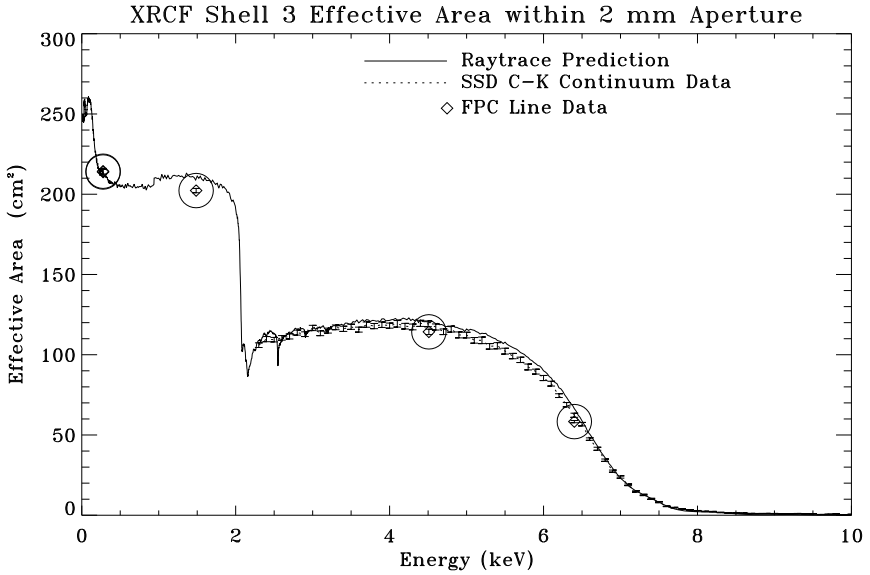

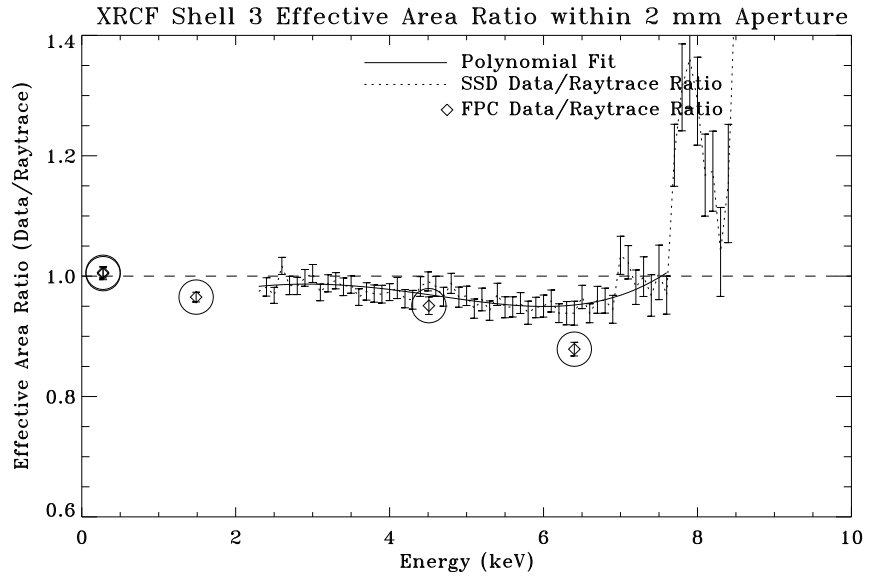

Figure 11.37: Calibration data vs. raytrace prediction. Top panel shows the XRCF Shell 3 effective area within 2 mm aperture. Bottom panel shows the effective area ratio of data/raytrace.

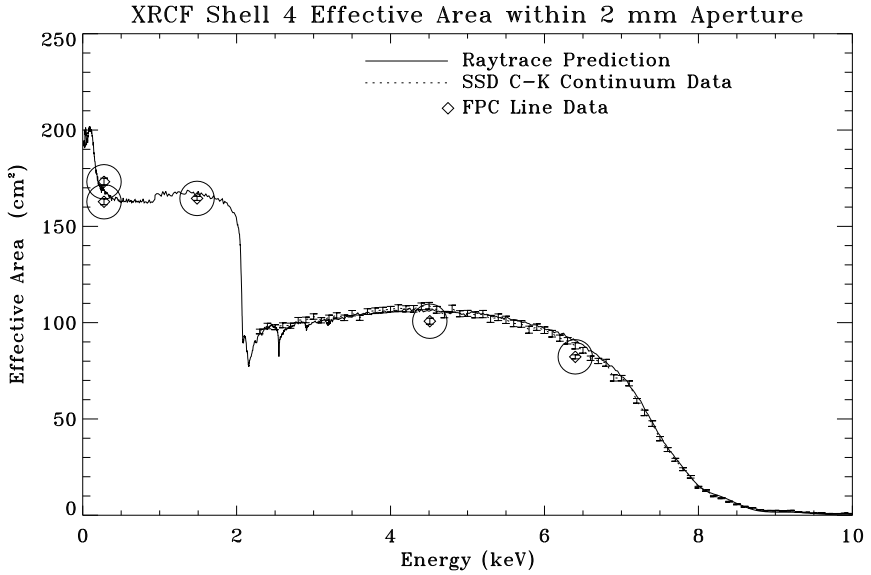

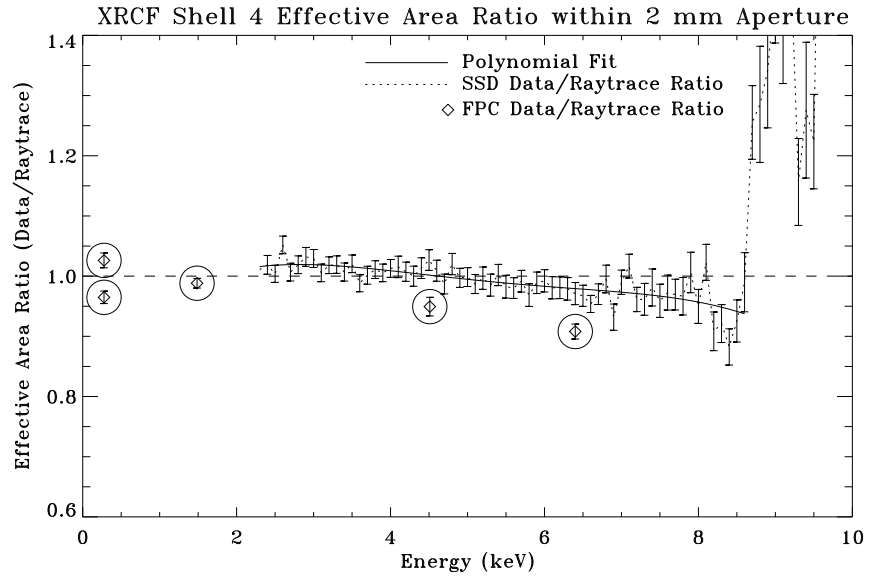

Figure 11.38: Calibration data vs. raytrace prediction. Top panel shows the XRCF Shell 4 effective area within 2 mm aperture. Bottom panel shows the effective area ratio of data/raytrace.

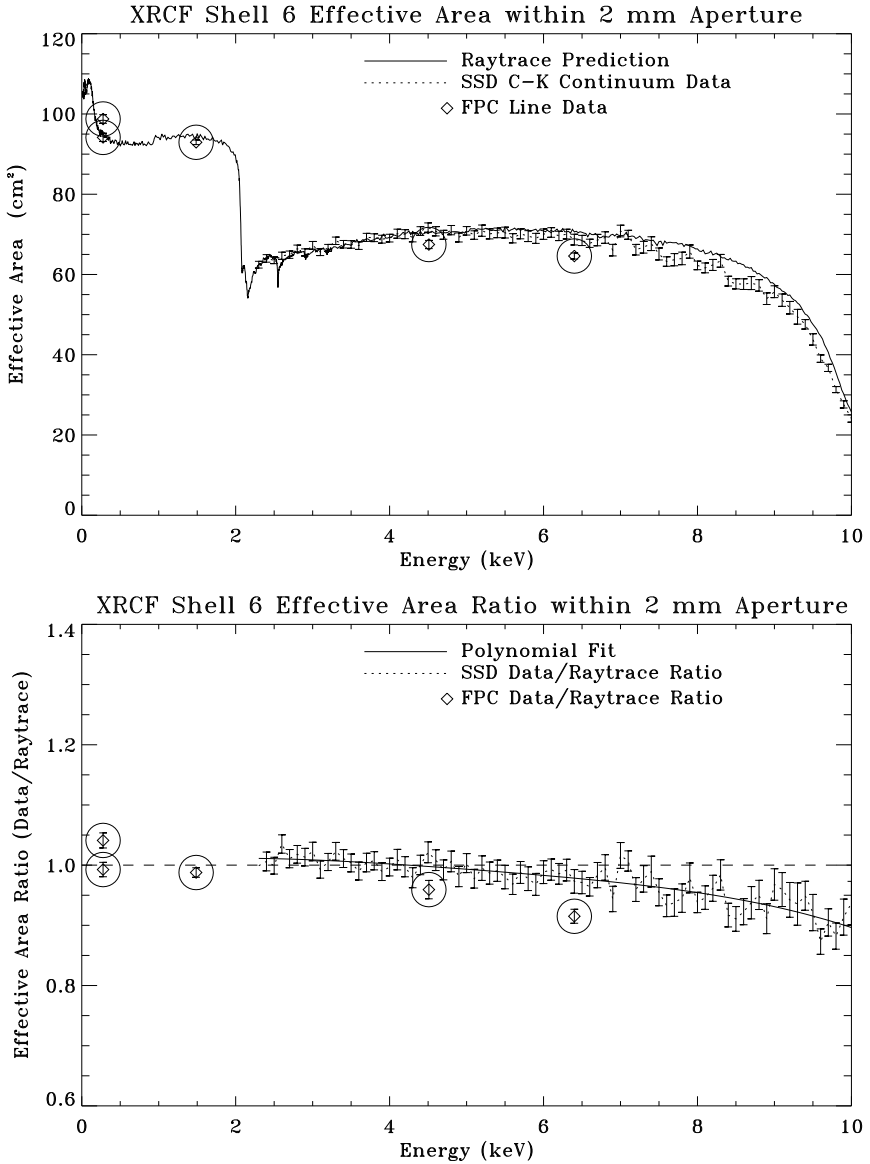

Figure 11.39: Calibration data vs. raytrace prediction. Top panel shows the XRCF Shell 6 effective area within 2 mm aperture. Bottom panel shows the effective area ratio of data/raytrace.

data and three of the seven FPC line spectral data (0.93 keV, 5.41 keV and 8.03 keV) are the direct measurements of the full HRMA. The data are below the raytrace prediction by ∼5–10% in the 2–10 keV band. In the raytrace prediction, there is a dip near the Ir M-edge (2.05 keV). The SSD C-continuum data could not reveal it due to the finite spectral resolution of the SSD. However, the SSD spectral line measurement at the 2.16 keV (Nb-L) did show a dip. The fluctuations in the EA ratio curves near the Ir M-edge in the 2.0–2.3 keV region are also due to the finite spectral resolution of the SSD.

In Figures 11.36–11.40, most of the FPC line data are below the SSD continuum data. Presently we do not know the exact cause of this. We hope to resolve this discrepancy as this work progresses.

Figures 11.36–11.40 can be accessed on the World Wide Web page:

http://hea-www.harvard.edu/MST/mirror/www/xrcf/hrma_ea.html

at the beginning of the web page, please click:

Shell 1 Effective Area within 2 mm aperture

Shell 3 Effective Area within 2 mm aperture

Shell 4 Effective Area within 2 mm aperture

Shell 6 Effective Area within 2 mm aperture

HRMA Effective Area within 2 mm aperture

11.15 Calibrating the HRMA Effective Area

The XRCF HRMA effective area raytrace predictions were originally generated based on the HRMA model which is accurate to the best of our knowledge, including the HRMA tilt and decenter measured during the calibration. However, as we can see in the previous section, the calibration data show that for energies higher than 2 keV, the measured effective area is substantially less than the predicted effective area by well more than the experimental errors, especially for shell 1. At least part of this discrepancy is due to differences in the way the raytrace model calculates reflectivity, compared to our derivation of optical constants via our synchrotron measurements. There are also some discrepancies between the mirror surface roughness scattering model and the data measured from the wing scan measurements (see Chapter 14). We are currently assessing and correcting for these differences. For the present, based on the principle that theory should yield to the experiment, we use the XRCF calibration data to scale down the raytrace empirically for both on-orbit and XRCF HRMA effective area predictions.

In order to smooth the Poisson noise in the correction factor, a fourth order polynomial is used to fit the deficit curve of the effective area ratio between 2.3 keV and 10 keV. The polynomial fit curves for the four shells and the HRMA are plotted as solid curves in the bottom panels of Figures 11.36–11.40. These polynomials as functions of energy are to be used to scale the raytrace prediction. For higher energies where the effective area drops to below a few cm^2 (i.e. $\geq$6.7 keV for shell 1, $\geq$7.9 keV for shell 3, and $\geq$9.0 keV for shell 4), there are not enough data to make a reasonable fit, and a ratio of unity is used.

Since the SSD data are not reliable for lower energies, FPC spectral line data for energies below 2.3 keV are used for scaling. The average ratios between the FPC data and the raytrace are used as the scaling factor. They are 1.0234 , 0.9983, 0.9998, 1.0136, and 1.0055, for shells 1,3,4,6 and the HRMA, respectively.

The errors for the scaling factors are:

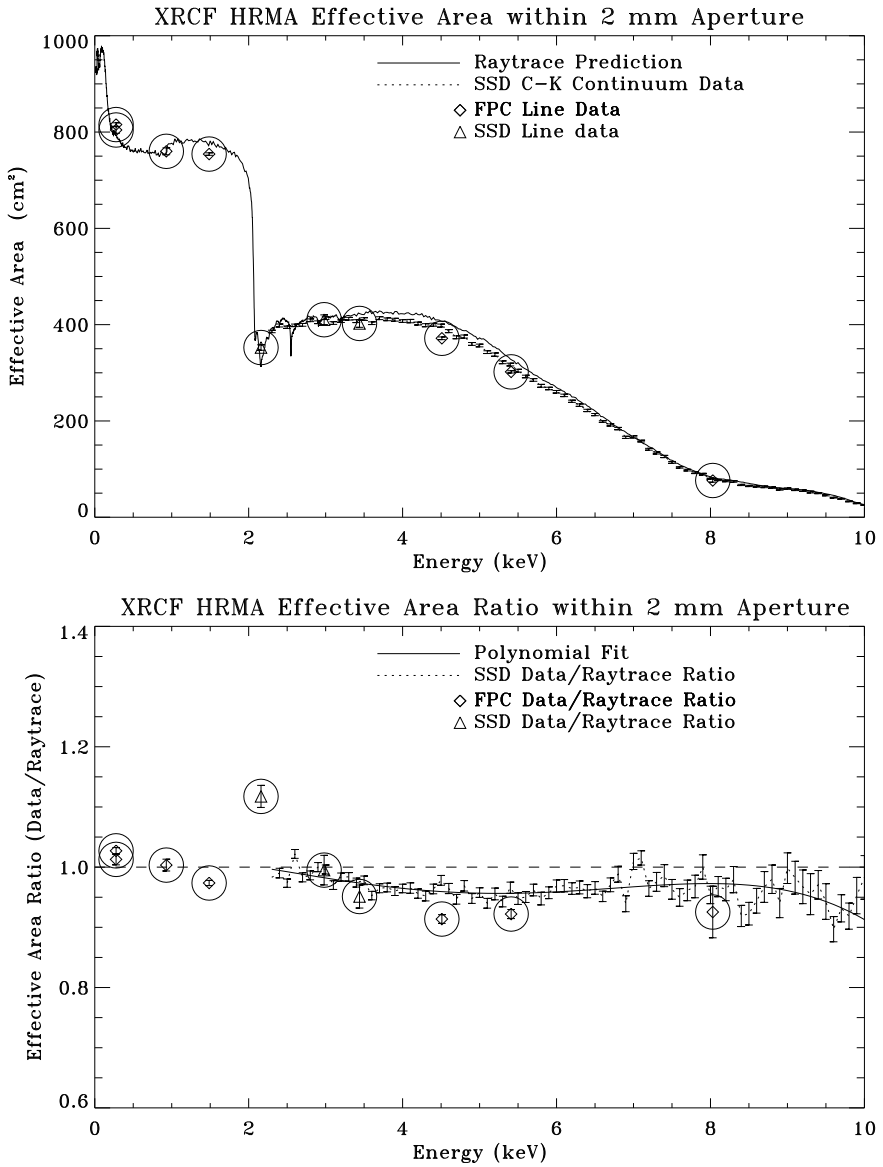

Figure 11.40: Calibration data vs. raytrace prediction. Top panel shows the XRCF HRMA effective area within 2 mm aperture. Bottom panel shows the effective area ratio of data/raytrace.

E < 2.3 keV:	FPC measurement errors	0.3–1.9%
	Deviations of the FPC data from the scaling factor	0.7–3.2%
	Statistical errors from raytrace simulation	<0.3%
	Total scaling factor errors	∼1.1–3.4%
E ≥ 2.3 keV:	Standard deviation of the polynomial fit	1.7–3.3%
	Deviation of each data point from the polynomial fit	0.2–6.0%
	Statistical errors from raytrace simulation	<0.3%
	Total scaling factor errors	∼2–7%

In the next three Sections we describe the raytrace predictions and the calibrated effective area at XRCF and on-orbit cases.

11.16 HRMA Effective Area Raytrace Predictions

The original raytrace predictions of the HRMA effective area for both the on-orbit and at XRCF cases were generated based on the HRMA model. The HRMA model includes mirror tilts and decenters measured at Kodak and XRCF, mirror low frequency surface maps from the HDOS metrology measurements, mirror CAP, pre- and post-collimators, apertures, ghost baffles, and mirror distortion due to epoxy cure shrinkage. For the XRCF case, the HRMA model also includes the finite source distance at the XRCF and the mirror distortion due to gravity.

The reflectivities are based on:[5]

E < 2 keV: Gullikson '95 optical constant table. (Henke et al., 1993)

E ≥ 2 keV: AXAF mirror witness flat synchrotron measurements made by Graessle et al. (Graessle et al., 1997)

The mirror surface roughness scattering is based on the Power Spectral Density (PSD) produced from the HDOS metrology measurements and calculated with a program "foldw1" written by Leon Van Speybroeck, which is based on the scattering theory by Beckmann and Spizzichino. (Beckmann and Spizzichino, 1963)

The XRCF HRMA trace-shell configuration file can be found at
http://hea-www.harvard.edu/MST/simul/raytrace/databases/ts_config/00Index.html
#xrcf_SAO1G+HDOS_HDOS-scat-980623_01

The on-orbit HRMA trace-shell configuration file can be found at
http://hea-www.harvard.edu/MST/simul/raytrace/databases/ts_config/00Index.html
#orbit_HDOS+HATS+XRCF_scat-980623_01

Figures 11.41–11.45 show the raytrace predicted effective areas and encircled energies of the four shells and the HRMA at the XRCF. The top panels shows the effective area curves within 2 mm, 35 mm diameter apertures, and 2π steradians. The bottom panels show the encircled energies of 2 mm and 35 mm apertures as fractions of that within 2π steradians.

Figures 11.46–11.50 show the raytrace predicted effective areas and encircled energies of the four shells and the HRMA on-orbit.

The purpose of showing these figures is to compare the encircled energy curves between the XRCF and the on-orbit cases.

[5]Because we used different optical constant tables for E < 2 keV and E ≥ 2 keV for the raytracing, there is a discontinuity at 2 keV in all the raytrace effective area curves. Obviously this discontinuity is not real and the optical constant in two tables should agree at 2 keV. We are currently working to resolve this discrepancy.

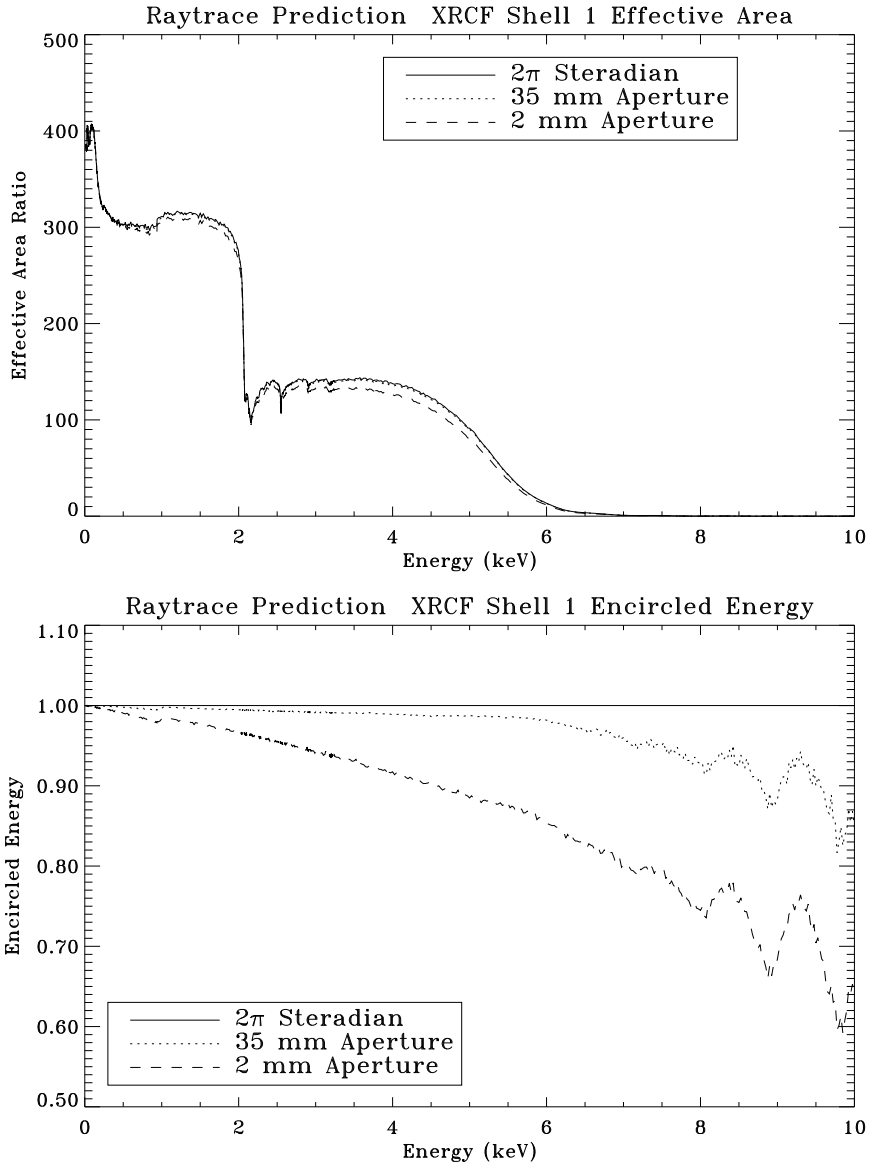

Figure 11.41: Raytrace prediction of XRCF Shell 1 effective area and encircled energy. Top panel shows the effective area curves within 2 mm, 35 mm apertures, and 2π steradian. Bottom panel shows the encircled energies of 2 mm and 35 mm apertures as fractions of that within 2π steradian.

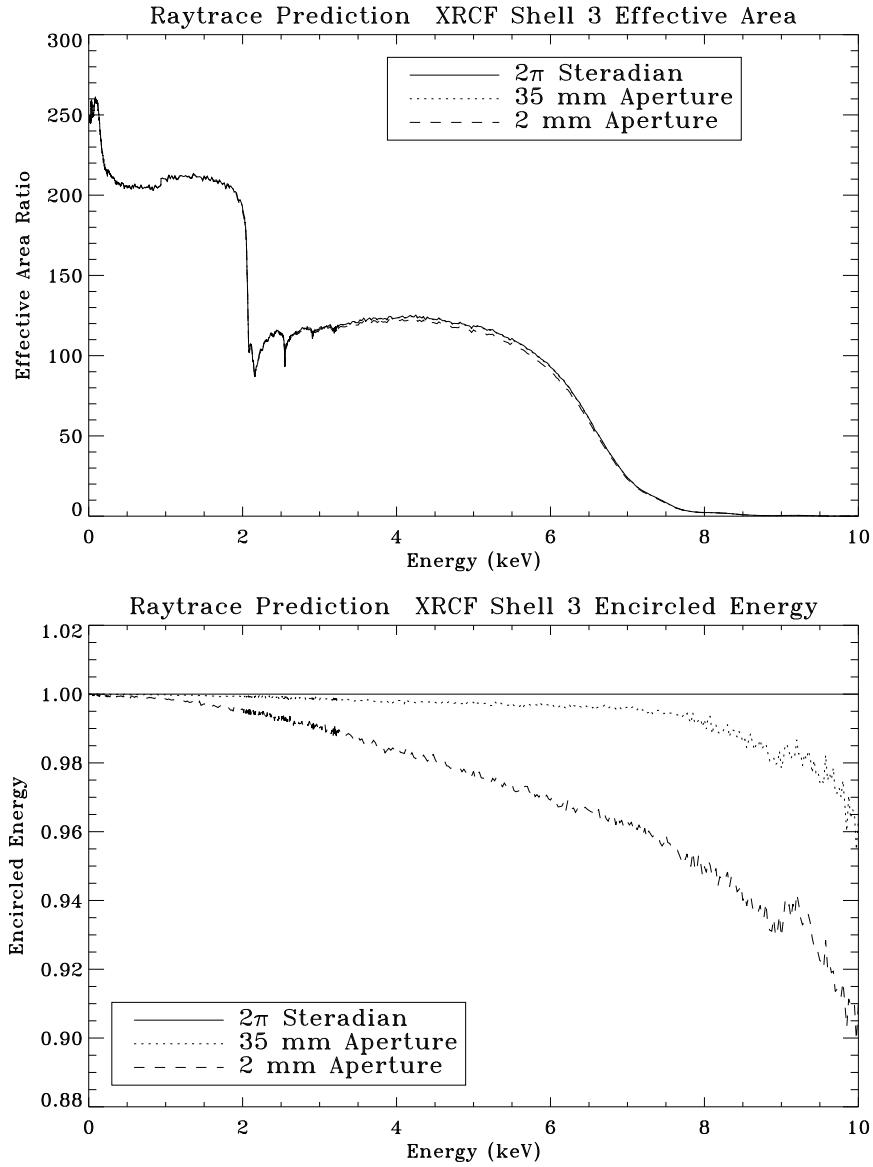

Figure 11.42: Raytrace prediction of XRCF Shell 3 effective area and encircled energy. Top panel shows the effective area curves within 2 mm, 35 mm apertures, and 2π steradian. Bottom panel shows the encircled energies of 2 mm and 35 mm apertures as fractions of that within 2π steradian.

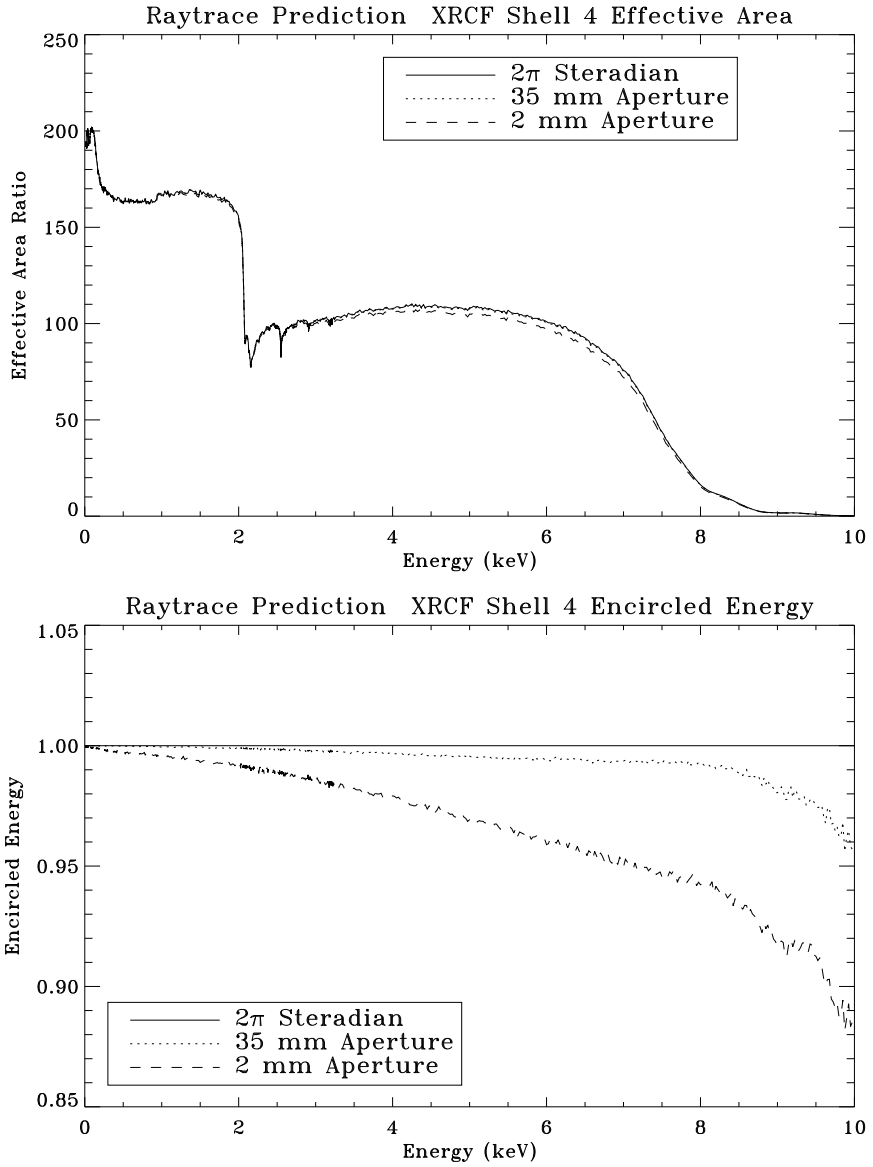

Figure 11.43: Raytrace prediction of XRCF Shell 4 effective area and encircled energy. Top panel shows the effective area curves within 2 mm, 35 mm apertures, and 2π steradian. Bottom panel shows the encircled energies of 2 mm and 35 mm apertures as fractions of that within 2π steradian.

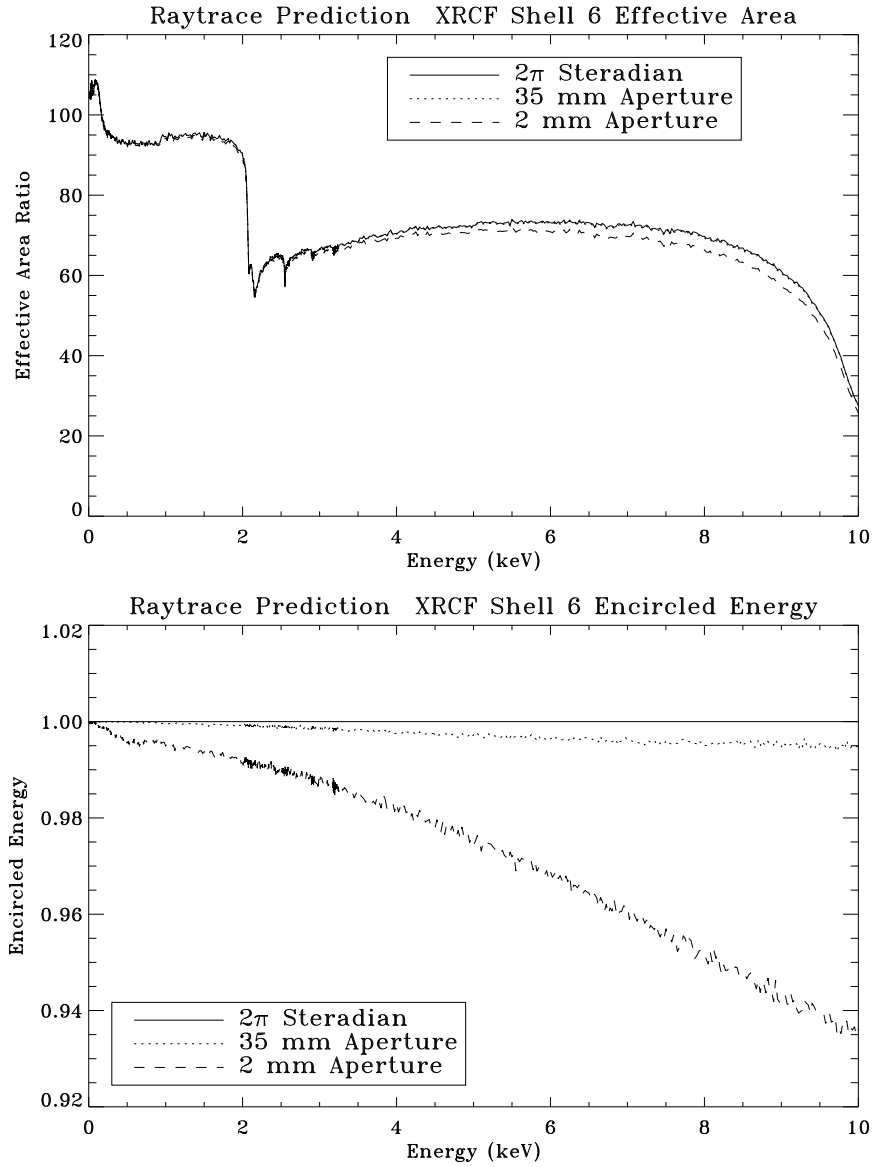

Figure 11.44: Raytrace prediction of XRCF Shell 6 effective area and encircled energy. Top panel shows the effective area curves within 2 mm, 35 mm apertures, and 2π steradian. Bottom panel shows the encircled energies of 2 mm and 35 mm apertures as fractions of that within 2π steradian.

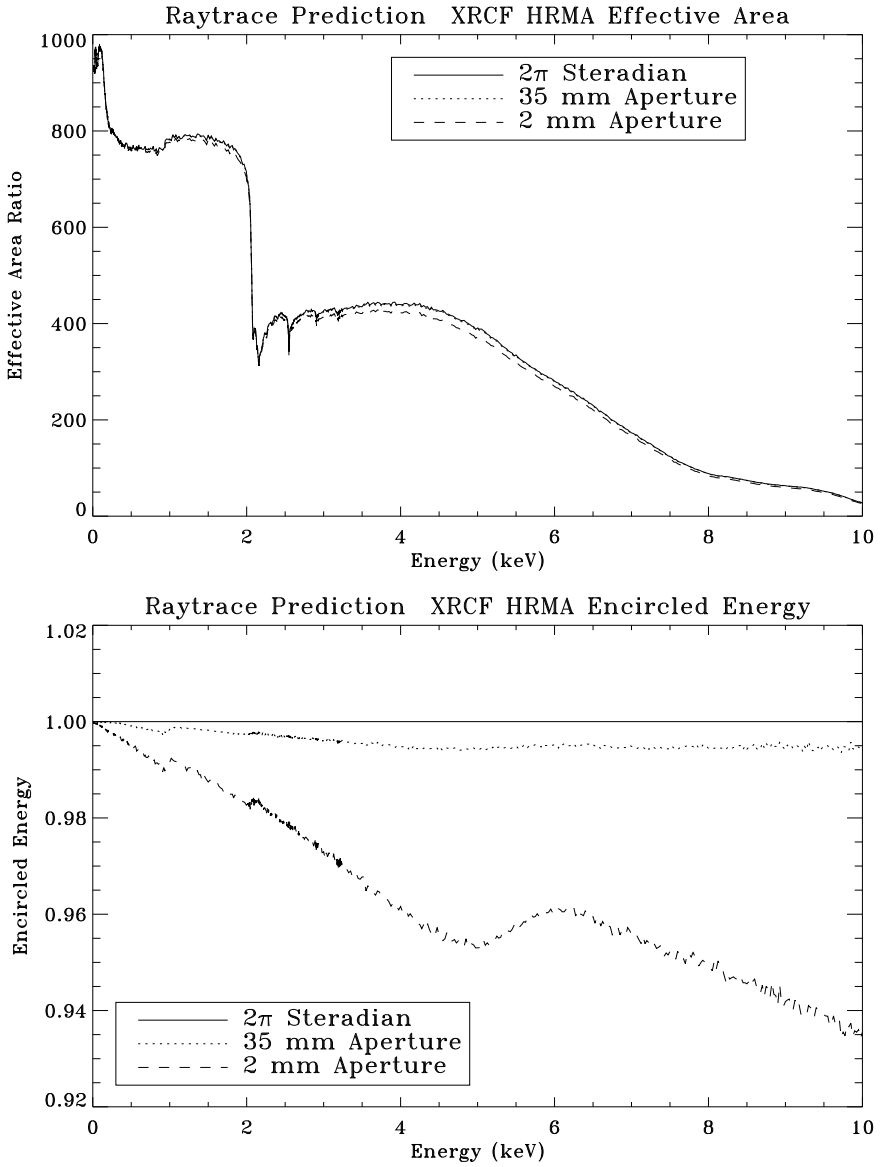

Figure 11.45: Raytrace prediction of XRCF HRMA effective area and encircled energy. Top panel shows the effective area curves within 2 mm, 35 mm apertures, and 2π steradian. Bottom panel shows the encircled energies of 2 mm and 35 mm apertures as fractions of that within 2π steradian.

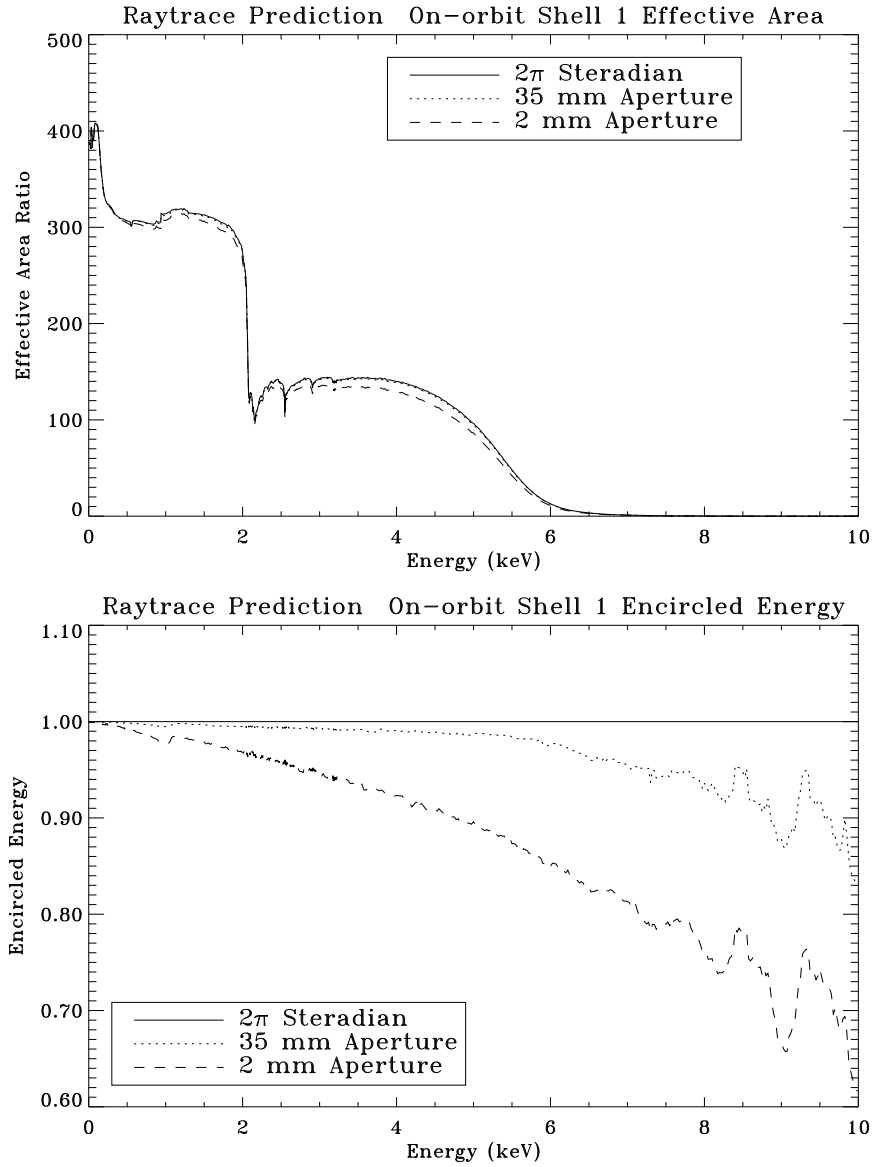

Figure 11.46: Raytrace prediction of on-orbit Shell 1 effective area and encircled energy. Top panel shows the effective area curves within 2 mm, 35 mm apertures, and 2π steradian. Bottom panel shows the encircled energies of 2 mm and 35 mm apertures as fractions of that within 2π steradian.

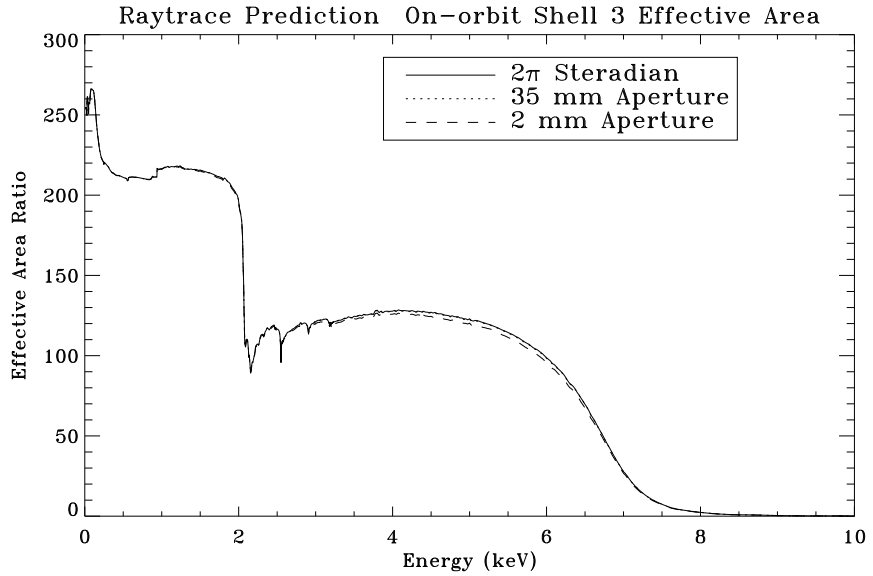

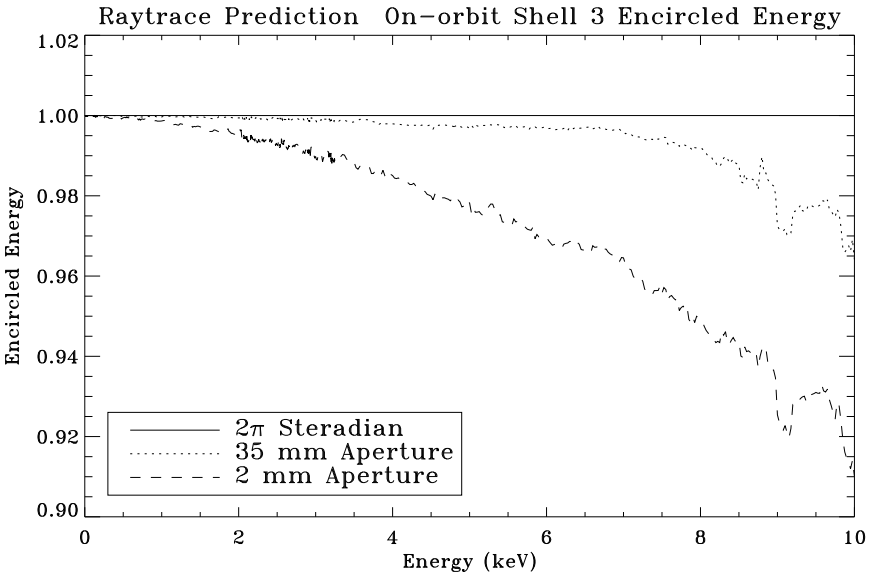

Figure 11.47: Raytrace prediction of on-orbit Shell 3 effective area and encircled energy. Top panel shows the effective area curves within 2 mm, 35 mm apertures, and 2π steradian. Bottom panel shows the encircled energies of 2 mm and 35 mm apertures as fractions of that within 2π steradian.

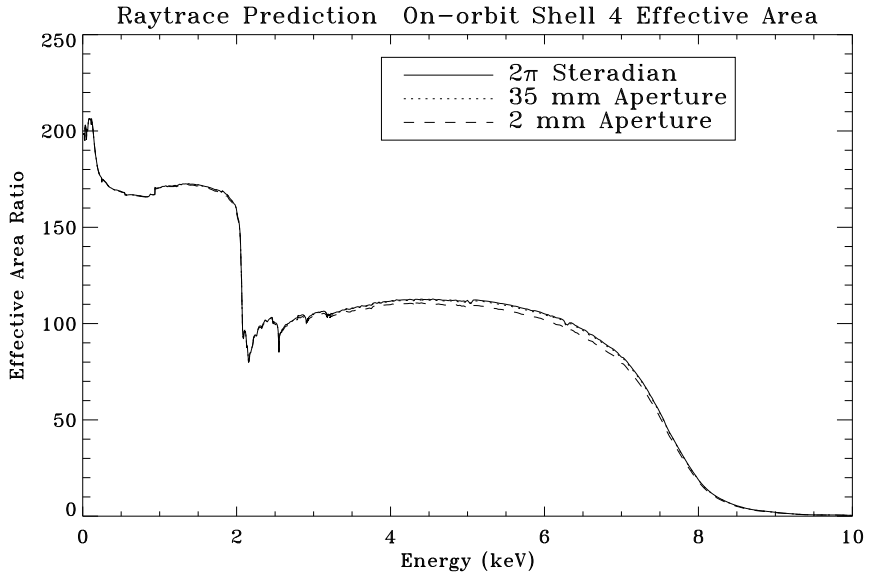

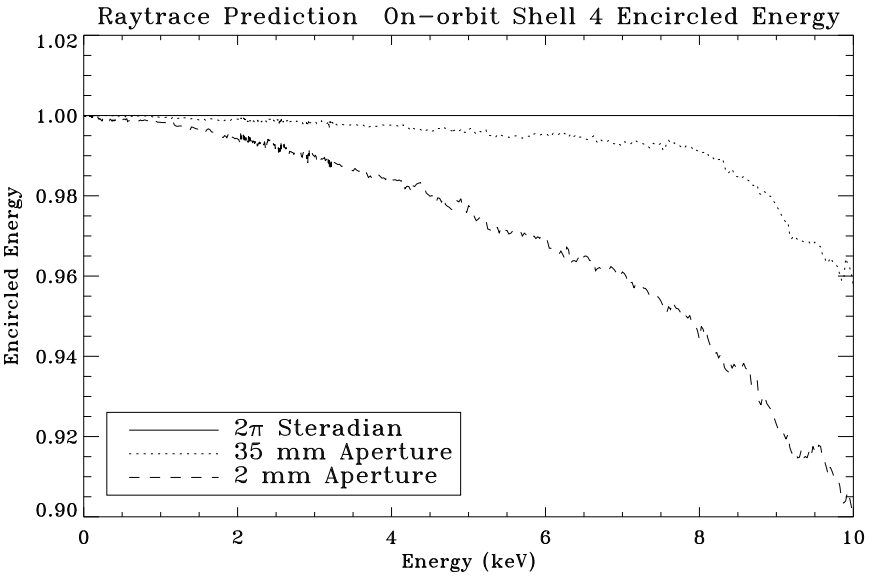

Figure 11.48: Raytrace prediction of on-orbit Shell 4 effective area and encircled energy. Top panel shows the effective area curves within 2 mm, 35 mm apertures, and 2π steradian. Bottom panel shows the encircled energies of 2 mm and 35 mm apertures as fractions of that within 2π steradian.

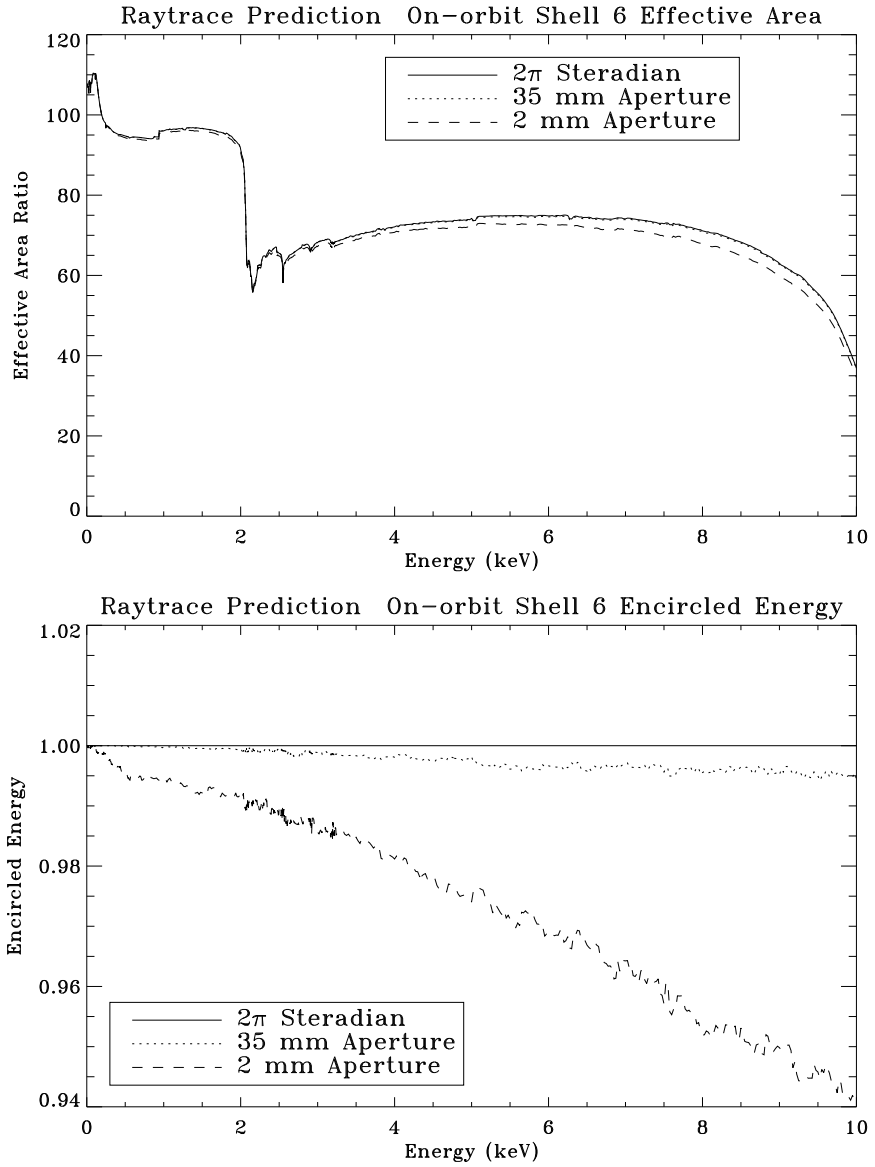

Figure 11.49: Raytrace prediction of on-orbit Shell 6 effective area and encircled energy. Top panel shows the effective area curves within 2 mm, 35 mm apertures, and 2π steradian. Bottom panel shows the encircled energies of 2 mm and 35 mm apertures as fractions of that within 2π steradian.

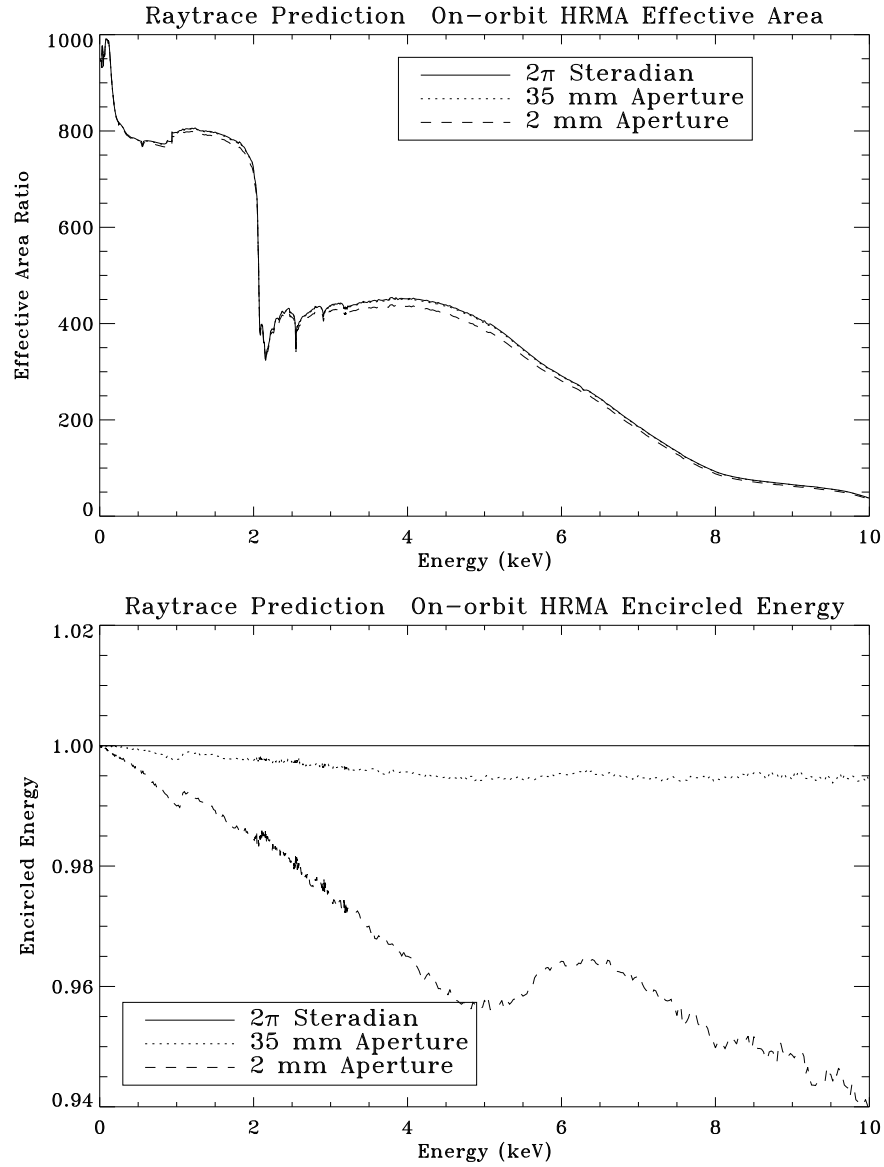

Figure 11.50: Raytrace prediction of on-orbit HRMA effective area and encircled energy. Top panel shows the effective area curves within 2 mm, 35 mm apertures, and 2π steradian. Bottom panel shows the encircled energies of 2 mm and 35 mm apertures as fractions of that within 2π steradian.

Since the SSD C-continuum effective area data we reduced are for only 2 mm aperture, we should be able to use these data to scale down the raytrace predicted XRCF effective area curve within 2 mm diameter. How about the XRCF effective area within larger apertures and 2π steradians? How about the on-orbit cases? Can we use the XRCF 2 mm aperture measurement to scale down other effective area curves the same way?

Let's first look at the XRCF cases. The fractional encircled energy within 2 mm aperture varies as a function of energy and from shell to shell. For shell 1 at 6.5 keV, it can be as low as 86% (see Figure 11.41). For other shells, the fractional encircled energy curve are all higher than 92%. Can we use the 2 mm aperture data to scale down the effective area within larger apertures and 2π steradians? The short answer is "we don't know", because we still don't know the exact cause or causes of the discrepancy between the data and the model. But we have some FPC spectral line measurements using the 35 mm diameter aperture (see Chapter 3). The data disagree with the raytrace prediction by about the same amount as the 2 mm aperture data did. As we can see the fractional encircled energy within 35 mm aperture are more than 99% for almost all the shells and all energies (see Figures 11.41–11.45). Therefore with good confidence we should be able to use the 2 mm aperture data scale down the XRCF effective area within larger apertures as well as within the 2π steradians.

Next let's look at the on-orbit cases. The effective area and fractional encircled energy curves are very similar to the same curves for the XRCF cases. Therefore we can, with the same confident level, scale down the on-orbit HRMA effective area prediction curve the same way as for the XRCF cases.

Therefore, we will use the 2 mm aperture calibration data to scale down the raytrace predicted effective areas within any apertures greater or equal to 2 mm diameter for both on-orbit and at XRCF cases.

11.17 XRCF HRMA Effective Area

Figures 11.51–11.53 show the XRCF HRMA and four shells effective areas within 2 mm, 35 mm diameters and 2π steradians, for the original raytrace and the calibrated curves with errors estimated in §11.15. Tables 11.7 – 11.9 list the values of the XRCF effective areas with energy grid of 0.1 keV.[6] The "rdb" tables on the web (see below) have denser energy grid.

These are our current best estimates for the HRMA effective area at the XRCF. Other calibration teams can use these data to calibrate their instruments. The "rdb" tables of the XRCF HRMA effective area, as well as Figures 11.51–11.53, can be accessed on the World Wide Web page:

http://hea-www.harvard.edu/MST/mirror/www/xrcf/hrma_ea.html

at the bottom of the web page, please click:

XRCF HRMA Effective Area within 2 mm aperture and its figure.

XRCF HRMA Effective Area within 35 mm aperture and its figure.

XRCF HRMA Effective Area within 2pi steradians and its figure.

[6] Careful readers will notice that the effective area of four shells do not exactly add up to the HRMA effective area listed in the tables. This is because, when generating these tables, we used polynomial curves to fit the deficit curve of the effective area ratio of the four shells and of the HRMA to smooth our the noise. This process produces the small discrepancy as seen here. However, the discrepancy is only 1-2% and well within the quoted errors.

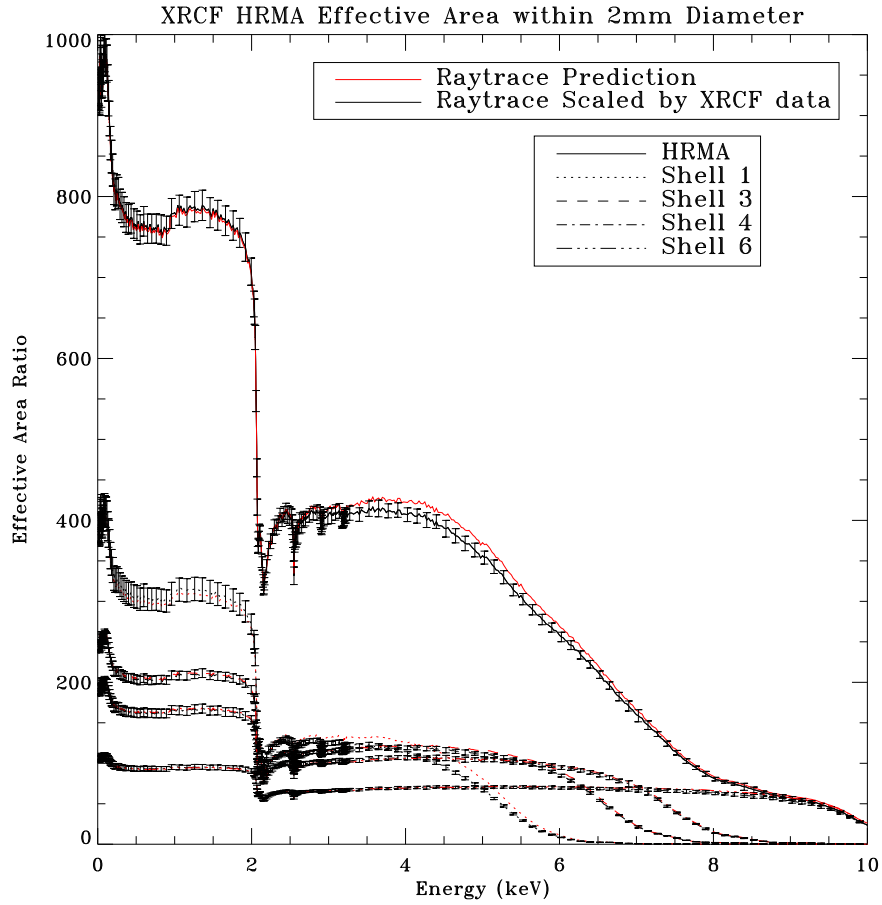

Figure 11.51: The XRCF HRMA and four shells effective areas within 2 mm aperture. The original raytrace predictions and the calibration data scaled raytrace predictions.

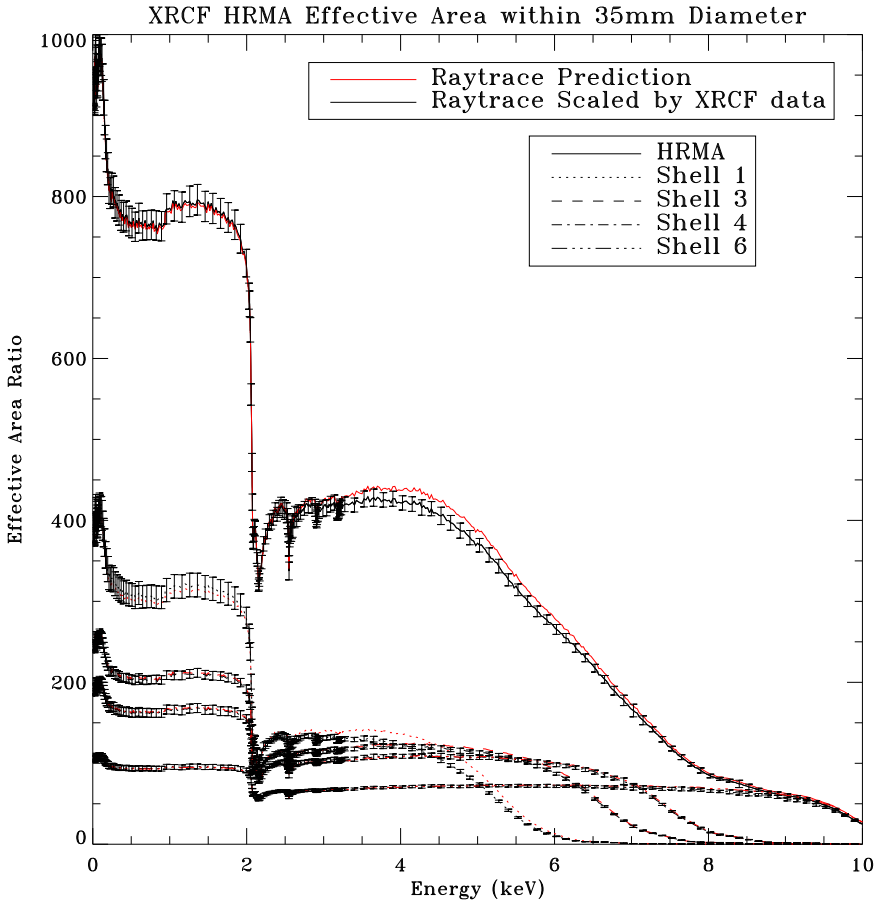

Figure 11.52: The XRCF HRMA and four shells effective areas within 35 mm aperture. The original raytrace predictions and the calibration data scaled raytrace predictions.

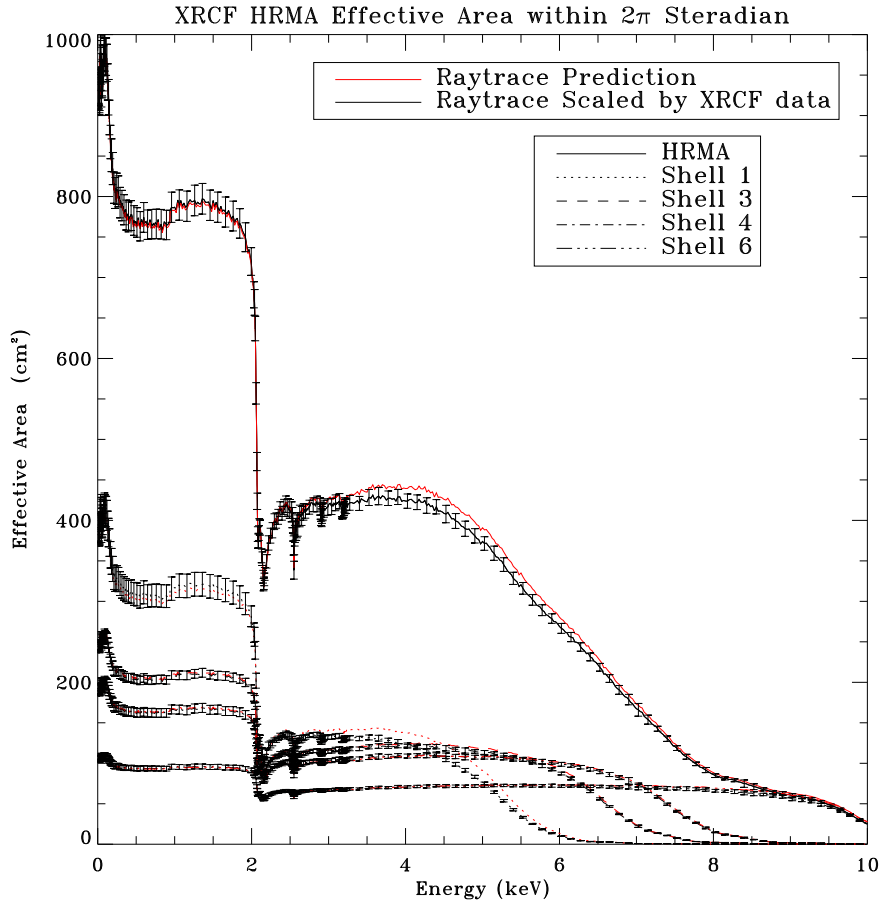

Figure 11.53: The XRCF HRMA and four shells effective areas within 2π steradian. The original raytrace predictions and the calibration data scaled raytrace predictions.

Table 11.7: XRCF HRMA Effective Area within 2 mm Aperture. Units: cm^2

Energy	Shell 1		Shell 3		Shell 4		Shell 6		HRMA	
(keV)	A_{eff}	Error	A_{eff}	Error	A_{eff}	Error	A_{eff}	Error	A_{eff}	Error
0.10	413.70	11.68	257.57	2.90	199.79	6.71	108.90	2.90	974.86	15.63
0.20	338.44	9.56	219.28	2.47	173.26	5.82	97.95	2.61	824.80	13.22
0.30	324.28	9.16	211.96	2.39	168.09	5.64	95.75	2.55	796.13	12.76
0.40	314.85	8.89	207.16	2.33	164.66	5.53	94.29	2.51	777.14	12.46
0.50	311.89	8.81	205.79	2.32	163.69	5.50	93.82	2.50	771.40	12.37
0.60	312.13	8.81	206.11	2.32	163.91	5.50	93.95	2.51	772.31	12.38
0.70	311.07	8.78	205.76	2.32	163.66	5.49	93.89	2.50	770.61	12.35
0.80	309.10	8.73	204.92	2.31	163.11	5.48	93.67	2.50	767.06	12.30
0.90	311.13	8.79	206.23	2.32	164.01	5.51	94.08	2.51	771.69	12.37
1.00	310.91	8.78	206.37	2.32	164.09	5.51	94.11	2.51	771.70	12.37
1.10	310.81	8.78	206.59	2.33	164.26	5.51	94.22	2.51	772.12	12.38
1.20	309.77	8.75	206.36	2.32	164.14	5.51	94.17	2.51	770.69	12.35
1.30	308.27	8.71	205.87	2.32	163.82	5.50	94.07	2.51	768.31	12.32
1.40	306.12	8.65	205.08	2.31	163.31	5.48	93.87	2.50	764.69	12.26
1.50	302.93	8.56	203.86	2.30	162.51	5.46	93.56	2.50	759.21	12.17
1.60	298.93	8.44	202.13	2.28	161.28	5.41	93.08	2.48	751.82	12.05
1.70	293.10	8.28	199.48	2.25	159.49	5.35	92.36	2.46	740.92	11.88
1.80	284.30	8.03	195.28	2.20	156.65	5.26	91.21	2.43	724.03	11.61
1.90	268.38	7.58	187.51	2.11	151.30	5.08	89.00	2.37	693.01	11.11
2.00	244.30	6.90	175.51	1.98	143.06	4.80	85.59	2.28	645.58	10.35
2.10	128.98	3.64	108.01	1.22	94.03	3.16	63.29	1.69	392.87	6.30
2.20	115.99	3.28	98.58	1.11	86.55	2.91	59.40	1.58	359.23	5.76
2.30	123.30	4.28	107.20	2.97	96.11	2.34	63.19	1.34	392.21	10.01
2.40	126.41	4.19	109.99	2.75	98.26	2.27	64.22	1.13	400.53	8.14
2.50	126.07	4.64	110.65	3.06	98.78	2.59	64.53	1.52	400.95	10.11
2.60	120.46	5.66	107.32	4.05	96.13	3.26	63.26	1.74	387.35	13.14
2.70	125.95	4.40	111.92	2.83	99.71	2.69	65.00	1.13	402.36	8.38
2.80	127.71	4.30	114.10	2.85	101.40	2.35	65.85	1.27	408.38	8.01
2.90	122.99	4.65	112.02	2.86	99.91	2.74	65.26	1.15	399.05	9.67
3.00	125.05	4.39	114.22	3.67	101.63	2.79	66.07	1.64	405.65	11.00
3.10	125.80	5.17	115.82	3.84	102.90	2.95	66.76	1.67	409.79	10.50
3.20	121.65	4.31	113.91	3.03	101.55	2.57	66.22	1.21	401.69	9.53
3.30	122.98	4.23	115.97	3.07	103.18	2.46	67.06	1.74	407.54	9.30
3.40	122.61	4.59	116.92	3.04	104.02	2.90	67.53	1.17	409.47	8.49
3.50	122.19	4.29	117.89	2.99	104.88	2.45	68.06	1.32	411.56	8.20
3.60	120.45	5.24	117.95	3.80	105.08	3.62	68.26	1.62	410.47	11.30
3.70	119.26	4.23	118.47	2.97	105.72	2.47	68.67	1.31	411.06	8.52
3.80	117.71	4.19	118.81	3.16	106.16	2.50	69.01	1.21	410.96	8.23
3.90	115.31	4.21	118.65	2.99	106.26	2.51	69.17	1.27	409.01	8.27
4.00	113.00	4.09	118.72	3.06	106.55	2.54	69.45	1.28	407.68	8.20
4.10	111.55	4.28	119.70	3.06	107.61	2.54	70.11	1.22	409.40	8.53
4.20	108.31	4.16	119.06	3.29	107.41	2.56	70.17	1.23	405.80	8.98
4.30	104.54	3.89	118.28	3.18	107.08	2.54	70.15	1.54	401.36	8.56

Table 11.7: XRCF HRMA Effective Area within 2 mm Aperture. Units: cm^2 (continued)

Energy	Shell 1		Shell 3		Shell 4		Shell 6		HRMA	
(keV)	A_{eff}	Error	A_{eff}	Error	A_{eff}	Error	A_{eff}	Error	A_{eff}	Error
4.40	101.42	3.83	118.23	3.25	107.33	2.76	70.45	1.29	399.21	8.11
4.50	97.13	3.81	117.26	3.54	106.95	3.08	70.45	1.73	393.98	8.87
4.60	92.14	3.54	116.02	3.20	106.36	2.54	70.38	1.29	387.44	7.95
4.70	85.36	3.28	115.29	3.13	106.44	3.47	70.72	1.51	380.39	10.35
4.80	79.90	3.24	114.16	3.40	105.99	2.82	70.70	1.28	373.55	7.78
4.90	73.87	2.91	113.12	3.03	105.65	2.75	70.76	2.01	366.27	9.97
5.00	67.43	2.94	111.53	2.94	104.93	2.52	70.64	1.27	357.41	7.34
5.10	60.03	2.40	110.03	3.06	104.42	2.54	70.64	1.51	347.72	8.70
5.20	52.71	2.23	108.32	2.87	103.72	2.58	70.54	1.29	337.52	6.86
5.30	45.06	1.98	106.61	3.12	103.10	2.76	70.56	1.33	327.02	8.64
5.40	37.68	1.67	104.28	2.98	102.04	2.55	70.36	1.24	315.44	6.63
5.50	30.55	1.33	101.64	2.70	100.88	2.49	70.16	1.27	303.60	6.20
5.60	24.35	1.05	98.85	2.59	99.75	2.42	70.03	1.62	292.71	5.98
5.70	19.26	0.94	96.01	2.61	98.69	2.45	69.92	1.26	283.09	6.06
5.80	15.07	0.79	92.98	2.52	97.68	2.75	69.90	1.29	274.45	5.80
5.90	11.10	0.51	89.26	2.34	96.62	2.55	69.91	1.55	265.25	5.76
6.00	8.58	0.54	85.45	2.24	95.45	2.40	69.80	1.26	257.54	6.01
6.10	6.56	0.36	80.92	2.34	93.96	2.30	69.63	1.48	249.31	6.24
6.20	5.02	0.29	75.69	2.34	92.24	2.28	69.39	1.25	240.65	4.87
6.30	3.83	0.61	69.78	2.07	90.46	2.21	69.19	1.50	231.66	4.80
6.40	2.93	0.16	63.01	1.81	88.39	2.22	68.97	1.27	221.87	4.49
6.50	2.27	0.12	55.61	1.81	85.81	2.11	68.58	1.23	211.02	4.71
6.60	1.75	0.24	48.20	1.50	83.63	3.01	68.45	1.42	200.94	4.65
6.70	1.34	0.24	40.58	1.34	81.15	2.28	68.50	1.23	190.66	3.95
6.80	1.87	0.08	34.24	0.90	78.01	2.21	68.23	1.54	180.86	4.83
6.90	1.54	0.06	28.45	1.25	74.07	3.44	67.79	2.16	170.72	6.05
7.00	1.26	0.05	23.40	0.74	69.88	2.12	67.50	3.38	161.24	6.34
7.10	1.04	0.04	18.96	0.50	64.76	3.82	67.11	2.92	151.40	7.19
7.20	0.88	0.04	15.38	0.70	58.52	1.68	66.18	1.20	140.78	2.83
7.40	0.59	0.03	9.34	0.34	45.85	1.14	66.37	1.26	122.05	2.52
7.60	0.44	0.02	6.01	0.51	33.96	1.56	65.58	1.80	105.96	3.93
7.80	0.32	0.01	3.89	0.34	24.20	0.61	64.68	1.39	93.13	1.85
8.00	0.24	0.01	2.55	0.23	16.49	0.44	63.64	2.46	83.02	2.74
8.20	0.18	0.01	1.74	0.06	10.91	0.28	62.44	1.67	75.44	1.96
8.40	0.14	0.01	1.25	0.03	7.18	0.18	61.36	1.16	70.17	1.57
8.60	0.11	0.00	0.89	0.04	4.57	0.12	59.62	2.07	65.52	1.69
8.80	0.08	0.00	0.70	0.02	2.94	0.35	57.84	1.35	61.92	2.73
9.00	0.06	0.00	0.51	0.01	1.96	0.07	55.55	1.29	58.56	1.78
9.20	0.05	0.00	0.38	0.01	1.36	0.11	52.30	1.07	54.64	1.16
9.40	0.04	0.00	0.29	0.01	0.95	0.03	48.20	1.75	50.09	1.31
9.60	0.03	0.00	0.23	0.01	0.72	0.02	42.22	1.77	43.81	2.21
9.80	0.03	0.00	0.18	0.00	0.53	0.02	33.83	1.31	35.12	1.62
10.00	0.02	0.00	0.14	0.00	0.39	0.01	24.70	0.63	25.69	0.82

Table 11.8: XRCF HRMA Effective Area within 35 mm Aperture. Units: cm^2

Energy	Shell 1		Shell 3		Shell 4		Shell 6		HRMA	
(keV)	A_{eff}	Error	A_{eff}	Error	A_{eff}	Error	A_{eff}	Error	A_{eff}	Error
0.10	414.16	11.70	257.64	2.90	199.94	6.71	108.96	2.91	975.58	15.64
0.20	339.13	9.58	219.38	2.47	173.48	5.82	98.07	2.62	825.92	13.24
0.30	325.13	9.18	212.09	2.39	168.38	5.65	95.93	2.56	797.57	12.79
0.40	315.89	8.92	207.28	2.33	165.01	5.54	94.52	2.52	778.86	12.49
0.50	313.16	8.84	205.88	2.32	164.04	5.51	94.12	2.51	773.39	12.40
0.60	313.68	8.86	206.23	2.32	164.30	5.52	94.24	2.51	774.64	12.42
0.70	312.90	8.84	205.90	2.32	164.08	5.51	94.16	2.51	773.22	12.40
0.80	311.22	8.79	205.08	2.31	163.52	5.49	93.95	2.51	769.98	12.34
0.90	313.54	8.85	206.42	2.33	164.47	5.52	94.38	2.52	775.00	12.42
1.00	313.63	8.86	206.58	2.33	164.60	5.53	94.44	2.52	775.44	12.43
1.10	313.88	8.86	206.83	2.33	164.81	5.53	94.55	2.52	776.27	12.44
1.20	313.27	8.85	206.64	2.33	164.70	5.53	94.52	2.52	775.33	12.43
1.30	312.21	8.82	206.21	2.32	164.44	5.52	94.43	2.52	773.50	12.40
1.40	310.44	8.77	205.48	2.31	163.96	5.50	94.26	2.51	770.37	12.35
1.50	307.70	8.69	204.31	2.30	163.17	5.48	93.95	2.51	765.41	12.27
1.60	304.05	8.59	202.61	2.28	162.03	5.44	93.51	2.49	758.52	12.16
1.70	298.53	8.43	200.01	2.25	160.27	5.38	92.79	2.47	748.00	11.99
1.80	290.06	8.19	195.88	2.21	157.47	5.29	91.66	2.44	731.59	11.73
1.90	274.29	7.75	188.11	2.12	152.14	5.11	89.48	2.39	700.72	11.23
2.00	250.12	7.06	176.13	1.98	143.89	4.83	86.08	2.30	653.24	10.47
2.10	132.29	3.74	108.44	1.22	94.62	3.18	63.66	1.70	397.51	6.37
2.20	119.18	3.37	98.99	1.12	87.13	2.92	59.76	1.59	363.71	5.83
2.30	126.92	4.41	107.71	2.98	96.78	2.36	63.60	1.35	397.56	10.15
2.40	130.39	4.32	110.53	2.76	98.97	2.29	64.65	1.14	406.34	8.26
2.50	130.31	4.80	111.23	3.08	99.52	2.61	64.97	1.53	407.10	10.27
2.60	124.71	5.86	107.93	4.07	96.88	3.28	63.71	1.76	393.56	13.35
2.70	130.67	4.56	112.60	2.85	100.52	2.71	65.49	1.14	409.22	8.52
2.80	132.75	4.47	114.83	2.87	102.29	2.37	66.39	1.28	415.77	8.16
2.90	128.09	4.85	112.76	2.88	100.81	2.76	65.80	1.16	406.53	9.85
3.00	130.54	4.59	115.03	3.70	102.58	2.82	66.65	1.65	413.72	11.22
3.10	131.60	5.41	116.69	3.87	103.92	2.98	67.38	1.68	418.35	10.72
3.20	127.52	4.52	114.84	3.05	102.58	2.59	66.85	1.22	410.40	9.74
3.30	129.23	4.45	116.94	3.10	104.32	2.48	67.73	1.76	416.87	9.51
3.40	129.15	4.83	117.95	3.06	105.20	2.93	68.25	1.18	419.27	8.69
3.50	129.02	4.53	118.95	3.02	106.11	2.48	68.79	1.34	421.80	8.40
3.60	127.46	5.55	119.05	3.84	106.36	3.67	69.02	1.64	421.03	11.59
3.70	126.51	4.48	119.69	3.00	107.05	2.51	69.45	1.33	422.11	8.75
3.80	125.17	4.46	120.13	3.19	107.58	2.53	69.83	1.23	422.50	8.46
3.90	122.90	4.49	120.01	3.02	107.74	2.54	70.06	1.29	420.89	8.51
4.00	120.76	4.38	120.14	3.10	108.08	2.57	70.37	1.30	419.93	8.45
4.10	119.52	4.58	121.17	3.10	109.20	2.58	71.04	1.24	422.06	8.79
4.20	116.31	4.47	120.64	3.34	109.03	2.60	71.12	1.25	418.72	9.26
4.30	112.54	4.19	119.90	3.22	108.76	2.58	71.17	1.57	414.47	8.84

Table 11.8: XRCF HRMA Effective Area within 35 mm Aperture. Units: cm^2 (continued)

Energy	Shell 1		Shell 3		Shell 4		Shell 6		HRMA	
(keV)	A_{eff}	Error	A_{eff}	Error	A_{eff}	Error	A_{eff}	Error	A_{eff}	Error
4.40	109.44	4.13	119.91	3.29	109.09	2.80	71.49	1.30	412.59	8.39
4.50	105.08	4.12	119.02	3.59	108.76	3.13	71.54	1.75	407.51	9.18
4.60	99.91	3.84	117.82	3.25	108.25	2.59	71.50	1.31	400.99	8.23
4.70	92.84	3.57	117.16	3.18	108.41	3.53	71.88	1.53	393.85	10.72
4.80	87.12	3.53	116.06	3.45	108.04	2.87	71.92	1.31	386.95	8.06
4.90	80.76	3.18	115.03	3.08	107.75	2.80	72.02	2.05	379.46	10.33
5.00	73.88	3.22	113.49	2.99	107.07	2.57	71.92	1.29	370.26	7.60
5.10	65.94	2.63	112.03	3.11	106.56	2.59	71.97	1.53	360.08	9.01
5.20	58.02	2.45	110.40	2.92	105.93	2.64	71.93	1.32	349.45	7.10
5.30	49.75	2.18	108.68	3.18	105.34	2.82	71.96	1.36	338.29	8.94
5.40	41.70	1.85	106.39	3.04	104.35	2.61	71.80	1.27	326.11	6.86
5.50	33.88	1.47	103.71	2.76	103.25	2.55	71.67	1.29	313.57	6.40
5.60	27.07	1.17	100.90	2.64	102.15	2.48	71.53	1.66	301.96	6.17
5.70	21.46	1.04	98.05	2.66	101.13	2.51	71.47	1.28	291.80	6.25
5.80	16.85	0.89	95.07	2.57	100.17	2.82	71.45	1.32	282.78	5.97
5.90	12.45	0.57	91.31	2.39	99.17	2.62	71.54	1.59	273.15	5.93
6.00	9.65	0.61	87.46	2.29	97.98	2.46	71.47	1.29	265.09	6.18
6.10	7.42	0.40	82.89	2.40	96.53	2.36	71.35	1.52	256.63	6.42
6.20	5.69	0.33	77.57	2.40	94.84	2.34	71.18	1.28	247.76	5.01
6.30	4.36	0.69	71.55	2.12	93.06	2.27	71.03	1.53	238.54	4.94
6.40	3.35	0.18	64.65	1.86	90.99	2.28	70.87	1.30	228.52	4.62
6.50	2.60	0.13	57.10	1.86	88.37	2.17	70.50	1.27	217.42	4.85
6.60	2.01	0.28	49.51	1.54	86.16	3.10	70.47	1.46	207.15	4.79
6.70	1.54	0.28	41.70	1.37	83.67	2.35	70.55	1.27	196.60	4.07
6.80	2.16	0.09	35.20	0.92	80.51	2.29	70.32	1.59	186.63	4.99
6.90	1.77	0.08	29.26	1.29	76.51	3.55	69.93	2.23	176.29	6.24
7.00	1.46	0.06	24.08	0.76	72.24	2.19	69.69	3.49	166.64	6.55
7.10	1.21	0.05	19.53	0.51	67.00	3.95	69.33	3.02	156.56	7.44
7.20	1.02	0.04	15.84	0.73	60.57	1.74	68.40	1.23	145.64	2.93
7.40	0.69	0.03	9.64	0.36	47.50	1.18	68.70	1.30	126.42	2.61
7.60	0.51	0.02	6.21	0.53	35.23	1.62	67.98	1.87	109.91	4.08
7.80	0.38	0.02	4.02	0.35	25.12	0.64	67.17	1.44	96.74	1.92
8.00	0.28	0.01	2.64	0.24	17.15	0.46	66.19	2.56	86.37	2.85
8.20	0.21	0.01	1.80	0.06	11.36	0.29	65.05	1.73	78.60	2.05
8.40	0.17	0.01	1.29	0.04	7.50	0.19	64.02	1.21	73.22	1.63
8.60	0.13	0.01	0.93	0.04	4.78	0.12	62.29	2.16	68.47	1.77
8.80	0.10	0.00	0.72	0.02	3.09	0.37	60.53	1.42	64.82	2.86
9.00	0.08	0.00	0.53	0.01	2.07	0.07	58.25	1.36	61.42	1.87
9.20	0.06	0.00	0.40	0.01	1.43	0.11	54.90	1.12	57.37	1.22
9.40	0.05	0.00	0.30	0.01	1.01	0.03	50.68	1.84	52.67	1.38
9.60	0.04	0.00	0.24	0.01	0.76	0.02	44.45	1.87	46.14	2.33
9.80	0.03	0.00	0.18	0.00	0.56	0.02	35.67	1.38	37.03	1.71
10.00	0.02	0.00	0.14	0.00	0.41	0.01	26.07	0.67	27.13	0.87

Table 11.9: XRCF HRMA Effective Area within 2π Steradian. Units: cm^2

Energy	Shell 1		Shell 3		Shell 4		Shell 6		HRMA	
(keV)	A_{eff}	Error	A_{eff}	Error	A_{eff}	Error	A_{eff}	Error	A_{eff}	Error
0.10	414.21	11.70	257.65	2.90	199.94	6.71	108.96	2.91	975.65	15.64
0.20	339.19	9.58	219.39	2.47	173.48	5.82	98.07	2.62	825.98	13.24
0.30	325.23	9.18	212.10	2.39	168.39	5.65	95.94	2.56	797.69	12.79
0.40	316.03	8.93	207.29	2.34	165.02	5.54	94.53	2.52	779.03	12.49
0.50	313.38	8.85	205.90	2.32	164.05	5.51	94.13	2.51	773.65	12.40
0.60	313.95	8.87	206.26	2.32	164.32	5.52	94.25	2.51	774.96	12.42
0.70	313.22	8.85	205.92	2.32	164.10	5.51	94.17	2.51	773.60	12.40
0.80	311.58	8.80	205.11	2.31	163.54	5.49	93.96	2.51	770.41	12.35
0.90	313.97	8.87	206.45	2.33	164.50	5.52	94.40	2.52	775.51	12.43
1.00	314.12	8.87	206.61	2.33	164.64	5.53	94.47	2.52	776.01	12.44
1.10	314.44	8.88	206.87	2.33	164.85	5.53	94.58	2.52	776.91	12.45
1.20	313.90	8.86	206.68	2.33	164.75	5.53	94.55	2.52	776.06	12.44
1.30	312.87	8.84	206.26	2.32	164.49	5.52	94.46	2.52	774.28	12.41
1.40	311.18	8.79	205.54	2.32	164.01	5.51	94.29	2.51	771.24	12.36
1.50	308.54	8.71	204.36	2.30	163.24	5.48	93.99	2.51	766.39	12.29
1.60	304.93	8.61	202.66	2.28	162.11	5.44	93.55	2.49	759.55	12.18
1.70	299.49	8.46	200.06	2.25	160.35	5.38	92.84	2.48	749.10	12.01
1.80	290.99	8.22	195.95	2.21	157.56	5.29	91.71	2.45	732.70	11.75
1.90	275.26	7.77	188.17	2.12	152.23	5.11	89.53	2.39	701.87	11.25
2.00	251.05	7.09	176.19	1.98	143.99	4.83	86.13	2.30	654.37	10.49
2.10	132.79	3.75	108.47	1.22	94.69	3.18	63.70	1.70	398.14	6.38
2.20	119.66	3.38	99.03	1.12	87.19	2.93	59.80	1.59	364.32	5.84
2.30	127.46	4.43	107.75	2.98	96.85	2.36	63.65	1.35	398.29	10.16
2.40	130.96	4.34	110.58	2.76	99.04	2.29	64.71	1.14	407.10	8.27
2.50	130.89	4.82	111.29	3.08	99.61	2.61	65.03	1.53	407.91	10.29
2.60	125.29	5.89	107.98	4.08	96.97	3.28	63.78	1.76	394.38	13.38
2.70	131.30	4.59	112.65	2.85	100.63	2.72	65.56	1.14	410.11	8.54
2.80	133.43	4.49	114.88	2.87	102.39	2.38	66.47	1.28	416.70	8.18
2.90	128.76	4.87	112.83	2.89	100.91	2.76	65.88	1.16	407.46	9.87
3.00	131.25	4.61	115.11	3.70	102.68	2.82	66.74	1.65	414.73	11.25
3.10	132.34	5.44	116.77	3.87	104.03	2.98	67.47	1.69	419.40	10.74
3.20	128.25	4.54	114.91	3.05	102.70	2.60	66.93	1.22	411.44	9.76
3.30	129.96	4.47	117.03	3.10	104.43	2.49	67.83	1.76	417.93	9.54
3.40	129.93	4.86	118.03	3.07	105.33	2.94	68.35	1.19	420.41	8.71
3.50	129.80	4.56	119.05	3.02	106.26	2.49	68.89	1.34	422.97	8.43
3.60	128.24	5.58	119.15	3.84	106.50	3.67	69.12	1.64	422.21	11.62
3.70	127.30	4.51	119.80	3.00	107.21	2.51	69.57	1.33	423.35	8.77
3.80	125.96	4.49	120.24	3.19	107.75	2.53	69.96	1.23	423.75	8.49
3.90	123.70	4.52	120.14	3.02	107.91	2.55	70.20	1.29	422.19	8.54
4.00	121.55	4.40	120.27	3.10	108.27	2.58	70.51	1.30	421.24	8.48
4.10	120.32	4.61	121.31	3.10	109.39	2.58	71.19	1.24	423.42	8.82
4.20	117.11	4.50	120.77	3.34	109.24	2.60	71.27	1.25	420.08	9.29
4.30	113.33	4.22	120.03	3.22	108.97	2.58	71.31	1.57	415.82	8.87

Table 11.9: XRCF HRMA Effective Area within 2π Steradian. Units: cm^2 (continued)

Energy	Shell 1		Shell 3		Shell 4		Shell 6		HRMA	
(keV)	A_{eff}	Error	A_{eff}	Error	A_{eff}	Error	A_{eff}	Error	A_{eff}	Error
4.40	110.22	4.16	120.03	3.30	109.32	2.81	71.65	1.31	413.95	8.41
4.50	105.83	4.15	119.15	3.59	109.00	3.14	71.71	1.76	408.87	9.21
4.60	100.62	3.87	117.96	3.25	108.50	2.59	71.67	1.31	402.34	8.26
4.70	93.51	3.59	117.31	3.19	108.66	3.54	72.06	1.54	395.17	10.76
4.80	87.75	3.56	116.23	3.46	108.28	2.88	72.09	1.31	388.25	8.08
4.90	81.34	3.20	115.18	3.08	108.00	2.81	72.20	2.05	380.70	10.36
5.00	74.42	3.25	113.63	3.00	107.32	2.58	72.11	1.29	371.46	7.62
5.10	66.44	2.65	112.18	3.11	106.83	2.60	72.16	1.54	361.26	9.04
5.20	58.46	2.47	110.54	2.93	106.19	2.64	72.13	1.32	350.56	7.12
5.30	50.13	2.20	108.83	3.18	105.61	2.83	72.16	1.36	339.35	8.97
5.40	42.02	1.86	106.51	3.04	104.63	2.62	72.02	1.27	327.11	6.88
5.50	34.16	1.49	103.85	2.76	103.53	2.56	71.87	1.30	314.50	6.42
5.60	27.30	1.18	101.04	2.64	102.44	2.49	71.75	1.66	302.87	6.19
5.70	21.65	1.05	98.18	2.67	101.42	2.51	71.68	1.29	292.65	6.27
5.80	17.00	0.90	95.20	2.58	100.46	2.83	71.66	1.32	283.58	5.99
5.90	12.57	0.57	91.44	2.39	99.46	2.62	71.74	1.59	273.92	5.95
6.00	9.75	0.61	87.59	2.29	98.27	2.47	71.68	1.29	265.83	6.20
6.10	7.50	0.41	83.01	2.40	96.81	2.37	71.57	1.53	257.36	6.44
6.20	5.76	0.33	77.69	2.41	95.12	2.35	71.40	1.29	248.46	5.02
6.30	4.42	0.70	71.66	2.13	93.32	2.28	71.25	1.54	239.21	4.96
6.40	3.39	0.18	64.75	1.86	91.26	2.29	71.08	1.30	229.17	4.63
6.50	2.64	0.13	57.18	1.86	88.64	2.18	70.71	1.27	218.04	4.87
6.60	2.05	0.28	49.58	1.54	86.43	3.11	70.68	1.46	207.74	4.80
6.70	1.57	0.28	41.76	1.38	83.93	2.36	70.76	1.27	197.18	4.09
6.80	2.20	0.09	35.26	0.93	80.75	2.29	70.54	1.59	187.19	5.00
6.90	1.81	0.08	29.31	1.29	76.75	3.56	70.14	2.23	176.82	6.26
7.00	1.49	0.06	24.13	0.76	72.47	2.20	69.92	3.50	167.17	6.57
7.10	1.23	0.05	19.57	0.51	67.21	3.96	69.55	3.03	157.06	7.46
7.20	1.04	0.04	15.88	0.73	60.77	1.75	68.63	1.24	146.12	2.94
7.40	0.71	0.03	9.67	0.36	47.65	1.19	68.94	1.31	126.85	2.62
7.60	0.53	0.02	6.22	0.53	35.34	1.62	68.22	1.87	110.30	4.09
7.80	0.39	0.02	4.04	0.35	25.21	0.64	67.40	1.45	97.08	1.92
8.00	0.29	0.01	2.65	0.24	17.21	0.46	66.42	2.56	86.68	2.86
8.20	0.22	0.01	1.81	0.06	11.41	0.29	65.26	1.74	78.88	2.05
8.40	0.17	0.01	1.30	0.04	7.53	0.19	64.22	1.22	73.48	1.64
8.60	0.13	0.01	0.94	0.04	4.81	0.12	62.50	2.16	68.73	1.77
8.80	0.10	0.00	0.73	0.02	3.11	0.37	60.72	1.42	65.04	2.87
9.00	0.08	0.00	0.54	0.01	2.08	0.07	58.45	1.36	61.64	1.87
9.20	0.06	0.00	0.40	0.01	1.45	0.11	55.09	1.13	57.59	1.22
9.40	0.05	0.00	0.30	0.01	1.02	0.03	50.85	1.85	52.86	1.39
9.60	0.04	0.00	0.24	0.01	0.77	0.02	44.61	1.87	46.31	2.33
9.80	0.03	0.00	0.19	0.00	0.57	0.02	35.80	1.39	37.18	1.71
10.00	0.03	0.00	0.15	0.00	0.42	0.01	26.17	0.67	27.24	0.87

11.18 On-orbit HRMA Effective Area Prediction

Figures 11.54–11.56 show the on-orbit HRMA and four shells effective areas within 2 mm, 35 mm diameters and 2π steradians,[7] for the original raytrace and the calibrated curves with errors estimated in §11.15. Tables 11.10 – 11.12 list the values of the on-orbit effective areas with energy grid of 0.1 keV.[6] The "rdb" tables on the web (see below) have denser energy grid.

These are our current best on-orbit effective area predictions for the HRMA. They can be used to make AXAF on-orbit performance predictions. The "rdb" tables of the predicted on-orbit HRMA effective area, as well as Figures 11.54–11.56, can be accessed on the World Wide Web page:

http://hea-www.harvard.edu/MST/mirror/www/orbit/hrma_ea.html

at the bottom of the web page, please click:

On-orbit HRMA Effective Area within 2 mm aperture and its figure.

On-orbit HRMA Effective Area within 35 mm aperture and its figure.

On-orbit HRMA Effective Area within 2pi steradians and its figure.

[7] Although it is not possible to use just a single shell on-orbit. The HETG operations do require the effective area predictions for Shells 1+3 and Shells 4+6 separately.

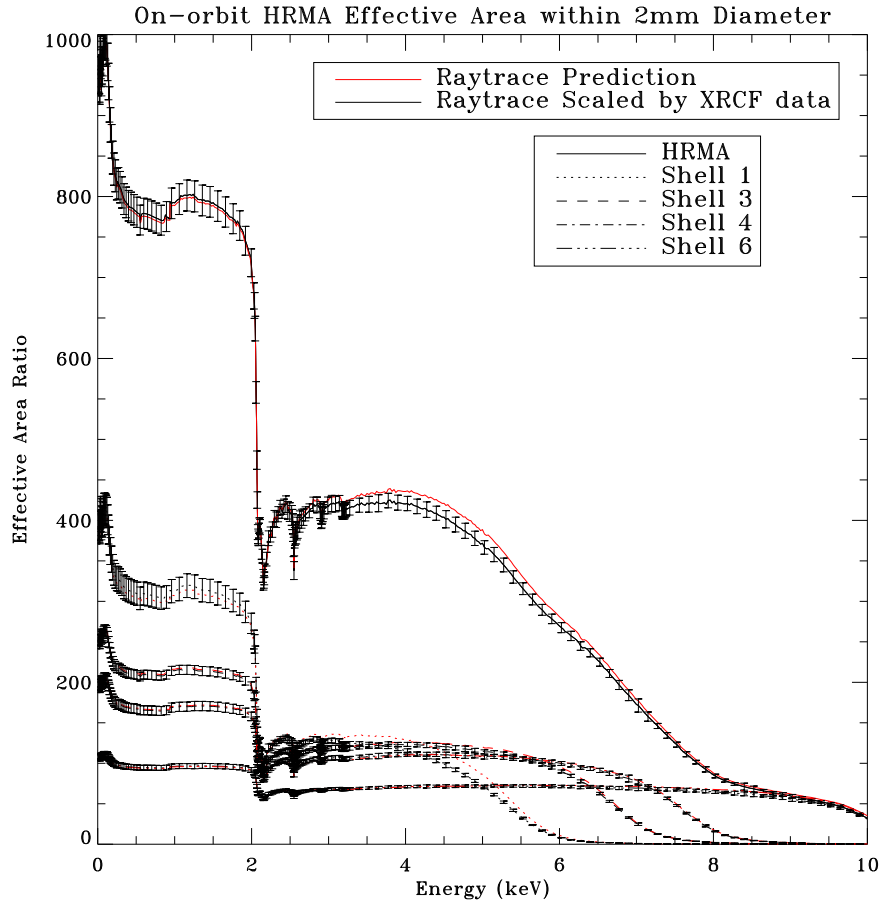

Figure 11.54: The on-orbit HRMA and four shells effective areas within 2 mm aperture. The original raytrace predictions and the calibration data scaled raytrace predictions.

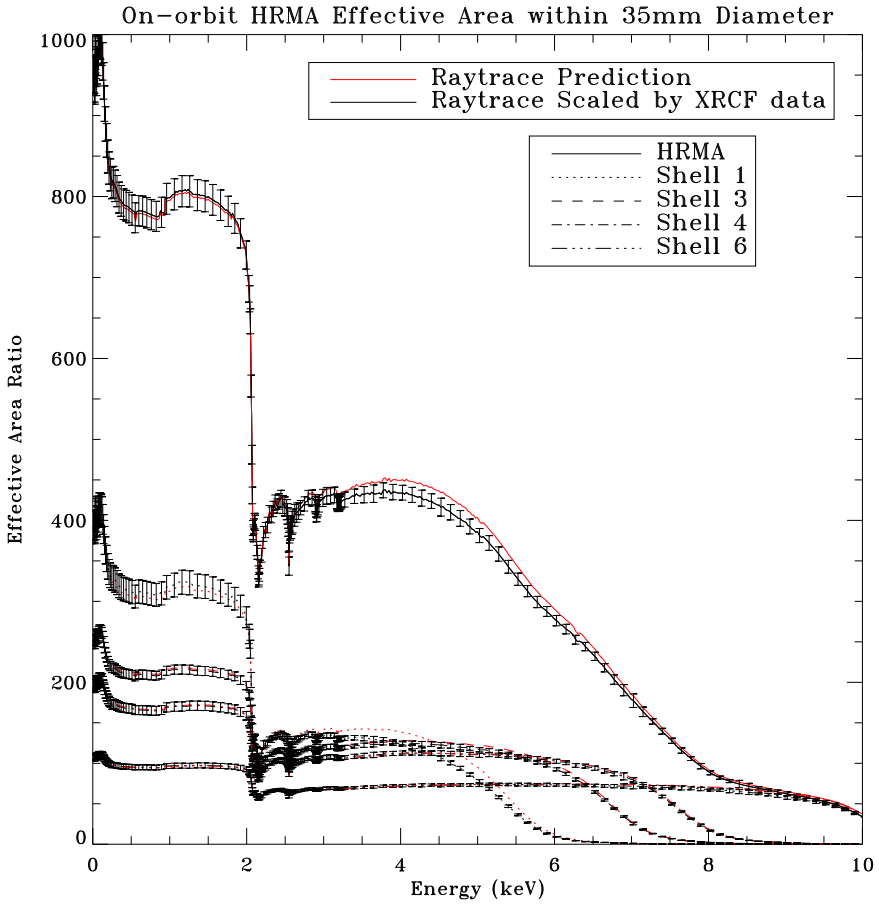

Figure 11.55: The on-orbit HRMA and four shells effective areas within 35 mm aperture. The original raytrace predictions and the calibration data scaled raytrace predictions.

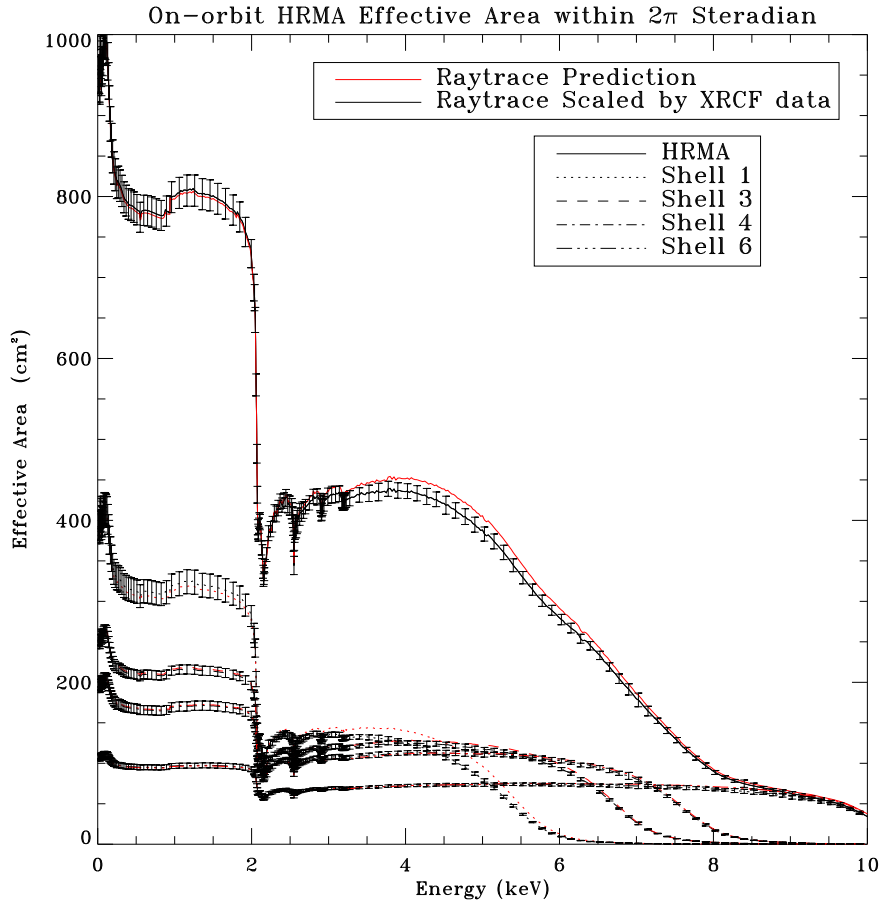

Figure 11.56: The on-orbit HRMA and four shells effective areas within 2π steradian. The original raytrace predictions and the calibration data scaled raytrace predictions.

Table 11.10: On-orbit HRMA Effective Area within 2 mm Diameter. Units: cm^2

Energy	Shell 1		Shell 3		Shell 4		Shell 6		HRMA	
(keV)	A_{eff}	Error	A_{eff}	Error	A_{eff}	Error	A_{eff}	Error	A_{eff}	Error
0.10	417.05	11.78	264.44	2.98	205.31	6.89	111.03	2.96	992.73	15.91
0.20	341.10	9.63	225.11	2.53	178.10	5.98	99.83	2.66	840.01	13.47
0.30	326.93	9.23	217.61	2.45	172.82	5.80	97.53	2.60	810.95	13.00
0.40	317.43	8.96	212.67	2.39	169.35	5.68	96.00	2.56	791.63	12.69
0.50	314.39	8.88	211.23	2.38	168.37	5.65	95.45	2.55	785.67	12.59
0.60	314.71	8.89	211.58	2.38	168.62	5.66	95.54	2.55	786.67	12.61
0.70	313.52	8.85	211.23	2.38	168.39	5.65	95.47	2.55	784.84	12.58
0.80	311.52	8.80	210.36	2.37	167.82	5.63	95.23	2.54	781.19	12.52
0.90	313.53	8.85	211.71	2.38	168.77	5.67	95.65	2.55	785.90	12.60
1.00	313.30	8.85	211.84	2.39	168.87	5.67	95.70	2.55	785.96	12.60
1.10	313.07	8.84	212.06	2.39	169.05	5.67	95.79	2.55	786.22	12.60
1.20	312.10	8.81	211.81	2.39	168.92	5.67	95.74	2.55	784.84	12.58
1.30	310.48	8.77	211.34	2.38	168.61	5.66	95.62	2.55	782.35	12.54
1.40	308.34	8.71	210.55	2.37	168.06	5.64	95.42	2.54	778.70	12.48
1.50	305.32	8.62	209.27	2.36	167.21	5.61	95.10	2.54	773.26	12.40
1.60	301.12	8.50	207.43	2.34	166.01	5.57	94.62	2.52	765.60	12.27
1.70	295.20	8.34	204.69	2.30	164.17	5.51	93.88	2.50	754.44	12.09
1.80	286.33	8.09	200.45	2.26	161.26	5.41	92.69	2.47	737.35	11.82
1.90	270.36	7.64	192.45	2.17	155.73	5.23	90.47	2.41	705.83	11.31
2.00	246.35	6.96	180.13	2.03	147.28	4.94	87.02	2.32	657.91	10.55
2.10	130.12	3.67	110.91	1.25	96.85	3.25	64.34	1.72	400.79	6.42
2.20	116.99	3.30	101.19	1.14	89.14	2.99	60.40	1.61	366.44	5.87
2.30	124.31	4.32	110.06	3.04	98.99	2.41	64.25	1.36	400.00	10.21
2.40	127.44	4.22	112.91	2.82	101.19	2.34	65.29	1.15	408.42	8.30
2.50	127.14	4.68	113.59	3.14	101.74	2.66	65.61	1.54	408.93	10.31
2.60	121.48	5.71	110.18	4.16	99.02	3.35	64.28	1.77	395.06	13.40
2.70	127.06	4.44	114.92	2.90	102.69	2.77	66.04	1.15	410.40	8.55
2.80	128.87	4.33	117.14	2.93	104.47	2.42	66.93	1.29	416.62	8.18
2.90	124.14	4.70	115.00	2.94	102.93	2.82	66.33	1.17	407.14	9.86
3.00	126.31	4.44	117.26	3.77	104.71	2.88	67.18	1.66	414.02	11.23
3.10	127.03	5.22	118.91	3.94	106.03	3.04	67.87	1.70	418.20	10.71
3.20	122.81	4.35	116.96	3.11	104.61	2.65	67.31	1.23	409.89	9.72
3.30	124.24	4.28	119.07	3.15	106.32	2.53	68.19	1.77	416.00	9.49
3.40	123.92	4.64	120.02	3.12	107.19	2.99	68.68	1.19	418.03	8.66
3.50	123.56	4.34	121.03	3.07	108.11	2.53	69.20	1.34	420.29	8.37
3.60	121.83	5.30	121.10	3.91	108.32	3.73	69.41	1.64	419.21	11.54
3.70	120.72	4.28	121.73	3.05	108.95	2.55	69.83	1.34	420.01	8.70
3.80	119.25	4.25	122.11	3.24	109.47	2.57	70.19	1.23	420.14	8.41
3.90	116.88	4.27	121.97	3.07	109.55	2.59	70.38	1.29	418.26	8.46
4.00	114.65	4.15	122.02	3.14	109.87	2.61	70.69	1.30	417.06	8.39
4.10	113.37	4.35	123.02	3.15	110.91	2.62	71.33	1.25	418.97	8.72
4.20	110.13	4.23	122.40	3.39	110.72	2.64	71.38	1.25	415.41	9.19
4.30	106.56	3.97	121.60	3.27	110.42	2.62	71.40	1.57	411.23	8.77

Table 11.10: On-orbit HRMA Effective Area within 2 mm Diameter. Units: cm^2 (continued)

Energy	Shell 1		Shell 3		Shell 4		Shell 6		HRMA	
(keV)	A_{eff}	Error	A_{eff}	Error	A_{eff}	Error	A_{eff}	Error	A_{eff}	Error
4.40	103.54	3.91	121.57	3.34	110.69	2.84	71.70	1.31	409.27	8.32
4.50	99.42	3.90	120.63	3.64	110.35	3.18	71.71	1.76	404.32	9.11
4.60	94.59	3.64	119.40	3.29	109.79	2.62	71.65	1.31	398.04	8.17
4.70	88.28	3.39	118.74	3.23	109.93	3.58	71.98	1.53	391.68	10.66
4.80	83.12	3.37	117.64	3.50	109.46	2.91	71.97	1.31	385.24	8.02
4.90	77.41	3.04	116.63	3.12	109.12	2.84	72.02	2.05	378.41	10.30
5.00	71.27	3.11	115.03	3.03	108.39	2.60	71.89	1.29	369.93	7.59
5.10	64.26	2.57	113.58	3.15	107.86	2.62	71.89	1.53	360.76	9.03
5.20	57.12	2.41	111.94	2.96	107.16	2.67	71.84	1.32	350.99	7.13
5.30	49.47	2.17	110.25	3.23	106.55	2.85	71.83	1.35	340.55	9.00
5.40	41.64	1.85	107.98	3.08	105.54	2.64	71.65	1.27	328.63	6.91
5.50	33.67	1.47	105.39	2.80	104.41	2.58	71.45	1.29	315.90	6.45
5.60	26.43	1.14	102.74	2.69	103.26	2.51	71.29	1.65	303.83	6.21
5.70	20.35	0.99	100.08	2.72	102.26	2.54	71.18	1.28	293.22	6.28
5.80	15.45	0.81	97.30	2.63	101.26	2.85	71.13	1.31	283.94	6.00
5.90	10.99	0.50	93.92	2.46	100.31	2.65	71.17	1.58	274.60	5.97
6.00	8.32	0.52	90.42	2.37	99.11	2.49	71.06	1.28	266.98	6.23
6.10	6.29	0.34	86.38	2.50	97.69	2.39	70.88	1.51	259.31	6.49
6.20	4.79	0.28	81.72	2.53	96.09	2.37	70.68	1.28	251.46	5.09
6.30	3.66	0.58	76.49	2.27	94.39	2.30	70.52	1.52	243.38	5.04
6.40	2.80	0.15	70.42	2.03	92.42	2.32	70.28	1.29	234.47	4.74
6.50	2.18	0.11	63.46	2.07	89.96	2.21	69.88	1.25	224.26	5.01
6.60	1.69	0.23	56.22	1.75	87.99	3.16	69.80	1.45	214.67	4.96
6.70	1.29	0.23	48.05	1.58	85.83	2.41	69.88	1.25	204.21	4.23
6.80	1.81	0.08	40.44	1.06	83.04	2.36	69.59	1.57	193.50	5.17
6.90	1.49	0.06	32.88	1.44	79.54	3.69	69.16	2.20	182.02	6.45
7.00	1.23	0.05	26.04	0.82	75.94	2.31	68.91	3.45	171.38	6.74
7.10	1.01	0.04	20.13	0.53	71.51	4.21	68.47	2.98	160.69	7.63
7.20	0.86	0.04	15.65	0.72	65.83	1.89	67.54	1.22	149.76	3.01
7.40	0.58	0.02	8.87	0.33	54.92	1.37	67.79	1.28	132.15	2.73
7.60	0.43	0.02	5.64	0.48	41.97	1.92	67.00	1.84	115.14	4.27
7.80	0.32	0.01	3.68	0.32	28.82	0.73	66.14	1.42	99.08	1.96
8.00	0.23	0.01	2.44	0.22	17.68	0.47	65.15	2.52	85.63	2.83
8.20	0.18	0.01	1.68	0.05	10.59	0.27	64.01	1.71	76.61	1.99
8.40	0.14	0.01	1.21	0.03	6.69	0.17	63.02	1.19	71.29	1.59
8.60	0.11	0.00	0.88	0.04	4.26	0.11	61.44	2.13	67.00	1.73
8.80	0.08	0.00	0.69	0.02	2.78	0.33	59.83	1.40	63.74	2.81
9.00	0.06	0.00	0.51	0.01	1.88	0.07	57.91	1.35	60.85	1.85
9.20	0.05	0.00	0.38	0.01	1.32	0.10	55.16	1.13	57.48	1.22
9.40	0.04	0.00	0.29	0.01	0.93	0.03	52.13	1.89	54.04	1.42
9.60	0.03	0.00	0.23	0.01	0.70	0.02	47.63	2.00	49.29	2.48
9.80	0.03	0.00	0.18	0.00	0.52	0.02	41.45	1.61	42.85	1.98
10.00	0.02	0.00	0.14	0.00	0.39	0.01	32.78	0.84	33.92	1.09

Table 11.11: On-orbit HRMA Effective Area within 35 mm Diameter. Units: cm^2

Energy	Shell 1		Shell 3		Shell 4		Shell 6		HRMA	
(keV)	A_{eff}	Error	A_{eff}	Error	A_{eff}	Error	A_{eff}	Error	A_{eff}	Error
0.10	417.51	11.79	264.48	2.98	205.36	6.89	111.07	2.96	993.31	15.92
0.20	341.81	9.65	225.18	2.54	178.17	5.98	99.95	2.67	840.98	13.48
0.30	327.68	9.25	217.70	2.45	172.94	5.81	97.75	2.61	812.12	13.02
0.40	318.34	8.99	212.76	2.40	169.48	5.69	96.30	2.57	793.05	12.71
0.50	315.56	8.91	211.32	2.38	168.48	5.66	95.87	2.56	787.44	12.62
0.60	316.08	8.93	211.69	2.38	168.75	5.66	95.98	2.56	788.69	12.64
0.70	315.25	8.90	211.34	2.38	168.52	5.66	95.88	2.56	787.20	12.62
0.80	313.53	8.85	210.51	2.37	167.95	5.64	95.64	2.55	783.87	12.57
0.90	315.88	8.92	211.88	2.39	168.94	5.67	96.07	2.56	788.97	12.65
1.00	315.93	8.92	212.05	2.39	169.07	5.68	96.14	2.56	789.38	12.65
1.10	316.15	8.93	212.31	2.39	169.28	5.68	96.25	2.57	790.18	12.67
1.20	315.53	8.91	212.12	2.39	169.17	5.68	96.22	2.57	789.23	12.65
1.30	314.37	8.88	211.68	2.38	168.90	5.67	96.12	2.56	787.30	12.62
1.40	312.54	8.83	210.92	2.38	168.40	5.65	95.94	2.56	784.05	12.57
1.50	309.90	8.75	209.71	2.36	167.60	5.63	95.63	2.55	779.12	12.49
1.60	306.15	8.65	207.95	2.34	166.44	5.59	95.18	2.54	772.04	12.38
1.70	300.58	8.49	205.27	2.31	164.62	5.53	94.46	2.52	761.33	12.20
1.80	291.97	8.25	201.05	2.26	161.75	5.43	93.30	2.49	744.59	11.94
1.90	276.13	7.80	193.07	2.17	156.27	5.25	91.08	2.43	713.27	11.43
2.00	251.91	7.11	180.80	2.04	147.83	4.96	87.62	2.34	665.21	10.66
2.10	133.33	3.77	111.36	1.25	97.23	3.26	64.82	1.73	405.24	6.50
2.20	120.06	3.39	101.64	1.14	89.52	3.01	60.84	1.62	370.72	5.94
2.30	127.84	4.44	110.58	3.06	99.43	2.43	64.75	1.37	405.12	10.34
2.40	131.31	4.35	113.49	2.83	101.68	2.35	65.81	1.16	414.05	8.41
2.50	131.25	4.83	114.22	3.16	102.26	2.68	66.15	1.55	414.87	10.46
2.60	125.60	5.91	110.83	4.18	99.56	3.37	64.86	1.79	401.09	13.60
2.70	131.61	4.60	115.62	2.92	103.30	2.79	66.67	1.16	417.05	8.68
2.80	133.74	4.50	117.90	2.94	105.12	2.44	67.58	1.30	423.73	8.32
2.90	129.08	4.88	115.79	2.96	103.60	2.84	66.98	1.18	414.39	10.04
3.00	131.57	4.62	118.12	3.80	105.42	2.90	67.86	1.68	421.75	11.44
3.10	132.64	5.46	119.83	3.97	106.81	3.06	68.59	1.71	426.47	10.93
3.20	128.54	4.55	117.93	3.13	105.43	2.67	68.05	1.24	418.40	9.92
3.30	130.26	4.49	120.11	3.18	107.20	2.55	68.95	1.79	425.01	9.70
3.40	130.22	4.87	121.13	3.15	108.13	3.02	69.47	1.21	427.51	8.86
3.50	130.11	4.57	122.19	3.10	109.10	2.55	70.02	1.36	430.17	8.57
3.60	128.56	5.60	122.31	3.95	109.35	3.77	70.27	1.66	429.46	11.82
3.70	127.67	4.52	122.98	3.08	110.05	2.58	70.73	1.35	430.66	8.92
3.80	126.39	4.50	123.43	3.28	110.61	2.60	71.11	1.25	431.15	8.63
3.90	124.19	4.54	123.35	3.10	110.77	2.61	71.32	1.31	429.65	8.69
4.00	122.11	4.42	123.50	3.18	111.12	2.64	71.63	1.32	428.79	8.63
4.10	121.01	4.64	124.59	3.19	112.27	2.65	72.34	1.26	431.21	8.98
4.20	117.90	4.53	124.02	3.43	112.12	2.67	72.43	1.27	427.99	9.47
4.30	114.27	4.25	123.27	3.31	111.87	2.65	72.46	1.59	423.90	9.04

Table 11.11: On-orbit HRMA Effective Area within 35 mm Diameter. Units: cm^2 (continued)

Energy	Shell 1		Shell 3		Shell 4		Shell 6		HRMA	
(keV)	A_{eff}	Error	A_{eff}	Error	A_{eff}	Error	A_{eff}	Error	A_{eff}	Error
4.40	111.34	4.20	123.31	3.39	112.22	2.88	72.80	1.33	422.29	8.58
4.50	107.13	4.20	122.45	3.69	111.90	3.22	72.84	1.78	417.43	9.40
4.60	102.18	3.93	121.27	3.34	111.38	2.66	72.80	1.34	411.19	8.44
4.70	95.61	3.67	120.66	3.28	111.56	3.63	73.20	1.56	404.74	11.02
4.80	90.21	3.66	119.61	3.56	111.18	2.96	73.24	1.33	398.29	8.29
4.90	84.26	3.31	118.62	3.18	110.91	2.88	73.34	2.09	391.39	10.65
5.00	77.76	3.39	117.08	3.09	110.23	2.65	73.25	1.31	382.72	7.85
5.10	70.28	2.81	115.67	3.21	109.76	2.67	73.30	1.56	373.22	9.34
5.20	62.64	2.65	114.06	3.02	109.12	2.72	73.28	1.34	363.03	7.38
5.30	54.37	2.38	112.41	3.29	108.54	2.91	73.32	1.38	352.03	9.30
5.40	45.91	2.03	110.18	3.15	107.57	2.69	73.18	1.29	339.52	7.14
5.50	37.23	1.62	107.60	2.86	106.46	2.63	73.03	1.32	326.04	6.66
5.60	29.31	1.27	104.94	2.75	105.40	2.56	72.91	1.69	313.31	6.40
5.70	22.67	1.10	102.28	2.78	104.40	2.59	72.85	1.31	302.08	6.47
5.80	17.26	0.91	99.52	2.69	103.48	2.92	72.83	1.34	292.31	6.17
5.90	12.32	0.56	96.12	2.52	102.55	2.71	72.93	1.62	282.44	6.14
6.00	9.35	0.59	92.66	2.42	101.42	2.54	72.86	1.31	274.61	6.40
6.10	7.09	0.39	88.56	2.56	100.03	2.45	72.75	1.55	266.70	6.67
6.20	5.41	0.31	83.81	2.59	98.43	2.43	72.58	1.31	258.55	5.23
6.30	4.14	0.66	78.47	2.33	96.72	2.36	72.43	1.56	250.21	5.19
6.40	3.18	0.17	72.28	2.08	94.80	2.38	72.24	1.33	241.13	4.88
6.50	2.48	0.13	65.18	2.12	92.31	2.27	71.88	1.29	230.71	5.15
6.60	1.92	0.27	57.79	1.79	90.35	3.25	71.85	1.49	220.96	5.11
6.70	1.48	0.26	49.42	1.63	88.20	2.48	71.93	1.29	210.25	4.36
6.80	2.07	0.09	41.60	1.09	85.38	2.42	71.71	1.62	199.32	5.33
6.90	1.71	0.07	33.86	1.49	81.80	3.80	71.31	2.27	187.59	6.64
7.00	1.41	0.06	26.84	0.85	78.14	2.37	71.11	3.56	176.73	6.95
7.10	1.17	0.05	20.76	0.54	73.63	4.34	70.73	3.08	165.84	7.88
7.20	0.99	0.04	16.15	0.74	67.83	1.95	69.81	1.26	154.65	3.11
7.40	0.68	0.03	9.16	0.34	56.65	1.41	70.17	1.33	136.64	2.82
7.60	0.50	0.02	5.83	0.50	43.38	1.99	69.47	1.91	119.28	4.43
7.80	0.37	0.02	3.81	0.33	29.84	0.76	68.67	1.48	102.82	2.04
8.00	0.28	0.01	2.53	0.23	18.35	0.49	67.73	2.62	89.01	2.94
8.20	0.21	0.01	1.74	0.06	11.02	0.28	66.64	1.78	79.77	2.08
8.40	0.16	0.01	1.26	0.03	6.97	0.18	65.69	1.24	74.31	1.66
8.60	0.13	0.01	0.91	0.04	4.44	0.11	64.11	2.22	69.92	1.81
8.80	0.10	0.00	0.71	0.02	2.90	0.34	62.55	1.46	66.65	2.94
9.00	0.08	0.00	0.53	0.01	1.97	0.07	60.63	1.41	63.70	1.94
9.20	0.06	0.00	0.40	0.01	1.38	0.11	57.83	1.18	60.27	1.28
9.40	0.05	0.00	0.30	0.01	0.98	0.03	54.73	1.99	56.74	1.49
9.60	0.04	0.00	0.24	0.01	0.74	0.02	50.09	2.10	51.83	2.61
9.80	0.03	0.00	0.18	0.00	0.55	0.02	43.63	1.69	45.11	2.08
10.00	0.02	0.00	0.14	0.00	0.41	0.01	34.62	0.89	35.82	1.15

Table 11.12: On-orbit HRMA Effective Area within 2π Steradian. Units: cm^2

Energy	Shell 1		Shell 3		Shell 4		Shell 6		HRMA	
(keV)	A_{eff}	Error	A_{eff}	Error	A_{eff}	Error	A_{eff}	Error	A_{eff}	Error
0.10	417.52	11.79	264.49	2.98	205.36	6.89	111.07	2.96	993.33	15.92
0.20	341.87	9.65	225.19	2.54	178.18	5.98	99.95	2.67	841.05	13.48
0.30	327.75	9.26	217.71	2.45	172.95	5.81	97.76	2.61	812.21	13.02
0.40	318.48	8.99	212.78	2.40	169.49	5.69	96.30	2.57	793.21	12.72
0.50	315.73	8.92	211.35	2.38	168.50	5.66	95.88	2.56	787.66	12.63
0.60	316.31	8.93	211.72	2.38	168.77	5.67	95.99	2.56	788.97	12.65
0.70	315.56	8.91	211.38	2.38	168.54	5.66	95.89	2.56	787.57	12.62
0.80	313.88	8.86	210.54	2.37	167.98	5.64	95.66	2.55	784.28	12.57
0.90	316.27	8.93	211.92	2.39	168.97	5.67	96.09	2.56	789.44	12.65
1.00	316.39	8.93	212.08	2.39	169.11	5.68	96.16	2.56	789.92	12.66
1.10	316.66	8.94	212.35	2.39	169.33	5.68	96.27	2.57	790.79	12.68
1.20	316.08	8.93	212.16	2.39	169.22	5.68	96.24	2.57	789.90	12.66
1.30	314.99	8.90	211.73	2.38	168.95	5.67	96.15	2.56	788.03	12.63
1.40	313.26	8.85	210.97	2.38	168.46	5.66	95.97	2.56	784.90	12.58
1.50	310.65	8.77	209.76	2.36	167.67	5.63	95.67	2.55	780.02	12.50
1.60	306.94	8.67	208.01	2.34	166.51	5.59	95.21	2.54	772.99	12.39
1.70	301.41	8.51	205.33	2.31	164.70	5.53	94.50	2.52	762.33	12.22
1.80	292.83	8.27	201.12	2.26	161.83	5.43	93.35	2.49	745.64	11.95
1.90	277.01	7.82	193.14	2.17	156.35	5.25	91.12	2.43	714.33	11.45
2.00	252.74	7.14	180.86	2.04	147.92	4.97	87.67	2.34	666.22	10.68
2.10	133.79	3.78	111.39	1.25	97.29	3.27	64.87	1.73	405.84	6.51
2.20	120.51	3.40	101.68	1.14	89.58	3.01	60.88	1.62	371.31	5.95
2.30	128.35	4.46	110.62	3.06	99.51	2.43	64.80	1.37	405.82	10.36
2.40	131.85	4.37	113.54	2.84	101.76	2.35	65.87	1.16	414.78	8.43
2.50	131.80	4.85	114.27	3.16	102.35	2.68	66.21	1.56	415.64	10.48
2.60	126.15	5.93	110.88	4.19	99.64	3.37	64.92	1.79	401.86	13.63
2.70	132.21	4.62	115.67	2.92	103.40	2.79	66.73	1.16	417.88	8.70
2.80	134.37	4.52	117.96	2.95	105.21	2.44	67.65	1.30	424.61	8.33
2.90	129.69	4.91	115.86	2.96	103.70	2.84	67.07	1.18	415.27	10.06
3.00	132.19	4.64	118.19	3.80	105.52	2.90	67.95	1.68	422.65	11.46
3.10	133.30	5.48	119.90	3.98	106.92	3.07	68.69	1.72	427.43	10.95
3.20	129.18	4.58	117.99	3.13	105.54	2.67	68.15	1.24	419.36	9.95
3.30	130.95	4.51	120.18	3.18	107.33	2.55	69.06	1.79	426.03	9.72
3.40	130.92	4.90	121.20	3.15	108.24	3.02	69.59	1.21	428.54	8.88
3.50	130.83	4.60	122.26	3.10	109.21	2.56	70.15	1.36	431.24	8.59
3.60	129.29	5.63	122.39	3.95	109.48	3.77	70.40	1.67	430.56	11.85
3.70	128.40	4.55	123.07	3.09	110.19	2.58	70.85	1.36	431.79	8.95
3.80	127.13	4.53	123.53	3.28	110.75	2.60	71.25	1.25	432.32	8.66
3.90	124.93	4.56	123.45	3.11	110.92	2.62	71.45	1.31	430.83	8.71
4.00	122.85	4.45	123.59	3.18	111.29	2.65	71.78	1.32	430.00	8.65
4.10	121.76	4.67	124.69	3.19	112.45	2.65	72.49	1.27	432.45	9.01
4.20	118.64	4.56	124.14	3.43	112.31	2.67	72.59	1.27	429.25	9.50
4.30	114.99	4.28	123.39	3.31	112.05	2.66	72.63	1.60	425.15	9.07

Table 11.12: On-orbit HRMA Effective Area within 2π Steradian. Units: cm^2 (continued)

Energy	Shell 1		Shell 3		Shell 4		Shell 6		HRMA	
(keV)	A_{eff}	Error	A_{eff}	Error	A_{eff}	Error	A_{eff}	Error	A_{eff}	Error
4.40	112.06	4.23	123.42	3.39	112.41	2.89	72.97	1.33	423.55	8.61
4.50	107.82	4.23	122.56	3.70	112.11	3.23	73.02	1.79	418.69	9.43
4.60	102.85	3.95	121.39	3.35	111.60	2.67	72.98	1.34	412.44	8.46
4.70	96.25	3.70	120.78	3.28	111.78	3.64	73.39	1.56	405.99	11.05
4.80	90.83	3.68	119.72	3.56	111.41	2.96	73.43	1.33	399.52	8.32
4.90	84.84	3.34	118.73	3.18	111.15	2.89	73.54	2.09	392.59	10.69
5.00	78.31	3.42	117.20	3.09	110.46	2.65	73.46	1.32	383.89	7.88
5.10	70.79	2.83	115.80	3.22	109.99	2.67	73.50	1.57	374.36	9.37
5.20	63.10	2.66	114.18	3.02	109.37	2.72	73.48	1.35	364.13	7.40
5.30	54.81	2.40	112.54	3.29	108.79	2.91	73.51	1.38	353.11	9.33
5.40	46.30	2.05	110.30	3.15	107.82	2.69	73.38	1.30	340.54	7.16
5.50	37.56	1.64	107.72	2.86	106.72	2.64	73.22	1.32	327.01	6.68
5.60	29.60	1.28	105.07	2.75	105.66	2.57	73.10	1.70	314.22	6.42
5.70	22.90	1.11	102.39	2.78	104.66	2.60	73.04	1.31	302.93	6.49
5.80	17.45	0.92	99.63	2.70	103.74	2.92	73.02	1.35	293.11	6.19
5.90	12.47	0.57	96.23	2.52	102.81	2.71	73.11	1.62	283.17	6.15
6.00	9.47	0.60	92.76	2.43	101.68	2.55	73.06	1.32	275.31	6.42
6.10	7.19	0.39	88.66	2.57	100.29	2.46	72.94	1.55	267.37	6.69
6.20	5.49	0.32	83.90	2.60	98.68	2.44	72.77	1.31	259.19	5.24
6.30	4.20	0.67	78.57	2.33	96.99	2.37	72.61	1.57	250.84	5.20
6.40	3.23	0.18	72.37	2.08	95.06	2.39	72.43	1.33	241.74	4.89
6.50	2.52	0.13	65.28	2.13	92.58	2.28	72.08	1.29	231.33	5.16
6.60	1.96	0.27	57.88	1.80	90.60	3.26	72.05	1.49	221.54	5.12
6.70	1.51	0.27	49.50	1.63	88.44	2.48	72.13	1.29	210.82	4.37
6.80	2.12	0.09	41.67	1.09	85.63	2.43	71.91	1.63	199.88	5.34
6.90	1.75	0.07	33.92	1.49	82.05	3.81	71.52	2.28	188.14	6.66
7.00	1.44	0.06	26.90	0.85	78.38	2.38	71.30	3.57	177.25	6.97
7.10	1.20	0.05	20.80	0.54	73.87	4.35	70.95	3.09	166.37	7.90
7.20	1.01	0.04	16.19	0.74	68.05	1.96	70.03	1.26	155.16	3.12
7.40	0.69	0.03	9.19	0.34	56.85	1.42	70.38	1.33	137.10	2.83
7.60	0.51	0.02	5.85	0.50	43.54	2.00	69.69	1.91	119.69	4.44
7.80	0.38	0.02	3.83	0.33	29.97	0.76	68.88	1.48	103.18	2.05
8.00	0.29	0.01	2.54	0.23	18.44	0.49	67.94	2.62	89.34	2.95
8.20	0.22	0.01	1.75	0.06	11.08	0.29	66.87	1.78	80.08	2.08
8.40	0.17	0.01	1.27	0.03	7.01	0.18	65.91	1.25	74.60	1.67
8.60	0.13	0.01	0.92	0.04	4.48	0.12	64.31	2.23	70.17	1.81
8.80	0.10	0.00	0.72	0.02	2.94	0.35	62.75	1.47	66.89	2.95
9.00	0.08	0.00	0.53	0.01	1.99	0.07	60.82	1.42	63.94	1.94
9.20	0.06	0.00	0.40	0.01	1.40	0.11	58.04	1.18	60.50	1.28
9.40	0.05	0.00	0.30	0.01	0.99	0.03	54.91	1.99	56.95	1.49
9.60	0.04	0.00	0.24	0.01	0.75	0.02	50.26	2.11	52.02	2.62
9.80	0.03	0.00	0.19	0.00	0.56	0.02	43.80	1.70	45.29	2.09
10.00	0.03	0.00	0.14	0.00	0.41	0.01	34.76	0.89	35.97	1.15

11.19 Conclusion

The HRMA calibration at the XRCF of MSFC made novel use of the X-ray continuum radiation from a conventional electron-impact source. Taking advantage of the good spectral resolution of solid-state detectors, continuum measurements proved advantageous in calibrating the effective area of AXAF's High-Resolution Mirror Assembly (HRMA) for the entire AXAF energy band.

The HRMA effective area was obtained by comparing the spectrum detected by a SSD at the focal plane with the spectrum detected by a beam normalization SSD in Building 500. Many systematic effects such as pileup, deadtime, beam uniformity, energy scale, icing, relative quantum efficiency, background, *etc.*, must be analyzed during the data reduction process.

In the data analysis, we did not use the actual SSD spectral response matrices. This could introduce an error as the energy resolutions of the two SSDs are slightly different. However, we did convolutions of the preliminary SSD spectral response matrices with the calibration data scaled raytrace predictions, and compared them with the measured effective area for each shell. The fit was reasonably good. Had we used the original raytrace prediction in the convolution, the fit would not be acceptable. This justifies the method we used to reduce the data and the calibrated effective area we generated. This work will be improved in the near future by using more detailed SSD response matrices calibrated at the BESSY to unfold the spectra and a pileup correction model as a continuous function of energy.

The results of the SSD C-continuum measurements show that the measured effective area is substantially less than the predicted effective area by well more than the experimental errors, especially for shell 1. Although we still don't have a good explanation for the cause or causes of this discrepancy on this important AXAF capability, we are currently assessing the reflectivity and surface scattering calculations in our raytrace model. When this is done, we will re-assess the differences between the data and the model, and, if necessary, apply similar, but smaller, polynomial corrections to our improved raytrace predictions.

Presently we have yet to achieve the calibration goal of 1% precision for the HRMA effective area. We expect to approach this goal as this work progresses.

Based on the SSD C-continuum Measurements at the XRCF, we have calibrated the HRMA effective area for its on-orbit performance as well as its actual values at the XRCF. The HRMA effective area is one of the most important AXAF capabilities. These calibrated values of the effective area can be used to make AXAF on-orbit performance predictions, and by other AXAF teams to calibrate their science instruments.

The HRMA effective area "rdb" tables and their figures are available on the World Wide Web pages for:

XRCF: $http://hea\text{-}www.harvard.edu/MST/mirror/www/xrcf/hrma\_ea.html$
On-orbit: $http://hea\text{-}www.harvard.edu/MST/mirror/www/orbit/hrma\_ea.html$

Chapter 12

HRMA Effective Area: Spectral Line Measurements

Richard J. Edgar

12.1 Introduction

This chapter describes the best effort to date to reduce data taken to determine the on-axis effective area of the HRMA shells. These experiments consist of electron impact point source (EIPS) measurements done in Phase 1, with flow proportional counters (FPC) and solid state detectors (SSD) used as both beam normalization detectors and at the HRMA focal point. In principle, since all the detectors of each type are nearly identical, most of the detector effects will cancel. In practice, at the few percent level, no two physical artifacts are identical, and so we will need to calibrate a great many effects and carefully remove them from the data.

12.2 FPC Data Reduction

The data were processed in much the same way as the generic XRCF FPC data, as described in §9.4. In order to improve the fidelity of the analysis, however, certain systematic effects need to be accounted for, which necessitates additional care in some aspects of the data reduction.

One such effect is to include the (rough) shape of the HRMA effective area curve in the analysis. Since the input spectrum is a strong line with a weak continuum, the main effect of modulating the spectrum with the HRMA effective area (as a function of energy) is to change the shape of the continuum. This does not change the counting rate at the line, but rather the shape of the continuum. Fitting the continuum well allows one to confidently separate continuum photons that fall in the region of the line from line photons, and to quote a counting rate due to line photons only, despite the poor intrinsic resolution of the FPC detectors.

Most of the tests covered here are encircled energy (EE) tests, which have many iterations using different sizes of pinhole apertures on the focal plane detector. After verifying that the counting rates measured by the BND-H detectors are time-independent to within 1.5% (often within 0.3%), the data from all these iterations (or those where a given detector was functioning, if it went offline for some of them) were co-added, to improve the signal to noise ratio for further analysis. In one case, Cr K–α, the beam flux was decaying monotonically with time, so we did not co-add the BND

Instr.	Line	E (keV)	Shell	TRW ID	Runid	
					35mm	2mm
FPC	C−Kα	0.277	1	D−IXF−EE−3.001	108597	108593
FPC	C−Kα	0.277	1	D−IXF−EE−3.012	108549	108545
FPC	C−Kα	0.277	3	D−IXF−EE−3.002	108627	108623
FPC	C−Kα	0.277	3	D−IXF−EE−3.013	108572	108568
FPC	C−Kα	0.277	4	D−IXF−EE−3.003	108658	108654
FPC	C−Kα	0.277	4	E−IXF−EE−3.014	110488	110484
FPC	C−Kα	0.277	6	D−IXF−EE−3.004	108689	108685
FPC	C−Kα	0.277	6	E−IXF−EE−3.015	110518	110513
FPC	Cu−Lα	0.930	all	D−IXF−EE−4.002	109397	109393
FPC	Al−Kα	1.486	1	D−IXF−EE−2.001	107326	107321
FPC	Al−Kα	1.486	3	D−IXF−EE−2.002	107358	107354
FPC	Al−Kα	1.486	4	D−IXF−EE−2.003	107388	107384
FPC	Al−Kα	1.486	6	D−IXF−EE−2.004a	107979	107975
SSD	Nb−Lα	2.166	all	D−IXS−MC−1.001	...	110126
SSD	Ag−Lα	2.980	all	E−IXS−EE−71.001	...	111193
SSD	Sn−Lα	3.444	all	D−IXS−EE−99.021	...	110097
FPC	Ti−Kα	4.510	1	D−IXF−EE−3.005	109125	109121
FPC	Ti−Kα	4.510	3	D−IXF−EE−3.006	109221	109217
FPC	Ti−Kα	4.510	4	D−IXF−EE−3.007	109157	109153
FPC	Ti−Kα	4.510	6	D−IXF−EE−3.008	109187	109183
FPC	Ti−Kα	4.510	all	D−IXF−3D−9.001	...	109242
FPC	Cr−Kα	5.410	all	E−IXF−EE−4.004	111904	111900
FPC	Fe−Kα	6.400	3	D−IXF−EE−3.009A	108232	108228
FPC	Fe−Kα	6.400	4	D−IXF−EE−3.010a	108350	108346
FPC	Fe−Kα	6.400	6	D−IXF−EE−3.011	108298	108294
FPC	Cu−Kα	8.030	all	D−IXF−EE−4.001	109360	109356

Table 12.1: Encircled Energy tests analyzed for the HRMA effective area

spectra.
A few of the effects which can be corrected are:

- Gain Nonuniformity in the open BND-H detectors
- Relative Quantum Efficiencies (RQE) of the detectors
- Beam Uniformity (BU) effects

Each of these is described in detail below.

In Table 12.1 we list the TRW ID numbers for each of the encircled energy tests we have analyzed in this effort. The corrections involve data from other tests, such as background runs, beam uniformity tests, and flat field tests. We list in Table 12.2 the TRW ID numbers of these other ancillary tests.

12.3 Gain Nonuniformity in the open BND-H detectors

Unlike the fpc_5 and focal plane FPC detectors, the BND-H detectors have a substantial amount of open area, approximately 3.6 × 9.9 cm. The response of these single-wire flow proportional

Line	E(keV)	BG TRW ID	BU TRW ID	RBG TRW ID	RQE TRW ID
C−Kα	0.277	D−IXF−BG−1.019	D−BND−BU−2.038	J−IXF−BG−1.027a	J−BND−BU−2.038
Cu−Lα	0.930	D−IXF−BG−1.001	D−BND−BU−2.001	J−IXF−BG−1.001	J−BND−BU−2.002
Al−Kα	1.486	D−IXF−BG−1.018b	D−BND−BU−2.036a	J−IXF−BG−1.026a	J−BND−BU−2.036
Nb−Lα	2.166	D−IXF−BG−1.007	D−BND−BU−2.013	J−IXF−BG−1.007	J−BND−BU−2.013
Ag−Lα	2.980	E−IXF−BG−1.008	E−BND−BU−2.015	J−IXF−BG−1.008	J−BND−BU−2.015
Sn−Lα	3.444	D−IXF−BG−1.010	J−BND−BU−2.019	J−IXF−BG−1.010	J−BND−BU−2.019
Ti−Kα	4.510	D−IXF−BG−1.015	D−BND−BU−2.030	J−IXF−BG−1.024	J−BND−BU−2.030
Cr−Kα	5.410	E−IXF−BG−1.012	E−BND−BU−2.023	J−IXF−BG−1.012	J−BND−BU−2.024
Fe−Kα	6.400	D−IXF−BG−1.013	D−BND−BU−2.028	J−IXF−BG−1.023	J−BND−BU−2.028
Cu−Kα	8.030	D−IXF−BG−1.002	D−BND−BU−2.004	*I−IAI−SG−5.024	*I−BND−BU−2.004

Table 12.2: Ancillary tests used in the present analysis. *Since no flat field tests were done at Cu-Kα in phase J, these are from phase I. The relative quantum efficiency for fpc_hs is assumed to be equal to that of fpc_hb.

counters has been found to be quite uniform across the wire (in the Y direction at XRCF), but the gain is significantly higher near the ends of the detectors. Prior to the calibration, the blocking plate apertures were reworked, giving a somewhat smaller open area and masking the ends of the counters where the gain was largest. However, there is still enough variation of gain along the wire that it must be taken into account in order to obtain acceptable fits to the spectra.

The fpc_hn detector could be used either open, or with a 36 mm circular aperture. When used with the 36 mm aperture, the gain nonuniformity effect is negligible.

We have used a technique involving two interlinked `JMKmod` models to fit these data, in order to account for the gain nonuniformity in these detectors. This is described in detail in §9.4.

12.4 FPC Beam Uniformity (BU) effects

The x-ray beam produced by the electron impact point source (EIPS) at XRCF is quite uniform. Beam Uniformity tests (BU) were conducted at each energy, and so the few percent variations in intensity with position across the HRMA entrance can be accounted for. These experiments (see Chapter 24) consisted of moving the fpc_hn around in front of the HRMA entrance, and to the position of each of the BND-H detectors. We can then calculate a beam uniformity factor for each detector (or the average over a given part of the HRMA) by:

$$BU_{det} = R(\text{fpc\_hn at det})/R(\text{fpc\_5}),$$

where the R variables are (fitted) count rate fluxes in detector counts s^{-1} cm^{-2}, projected to the HRMA entrance plane. The normalization to the fpc_5 rate controls for possible time-dependence of the beam strength. In Chapter A, we list the aperture areas and source distances used in this reduction effort.

12.5 Relative Quantum Efficiencies (RQE) of the FPC detectors

Data from the Phase I and J flat field tests were analyzed to compute relative quantum efficiencies for the HXDS detectors. The results of the analysis of these data are summarized in §3.5.3.

These tests were conducted in much the same manner as the Beam Uniformity tests during the HRMA calibration. In this case, the fpc_hn was positioned in turn in front of each of the other

FPC detectors (the BND-H detectors, and the fpc_x2). Some of the exposures were done with the fpc_hn open, and some with the 36 mm circular aperture. Thus double `JMKmod` fits must be done to analyze these data. When the 36 mm aperture is in use, the norm of the second `JMKmod` fits to a very small fraction of the main model component. A beam uniformity factor can be computed for each detector position from the same flat field data (not to be confused with the BU factors from the main HRMA calibration, discussed above), and the relative quantum efficiency can be computed:

$$RQE_{det} = \frac{R_{det}}{R_{\text{fpc\_hn}}} \times \frac{BU_{\text{fpc\_hn}}}{BU_{det}}.$$

It is a worthwhile exercise to work through the units in this equation. The first ratio of R variables is in detector counts per fpc_hn count, measured at the fpc_hn home position. The BU factors are in fpc_hn counts at the home position, and at the position of the detector in question, respectively:

$$RQE_{det} \sim \frac{det \text{ counts}}{\text{fpc\_hn counts at home}} \times \frac{\text{fpc\_hn counts at home/fpc\_5 counts}}{\text{fpc\_hn counts at } det\text{/fpc\_5 counts}}.$$

Since the counters were operated at systematically different temperatures during the Phase 1 HRMA calibration and the Phase J flat field measurements, corrections have been made in accordance with the method described in §3.5.4. This amounts to less than 2% and is most important at high energies, and just below 3 keV. The effect arises because the pressure of the gas in the FPCs was controlled and quite stable at 400 torr, and so the density of the gas varies inversely as the absolute temperature. This in turn makes the optical depth of the gas vary, and so at high energies where this optical depth is not large, the quantum efficiency of the counters can be affected.

Note that no direct RQE measurement is available for fpc_hs at Cu K–α. We assume that the RQE for this detector is the same as for fpc_hb, which is true at other high energies (see Table 3.5).

12.6 Corrected HRMA Entrance Flux: FPC detectors

Now that we have corrections for beam uniformity and relative quantum efficiency, we can combine these with the BND data to compute a corrected flux at the HRMA entrance. Note that, since the QE corrections are relative to the fpc_hn, all corrected fluxes are in units of fpc_hn counts s^{-1} cm^{-2}. For each detector,

$$F_{det} = \frac{\langle BU_{HRMA} \rangle}{BU_{det}} \times \frac{R_{det}}{RQE_{det}},$$

where R_{det} is the count rate flux in the detector in question, in counts s^{-1} cm^{-2}, projected to the HRMA entrance plane. The quantity $\langle BU_{HRMA} \rangle$ is the average beam uniformity factor over the exposed portion of the HRMA.

The four corrected fluxes due to the four BND-H detectors are then averaged to give $\langle F \rangle$:

$$\langle F \rangle = \frac{1}{4} \sum_{BND} F_{BND}.$$

12.7 Effective Areas: FPC detectors

We then put the above corrections together to produce a number for the effective area of the HRMA at each energy for each mirror combination exposed.

$$A_{eff} = \frac{C_{\mathsf{fpc\_x2}}/RQE_{\mathsf{fpc\_x2}}}{\langle F\rangle},$$

where $C_{\mathsf{fpc\_x2}}$ is the count rate in the fpc_x2. Note that dividing by the RQE for this detector puts the numerator in units of fpc_hn counts s^{-1}, so that the effective area comes out in units of cm^2.

We give these values in Table 12.3 (for 35 mm apertures) and Table 12.4 (for 2 mm apertures). Also listed in the tables are the average BND fluxes, and various contributions to the error (see next section).

For comparison with ray trace models, we show the data derived here on plots of effective area vs. energy for each shell, and for the HRMA ensemble in Figures 12.1to12.6. The ray trace models shown here are those from model xrcf_SA01G+HDOS_HDOS-scat-970220_03, which is described in Chapter 10. The HRMA ensemble points at C, Al, Ti, and Fe K–α (0.277, 1.49, 4.51, and 6.4 keV) are sums of the single shell effective areas (assuming 4.1 and 4.7 cm^2 effective area for shell 1, for 2 mm and 35 mm apertures respectively, at Fe K–α, numbers obtained from the SSD continuum experiments, Chapter 11). Those at the other energies are direct measurements with the full HRMA. In Figures 12.4to12.6, which show results using the 2 mm aperture, we also show the effective area measured with the SSD continuum experiments, described more fully in Chapter 11. Continuum points below 1.3 keV have been excluded, as systematic effects dominate the measurement in this band. Note that there were both single-shell and full-HRMA measurements with 2 mm apertures at Ti K–α.

12.8 Error Analysis: FPC detectors

The quoted errors on the effective areas include several effects. Each JMKmod fit has uncertainties which include statistical errors and a few systematic effects which we have not corrected for.

We have included the average corrected BND fluxes $\langle F\rangle$, the RMS deviation among the four individual corrected BND fluxes δF_{dev}, the propagated fitting (including statistical) error in each BND flux δF_{prop}, and the standard deviation of the mean of the four BND fluxes, in Table 12.3 and Table 12.4.

This last quantity $\sigma_{\langle F\rangle}$ is used as the error on the BND flux for further computation, including the effective area.

$$\delta F_{dev} = \Big(\frac{1}{3}\sum_{BND}(F_{BND} - \langle F\rangle)^2\Big)^{1/2}$$

$$\delta F_{prop} = \Big(\frac{1}{4}\sum_{BND}\sigma^2_{F_{BND}}\Big)^{1/2}$$

$$\sigma_{\langle F\rangle} = \Big(\frac{1}{3\times 4}\sum_{BND}(F_{BND} - \langle F\rangle)^2\Big)^{1/2}$$

We find that the HRMA-averaged fluxes derived from the different BND-H detectors for a given test sometimes disagree in a statistically significant manner, even after correction for beam uniformity and relative quantum efficiency effects. The situation is summarized in Table 12.3 and

EE TRW ID	E (keV)	Line	Shell	$\langle F\rangle$	δF_{dev}	δF_{prop}	$\sigma_{\langle F\rangle}$	$A_{\rm eff}$
D−IXF−EE−3.001	0.277	C−Kα	1	4.273	0.154	0.035	0.077	338.143 ± 6.503
D−IXF−EE−3.012	0.277	C−Kα	1	4.438	0.025	0.037	0.012	327.784 ± 2.322
D−IXF−EE−3.002	0.277	C−Kα	3	4.310	0.037	0.035	0.019	215.486 ± 1.853
D−IXF−EE−3.013	0.277	C−Kα	3	4.449	0.030	0.036	0.015	217.122 ± 1.753
D−IXF−EE−3.003	0.277	C−Kα	4	4.265	0.063	0.035	0.032	178.157 ± 1.930
E−IXF−EE−3.014	0.277	C−Kα	4	4.070	0.037	0.034	0.018	164.369 ± 1.532
D−IXF−EE−3.004	0.277	C−Kα	6	4.269	0.041	0.035	0.021	97.197 ± 1.054
E−IXF−EE−3.015	0.277	C−Kα	6	4.066	0.032	0.033	0.016	94.222 ± 1.025
...EE−3.00[1,2,3,4]	0.277	C−Kα	sum	...	...	...	...	828.982 ± 7.111
...EE−3.01[2,3,4,5]	0.277	C−Kα	sum	...	...	...	...	803.498 ± 3.444
D−IXF−EE−4.002	0.930	Cu−Lα	all	2.198	0.029	0.025	0.014	758.110 ± 7.148
D−IXF−EE−2.001	1.486	Al−Kα	1	17.645	0.117	0.144	0.058	304.951 ± 2.042
D−IXF−EE−2.002	1.486	Al−Kα	3	36.194	0.282	0.295	0.141	203.237 ± 1.345
D−IXF−EE−2.003	1.486	Al−Kα	4	49.420	0.353	0.403	0.177	166.329 ± 1.061
D−IXF−EE−2.004a	1.486	Al−Kα	6	36.313	0.172	0.296	0.086	94.116 ± 0.581
...EE−2.00[1,2,3,4a]	1.486	Al−Kα	sum	...	...	...	...	768.633 ± 2.728
D−IXF−EE−3.005	4.510	Ti−Kα	1	19.842	0.469	0.158	0.235	103.870 ± 1.482
D−IXF−EE−3.006	4.510	Ti−Kα	3	19.926	0.489	0.159	0.244	116.448 ± 1.699
D−IXF−EE−3.007	4.510	Ti−Kα	4	19.875	0.518	0.159	0.259	103.824 ± 1.606
D−IXF−EE−3.008	4.510	Ti−Kα	6	19.920	0.507	0.159	0.253	70.427 ± 1.059
...EE−3.00[5,6,7,8]	4.510	Ti−Kα	sum	...	...	...	...	394.569 ± 2.964
E−IXF−EE−4.004	5.410	Cr−Kα	all	67.320	0.550	0.705	0.275	327.220 ± 2.464
D−IXF−EE−3.009A	6.400	Fe−Kα	3	43.304	0.506	0.585	0.253	61.867 ± 0.729
D−IXF−EE−3.010a	6.400	Fe−Kα	4	31.933	0.469	0.431	0.234	88.785 ± 1.118
D−IXF−EE−3.011	6.400	Fe−Kα	6	43.179	0.491	0.583	0.246	68.795 ± 0.797
...EE−3.0[09A,10a,11]	6.400	Fe−Kα	sum	...	...	...	...	224.146 ± 1.558
D−IXF−EE−4.001	8.030	Cu−Kα	all	43.685	2.917	1.545	1.459	82.929 ± 3.821

Table 12.3: Effective Area results for 35 mm apertures and average BND fluxes with error contributions. Note that the summed result at Fe K–α includes 4.7 ± 0.1 cm^2 for shell 1, obtained from ssd continuum measurements.

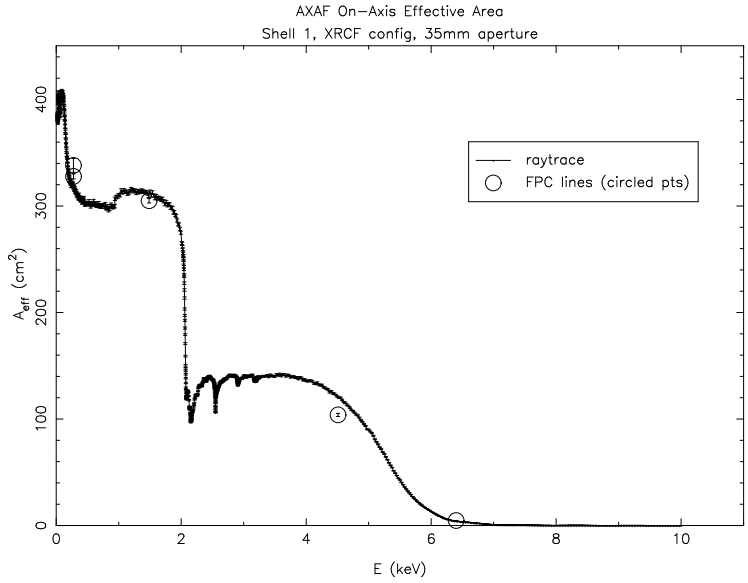

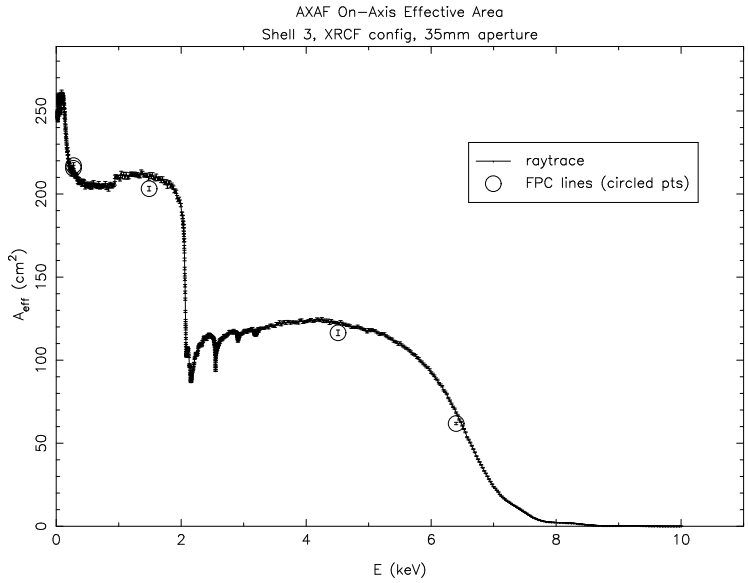

Figure 12.1: Measurements and Ray traces for effective area through 35 mm pinholes for shells 1 and 3.

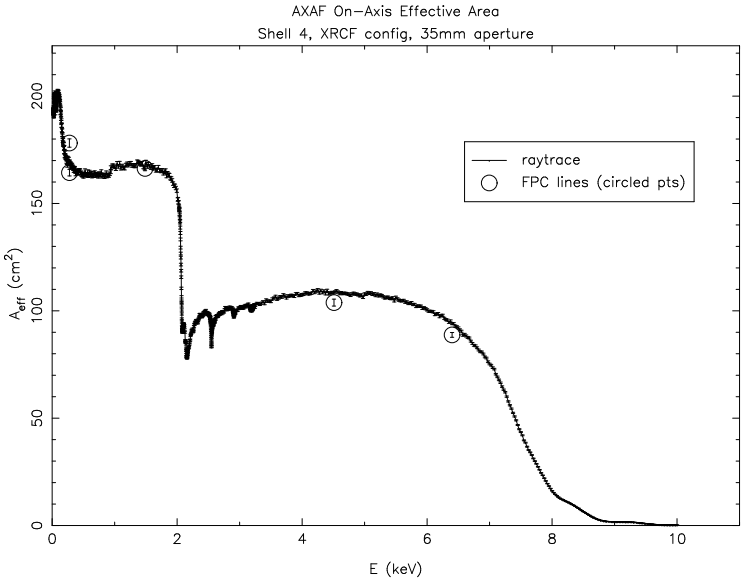

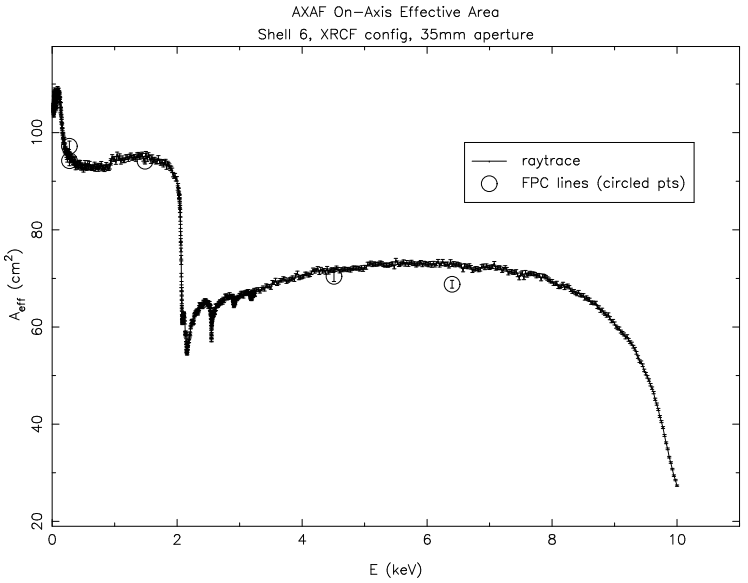

Figure 12.2: Measurements and Ray traces for effective area through 35 mm pinholes for shells 4 and 6.

EE TRW ID	E (keV)	Line	Shell	$\langle F \rangle$	δF_{dev}	δF_{prop}	$\sigma_{\langle F \rangle}$	$A_{\rm eff}$
D−IXF−EE−3.001	0.277	C−Kα	1	4.273	0.154	0.035	0.077	332.949 ± 6.407
D−IXF−EE−3.012	0.277	C−Kα	1	4.438	0.025	0.037	0.012	329.784 ± 2.351
D−IXF−EE−3.002	0.277	C−Kα	3	4.310	0.037	0.035	0.019	213.863 ± 1.837
D−IXF−EE−3.013	0.277	C−Kα	3	4.449	0.030	0.036	0.015	214.354 ± 1.725
D−IXF−EE−3.003	0.277	C−Kα	4	4.265	0.063	0.035	0.032	173.135 ± 1.883
E−IXF−EE−3.014	0.277	C−Kα	4	4.070	0.037	0.034	0.018	162.788 ± 1.540
D−IXF−EE−3.004	0.277	C−Kα	6	4.269	0.041	0.035	0.021	98.756 ± 1.082
E−IXF−EE−3.015	0.277	C−Kα	6	4.066	0.032	0.033	0.016	94.168 ± 1.028
...EE−3.00[1,2,3,4]	0.277	C−Kα	sum	...	...	...	...	818.704 ± 7.010
...EE−3.01[2,3,4,5]	0.277	C−Kα	sum	...	...	...	...	801.094 ± 3.454
D−IXF−EE−4.002	0.930	Cu−Lα	all	2.198	0.029	0.025	0.014	760.004 ± 7.163
D−IXF−EE−2.001	1.486	Al−Kα	1	17.645	0.117	0.144	0.058	294.526 ± 1.874
D−IXF−EE−2.002	1.486	Al−Kα	3	36.194	0.282	0.295	0.141	202.294 ± 1.335
D−IXF−EE−2.003	1.486	Al−Kα	4	49.420	0.353	0.403	0.177	164.509 ± 1.049
D−IXF−EE−2.004a	1.486	Al−Kα	6	36.313	0.172	0.296	0.086	92.950 ± 0.574
...EE−2.00[1,2,3,4a]	1.486	Al−Kα	sum	...	...	...	...	754.279 ± 2.593
D−IXS−MC−1.001	2.166	Nb−Lα	all	2.203	...	...	0.036	352.451 ± 5.700
E−IXS−EE−71.001	2.980	Ag−Lα	all	6.661	...	...	0.157	410.267 ± 10.066
D−IXS−EE−99.021	3.444	Sn−Lα	all	1.577	...	...	0.029	402.518 ± 8.033
D−IXF−EE−3.005	4.510	Ti−Kα	1	19.842	0.469	0.158	0.235	89.066 ± 1.280
D−IXF−EE−3.006	4.510	Ti−Kα	3	19.926	0.489	0.159	0.244	113.921 ± 1.659
D−IXF−EE−3.007	4.510	Ti−Kα	4	19.875	0.518	0.159	0.259	100.747 ± 1.556
D−IXF−EE−3.008	4.510	Ti−Kα	6	19.920	0.507	0.159	0.253	67.477 ± 1.016
D−IXF−3D−9.001	4.510	Ti−Kα	all	12.670	0.327	0.153	0.163	362.434 ± 5.688
...EE−3.00[5,6,7,8]	4.510	Ti−Kα	sum	...	...	...	...	371.211 ± 2.801
E−IXF−EE−4.004	5.410	Cr−Kα	all	68.016	0.834	0.712	0.417	307.146 ± 2.700
D−IXF−EE−3.009A	6.400	Fe−Kα	3	43.304	0.506	0.585	0.253	58.346 ± 0.691
D−IXF−EE−3.010a	6.400	Fe−Kα	4	31.933	0.469	0.431	0.234	82.246 ± 1.042
D−IXF−EE−3.011	6.400	Fe−Kα	6	43.179	0.491	0.583	0.246	64.605 ± 0.753
...EE−3.0[09A,10a,11]	6.400	Fe−Kα	sum	...	...	...	...	209.307 ± 1.463
D−IXF−EE−4.001	8.030	Cu−Kα	all	43.685	2.917	1.545	1.459	76.331 ± 3.519

Table 12.4: Effective Area results for 2 mm apertures, and average BND fluxes with error contributions. Note that the summed result at Fe K–α includes 4.1 ± 0.1 cm^2 for shell 1, obtained from ssd continuum measurements.

Table 12.4. The cause of this discrepancy is currently not understood. The comparison between δF_{dev} and δF_{prop} shows that they are in general comparable (as they should be if the dominant error is statistical), with the notable exception of Ti K–α.

12.9 SSD Data Analysis

There were three measurements of the HRMA effective area using spectral lines and the solid state detectors, with 2 mm apertures. These are listed in Table 12.1; they have TRW ID numbers containing the string "IXS" ("I"maging test (*i.e.* no gratings), with the H"X"DS, "S"SD detector). These tests were done at L-line complexes of Nb, Ag, and Sn, which in most cases would present significant challenges to FPC data analysis.

After verifying that the source is temporally stable within measurement errors, for those tests with multiple exposures, the ssd_5 spectra were summed. The data were then reduced by fitting the ssd_x and ssd_5 spectra with the JMKmod model, as described in Chapter 9. Great care was taken to arrive at physically reasonable values for the fitted parameters, including ratios of L-complex lines. Thanks are due to Allyn Tennant for advice on the Ag L–α fits.

Note that the use of a single beam normalization detector (ssd_5) avoids the problems discussed above with disagreements between BND fluxes. This perhaps makes the errorbars not comparable with those from the FPC tests, since this systematic effect is not present in these data.

The resulting fluxes require at least three corrections:

- Dead Time
- Beam Uniformity
- Relative Quantum Efficiency

These corrections proceed in ways analogous to those discussed above for the case of FPC detectors. A notable difference is that the beam normalization detector, ssd_5, is much closer to the source, and so beam uniformity tests must be conducted with the fpc_5 detector, and no other detector is available to control for temporal instability in the beam.

Beam uniformity factors are defined as follows:

$$BU_{\rm ssd\_5} = \frac{R(\text{fpc\_5 at ssd\_5})}{< R(\text{fpc\_5}) >_{HRMA}}.$$

In two of the cases, there exist fpc_5 beam maps done in close temporal proximity to the effective area test, and these are used. In the remaining case, Sn L–α, the high voltage for the fpc_5 was offline, so no such test was conducted. We have therefore taken beam uniformity factors from the Phase J flat field data to make this correction.

Dead time corrections are done according to the procedure outlined in Chapter 5. The initial analysis is done using the Gedcke-Hale deadtime estimates in the file headers. The pulser peak is then examined to determine how the number of counts detected compares to the number of counts injected (recorded in the file headers). The ratio of these quantities is the live time fraction. A correction factor is obtained by dividing the Gedcke-Hale live time fraction by the true value.

Relative quantum efficiency corrections are done by assuming, as shown in Chapter 11, that the ratio

$$\frac{QE(\text{ssd\_5})}{QE(\text{ssd\_x})} = 1.0141 \pm 0.0089.$$

This is not strictly correct for these low energies, especially below about 3 keV, since the ice thickness on the ssd_x window is unknown, and can have striking effects at such energies. Even so,

the 1.1% stated uncertainty on the relative quantum efficiency of the two detectors is the largest contribution to the errors of these effective area measurements.

12.10 Monochromator/FPC Effective Area Measurements

This section reports a still-in-progress analysis of the phase D and E monochromator measurements of the on-axis HRMA effective area. There are two series of measurements: the DCM measurements from phase D, and the HIREFS measurements from phase E. What follows relies on much advice from the Project Science people, especially Doug Swartz.

The HIREFS tests, which were single runs at single energies from 0.124 to 0.247 keV, have proven not very useful. This seems to be primarily because of beam uniformity problems, which are very severe due to the geometry of this monochromator; often the various BND detectors disagree as to the input flux by factors of five. This results in huge error bars. Since the beam uniformity was not in general measured at the same settings as used in the effective area tests, these data seem to be essentially worthless.

The DCM data from test D-IXF-EA-21.001 suffer from a similar problem. This test was a scan from 0.75 to 2.3 keV in steps of 50 eV. Since the strong tungsten M lines at 1.775 and 1.834 keV are in this band pass, severe beam uniformity problems resulted.

However, the situation is much better for the other 3 DCM scans, tests D-IXF-EA-2[234].001. The lack of strong tungsten lines and the broad spatially and spectrally uniform region at the HRMA entrance makes it possible to learn something from these data. All of these experiments were done with the full HRMA and 35 mm apertures. In 3 scans, they cover the range from 2.1 to 9 keV.

We have reduced the data in the usual way, fitting the FPC spectra using a `JMKmod` model consisting of no continuum, a background model (fit to background spectra and then fixed during spectral fits), and a series of spectral lines representing the first four orders of the advertised DCM energy. The first order flux only is used in the HRMA calibration. There are some interesting effects that occur in high orders when, for example, the fourth order nearly matches the tungsten L-α line; the fpc_hs sees it strongly and the other detectors do not.

We find for reasons that are not understood that the fpc_hn often disagrees with the other BND detectors as to the HRMA entrance flux; thus to minimize the error bars, it was excluded from the analysis.

We plot in Figure 12.7 the results of these analyses, using the fpc_ht, fpc_hb, and fpc_hs as normalization detectors, and making no corrections for relative quantum efficiencies or beam non-uniformities or other effects. We also show the FPC/EIPS spectral line data with 35 mm pinholes discussed above, for comparison. This plot is similar in spirit to the comparison between SSD continuum and EIPS line effective area measurements in Figure 12.6.

Several interesting effects are apparent in these data:

- The iridium M edges (the small depressions in the effective area curve between 2 and 3 keV) seem to appear in the data, just as predicted. This is of interest since other experiments (such as grating observations of the carbon continuum source) seem to indicate they are absent; while still another observation (the Nb L–α line SSD measurement discussed above) says that at least the M-IV edge is present. The presence and depths of these edge features can be used as a diagnostic of hydrocarbon contamination on the HRMA surfaces.

- The feature at 3.2 keV is almost certainly a feature of the QE of the FPC detectors, as it is coincident with the Ar K edge, at which energy the FPC QE jumps from $\sim$ 50% to unity. However, the analysis in Chapter 3 suggests that the fpc_x2 is the least sensitive of the detectors below the Ar edge, which implies that the jump in the raw effective area should go the other way:

$$A_{eff} = \frac{C_x/QE_x}{F_{BND}/ < QE >_{BND}}. \tag{12.1}$$

  Thus the effective area prior to correction for QE effects should vary inversely as the relative QE of the fpc_x2. But we observe it to jump *down* instead of the expected jump up. This effect is still under investigation.

- Some of the rattiness in the data in the 7–9 keV range is due to interaction with tungsten lines in the rotating anode source. With more care, and selection of points, this can be cleaned up a bit.

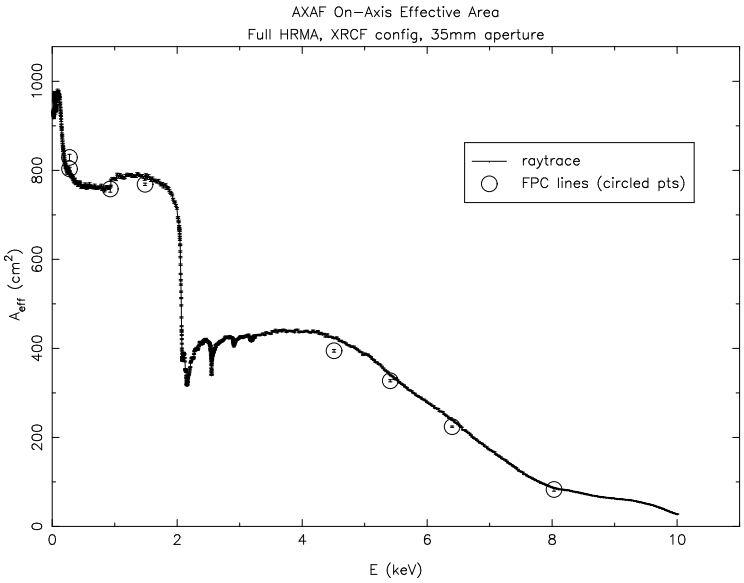

Figure 12.3: Measurements and Ray traces for effective area through 35 mm pinholes for the HRMA ensemble.

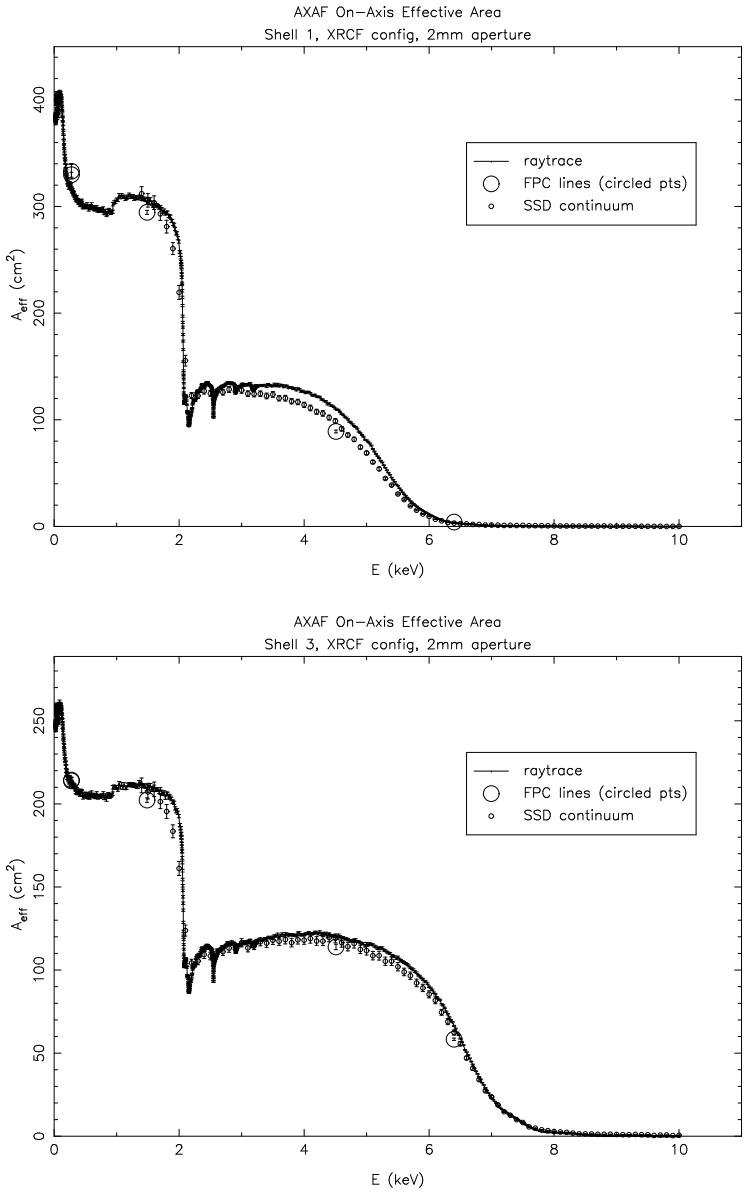

Figure 12.4: Measurements and Ray traces for effective area through 2 mm pinholes for shells 1 and 3. Both fpc_ and SSD continuum measurements are shown.

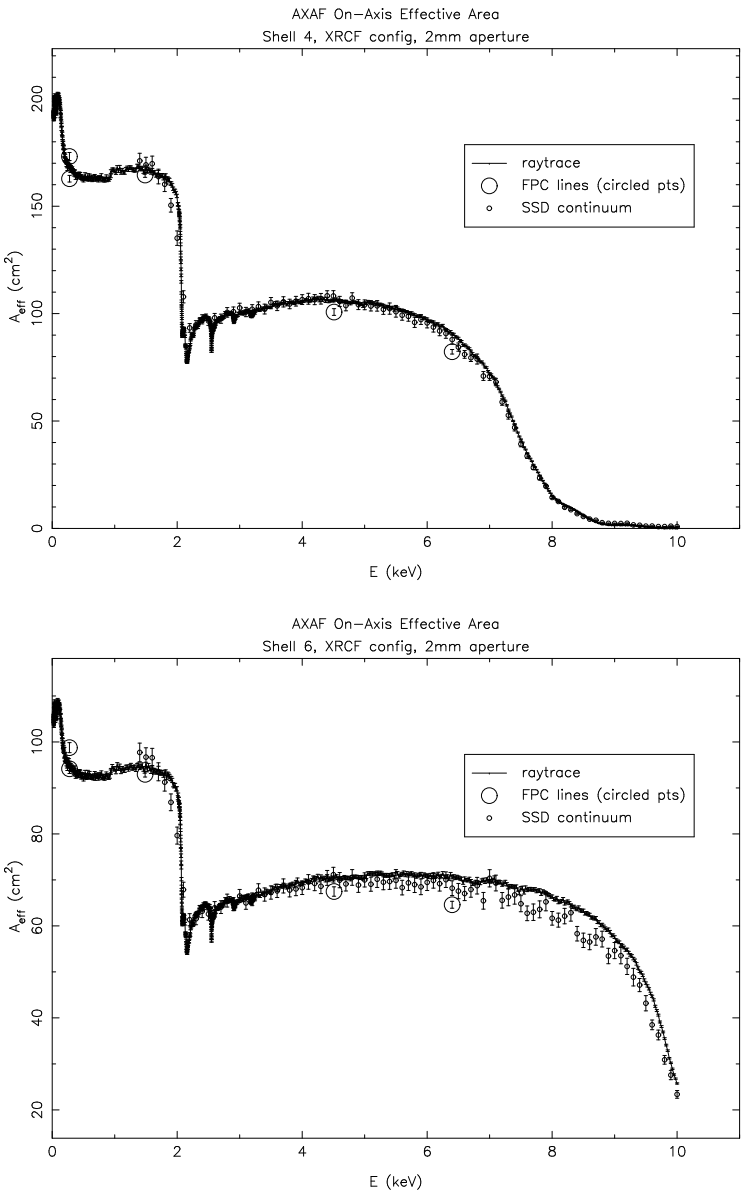

Figure 12.5: Measurements and Ray traces for effective area through 2 mm pinholes for shells 4 and 6. Both fpc_ and SSD continuum measurements are shown.

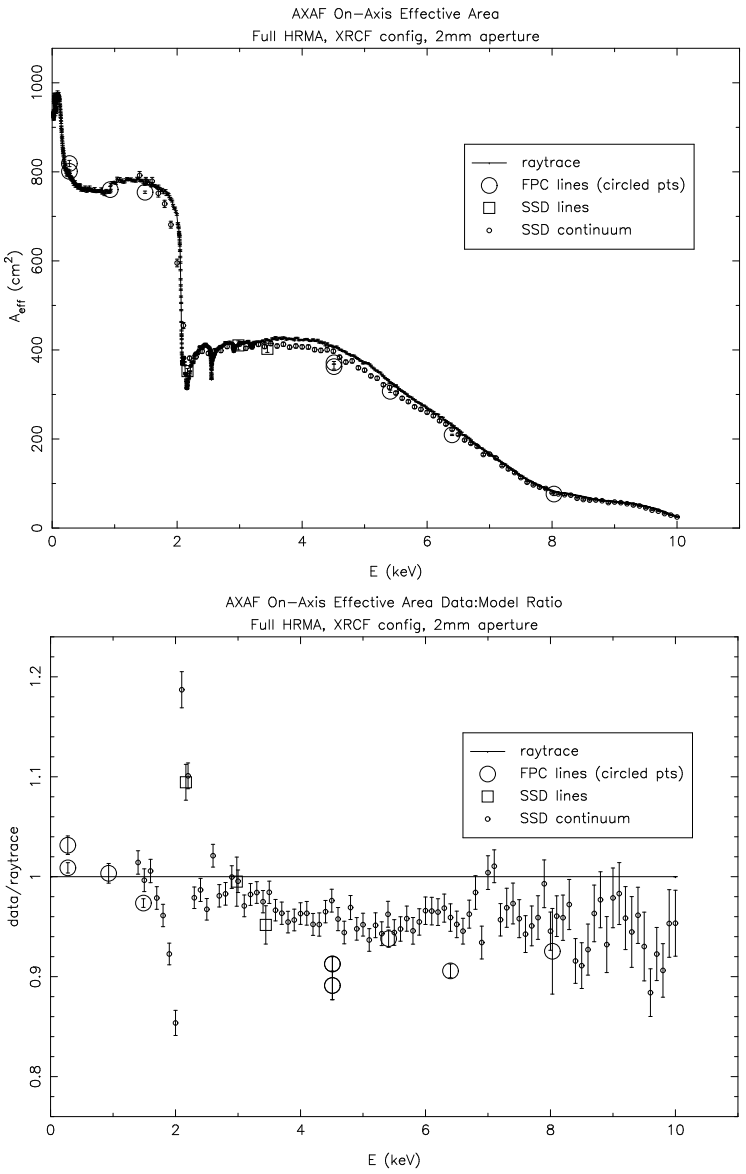

Figure 12.6: Measurements and Ray traces for effective area through 2 mm pinholes for the HRMA ensemble. Data shown include FPC and SSD line measurements and SSD continuum measurements. The lower panel shows ratios of the measurements to raytrace models.

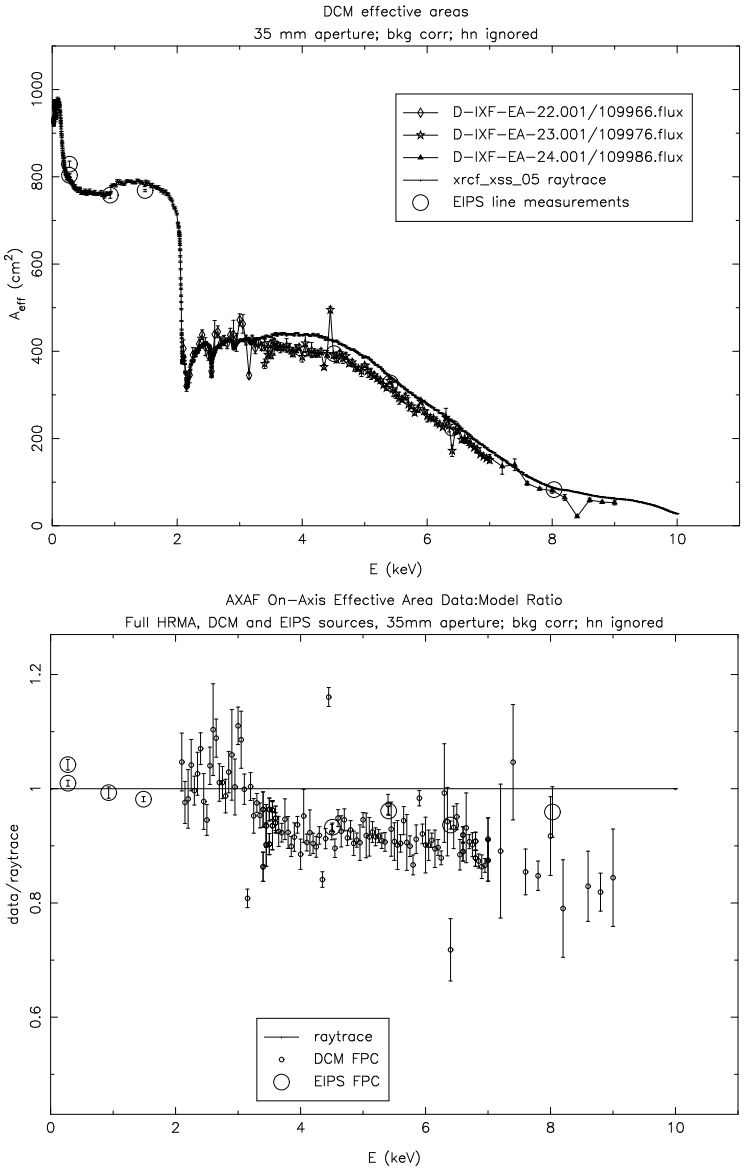

Figure 12.7: Measurements and Ray traces for effective area through 35 mm pinholes for the HRMA ensemble. Data shown include DCM measurements (small points) and FPC line measurements. The lower panel shows ratios of the measurements to raytrace models.

Chapter 13

Fitting the HRMA Effective Area

Michael Tibbetts

13.1 Introduction

This chapter deals with the effort to improve the agreement between the XRCF effective area data and the HRMA mirror models. We consider the effective areas derived from the solid state detector (SSD) continuum data, and attempt to fit the data by allowing the surface roughness value, σ, in the model to vary. Since σ is energy independent, we would expect to fit the effective area with a single value of σ for each optic. However, with the SSD continuum data, it is only possible to isolate each shell, a hyperboloid-paraboloid pair. The fits are further complicated by the fact that the optical constants for each optic were determined from a single witness coupon from the p6 optic, coupon 065. The optical constants for this coupon were determined by fitting reflectivity data taken by the MST synchrotron group. Due to limitations on the range of the energy scale available with a given setup at the synchrotron, the reflectivity data were taken over multiple energy ranges. Each energy range was fit independently by varying the value of σ in the model of the witness coupon. Thus, the SSD continuum simulations contain optical constants derived from measurements of a single optic but applied to all optics. Also, the optical constants from the synchrotron reflectivity data allow the value of σ to vary between energy ranges.

In fitting the SSD continuum data, we begin by fitting the effective area with a single value of σ applied over the entire energy range. It will be shown that the effective areas derived in this manner fit the data poorly. From there we fit the data over multiple energy ranges corresponding to the energy ranges used in deriving the optical constants from the synchrotron data. These fits show varied results based on energy range and shell.

13.2 Mirror Model

The simulations treat the mirrors as multi-layered surfaces comprised of a layer of Iridium, a layer of Chromium, and a layer of Zerodur in a vacuum, as illustrated in figure 13.1.

At the interface of each layer, including the vacuum-Iridium interface, the simulations calculate the reflection and transmission coefficients. The reflection coefficient, r_t, for the top interface can be calculated recursively using the following formula:

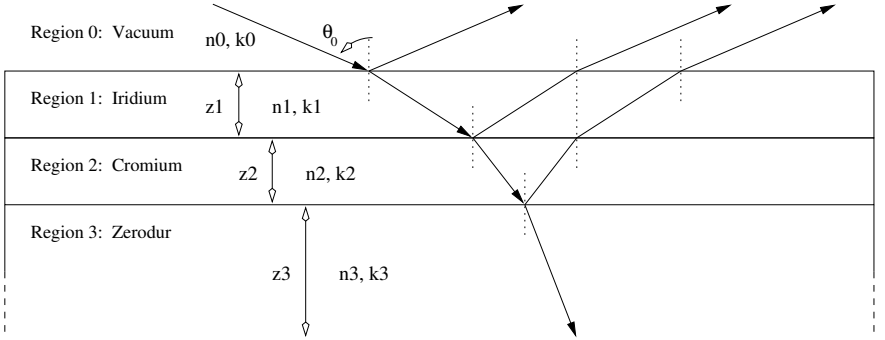

Figure 13.1: Reflection and transmission through a multi-layer mirror.

$$r_t = r_{ij} + \frac{r_b t_{ij} t_{ji} e^{2i\beta_j}}{1 + r_{ij} r_b e^{2i\beta_j}} \tag{13.1}$$

where r_{ij} is the reflection coefficient for the interface between the i-th and j-th layers, r_b is the reflection coefficient from the bottom layer, t_{ij} and t_{ji} are the transmission coefficients into and out of the interface, and β_j is defined below.

$$\beta_j = \frac{2\pi n_j z_j \cos\theta_j}{\lambda} \tag{13.2}$$

where n_j is the optical constant from layer j, z_j is the layer thickness, θ_j is the incidence angle, and λ is the wavelength. The reflection coefficients above are obtained from a modified version of the Fresnel equations:

$$r^s_{ij} = \frac{n_i \cos\theta_i - n_j \cos\theta_j}{n_i \cos\theta_i + n_j \cos\theta_j} \exp^{-2[\frac{2\pi\sigma_{ij}\cos\theta_i}{\lambda}]^2} \tag{13.3}$$

$$r^p_{ij} = \frac{n_i \cos\theta_j - n_j \cos\theta_i}{n_i \cos\theta_j + n_j \cos\theta_i} \exp^{-2[\frac{2\pi\sigma_{ij}\cos\theta_i}{\lambda}]^2} \tag{13.4}$$

where $\exp^{-2[\frac{2\pi\sigma_{ij}\cos\theta_i}{\lambda}]^2}$ is the Debye-Waller factor at the interface between layers i and j accounting for the reflection lose due to scattering. It is in this modifying factor that the surface roughness term, σ, is applied. From equations 13.3 and 13.4, we see that a different value of σ can be applied for each surface interface.

We know that the optical constants derived from the synchrotron measurements fit the value of σ for each interface separately. However, it was determined that the value of σ used for the vacuum Iridium interface was the dominant factor and so we simplify and use the same value of σ at each interface.

13.3 Setup

The simulations represent measurements with a 2mm aperture located on-axis at the focal plane. The rays use the `xrcf_xss_03` configuration of `trace-xrcf1`. Complete descriptions of the software and this configuration can be found at:

http://hea-www.harvard.edu/MST/simul/raytrace/databases/ts_config/00Index.html. Each simulated effective area has a statistical error $\leq 1\%$, corresponding to poisson statistics for the number of photons in the simulation. In order to get a feel for systematic variations in the simulations, due to the probabilistic nature of the reflectivity in the simulations, we ran 10 distinct simulations of each data set. Each simulation was started with a different seed for the random number generator in the simulation. This allows us to gain an understanding of any systematic variations in the experiment.

13.4 Fitting

We began by fitting the SSD continuum data over the range of 2 to 10.5 KeV with a single value of σ for the entire energy range. Since the value of σ should be independent of energy, we would expect a single value to provide a good fit. Figures 13.2to13.5 show the results of the 10 simulated data sets to the SSD data over the entire energy range for shells 1, 3, 4, and 6. Table 13.1 shows the resulting reduced χ^2 of the fits. The reduced χ^2 of the fits indicate that a single value of σ over the entire energy range fits the data poorly.

From there, we broke up the SSD continuum data and fit each energy range used to determine the optical constants independently. The energy ranges are 2.01 to 2.4 KeV, 2.25 to 2.9 KeV, 2.8 to 4 KeV, 3.9 to 7 KeV, 5 to 8.5 KeV, 8 to 12 KeV. For each energy range, except 2.01 to 2.4 KeV, we took 5 or 6 evenly distributed data points from the SSD continuum data to constitute the data set to be fit. For the 2.01 to 2.4 KeV range, we were only able to get two points at the higher end of the range. Results of the fits are in Figures 13.6to13.29.

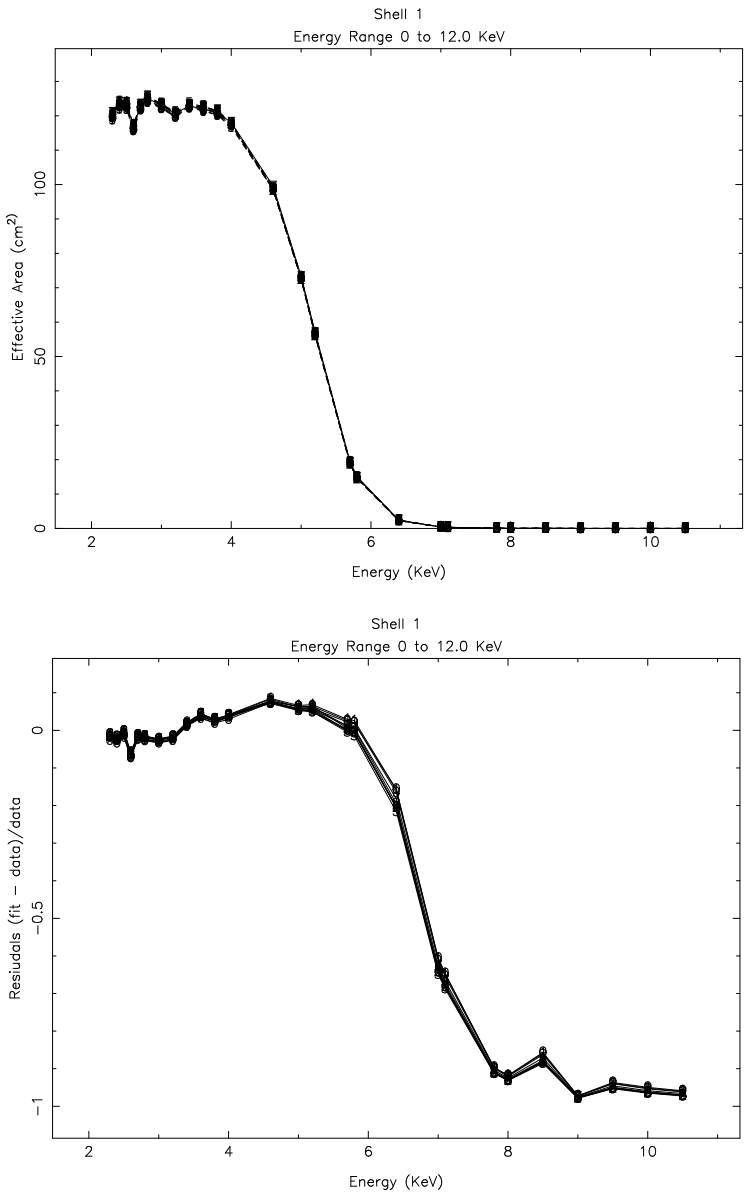

Figure 13.2: SSD continuum data and model effective area and residuals through 2mm pinhole for shell 1.

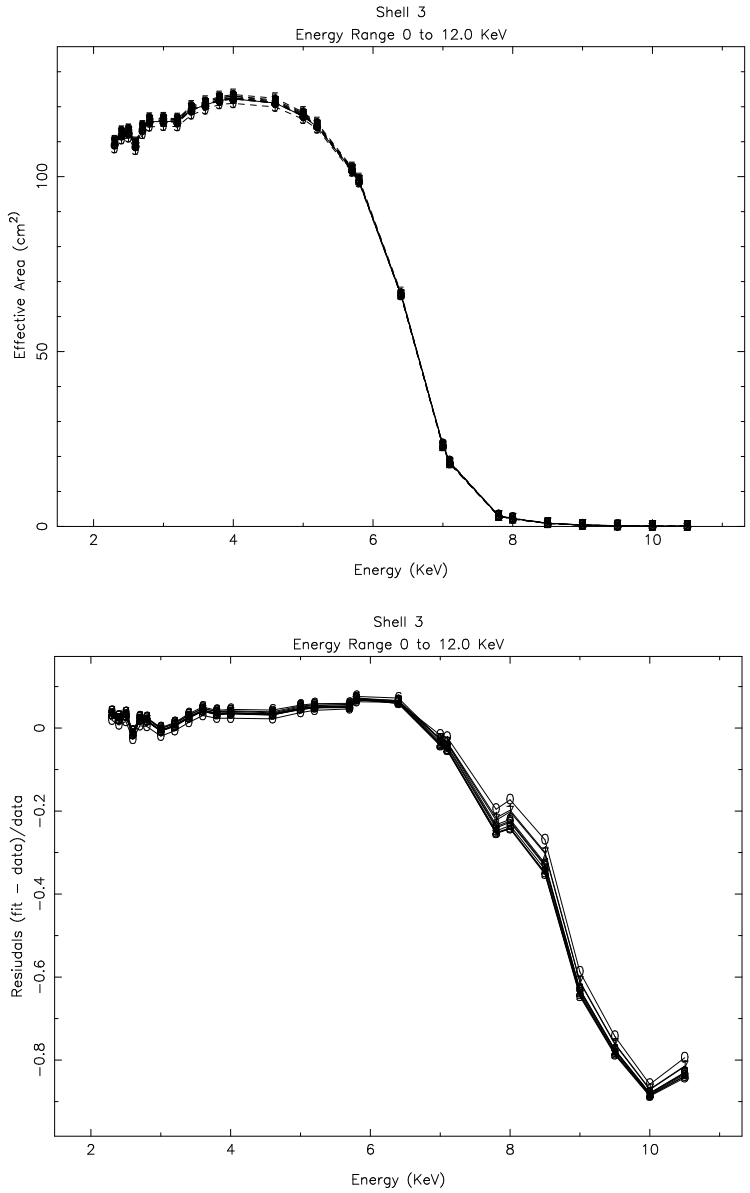

Figure 13.3: SSD continuum data and model effective area and residuals through 2mm pinhole for shell 3.

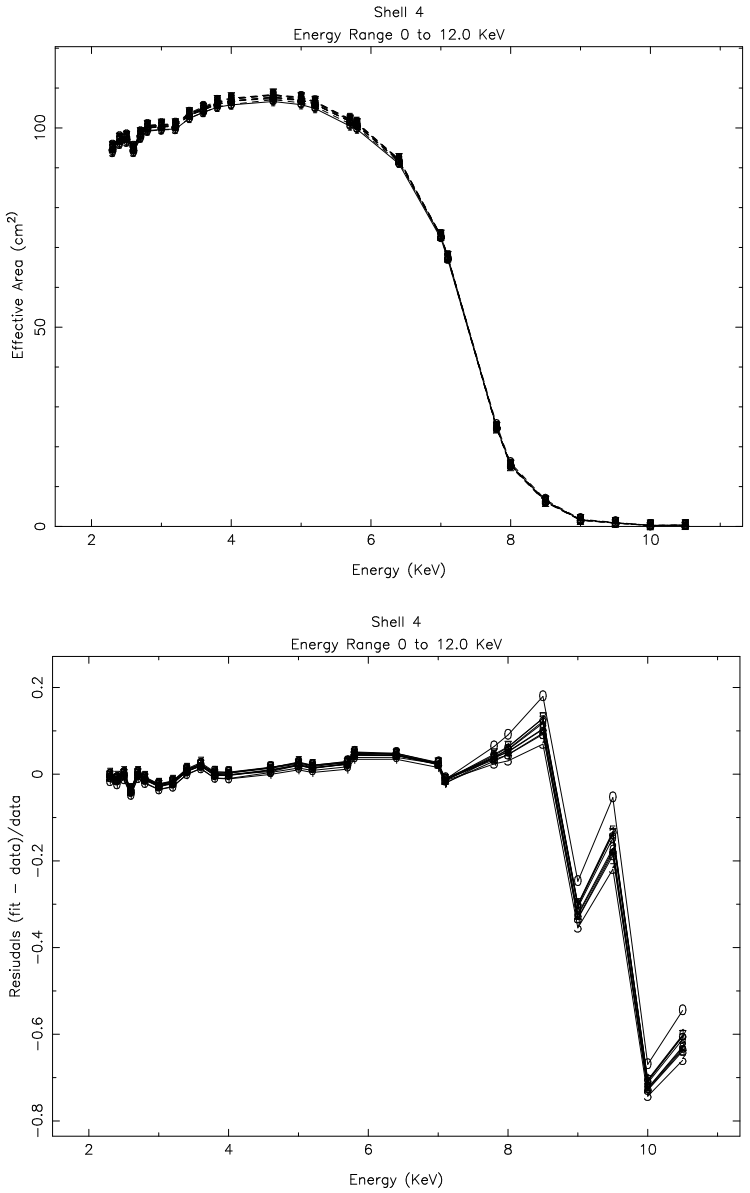

Figure 13.4: SSD continuum data and model effective area and residuals through 2mm pinhole for shell 4.

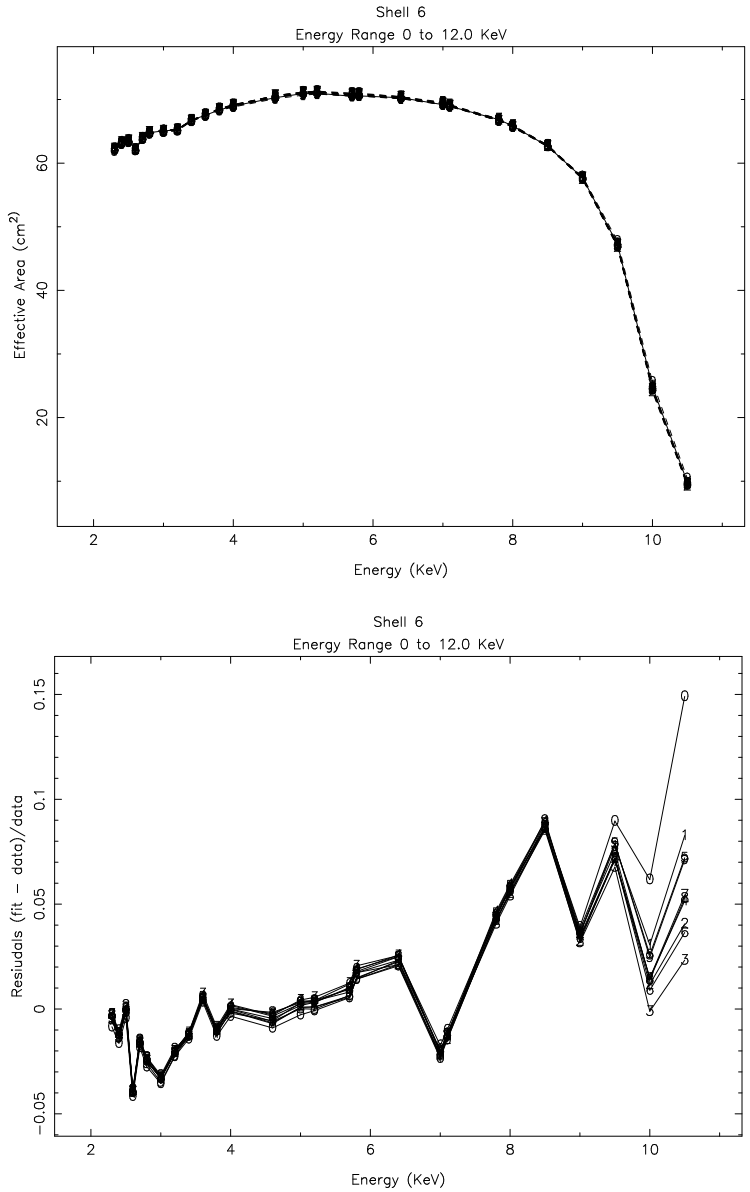

Figure 13.5: SSD continuum data and model effective area and residuals through 2mm pinhole for shell 6.

Shell	Energy	Seed	Reduced χ^2	σ_{Aeff}
1	0.00 12.00	1	19.2330	7.6656
1	0.00 12.00	2	19.7227	8.1168
1	0.00 12.00	3	19.9562	8.1910
1	0.00 12.00	4	19.9521	8.0996
1	0.00 12.00	5	19.8950	8.1240
1	0.00 12.00	6	19.6568	8.1425
1	0.00 12.00	7	19.6705	7.9039
1	0.00 12.00	8	19.7442	8.0414
1	0.00 12.00	9	19.2286	7.7272
1	0.00 12.00	10	19.2790	7.5835
3	0.00 12.00	1	13.3453	4.0237
3	0.00 12.00	2	15.3185	4.5000
3	0.00 12.00	3	15.8722	4.8129
3	0.00 12.00	4	14.9886	4.7114
3	0.00 12.00	5	14.4998	4.6099
3	0.00 12.00	6	15.8168	4.5000
3	0.00 12.00	7	13.3185	4.0564
3	0.00 12.00	8	14.9630	4.7026
3	0.00 12.00	9	14.4518	4.5000
3	0.00 12.00	10	11.3052	3.4314
4	0.00 12.00	1	5.0807	3.7612
4	0.00 12.00	2	5.2083	4.4369
4	0.00 12.00	3	5.4712	4.9685
4	0.00 12.00	4	5.1740	4.5000
4	0.00 12.00	5	5.0365	3.9478
4	0.00 12.00	6	5.3174	4.5000
4	0.00 12.00	7	5.0377	3.9362
4	0.00 12.00	8	5.2685	4.6244
4	0.00 12.00	9	5.0129	4.0726
4	0.00 12.00	10	5.4154	2.5079
6	0.00 12.00	1	2.6173	4.9975
6	0.00 12.00	2	2.3277	6.1460
6	0.00 12.00	3	2.4088	6.5383
6	0.00 12.00	4	2.6018	5.9270
6	0.00 12.00	5	2.6323	5.3034
6	0.00 12.00	6	2.4617	6.2584
6	0.00 12.00	7	2.4635	5.6968
6	0.00 12.00	8	2.4132	5.9473
6	0.00 12.00	9	2.6884	5.4510
6	0.00 12.00	10	3.1549	2.5405

Table 13.1: Shells 1, 3, 4, and 6 reduced χ^2 and σ

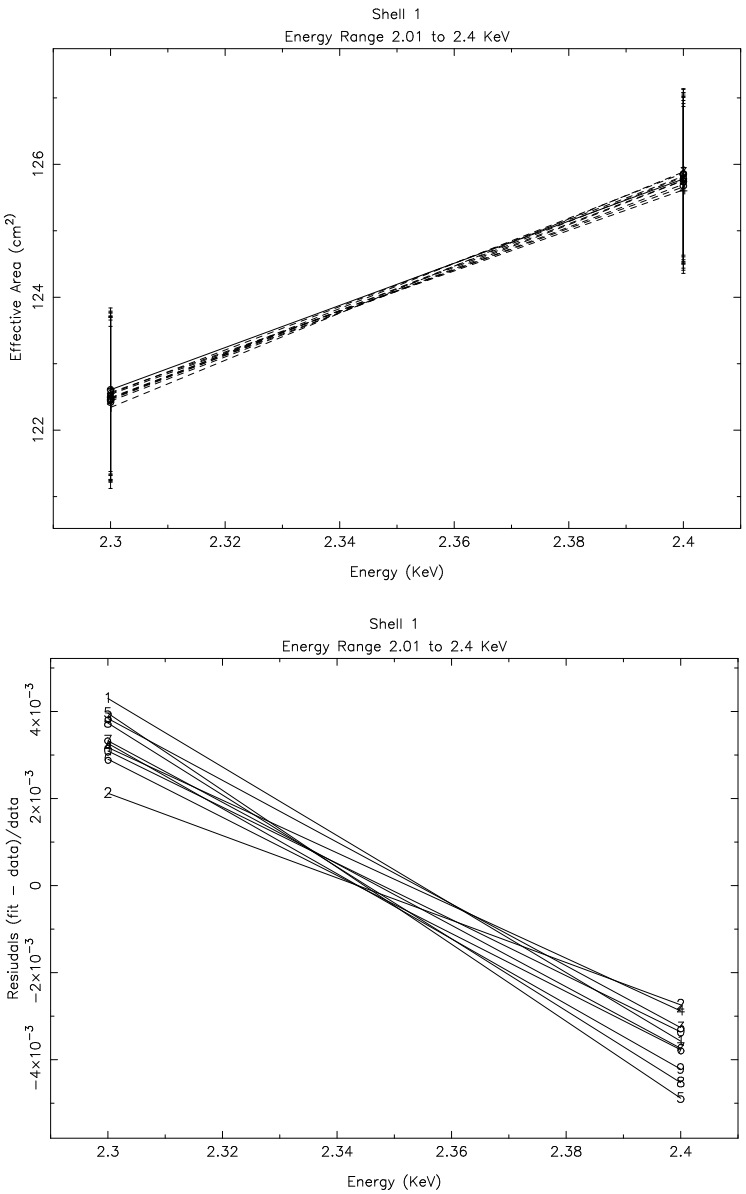

Figure 13.6: SSD continuum data and model effective area and residuals through 2mm pinhole for shell 1 between 2.01 and 2.4 keV.

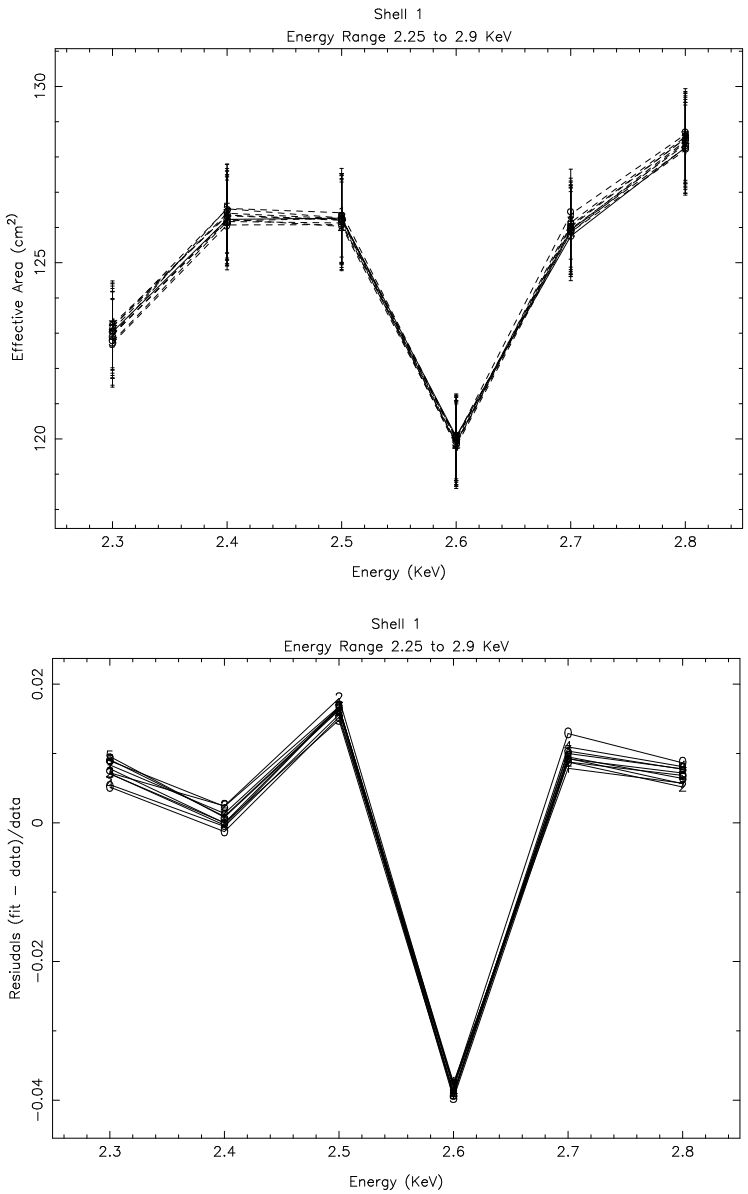

Figure 13.7: SSD continuum data and model effective area and residuals through 2mm pinhole for shell 1 between 2.25 and 2.9 keV.

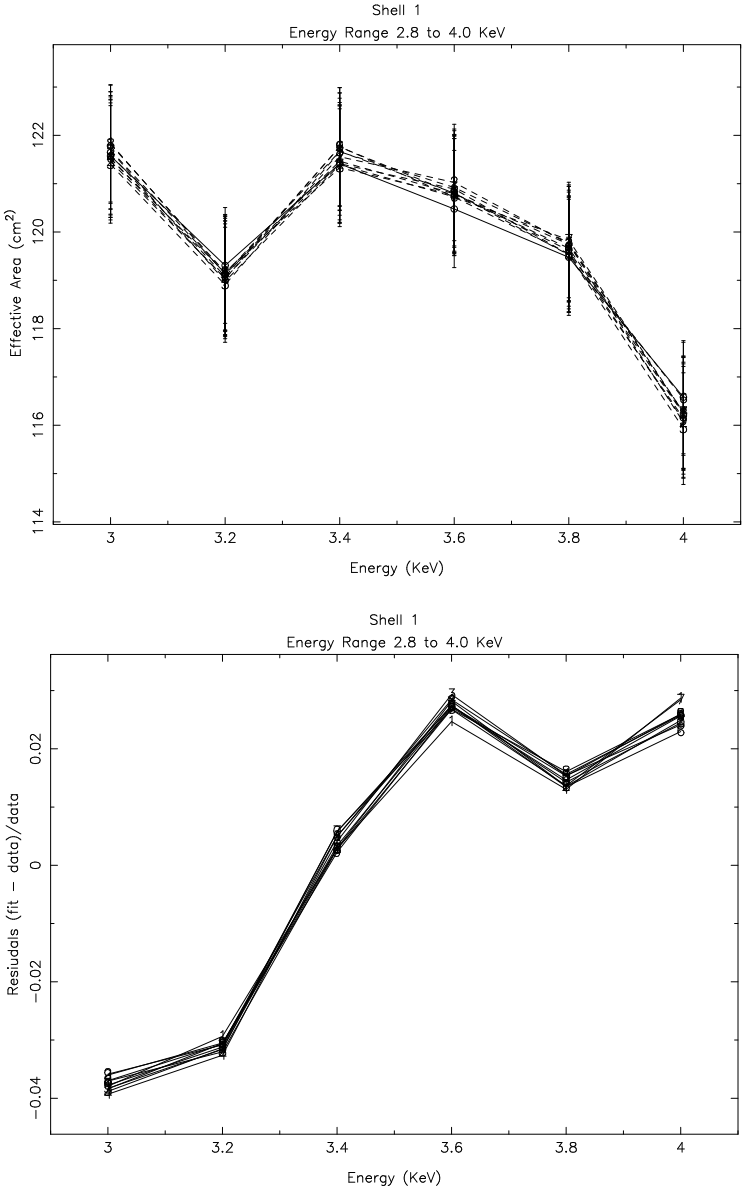

Figure 13.8: SSD continuum data and model effective area and residuals through 2mm pinhole for shell 1 between 2.8 and 4.0 keV.

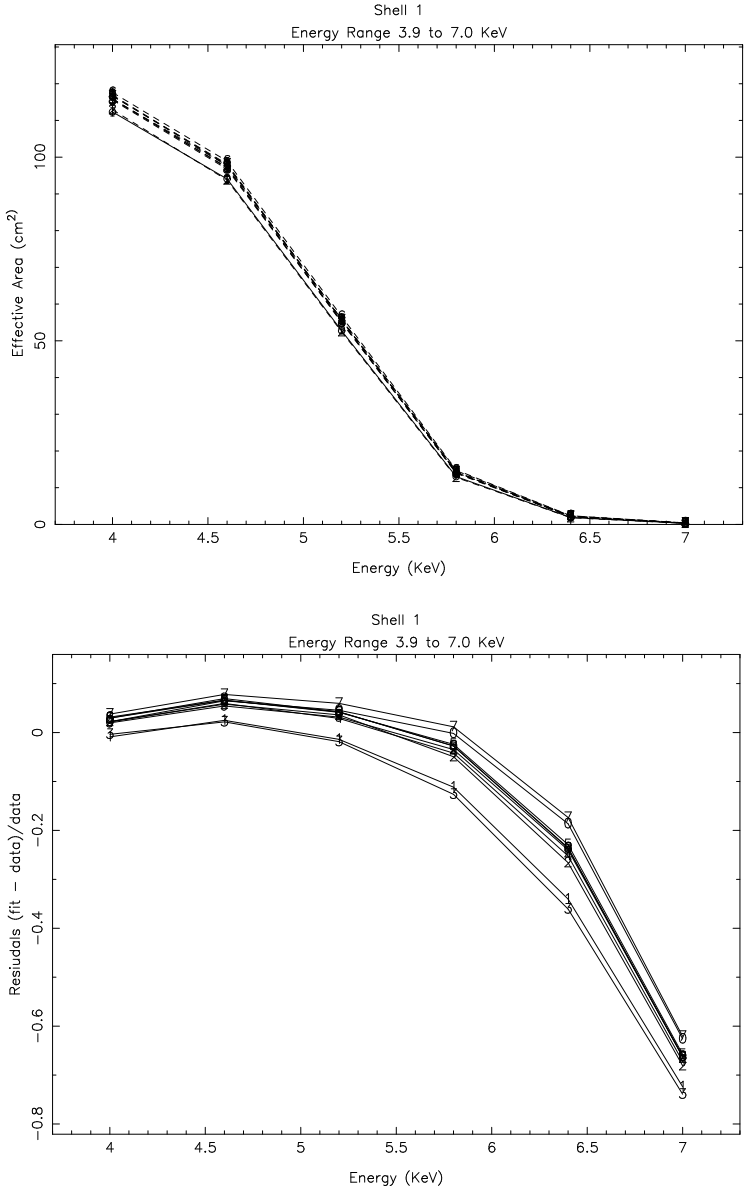

Figure 13.9: SSD continuum data and model effective area and residuals through 2mm pinhole for shell 1 between 3.9 and 7.0 keV.

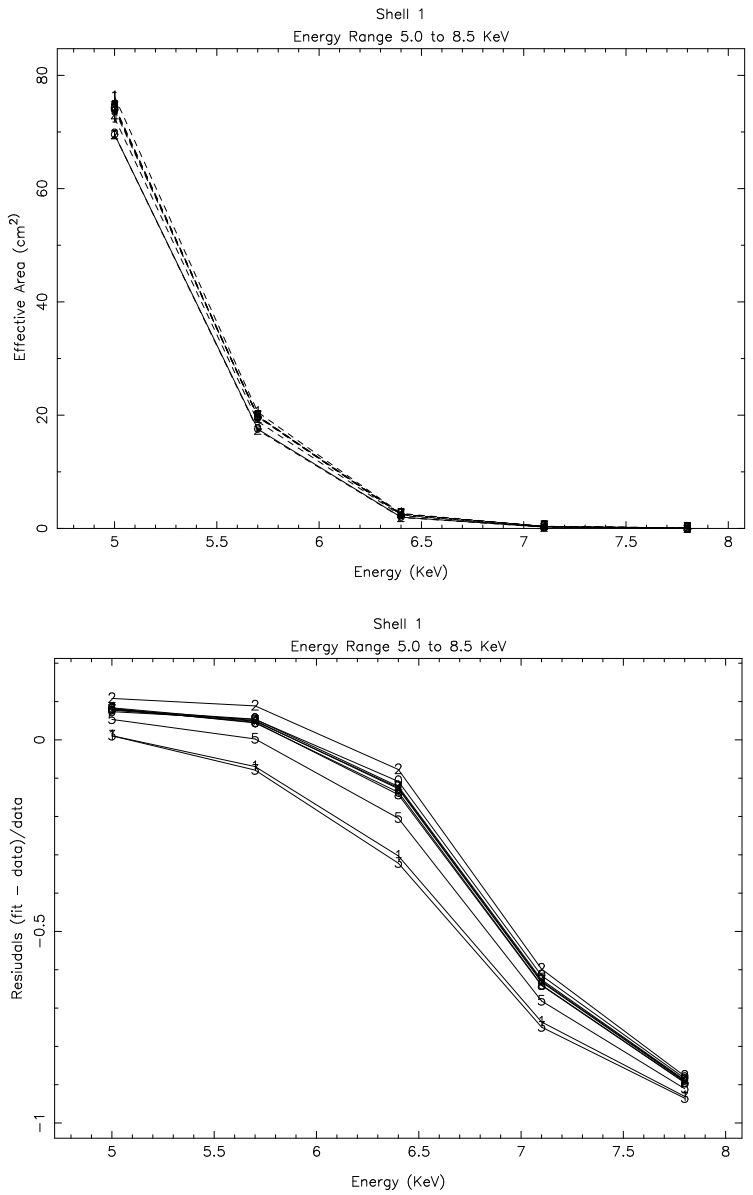

Figure 13.10: SSD continuum data and model effective area and residuals through 2mm pinhole for shell 1 between 5.0 and 8.5 keV.

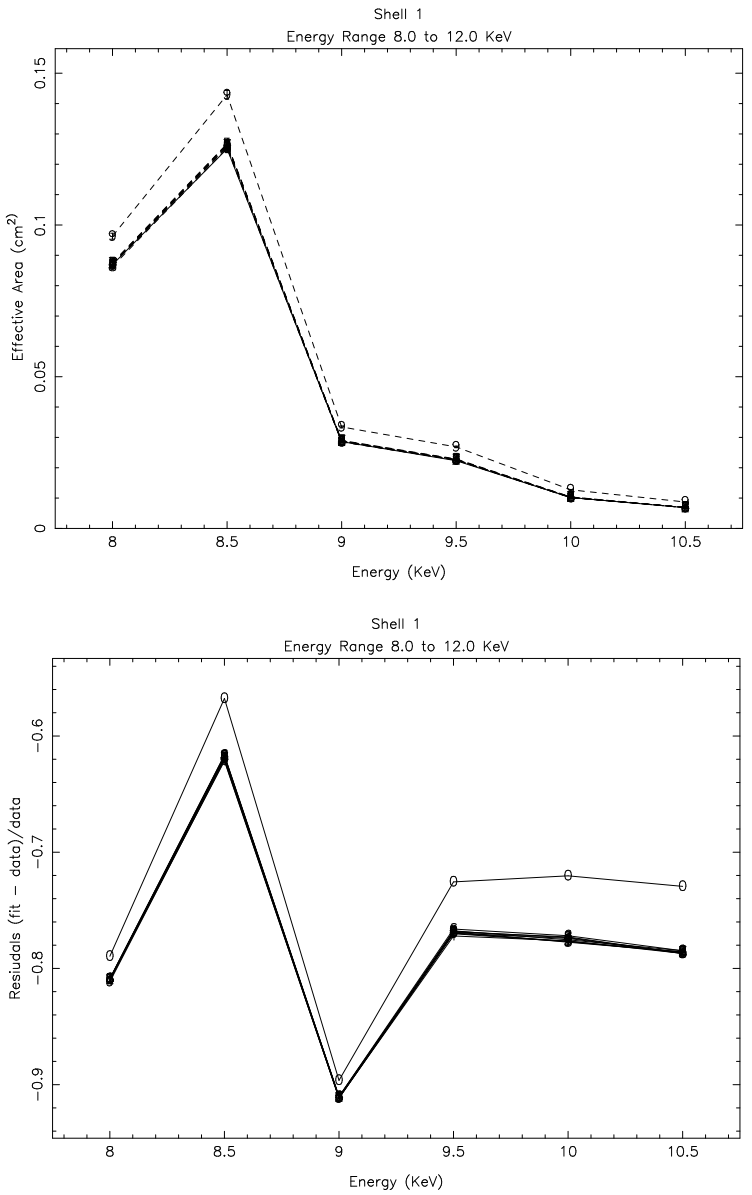

Figure 13.11: SSD continuum data and model effective area and residuals through 2mm pinhole for shell 1 between 8.0 and 12.0 keV.

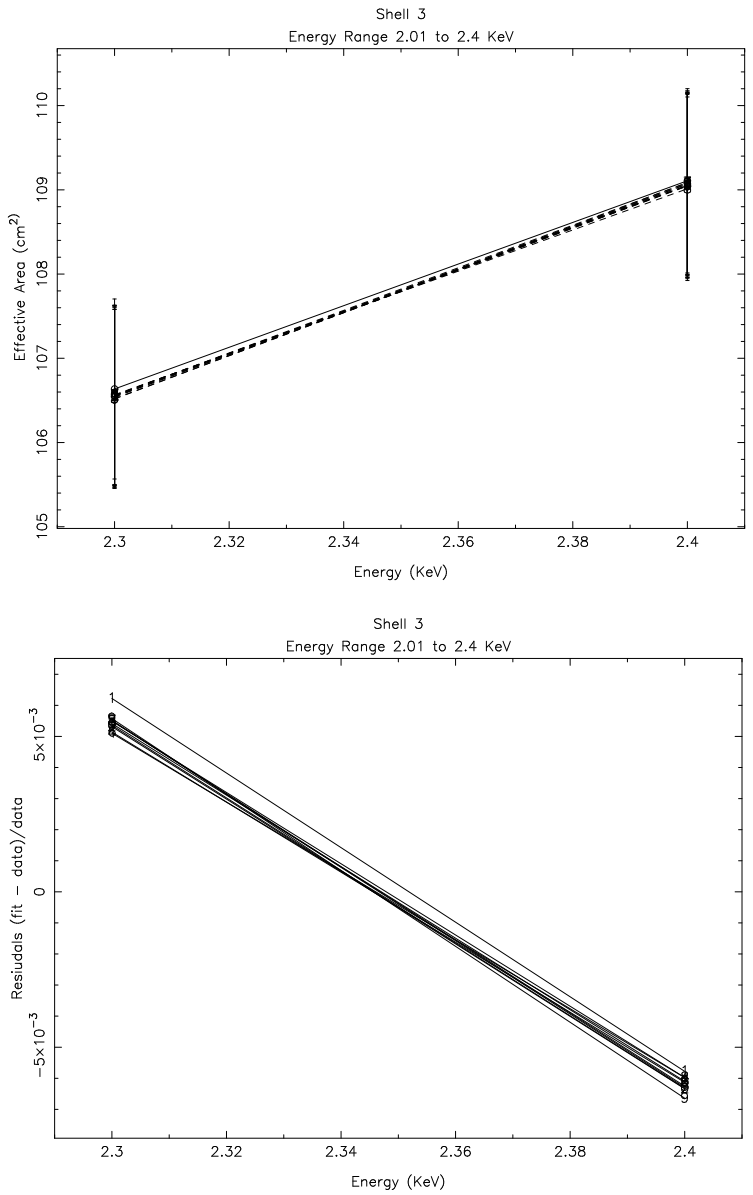

Figure 13.12: SSD continuum data and model effective area and residuals through 2mm pinhole for shell 3 between 2.01 and 2.4 keV.

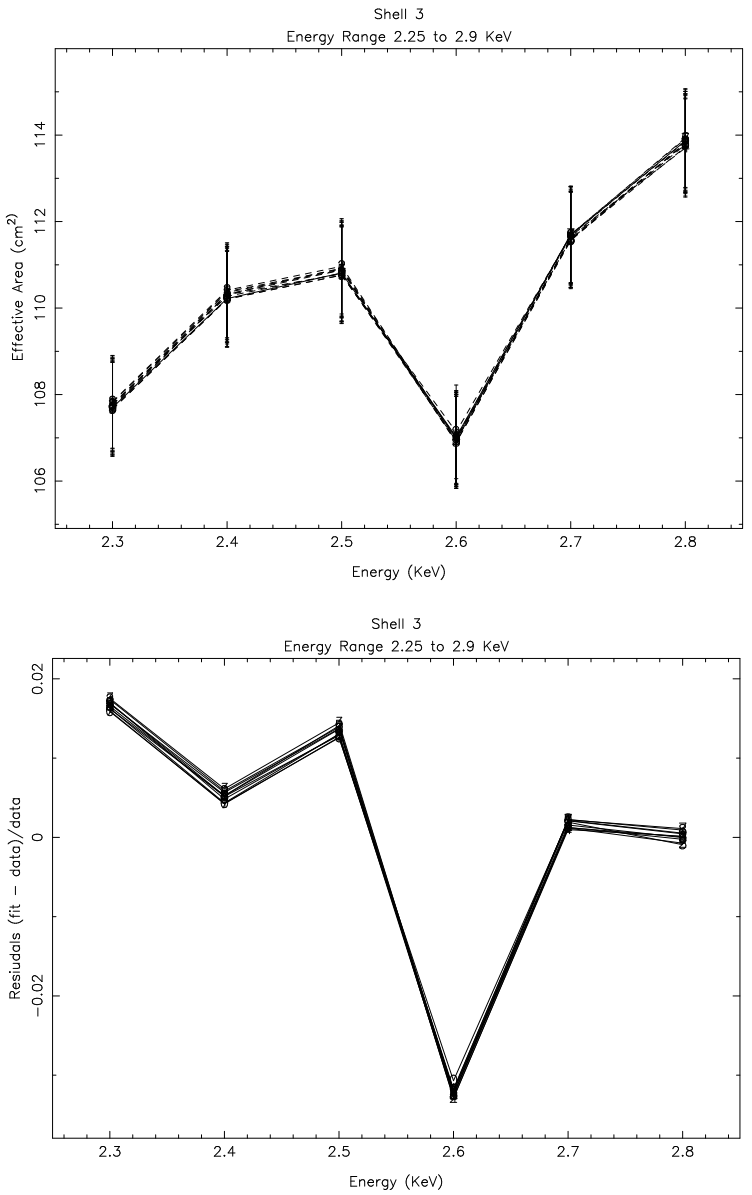

Figure 13.13: SSD continuum data and model effective area and residuals through 2mm pinhole for shell 3 between 2.25 and 2.9 keV.

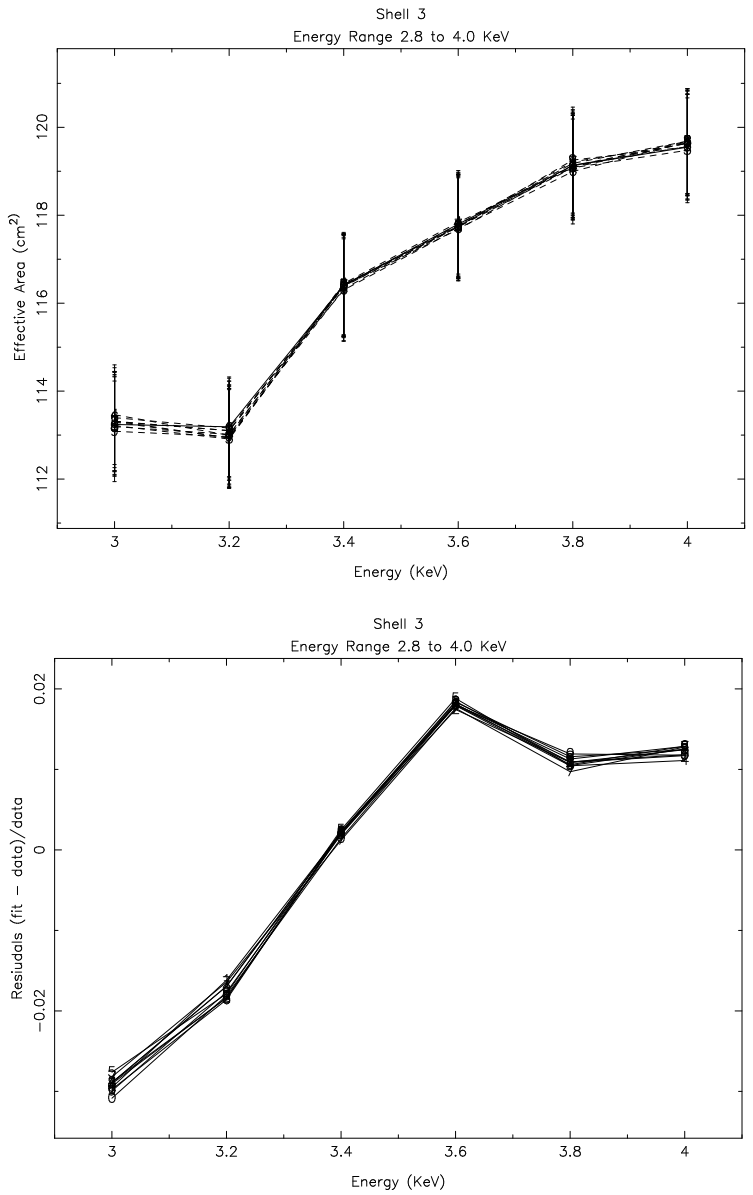

Figure 13.14: SSD continuum data and model effective area and residuals through 2mm pinhole for shell 3 between 2.8 and 4.0 keV.

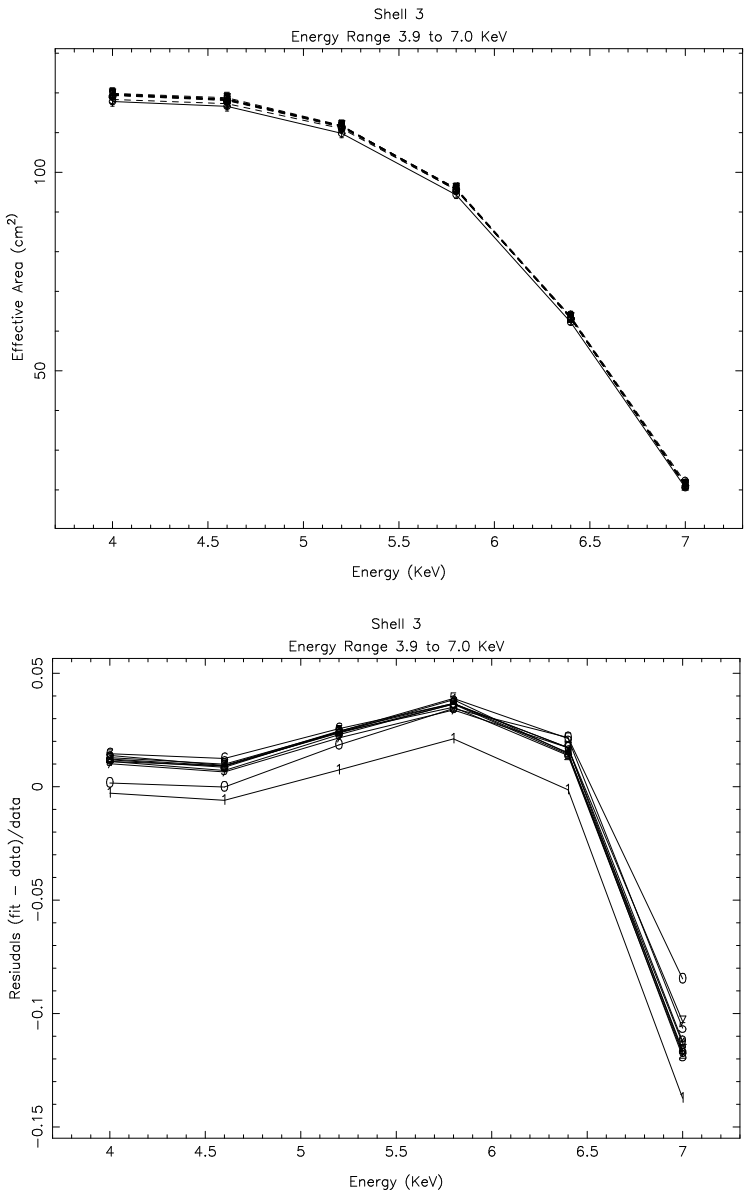

Figure 13.15: SSD continuum data and model effective area and residuals through 2mm pinhole for shell 3 between 3.9 and 7.0 keV.

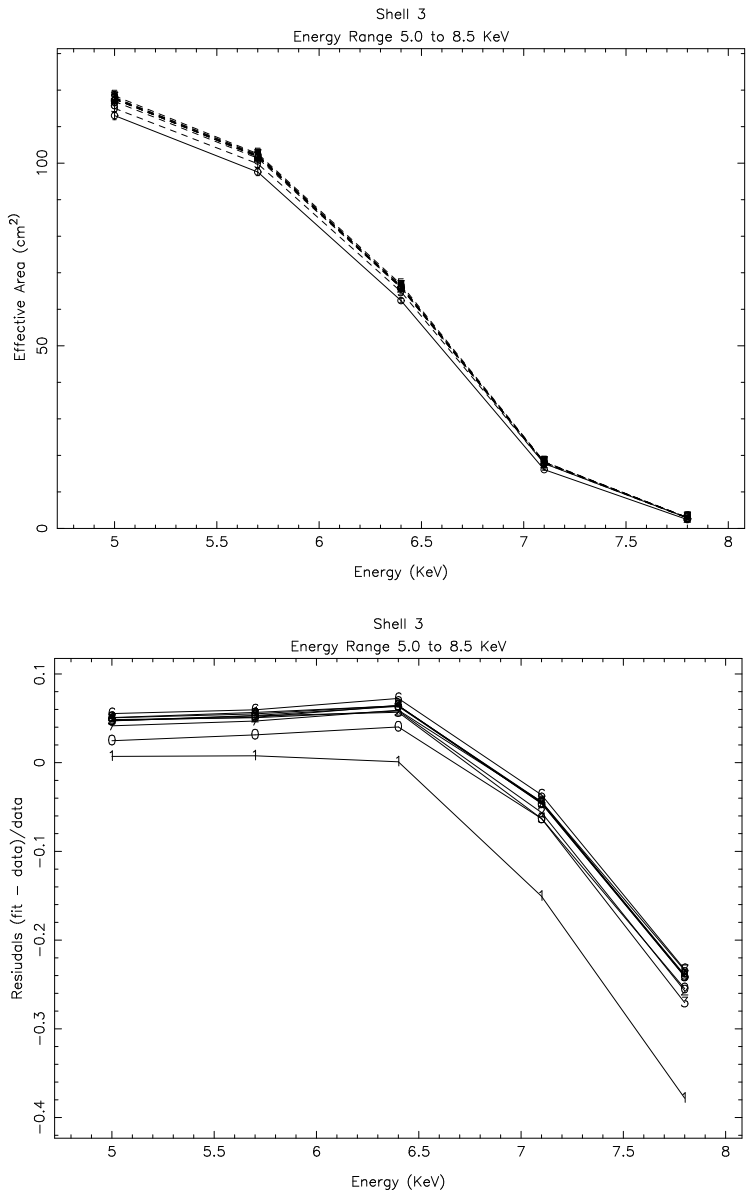

Figure 13.16: SSD continuum data and model effective area and residuals through 2mm pinhole for shell 3 between 5.0 and 8.5 keV.

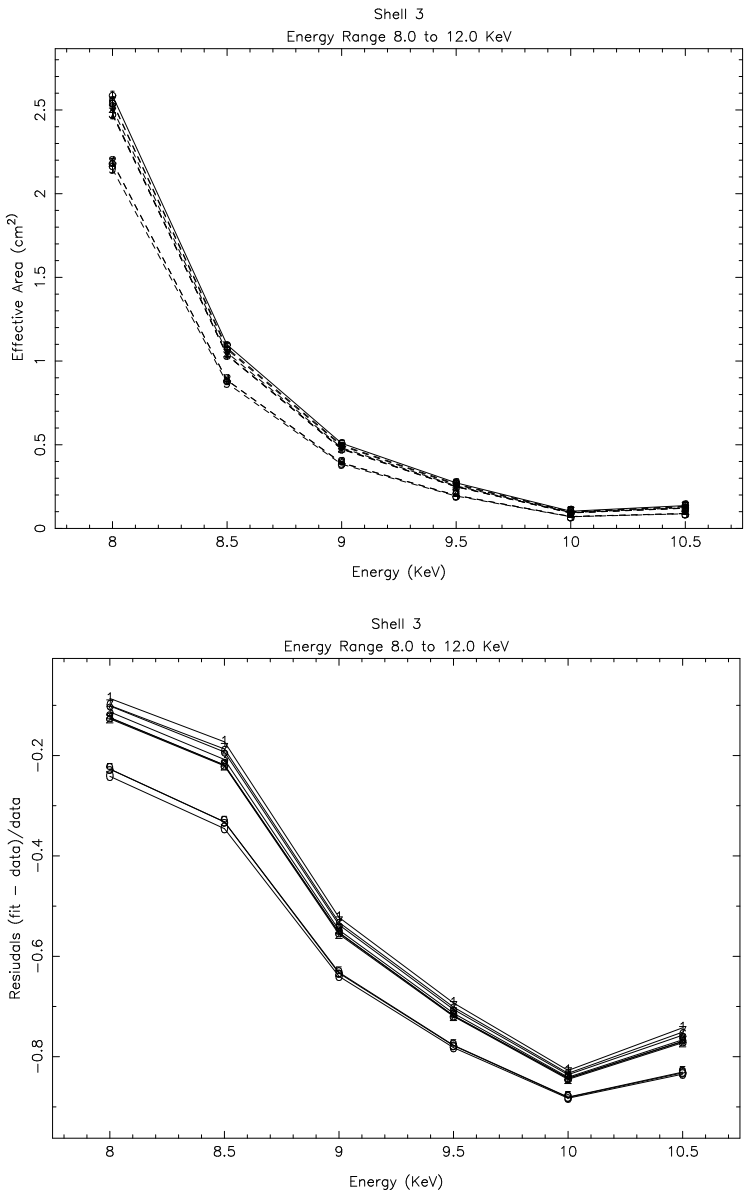

Figure 13.17: SSD continuum data and model effective area and residuals through 2mm pinhole for shell 3 between 8.0 and 12.0 keV.

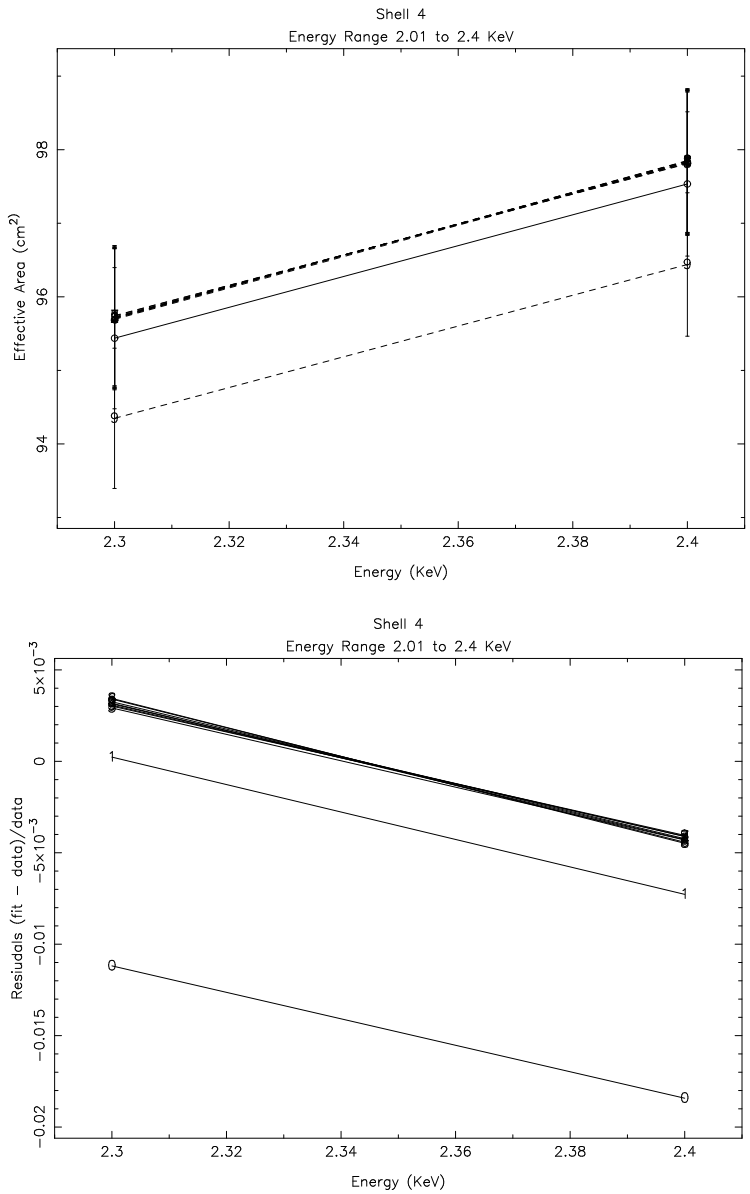

Figure 13.18: SSD continuum data and model effective area and residuals through 2mm pinhole for shell 4 between 2.01 and 2.4 keV.

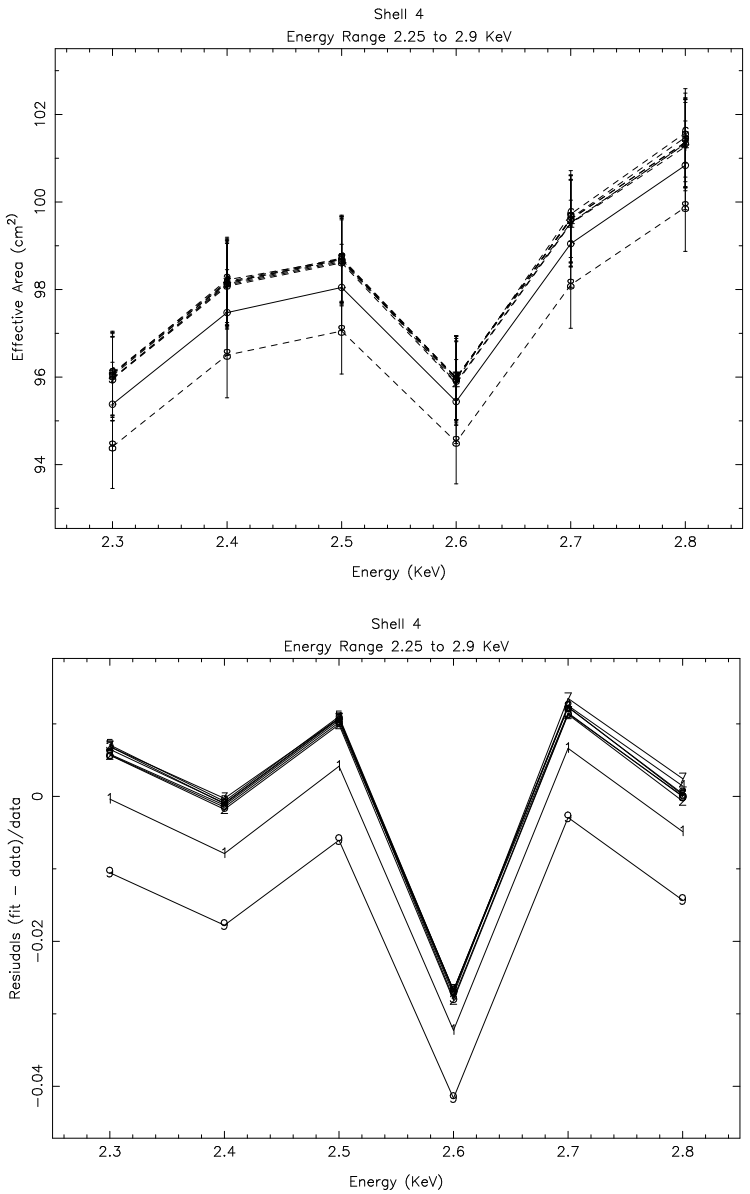

Figure 13.19: SSD continuum data and model effective area and residuals through 2mm pinhole for shell 4 between 2.25 and 2.9 keV.

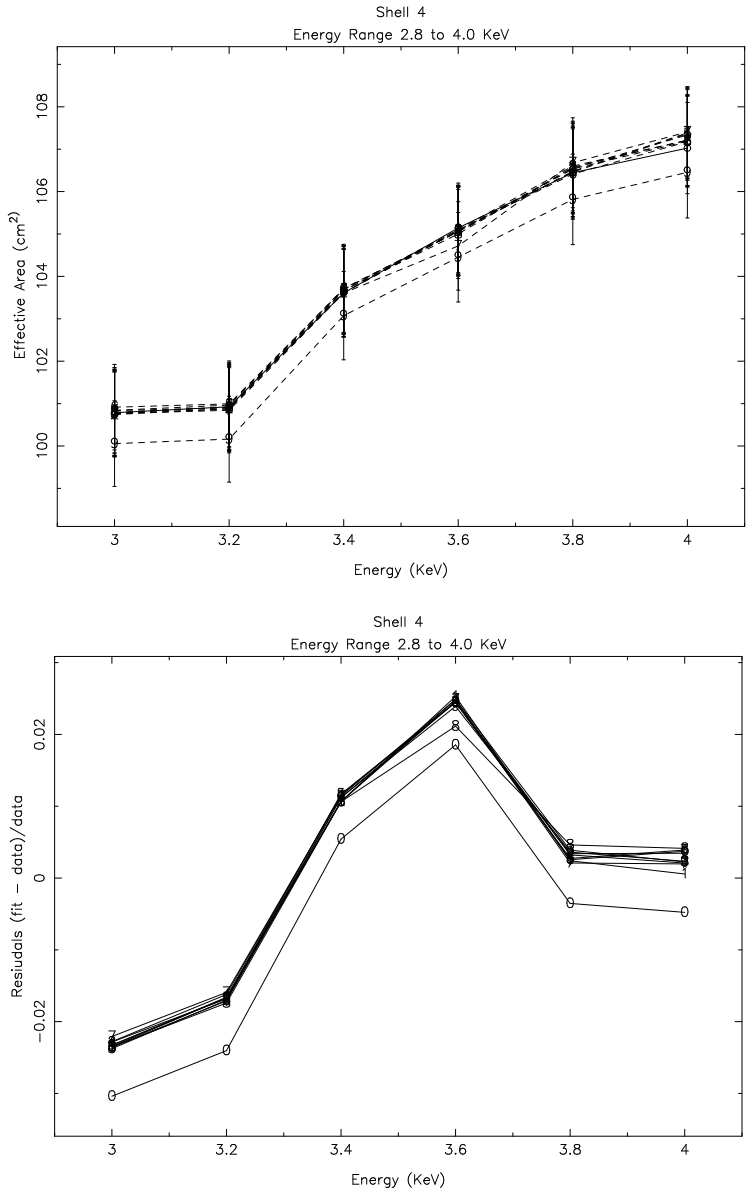

Figure 13.20: SSD continuum data and model effective area and residuals through 2mm pinhole for shell 4 between 2.8 and 4.0 keV.

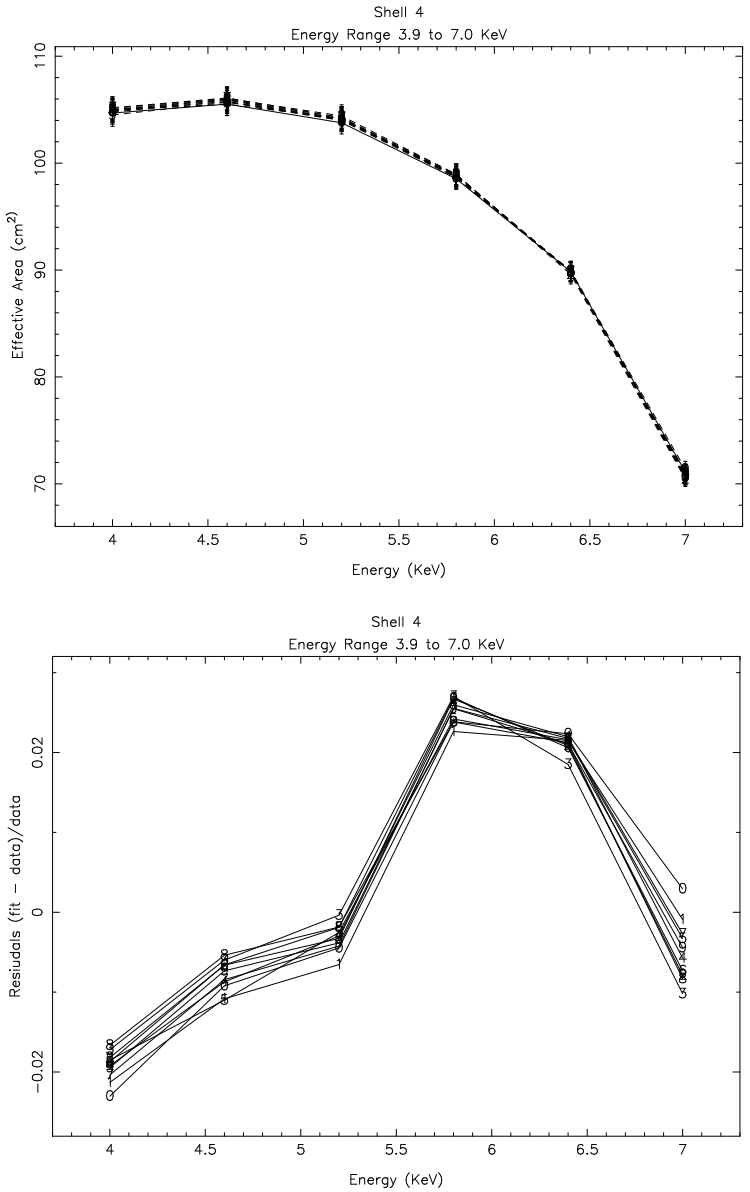

Figure 13.21: SSD continuum data and model effective area and residuals through 2mm pinhole for shell 4 between 3.9 and 7.0 keV.

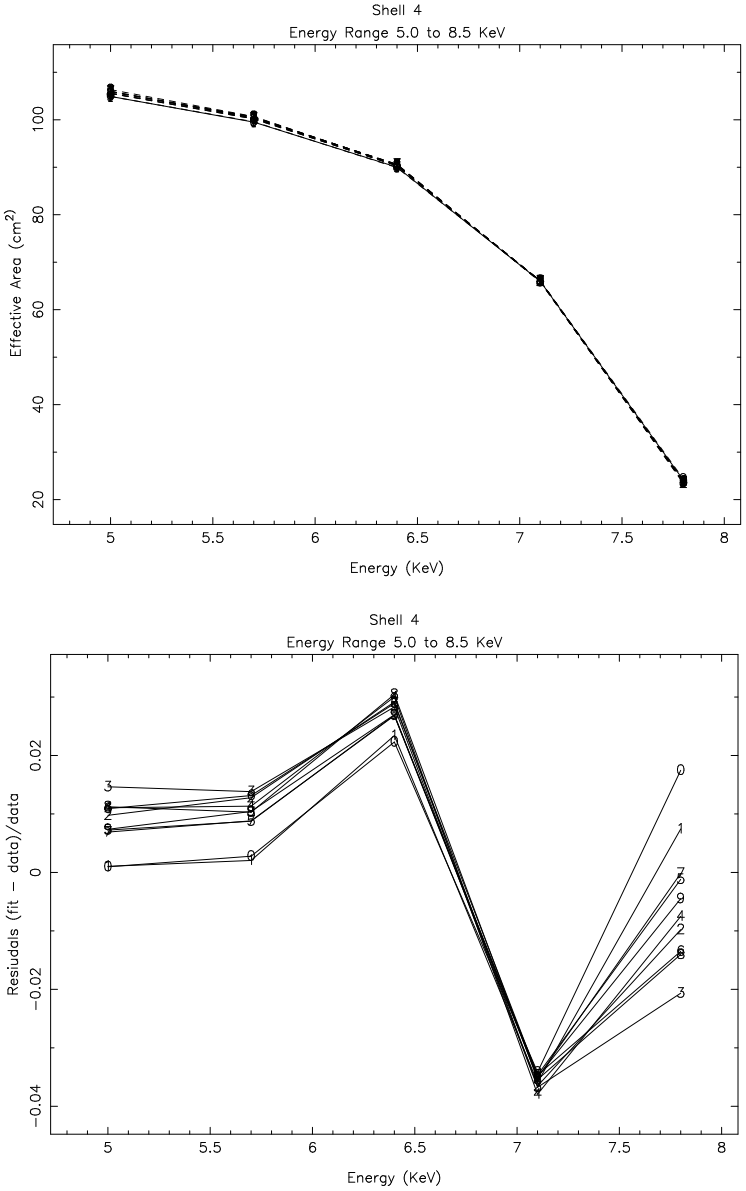

Figure 13.22: SSD continuum data and model effective area and residuals through 2mm pinhole for shell 4 between 5.0 and 8.5 keV.

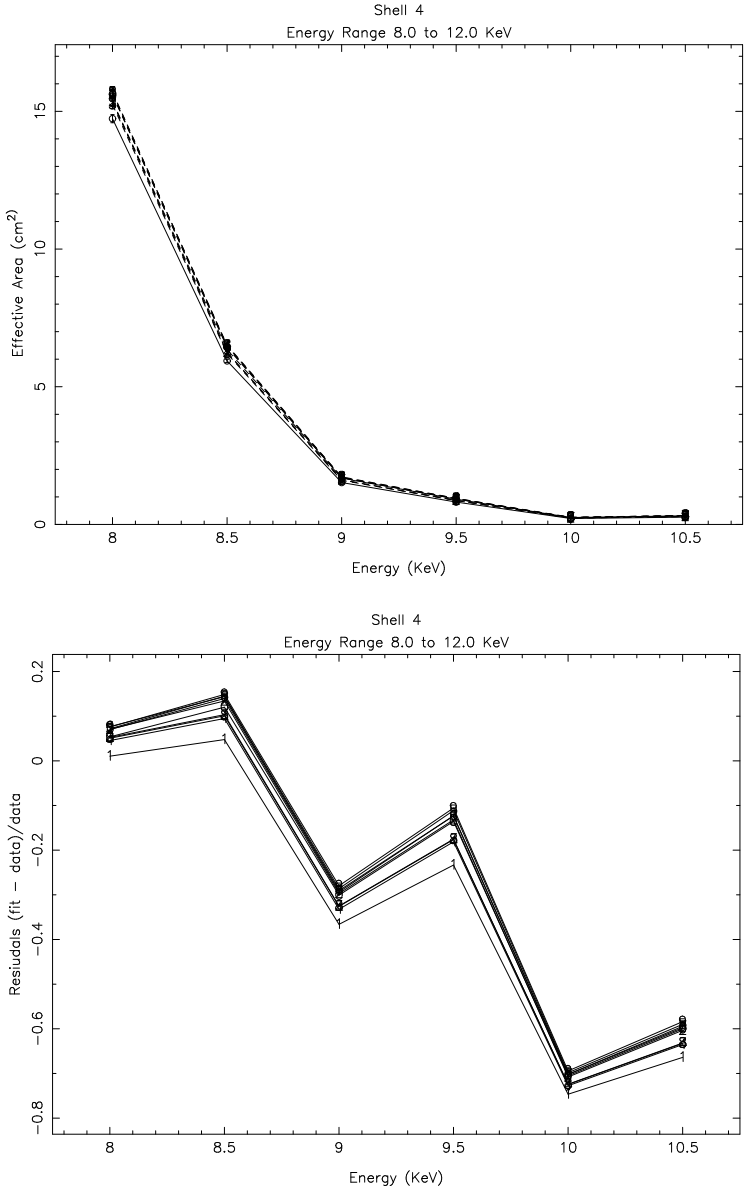

Figure 13.23: SSD continuum data and model effective area and residuals through 2mm pinhole for shell 4 between 8.0 and 12.0 keV.

Since the optical constants used in the model were derived by fitting reflectivity data from witness flats of the mirror, we would expect to get the same values of σ out of the fits to effective area as were used in the fits to reflectivity. Tables 13.2 to 13.5 show the reduced χ^2 of each fit for shells 1, 3, 4, and 6. Also present are the values of σ determined by the fit and the expected value of σ from the synchrotron fits to the reflectivity.

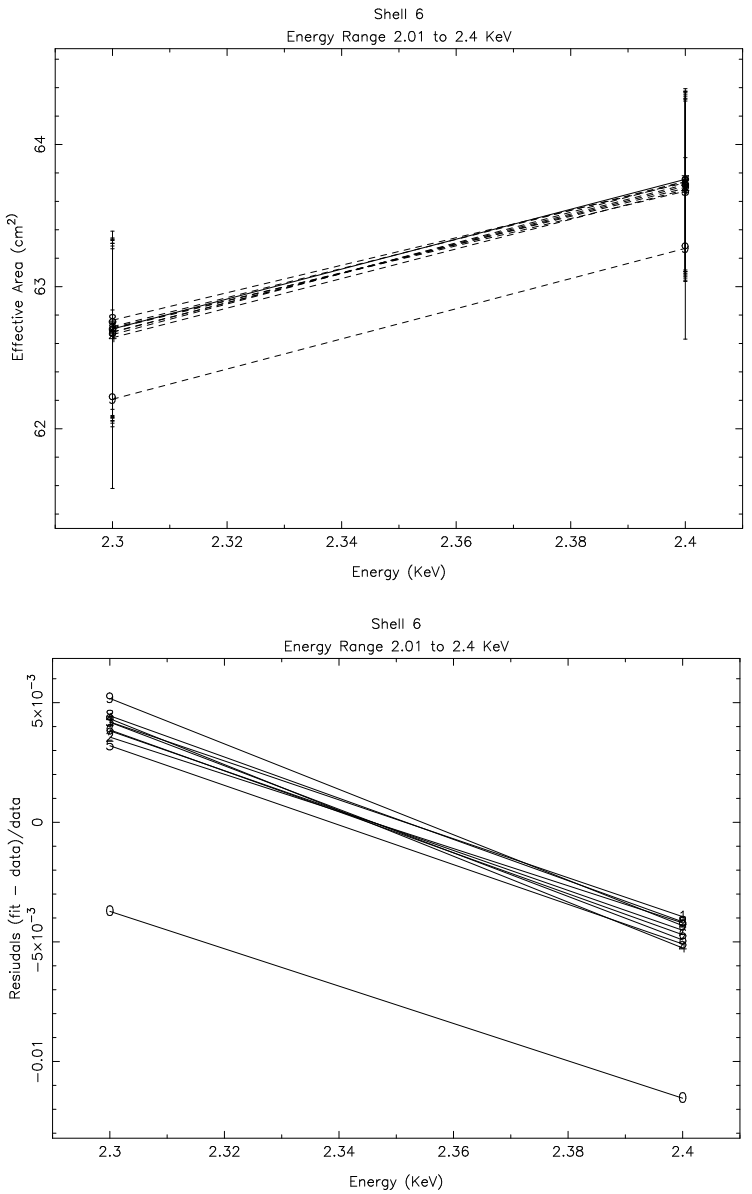

Figure 13.24: SSD continuum data and model effective area and residuals through 2mm pinhole for shell 6 between 2.01 and 2.4 keV.

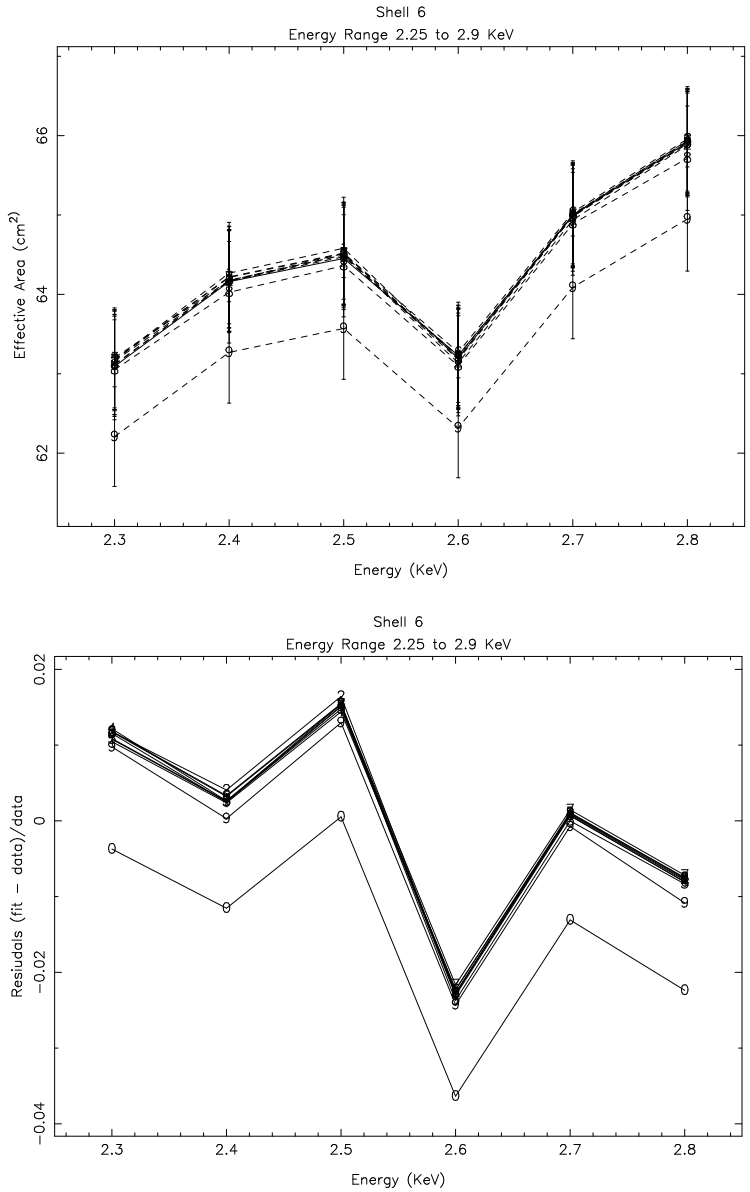

Figure 13.25: SSD continuum data and model effective area and residuals through 2mm pinhole for shell 6 between 2.25 and 2.9 keV.

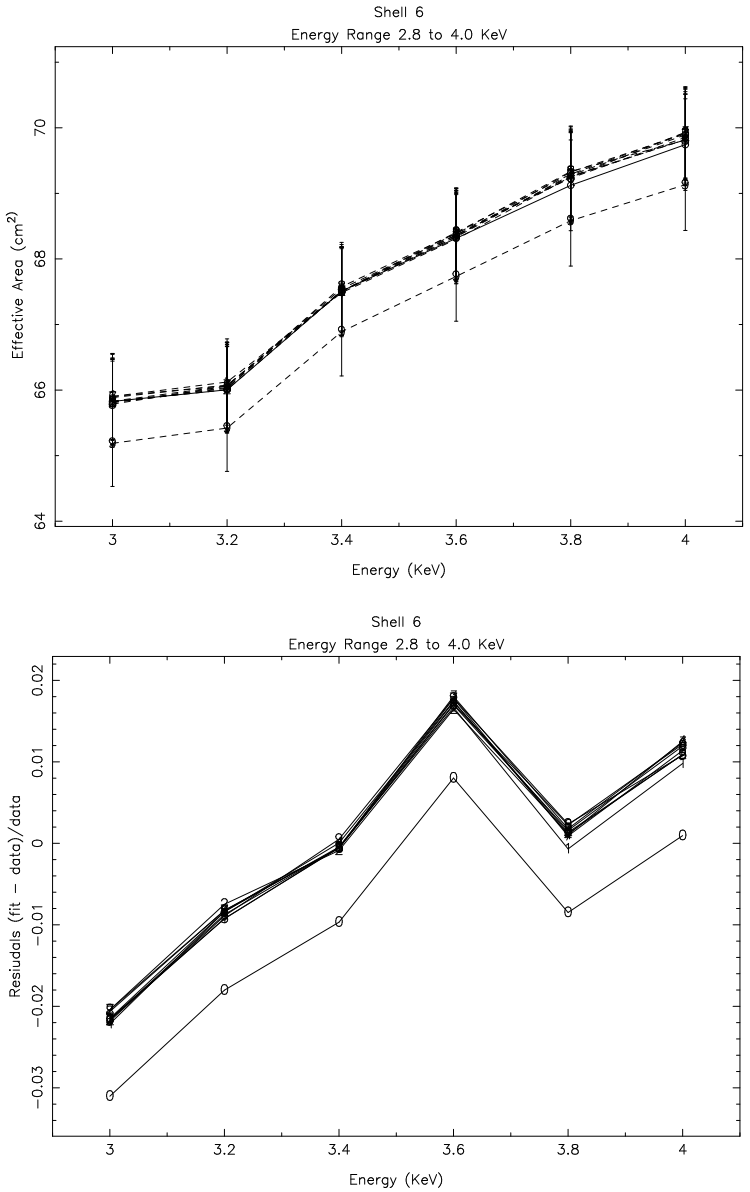

Figure 13.26: SSD continuum data and model effective area and residuals through 2mm pinhole for shell 6 between 2.8 and 4.0 keV.

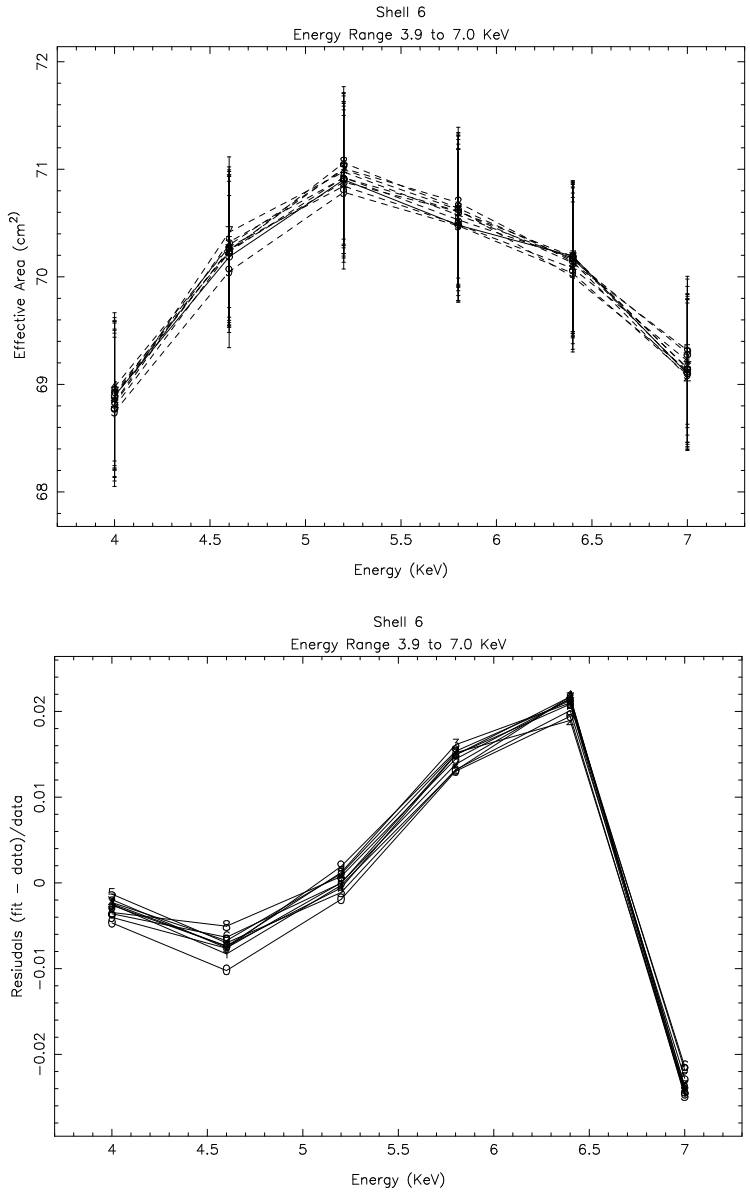

Figure 13.27: SSD continuum data and model effective area and residuals through 2mm pinhole for shell 6 between 3.9 and 7.0 keV.

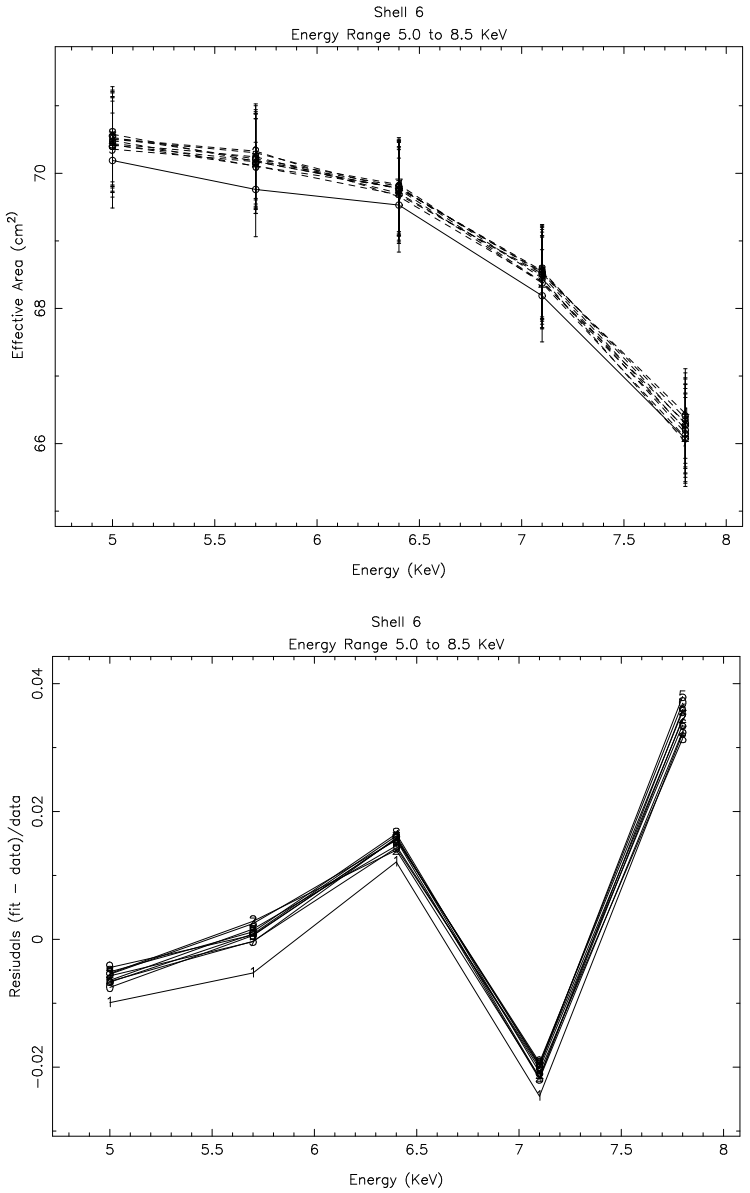

Figure 13.28: SSD continuum data and model effective area and residuals through 2mm pinhole for shell 6 between 5.0 and 8.5 keV.

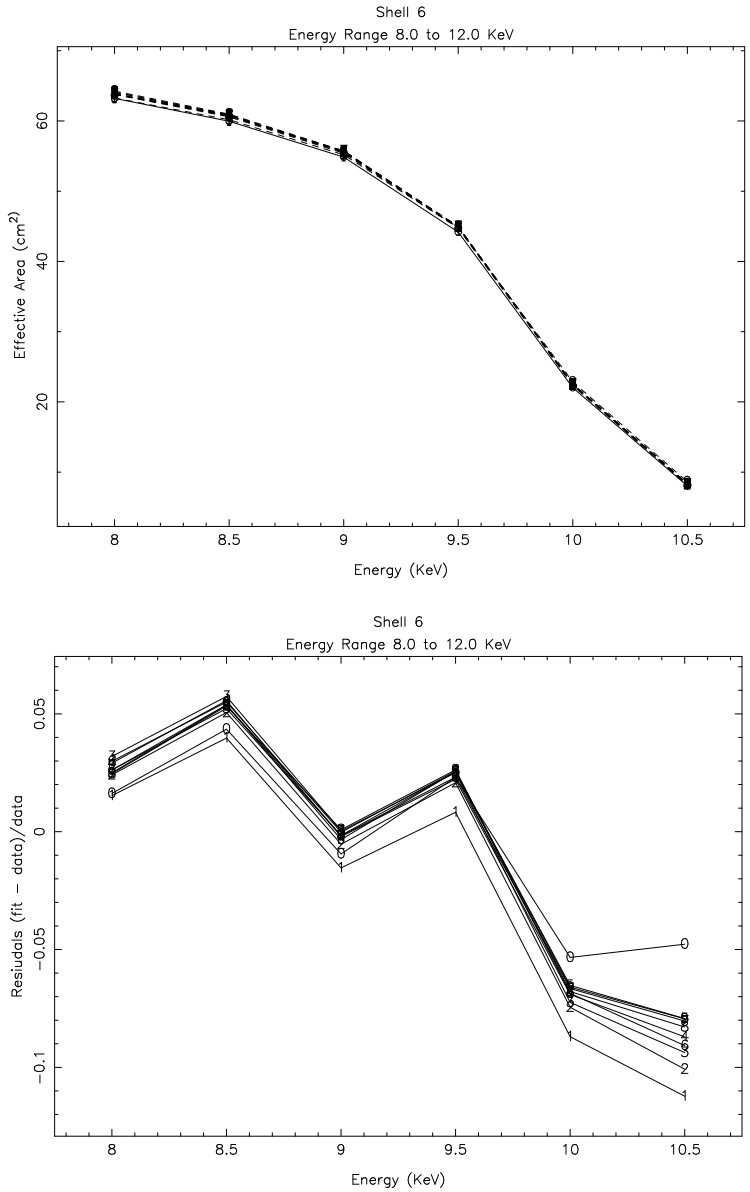

Figure 13.29: SSD continuum data and model effective area and residuals through 2mm pinhole for shell 6 between 8.0 and 12.0 keV.

Energy	Avg Reduced χ^2	$\sigma_{\rm refl}$	Avg $\sigma_{\rm Aeff}$	Avg Residuals
2.01 2.40	0.1278 ± 0.0395	3.9000	7.0903 ± 0.4286	0.8180 ± 0.1099
2.25 2.90	2.3021 ± 0.0737	4.0454	6.8986 ± 0.3962	0.7053 ± 0.0980
2.80 4.00	4.7686 ± 0.2173	3.9000	8.3107 ± 0.2848	1.1310 ± 0.0730
3.90 7.00	19.8605 ± 3.2391	4.2000	8.4641 ± 0.4910	1.0153 ± 0.1169
5.00 8.50	51.0264 ± 4.5356	5.0229	7.7920 ± 0.6637	0.5513 ± 0.1321
8.00 12.00	25.1500 ± 0.5527	4.1000	4.4307 ± 0.2190	0.0807 ± 0.0534

Table 13.2: Shell 1 reduced χ^2 and σ

Energy	Avg Reduced χ^2	$\sigma_{\rm refl}$	Avg $\sigma_{\rm Aeff}$	Avg Residuals
2.01 2.40	0.3366 ± 0.0197	3.9000	6.4552 ± 0.6770	0.6552 ± 0.1736
2.25 2.90	1.7679 ± 0.0841	4.0454	5.6774 ± 0.7523	0.4034 ± 0.1859
2.80 4.00	1.8648 ± 0.0849	3.9000	6.0162 ± 0.6157	0.5426 ± 0.1579
3.90 7.00	4.0426 ± 0.5962	4.2000	6.1872 ± 0.3849	0.4732 ± 0.0916
5.00 8.50	13.2666 ± 2.8037	5.0229	4.7625 ± 0.6406	−0.0518 ± 0.1275
8.00 12.00	41.5906 ± 7.0247	4.1000	3.1486 ± 0.9921	−0.2321 ± 0.2420

Table 13.3: Shell 3 reduced χ^2 and σ

Energy	Avg Reduced χ^2	$\sigma_{\rm refl}$	Avg $\sigma_{\rm Aeff}$	Avg Residuals
2.01 2.40	0.3831 ± 0.7059	3.9000	2.9182 ± 1.3416	−0.2517 ± 0.3440
2.25 2.90	NaN ± NaN	4.0454	NaN ± NaN	NaN ± NaN
2.80 4.00	1.7732 ± 0.1474	3.9000	3.6187 ± 1.1911	−0.0721 ± 0.3054
3.90 7.00	1.1075 ± 0.0877	4.2000	5.6987 ± 0.7249	0.3568 ± 0.1726
5.00 8.50	1.6899 ± 0.2663	5.0229	5.3255 ± 0.5466	0.0602 ± 0.1088
8.00 12.00	18.4686 ± 0.9141	4.1000	4.0980 ± 0.4578	−0.0005 ± 0.1116

Table 13.4: Shell 4 reduced χ^2 and σ

Energy	Avg Reduced χ^2	$\sigma_{\rm refl}$	Avg $\sigma_{\rm Aeff}$	Avg Residuals
2.01 2.40	0.2408 ± 0.1608	3.9000	4.2988 ± 1.6719	0.1022 ± 0.4287
2.25 2.90	1.1571 ± 0.3869	4.0454	3.2510 ± 1.4316	−0.1964 ± 0.3539
2.80 4.00	1.0332 ± 0.1939	3.9000	4.0534 ± 1.2651	0.0393 ± 0.3244
3.90 7.00	0.6554 ± 0.0376	4.2000	5.7636 ± 1.1746	0.3723 ± 0.2797
5.00 8.50	1.1330 ± 0.0711	5.0229	6.4072 ± 1.0825	0.2756 ± 0.2155
8.00 12.00	2.8458 ± 0.4875	4.1000	8.2877 ± 0.3880	1.0214 ± 0.0946

Table 13.5: Shell 6 reduced χ^2 and σ

13.5 Resulting Fits

Figures 13.2to13.5 show the effective areas and residuals from fits to the data over the energy range of 2 to 10.5 KeV. For each shell we see that the quality of the fit deteriorates as the energy increases. For shell 1, the simulated effective areas are within 5% of the data up to 4 KeV, shell 3 is within 5% up to 5 KeV, shell 4 is within 5% up to 7 KeV, and shell 6 is within 5% up to 8 KeV. In each shell, this corresponds with the cut-off energy of the shell where the effective area drops sharply. The data at higher energies, after the cut off, prove difficult to fit as the signal to noise decreases. Thus, the reduced χ^2 of the fits are fairly high, ≈ 20 for shell 1, ≈ 13 for shell 3, ≈ 5 for shell 4, and ≈ 2.5 for shell 6 where the cut off is at a much high energy.

In order to compensate for the difficulty of fitting the entire energy range at once, the data were independently fit over each of the energy ranges used in the synchrotron experiment. Figures 13.6to13.29 illustrate the results of these fits. Notice that the fits get worse for the higher energy ranges, with the effect becoming more pronounced from shell 6 to shell 1. By fitting σ over mulitple energy ranges, the fits improve on the whole. However, despite better fits within the various energy ranges, we do not see the fitted values of σ, σ_{Aeff}, agreeing with the values derived from the synchrotron experiment, σ_{refl}, in Tables 13.2 to 13.5. It should also be noted that thevalues of σ vary from energy range to energy range. While this reflects how σ was handled in deriving the optical constants for the model, it does not reflect the physical nature of σ, a surface grating term. Thus, the quality of the fits have improved to the detriment of the physical model.

Chapter 14

Wing Scans: Data Reduction and Pinhole Effective Areas

Terrance J. Gaetz

In this chapter we discuss the data taken for the wing scan experiments at XRCF; in the next chapter the data are analyzed to extract information about the mirror surfaces. In the encircled energy experiments (see Chapter 16), the energy passing within concentric pinholes from 10 μm diameter up to 35 mm diameter was measured. The wing scans provide information on the PSF wings in some directions out to 105 mm from the image core. The wing scan experiment was designed to map out the far wings of the Point Spread Function, or PSF, at angles $\gtrsim$1 mm (about $20''$ away from the core). Because of time constraints, only a selected portions of the wings could be mapped in detail. This was accomplished by a series of horizontal (Y) or vertical (Z) pinhole scans through the PSF. The pinhole diameters were 1, 4, 10, 20, and 35 mm; the scan was centered on the core of the PSF, and up to 3 points were sampled to either side (*i.e.*, $-3D_{ap}$, $-2D_{ap}$, $-1D_{ap}$, 0, $+1D_{ap}$, $+2D_{ap}$, $+3D_{ap}$).

The quadrant shutters were used to isolate quadrants of individual mirror pairs; see Chapter C for a description of the quadrant shutter nomenclature. Wing scans were performed at various energies for each quadrant of each mirror pair. The combinations of quadrant, energy, and pinhole diameter for the single quadrant wing scans are given in Table 14.3. In addition, a small number of double-quadrant wing scans were performed. In these scans, opposing quadrants for a given shell were open and the HRMA was at zero pitch and yaw; because of the presumed symmetry of the HRMA, data were taken only for points to one side of the HRMA ($+D_{ap}$, $+2D_{ap}$, and $+3D_{ap}$ for a given aperture diameter D_{ap}). Because of problems with shutters sticking, the 4N4S and 6N6S scans were performed with shutter 3B also open (*i.e.*, they were really 4N4S3B and 6N6S3B scans). In order to correct for this, additional 3B Z-scans were performed for the 1 mm and 4 mm pinholes only. These pinhole measurements are listed in Table 14.2.

The far wings of the PSF result mainly from scattering by the optic surfaces, primarily scattering from microroughness. In principle dust scattering could also contribute but any dust component was expected to be small because of the cleanliness of the AXAF optics. For grazing incidence reflection, scattering by microroughness is predominantly in-plane with only a small out-of-plane component. Consequently, Y-scans were performed for the North and South quadrants, while Z-scans were used for the Top and Bottom quadrants; a Y-scan was also performed at C-Kα for the shell 6 bottom quadrant in order to look for out-of-plane scattering resulting from any dust contamination. In addition, a very small number of Y-scans were performed at Al-Kα for the shell 3 bottom quadrant.

Table 14.1: XRCF Single Quadrant Wing Scan Measurements (by shell)

Energy (keV)	diam (mm)	T1	N1	B1	S1	T3	N3	B3	S3	T4	N4	B4	S4	T6	N6	B6	S6
0.277	1														○		
0.277	4														○		
0.277	10														○		
0.277	20														○		
0.277	35																
1.486	1	○	○	○	○	○	○	○	○	○	○	○	○	○	○	○	○
1.486	4	○	○	○	○	○	○	○	○	○	○	○	○	○	○	○	○
1.486	10	○	○	○	○		○		○		○		○		○		○
1.486	20	○	○	○	○	○	○	○	○	○	○	○	○	○	○	○	○
1.486	35		○		○		○		○		○		○		○		○
4.51	1	○	○	○	○				○				○				○
4.51	4	○	○	○	○				○				○				○
4.51	10	○	○	○	○				○				○				○
4.51	20	○	○	○	○				○				○				○
4.51	35		○		○				○				○				○
5.41	1								○				○				○
5.41	4								○				○				○
5.41	10								○				○				○
5.41	20								○				○				○
5.41	35								○				○				○
6.4	1					○	○	○	○	○	○	○	○	○	○	○	○
6.4	4					○	○	○	○	○	○	○	○	○	○	○	○
6.4	10					○	○	○	○	○	○	○	○	○	○	○	○
6.4	20					○	○	○	○	○	○	○	○	○	○	○	○
6.4	35						○				○		○		○		○
8.03	1												○	○	○†	○	○
8.03	4												○	○	○†	○	○
8.03	10												○	○	○†	○	○
8.03	20												○	○	○†	○	○
8.03	35												○		○†		○

†CMBD indicates yaw = $-1.88'$; other logs indicate that yaw = $+1.88'$ was actually used.

In order to expose as much of the optic as is possible given the finite source distance at XRCF, the tests were done one quadrant at a time with the mirror assembly pitched or yawed a few minutes of arc so that the diverging rays from the source would strike the mirror approximately parallel to the mirror assembly axis of rotational symmetry (closer to on-orbit, infinite source distance conditions). Nominally, the pitch or yaw should have been $3.56'$, $2.87'$, $2.53'$, or $1.88'$ for shells 1, 3, 4, and 6, respectively. Because of confusion about the orientation of the optical axis relative to the facility axis, some yaw offsets were in reality about 1 arcmin away from the intended value; the actual pitch/yaw combinations are given in Table 14.3 below.

In one case (shell 6N at Cu-Kα, the CMDB indicates a requested yaw of $-1.88'$ instead of the

Table 14.2: XRCF Double Quadrant Wing Scan Measurements

Energy (keV)	diam (mm)	4N4S3B	6N6S3B	3B
1.486	1	∘	∘	∘
1.486	4	∘	∘	∘
1.486	10	∘	∘	
1.486	20	∘	∘	
1.486	35	∘	∘	

expected $+1.88'$. This error was apparently caught on the floor; the available logs indicate that the test was actually performed at $+1.88'$. As noted in §D.7.2, the yaw axial reference was off by $-1'$ relative to the optical axis; thus, the actual off-axis angle for this test was yaw = $+0.88'$.

Table 14.3: Single Quadrant Pitch/Yaw values

Quadrant	energies	pitch($'$)	yaw($'$)
1T	Al, Ti	+3.56	+0.0
1N	Al, Ti	+0.0	+2.56†
1B	Al, Ti	−3.56	+0.0
1S	Al, Ti	+0.0	−4.56†
3T	Al, Fe	+2.87	+0.0
3N	Al, Fe	+0.0	+1.87†
3B	Al, Fe	−2.87	+0.0
3S	Al, Fe	+0.0	−3.87†
	Ti, Cr	+0.0	−2.87
4T	Al, Fe	+2.53	+0.0
4N	Al, Fe	+0.0	+1.53†
4B	Al, Fe	−2.53	+0.0
4S	Al, Fe, Cu	+0.0	−3.53†
	Ti, Cr	+0.0	−2.53
6T	Al, Fe, Cu	+1.88	+0.0
6N	Al, Fe	+0.0	+0.88
	Cu	+0.0	+0.88††
6B	Al, Fe	−1.88	+0.0
6S	Al, Fe, Cu	+0.0	−2.88†
	Ti, Cr	+0.0	−1.88

† Error of $1'$ in yaw zero reference

†† The CMDB indicates a yaw of $-1.88'$; other logs indicate that the HRMA was set to yaw = $+1.88'$. Adding the yaw axial offset error of $-1'$ gives yaw = $+0.88'$.

Pitching and yawing the HRMA allowed a better sampling of the length of the optic for a given shell shell and quadrant; at the same time, it complicates the interpretation of the data: in the on-axis case, the incident graze angle is nominally a function of the axial distance of the ray intercept along the optic. With the tilted optic, the graze angle varies with azimuth as well. Consequently,

the approach we take is to perform a raytraces which simulate the XRCF experiments as closely as possible. The raytraces were performed with the HRMA pitched or yawed according to the values as specified in the CMDB, but modified as necessary for the yaw reference error; see Table 14.3 and §D.7.2. The raytrace model was based on configuration `xrcf_SA01G+HD0S_HD0S-scat-980623_01`; note that this does *not* include finite source size effects or multilayer (and multilayer gradation) reflectivity effects. The smallest pinhole size used was 1 mm diameter, much larger than the projected source dimensions, so neglect of the finite source size is not significant in this case. The ("rough") multilayer reflectivity effects are of order 10%, small enough to be neglected in this first pass through the data analysis.

Currently, no mesh correction is applied to the raytrace simulations; again this is expected to be at most a 10% effect. As a test of this, a limited number of wing scan raytraces were performed including a simulation of the mesh (Table 14.4). As expected, the off-axis points are consistent with an overall mesh correction of about 10%. Note that the raytrace model currently underpredicts the measured wing scan X-ray data, so including the mesh correction will make the disagreement slightly worse.

Table 14.4: Effect of Mesh on Wing Scans

trwid	diam	iter	$N_{\rm nomesh}$	$N_{\rm mesh}$	ratio	error
D-IXF-PW-6.014a	1	0	914	884	0.967	0.046
D-IXF-PW-6.014a	1	1	2413	2327	0.965	0.028
D-IXF-PW-6.014a	1	2	7233	6970	0.964	0.016
D-IXF-PW-6.014a	1	3	922442	921402	0.999	0.0015
D-IXF-PW-6.014a	1	4	10019	8473	0.847	0.012
D-IXF-PW-6.014a	1	5	2984	2725	0.914	0.024
D-IXF-PW-6.014a	1	6	1059	969	0.915	0.041
D-IXF-PW-6.018	35	2	3098	2787	0.90	0.023
D-IXF-PW-6.018	35	3	1034352	1023056	0.989	0.0014
D-IXF-PW-6.018	35	4	2378	2124	0.89	0.027

14.1 Pinhole Effective Areas

The basic data obtained in the experiment were the effective areas measured for pinhole scans through the image. In this section we describe the reduction of the X-ray measurements and the raytrace simulation procedure.

14.1.1 X-ray data reduction

During Phase 1 at the XRCF, the HRMA effective area was measured at numerous spectral lines. The source used was the electron impact point source (EIPS). The anode selected, in concert with the high voltage used in the source, dictates the spectrum, both line and continuum, emitted by the source. Much of the continuum flux is absorbed by a filter placed between the source and the beam-line (and hence all the detectors). This filter is chosen in such a way as to have an optical depth of 2 or 4 at the line in question, and so it is optically much thicker at slightly higher energies where it has an absorption edge. Various pinholes can be positioned in front of the focal plane

detector to act as an aperture stop. In the wing scan experiments the pinhole diameters used were 1 mm, 4 mm, 10 mm, 20 mm, and 35 mm.

The pulse height spectral data were reduced using the method described in Chapter 9. Because the off-axis focal plane instrument often sees very low counting rates (only a few counts per bin) and can be dominated by background, we used the C-statistic ((Cash, 1979) and (Nousek and Shue, 1989)). We have also used the distributed gain double-`JMKmod` method (§9.4) to fit the BND-H data, which have relatively high signal-to-noise ratios.

The BND detectors are used to measure the photon flux density at the HRMA entrance, which is determined by dividing the count rate from each detector by the open area of its aperture (corrected for mesh transmission), and averaging the results. This average is then divided into the count rate from the focal plane detector, giving a quantity which has units of cm^2, known as the effective area. The quantities of interest here are the effective areas measured through pinholes positioned in front of the focal plane detector. In addition to the pinhole measurements in the wing scans, the on-axis effective area measured through a 35 mm pinhole was used to normalize the wing scan data; see the discussion below.

14.1.2 Raytrace simulations of the pinhole experiments

The wing scan raytraces were performed as very long raytraces (incident ray density of 500 rays/mm^2) in which the rays were processed by the `pinhole` module. The `pinhole` module tallies the total number of rays and total ray weight for rays which would have passed through a virtual pinhole with a given radius and position. An array of (possibly overlapping) virtual pinholes of arbitrary sizes can be processed together. In these simulations, the rays were processed through pinholes positioned between −105 mm and +105 mm with 0.1 mm spacing, for pinhole diameters 1, 4, 10, 20, and 35 mm. In each case the conditions of the actual X-ray experiment were replicated as well as possible including the finite X-ray source distance and the pitch or yaw of the HRMA. The quadrant shutters were modeled using opaque apertures shaped and positioned according to the specifications of the aperture assembly drawings (aperture `quad_shutter_05.lua`).

The pinhole effective areas were evaluated by dividing the total ray weight for rays passing through the pinhole by the known ray density at the HRMA entrance. The statistical error on the pinhole effective area was estimated by dividing the pinhole effective area by the square root of the number of rays passing through the pinhole (appropriate for Poisson statistics).

14.2 The Experiment as Performed

The analysis of the wing scan experiment was complicated by several aspects of the as-run experiment. In particular, the execution of the pinhole experiments with nonzero HRMA pitch resulted in a shift of the HRMA focus which was not (for the most part) captured by the FOA tables; consequently, the distance between pinhole center and focus based only on the HXDA stage logs and the FOA table in many cases needs to have a pitch correction applied. In addition, the confusion engendered by the built-in HRMA decenter error (Coma-free decenter; see Chapter 30) resulted in the HRMA bore sight being offset by $1'$ in yaw for part of the testing; as a result, in some cases the actual yaw values differed by $1'$ from the intended values (*i.e.*, those requested in the CMDB). Finally, the mapping of the wings relies on using the quadrant shutters to isolate individual mirror shells and quadrants. Some of the pinhole scans reach sufficiently far off-axis that vignetting by closed shutters for adjacent shells becomes important, particularly for shells 3 and 4 which are physically close together. These issues are addressed in more detail in the following sections.

14.2.1 History of the Pitch Problem

For the XRCF data, the pinhole positions relative to the focus were calculated using `calcstage4`. In the `calcstage4` calculation the pinhole location relative to the focus is determined by using the stage logs and the contemporaneous focus position appropriate to the shell(s) in use is determined from the FOA tables. The distance (X, Y, Z) of the pinhole from the focus is evaluated by differencing the two sets of values:

$$X = X_{pinhole} - X_{focus} \tag{14.1}$$
$$Y = Y_{pinhole} - Y_{focus} \tag{14.2}$$
$$Z = Z_{pinhole} - Z_{focus} \tag{14.3}$$

Note that currently the only information that `calcstage4` has about the focus position is that found in the FOA tables; if the FOA table is incorrect about where the focus happens to be, then `calcstage4` will get the wrong answer.

Because an aft vertical actuator was stuck during phase 1E, pitch motions during phase 1E were carried out using only the forward vertical actuator. This resulted in a pitch motion about a point other than the HRMA node, so any pitch motions caused the HRMA node (and hence, the finite conjugate focal point) to shift vertically. These vertical shifts in focus location can be large ($\lesssim 1$ mm) compared to the size of the smallest pinhole used in the wing scans (1 mm diameter). It is therefore important to understand the relation between HRMA pitch moves and the FOA tables.

In order to determine how the experiment was really performed, the XRCF 2nd Floor Shift Reports, the Project Science/Telescope Scientist logs, and the EKC shift reports were examined. The first wing scan experiment in Phase 1E was a wing scan of quadrant 6B with an EIPS C-Kα source and with the HRMA pitched by $-1.88'$. A set of Y-scans was performed (E-IXF-PW-2.001–5, day 028/029) followed by a set of Z-scans (E-IXF-PW-2.010–13, day 029). During the the first sequence of 1 mm pinhole Y-scan measurements (E-IXF-PW-2.001) it was discovered that the scan was approximately 500 μm too low. It was realized that this was because the pinhole positions were calculated relative to the FOA values for the focus position and that the FOA value was now offset from the real focus of the pitched HRMA. In order to compensate for this, the FOA table was adjusted by 504 μm in Z for the rest of the quadrant 6B C-Kα wing scans (4 mm, 10 mm, 20 mm, 35 mm Y-scans, 1 mm, 4 mm, 10 mm, 20 mm Z-scans) based on a beam centering with the 70 μm pinhole. Following the C-Kα wing scans, the FOA values were reset back to the nominal values. The actual pitch correction should have been 609 μm in Z, so the FOA table correction was about 105 μm shy of the appropriate correction. Consequently, the `calcstage4` values for the distance of the pinhole from the focus were nearly correct for these pinholes, but additional $\Delta Z_{focus} = +105$ μm pitch correction needs to be applied. (The additional pitch correction we actually applied was $\Delta Z_{focus} = +94$ μm; the effect of the remaining 11 μm discrepency is negligible for these wing scan measurements.)

It was initially suggested that a similar FOA adjustment be made for all the subsequent HRMA pitch moves. It was decided instead to aim for an automated approach whereby the pitch correction would be applied to the pinhole locations during the CMDB processing; these fixes were incorporated into the software during shift A, 1997 Feb 2 (day 033). Note that for the period between the end of the 6B C-Kα wing scans on day 029 and CMDB fixes of day 033, any pitch corrections would have been entered manually into the pinhole locations files.

Node Shift in HRMA Pitch Moves

Because the HRMA pitch motions were performed with the aft vertical actuators fixed, the actual pitch motion was a rotation about the line defined by the aft vertical actuator locations. This produced a vertical shift of the HRMA node which displaced the focal point at the instrument plane.

In comparing the raytraces to the XRCF pinhole data, the XRCF Z coordinates relative to the contemporary FOA were corrected for the shift in the focus by subtracting off a pitch correction. To first order, the vertical shift in the node is the product of the sine of the pitch angle change and the axial offset between the fixed actuator station and the node. The axial distance between the node and the actuator is 43 inches (= 1092.2 mm), from which

$$\Delta Z_{node} = -1092.2 \ \sin\Delta\theta_{pitch} \text{ mm} \tag{14.4}$$

where $\Delta\theta_{pitch}$ is the change (in radians) in the HRMA pitch. In the thin lens approximation, the focus moves by

$$\Delta Z_{focus} = \frac{\Delta Z_{node}}{D_{source}} \times (D_{source} + D_{focus}) \tag{14.5}$$

where $D_{source} = 527297$ mm is the distance between the HRMA node and the X-ray source, and $D_{focus} = 10256$ mm is the nominal distance from the HRMA node to the finite conjugate focus. In making the above estimates, the node was assumed to be 18.1 mm aft of CAP "Datum A". Substituting for the various distances, the vertical shift in focus is approximately:

$$\Delta Z_{focus} = -1.1134 \times 10^6 \sin\theta_{pitch} \, \mu\text{m} \tag{14.6}$$

or,

$$\frac{\Delta Z_{focus}}{\Delta\theta_{pitch}} \simeq -323.9 \ \mu\text{m/arcmin}. \tag{14.7}$$

Pitch Corrections Applied

Most of the wing scans with HRMA at nonzero pitch were performed with the FOA table values appropriate to HRMA at zero pitch; the requisite pitch corrections were applied to the requested pinhole locations. `calcstage4` calculates the pinhole location based on the stage logs; the resulting physical location for the pinhole will be calculated correctly. In analyzing the wing scans, the distance of the pinhole center from the current focal point is needed; the `calcstage4` evaluation of the focus position is based on the FOA entry and that is incorrect because of the HRMA node shift (and resultant shift in focus). `calcstage4` reports the difference between the pinhole location and the focus position, so a pitch correction needs to be *subtracted* from the `calcstage4` Z value. Based on equation (Eq. D.6), the pinhole Z value reported by `calcstage4` was corrected by

$$\Delta Z_{corr} = Z - \Delta Z_{focus}. \tag{14.8}$$

An exception was the wing scan for shell 6B for which the FOA was partially compensated for the pitch-induced focus change (§D.7.1); in this case, the Z values were corrected by -94 μm to account for the slight undercorrection of the FOA adjustment.

14.2.2 Yaw Reference Error

Early in Phase 1D, an attempt was made to determine the HRMA X-ray bore sight by using the variation of effective area as the HRMA was pitched and yawed. At the time, the presence of the coma-free decenter error in the HRMA mirror alignment was not yet known; this error causes the off-axis effective area profiles to be nonsymmetric about the optical axis. This led to an initial confusion as to alignment of the mirror bore sight to the facility optical axis; the reference axis for pitch and yaw ended up being offset by about $1'$ in yaw starting at IAP 5 (day 005, 16:11) through the end of phase 1D. Consequently, the actual yaws ended up being offset by $1'$ from the requested values, and because of this, some yaw values in Table 14.3 differ from the requested CMDB values. This does not directly affect the XRCF data reduction; the yaws were off, but the FOA was determined based on the contemporary yaw zero reference. However, this offset does need to be included in the comparison raytraces.

14.2.3 Vignetting by Quadrant Shutters

In the plots of pinhole effective areas, the raytrace results are displayed at 0.1 mm intervals for the 1 mm diameter pinhole, 0.4 mm intervals for the 4 mm pinhole, and at 1 mm intervals for the 10, 20, and 35 mm pinholes.

Although the scattering formulation currently being used in the raytracing is symmetric with regard to scattering toward or away from the surface, the raytrace pinhole effective areas do show an asymmetry in deflections towards or away from the mirror surface. This is at least in part because of the off-axis vignetting by the quadrant shutter blades. The quadrant shutter vignetting is particularly noticeable in the larger pinholes for shells 3 and 4; see Figure 14.1. In Figure 14.2 the results *for a single mirror pair*, MP3, are compared with only the 3S quadrant open and with the all the S quadrants open. (This latter experiment could not be done at XRCF because closing the 1S, 4S, and 6S shutters is necessary in order to isolate shell 3.) It is evident that the 1S and 4S shutter blades can significantly vignette the wing scan observations for shell 3S; similar observations apply to the other shells.

The reason for the drop-off away from the mirror (shell 3) or towards the mirror (shell 4) can be seen in Figure 14.3. In this figure, ray position *vs.* ray azimuth is plotted at the axial location for the quadrant shutters. In each case, only one quadrant shutter is open. The horizontal and vertical lines indicate the limiting edges of the adjacent shutter blades. For 35 mm diameter pinholes, shell 3 begins to be vignetted by the adjacent shell 4 shutter blade by the time the pinhole is only 30 mm off-axis. Note that at the shutter assembly position, the X-rays are on cones converging towards the focus. Consequently, scattering towards the mirror surface shows up as deflections towards larger radius at the shutter plane; similarly scattering away from the mirror surface produces deflections towards smaller radius at the shutter plane.

14.3 Pinhole Effective Areas: X-ray data *vs* Raytrace

The effective area through a pinhole of a given radius as a function of the pinhole off-axis position provides the most direct comparison between the XRCF data and the raytrace simulations. The X-ray data and the raytrace pinhole effective areas are compared in the following subsections. Each page provides plots comparing the XRCF data *vs.* raytrace data for different pinhole diameters for a given shell, quadrant, and energy; the figures are presented in the order: shell, quadrant (T, N, B, or S), and energy.

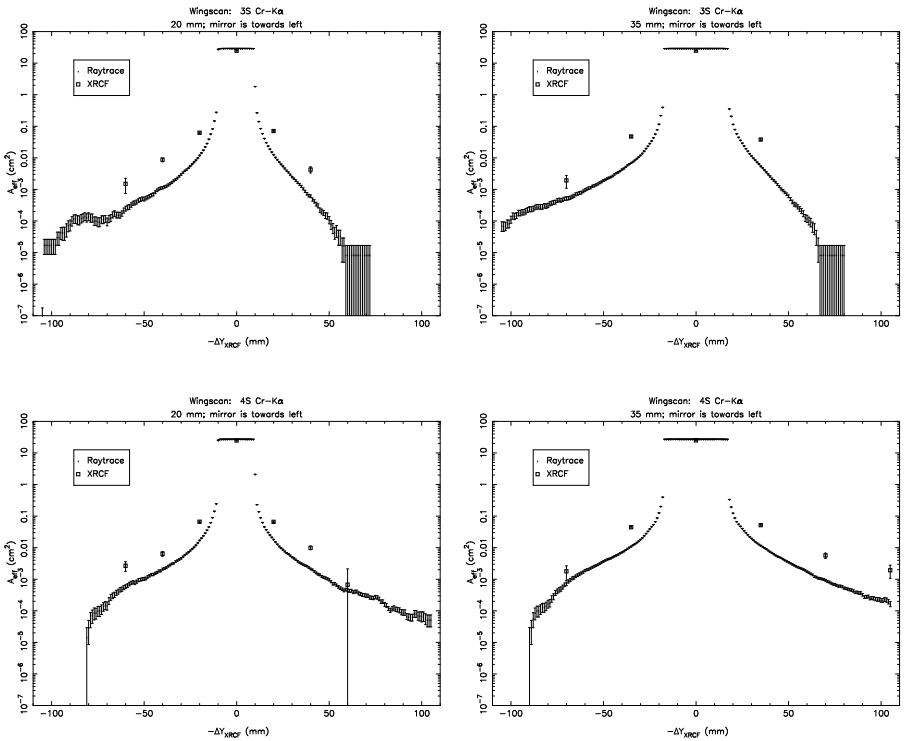

Figure 14.1: Effect of quadrant shutter vignetting: shell 3 *vs.* shell 4. Note that Shell 3 is vignetted away from the mirror while shell 4 is vignetted towards the mirror, consistent with Figure 14.3.

14.3.1 Single Quadrant Wing Scan Pinhole Data

In this section the XRCF single quadrant wing scan pinhole effective area measurements are compared to the raytrace simulations of the same configurations. The list of sampled pinhole measurements is summarized in Table 14.1. In the plots of pinhole effective areas, all the XRCF data points are plotted. The raytrace results are displayed at 0.1 mm intervals for the 1 mm diameter pinhole, 0.4 mm intervals for the 4 mm pinhole, and at 1 mm intervals for the 10, 20, and 35 mm pinholes (see Chapter 14).

The central portion of the profile appears flat up to a distance of about half the pinhole diameter away from the center; in this regime, the sharply peaked core of the PSF falls entire within the pinhole and the effective area varies slowly as different portions of the wings are included together with the core. The pinhole effective area drops off rapidly as the core moves outside the pinhole, then more slowly as the near-wings of the PSF are also excluded from the pinhole. The wing scan experiment is concerned with the outer wings of the PSF.

For the smallest pinholes, the agreement with the raytrace simulations is often quite good. The distribution is often approximately symmetric about the center (for example, 1T Ti-Kα, Figure 14.8), (for example, 1S Al-Kα, Figure 14.7), but markedly asymmetric in other cases, (for example, 4S Al-Kα, Figure 14.25). In the cases with marked asymmetry, the point(s) in the direction corresponding to scattering away from the mirror surface tend to be higher than those towards the mirror surface. A notable exception is the 6B C-Kα in-plane scan. The distribution for the 1 mm pinhole looks reasonably symmetric, but in the 4 mm scan, the point 4 mm inwards is an order of magnitude higher than the point 4 mm outwards. (The central point was omitted for the 4, 10, and 20 mm scans; no 35 mm scan was done in this case.) Examination of the raw data indicates that the difference is real; the available information on pinhole positions and tolerances indicate that these are accurate as well. Currently we have no explanation for this difference. (See also the 6B C-Kα out-of-plane scan (§14.3.2) which took place immediately prior to the in-plane scan.)

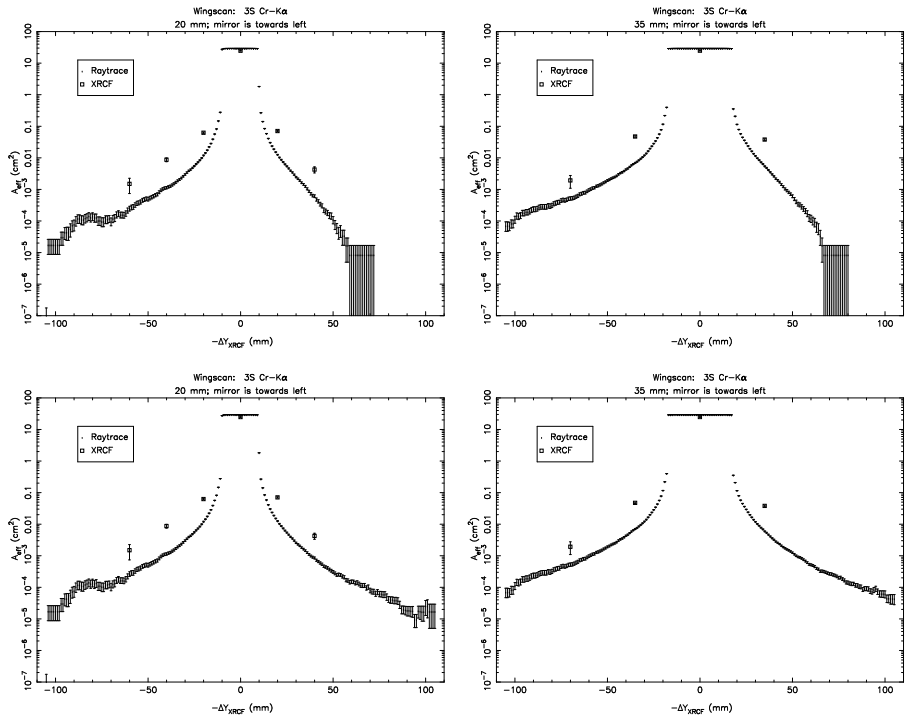

Figure 14.2: Effect of quadrant shutter vignetting. The top panels were raytraced for shell 3 alone and with quadrant configuration `cccc-ccco-cccc-cccc` while the bottom panels were traced with shell 3 alone but with all the South shutters open (quadrant shutter configuration `ccco-ccco-ccco-ccco`).

In general, the agreement between the X-ray data and the simulations gets worse for larger off-axis angles, particularly for the larger pinholes. The raytrace simulations for the larger pinholes also show effects of vignetting by the adjacent quadrant shutter blades (see Chapter 14 for further details.)

Further analysis of the wing scan experiment (including derivation of surface brightness profiles

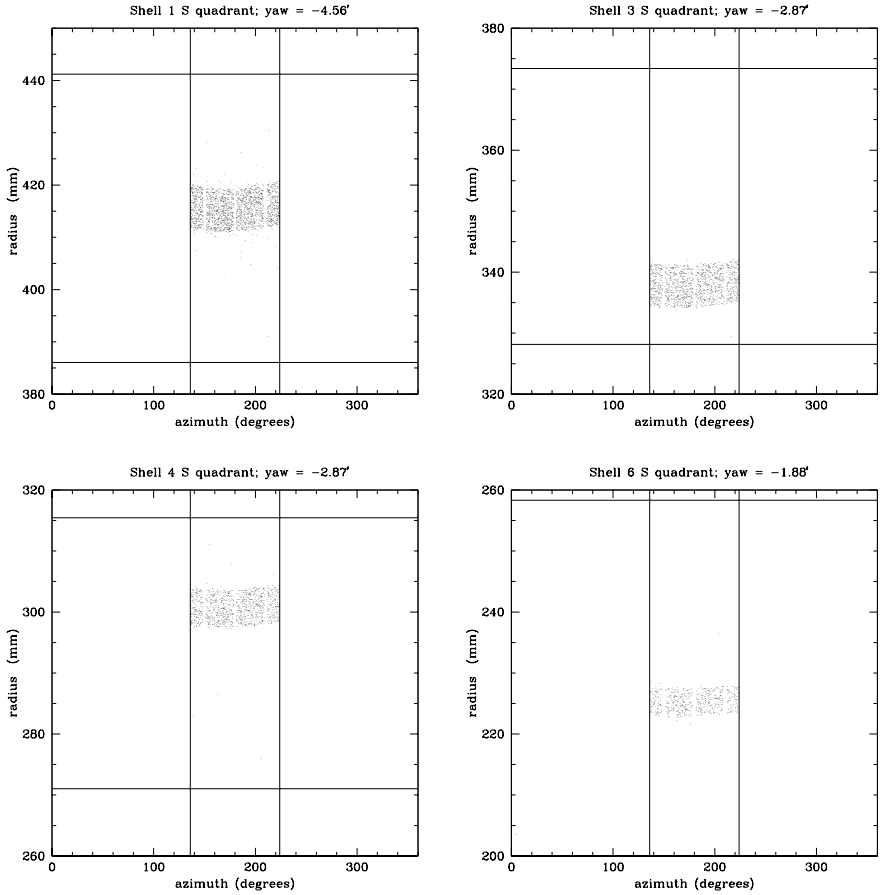

Figure 14.3: Quadrant shutter vignetting. The figures are spot diagrams for ray positions at the planes of the quadrant shutter blades. The vertical and horizontal lines indicate the limiting edges for the adjacent, closed quadrant shutters. Top Left: 1S (configuration `ccco-cccc-cccc-cccc`). Top Right: 3S (configuration `cccc-ccco-cccc-cccc`). Bottom Left: 4S (configuration `cccc-cccc-ccco-cccc`). Bottom Right: 6S (configuration `cccc-cccc-cccc-ccco`).

and corresponding PSD's) is provided in Chapter 15.

Shell 1 Single Quadrant Scans

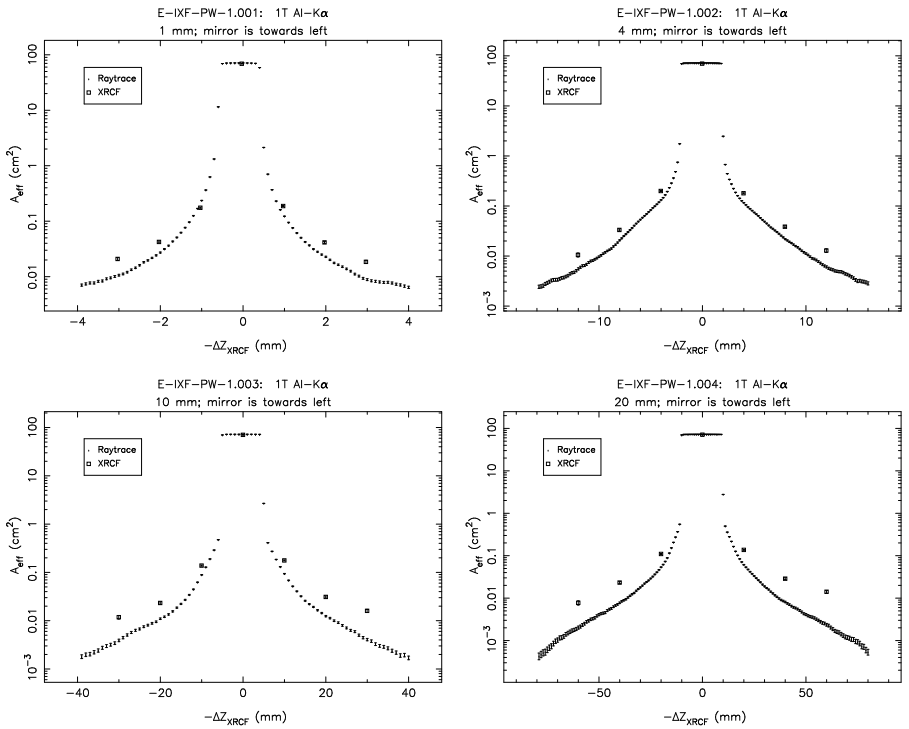

Figure 14.4: Pinhole effective areas; Shell 1T at Al-Kα.

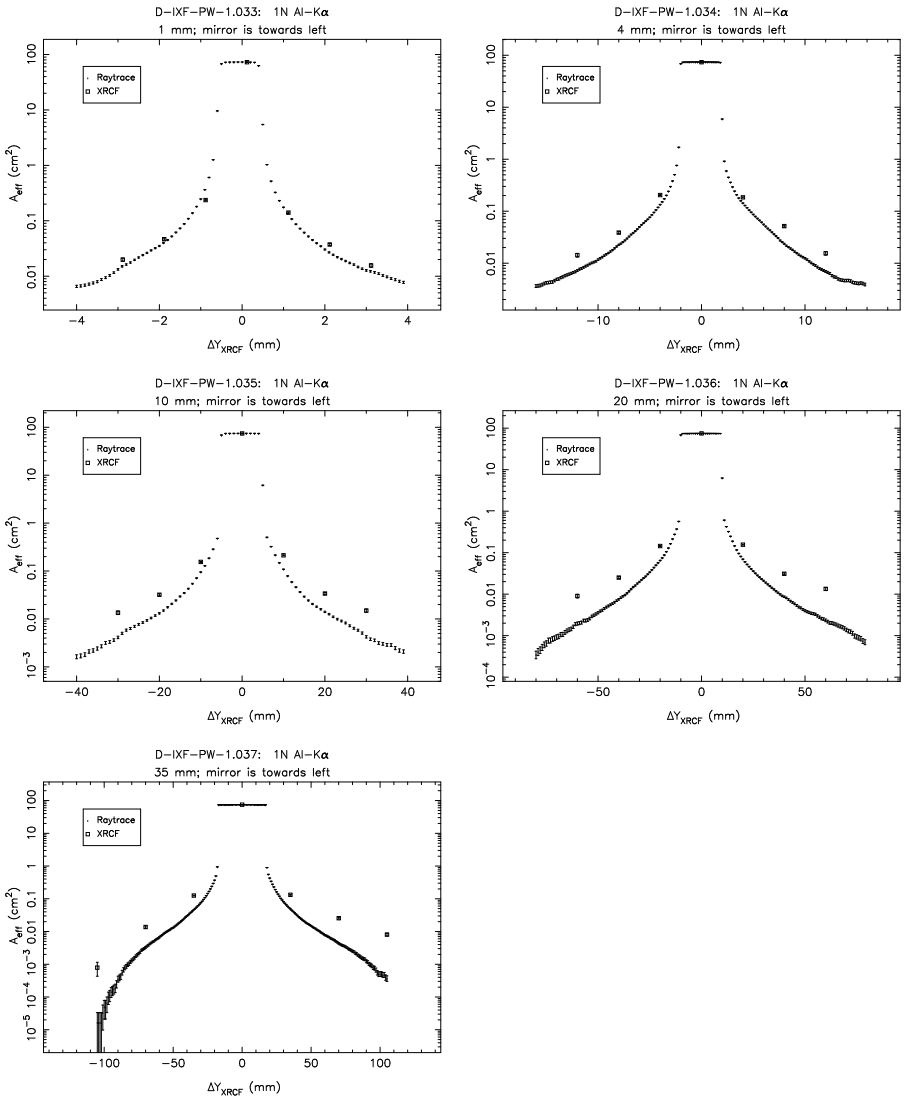

Figure 14.5: Pinhole effective areas; Shell 1N at Al-Kα.

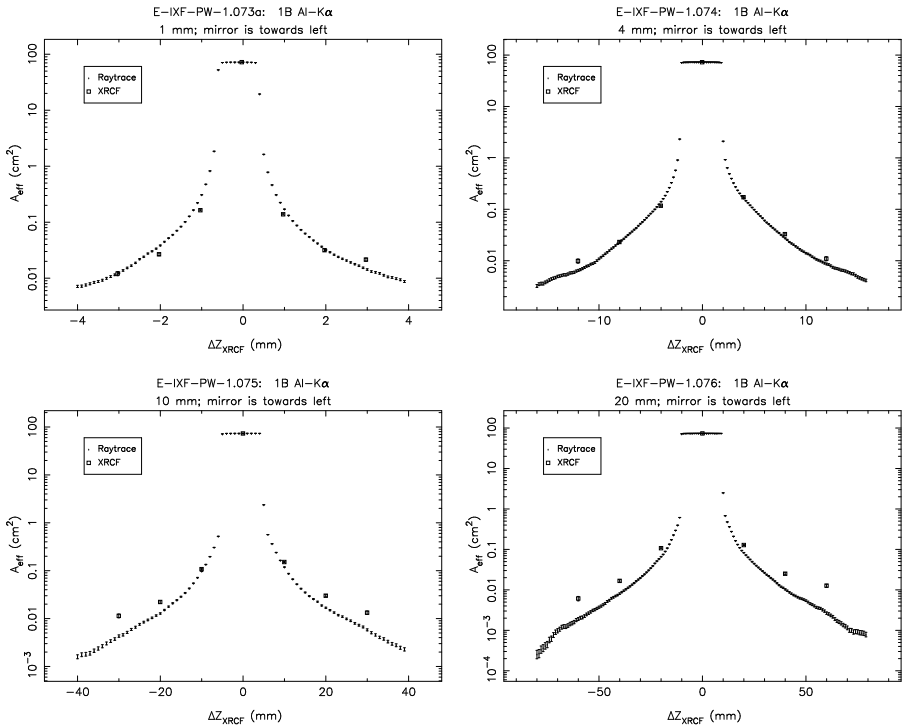

Figure 14.6: Pinhole effective areas; Shell 1B at Al-Kα.

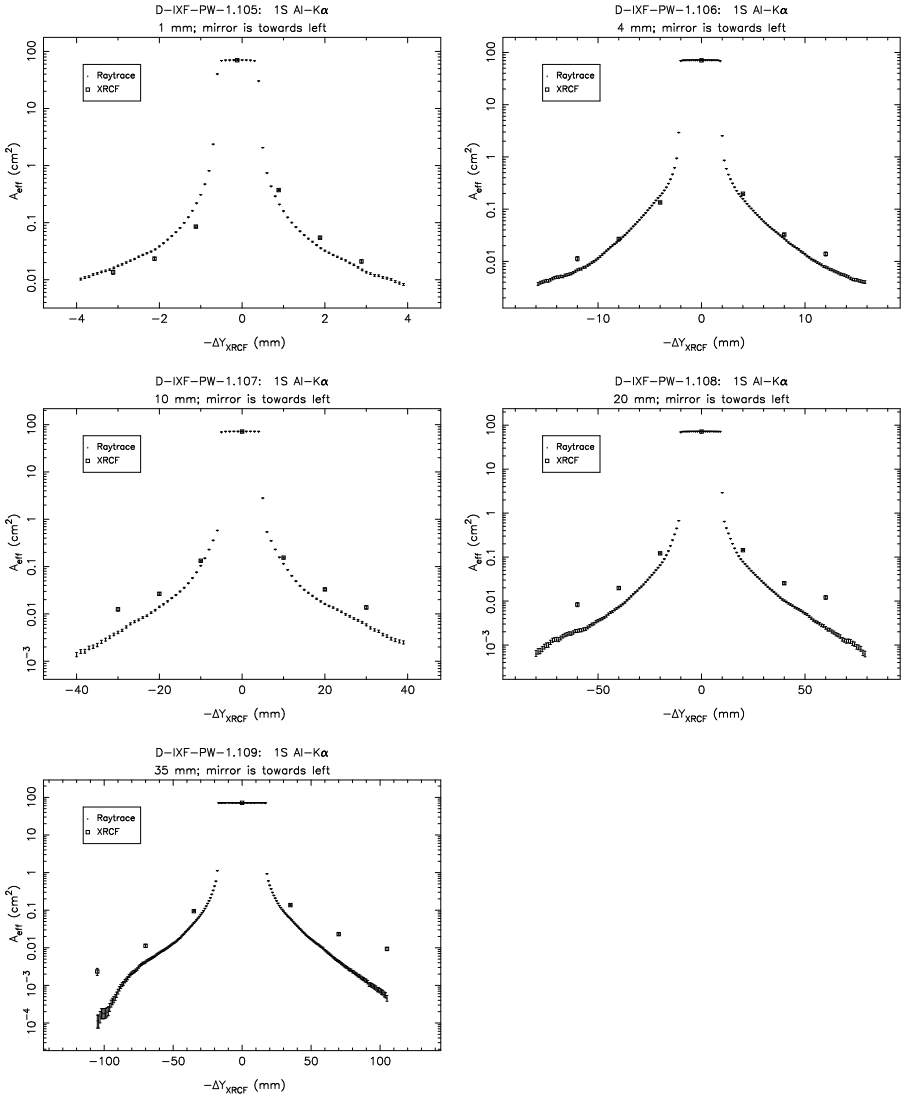

Figure 14.7: Pinhole effective areas; Shell 1S at Al-Kα.

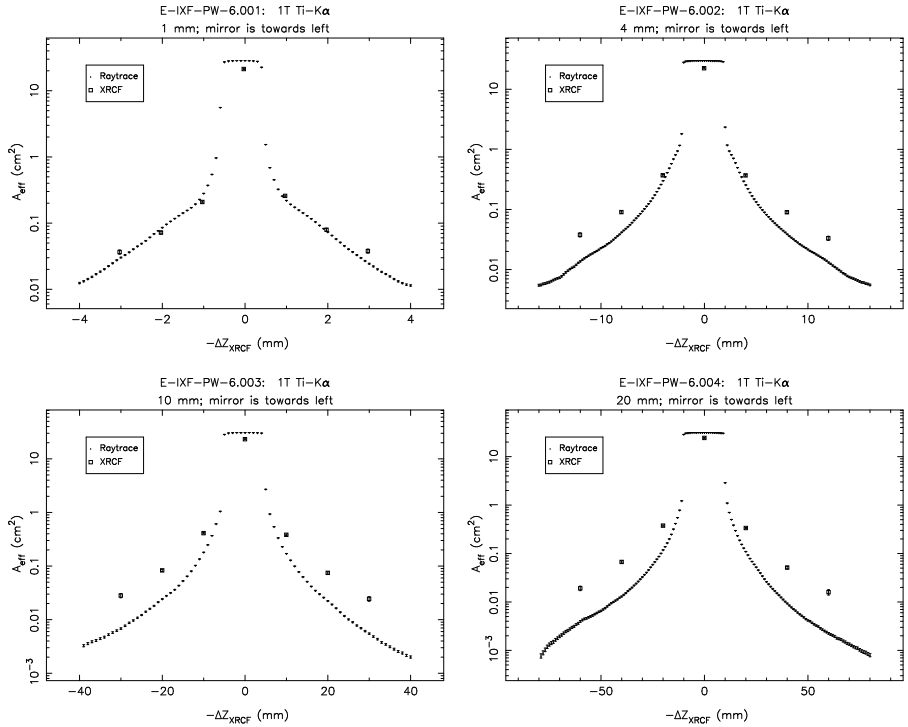

Figure 14.8: Pinhole effective areas; Shell 1T at Ti-Kα.

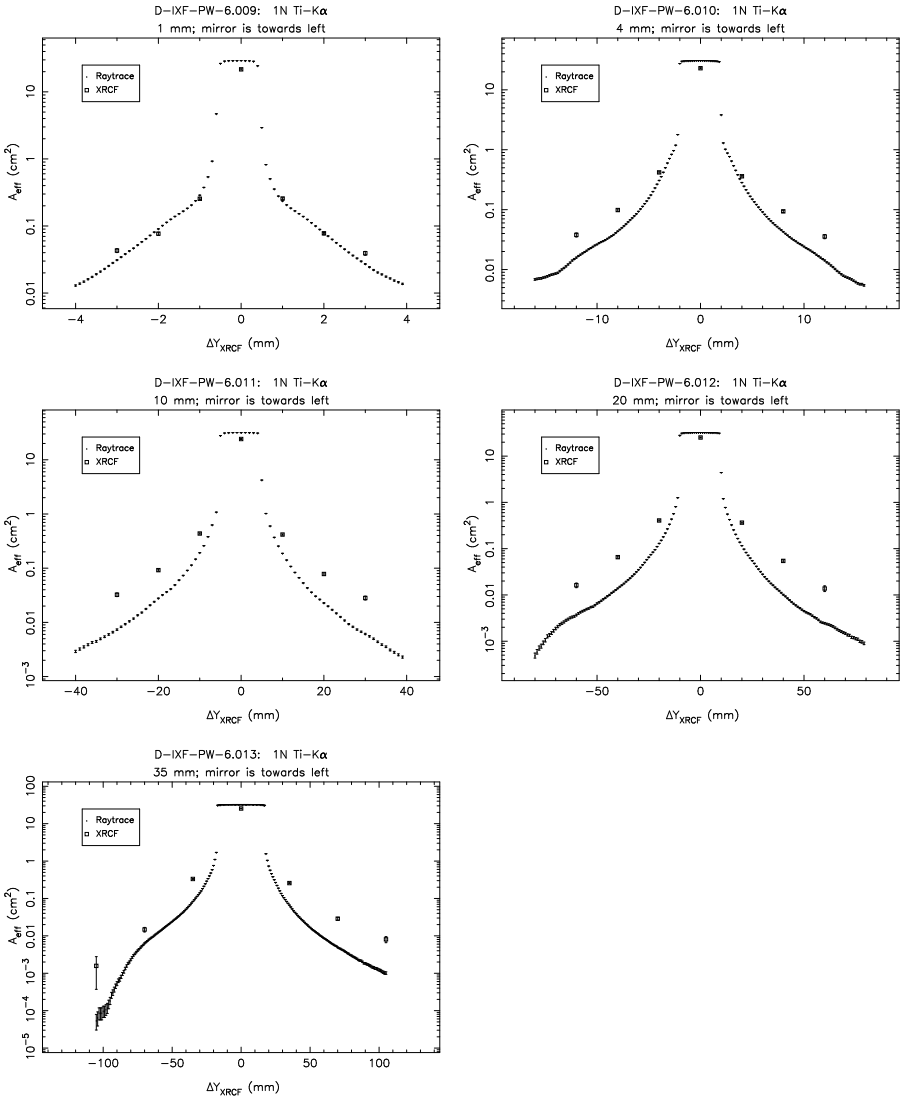

Figure 14.9: Pinhole effective areas; Shell 1N at Ti-Kα.

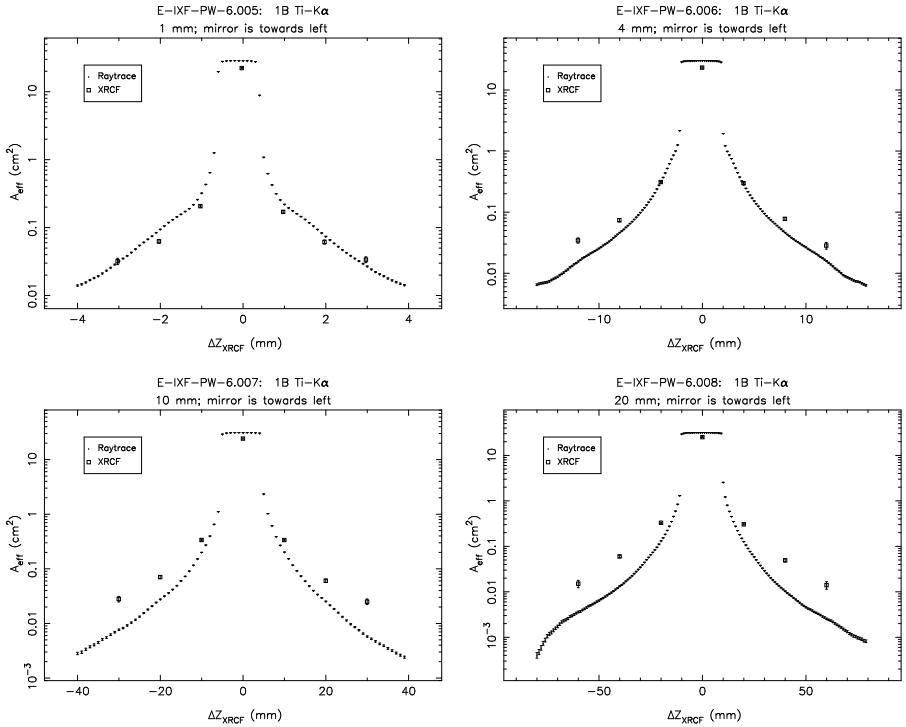

Figure 14.10: Pinhole effective areas; Shell 1B at Ti-Kα.

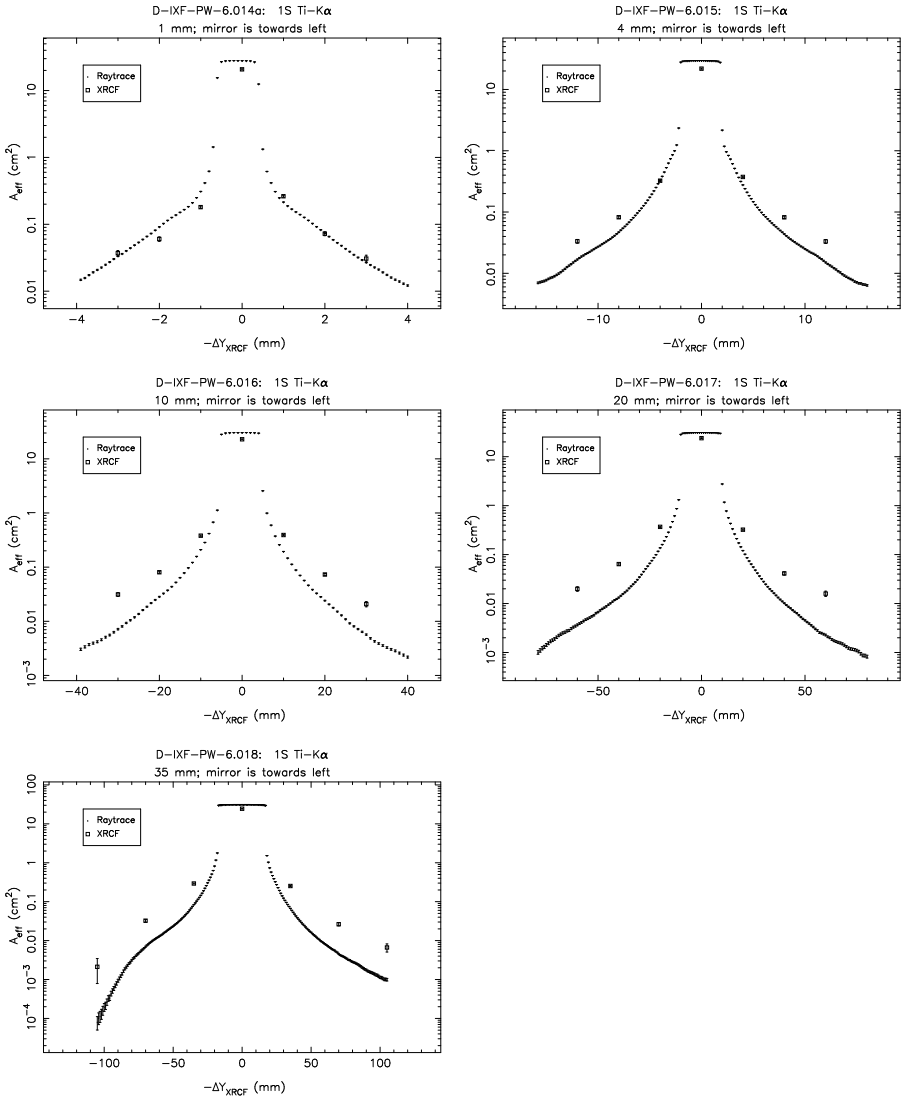

Figure 14.11: Pinhole effective areas; Shell 1S at Ti-Kα.

Shell 3 Single Quadrant Scans

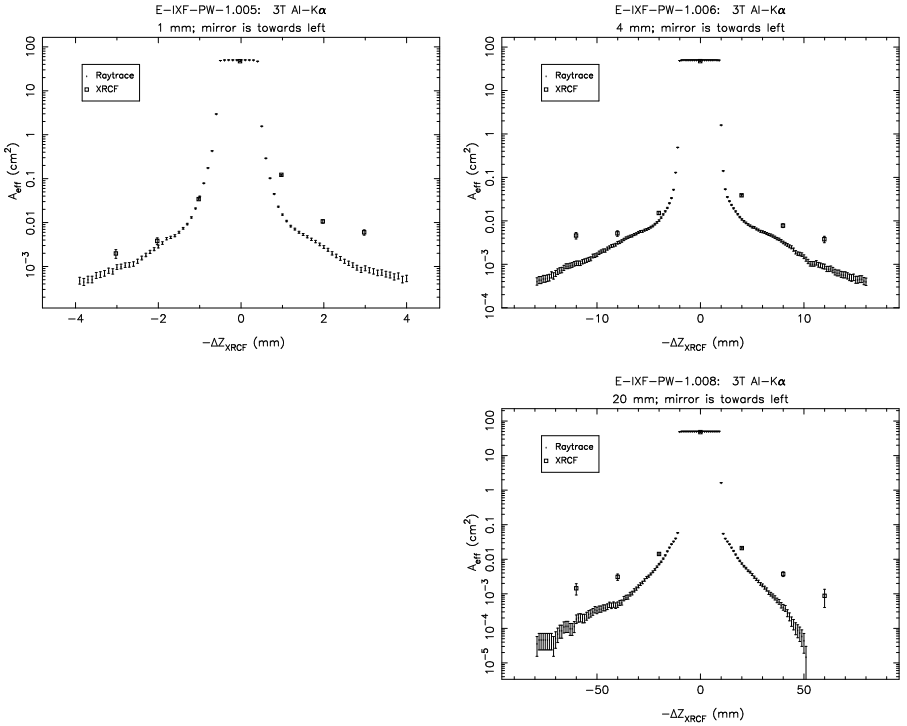

Figure 14.12: Pinhole effective areas; Shell 3T at Al-Kα.

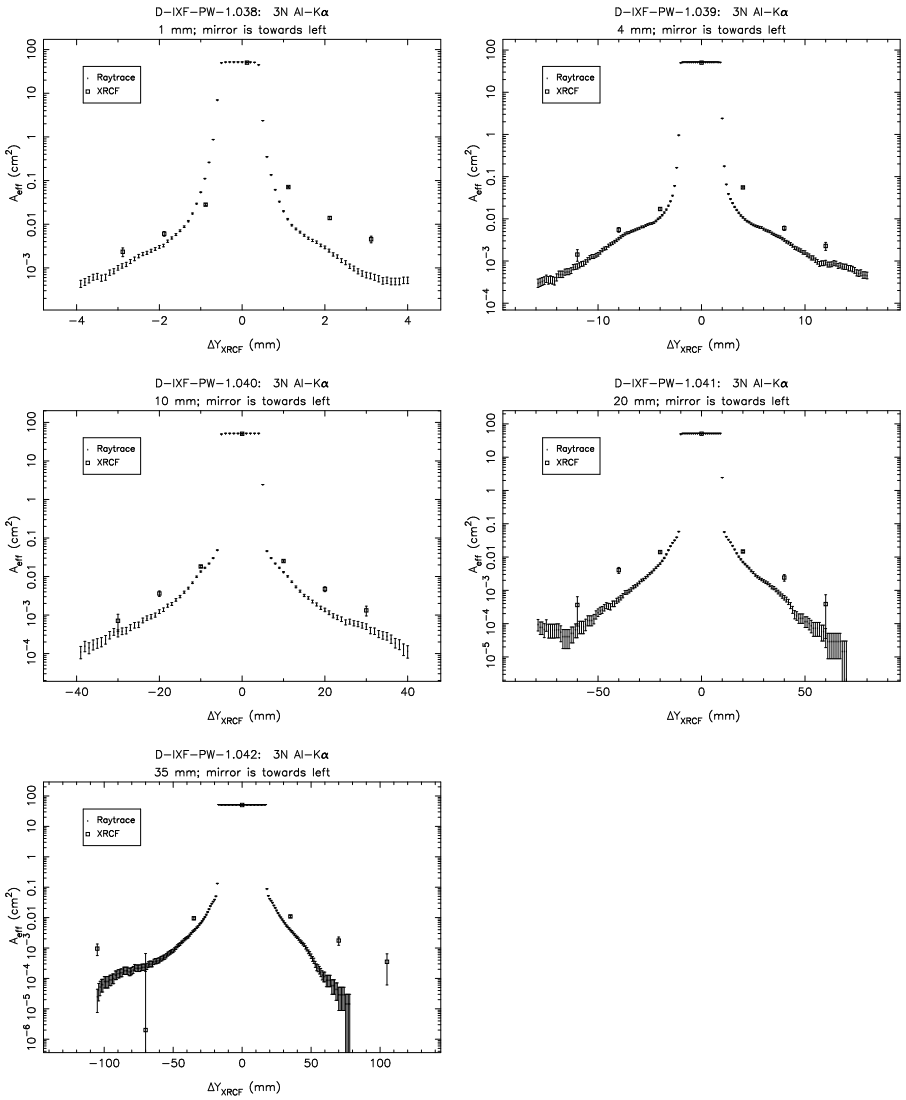

Figure 14.13: Pinhole effective areas; Shell 3N at Al-Kα.

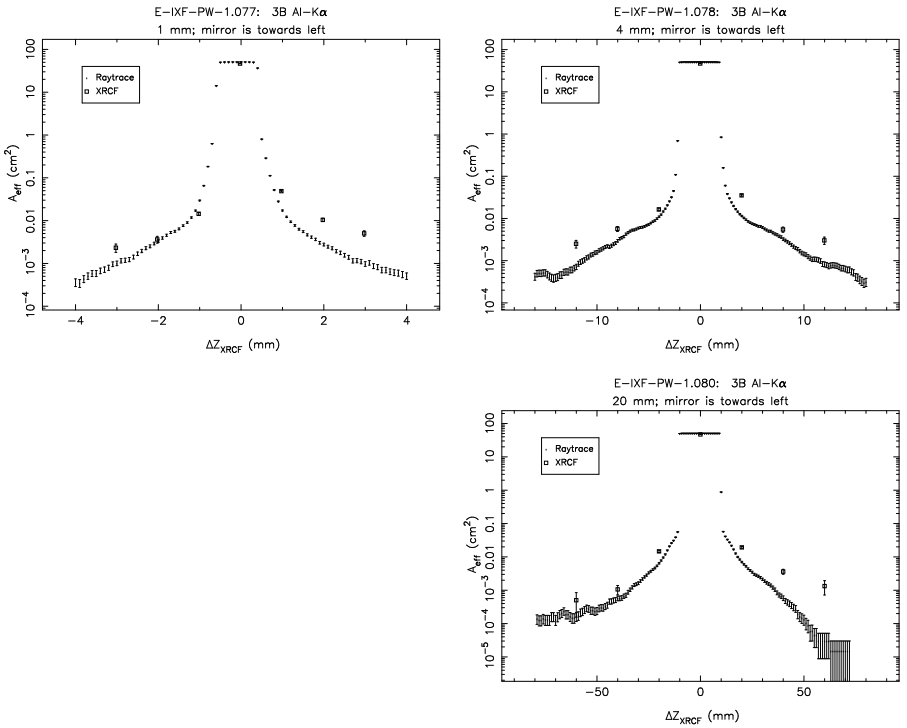

Figure 14.14: Pinhole effective areas; Shell 3B at Al-Kα.

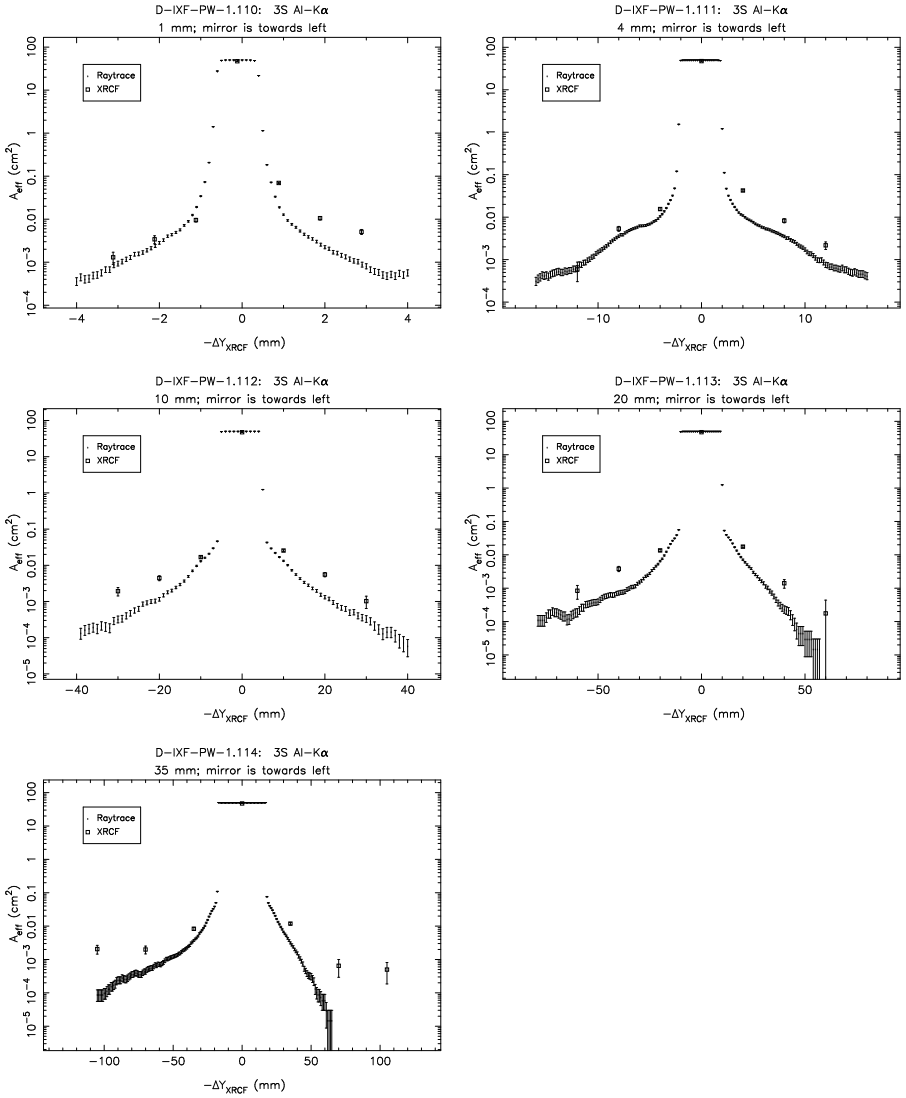

Figure 14.15: Pinhole effective areas; Shell 3S at Al-Kα.

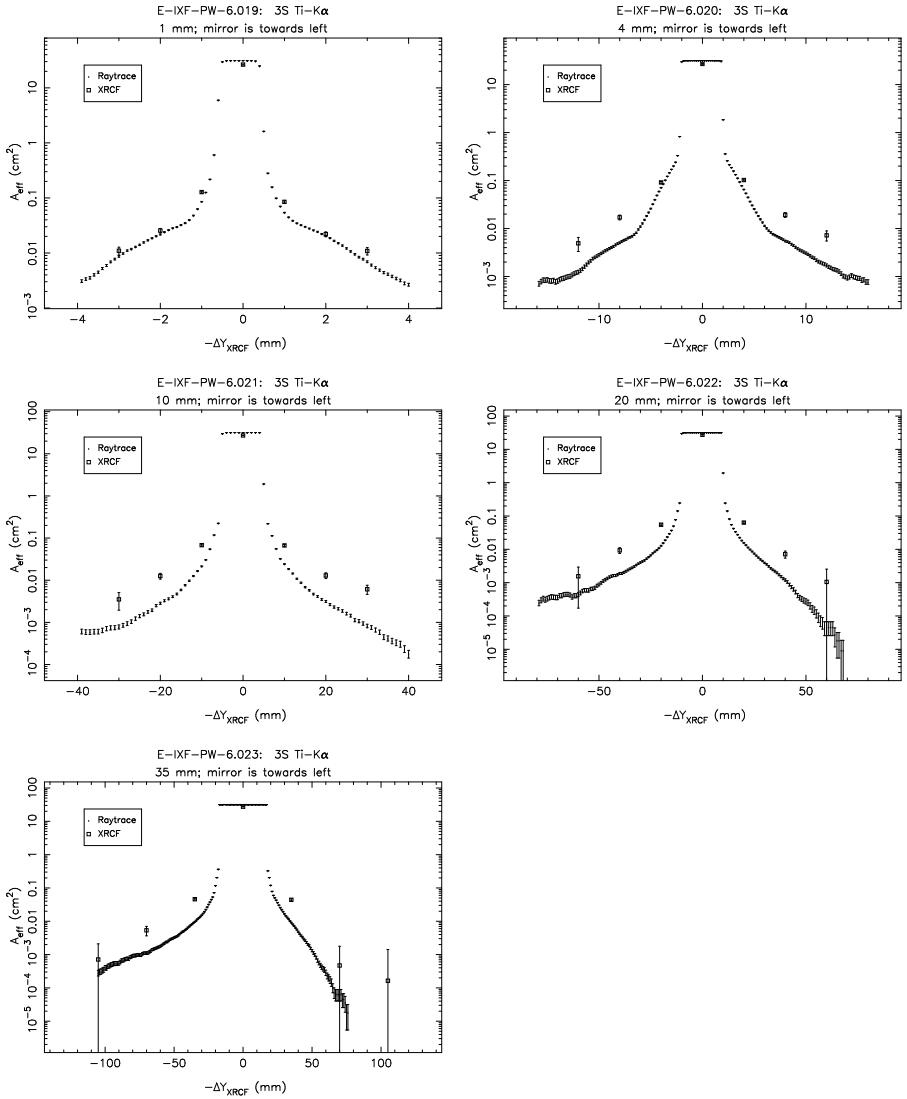

Figure 14.16: Pinhole effective areas; Shell 3S at Ti-Kα.

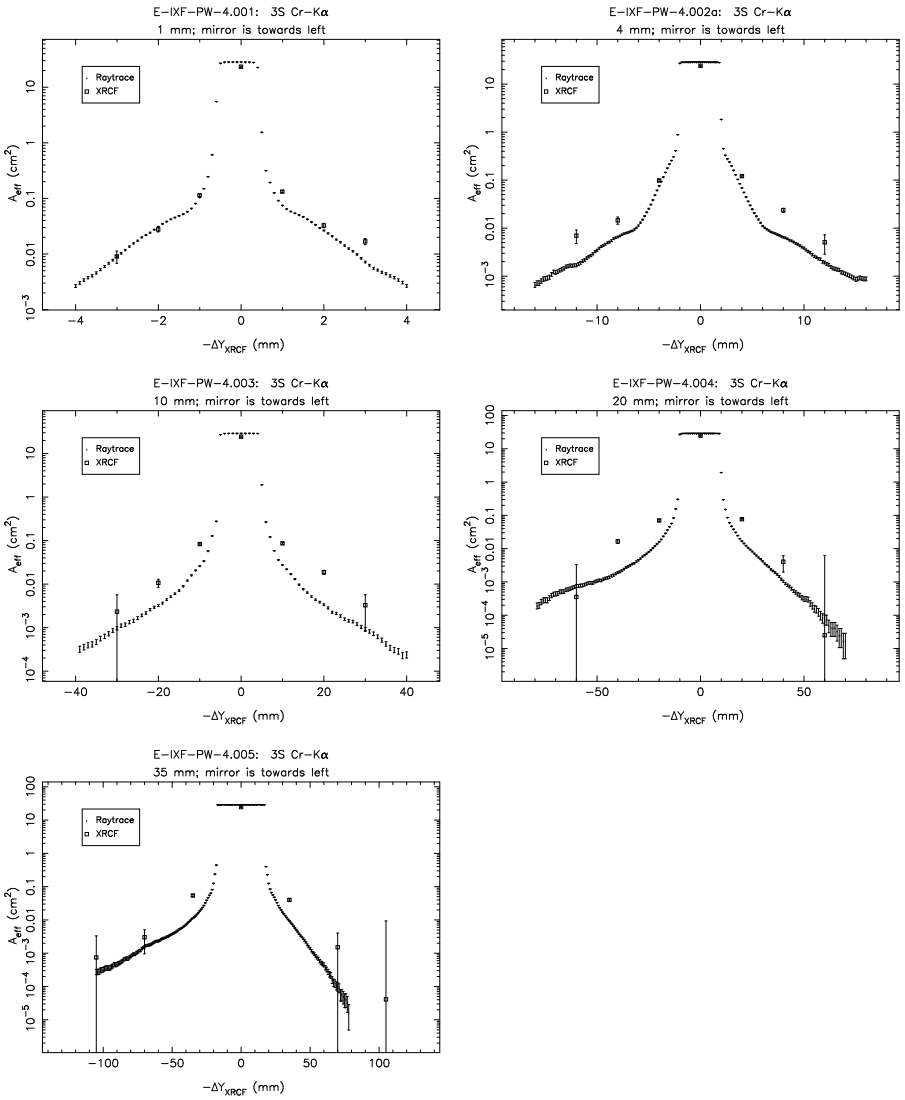

Figure 14.17: Pinhole effective areas; Shell 3S at Cr-Kα.

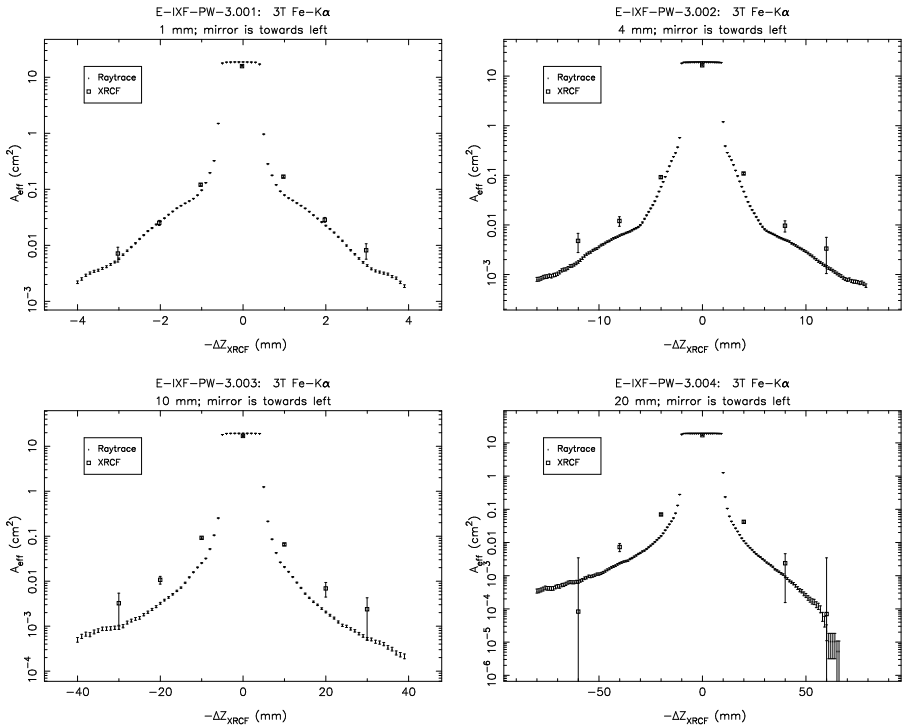

Figure 14.18: Pinhole effective areas; Shell 3T at Fe-Kα.

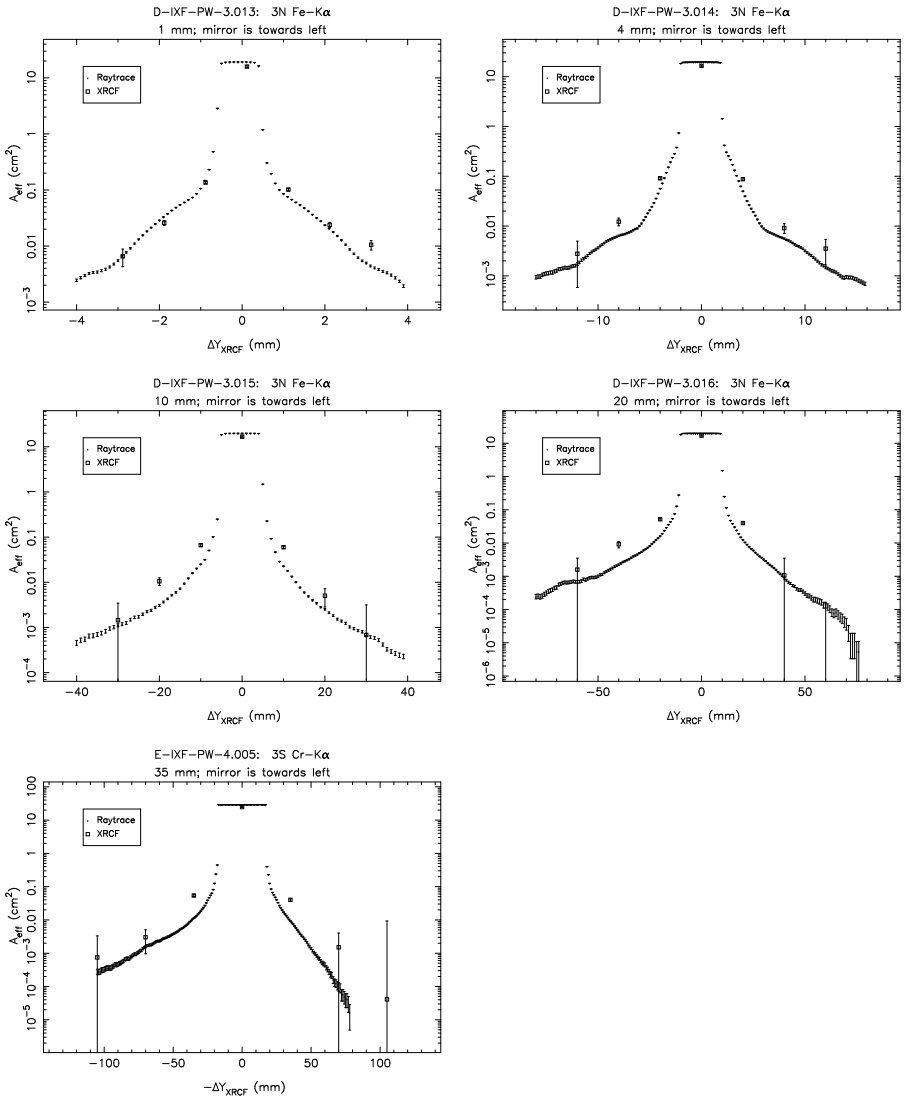

Figure 14.19: Pinhole effective areas; Shell 3N at Fe-Kα.

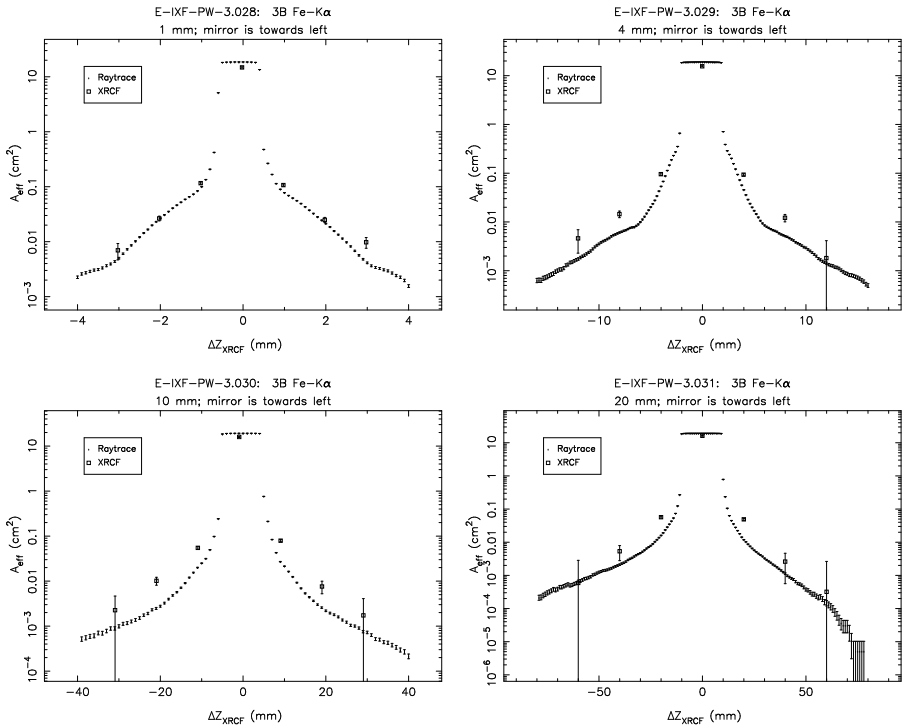

Figure 14.20: Pinhole effective areas; Shell 3B at Fe-Kα.

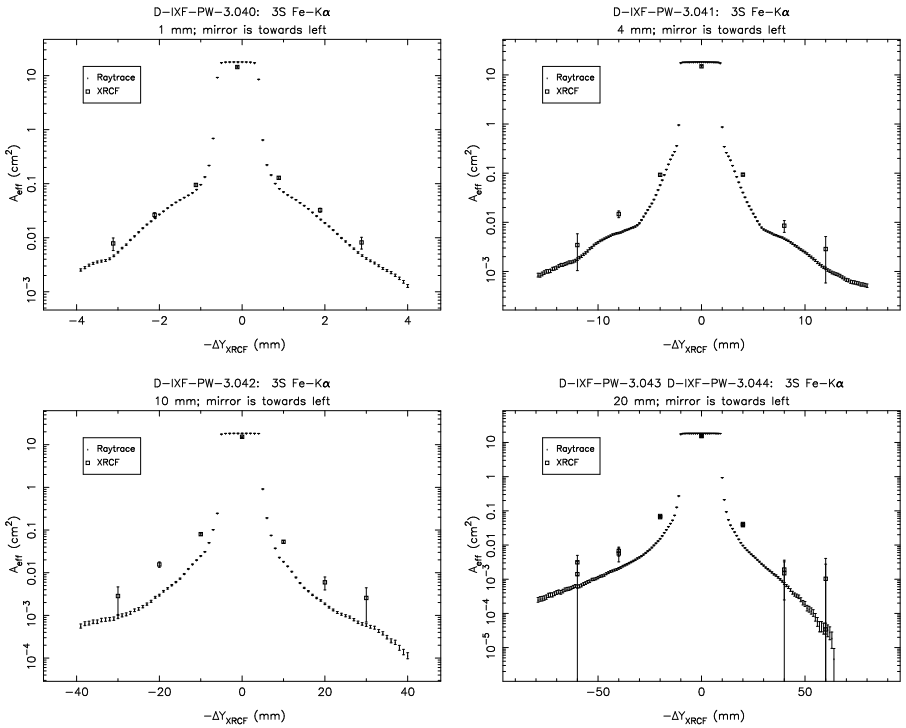

Figure 14.21: Pinhole effective areas; Shell 3S at Fe-Kα.

Shell 4 Single Quadrant Scans

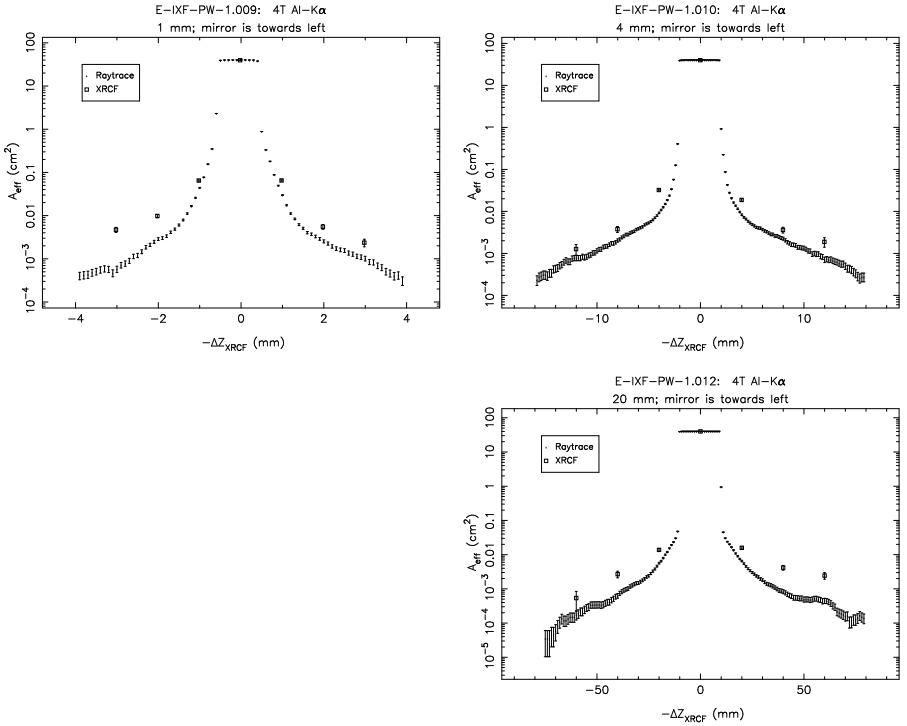

Figure 14.22: Pinhole effective areas; Shell 4T at Al-Kα.

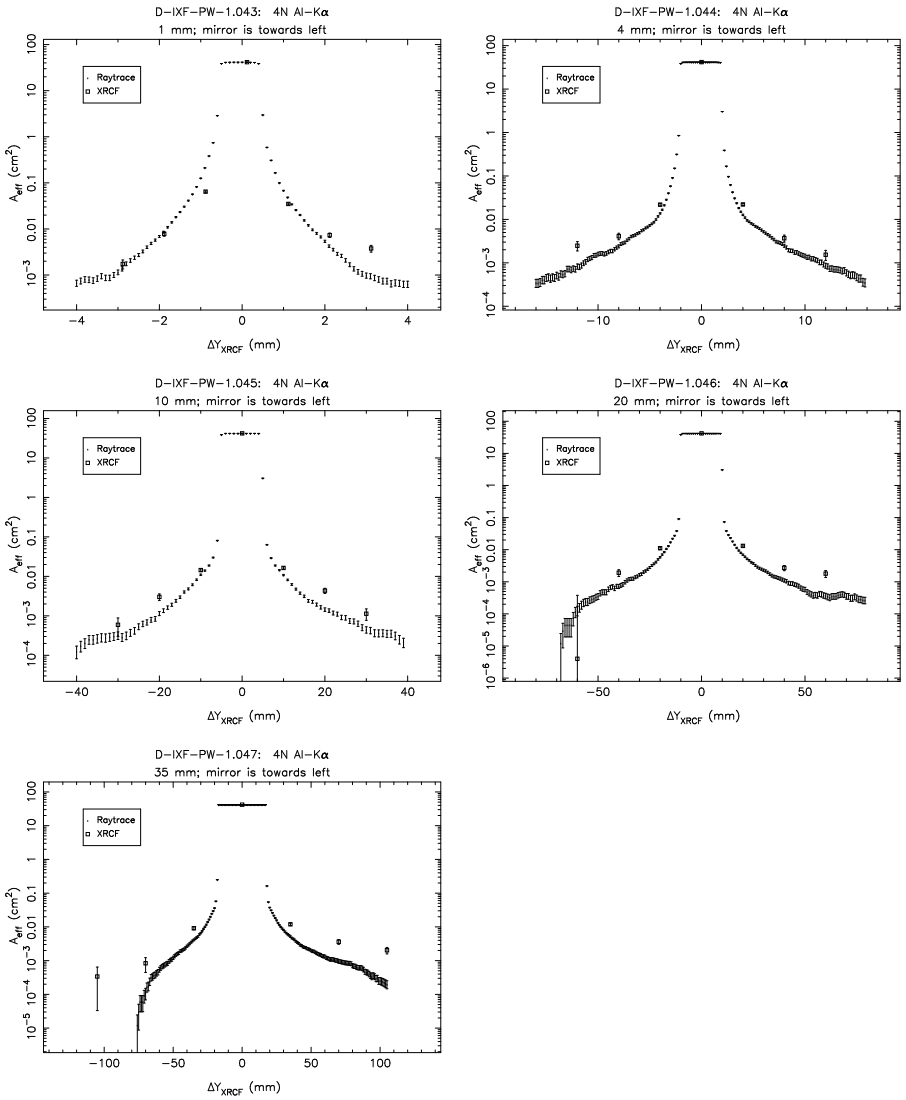

Figure 14.23: Pinhole effective areas; Shell 4N at Al-Kα.

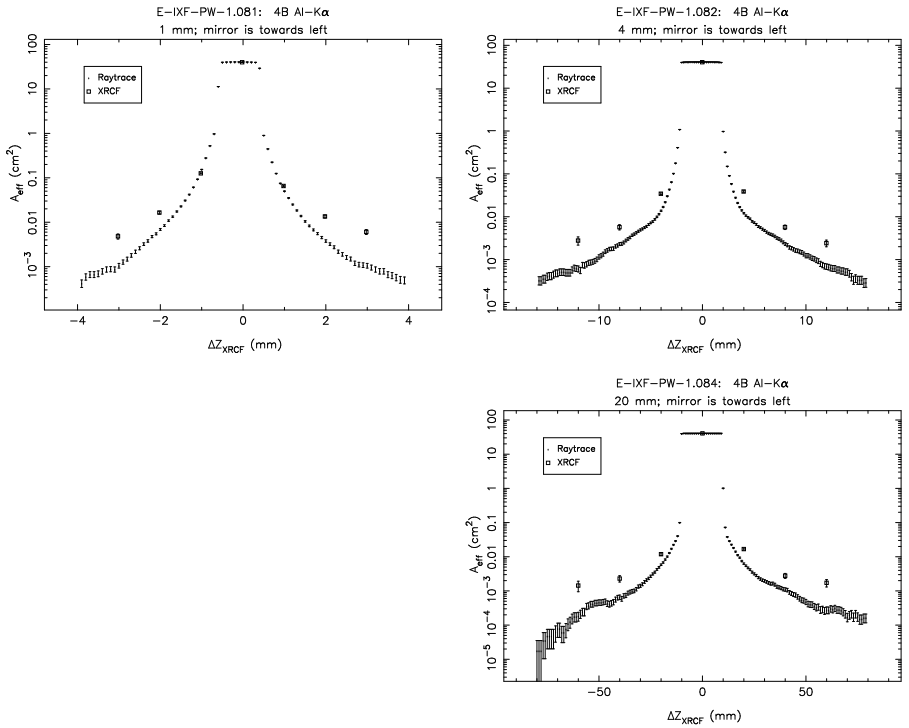

Figure 14.24: Pinhole effective areas; Shell 4B at Al-Kα.

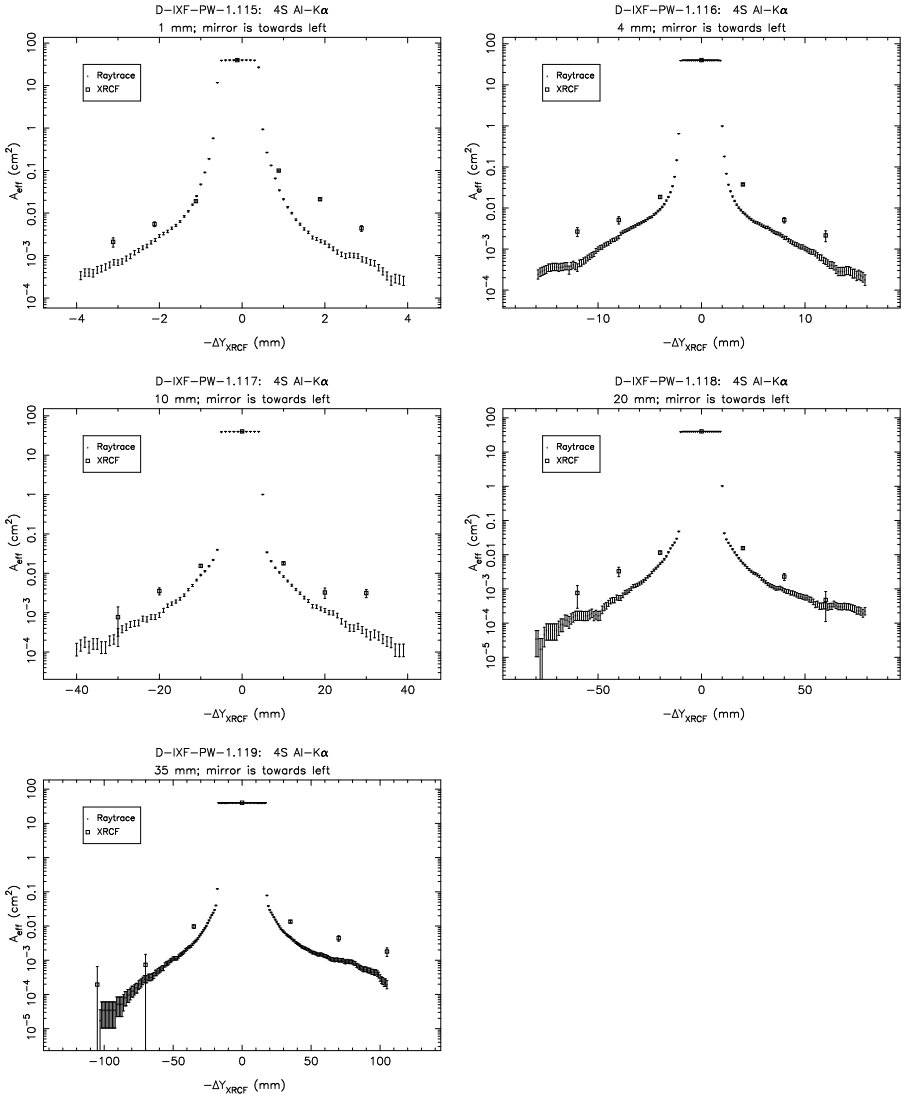

Figure 14.25: Pinhole effective areas; Shell 4S at Al-Kα.

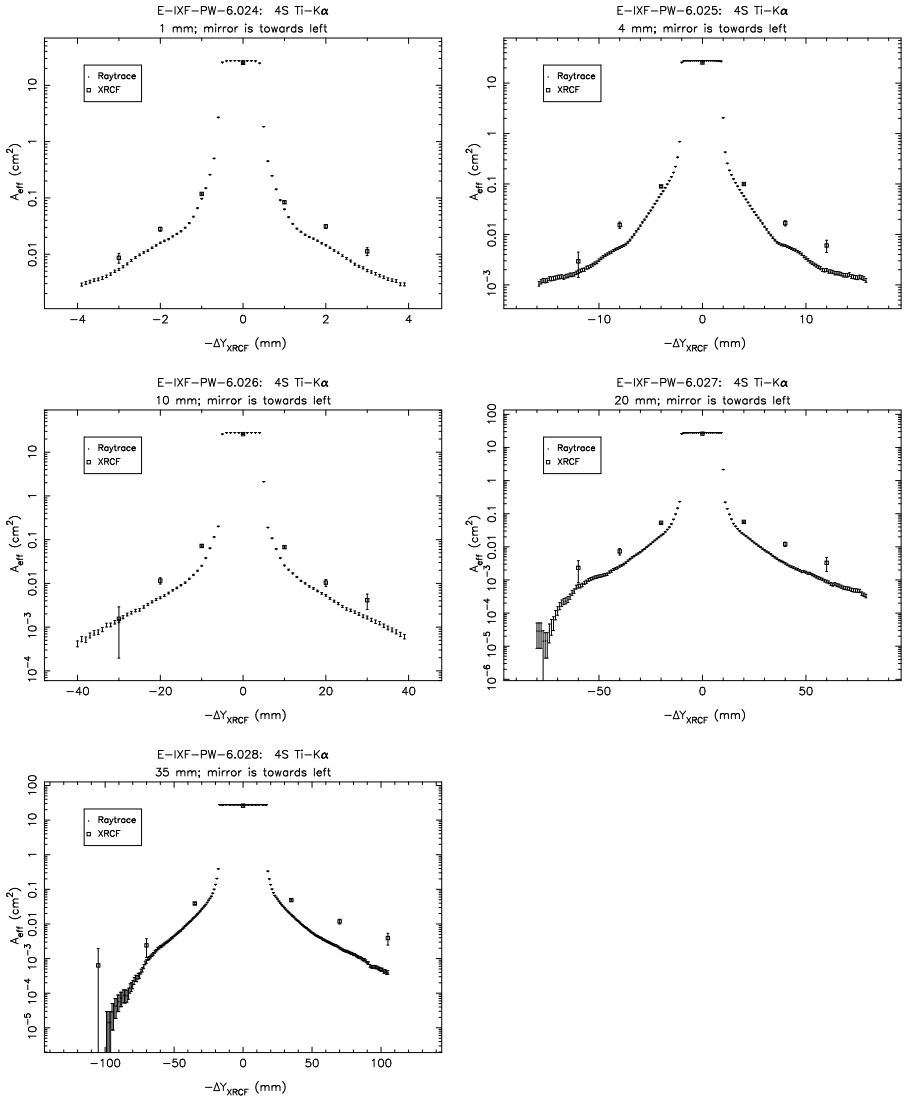

Figure 14.26: Pinhole effective areas; Shell 4S at Ti-Kα.

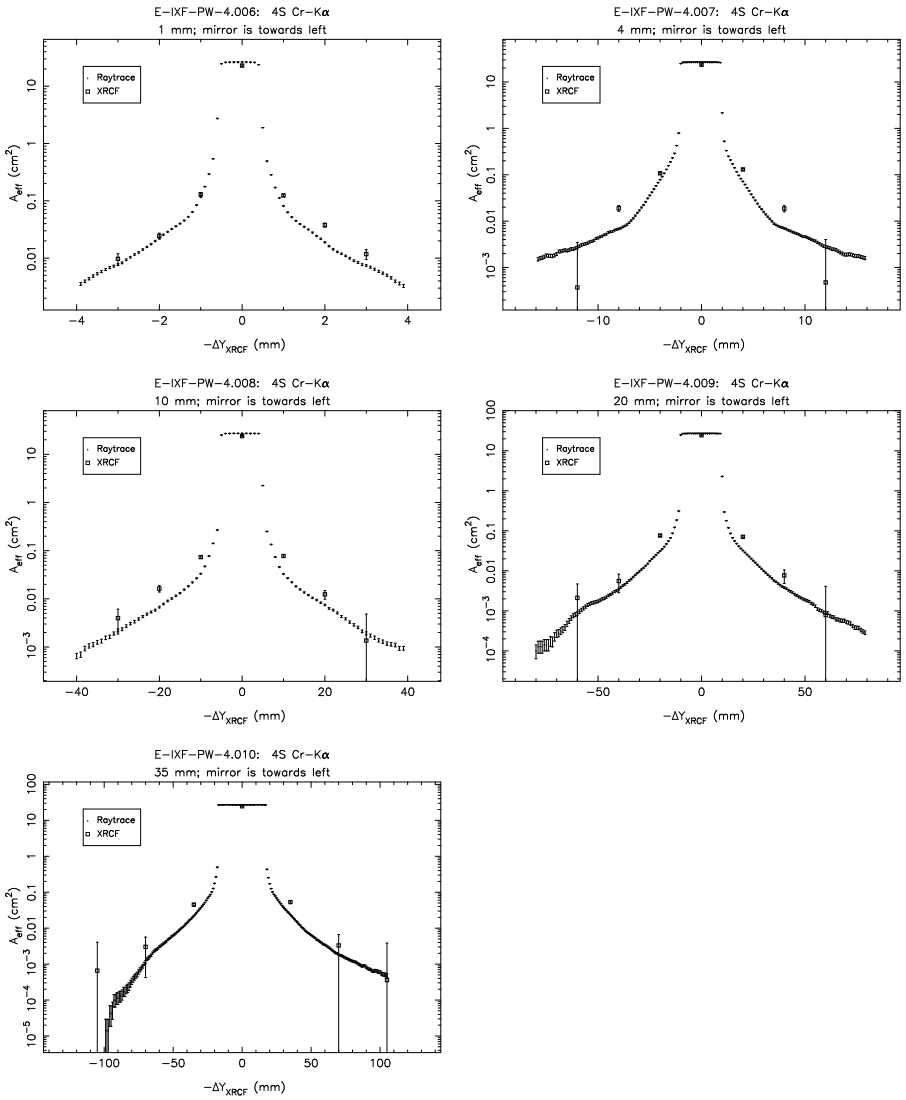

Figure 14.27: Pinhole effective areas; Shell 4S at Cr-Kα.

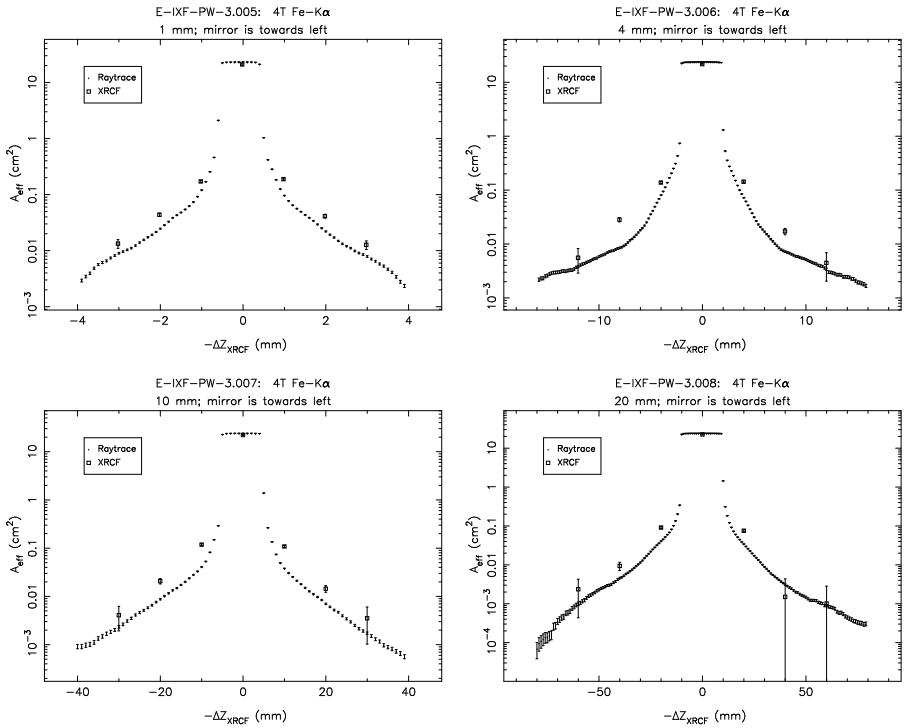

Figure 14.28: Pinhole effective areas; Shell 4T at Fe-Kα.

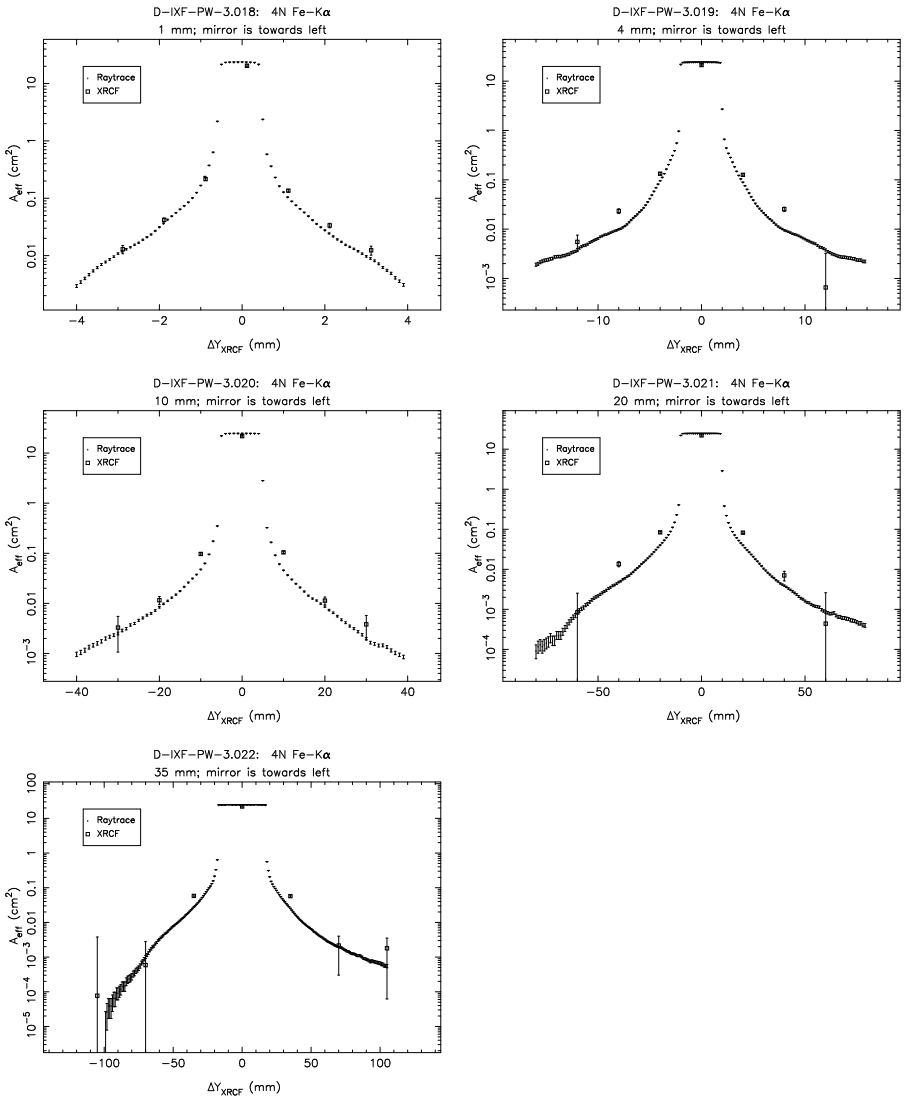

Figure 14.29: Pinhole effective areas; Shell 4N at Fe-Kα.

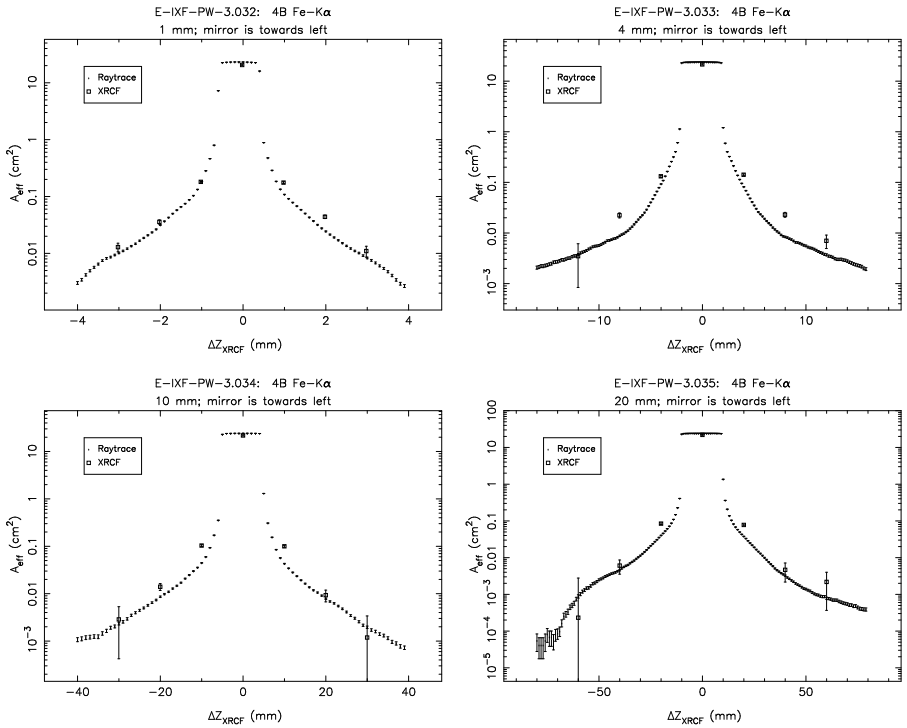

Figure 14.30: Pinhole effective areas; Shell 4B at Fe-Kα.

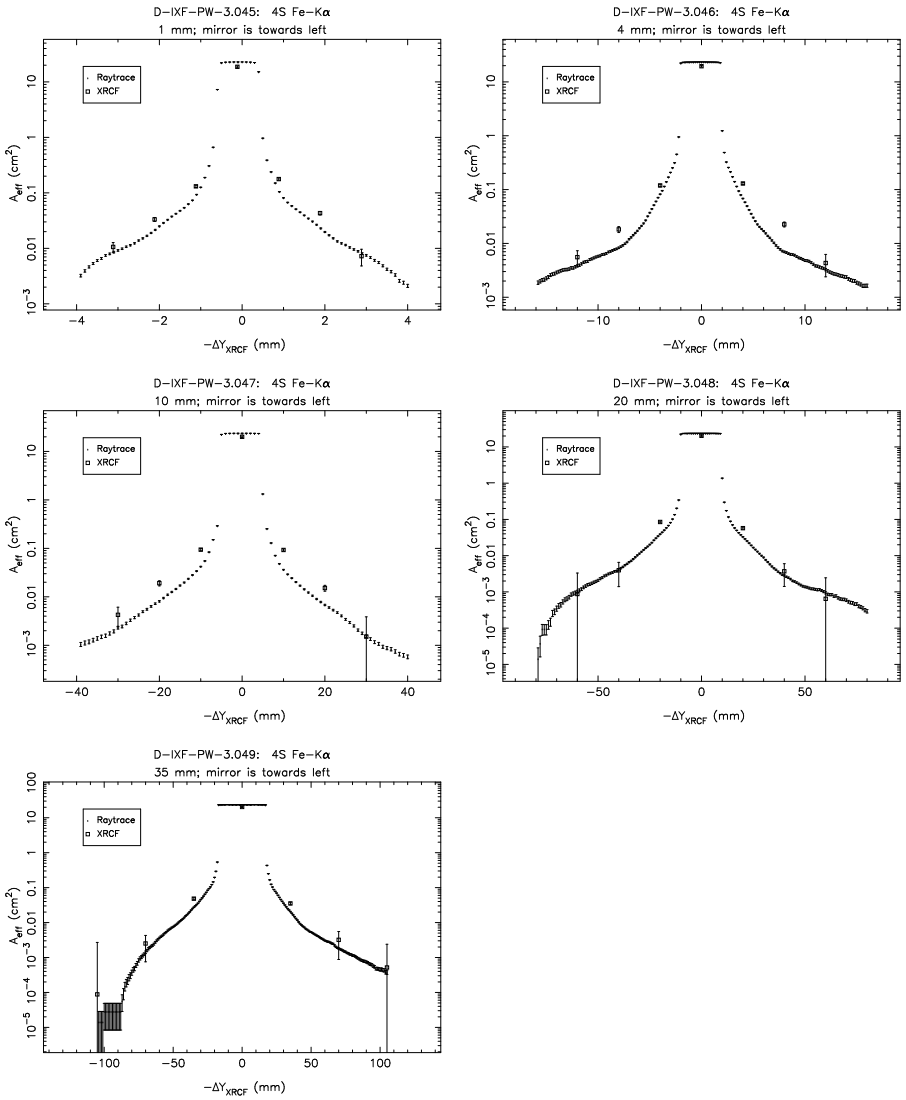

Figure 14.31: Pinhole effective areas; Shell 4S at Fe-Kα.

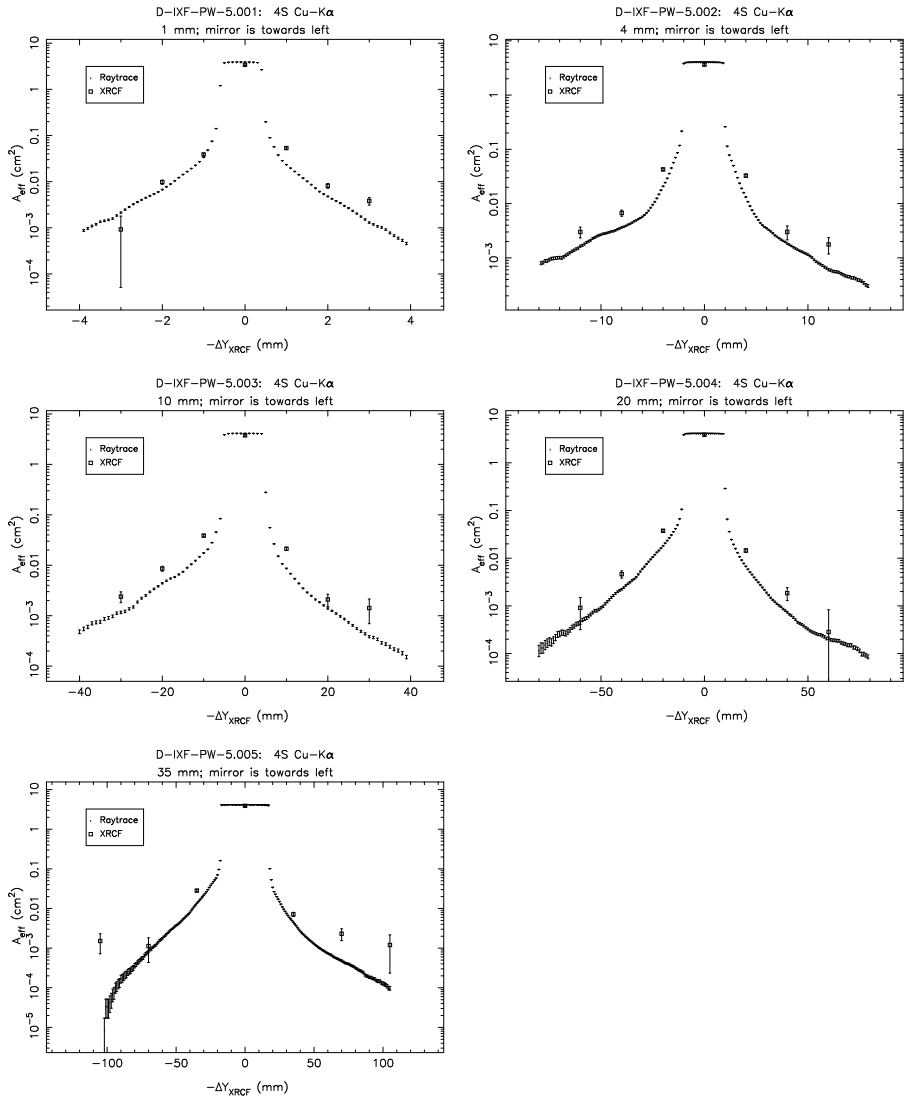

Figure 14.32: Pinhole effective areas; Shell 4S at Cu-Kα.

Shell 6 Single Quadrant Scans

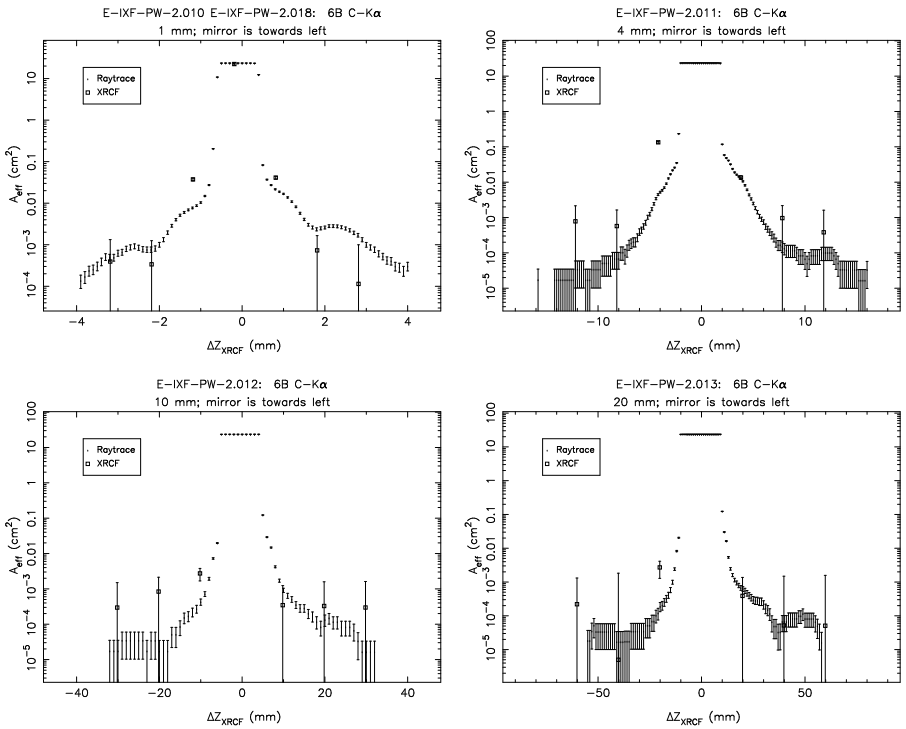

Figure 14.33: Pinhole effective areas; Shell 6B at C-Kα. The 4 mm pinhole effective area at $\Delta Z_{XRCF} = -4$ mm appears to be strongly discrepant; see §14.3.2.

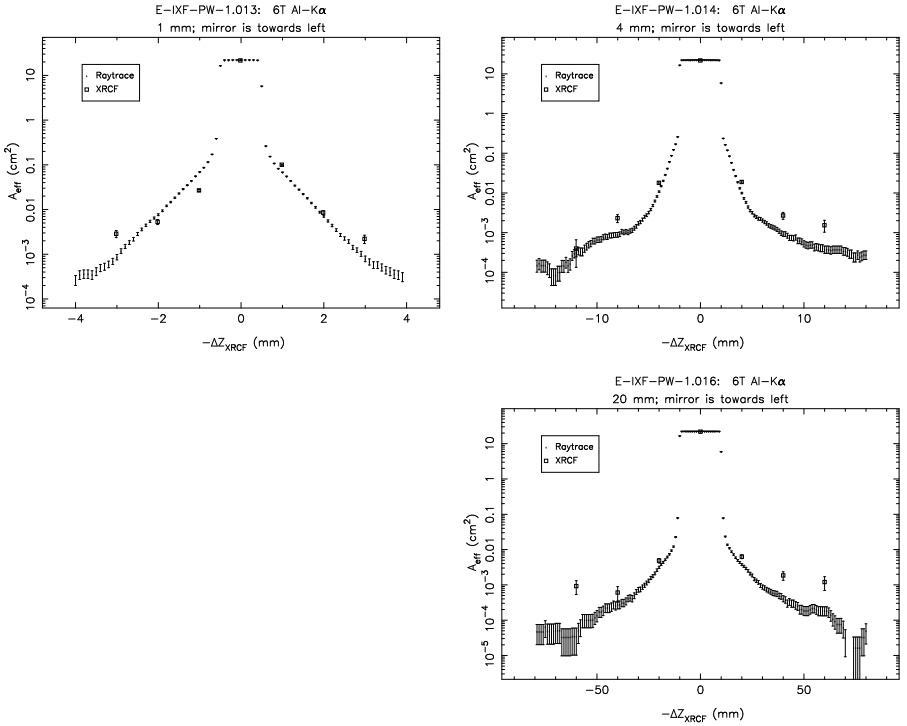

Figure 14.34: Pinhole effective areas; Shell 6T at Al-Kα.

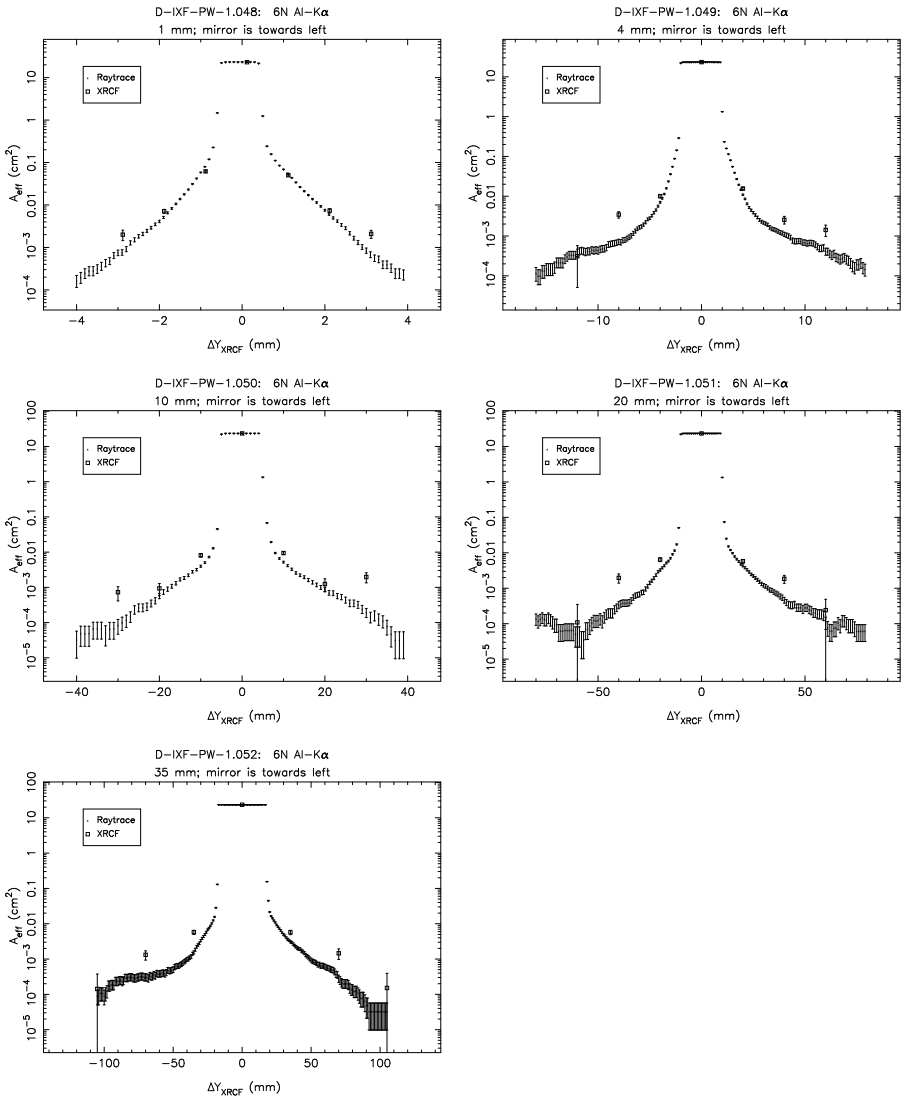

Figure 14.35: Pinhole effective areas; Shell 6N at Al-Kα.

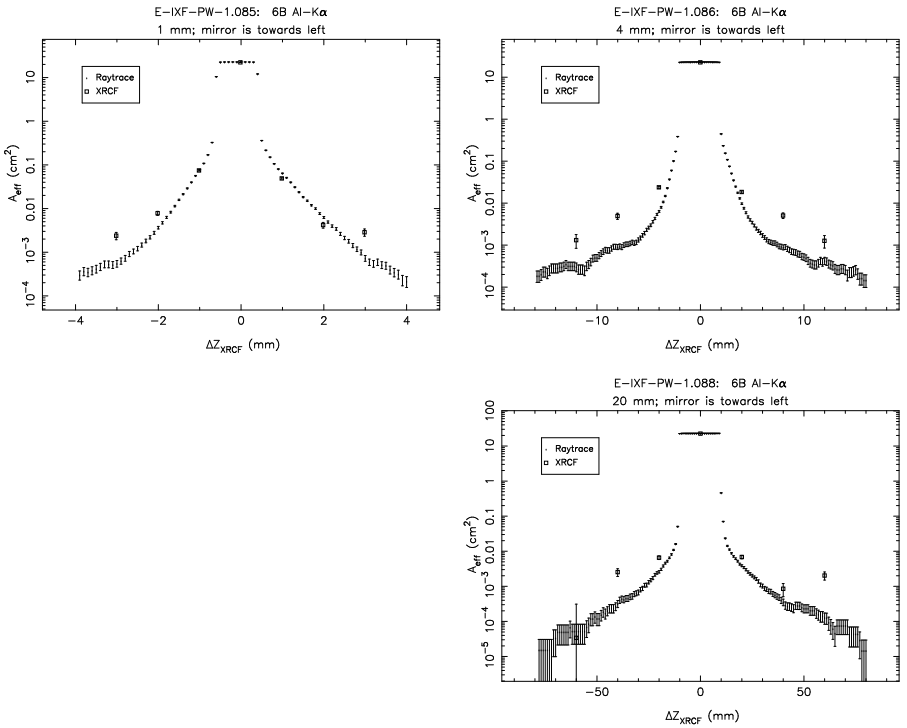

Figure 14.36: Pinhole effective areas; Shell 6B at Al-Kα.

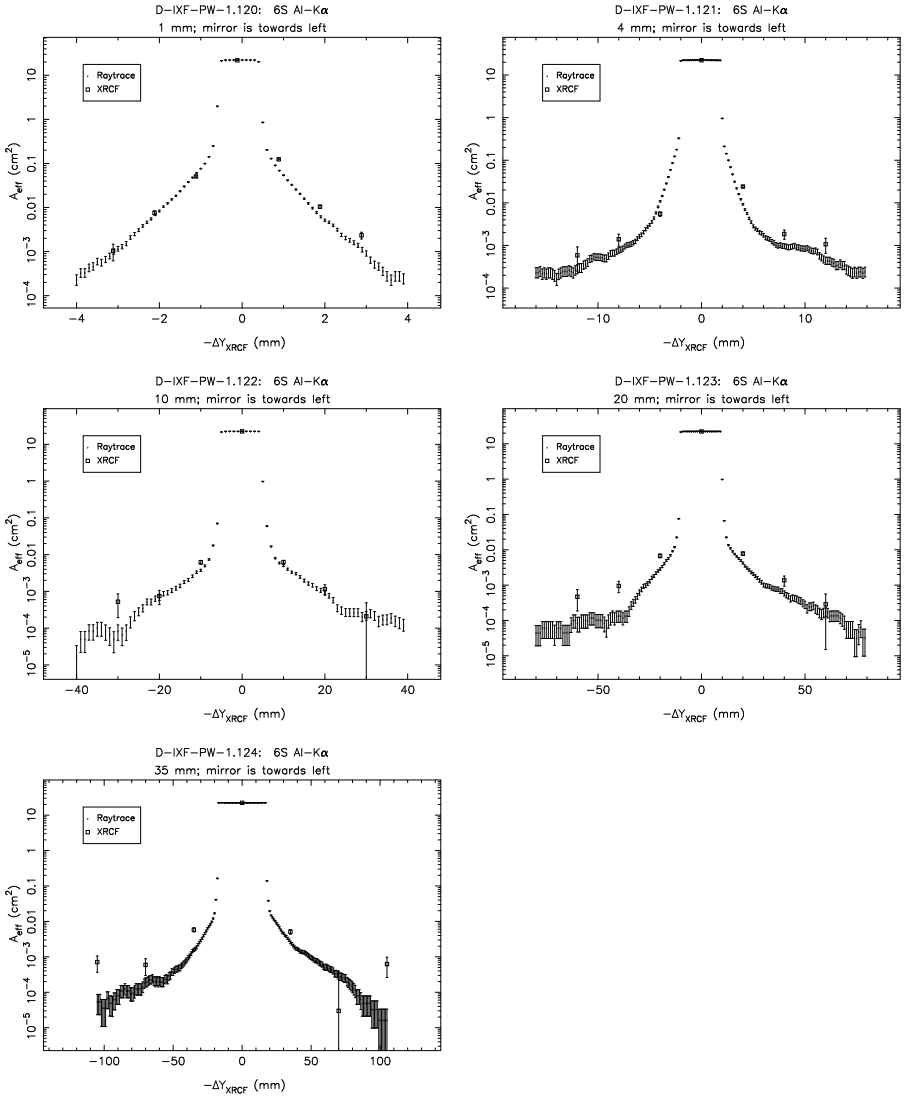

Figure 14.37: Pinhole effective areas; Shell 6S at Al-Kα.

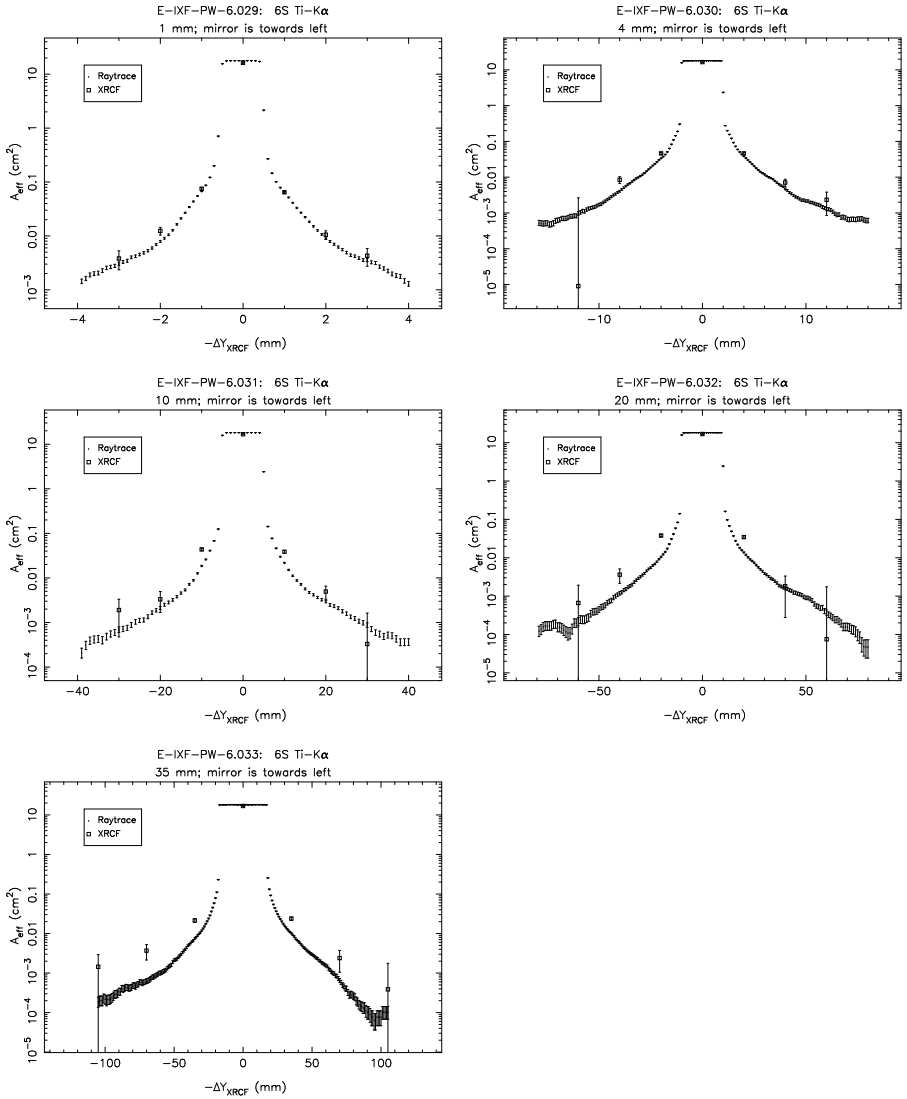

Figure 14.38: Pinhole effective areas; Shell 6S at Ti-Kα.

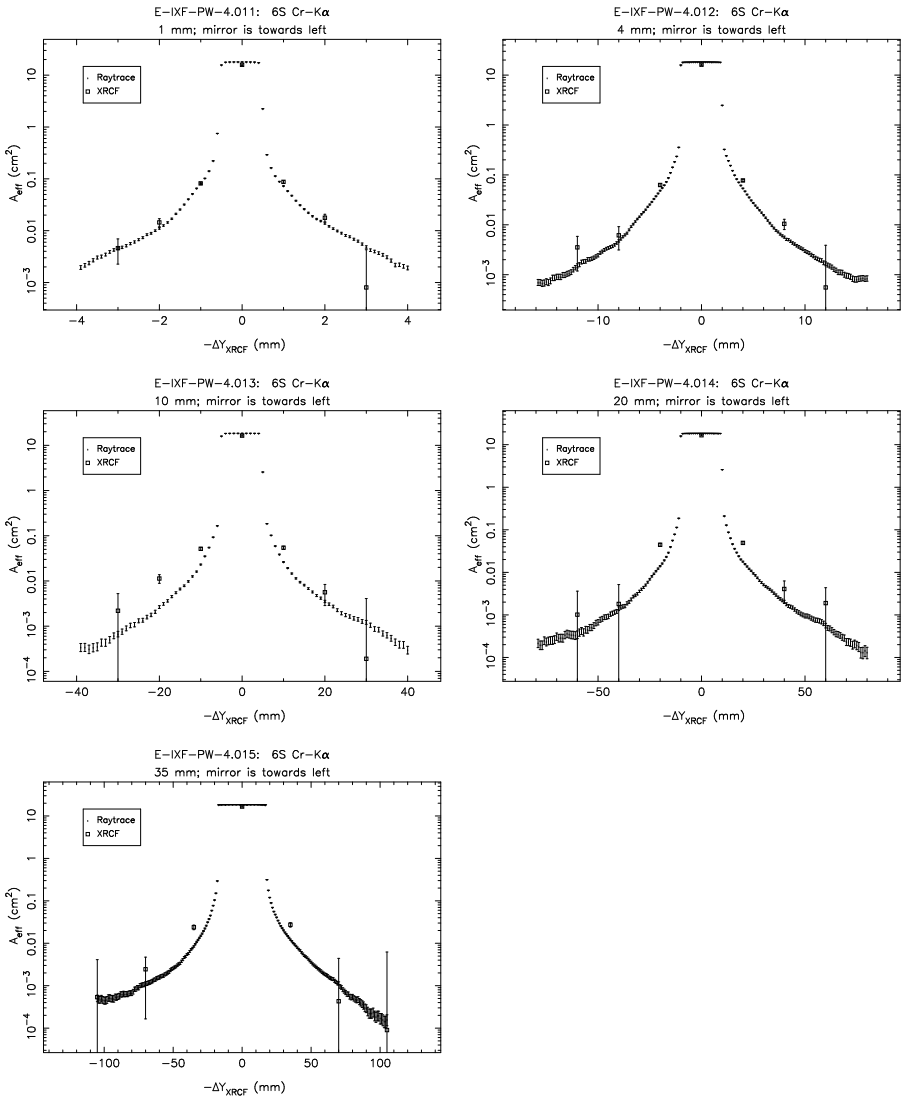

Figure 14.39: Pinhole effective areas; Shell 6S at Cr-Kα.

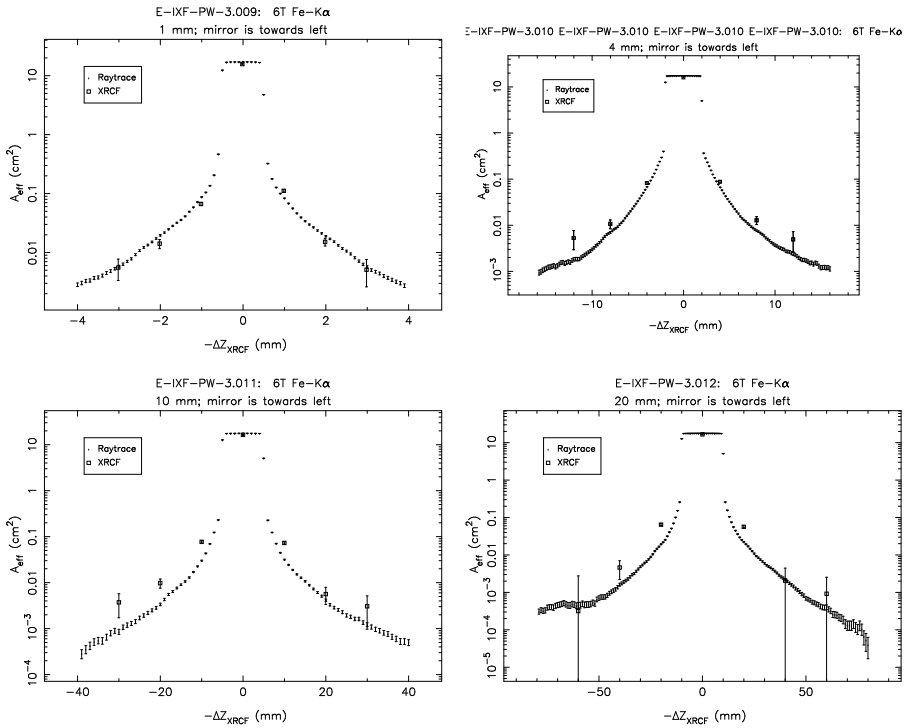

Figure 14.40: Pinhole effective areas; Shell 6T at Fe-Kα.

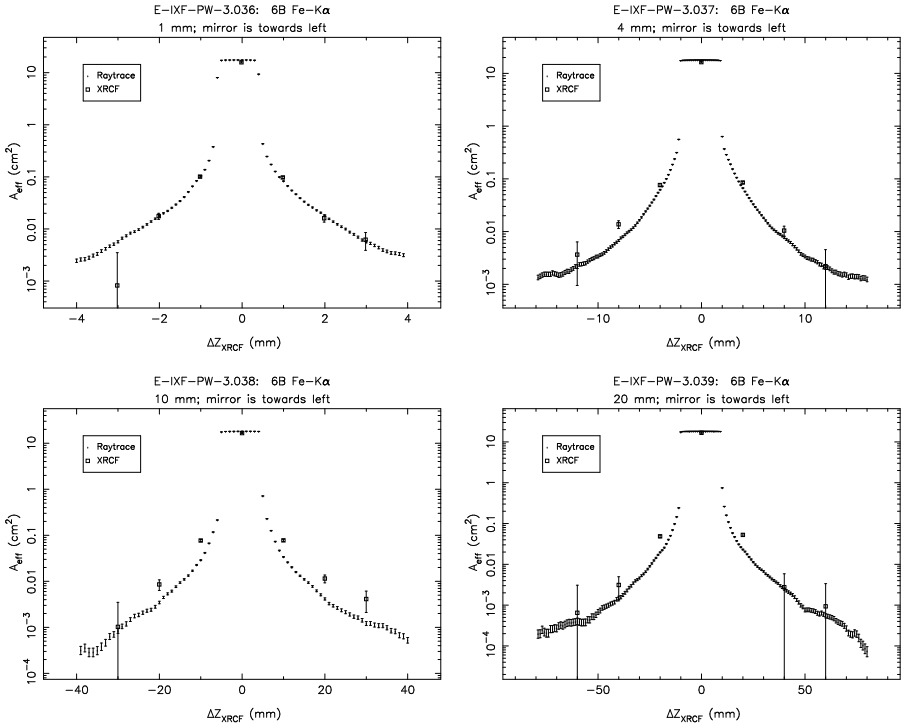

Figure 14.41: Pinhole effective areas; Shell 6B at Fe-Kα.

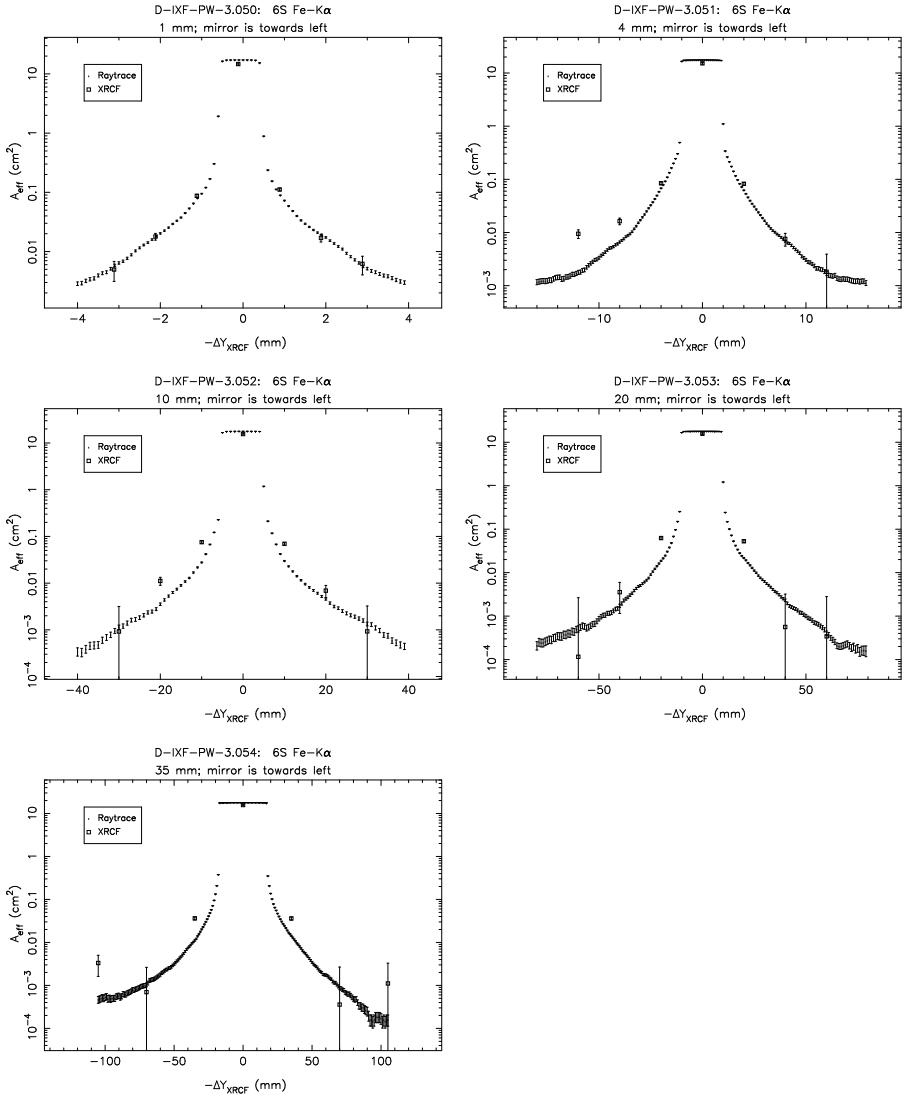

Figure 14.42: Pinhole effective areas; Shell 6S at Fe-Kα.

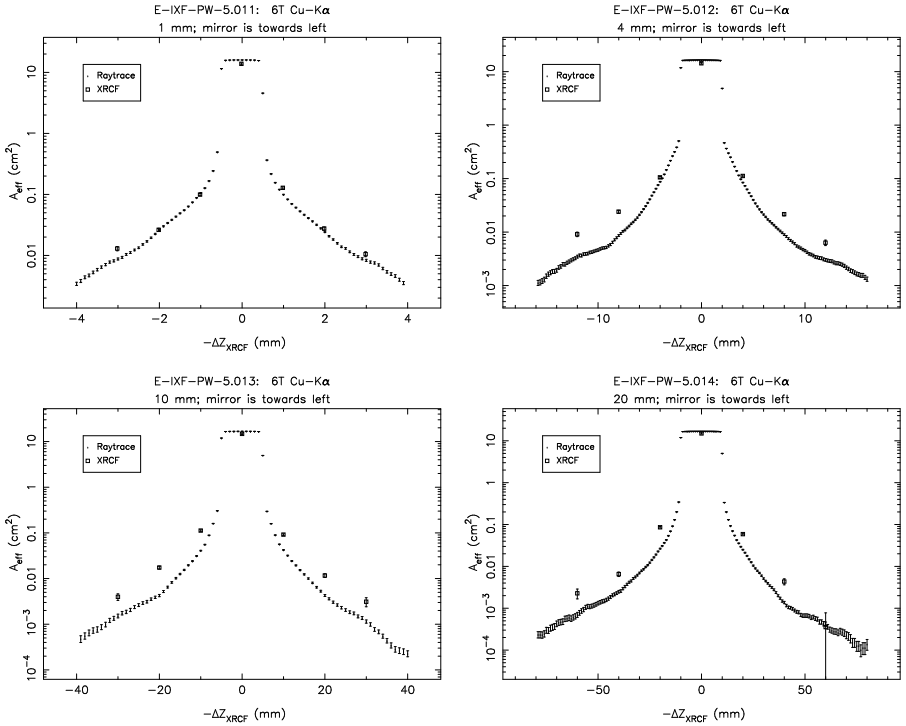

Figure 14.43: Pinhole effective areas; Shell 6T at Cu-Kα.

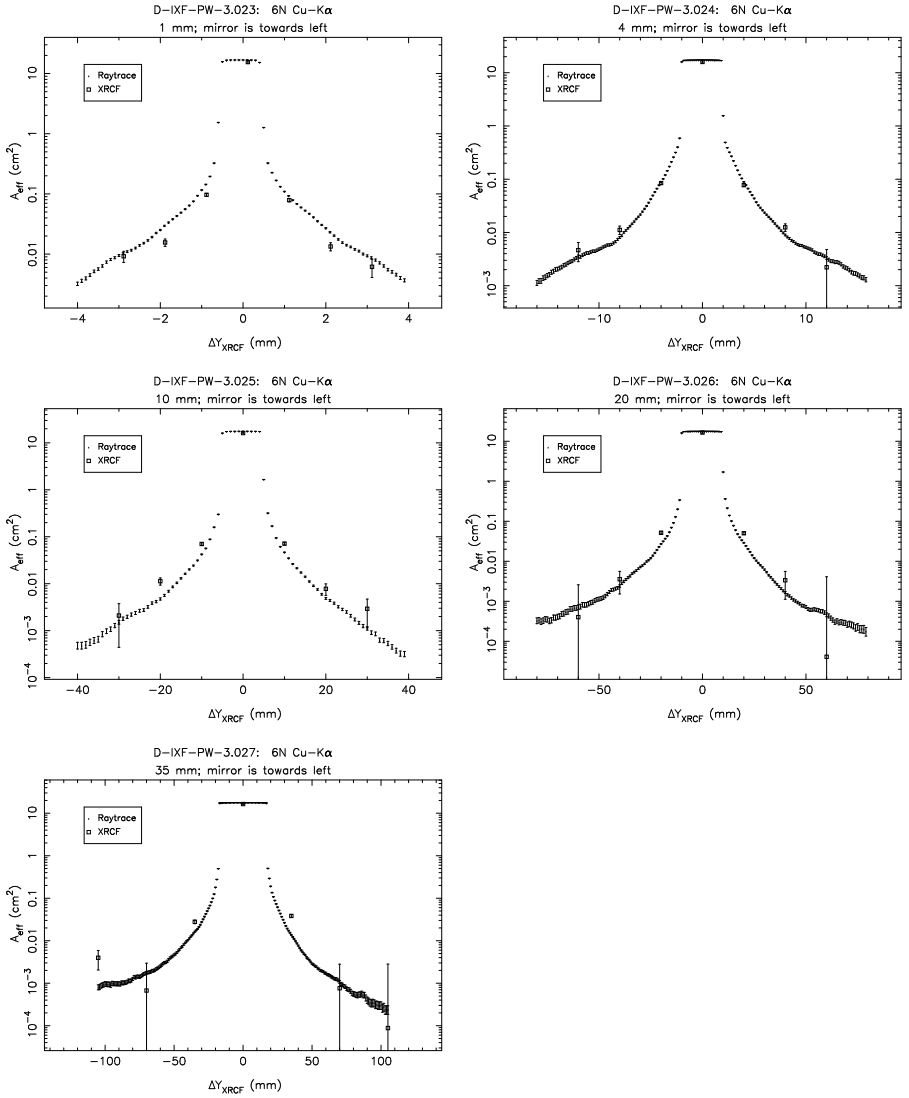

Figure 14.44: Pinhole effective areas; Shell 6N at Cu-Kα.

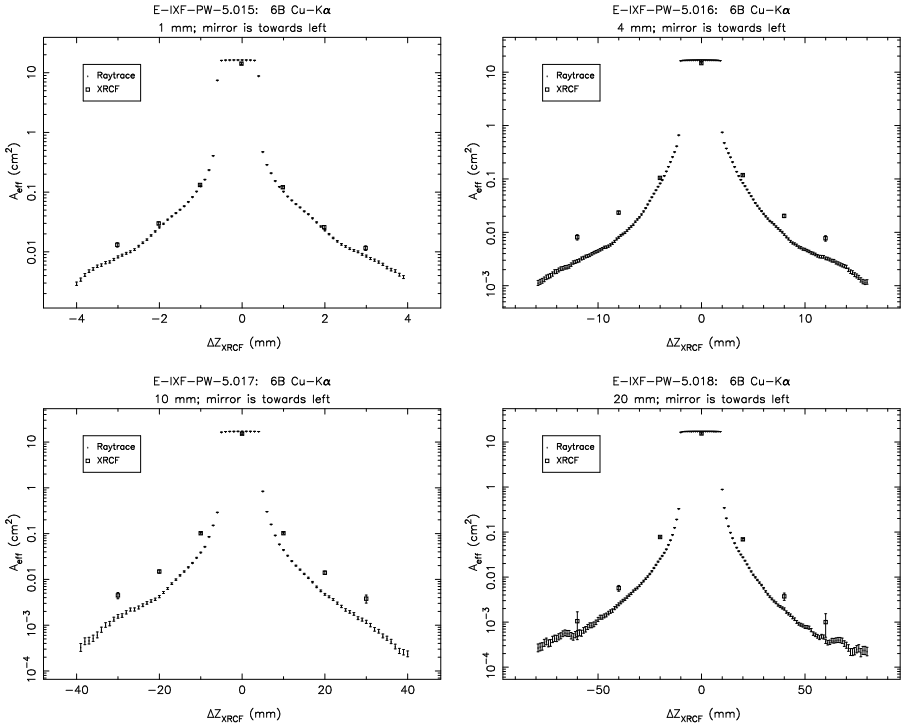

Figure 14.45: Pinhole effective areas; Shell 6B at Cu-Kα.

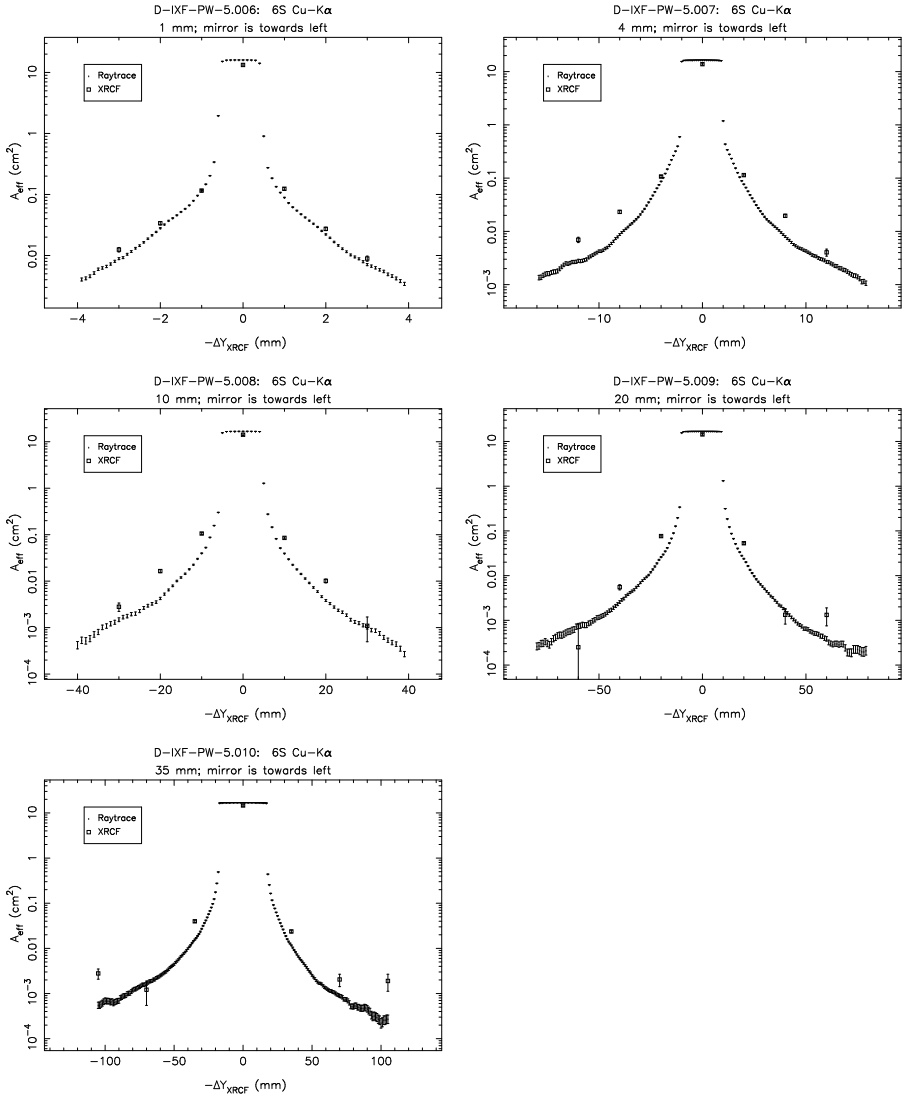

Figure 14.46: Pinhole effective areas; Shell 6S at Cu-Kα.

14.3.2 Transverse (out of plane) Wing Scan Pinhole Data

In this section the transverse pinhole scans at C-Kα are presented. A single set of "out-of-plane" scans was performed for quadrant 6B. These were in the Z direction rather than the Y direction; they may be compared to the normal "in-plane" scans in Figure 14.33.

The Y scans were performed with 1, 4, 10, 20, and 35 mm diameter pinholes. In the course of the 1 mm scans, it was discovered that the scan was approximately 500 μm too low. The reason for this is discussed in §D.7.1.

The FOA table was adjusted between the 1 mm and the 4 mm pinhole scan, so the 4, 10, 20, and 35 mm pinhole scans were at approximately the correct Z value. (It is believed that the data were taken approximately 100 μm too low, but this should not be a significant error; see §D.7.1.)

For the 1 mm pinhole raytrace simulation, the scan was along $Z = -0.6$ mm; the scan misses the core of the pinhole, resulting in a peaked distribution of pinhole effective area with pinhole position, rather than the flat-topped distribution more typically seen in the raytraces. Note also that in the raytraces, the handling of the out-of-plane scattering is simplistic: the out-of-plane scattering distribution is taken to be the in-plane scattering distribution scaled by the sine of the graze angle.

In examining the X-ray data for the 4 mm pinhole, it is notable that the pinhole effective area is definitely nonzero at -4 mm, but basically only an upper limit at $+4$ mm; see also the corresponding 6B C-Kα in-plane scan (Figure 14.33) conducted just after this scan. Again, examination of the raw data indicates that the difference is real and the available information on pinhole positions and tolerances indicate that these are accurate too. Unlike the in-plane case, in which the scattering distribution towards or away from the mirror is not necessarily symmetric about the peak, in this out-of-plane case, the expectation is that the situation should fully symmetric about the peak. The asymmetry in the 4 mm pinhole data is therefore puzzling. In both the in-plane and the out-of-plane cases for the 6B C-Kα scans, the 4 mm pinhole results are inconsistent with the 1 mm pinhole results based on relative pinhole areas. The 4 mm effective area at 4mm off-axis should be at most 16 times the 1 mm effective areas at 2 and 3 mm off-axis. Because we expect the surface brightness to be steeply falling, this should be a strong upper limit. Instead, the 4 mm effective area is a factor of 30 larger than the 1 mm effective areas for the out-of-plane case (Figure 14.47). In the case of the in-plane scan (Figure 14.33) the discrepency is even worse, with the 4 mm effective area more than a hundred times larger than can be accounted for by the 1 mm effective areas (even assuming a flat brightness distribution). Currently we have no explanation for these discrepencies.

Because of problems with shutters sticking, the 4N4S and 6N6S scans were performed with shutter 3B also open (*i.e.*, they were really 4N4S3B and 6N6S3B scans) In order to correct for this, additional 3B Z-scans at Al-Kα were performed for the 1 mm and 4 mm pinholes (see Figure 14.48); these provide an additional (albeit limited) sample of the out-of-plane wings. As noted in §14.3.3, the scan was only in one direction off-axis because of the presumed symmetry of the out-of-plane scattering.

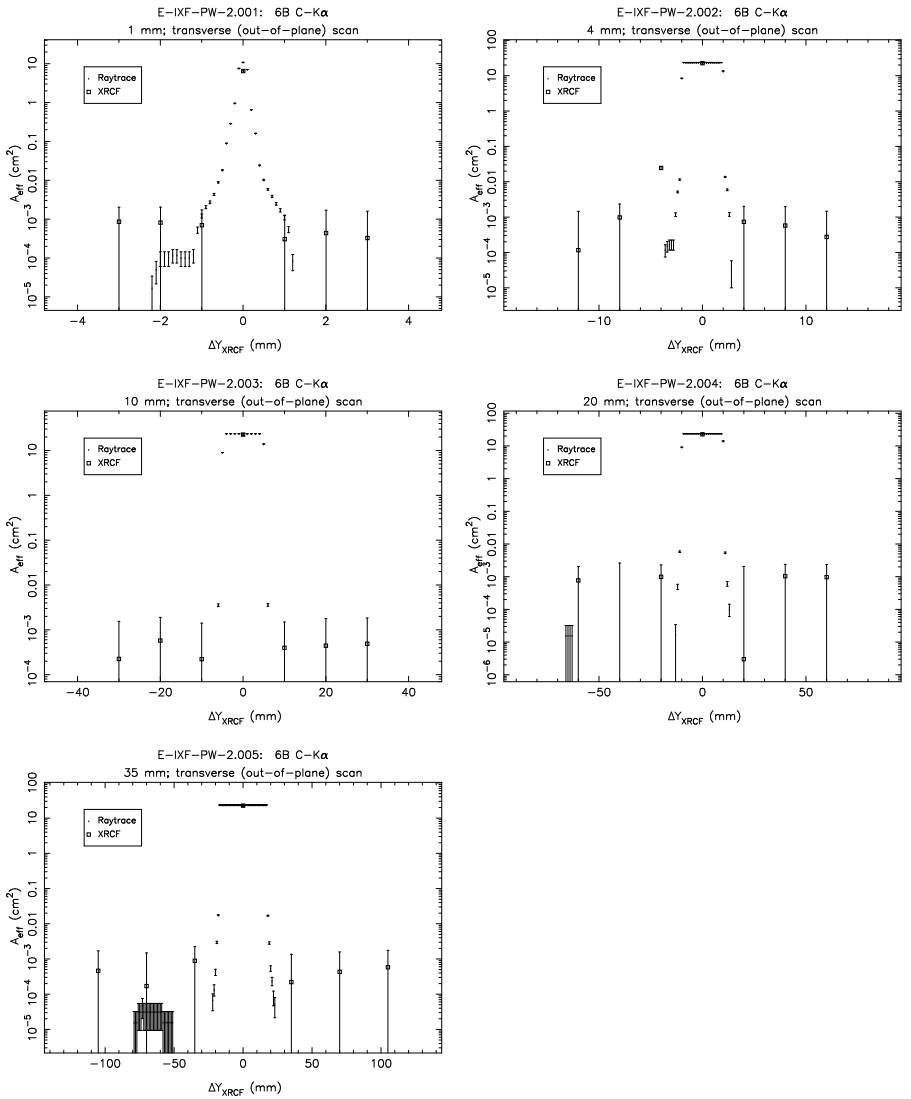

Figure 14.47: Pinhole effective areas; Shell 6B at C-Kα (*transverse scans*).

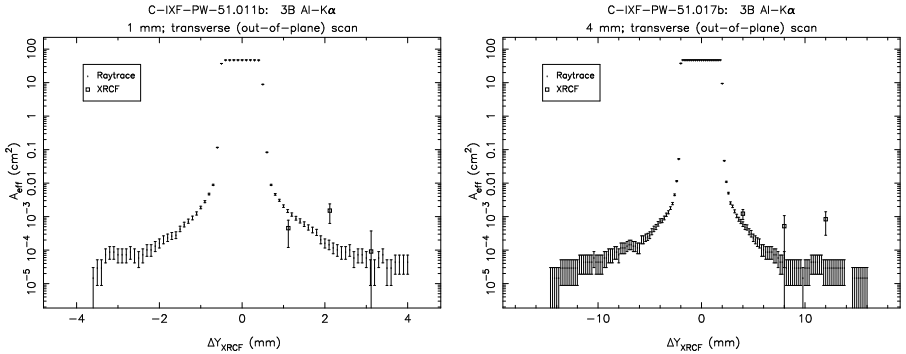

Figure 14.48: Pinhole effective areas. Left: 1 mm pinhole scan, Shell 3B at Al-Kα. Right: 4 mm pinhole scan, Shell 3B at Al-Kα. These 3B Y–scans were performed in order to correct the in-plane 4N4S and 6N6S scans which were made with the 3B shutter stuck open. (*transverse scans*).

14.3.3 Double Quadrant Wing Scan Pinhole Data

In this section the XRCF double quadrant wing scan pinhole effective area measurements are compared to the raytrace simulations of the same configurations. Unlike the single quadrant scans presented in §14.3.1, the HRMA was nominally at zero yaw and pitch. Because the profiles were expected to be symmetric, scans were performed only for points to one side ($+D_{ap}$, $+2D_{ap}$, and $+3D_{ap}$ for a given aperture diameter D_{ap}). Because of problems with shutters sticking, the 4N4S and 6N6S scans were performed with shutter 3B also open (*i.e.*, they were really 4N4S3B and 6N6S3B scans). In order to correct for this, additional 3B Z-scans at Al-Kα were performed for the 1 mm and 4 mm pinholes (see Figure 14.48).

Shell 4 Double Quadrant Scans

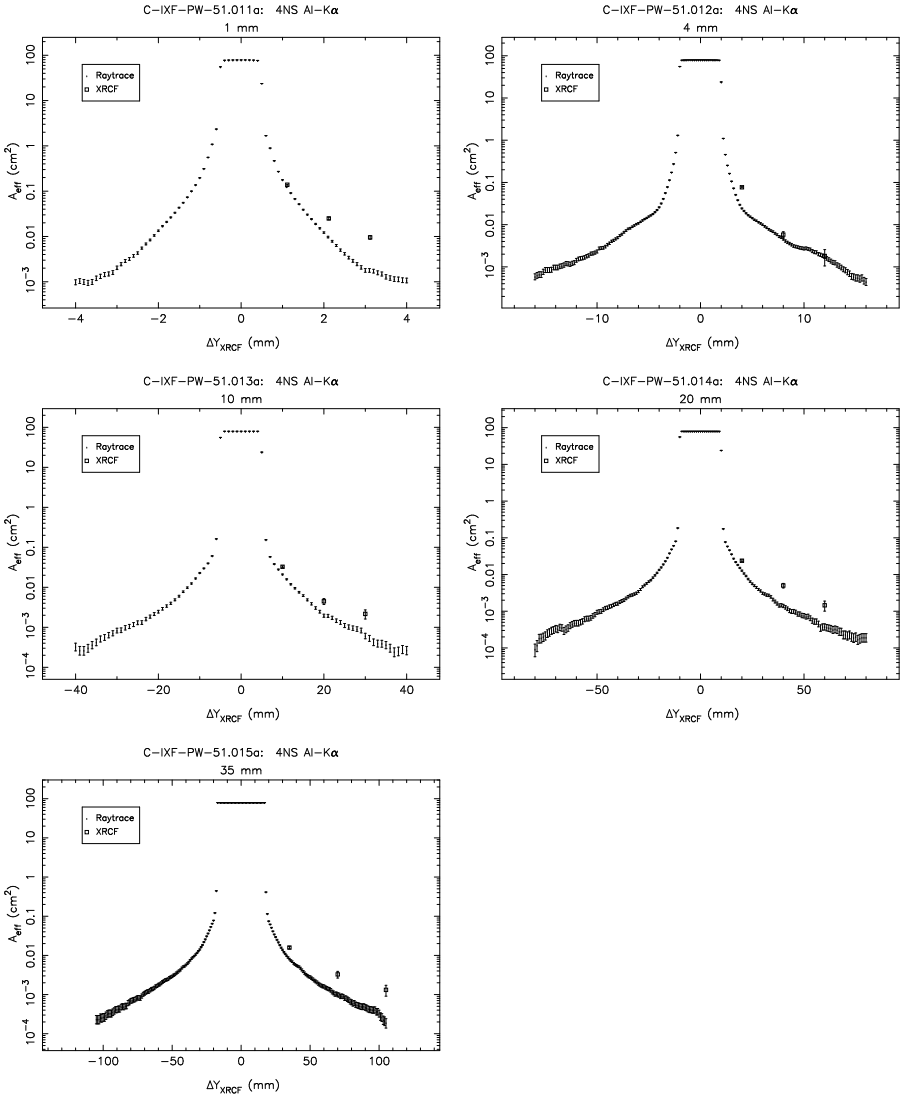

Figure 14.49: Pinhole effective areas; Shell 4NS at Al-Kα.

Shell 6 Double Quadrant Scans

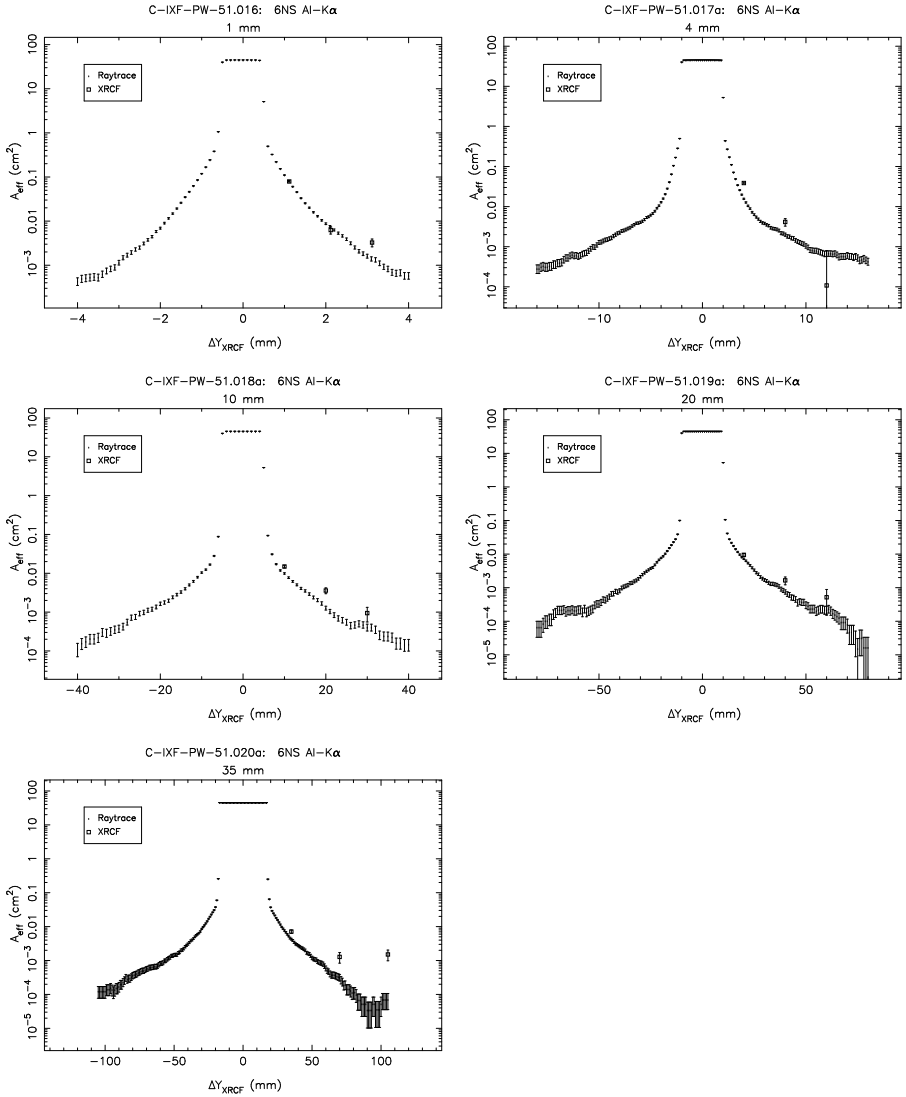

Figure 14.50: Pinhole effective areas; Shell 6NS at Al-Kα.

14.4 Discussion and Outstanding Issues

Other than for the effects of quadrant shutter vignetting, the raytrace data suggest that the pinhole effective area distribution is approximately symmetric. (Note, however, that the raytraces have a built-in symmetry in that the same scattering function is used for scattering both towards and away from the mirror surface; in reality, the distribution in the two directions is expected to be different.) For the most part, the X-ray data also show approximate symmetry. However, in a number of cases, the profiles appear to be markedly asymmetric: see 1S, 3T, 3N, 3B, 3T, 3S, 4S, 6T at Al-Kα. There seem to be no obvious trends. Based on the way the mirrors were manufactured, one would expect the same basic scattering properties for each quadrant, but at Al-Kα, while all four shell 3 quadrants show asymmetries in the 1 mm pinhole data, in shells 1, 4, and 6 only one quadrant shows such a marked asymmetry. Some part of the asymmetry may arise because of misalignment of the pinhole scan to the core of the image, particularly for the innermost points which are on a steeply falling portion of the wings. In a case like the 3T Al-Kα 1 mm pinhole data, this does not appear plausible, though.

A peculiar case is that of the 6B C-Kα in-plane scans (Figure 14.33) and out-of-plane scans (§14.3.2). In both cases, the 4 mm pinhole scans show large asymmetries between the effective areas for pinholes 4 mm to either side of the core. This is particularly puzzling in the case of the out-of-plane scan in which the the symmetry of the experiment leads one to expect a symmetric distribution. In contrast to the 4 mm pinhole data, the 1 mm pinholes do not show strong evidence for the asymmetry. Any pinhole positional errors large enough to reconcile the data (of order 1 or 2 mm) are improbably large compared to the known tolerances on pinhole positioning, and errors of this magnitude (arising, say, from an incorrect value in the FOA table) would have been detected in other experiments using smaller pinholes. Furthermore, the effective area found for the 4 mm pinhole position 4 mm off-axis is *strongly inconsistent* with the 1 mm pinhole measurements at 2 and 3 mm off-axis. Currently we have no explanation for these anomalies in the 6B C-Kα pinhole scan 4 mm pinhole effective areas.

14.5 Raytrace and Data Reduction Versions

The data reductions described in this chapter used the following software versions:

```
FitAll2 script:             1.12 $Date: 1998/06/11 13:55:25 $
calcstage4 script:          1.7 1998/04/16 18:55:00
Wingscan script:            1.6 1998/05/14 18:23:07
```

The raytrace simulations described in this chapter used the following software versions:

```
raytrace script:            trace-shell5
raytrace configuration:     xrcf_SAO1G+HDOS_HDOS-scat-980623_01.cnf
quadrant shutter script:    quad_shutter_05.lua
```

The raytraces used for evaluating the mesh correction (Table 14.4) also include updated optical constants, and a "modified Debye-Waller" treatment of the effects of interface gradients in the multilayer stack. These raytraces used the following software:

```
raytrace script:            trace-xrcf1
raytrace configuration:     xrcf_xss_05.cnf
quadrant shutter script:    quad_shutter_05.lua
mesh module:                D951201
```

Chapter 15

Wing Scans: Analysis

Terrance J. Gaetz

In this chapter we discuss the analysis of the wing scan experiment at XRCF. The experiment was designed to map out the far wings of the Point Spread Function, or PSF, at angles $\gtrsim$1 mm (about 20″ away from the core) by using a series of pinhole scans across the PSF. Because of time constraints, only selected portions of the wings could be mapped in detail; a series of horizontal (Y) or vertical (Z) pinhole scans were sampled using pinhole diameters of 1, 4, 10, 20, and 35 mm. Quadrant shutters were used to isolate quadrants of individual mirror pairs; in order to provide illumination of the surface more nearly resembling on-orbit conditions, the HRMA was also pitched or yawed by the mean graze angle for the shell in question. The experiment, the reduction of the X-ray data, and the raytrace simulations of the pinhole measurements are discussed in more detail in Chapter 14.

The analysis of these data can provide information about two properties of the mirror: First, they allow the measurement of the RMS surface roughness of the mirrors, and a diagnosis of the amount of dust on the optics (if any). Second, by simply looking at the surface brightness as a function of off-axis angle, we can extrapolate the wings of the point spread function to discover how much of the effective area falls outside of the largest pinhole used in the Encircled Energy tests. This allows us to correct the measured effective areas at selected energies for scattering beyond the largest aperture used.

In this chapter we discuss the analysis of X-ray wing scan data and the analysis of raytrace simulations of the wing scan experiment. The knowledge of the PSD based on the mirror metrology measurements is briefly discussed. The pinhole effective areas are combined to form surface brightness profiles for each of the sampled quadrants and energies, and the surface brightness profiles are in turn combined into PSD's in the form of "$2W_1$" profiles. As a consistency check, the surface brightness profile is compared to that obtained by differentiating the effective area function in the one case which permits a relatively low-noise numerical derivative.

15.1 PSD based on HDOS metrology

Prior to X-ray testing at XRCF, knowledge of the microroughness of the HRMA optics depended on measurements of the HRMA mirror metrology performed at the Hughes Danbury Optical Systems, Inc. (HDOS) in Danbury, CT. Measurements were performed for each mirror after final polishing but before the mirror was shipped to OCLI for coating. The instruments used in the metrology were the CIDS (Circularity and Inner Diameter Station), the PMS (Precision Metrology Station), and the MPMI or WYKO (Micro Phase Measuring Interferometer, a slightly modified WYKO Corporation instrument). The CIDS was used to determine circularity and the inner diameters of the HRMA shells. The PMS was used to measure along meridians. With these two instruments, HDOS essentially measured both the 'hoops' and 'staves' of each 'barrel' (optic), and thus mapped the entire surface. Finally, microroughness was sampled on each mirror using the WYKO.

The HDOS mirror metrology was processed by the AXAF Telescope Scientist into a low-frequency mirror map (based on PMS axial scan data and CIDS circularity data) and high frequency errors (based on WYKO measurements). These data were split into two pieces and processed into a mirror map for low-frequency errors (modeled in the raytrace using 2D splines periodic in one direction) and high frequency components (treated in the raytrace statistically as a scattering component).

The mirror map files represent a combination of PMS axial scan data and CIDS circularity data. Each of these files had solid body translations and rotations removed and was divided into two complementary maps by passing the data through a filter; the low pass portions were combined with the modeled distortions induced by the mirror supports (1G and epoxy-induced distortions), fit with 2D spline functions, and used deterministically in the ray-tracing. The high frequency portions were combined with the WYKO data and treated statistically in the raytraces. The standard HDOS filter was used for the separation; the parameters were such that the transition between low and high frequency pass bands occurred from 0.02 to 0.03 mm^{-1}.

The WYKO data at each magnification ($\times$1.5, $\times$10, and $\times$40) were combined into mean PSD files, and these files were processed with the program `foldw1` (which is similar to the HDOS program `eegraz`) to calculate scattering distributions. The calculation was based on the Kirchoff theory of scattering Beckmann and Spizzichino (1963). The PSD files do not agree perfectly in the overlap regions, so a linear weighting was used in the overlap regions such that the weight given to the lower frequency file would decrease from 1.0 to 0.0 while the weight given to the high frequency file would increase from 0.0 to 1.0. The frequency intervals are, in units of mm^{-1}, 0.000 to 0.226, 0.226 to 0.5, 0.5 to 1.5, 1.5 to 2.0, 2.0 to 5.0, 5.0 to 10.0, and 10.0 to 1000.0.

Because the mirror surface roughness is worse near the end of each mirror, the PSDs were calculated for a set of axial zones (ranging from 5 to 11 zones) for each optic, with a center zone covering about 80% of the mirror surface and end zones covering the rest.

15.2 Surface Brightness Profiles

Once the wing scan pinhole effective areas are obtained (see Chapter 14), the next level of processing is to stitch together the pinhole effective areas into surface brightness profiles for a given shell, quadrant, and energy. The pinhole effective area is converted to a surface brightness, ψ, normalized to the effective area within a 35 mm diameter pinhole on-axis and scaled by a factor of $2 \times 88/360$ to account for the fact that the experiment used a single quadrant at a time. The effective area measured within a 35 mm diameter on-axis pinhole will be denoted A_{eff}^{tot}; in the raytrace simulation, A_{eff}^{tot} was evaluated from an on-axis raytrace with a 35 mm diameter pinhole at the appropriate axial location.

The *scaled* on-axis 35 mm effective area is a_{eff}^{tot}, where

$$a_{\mathit{eff}}^{tot} = 2 \times \frac{88}{360} A_{\mathit{eff}}^{tot}. \tag{15.1}$$

The factor 88/360 arises because each "quadrant" is really 88° (because of the overlap of adjacent closed quadrants). The factor of 2 comes about because scattering is predominantly in-plane so

that the scattered flux at a given off-axis location comes primarily from two opposing portions of the mirror; having only one shutter open should provide about half the flux, provided that the pinhole doesn't actually contain the core of the PSF. This factor should be verified by raytrace experiments; however, obtaining sufficiently small errors would require significantly longer raytraces than performed thus far.

The surface brightness is estimated as

$$\psi = w \times \frac{A_{eff}}{a_{eff}^{tot}} \times \frac{4F_{fc}^2}{\pi d^2}, \tag{15.2}$$

where w is a wing correction factor (see below), F_{fc} is the telescope finite conjugate focal length (taken to be 10.252500 m), A_{eff} is the measured effective area through the off-centered aperture of diameter d obtained as part of the wingscan test, and a_{eff}^{tot} the rescaled on-axis 35 mm effective area with all four quadrants exposed (see Eq. Eq. 15.1).

The surface brightness, ψ, should really be normalized to $\int_{2\pi} \psi \, d\Omega = 1$; by normalizing to a 35 mm diameter pinhole we neglect the flux which falls outside the pinhole. This is at most a 4% **(TBR)** effect for the XRCF data (and usually smaller), and an even smaller effect in the case of the current raytrace simulations.

In evaluating the surface brightness, the pinhole effective areas need to be corrected for the fact that the pinhole has a finite diameter and samples the wings of a PSF which is falling steeply with radius. Consequently, the flux can vary strongly with position within the pinhole; in some cases the pinhole diameter is as large as the pinhole off-axis distance, so the effect can be significant. The analysis currently assumes that the brightness falls as a power law across the width of a pinhole, *i.e.*

$$\psi = \psi_0 \theta^{-\gamma}, \tag{15.3}$$

with γ constant across the pinhole. The pinhole correction then becomes the factor

$$w \approx \frac{1}{{}_2F_1\left(\frac{\gamma}{2}, \frac{\gamma}{2}, 2; \frac{a^2}{r^2}\right)} \tag{15.4}$$

where a is the pinhole radius, r is the off-axis distance, and ${}_2F_1$ is a hypergeometric function.

The value of γ was obtained by using the local logarithmic derivative of the fit function (Eq. 15.5) at the location of the pinhole center (see below).

The surface brightness data are fit with functions of the form

$$\psi(R) = aR^{-b}e^{-R/c} \tag{15.5}$$

where R is the distance (in mm) in the $Y - Z$ plane of the pinhole center from the finite conjugate focus; R is related to off-axis angle θ by

$$\theta \approx R/F_{fc}, \tag{15.6}$$

where F_{fc} is the distance from the HRMA node to the finite conjugate focus.

It is necessary to obtain the wing correction iteratively. We begin by assuming $\gamma = 2$, compute surface brightnesses, and fit the surface brightness to an exponentially truncated power law (Eq. Eq. 15.5). In the case of $\gamma = 2$, the hypergeometric function reduces to

$${}_2F_1\left(1, 1, 2; \frac{a^2}{r^2}\right) = -\frac{\ln(1-z)}{z} \tag{15.7}$$

We take the logarithmic derivative of this function to obtain the local power-law index γ at each data point θ, recompute the wing correction using the hypergeometric function, and iterate until

$$\Delta \equiv \sum_{\text{ap pos}} \left(\frac{w_{old} - w_{new}}{w_{old}}\right)^2 \leq 0.01 \tag{15.8}$$

or 5 iterations, whichever is smaller. In the case of the data from raytrace simulations, 5 iterations were always performed. The raytrace data are not fit well by this form; the raytrace surface brightness profiles contain much structure from the underlying assumed surface PSD, so an unconstrained fit can be a poor approximation to the overall data set. In particular, in attempting to reduce large χ^2 contributions from large curvature portions at small radius, the unconstrained fit may introduce a relatively small value for the exponential cutoff scale length so that the fit function cuts off well before the data. It was decided against attempting to fit more realistic functions to the raytrace data; ultimately we need to compare against the fits to the XRCF data, and the sparseness of the XRCF data set would not support a functional form with even more free parameters. In order to reduce the problems with the exponential cutoff scale, the exponential scale length parameter for the raytrace fits was typically limited to a range of values (typically 20 – 10000 mm); the lower limit was a value chosen (by trial and error) to reproduce the overall shape of the curve at large radii. This worked in some cases (*e.g.*, Figure 15.3) but not very well in other cases (*e.g.*, Figure 15.6). For the present we use the same limits for the exponential cutoff, but future analyses should consider applying different limit ranges on a case by case basis. The XRCF data sets were much sparser and this seems to have been less of a problem; see the shell 6 fits, however.

As noted in §14.2.3, vignetting resulting from the adjacent closed quadrant shutters can be significant. Because of this, separate fits were made for scattering towards the optic (*i.e.*, towards larger radii at the focal plane) and away from the optic (towards smaller radii at the focal plane) for each shell, quadrant, and energy. In the case of the raytrace data, the data points subject to vignetting were removed from the plots and the fits; the adopted cutoffs are listed in Table 15.1.

Table 15.1: Wing scan shutter vignetting cutoffs

Shell	Towards optic (mm)	Away from optic (mm)
1	70	500
3	500	30
4	50	500
6	500	500

The XRCF data are compared to the raytrace simulations in the following tables and figures. In the following, §15.2.1 presents the surface brightness data for the shell 1 single quadrant wing scans in the order: quadrant, energy. Similarly, §15.2.2, §15.2.3, and §15.2.4 present the single quadrant wing scan data for shells 3, 4, and 6, respectively. Finally, §15.2.5 presents the surface brightness data for the shell 4 and shell 6 double-quadrant wing scans. Tables 15.2 to 15.8 present the parameters for the fits to the XRCF data points and to the raytrace data. The fits are also used to evaluate the fractional excess effective area falling outside the largest (35 mm diameter pinhole); this is at most ∼4% (**TBR**) in the case of the XRCF data and at most ∼2% (**TBR**) for the raytrace simulations. Note that in most cases the fractional excess effective area is considerably smaller than the worst case.

The agreement between the XRCF data and the raytrace simulations seems to be reasonably good for the smallest pinholes. The data for the 1S scan at Al-Kα seem to show considerably more

scattering in the direction away from the optic than towards the optic. This is also particularly noticeable in all four quadrants for the the Al-Kα scans shell 3, and for quadrant 4S. This effect seems to be less prominent in the other quadrant/shell/energy combinations. The reason for – and significance of – this effect is not well understood at present.

15.2.1 Shell 1 scans

Table 15.2: Surface brightness fits and fractional excess effective area beyond the 35 mm pinhole. (Raytrace simulations and XRCF data, Shell 1)

Type	Quad	Line	Dir	a	b	c	fractional extra area
sim	1T	Al	in	177526.000	2.447	145.081	0.001618
sim	1T	Al	out	100141.600	2.039	32.969	0.001009
sim	1N	Al	in	188074.000	2.414	100.808	0.001539
sim	1N	Al	out	140240.000	2.145	36.331	0.001089
sim	1B	Al	in	229218.000	2.540	354.215	0.002089
sim	1B	Al	out	142126.000	2.074	33.888	0.001309
sim	1S	Al	in	239490.000	2.442	68.289	0.001245
sim	1S	Al	out	135748.000	2.063	32.608	0.001222
sim	1T	Ti	in	638360.000	2.083	22.409	0.002511
sim	1T	Ti	out	491692.000	1.982	20.000	0.002182
sim	1N	Ti	in	651161.000	2.069	22.748	0.002793
sim	1N	Ti	out	544555.000	1.992	20.000	0.002326
sim	1B	Ti	in	715540.000	2.108	23.324	0.002788
sim	1B	Ti	out	514720.000	1.923	20.000	0.002870
sim	1S	Ti	in	709070.000	2.053	20.000	0.002390
sim	1S	Ti	out	495692.000	1.923	20.000	0.002761
xrcf	1T	Al	in	174886.000	2.202	374.817	0.007554
xrcf	1T	Al	out	161181.000	2.061	188.814	0.009362
xrcf	1N	Al	in	146541.000	1.933	48.627	0.004132
xrcf	1N	Al	out	151190.000	1.965	88.460	0.007418
xrcf	1B	Al	in	135389.000	2.271	10000.000	0.008287
xrcf	1B	Al	out	123336.000	1.947	76.618	0.005657
xrcf	1S	Al	in	90294.800	1.837	47.734	0.003680
xrcf	1S	Al	out	209820.000	2.214	10000.000	0.017700
xrcf	1T	Ti	in	588435.000	1.640	32.729	0.028977
xrcf	1T	Ti	out	650222.000	1.713	29.945	0.020186
xrcf	1N	Ti	in	654973.000	1.624	26.366	0.022367
xrcf	1N	Ti	out	741870.000	1.851	39.998	0.021932
xrcf	1B	Ti	in	564424.000	1.803	63.980	0.038846
xrcf	1B	Ti	out	477645.000	1.605	27.270	0.018891
xrcf	1S	Ti	in	518891.000	1.634	30.179	0.022434
xrcf	1S	Ti	out	686177.000	1.759	32.517	0.020691

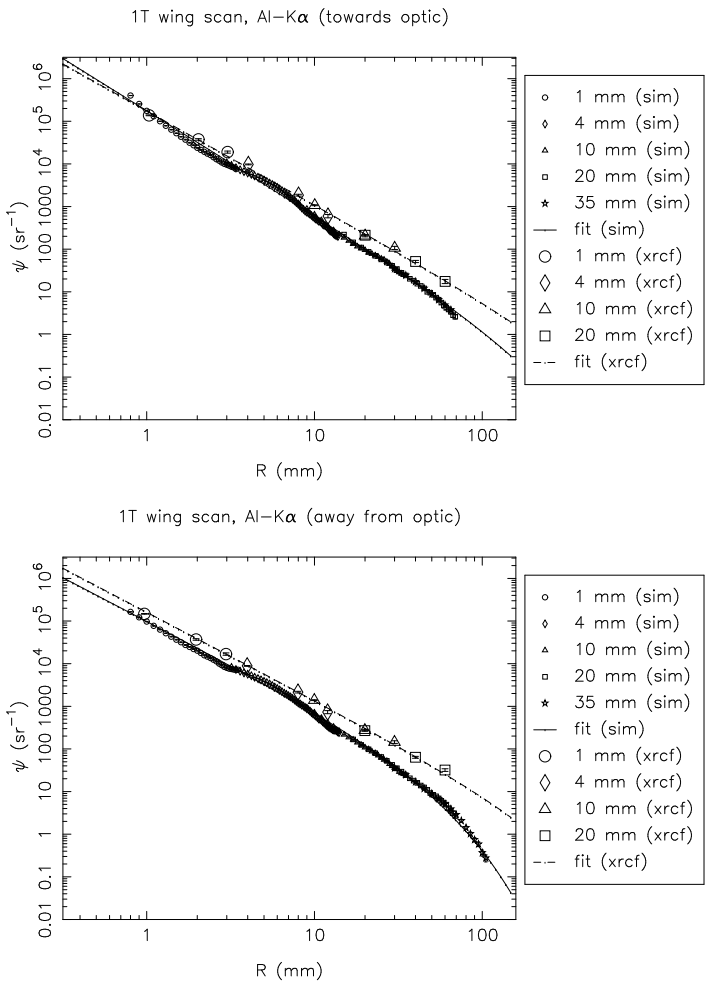

Figure 15.1: Shell 1T: Al-Kα surface brightness, towards and away from the optic

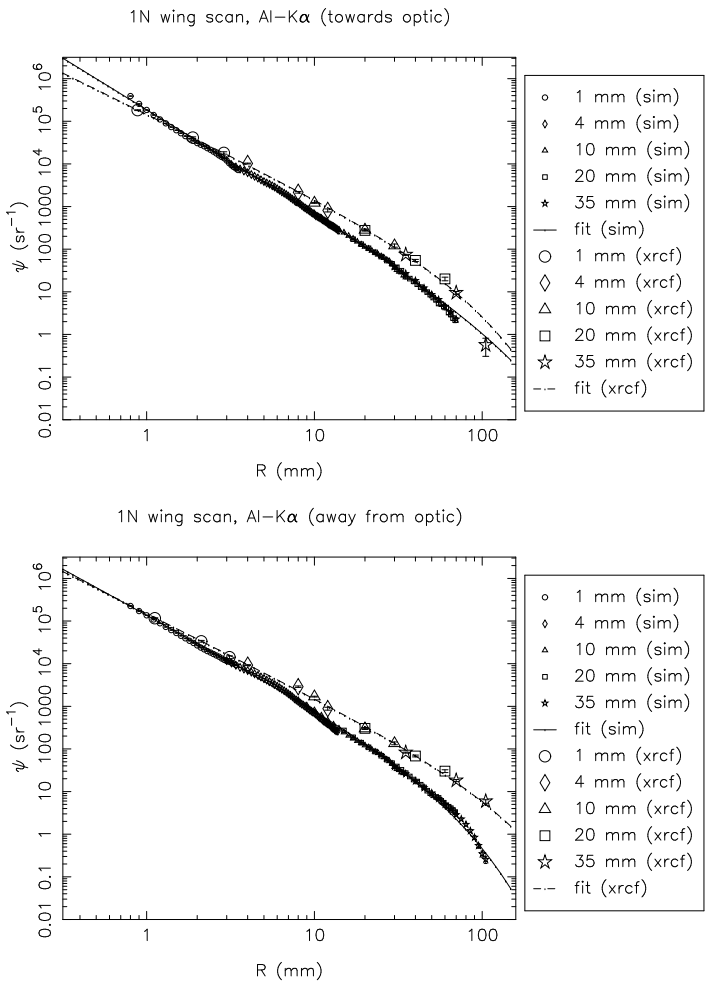

Figure 15.2: Shell 1N: Al-Kα surface brightness, towards and away from the optic

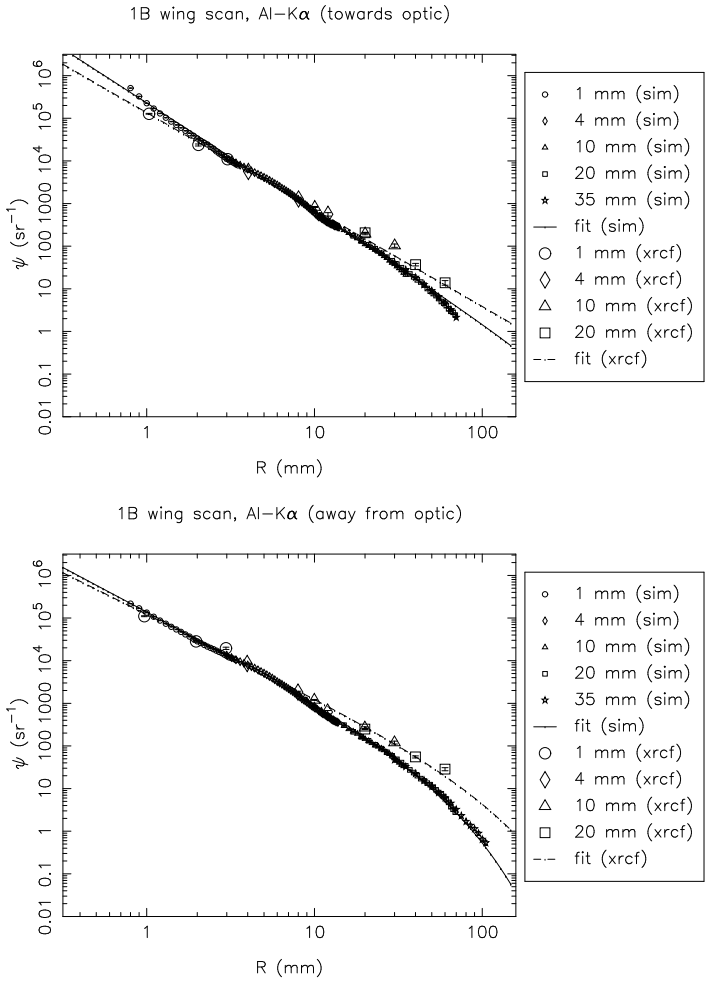

Figure 15.3: Shell 1B: Al-Kα surface brightness, towards and away from the optic

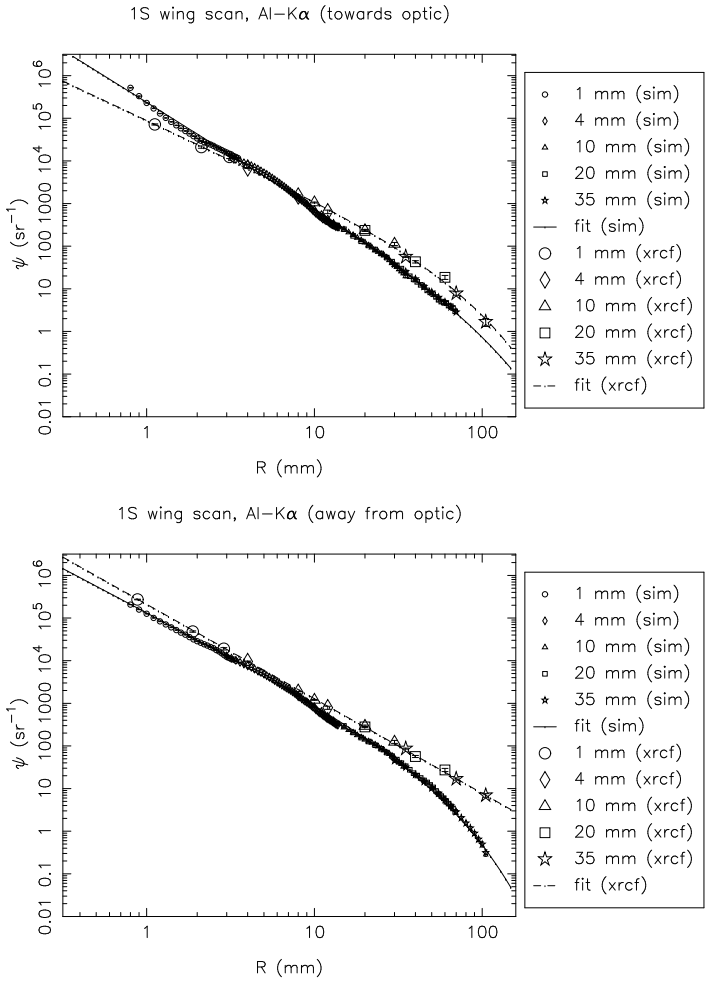

Figure 15.4: Shell 1S: Al-Kα surface brightness, towards and away from the optic

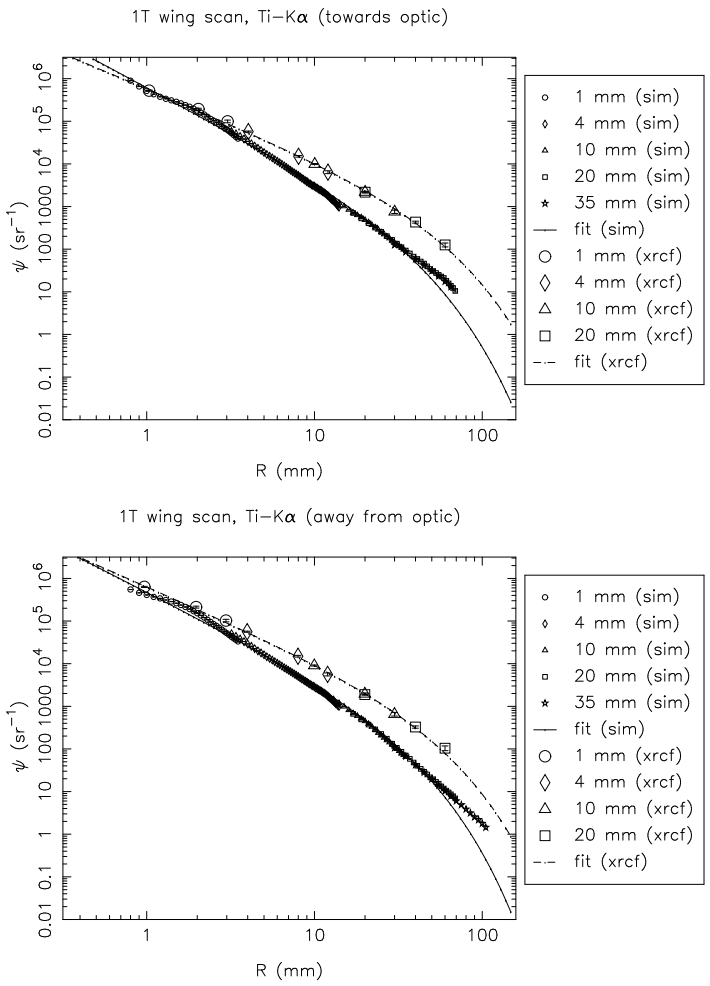

Figure 15.5: Shell 1T: Ti-Kα surface brightness, towards and away from the optic

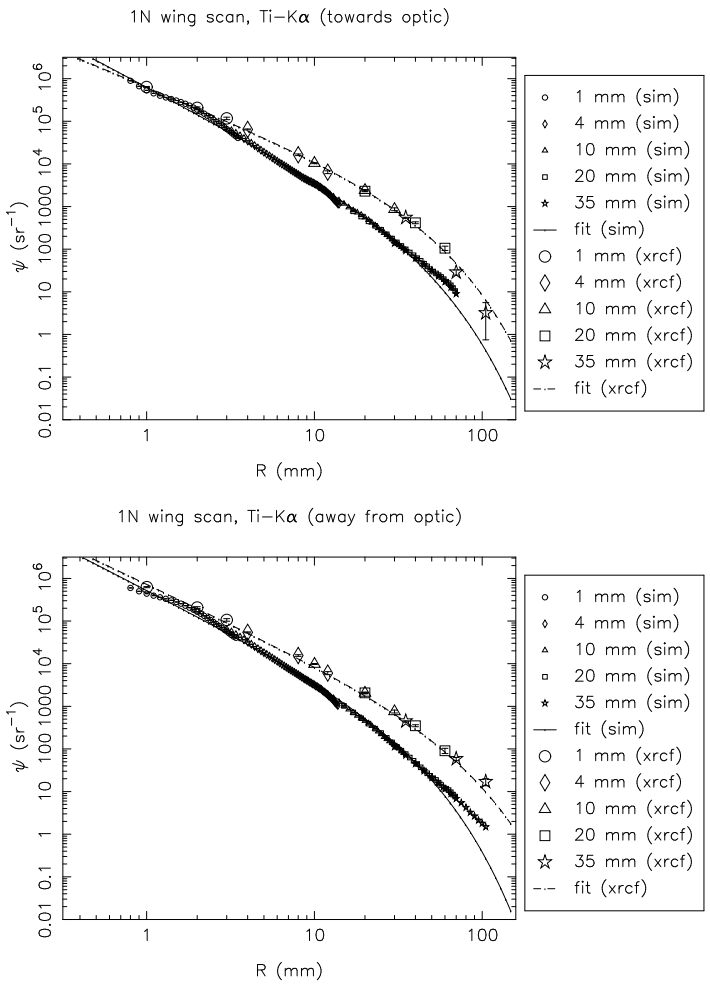

Figure 15.6: Shell 1N: Ti-Kα surface brightness, towards and away from the optic

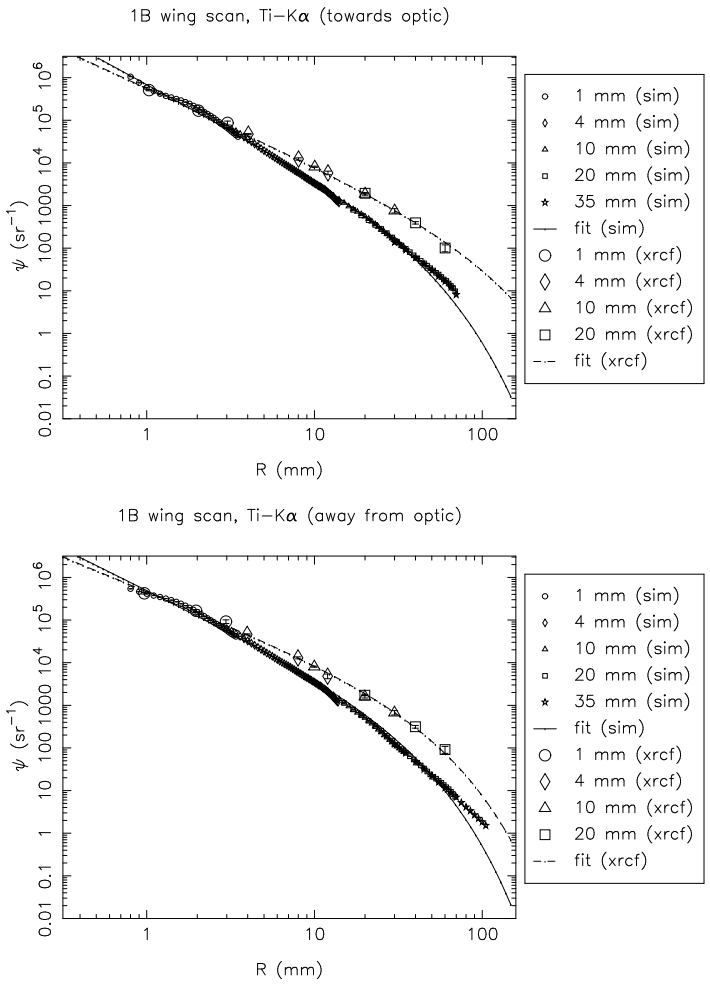

Figure 15.7: Shell 1B: Ti-Kα surface brightness, towards and away from th e optic

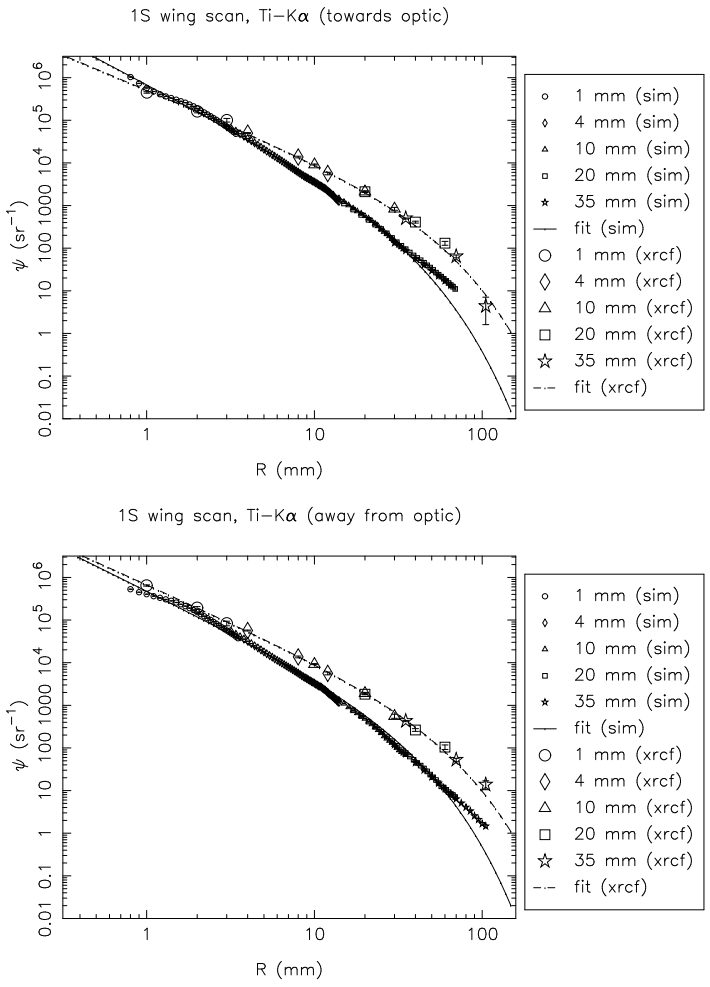

Figure 15.8: Shell 1S: Ti-Kα surface brightness, towards and away from the optic

15.2.2 Shell 3 scans

Table 15.3: Surface brightness fits and fractional excess effective area beyond the 35 mm pinhole. (Raytrace simulations, Shell 3)

Type	Quad	Line	Dir	a	b	c	fractional extra area
sim	3T	Al	in	33670.200	2.630	10000.000	0.000318
sim	3T	Al	out	18158.600	2.123	70.000	0.000361
sim	3N	Al	in	43456.300	2.810	10000.000	0.000173
sim	3N	Al	out	21399.700	2.290	164.721	0.000415
sim	3B	Al	in	33533.400	2.612	10000.000	0.000345
sim	3B	Al	out	20187.700	2.193	70.000	0.000301
sim	3S	Al	in	33600.500	2.621	10000.000	0.000332
sim	3S	Al	out	15612.400	2.026	70.000	0.000466
sim	3S	Ti	in	186937.000	2.570	70.000	0.000591
sim	3S	Ti	out	124877.000	2.335	70.000	0.001034
sim	3S	Cr	in	246429.000	2.579	70.000	0.000749
sim	3S	Cr	out	176035.000	2.408	70.000	0.001081
sim	3T	Fe	in	349548.000	2.561	85.408	0.001361
sim	3T	Fe	out	270453.000	2.539	70.000	0.000968
sim	3B	Fe	in	353953.000	2.603	117.001	0.001461
sim	3B	Fe	out	254630.000	2.510	70.000	0.001028
sim	3N	Fe	in	377381.000	2.626	148.135	0.001626
sim	3N	Fe	out	293686.000	2.532	70.000	0.001081
sim	3S	Fe	in	362943.000	2.575	70.000	0.001125
sim	3S	Fe	out	226964.000	2.524	70.000	0.000866

Table 15.4: Surface brightness fits and fractional excess effective area beyond the 35 mm pinhole. (XRCF data, Shell 3)

Type	Quad	Line	Dir	a	b	c	fractional extra area
xrcf	3T	Al	in	42694.600	2.545	10000.000	0.000615
xrcf	3T	Al	out	139570.000	2.700	10000.000	0.000937
xrcf	3N	Al	in	25452.400	1.980	42.306	0.000486
xrcf	3N	Al	out	123052.000	2.509	71.304	0.000507
xrcf	3B	Al	in	18670.600	1.721	20.099	0.000231
xrcf	3B	Al	out	55033.600	2.205	77.562	0.000863
xrcf	3S	Al	in	16015.000	1.783	30.189	0.000382
xrcf	3S	Al	out	62529.500	2.125	25.698	0.000281
xrcf	3S	Ti	in	278681.000	2.231	122.589	0.005740
xrcf	3S	Ti	out	195982.000	1.925	31.936	0.002944
xrcf	3S	Cr	in	260346.000	2.095	65.196	0.005399
xrcf	3S	Cr	out	310305.000	2.009	25.242	0.002115
xrcf	3T	Fe	in	560465.000	2.253	459.946	0.020630
xrcf	3T	Fe	out	736608.000	2.304	33.052	0.002609
xrcf	3B	Fe	in	568188.000	2.304	232.852	0.012476
xrcf	3B	Fe	out	484538.000	2.107	29.203	0.003001
xrcf	3N	Fe	in	422225.000	2.114	59.864	0.007351
xrcf	3N	Fe	out	563223.000	2.168	21.617	0.001465
xrcf	3S	Fe	in	503919.000	2.113	58.980	0.008658
xrcf	3S	Fe	out	428822.000	2.027	20.240	0.001646

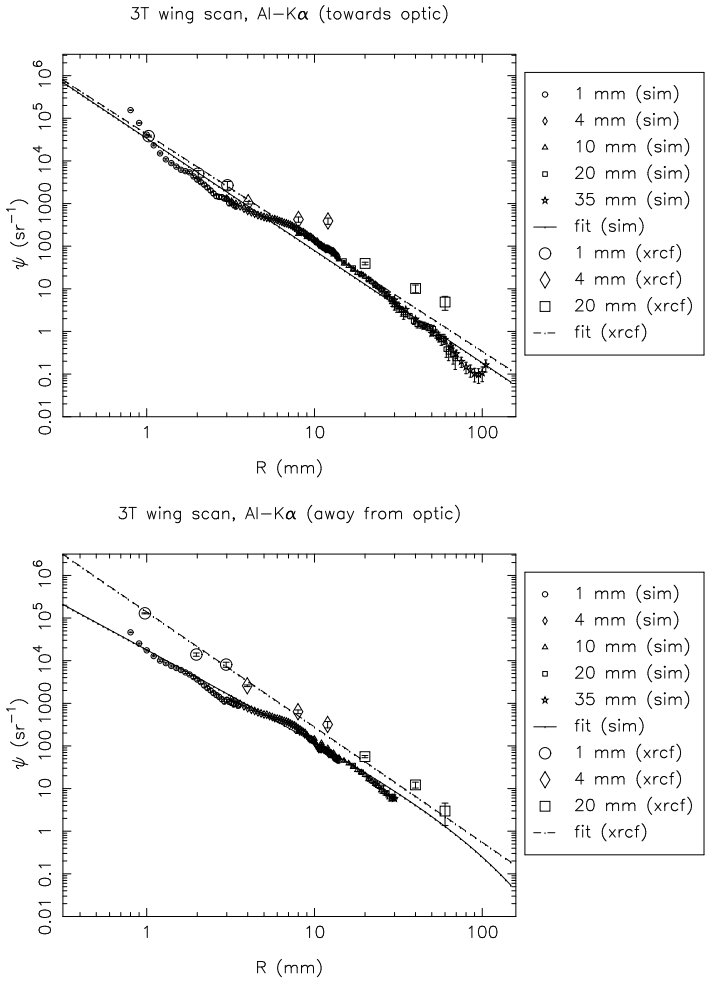

Figure 15.9: Shell 3T: Al-Kα surface brightness, towards and away from the optic

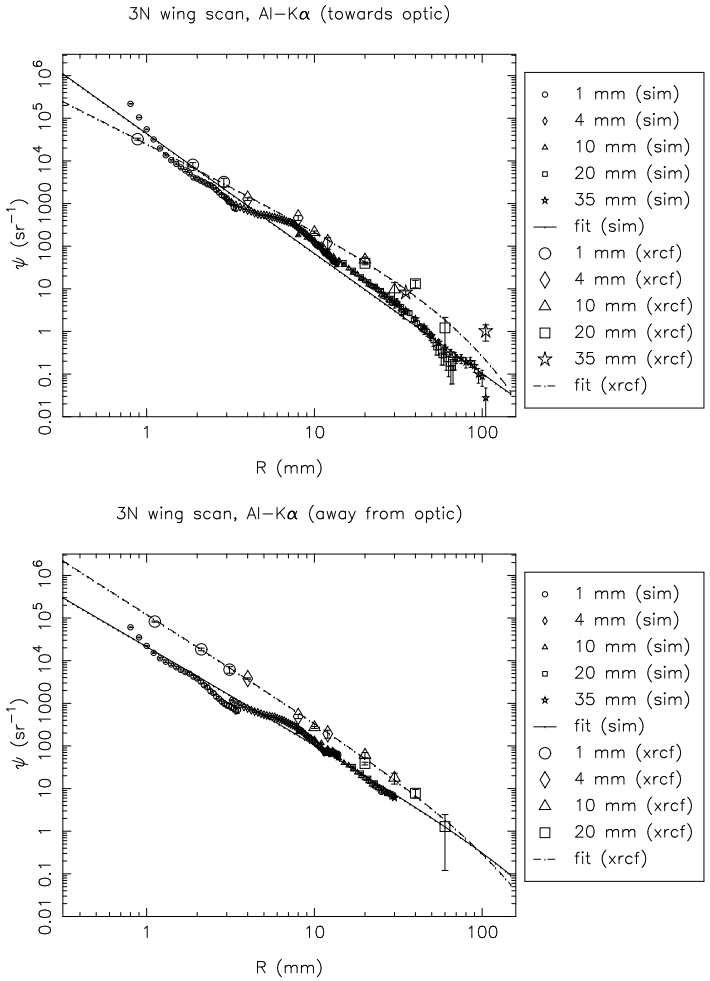

Figure 15.10: Shell 3N: Al-Kα surface brightness, towards and away from the optic

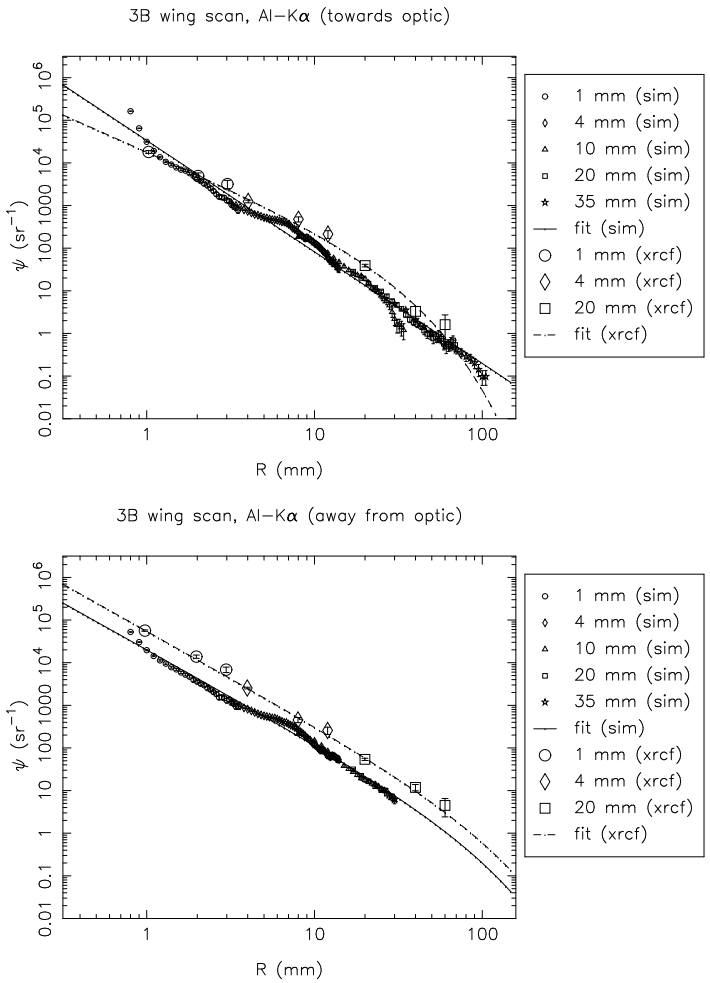

Figure 15.11: Shell 3B: Al-Kα surface brightness, towards and away from the optic

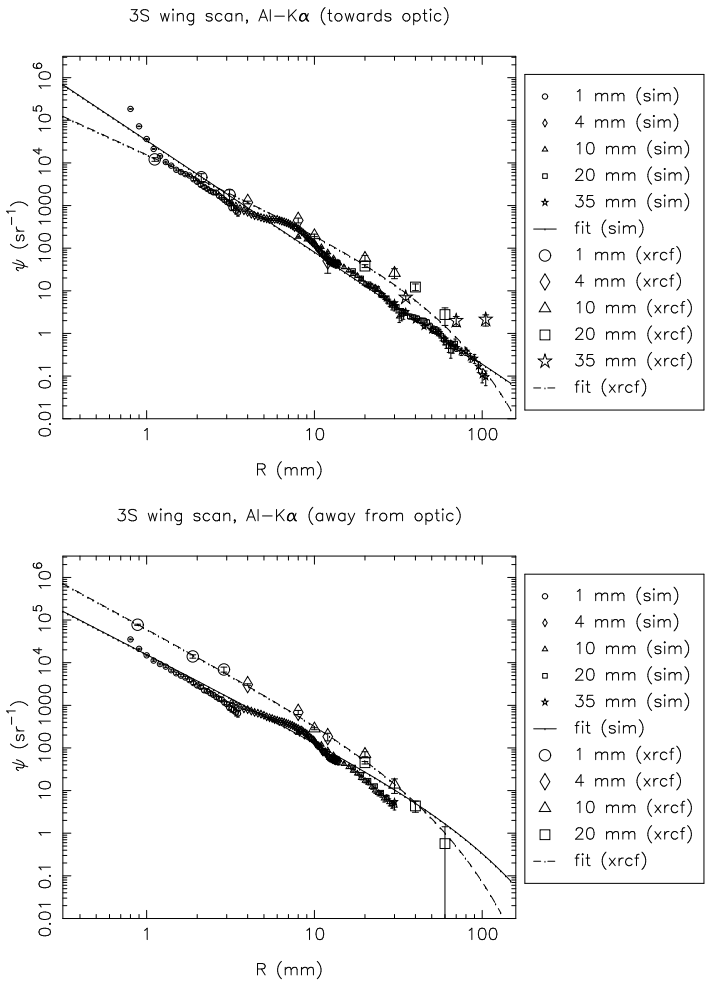

Figure 15.12: Shell 3S: Al-Kα surface brightness, towards and away from the optic

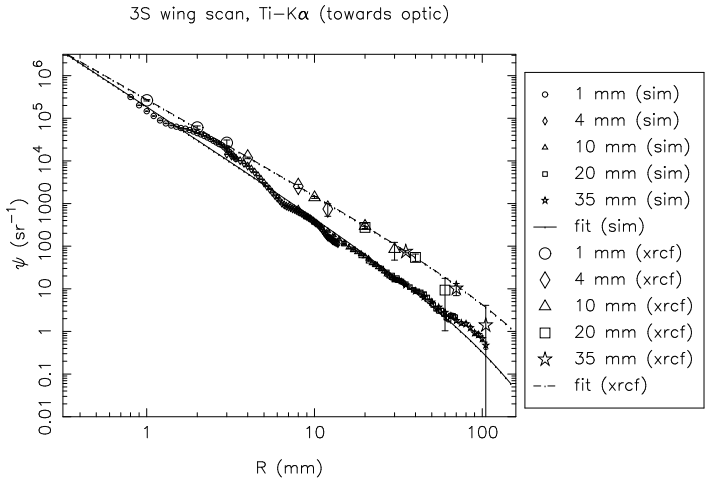

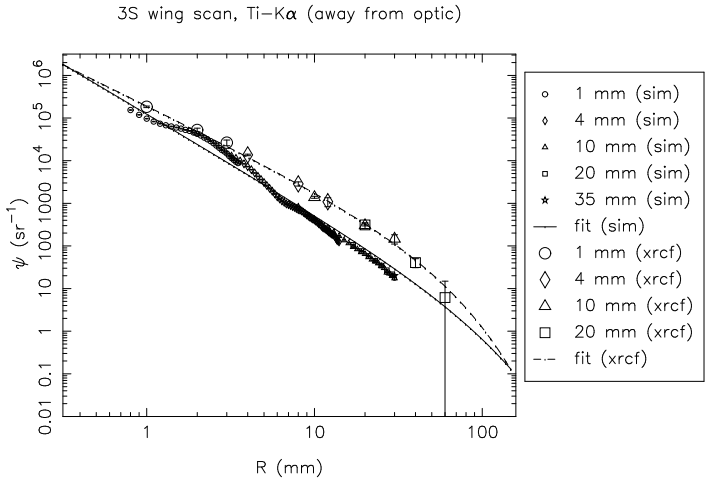

Figure 15.13: Shell 3S: Ti-Kα surface brightness, towards and away from the optic

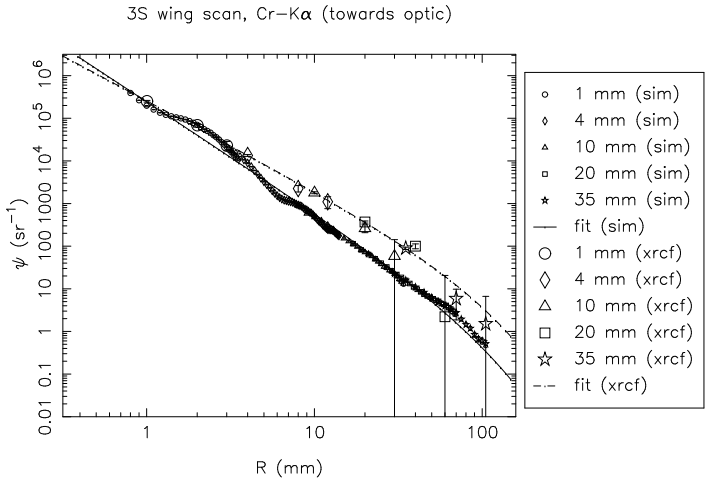

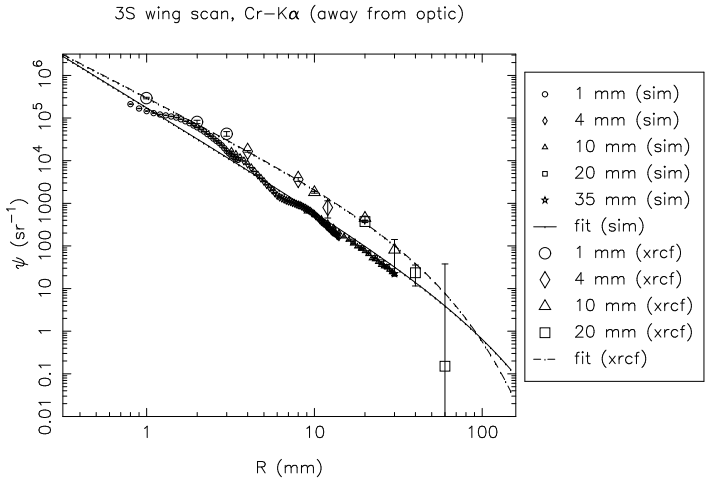

Figure 15.14: Shell 3S: Cr-Kα surface brightness, towards and away from the optic

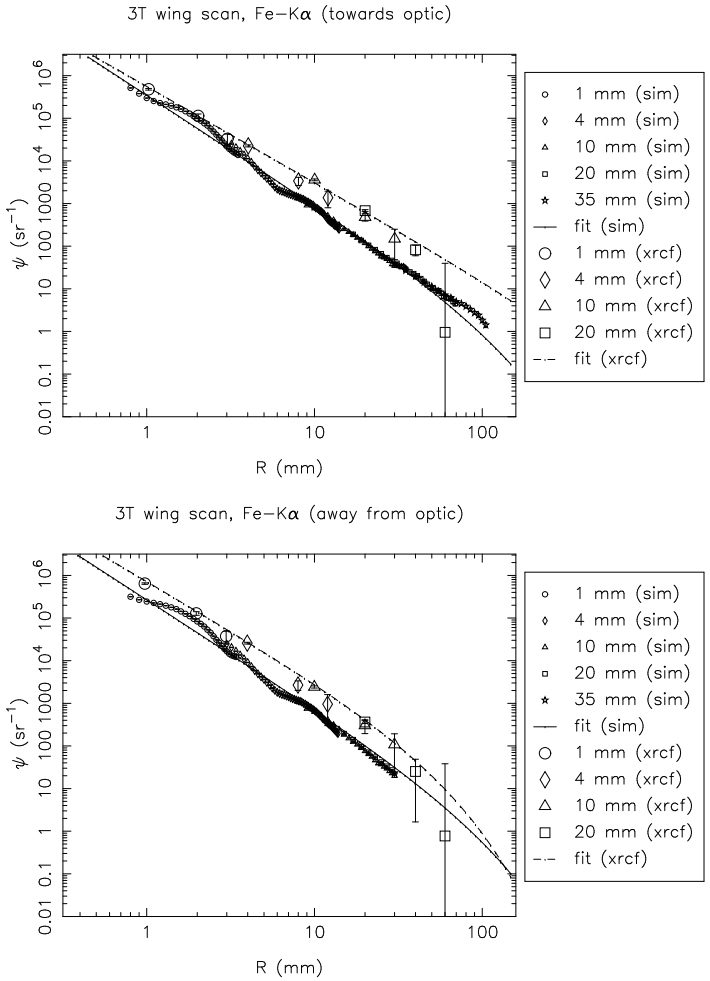

Figure 15.15: Shell 3T: Fe-Kα surface brightness, towards and away from the optic

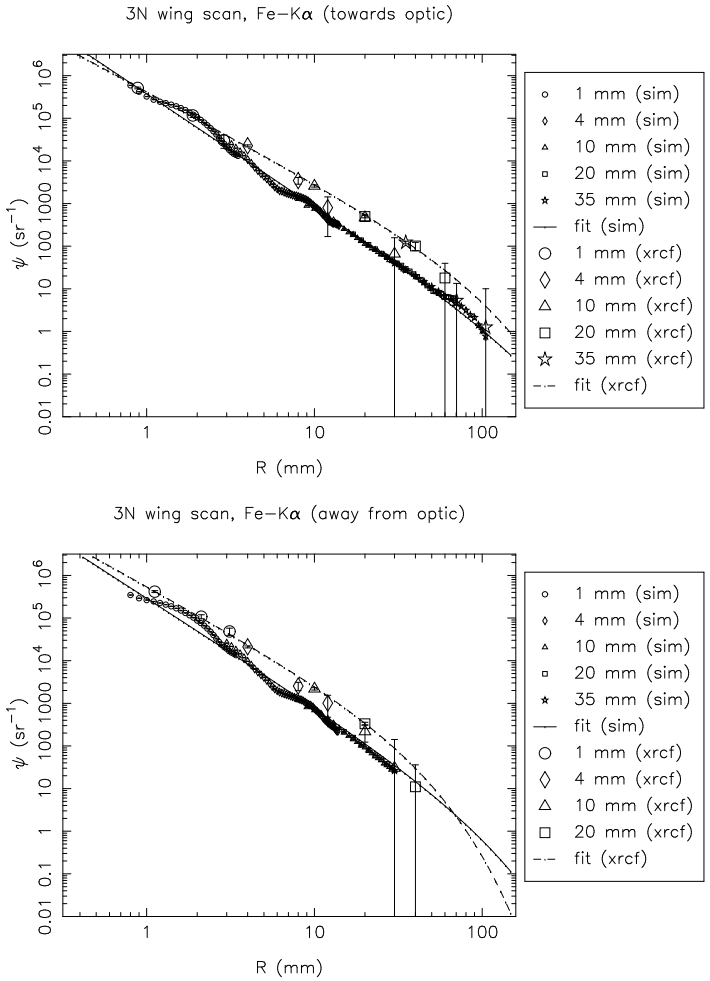

Figure 15.16: Shell 3N: Fe-Kα surface brightness, towards and away from the optic

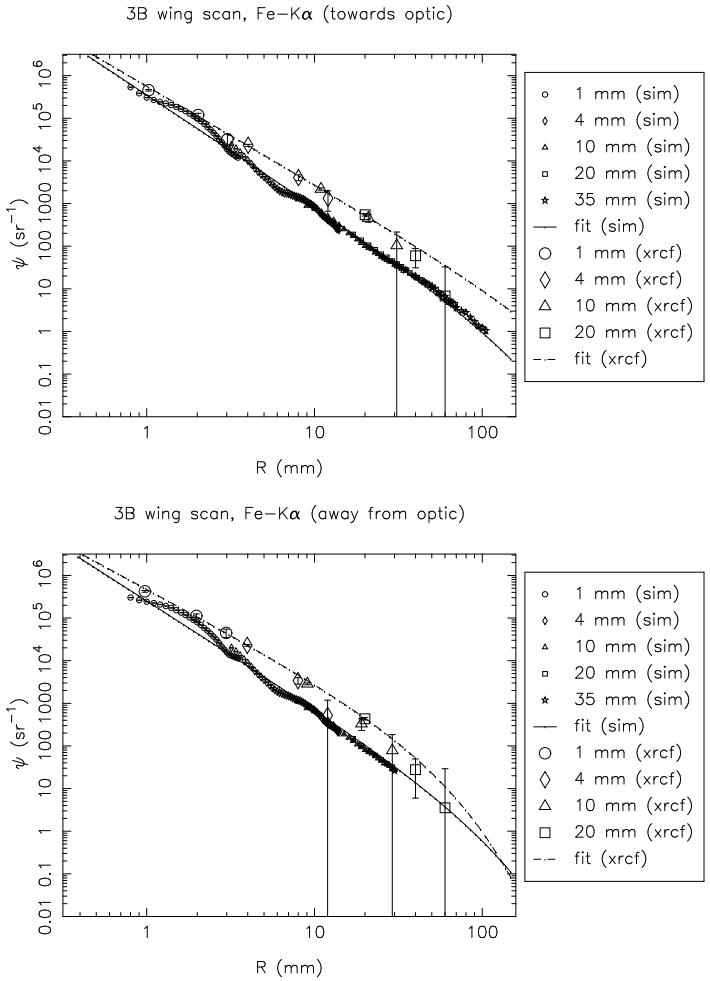

Figure 15.17: Shell 3B: Fe-Kα surface brightness, towards and away from the optic

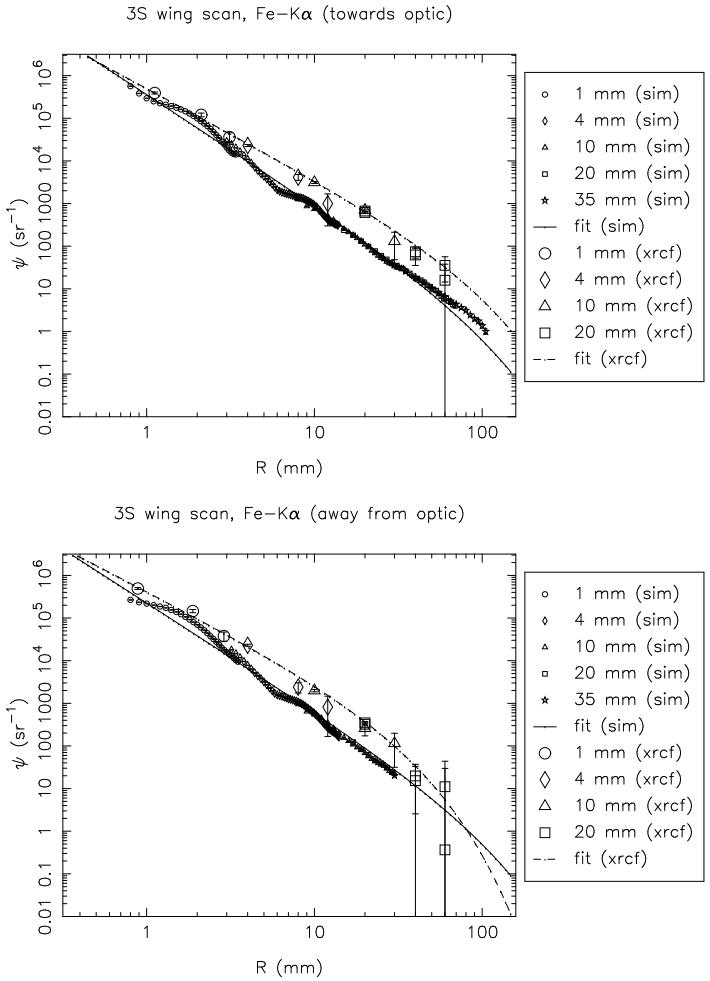

Figure 15.18: Shell 3S: Fe-Kα surface brightness, towards and away from the optic

15.2.3 Shell 4 scans

Table 15.5: Surface brightness fits and fractional excess effective area beyond the 35 mm pinhole. (Raytrace simulations, Shell 4)

Type	Quad	Line	Dir	a	b	c	fractional extra area
sim	4T	Al	in	45522.100	2.862	10000.000	0.000143
sim	4T	Al	out	29538.700	2.500	10000.000	0.000535
sim	4N	Al	in	133732.000	3.433	10000.000	0.000034
sim	4N	Al	out	72861.700	2.880	10000.000	0.000209
sim	4B	Al	in	155290.000	3.686	10000.000	0.000014
sim	4B	Al	out	54287.800	2.719	10000.000	0.000333
sim	4S	Al	in	48438.200	2.912	10000.000	0.000120
sim	4S	Al	out	23695.800	2.435	10000.000	0.000601
sim	4S	Ti	in	207308.000	2.531	278.904	0.001804
sim	4S	Ti	out	148785.000	2.320	85.397	0.001574
sim	4S	Cr	in	271072.000	2.517	597.682	0.003174
sim	4S	Cr	out	200191.000	2.321	70.615	0.001770
sim	4T	Fe	in	309523.000	2.447	600.865	0.005007
sim	4T	Fe	out	254766.000	2.354	70.000	0.001953
sim	4N	Fe	in	420038.000	2.549	8658.530	0.005870
sim	4N	Fe	out	330389.000	2.390	70.000	0.002183
sim	4B	Fe	in	457006.000	2.622	10000.000	0.004478
sim	4B	Fe	out	284517.000	2.365	70.000	0.002078
sim	4S	Fe	in	330882.000	2.487	5767.630	0.006168
sim	4S	Fe	out	222297.000	2.317	70.000	0.001980
sim	4S	Cu	in	489937.000	2.355	10000.000	0.018923
sim	4S	Cu	out	316625.000	2.401	95.931	0.002631

Table 15.6: Surface brightness fits and fractional excess effective area beyond the 35 mm pinhole. (XRCF data, Shell 4)

Type	Quad	Line	Dir	a	b	c	fractional extra area
xrcf	4T	Al	in	113177.000	2.656	10000.000	0.000940
xrcf	4T	Al	out	90027.300	2.756	10000.000	0.000462
xrcf	4N	Al	in	64983.900	2.475	6510.170	0.001299
xrcf	4N	Al	out	67406.900	2.523	10000.000	0.001084
xrcf	4B	Al	in	163766.000	2.881	10000.000	0.000469
xrcf	4B	Al	out	88631.200	2.352	89.746	0.000857
xrcf	4S	Al	in	37857.300	2.152	77.512	0.000741
xrcf	4S	Al	out	106539.000	2.529	10000.000	0.001662
xrcf	4S	Ti	in	281656.000	2.156	54.267	0.003672
xrcf	4S	Ti	out	222767.000	2.077	91.891	0.007020
xrcf	4S	Cr	in	311700.000	2.121	57.218	0.005000
xrcf	4S	Cr	out	323288.000	2.089	47.867	0.004719
xrcf	4T	Fe	in	575581.000	2.220	85.123	0.009246
xrcf	4T	Fe	out	576353.000	2.161	33.536	0.003687
xrcf	4N	Fe	in	462355.000	2.123	51.746	0.006503
xrcf	4N	Fe	out	504010.000	2.151	47.334	0.005633
xrcf	4B	Fe	in	593296.000	2.317	184.370	0.010897
xrcf	4B	Fe	out	549030.000	2.131	31.303	0.003510
xrcf	4S	Fe	in	476664.000	2.171	46.147	0.004748
xrcf	4S	Fe	out	406663.000	1.985	19.077	0.001580
xrcf	4S	Cu	in	842582.000	1.885	42.887	0.024146
xrcf	4S	Cu	out	1173790.000	2.335	48.786	0.006481

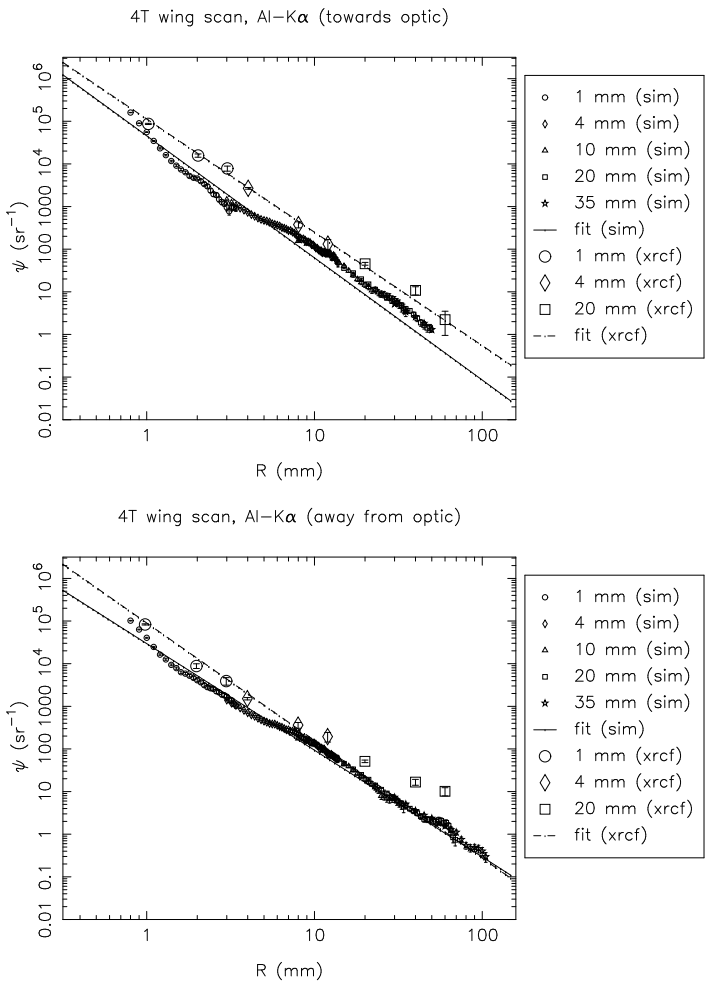

Figure 15.19: Shell 4T: Al-Kα surface brightness, towards and away from the optic

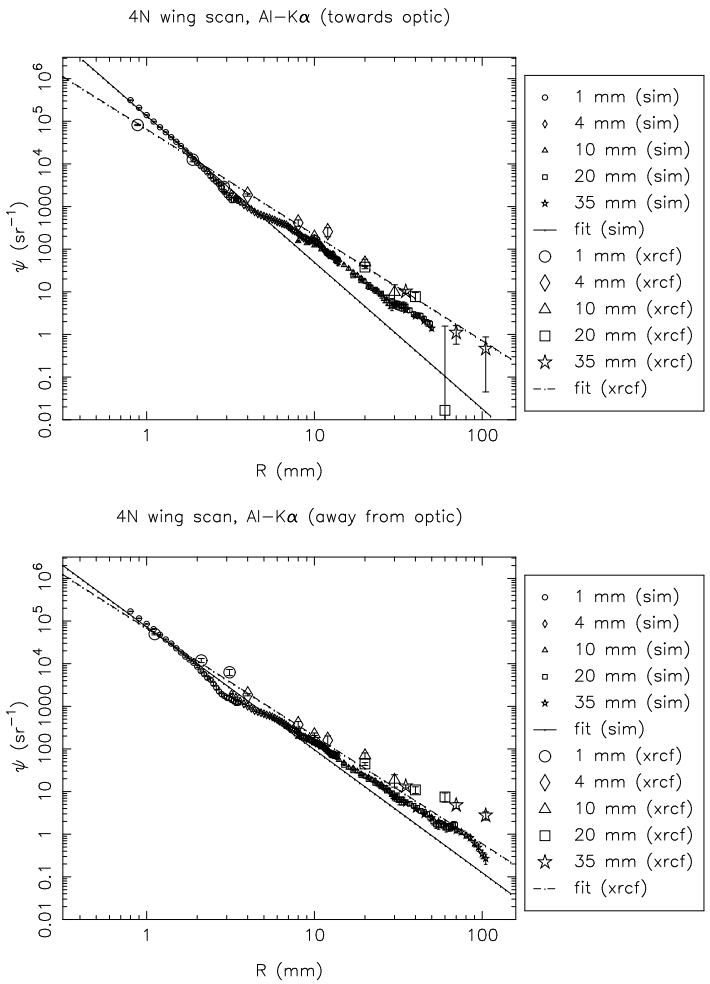

Figure 15.20: Shell 4N: Al-Kα surface brightness, towards and away from the optic

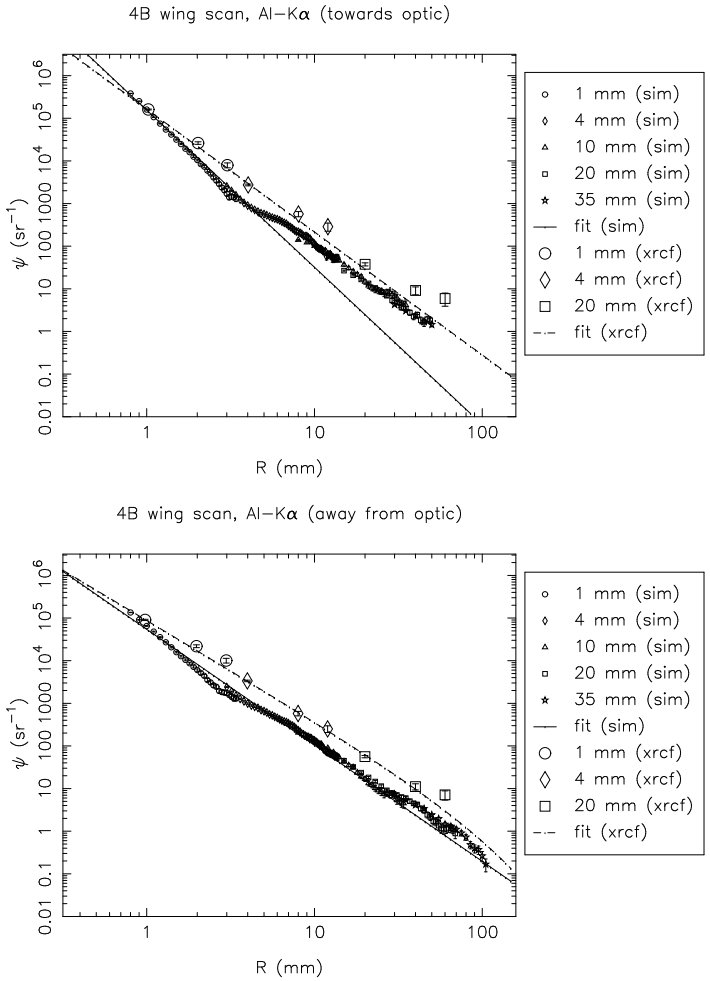

Figure 15.21: Shell 4B: Al-Kα surface brightness, towards and away from the optic

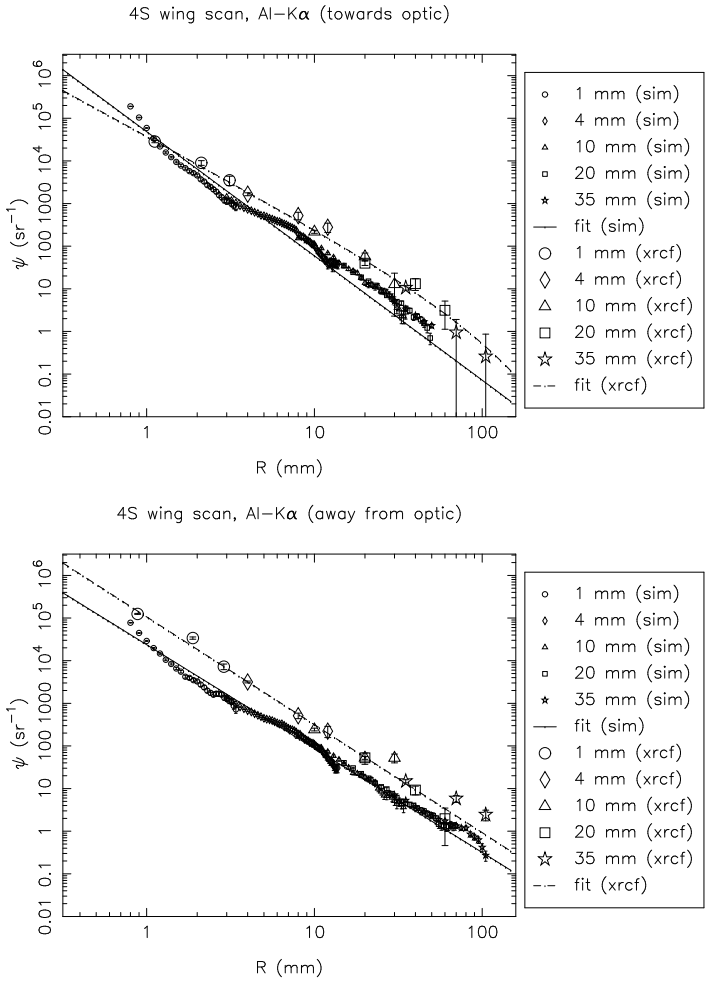

Figure 15.22: Shell 4S: Al-Kα surface brightness, towards and away from the optic

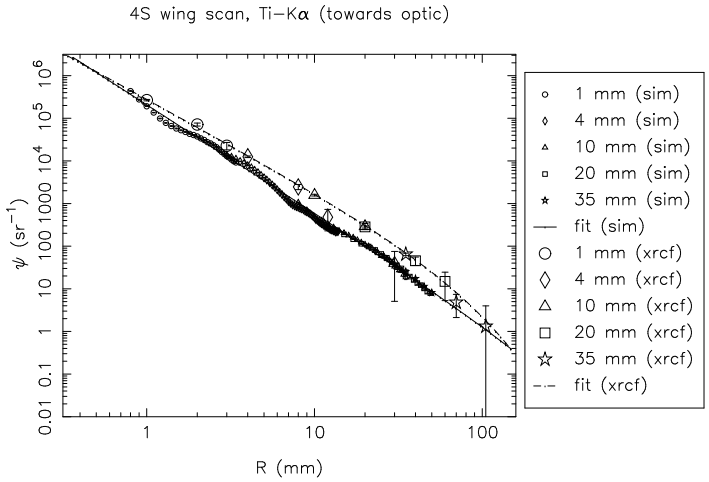

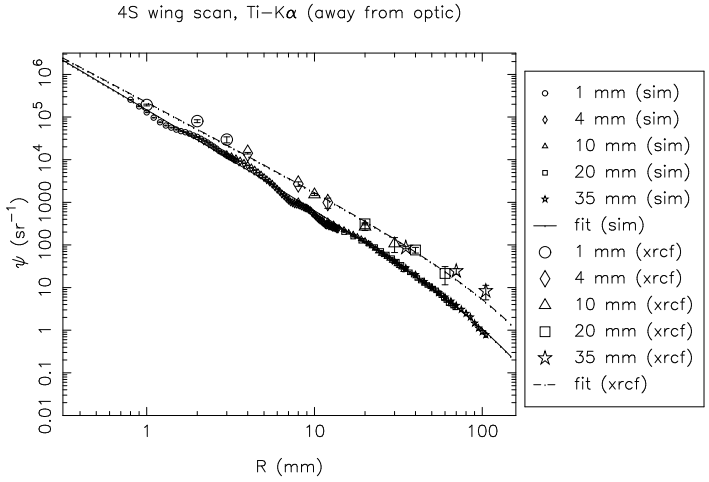

Figure 15.23: Shell 4S: Ti-Kα surface brightness, towards and away from the optic

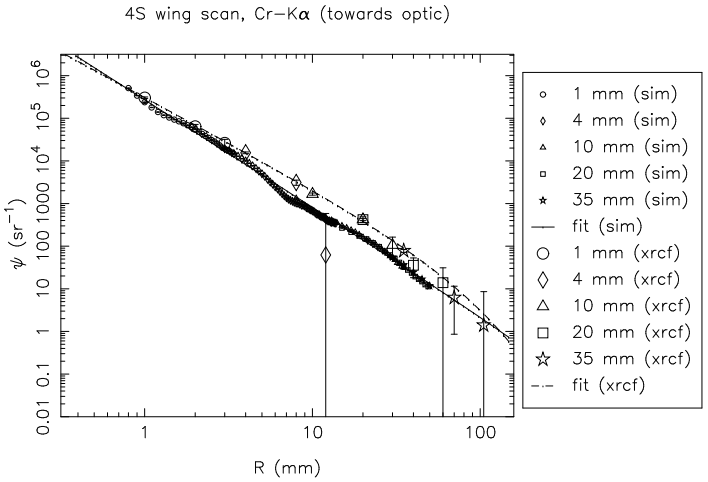

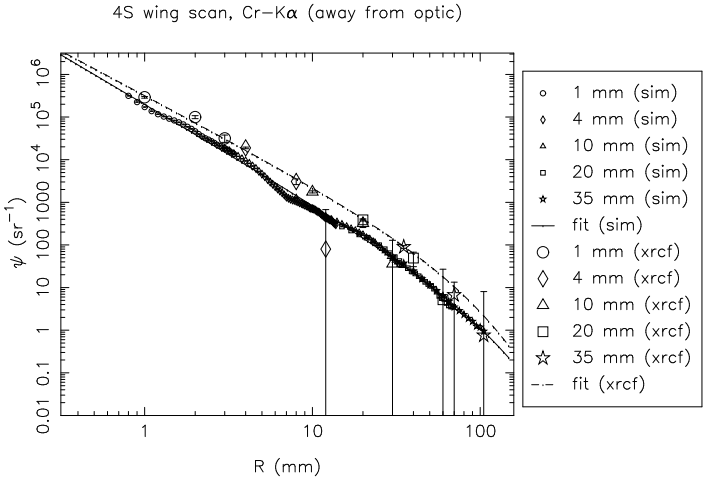

Figure 15.24: Shell 4S: Cr-Kα surface brightness, towards and away from the optic

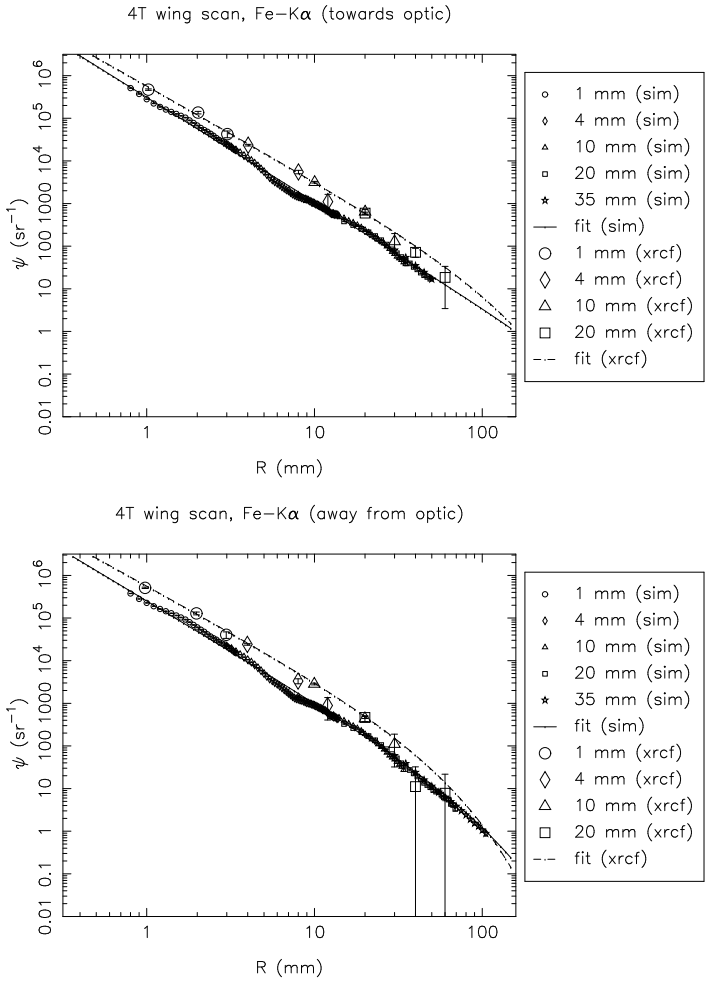

Figure 15.25: Shell 4T: Fe-Kα surface brightness, towards and away from the optic

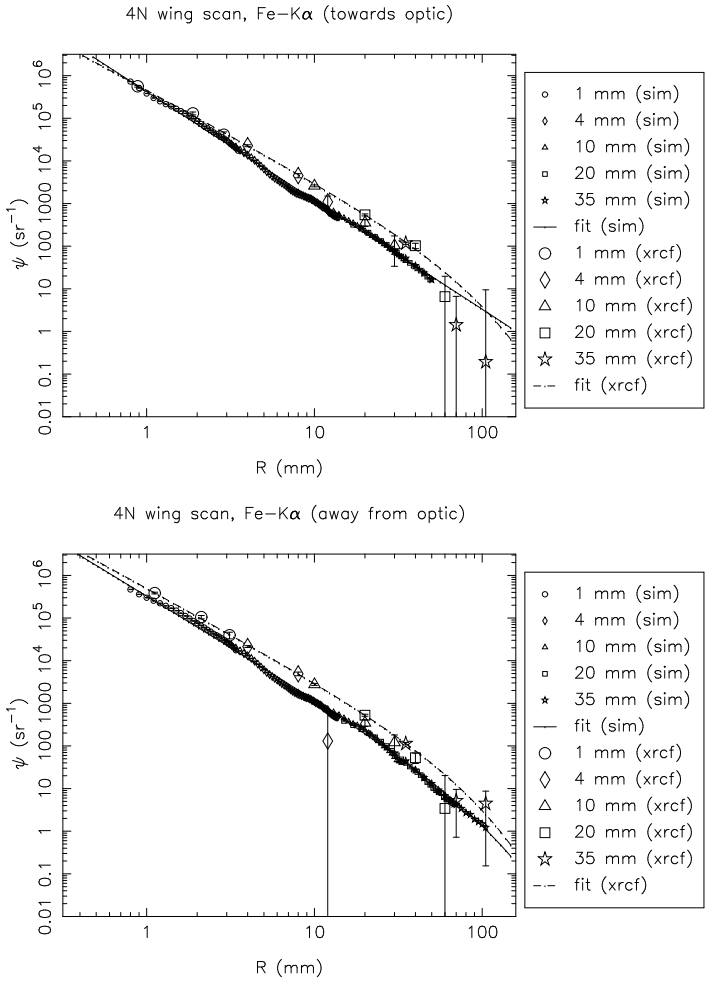

Figure 15.26: Shell 4N: Fe-Kα surface brightness, towards and away from the optic

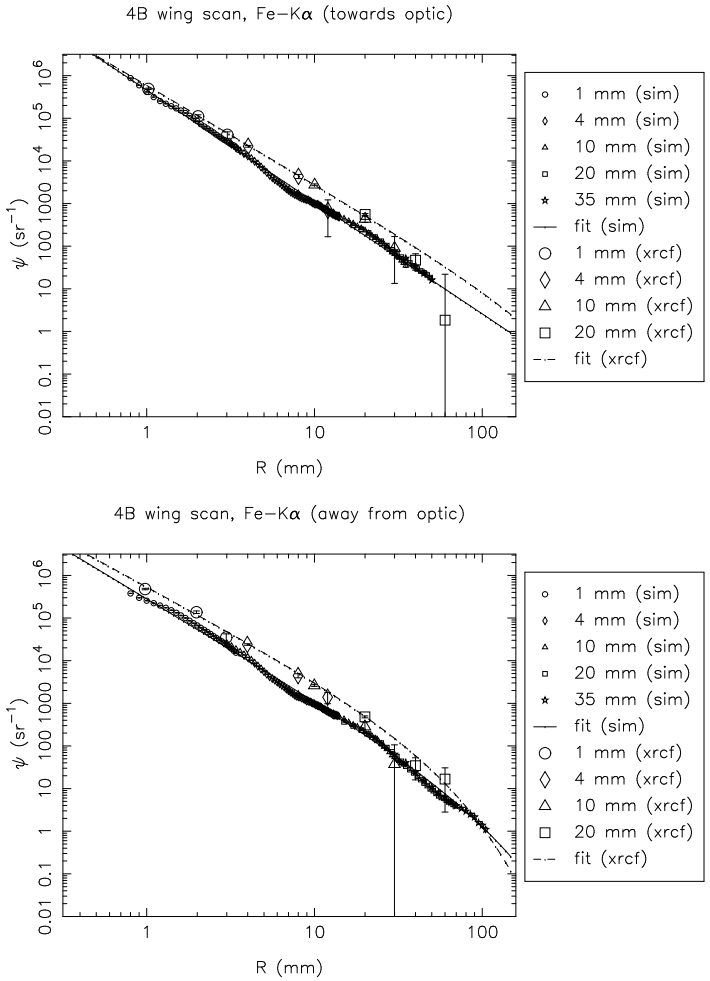

Figure 15.27: Shell 4B: Fe-Kα surface brightness, towards and away from the optic

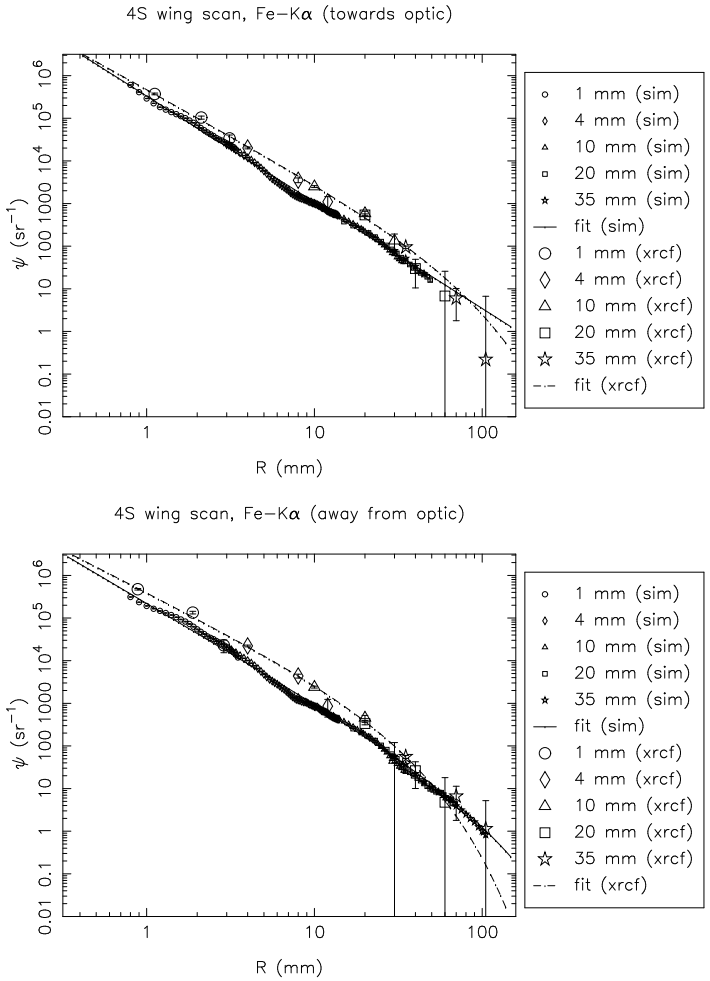

Figure 15.28: Shell 4S: Fe-Kα surface brightness, towards and away from the optic

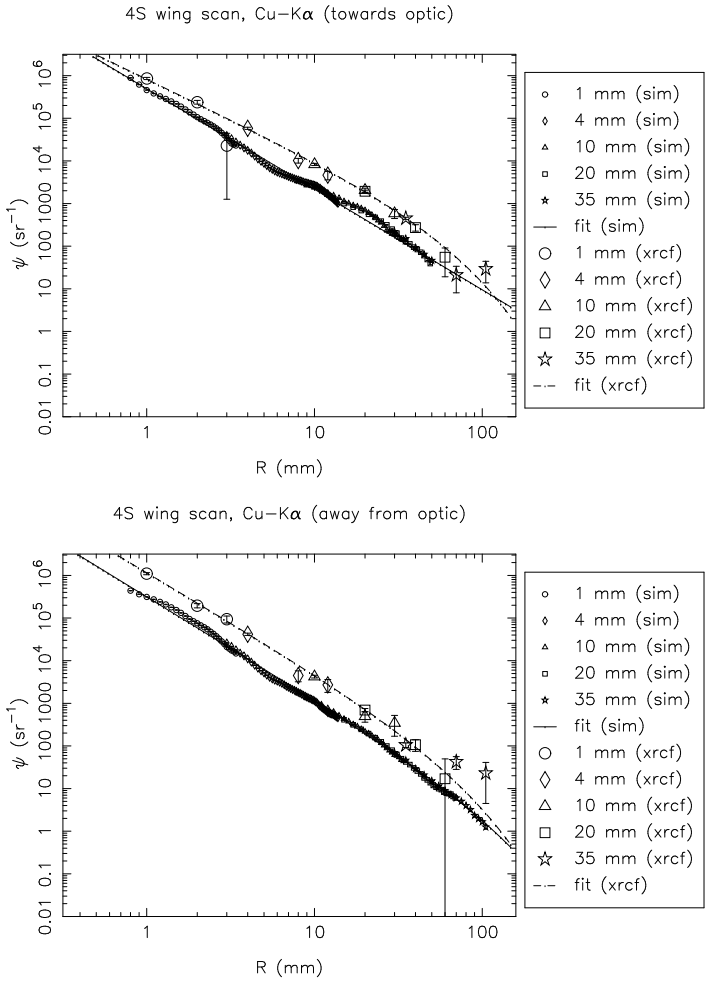

Figure 15.29: Shell 4S: Cu-Kα surface brightness, towards and away from the optic

15.2.4 Shell 6 scans

Table 15.7: Surface brightness fits and fractional excess effective area beyond the 35 mm pinhole. (Raytrace simulations, Shell 6)

Type	Quad	Line	Dir	a	b	c	fractional extra area
sim	6B	C	in	25912.900	3.142	70.000	0.000008
sim	6B	C	out	30915.300	2.895	70.000	0.000026
sim	6T	Al	in	121092.000	3.146	10000.000	0.000105
sim	6T	Al	out	116395.000	3.095	10000.000	0.000127
sim	6N	Al	in	101486.600	3.262	10000.000	0.000053
sim	6N	Al	out	120531.000	3.058	10000.000	0.000155
sim	6B	Al	in	122030.000	3.475	10000.000	0.000026
sim	6B	Al	out	109760.000	3.109	10000.000	0.000112
sim	6S	Al	in	134708.000	3.231	10000.000	0.000081
sim	6S	Al	out	96170.800	3.019	10000.000	0.000147
sim	6S	Ti	in	199568.000	2.518	70.000	0.000779
sim	6S	Ti	out	193288.000	2.421	70.000	0.001121
sim	6S	Cr	in	246680.000	2.482	70.000	0.001115
sim	6S	Cr	out	232063.000	2.388	70.000	0.001543
sim	6T	Fe	in	292414.000	2.415	70.000	0.001741
sim	6T	Fe	out	284040.000	2.373	70.000	0.002010
sim	6N	Fe	in	298852.000	2.414	70.000	0.001789
sim	6N	Fe	out	305030.000	2.354	70.000	0.002333
sim	6B	Fe	in	335773.000	2.506	70.000	0.001378
sim	6B	Fe	out	279676.000	2.356	70.000	0.002125
sim	6S	Fe	in	317636.000	2.464	70.000	0.001548
sim	6S	Fe	out	246516.000	2.352	70.000	0.001903
sim	6T	Cu	in	388002.000	2.394	70.000	0.002519
sim	6T	Cu	out	383320.000	2.453	70.000	0.001953
sim	6N	Cu	in	415306.000	2.415	70.000	0.002471
sim	6N	Cu	out	417002.000	2.436	70.000	0.002275
sim	6B	Cu	in	442238.000	2.470	70.000	0.002105
sim	6B	Cu	out	387613.000	2.437	70.000	0.002108
sim	6S	Cu	in	431805.000	2.439	70.000	0.002333
sim	6S	Cu	out	330644.000	2.368	70.000	0.002390

Table 15.8: Surface brightness fits and fractional excess effective area beyond the 35 mm pinhole. (XRCF data, Shell 6)

Type	Quad	Line	Dir	a	b	c	fractional extra area
xrcf	6B	C	in	107596.000	2.926	50.000	0.000058
xrcf	6B	C	out	61652.600	2.939	50.000	0.000031
xrcf	6T	Al	in	76735.100	2.176	12.628	0.000041
xrcf	6T	Al	out	194262.000	3.076	10000.000	0.000230
xrcf	6N	Al	in	103493.200	2.751	10000.000	0.000544
xrcf	6N	Al	out	169376.000	2.860	10000.000	0.000534
xrcf	6B	Al	in	168171.000	2.846	10000.000	0.000566
xrcf	6B	Al	out	103630.200	2.655	10000.000	0.000865
xrcf	6S	Al	in	193325.000	3.605	10000.000	0.000024
xrcf	6S	Al	out	209454.000	2.982	10000.000	0.000378
xrcf	6S	Ti	in	255254.000	2.216	98.125	0.004716
xrcf	6S	Ti	out	222456.000	2.161	76.943	0.004162
xrcf	6S	Cr	in	258517.000	2.108	46.722	0.003380
xrcf	6S	Cr	out	284988.000	2.073	38.094	0.003186
xrcf	6T	Fe	in	286282.000	1.911	35.797	0.005547
xrcf	6T	Fe	in	418386.000	2.104	40.853	0.004595
xrcf	6T	Fe	out	286282.000	1.911	35.797	0.005547
xrcf	6T	Fe	out	418386.000	2.104	40.853	0.004595
xrcf	6N	Fe	in	284232.000	1.840	19.108	0.001944
xrcf	6N	Fe	out	360357.000	2.108	46.673	0.004705
xrcf	6B	Fe	in	421488.000	2.182	55.439	0.005070
xrcf	6B	Fe	out	376848.000	2.039	36.442	0.004500
xrcf	6S	Fe	in	399255.000	2.052	38.782	0.004994
xrcf	6S	Fe	out	309988.000	1.994	36.596	0.004464
xrcf	6T	Cu	in	426542.000	1.872	24.960	0.004861
xrcf	6T	Cu	out	511460.000	1.981	20.652	0.002465
xrcf	6N	Cu	in	478480.000	1.807	14.549	0.001680
xrcf	6N	Cu	out	478914.000	1.917	17.547	0.001933
xrcf	6B	Cu	in	548984.000	2.065	32.972	0.004997
xrcf	6B	Cu	out	478089.000	1.893	19.165	0.002684
xrcf	6S	Cu	in	467525.000	1.887	19.009	0.002630
xrcf	6S	Cu	out	483961.000	1.957	15.265	0.001114

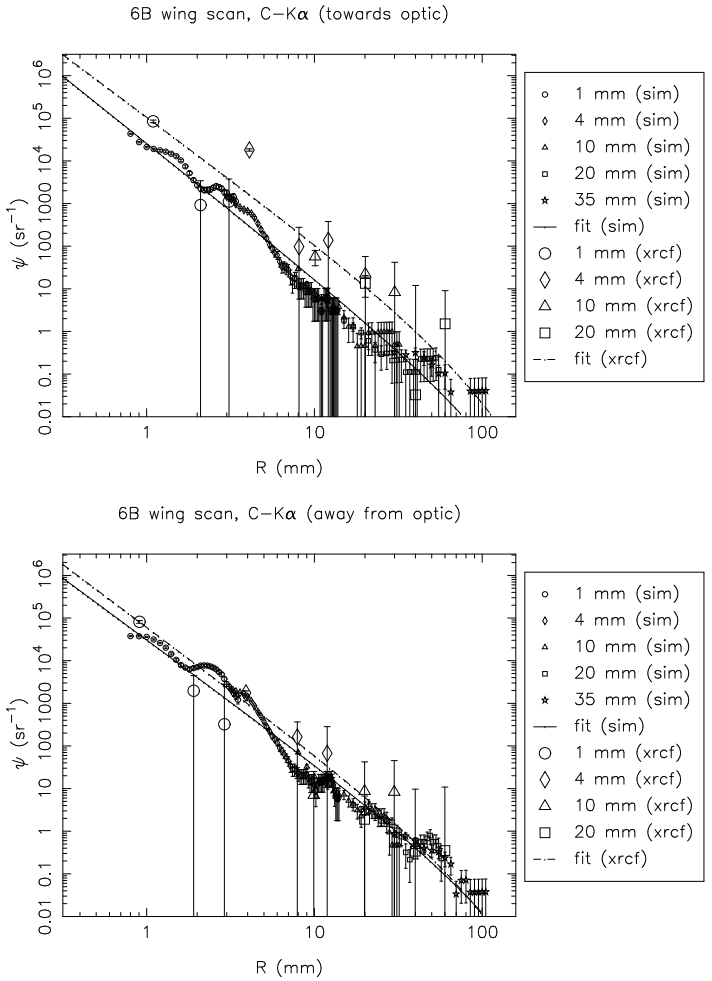

Figure 15.30: Shell 6B: C-Kα surface brightness, towards and away from the optic

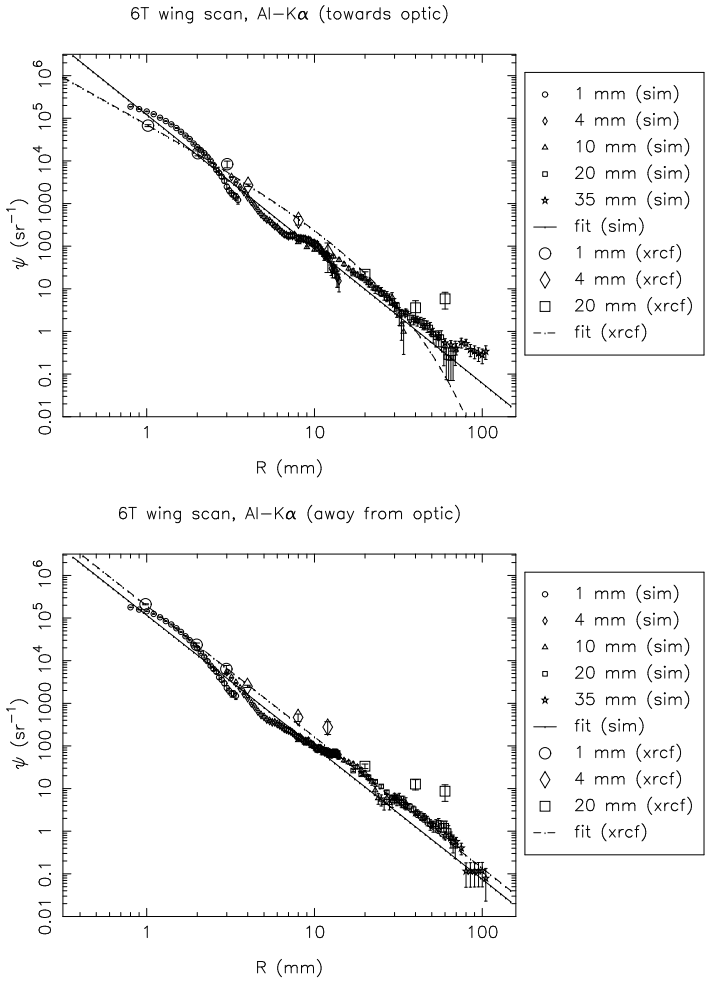

Figure 15.31: Shell 6T: Al-Kα surface brightness, towards and away from the optic

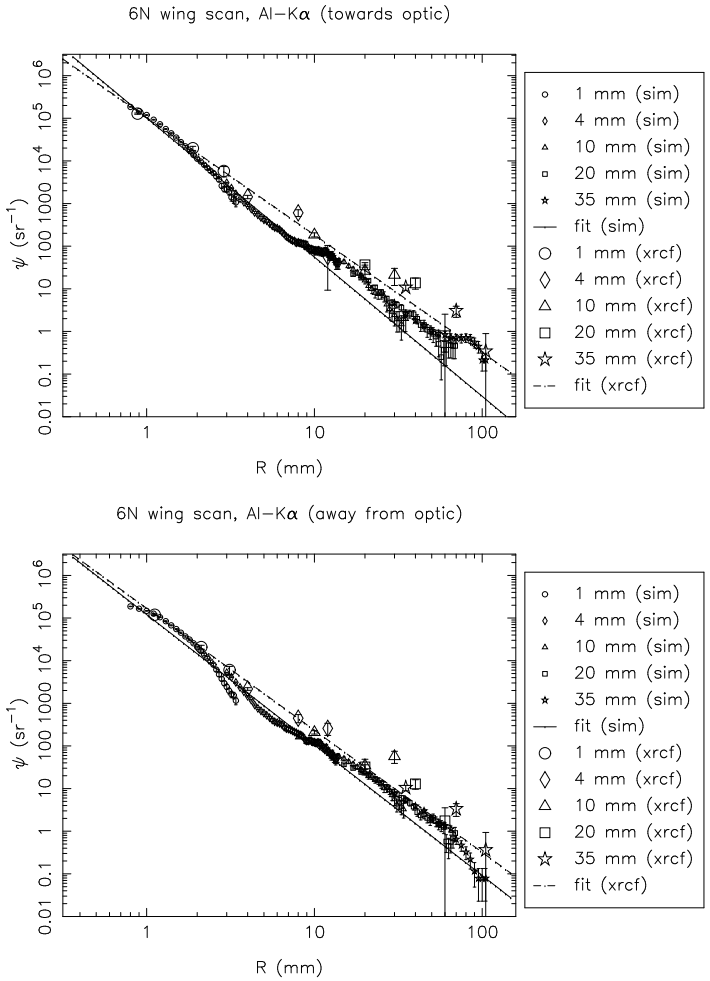

Figure 15.32: Shell 6N: Al-Kα surface brightness, towards and away from the optic

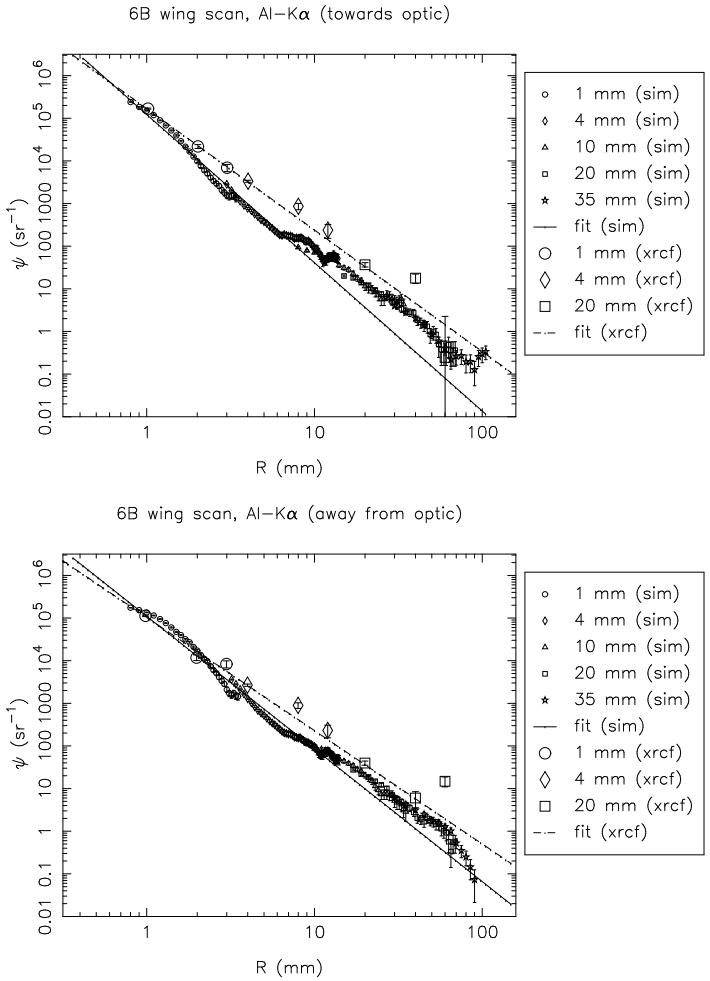

Figure 15.33: Shell 6B: Al-Kα surface brightness, towards and away from the optic

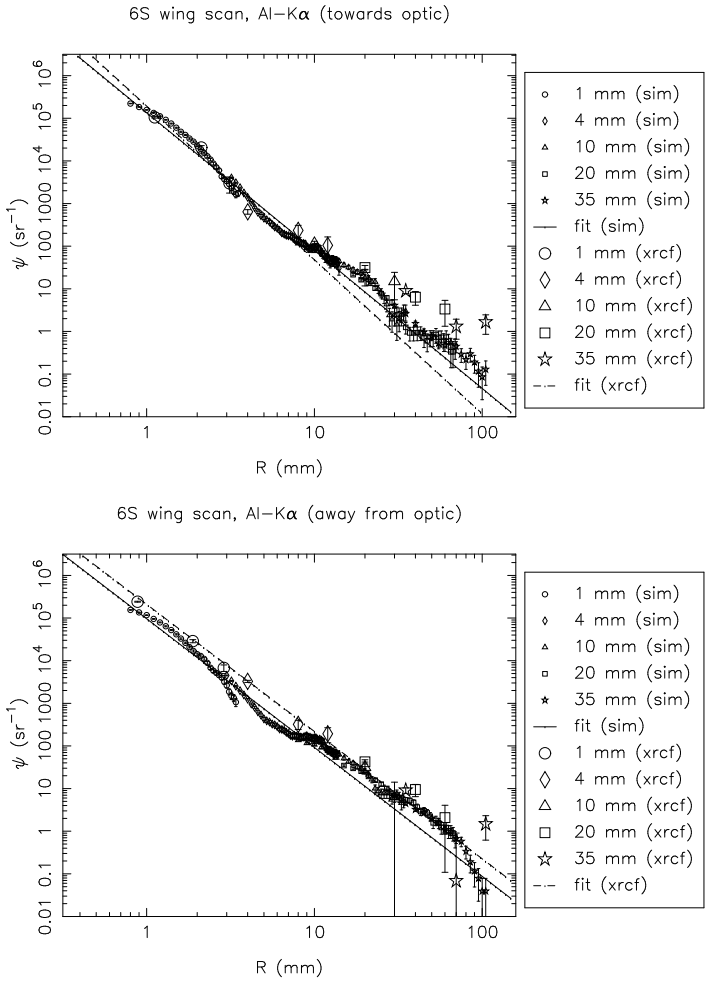

Figure 15.34: Shell 6S: Al-Kα surface brightness, towards and away from the optic

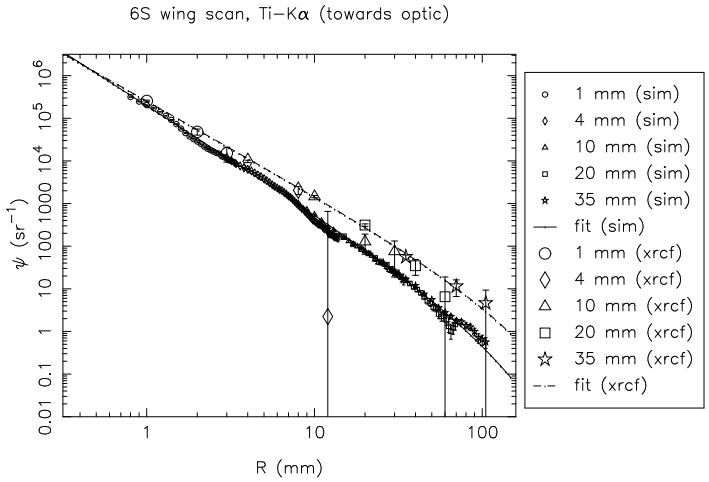

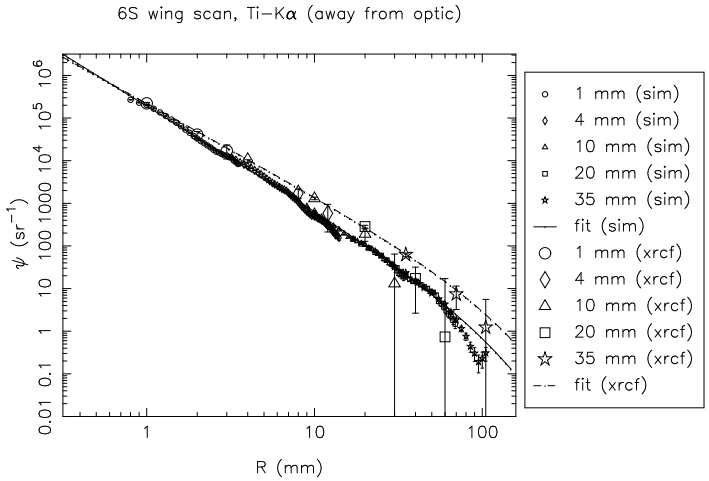

Figure 15.35: Shell 6S: Ti-Kα surface brightness, towards and away from the optic

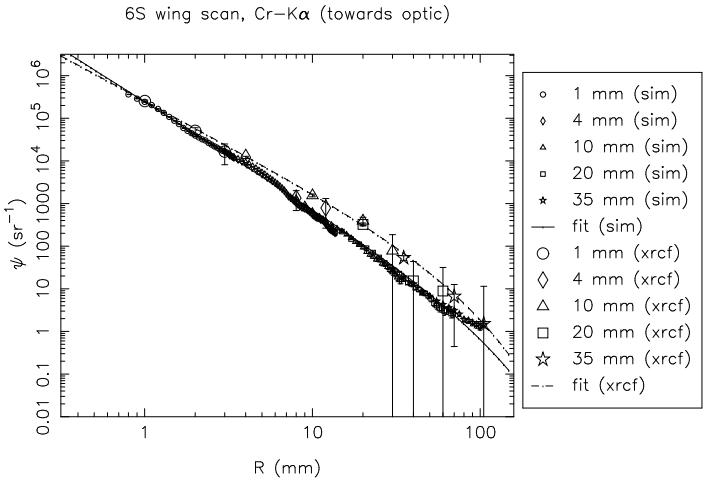

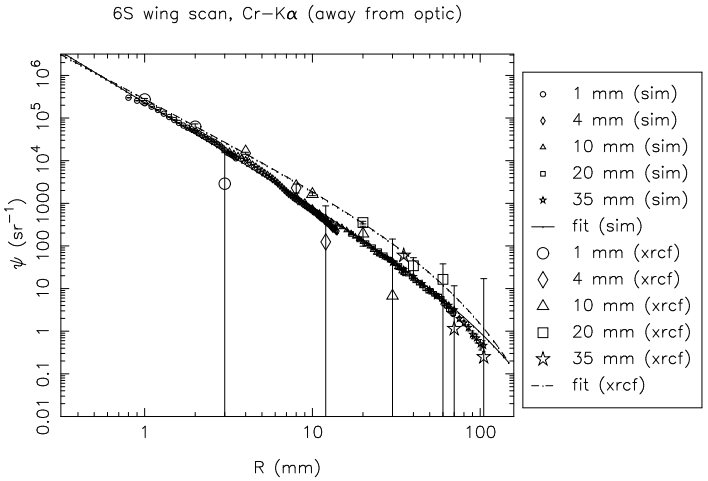

Figure 15.36: Shell 6S: Cr-Kα surface brightness, towards and away from the optic

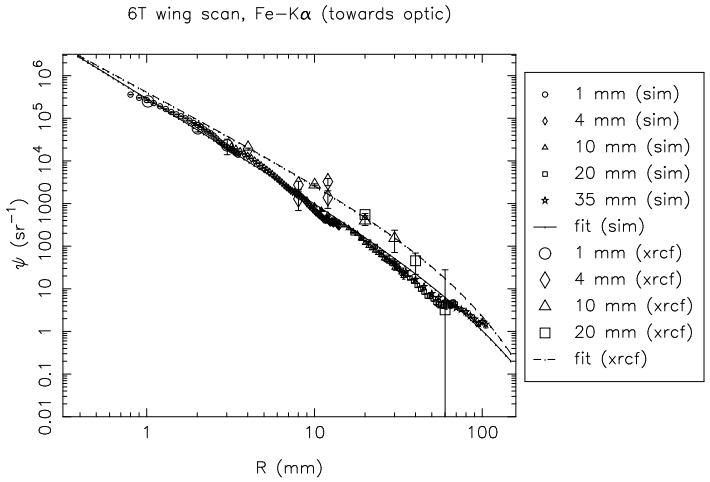

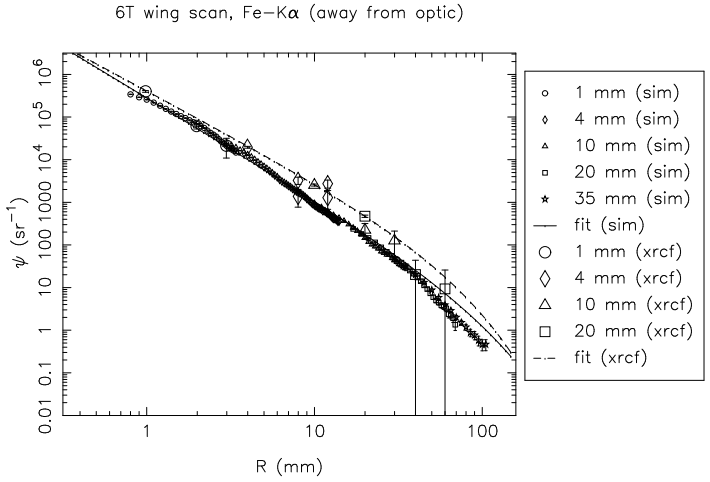

Figure 15.37: Shell 6T: Fe-Kα surface brightness, towards and away from the optic

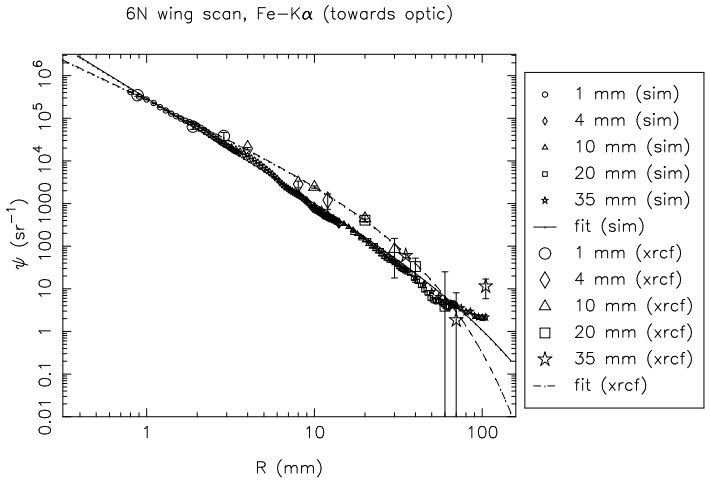

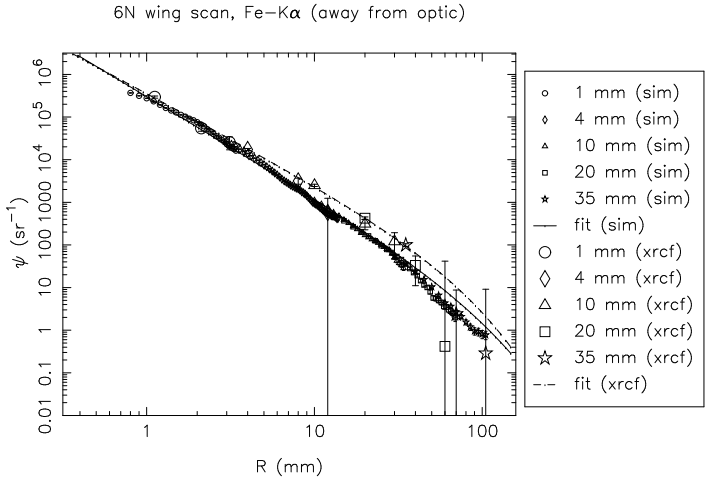

Figure 15.38: Shell 6N: Fe-Kα surface brightness, towards and away from the optic

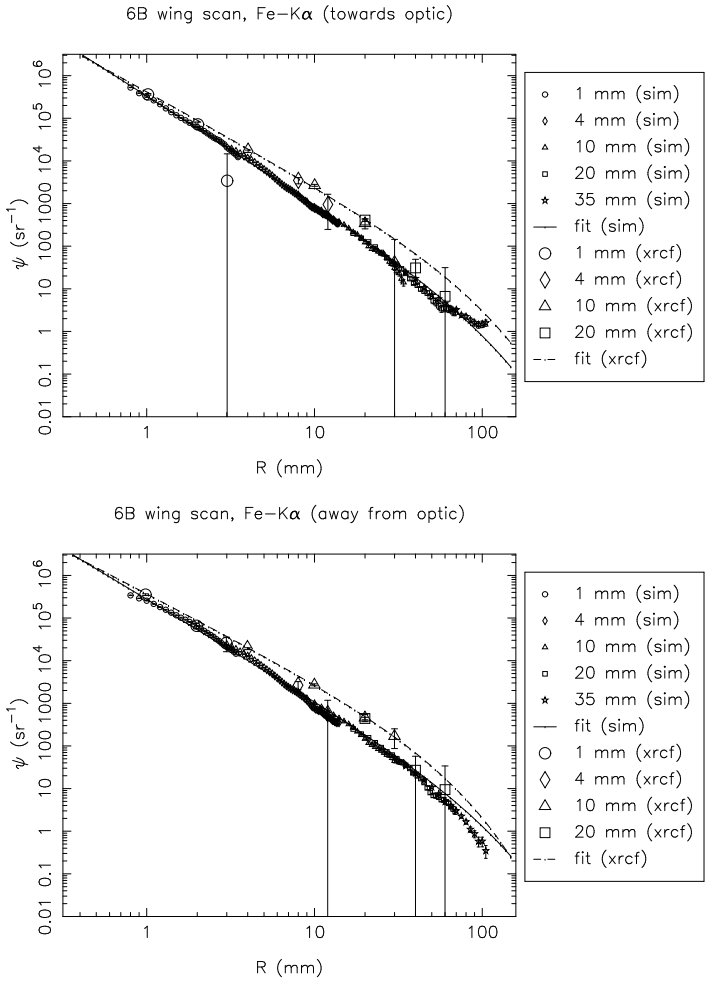

Figure 15.39: Shell 6B: Fe-Kα surface brightness, towards and away from the optic

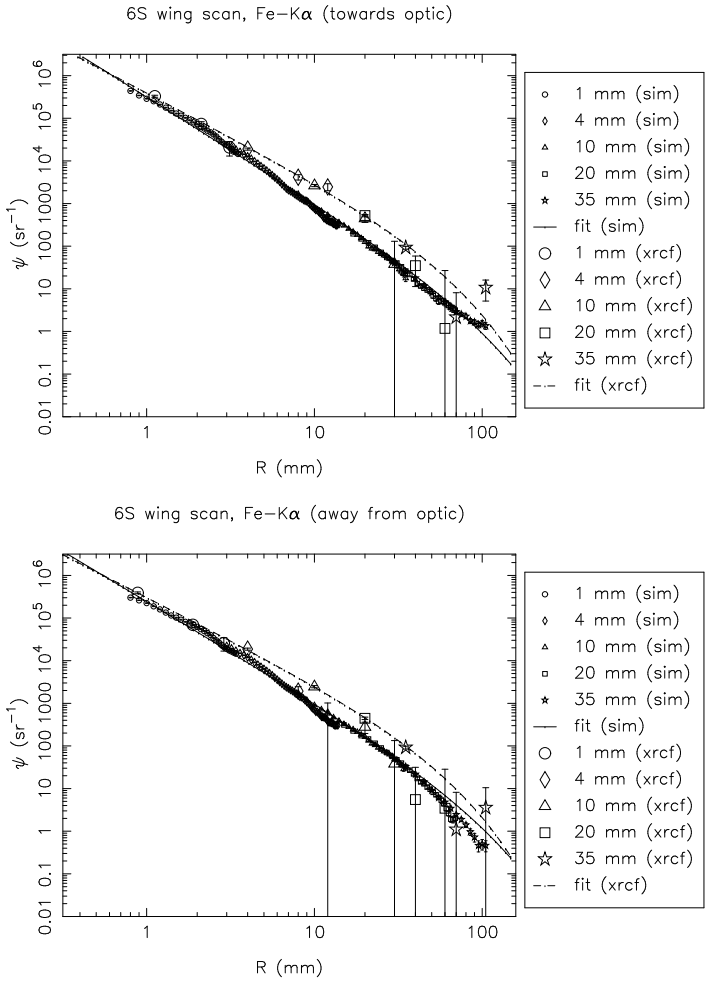

Figure 15.40: Shell 6S: Fe-Kα surface brightness, towards and away from the optic

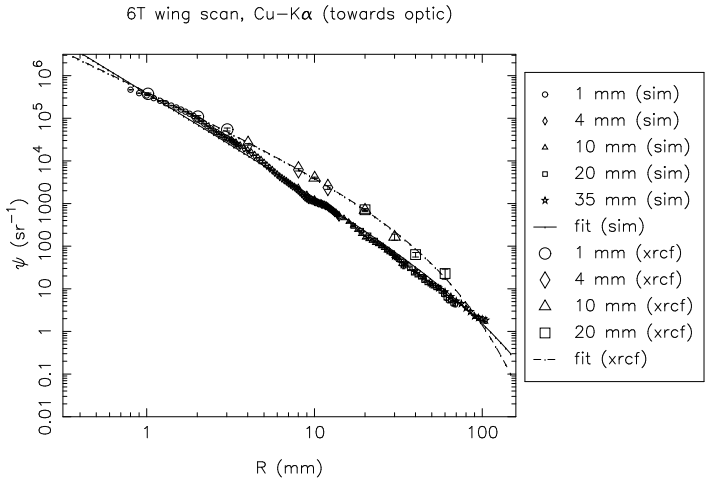

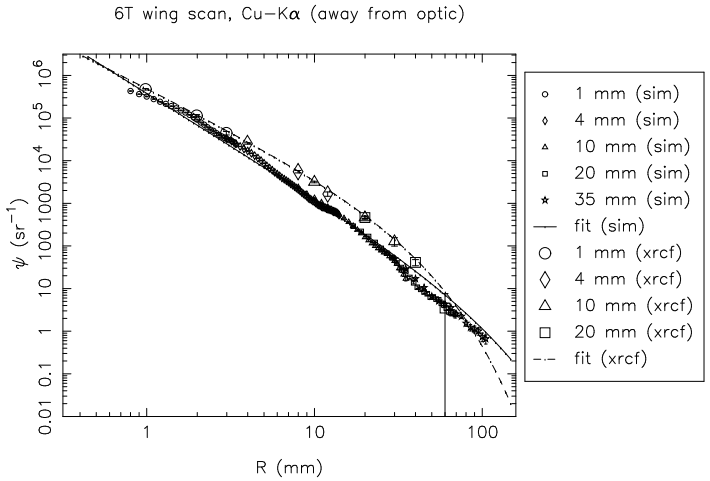

Figure 15.41: Shell 6T: Cu-Kα surface brightness, towards and away from the optic

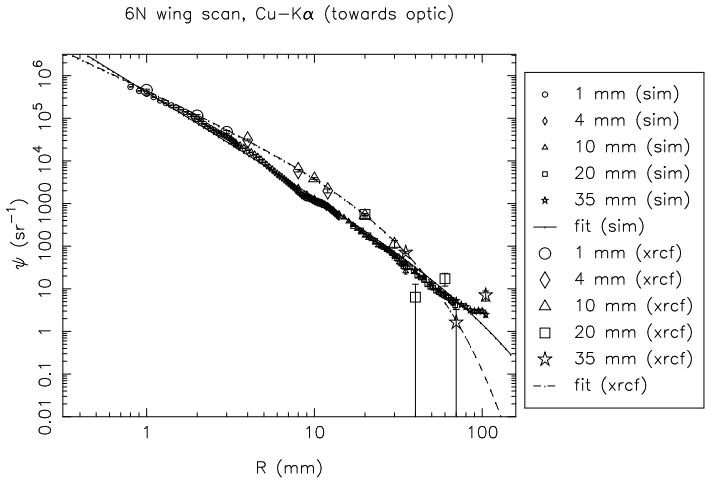

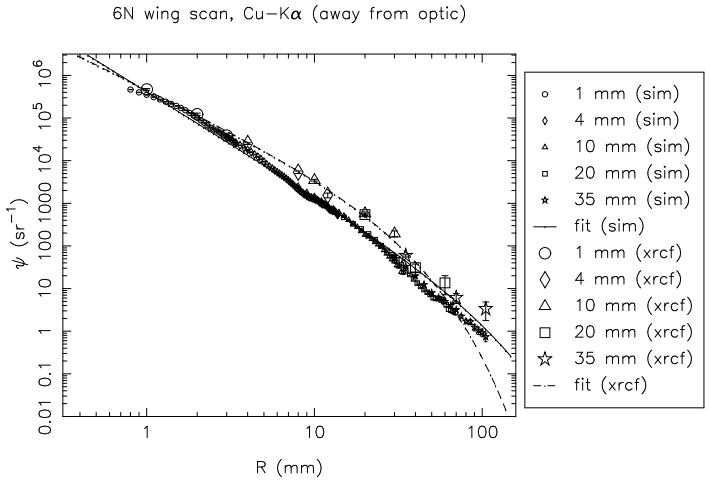

Figure 15.42: Shell 6N: Cu-Kα surface brightness, towards and away from the optic

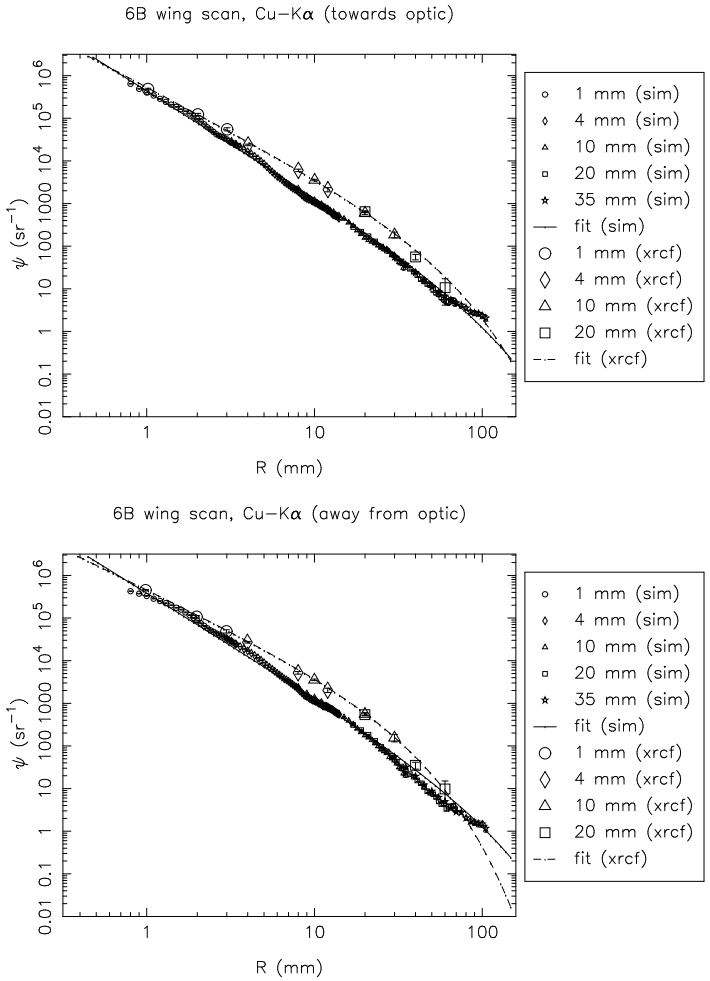

Figure 15.43: Shell 6B: Cu-Kα surface brightness, towards and away from the optic

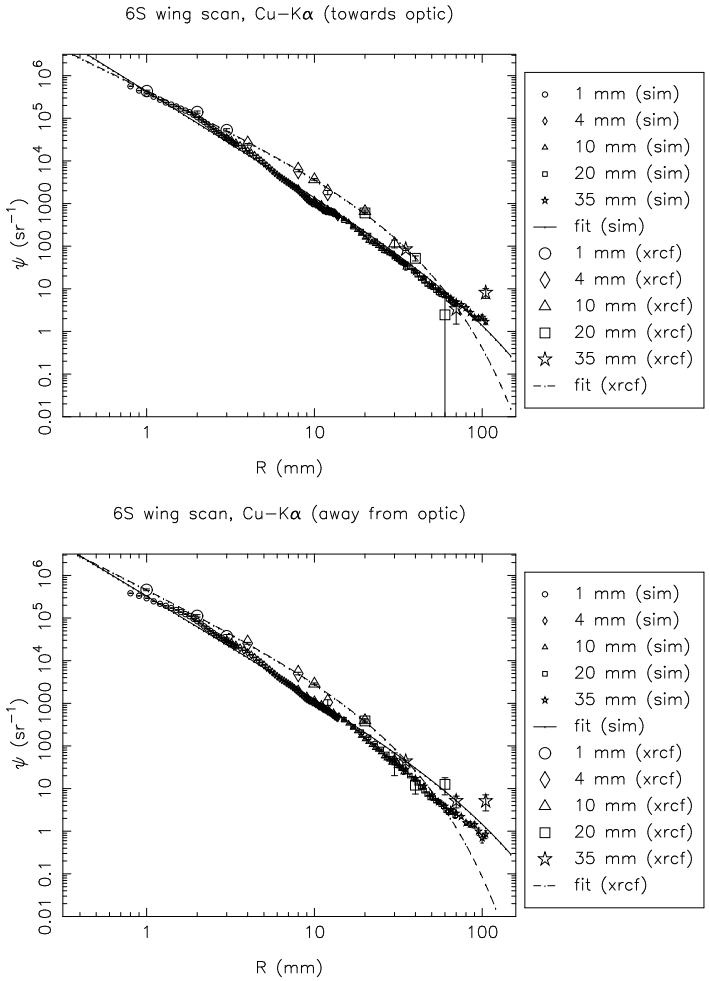

Figure 15.44: Shell 6S: Cu-Kα surface brightness, towards and away from the optic

15.2.5 Double Quadrant Scans

Table 15.9: Surface brightness fits and fractional excess effective area beyond the 35 mm pinhole. (Raytrace simulations and XRCF data, Shell 4N 4S)

Type	Quad	Line	Dir	a	b	c	fractional extra area
sim	4NS	Al	both	202617.000	3.204	10000.000	0.000137
xrcf	4NS	Al	both	254343.000	2.500	54.593	0.000825

Table 15.10: Surface brightness fits and fractional excess effective area beyond the 35 mm pinhole. (Raytrace simulations and XRCF data, Shell 6N 6S)

Type	Quad	Line	Dir	a	b	c	fractional extra area
sim	6NS	Al	both	195929.000	3.167	10000.000	0.000156
xrcf	6NS	Al	both	236995.000	2.500	35.660	0.000437

The surface brightness profiles for the double-quadrant scans are presented in Figure 15.45.

15.3 Out-of-Plane Scattering

Two sets of wing scans were conducted for which the scan was transverse to the direction of the quadrant. The first was the set of 6B Y-scans performed at C-Kα; these scans were intended to look for signs of dust scattering. The scattering from microroughness is mainly in-plane, and an excess out-of-plane component might be produced by dust scattering. The second set of scans were the 3B Y-scans at Al-Kα. These were performed in order to correct the double-quadrant wing scans (6N6S, 4N4S) for the fact that the 3B quadrant shutter was sticking and was open during the scans. The surface brightnesses based on these scans are plotted in Figure 15.46. For comparison, in-plane scans for the same shell and quadrant are also shown. Note, however, that the 3B out-of-plane scans were with HRMA at zero pitch and yaw, while the 3B in-plane scans were performed with HRMA yawed.

The out-of-plane component for the scattering due to microroughness is expected to be smaller than the in-plane component by a factor of order $\sin\alpha$ where α is the graze angle for the given shell. For shell 3 this factor would be about 1/83, while for shell 6 the factor would be about 1/130. The raytrace for the transverse scan for shell 6B at C-Kα suggests that the raytrace model may be lower in wing surface brightness by perhaps a factor of 10; however, the raytrace has very few counts in the wings, and the 10 mm pinhole positions show no counts this far into the wings. Longer raytraces are needed before the questions can be answered definitively. It is also worth noting that in the current scattering model, the out-of-plane component is calculated as $\sin\alpha$ times the in-plane component; this treatment may be too simplistic. The 3B out-of-plane scan data indicate a flatter slope than in the raytrace data, but this probably is not significant given the small number of data points and the large uncertainties in the values.

In Chapter 14, it was noted that the X-ray data for the 4 mm pinhole effective areas were peculiar in that the pinhole effective area for the position 4 mm to one side of the core was more than a factor of 10 larger than the corresponding position on the other side of the core (both for

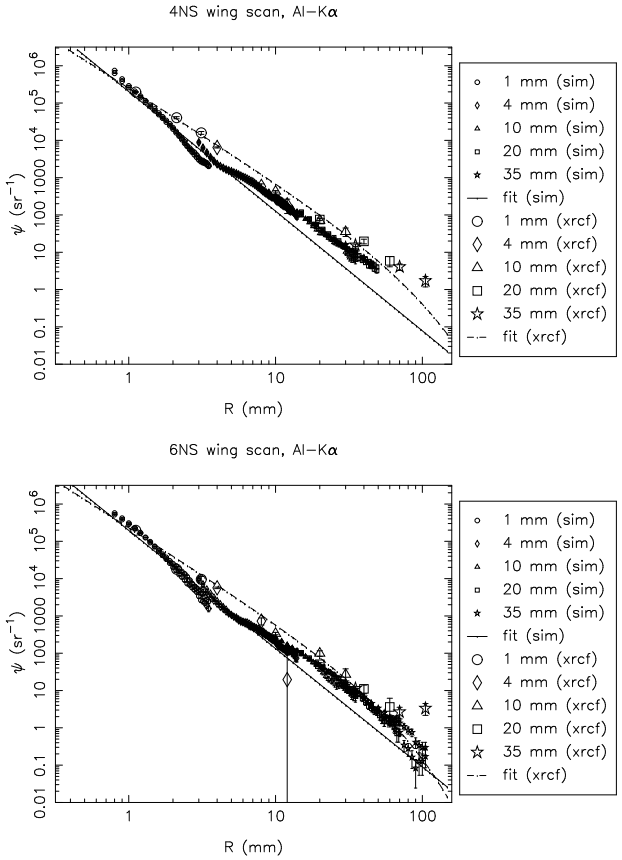

Figure 15.45: Double quadrant wing scan surface brightness: Al-Kα. Top: Shell 4, N and S quadrant. Bottom: Shell 6, N and S quadrant.

the in-plane and out-of-plane cases). In Figure 15.46 these are the diamond-shaped points at $R = 4$ mm.

15.4 Comparison with Encircled Energy Data

In order to show the consistency between the wing scan surface brightness data and the encircled energy data, we have plotted in Figure 15.47 the surface brightness profile measured in two different ways, for the one case for which this is feasible. The encircled energy tests are described in Chapter 16; these tests give a measurement of the surface brightness integrated out to the radius of a given aperture centered on the peak of the distribution, so numerically differentiating the effective area *vs.* radius curve gives us the surface brightness profile. In order to make a direct

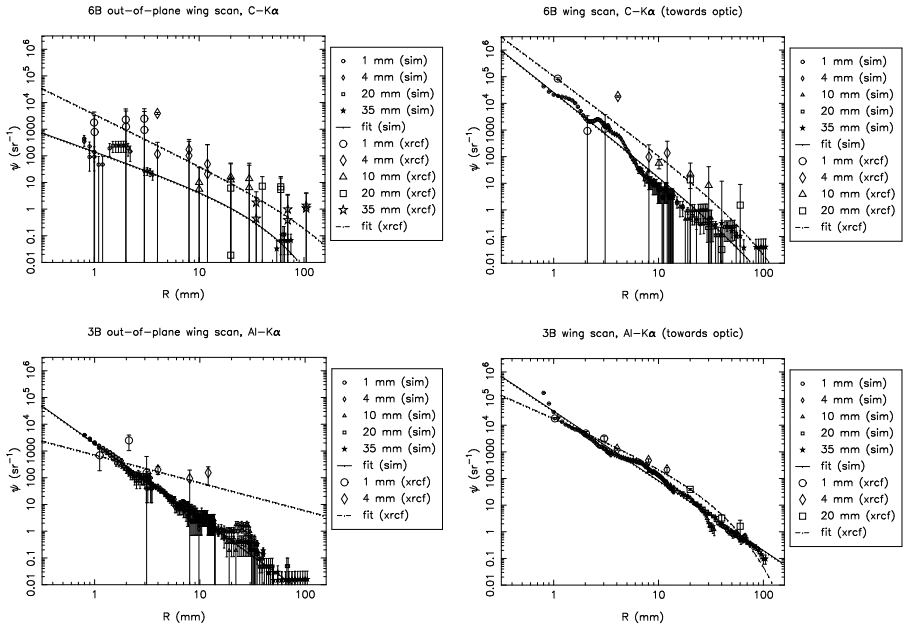

Figure 15.46: Out-of-plane scans, compared to in-plane scans. Top left: 6B Y scan at C-Kα (out of plane). Top right: 6B Z scan at C-Kα (in plane, towards optic). Bottom left: 3B Y scan at Al-Kα (out of plane). Bottom right: 3B Z scan at Al-Kα (in plane).

comparison with the wingscan surface brightness measurements, the surface brightness obtained by differentiating the effective area curve was scaled by a factor of $2 \times 88/360$ times the effective area within an on-axis 35 mm diameter pinhole, to account for the fact that the wing scans were done one quadrant at a time (see §15.2). This surface brightness and that for the 1S Ti-Kα wing scan are plotted in Figure 15.47. The case of Ti K-α for Shell 1 is unique in that the encircled energy curve is both steep enough in the outer parts and well enough measured that the numerical derivative can be computed with finite error bars. Other cases examined showed the wing scan data at a level not inconsistent with the encircled energy data, but due to the large error bars on the latter, no stronger conclusions can be drawn. Note also the HRMA was yawed by $-1'$ during this effective area experiment and by $-4.56'$ in this wing scan measurement (see §D.7.2 and Table 14.3).

15.5 "$2W_1$" Profiles

Finally, given the surface brightness profiles for various energies, the "$2W_1$" functions describing the surface can be evaluated. The value of $2W_1$ is based on equation (7) of O'Dell et al. (1992):

$$2W_1(f) \simeq \frac{f\psi(\theta)\lambda^4}{16\pi \sin^4 \alpha} \tag{15.9}$$

where $f = \theta \sin\alpha/\lambda$ is the spatial frequency, θ is the off-axis angle, α is the mean graze angle for the mirror shell, λ is the X-ray wavelength, and ψ is the surface brightness normalized to a scaled on-axis effective area measured using the largest 35 mm pinhole (see §15.2 and also the MST preliminary report).

It should be emphasized that the PSD thus calculated is *per surface*.

The resulting $2W_1$ data are fit with functions of the form

$$2W_1(f) = af^{-b}e^{-f/c}. \tag{15.10}$$

Again, the raytrace data are not fit well by this particular form; as for the surface brightness fits to the raytrace data, the exponential scale length parameter was limited to fall within a given range of values, in this case 190–10000. The lower limit (obtained by trial and error) was chosen to reproduce approximately the overall shape of the curve at large radius. As before, the overall shape fits reasonably well in some cases but not in others; in future analyses, different limit ranges should be applied on a case by case basis.

In the following tables and figures, the $2W_1$ obtained from the X-ray data are compared to the $2W_1$ based on the raytrace simulations.

The agreement between the XRCF data and the raytrace simulations seems to be generally better towards smaller f values. The agreement towards larger f gets significantly worse, particularly for the larger shells. The raytrace models for shell 6 indicate a high shoulder towards small f; the X-ray data shows some support for this (see Figures 15.60–15.63).

The mean-square "roughness" values derived from the fits also shows the increasing discrepancy towards larger values for spatial frequency. The σ^2 evaluated for 1–10 mm^{-1} agree much better

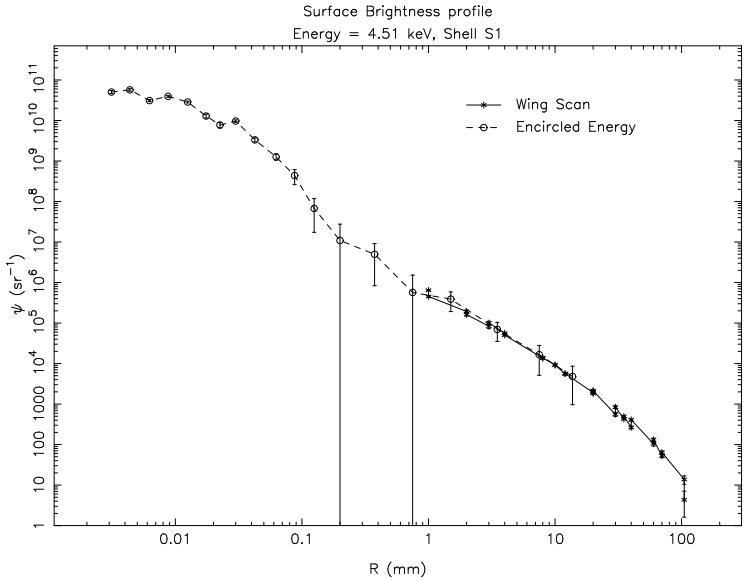

Figure 15.47: Surface Brightness *vs.* Radius for Shell 1S at Ti K-α. This is a composite plot based on both wing scan data and an encircled energy test.

than the values for 100–1000 mm^{-1}. Comparing the values derived from the fits by integrating from 1–1000 mm^{-1}, it can be seen that for shells 1 and 3, the XRCF values are about a factor of two higher than the raytrace values, about a factor of 1.7 higher for shell 4, and about 1.3 times higher for shell 6; generally, the discrepancy tends to be smaller for the smaller shells. The values for the XRCF data fits for scattering towards *vs.* away from the optic seem to be comparable except in the case of shell 3, in which case the derived roughness is considerably larger for directions away from the optic than towards the optic. As noted in the discussion of the surface brightnesses, this effect (if real, and not an artifact of the reductions and analysis) is currently not understood.

Finally, derived roughnesses from the double-quadrant scans (integrated over 1–1000 mm^{-1}) are about 3 to 3.5 times larger than the corresponding single-quadrant scans. The data were processed for the double-quadrant scans using the same value for a_{eff}^{tot} as in the single quadrant scans (see Eq. Eq. 15.1); this factor should have been a factor of two larger for the double-quadrant scans (two quadrants now contribute) so a factor of 2 of the discrepancy is explained by the normalization factor. The remaining discrepancy may be in part a result of the differences in the experimental setup (*e.g.*, the HRMA was not pitched or yawed in the double-quadrant scans), or a bias resulting from the paucity of double-quadrant data points. However, the discrepency appears to be larger than can be easily explained by such effects.

15.5.1 Shell 1 scans

Table 15.11: Single quadrant wingscan $2W_1$ fits and mean square roughness (Raytrace simulation and XRCF data, Shell 1)

Type	Quad	Dir	a	b	c	σ^2_{1-10}	σ^2_{10-100}	$\sigma^2_{100-1000}$	σ^2_{1-1000}
sim	1T	in	6.935	1.238	190.000	12.062	5.935	1.060	19.056
sim	1T	out	3.828	1.104	190.000	7.689	5.111	1.177	13.978
sim	1N	in	6.914	1.221	190.000	12.249	6.269	1.158	19.676
sim	1N	out	4.612	1.129	190.000	9.011	5.663	1.244	15.918
sim	1B	in	7.941	1.247	190.000	13.689	6.608	1.161	21.458
sim	1B	out	3.863	1.069	190.000	8.059	5.783	1.420	15.263
sim	1S	in	7.969	1.247	190.000	13.738	6.631	1.165	21.534
sim	1S	out	3.692	1.068	190.000	7.711	5.548	1.366	14.625
xrcf	T	in	6.100	1.009	761.127	13.830	12.944	8.396	35.170
xrcf	T	out	5.791	0.947	271.357	13.975	13.888	5.783	33.647
xrcf	N	in	5.891	0.921	182.656	14.553	14.440	4.498	33.491
xrcf	N	out	5.350	0.895	210.773	13.670	14.729	5.493	33.892
xrcf	B	in	5.824	1.062	800.000	12.438	10.335	6.093	28.866
xrcf	B	out	3.948	0.870	236.156	10.415	12.077	5.208	27.700
xrcf	S	in	3.844	0.871	245.184	10.135	11.789	5.236	27.160
xrcf	S	out	7.816	1.041	314.447	16.965	13.871	5.347	36.184

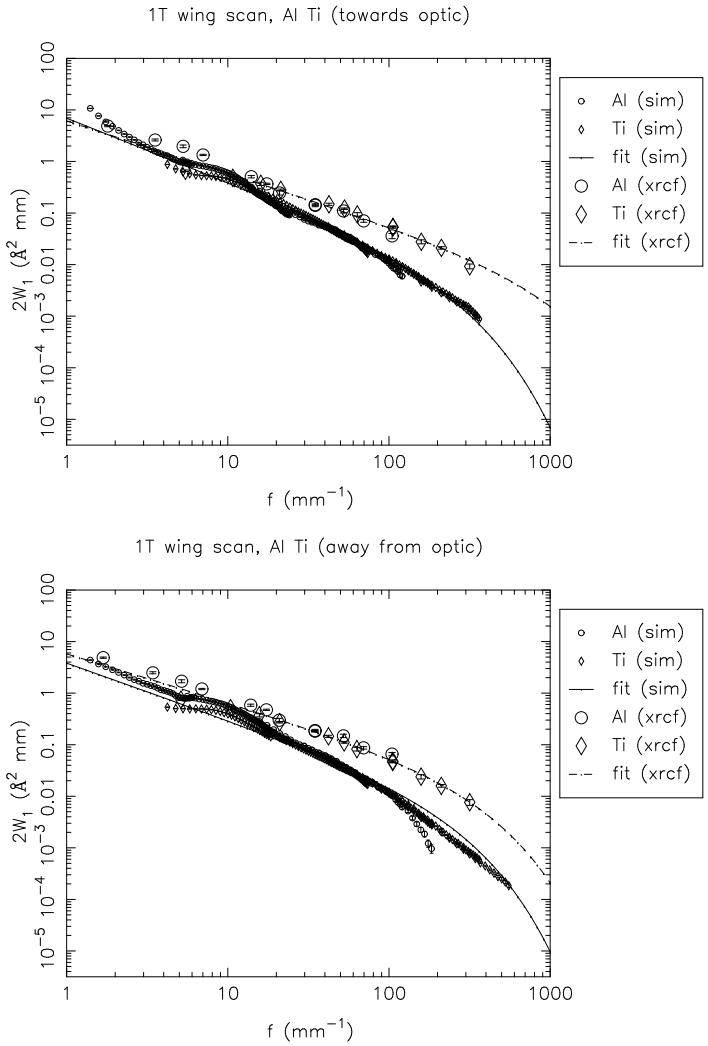

Figure 15.48: Shell 1T: $2W_1$ profiles, towards and away from the optic. XRCF data (*xrcf*) *vs.* raytrace data (*sim*).

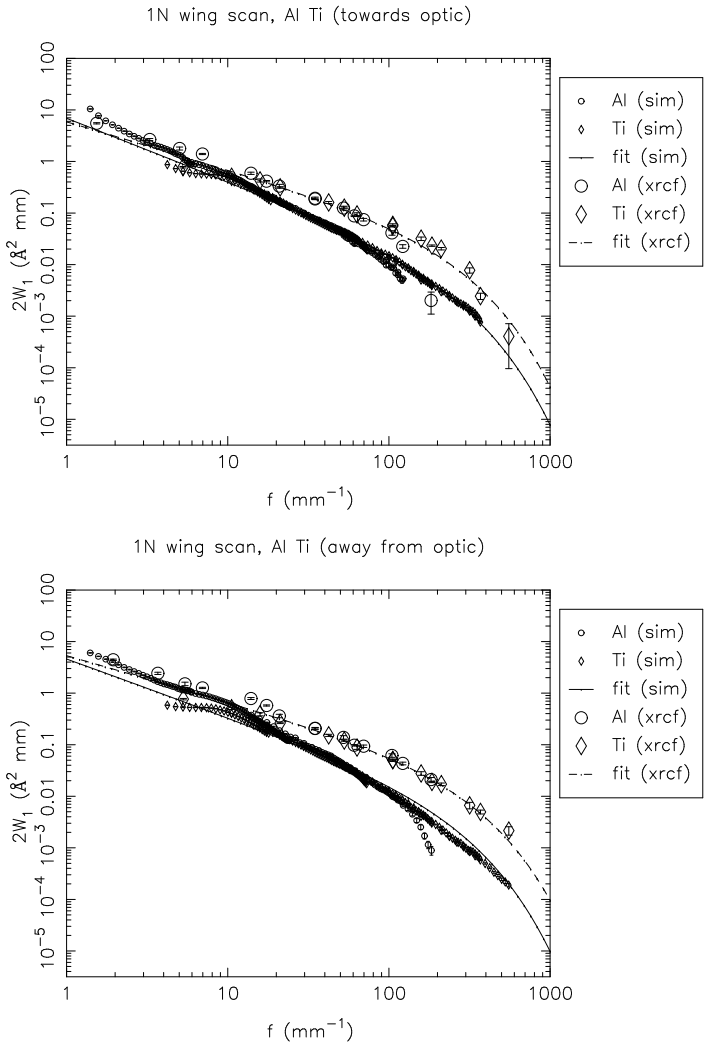

Figure 15.49: Shell 1N: $2W_1$ profiles, towards and away from the optic. XRCF data (*xrcf*) *vs.* raytrace data (*sim*).

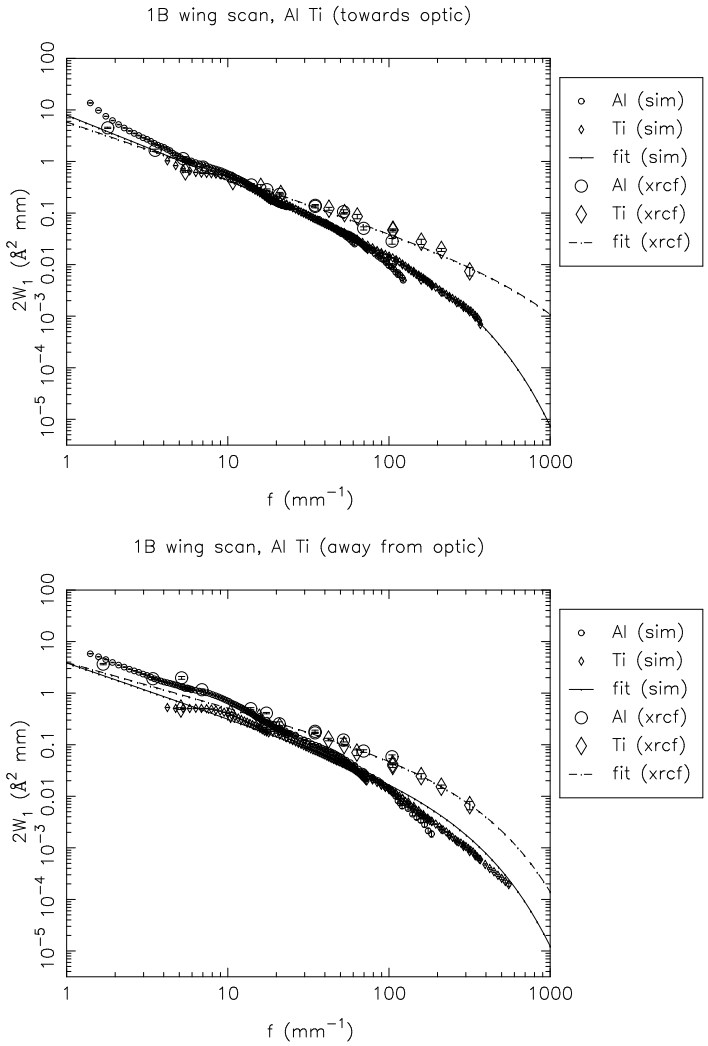

Figure 15.50: Shell 1B: $2W_1$ profiles, towards and away from the optic. XRCF data (*xrcf*) *vs.* raytrace data (*sim*).

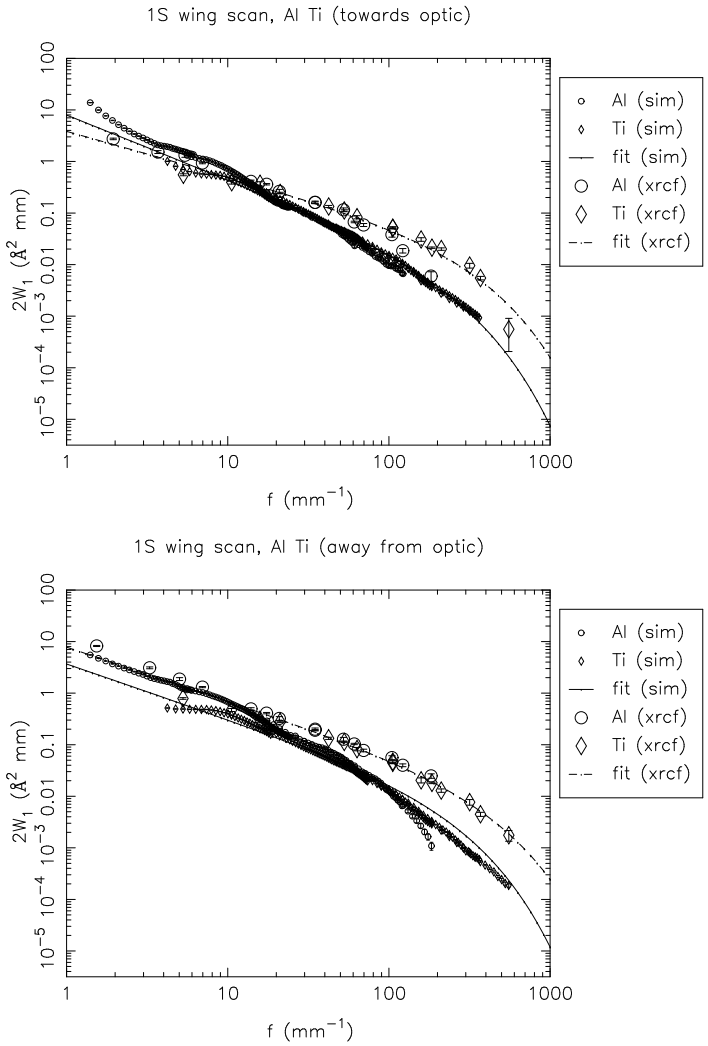

Figure 15.51: Shell 1S: $2W_1$ profiles, towards and away from the optic. XRCF data (*xrcf*) *vs.* raytrace data (*sim*).

15.5.2 Shell 3 scans

Table 15.12: Single quadrant wingscan $2W_1$ fits and mean square roughness (Raytrace simulation and XRCF data, Shell 3)

Type	Quad	Dir	a	b	c	σ^2_{1-10}	σ^2_{10-100}	$\sigma^2_{100-1000}$	σ^2_{1-1000}
sim	3T	in	3.999	1.555	2622.350	5.191	1.431	0.360	6.982
sim	3T	out	2.563	1.401	190.000	3.786	1.294	0.169	5.250
sim	3N	in	4.831	1.582	666.650	6.099	1.533	0.278	7.911
sim	3N	out	2.729	1.376	190.000	4.131	1.493	0.205	5.829
sim	3B	in	4.254	1.542	454.649	5.557	1.502	0.256	7.316
sim	3B	out	2.509	1.389	190.000	3.750	1.318	0.176	5.244
sim	3S	in	3.960	1.508	210.044	5.296	1.445	0.166	6.907
sim	3S	out	2.341	1.400	190.000	3.462	1.187	0.155	4.803
xrcf	T	in	3.283	1.215	800.000	5.936	3.477	1.475	10.888
xrcf	T	out	12.797	1.712	500.000	14.402	2.656	0.329	17.386
xrcf	N	in	2.537	1.138	360.117	4.954	3.295	1.142	9.390
xrcf	N	out	12.378	1.609	488.997	15.230	3.548	0.542	19.320
xrcf	B	in	2.069	1.021	168.669	4.546	3.558	0.855	8.959
xrcf	B	out	5.237	1.336	443.104	8.332	3.592	0.930	12.854
xrcf	S	in	2.243	1.084	287.982	4.635	3.407	1.136	9.177
xrcf	S	out	3.704	1.217	210.807	6.600	3.460	0.703	10.763

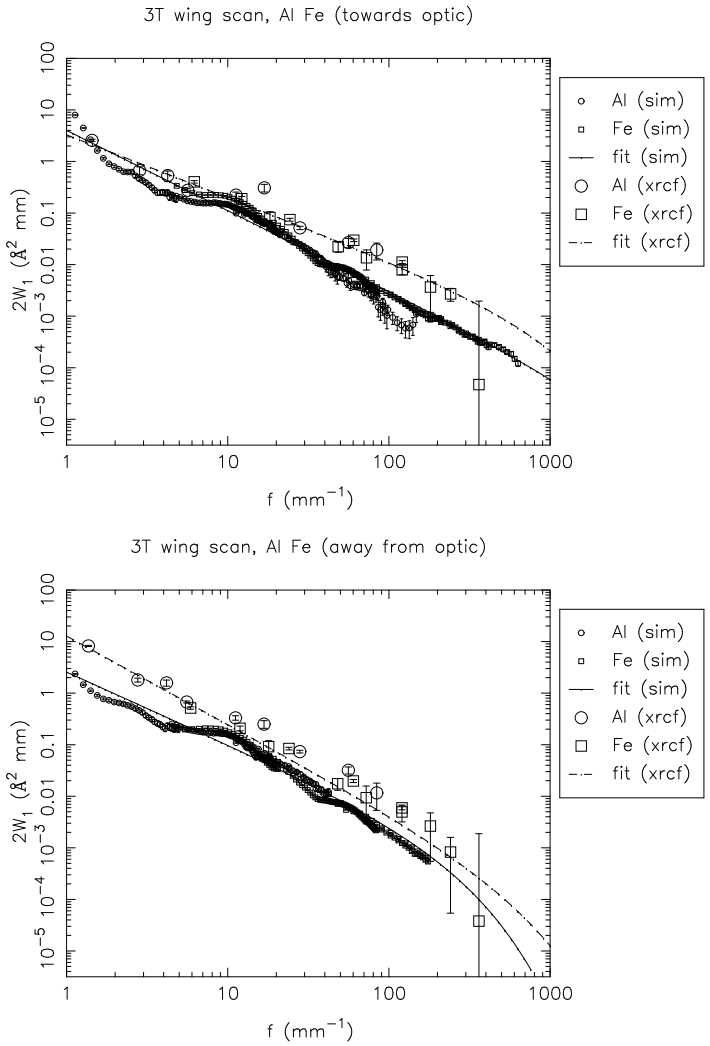

Figure 15.52: Shell 3T: $2W_1$ profiles, towards and away from the optic. XRCF data (*xrcf*) *vs.* raytrace data (*sim*).

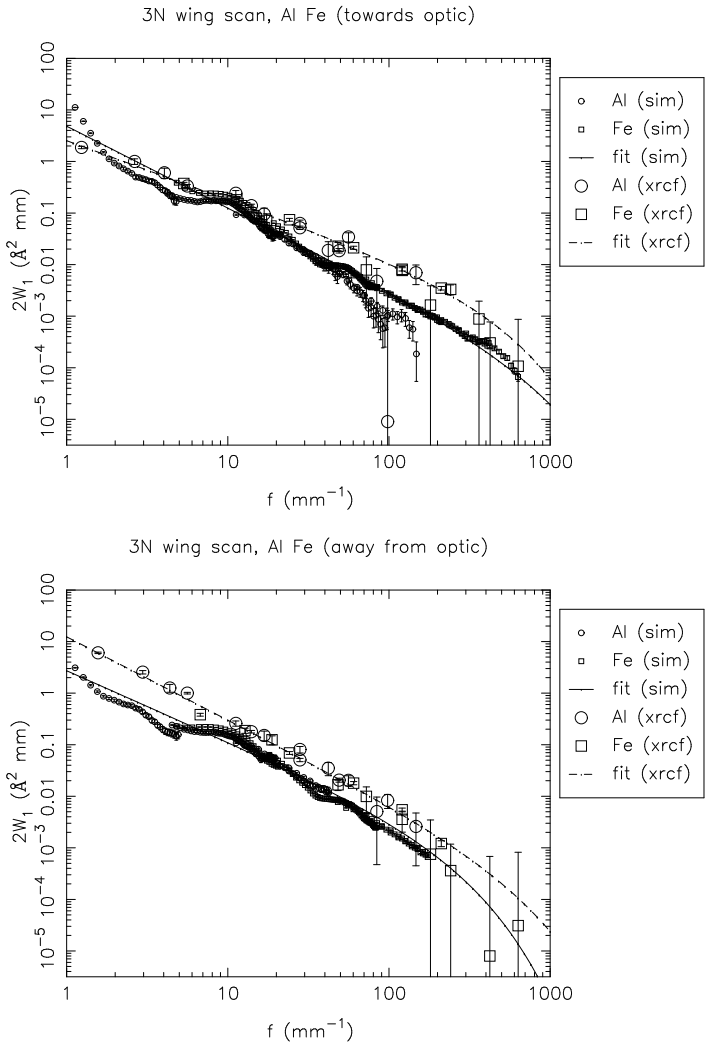

Figure 15.53: Shell 3N: $2W_1$ profiles, towards and away from the optic. XRCF data (*xrcf*) *vs.* raytrace data (*sim*).

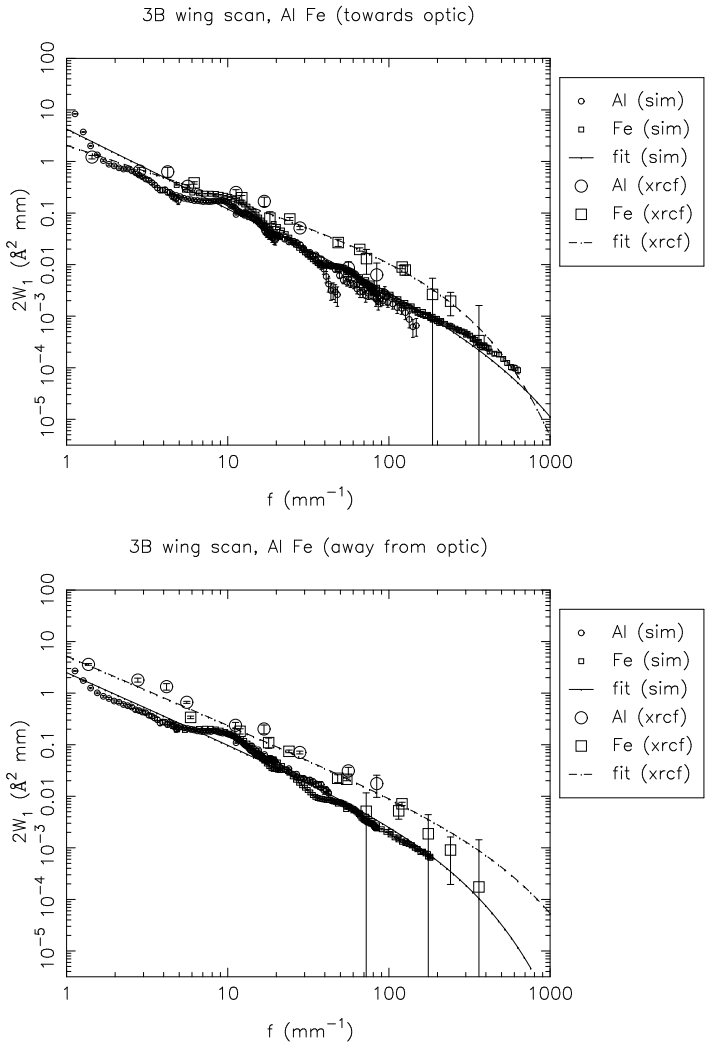

Figure 15.54: Shell 3B: $2W_1$ profiles, towards and away from the optic. XRCF data (*xrcf*) *vs.* raytrace data (*sim*).

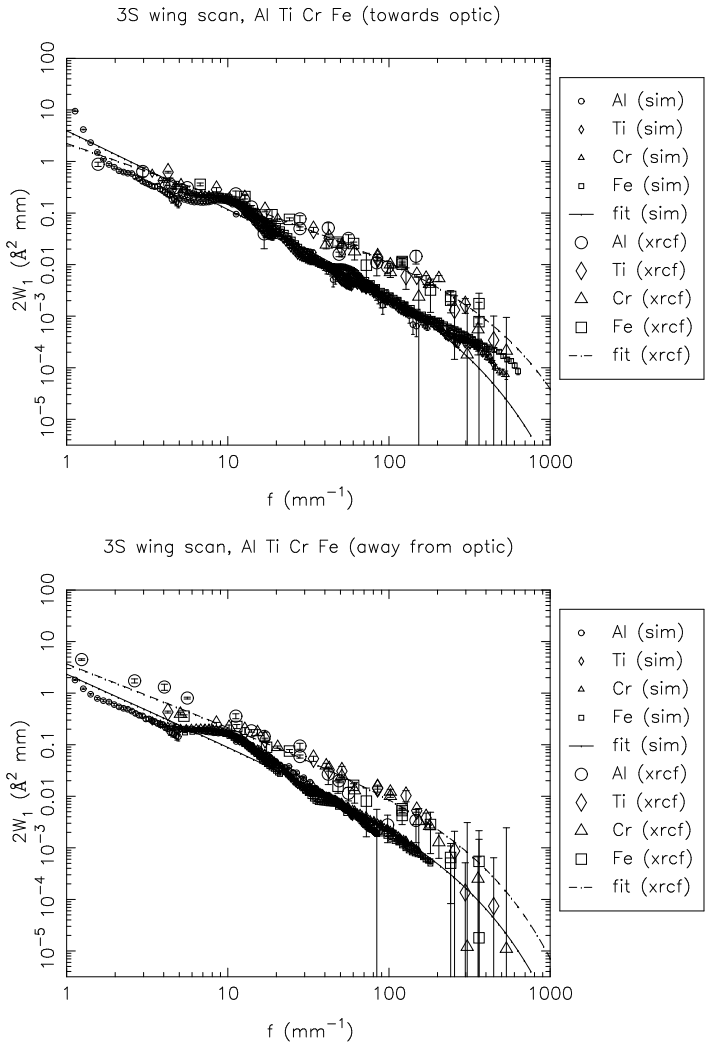

Figure 15.55: Shell 3S: $2W_1$ profiles, towards and away from the optic. XRCF data (*xrcf*) *vs.* raytrace data (*sim*).

15.5.3 Shell 4 scans

Table 15.13: Single quadrant wingscan $2W_1$ fits and mean square roughness (Raytrace simulation and XRCF data, Shell 4)

Type	Quad	Dir	a	b	c	σ^2_{1-10}	σ^2_{10-100}	$\sigma^2_{100-1000}$	σ^2_{1-1000}
sim	4T	in	4.183	1.462	10000.000	5.929	2.042	0.685	8.656
sim	4T	out	3.013	1.363	346.607	4.657	1.854	0.398	6.909
sim	4N	in	14.699	1.945	10000.000	13.784	1.560	0.173	15.518
sim	4N	out	4.619	1.438	434.562	6.648	2.268	0.470	9.386
sim	4B	in	17.226	2.029	10000.000	15.176	1.418	0.130	16.724
sim	4B	out	3.610	1.384	337.913	5.466	2.073	0.421	7.960
sim	4S	in	4.815	1.481	10000.000	6.702	2.208	0.709	9.619
sim	4S	out	2.768	1.367	427.547	4.270	1.713	0.409	6.392
xrcf	T	in	11.518	1.600	800.000	14.320	3.478	0.641	18.440
xrcf	T	out	8.829	1.563	500.000	11.323	2.933	0.498	14.754
xrcf	N	in	6.997	1.413	800.000	10.354	3.857	1.067	15.278
xrcf	N	out	7.095	1.358	500.000	11.053	4.567	1.195	16.815
xrcf	B	in	20.062	1.791	800.000	21.185	3.323	0.404	24.912
xrcf	B	out	10.651	1.505	500.000	14.407	4.259	0.818	19.484
xrcf	S	in	4.283	1.189	319.651	7.907	4.634	1.347	13.888
xrcf	S	out	5.439	1.259	259.463	9.307	4.557	1.001	14.865

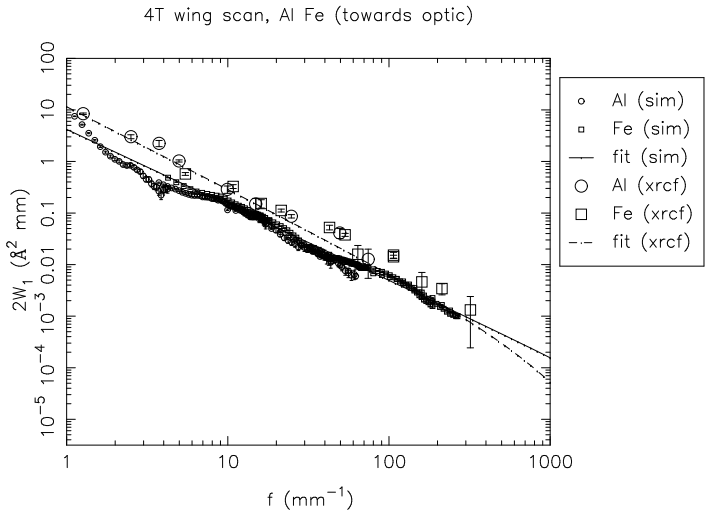

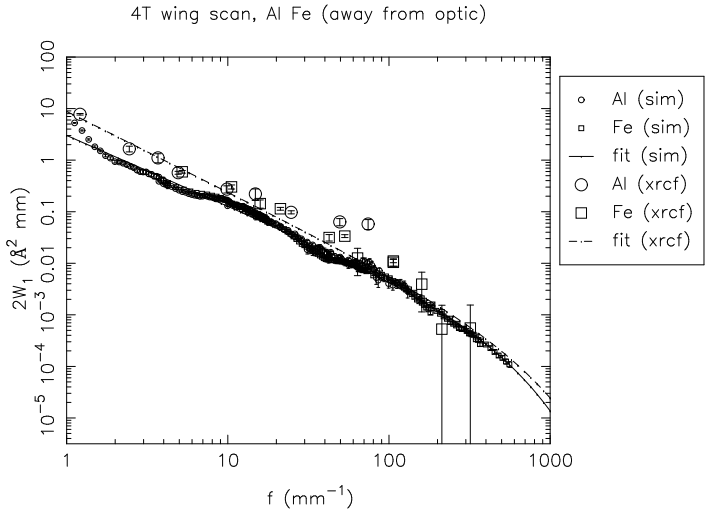

Figure 15.56: Shell 4T: $2W_1$ profiles, towards and away from the optic. XRCF data (*xrcf*) *vs.* raytrace data (*sim*).

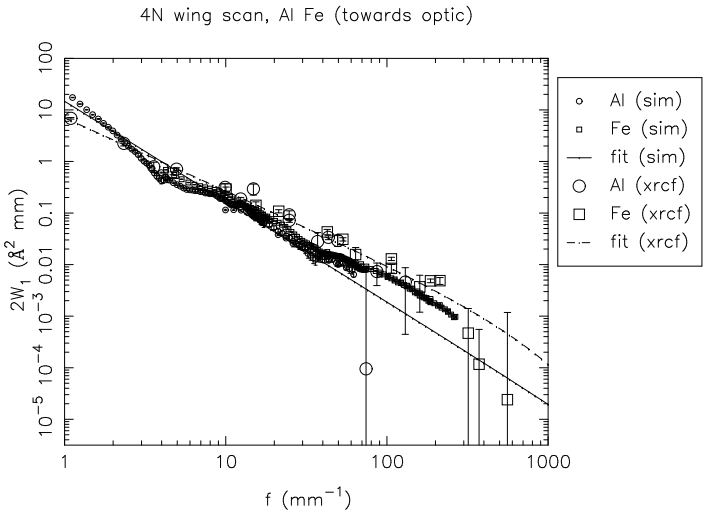

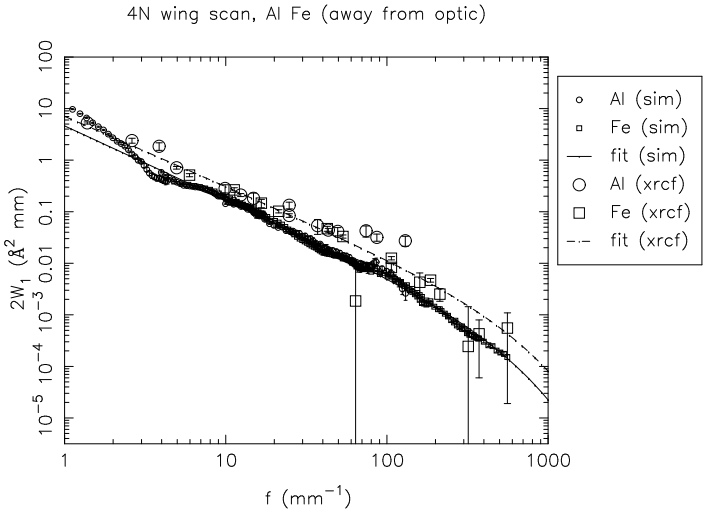

Figure 15.57: Shell 4N: $2W_1$ profiles, towards and away from the optic. XRCF data (*xrcf*) *vs.* raytrace data (*sim*).

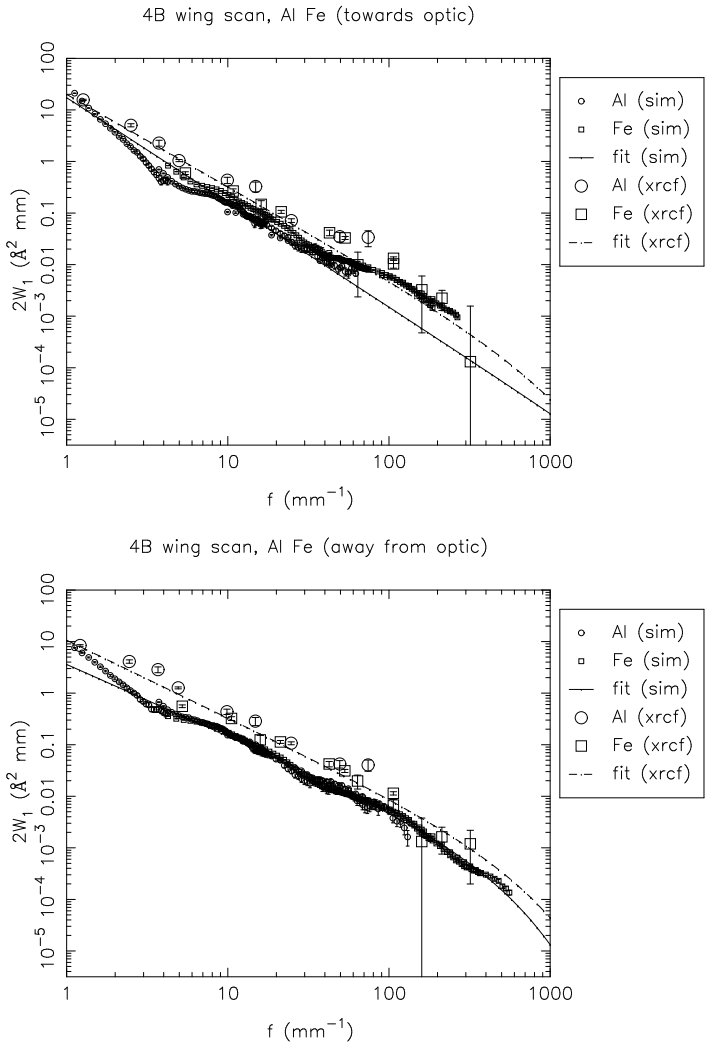

Figure 15.58: Shell 4B: $2W_1$ profiles, towards and away from the optic. XRCF data (*xrcf*) *vs.* raytrace data (*sim*).

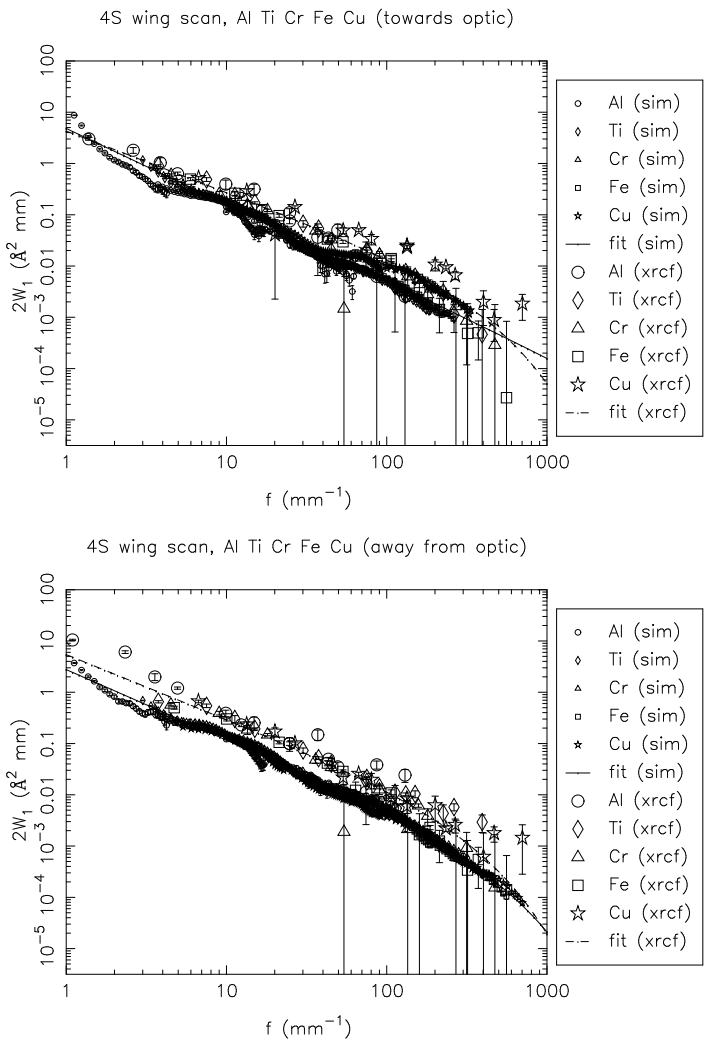

Figure 15.59: Shell 4S: $2W_1$ profiles, towards and away from the optic. XRCF data (*xrcf*) *vs.* raytrace data (*sim*).

15.5.4 Shell 6 scans

Table 15.14: Single quadrant wingscan $2W_1$ fits and mean square roughness (Raytrace simulation and XRCF data, Shell 6)

Type	Quad	Dir	a	b	c	σ^2_{1-10}	σ^2_{10-100}	$\sigma^2_{100-1000}$	σ^2_{1-1000}
sim	6T	in	5.441	1.365	190.000	8.323	3.083	0.432	11.838
sim	6T	out	4.866	1.334	190.000	7.680	3.052	0.454	11.187
sim	6N	in	5.842	1.387	190.000	8.751	3.089	0.415	12.254
sim	6N	out	5.273	1.329	190.000	8.366	3.364	0.506	12.236
sim	6B	in	10.047	1.644	1523.130	12.037	2.685	0.516	15.238
sim	6B	out	4.877	1.334	190.000	7.697	3.059	0.455	11.211
sim	6S	in	6.953	1.456	190.734	9.743	2.946	0.347	13.036
sim	6S	out	4.869	1.343	190.000	7.617	2.968	0.434	11.019
xrcf	T	in	3.785	1.027	172.717	8.264	6.412	1.558	16.233
xrcf	T	out	15.978	1.658	500.000	18.834	3.929	0.545	23.308
xrcf	N	in	4.932	1.081	107.681	10.005	6.201	0.810	17.017
xrcf	N	out	6.979	1.232	153.534	12.167	5.858	0.868	18.893
xrcf	B	in	28.228	2.147	800.000	22.787	1.581	0.088	24.456
xrcf	B	out	6.293	1.208	194.071	11.304	5.973	1.151	18.428
xrcf	S	in	4.812	1.089	135.492	9.745	6.277	1.061	17.084
xrcf	S	out	6.796	1.225	120.423	11.859	5.514	0.637	18.010

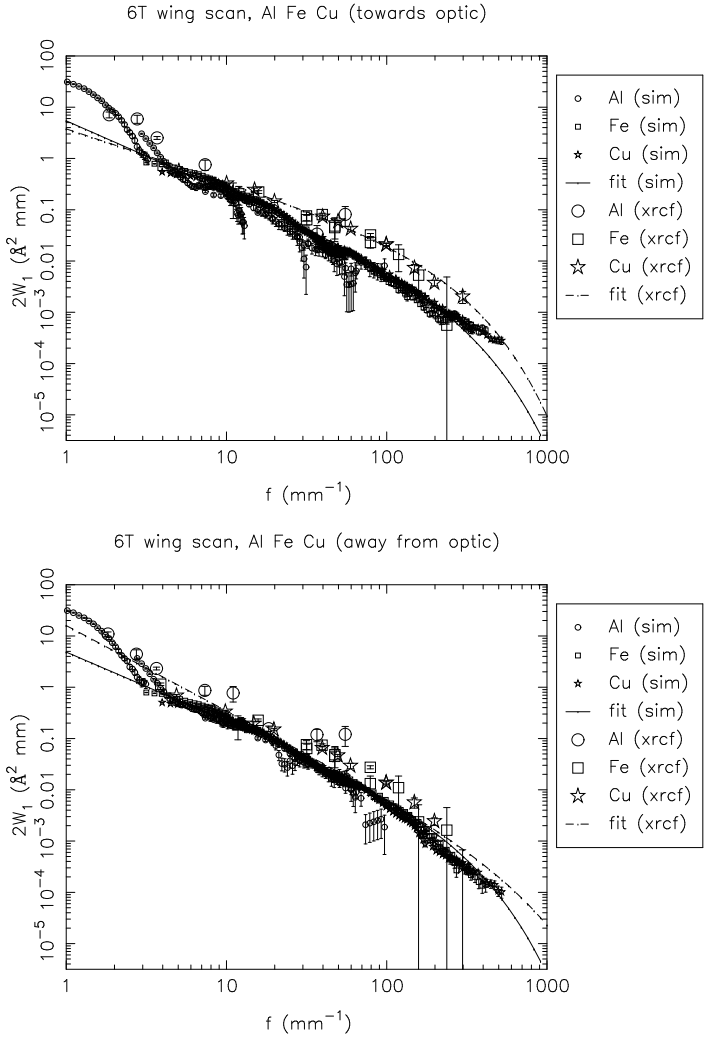

Figure 15.60: Shell 6T: $2W_1$ profiles, towards and away from the optic. XRCF data (*xrcf*) *vs.* raytrace data (*sim*).

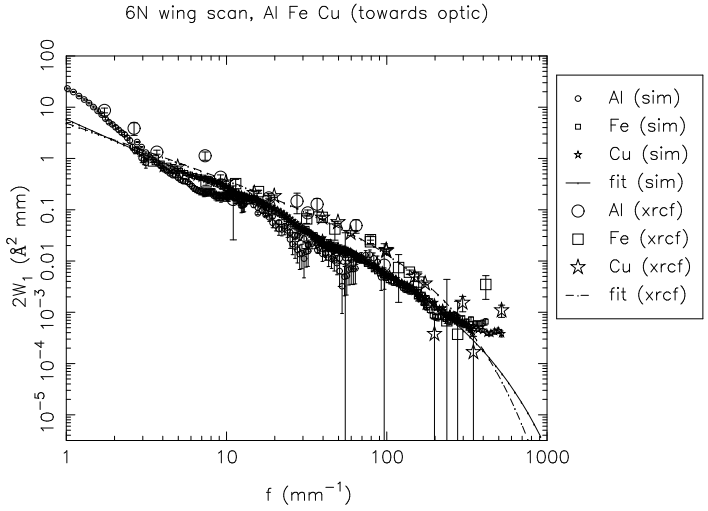

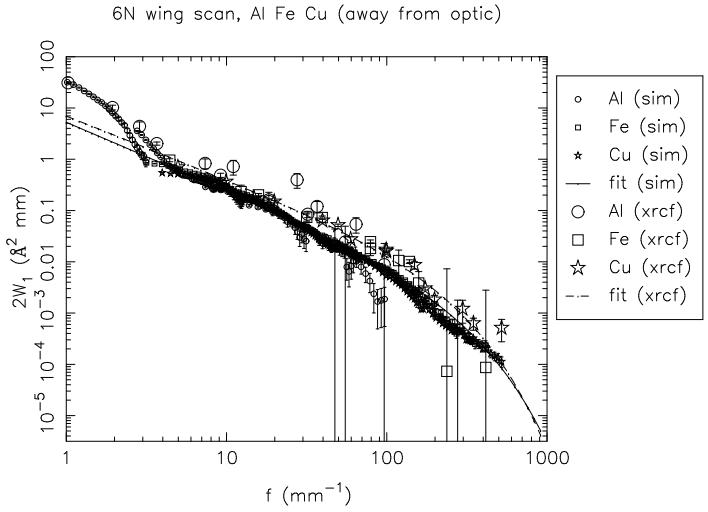

Figure 15.61: Shell 6N: $2W_1$ profiles, towards and away from the optic. XRCF data (*xrcf*) *vs.* raytrace data (*sim*).

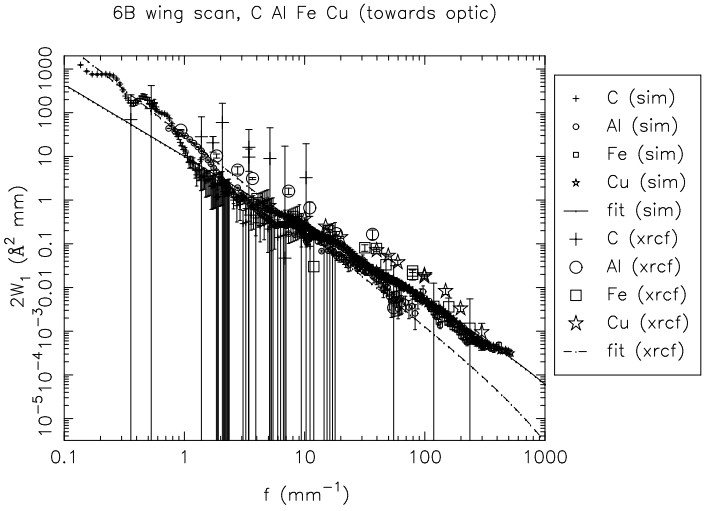

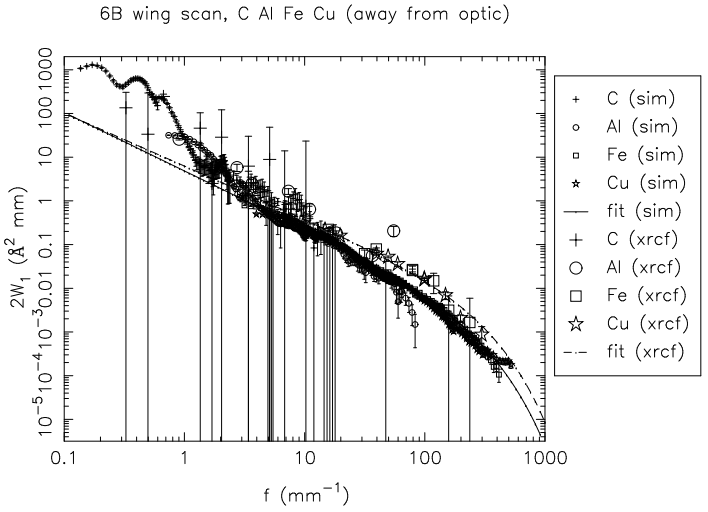

Figure 15.62: Shell 6B: $2W_1$ profiles, towards and away from the optic. XRCF data (*xrcf*) *vs.* raytrace data (*sim*).

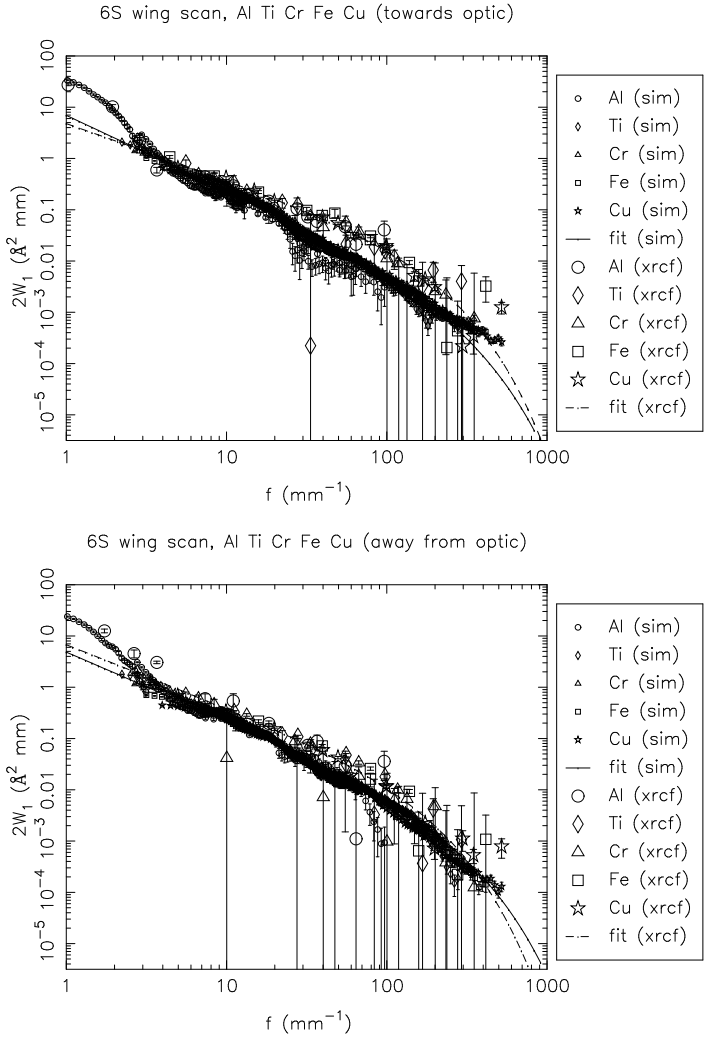

Figure 15.63: Shell 6S: $2W_1$ profiles, towards and away from the optic. XRCF data (*xrcf*) *vs.* raytrace data (*sim*).

15.5.5 2 Quadrant Scans

Table 15.15: Double quadrant wingscan $2W_1$ fits and mean square roughness (Raytrace simulation and XRCF data, Shell 4NS)

Type	Quad	Dir	a	b	c	σ^2_{1-10}	σ^2_{10-100}	$\sigma^2_{100-1000}$	σ^2_{1-1000}
sim	4NS	both	40.548	2.293	1000.000	29.687	1.480	0.062	31.230
xrcf	NS	both	38.249	1.763	800.000	41.332	6.912	0.893	49.138

Table 15.16: Double quadrant wingscan $2W_1$ fits and mean square roughness (Raytrace simulation and XRCF data, Shell 6NS)

Type	Quad	Dir	a	b	c	σ^2_{1-10}	σ^2_{10-100}	$\sigma^2_{100-1000}$	σ^2_{1-1000}
sim	6NS	both	49.306	2.280	1000.000	36.424	1.874	0.081	38.379
xrcf	NS	both	32.181	1.500	200.000	43.321	11.952	1.343	56.616

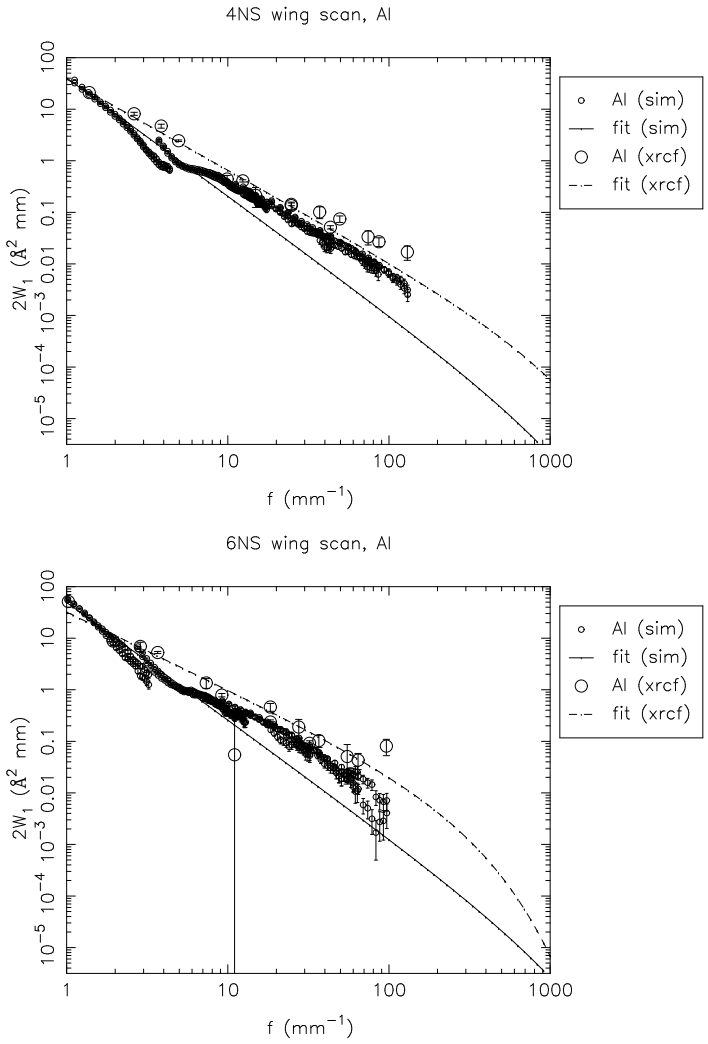

Figure 15.64: Double quadrant wing scans. Top: Shell 4 N and S quadrants: $2W_1$ profiles. Bottom: Shell 4 N and S quadrants: $2W_1$ profiles. XRCF data (*xrcf*) *vs.* raytrace data (*sim*).

15.6 Outstanding Analysis Issues

The analysis can be improved in a number of ways:

- In the case of the raytrace simulations, the fits to the surface brightness data and to the $2W_1$ data are not very good in many cases. The raytrace data show structure which is not captured by the simple fit function; on the other hand, the XRCF data set is sparse enough that a more elaborate fitting function is not really justified. In the raytrace fits, a lower limit to the exponential cutoff scale was specified. This was estimated by inspecting the resulting fits; the same cutoff value was used for all of the ψ fits (and similarly, for the $2W_1$ fits). Consequently, the fit at large radius can be bad. This affects the estimates of the fractional effective area outside the 35 mm pinhole (in the case of the ψ fits) or the mean square roughness σ^2 (in the case of the $2W_1$ fits).
- The truncation of the raytrace data sets to remove points affected by shutter vignetting was done by estimating a cutoff based on visual inspection of the curves. Raytraces with/without adjacent shutters in (shutters for other shells in the same quadrant) would provide a better handle on when the shutter vignetting kicks in.
- The surface brightness, ψ, is scaled by a a factor $2 \times 88/360$ to account for the fact that the experiment used a single quadrant at a time. This should be checked against raytraces for 1 *vs.* 4 quadrants open in a given direction, *e.g.*, nS *vs.* 1S3S4S6S, and for on-axis versus tilted HRMA cases. However, such raytraces would have to be much longer than the ones used in the current analysis. For now, this effect should more or less scale out because the raytraces were processed in the same way as the XRCF data.
- The comparison of scattering towards *vs.* away from the optic has only been given a cursory examination; further work needs to be done to determine whether there are discernible trends from quadrant to quadrant.
- The transverse wing scan data poorly understood at present. They are significantly below the corresponding in-plane measurements, but they need to be compared to raytraces in order to assess whether they are consistent with the scattering calculations.
- The double-quadrant wing scan data are *very* sparse; the analysis and interpretation of these data are incomplete at present.

15.7 Implications for Scattering Models

From the foregoing it is clear the raytrace scattering model needs to be improved. The raytraces consistently underpredict the pinhole effective area for the larger pinholes. The surface brightness plots and the $2W_1$ plots indicate a steeper power-law slope than is seen in the wing scan data. The mean-square roughness for spatial frequencies $1 - 1000$ mm^{-1} as deduced from the XRCF wing scan data are larger than that from the raytrace by about a factor of two for shells 1, 3, and 4, and about a factor 1.3 for shell 6. The disagreement between X-ray determinations and raytrace estimates get worse for larger spatial frequency f; this can also be seen in the figures in that the slopes of the $2W_1$ curves based on XRCF data tend to be flatter than the $2W_1$ curves obtained from the raytraces. The derived roughness parameter, σ^2, obtained by integrating the $2W_1$ functions over some passband, show puzzling variations: in quadrants 1S, 3T, 3N, 3B, 3S, and 4S, the σ^2 derived from the fits for scattering away from the optic surface are considerably larger than those for scattering towards the optic surface. In addition, the roughness derived from the double-quadrant scans is a factor of about 2 larger than that obtained from the single quadrant scans (taking into account the difference in normalization); this may result in part from the different illumination

pattern (tilted *vs.* untilted HRMA), but further investigation is warranted.

Chapter 16

Encircled Energy

Diab Jerius

In this chapter we present a set of encircled energy curves, measured at various energies and for various mirror combinations.

The experiments and data reductions were described in Chapter 12 and Chapter 9, respectively. We present here plots of the effective area captured within a circular aperture centered on the focused image, as functions of the aperture diameter.

Some of the experiments were done one shell at a time, on axis, at the C K-α, Al K-α, Ti K-α, and Fe K-α lines. Also done on-axis were full-HRMA measurements at the Cu L-α, Cr K-α, and Cu K-α lines. In addition, there were "ends survey" tests done, in which one quadrant of a single mirror shell was exposed, and the HRMA tilted in pitch or yaw to simulate an infinite source distance. This illuminates a larger fraction of the length of the optic, and allows one to search for effects of larger surface roughness near the ends of the optic.

A few encircled energy tests were done with the solid state detectors, both with the continuum source (EIPS with graphite target, 15 kV, and a beryllium target), and with selected lines such as Ag and Sn L-α. The analysis of these data lag behind the simpler FPC spectra, and are not reported here.

The natural units for the measured points in an encircled energy experiment are cm^2, since the measured quantity is the effective area, integrated over the aperture. There are occasional points where, due to experimental error, the error bars are large and the points lie off the trend line. In most cases these points are within the calculated error bar of the trend line, so few real excursions exist. Those excursions which are real are cases in which the aperture was not properly centered on the image, and so the flux measured in the pinhole is less than it should have been. These points should be ignored.

Current ray trace models do not yet incorporate an accurate image of the source's spatial structure, and so are not comparable to the data. The source is believed to subtend an angle of $0.2''$ or so as seen from the HRMA, and so the core of the image is somewhat more diffuse than the point-source ray trace models predict. The normalization of the curves are also somewhat discrepant. This effect is discussed elsewhere in this document, in the chapters on effective areas (Chapter 12 and Chapter 11). However, except for the inner core of the image, the shapes of the encircled energy curves match the simulations quite closely.

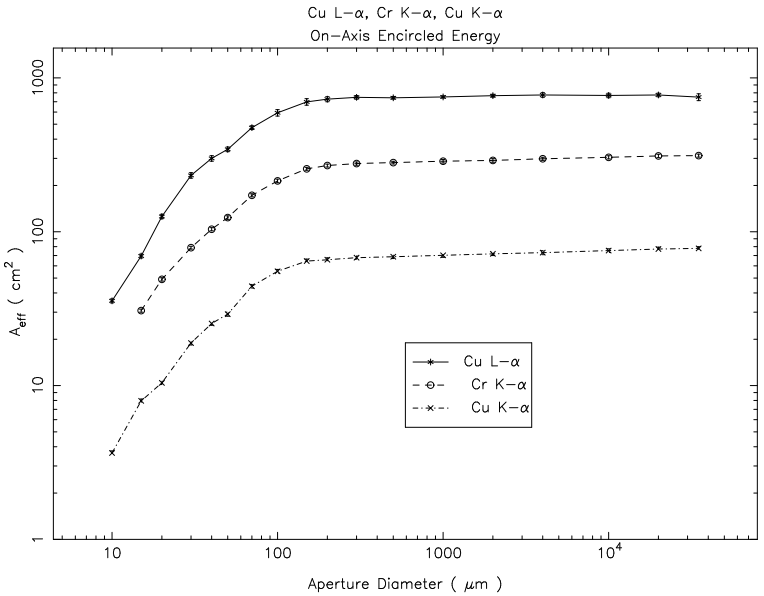

Figure 16.1: On-axis Full-HRMA Copper L- and K-α and Chromium K-α Encircled Energy

16.1 Comparison of Encircled Energy Measurements to Simulations

Figures 16.4to16.8 show comparisons of the measured FPC encircled energies to the simulations. In general the agreement is quite good. The inner cores disagree in part because the simulations treat the XSS as a point source. Additionally, the smaller pinholes were not reliably centered.

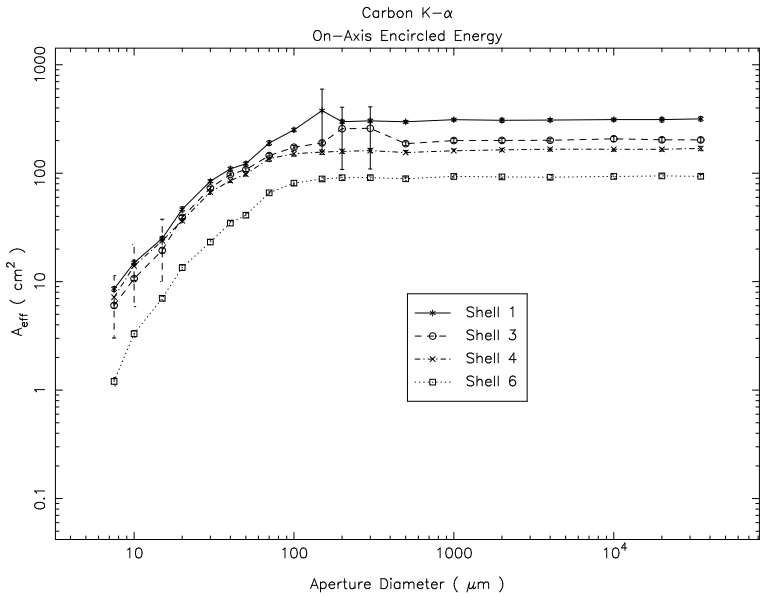

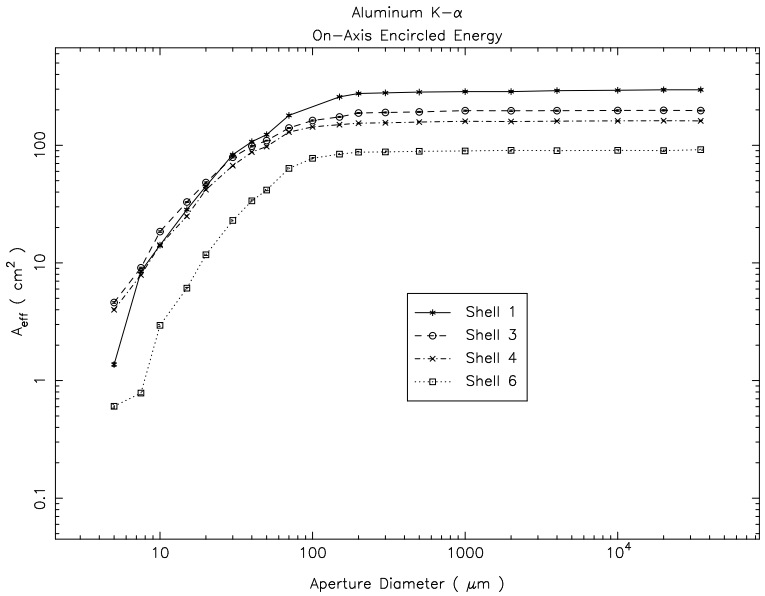

Figure 16.2: On-axis Carbon and Aluminum K-α Encircled Energy

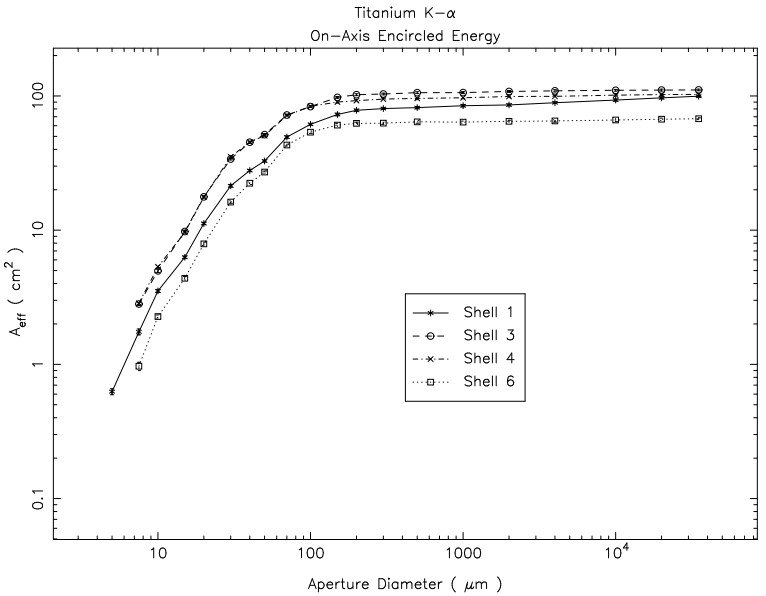

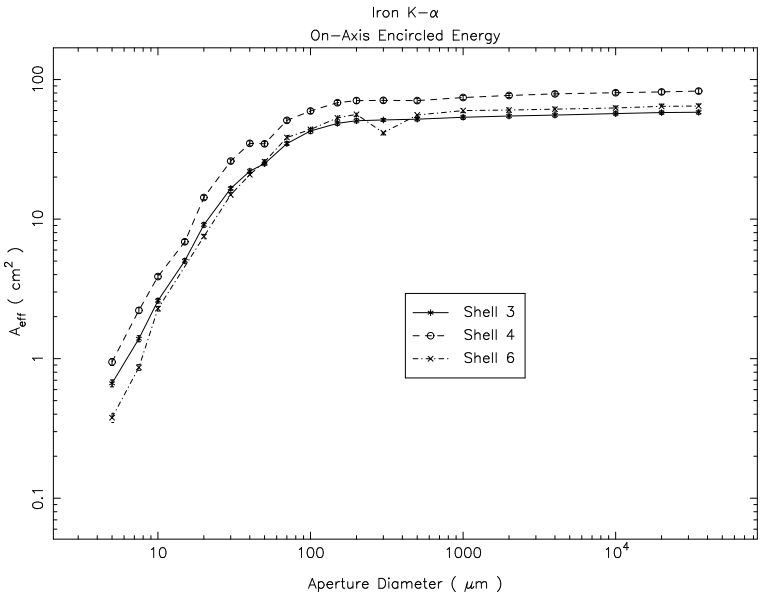

Figure 16.3: On-axis Titanium and Iron K-α Encircled Energy

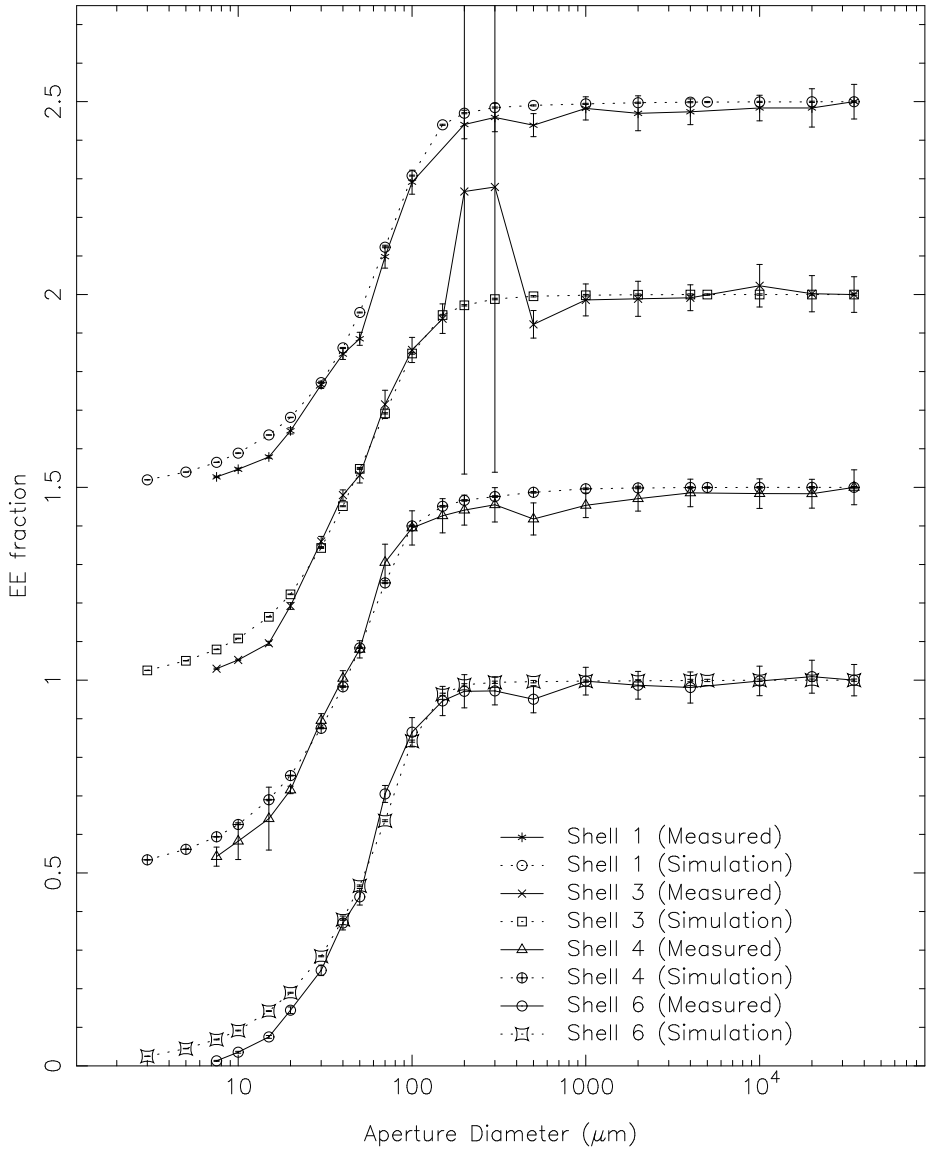

Figure 16.4: Encircled Energy Fractions at 0.277 keV. The values for Shells 1–3 have been shifted upwards for clarity.

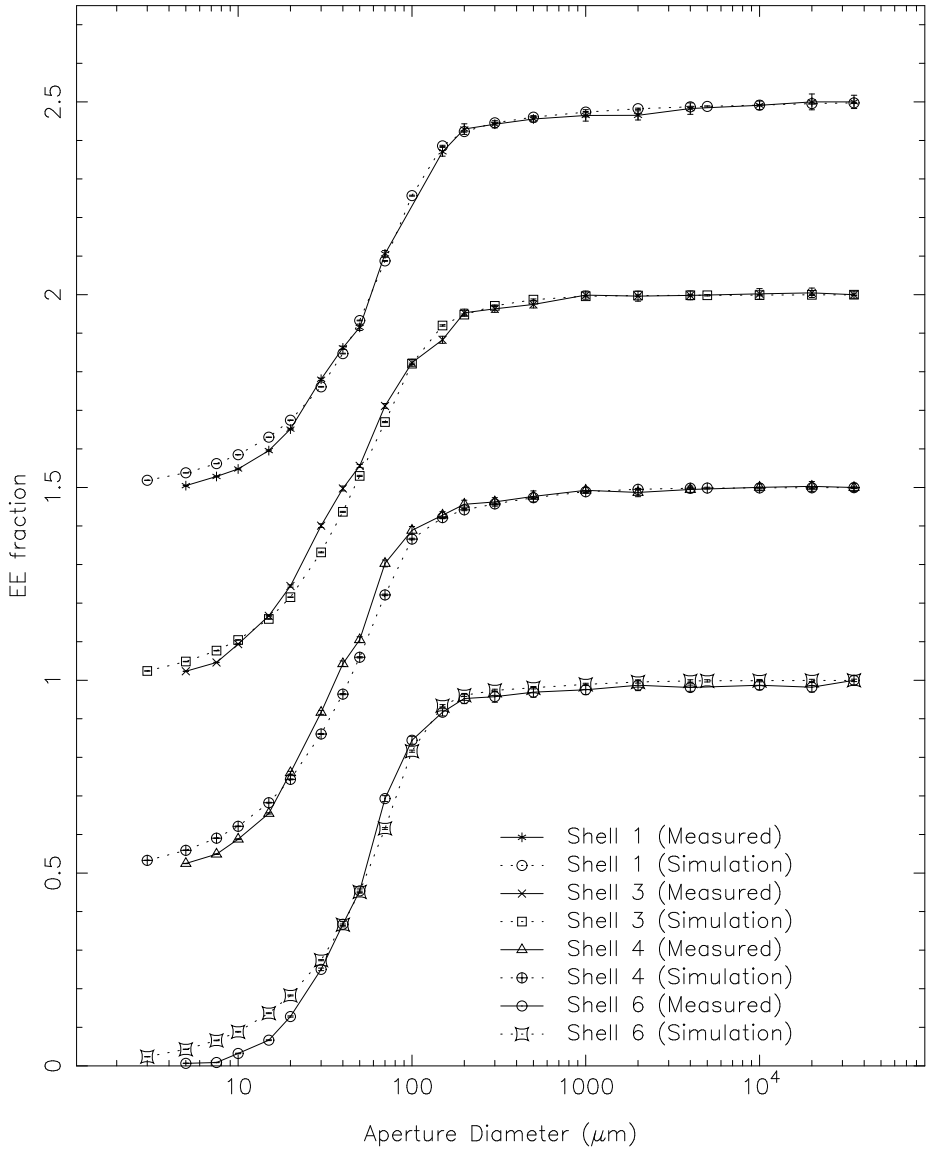

Figure 16.5: Encircled Energy Fractions at 1.486 keV. The values for Shells 1–3 have been shifted upwards for clarity.

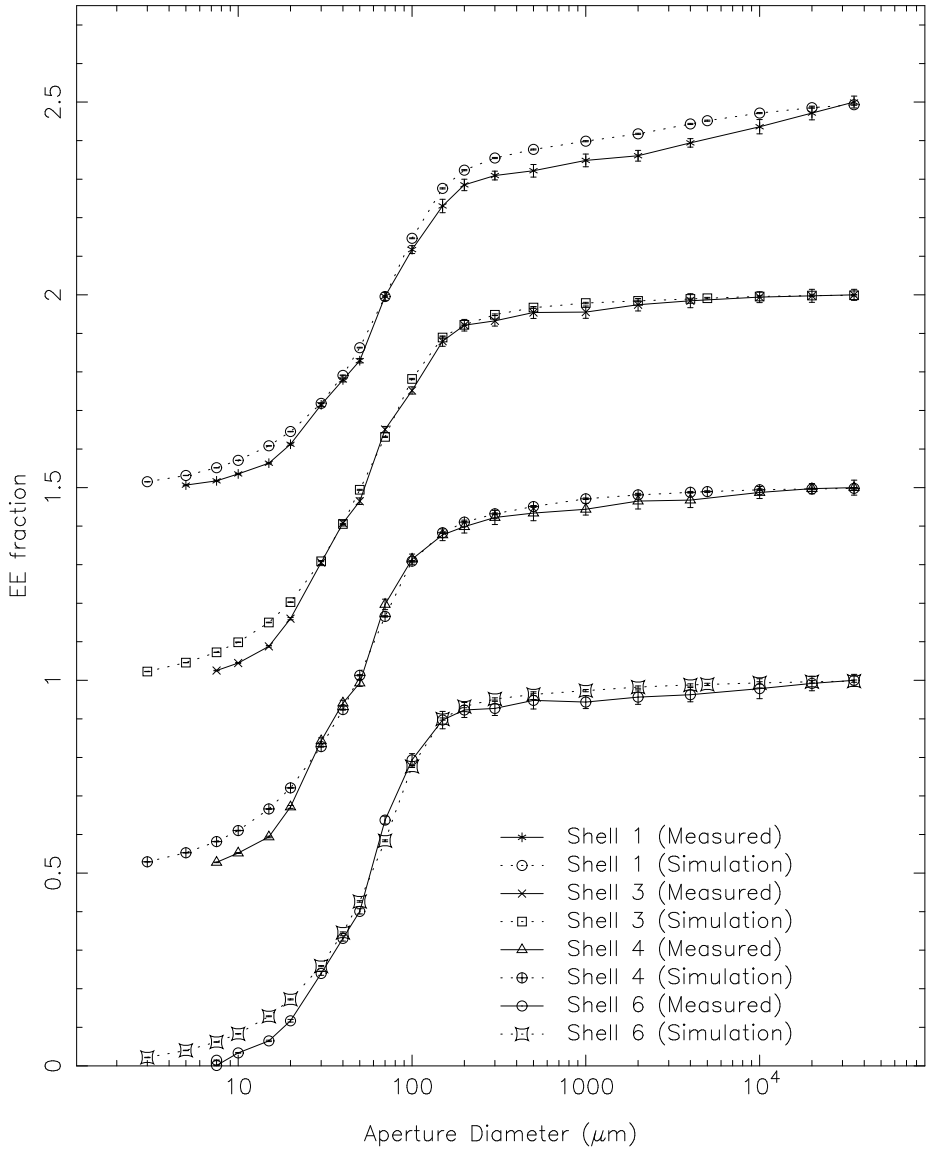

Figure 16.6: Encircled Energy Fractions at 4.51 keV. The values for Shells 1–3 have been shifted upwards for clarity.

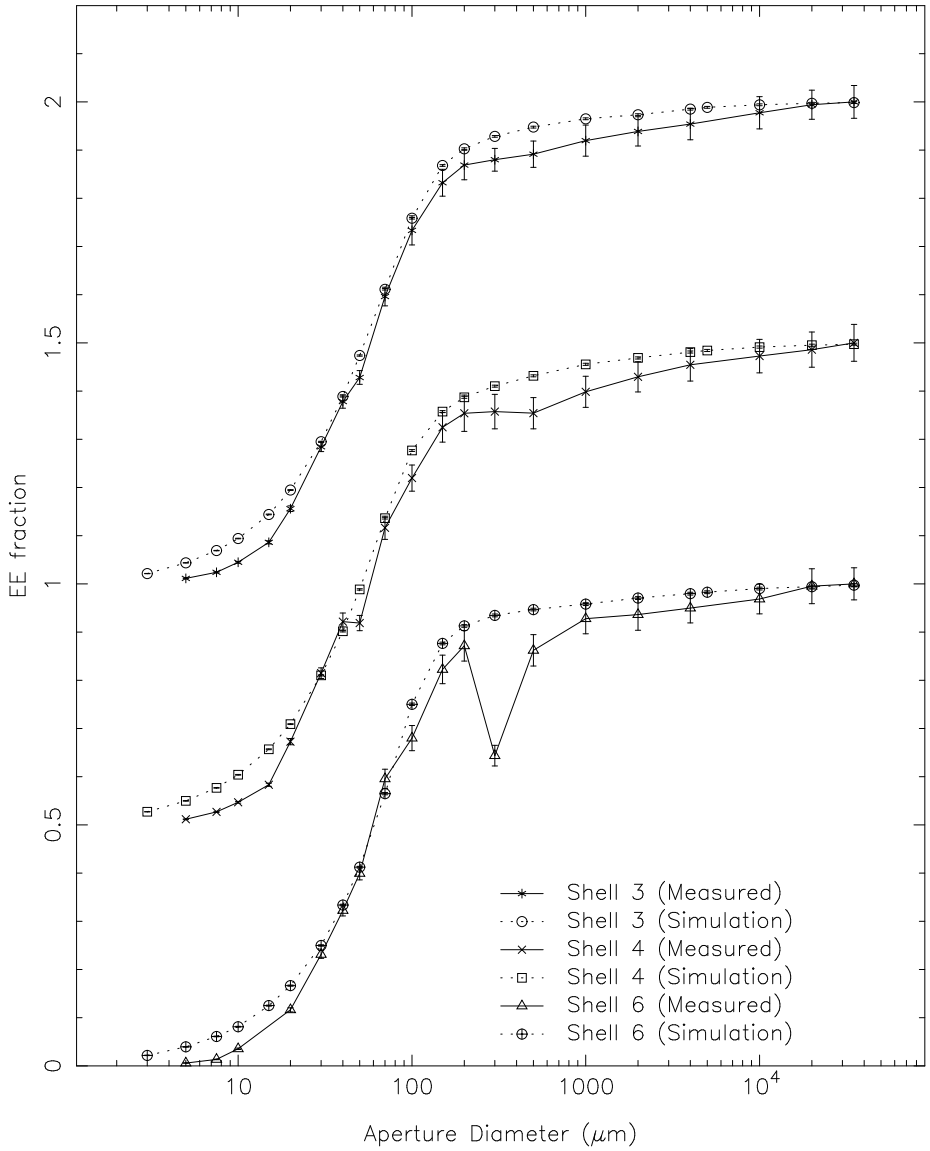

Figure 16.7: Encircled Energy Fractions at 6.4 keV. The values for Shells 3 and 4 have been shifted upwards for clarity.

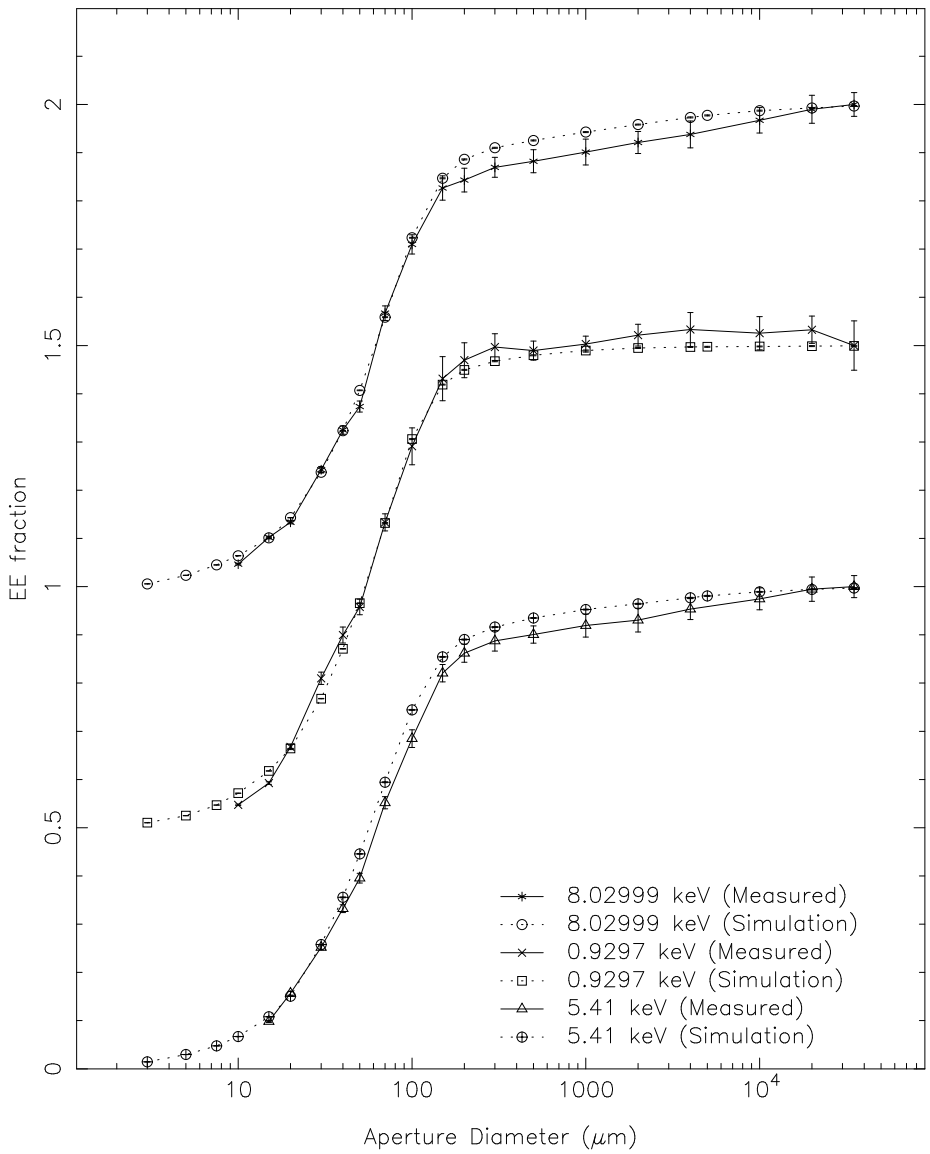

Figure 16.8: HRMA Encircled Energy Fractions. The values for higher energies have been shifted upwards for clarity.

Chapter 17

Off Axis Effective Area

Chapter 18

HRMA Ring Focus Measurements

Ping Zhao

18.1 Introduction

The HRMA ring focus measurement is an essential part of the AXAF ground calibration. It allows diagnosis of features not evident in the focal plane.

During the calibration, the HRMA was mounted horizontally. Because each of the eight mirror shells was bonded with epoxy to 12 invar pads around outside of the shell, the shells were distorted by small but measurable amounts by the mechanical support system due to gravity, thermal effects, and strain in the epoxy bonds. Furthermore, the moisture gain or loss in the epoxy bond (as it cures) changes the thickness of the epoxy bonds, and therefore causes the mirror distortions vary with time.

To ensure a scientifically successful mission and to predict the AXAF on-orbit performance, these distortions need to be measured carefully and their impact needs to be assessed. For example, the gravity distortion needs to be removed and the epoxy strain and its change with time needs to be evaluated for on-orbit performance predictions.

The HRMA ring focus measurements were designed and carried out for the above purpose. The ring focus is a sharply focused ring formed by the X-rays before they reach the HRMA focal plane (Griner et al., 1985; Zissa and Korsch, 1986). It is caused by spherical aberrations due to the finite source distance at the XRCF. There are four rings, one for each of the four shells of the HRMA.

The HRMA ring focus measurements were made with a High Speed Imager (HSI)[1] and a High Resolution Camera (HRC)[2], both microchannel plate X-ray detectors. The measurements reveal aspects of the mirror surface figures and distortions which are difficult or impossible to detect in the focal plane. The measurement results show periodic modulations of the ring width which were caused by gravity and strain in the epoxy bonds. The strongest component of the modulation has 12-fold symmetry due to the 12 flexures that support each mirror shell. Five ring focus HSI images and one HRC images were taken at different energies during the HRMA calibration (from 1996/12/20 to 1997/04/10). By examining the small changes in the ring width, temporal effects (such as changes in epoxy strain) can be diagnosed.

[1]The High Speed Imager (HSI) is part of the HRMA X-ray Detection System (HXDS).

[2]The High Resolution Camera (HRC) is one of the two AXAF detectors, P.I.: S. Murray(Murray et al., 1997).

The HRMA ring focus measurements were planned because of the success of similar measurements done for the VETA-I (Verification Engineering Test Article I) experiment in 1991 (Zhao et al., 1993). The data analysis here is based on that described in Zhao et al. (1993).

In this chapter we discuss the ring focus measurement results, ring focus model, the epoxy strain issue and its effect on the HRMA on-orbit performance. In §18.2 we describe the ring focus measurements and the data obtained. In §18.3 we discuss the data analysis. In §18.4 we present the measurement results with figures. In §18.5 we describe the ring focus models. In §18.6 we compare the data with the models. Finally, in §18.7 we summarize the ring focus measurements, our current assessment to the HRMA mirror deformation, evaluate the epoxy strain change between the ground calibration and on-orbit, and discuss the impact on the HRMA on-orbit performance.

18.2 Measurements and Data

Based on raytrace simulations, the ring focus plane was calculated to be 65.2 mm towards the HRMA from the focal plane (or 10209.3 mm from the CAP datum A – front surface of the Central Aperture Plate). The ring focus measurements were made in this plane. Five long exposure (1800 seconds) images were taken between 1996/12/23 and 1997/02/10 with an HSI detector. Then two months later, on 1997/04/10, an HRC image was taken with 6000 second integration time. Table 18.1 lists these six ring focus images. There was a repress (the test vacuum chamber was repressurized and opened) between the first and the second ring focus measurements, another repress between the fourth and the fifth measurements, and two represses between the fifth and the sixth measurements. Work was done on the HRMA alignment mechanism (actuators) during the first two repress cycles.

Table 18.1: HRMA Ring Focus Measurement data

Date (GMT)	Run ID	TRW ID	Source	Defocus	Detector	Integration time
961223	106856	C-IXH-RF-1.005	Al-K	65.2 mm	HSI	1800 seconds
970110	108185	D-IXH-RF-1.003	Fe-K	65.2 mm	HSI	1800 seconds
970115	108944	D-IXH-RF-1.002	C-K	65.2 mm	HSI	1800 seconds
970124	110004	D-IXH-RF-1.005	Al-K	65.2 mm	HSI	1800 seconds
970210	111804	E-IXH-RF-1.007	Al-K	65.2 mm	HSI	1800 seconds
970410	114828	G-IHI-RF-7.007	Mg-K	65.2 mm	HRC	6000 seconds

Figures 18.1through18.6 show these six ring focus images. Four rings in each figure are X-ray images from the four mirror shells of the HRMA. The images shown are as seen from the mirror looking towards the focal plane – top is the top, bottom is the bottom, left is the north and right is the south of the XRCF. The 12 gaps around the rings are the shadows of the supporting struts in the apertures and collimators.[3] A scale bar at the bottom of each figure shows the size of 1 mm or 20.2″. At the 65.2 mm defocus, the mean radii of the four rings are 3.88 mm, 3.10 mm, 2.73 mm, and 2.05 mm for shells 1,3,4, and 6, respectively.

In the five HSI images, the right (south) sides of the images are brighter than the left. This is because the HSI quantum efficiency is a function of incident angle; the HSI pores were tilted about

[3]From the 12 gap positions, it was found that the orientation of the HSI was slightly misaligned with respect to the HRMA (the HSI was rotated 0.7° clockwise, so the HRMA images appeared on the HSI were rotated 0.7° counterclockwise). This misalignment was considered in the data analysis.

6° from the detector normal, and about 10° below the south.[4]. In the HRC image this effect is not noticeable as the HRC quantum efficiency is not strongly dependent on the incident angle.

Near the 12 gaps of each ring, the ring width bulges out. This is primarily due to the effect of gravity induced distortions from the 12 mirror holders at those locations; we will discuss this later. In Figure 18.2, ring 1 (the largest ring) is very faint. This is because it is an Fe-K (6.4 keV) image. At this energy, the critical angle of reflection for Ir is 45.3 arcmin, while mirror P1 has a mean grazing angle of about 55.1 arcmin at the XRCF. This is beyond the critical angle, so there is not much reflection at 6.4 keV from shell 1. (The same is true for on-orbit operation, where shell 1 has a mean grazing angle of 51.3 arcmin.)

18.3 Data Analysis

Both HSI and HRC ring focus image data were digitized to a qpoe format in a 4096×4096 readout array with pixel size of $(6.43\mu\text{m})^2$. HSI has a spatial resolution of ∼14 μm (FWHM) and HRC has a spatial resolution of ∼20 μm (FWHM). Each image collected 1–2 million photons. Before the data analysis, the images were processed to remove artifacts. One of the processes is called degap. The image readout is a crossed grid charge detector, which consists of two orthogonal planes of wires electrically separated from each other. These two wire plates are located behind the microchannel plate stack to collect the charge. The electron charge cloud has a core/halo type of structure and spreads over several wires. A fine position algorithm was developed to determine the centroid of the charge cloud to a small fraction of the wire spacing. An artifact due to this algorithm is 16 vertical and 16 horizontal gaps left in the raw images (Chappell and Murray, 1989). The degap process restores the image so that each pixel appears at its actual location. By examining the final images, the residual gaps or pixel overlaps were determined to be less than one pixel wide.

Each degapped ring image was divided into annuli and pie sectors, using IRAF (Image Reduction and Analysis Facility). Each ring image was divided into annuli of one pixel (6.43 μm) wide. Each sector was chosen to be 2° wide, which gives adequate statistical errors and azimuthal resolution. Photon counts in each cell of the annulus-sector grid were tabulated. Radial profiles across each ring for each azimuthal angle were plotted; Figures 18.7–18.10 show some ring profile examples. For most parts of the ring, the radial profiles are single peaked. Near the 12 gaps (except the top and the bottom gap), the radial profiles are double or even triple-peaked. This is because the mirror was slightly deformed at the 12 support points due to gravity (see §18.5).

The ring width RMS and FWHM, and the ring mean radius were calculated for each radial profile.[5] There are a large number of scattered photons in each image. Because a photon far from the ring can carry a large statistical weight, the above calculations are meaningless without clipping. Therefore, a window of 320 μm was set around each ring before performing the calculations. Inside this window, focused photons were overwhelmingly dominant over the scattered photons. Photons outside this window were scattered photons and therefore were ignored.

The ring width RMS was chosen to represent the ring width because it carries a better statistical value than the FWHM.[6] The ring radii were affected by the detector plate scale non-uniformity, which is not very well known. Hence the ring radii are not analyzed here.

[4]From the ring focus data, the relative HSI quantum efficiency curve can be obtained since the X-ray incident angle can be very precisely determined and varies around the ring (see Chapter 7)

[5]The incident-angle-dependent QE of the HSI and HRC does not affect the values of RMS, FWHM, or the ring mean radius, although it does affect the errors as the number of detected photons varies. Different energies (except Fe-K) also should not affect these values as the analysis only use the focused rays.

[6]The RMS is calculated from all the data points within the window, while the FWHM is only based on three points.

18.4 Results

For each of the six images, the ring width RMS variation for each ring was plotted as a function of the azimuthal angle. Figures 18.11–18.14 show the ring width RMS variations for the image with run ID 110004. The top panels show the data points with error bars (the RMS calculated from those 180 angular sector profiles but with the data falling into the 12 gaps removed) as a function of the azimuthal angle, where 0° is at the top of the ring; 90° is to the south; 180° is at the bottom; and −90° is to the north. A modulation with a 30° period is clearly shown in this figure. Each middle panel is a spline fit to the data. Each bottom panel is the Fourier transformation of the data, plotted as the modulation power vs. the frequency in one circumference. The modulation has dominant frequencies of 2 (180° period), 12 (30° period) and its higher harmonics.

Figures 18.15–18.18 are the summary figures for the HRMA ring focus measurements. They show the ring width RMS variations and their Fourier transforms for all four rings from all six measurements. The six ring focus measurements were made over a time span of 3.5 months during the calibration. The purpose was to see if there were any changes with time in the ring structure, especially the 12 fold symmetry, in order to determine the change in the epoxy strain.

Rings with the Fe-K source (the dotted curve) have greater width because Fe-K has higher energy (6.4 keV), and therefore more scattering, which broadens the rings. Ring 1 for Fe-K is especially wide and noisy. This is because there were not many photons in ring 1 as mentioned before (see Figure 18.2). For shells 3, 4 and 6, the Fe-K rings are broader but basically match the profiles from other sources.

Data taken with Al-K and C-K source have enough counts and less scattering. They are used to do the comparison for the epoxy strain effect.

All the curves have 12 dominant split peaks at 30° multiples. They are primarily due to the gravity, and possibly also thermal, and epoxy strain effects. Since each shell was held at 12 rather small areas (the largest shells were epoxy bonded to 2 inch diameter invar pads), gravity caused local distortions at those 12 locations. The distortions along the sides of the mirror were more severe than at the top or bottom. These local distortions would cause a shifted 12-fold symmetry (i.e. 12 ± 1 and 12 ± 2 fold) and higher harmonics (i.e. 24, 24 ± 1 and 24 ± 2 fold). A 2-fold symmetry also exists due to the fact that the amplitude of the side distortions are much larger than that from the top and bottom. The 2-fold symmetry is slightly upset because the epoxy gaps are not uniform at each of the 12 bonds.

18.5 Ring Focus Models

To understand the results of the HRMA ring focus measurements, we developed ring focus models. The ring focus models are computer generated images obtained by ray-tracing to simulate the X-rays passing through the HRMA mirror and the test system. Details such as scattering due to mirror surface roughness and the detector response were also simulated. The same analysis used for the real data was applied to the model images. As an example, Figure 18.19 is a HRMA model ring focus image with the epoxy strain set at −0.35% (i.e. an inward bump of 0.35% of the epoxy thickness at the bonding points; see below).

The ring focus models include the following elements:

1. HRMA mirror surface map from the HDOS.
2. HRMA mirror assembly errors as deduced from the EKC HATS data.
3. HRMA decenters and tilts as measured during the HRMA calibration at the XRCF.

4. Gravity (1-g) distortions modeled by SAO.
5. Epoxy strain distortions modeled by SAO.
6. Thermal effects.
7. Finite source distance.
8. HRMA apertures and their supporting struts.
9. HRMA mirror reflectivity and scattering due to surface micro-roughness.
10. HSI and HRC detector resolutions.

The HRMA mirror surface (low frequency) maps are from data obtained from the Hughes Danbury Optical Systems, Inc. (HDOS) metrology measurements. The HRMA mirror assembly errors were deduced from data obtained from the Eastman Kodak Company (EKC). Because mirror shells were made slightly different from ideal shells, they had to be bonded slightly different from the design positions in order to obtain the best on-orbit parfocalization. The HRMA decenter and tilt errors (H shells with respect to P shells) errors were measured and analyzed during the calibration (Gaetz et al., 1997).

The SAO 1-g model is a full 360 degree Finite Element Analysis (FEA) model. Twelve tangential flexures support each optic. In a 1-g vertical field, the FEA model shows that the flexures at the sides of the optic each support about 17% of the optic's weight, the flexures 30° above and below the sides support about 12% of the optic's weight and the flexures 60° above and below the sides support about 4% of the optic's weight. The flexures at the top and bottom support essentially no weight because of their flexibility. The flexures that are more highly loaded cause the optic to twist more about the optical axis (producing a so-called circumferential slope). At the side locations (±90°), the gravity causes a large slope change on the optic across the centerline of the flexure such that optic above the ±90° was pushed in while below the ±90° was pulled out. The peak-to-valley distortion (±85° to ±95°) was about 0.37μm. Therefore there are inward dimples centered at around ±85° and outward dimples centered at around ±95°. At the 30° above and below the side locations, the slope change is about 1/2 of that occurs at the side locations. At the 60° above and below, the slope change is about 1/6 of that. At the top and bottom of the optic, there is essentially no slope change as there is no twisting effect by the gravity. A more detailed analysis of the SAO 1-g model can be found in SAO memo by L.M. Cohen (Cohen, 1997).

The epoxy strain was measured on test flats at EKC. The results show two kinds of effects: (1) An in-plane cure shrinkage of about 0.075% and a "through-the-thickness" (TTT, through the 0.0075" nominal thickness direction) shrinkage of about 2% took place within a few days after bonding; (2) Long term epoxy strains of order 1% due to moisture gain and loss in the epoxy, −1% (inward bump) in the fully dried condition and +1% (outward bump) in the fully moist. For effect (1), we assume that about 1 week after each optic is bonded, there were 12 outward bumps. Those outward bumps were due to the large (−2%) TTT strain which causes the optic to be pulled outward while the flexure is pulled inward. The magnitude of this outward bump is the equivalent to an epoxy moisture strain of about +0.32%. For the effect (2), the epoxy strain will change based on the moisture. The time constant for this effect is order of months. A more detailed analysis of the epoxy strain effects can be found in SAO memo by L.M. Cohen (Cohen, 1997).

For the thermal effects, a uniform temperature change of 11.1°F is equivalent to an epoxy strain of 1%. The optics were bonded at the EKC at an average temperature of 69.83°F, whereas

the temperatures during the ring focus measurements were 69.79±0.05°F. This small temperature change is negligible (equivalent to an epoxy strain of 0.0036%).

The finite source distance in the model is 527.27904 meters from the CAP datum A plane. The geometries of the HRMA apertures and their supporting struts are well defined.

The mirror reflectivity was calculated using the optical constants tabulated by Henke et al. (Henke et al., 1993) (0.1–2 keV) and synchrotron measurements made by Graessle et al. (Graessle et al., 1997) (2–12 keV). The mirror surface roughness data from the HDOS WYKO measurements were processed using a program "foldw1", written by L.P. Van Speybroeck, to calculate scattering distributions. The calculation was based on the scattering theory by Beckmann and Spizzichino (Beckmann and Spizzichino, 1963).

The HSI and HRC detectors have spatial resolutions (FWHM) of 14 μm and 20 μm, respectively. Both detectors have read out pixel size of 6.43 μm.

Of all the elements mentioned above, the 1-g deformation and the epoxy strain are the two central issues for the modeling. While the gravity is constant during the ground tests, epoxy strain can change. That is why we made several measurements during the calibration to determine the epoxy strain change. However, the gravity effect is very strong and the epoxy strain only exhibit very small effect on the ring focus RMS width where the gravity effect dominates.

Figure 18.20 shows the model of ring 1 with Al-K source and all the model elements except the gravity and the epoxy strain effects. The ring width RMS is about 0.5 arcsec with a random noise of the order of 0.1 arcsec. This "noisy" ring width is due to the actual mirror surface imperfection as measured at the HDOS. (For an ideal mirror, the ring width RMS should be 0.01 arcsec with no noise.) As seen from its Fourier transform, there is no noticeable modulations to the general "noisy" shape (the largest term is only 0.015 arcsec. This indicates that there is no significant "structure" in the mirror.

Figure 18.21 shows the model of ring 1 with the 1-g effect but still without the epoxy strain effect. The ring width RMS displays significant split peaks at 30° multiples, except at the top and bottom of the ring. This is the gravity twisting effect at the optic holding points as expected. Notice the base line of this curve is still at about 0.5 arcsec which is set by the mirror surface figure (imperfection). The Fourier transform of the data shows dominant 12 fold symmetry and the second harmonics due to the 12 split peaks, and 2 fold symmetry due to the fact that the peaks are much larger at the sides than at the top and bottom.

Figure 18.22 shows the model of ring 1 with epoxy strain effects in addition to 1-g effects. The top panel shows the mirror with (−2%) TTT initial epoxy cure plus the long term epoxy strains for 1% (fully moist condition) to −1% (fully dried condition). The solid line is the 0.0% moist, i.e. no long term epoxy strain beyond the initial -2% TTT cure strain. When the moisture increases, the epoxy strain would enforce an outward bump at each supporting point. This bump would increase the outward dimple below each supporting point due to the gravity twist, and decrease the inward dimple above each supporting point due to the gravity twist. When the moisture decreases, the epoxy strain would enforce an inward bump at each supporting point, and the effect is reversed. This epoxy strain effect is shown clearly in the Figure 18.22: When the moisture increases (0.5% and 1.0% moist), the peaks 5° outside the 30° multiples (below the supporting points) increase while the peaks 5° inside the 30° multiples (above the supporting points) decrease. When moisture decreases (-0.5% and -1.0% moist), the inside peaks increase while the outside peaks decrease.

As we can see, the effect of epoxy strain change is very dramatic at this 1% level. The actual data (Figures 18.15–18.18) show little noticeable effect like this. Therefore we conclude that the epoxy strain change must be significantly less than 1%.

18.6 Comparison of Data with the Model

To see if there were any changes in the ring structure, we compare the ring focus data taken on 1996/12/23, 1997/02/10 and 1997/04/10. The first two images were taken with the HSI at the beginning and the end of the phase 1 calibration, separated by 1.5 months. The third image was taken with the HRC two months later, in the phase 2 calibration. Figures 18.23–18.26 show the comparison. As in Figures 18.15–18.18, the top panels show the ring width RMS variations and the bottom panels show their Fourier transforms. As it can be seen, there are indeed changes in the ring structure during the calibration period. Generally, there were relatively larger change between 1996/12/23 and 1997/02/10, and relatively smaller change between 1997/02/10 and 1997/04/10.

For a closer look, Figures 18.27–18.30 show the ring width RMS change from 1996/12/23 to 1997/02/10. They were both taken with the Al-K source. The top panels show the two RMS curves. For most of the double peaks, especially on the left (north), the inside peaks increased while the outside peaks decreased. According to the analysis in the previous section, this indicates the possibility of inward bump at the flexures due to the moisture decrease in the epoxy. However, this change is not very consistent. On the right side of ring 1, there is very little change. Peaks at 150° from all four rings and some peaks on the right side of ring 3 seem have the opposite change (i.e. inside peaks decreased while outside peaks increased). The second panels show the Fourier transforms of the above two curves. The third panels show the differences of the two RMS curves (RMS of 1997/02/10 minus RMS of 1996/12/23). The bottom panels show the Fourier transform of the difference. In general, the changes in the RMS width are very small – at the 0.1 arcsec level.

Figures 18.31–18.34 show the ring width RMS change from 1997/02/10 to 1997/04/10. Generally, the changes were smaller during that two months period comparing to the first month and half (compare the third, RMS difference, panel for each ring). This indicates the HRMA is likely stabilized from epoxy strain distortion after the first month and half in the calibration chamber.

The small change in the ring width could be due to the temperature, gravity or the epoxy strain. The temperature during the measurements, as mentioned earlier, was very constant and very close to the temperature as the HRMA was assembled. Therefore the temperature effect is negligible. Gravity could have caused small changes if the HRMA support conditions were changed during that period. This is possible as the test vacuum chamber was opened a few times and work was done on the HRMA actuators. However, we do not have enough convincing data and information to model this scenario. Supposing the change was purely due to the epoxy strain, which is the most likely case, we can give a estimate of the change based on our model.

Figure 18.35 shows the model for ring 1 with the epoxy strain of -2% TTT plus 0.0% and -0.3% moist. The four panels show the same curves as shown in Figure 18.27 with the same scale. As mentioned above, most of the epoxy strain changes seem occurred in phase 1, i.e. between 1996/12/23 and 1997/02/10. We compare Figure 18.35 with Figure 18.27, and see many similarities and also differences:

1. The width RMS curves (top panels) of both data and model have the same base line of about 0.5 arcsec. This indicates that the model for the mirror surface figure is correct.

2. Both curves (top panels) have 12 dominant split peaks at 30° multiples. Both of their Fourier transforms (second panels) have dominant 2, 12 and 24 fold symmetries and about the same magnitude of 12 ± 1, ±2 and 24 ± 1, ±2 components. This indicates that the 1-g model is right.

3. The model has larger modulation amplitude than that of the data (top and second panels). This indicates that the epoxy strain change is likely less than 0.3%.

4. The model show the inside peaks increase and outside peaks decrease on both sides of the curve (top panels) due to the epoxy moisture loss , while the data only shows this effect on the left side (-180° to 0°). This could be due to the HRMA loading condition changed during the test. It could also be due to the epoxy moisture condition was not uniform to begin with.

5. The RMS difference curves show similar structures between the data and the model. Only the data has smaller amplitude on the right side (0° to 180°); this agrees with the discussion in the previous paragraph.

18.7 Conclusion

The HRMA ring focus measurements were made with the HSI and HRC detectors during the HRMA calibration. From 1996/12/23 to 1997/04/10, five HSI images and one HRC image were taken. The data show the RMS ring width has 12 dominate split peaks around the center line of the 12 mirror holding flexures. The ring focus model was generated using raytracing, considering all the relevant factors from the mirror surface figure to the XRCF test environment. By comparing the ring focus data and the ring focus models, we are able to assess the mirror surface figures as well as the mechanical support system distortions which are very difficult to detect in the focal plane. We also estimated the epoxy strain effects on the mirror for its on-orbit performance.

These are the conclusions of this study:

1. In general, the model and the data agree well. Effects of mirror surface figure, assembly errors, decenter and tilt, finite source distance, gravity etc. are clearly shown in the model and agree with the data.

2. Inside peaks increased and outside peaks decreased during the first month and half of the calibration. This is consistent with the theoretical model of epoxy strain due to moisture loss.

3. Comparing the data with the model, the actual change in the epoxy strain is very small ($\sim$0.3%). The small epoxy strain change could be because most of the moisture loss in the epoxy bond occurred before the beginning of ring focus measurements, due to the HRMA vacuum exposure and dry nitrogen purge used after the final assembly.

4. Changes between 2/10 and 4/10 are even smaller than the changes occurred between 12/23/96 and 2/10/97. This indicates the HRMA has likely stabilized from epoxy strain distortion after the first month and half in the calibration chamber.

5. The small change of the epoxy strain and its stabilization observed during the calibration interval lead us to expect no more serious changes between the calibration and flight performance. Even in a worst case, it is unlikely the epoxy strain effect on-orbit will be more than 0.5% due to moisture loss. A raytrace calculation with the 1-g effect removed shows that this case will degrade the AXAF performance by no more than 5% from a one arc second diameter encircled energy for mirror pair 1. The change of the epoxy strain on other shells is even less than that measured on shell 1, and hence the total effect should be less than 5% loss for the whole HRMA.

6. We should be able to predict the HRMA on-orbit performance using the ground calibration data.

Here is the bottom line: HRMA IS AN EXCELLENT MIRROR. IT WILL STAY THAT WAY ON ORBIT!

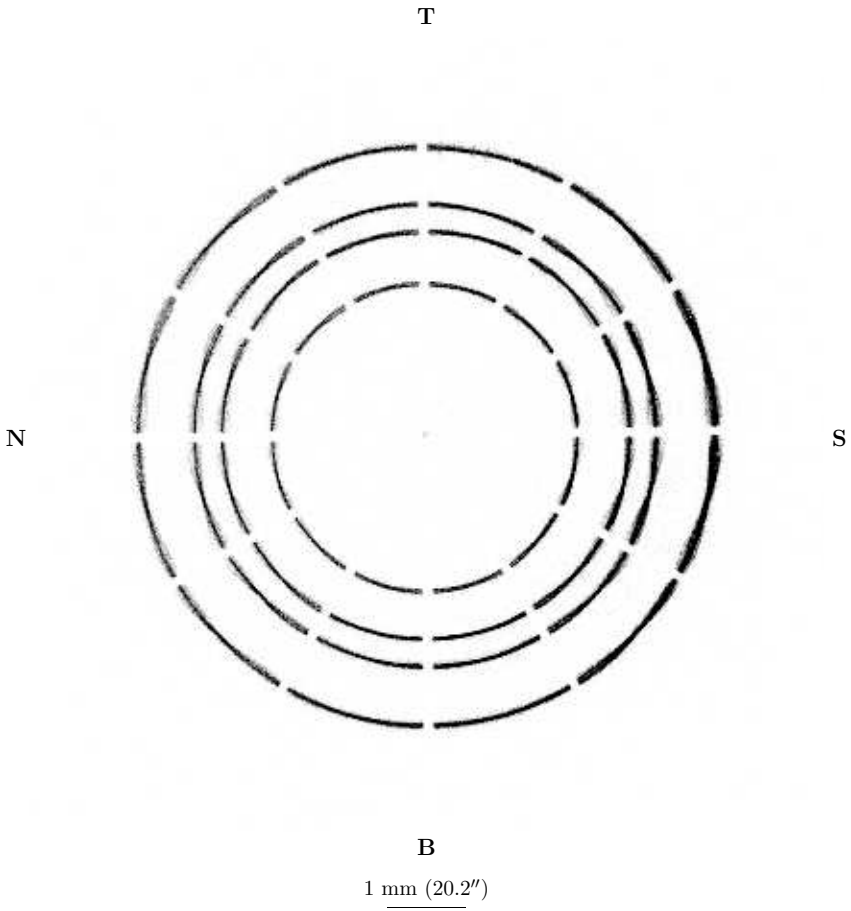

Figure 18.1: The HRMA ring focus HSI image. Date: 1996/12/23; TRW ID: C-IXH-RF-1.005; Run ID: 106856; Source: Al–K; Defocus: 65.2 mm; Integration time: 1800 seconds.

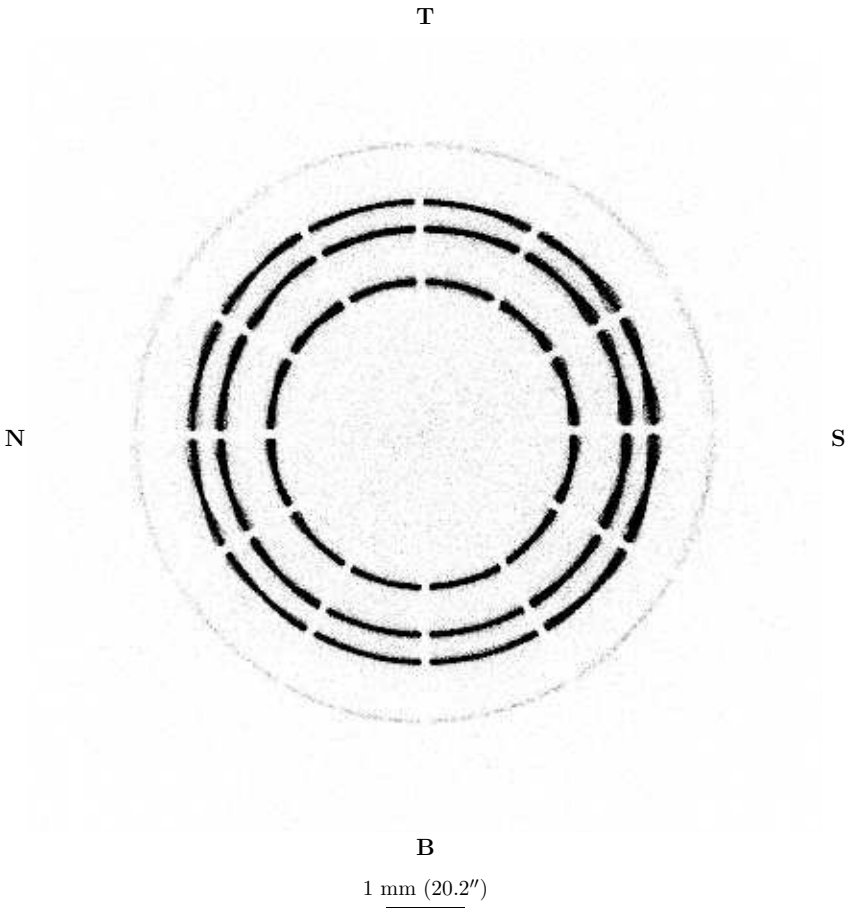

Figure 18.2: The HRMA ring focus HSI image. Date: 1997/01/10; TRW ID: D-IXH-RF-1.003; Run ID: 108185; Source: Fe–K; Defocus: 65.2 mm; Integration time: 1800 seconds.

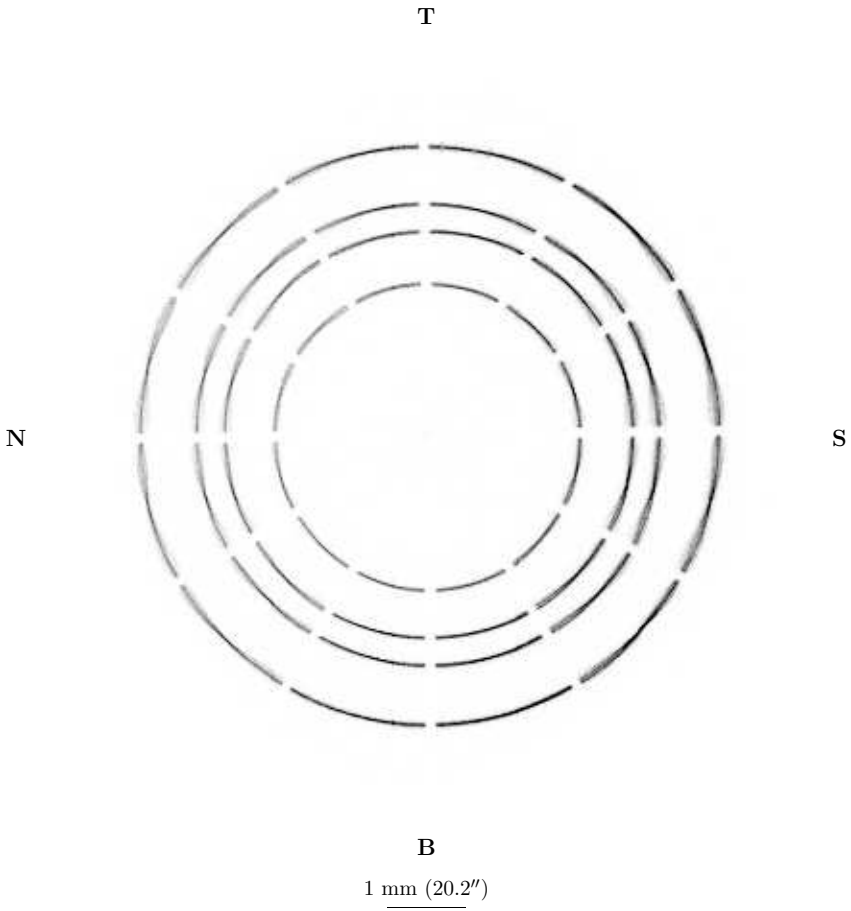

Figure 18.3: The HRMA ring focus HSI image. Date: 1997/01/15; TRW ID: D-IXH-RF-1.002; Run ID: 108944; Source: C–K; Defocus: 65.2 mm; Integration time: 1800 seconds.

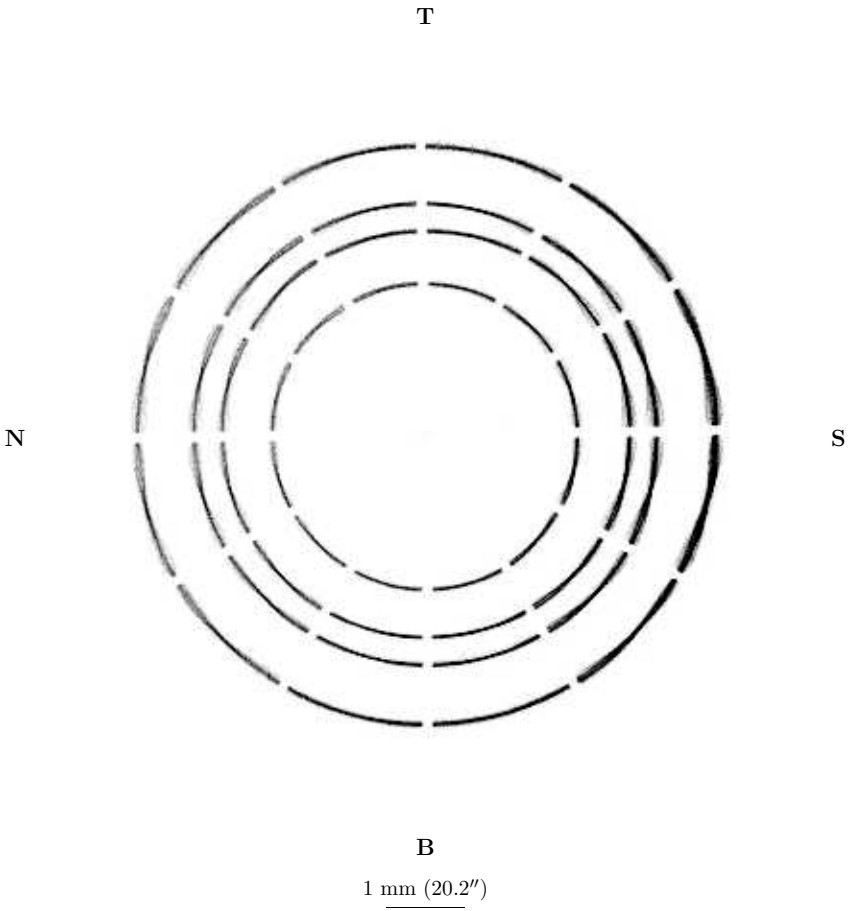

Figure 18.4: The HRMA ring focus HSI image. Date: 1997/01/24; TRW ID: D-IXH-RF-1.005; Run ID: 110004; Source: Al–K; Defocus: 65.2 mm; Integration time: 1800 seconds.

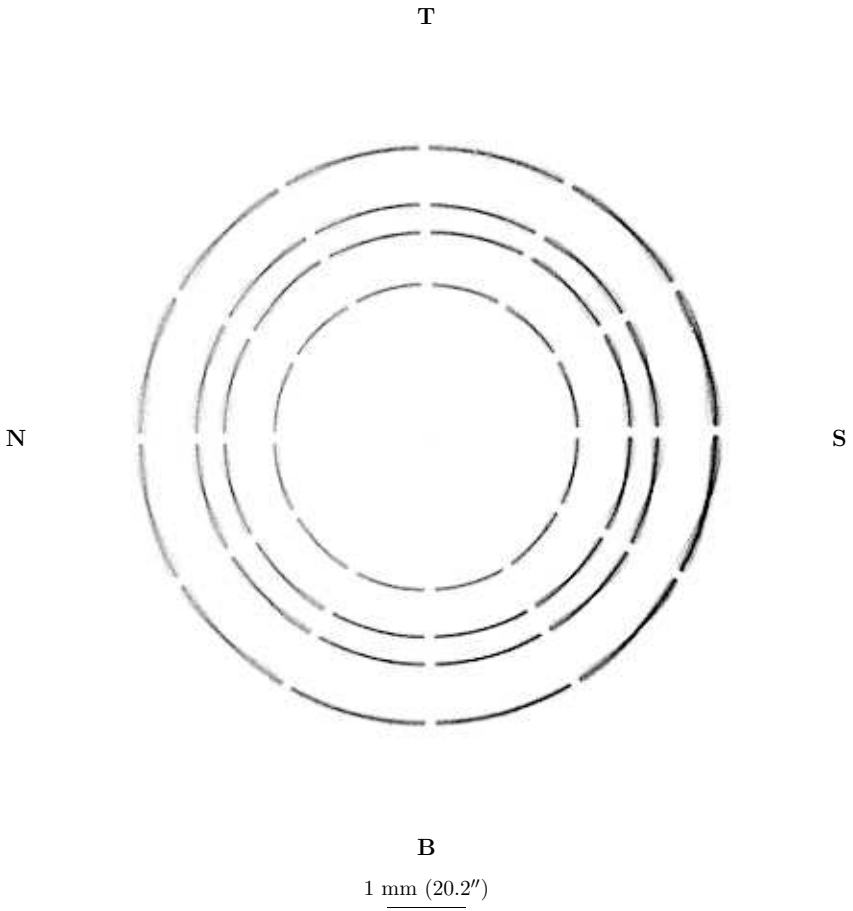

Figure 18.5: The HRMA ring focus HSI image. Date: 1997/02/10; TRW ID: E-IXH-RF-1.007; Run ID: 111804; Source: Al–K; Defocus: 65.2 mm; Integration time: 1800 seconds.

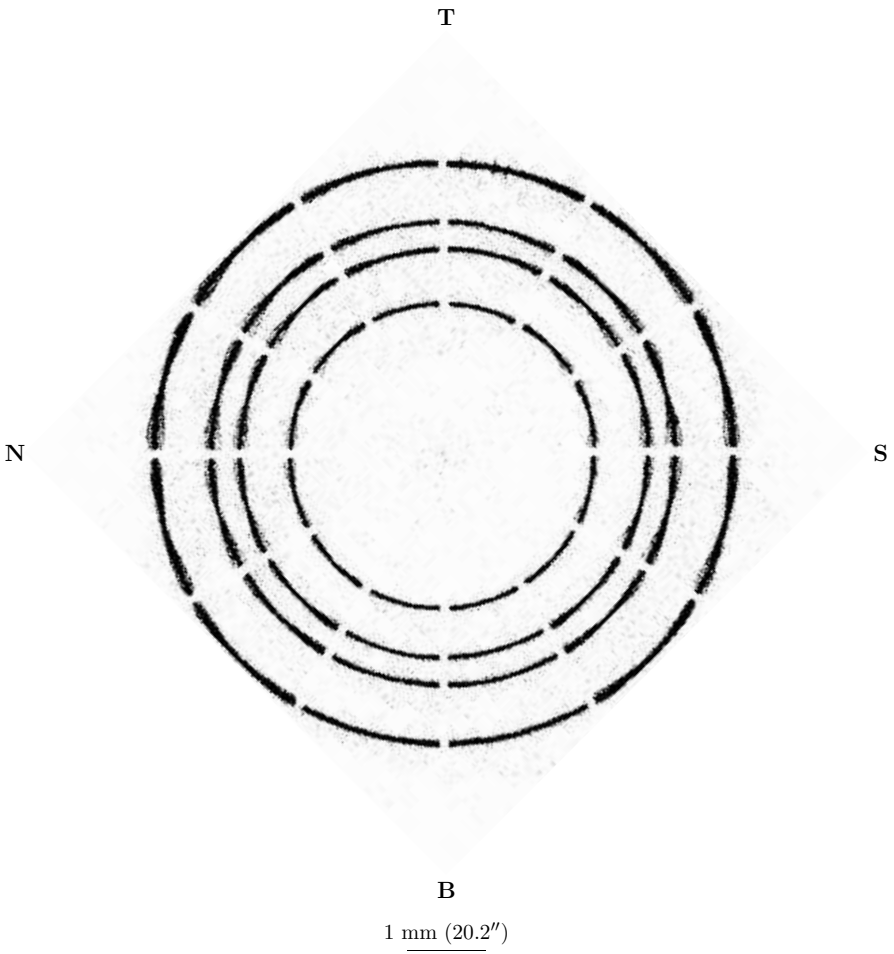

Figure 18.6: The HRMA ring focus HRC image. Date: 1997/04/10; TRW ID: G-IHI-RF-7.007; Run ID: 114828; Source: Mg–K; Defocus: 65.2 mm; Integration time: 6000 seconds.

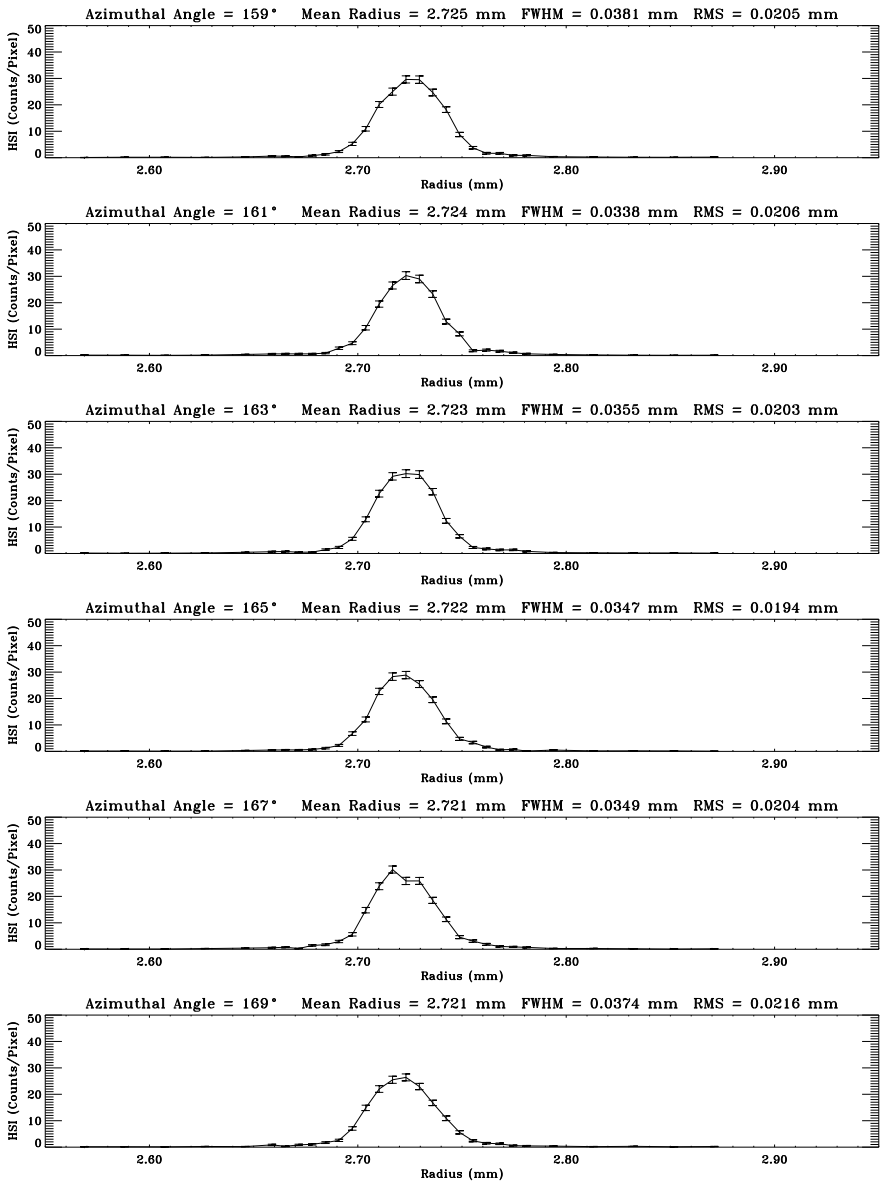

Figure 18.7: Radial profiles for ring 4. Date: 1997/01/24; TRW ID: D-IXH-RF-1.005; Run ID: 110004; Source: Al–K; Defocus: 65.2 mm.

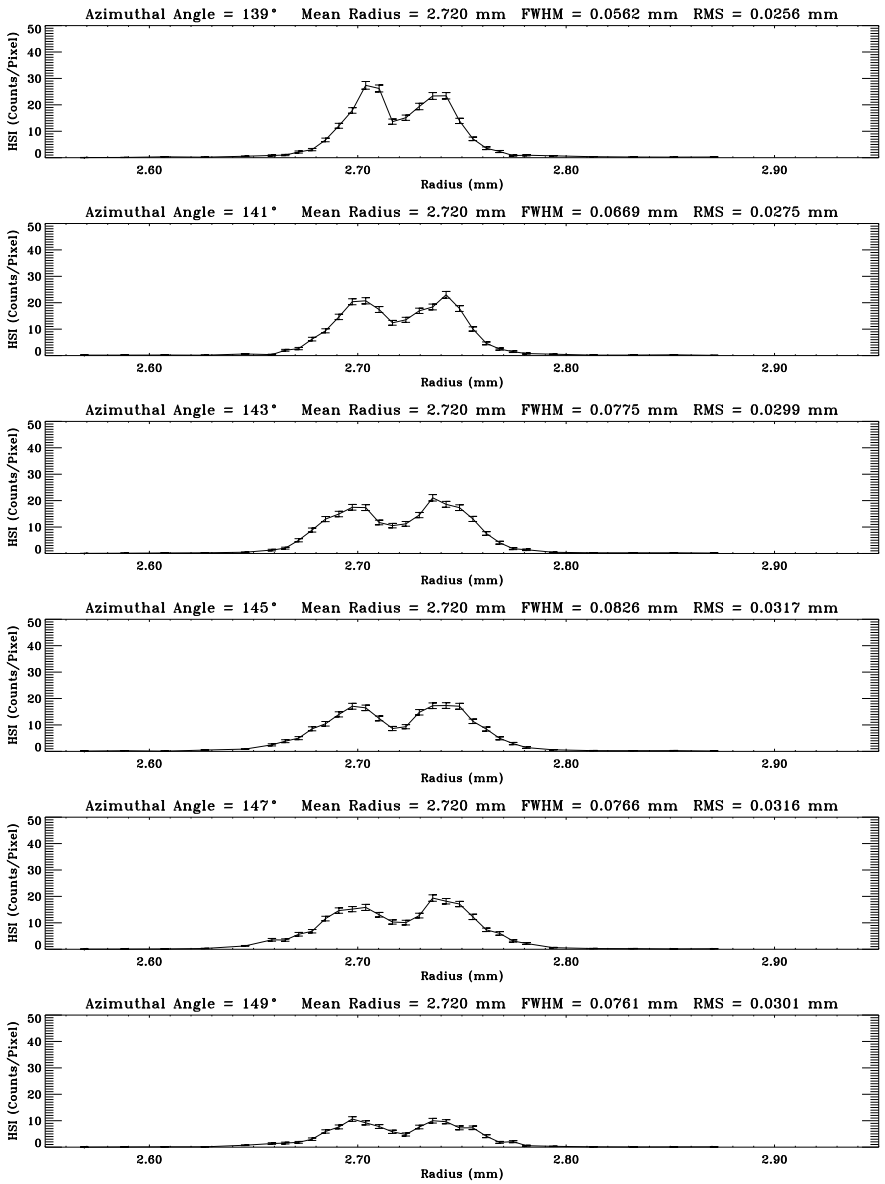

Figure 18.8: Radial profiles for ring 4. Date: 1997/01/24; TRW ID: D-IXH-RF-1.005; Run ID: 110004; Source: Al–K; Defocus: 65.2 mm.

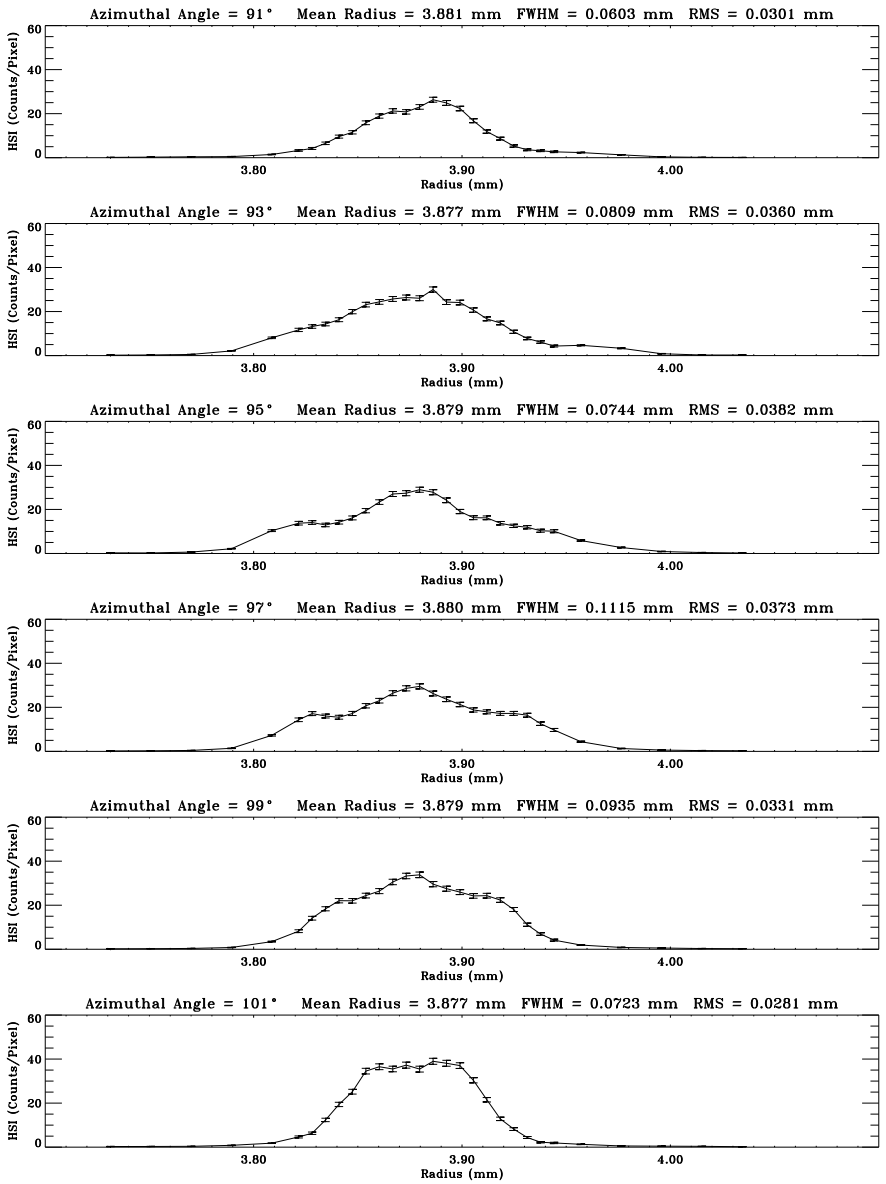

Figure 18.9: Radial profiles for ring 1. Date: 1997/01/24; TRW ID: D-IXH-RF-1.005; Run ID: 110004; Source: Al–K; Defocus: 65.2 mm.

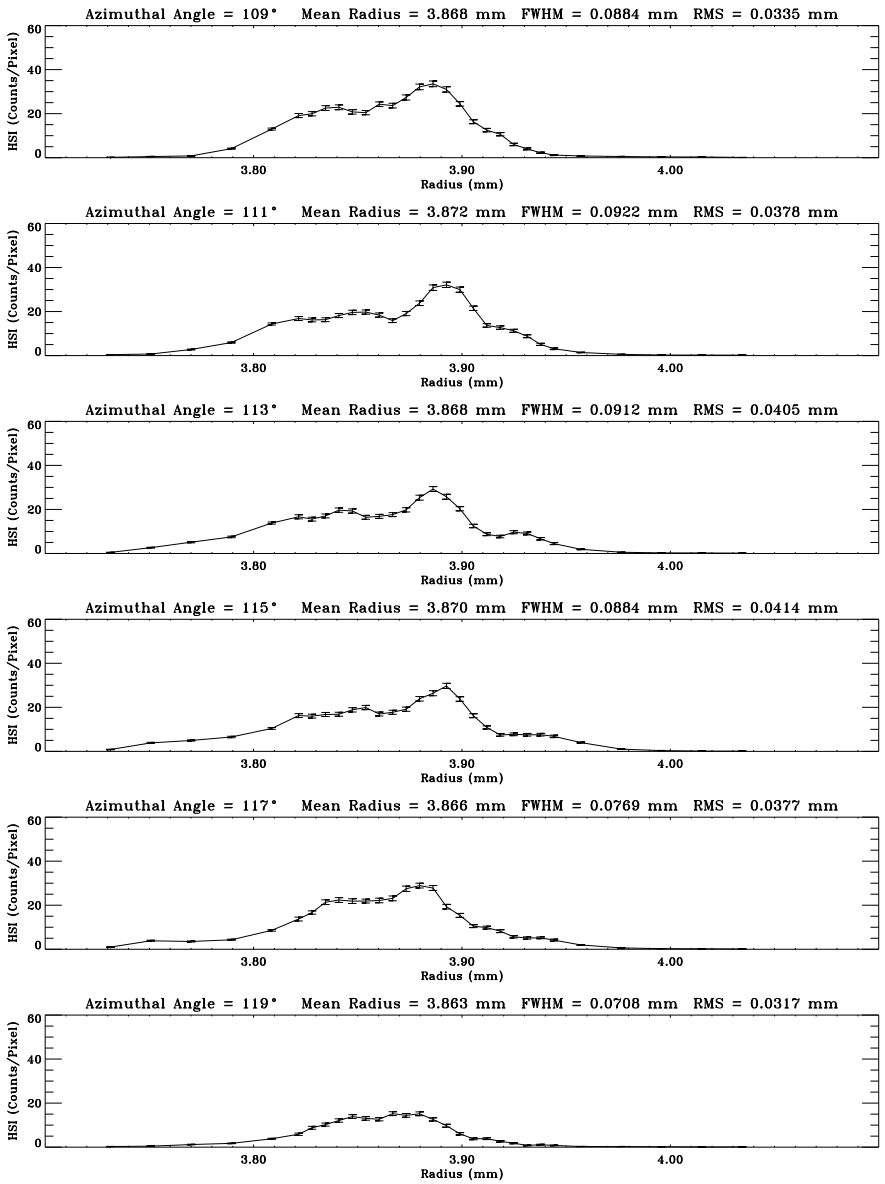

Figure 18.10: Radial profiles for ring 1. Date: 1997/01/24; TRW ID: D-IXH-RF-1.005; Run ID: 110004; Source: Al–K; Defocus: 65.2 mm.

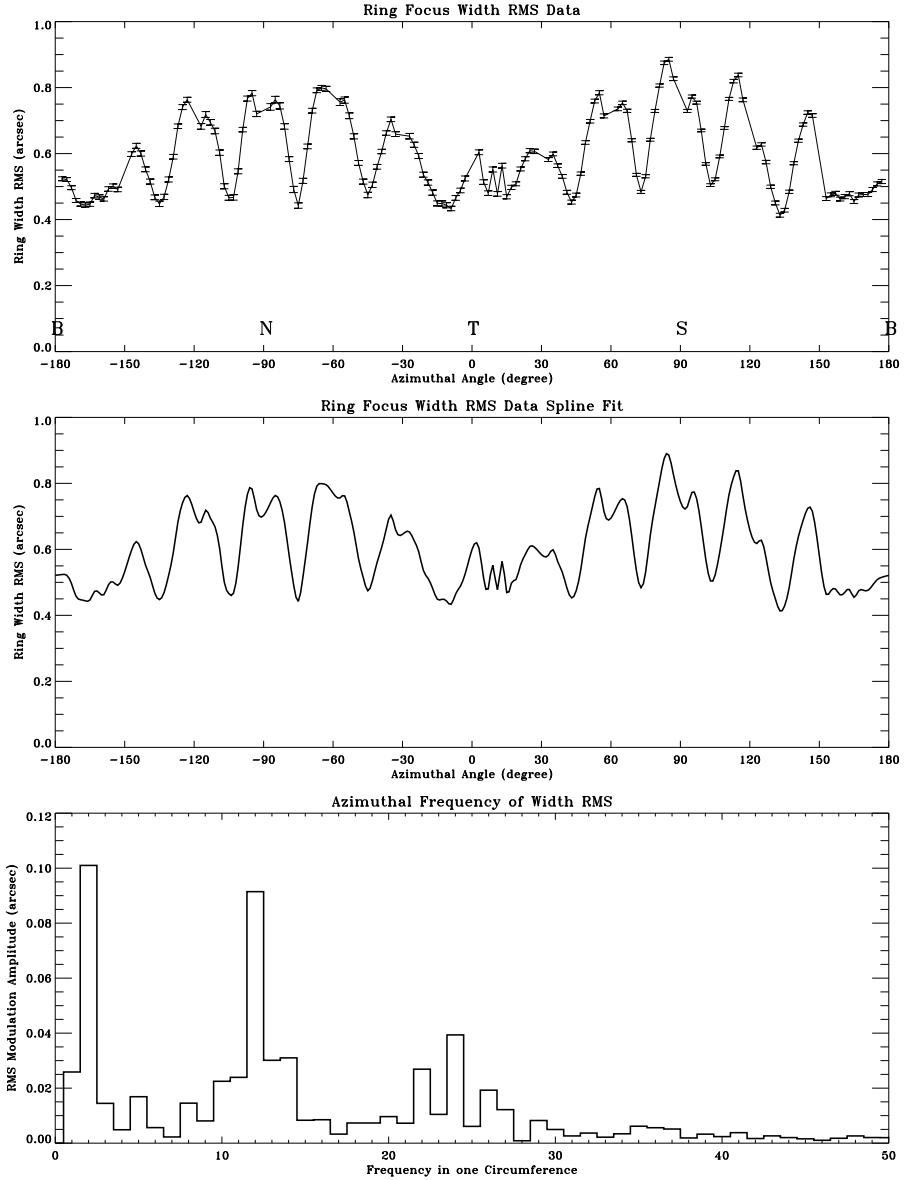

Figure 18.11: The Ring width RMS for ring 1. Date: 1997/01/24; TRW ID: D-IXH-RF-1.005; Run ID: 110004; Source: Al–K; Defocus: 65.2 mm.

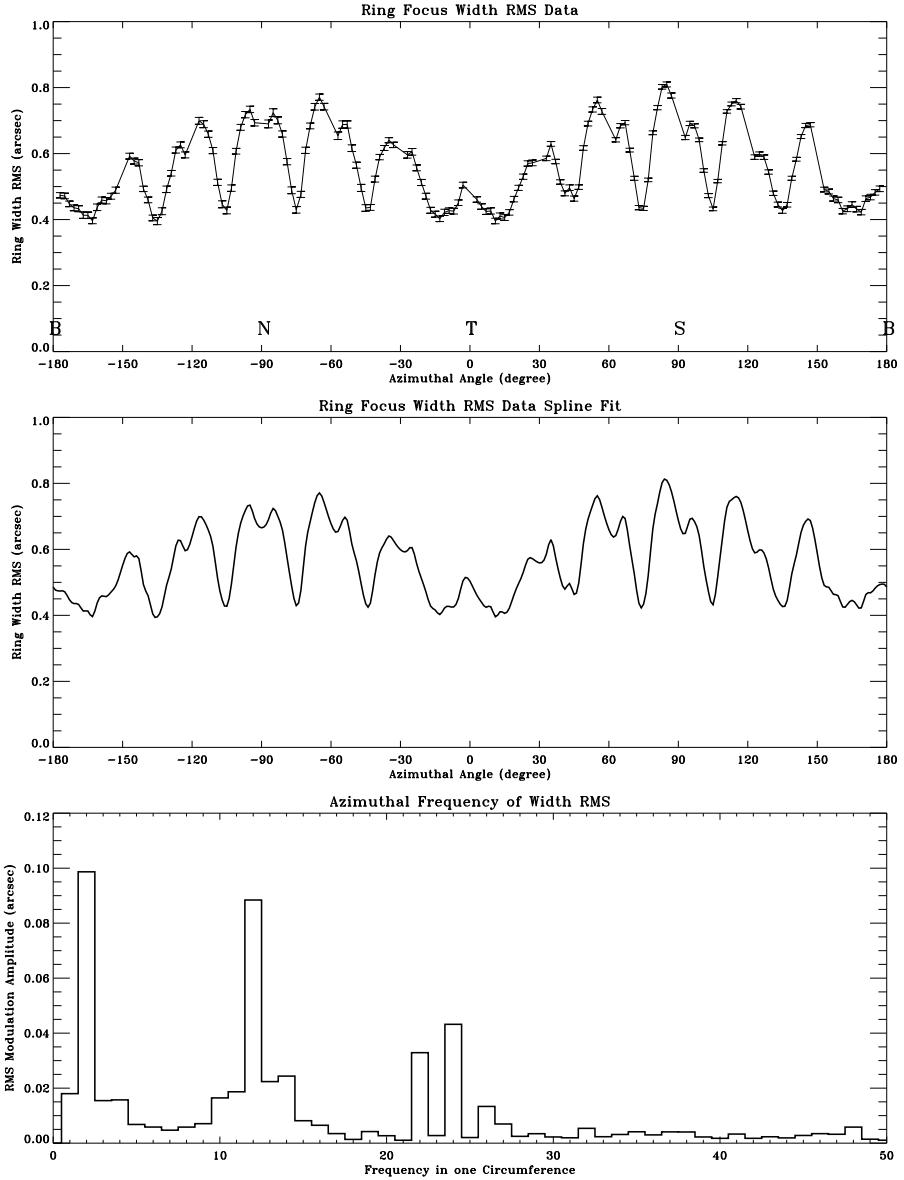

Figure 18.12: The Ring width RMS for ring 3. Date: 1997/01/24; TRW ID: D-IXH-RF-1.005; Run ID: 110004; Source: Al–K; Defocus: 65.2 mm.

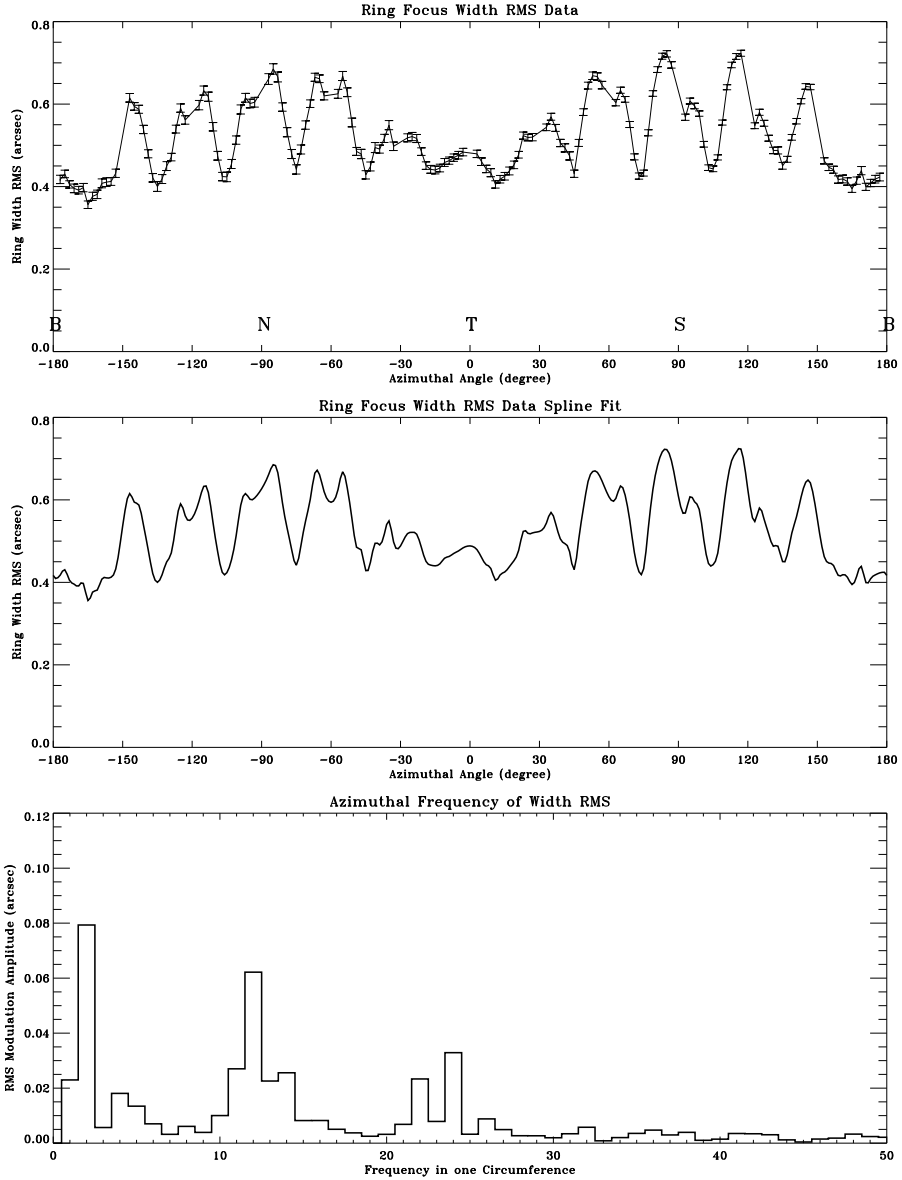

Figure 18.13: The Ring width RMS for ring 4. Date: 1997/01/24; TRW ID: D-IXH-RF-1.005; Run ID: 110004; Source: Al–K; Defocus: 65.2 mm.

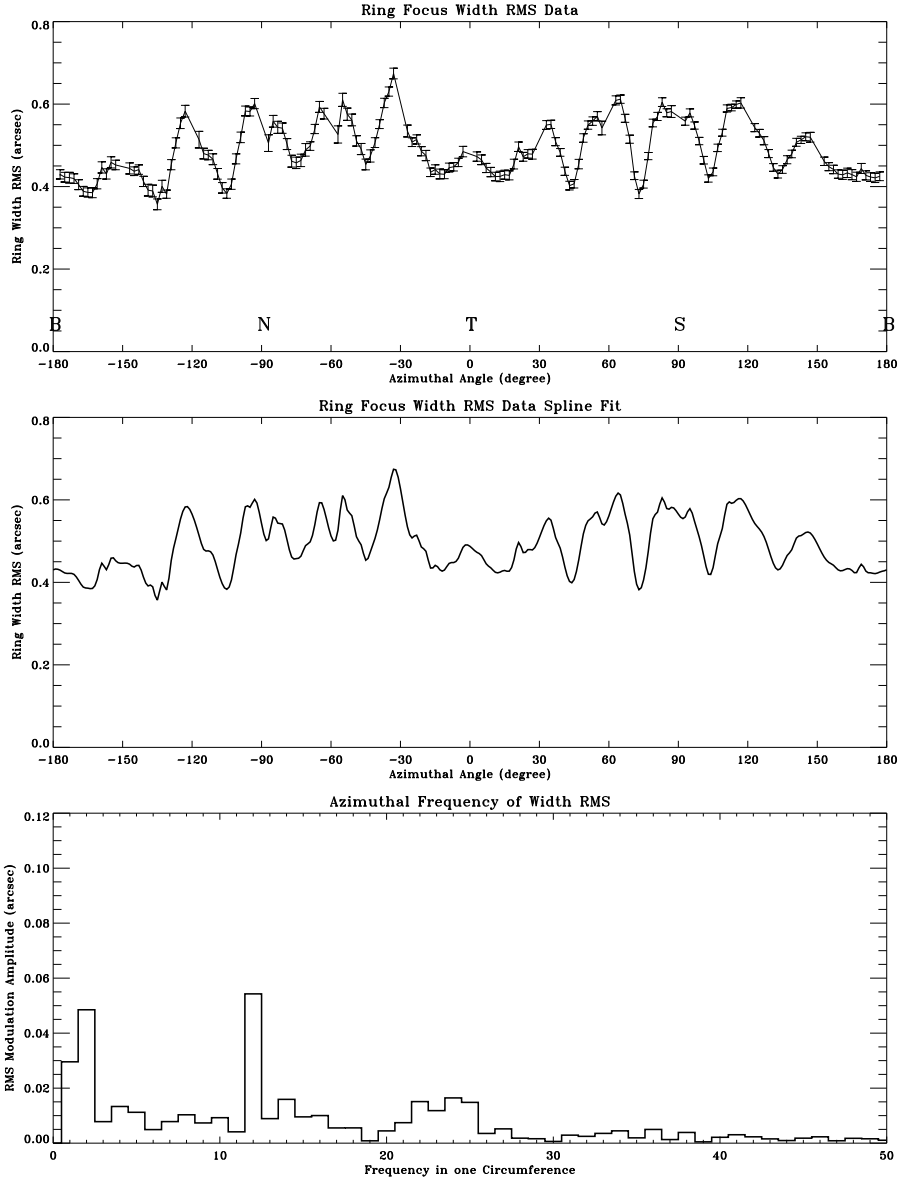

Figure 18.14: The Ring width RMS for ring 6. Date: 1997/01/24; TRW ID: D-IXH-RF-1.005; Run ID: 110004; Source: Al–K; Defocus: 65.2 mm.

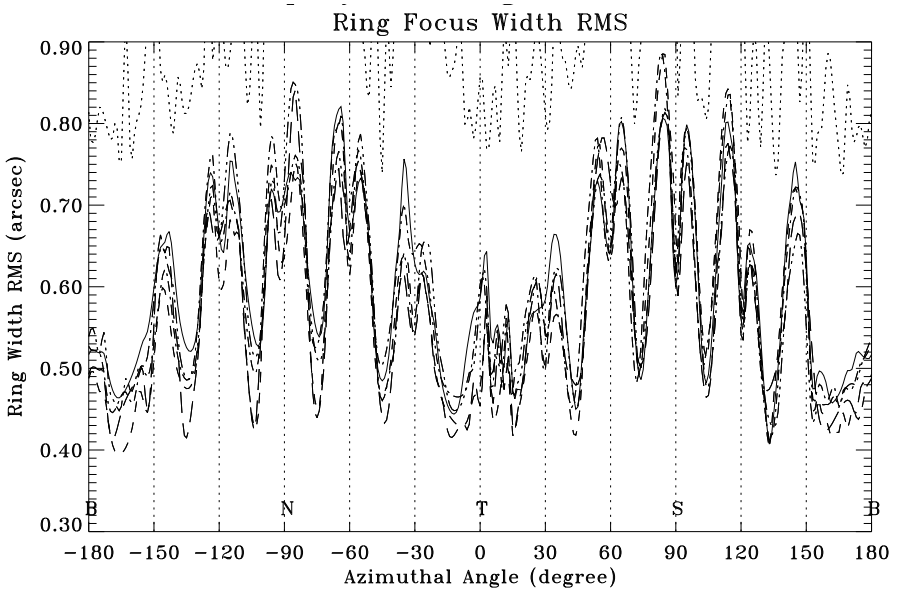

Figure 18.15: The Ring width RMS for ring 1, from all six ring focus measurements.

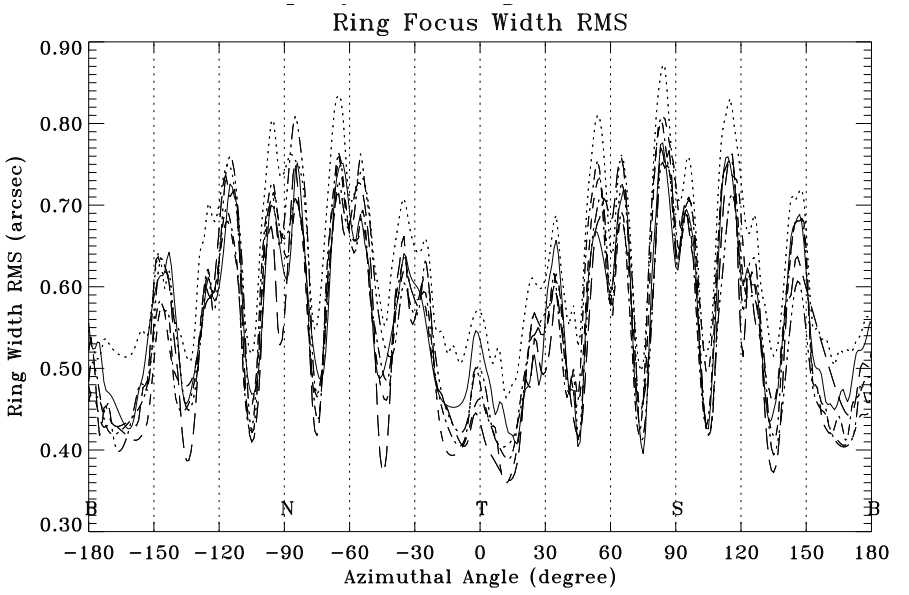

Figure 18.16: The Ring width RMS for ring 3, from all six ring focus measurements.

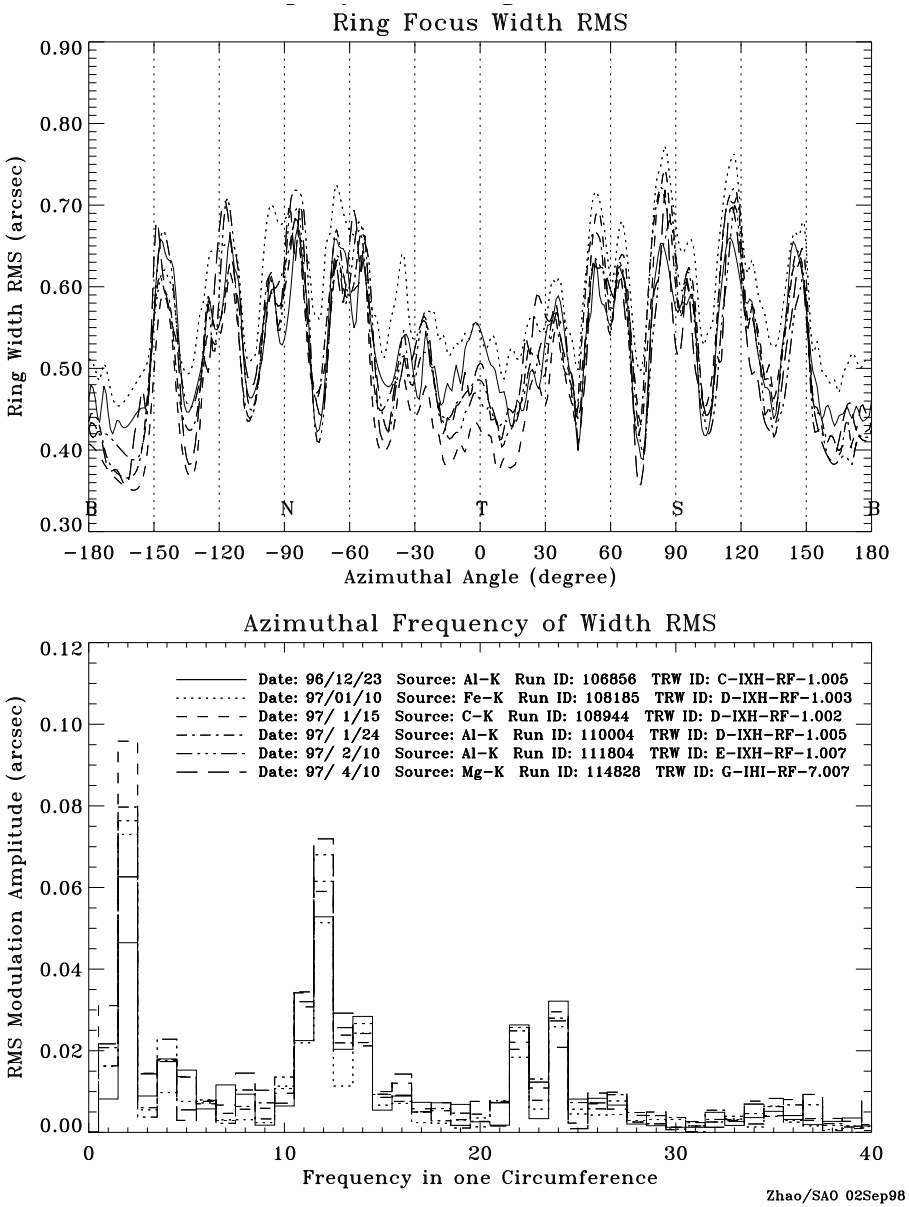

Figure 18.17: The Ring width RMS for ring 4, from all six ring focus measurements.

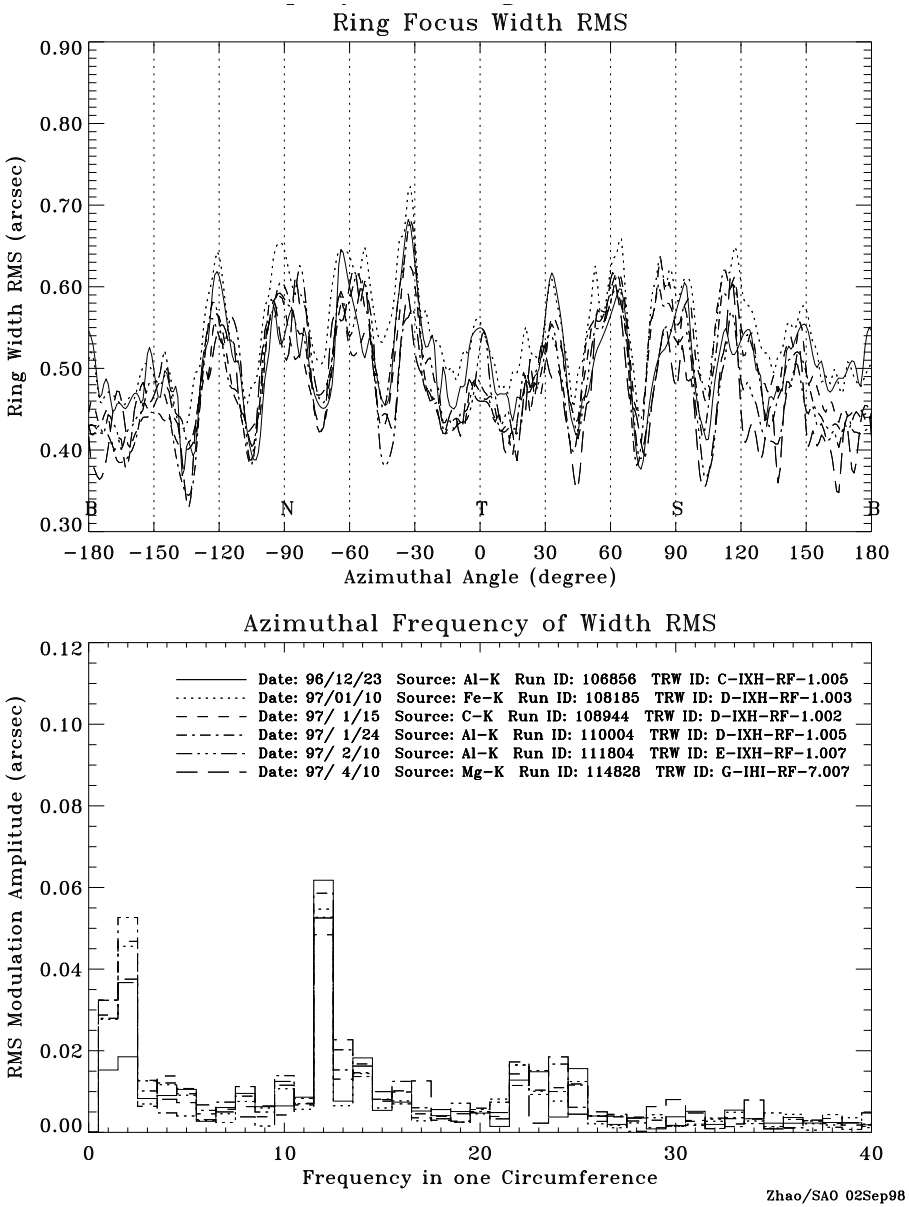

Figure 18.18: The Ring width RMS for ring 6, from all six ring focus measurements.

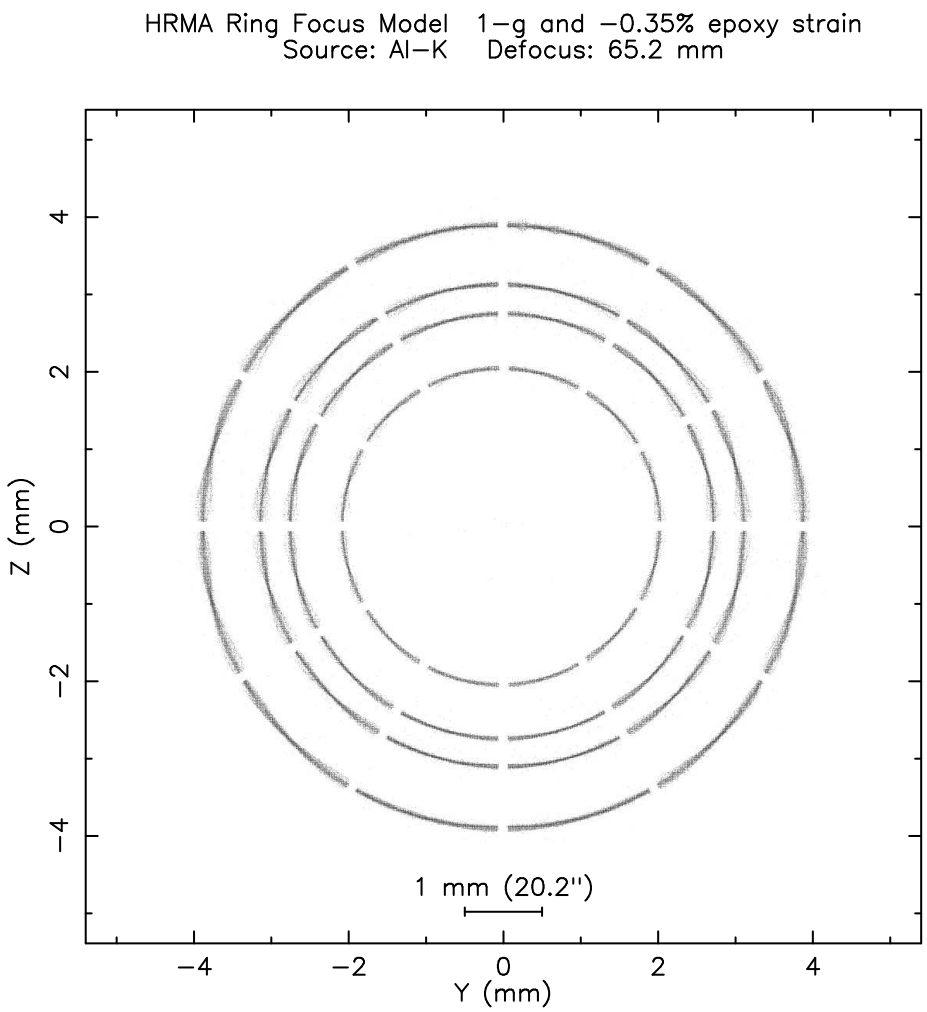

Figure 18.19: The HRMA ring focus model with -0.5% epoxy strain. Source: Al-K; Defocus: 65.2 mm

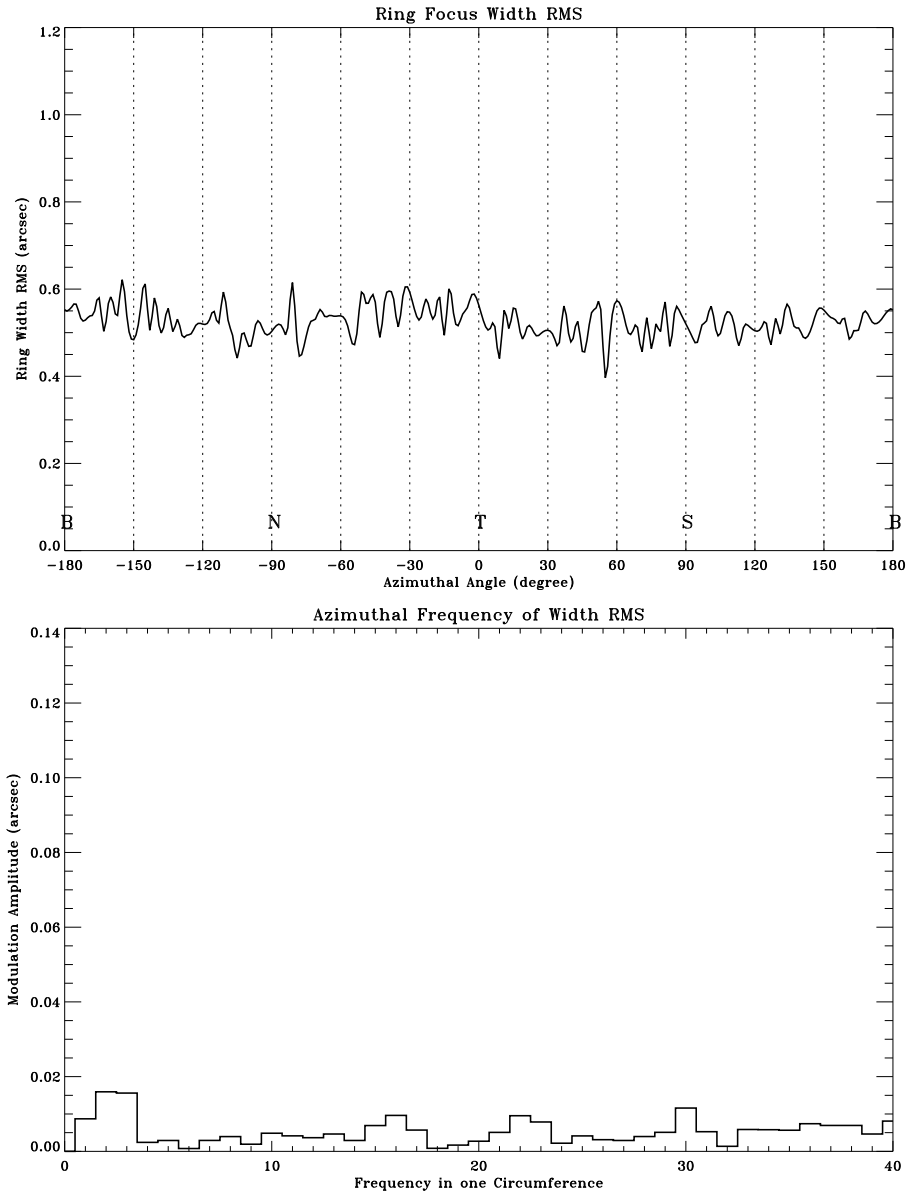

Figure 18.20: HRMA ring focus model: Ring 1, Al-K source, no gravity, no epoxy strain.

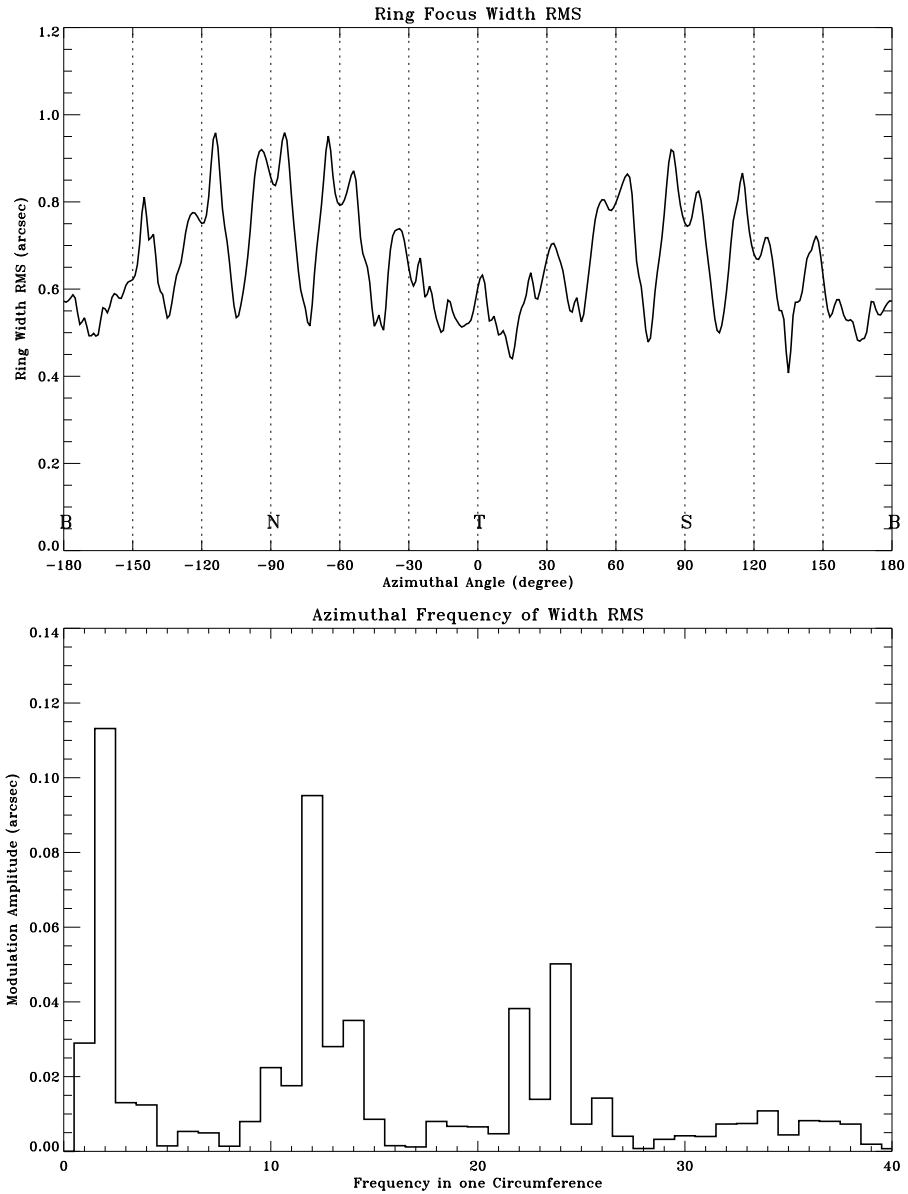

Figure 18.21: HRMA ring focus model: Ring 1, Al-K source, with gravity, no epoxy strain.

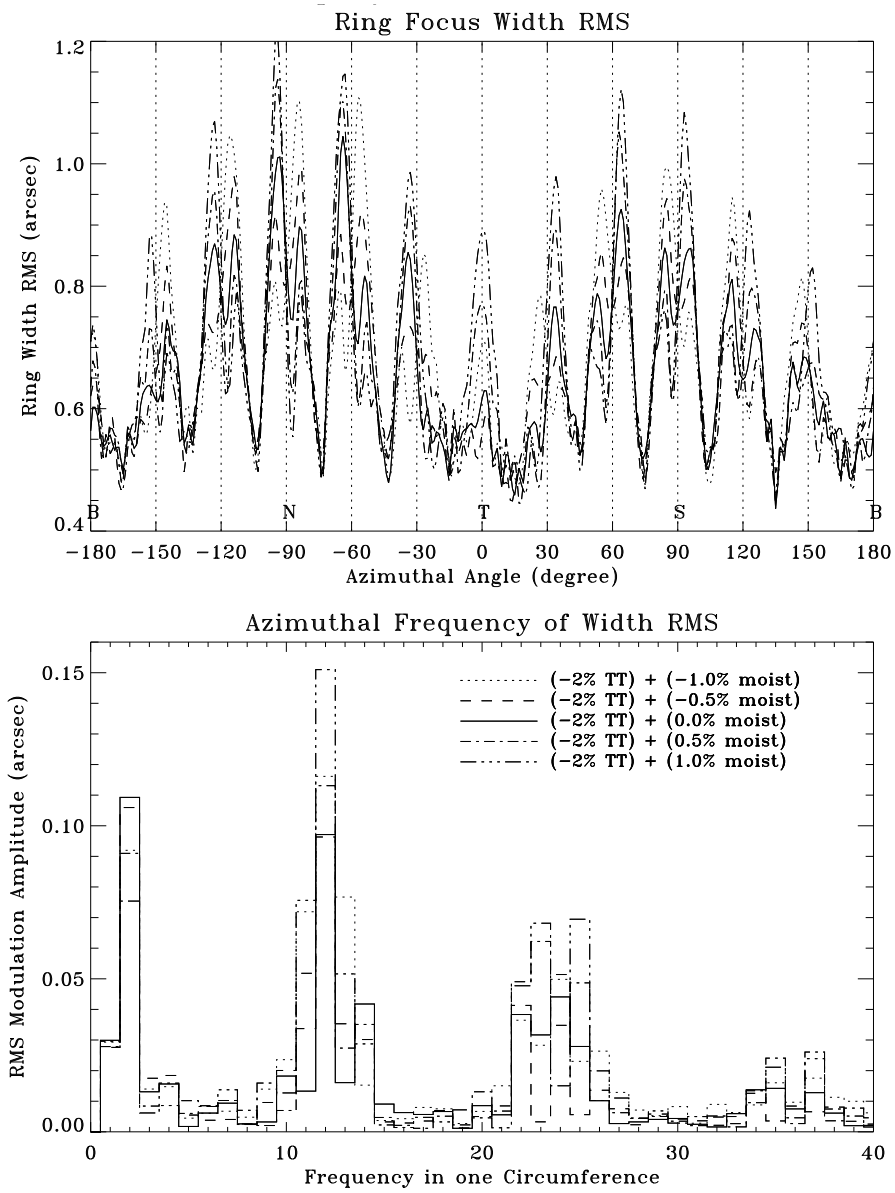

Figure 18.22: HRMA ring focus model: Ring 1, Al-K source, with gravity and epoxy strain change.

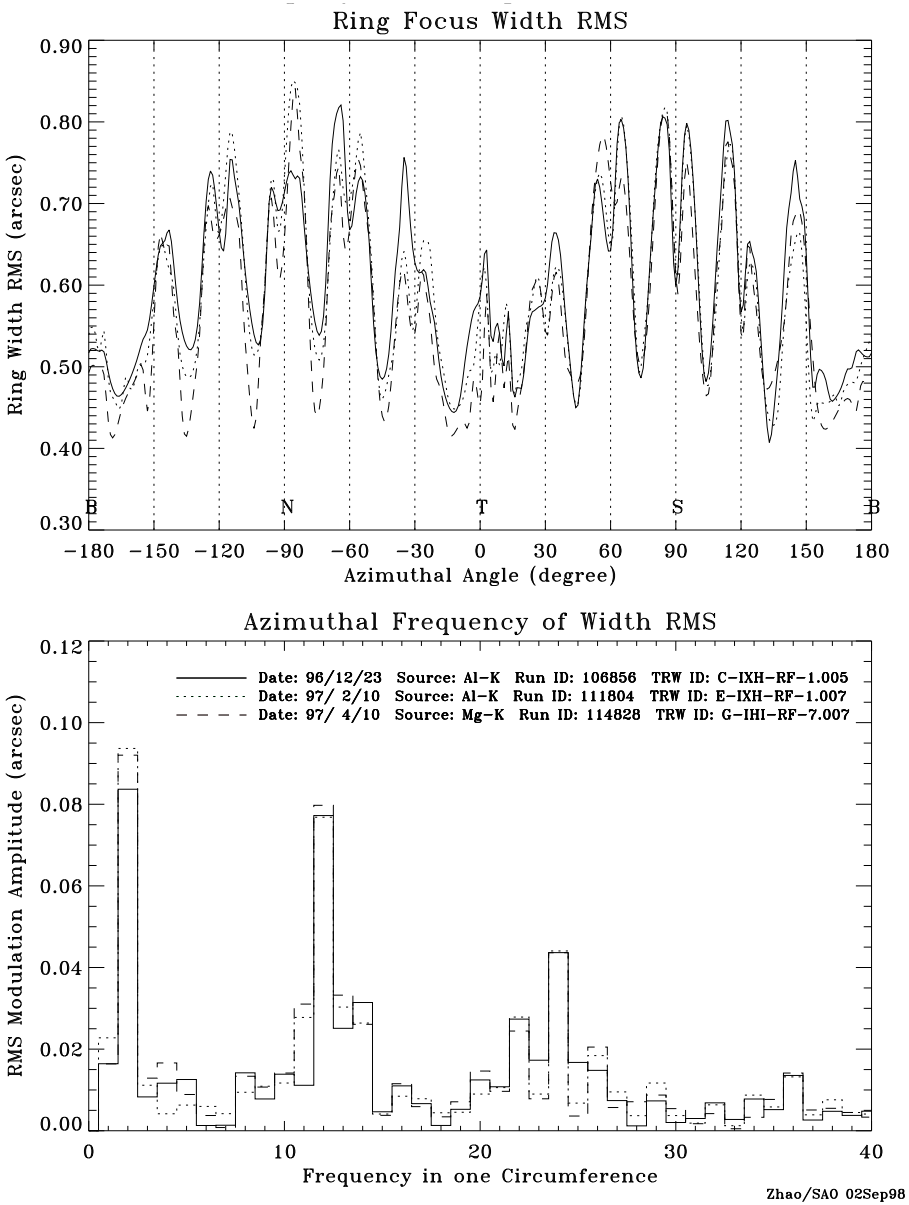

Figure 18.23: The Ring width RMS for ring 1, from three ring focus measurements on 1996/12/23, 1997/02/10 and 1997/04/10.

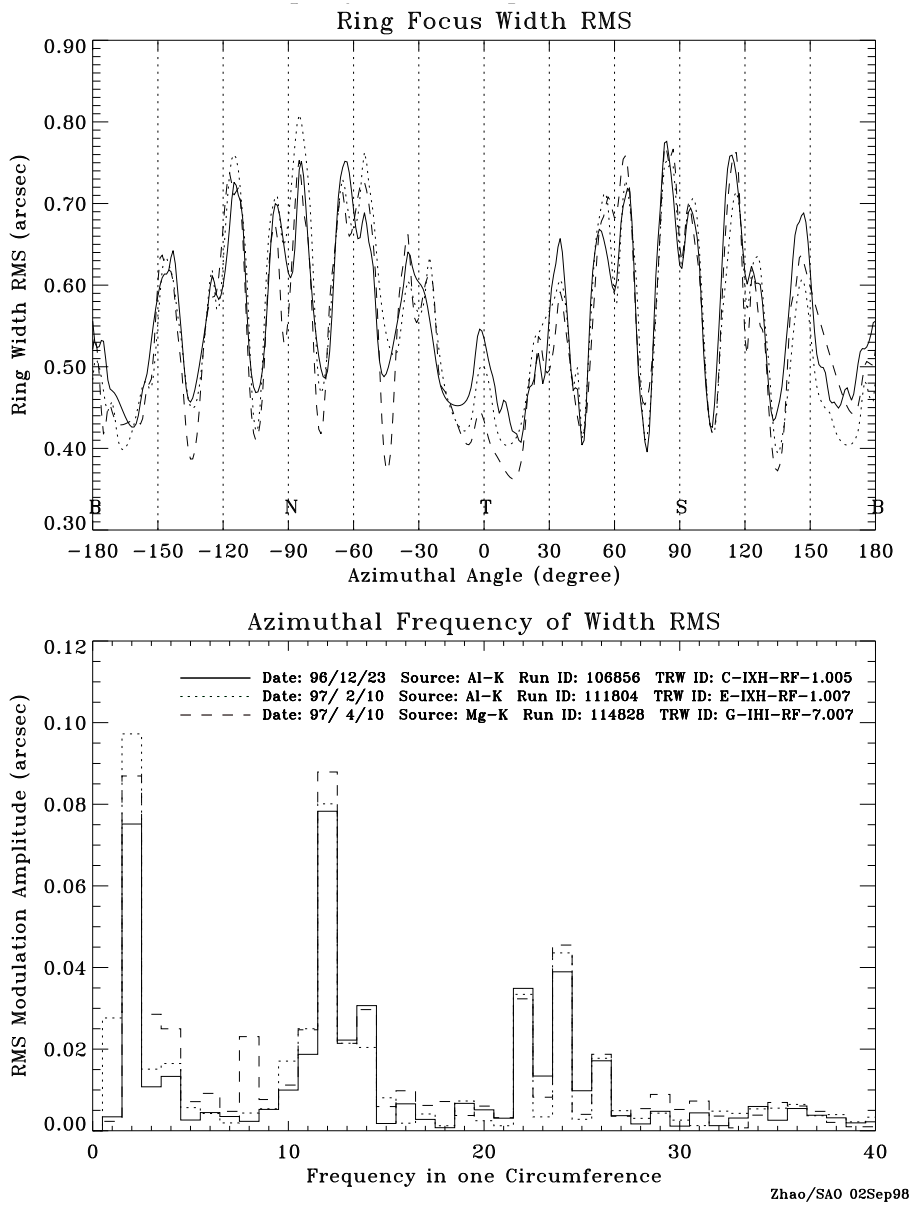

Figure 18.24: The Ring width RMS for ring 3, from three ring focus measurements on 1996/12/23, 1997/02/10 and 1997/04/10.

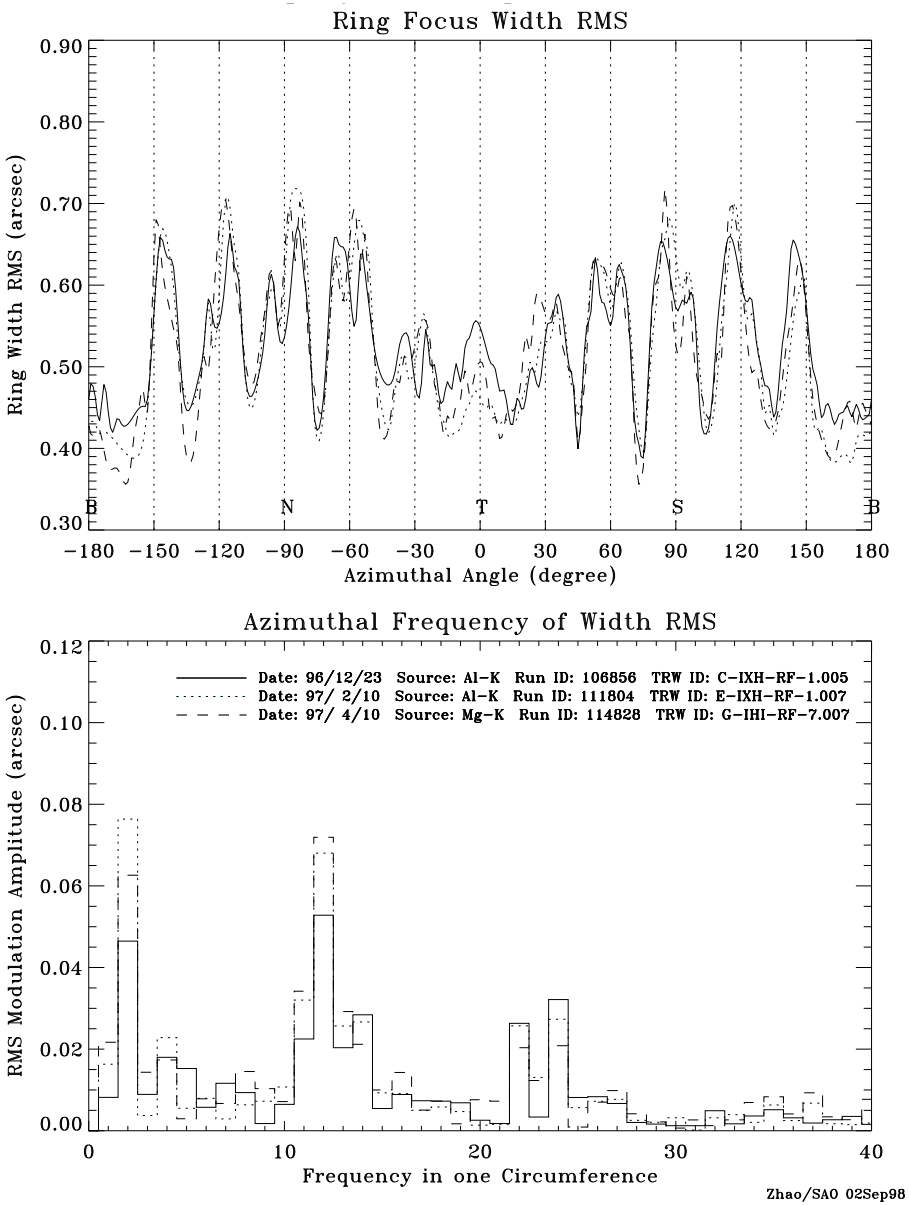

Figure 18.25: The Ring width RMS for ring 4, from three ring focus measurements on 1996/12/23, 1997/02/10 and 1997/04/10.

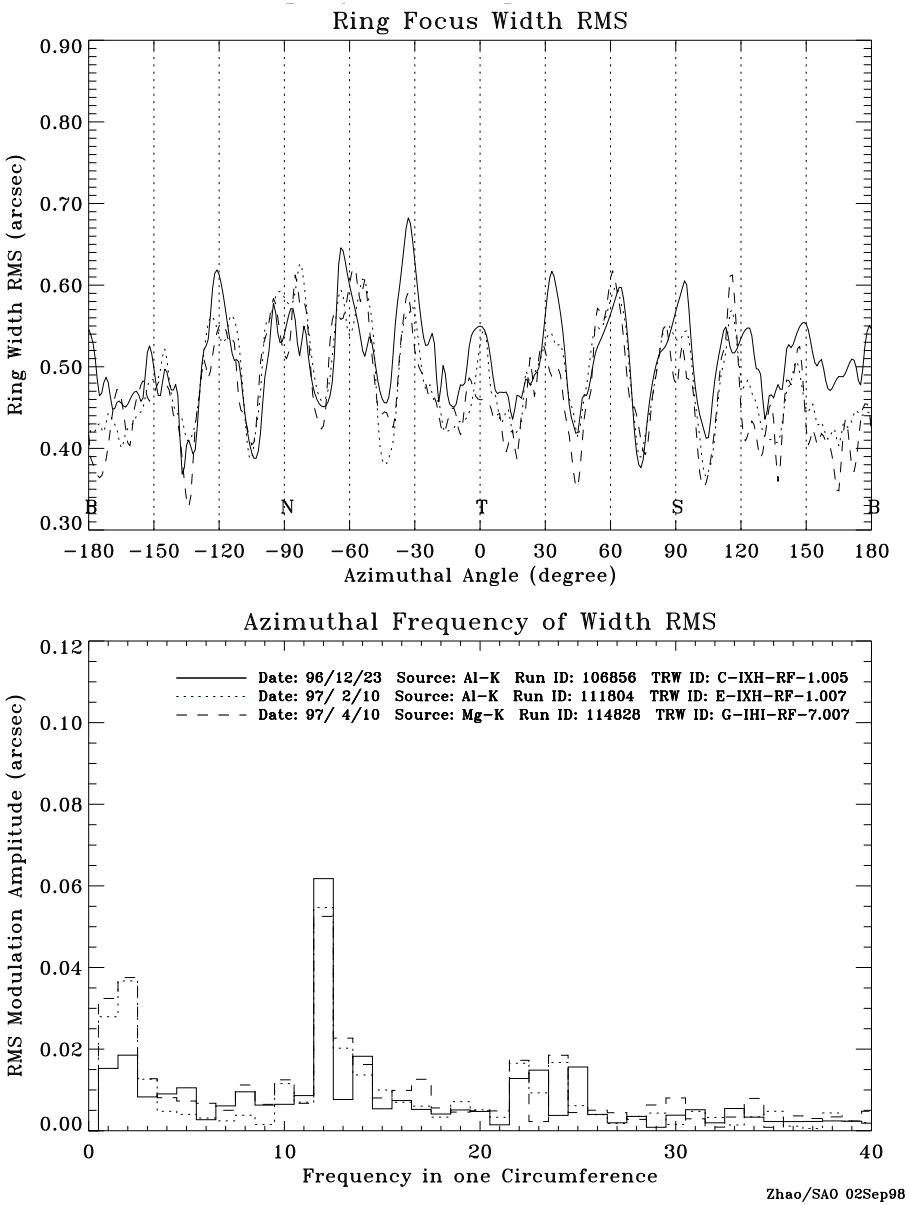

Figure 18.26: The Ring width RMS for ring 6, from three ring focus measurements on 1996/12/23, 1997/02/10 and 1997/04/10.

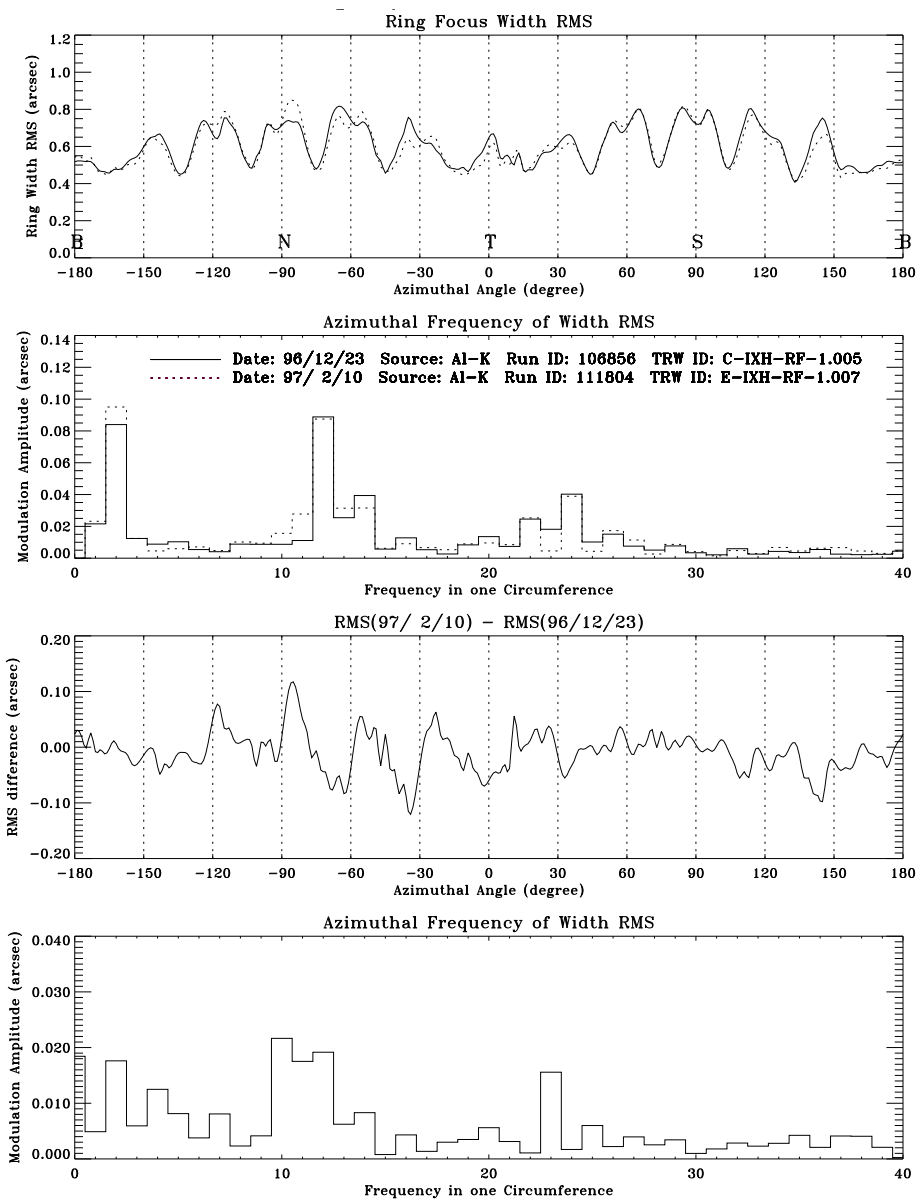

Figure 18.27: HRMA ring focus Data: Ring 1, Al-K source, data of 1996/12/23 and 1997/02/10 and their difference.

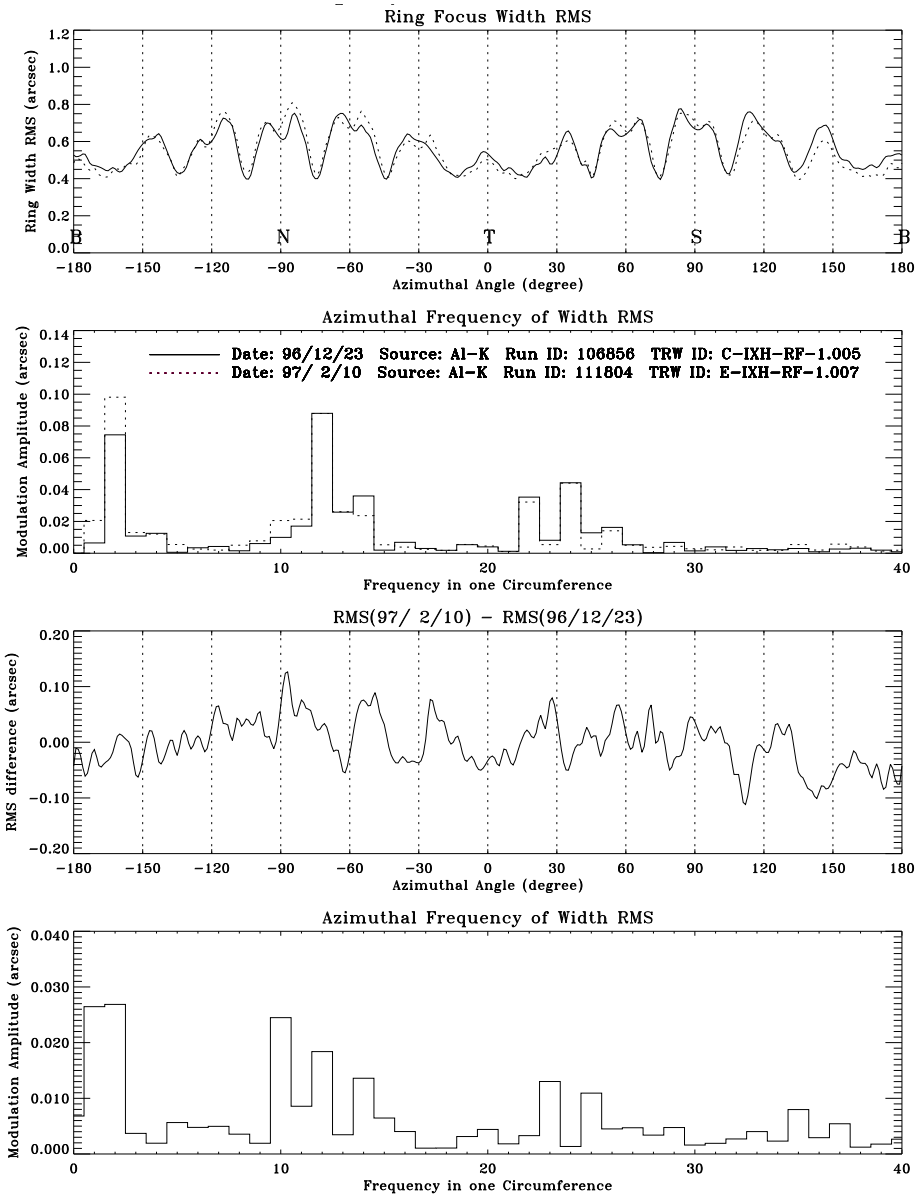

Figure 18.28: HRMA ring focus Data: Ring 3, Al-K source, data of 1996/12/23 and 1997/02/10 and their difference.

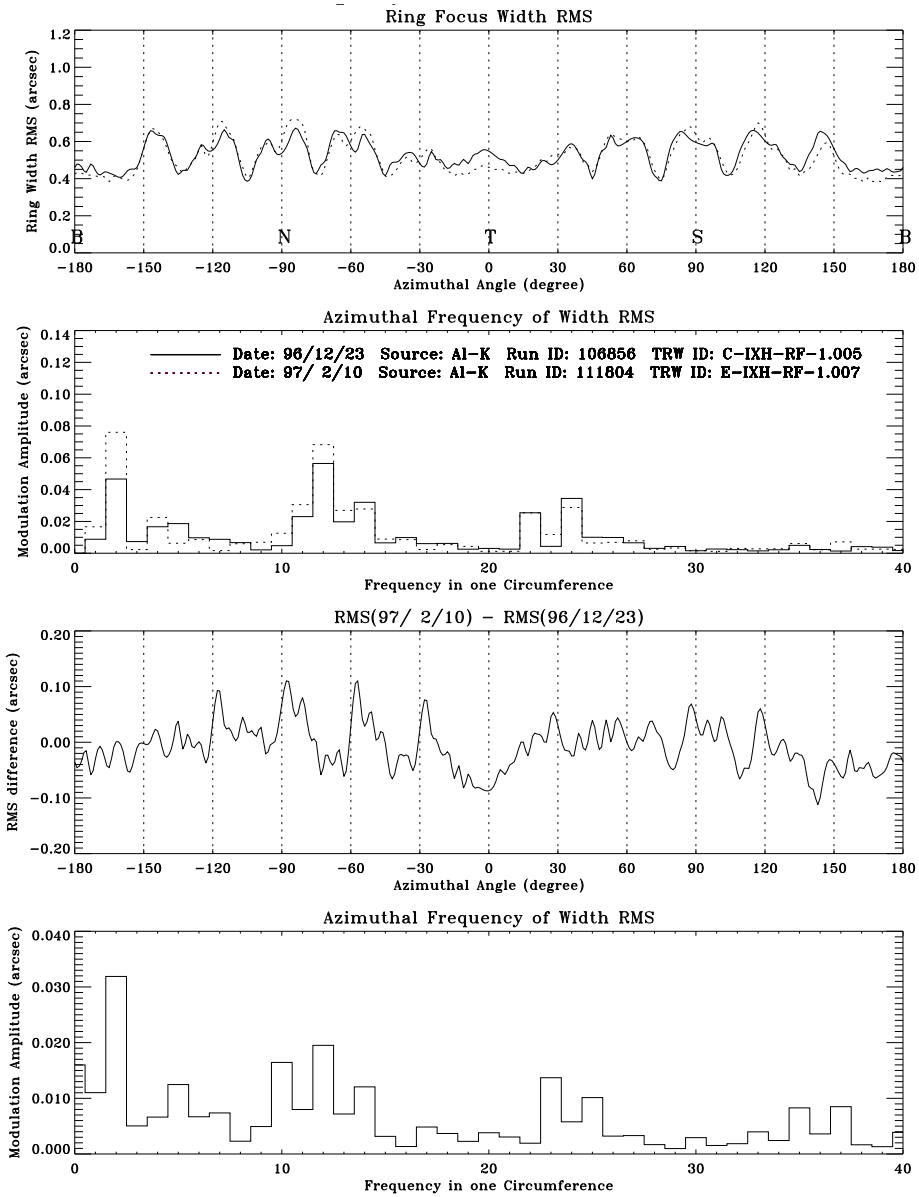

Figure 18.29: HRMA ring focus Data: Ring 4, Al-K source, data of 1996/12/23 and 1997/02/10 and their difference.

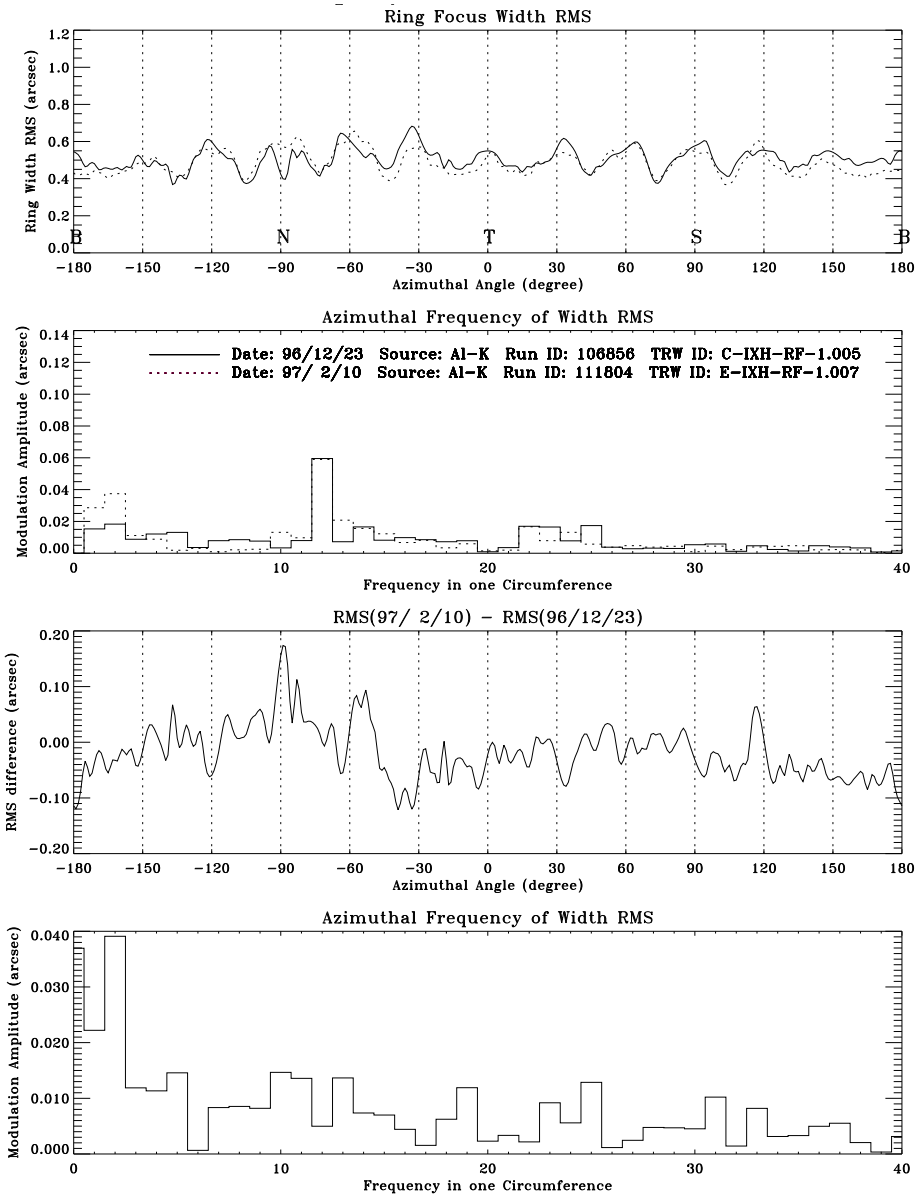

Figure 18.30: HRMA ring focus Data: Ring 6, Al-K source, data of 1996/12/23 and 1997/02/10 and their difference.

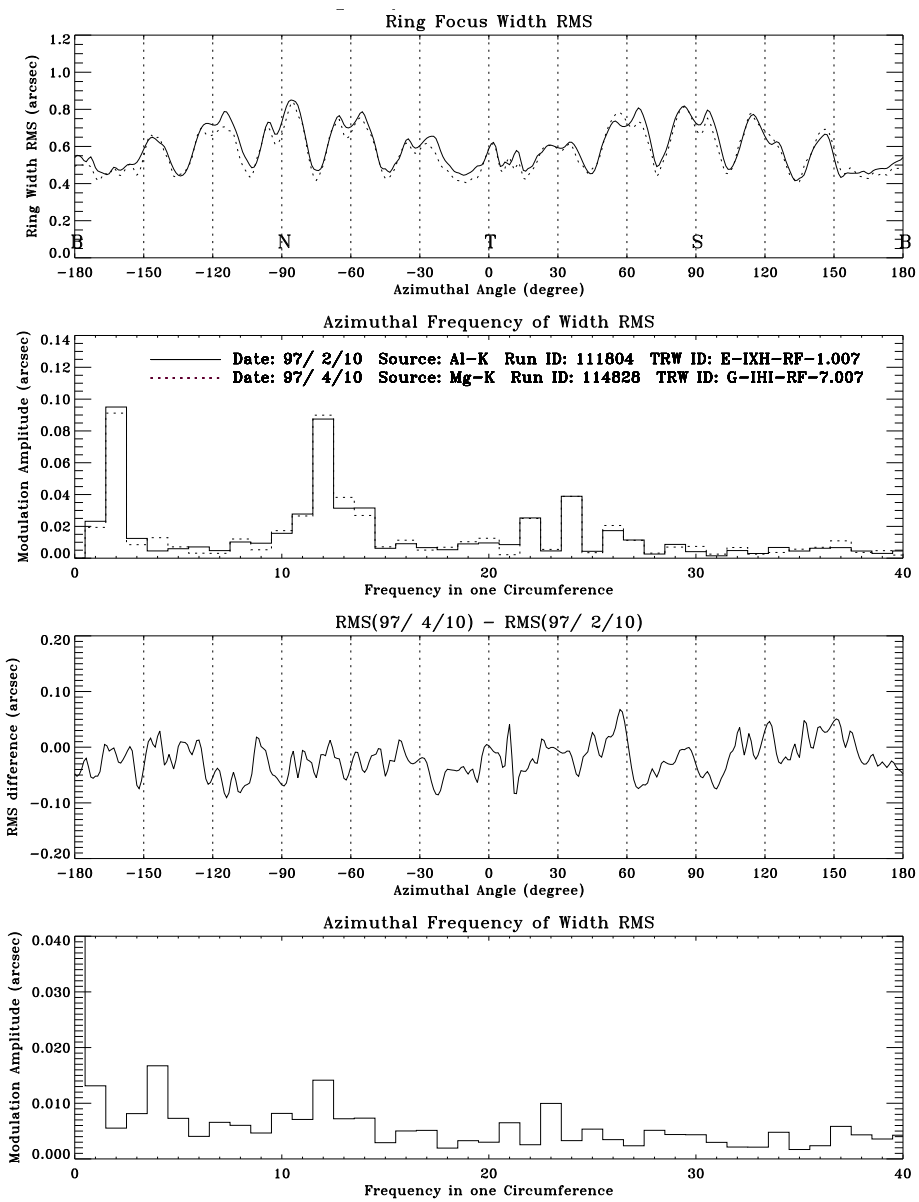

Figure 18.31: HRMA ring focus Data: Ring 1, Al-K source, data of 1997/02/10 and 1997/04/10 and their difference.

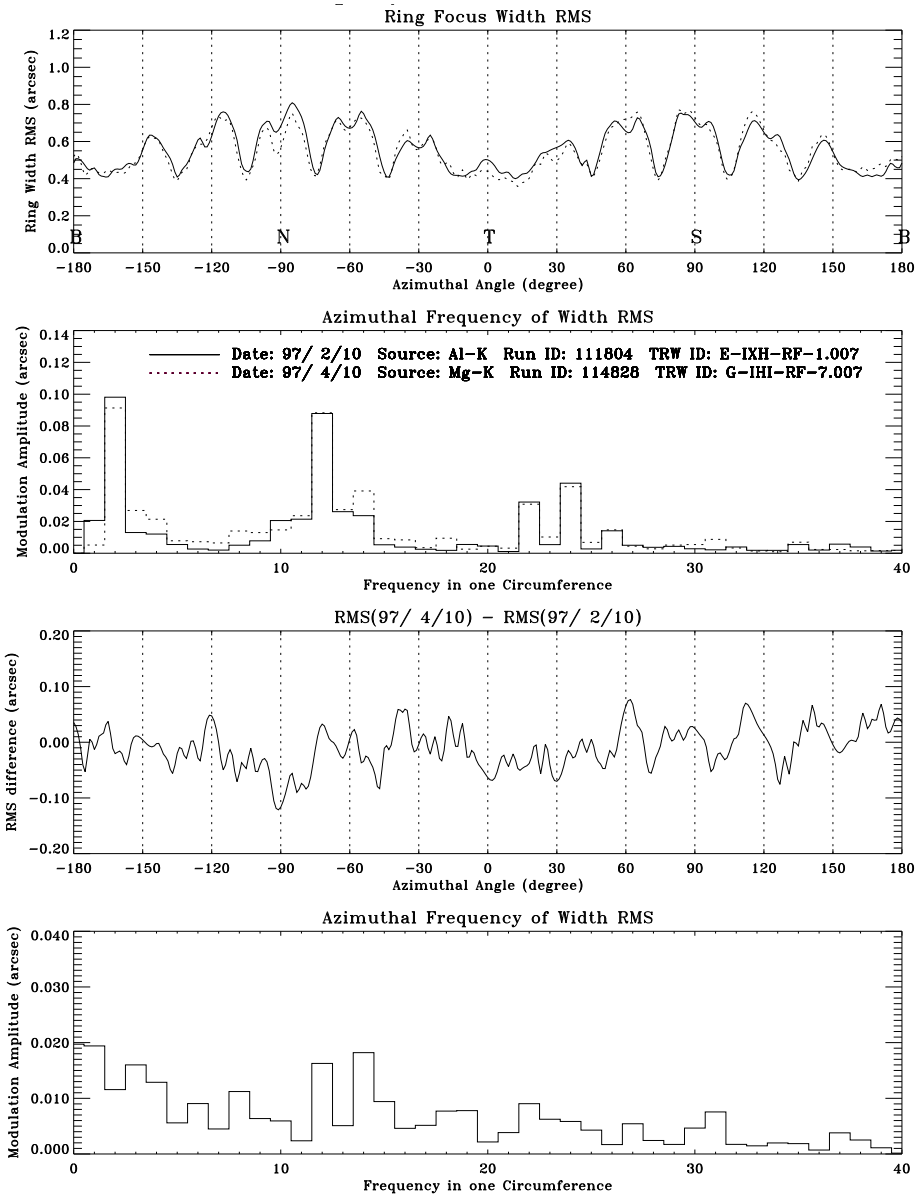

Figure 18.32: HRMA ring focus Data: Ring 3, Al-K source, data of 1997/02/10 and 1997/04/10 and their difference.

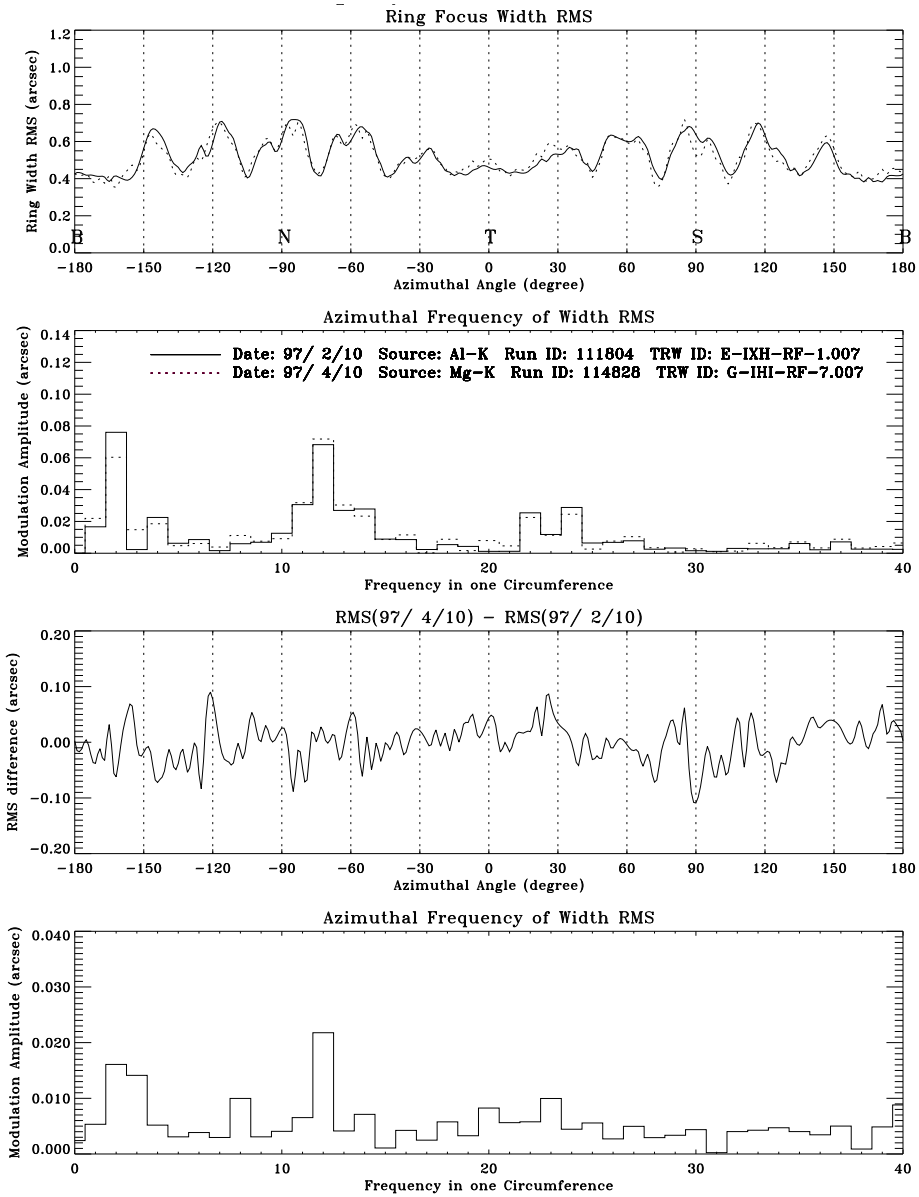

Figure 18.33: HRMA ring focus Data: Ring 4, Al-K source, data of 1997/02/10 and 1997/04/10 and their difference.

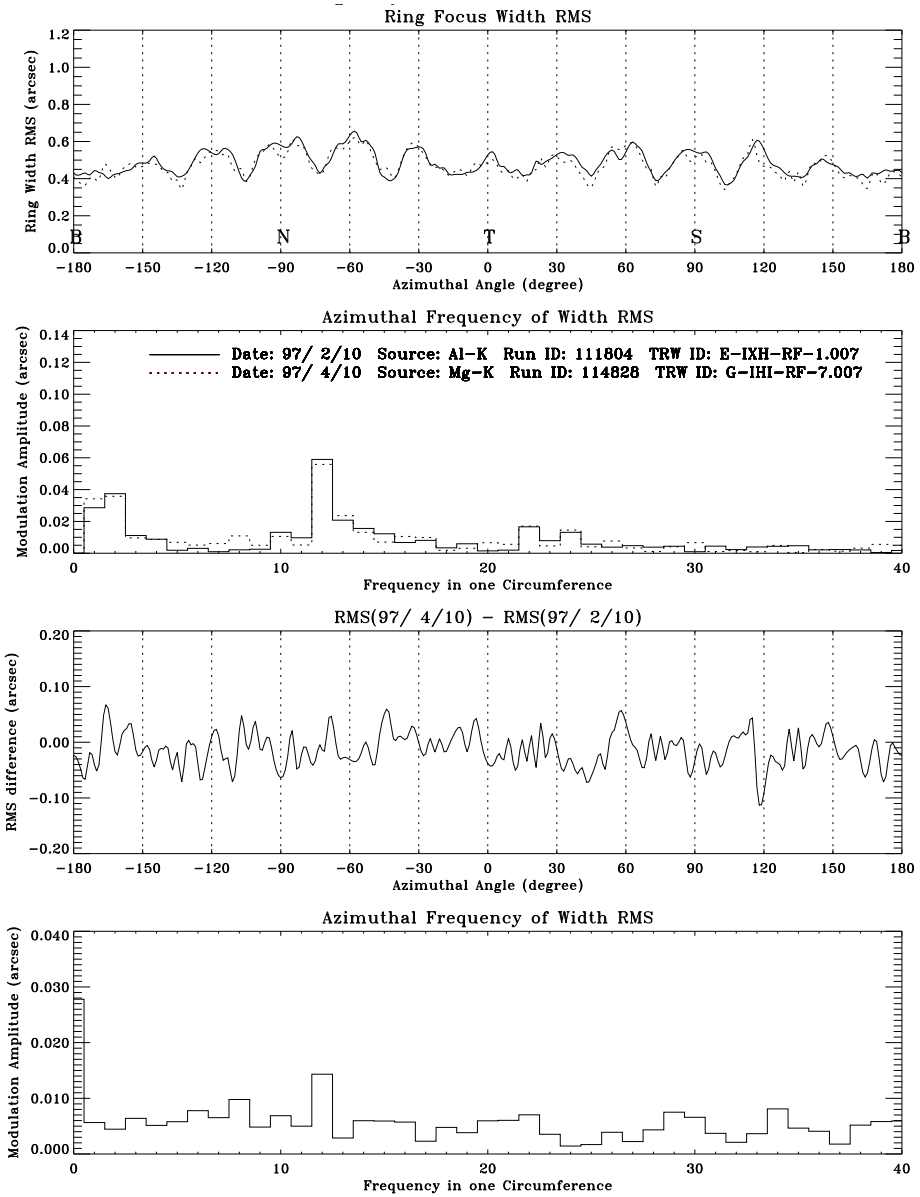

Figure 18.34: HRMA ring focus Data: Ring 6, Al-K source, data of 1997/02/10 and 1997/04/10 and their difference.

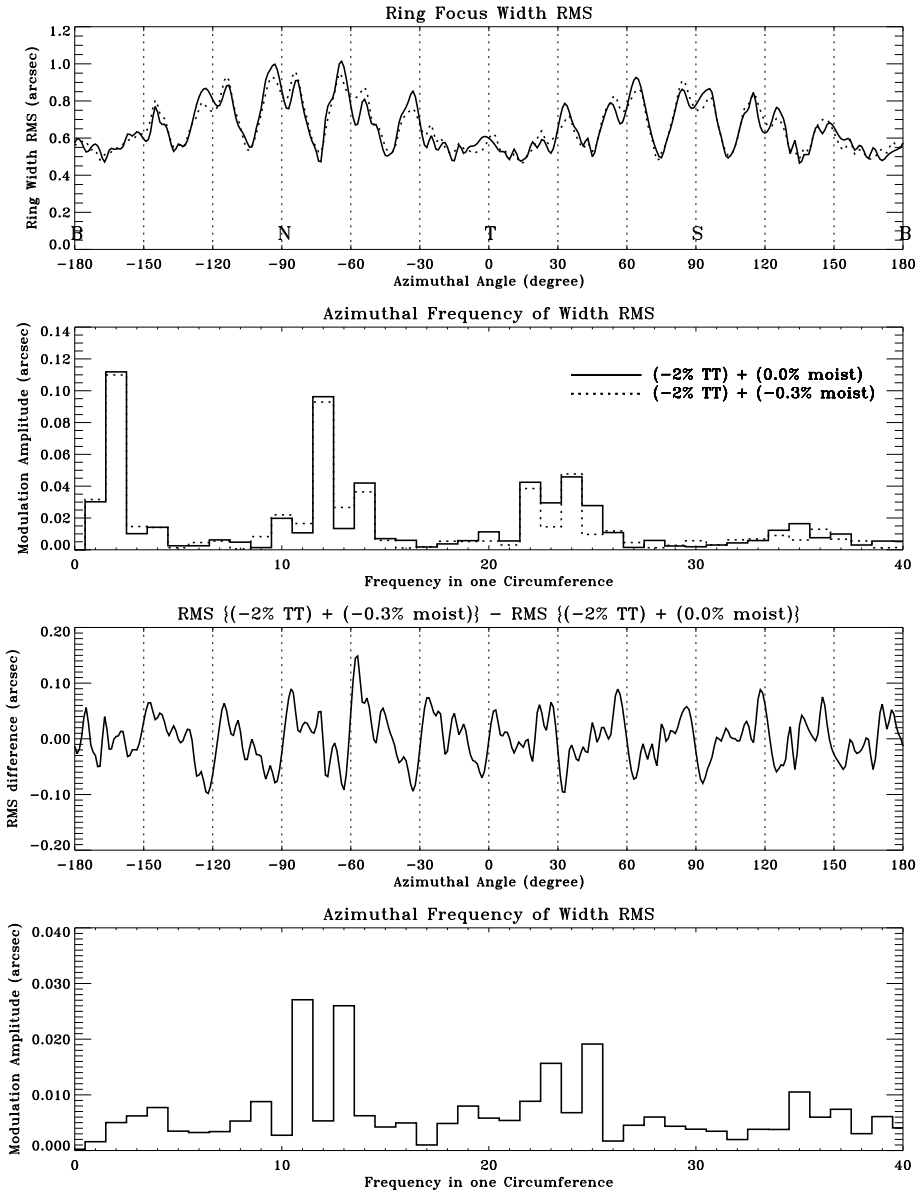

Figure 18.35: HRMA ring focus model: Ring 1, Al-K source, epoxy strain with 0.0% and -0.3% moist and their difference.

Chapter 19

HRMA PSF

Chapter 20

HRMA Ghost Image Properties

Terrance J. Gaetz

20.1 Ghost Images – Geometry

Ghost images occur when photons reach the focal plane after missing the paraboloid or the hyperboloid of a given mirror pair. The ghost rays can be classified into the following types:

- nonreflected rays: missed both the P (paraboloid) and the H (hyperboloid) optics of a given mirror pair.
- P-ghosts: missed the P mirror.
- H-ghosts: missed the H mirror.

The HRMA was designed to suppress ghost images within $14'$ of the optical axis. This was accomplished by X-ray baffles at the location of the first thermal precollimator plate and X-ray baffles at the aft surface of the HRMA Central Aperture Plate (CAP). In addition, an X-ray baffle is needed in the P6 cavity. A description of the X-ray baffle design is given in Gaetz (1993).

The behavior of the ghost images can be understood qualitatively as follows. If a Wolter Type-I mirror pair were completely unbaffled, ghost rays would reach the focal plane even in the on-axis case. Individual mirror elements do not focus rays at the same location as a mirror pair: the paraboloidal mirror elements focus rays behind the mirror pair focal plane, while the hyperboloidal mirror elements focus rays ahead of the pair focal plane (see Figure 20.1)

Rays which are parallel to the optical axis and which hit the P optic will also reflect off the H optic (neglecting the effects of scattering and assuming a perfectly aligned system). Because the H optics are actually slightly over-long compared to the matching P optics, there is a slight range of off-axis angles (in the as-designed system) where rays hitting the P optic will continue to hit the H optic. Eventually, though, the off-axis angle becomes steep enough that rays hitting near the front of the P will be reflected too steeply to hit the H optic; such rays become ghost rays if they are not blocked (Figure 20.2). Rays which are parallel to the optical axis and hit the hyperboloid will reach the focal plane as ghost rays (in an unbaffled system) but well outside the the detector area; to lowest order, the radius of this H-ghost ring is half the radius of the mirror pair.

The behavior of the ghost images can be understood qualitatively by considering the reflection properties of individual paraboloid or hyperboloid mirrors. Consider a paraboloidal mirror element by itself (*i.e.*, in the absence of its companion hyperboloid); rays from an on-axis point source at infinity will produce an out-of-focus ring at the (mirror pair) focal plane. In this case, the focus of

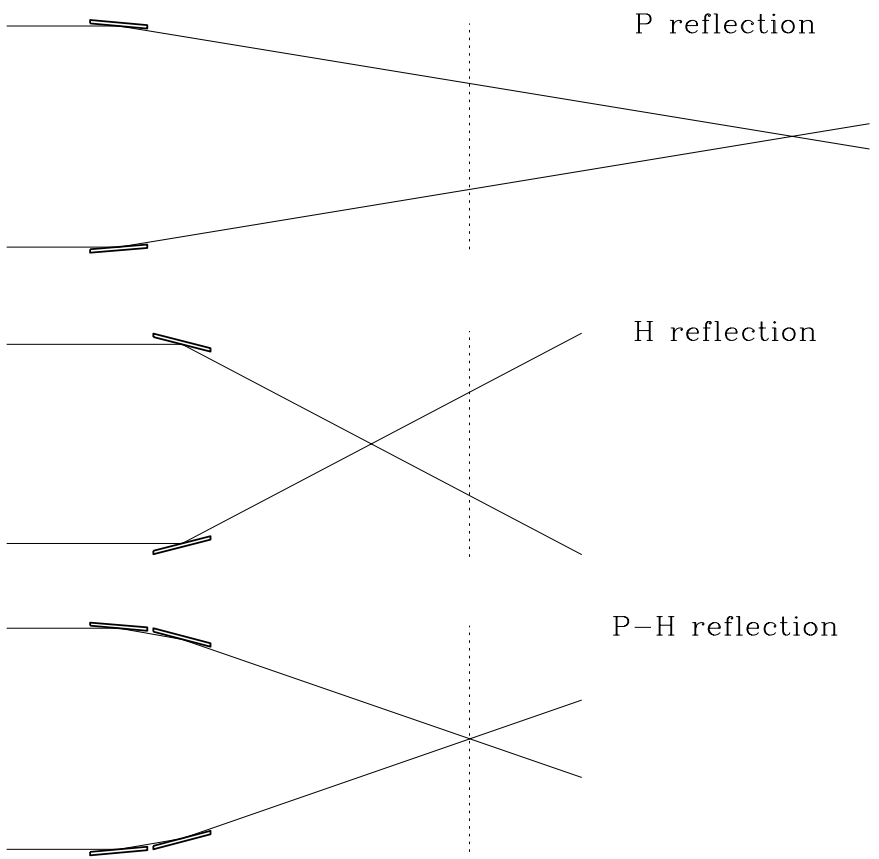

Figure 20.1: Schematic diagram of rays reflected from a single P or H mirror element compared to the P and H combination of the Wolter type I design. The dashed line indicates the focal plane for the mirror pair.

the optic is behind the system focus so that the $+Y$ portion of the out of focus ring is produced by the $+Y$ portion of the optic. A hyperboloidal mirror element by itself also produces an out of focus ring; however, because the hyperboloid focuses the rays ahead of the focal plane, the image is inverted and the $-Y$ portion of the image is produced by the $+Y$ portion of the optic. In reality, the on-axis rays which hit the P optic will also reflect from the companion H optic and reach the system focus. In the absence of baffles, rays which miss the P optic will hit the H optic and become single reflection H-ghosts, or miss both the P and H optics and become nonreflected ghosts. The HRMA baffles are designed to reject non-reflected ghost rays, and to prevent single reflection ghosts from hitting within the central $14'$ of the focal plane, while at the same time not vignetting doubly-reflected rays incident within $14'$ of the optical axis.

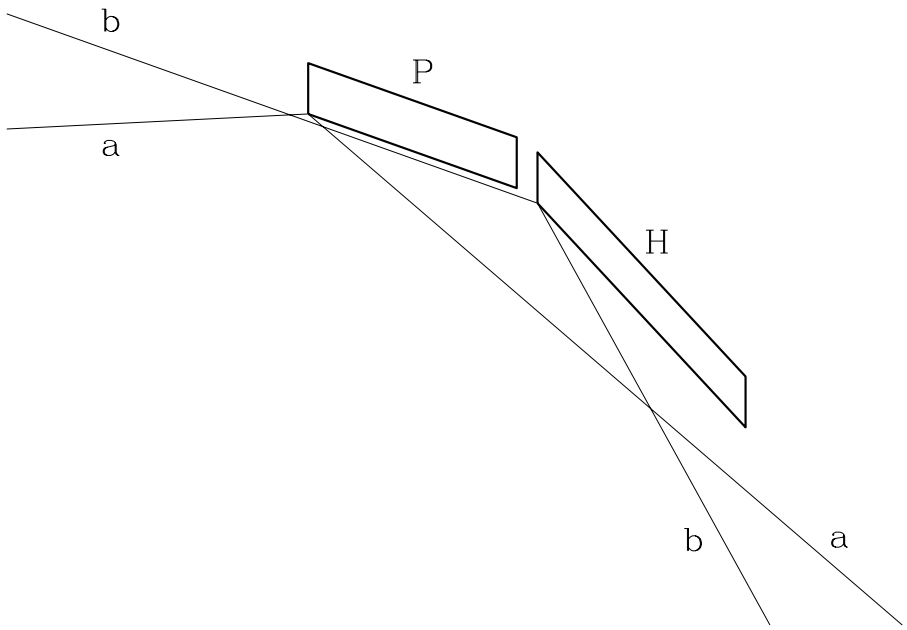

Figure 20.2: Schematic diagram of single reflection ghosts. Ray a strikes the parabola with too steep a positive slope and the reflected ray misses the aft end of the hyperbola becoming a "P ghost". Ray b is an example of an "H ghost".

Note that the finite length of the optics produces edges which vignette the rays. In the AXAF mirror design, the H optics are slightly over-long compared to the P optics: for perfect optics and perfect alignment, the set of rays parallel to the axis which illuminate the P optics are reflected and illuminate almost all of the companion H optics; however, a narrow band at the forward and aft end of each H optic is unilluminated.

As a source moves further and further off-axis, the rings of singly-reflected rays deforms inward (along the axis containing the source and the optical axis). The ring forms a cusp (cardioid-like) when the off-axis angle is comparable to the graze-angle of the mirror; thereafter, the ghost ring forms a double-loop (very much like a limaçon); both branches of the limaçon grow, and the smaller loop eventually crosses the optical axis unless appropriate X-ray baffles are in place (see Figure 20.3).

20.2 Ghost Baffle Design

In Figure 20.4, possible locations of X-ray baffles in Wolter type I systems are indicated, together with the vignetting constraints. The utility of ghost baffles at each of these locations is discussed by

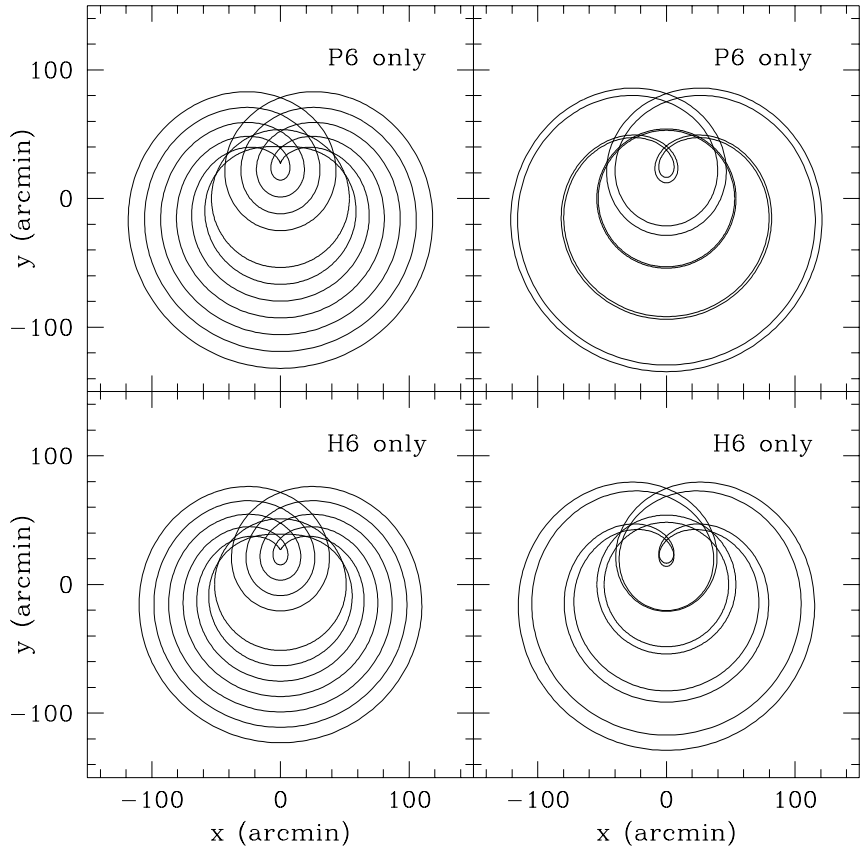

Figure 20.3: The left panels shows the images of rays from a point source at infinity and intercepting a mirror element at its midplane; curves are shown for source off-axis angles of 0, 12.5, 25, 37.5, 50, 62.5, and 75 arcmin. The right panels show the images of rays reflecting from the forward and aft edges of an individual mirror element; curves are shown for off-axis angles of 0, 37.5, and 75 arcmin. In each case only a single mirror element of the mirror pair is considered; the companion mirror element is absent, and the system is assumed to be unbaffled.

Austen and Torgenson (1980); they note that interior baffles (locations I_P and I_H are preferable, but baffling at F, C, or A is usually mechanically more practical. The baffles at the the A position serve to exclude ghost rays *outside* some radius from the optical axis, so they are not relevant to the problem of excluding ghost rays near the optical axis. The original ghost baffle design included baffles only at F and C; this design would not meet the requirement of the AXAF-I *Projects Requirement Document* (PRD) *Level II* (originally a *keep-out* zone of $15'$), and it was

suggested that the requirement be relaxed. Gaetz (1993) showed that the addition of a baffle at the I_P position for P6 would allow the ghost exclusion requirement to be met; the final baffle design included a P6 interior baffle. Based on subsequent manufacturing tolerance concerns, the PRD *Level II* requirement was relaxed to $14'$ from the optical axis. In the following, we briefly discuss the baffling of P-ghosts, H-ghosts, and the vignetting implications.

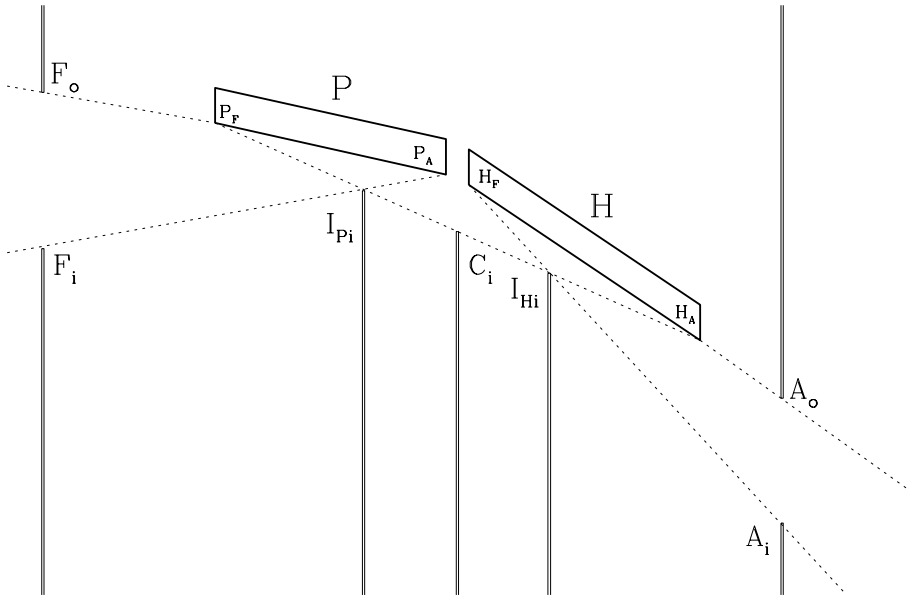

Figure 20.4: Schematic diagram of baffles for Wolter type I optics. The dashed lines originating at the forward and aft ends of the optics indicate the vignetting angles. The dashed line connecting the forward edge of the paraboloid (P) to the aft edge of the hyperboloid (H) indicates a limiting "good" ray. Potential baffle locations are forward of the optics (F), between the P and H (C), aft of the optics (A), interior to the paraboloid (I_P), or interior to the hyperboloid (I_H).

20.2.1 Control of Single Reflection Ghosts

The limiting H ghost ray is determined by baffle F_i and either I_{Pi} or C_i. In the AXAF-I HRMA design, baffling at F_i, F_o, and C_i works for the outer three shells (P1H1, P3H3, and P4H4), but is not adequate for the innermost shell (P6H6). However, as noted above, it turns out that a baffle at the location I_{Pi} enables the simultaneous vignetting/ghost ray requirements to be met, at least for ideal conditions; Figure 20.5 schematically indicates how the ghost baffle system works.

The addition of a baffle at I_P improves the control of H ghosts by reducing magnitude of the slope of the limiting ray for a given choice of vignetting angle θ_{Vo}; the degree of relief is limited by the need for the baffle to avoid the $F_i - P_A$ vignetting cone and the $P_F - H_A$ cone. Figure 20.6 schematically indicates how the ghost baffle system works.

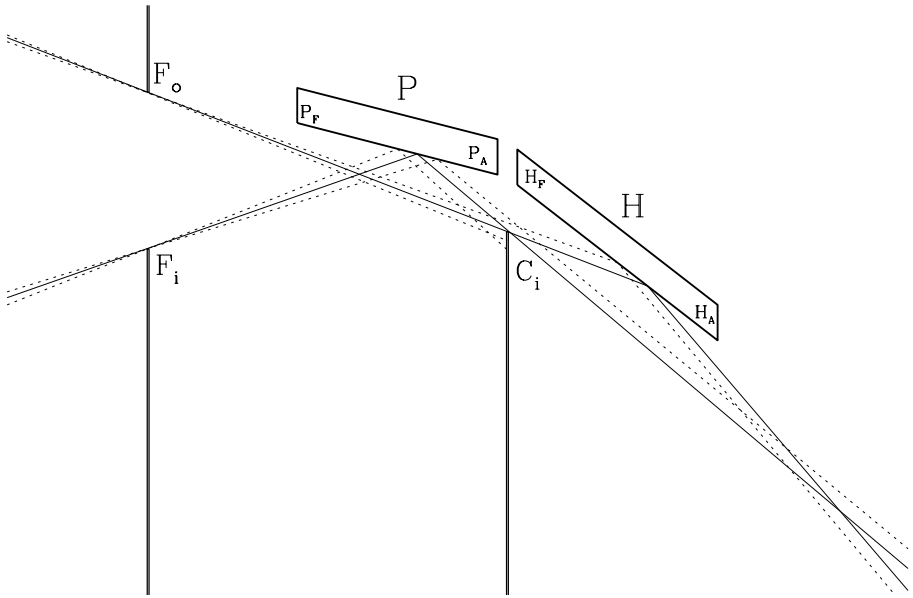

Figure 20.5: Control of ghost rays using baffles at F_i, F_o, and C_i. The P ghosts are controlled by the baffles F_i and C_i. The solid curve touching F_i indicates the limiting P ghost ray: steeper rays are blocked by the baffle C_i; shallower rays have a shallower angles after reflection and intercept the focal plane further out than the limiting ray. H ghosts are controlled by the baffles F_o and C_i. The solid curve through F_o indicates a limiting ghost ray: steeper rays are blocked by C_i; shallower rays have a steeper angles after reflection and intercept the focal plane further out than the limiting ray.

20.3 HSI Images of Ghosts

Ghost images are evident in the HSI off-axis images for angles $25'$ and greater. The basic features in the $30'$ off-axis images are shown in Figure 20.7

In Table 20.1, the off-axis HSI images which include P6 or H6 ghosts are listed.

At the angles for which HSI images were obtained, only single reflection P6 or H6 ghosts are visible. In the $25'$ off-axis images at Ti-Kα and Fe-Kα (Figure 20.9), part of the H6 loop (lower left corner of each image) is occulted by one of the cusps of the HSI mask. The full inner part of the H6 loop is visible in the $25'$ C-Kα image because the image is centered near the top of the detector; in this case most of one of the large lobes is lost. The Al-Kα image (MP6 only) is at about $24'$ off-axis, and the H6 ghost is in the problem of cusping. (Note that the off-axis direction also differs by $90°$ from the other images.) Comparing the difference between the image at $\sim 24'$ (H6 ghost image cusping, and hasn't yet reached the direct image) *versus* the images at $\sim 25'$ (ghost image forms a loop passing through the direct image) indicates that the ghost images in this angle range provide a sensitive measure of the actual angle the HRMA makes with the beamline axis.

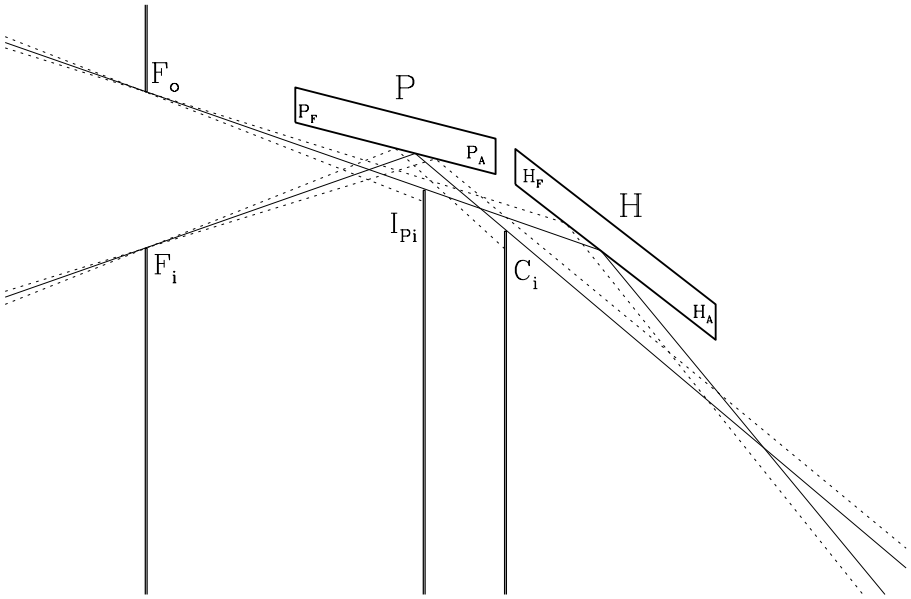

Figure 20.6: Control of ghost rays using baffles at F_i, F_o, I_{Pi}, and C_i. The P ghosts are controlled as in Figure 20.5. The H ghosts are controlled by the baffles F_o and I_{Pi}. The solid curve again indicates a limiting ghost ray: steeper rays are blocked by I_{Pi}; shallower rays have a steeper angle after reflection and intercept the focal plane further out than the limiting ray.

Table 20.1: Phase 1 Off-Axis Images with P6 or H6 ghosts

TRW ID	RunID	Energy (keV)	Shell	nominal pitch (′)	nominal yaw (′)	defocus (mm)	Counts
E-IXH-PI-6.006	110701	0.277	HRMA	−21.21	21.21	44.7368	32438
E-IXH-PI-21.006	111089	4.51	HRMA	−21.21	21.21	44.7368	58039
E-IXH-PI-11.006	110893	6.4	HRMA	−21.21	21.21	44.7368	282273
E-IXH-PI-6.005	110700	0.277	HRMA	−17.68	17.68	31.1065	48864
E-IXH-PI-52.001	111765	1.486	6	16.42	17.68	85.0136	98126
E-IXH-PI-21.005	111088	4.51	HRMA	−17.68	17.68	31.1065	56639
E-IXH-PI-11.005	110892	6.4	HRMA	−17.68	17.68	31.1065	128426

20.4 Determination of Off-axis Angle Using Ghosts

The sampled angles are particularly interesting in that they occur near the angles at which the P6 and H6 ghosts cusp and turn into loops. The fact that the both the direct image and the H6

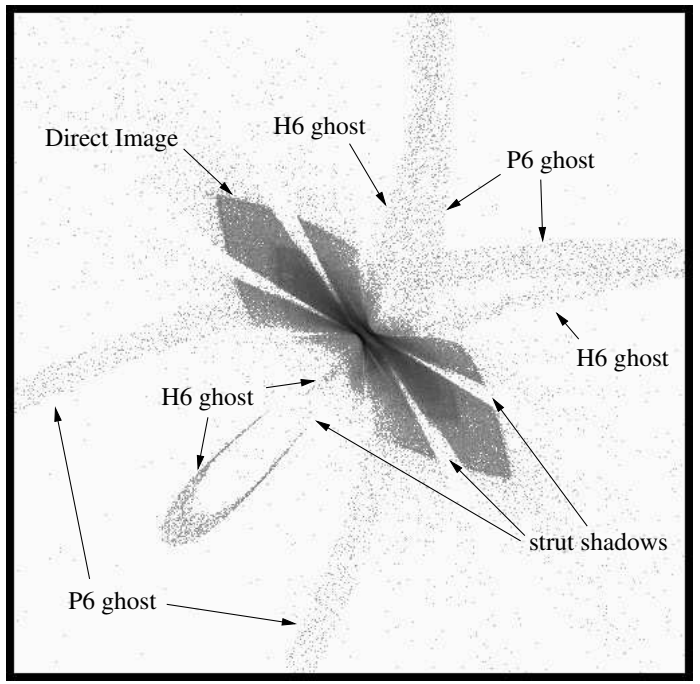

Figure 20.7: Off-axis image with ghosts. (Simulation of E-IXH-PI-11.006, runid 110893; Fe-Kα, 30′ off-axis.). At this angle, the single-reflection P ghost and single reflection H ghost can be readily discerned.

ghost loop are visible at the same time make these images useful for measuring the actual off-axis angle of the MP6 shell relative to the facility optical axis. The anomalies of the line PRF relative to the simulated line width suggest that the assumed Initial Actuator Position (IAP) of the HRMA may be off by ∼1/4 arcmin in yaw from the best value based on available records. The simulated images at 25′ and 30′ off-axis also suggest that the IAP may be systematically in error by an amount of that order.

The size of the H6 ghost loop and its position are sensitive indicators for the magnitude of the off-axis angle, θ; it can be estimated to within $\sim\pm 0.05'$. The azimuth of the off-axis angle, ϕ, is trickier to determine; accurate evaluation involves evaluation of subtle variations in feature locations as the azimuth varies on a scale of degrees or less. In Figure 20.10, typical critical features are indicated; Figure 20.11, simulations varying θ and ϕ are presented.

The determination of the HRMA orientation by this technique is currently ongoing; results will be presented as they become available.

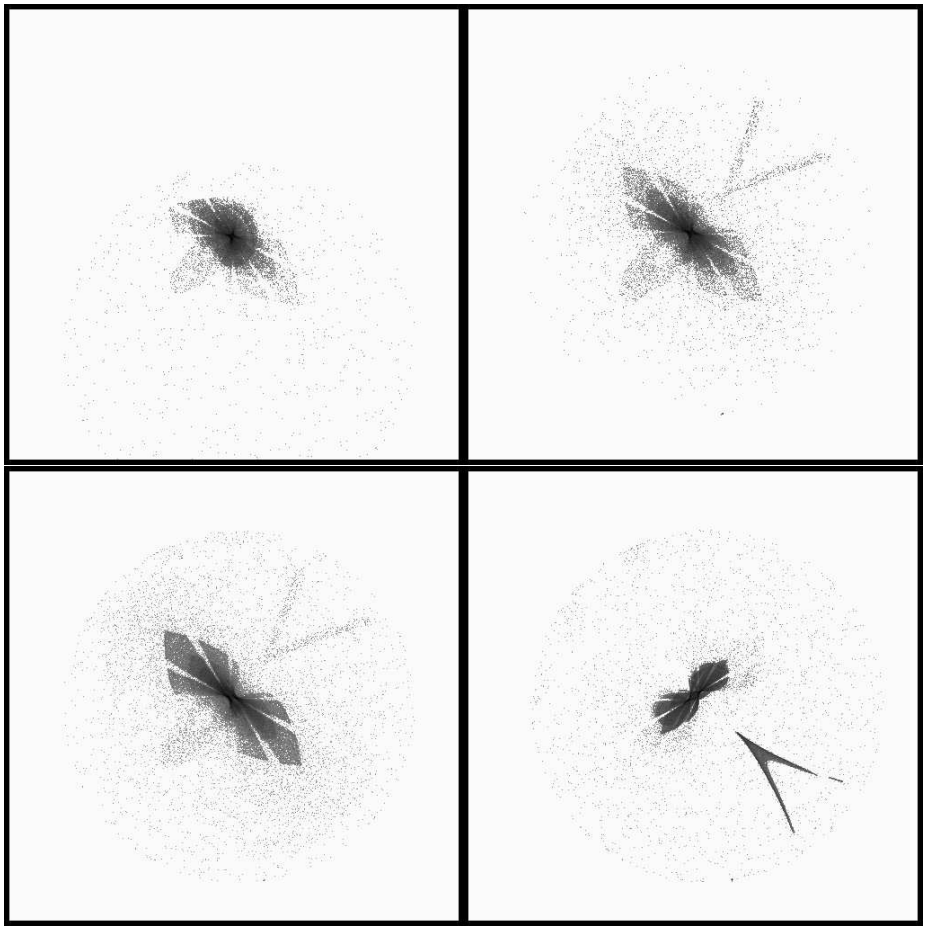

Figure 20.8: HSI images of ghosts at 25′ off-axis. Upper left: C-Kα (E-IXH-PI-6.005, runid 110700, 48864 counts) Upper right: Ti-Kα (E-IXH-PI-21.005, runid 111088, 56639 counts) Lower left: Fe-Kα (E-IXH-PI-21.005, runid 110892, 128426 counts) Lower right: Al-Kα (E-IXH-PI-52.001, runid 111765, 98126 counts) The image at Al-Kα was taken using the quadrant shutters to isolate mirror shell 6; because of actuator constraints, the off-axis angle was closer to 24′ off-axis, which is why the P-ghost has not formed a loop yet. In addition, the azimuth for the Al-Kα exposure differed by 90° from that used for the other energies.

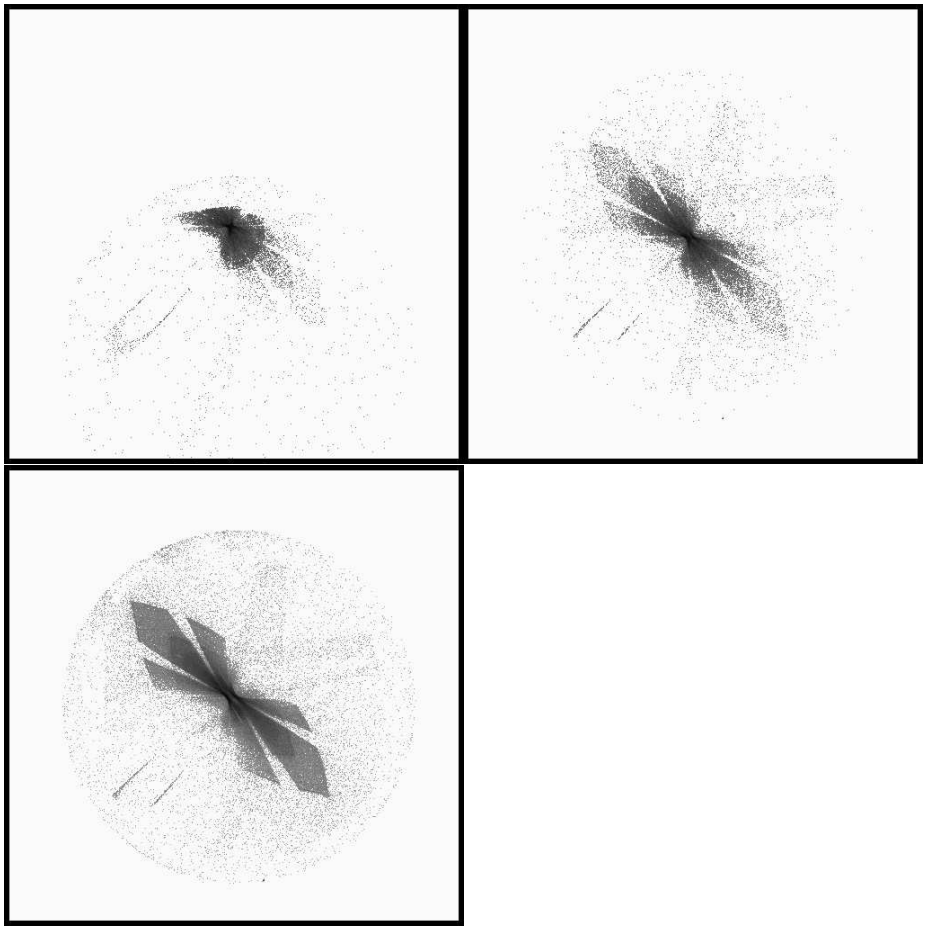

Figure 20.9: HSI full HRMA images of ghosts at 30′ off-axis. Upper left: C-Kα (E-IXH-PI-6.006, runid 110701, 32438 counts) Upper right: Ti-Kα (E-IXH-PI-21.006, runid 111089, 58039 counts) Lower left: Fe-Kα (E-IXH-PI-21.006, runid 110893, 282273 counts) Note that one of the cusps of the HSI mask occults part of the H6 ghost loop in the lower right of the Ti-Kα and Fe-Kα images.

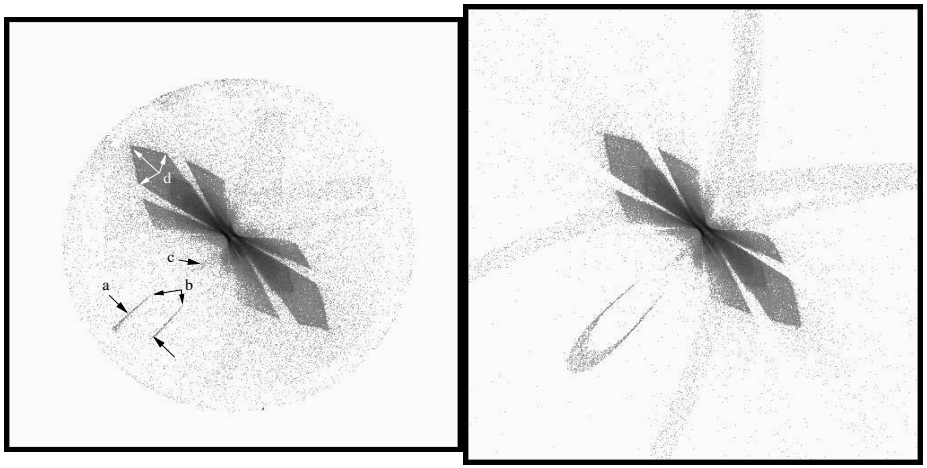

Figure 20.10: Determination of off-axis angle using the ghost in the 30′ off-axis Fe-α HSI image (E-IXH-PI-11.006, runid 110893). The planned angle was $\theta = 30'$, $\phi = -45°$. The value calculated from the actuator readings and relative to IAP7c2 is $\theta = 30.01952'$, $\phi = -45.0351°$. Top. The ghost loop is truncated lower left by the HSI mask cusp. The distance a is sensitive to the magnitude of the off-axis angle. The features b, c, and d help to refine the direction of the off-axis angle. Bottom. Simulation, ($\theta = 30.3039'$, $\phi = -44.75°$), almost matches the HSI image. The smaller ghost loop comes from one of the twelve open slots of the P6H6 optic; the gaps adjacent to feature b are produced by the support strut shadows. Feature c is the image of the next segment just beginning to appear. A large second ghost loop is also visible as a faint large loop.

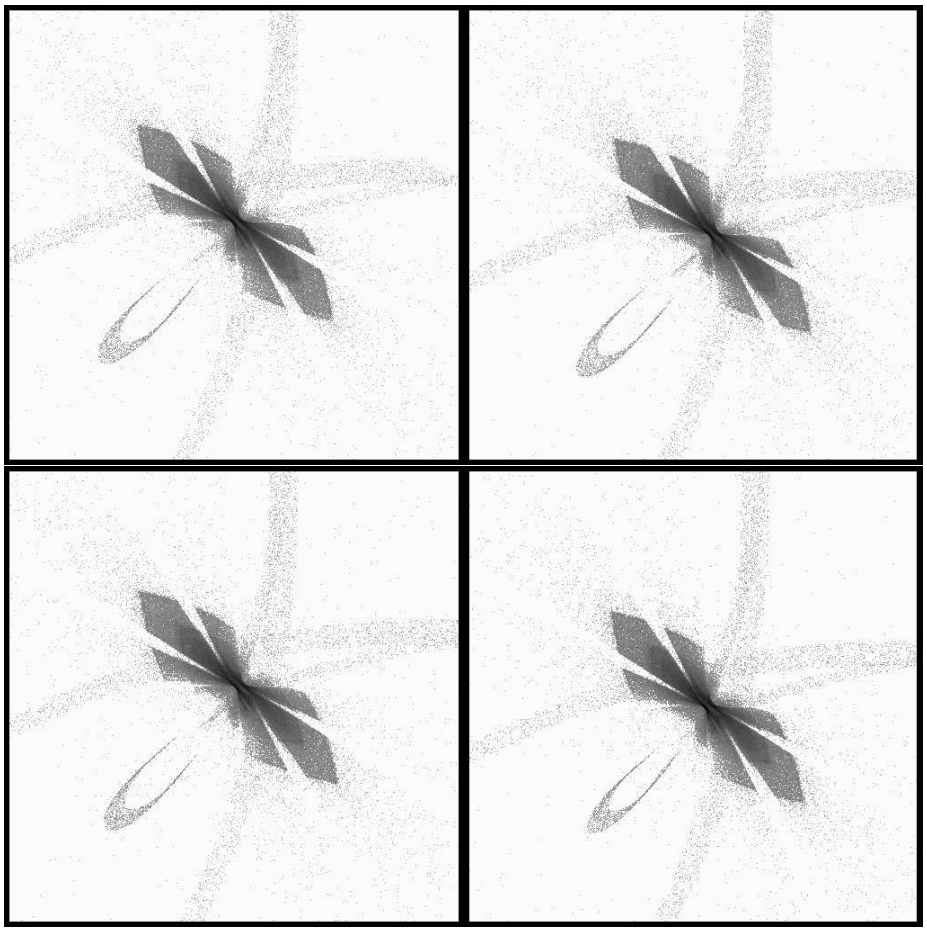

Figure 20.11: Top Left: $\theta = 30.3038'$, $\phi = -44°$ (Pitch, yaw = [$-21.0510'$, $21.7990'$]). Top Right: $\theta = 30.3038'$, $\phi = -44.5°$ (Pitch, yaw = [$-21.2400'$, $21.6140'$]). Bottom Left: $\theta = 30.3038'$, $\phi = -45°$ (Pitch, yaw = [$-21.4280'$, $21.4280'$]). Bottom Right: $\theta = 30.0921'$, $\phi = -44.3618°$ (Pitch, yaw = [$-21.0400'$, $21.5140'$]). Simulations for varying θ and ϕ. Comparing the bottom right figure with the others, it is evident that the width at a (see Figure 20.10) is sensitive to the off-axis angle θ; we estimate that the width of this feature restricts the value of θ to about $30.3' \pm 0.05$. Note also that as θ becomes more negative, the "horns" (feature b) on the smaller loop shift systematically. The feature c (see Fig. 1) shifts systematically with ϕ. The relative lengths of the segments at c also vary systematically. These features allow the value of ϕ to be estimated as about $44.675° \pm 0.15$.

Chapter 21

Analysis of the "Mesh-Plane" HSI Image

Terrance J. Gaetz

In this chapter the analysis of the HSI "Mesh-plane" HSI images is considered.

21.1 Mesh-Plane HSI Image

It was noted from the time of the initial out-of-focus "first light" HSI images that such images might contain structure which could be used to assess the HRMA alignment. A number of out of focus exposures were made to study different aspects of the HRMA, most notably the ring focus tests (see Chapter 18). In addition, exposures were taken at what was then thought to be the mesh plane for the FPC detectors. The mesh plane was taken to be 9.7 mm behind the aperture plate, so that when the focus is at the aperture plane, the mesh plane would be 9.7 mm out of focus. Subsequent measurements indicate that the actual spacing between the mesh plane and the aperture plane was 9.12 ± 0.15 mm. The "mesh plane" HSI exposures were requested at 9.7 mm out of focus, and the defocus value derived from the stage logs is consistent with 9.7 mm. It should also be noted that there may be some uncertainty in the relative axial location of the HSI relative to the FPC aperture plane; the value was originally measured before the HSI MCP failed and was replaced.

The images are too far from the finite conjugate focus to be of much help in assessing the shell-to-shell alignment, but are of great interest for assessing the effects of epoxy-induced distortion of the optic; the ring focus images are analyzed in detail in Chapter 18.

The "mesh plane" exposures turn out to provide useful alignment information and may also yield information on mirror deformations. Two mesh plane HSI exposures were taken, `hsi107550` and `hsi111803i0` (see Table 21.1). One image, `hsi111803i0`, is deep enough to provide useful information for assessing mirror shape and refining the HRMA alignment parameters; in this chapter, the analysis will concentrate on the `hsi111803i0` exposure.

The `hsi111803i0` image was taken at 9.7 mm aft of the focal plane. The image is far enough out of focus so that the rings from the individual shells are almost separated, but near enough to focus that the asymmetries and image deformations can be picked out. As such, this image will be important both for refining the alignment estimates, and for improving our understanding of the 1G mirror structural models.

The degapped HSI images `hsi107550` and `hsi111803i0` are shown in Figure 21.1. These image shows a number of interesting features, including:

Table 21.1: Mesh Plane HSI images

Date	TRW Test ID	runid	energy (keV)	exposure time (sec)	valid events
04 Jan 1997	D-IXH-PI-3.003	107550	1.49	104.002556	52073
10 Feb 1997	E-IXH-RF-18.002	111803	1.49	1032.847290	607305

- a distinctive braiding resulting from the 1G-induced distortions
- an enhanced central spot where the in-plane scattering planes intersect (visible in the `hsi11803i0` image.
- the spoke shadows do not line up across the image; rather they are radial with respect to the enhanced central spot. Close inspection reveals offsets in the strut shadows between different shells; this is maybe most noticeable at the bottom of the image in comparing shell 4 to shell 6.
- mirror pair six (the smallest ring) is displaced down and somewhat to the left relative to the other rings.
- the larger rings show small displacements relative to each other.

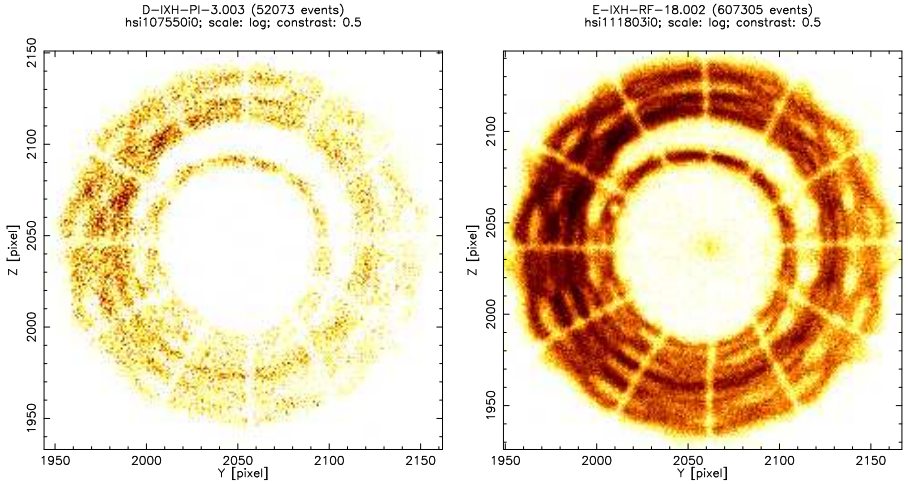

Figure 21.1: The two "mesh plane" HSI images. Left: hsi107550i0 image, stretch=log. Right: hsi111803i0 image, stretch=log.

21.2 Raytrace Simulations

To learn more about the implications of this image we turn to high fidelity raytrace models based on the SAO and the EKC finite element mechanical models for the distortion of the mirrors when supported horizontally under a 1G load. In the raytrace, the EIPS source distance was taken to be 527522 mm from the HRMA node, which is 18 mm from the P side of the CAP. Consequently, the source distance from the CAP DATUM –A– plane is 527504 mm.

Table 21.2: Focus distance from CAP Datum –A– plane for EIPS Al-Kα source

1G model	Focus (mm)
SAO 1G model	10274.777
EKC 1G model	10274.691

Table 21.3: Vertical/Horizontal ratios for meshplane HSI image

Mirror Pair	HSI image	raytrace
1	0.99	0.95
6	1.08	1.02

Focus at Al-Kα was determined by raytraces with ray density 6 mm^{-2} resulting in the values given in Table 21.2

Figure 21.2 compares the raytraced images based on the SAO and the EKC mechanical models with the `hsi111803i0` image; for reference, a raytrace with no 1G distortions is included. All three raytraces are based on the rigid body alignment model (EKCHDOS06) described in Jerius (1997).

Several things can be discerned by comparing these images:

- The overall scale of the HSI image appears to be slightly larger than the raytrace models. This suggests that the axial location for the ray projection may not be quite right.
- The shell 6 ring appears to be displace downwards more in the HSI image than in the raytraces. This suggests that the rigid body "tilt" parameters may be slightly off.
- Close examination of the XRCF image shows that the innermost and outermost shells are relatively cleanly visible; the middle two mirror pairs are somewhat more confused and care is needed in interpreting the image. It may be possible to slice out rings 1 and 6 from the HSI image; rings 3 and 4 are too close together and overlap in places.
- The ratio of the vertical to horizontal dimensions differs somewhat between the XRCF image and the raytrace simulations. Crude estimates of the vertical to horizontal ratios for the SAO 1G model are compared to the estimates for the HSI image in Table 21.3. This suggests that the mechanical models predict somewhat more ovalization than is seen in the XRCF data.
- The shape of the shell 6 ring is slightly different than in the raytrace model.

We address these issues in the following sections.

21.3 Analysis of the Image

In order to assess the HSI image, the image was clipped into three quasi-elliptical annuli covering mainly shell 6, shells 3 plus 4, and mainly shell 1. Each annulus was bounded by an ellipse. The annuli used for the HSI image are given in Table 21.4; these cuts are plotted in Figure 21.3. For comparison, Figure 21.4 shows raytrace simulations based on the SAO 1G model. **needed: similar figures for EKC model.**

The shell 1 and shell 6 rings were analyzed using the ring analysis software. The mean ring radius for the HSI rings as a function of azimuth is plotted in Figure 21.5. For comparison, the same analysis is presented for the SAO 1G model. **To be done: a similar treatment for the**

Table 21.4: Parameters for the quasi-elliptical annuli used to split apart the hsi111803i0 image

Mirror Pair	a_i	a_i/b_i	Y_i	Z_i	a_o	a_o/b_o	Y_o	Z_o
1	83	1.03	2057	2038	104	1.03	2037	2037
3+4	59	1.07	2055	2035	83	1.03	2057	2038
6	40	1.07	2055	2035	59	1.07	2055	2035

Table 21.5: Ring radius parameters.

Mirror Pair	$R_{hsi,avg}$ (HSI pixel)	$R_{raytrace,avg}$ (HSI pixel)	ratio	ΔF (mm)
1	93.22	87.41	1.066	0.640
6	52.44	47.45	1.105	1.020

EKC 1G model. Also, Fourier analysis of the curve. Can we dig out ovalization and trefoil (to compare to the models)? Can we get a tilt estimator out of it?

In Table 21.5 some parameters of the ring fits are presented. The $R_{hsi,avg}$ column gives the mean radius for the rings in the HSI image, while $R_{raytrace,avg}$ gives the values for the raytraces. The ratio column is $R_{hsi,avg}/R_{raytrace,avg}$. The ΔF column lists the additional defocus distance needed to make the mean ring radius in the raytrace match the mean ring radius in the HSI image, assuming that defocus is the only effect operating. **The raytrace setup needs to be rechecked to make sure I haven't entered a distance incorrectly or something. If that doesn't explain it, we need some comment on this. How much can be plausibly attributed to the HSI position relative to the FPCs? How much is a result of mirror deformations (1G or other) biasing the radius estimator? My earlier estimates based on measuring the image with a ruler gave a defocus correction of about 0.4 mm compared to 0.64 and 1.02 here. ???**

21.3.1 Axial position of the image

Recent reexamination of the XRCF focus data indicates that the axial position of the HRMA is not repeatable at the level of
`http://hea-www.harvard.edu/MST/simul/xrcf/HRMA/focus/hsi_offset/index.html`

21.4 Updating the Tilts

As noted above, the displacement of the shell 6 ring relative to the others seems to be somewhat larger than in the raytrace models based on the EKCHDOS06 version of the rigid-body parameters. In the analysis of the mirror "tilts" based on the quadrant shutter focus studies (see Jerius (1997)) it was found that the "Y-tilts" were larger than predicted by the models. Based on comparison with the predictions of the EKC 1G model and the SAO 1G model, it was concluded that the discrepancy was likely a result of 1G tilts not captured by the modeling.

These additional Y-tilts are here applied to the raytrace model; the Y-tilt differences *only* from line E of Table 11.2 of Jerius (1997) were applied. In addition, a 0.1 $''$ Z-tilt was applied to shell

6 only in order to improve agreement with the HSI image. These are relative P to H tilts for individual mirror pairs. In order to retain nearly the same parfocalization as before, the additional tilts were applied half to the P optics and half to the H optic of a given mirror pair, but with opposite signs.

To get the overall scales to match, I had to project the raytrace an additional 0.4 mm or so; the stage logs indicate that the HSI image was taken at 9.7 mm back from the on-axis HRMA focus; the reason for this difference needs to be elucidated. The XRCF focus is calculated using quad-shutters while the raytrace focus is determined using saofocus with scattering turned off (minimizing rms blur); could the difference in focus algorithms be introducing an offset in where the focus appears to be?

(Note added 980501: source distance error for the EIPS distance in the raytrace may account for 0.1 mm or so of the discrepancy.)

(Note added 980826: The source distance has been fixed, but not all the raytraces have been redone yet. The "ring focus" style analysis above indicates a larger than that I estimated here; what about the effects of mirror deformations?) Figure 21.6 compares the HSI image to the raytrace results with 0.5, 1, and 1.5 times the additional Y-tilts. Similarly, Figure 21.7, shows the effect of adding 0, 1, and 2 times the additional Z-tilt to a model to which the additional Y-tilts have already been added.

In Figure 21.8 the raytrace model (including the additional tilts based on the quadrant shutter data) is compared to the HSI image.

21.5 Mirror Distortions

based on Fourier Analysis above, or by empirically comparing raytrace models to the HSI image. Extract the 2nd & 3rd order DDR's from WAP's Assembly Strain `.DFR` files and compare.

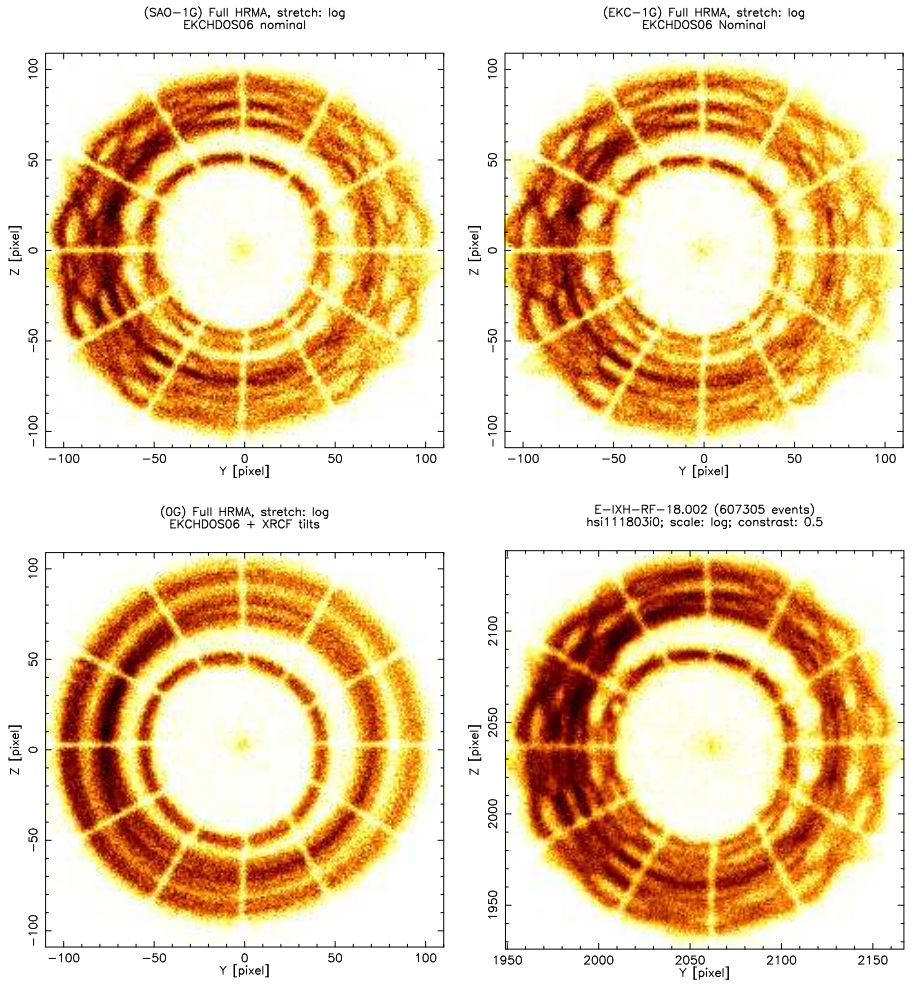

Figure 21.2: Raytrace simulation comparing the SAO and the EKC 1G mechanical models. These traces differ only in the 1G model used; all other components (alignment parameters, assembly strain terms, epoxy shrinkage) are the same. The rigid body alignment terms are those given in the MST Phase 1 preliminary report (EKCHDOS06 rigid body terms). Top Left: SAO 1G nominal case, EKCHDOS06 rigid body terms, log stretch. Top Right: EKC 1G nominal case, EKCHDOS06 rigid body terms, log stretch. Bottom Left: 0G case, EKCHDOS06 rigid body terms, XRCF tilt corrections, log stretch. Bottom Right: hsi111803i0 image, log stretch.

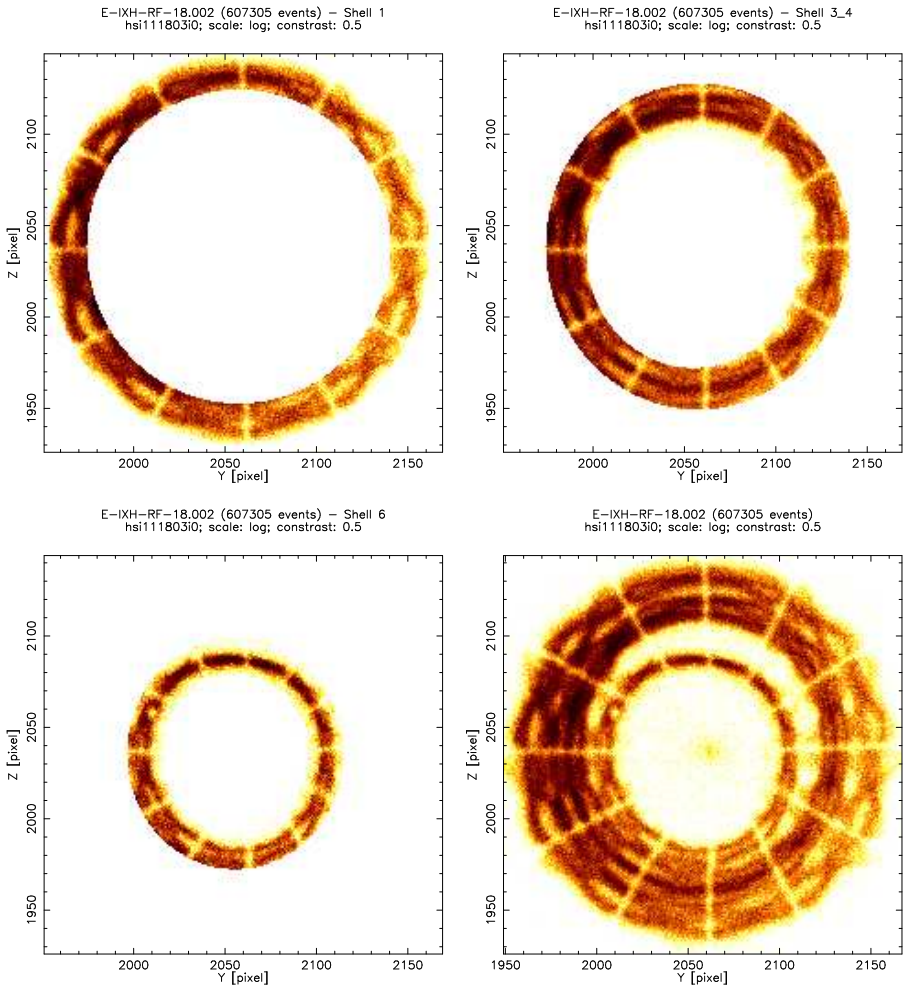

Figure 21.3: Division of hsi111803i0 image into annuli. Top left: shell 1, stretch=log. Top right: shell 3 + 4, stretch=log. Bottom left: shell 6, stretch=log. Bottom right: full hsi111803i0 image, stretch=log.

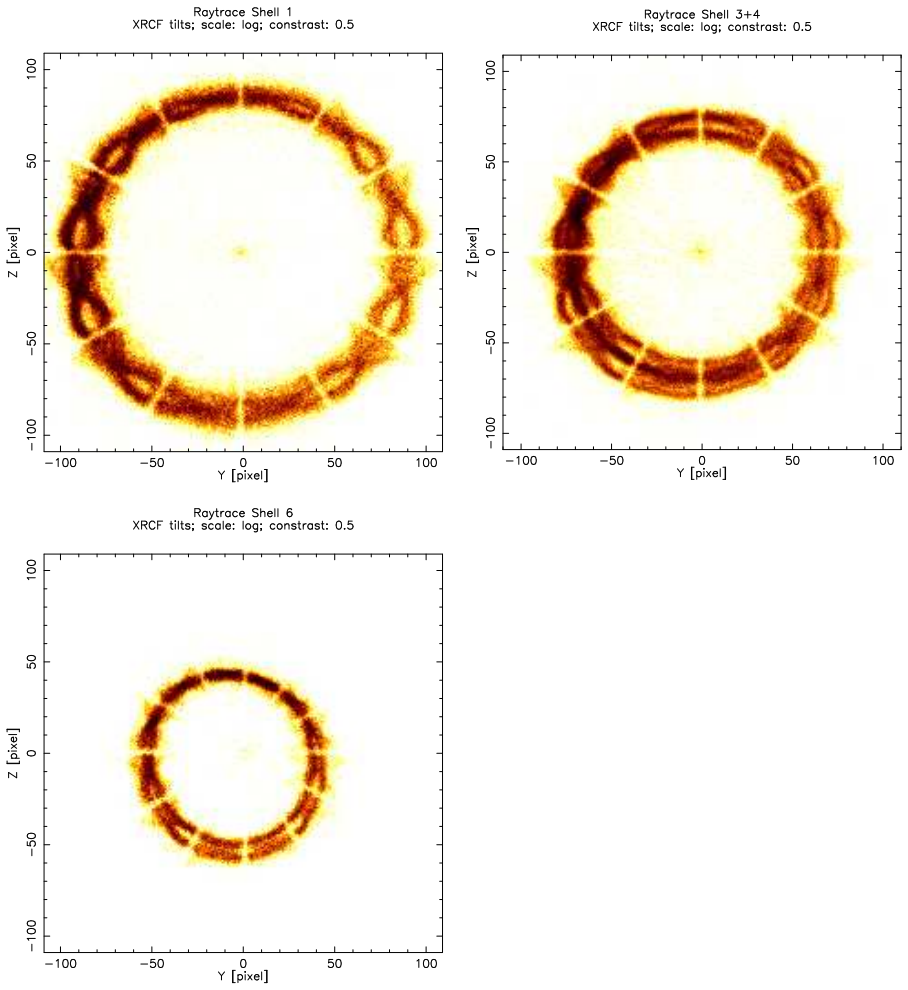

Figure 21.4: Raytraces for individual HRMA shells, or Mirror Pairs (MP), at the "mesh plane". Top left: shell 1, stretch=log. Top right: shell 3 + 4, stretch=log. Bottom left: shell 6, stretch=log.

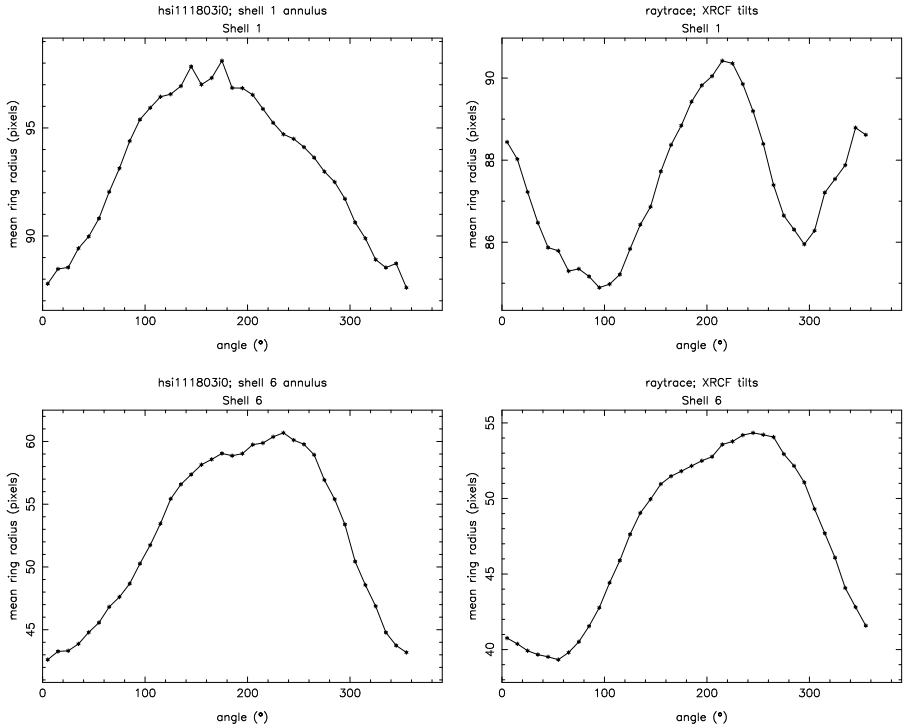

Figure 21.5: Ring radius for individual shells. Top left: shell 1, hsi111803i0 image. Top right: shell 1, raytrace. Bottom left: shell 6, hsi111803i0 image. Bottom right: shell 6, raytrace.

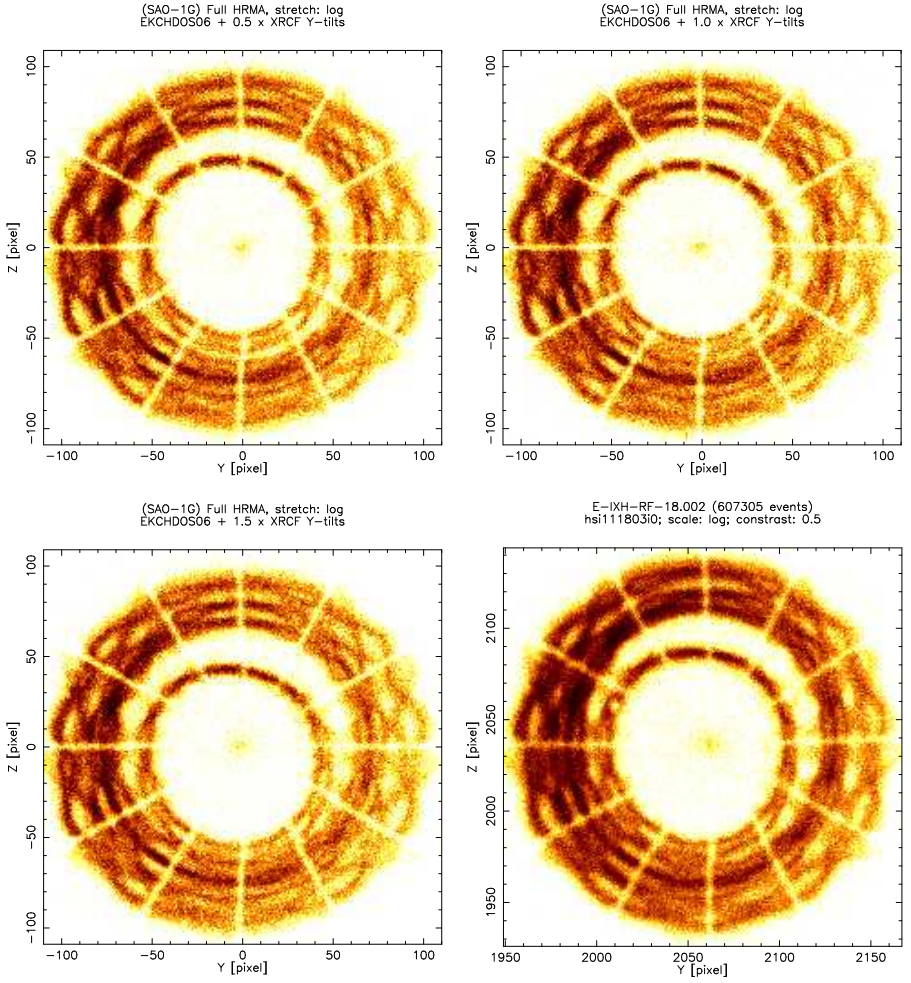

Figure 21.6: Raytraces with varying Y-tilts compared to hsi111803 image. Top left: 0.5×XRCF Y-tilts, stretch=log. Top right: 1.0×XRCF Y-tilts, stretch=log. Bottom left: 1.5×XRCF Y-tilts, stretch=log. Top right: hsi111803i0 image, stretch=log. The images are sqrt stretched.

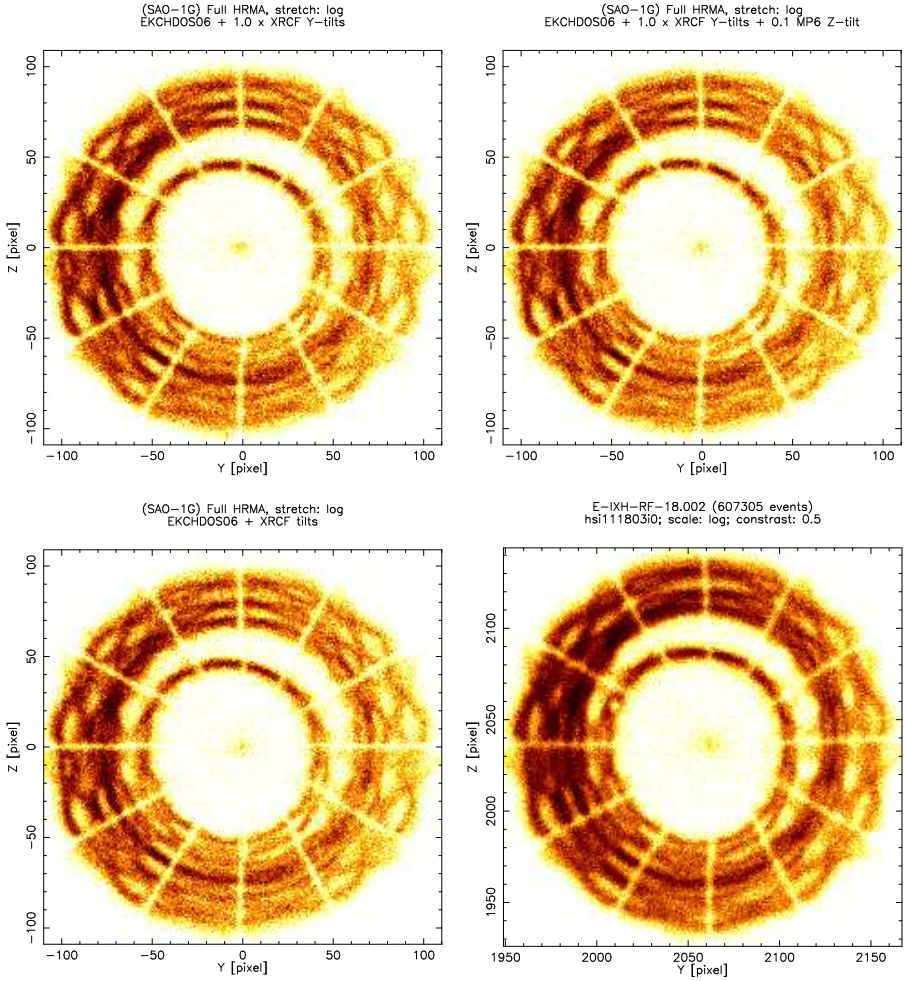

Figure 21.7: Raytraces with varying Z-tilts compared to hsi111803 image. Top left: XRCF Y-tilts; 0.0″ added P6 Z-tilt, stretch=log. Top right: XRCF Y-tilts; 0.2″ added P6 Z-tilt, stretch=log. Bottom left: XRCF Y-tilts; 0.1″ added P6 Z-tilt, stretch=log. Top right: hsi111803i0 image, stretch=log.

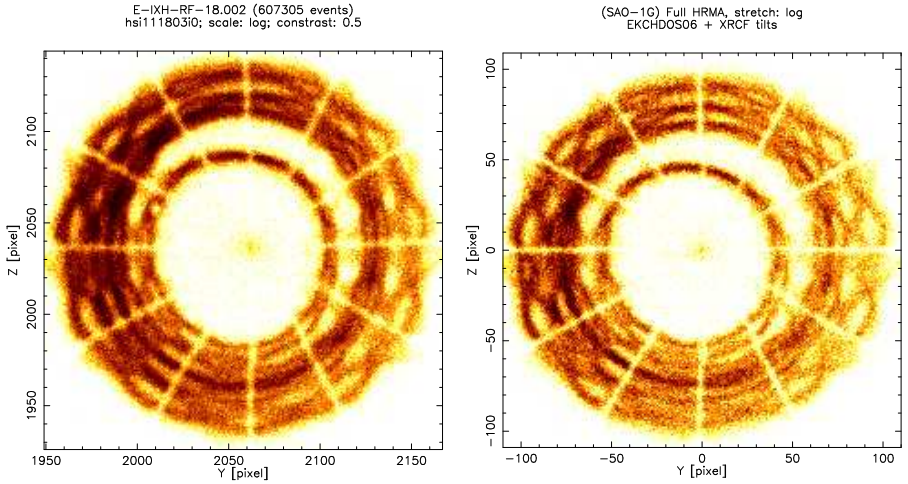

Figure 21.8: Comparison of XRCF mesh plane HSI image (top) and raytrace simulations (bottom). Left: hsi111803i0 image, linear stretch. Right: HRMA raytrace, SAO-1G model, EKCHDOS06 rigid body terms, XRCF tilt correction, log stretch.

Chapter 22

Off-Axis imaging: comparing HSI images to raytrace models

Terrance J. Gaetz

A number of off-axis HSI exposures were made in order to explore the off-axis PSF. It was initially planned to take full HRMA exposures at $10'$ and $20'$ (pure *yaw*), and at $5'$, $15'$, $25'$, and $30'$ ($pitch = -yaw$); they were to be taken at four energies, C-Kα (0.277 keV), Al-Kα (1.486 keV), Ti-Kα (4.51 keV), and Fe-Kα (6.4 keV). The initial exposures (C-Kα) showed structure which supported the speculation that the observed imbalances in the flux balance tests were due to an internal Parabola to Hyperbola decenter error. Further off-axis images, together with raytrace analysis, indicated that at least two shells had decenter errors. It was decided to replace the planned set of full HRMA exposures with a set of single-shell exposures; in order to provide more coverage of the off-axis direction, the $30'$ single shell exposures were taken with $pitch \simeq yaw$ rather than $pitch = -yaw$ as was done for the other energies. Analysis of these images, together with raytrace simulations of the effects of mirror misalignments, allowed a set of rigid-body decenters (plus compensating tilts) to be derived; this is discussed more fully in Chapter 30.

In this chapter the high fidelity raytrace model is used to compare raytraced images (based on the derived rigid-body parameter sets) with the HSI off-axis images obtained at XRCF. The raytrace images include the effects of the HSI angle-dependent relative quantum efficiency.

In Table 22.1, the off-axis HSI images are listed.

22.1 Off-axis HSI Images (Full HRMA)

the 25 and $30'$ off-axis images show ghost images. The positions and shapes of the ghosts are very sensitive to off-axis angle; the pitch and yaw need to be tweaked to get better agreement for the ghosts.

Table 22.1: Phase 1 Off-Axis Images (Full HRMA)

TRW ID	RunID	Energy	Shell	pitch	yaw	defocus	Counts
E-IXH-PI-6.001	110594	0.277	HRMA	−3.54	3.54	1.4384	103775
E-IXH-PI-7.002	110639	0.277	HRMA	0	−10	5.6211	103208
E-IXH-PI-6.003	110668	0.277	HRMA	−10.61	10.61	12.1095	100412
E-IXH-PI-7.004	110669	0.277	HRMA	0	−20	20.6847	73019
E-IXH-PI-6.005	110700	0.277	HRMA	−17.68	17.68	31.1065	48864
E-IXH-PI-6.006	110701	0.277	HRMA	−21.21	21.21	44.7368	32438
E-IXH-PI-12.004	110887	6.4	HRMA	0	−20	20.6847	81715
E-IXH-PI-12.002	110888	6.4	HRMA	0	−10	5.6211	98095
E-IXH-PI-11.001	110889	6.4	HRMA	−3.54	3.54	1.4384	93828
E-IXH-PI-11.003	110890	6.4	HRMA	−10.61	10.61	12.1095	96178
E-IXH-PI-11.005	110892	6.4	HRMA	−17.68	17.68	31.1065	128426
E-IXH-PI-11.006	110893	6.4	HRMA	−21.21	21.21	44.7368	282273
E-IXH-PI-22.004	111084	4.51	HRMA	0	−20	20.6847	74416
E-IXH-PI-22.002	111085	4.51	HRMA	0	−10	5.6211	103047
E-IXH-PI-21.001	111086	4.51	HRMA	−3.54	3.54	1.4384	99238
E-IXH-PI-21.003	111087	4.51	HRMA	−10.61	10.61	12.1095	98197
E-IXH-PI-21.005	111088	4.51	HRMA	−17.68	17.68	31.1065	56639
E-IXH-PI-21.006	111089	4.51	HRMA	−21.21	21.21	44.7368	58039
E-IXH-PI-50.001	111757	1.486	6	0	−20	54.1046	90934
E-IXH-PI-50.002	111758	1.486	4	0	−20	30.2079	80047
E-IXH-PI-50.003	111759	1.486	3	0	−20	23.6882	58430
E-IXH-PI-50.004	111760	1.486	1	0	−20	15.5253	84628
E-IXH-PI-51.001	111761	1.486	6	−10.61	10.61	30.3917	87750
E-IXH-PI-51.002	111762	1.486	4	−10.61	10.61	17.4109	86283
E-IXH-PI-51.003	111763	1.486	3	−10.61	10.61	13.6771	85855
E-IXH-PI-51.004	111764	1.486	1	−10.61	10.61	9.0284	86542
E-IXH-PI-52.001	111765	1.486	6	16.42	17.68	85.0136	98126
E-IXH-PI-52.002	111766	1.486	4	16.42	17.68	46.4008	75388
E-IXH-PI-52.003	111767	1.486	3	16.42	17.68	36.0489	67708
E-IXH-PI-52.004	111768	1.486	1	16.42	17.68	23.6816	75210

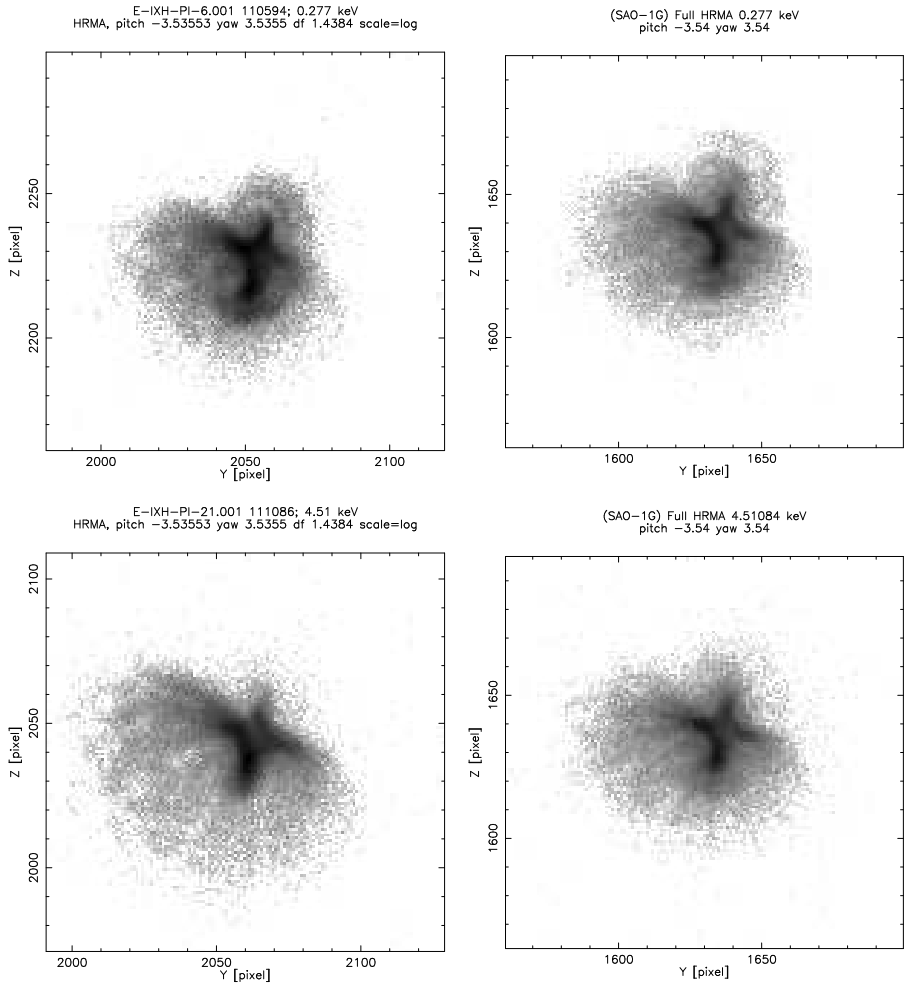

Figure 22.1: Top left: hsi110594i0 X-ray image; 5′ off-axis, C-Kα. (1 × 1 HSI pixel.) Top right: Raytrace; 5′ off-axis, C-Kα. (1 × 1 HSI pixel.) Bottom left: hsi111086i0 X-ray image; 5′ off-axis, Ti-Kα. (1 × 1 HSI pixel.) Bottom right: Raytrace; 5′ off-axis, Ti-Kα. (1 × 1 HSI pixel.) The images are log stretched.

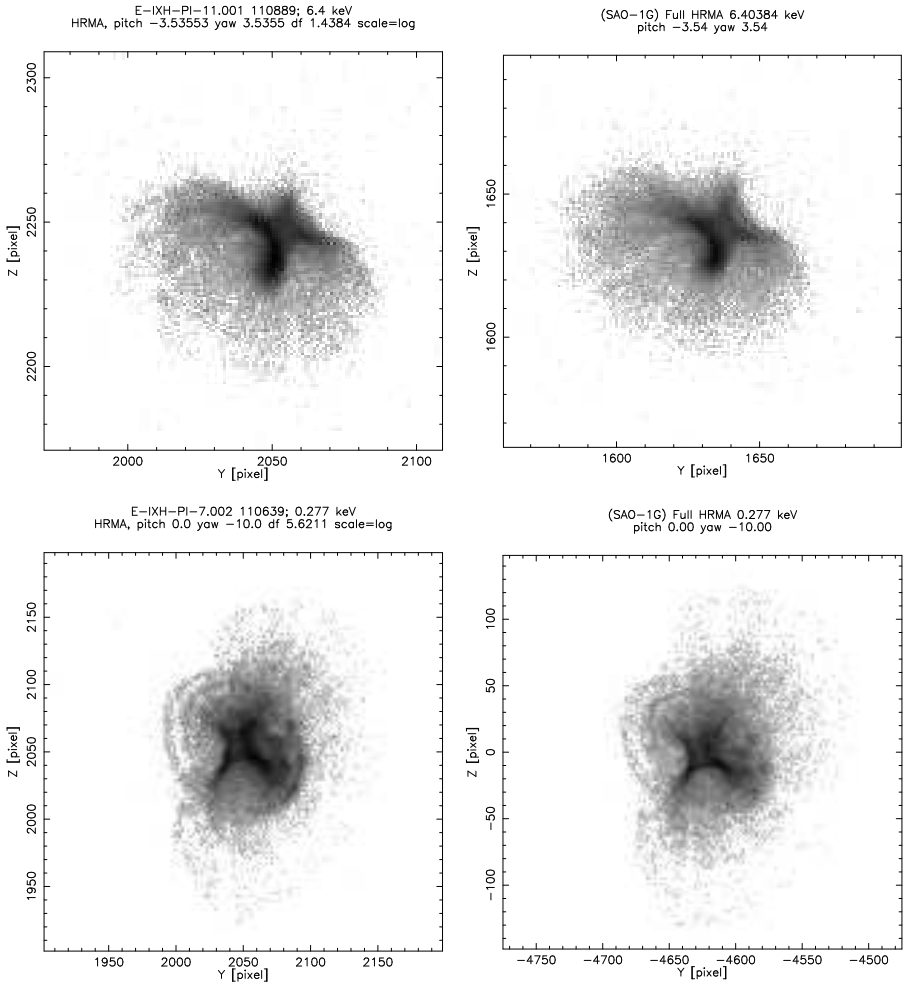

Figure 22.2: Top left: hsi110889i0 X-ray image; 5′ off-axis, Fe-Kα. (1 × 1 HSI pixel.) Top right: Raytrace; 5′ off-axis, Fe-Kα. (1 × 1 HSI pixel.) Bottom left: hsi111086i0 X-ray image; 10′ off-axis, C-Kα. (2 × 2 HSI pixels.) Bottom right: Raytrace; 10′ off-axis, C-Kα. (2 × 2 HSI pixels.) The images are log stretched.

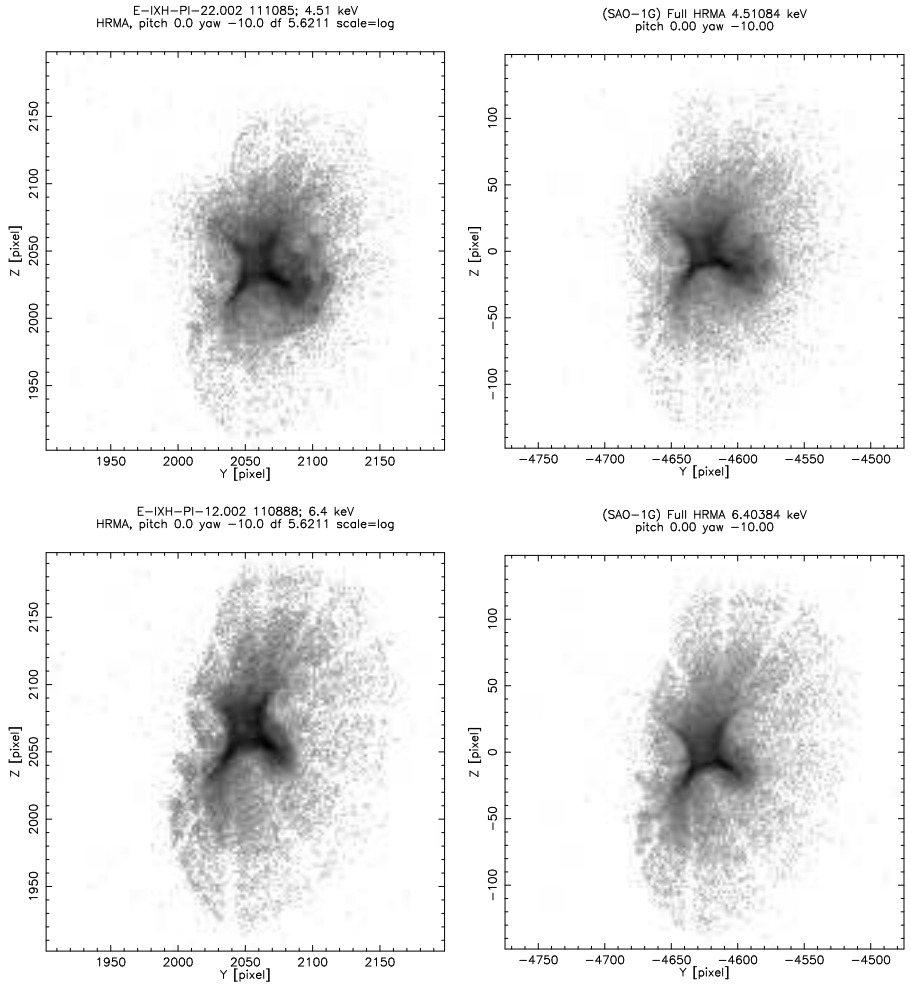

Figure 22.3: Top left: hsi111085i0 X-ray image; 10′ off-axis, Ti-Kα. (2×2 HSI pixels.) Top right: Raytrace; 10′ off-axis, Ti-Kα. (2×2 HSI pixels.) Bottom left: hsi110888i0 X-ray image; 10′ off-axis, Fe-Kα. (2×2 HSI pixels.) Bottom right: Raytrace; 10′ off-axis, Fe-Kα. (2×2 HSI pixels.) The images are log stretched.

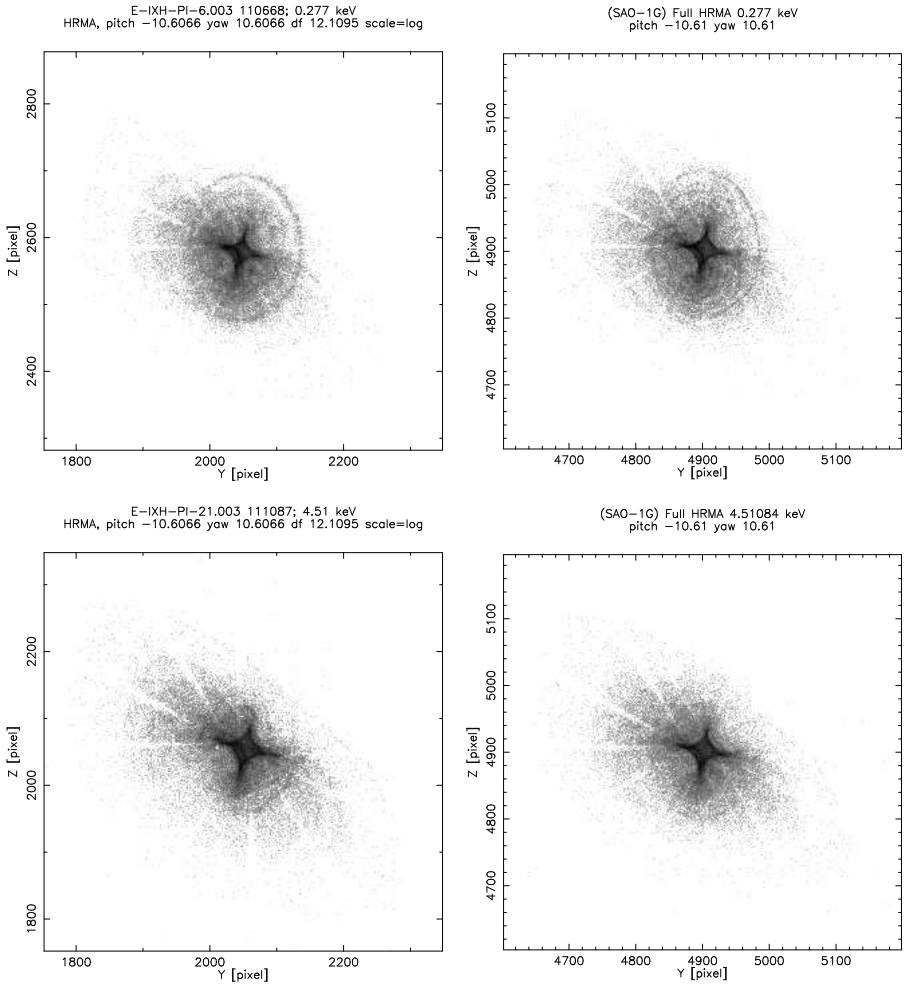

Figure 22.4: Top left: hsi110668i0 X-ray image; 15′ off-axis, C-Kα. (2×2 HSI pixels.) Top right: Raytrace; 15′ off-axis, C-Kα. (2×2 HSI pixels.) Bottom left: hsi111087i0 X-ray image; 15′ off-axis, Ti-Kα. (2×2 HSI pixels.) Bottom right: Raytrace; 15′ off-axis, Ti-Kα. (2×2 HSI pixels.) The images are log stretched.

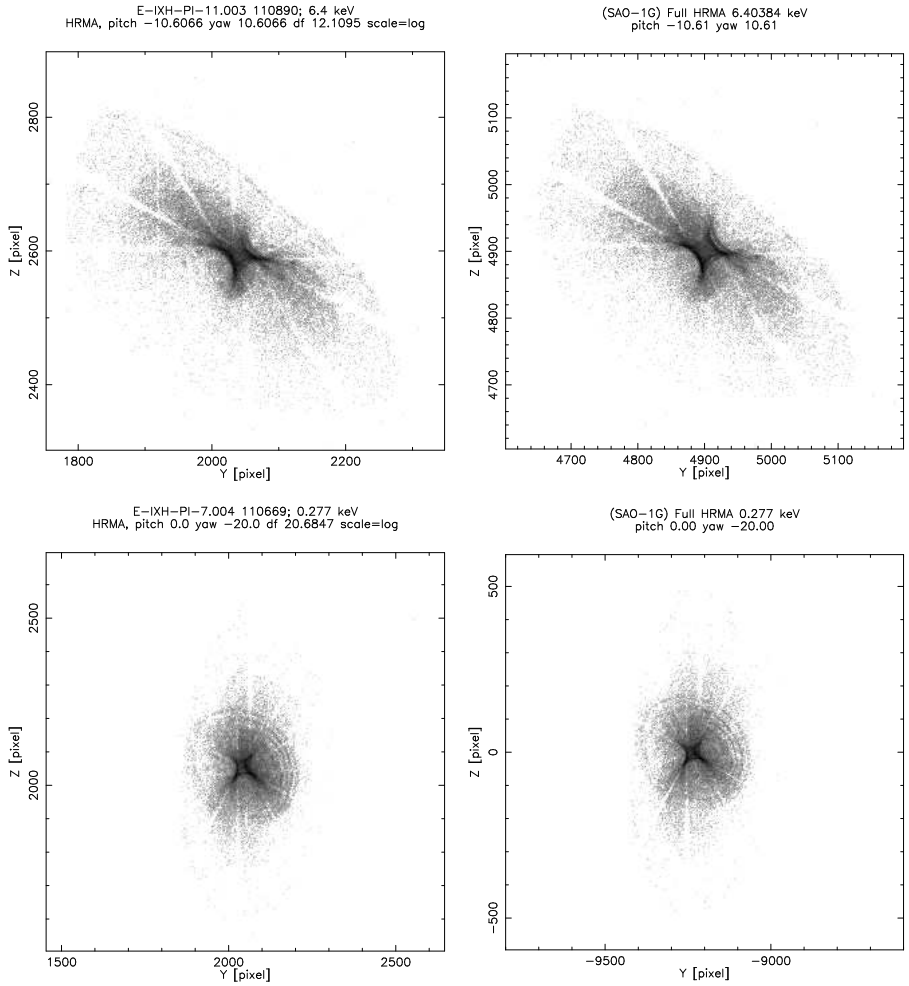

Figure 22.5: Top left: hsi110890i0 X-ray image; 15′ off-axis, Fe-Kα. (4×4 HSI pixels.) Top right: Raytrace; 15′ off-axis, Fe-Kα. (4×4 HSI pixels.) Bottom left: hsi110669i0 X-ray image; 20′ off-axis, C-Kα. (4×4 HSI pixels.) Bottom right: Raytrace; 20′ off-axis, C-Kα. (4×4 HSI pixels.) The images are log stretched.

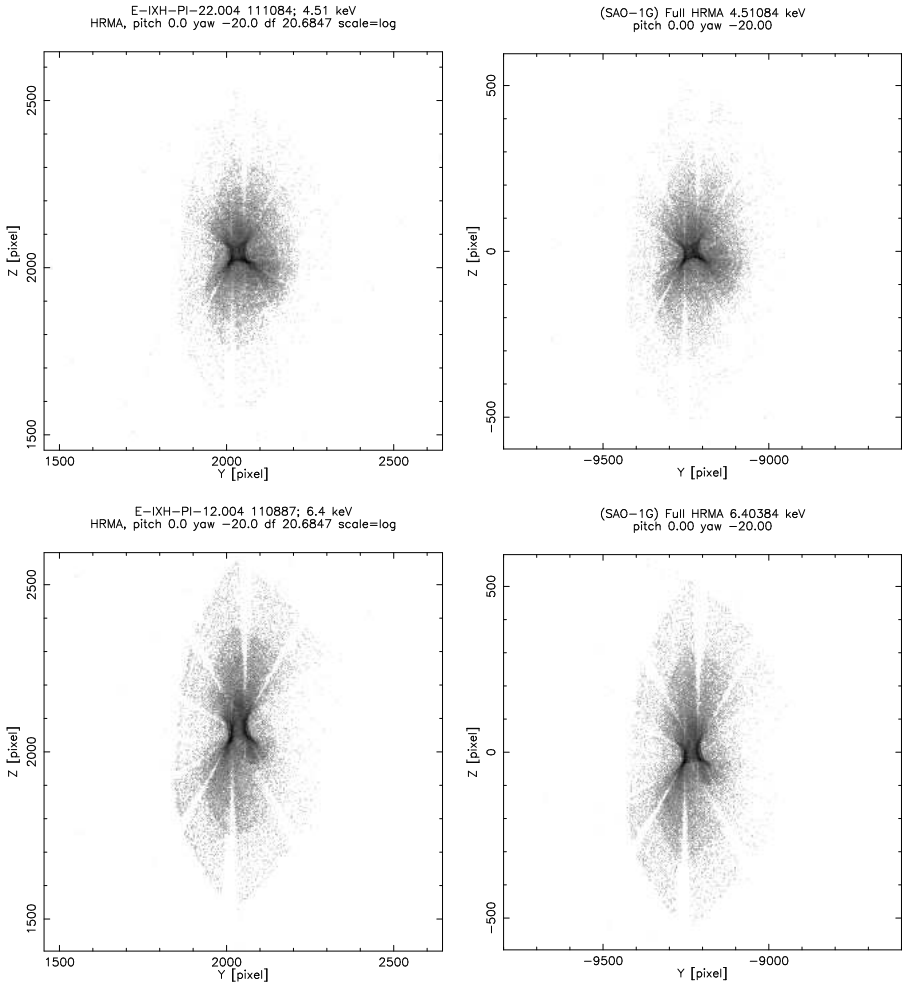

Figure 22.6: Top left: hsi111084i0 X-ray image; 20′ off-axis, Ti-Kα. (4×4 HSI pixels.) Top right: Raytrace; 20′ off-axis, Ti-Kα. (4×4 HSI pixels.) Bottom left: hsi110887i0 X-ray image; 20′ off-axis, Fe-Kα. (4×4 HSI pixels.) Bottom right: Raytrace; 20′ off-axis, Fe-Kα. (4×4 HSI pixels.) The images are log stretched.

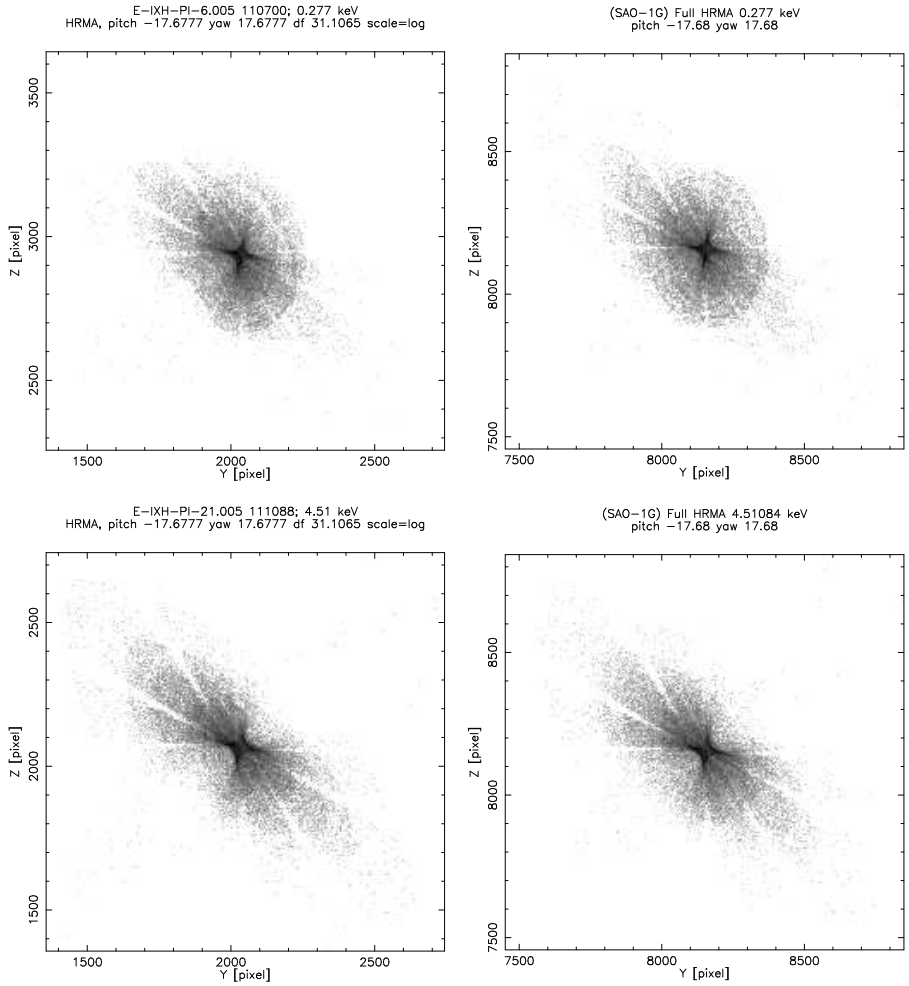

Figure 22.7: Top left: hsi110700i0 X-ray image; 25′ off-axis, C-Kα. (6×6 HSI pixels.) Top right: Raytrace; 25′ off-axis, C-Kα. (6×6 HSI pixels.) Bottom left: hsi11108i0 X-ray image; 25′ off-axis, Ti-Kα. (6×6 HSI pixels.) Bottom right: Raytrace; 25′ off-axis, Ti-Kα. (6×6 HSI pixels.) The images are log stretched.

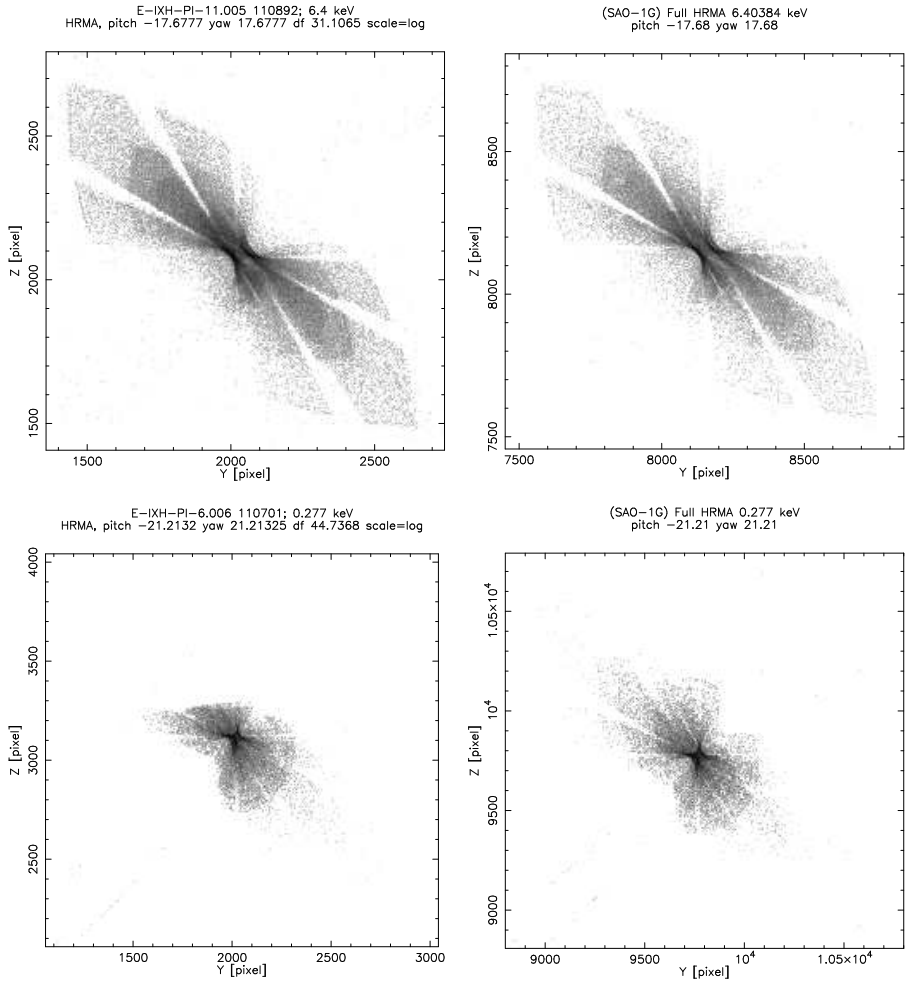

Figure 22.8: Top left: hsi110892i0 X-ray image; 25′ off-axis, Fe-Kα. (6×6 HSI pixels.) Top right: Raytrace; 25′ off-axis, Fe-Kα. (6×6 HSI pixels.) Bottom left: hsi11070li0 X-ray image; 30′ off-axis, C-Kα. (8×8 HSI pixels.) Bottom right: Raytrace; 30′ off-axis, C-Kα. (8×8 HSI pixels.) The images are log stretched. The C-Kα 35′ image was taken near the edge of the HSI detector; this caused part of the image to fall off the detector.

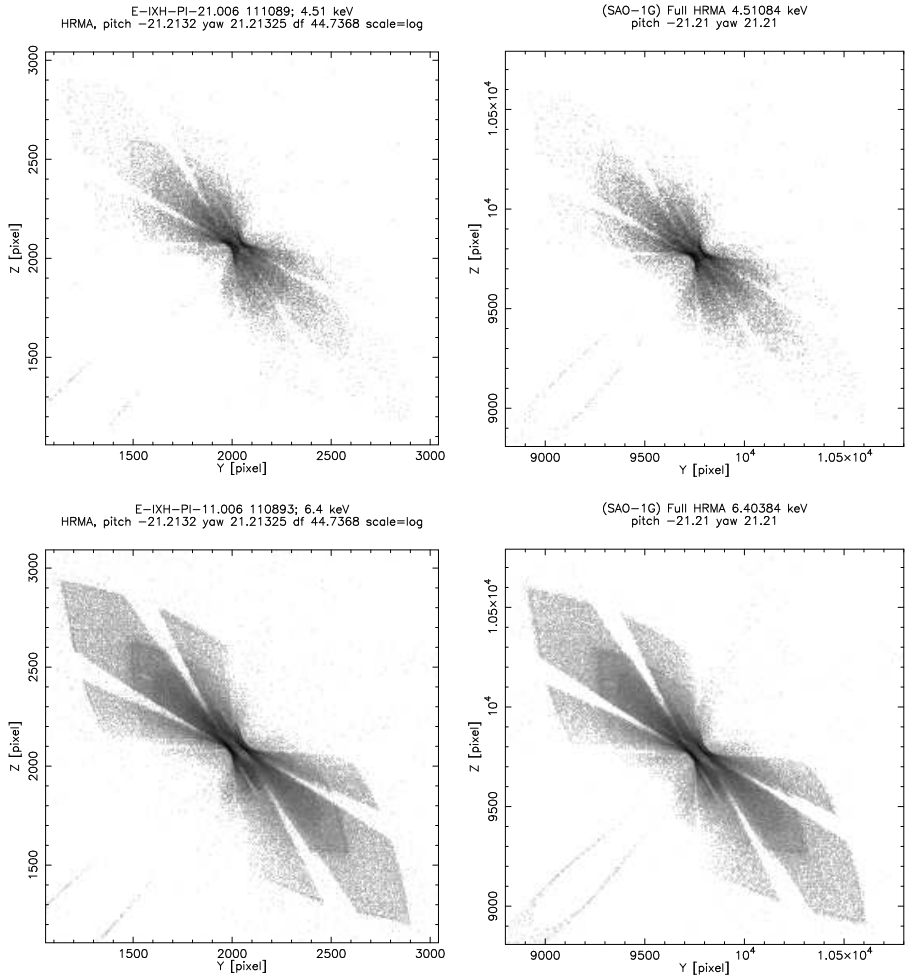

Figure 22.9: Top left: hsi111089i0 X-ray image; 30′ off-axis, Ti-Kα. (8×8 HSI pixels.) Top right: Raytrace; 30′ off-axis, Ti-Kα. (8×8 HSI pixels.) Bottom left: hsi110893i0 X-ray image; 30′ off-axis, Fe-Kα. (8×8 HSI pixels.) Bottom right: Raytrace; 30′ off-axis, Fe-Kα. (8×8 HSI pixels.) The images are log stretched.

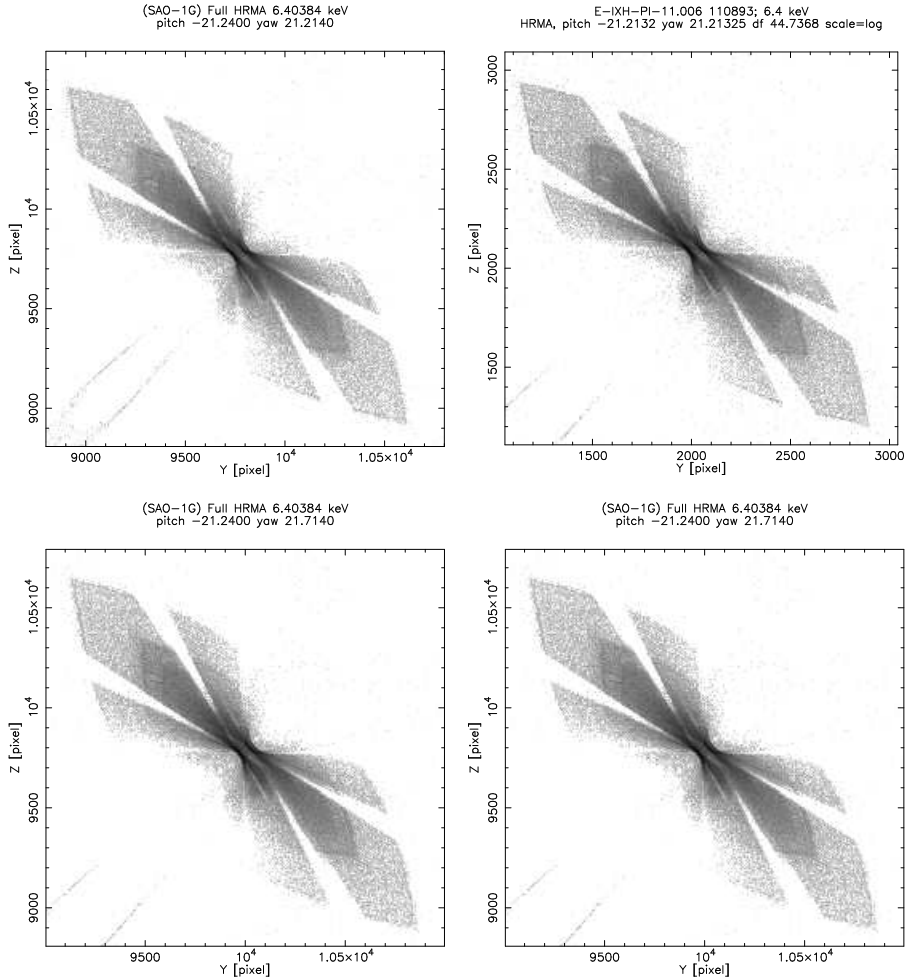

Figure 22.10: Top left: Raytrace; nominal IAP setting. (8×8 HSI pixels.) Top right: hsi110893i0 X-ray image; 30′ off-axis, Fe-Kα. (8×8 HSI pixels.) Bottom left: Raytrace; nominal IAP + 0.5 arcmin yaw. (8×8 HSI pixels.) Bottom right: Raytrace; nominal IAP + 0.5 arcmin yaw. (8×8 HSI pixels.) The images are log stretched.

22.2 Off-axis HSI Images (Single Shell)

In order to better diagnose the coma-free decenters, a planned set of full-HRMA off-axis images at Al-Kα was replaced by a set of single shell images at Al-Kα. These were used to diagnose the magnitude and direction of the decenters (see Chapter 30).

In addition, it is apparent that the quadrant shutters are vignetting the single shell images. This is particularly noticeable in the 20 and 25′ off-axis single shell images. These can be used to refine the knowledge of misalignment of the quadrant shutter assembly. **Work in progress; to be done: raytraces with the misaligned quadrant shutters.**

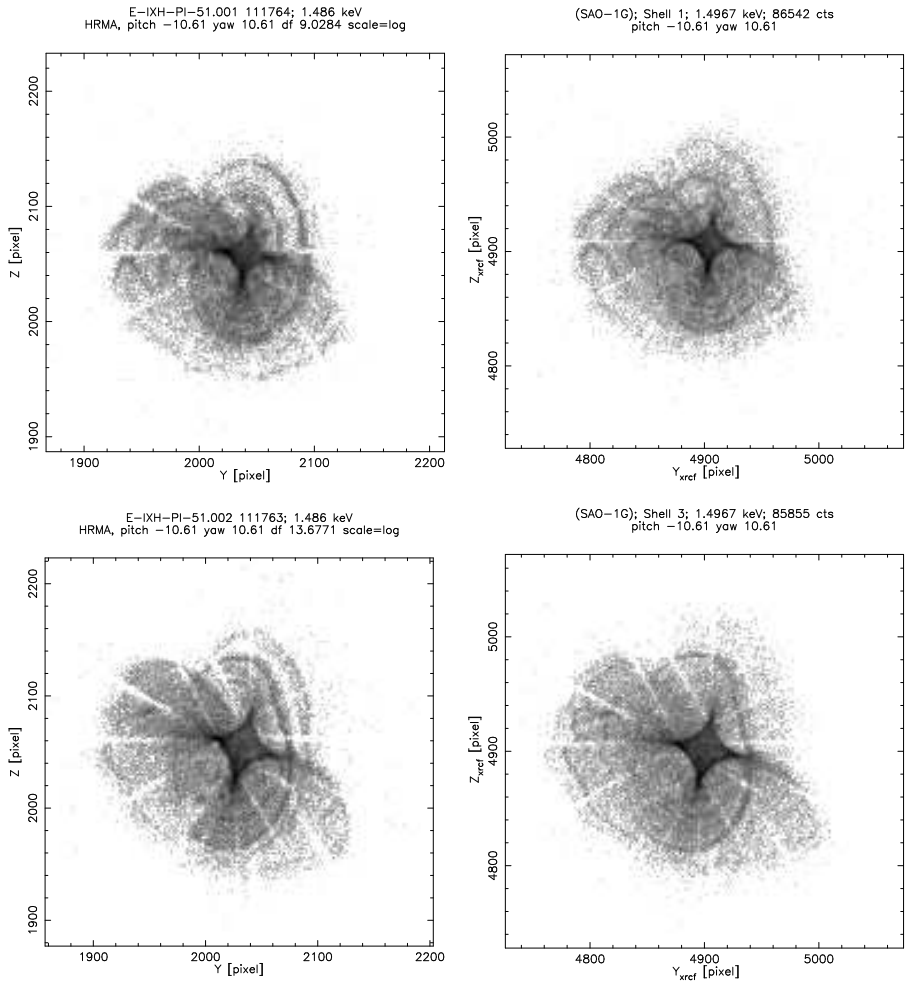

Figure 22.11: Top left: hsi111764i0 X-ray image; shell 1, 15′ off-axis, Al-Kα. (2×2 HSI pixels.) Top right: Raytrace; shell 1, 15′ off-axis, Al-Kα. (2×2 HSI pixels.) Bottom left: hsi111763i0 X-ray image; shell 3, 15′ off-axis, Al-Kα. (2×2 HSI pixels.) Bottom right: Raytrace; shell 3, 15′ off-axis, Al-Kα. (2×2 HSI pixels.) The images are log stretched.

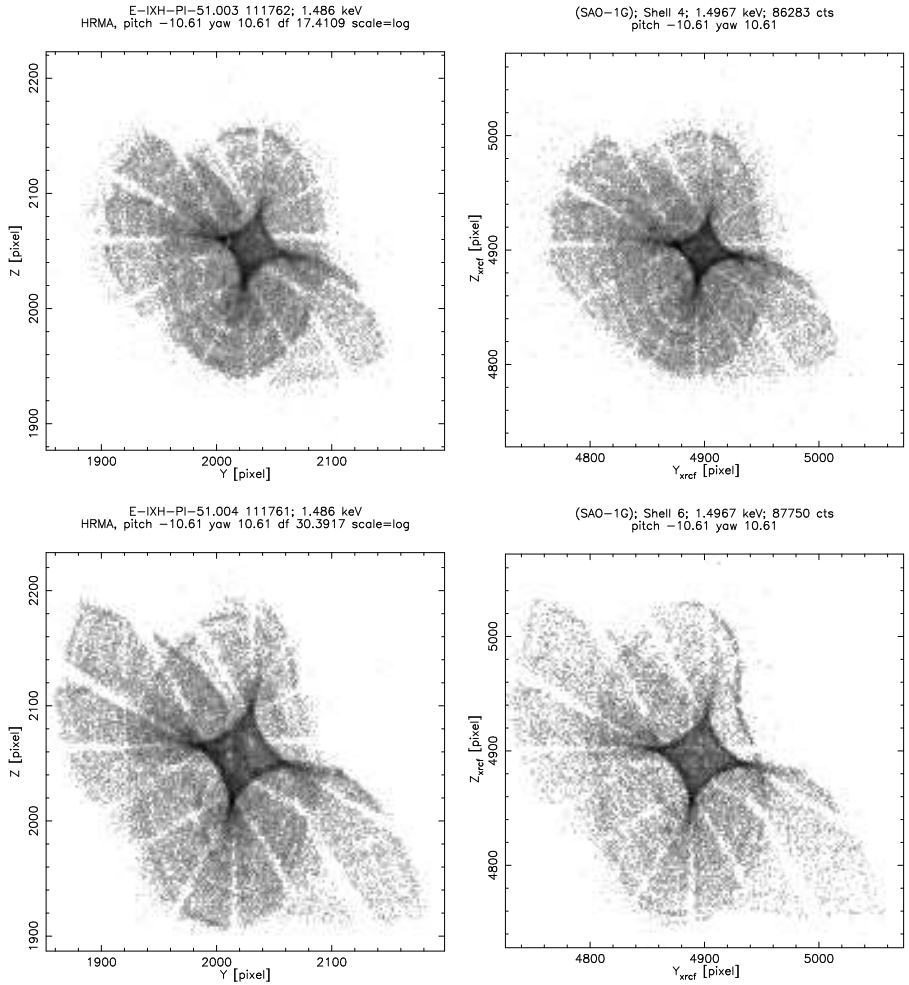

Figure 22.12: Top left: hsi111762i0 X-ray image; shell 4, 15′ off-axis, Al-Kα. (2×2 HSI pixels.) Top right: Raytrace; shell 4, 15′ off-axis, Al-Kα. (2×2 HSI pixels.) Bottom left: hsi111761i0 X-ray image; shell 6, 15′ off-axis, Al-Kα. (2×2 HSI pixels.) Bottom right: Raytrace; shell 6, 15′ off-axis, Al-Kα. (2×2 HSI pixels.) The images are log stretched.

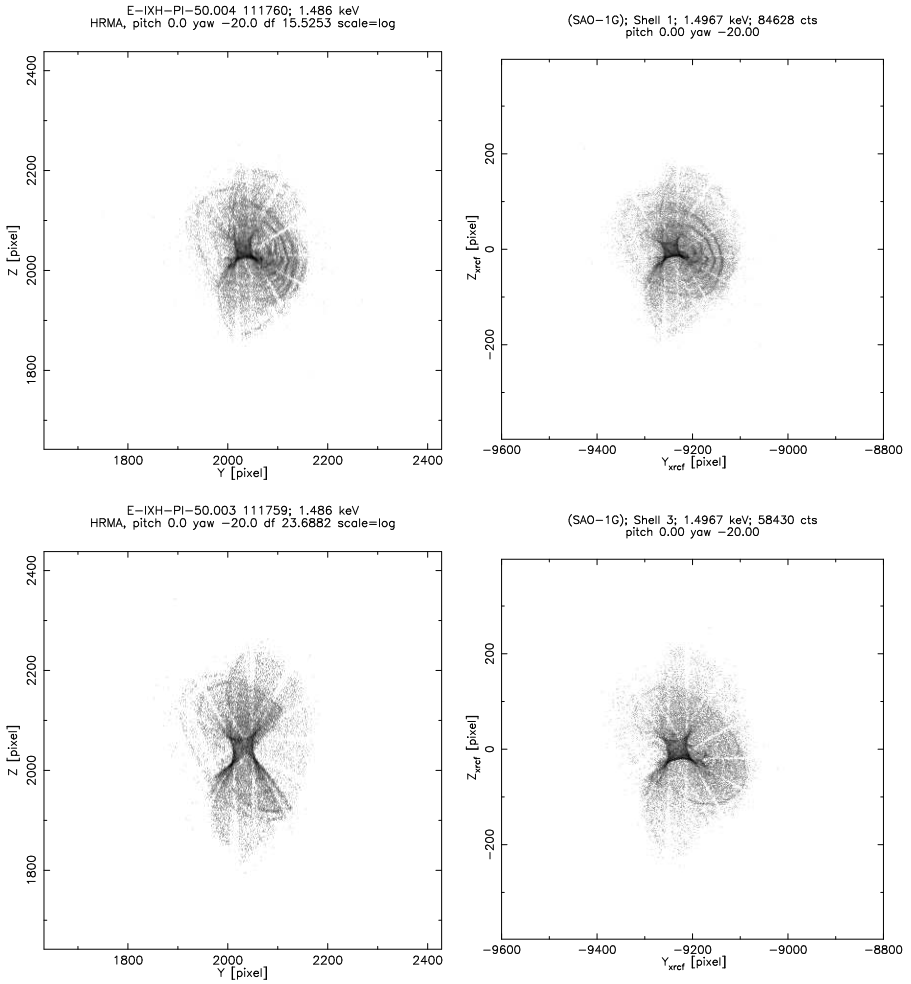

Figure 22.13: Top left: hsi111760i0 X-ray image; shell 1, 20′ off-axis, Al-Kα. (2×2 HSI pixels.) Top right: Raytrace; shell 1, 20′ off-axis, Al-Kα. (2×2 HSI pixels.) Bottom left: hsi111759i0 X-ray image; shell 3, 20′ off-axis, Al-Kα. (2×2 HSI pixels.) Bottom right: Raytrace; shell 3, 20′ off-axis, Al-Kα. (2×2 HSI pixels.) The images are log stretched.

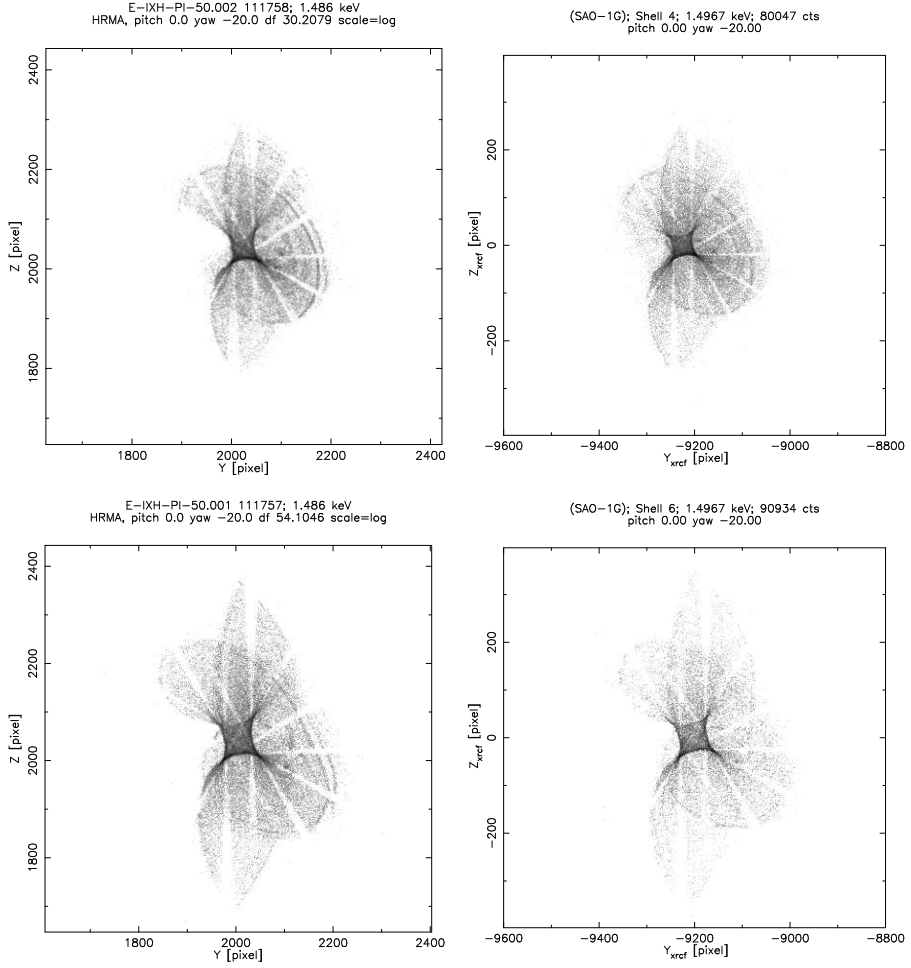

Figure 22.14: Top left: hsi111758i0 X-ray image; shell 4, 20′ off-axis, Al-Kα. (2×2 HSI pixels.) Top right: Raytrace; shell 4, 20′ off-axis, Al-Kα. (2×2 HSI pixels.) Bottom left: hsi111757i0 X-ray image; shell 6, 20′ off-axis, Al-Kα. (2×2 HSI pixels.) Bottom right: Raytrace; shell 6, 20′ off-axis, Al-Kα. (2×2 HSI pixels.) The images are log stretched.

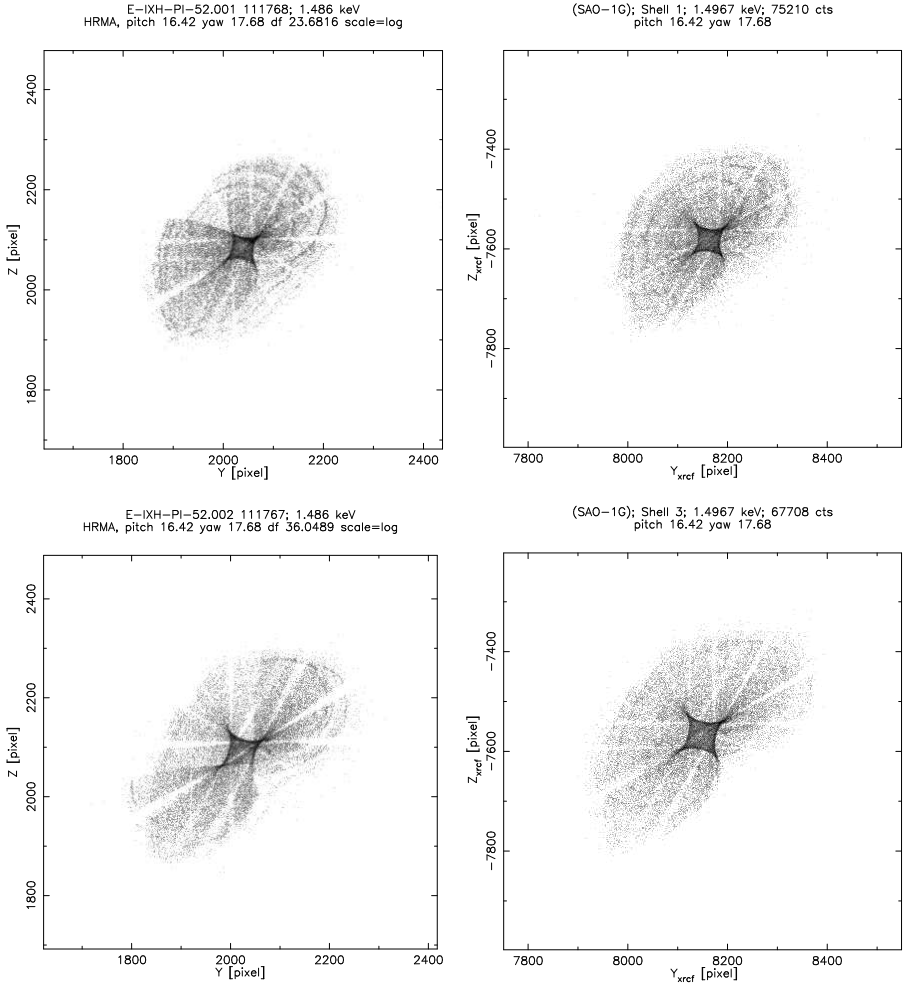

Figure 22.15: Top left: hsi111768i0 X-ray image; shell 1, 24′ off-axis, Al-Kα. (2×2 HSI pixels.) Top right: Raytrace; shell 1, 24′ off-axis, Al-Kα. (2×2 HSI pixels.) Bottom left: hsi111767i0 X-ray image; shell 3, 24′ off-axis, Al-Kα. (2×2 HSI pixels.) Bottom right: Raytrace; shell 3, 24′ off-axis, Al-Kα. (2×2 HSI pixels.) The images are log stretched.

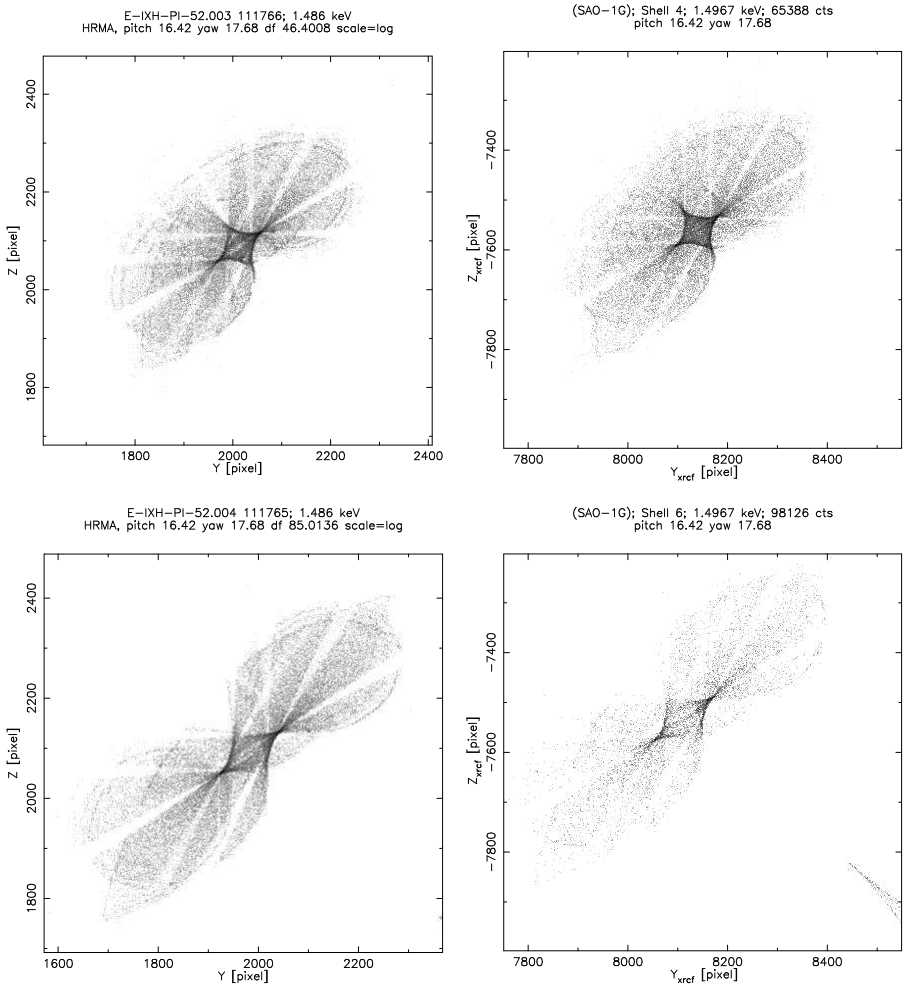

Figure 22.16: Top left: hsi111766i0 X-ray image; shell 4, 24′ off-axis, Al-Kα. (2×2 HSI pixels.) Top right: Raytrace; shell 4, 24′ off-axis, Al-Kα. (2×2 HSI pixels.) Bottom left: hsi111765i0 X-ray image; shell 6, 24′ off-axis, Al-Kα. (2×2 HSI pixels.) Bottom right: Raytrace; shell 6, 24′ off-axis, Al-Kα. (2×2 HSI pixels.) The images are log stretched.

Chapter 23

Predictions of the On-orbit Performance

Chapter 24

EIPS Beam Uniformity

John Everett

This chapter contains an overview of the Electron Impact Point Source (EIPS) Beam Uniformity (BU) measurements taken at XRCF and our analysis of them. (There were also DCM and HIREFS BU measurements taken, but those have been analyzed by the Project Science team, and their results are available from their web site at `http://wwwastro.msfc.nasa.gov/xray/xraycal/`. There appear to have been no BU tests taken with the Penning source.)

24.1 Beam Uniformity Tests

After each source and filter change at XRCF, a Beam Uniformity (BU) scan was taken to determine if the beam flux was non-uniform at the entrance aperture of the HRMA. The possibility of beam non-uniformity is important not only to tests that examine the response of different parts of the mirrors (such as shutter tests or Ring Focus measurements) but also to the use of the four Flow Proportional Counters (FPCs) in front of the HRMA for flux normalization: if there is a spatial non-uniformity in the beam, it is no longer strictly valid to find the flux at the face of the HRMA by averaging the flux detected in the four FPCs. One must employ a beam uniformity map to determine the actual flux 'seen' by the HRMA.

There were two different types of BU scans taken. The most accurate type of BU test was executed at the face of the HRMA with the "North" Flow Proportional Counter (one of the FPCs at the face of the HRMA; known as fpc_hn for Flow Proportional Counter at the HRMA, North). This detector carried out a 40 point scan with four points at the home positions of the fpc_h detectors, and the rest closely following the entrance apertures of the mirror shells. One can see this pattern in a plot from our analysis code, shown in Figure 24.1. fpc_hn had a 36 mm diameter hole defining its aperture for many of these BU scans. For some scans, the fpc_hn's fully open aperture was used, which caused problems when the open aperture extended beyond the X-ray beam at the fpc_ht and fpc_hb positions; those points have been identified and excluded from our analysis.

The second type of BU test was (commonly) a seven point scan done with the FPC in Building 500 (and therefore known as a FPC-500 scan), about 38 meters from the source building, and about 460 meters in front of the HRMA. These were fairly simple scans where two of the points coincided with the home positions of the fpc_5 and ssd_5 detectors with the other five sampling the main X-ray beam that would illuminate the HRMA. A sample FPC-500 beam scan is shown in

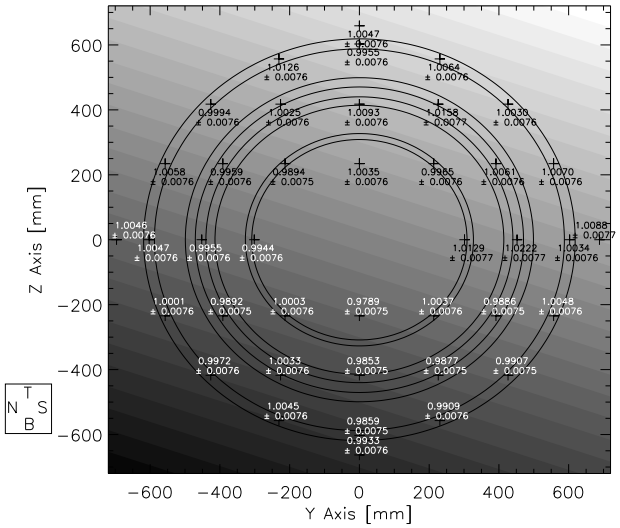

Figure 24.1: fpc_hn Scan Pattern with Polynomial Fit to Normalized Count Rates. The data was taken for MST Run ID 108363 (TRW ID D-BND-BU-2.038) on January 11, 1997 with the C-Kα EIPS anode. The concentric annuli represent the positions of the HRMA mirror shells.

Figure 24.2 (excluding the two data points taken out of the central X-ray beam). The fpc_5 used either the 4, 12, or 36 mm aperture for these scans.

24.2 Beam Uniformity Analysis

For our first cut at analyzing the BU data, we used the HXDS `.sum` files, which contain counts from each of the detectors (determined by a sum of all of the counts in a specified Region of Interest, or ROI) as well as live time information. After completing our 'quick-look' analysis using this method, we fit each of the spectra individually using XSPEC and JMKmod. For our XSPEC results, I heavily used the collection of XSPEC `.xcm` files that Dick Edgar has collected as a result of extensive XSPEC/JMKmod work.

An IDL program was developed that reads in the resultant count rates from either the HXDS `.sum` files or the XSPEC `.flux` files for the fpc_h and fpc_5 detectors, calculates the flux, and then determines a normalized flux. For the fpc_h tests, that normalized flux is derived by first taking the ratio of the fpc_h count rate to the fpc_5 count rate for each data point. The average of that normalized count rate is then calculated, and then divided back into the normalized count rate. Uncertainties are estimated using Poisson statistics.

For the FPC-500 scans, a second set of count rates is not available, so the program simply averages all of the fpc_5 count rates, and then divides the average into the all of count rates to derive a normalized count rate for each data point. This assumes that the source is constant in

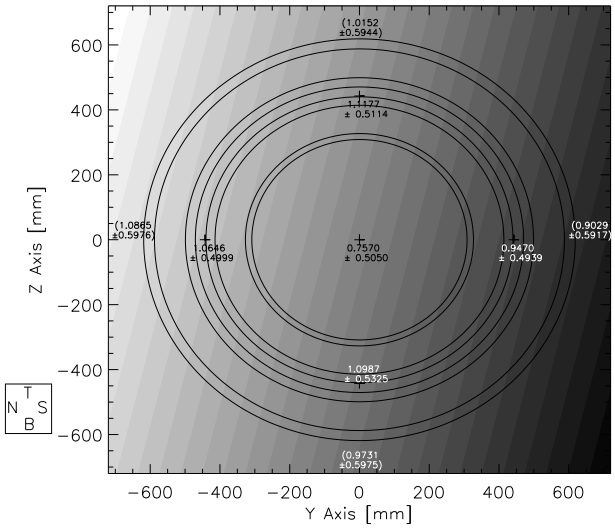

Figure 24.2: fpc_5 Scan Pattern with Polynomial Fit to Normalized Count Rates. The data in this figure is from MST Run ID 110285 (TRW ID E-BND-BU-2.043) taken on January 28, 1997 with the C-Kα EIPS source. The program has extrapolated, from the polynomial fit, to predict values for the fluxes read at the home positions of the fpc_h detector home positions, indicated in parentheses.

time, but that seems to be true to high accuracy for almost all of the EIPS sources (except perhaps those with significant spectral contamination), and also, the FPC-500 scans were run for shorter integration (and overall) times than the FPC-HN scans, so time variability should be even less of a concern. As above, uncertainties are computed using Poisson statistics.

The program then projects the detector scan points back to the location of the HRMA entrance aperture and fits either a smoothed surface or a simple, first order polynomial over the data points, depending on user input. The smooth surface fit is found via an interpolation scheme that first tiles the coordinate grid with triangles whose vertices are data points, and then uses a fifth order polynomial fit to interpolate between the data points and extrapolate outside of the data (Akima, 1978). This produces a smooth surface that the program then uses to map out the flux as a function of mean mirror radius and azimuth. This method produces a map that very closely follows the data points, and was used initially as the basis for all of our BU analysis. These smooth fitting results are still available, although we almost exclusively use first order polynomials fits, now.

For fitting, the simplest function we can fit to the data is a single constant. We might hope that this constant would be the best fit, thus showing that the beam is indeed uniform within statistical uncertainty. We can compare that constant to fits of other functions that we might believe to be physically valid. For the Electron Impact Point Source (EIPS) and the Penning Source, the variations we might expect to see come mostly from some variation in the thickness of the filter in front of the source, which we might model with a simple slanted plane (in XRCF coordinates,

where y and z are in millimeters from the center of the HRMA, whose calculated position for each BU run is given in the buTableEIPS.rdb, an rdb table mentioned in more detail below):

$$(Normalized\ Count\ Rate)_i = a + by_i + cz_i$$

We have tried fitting this function to all of our analyzed EIPS data, and in many cases, it yields a χ^2_ν close to unity. After this fit, the program then plots the fit as a function of mean mirror shell radius and azimuth, and also plots the data points that are close to that mirror shell, for comparison. Results for MST Run ID 112357 (TRW ID F-BND-BU-71.001, taken on February 25, 1997 with the Al-Kα EIPS anode) are shown below in Figures 24.3through24.5. The fits shown in those figures show a maximum variation of the fit of about 2.5 percent. This is actually very common for the EIPS BU maps: most fits vary only as much as 1 to 2 percent (two exceptions are MST Run IDs 110147 and 113089 (2.29 keV and 1.25 keV, respectively), which have much greater variations), and the maximum variation is usually found over the outermost shell, as one might expect.

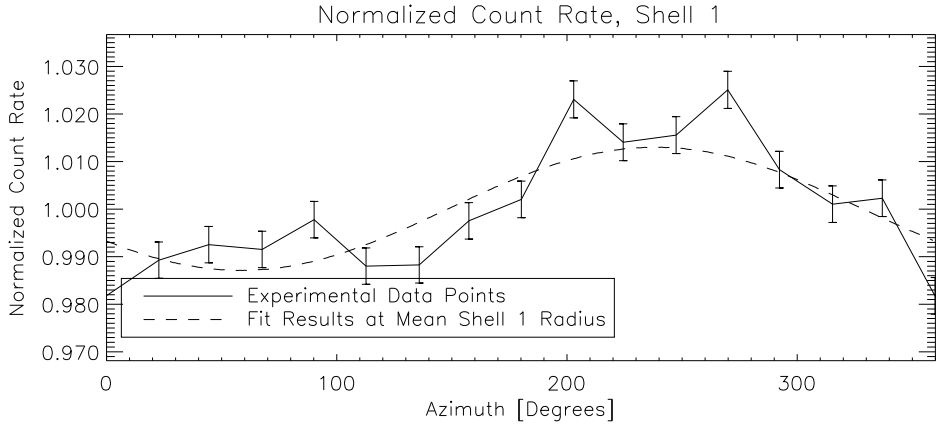

Figure 24.3: Variation in fit and data points as a function of azimuth for mirror Shell 1. The data is from MST Run ID 112357 (TRW ID F-BND-BU-71.001), which was taken on February 25, 1997 with the Al-Kα EIPS anode.

The question still remains, however, of whether those equations actually fit the data any better (within statistical uncertainties) than a simple constant. We can apply the F test to determine whether the addition of the extra parameters in the above equations actually yields a better fit (Bevington and Robinson, 1992, pg. 208-209). For a catalog of all of our fits and F test results to present date, please see the BU webpage at URL

`http://asc.harvard.edu/cal/Links/Compiled/hrma/bumap.html`.

All of our PostScript plots, as well as an rdb table (`buTableEIPS.rdb`) collecting all of the individual BU results, can be found on of this main web page. A listing of some of the columns from the rdb table is shown in Table 24.1.

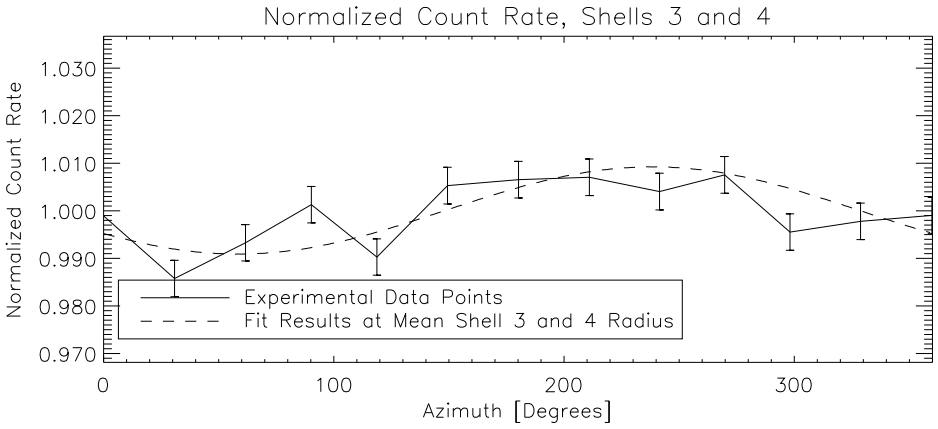

Figure 24.4: Variation in fit and data points as a function of azimuth for mirror Shells 3 and 4. The data is from MST Run ID 112357 (TRW ID F-BND-BU-71.001), which was taken on February 25, 1997 with the Al-Kα EIPS anode.

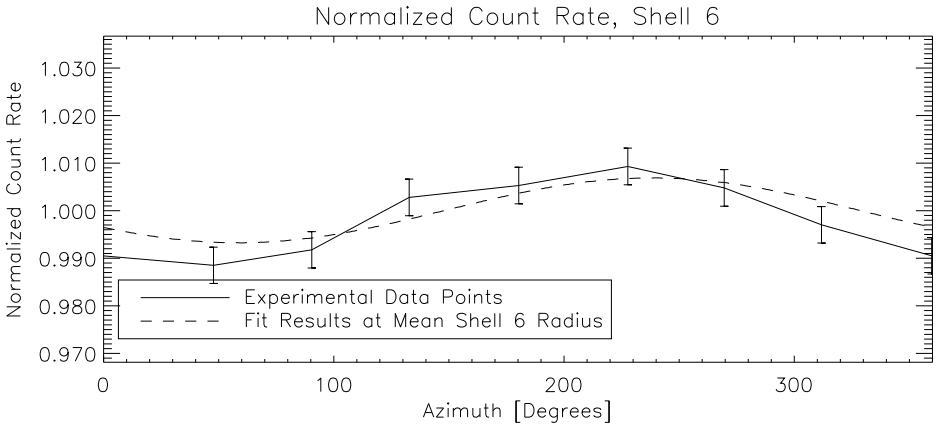

Figure 24.5: Variation in fit and data points as a function of azimuth for mirror Shell 6. The data is from MST Run ID 112357 (TRW ID F-BND-BU-71.001), which was taken on January 11, 1997 with the Al-Kα EIPS anode.

Table 24.1: Fit Results for all EIPS BU Tests. The results of the slanted-plane fits to all of the BU EIPS scans are presented in this table, along with F Test results for comparing constant fits to slanted plane fits. Of the two χ^2_ν values listed, the first ($\chi^2_{\nu,fit}$) is the χ^2_ν for the fit of the slanted plane, and the second ($\chi^2_{\nu,const}$) is the χ^2_ν for a constant value. For tests with F_χ greater than F_{upper}, the slanted plane gives a significantly improved fit over the simple constant.

TRW_ID	Energy	a σ_a	b σ_b	c σ_c	$\chi^2_{\nu,fit}$ F_χ	$\chi^2_{\nu,const}$ F_{upper}
C−BND−BU−2.035	1.490	1.00009 0.00282	−3.40815e−05 1.01327e−05	2.64936e−06 1.00390e−05	2.905 3.919	4.298 99.000
C−BND−BU−2.036	1.490	1.00002 0.00120	−1.14747e−05 3.25334e−06	−2.67304e−06 3.25856e−06	1.717 7.646	1.966 5.229
C−BND−BU−60.009	0.280	1.00046 0.00769	7.49000e−05 2.74978e−05	8.89622e−06 2.75552e−05	0.792 9.496	2.277 99.000
C−BND−BU−60.010	0.280	1.00000 0.00330	−1.18128e−06 8.93709e−06	2.79435e−06 8.95807e−06	0.974 0.118	0.927 5.229
C−BND−BU−60.007	1.490	1.00001 0.00287	−7.75767e−06 1.02841e−05	9.68478e−06 1.02164e−05	1.833 0.801	1.284 99.000
C−BND−BU−60.008	1.490	1.00002 0.00121	−9.50628e−06 3.27804e−06	−8.92112e−06 3.29079e−06	1.903 8.302	2.211 5.229
D−BND−BU−2.035	1.490	1.00002 0.00267	−1.60653e−05 9.53059e−06	−4.77157e−06 9.55453e−06	0.468 6.600	1.007 99.000
D−BND−BU−2.036	1.490	1.00006 0.00112	−1.87262e−05 3.03715e−06	−5.50266e−06 3.04106e−06	1.727 23.921	2.698 5.229
D−BND−BU−2.035a	1.490	1.00000 0.00266	−7.25887e−06 9.52932e−06	−6.57621e−06 9.46761e−06	1.873 0.567	1.202 99.000
D−BND−BU−2.036a	1.490	1.00003 0.00113	−8.53965e−06 3.05151e−06	−1.13365e−05 3.05394e−06	1.587 13.629	2.060 5.229
D−BND−BU−2.026	0.700	0.99998 0.00540	2.50514e−06 1.42596e−05	1.18393e−05 1.57974e−05	1.448 0.408	1.386 5.268
D−BND−BU−2.028	6.400	1.00001 0.00193	−6.54080e−06 5.27699e−06	5.91494e−06 5.21743e−06	1.755 1.614	1.738 5.229
D−BND−BU−2.025a	0.705	1.00003 0.00918	1.19024e−05 3.27523e−05	−2.68191e−05 3.29316e−05	0.577 1.379	0.487 99.000
D−BND−BU−2.027	6.400	1.00000 0.00319	9.08200e−06 1.15067e−05	−2.46893e−06 1.12980e−05	7.183 0.093	3.759 99.000
D−BND−BU−2.037	0.280	1.00000 0.00308	−3.67794e−06 1.10166e−05	−2.62435e−07 1.09712e−05	0.533 0.210	0.295 99.000
D−BND−BU−2.038	0.280	1.00002 0.00120	4.08737e−06 3.25662e−06	1.18176e−05 3.27716e−06	1.138 12.802	1.453 5.229
D−BND−BU−2.033	1.250	1.00002 0.00422	−2.49726e−06 1.50488e−05	−1.75724e−05 1.51067e−05	0.940 1.469	0.815 99.000
D−BND−BU−2.034	1.250	1.00005 0.00186	−9.73956e−06 4.90488e−06	−1.34318e−05 5.44204e−06	1.762 5.724	1.940 5.268
D−BND−BU−2.029	4.510	1.00000 0.00182	1.10422e−05 6.53577e−06	1.10743e−05 6.49357e−06	1.811 3.182	2.346 99.000

Table 24.1: Fit Results for all EIPS BU Tests, continued.

TRW_ID	Energy	a σ_a	b σ_b	c σ_c	$\chi^2_{\nu,fit}$ F_χ	$\chi^2_{\nu,const}$ F_{upper}
D−BND−BU−2.030	4.510	0.99997	−1.64676e−06	4.26492e−06	0.776	0.808
		0.00101	2.72908e−06	2.73519e−06	3.598	5.229
D−BND−BU−2.007	0.520	1.00001	5.68058e−06	−2.87124e−06	0.470	0.705
		0.00130	4.63578e−06	4.65411e−06	4.007	99.000
D−BND−BU−2.001	0.930	1.00000	−1.00829e−05	8.18246e−06	1.760	1.174
		0.00336	1.19714e−05	1.20005e−05	0.667	99.000
D−BND−BU−2.003	8.030	1.00005	−1.19268e−05	2.99188e−05	0.370	1.346
		0.00418	1.49258e−05	1.49476e−05	12.544	99.000
D−BND−BU−2.004	8.030	1.00000	−8.48486e−07	7.40074e−06	1.029	1.023
		0.00189	4.98332e−06	5.49646e−06	1.791	5.268
D−BND−BU−2.020	3.440	0.99987	5.85193e−06	7.37793e−06	0.868	0.832
		0.00602	1.62181e−05	1.65826e−05	0.361	5.229
D−BND−BU−2.014	2.040	1.00373	2.28540e−05	4.10903e−05	21.851	22.984
		0.00184	4.62379e−06	5.37765e−06	3.712	5.362
D−BND−BU−2.013	2.040	1.00007	2.67702e−05	1.44823e−05	0.492	1.093
		0.00464	1.65118e−05	1.66111e−05	6.886	99.000
D−BND−BU−2.017	2.290	1.00002	−5.41036e−06	−2.00972e−05	1.342	1.157
		0.00417	1.47938e−05	1.49365e−05	1.449	99.000
D−BND−BU−2.018	2.290	1.00050	−4.53942e−05	−2.89089e−05	3.455	8.193
		0.00144	3.87923e−06	3.92420e−06	55.476	5.229
D−BND−BU−2.005	0.850	1.00001	4.94521e−06	−7.79643e−06	0.021	0.111
		0.00408	1.45350e−05	1.45812e−05	19.482	99.000
D−BND−BU−2.041	0.110	1.00016	−5.09332e−05	9.72039e−06	4.163	3.931
		0.00532	1.90605e−05	1.91309e−05	1.777	99.000
D−BND−BU−2.039	0.180	1.00003	−2.11774e−05	4.82300e−06	1.165	1.193
		0.00388	1.39015e−05	1.38396e−05	2.096	99.000
D−BND−BU−2.040	0.180	1.00000	1.64747e−06	1.60597e−06	1.255	1.199
		0.00129	3.41389e−06	3.75790e−06	0.331	5.268
E−BND−BU−2.043	0.277	1.00001	−1.88833e−06	−9.16368e−06	0.160	0.738
		0.00161	5.76348e−06	5.76616e−06	16.413	99.000
E−BND−BU−2.044	0.277	1.00001	−9.32083e−06	−2.12630e−06	1.609	1.691
		0.00140	3.77800e−06	3.78893e−06	3.980	5.229
E−BND−BU−2.027	6.400	1.00000	−5.71183e−06	−1.27929e−05	4.732	2.717
		0.00332	1.19438e−05	1.18052e−05	0.297	99.000
E−BND−BU−2.028	6.400	1.00000	−2.02997e−06	2.56462e−06	1.495	1.428
		0.00201	5.44052e−06	5.45186e−06	0.242	5.229
E−BND−BU−2.029	4.510	1.00006	1.35422e−05	2.67904e−05	0.026	1.364
		0.00362	1.29632e−05	1.29008e−05	206.730	99.000
E−BND−BU−2.030	4.510	1.00001	7.93309e−06	7.19870e−06	0.486	0.625
		0.00156	4.22701e−06	4.22119e−06	13.235	5.229
E−BND−BU−2.015	2.980	0.99998	4.18590e−06	−9.32613e−06	0.181	0.251
		0.00357	1.26866e−05	1.27888e−05	3.541	99.000
E−BND−BU−2.016	2.980	1.00000	−4.15124e−06	2.93009e−06	1.195	1.158

Table 24.1: Fit Results for all EIPS BU Tests, continued.

TRW_ID	Energy	a σ_a	b σ_b	c σ_c	$\chi^2_{\nu,fit}$ F_χ	$\chi^2_{\nu,const}$ F_{upper}
		0.00192	5.19438e−06	5.22246e−06	0.798	5.229
E−BND−BU−2.001	0.930	1.00000	−1.32484e−05	8.31557e−06	0.425	0.628
		0.00339	1.21639e−05	1.20843e−05	3.902	99.000
E−BND−BU−2.003	8.030	0.99994	9.74866e−06	−2.44388e−05	6.306	3.827
		0.00451	1.62158e−05	1.59987e−05	0.427	99.000
E−BND−BU−2.035	1.490	1.00005	−9.19765e−06	−2.15445e−05	0.674	3.435
		0.00186	6.66013e−06	6.65414e−06	18.372	99.000
E−BND−BU−2.023	5.410	1.00022	4.79380e−05	2.70673e−05	4.844	6.023
		0.00404	1.45592e−05	1.43369e−05	2.974	99.000
F−BND−BU−71.001	1.490	1.00007	−1.12402e−05	−1.82670e−05	2.608	6.928
		0.00061	1.62379e−06	1.62742e−06	66.600	5.229
F−BND−BU−71.002	0.930	1.00001	−1.98478e−06	6.29006e−06	1.351	1.680
		0.00069	2.56810e−06	2.55593e−06	4.924	7.559
F−BND−BU−71.003	8.030	1.00000	4.99967e−06	6.57708e−06	2.409	2.631
		0.00084	2.24960e−06	2.25276e−06	5.606	5.229
F−BND−BU−71.002a	0.930	1.00001	−5.42720e−06	3.81035e−06	0.522	0.964
		0.00071	2.63520e−06	2.63484e−06	12.133	7.559
F−BND−BU−71.003a	8.030	0.99999	1.15272e−06	2.98672e−06	1.280	1.239
		0.00123	3.25124e−06	3.28865e−06	0.744	5.229
F−BND−BU−71.008	6.400	1.00012	2.54596e−05	−2.25740e−05	4.173	6.310
		0.00134	3.55175e−06	3.57589e−06	21.974	5.229
F−BND−BU−71.009	0.700	1.00003	−1.59876e−05	−1.36148e−05	0.933	0.963
		0.00452	1.20756e−05	1.20788e−05	3.241	5.229
F−BND−BU−71.023	6.400	0.99376	5.99711e−05	−1.04384e−06	182.133	150.426
		0.00696	1.57501e−05	1.29900e−05	0.085	8.022
F−BND−BU−71.007	0.280	1.00000	−6.00555e−06	5.05003e−06	71.204	69.135
		0.00037	9.99948e−07	9.97364e−07	0.867	5.229
F−BND−BU−71.010	4.510	1.00004	1.17268e−07	9.81362e−06	0.673	0.708
		0.00230	6.83280e−06	5.95102e−06	4.041	5.229
F−BND−BU−71.011	0.450	1.00146	5.81334e−05	−1.56096e−04	0.698	1.138
		0.01714	6.35006e−05	6.42413e−05	9.569	7.559
F−BND−BU−71.006	0.520	1.00015	3.92564e−05	−8.36074e−06	1.545	1.611
		0.00635	1.69182e−05	1.69814e−05	3.648	5.229
F−BND−BU−71.005	1.740	1.00038	−3.49262e−05	4.89348e−05	2.118	3.865
		0.00265	7.06815e−06	7.06251e−06	34.148	5.229
F−BND−BU−71.013	0.850	1.00033	3.68032e−05	6.04605e−05	1.270	3.596
		0.00343	1.27796e−05	1.28204e−05	23.976	7.559
F−BND−BU−71.004	1.250	1.00158	3.73415e−05	−9.94471e−05	3.662	43.366
		0.00101	2.69061e−06	2.69081e−06	424.884	5.229
G−BND−BU−81.007	0.280	1.00003	−6.51892e−06	−1.47677e−05	1.180	1.463
		0.00165	4.39884e−06	4.41322e−06	11.370	5.229
G−BND−BU−81.022	0.110	1.00054	2.57768e−04	−3.46909e−04	0.179	2.518
		0.01827	9.62680e−05	1.81749e−04	41.218	4999.536

Table 24.1: Fit Results for all EIPS BU Tests, continued.

TRW_ID	Energy	a σ_a	b σ_b	c σ_c	$\chi^2_{\nu,fit}$ F_χ	$\chi^2_{\nu,const}$ F_{upper}
G−BND−BU−81.021	0.180	1.00001	−2.05933e−05	2.78142e−05	0.216	0.237
		0.01152	3.08143e−05	3.06438e−05	5.918	5.229
G−BND−BU−81.011	0.450	1.00057	−3.44642e−05	1.38253e−05	0.868	0.750
		0.01731	6.46812e−05	6.39322e−05	0.371	7.559
G−BND−BU−81.006	0.520	0.99992	−1.52032e−05	3.78581e−05	1.326	1.302
		0.01173	3.14650e−05	3.14308e−05	1.271	5.229
G−BND−BU−81.005	1.740	1.00028	−2.82025e−05	3.60225e−05	2.387	4.658
		0.00177	4.74495e−06	4.72368e−06	39.103	5.229
G−BND−BU−81.009	0.700	1.00271	2.45266e−04	6.46635e−05	2.223	2.453
		0.02606	6.96864e−05	6.93748e−05	6.040	5.229
G−BND−BU−81.013	0.850	1.00002	−5.01848e−06	5.97849e−06	0.673	0.682
		0.00251	6.43125e−06	6.48740e−06	2.155	7.559
G−BND−BU−81.002	0.930	1.00001	−9.88465e−06	−2.82025e−06	0.980	0.978
		0.00288	7.37642e−06	7.39165e−06	1.982	7.559
G−BND−BU−81.004	1.250	1.00005	−1.11282e−05	−2.02036e−05	1.062	1.911
		0.00145	3.88464e−06	3.88691e−06	33.189	5.229
I−BND−BU−2.022	1.740	1.00093	−1.77308e−05	3.12021e−05	9.370	30.440
		0.00108	2.63264e−06	2.29864e−06	24.486	8.649
I−BND−BU−2.008	0.520	1.00010	−9.36616e−07	−1.58046e−06	1.745	1.434
		0.00139	3.21912e−06	2.96713e−06	0.213	8.649
I−BND−BU−2.028	6.400	1.00008	−6.20802e−06	6.28369e−06	1.403	1.903
		0.00151	3.85321e−06	2.75128e−06	5.567	8.649
I−BND−BU−2.004	8.030	0.99996	−4.47744e−06	−3.83342e−07	5.261	4.451
		0.00109	2.90911e−06	2.20397e−06	0.460	8.649
I−BND−BU−2.030	4.510	0.99994	7.50034e−07	−8.42752e−07	0.550	0.448
		0.00180	4.77674e−06	3.65354e−06	0.143	8.649
I−BND−BU−2.016	1.490	1.00087	−2.15739e−05	−9.88483e−06	2.281	7.884
		0.00121	3.24823e−06	2.43388e−06	26.567	8.649
I−BND−BU−2.129	0.520	1.00723	−2.69526e−05	−1.21810e−04	1.208	1.103
		0.01019	2.35998e−05	2.49247e−04	1.130	8.649

24.3 Future Directions

Shortly, we will complete the first pass of analysis using XSPEC and JMKmod, and after that, the majority of BU analysis will be complete. Further analysis of the variation of the beam between tests, and the variation of a given EIPS flux over different BU tests, are possible future areas of concentration. Also, we may wish to try other fitting functions to improve the simple polynomial fits to the data. Comparisons of these BU maps with Phase I and J flat field calibration BU maps (which had higher statistics, although at fewer points) would be useful. In addition, we might improve the normalization statistics for our fpc_hn BU tests by including ssd_5 flux measurements when possible.

24.4 Acknowledgments

Thanks to the following people, who helped me from the start of this project through to its latest incarnation: Mark Freeman, who started this program long ago, Jeremy Drake and Diab Jerius, who helped me push it further, Deron Pease for throwing megabytes of data through it, and Dick Edgar and Kendra Michaud for their help with fitting with JMKmod and XSPEC.

Chapter 25

HRMA Ring Focus Shutter Test

Ping Zhao

25.1 Introduction

The HRMA ring focus shutter test was designed to measure the HRMA shutter positions. During the HRMA calibration in early January 1997, it was found that the throughput of the HRMA top and bottom quadrants were unequal. For shell 6 it differed by as much as 10%. An early suggestion was that the shutters behind the HRMA were not positioned properly. For example, if the North or/and South shutters were blocking part of the bottom quadrant, the throughput asymmetry would occur. Also, if one shutter were blocking a slice of neighboring shell, the asymmetry could happen.

The quadrant shutter assembly, mounted behind the H shells, contained four shutters for each mirror. The shutters were named according to their positions: T(op), B(ottom), N(orth) and S(outh). Each shutter blade is 92 degrees wide to ensure complete blocking when all four shutters are closed.

25.2 Measurements

The ring focus shutter tests were made with the HSI at the ring focus position (65.2 mm defocus) and with either T & B shutters or N & S shutters open for one shell only. The eight shutter test images were taken on 15 Jan 1997 with the C-K EIPS source, immediately following the ring focus test (with run ID 108944), which had all 16 shutters open. Image 108944 had an integration time of 1800 sec. The shutter tests had integration times ranging from 200 to 600 sec; Table 25.1 lists these eight shutter tests.

25.3 Data Analysis

Figures 25.1–25.8 show the eight shutter test images as listed in Table 25.1. The image orientations are looking towards the HSI from the HRMA, i.e. the top, left, bottom, and right of each image corresponds to the Top, North, Bottom, and South at the XRCF. The mean radii of the rings from the four shells are 3.88 mm, 3.10 mm, 2.73 mm, and 2.05 mm, respectively.

Table 25.1: HRMA Ring Focus Shutter Test Data
Date: 15 Jan 1997 Source: C-Kα Defocus: 65.2 mm

Run ID	TRW ID	Shell	Shutters open	Defocus	Integration
108945	D-IXH-RF-17.001	1	T + B	65.2 mm	200 sec
108946	D-IXH-RF-17.002	1	N + S	65.2 mm	200 sec
108947	D-IXH-RF-17.003	3	T + B	65.2 mm	200 sec
108948	D-IXH-RF-17.004	3	N + S	65.2 mm	300 sec
108949	D-IXH-RF-17.005	4	T + B	65.2 mm	360 sec
108951	D-IXH-RF-17.006	4	N + S	65.2 mm	360 sec
108953	D-IXH-RF-17.007	6	T + B	65.2 mm	600 sec
108954	D-IXH-RF-17.008	6	N + S	65.2 mm	600 sec

To analyze the data, each image pair was combined to make a full ring. Figures 25.9–25.12 show the four combined full rings.[1] Each ring was sliced into 360 sectors with 1 degree per sector. The intensity of each sector (counts/second/sector) was then measured using the IRAF/imcnts package and plotted as a function of azimuthal angle.

25.4 Results

Figures 25.13–25.16 illustrate the results of the ring focus shutter test for the four shells. There are five panels in each figure:

1. The top panel shows the HSI intensity of the corresponding ring from run 108944 (C-Kα source, 1800 sec exposure time), which was taken with all the shutters open. The intensity variation is due to the quantum efficiency of the HSI which depends on the incident angle of the X-ray. There are intensity dips at 30 degree multiples. These are due to the supporting struts blocking the rays.

2. The second panel is the HSI intensity from the shutter tests. In addition to the intensity dips at 30 degree multiples, there are dips at $\pm$45 and $\pm$135 degrees. These are due to the shutter overlaps: each shutter is designed to be 92 degrees wide, so each open quadrant should be 88 degrees wide. The figures show that those dips are 2-3 degrees wide as expected. And their positions are within 1-2 degrees from the expected values.

3. The third panel is the ratio of the above two panels. The dips at $\pm$45 and $\pm$135 degrees are still there as expected. There are also spikes (both positive and negative) at 30 degree multiples. Because the HSI was moved between these tests, the gaps were not aligned exactly.

4. The fourth panel is the third panel with the spikes and dips removed. It looks pretty flat.

5. The fifth panel shows the data from the fourth panel binned into 15 degree bins and fitted to a straight line. The straight line is the average ratio over the entire ring. The straight line fits these data very well.

[1] In Figure 25.9, a quasi-elliptical scattering pattern, clocked about 7 degrees clockwise, appears above and below the shell 1 ring. In Figure 25.11, there is a very faint ring outside the shell 4 ring. There is also a faint scattering pattern on the north side of the ring 3 (Figure 25.10). These were probably caused by the reflections from the mirror ends, which, for the last a few millimeters, have a slightly different tangent from the designed surface.

These figures answer the question of whether the shutters were mounted and positioned properly. As we can see, the ratios of the ring focus test and the shutter tests are nearly constant (other than the spikes and dips) with values between 2.89 and 2.99. The magnitude of these ratios is due to the source intensity difference between the run 108944 and the shutter test runs). These results tell us that the shutters were not blocking anything other than their assigned areas. If there were any unwanted blocking in the azimuthal direction, there would have been dips wider than 2-3 degrees at the ± 45 and ± 135 degree locations. If there were any unwanted blocking in the radial direction, the intensity ratio in that quadrant would have systematically dropped below the overall average ratio.

25.5 Conclusion

The conclusion is: based on the HSI ring focus shutter test, all the shutters were mounted properly. They only block rays in their assigned area when closed. The HRMA shutters do not block on-axis rays beyond design expectations. (Note, however, the design requirements did allow the shutters to vignette off-axis rays, as discussed in Chapter 15). The HRMA throughput asymmetry was not due to shutter vignetting. (Later, the throughput asymmetry was attributed to the decenters between the P shells and the H shells. See Chapter 30 of this report.)

HRMA Ring Focus Shutter Test Images

Source: C-Kα, Defocus: 65.2 mm

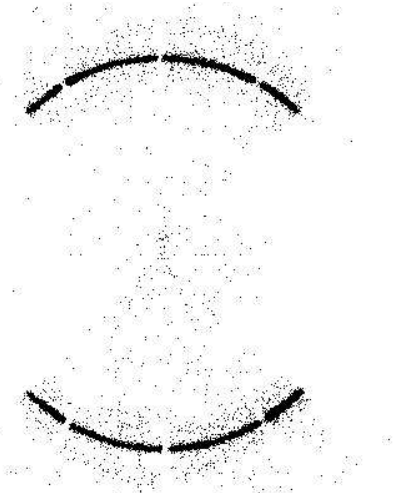

Figure 25.1: D-IXH-RF-17.001, 108945, Shell 1 TB, 200 sec.

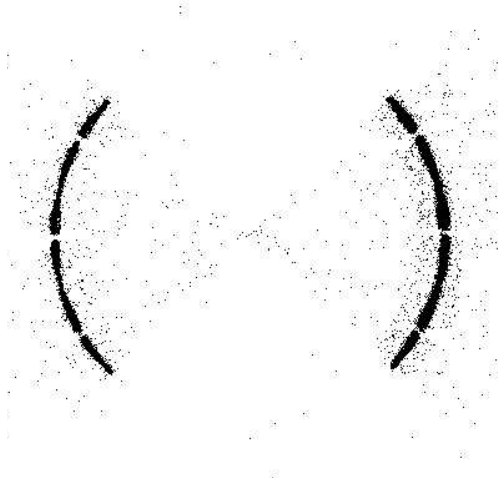

Figure 25.2: D-IXH-RF-17.002, 108946, Shell 1 NS, 200 sec.

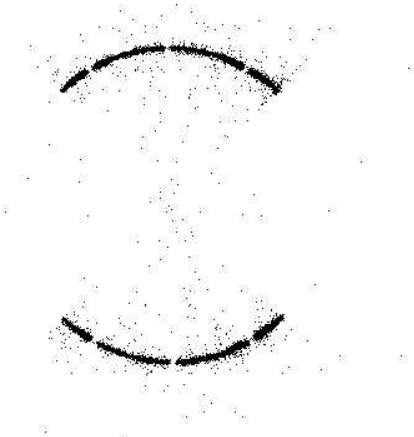

Figure 25.3: D-IXH-RF-17.003, 108947, Shell 3 TB, 200 sec.

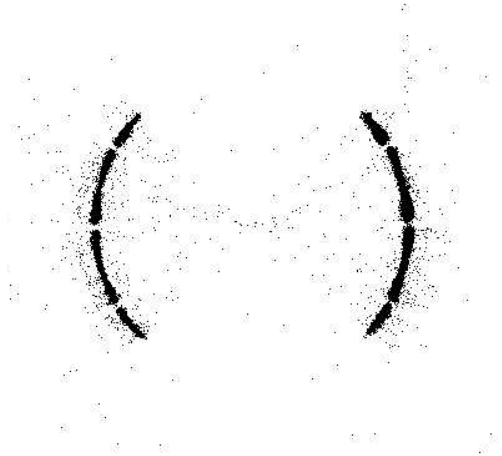

Figure 25.4: D-IXH-RF-17.004, 108948, Shell 3 NS, 300 sec.

HRMA Ring Focus Shutter Test Images
Source: C-Kα, Defocus: 65.2 mm

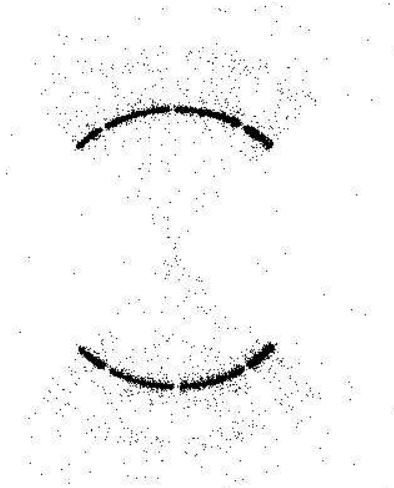

Figure 25.5: D-IXH-RF-17.005, 108949, Shell 4 TB, 360 sec.

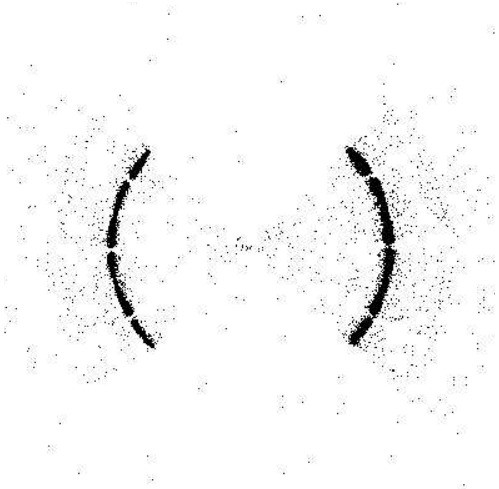

Figure 25.6: D-IXH-RF-17.006, 108951, Shell 4 NS, 360 sec.

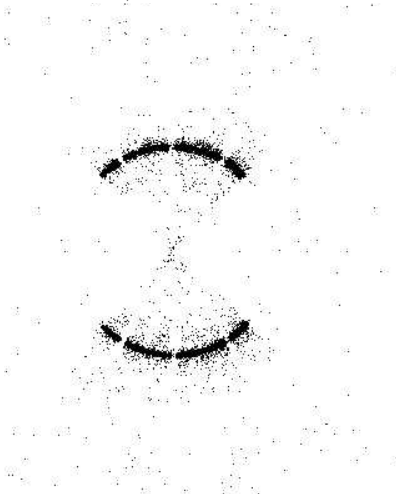

Figure 25.7: D-IXH-RF-17.007, 108953, Shell 6 TB, 600 sec.

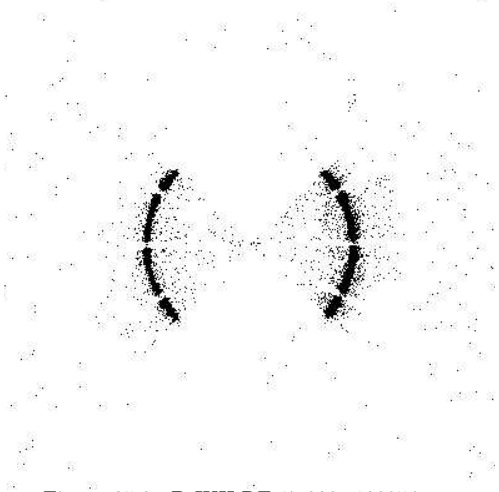

Figure 25.8: D-IXH-RF-17.008, 108954, Shell 6 NS, 600 sec.

HRMA Ring Focus Shutter Test Combined Images
Source: C-Kα, Defocus: 65.2 mm

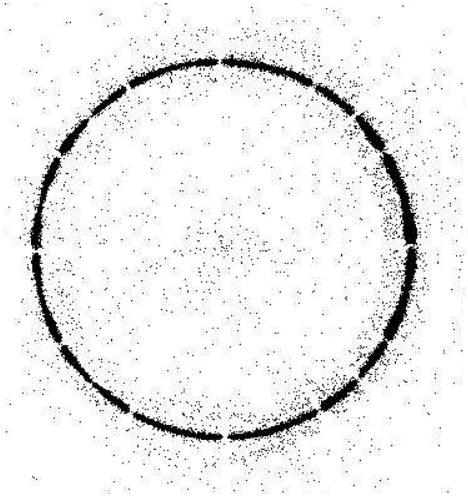

Figure 25.9: 108945 & 108946, Shell 1, 200 + 200 sec.

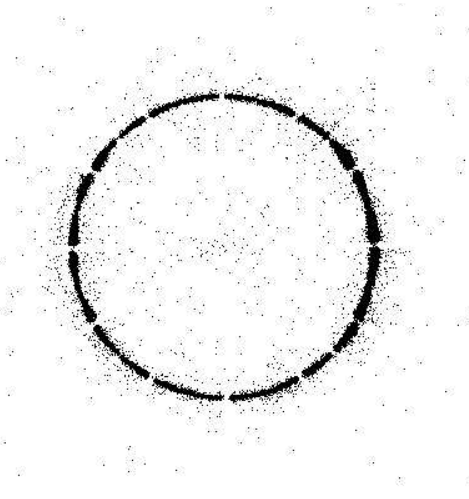

Figure 25.10: 108947 & 108948, Shell 3, 200 + 300 sec.

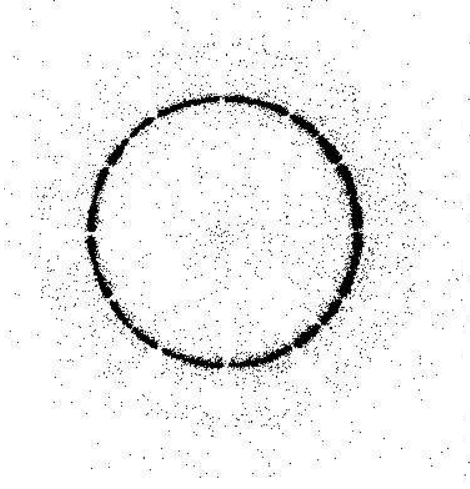

Figure 25.11: 108949 & 108951, Shell 4, 360 + 360 sec.

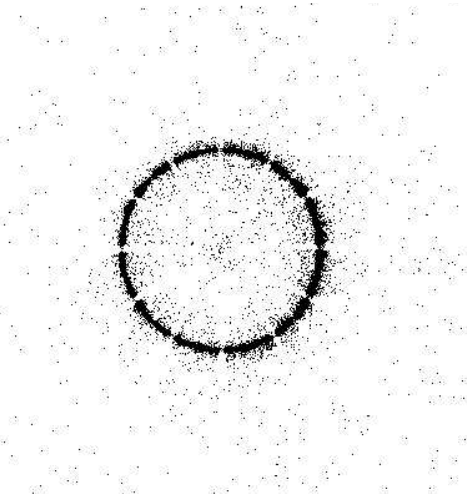

Figure 25.12: 108953 & 108954, Shell 6, 600 + 600 sec.

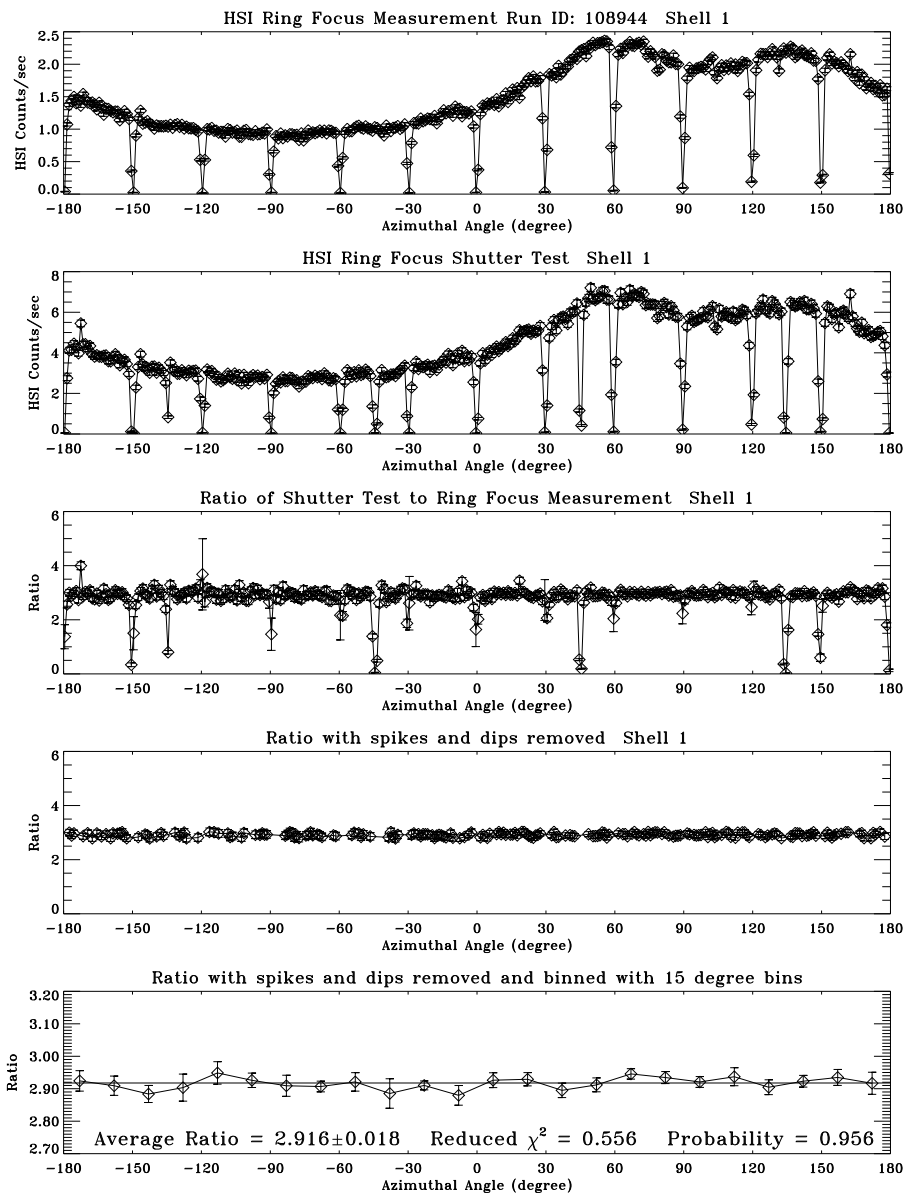

Figure 25.13: The HRMA ring focus shutter test results. Shell 1

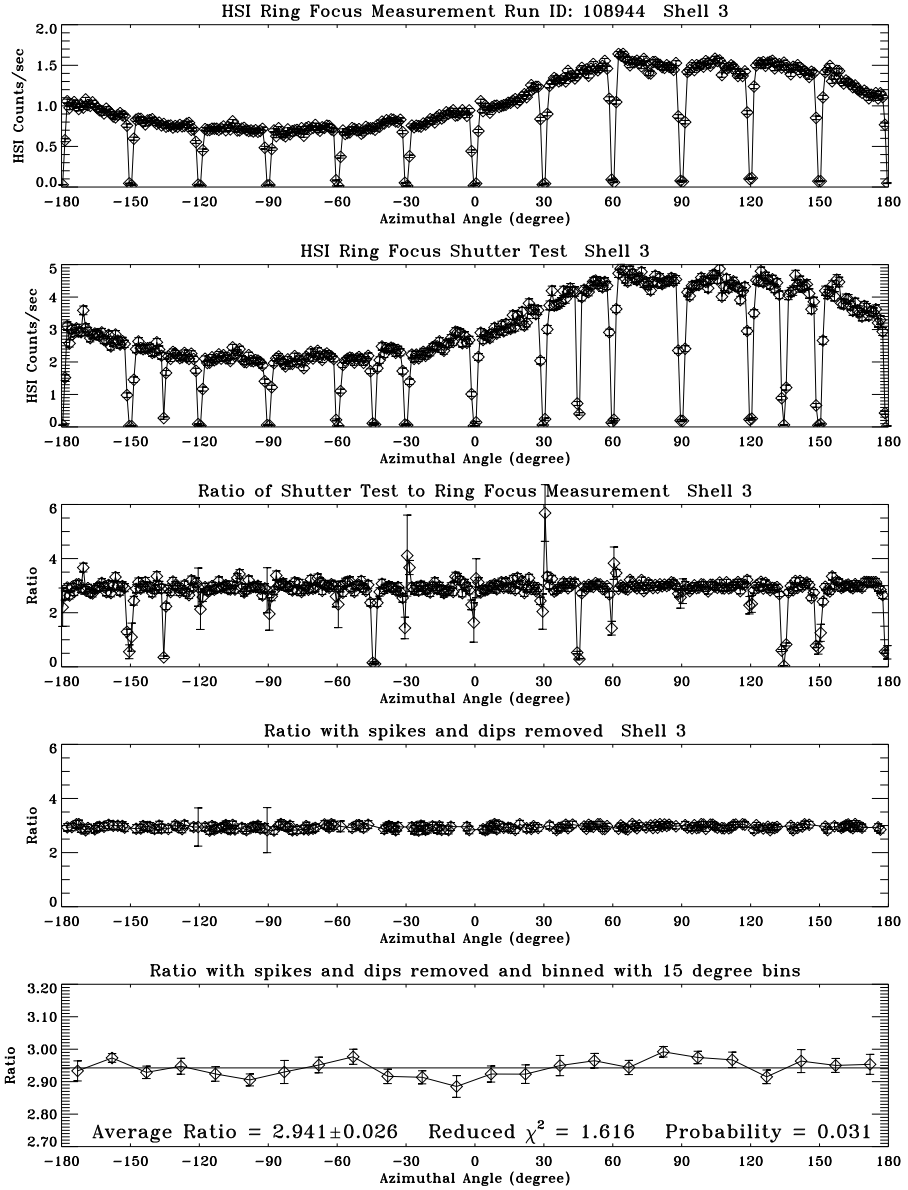

Figure 25.14: The HRMA ring focus shutter results. Shell 3

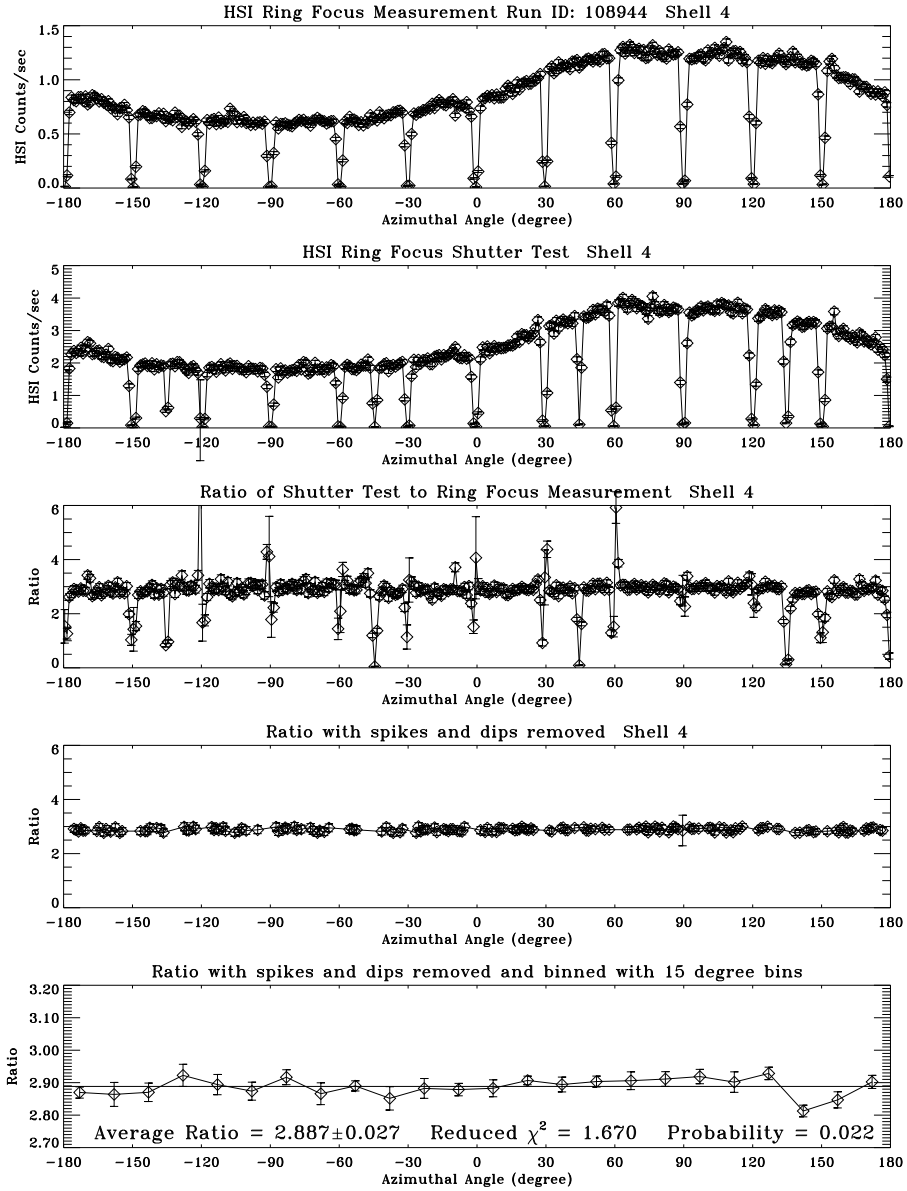

Figure 25.15: The HRMA ring focus shutter results. Shell 4

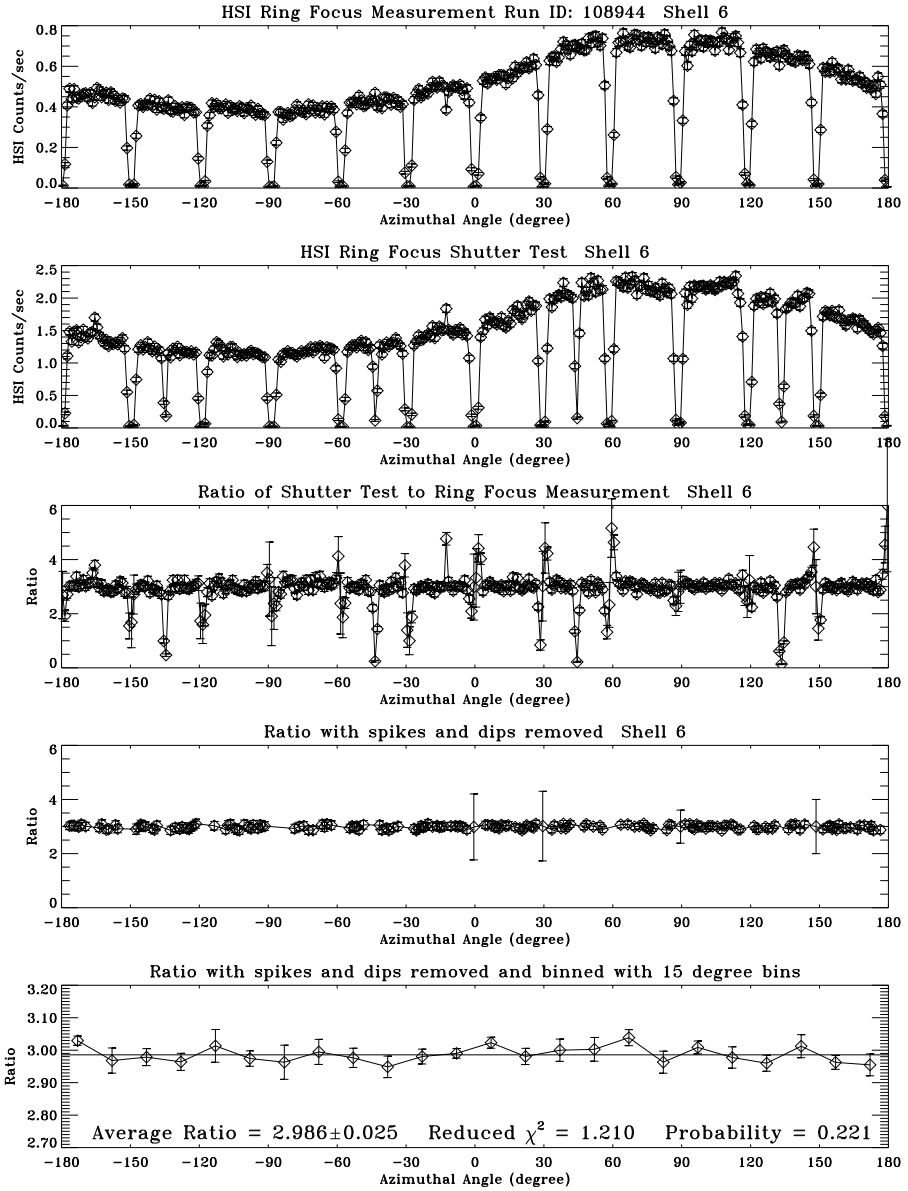

Figure 25.16: The HRMA ring focus shutter results. Shell 6

Chapter 26

HRMA Focus Measurements and Raytrace Update

William Podgorski

26.1 HRMA Focus Measurements at XRCF

Two dimensional HXDS FPC pinhole scans were made on a shell-by-shell and quadrant-by-quadrant basis on three separate occasions during the Phase 1 HRMA XRCF testing period. These scans were used to calculate the best focus position of each of the four HRMA shells as well as the relative P-H tilts. We have analyzed these data and updated our raytrace model of the HRMA to include the XRCF measured focus results. We have not yet incorporated the XRCF measured intra-shell mirror tilts. In this section we describe these measurements and the subsequent analysis.

Centroids determined from a shell's quadrant images yield four pairs of coordinate values. From these, two focus estimates may be constructed:

$$\Delta_{Y,i} = 0.995 \frac{\pi}{4\sqrt{2}} \frac{F}{R_i} (Y_{i,N} - Y_{i,S})$$
$$\Delta_{Z,i} = 0.995 \frac{\pi}{4\sqrt{2}} \frac{F}{R_i} (Z_{i,T} - Z_{i,B})$$

where $\Delta_{Y,Z}$ are the focus error estimates; R_i is the nodal radius for the mirror pair, and F is the distance from the mirror node to the (finite conjugate) focus. (The 0.995 factor accounts for the fact that the quadrants are really only 88°.) A disagreement between these two focus error estimates may be indicative of astigmatism, either intrinsic to the optic or resulting from 1g distortions. In addition, two alignment estimators can be formed:

$$tilt_{Y,i} = 0.978 \frac{\pi}{4F_i'} (Y_{i,N} + Y_{i,S} - Y_{i,T} - Y_{i,B})$$
$$tilt_{Z,i} = 0.978 \frac{\pi}{4F_i'} (Z_{i,N} + Z_{i,S} - Z_{i,T} - Z_{i,B})$$

where F_i' is the distance from the body center of the H optic to the *far focus* of the H. (The 0.978 factor is a correction for 88° quadrants.)

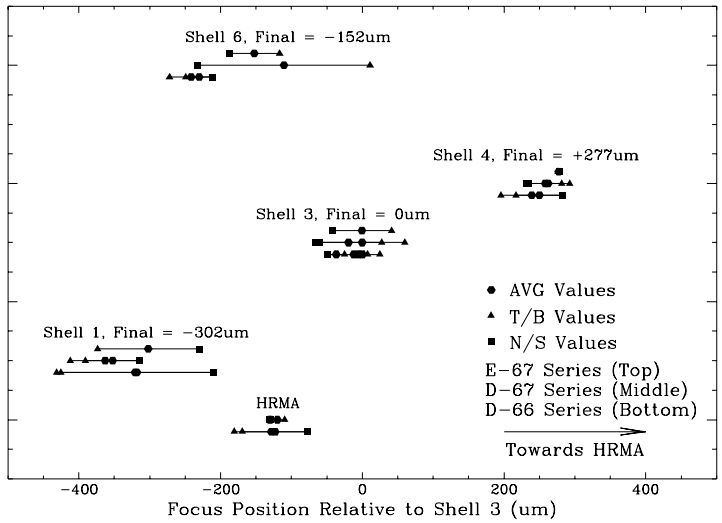

Figure 26.1: HRMA Focus Data: Focal positions are shown in μm relative to the Shell 3 focus. A positive difference represents a focus position closer to the HRMA than the Shell 3 focus (this is the XRCF sign convention and *not* that of `SAOsac`). The data are taken from three series of tests, and are shown stacked – the legend describes the stacking order. Note that there were no HRMA tests in series E-67.

The HRMA focus data from the three measurement sets performed are summarized in Figure 26.1. Five groups of data are shown, the four individual shells and the complete HRMA. For the four HRMA shells three data lines are shown, representing the initial (D-66 series), intermediate (D-67 series), and final (E-67 series) data. The focus of a shell may be calculated from either the *top* and *bottom* quadrants or the *north* and *south* quadrants. The average of these two foci was used as the shell focus position. The difference between the T/B focus and the N/S focus may be due to either astigmatism in the mirrors or to measurement error (a certain amount of separation is also induced by the 1G test environment).

The best dataset was E-67, the last one taken; more was known about the shell image qualities beforehand and more time was allocated to capture all of the flux from each quadrant of each shell, compared to the earlier data. The relative foci from these measurements are shown in Table 26.1.

Table 26.1: Best Estimate of XRCF Measured Focus of Shells, relative to Shell 3

Shell	F_N - F_3 (μm)
1	−302
3	0
4	+277
6	−152

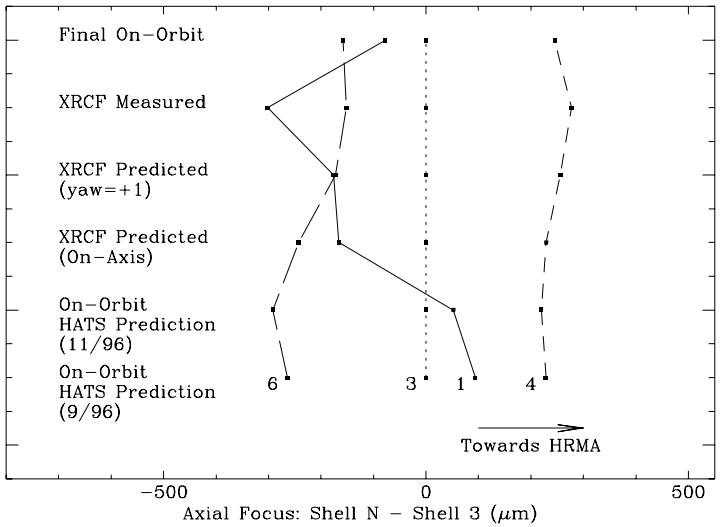

Figure 26.2: HRMA Focus History

Positive numbers represent focus positions closer to the HRMA, or shorter overall focal lengths.

In Figure 26.2 the XRCF measured focus data are compared with various focus predictions for both the on-orbit (infinite source distance, no gravity) and XRCF (finite source distance, 1G) conditions. Six different cases are shown, presented vertically with the focus values of each shell connected by lines. The bottom two cases represent the pre-calibration predictions of *on-orbit* focus from the Kodak HATS data. The bottom set of data is from the September 1996 testing, after all alignments but prior to HRMA final assembly. The next set up represents data from Kodak's November 96 HRMA Acceptance Test Procedure (ATP), after HRMA final assembly at Kodak and just prior to shipment to XRCF. Both sets of data show that the foci of the shells span about 500 μm, with the ordering of the foci as (6 – 3 – 1 – 4) in order of *decreasing* focal lengths.

The middle two cases shown in Figure 26.2 represent pre-calibration predictions of XRCF focus from the November 1996 Kodak test data, for HRMA yaw angles of both zero and one arc minute. Table 26.2 presents a comparison of predictions of the on-orbit and XRCF focal distances, relative to the P side of the HRMA CAP. The overall change in focal distance is about 195mm (longer at XRCF). However, the most interesting feature shown is that the Shell 1 focal distance increases much more (about 250 μm) than that of the other 3 shells. In Figure 26.2 this feature is shown clearly as the Shell 1 focus moves from a position between 3 and 4, for the on-orbit case, to a position further away from the HRMA, now between 6 and 3. This behavior was initially considered to be an anomaly and possibly a mistake, since raytrace studies using the *ideal* HRMA optic prescriptions and spacings did *not* give this result. However, when the as-built P1 and H1 surface prescriptions and mirror axial spacings are used this feature is seen (this result has been confirmed by Dave Zissa and Paul Glenn).

The "XRCF measured" case in Figure 26.2 shows what is considered to be the best estimate

Table 26.2: Comparison of pre-XRCF Predictions of On-orbit and XRCF HRMA foci

Shell	Focus relative to P side of CAP(mm) F_{XRCF}	$F_{\mathrm{On-Orbit}}$	ΔF	$\Delta F - \Delta F_{\mathrm{Shell3}}$
1	10274.9145004675	10079.6696878001	195.2461	0.2949
3	10274.7304206266	10079.779404296	194.9512	0.0000
4	10274.3675449462	10079.4606206727	194.9062	−0.0449
6	10274.7562744271	10079.7697370664	194.9863	0.0352

from XRCF testing of the shell-to-shell relative focus. This is from the data in Table 26.1, discussed above. We see that there is is a discrepancy of about 200 μm in the position of the Shell 1 focus at XRCF as compared with the predictions based on Kodak optical test data. At XRCF, Shell 1 had the longest focal distance, a result which was consistent over all of the testing. In discussion with L. Van Speybroeck (AXAF Telescope Scientist), we decided that the XRCF data was most likely more accurate than the Kodak optical test data, and that we should use this data as the basis for our HRMA model. The process of incorporating the XRCF data into our raytrace model is discussed below. The end result is shown as the top case in Figure 26.2. This assumption makes the predicted HRMA performance somewhat better, as the span of the foci is a bit smaller. It is now baselined in SAO's HRMA raytrace model.

26.2 Update of SAO HRMA Raytrace Model from XRCF Focus Data

In the pre-calibration SAO baseline mirror definition file, `EKCHDOS04`, the shell relative foci were set equal to those measured in the Kodak optical tests. This was done by adjusting the CAP-to-H mirror spacing so that the relative foci as determined by raytracing were equal to that measured in the optical tests. In the updated, post-calibration, SAO baseline, derived from XRCF testing, the CAP-to-mirror spacings are set to the values measured at Kodak for both P and H mirrors, and the relative foci were adjusted by making slight changes to the average cone angles of the mirrors. These cone angles were adjusted until the raytraced foci, at the XRCF finite source distance, were close to the XRCF measured relative foci. The shell 3 focus was left unchanged, and the foci of the other shells were adjusted relative to that of shell 3. The as-measured mirror data (from Kodak and HDOS) are given in Table 26.3. The data in Table 26.3 were used in the updated mirror definition file, `EKCHDOS06`.

Alteration of the cone angles was done by adding an additional "deformation" to the optics described by a Fourier-Legendre polynomial with three Legendre terms and no Fourier terms. The only non-zero term, the l_1 term, is equal to −0.001mm for the P optics and +0.001mm for the H optics (two term L-F files would have sufficed for this application). A single numerical scaling factor for these deformations was determined for each shell, and was used for both the P and H optics. The value of these multipliers was determined by trial-and-error by running tests with the full XRCF raytrace model including the `EKCHDOS06` mirror database :

Shell	Multiplier
1	0.0872
3	0.0
4	0.0150
6	0.0461

Table 26.3: As Measured Optic lengths and distances

Shell	L_P (mm)	L_H (mm)	CAP (mm)	P-CAP (in)	H-CAP (in)	ZC_P (mm)	ZC_H (mm)
1	842.2150	842.1920	49.911	0.2153	0.3940	-426.5761	481.0146
3	842.2080	842.1970	49.911	0.6144	0.3905	-436.7098	480.9282
4	842.2080	842.2250	49.911	0.7580	0.3860	-440.3572	480.8279
6	842.2090	842.2000	49.911	0.9440	0.3230	-445.0821	479.2152

L_P	Length of P Mirror
L_H	Length of H Mirror
CAP	Thickness of CAP
P-CAP	Distance from P side of CAP to P mirror
H-CAP	Distance from H side of CAP to H mirror
ZC_P	Z co-ordinate of center of P mirror in SAO raytrace co-ordinates
ZC_H	Z co-ordinate of center of H mirror in SAO raytrace co-ordinates

Table 26.4: Final Mirror Focal Positions at XRCF and on orbit

	XRCF			On Orbit	
	Raytrace		Meas.	Raytrace	
Shell	F_N (mm)	-(F_N - F_3) (μm)	F_N - F_3 (μm)	F_N (mm)	-(F_N - F_3) (μm)
1	10275.0342	-305	-302	10079.8359	-77
3	10274.7295	0	0	10079.7588	0
4	10274.4551	274	277	10079.5137	245
6	10274.8730	-144	-152	10079.9170	-158

The resultant deformations are summed with the other mirror distortions to create the final mirror maps.

In Table 26.4, raytrace results using these offset files plus the new `EKCHDOS06` mirror database are given for both the XRCF and on-orbit cases, plus the measured XRCF relative foci (repeated for convenience from Table 26.1. The raytraced F_N are measured relative to the P side of the CAP in the raytrace (`SAOsac`) coordinate system. The foci relative to Shell 3 are presented in the XRCF coordinate system (recall from Figure B.1 that the `SAOsac` Z optical axis coordinate is flipped with respect to the XRCF X coordinate). A positive relative focus again indicates a focus value closer to the HRMA. The results from the on-orbit raytrace (the last column in Table 26.4) are also plotted as "Final On-Orbit" in Figure 26.2.

Test data are given in Tables 26.5 through 26.7.

Table 26.5: Test Data for HRMA Focus Tests: D-66 Series

Date	TRW Test ID	Shell	PrimeX [μm]	δF_y [μm]	δF_z [μm]	Yaw [′]	Pitch [′]
01/02/97	D-IXF-P2-66.001	3	−32566	180.8	178.7	0	0
01/02/97	D-IXF-P2-66.002						
01/02/97	D-IXF-P2-66.003						
01/02/97	D-IXF-P2-66.004						
01/02/97	D-IXF-P2-66.005	3	−32566	180.8	166.8	0	0
01/02/97	D-IXF-P2-66.002						
01/02/97	D-IXF-P2-66.003						
01/02/97	D-IXF-P2-66.004						
01/02/97	D-IXF-P2-66.026	3	−32804	−15.0	−39.1	0	0
01/02/97	D-IXF-P2-66.027						
01/02/97	D-IXF-P2-66.028						
01/02/97	D-IXF-P2-66.029						
01/02/97	D-IXF-P2-66.030	3	−32804	−15.0	−88.8	0	0
01/02/97	D-IXF-P2-66.027						
01/02/97	D-IXF-P2-66.028						
01/02/97	D-IXF-P2-66.029						
01/02/97	D-IXF-P2-66.006	4	−32563	−106.0	−18.7	0	0
01/02/97	D-IXF-P2-66.007						
01/03/97	D-IXF-P2-66.008						
01/03/97	D-IXF-P2-66.009						
01/03/97	D-IXF-P2-66.010	4	−32563	−106.0	−40.0	0	0
01/03/97	D-IXF-P2-66.007						
01/03/97	D-IXF-P2-66.008						
01/03/97	D-IXF-P2-66.009						
01/03/97	D-IXF-P2-66.011	6	−33060	−108.9	−47.9	0	0
01/03/97	D-IXF-P2-66.012						
01/03/97	D-IXF-P2-66.013						
01/03/97	D-IXF-P2-66.014						
01/03/97	D-IXF-P2-66.015	6	−33060	−108.9	−70.7	0	0
01/03/97	D-IXF-P2-66.012						
01/03/97	D-IXF-P2-66.013						
01/03/97	D-IXF-P2-66.014						
01/03/97	D-IXF-P2-66.016	1	−32962	−11.5	209.2	0	0
01/03/97	D-IXF-P2-66.017						
01/03/97	D-IXF-P2-66.018						
01/03/97	D-IXF-P2-66.019						
01/03/97	D-IXF-P2-66.020	1	−32962	−11.5	203.2	0	0
01/03/97	D-IXF-P2-66.017						
01/03/97	D-IXF-P2-66.018						
01/03/97	D-IXF-P2-66.019						

Table 26.5: Test Data for HRMA Focus Tests: D-66 Series, continued

Date	TRW Test ID	Shell	PrimeX [μm]	δF_y [μm]	δF_z [μm]	Yaw [′]	Pitch [′]
01/03/97	D-IXF-P2-66.021	1346	−32866	−49.4	54.7	0	0
01/03/97	D-IXF-P2-66.022						
01/03/97	D-IXF-P2-66.023						
01/03/97	D-IXF-P2-66.024						
01/03/97	D-IXF-P2-66.025	1346	−32866	−49.4	43.2	0	0
01/03/97	D-IXF-P2-66.022						
01/03/97	D-IXF-P2-66.023						
01/03/97	D-IXF-P2-66.024						

Table 26.6: Test Data for HRMA Focus Tests: D-67 Series

Date	TRW Test ID	Shell	PrimeX [μm]	δF_y [μm]	δF_z [μm]	Yaw [′]	Pitch [′]
01/05/97	D-IXF-P2-67.001	3	−32782	41.5	−52.6	−1	0
01/05/97	D-IXF-P2-67.002						
01/05/97	D-IXF-P2-67.003						
01/05/97	D-IXF-P2-67.004						
01/05/97	D-IXF-P2-67.005	3	−32776	41.5	−79.0	−1	0
01/05/97	D-IXF-P2-67.002						
01/05/97	D-IXF-P2-67.003						
01/05/97	D-IXF-P2-67.004						
01/05/97	D-IXF-P2-67.006	4	−32499	22.9	−23.1	−1	0
01/05/97	D-IXF-P2-67.007						
01/05/97	D-IXF-P2-67.008						
01/05/97	D-IXF-P2-67.009						
01/05/97	D-IXF-P2-67.010	4	−32502	22.9	−37.9	−1	0
01/05/97	D-IXF-P2-67.007						
01/05/97	D-IXF-P2-67.008						
01/05/97	D-IXF-P2-67.009						
01/05/97	D-IXF-P2-67.011	6	−32984	5.3	−238.1	−1	0
01/05/97	D-IXF-P2-67.012						
01/06/97	D-IXF-P2-67.013						
01/06/97	D-IXF-P2-67.014						
01/06/97	D-IXF-P2-67.015	6	−32984	5.3	−238.1	−1	0
01/06/97	D-IXF-P2-67.012						
01/06/97	D-IXF-P2-67.013						
01/06/97	D-IXF-P2-67.014						
01/06/97	D-IXF-P2-67.016	1	−33058	12.9	111.1	−1	0
01/06/97	D-IXF-P2-67.017						
01/06/97	D-IXF-P2-67.018						
01/06/97	D-IXF-P2-67.019						
01/06/97	D-IXF-P2-67.020	1	−33058	12.9	89.9	−1	0
01/06/97	D-IXF-P2-67.017						
01/06/97	D-IXF-P2-67.018						
01/06/97	D-IXF-P2-67.019						
01/06/97	D-IXF-P2-67.021	1346	−32861	26.3	26.0	−1	0
01/06/97	D-IXF-P2-67.022						
01/06/97	D-IXF-P2-67.023						
01/06/97	D-IXF-P2-67.024						
01/06/97	D-IXF-P2-67.025	1346	−32861	26.0	5.6	−1	0
01/06/97	D-IXF-P2-67.022						
01/06/97	D-IXF-P2-67.023						
01/06/97	D-IXF-P2-67.024						

Table 26.7: Test Data for HRMA Focus Tests: E-67 (Final) Series

Date	TRW Test ID	Shell	PrimeX [μm]	δF_y [μm]	δF_z [μm]	Yaw [′]	Pitch [′]
02/07/97	E-IXF-P2-67.001	3	−32562	−282.03	−365.2	0	0
02/07/97	E-IXF-P2-67.002						
02/07/97	E-IXF-P2-67.003						
02/07/97	E-IXF-P2-67.004						
02/07/97	E-IXF-P2-67.006	4	−31970	−9.64	−8.2	0	0
02/07/97	E-IXF-P2-67.007						
02/07/97	E-IXF-P2-67.008						
02/07/97	E-IXF-P2-67.009						
02/07/97	E-IXF-P2-67.011	6	−32341	85.09	13.6	0	0
02/07/97	E-IXF-P2-67.012						
02/07/97	E-IXF-P2-67.013						
02/07/97	E-IXF-P2-67.014						
02/07/97	E-IXF-P2-67.016	1	−32589	−120.6	22.6	0	0
02/07/97	E-IXF-P2-67.017						
02/07/97	E-IXF-P2-67.018						
02/07/97	E-IXF-P2-67.019						

26.3 Updated deformation and sum files

In `SAOsac` terminology Legendre-Fourier DFR "offset" files were created to describe the deformation to the optics which provides the required change in optic cone angle:

`p`N`_off.DFR` (where $N = 1, 3, 4, 6$):

```
P  Deformation                                              3    0
   0.00000E+00   -1.00000E-03    0.00000E+00
```

`h`N`_off.DFR` (where $N = 1, 3, 4, 6$):

```
H  Deformation                                              3    0
   0.00000E+00    1.00000E-03    0.00000E+00
```

So-called "sum" files direct the summation of the various distortions and their magnitudes (i.e. the scaling factor mentioned above). The Shell 1 files look like this:

`p1_xrcf_sum_off.files` :

```
p1_xrcf_sum_off.SPL 422 288
/proj/axaf/Syseng/models/hrma-xrcf/xrcf_2wks/p1_xrcf_sum.SPL 1.000 0.000
p1_off.DFR 0.0872 0.000
```

`h1_xrcf_sum_off.files` :

```
h1_xrcf_sum_off.SPL 422 288
/proj/axaf/Syseng/models/hrma-xrcf/xrcf_2wks/h1_xrcf_sum.SPL 1.000 0.000
h1_off.DFR 0.0872 0.000
```

The "sum" files have names of the form ***xn*** `_xrcf_sum_off.SPL` where $x = \{$p, h$\}$ and $n = \{1, 3, 4, 6\}$.

All of these files are located in

`/proj/axaf/Syseng/models/hrma-xrcf/xrcf_2wks_offset/`

on the CfA Central Engineering and High Energy Astrophysics LANs.

Chapter 27

Rigid-Body Misalignment Parameters

Terrance J. Gaetz

In this chapter the incorporation of the rigid-body misalignment parameters into the raytrace model is discussed. In §27.1 the extraction of mirror rigid body parameters from the HATS optical data is discussed; in particular we are concerned with the focal plane image lateral parfocalization ("focal plane decenters") and the residual tilts. Other rigid body parameters are axial parfocalization (discussed in Chapter 26) and relative P to H decenters (*tilt-compensated decenters* (discussed in Chapter 30). The axial parfocalization was accommodated in the models by placing the mirrors at the as-measured positions and making a slight adjustment to the mirror maps. The remaining rigid body parameters were treated by adjusting the lateral position and tilts of the individual mirror elements; the construction of this rigid body database is described in §27.2. The database is based upon HATS measurements of the lateral parfocalization and residual tilt, and the X-ray measurements of the tilt-compensated decenters (Chapter 30).

27.1 HATS Data

During HRMA buildup, the alignment state of the HRMA optics was assessed using the Eastman Kodak Company HATS system (HRMA Alignment Test System). In the HATS tower configuration the HRMA optics were supported vertically in an assembly and testing tower (H optics upper, P optics lower) suspended above an optical flat (the Autocollimating Flat, or ACF); the configuration is illustrated schematically in Figure 27.1. An aperture mask with 24 evenly spaced apertures for each test zone (*i.e.*, mirror shell) was placed above the ACF. The aperture mask also carried a Tilt Reference Indicator (TRI, consisting of a pair of autocollimators, one looking down at the ACF, and the other looking up at a flat mounted in the CAP) which monitored the parallelism between the CAP and the ACF. HATS includes a Centroid Detector Assembly (CDA) mounted on rails at the top of the tower; this was used to assess the alignment of the optics at the 20 m (folded path) P focus or at the 10 m system focus. The alignment of the HRMA was probed using a double-pass system in which a directable laser beam from the CDA source (S) was reflected off an H, a P, the ACF, the P and H again, finally reaching the CDA detector (D); the centroids of the returned beam and an internal reference beam were measured using a quad-cell detector.

For a given mirror pair, the HATS measures the double-pass centroids for a set of 24 apertures equally spaced in azimuth around the optic. The alignment test is basically a double-pass Hartmann test of the X-ray optics. The test laser acts as a pencil beam probing a single azimuth (about the optical axis). The alignment state (and some low-order deformations of the optics) can be assessed

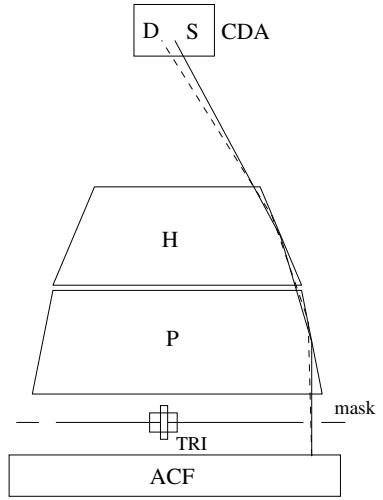

Figure 27.1: Schematic diagram of HATS double-pass configurations. A beam originates at source S, reflects from the H, the P, the Autocollimating Flat (ACF), the P and H again, and finally reaches detector D. The variation in the return beam centroid location with azimuth of the test beam provides information on mirror alignment.

by analyzing the variation in centroid location of the return beam as a function of the pointing azimuth. For example, if the CDA source/detector plane is in front of the HRMA focus (between the focus and the HRMA), the centroids will move along a defocus circle in phase with the beam azimuth (in-phase "1θ" variation). A relative tilt between the P and H, or a relative decenter between the optics produces coma which manifests as a "2θ" variation: the centroid position angle varies twice as quickly as the test beam azimuth varies. A lateral parfocalization error shows up as a relative displacement of the whole set of centroid positions; tilt and relative decenter can both change the lateral parfocalization.

These misalignment coefficients are clearly amenable to a Fourier analysis in which the appropriate low-order Fourier coefficients are interpreted in terms of misalignments. For a double-pass configuration containing both a P optic and its corresponding H optic, the coefficients relevant to rigid-body alignment are given in Table 27.1, in which Q_n is the Fourier coefficient of order n, and Re and Im indicate the real and imaginary components, respectively. The relations between the Fourier decomposition and HRMA alignment are described more fully in Lewis (1993).

Table 27.1: HATS Fourier Coefficients (ATP augmented data set)

Fourier Coefficient	Rigid Body Term
$Re(Q_0)$ and $Im(Q_0)$	lateral focus error
$Re(Q_1)$	axial focus error
$Re(Q_2)$ and $Im(Q_2)$	residual coma

Basically, Q_0 gives the displacement of the image in the focal plane, $Re(Q_1)$ gives the radius of the cone of rays (defocus circle, positive in front of the focal point, negative behind the focal point), and Q_2 provides the size and orientation of the 2θ coma circle. Because this is a double-pass experiment, the actual parfocalization and coma errors for a point source at infinity are a factor of two smaller than the Q_n coefficients. Although the interpretation of the HATS Q_0 and Q_2 Fourier coefficients is straightforward, the interpretation of Q_1 is complicated by a number of axially symmetric biases including deformation of the CAP under load, curvature of the ACF, "dimples" induced by the mirror supports under 1g, and refraction by radial temperature gradients within the HRMA.

27.1.1 November 1996 HATS ATP (Augmented) Data Set

The final HATS test data (Acceptance Test Procedure, or ATP) were obtained on November 9 and 10, 1996. We augment the original 9 ATP tests with an additional 15 tests performed at that time to obtain an augmented ATP data set as indicated in Table 27.2. We evaluated the means and standard deviations of the Fourier coefficients for this augmented test sequence; the Fourier coefficients evaluated and averaged using the SAO-written `PV-WAVE` package `hats_plot`. The means and errors used for the following analysis were taken from the output file `/ceaxaf1/ekc/HATS_data/hrma_atp/AZMIS.avg`; the errors quoted are the standard deviations of the set of Fourier coefficients obtained for the 24 individual alignment tests in the augmented HATS ATP data set. The Fourier coefficients relevant to rigid-body mirror element alignment are given in Table 27.3.

Table 27.2: HATS ATP (Augmented) Data

11/09/1996	21:49:36.000†	11/10/1996	07:35:05.000
11/09/1996	22:39:14.000†	11/10/1996	08:19:18.000
11/09/1996	23:44:28.000	11/10/1996	09:03:20.000†
11/10/1996	00:28:20.000†	11/10/1996	09:48:05.000†
11/10/1996	01:12:16.000†	11/10/1996	10:32:04.000†
11/10/1996	01:56:05.000†	11/10/1996	11:16:26.000†
11/10/1996	03:10:53.000	11/10/1996	12:00:32.000†
11/10/1996	03:54:49.000	11/10/1996	12:44:35.000†
11/10/1996	04:38:47.000	11/10/1996	13:28:30.000†
11/10/1996	05:22:45.000	11/10/1996	14:12:29.000†
11/10/1996	06:06:47.000	11/10/1996	14:56:24.000†
11/10/1996	06:50:54.000	11/10/1996	15:40:26.000†

†not in original HATS ATP data set

As noted above, the interpretation of Q_1 is complicated by a number of axially symmetric biases; see Chapter 26 for further discussion of axial parfocalization. The raytrace model for the axial parfocalization was updated by correcting the axial placements of the mirrors and adjusting the cone angles in the mirror maps; consequently the axial parfocalization is not discussed further here (see Chapter 26).

The HATS test procedure yields only relative values for the parfocalization so $\langle Q_0 \rangle = [-5.48, 9.42]$, the R^2-weighted mean, was subtracted from Q_0; R is an effective radius for the mirror pair and was taken from Waldman (1995). The resulting Q_n values are given in Table 27.4.

Relative rigid body misalignments of the P to H optics in either decenter or tilt can cause a

Table 27.3: HATS Fourier Coefficients

		units	MP1	MP3	MP4	MP6
1	$Re(Q_0)$	(μm)	−11.49±9.42	−0.18±9.40	−1.31±9.66	−3.78±9.24
2	$Im(Q_0)$	(μm)	7.62±8.89	13.43±8.77	9.89±9.00	4.89±9.08
3	$Re(Q_1)$	(μm)	−24.65±1.09	−11.98±2.42	−30.67±1.35	6.81±1.94
4	$Re(Q_2)$	(μm)	−8.66±0.35	6.26±0.58	5.76±0.27	29.68±0.62
5	$Im(Q_2)$	(μm)	2.60±0.30	−1.93±0.59	−0.76±0.38	−3.07±0.44

Table 27.4: HATS Fourier Coefficients: r^2-weighted Q_0 removed

		units	MP1	MP3	MP4	MP6
1	$Re(Q_0)$	(μm)	−5.97±9.42	5.30±9.40	4.17±9.66	1.69±9.24
2	$Im(Q_0)$	(μm)	−1.71±8.89	4.10±8.77	0.57±9.00	−4.43±9.08
3	$Re(Q_1)$	(μm)	−24.65±1.09	−11.98±2.42	−30.67±1.35	6.81±1.94
4	$Re(Q_2)$	(μm)	−8.66±0.35	6.26±0.58	5.76±0.27	29.68±0.62
5	$Im(Q_2)$	(μm)	2.60±0.30	−1.93±0.59	−0.76±0.38	−3.07±0.44

comatic image distortion in the focal plane. The coma circle diameter in the focal plane is related to a pure H relative decenter or a pure H relative tilt angle as:

	1″ H tilt	1 mm H decenter
Coma circle radius (″)	1	10
Coma circle radius (μm)	48.5	488

The breakdown between mirror element tilt and decenter is not uniquely determined by the coma as measured on-axis. Because both tilt and decenter introduce coma, the net coma can vanish for some combination movements; in particular, for combinations of H tilt + H decenter which are equivalent to a pure rotation about the H far focus, the comas introduced by the decenter and the tilt cancel each other leaving the net coma unchanged. We therefore factor the decenter and tilt into two components:

- coma; appears even on-axis
- tilt-compensated decenter; no on-axis coma, but an additional off-axis aberration appears (see Chapter 30).

We interpret the coma as a pure body-centered tilt of the H relative to its companion P optic. In the rest of this section, *tilt* refers to the corresponding component of on-axis coma expressed as a tilt of the H optic unless otherwise noted.

From the Q_0 and Q_2 coefficients it is straightforward to obtain the residual coma and lateral parfocalization:

Table 27.5:

$\Delta X_{DPSAOsac}$	=	$+\Delta X_{SAOsac}$	=	$+Re(Q_0)/2$
$\Delta Y_{DPSAOsac}$	=	$-\Delta Y_{SAOsac}$	=	$+Im(Q_0)/2$
$azmis_{DPSAOsac}$	=	$-azmis_{SAOsac}$	=	$-Re(Q_2)/(2F_H)$
$elmis_{DPSAOsac}$	=	$+elmis_{SAOsac}$	=	$+Im(Q_2)/(2F_H)$

where $F_H = 9607$ mm is an effective focal length for HATS measurements (Waldman, 1995); the extra factors of 2 arise because this is a double-pass measurement. The numerical values for the lateral parfocalization and residual tilts are given in Table 27.6.

Table 27.6: Summary: HRMA Lateral Parfocalization and On-Axis Coma (SAOsac coordinates)

		units	MP1	MP3	MP4	MP6
Lateral Parfocalization	δX	(μm)	−3.00	+2.65	+2.08	+0.84
Lateral Parfocalization	δY	(μm)	+0.86	−2.05	−0.28	−2.22
On-Axis Coma	*elmis*	($''$)	+0.02926	−0.02069	−0.00423	−0.03292
On-Axis Coma	*azmis*	($''$)	−0.09019	+0.06720	+0.06188	+0.31865

27.1.2 Conversion of HATS data to Rigid Body Coefficients

On-Axis Coma: Tilt and Decenter

The coma measures a combination of relative P to H tilt and P to H decenter. As noted above, we decompose the mirror decenters and tilts into two components: pure body-centered H tilt, and a (coma-free) tilt-compensated H decenter. We assign all of the measured on-axis coma to a pure body-centered tilt; the tilt-compensated decenter is incorporated into the model in §27.2. When a body-centered tilt is applied to the H optic, the lateral focus position also shifts and this affects the lateral parfocalization. We restore lateral parfocalization to the measured values by applying a decenter to the mirror pair as a whole. In terms of the HATS Fourier coefficients, the corrected mirror pair body-centered decenter is given by in Table 27.7 where

$$Q_0' = Q_0 - Q_2^\star$$

and * indicates complex conjugate.

From these adjusted Q_0' and Q_2 values we derive the body-centered HATS-based decenter values (δX, δY) and tilts (`elmis`, `azmis`), in the `SAOsac` double-pass raytrace coordinates (see Tables 27.7 and 27.8). These can be converted from double-pass `SAOsac` to standard `SAOsac` coordinates using the relations in Chapter B; the results are given in Table 27.9.

27.2 Construction of the Mirror Rigid-Body Database

In this section we summarize the current rigid-body mirror database used as the basis for our raytrace models. We start with an ideal "OSAC"-style mirror prescription; the OSAC mirror conic

Table 27.7: Conversion to Rigid Body Misalignment

$\Delta X_{\mathrm{MP},DPSAOsac}$	=	$+\Delta X_{\mathrm{MP},SAOsac}$	=	$+Re(Q_0')/2$
$\Delta Y_{\mathrm{MP},DPSAOsac}$	=	$-\Delta Y_{\mathrm{MP},SAOsac}$	=	$+Im(Q_0')/2$
$azmis_{\mathrm{H},DPSAOsac}$	=	$-azmis_{\mathrm{H},SAOsac}$	=	$-Re(Q_2)/(2F_H)$
$elmis_{\mathrm{H},DPSAOsac}$	=	$+elmis_{\mathrm{H},SAOsac}$	=	$+Im(Q_2)/(2F_H)$

Table 27.8: Body-center rigid body coefficients (*double-pass* coordinate system)

Coefficient	units	MP1	MP3	MP4	MP6
$\delta X_{dp,P}$	(μm)	1.347	−0.482	−0.796	−13.995
$\delta Y_{dp,P}$	(μm)	0.446	1.087	−0.097	−3.748
$\mathrm{azmis}_{dp,P}$	($''$)	0.0	0.0	0.0	0.0
$\mathrm{elmis}_{dp,P}$	($''$)	0.0	0.0	0.0	0.0
$\delta X_{dp,H}$	(μm)	1.347	−0.482	−0.796	−13.995
$\delta Y_{dp,H}$	(μm)	0.446	1.087	−0.097	−3.748
$\mathrm{azmis}_{dp,H}$	($''$)	0.09019	−0.067200	−0.061875	−0.318647
$\mathrm{elmis}_{dp,H}$	($''$)	0.02926	−0.020686	−0.004233	−0.032918

is described by

$$r^2 = \rho_0^2 + 2Kz - Pz^2 \tag{27.1}$$

where r is the radius corresponding to location z along the axis; z is measured from the body center of the optic so ρ_0 is just the radius corresponding to the body center. The adopted mirror parameters, incorporating the effects of the end-cut, are given in Table 27.10 (Zhao, 1996).

To this we apply the decenters and tilts implied by the HATS optical measurements (Table 27.9), and the as-measured optic axial positions (see Chapter 26) to obtain Table 27.11. Recall that we are working in our standard `SAOsac` raytrace coordinate system so Z_0 is along the optical axis (positive *from* HRMA *towards* the detectors).

To this basic configuration we apply the optic-to-optic decenters as derived from the off-axis X-ray images (Chapter 30). The mirror (body-center) decenters must also be consistent with the optically determined (focal plane) decenters and coma. This was achieved as follows: A pure rigid body rotation of an H optic about its far focus preserves the coma in the focal plane. For ideal optics the distance from H body center to H far focus is 19668.11899 mm. Raytraces studies show that a tilt-compensated H decenter also shifts the focal plane centroid of the double-pass image by about 1.023902 times the magnitude of the relative H decenter; we can correct for this can be corrected by applying a compensating decenter of the mirror pair as a whole by an amount equal to $0.5 \times 1.023902 \times H_{\mathrm{decenter}}$. (The extra factor of 0.5 results because of the double-pass nature of the HATS alignment test.) That is, if the H to P decenter component of a tilt-compensated decenter of the H is $[\delta x_H, \delta y_H]$, the compensating tilt (in radians) is:

$$\delta elmis = -\frac{\delta y_H}{19668.11899}, \tag{27.2}$$

$$\delta azmis = -\frac{\delta x_H}{19668.11899} \tag{27.3}$$

and the compensating mirror *pair* decenter is $-0.5 \times 1.023902 \times [\delta x_H, \delta y_H]$.

In summary, the procedure for incorporating the P to H decenter is:

Table 27.9: Body-center rigid body coefficients (standard SAOsac coordinate system)

Coefficient	units	MP1	MP3	MP4	MP6
δX_P	(μm)	1.347	−0.482	−0.796	−13.995
δY_P	(μm)	−0.446	−1.087	0.097	3.748
azmis$_P$	($''$)	0.0	0.0	0.0	0.0
elmis$_P$	($''$)	0.0	0.0	0.0	0.0
δX_H	(μm)	1.347	−0.482	−0.796	−13.995
δY_H	(μm)	−0.446	−1.087	0.097	3.748
azmis$_H$	($''$)	−0.09019	0.067200	0.061875	0.318647
elmis$_H$	($''$)	0.02926	−0.020686	−0.004233	−0.032918

Table 27.10: SAOsac mirror parameters, baseline optic prescription

Mirror	P (dimensionless)	K (mm)	ρ_0 (mm)
p1	0.0	−8.9333113530131421	606.86080963697918
p3	0.0	−5.7939624154424676	488.46244215611011
p4	0.0	−4.5165799273846270	431.26225933154404
p6	0.0	−2.4957050467401789	320.56977725634789
h1	−1.7797716637950735E-03	−26.0506034413416841	579.89015840093919
h3	−1.1532395834759916E-03	−16.875942397594130	466.64379784205380
h4	−8.9864417477996457E-04	−13.150318066441841	411.91935912458604
h6	−4.9625995845653374E-04	−7.2620248152618760	306.09851668776219

1. Start with the baseline ideal optics prescription (Table 27.10).

2. Apply a mirror decenter/tilt combination which reproduces the optical measurements of the focal plane decenter and coma, and as-measured optic spacing (Table 27.11.)

3. Apply relative decenters to the H optics (Table 30.3).

4. Apply a compensating tilt to each H optic such that the combined decenter (Table 30.3) plus tilt is equivalent to a pure rotation of the H body center about the H far focus.

5. Decenter to the mirror pair as a whole by −1.023902 times half of the H decenter from Table 30.3 to restore lateral parfocalization.

The resulting rigid-body parameters are given in Table 27.12. These rigid-body data were incorporated into an updated raytrace mirror database; the current mirror database is `/proj/axaf/simul/databases/mirror/EKCHDOS06.rdb`. As noted in Chapter 26, the axial parfocalization correction was incorporated into the mirror maps by adjusting the mirror cone angles. The current HRMA model (`trace-shell4` configuration file, `xrcf_SAO1G+HDOS_HDOS-scat-970220_03`), incorporates the adjusted mirror maps.

The rigid-body configuration in Table 27.12 was converted into the SAOsac (double-pass) coordinate system using the transformations in Table B.2 and raytraced in a double-pass configuration; the optics were assumed to be otherwise ideal. The Fourier coefficients relevant to focal plane

Table 27.11: SAOsac mirror parameters, decenters and tilts from ATP data; as-measured axial mirror positions

Mirror	X_0 (mm)	Y_0 (mm)	Z_0 (mm)	azmis ($''$)	elmis ($''$)
P1	0.001347	−0.000446	−426.5761	0.0	0.0
P3	−0.000482	−0.001087	−436.7098	0.0	0.0
P4	−0.000796	0.000097	−440.3572	0.0	0.0
P6	−0.013995	0.003748	−445.0821	0.0	0.0
H1	0.001347	−0.000446	481.0146	−0.09019	0.02926
H3	−0.000482	−0.001087	480.9282	0.067200	−0.020686
H4	−0.000796	0.000097	480.8279	0.061875	−0.004233
H6	−0.013995	0.003748	479.2152	0.318647	−0.032918

Table 27.12: Rigid-Body Mirror Parameters (EKCHDOS06)

Mirror	X_0 (mm)	Y_0 (mm)	Z_0 (mm)	azmis ($''$)	elmis ($''$)
P1	0.1239	0.2151	−426.5761	0.0	0.0
P3	0.08675	0.2437	−436.7098	0.0	0.0
P4	0.08634	0.2168	−440.3572	0.0	0.0
P6	0.08625	0.2245	−445.0821	0.0	0.0
H1	−0.1154	−0.2060	481.0146	2.4194219	4.4454479
H3	−0.08365	−0.2345	480.9282	1.8542174	4.9943249
H4	−0.08386	−0.2065	480.8279	1.8468078	4.4350269
H6	−0.1096	−0.2067	479.2152	2.3720568	4.4891913

decenter and residual coma were evaluated and compared to the HATS-derived values given in Table 27.4; the resulting values are listed in Table 27.13. The values agree to better than 0.4 μm; this is satisfactory agreement, well within the measurement uncertainties for Q_0 and comparable to the measurement uncertainties for Q_2 (Table 27.3).

27.3 Future Directions

This is a preliminary assessment of the mirror rigid-body orientation parameters. As our data reductions and analyses are refined, the improved estimates of axial parfocalization (Chapter 26) and tilt-compensated decenters (Chapter 30) will be incorporated into the model.

The analysis of the optical alignment data can also be improved: various double-pass raytrace analyses were based on optics which were ideal other than for the misalignments. Because raytraces indicate that Fourier decomposition is insensitive to details of the mirror map (other than the axial parfocalization, as noted above), this is not expected to change the estimates appreciably.

Preliminary raytrace investigations indicate that the tilt-compensated decenters do not significantly bias the HATS-based measurements of the coma or parfocalization. It is possible that the tilt-compensated decenters affect some of the higher-order HATS residuals, though.

Finally, an assessment of the lateral parfocalization at XRCF needs to be made. Measurement

Table 27.13: Fourier Coefficients: HATS *vs.* raytrace

mirror	units	data	MP1	MP3	MP4	MP6
$Re(Q_0)$	(μm)	ATP Data	−5.9709	5.2962	4.1713	1.6929
$Re(Q_0)$	(μm)	raytrace	−5.6195	5.2857	4.1754	1.6076
$Re(Q_0)$	(μm)	residual	−0.3514	0.0105	−0.0041	0.0853
$Im(Q_0)$	(μm)	ATP Data	−1.7083	4.1013	0.5668	−4.4305
$Im(Q_0)$	(μm)	raytrace	−1.7612	4.1548	0.2073	−4.4666
$Im(Q_0)$	(μm)	residual	0.0529	−0.0535	0.3595	0.0361
$Re(Q_2)$	(μm)	ATP Data	−8.6649	6.2598	5.7638	29.6826
$Re(Q_2)$	(μm)	raytrace	−8.3901	6.2643	5.7719	29.6405
$Re(Q_2)$	(μm)	residual	−2.0748	−0.0045	−0.0081	0.0421
$Im(Q_2)$	(μm)	ATP Data	2.6014	−1.9269	−0.7608	−3.0664
$Im(Q_2)$	(μm)	raytrace	2.7256	−1.9222	−0.3803	−3.0516
$Im(Q_2)$	(μm)	residual	−0.1242	−0.0047	−0.3805	−0.0148

the lateral parfocalization in X-rays is complicated by several factors: tilts induced by 1g distortion of HRMA as supported in the horizontal XRCF configuration, maintaining stability and accuracy of absolute centroid positions over long timescales, and the large pinholes (10 μm or 20 μm). Although the X-ray measurements may not improve on the HATS values, the X-ray centroids will provide additional constraints on the 1g model. (In the optical HATS measurements the HRMA was supported vertically, so no appreciable 1g-induced tilts are introduced.)

Chapter 28

HRMA Tilts at XRCF

William Podgorski

In this section we discuss HRMA rigid body misalignments (relative P-H tilt and decenter). Data is presented from the optical alignments at Kodak, from the XRCF calibration and from various analyses.

Relative rigid body misalignments of the P to H optics in either decenter or tilt cause a comatic image distortion in the focal plane. This distortion is a "coma circle" in which the position of the rays in the coma circle moves around the circle twice as the input ray bundle (to the shell) varies once around the shell input aperture. Figure 28.1 illustrates this. The coma circle diameter in the focal plane is related to the P-H decenter and tilt angle as follows:

	1″ P-H tilt	1 mm P-H decenter
Coma circle radius (″)	1	10
Coma circle radius (μm)	48.5	488

28.1 Coordinate Systems and tilt angles

Since tilt and decenter both produce coma in the image plane we will interpret this coma as a tilt of the H optic relative to the P optic. Three different coordinate systems and sets of tilt angles have been used (see also Chapter B and Figure B.1):

- HRMA Coordinates (θ_Y, θ_Z)
- `SAOsac` Raytrace Coordinates (*azmis*, *elmis*)
- XRCF Coordinates ($tilt_Y$, $tilt_Z$)

The tilt angles are interpreted as a rotation of the H optic about a given coordinate axis, relative to the perfectly aligned P optic. The rotation axes are as follows (again see Figure B.1);

Coordinates	H Angle	Rotation axis
HRMA	θ_Y	+Y-HRMA
	θ_Z	+Z-HRMA
SAOSAC	*azmis*	+Y-OSAC
	elmis	−X-OSAC
XRCF	$tilt_Y$	+Y-XRCF
	$tilt_Z$	+Z-XRCF

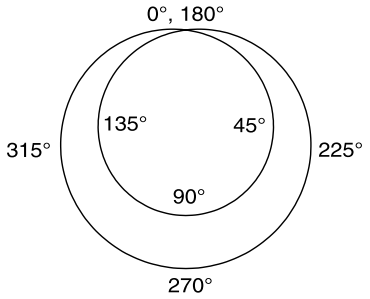

Figure 28.1: Schematic of coma circle (2θ) image distortion. The limaçon is the pattern of the photons at the focal surface. The angles refer to the azimuth of the optic at which the photons were reflected.

Tilt angle relationships:

$$\begin{aligned} azmis &= -\theta_Z = +tilt_Z \\ elmis &= -\theta_Y = +tilt_Y \end{aligned}$$

Table 28.1 provides a summary of relative tilt angles (H with respect to P) for various conditions. The four HRMA shells are given with the two tilt angles per shell. These angles are shown in terms of the XRCF angles, $tilt_Y$ and $tilt_Z$. The tilt angles as measured at Kodak by the HATS (in the final ATP measurements) are shown in line 1. In lines 2 and 3 the XRCF 1G *corrections* to the tilt angles are given for both SAO's FEA model and EKC's FEA model. Note that the corrections are about XRCF Y only, Y being the horizontal axis at XRCF. Lines 4 through 9 present various raytrace predictions of the tilt angles, based on various HRMA models and using a simulated quad shutter tilt calculation. The cases are defined as follows:

EKCHDOS04 Based on Kodak test data of 9/96 with *no* decenter, full XRCF mirror maps (SAO)

EKCHDOS04_low Based on Kodak test data of 9/96 with *no* decenter, mirror map includes only 3 term Legendre fit of surface (no 1G)

EKCHDOS04_low_off Based on Kodak test data of 9/96 with *no* decenter, mirror map includes only 3 term Legendre fit of surface (no 1G), HRMA pointed 1′ off-axis in azimuth

EKCHDOS05 Based on Kodak ATP test data of 11/96 with XRCF measured decenter, full XRCF mirror maps (SAO), axial spacing as in `EKCHDOS04`

EKCHDOS05_low Based on Kodak ATP test data of 11/96 with XRCF measured decenter, mirror map includes only 3 term Legendre fit of surface (no 1G)

EKCHDOS06 Based on Kodak ATP test data of 11/96 with XRCF measured decenter, full XRCF mirror maps (SAO), axial spacing derived from XRCF measurements

EKCHDOS06_off Based on Kodak ATP test data of 11/96 with XRCF measured decenter, full XRCF mirror maps (SAO), axial spacing derived from XRCF measurements, HRMA pointed 1′ off-axis in azimuth

Table 28.1: HRMA Tilt Angles

	Model	Shell 1		Shell 3		Shell 4		Shell 6	
		Y [″]	Z [″]	Y [″]	Z [″]	Y [″]	Z [″]	Y [″]	Z [″]
1	Kodak ATP HATS	0.03	−0.09	−0.02	0.07	0.00	0.06	−0.03	0.32
2	XRCF 1G Corr(SAO)	−0.24	0.00	−0.08	0.00	−0.12	0.00	−0.12	0.00
3	XRCF 1G Corr(EKC)	−0.23	0.00	−0.18	0.00	−0.21	0.00	−0.33	0.00
4	EKCHDOS04	−0.19	−0.15	−0.08	0.03	−0.13	0.07	−0.29	0.27
5	EKCHDOS04_low	0.04	−0.11	−0.03	0.06	0.00	0.05	−0.09	0.27
6	EKCHDOS04_low_off	0.04	0.04	−0.03	0.23	0.00	0.23	−0.09	0.47
7	EKCHDOS05	−0.01	−0.03	0.13	0.11	0.05	0.15	−0.05	0.38
8	EKCHDOS05_low	0.20	0.00	0.18	0.14	0.17	0.13	0.15	0.39
9	EKCHDOS06	−0.01	−0.03	0.13	0.11	0.04	0.15	−0.05	0.38
10	EKCHDOS06_off	−0.01	0.12	0.12	0.29	0.05	0.34	−0.05	0.58
11	Measured 1/5-6/97†	−0.15	−0.14	−0.05	−0.06	−0.04	−0.08	−0.44	0.18
12	Measured 1/5-6/97	−0.17	−0.14	−0.07	−0.05	−0.05	−0.07		
13	Measured 2/7-8/97	−0.14	−0.02	−0.05	0.12	−0.04	0.04	−0.43	0.36
14	Kodak ATP+SAO XRCF	−0.21	−0.09	−0.10	0.07	−0.12	0.06	−0.15	0.32
15	Kodak ATP+EKC XRCF	−0.20	−0.09	−0.20	0.07	−0.12	0.06	−0.36	0.32

†XRCF tilts measured 1′ off-axis in azimuth

Lines 11, 12 and 13 give the measured XRCF tilt angles for 3 different cases, using the quad shutter calculations. Lines 11 and 12 present data from tests on 1/5/97 and 1/6/97, when the HRMA was 1′ off-axis in azimuth. The data in line 11 is the initial baseline tilt data from these tests. The data in line 12 is repeatability data in which the *top* quadrant was re-measured and used in conjunction with the initial data from the other three quadrants. The data in lines 11 and 12 should be the same. The data in line 13 is from the last series of focus/tilt measurements in Phase 1 (at Al Kα), taken on 2/7/97 and 2/8/97. An important difference between this data and the data taken in early January is that the HRMA was on-axis for the February data, but was +1′ off-axis in azimuth when the January data was taken.

Lines 14 and 15 give the arithmetic sums of the Kodak ATP tilt angles plus the XRCF 1G tilts for the SAO model (line 14) and the EKC model (line 15).

28.2 Tilt Measurements

Examination of the measured tilt data in Table 28.1 (lines 11 - 13) shows excellent agreement for all of the $tilt_Y$ measurements, with a span of only 0.03″ over all shells for the three sets of data. There are larger differences between the January and February data in $tilt_Z$, however. The February data show, for all four shells, numerically larger values of $tilt_Z$, the differences ranging from about 0.10″ to 0.20″. This discrepancy is due to the difference in HRMA alignment, specifically the 1′ azimuth off-axis angle. Simulations show the same trend in tilt angles as the HRMA azimuth is varied. Comparison of raytrace cases `EKCHDOS04_low` *vs.* `EKCHDOS04_low_off` and `EKCHDOS06` *vs.* `EKCHDOS06_off` show that the $tilt_Z$ angles do increase as the HRMA azimuth is increased, by about the same amounts as seen in the measurements. In Table 28.2 the 1/5-6/97 data has been adjusted for the off-axis azimuth effect, line B, and compared with the 2/7-8/97 data, line C. The agreement is excellent, and we will therefore use the tilt values measured in 2/97 as our reference measurement, with the HRMA at an on-axis condition.

Table 28.2: Summary of HRMA Tilt Angles

	Model	Shell 1		Shell 3		Shell 4		Shell 6	
		Y [″]	Z [″]	Y [″]	Z [″]	Y [″]	Z [″]	Y [″]	Z [″]
A	Offaxis Az delta	0.00	0.15	-0.01	0.18	0.01	0.19	0.00	0.20
B	1/5-6/97 + Az delta	-0.15	0.01	-0.05	0.12	-0.04	0.11	-0.44	0.38
C	Measured 2/7-8/97	-0.14	-0.02	-0.05	0.12	-0.04	0.04	-0.43	0.36
D	EKCHDOS06	-0.01	-0.03	0.13	0.11	0.04	0.15	-0.05	0.38
E	(Data - Model)	-0.13	0.01	-0.18	0.01	-0.08	-0.11	-0.38	-0.02

28.3 Comparison with models

The raytrace simulation denoted as `EKCHDOS06` represents our best model of the HRMA at the XRCF to date. Calculations of tilt angles were made from it using the `wedge` program to simulate the quadrant shutters, in conjunction with the HXDS shutter focus algorithm. A comparison of the modeled tilts with measured tilts may be seen by comparison of lines C and D in Table 28.2. The differences in modeled vs. measured tilts are given in line E of Table 28.2. The differences in $tilt_Z$ are smaller than in $tilt_Y$. These differences may indicate a lack of accuracy in the XRCF 1G modeling of rigid body tilts, since only $tilt_Y$ is affected by gravity in XRCF testing, and it has the larger differences.

28.4 Future work

We plan to investigate the 1G models of the HRMA with respect to tilt to try to determine if there are modeling issues which may affect the tilts. If not, then we will "tune" the 1G models to the XRCF measured data, so that the modeled tilts are close to the measured tilts. This procedure is based on the assumption that the tilt data from the Kodak HATS tests is correct, as well as the XRCF data, and that the most likely source of error is the 1G model. This conclusion is supported by the agreement seen in the $tilt_Z$ values, which are not affected by gravity. One important result which follows from this assumption is that shell 6 will have significantly better performance on-orbit that at XRCF, since a large fraction of the $tilt_Y$ seen at XRCF is gravity induced. This assumption will be checked by examination of on-orbit image properties at high energies.

28.5 Quad shutter tilt data from XRCF tests

28.5.1 Shell 1

Runid	Date	TRW ID	Shell / Quad	Center [μm] Y	Z
107656	01/06/97	D-IXF-P2-67.016	1T	-307159.66	10676.87
107657	01/06/97	D-IXF-P2-67.017	1N	-307147.69	10683.71
107659	01/06/97	D-IXF-P2-67.018	1B	-307152.50	10665.15
107660	01/06/97	D-IXF-P2-67.019	1S	-307146.31	10677.72

Y Tilt = -0.153014
Z Tilt = -0.143143

107663	01/06/97	D-IXF-P2-67.020	1T	-307159.59	10674.64
107657	01/06/97	D-IXF-P2-67.017	1N	-307147.69	10683.71
107659	01/06/97	D-IXF-P2-67.018	1B	-307152.50	10665.15
107660	01/06/97	D-IXF-P2-67.019	1S	-307146.31	10677.72

Y Tilt = -0.170591
Z Tilt = -0.143143

111470	02/07/97	E-IXF-P2-67.016	1T	-307110.59	10624.46
111471	02/07/97	E-IXF-P2-67.017	1N	-307102.25	10630.90
111474	02/07/97	E-IXF-P2-67.018	1B	-307109.31	10622.07
111475	02/07/97	E-IXF-P2-67.019	1S	-307115.00	10633.48

Y Tilt = -0.140715
Z Tilt = -0.0209302

28.5.2 Shell 3

Runid	Date	TRW ID	Shell / Quad	Center [μm] Y	Z
107637	01/05/97	D-IXF-P2-67.001	3T	-307167.59	10676.34
107638	01/05/97	D-IXF-P2-67.002	3N	-307156.75	10688.66
107639	01/05/97	D-IXF-P2-67.003	3B	-307150.00	10680.82
107640	01/05/97	D-IXF-P2-67.004	3S	-307153.22	10674.62

Y Tilt = -0.0482356
Z Tilt = -0.0603847

107641	01/05/97	D-IXF-P2-67.005	3T	-307166.53	10674.11
107638	01/05/97	D-IXF-P2-67.002	3N	-307156.75	10688.66
107639	01/05/97	D-IXF-P2-67.003	3B	-307150.00	10680.82
107640	01/05/97	D-IXF-P2-67.004	3S	-307153.22	10674.62

Y Tilt = -0.0658127
Z Tilt = -0.0517239

111451	02/07/97	E-IXF-P2-67.001	3T	-307116.59	10613.04
111452	02/07/97	E-IXF-P2-67.002	3N	-307110.19	10634.03
111453	02/07/97	E-IXF-P2-67.003	3B	-307112.28	10644.09
111454+7†	02/07/97	E-IXF-P2-67.004	3S	-307134.19	10629.06

†This run included an extra 1D scan

Y Tilt = -0.0469876
Z Tilt = 0.122213

28.5.3 Shell 4

Runid	Date	TRW ID	Shell / Quad	Center [μm] Y	Z
107642	01/05/97	D-IXF-P2-67.006	4T	-307163.59	10677.85
107644	01/05/97	D-IXF-P2-67.007	4N	-307153.69	10685.39
107645	01/05/97	D-IXF-P2-67.008	4B	-307152.19	10679.59
107646	01/05/97	D-IXF-P2-67.009	4S	-307151.97	10677.10

Y Tilt = -0.0397929
Z Tilt = -0.0798714

107647	01/05/97	D-IXF-P2-67.010	4T	-307162.38	10676.75
107644	01/05/97	D-IXF-P2-67.007	4N	-307153.69	10685.39
107645	01/05/97	D-IXF-P2-67.008	4B	-307152.19	10679.59
107646	01/05/97	D-IXF-P2-67.009	4S	-307151.97	10677.10

Y Tilt = -0.0484686
Z Tilt = -0.0702483

111458	02/07/97	E-IXF-P2-67.006	4T	-307114.69	10629.45
111459	02/07/97	E-IXF-P2-67.007	4N	-307119.09	10630.60
111460	02/07/97	E-IXF-P2-67.008	4B	-307119.66	10630.07
111461	02/07/97	E-IXF-P2-67.009	4S	-307119.84	10634.37

Y Tilt = -0.0429504
Z Tilt = 0.0358459

28.5.4 Shell 6

Runid	Date	TRW ID	Shell / Quad	Center [μm] Y	Z
107655	01/05/97	D-IXF-P2-67.015	6T	-307157.16	10641.41
107652	01/05/97	D-IXF-P2-67.012	6N	-307162.00	10681.58
107653	01/06/97	D-IXF-P2-67.013	6B	-307143.06	10654.70
107654	01/06/97	D-IXF-P2-67.014	6S	-307161.69	10669.99

Y Tilt = -0.43721
Z Tilt = 0.184763

111462	02/07/97	E-IXF-P2-67.011	6T	-307109.50	10600.10
111463	02/07/97	E-IXF-P2-67.012	6N	-307136.59	10626.19
111466	02/07/97	E-IXF-P2-67.013	6B	-307113.44	10599.34
111467	02/07/97	E-IXF-P2-67.014	6S	-307131.88	10628.12

Y Tilt = -0.432541
Z Tilt = 0.359181

Chapter 29

HRMA Off-Axis Focal Positions

William Podgorski

For off-axis angles the optimum focal surface of the HRMA is closer to the HRMA than that for on-axis. This displacement depends on both off-axis angle and shell. A raytrace simulation of the offset of the best off-axis focus from the best on-axis focus was made using SAO's XRCF HRMA model (model `xrcf_SAO1G+HDOS_HDOS-scat-old_02`, which does not implement the XRCF-determined decenter). This data is presented in Table 29.1.

Table 29.1: Offset from on-axis focus (mm), + towards HRMA

Angle [′]	System	Shell 1	Shell 3	Shell 4	Shell 6
0	0.0000	0.0000	0.0000	0.0000	0.0000
5	1.4384	1.0905	1.5921	2.0559	3.6470
10	5.6211	4.0979	6.2833	8.0436	14.0232
15	12.1095	9.0284	13.6771	17.4109	30.3917
20	20.6847	15.5253	23.6882	30.2079	54.1046
25	31.1065	23.6816	36.0489	46.4008	85.0136
30	44.7368	34.0254	51.7845	66.5531	122.6774

A series of tests was run on 1/30/97 and 1/31/97 to measure the best focus using the HSI and the quad shutter focus procedure. The starting point (in PrimeX) for each measurement was the on-axis best focus, as determined by the quad shutter focus procedure using the FPC. The FPC facility optical axis (FOA) in place during this test series is listed in Table 29.2.

Since Table 29.2 is determined for the HXDS FPC's, the PrimeX offset between the HSI and fpc_x2 (20 μm aperture) must be added to the PrimeX values in the table to obtain the initial

Table 29.2: HXDS FOA Values During Off-Axis Tests

IRIG	Shell	Prime X	Prime Y	PCAZ
030102900000	all	−32679	−307153	10543
030102901000	1	−32912	−307153	10543
030102901000	3	−32561	−307153	10543
030102902000	4	−32292	−307153	10543
030102903000	6	−32664	−307153	10543

PrimeX values for the HSI. At the time of these tests the PrimeX value carried for the 20 μm aperture for fpc_x2 was -43500 μm. The PrimeX value carried for the HSI was -46475 μm, so 2975 μm must be subtracted from the PrimeX values in Table 29.2 to yield the on-axis best focus values for the HSI. These values are listed in Table 29.3.

Table 29.3: HSI PrimeX Values for Best On-Axis Focus

Shell	PrimeX_{00} [mm]
HRMA	−35.6540
1	−35.8870
3	−35.5360
4	−35.2670
6	−35.6390

The measured data from the 20 tests (some with 2 iterations) are listed in Table 29.4. The data given are:

TRW ID	Test ID
RunID	One of 4 RunID's from the Quad shutter test
θ	Off-axis angle
ϕ	Clocking of the off-axis angle relative to XRCF-Y (see Figure B.1).
Shell	HRMA shell number
PrimeX	Initial PrimeX stage position during test
ΔX	Change in PrimeX for best focus from HSI measurement and shutter focus calculation
$\delta\text{F}_{\text{meas}}$	$\text{PrimeX}/1000 - \Delta X/1000 - \text{PrimeX}_{00}$
$\delta\text{F}_{\text{sim}}$	Simulated shift in focal position from the on-axis focal position
ΔF	$\delta\text{F}_{\text{meas}} - \delta\text{F}_{\text{sim}}$

$\delta\text{F}_{\text{meas}}$ and $\delta\text{F}_{\text{sim}}$ are plotted in Figure 29.1.

Table 29.4: Off-Axis Focus Test Data

TRW ID	RunID	θ [′]	ϕ [°]	Shell	PrimeX [μm]	ΔX [μm]	δF_{meas} [mm]	δF_{sim} [mm]	ΔF [mm]
E-IXH-SF-15.001	110553	5	135	All	−34215.08	−613	2.0519	1.4384	0.6135
E-IXH-SF-15.001	110560	5	135	All	−33603.14	49	2.0019	1.4384	0.5635
E-IXH-SF-15.002	110561	5	135	1	−34860.02	−450	1.4770	1.0905	0.3865
E-IXH-SF-15.002	110568	5	135	1	−34408.06	−9	1.4879	1.0905	0.3974
E-IXH-SF-15.003	110569	5	135	3	−33942.11	−412	2.0059	1.5921	0.4138
E-IXH-SF-15.003	110577	5	135	3	−33528.65	10	1.9973	1.5921	0.4052
E-IXH-SF-15.004	110578	5	135	4	−33209.18	−384	2.4418	2.0559	0.3859
E-IXH-SF-15.004	110585	5	135	4	−32823.22	−4	2.4478	2.0559	0.3919
E-IXH-SF-15.005	110586	5	135	6	−31990.30	−407	4.0557	3.6470	0.4087
E-IXH-SF-15.005	110593	5	135	6	−31579.34	788	3.2717	3.6470	-0.3753
E-IXH-SF-15.006	110595	10	0	All	−30030.50	−35	5.6585	5.6211	0.0374
E-IXH-SF-15.006	110603	10	0	All	−29995.50	−7	5.6655	5.6211	0.0444
E-IXH-SF-15.007	110607	10	0	1	−31786.82	186	3.9142	4.0979	-0.1837
E-IXH-SF-15.007	110611	10	0	1	−31972.80	50	3.8642	4.0979	-0.2337
E-IXH-SF-15.008	110618	10	0	3	−29252.07	487	5.7969	6.2833	-0.4864
E-IXH-SF-15.008	110619	10	0	3	−29739.53	44	5.7525	6.2833	-0.5308
E-IXH-SF-15.009	110623	10	0	4	−27221.28	726	7.3197	8.0436	-0.7239
E-IXH-SF-15.009	110630	10	0	4	−27949.21	−59	7.3768	8.0436	-0.6668
E-IXH-SF-15.010	110631	10	0	6	−21614.34	1160	12.8647	14.0232	-1.1585
E-IXH-SF-15.010	110638	10	0	6	−22775.72	−195	13.0583	14.0232	-0.9649
E-IXH-SF-15.011	110640	15	135	All	−23542.15	315	11.7968	12.1095	-0.3127
E-IXH-SF-15.011	110647	15	135	All	−23858.61	38	11.7574	12.1095	-0.3521
E-IXH-SF-15.012	110648	15	135	1	−26923.31	845	8.1187	9.0284	-0.9097
E-IXH-SF-15.012	110655	15	135	1	−27770.22	−34	8.1508	9.0284	-0.8776
E-IXH-SF-15.013	110656	15	135	3	−21857.31	898	12.7807	13.6771	-0.8964
E-IXH-SF-15.014	110660	15	135	4	−17854.21	791	16.6218	17.4109	-0.7891
E-IXH-SF-15.015	110664	15	135	6	−5245.48	−329	30.7225	30.3917	0.3308
E-IXH-SF-15.016	110670	25	135	All	−4546.05	−1058	32.1660	31.1065	1.0595
E-IXH-SF-15.016	110677	25	135	All	−3487.15	−32	32.1988	31.1065	1.0923
E-IXH-SF-15.017	110678	25	135	1	−12202.78	−1143	24.8272	23.6816	1.1456
E-IXH-SF-15.018	110682	25	135	3	514.45	578	35.4725	36.0489	-0.5765
E-IXH-SF-15.019	110688	25	135	4	11135.89	1060	45.3429	46.4008	-1.0579
E-IXH-SF-15.020	110692	25	135	6	49377.06	587	84.4291	85.0136	-0.5845

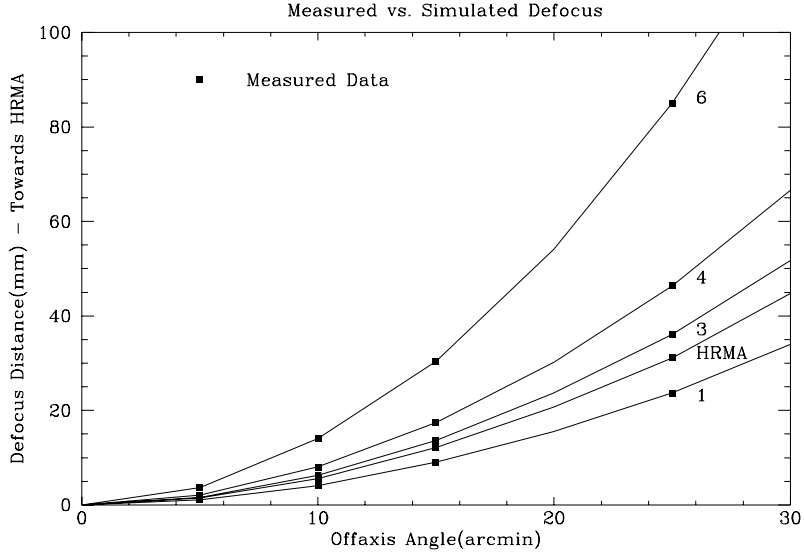

Figure 29.1: Measured vs. Simulated Off-Axis Focus Data

Chapter 30

Internal Tilt-Compensated Coma-Free Decenter of the AXAF mirrors

Terrance J. Gaetz

This chapter discusses the investigation and analysis of one of the major "minor mysteries" encountered during Phase 1 testing at XRCF. The first two sections (§30.1 and §30.2) provide a brief description of the investigation which led to the discovery of the "tilt-compensated" (*i.e.*, *coma-free*) decenters between the P and H optics in the HRMA. Although the decenter was first detected in quadrant flux balance measurements, detailed off-axis X-ray images led to a much more powerful approach to determining the decenter values. The detailed morphology of the X-ray images is discussed in §30.3. The measurements of the tilt-compensated decenters are described in §30.4. Finally, in §30.5 some suggestions are made for future investigation.

30.1 Quadrant Shutter Flux Balance

During the attempts to assess the relation between the HRMA optical axis and the FOA, a series of quad-shutter flux balance experiments were performed. These tests were part of an attempt to measure the misalignment of the HRMA optical axis relative to the Facility Optical Axis (FOA) by the variation in the amount of flux detected through individual mirror quadrants. For example, as the HRMA pitch is changed, one would expect the relationship between the fluxes from the Top and Bottom quadrants to change. The "2nd Floor" scientists at XRCF noted anomalies which were difficult to explain: an asymmetry of 6 or 7% between the Shell 6 top and bottom shutter fluxes (and correspondingly smaller asymmetries for the larger shells) even though other evidence suggested that HRMA axis alignment to the FOA in pitch was really rather close.

Various suggestions were considered. The effects of vignetting by various baffles and obstructions were investigated, but in each case the required decenters were too large to be plausible (*e.g.*, decenters of the precollimator by several millimeters), the size of the effect was too small, or the effect did not fit the observed trends very well. Tests at ring focus exonerated the shutter assembly itself (see Chapter 25). Finally it was suggested by that an internal relative decenter between the P and H optic might explain the anomalies. Preliminary raytrace investigations showed that a pure decenter of several hundred μm could affect the flux balance in the way observed. Because such large decenters would have been immediately noticed in the optical coma measurements (Chapter 27), it was postulated that a coma-free combination of decenter plus tilt ("tilt-compensated decenter") was responsible. In the case of an H optic, this motion is a rigid-body rotation of the H optic about its far focus; the coma from the tilt component of the motion exactly cancels the coma produced by the decenter component. Further raytraces showed that the decenter component of the tilt-compensated decenter accounted for most of the flux balance anomaly; although the tilt compensation is needed to account for the observed coma, the tilt compensation modified the flux balance discrepencies by $\lesssim$10%.)

C. Atkinson (EKC) reviewed the assembly procedure and came up with a scenario whereby an initial decenter could have been introduced between P6 and the optical axis and which would naturally lead to each of the mirror pairs having approximately the same tilt-compensated decenters; tolerances are such that a relative decenter of a few hundred μm are possible.

Noise and systematic errors made it difficult to obtain good values of the decenters from the flux balance differences alone.

30.2 Off-Axis X-ray Images

Off-axis HSI images for the whole HRMA were taken at a number of off-axis angles and energies (see Table 30.1). These off-axis images showed a peculiar pincushion-like cuspy feature in the core and this proved to be the breakthrough needed for understanding the P to H decenters. Preliminary raytrace studies confirmed that a P to H decenter of several hundred μm could generate pincushion-like cusps in off-axis images qualitatively similar to those observed. The off-axis images established tilt-compensated decenter as the most likely explanation for the flux balance results; any explanation in terms of obscuration or vignetting would fail to account for the distinctive characteristic features in the off-axis X-ray images.

Considerable effort was expended in attempting to deduce the optic decenters from the available full-HRMA images at different energies; T. Gaetz (SAO) determined that two mirror pairs (at least) exhibited a tilt-compensated decenter, probably of about the same magnitude and direction, but the complexity of four overlapping images made it very difficult to make further progress. (Even the identification between pincushion and responsible mirror shell was problematic; some of the tentative identifications proved to be incorrect.)

In order to diagnose the P to H decenters which seemed to be implied by the quadrant flux balance data and the full-HRMA off-axis images, a series of off-axis images for individual mirror pairs was requested and obtained. These images were all at Al-Kα (see Table 30.2) and are plotted in Figures 30.1, 30.2, and 30.3.

Systematic raytrace investigations were undertaken to understand the effect of tilt-compensated decenter on off-axis images (T.Gaetz, SAO); as a result of these studies, a scheme was developed for deriving the decenter parameters based on detailed measurements of image features. The results of these studies and the resulting tilt-compensated decenter parameters as assessed from the X-ray images are described below.

30.3 Morphology of the Off-axis X-ray Images

The off-axis images taken at XRCF show two distinctive features: a pair of overlapping large, approximately oval lobes, and a small pincushion-like caustic in the core. This section discusses the morphology of these features and their dependence on decenter magnitude and direction relative to the off-axis source direction.

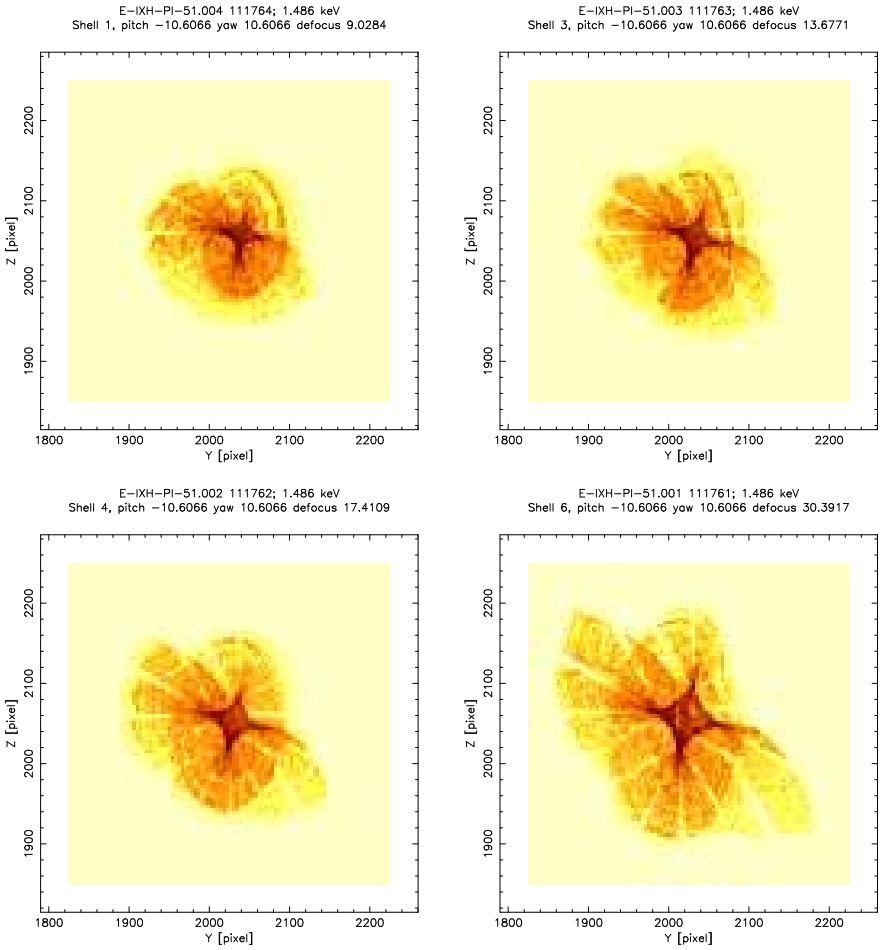

Figure 30.1: Off-axis images for individual shells; pitch = $-10.61'$, yaw = $10.61'$. Pixel width $6.43\,\mu$m; binned to 4×4 pixels. Two large overlapping lobes and a dense central pincushion can be seen; the light lanes are shadows of the CAP struts. The concentric ridges in the large lobes result from low-frequency surface errors on the mirrors. (X-ray data; logarithmic stretch)

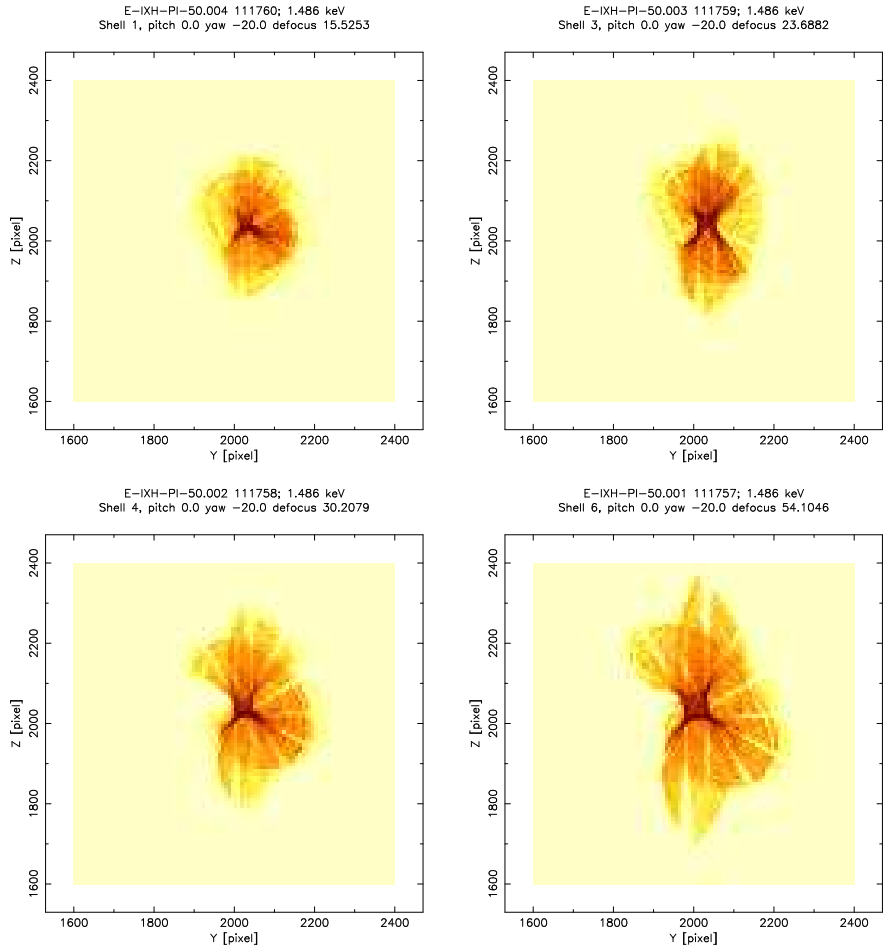

Figure 30.2: Off-axis images for individual shells; pitch = $0'$, yaw = $-20'$. Pixel width $6.43\,\mu$m; binned to 8×8 pixels. Two large overlapping lobes and a dense central pincushion can be seen; the light lanes are shadows of the CAP struts. The concentric ridges in the large lobes result from low-frequency surface errors on the mirrors. (X-ray data; logarithmic stretch)

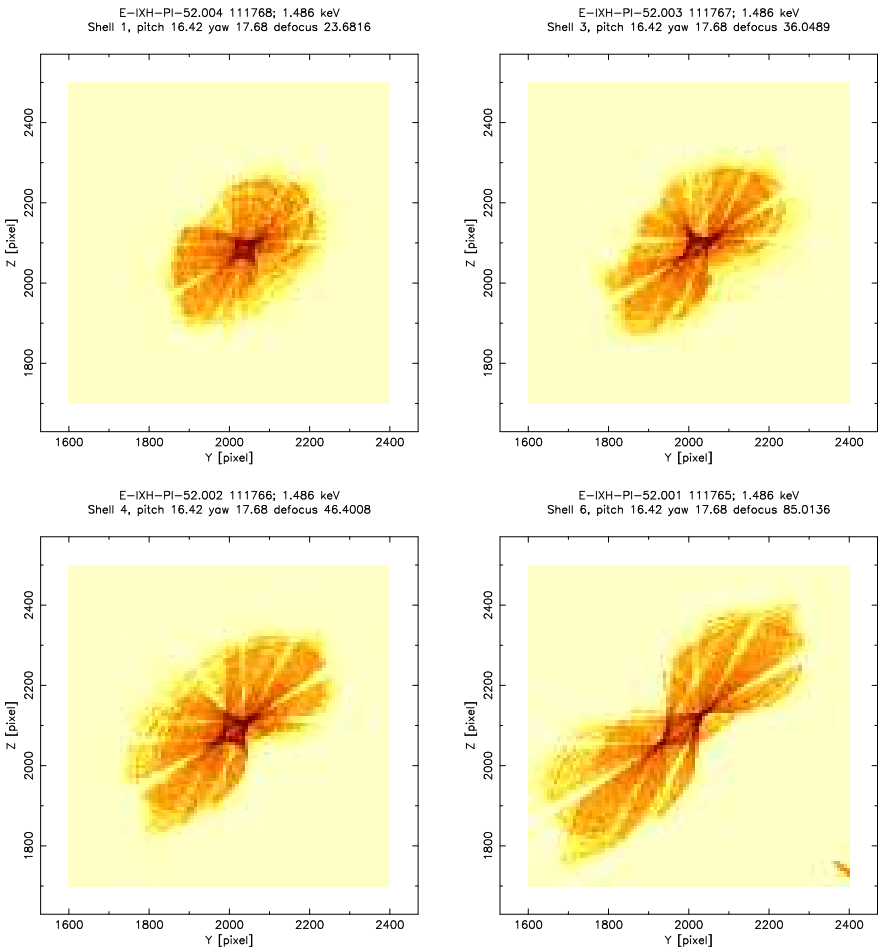

Figure 30.3: Off-axis images for individual shells; pitch = 16.42′, yaw = 17.68′. Pixel width 6.43 μm; binned to 8×8 pixels. Two large overlapping lobes and a dense central pincushion can be seen; the light lanes are shadows of the CAP struts. The concentric ridges in the large lobes result from low-frequency surface errors on the mirrors. (X-ray data; logarithmic stretch)

Table 30.1: Phase 1 Off-Axis Images (Full HRMA)

TRW ID	RunID	Energy	Shell	pitch	yaw	defocus
E-IXH-PI-6.001	110594	0.277	HRMA	−3.54	3.54	1.4384
E-IXH-PI-7.002	110639	0.277	HRMA	0	−10	5.6211
E-IXH-PI-6.003	110668	0.277	HRMA	−10.61	10.61	12.1095
E-IXH-PI-7.004	110669	0.277	HRMA	0	−20	20.6847
E-IXH-PI-6.005	110700	0.277	HRMA	−17.68	17.68	31.1065
E-IXH-PI-6.006	110701	0.277	HRMA	−21.21	21.21	44.7368
E-IXH-PI-12.004	110887	6.4	HRMA	0	−20	20.6847
E-IXH-PI-12.002	110888	6.4	HRMA	0	−10	5.6211
E-IXH-PI-11.001	110889	6.4	HRMA	−3.54	3.54	1.4384
E-IXH-PI-11.003	110890	6.4	HRMA	−10.61	10.61	12.1095
E-IXH-PI-11.005	110892	6.4	HRMA	−17.68	17.68	31.1065
E-IXH-PI-11.006	110893	6.4	HRMA	−21.21	21.21	44.7368
E-IXH-PI-22.004	111084	4.51	HRMA	0	−20	20.6847
E-IXH-PI-22.002	111085	4.51	HRMA	0	−10	5.6211
E-IXH-PI-21.001	111086	4.51	HRMA	−3.54	3.54	1.4384
E-IXH-PI-21.003	111087	4.51	HRMA	−10.61	10.61	12.1095
E-IXH-PI-21.005	111088	4.51	HRMA	−17.68	17.68	31.1065
E-IXH-PI-21.006	111089	4.51	HRMA	−21.21	21.21	44.7368

30.3.1 Off-Axis Images: Large Lobes

The off-axis images show two large approximately oval lobes; these are a facility effect resulting from the spherical aberration which is introduced by the finite source distance at XRCF. Symmetry considerations indicate that for an ideal perfectly aligned telescope, these lobes should be symmetric about a line containing the off-axis image and the optical axis. The observed large lobes are asymmetric and also tilted relative to each other; this is a consequence of the tilt-compensated decenter within the mirror pair. The lighter swaths through the image result from shadowing by support struts, predominantly those in the Central Aperture Plate.

The approximately concentric ripples in the large lobes result from the low-order mirror surface errors; these are also caustics, analogous to the pattern of bright lines on the bottom of a swimming pool caused by the ripples on the water surface. In this case they result from axial ripples on the mirror surface. The agreement between the location and shape of the ripples in the X-ray data as compared to the raytraces is an indication of the fidelity of the low-order mirror maps used in the raytrace. The ripples are more noticeable in the Shell 1 images; Figure 30.7 shows them at a different contrast setting.

The relative balance between the sizes of the lobes is sensitive to the axial position of the detector; at the best off-axis focus for the mirror pair, these lobes are comparable in size. The relative shape and orientation of the lobes depends on the direction of the decenter relative to the direction of the off-axis source (working in HRMA-centered coordinates). In addition to the offsets in the large lobes, a relative P to H decenter produces a pincushion-shaped caustic at best (off-axis)

Table 30.2: Phase 1 Off-Axis Images (Individual Shell)

TRW ID	RunID	Energy	Shell	pitch	yaw	defocus
E-IXH-PI-50.001	111757	1.486	6	0	−20	54.1046
E-IXH-PI-50.002	111758	1.486	4	0	−20	30.2079
E-IXH-PI-50.003	111759	1.486	3	0	−20	23.6882
E-IXH-PI-50.004	111760	1.486	1	0	−20	15.5253
E-IXH-PI-51.001	111761	1.486	6	−10.61	10.61	30.3917
E-IXH-PI-51.002	111762	1.486	4	−10.61	10.61	17.4109
E-IXH-PI-51.003	111763	1.486	3	−10.61	10.61	13.6771
E-IXH-PI-51.004	111764	1.486	1	−10.61	10.61	9.0284
E-IXH-PI-52.001	111765	1.486	6	16.42	17.68	85.0136
E-IXH-PI-52.002	111766	1.486	4	16.42	17.68	46.4008
E-IXH-PI-52.003	111767	1.486	3	16.42	17.68	36.0489
E-IXH-PI-52.004	111768	1.486	1	16.42	17.68	23.6816

focus; this is discussed further in §30.3.2.

Some of the XRCF single-shell off-axis images show obvious indentations in the large lobes. In some cases (e.g., Shells 3 and 4 at pitch $= 0'$, yaw $= -20'$, Shells 1 and 3 at pitch $= 16.42'$, yaw $= 17.68'$) this appears to be a result of vignetting by the shutter assembly; preliminary raytraces show that a shutter assembly decenter of about 2 mm appears to be consistent with these results. In other cases the indentations arise from the morphology of the off-axis images: Shells 1 and 6 at pitch $= 0'$, yaw $= -20'$ appears to be consistent with no additional vignetting by the shutter assembly.

A raytrace experiment was performed in which the relative direction between the off-axis source and the decenter direction was systematically varied. (The pitch and yaw of the shell were assumed fixed and the decenter direction varied.) The results are shown in Figure 30.4; a close-up of the pincushion core is shown in Figure 30.5. Note that the smaller of the large lobes and the orientation of the cuspy pincushion rotate oppositely to the change in decenter direction and at approximately half the rate that the decenter varies. The size of the pincushion also varies somewhat with relative angle between off-axis source direction and P to H mirror decenter direction. Note that the lobes and the pincushion core both show the expected bilateral symmetry when the decenter direction and the off-axis direction are parallel ($\phi = 0°$ and $\phi = 180°$.)

30.3.2 Off-Axis Images: Pincushion Caustics

The pincushion caustics are also a consequence of the tilt-compensated decenter in the optics. Raytrace studies show that the dimension of the pincushion scales inversely with the mirror pair nodal radius. The pincushion gets larger as the magnitude of the off-axis angle increases (for constant tilt-compensated decenter) and also gets larger as the magnitude of the tilt-compensated decenter increases (for constant source off-axis angle). For fixed magnitude of off-axis angle and tilt-compensated decenter, the pincushion size and the orientation of the axes of the pincushion

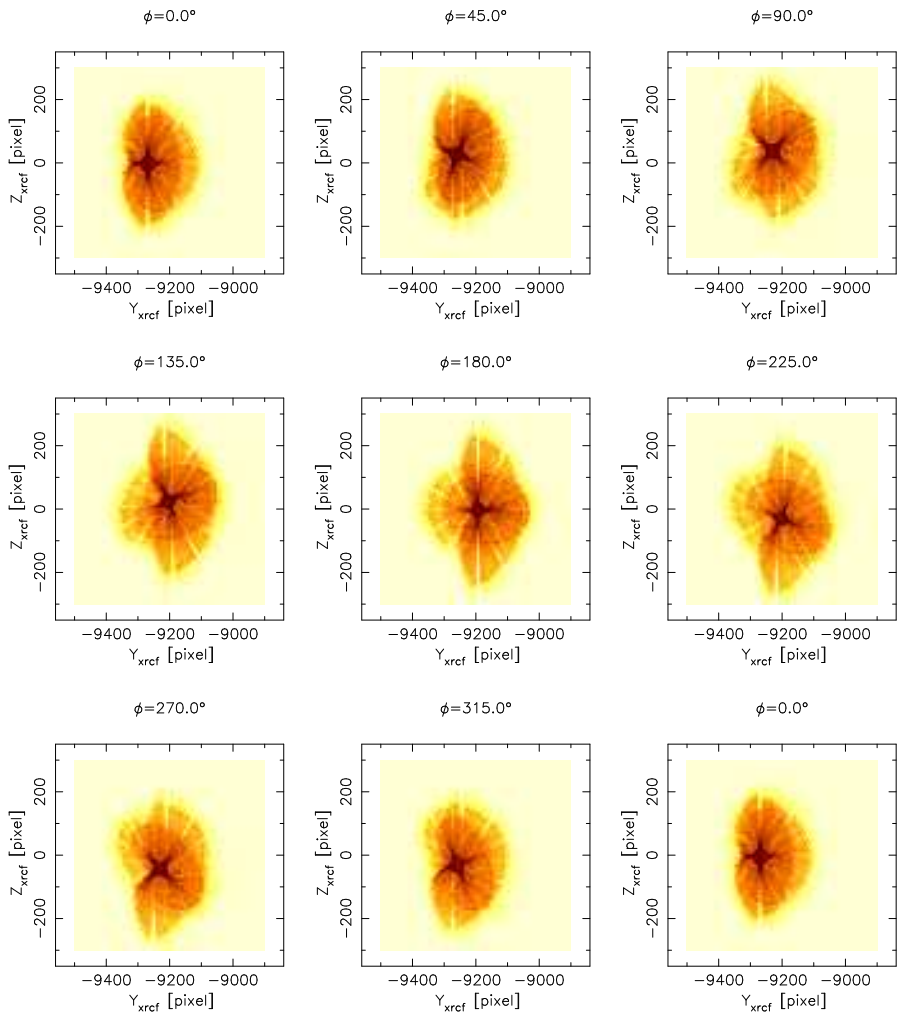

Figure 30.4: Variation of off-axis image with angle between source and decenter direction. Shell 3, pitch $= 16.42'$, yaw $= 17.68'$. Pixel width 6.43 μm; binned to 8×8 pixels. (Raytrace data; logarithmic stretch)

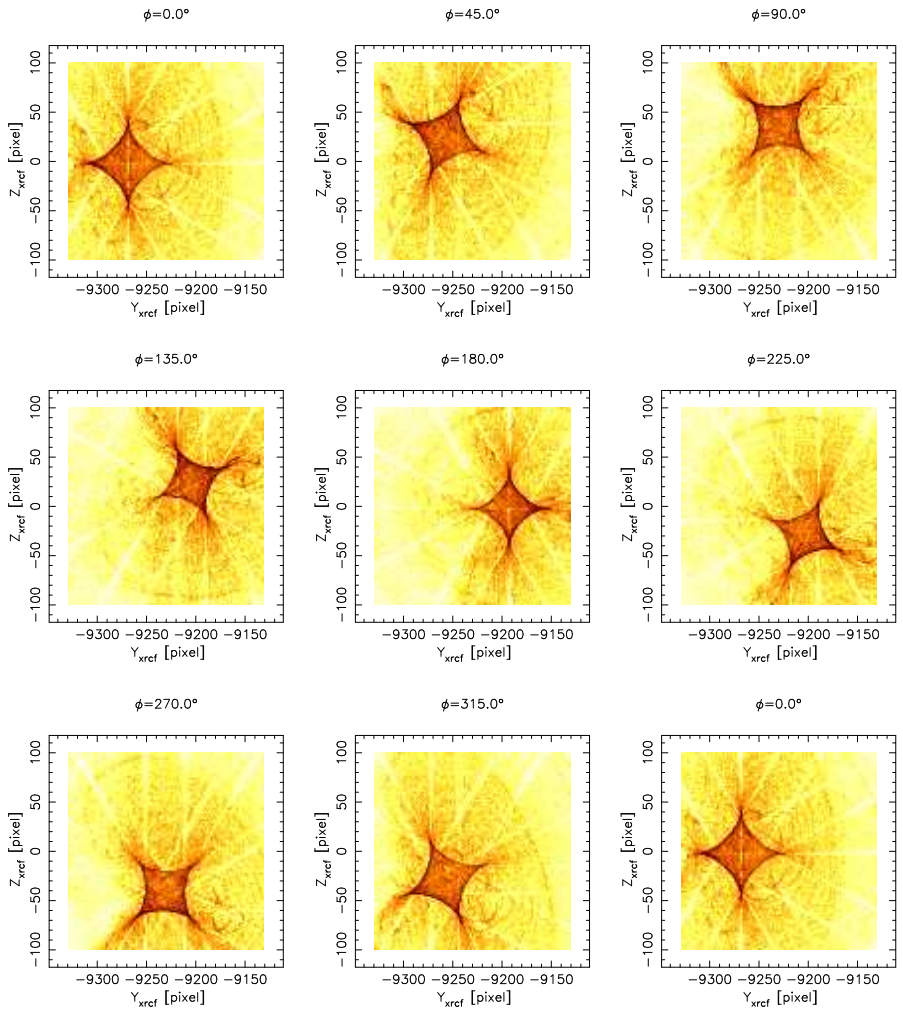

Figure 30.5: Variation of off-axis image with angle between source and decenter direction. Shell 3, pitch = 16.42′, yaw = 17.68′. Pixel width 6.43 μm; binned to 1×1 pixels. (Raytrace data; logarithmic stretch)

vary with relative angle between off-axis direction and the decenter direction. Symmetry considerations suggest that the pincushion should show full bilateral symmetry about the decenter direction when the decenter direction is parallel or anti-parallel to the off-axis direction, and this is seen in Figure 30.5 ($\phi = 0°$ and $\phi = 180°$ cases, where ϕ is the angle between the decenter direction and the projection onto the focal plane of the off-axis source direction); the corners of the pillbox are aligned with the decenter direction. Closer scrutiny of Figure 30.5 shows that the pincushion size varies systematically with angle between decenter direction (at fixed decenter magnitude) and (fixed) off-axis direction. The pincushion orientation changes by 90° as the ϕ changes by 180° so the pincushion rotates about half as rapidly as ϕ varies. Detailed measurements show that the factor of 1/2 is only approximate, but by symmetry, the pincushion rotation between $\phi = 0°$ and $\phi = 180°$ must be exactly 90° in the limit of otherwise ideal optics.

Raytracing also shows that the size and orientation of the pincushion is insensitive to the axial location of the detector; the basic structure of the pincushion is the same even with focal errors as large as several mm (though differences become readily apparent if the image is sufficiently out of focus that the pincushion unravels).

30.4 Measuring the Tilt-Compensated Decenter

Raytrace studies revealed an important feature of the tilt-compensated decenters: for constant off-axis angle and in the neighborhood of a given decenter value, the variation of the *pincushion size* with *decenter magnitude* and the variation of *pincushion orientation* with *decenter direction* are relatively uncoupled from each other. This means that once an initial estimate of the decenter parameters is obtained, the decenter magnitude and direction can be refined by using the sensitivities of pincushion size and orientation to decenter magnitude and direction to refine the estimate.

The above procedure was carried out for the single-shell pitch = 0′, yaw = −20′ measurements. The approximate direction of the decenter was be assessed from the morphology of the large lobes; this also removes the $\pi/2$ angular ambiguity in the pincushion orientation (see Figure 30.4). Raytraces were used to provide an initial estimate for the magnitude and direction; the same initial values were assumed for all four shells. The relative sizes of the large lobes do depend sensitively on focal position and serve as an additional check that the images were taken at very nearly the best off-axis focus for the individual shell; examination of the X-ray data indicates that the individual shell images were taken near best focus.

The decenter magnitude and direction can be determined by measuring the pincushions in the X-ray data and simulation (on an expanded scale to make measurement easier). Figure 30.9 shows and expanded view of the the pincushion cores in the pitch= 0′, yaw= 20′ images, and Figure 30.10 shows the equivalent images based on raytraces using the mirror rigid-body model obtained in Chapter 27.

Figure 30.6 shows the measurement schematically. The width, w, of the pincushion along a slice through the narrow portion of the pincushion (midway up the box) was measured. In addition, the angle, θ between the Y axis and a line connecting opposing corners (at $\sim +45°$) was measured. These metrics were compared with those in raytraced images. Once reasonably good agreement was obtained, a raytrace study established the sensitivity of box width w to decenter magnitude and also the sensitivity of box orientation θ to decenter direction; it was found that for Shell 6 the pincushion width w varied with decenter magnitude as 123 pixels mm^{-1} of decenter (1 pixel= 6.43 μm); the sensitivity scales inversely with the mirror nodal radius. (Note that the sensitivities may depend on the approximate magnitude of the tilt-compensated decenter and its direction relative to the off-axis source direction.)

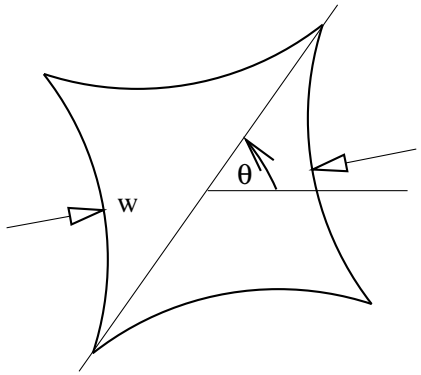

Figure 30.6: Schematic diagram of pincushion measurement. The width, w is measured across the narrow part of the pincushion. The orientation, θ, is measured using the diagonal of the pincushion.

As an illustration of the procedure, consider Figures 30.7and30.8 (Shell 1; pitch= $0'$, yaw= $-20'$). In Figure 30.7 a raytrace using the current best estimate for Shell 1 tilt-compensated decenter (upper left panel) is compared to the X-ray image (lower right panel). The effects of increasing (decreasing) the tilt-compensated decenter by 0.1 mm is shown in the lower left (upper right) panel; the change in pincushion size is clearly visible. Similarly, in Figure 30.7 the current best estimate for Shell 1 coma-free decenter+tilt (upper left panel) is compared to the X-ray image (lower right panel). The decenter is direction changed by $-24°$ (upper right) or $+24°$ (lower left); note the change in pincushion orientation. In this case it is also possible to see a darker bar across the pincushion at about 120° from about halfway across the bottom of the box; the position of this bar changes with pincushion orientation, and the agreement in bar position is quite good between the X-ray data and the current best raytrace model. (This bar is even more clearly visible in the upper left panels of Figures 30.9and30.10; a similar feature is seen in the upper right panel of Figure 30.10, but vignetting by the shutter assembly obscures that portion of the image in the corresponding X-ray data (upper right panel of Figure 30.9).)

Note that the X-ray image cores and the raytrace image cores differ in detail for at least two reasons: angle-dependent sensitivity of the HSI detector and vignetting by the quadrant shutter assembly; for example, note the vignetting evident in the bottom of the pincushion for Shell 3 and the top of the pincushion for Shell 4 in Figure 30.9. Nevertheless, the diagnostic features (pincushion size and orientation) are visible clearly enough to allow a good determination of decenter direction and magnitude. Where visible, agreement in the pincushion substructure between the X-ray data and the raytraces provides further support for the accuracy of the tilt-compensated decenter values.

The estimated relative decenters of the H mirrors relative to their mating P mirrors are given in Table 30.3. Note that these decenters are given in `SAOsac` raytrace coordinates (see Chapter B);

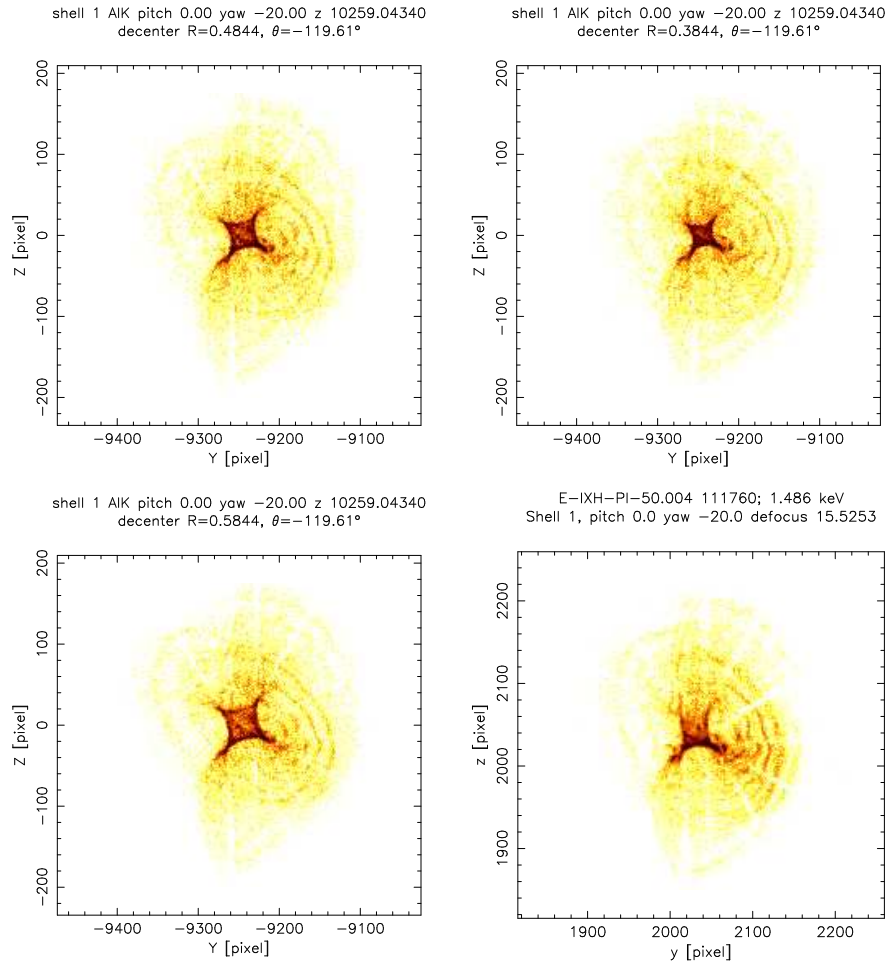

Figure 30.7: Off-axis images (Shell 1; pitch = $0'$, yaw = $-20'$). Top left: Current raytrace model. Top right: decenter magnitude $\Delta R_0 - 0.1$ mm. Bottom left: decenter magnitude $\Delta R_0 + 0.1$ mm. Bottom right: HSI image (X-ray data) (to same scale). Pixel width 6.43 μm; binned to 2×2 pixels. Logarithmic stretch.

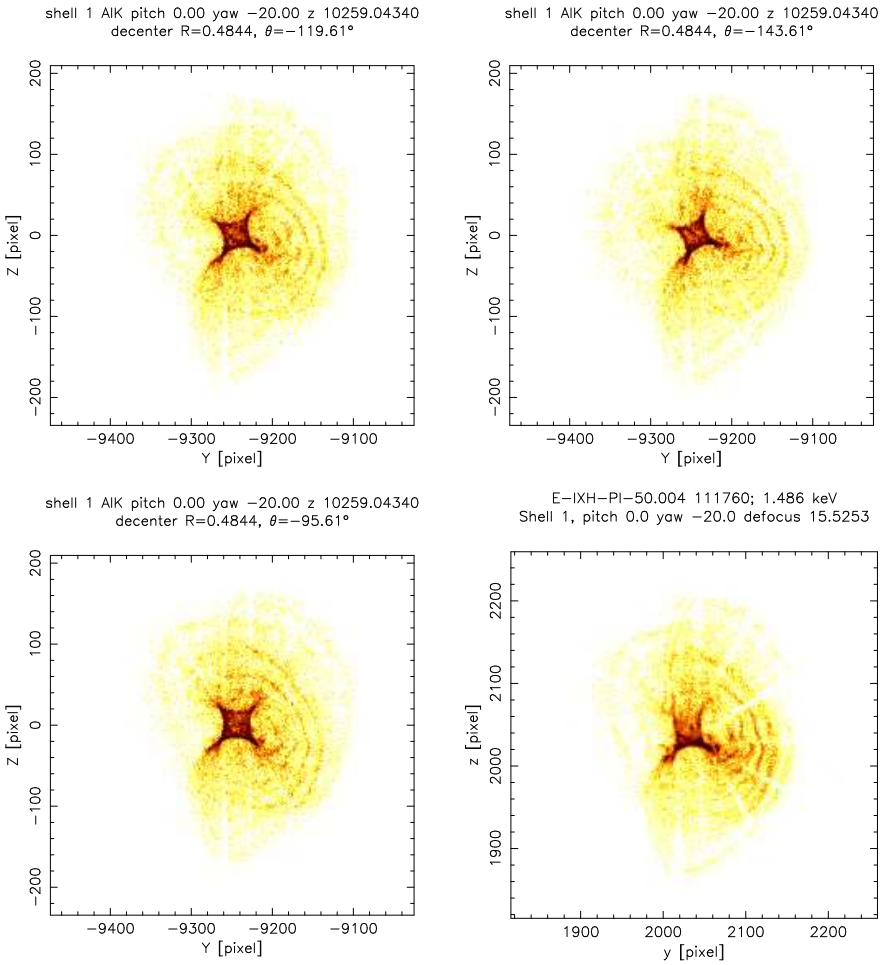

Figure 30.8: Off-axis images (Shell 1; pitch = 0′, yaw = −20′). Top left: Current raytrace model. Top right: decenter direction $\Delta\phi_0 - 24°$. Bottom left: decenter direction $\Delta\phi_0 + 24°$. Bottom right: HSI image (X-ray data) (to same scale). Pixel width 6.43 μm; binned to 2×2 pixels. Logarithmic stretch.

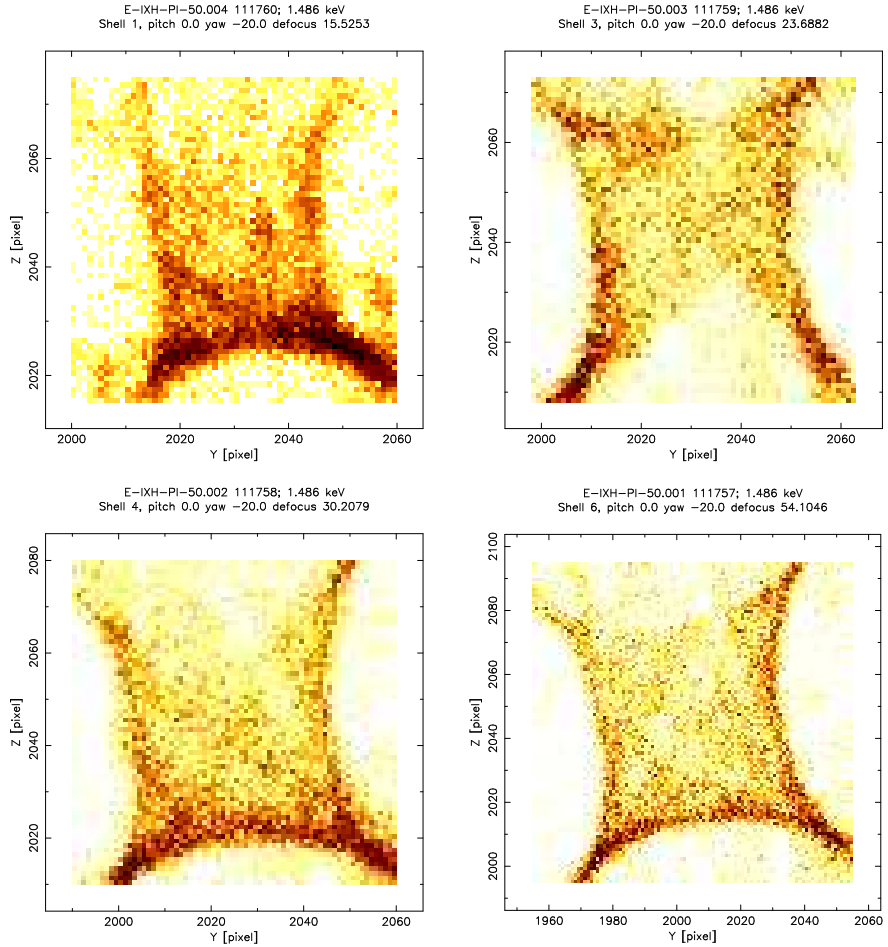

Figure 30.9: Core pincushions of off-axis images for individual shells; pitch = 0′, yaw = −20′. Pixel width 6.43 μm; binned to 1×1 pixels. (X-ray data; logarithmic stretch)

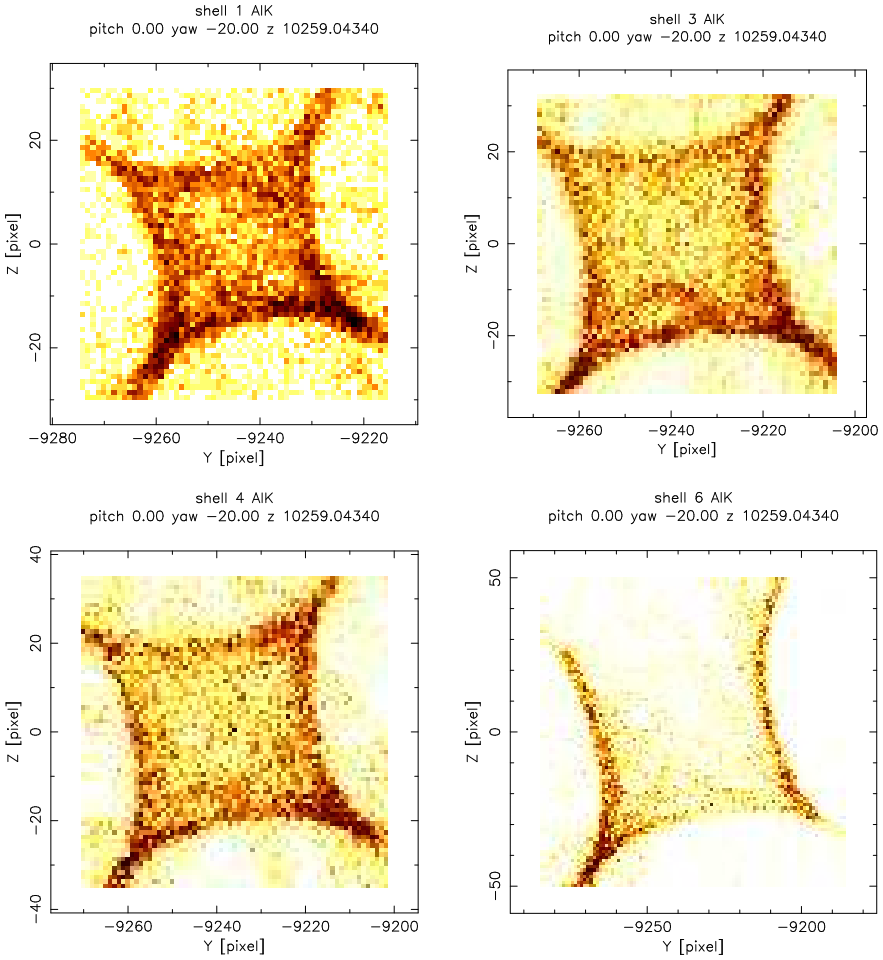

Figure 30.10: Core pincushions of off-axis images for individual shells based on current SAO raytrace model; pitch = 0′, yaw = −20′. Pixel width 6.43 μm; binned to 1 × 1 pixels. (Raytraced; logarithmic stretch)

Table 30.3: Measured Tilt-Compensated Decenters

	decenter†		decenter†	
mirror	magnitude (mm)	angle (deg)	Δx_0 (mm)	Δy_0 (mm)
h1	0.4844	−119.61	−0.2393	−0.4211
h3	0.5077	−109.61	−0.1704	−0.4782
h4	0.4562	−111.90	−0.1702	−0.4233
h6	0.4736	−114.42	−0.1958	−0.4312

†coma from decenter cancelled by compensating tilt

angle is measured from the `SAOsac` raytrace $+X$ axis with $+Y$ at $+90°$ (see Figure B.1);

$$X_{SAOsac} = -Y_{XRCF} \tag{30.1}$$
$$Y_{SAOsac} = +Z_{XRCF} \tag{30.2}$$
$$Z_{SAOsac} = -X_{XRCF} \tag{30.3}$$
$$\tag{30.4}$$

Note that the actual body-centered decenter and tilt for each optic must also be consistent with optical measurements at EKC at the end of HRMA buildup. The construction of the mirror rigid-body database (based on the above tilt-compensated decenter and the X-ray and optical measurements of the alignment) is discussed in Chapter 27; the current mirror database is `/proj/axaf/simul/databases/mirror/EKCHDOS06.rdb`.

The current HRMA model (`trace-shell4` configuration file `xrcf_SAO1G+HDOS_HDOS-scat-970220_03`) was raytraced for each mirror pair and off-axis angle combination as listed in Table 30.2. The raytraces accumulated a total ray weight of about 100000 per image (comparable to the number of events in the X-ray images). The raytrace fractional weights were converted statistically into unit weights (`mxwldmn`) and blurred to the HSI resolution (`mcp` using the `/proj/axaf/simul/databases/detectors/hsi.par` specification file. The images *do not*, however, incorporate the angle-dependent HSI detector quantum efficiency, nor do they include the vignetting introduced by the quadrant shutter assembly at these large off-axis angles. The raytraces of the HRMA model are plotted in Figures 30.11, 30.12, and 30.13; these can be compared with the X-ray images in Figures 30.1, 30.2, and 30.3.

30.5 Future Directions

This chapter represents a preliminary attempt at extracting the tilt-compensated H to P decenters from the X-ray data. It is thought that the decenters are accurate to better than 10%. The current estimate is based on single-shell data at a single off-axis angle (pitch = 0′, yaw = −20′). Single-shell off-axis X-ray images were obtained in two other directions; inspection of the raytrace data in Figures 30.11and30.13 compared to the X-ray data in Figures 30.1and30.3 shows good qualitative agreement. (Some of the detailed differences between the images are caused by vignetting by the quad shutter assembly at these large off-axis angles.) The single-shell data taken at the other two off-axis angles can be used to provide additional estimates of the tilt-compensated decenters;

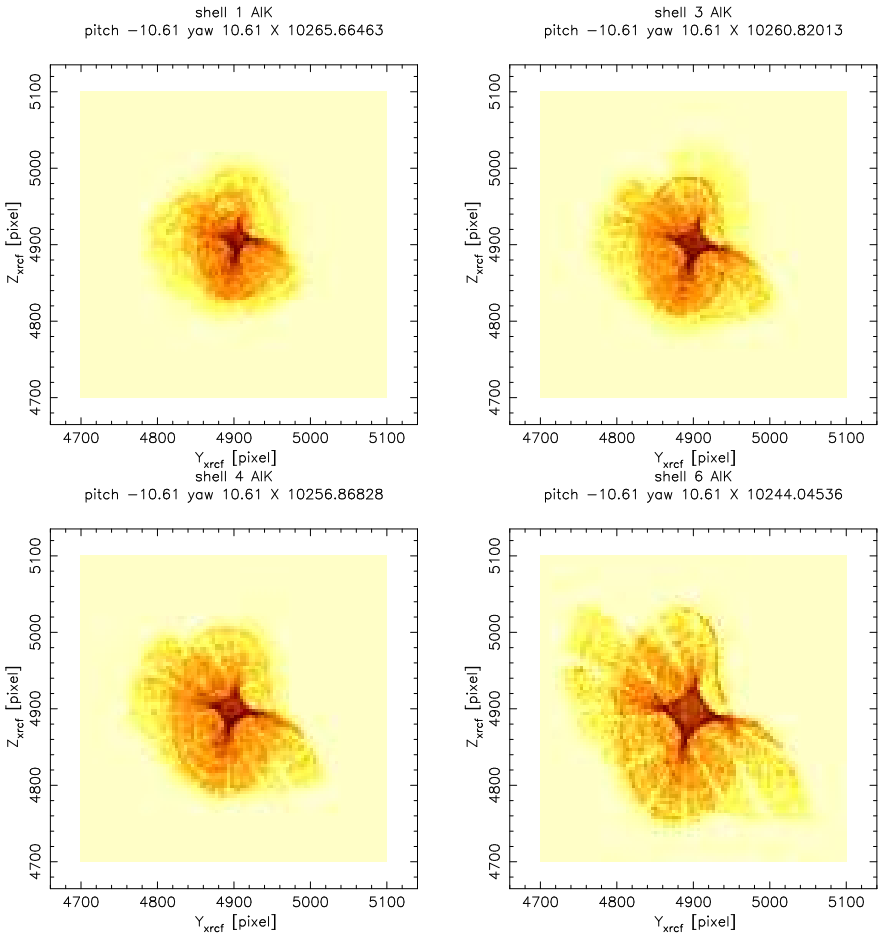

Figure 30.11: Off-axis images for individual shells; pitch = $-10.61'$, yaw = $10.61'$. Pixel width $6.43\,\mu$m; binned to 4×4 pixels. Two large overlapping lobes and a dense central pincushion can be seen; the light lanes are shadows of the CAP struts. The concentric ridges in the large lobes result from low-frequency surface errors on the mirrors. (Raytrace data; logarithmic stretch)

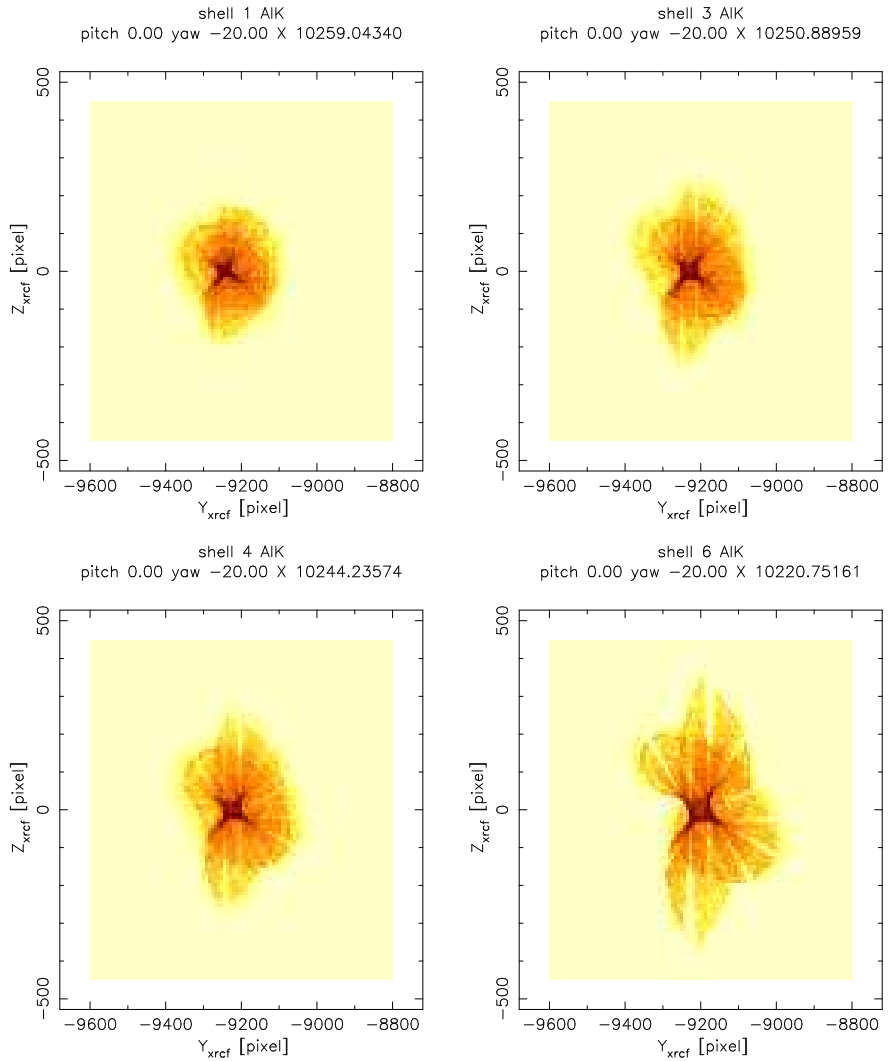

Figure 30.12: Off-axis images for individual shells; pitch = $0'$, yaw = $-20'$. Pixel width $6.43\,\mu$m; binned to 8×8 pixels. Two large overlapping lobes and a dense central pincushion can be seen; the light lanes are shadows of the CAP struts. The concentric ridges in the large lobes result from low-frequency surface errors on the mirrors. (Raytrace data; logarithmic stretch)

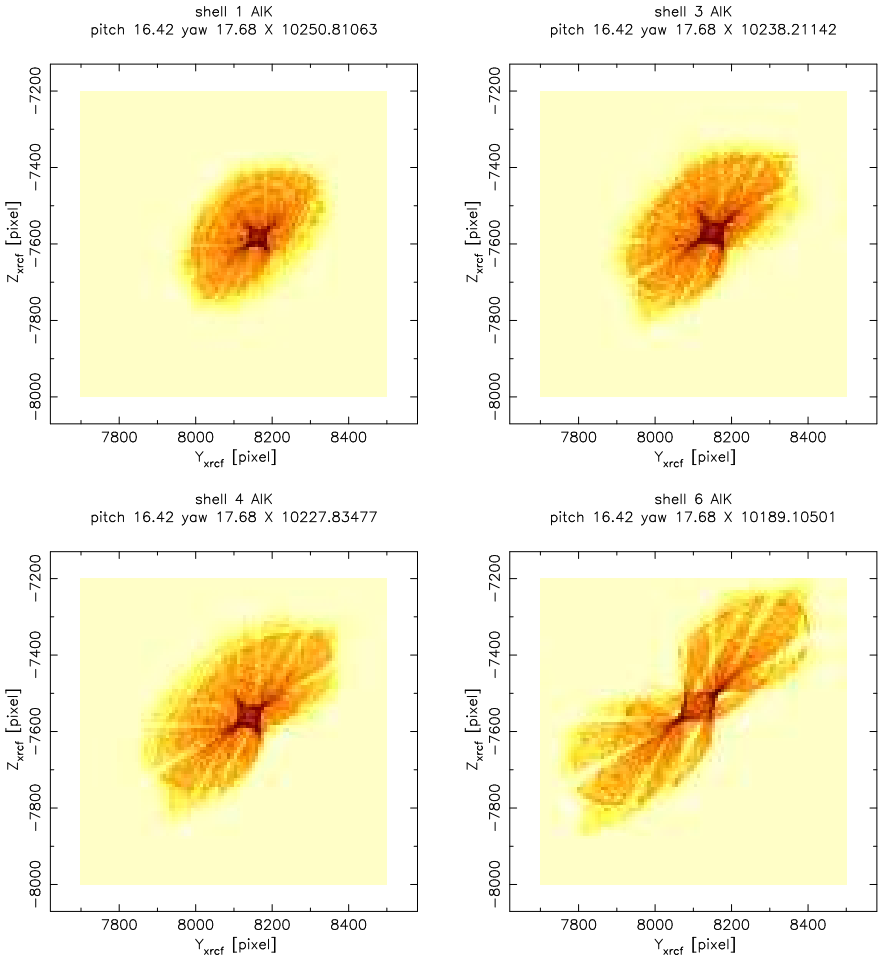

Figure 30.13: Off-axis images for individual shells; pitch = 16.42′, yaw = 17.68′. Pixel width 6.43 μm; binned to 8×8 pixels. Two large overlapping lobes and a dense central pincushion can be seen; the light lanes are shadows of the CAP struts. The concentric ridges in the large lobes result from low-frequency surface errors on the mirrors. (Raytrace data; logarithmic stretch)

this will produce a better estimate and allow an assessment of the measurement errors. The model can also be checked against the full-HRMA off-axis images at different energies obtained during Phase 1 of the XRCF testing.

Preliminary raytrace studies show that the HATS Fourier coefficients associated with rigid body alignment are insensitive to a tilt-compensated decenter. The effects may show up in the higher Fourier components but noise in the data may make it impractical to extract a value. Further preliminary studies indicate that a tilt-compensated decenter has little effect on the quadrant shutter focus estimators (of order 10 μm axially) but could produce a significant bias in the tilt estimates. The analysis in Chapter 28 compared against a model incorporating the estimated tilt-compensated decenter, so whatever bias the decenter introduces is also present in the modeling. Care must be taken, however, in attempting a breakdown into individual components until this bias is better understood.

The effects of the tilt-compensated decenter on the analysis and interpretation of the other calibration data needs to be investigated. Although the tilt-compensated decenter does not produce on-axis coma on-orbit, the finite source distance at XRCF produces an effective spherical aberration which may make the tilt-compensated decenter effects visible in images even on-axis: preliminary raytraces indicate that the on-axis blur circle should be asymmetric. The available on-axis data also needs to be checked to determine whether they are consistent with the measured tilt-compensated decenter values.

The single-shell off-axis images show signs of vignetting by the closed shutters for adjacent shells. It may be possible to ascertain the lateral decenter of the shutter assembly relative to the optical axis by making use of the full set of off-axis images for the individual shells Preliminary raytraces indicate a horizontal decenter by about 2 mm; a further study could refine the decenter of the shutter assembly. Because we have pure yaw cases but not pure pitch cases, it will be easier to constrain the Y_{XRCF} component than the Z_{XRCF} component of the shutter assembly decenter.

Finally, some of the images (single-shell and full HRMA) at large off-axis angles show single-reflection ghost images. Once the tilt-compensated decenters and other alignments of the HRMA are well determined, it may be possible to deduce something about the as-built X-ray baffle placement from the shapes of the off-axis images and the ghost images.

Appendix A

Incidental Data Tables

Richard J. Edgar

A.1 Introduction

This chapter contains data tables used in the analysis or simulation of the data described in this report.

The detector locations for the various phases of XRCF testing are summarized in Table A.1. During the flatfield testing prior to the HRMA calibration in November 1996, the detectors were arranged as in phases C, D & E. We also include, for completeness, the detector locations during Phase 2 of the HRMA calibration (phases F, G, & H) when flight instruments (or the ACIS-2C) were in the focal plane. **Instruments are referred to throughout this document by the positions they occupied during phases C, D, & E of the XRCF HRMA calibration.** However, the data files themselves give detectors their names based on their positions at the time of the test.

Phase:	CDE	FGH	I	J
location				
HXDA	fpc_x1	...	...	fpc_5
	fpc_x2	...	...	fpc_x2
	ssd_x	...	...	ssd_5
BND-H	fpc_hn	fpc_hn	fpc_hn	fpc_hn
	fpc_hb	fpc_hb	fpc_hb	fpc_hb
	fpc_ht	fpc_ht	fpc_ht	fpc_ht
	fpc_hs	fpc_hs	fpc_x2	fpc_hs
BND-500	fpc_5	fpc_5	fpc_5	fpc_x1*
	ssd_5	ssd_5	ssd_5	ssd_x

Table A.1: HXDS detector locations in XRCF testing phases. *Note that fpc_x1 (the original fpc_5) was not working during phase J

instrument	aperture	ap_size	A (cm^2)	A* (cm^2)
fpc_5	fpc_5_1	1	.008518 ± 4.26*e*-4	.008518 ± 4.26*e*-4
fpc_5	fpc_5_4	4	.1142 ± .0015	.1142 ± .0015
fpc_5	fpc_5_12	12	1.023 ± .0041	1.023 ± .0041
fpc_5	fpc_5_36	36	9.216 ± .0129	9.216 ± .0129
fpc_hn	fpc_hn_full	full	32.2781 ± .16	32.24 ± .16
fpc_hn	fpc_hn_36	36	9.190 ± .0129	9.14 ± .05
fpc_hs	fpc_hs_full	full	32.2684 ± .16	32.24 ± .16
fpc_x2	fpc_hs_37	37	9.5965 ± .0037	9.59 ± .05
fpc_ht	fpc_ht_full	full	32.3048 ± .16	32.24 ± .16
fpc_hb	fpc_hb_full	full	32.2435 ± .16	32.24 ± .16
ssd_5	ssd_5_5000	5000	0.1958 ± .003916	0.1958 ± .003916
ssd_5	ssd_5_2000	2000	3.130*e*-2 ± 6.260*e*-4	3.130*e*-2 ± 6.260*e*-4
ssd_5	ssd_5_500	500	1.975*e*-3 ± 3.950*e*-5	1.975*e*-3 ± 3.950*e*-5
ssd_5	ssd_5_200	200	3.173*e*-4 ± 6.346*e*-6	3.173*e*-4 ± 6.346*e*-6
ssd_5	ssd_5_100	100	8.168*e*-5 ± 1.6336*e*-6	8.168*e*-5 ± 1.6336*e*-6

Table A.2: BND aperture areas. The ap_size column is the nominal diameter in mm, the ap_area column is the aperture area in cm^2, corrected for mesh transmission of 0.9025, except in the case of the fpc_5 1 mm aperture, which is centered in a 2 mm mesh cell, and so no mesh correction is appropriate. *The last column contains newly measured areas (see Table 3.2), not used in the present analysis, but in most cases not very different from the older values.

src	object	d (cm)
eips	fpc_5	3743.3 ± 0.5
eips	ssd_5	3819.9 ± 0.6
eips	fpc_hn	52400.1 ± 0.8
eips	fpc_hs	52431.6 ± 0.8
eips	fpc_ht	52431.6 ± 0.8
eips	fpc_hb	52431.6 ± 0.8
eips	hrma_node	52752.2 ± 0.4
eips	cap_datum_a	52750.385 ± 0.4
eips	hrma_ent	52601.221 ± 0.4
eips	acis	53752.2 ± 30
eips	fpc_x2	53752.2 ± 30
eips	fpc_x1	53752.2 ± 30
eips	ssd_x	53752.2 ± 30

Table A.3: Distances from XSS sources to HXDS and HRMA equipment in cm. From Project Science compilation. Note that the distances to the focal plane instruments are used only in the analysis of flat field data (phases I and J).

Appendix B

Coordinate Systems

Terrance J. Gaetz

In this appendix we summarize the relations between various coordinate systems of interest; these include:

Tower:	HRMA Alignment Test System Tower at EKC (HATS measurements)
`DPSAOsac`:	Double-pass raytraces to simulate HATS measurements
`SAOsac`:	standard raytraces (*e.g.*, XRCF conditions)
XRCF:	coordinate system at the XRCF test facility
HRMA:	HRMA-based coordinate system aligned with the standard AXAF coordinate directions

Figure B.1 illustrates the different coordinate systems. Note that the XRCF coordinates differ from the standard HRMA/AXAF coordinate system by a flip of 180° about the X_{HRMA} axis, while the `DPSAOsac` coordinates differ from the standard `SAOsac` coordinates by a flip of 180° about the X_{SAOsac} axis (the Y_{HRMA} axis). Note also that we are primarily concerned here with the directions of the coordinate axes rather than the location of the coordinate origin.

The SAO/MST raytrace system, `SAOsac`, specifies rigid-body positioning in terms of the location and orientation of the body-center of the optic. The body-center "tilt" coordinates are `azmis` and `elmis`, where

`azmis`:	positive rotation about an axis parallel to the `SAOsac` Y axis; positive rotation is right-hand-rule rotation with angle increasing from the $+Z$ axis towards the $+X$ axis. (X' axis is the new X axis after `azmis` rotation; Z' axis is the new Z axis after `azmis` rotation).
`elmis`:	negative rotation about an axis parallel to `SAOsac` X' axis; positive rotation is right-hand-rule with angle increasing from the $+Y$ axis towards the $+Z'$ axis. Positive `elmis` rotation takes $+Z'$ axis towards the $+Y$ axis.

For completeness, the corresponding conventions for mirror element rotations in the HRMA and XRCF coordinates are

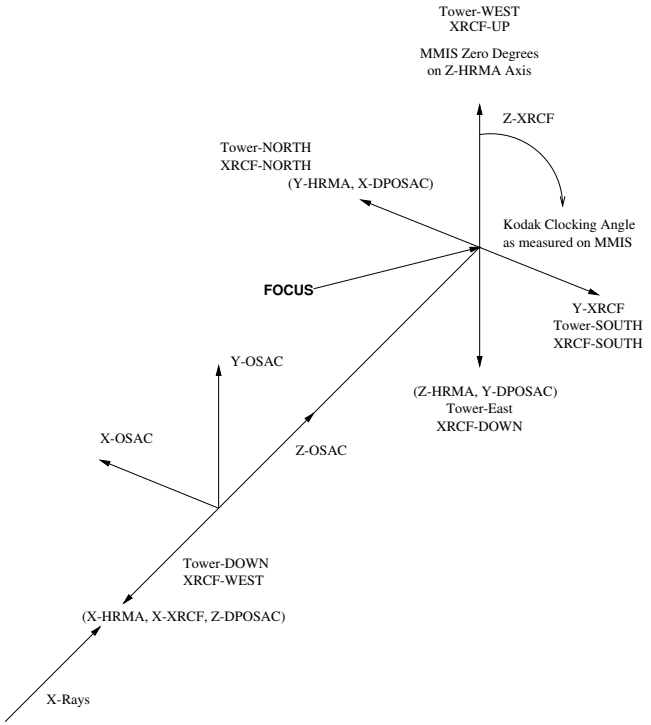

Figure B.1: Relations between HATS tower, XRCF, and `SAOsac` coordinates

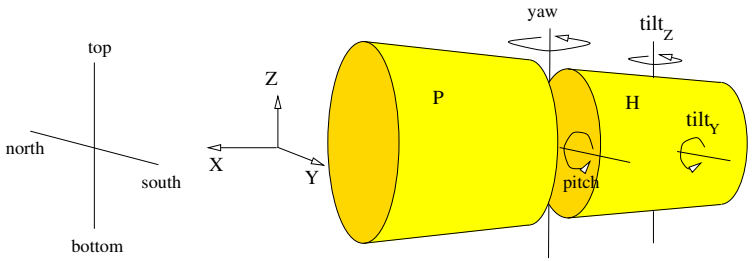

Figure B.2: Schematic of XRCF coordinate and rotation conventions

θ_Y: positive rotation about an axis parallel to the `HRMA` $+Y$ axis; positive rotation is right-hand-rule rotation with angle increasing from the $+Z$ axis towards the $+X$ axis.

θ_Z: positive rotation about an axis parallel to the `HRMA` $+Z$ axis; positive rotation is right-hand-rule rotation with angle increasing from the $+X$ axis towards the $+Y$ axis.

and

$tilt_Y$: positive rotation about an axis parallel to the `XRCF` $+Y$ axis; positive rotation is right-hand-rule rotation with angle increasing from the $+Z$ axis towards the $+X$ axis.

$tilt_Z$: positive rotation about an axis parallel to the `XRCF` $+Z$ axis; positive rotation is right-hand-rule rotation with angle increasing from the $+X$ axis towards the $+Y$ axis.

At the XRCF, the orientation of the HRMA as a whole was specified by *pitch* and *yaw*:

pitch: positive rotation about an axis parallel to the `XRCF` $+Y$ axis. Positive rotation is right-hand-rule rotation with angle increasing from the $+Z$ axis towards the $+X$ axis.

yaw: positive rotation about an axis parallel to the `XRCF` $+Z$ axis. Positive rotation is right-hand-rule rotation with angle increasing from the $+X$ axis towards the $+Y$ axis.

The raytrace simulations are always performed in the appropriate `SAOsac` coordinate system; the orientation of the HRMA relative to the source is given by *bundle_el* and *bundle_az*, the direction *from* the source *towards* HRMA. The relation between *pitch*, *yaw*, *bundle_el*, and *bundle_az* are summarized in Table B.1.

Table B.1: Relations between coordinate systems

$+bundle\_el_{SAOsac}$	=	$-bundle\_el_{DPSAOsac}$	=	$-pitch$
$+bundle\_az_{SAOsac}$	=	$-bundle\_az_{DPSAOsac}$	=	$-yaw$

The relations between coordinate directions are summarized in Table B.2.

Table B.2: Relations between coordinate systems

$+Y_{XRCF}$	=	$-Y_{HRMA}$	=	$-X_{SAOsac}$	=	$-X_{DPSAOsac}$		
$+Z_{XRCF}$	=	$-Z_{HRMA}$	=	$+Y_{SAOsac}$	=	$-Y_{DPSAOsac}$		
$+X_{XRCF}$	=	$+X_{HRMA}$	=	$-Z_{SAOsac}$	=	$+Z_{DPSAOsac}$		
$+tilt_Y$	=	$-\theta_Y$	=	$+elmis_{SAOsac}$	=	$+elmis_{DPSAOsac}$	=	$+pitch$
$+tilt_Z$	=	$-\theta_Z$	=	$+azmis_{SAOsac}$	=	$-azmis_{DPSAOsac}$	=	$+yaw$

Appendix C

Quadrant Shutter Nomenclature

Terrance J. Gaetz

A quadrant shutter assembly mounted between the HRMA and the detectors allowed individual quadrants of individual mirror pairs (shells) to be examined. The quadrant shutter assembly was mounted on the same ground support equipment (GSE) as the HRMA so the shutter assembly followed the pitch/yaw motions of the HMRA. The quadrant shutters consisted of a set of 16 separately controllable opaque blades which could be placed in the beam to block X-rays reflected by quadrants of the mirror. The shapes of the blades were designed so that by having all but one shutter blade in the beam allows rays from a single quadrant of a single mirror pair to pass. This allowed access to any quadrant/mirror pair combination. The shutter locations were named after the cardinal directions at the XRCF: N(orth), T(op), B(ottom), S(outh). Individual shutters were sometimes referred to by using letter-number combinations indicating mirror quadrant and shell (*e.g.*, 3N or N3 for the North quadrant of shell 3). To simplify specification of shutter combinations in the CMDB, a code consisting of a string of 16 letters was used; each letter was either `o`, indicating that the quadrant was open, or `c`, indicating that quadrant closed (*i.e.*, the beam was blocked). The code specified shutter configurations in groups of four, one group of four per mirror pair, in the order: mirror pair 1, 3, 4, 6. Within a group of four for an individual mirror pair, the letters indicated the state of individual quadrant shutters, in the order T, N, B, S. For ease of reading, the `quad_shutter` aperture raytrace module requires a character (typically a space or underscore) separating each group of four quadrants. Thus, the state with all quadrant shutters closed except for the Bottom quadrant of shell 3 could be indicated by `3B`, `B3`, `ccccccoccccccccc` (CMDB), or `cccc_ccoc_cccc_cccc` (raytrace `quad_shutter` module).

Table C.1: Quadrant Shutter Nomenclature

Quadrant	Direction			Code
T	$+Z_{XRCF}$	$-Z_{AXAF}$	$+Y_{raytrace}$	`occc`
N	$-Y_{XRCF}$	$+Y_{AXAF}$	$+X_{raytrace}$	`cocc`
B	$-Z_{XRCF}$	$+Z_{AXAF}$	$-Y_{raytrace}$	`ccoc`
S	$+Y_{XRCF}$	$-Y_{AXAF}$	$-X_{raytrace}$	`ccco`

Appendix D

Appendix: HRMA Pointing at XRCF

Richard J. Edgar

D.1 Introduction

In this chapter we describe the HRMA pointing actuator system, and the method that was used to reconstruct to the best extent possible the actual pointing of the HRMA during each test at XRCF.

The HRMA pointing actuator system is described elsewhere (XC-05?) in much more detail. The HRMA was mounted on a table-like fixture in the vacuum tank at XRCF. Basically, the yaw motion was controlled by two screw-type actuators symmetrically placed at the forward (actuator 4) and aft (actuator 5) ends of this fixture, one of which gets longer and the other shorter by the same amount, to rotate the HRMA about a vertical axis passing through the node. The pitch motion is similar: there are two vertical actuators at the aft end of the fixture (downstream from the x-ray beam's point of view; actuators 7 and 8 on the near and far sides, respectively as seen from the control room) and one at the front (actuator 6). Nominal operations call for the forward actuator to shorten and the two aft actuators to lengthen in order to pitch the front of the HRMA down, rotating it about a horizontal axis through its node.

There is also an axial actuator (actuator 3) that can control the motion of the HRMA along the beam direction. This can be used to compensate for axial motions of the node (if any) generated by pitch and yaw maneuvers.

The HRMA Actuator Control System (HACS) software was intended to run the actuators in the above manner, and report the output of the encoders attached to each actuator, via the DLRS, to the data archive. It was often the case, however, that the hardware was not in optimal working condition, and so the actuators were controlled manually by EKC personnel, and troubleshooting efforts were concentrated (quite properly) on getting the hardware to work, and not, in many cases, on recording the details of the tests performed. Especially in Phase 1, therefore, the record is somewhat spotty, and sometimes altogether missing.

We have done what we could to reconstruct the sequence of events and come up with a best-guess set of HRMA pitch and yaw pointing values for each known test (delimited and designated by TRW ID glyphs).

D.2 Sources of Information

There are several logs, some hand-entered and some computer-generated, which contain information on the HRMA pointing. Some are indexed on time alone, and others have more identifying information in them, such as TRW ID's. It is therefore necessary to have a list of what tests were done, what TRW ID's were used, in what order, and at what start and stop times.

D.2.1 Test Order and Times

In many cases the Test Conductor log (TC log) contains all the necessary information about times and test identification, and can be parsed by an automated script. Perhaps 90% of the tests fall into this category. The archive group has done this parsing, and generated a list of start, stop and abort times for each TRW_ID which has the appropriate entries in the TC log. The times in the TC log were generated automatically, and some of the other entries are generated by scripts and other autonomous processes. Other entries are generated manually, and so the format varies, and in some cases there are typographical errors. This renders some sections of the TC log difficult to parse with an automated script. Manual inspection is required.

Also produced by the test conductors was a spread sheet known as the Time-lines, with (manually generated) local times of starting and stopping each test, and what the disposition of the test was (executed, aborted, skipped, etc.).

A third source of information is the (manually generated) Project/Telescope Scientist's log (PTS log). This contains comments on a test-by-test basis in most cases on what was happening, cursory results, failures, etc., and has proven invaluable.

A detailed manual inspection of the entire Test Conductor log was conducted, comparing it with the Time-lines, the PTS log, and the "DRAFT as-run CMDB" (calibration measurement data base). A sequential list of tests with approximate start and stop times was assembled. In some cases there are disagreements as to what TRW_ID to use for a given test or two tests conducted simultaneously (e.g. focal plane background/setup tests and BND beam maps), and so a modicum of intelligence is required for this task.

The tables themselves are available from the MST web page,

`http://hea-www.harvard.edu/MST/simul/simul-home.pl`

under "Facility Data."

D.2.2 Actuator Encoder Readouts

The readouts of the pitch and yaw actuator readouts were (sometimes) recorded in one of three sources:

- The `hrmapos` logs, generated by the HACS software and sent to the archive via the DLRS;
- The Test Conductor Logs, in messages sent from Kodak to the test conductor containing (manually entered) actuator values; and
- The Eastman Kodak Company logs (EKC logs), written in Microsoft Word by EKC personnel, containing (manually entered) times and actuator values.

The `hrmapos` logs are available only when the HACS software was being used to control HRMA pitch and yaw pointing. This time period covers about 20 hours on December 31, 1996 (the

beginning of Phase D), and nearly all of Phase 2 of XRCF testing (sub-phases F, G, and H). The contents of these data records include irig times, readouts of all actuators, and intended and actual pitch and yaw. Where these are available, they are used.

Where the `hrmapos` logs are not available, it is often the case that either the TC log or the EKC logs (or both) have entries recording actuator values. Both logs have manually entered actuator values, and are subject to typographical errors (mercifully quite rare). The time tags are also the times the values are recorded, not the time of the maneuver that changed them. Often, but not always, the actuator values are reported during the data-taking phase of the test they apply to, so a large majority of the tests can be associated with actuator values by taking the last set of actuator values prior to the test's end time. An even larger number of tests can be accommodated in this manner by presuming that the clock used in the EKC logs is about 1 minute slow, compared to the TC clock (which was irig-synchronized).

D.3 Initial Actuator Position (IAP)

There was considerable confusion early in Phase D of the XRCF testing about the relative pointing of the x-ray optics (the HRMA) and the optical XRCF Alignment Reference Mirror (the ARM-X). This, and the failure of the aft far pitch actuator, resulted in the issuance of multiple sets of "Initial Actuator Positions," i.e. a table of what the actuator readouts are when the telescope is pointed on-axis. Some of these were known later to be in error, and are superseded by later IAPs. In the case of the Phase 1 IAP5, it was eventually decided that the ARM-X alignment, IAP4, was closer to the truth than IAP5 (generated from x-ray data). IAP5 was used for most of Phase D, so there is a systematic error in pointing by one arcminute in yaw for most of the Phase D tests.

The IAP table given in Table D.1 is based on the one in Matthews (1997), updated and completed based on information mostly from the EKC logs. We have added entries for phase 2 (the bottom half of the table), phase 1C (first entry), and several IAP7c entries not in Matthews' table. The columns are:

- IAP: the identifier of the inital actuator position system. Note that names are re-used in phase 2.
- "true start": for those IAPs believed to be close to the truth, this is the starting IRIG time when they are effective.
- "start": the IRIG time when the IAP was established.
- "el" and "az": for phase 1D IAPs, this is the offset between the IAP and IAP4, which we ultimately chose as the truth.
- a3–a8: actuator readouts at pitch = yaw = 0.
- "comments": comments on alignment standard, etc.

D.4 Actuator Failures

Phase 1, sub-phase C of the testing (December 20–24, 1996) was conducted with the HRMA blocked in place, aligned optically to the ARM-X, as the pitch and yaw actuators were not yet ready for use. We have presumed that these pitches and yaws are zero, though x-ray evidence for this is lacking (or has not been examined in detail).

IAP	true start	start	el	az	a3	a4	a5	a6	a7	a8	comments
C	355/03:00:00	355/03:00:00	0	0							Dummy for phase C
IAP		364/18:00:00	0	0	105511	−1299	1732	−77341	−195144	−194671	original pre−vacuum IAP
IAP2		001/05:00:00	−1.07	−1.33	105511	−1299	1732	−209714	−327517	−302289	Initial failure IAP (calculated on encoder counts)
IAP3		001/12:15:00	−1.47	−0.51	108177	−4499	4919	−199949	−327517	−302289	X−ray beam scans (−0.4 El, 0.918 Az wrt IAP2)
IAP4	364/18:00:00	002/18:22:00	0.00	0.00	105513	−9000	4388	−235959	−326740	−302863	Vacuum alignment to ARM−X
IAP5		005/16:11:00	0.00	−1.00	105513	−5098	503	−235959	−326740	−302863	Autocol. from Source End −1 min Az bias from IAP 4 based on X−ray data
IAP6	026/08:08:00	026/08:08:00	0.00	−1.00	0	0	0	0	0	0	Same as IAP5 just encoders were zeroed with rack shut off
7−air		027/20:00:00			105512	−7124	2621	−690294	0	0	Aligned ARM−X air, GSE at 70 degrees F
IAP7		028/15:01:00			109977	−6410	1907	−674729	0	0	Aligned ARM−X, GSE at 67 degrees F
IAP7a		029/16:52:00			109977	−9007	4504	−674729	0	0	Aligned ARM−X, GSE @ 55 degrees F (47 arcsec in yaw from IAP7a)
IAP7b		029/20:32:00			108450	−9007	4504	−680054	0	0	Aligned ARM−X, GSE @ 54 degrees F (7 arcsec in pitch from IAP7a)
IAP7c1		031/19:34:00			106688	−9006	4500	−686918	0	0	+32 arcsec pitch wrt ARM−X (filled in from EKC log 031/19:34)
IAP7c2	027/20:00:00	031/21:07:00			110914	−9006	4500	−672068	0	0	ref: Texter via O'Dell 9 Jun 1998 e−mail (filled in from TC log 031/21:29:25)
IAP8	040/09:30:00	040/09:30:00			0	0	0	0	0	0	Aligned ARM−X, GSE @ 52.5 (encoders not zero at home)
IAP1	051/17:38:00	051/17:38:00			−52184	253479	95507	−49082	−286211	−286111	YPP=−.4411" ZPP=−.2285"
IAP2	059/09:14:00	059/09:14:00									first mention of IAP2
IAP3	059/17:38:00	059/17:38:00									see EKC log this date
IAP4	064/20:38:00	064/20:38:00									see EKC log this date
IAP5	079/06:53:00	079/06:53:00			−50569	253282	95862	−47306	−276427	−276278	see EKC worksheet
IAP6	100/08:00:00	100/08:00:00									see EKC log this date
IAP5	100/09:30:00	100/09:30:00			−50569	253282	95862	−47306	−276427	−276278	see EKC log this date (return to IAP5)
IAP7	109/14:30:00	109/14:30:00			−48718	253282	95901	−42699	−278746	−278611	see EKC log this date

Table D.1: IAP table for both phases.

The first day of phase D, at about 22:57 GMT on December 31, 1996, the aft far pitch actuator (actuator 8) got stuck in a non-zero pitch position. After much consultation, the decision was made to keep the aft near pitch actuator matched with the far one, and (after finishing a set of pitch alignment tests then in progress) shorten the forward pitch actuator (number 6) to align to the beam. This resulted in the entire telescope being $\sim$ 500 microns lower than the design position. Phase D was then conducted using pitch fixed at zero, though many non-zero yaw tests were performed. The zero-reference for the pitch was apparently taken with respect to the ARM-X.

For a period of about 3–4 days following the actuator failure, no data are available about the pointing of the mirror. We have therefore had no choice but to adopt the CMDB pitches and yaws as "as-run" values, and corrected them to "true" values using the azimuth and elevation offsets from IAP4 from the IAP table. This presumes that EKC was successful in executing the planned CMDB maneuvers.

A similar difficulty was encountered in phase E, but the workaround consisted of fixing both aft pitch actuators, and using the forward pitch actuator to pitch the HRMA, rotating not about the node (as designed) but about the stuck actuators. This results in vertical motion of the node, and so the image moves vertically by about 323.9 microns per arcminute of pitch. In most cases this motion was not recorded in the FOA tables of the HXDS equipment, and so the `calcstage4` script cannot correctly compute the Z distance from the aperture center to the beam. Pitch corrections have been applied to the data when appropriate (notably wing scans).

It appears to this author [RJE] that the pitch and yaw actuators and the HACS software worked as designed throughout phase 2 of the XRCF testing. Data from the `hrmapos` log is available for all but a few of the phase 2 tests, and we have used them almost exclusively for phase 2.

D.5 Data Processing

We have constructed a script that parses the EKC logs (turned into ASCII files by Terry Gaetz, saving them as text from Microsoft Word, running under Citrix, a Windows emulator) and returns an RDB table containing times and actuator values. A similar script parses the actuator values out of the TC log. These are then merged with the `hrmapos` log and the table of TRW_ID start & stop times, augmented with `HRMA_pitch` and `HRMA_yaw` fields out of the DRAFT as-run CMDB (the version dated 26 January 1999). The results are sorted on time, using the end time for each TRW_ID.

Given actuator values, it is possible to compute pitch and yaw, using a recipe and formulae from Gary Matthews' excellent document "Encoder Values, IAP, and What It Means To Me" [Matthews (1997)]. This document describes the geometry, the operation of the actuator system with a stuck actuator, and how to compute HRMA pointing given actuator readout values.

The output of these scripts is a table of pitch and yaw as a function of time and TRW_ID, sometimes with multiple sources and sometimes with no source at all (other than the CMDB). As-run pitches and yaws can then be compared to as-ordered pitches and yaws from the CMDB, and discrepancies noted and investigated. In a few dozen cases, there are obvious typographical errors (extra commas, missing or duplicated digits, etc.), or time errors (caused in general by reporting the values after the following test had begun). These were corrected, by a script which runs on the fly during the log file parsing and table generation process. The remaining tests which differ by more than a few hundredths of an arcminute are listed in §D.6, with conjectures about the cause of the discrepancy.

Another script was then developed that took the above merged log, selected one source for each test, recorded the best-available values for the pitch and yaw actuators, and then used two IAP

bases to compute the pitch and yaw. These then represent the "as-run" values (what the operators on the floor at the time of the test would have seen), and the "true" values (what we believe with benefit of hindsight were the pointings relative to the facility optical axis). Also included for reference were the "planned" values from the CMDB.

Work is in progress to analyze other x-ray data to obtain better values for the offsets between the mirror axis and the facility optical axis. Data which bear on the question include some of the line shape function tests (slit scans of the focused image) and off-axis images, whose detailed structure provides much information on the alignment and pointing of each shell of the telescope.

D.6 Discrepant Tests

There were a few tests where the final results show a discrepancy of more than 0.04 arcminutes between the CMDB planned pitch and/or yaw, and the as-run values. These are listed below for reference, with my opinions [RJE] about the cause of the discrepancy.

D.6.1 Phase 1

- Tests D-IXH-PI-3.00[67][ab] were changed on the floor from $(p, y) = (0, 0)$ to yaws of ± 1 arcminute.
- Tests D-LXH-3D-20.00[89] requested yaw of 1 arcmin, and seem to have $-1'$ with respect to the then-current IAP5. Because of the $1'$ yaw difference between IAP5 and IAP4 (believed to be correct), this gives actual yaws of $-2'$ This seems to be a mistake on the part of EKC.
- Test D-LXH-3D-30.001 requested yaw of $+1'$ and was run with zero with respect to the then-current IAP5. As above, this results in actual yaw of $-1'$
- Tests E-IXH-PI-52.00[1234] were off-axis single-shell `hsi` images. The planned pointing was $(17.6777, 17.6777)$, but the pitch actuator pegged when it reached $16.437'$ with respect to IAP8. The tests were run in this position.
- IAP7 was known to be "off" by 15 arcsec in yaw, but was used anyway. This results in a series of tests from irig time 028/21:11 to 029/10:40 with as-run yaw 0.25 arcmin larger than the planned yaw. These tests include carbon EIPS tests E-IXH-PI-13.001, E-IXH-SF-12.001, the E-IXF-PW-2 series, and the E-IXS-MC-16 series.
- There appears to be a sign error in reporting actuator A3 at 031/03:58. If something is done with the axial position of the HRMA, this should be investigated. Tests E-IXH-SF-15.01[1-4] and E-IXH-PI-6.003 are the only ones impacted.

D.6.2 Phase 2

- IAP1 was a bit off, but this was known at the time, so the as-run pitch was $0.280'$ too high, and the as-run yaw is $0.055'$ too high. But the actuals are right on.
- There is an error or bug in the `hrmapos` data for test F-I2C-EA-11.002a, at irig time 062/10:40. This causes the as-run pitch to be erroneously reported as zero. The actual pitch is correct, however.

- On day 083 a change was made on the floor with the concurrence of the PTS and TC. G-IHS-EA tests with CMDB pitches of ±2.9, 2.95, or 3.0 arcmin were run with the same sign, but with the absolute value of the pitch equal to 2.68′
- On day 088 the IRIG clock problem makes synchronizing the `hrmapos` data with the test list very hard. The correct moves were (mostly) done in the correct order, so application of a time offset yields the plausible result that everything was done as planned.
- On day 093 there were changes made in tests G-IHS-EA-60.032 and 036. The CMDB yaw of 14.8′ was changed to 13.8′
- On days 094 through 096 there were occasional changes of sign in pitch or yaw, attributable to EKC operator error (in my opinion). The tests in question are G-IHI-EA-3.109, 3.067, 4.016, 3.075, and 3.083.
- Nine tests in the 99 series in phases G and H have erroneous pitch and/or yaw values in the CMDB. This is not surprising since 99-series tests are created on the floor and the CMDB is reconstructed after the fact.
- The test conductor ordered various non-CMDB pitches and yaws on day 112, in tests H-IAS-PI-7.010, 015, 011, 016, 002, 005, and H-HAS-PI-1.012.

D.7 The Pitch Problem and its Effect on Wing Scan Data

D.7.1 History of the Pitch Problem

For the XRCF data, the pinhole positions relative to the focus were calculated using `calcstage4`. In the `calcstage4` calculation the pinhole location relative to the focus is determined by using the stage logs and the contemporaneous focus position appropriate to the shell(s) in use is determined from the FOA tables. The distance (X, Y, Z) of the pinhole from the focus is evaluated by differencing the two sets of values:

$$X = X_{pinhole} - X_{focus} \tag{D.1}$$
$$Y = Y_{pinhole} - Y_{focus} \tag{D.2}$$
$$Z = Z_{pinhole} - Z_{focus} \tag{D.3}$$

Note that currently the only information that `calcstage4` has about the focus position is that found in the FOA tables; if the FOA table is incorrect about where the focus happens to be, then `calcstage4` will get the wrong answer.

Because an aft vertical actuator was stuck during phase 1E, pitch motions during phase 1E were carried out using only the forward vertical actuator. This resulted in a pitch motion about a point other than the HRMA node, so any pitch motions caused the HRMA node (and hence, the finite conjugate focal point) to shift vertically. These vertical shifts in focus location can be large ($\lesssim 1$ mm) compared to the size of the smallest pinhole used in the wing scans (1 mm diameter). It is therefore important to understand the relation between HRMA pitch moves and the FOA tables.

In order to determine how the experiment was really performed, the XRCF 2nd Floor Shift Reports, the Project Science/Telescope Scientist logs, and the EKC shift reports were examined. The first wing scan experiment in Phase 1E was a wing scan of quadrant 6B with an EIPS C-Kα source and with the HRMA pitched by $-1.88'$. A set of Y-scans was performed (E-IXF-PW-2.001–5, day 028/029) followed by a set of Z-scans (E-IXF-PW-2.010–13, day 029). During the the first

sequence of 1 mm pinhole Y-scan measurements (E-IXF-PW-2.001) it was discovered that the scan was approximately 500 μm too low. It was realized that this was because the pinhole positions were calculated relative to the FOA values for the focus position and that the FOA value was now offset from the real focus of the pitched HRMA. In order to compensate for this, the FOA table was adjusted by 504 μm in Z for the rest of the quadrant 6B C-Kα wing scans (4 mm, 10 mm, 20 mm, 35 mm Y-scans, 1 mm, 4 mm, 10 mm, 20 mm Z-scans) based on a beam centering with the 70 μm pinhole. Following the C-Kα wing scans, the FOA values were reset back to the nominal values. The actual pitch correction should have been 609 μm in Z, so the FOA table correction was about 105 μm shy of the appropriate correction. Consequently, the `calcstage4` values for the distance of the pinhole from the focus were nearly correct for these pinholes, but additional $\Delta Z_{focus} = +105$ μm pitch correction needs to be applied. (The additional pitch correction we actually applied was $\Delta Z_{focus} = +94$ μm; the effect of the remaining 11 μm discrepency is negligible for these wing scan measurements.)

It was initially suggested that a similar FOA adjustment be made for all the subsequent HRMA pitch moves. It was decided instead to aim for an automated approach whereby the pitch correction would be applied to the pinhole locations during the CMDB processing; these fixes were incorporated into the software during shift A, 1997 Feb 2 (day 033). Note that for the period between the end of the 6B C-Kα wing scans on day 029 and CMDB fixes of day 033, any pitch corrections would have been entered manually into the pinhole locations files.

Node Shift in HRMA Pitch Moves

Because the HRMA pitch motions were performed with the aft vertical actuators fixed, the actual pitch motion was a rotation about the line defined by the aft vertical actuator locations. This produced a vertical shift of the HRMA node which displaced the focal point at the instrument plane.

In comparing the raytraces to the XRCF pinhole data, the XRCF Z coordinates relative to the contemporary FOA were corrected for the shift in the focus by subtracting off a pitch correction. To first order, the vertical shift in the node is the product of the sine of the pitch angle change and the axial offset between the fixed actuator station and the node. The axial distance between the node and the actuator is 43 inches (= 1092.2 mm), from which

$$\Delta Z_{node} = -1092.2 \ \sin \Delta\theta_{pitch} \text{ mm} \tag{D.4}$$

where $\Delta\theta_{pitch}$ is the change (in radians) in the HRMA pitch. In the thin lens approximation, the focus moves by

$$\Delta Z_{focus} = \frac{\Delta Z_{node}}{D_{source}} \times (D_{source} + D_{focus}) \tag{D.5}$$

where $D_{source} = 527297$ mm is the distance between the HRMA node and the X-ray source, and $D_{focus} = 10256$ mm is the nominal distance from the HRMA node to the finite conjugate focus. In making the above estimates, the node was assumed to be 18.1 mm aft of CAP "Datum A". Substituting for the various distances, the vertical shift in focus is approximately:

$$\Delta Z_{focus} = -1.1134 \times 10^6 \sin\theta_{pitch} \, \mu\text{m} \tag{D.6}$$

or,

$$\frac{\Delta Z_{focus}}{\Delta\theta_{pitch}} \simeq -323.9 \ \mu\text{m/arcmin}. \tag{D.7}$$

Pitch Corrections Applied

Most of the wing scans with HRMA at nonzero pitch were performed with the FOA table values appropriate to HRMA at zero pitch; the requisite pitch corrections were applied to the requested pinhole locations. `calcstage4` calculates the pinhole location based on the stage logs; the resulting physical location for the pinhole will be calculated correctly. In analyzing the wing scans, the distance of the pinhole center from the current focal point is needed; the `calcstage4` evaluation of the focus position is based on the FOA entry and that is incorrect because of the HRMA node shift (and resultant shift in focus). `calcstage4` reports the difference between the pinhole location and the focus position, so a pitch correction needs to be *subtracted* from the `calcstage4` Z value. Based on equation (Eq. D.6), the pinhole Z value reported by `calcstage4` was corrected by

$$\Delta Z_{corr} = Z - \Delta Z_{focus}. \tag{D.8}$$

An exception was the wing scan for shell 6B for which the FOA was partially compensated for the pitch-induced focus change (§D.7.1); in this case, the Z values were corrected by -94 μm to account for the slight under correction of the FOA adjustment.

D.7.2 Yaw Reference Error

Early in Phase 1D, an attempt was made to determine the HRMA X-ray bore sight by using the variation of effective area as the HRMA was pitched and yawed. At the time, the presence of the coma-free decenter error in the HRMA mirror alignment was not yet known; this error causes the off-axis effective area profiles to be non-symmetric about the optical axis. This led to an initial confusion as to alignment of the mirror bore sight to the facility optical axis; the reference axis for pitch and yaw ended up being offset by about $1'$ in yaw starting at IAP 5 (day 005, 16:11) through the end of phase 1D. Consequently, the actual yaws ended up being offset by $1'$ from the requested values, and because of this, some yaw values in Table 14.3 differ from the requested CMDB values. This does not directly affect the XRCF data reduction; the yaws were off, but the FOA was determined based on the contemporary yaw zero reference. However, this offset does need to be included in the comparison raytraces.

Appendix E

HRMA Dimensional Data

Terrance J. Gaetz

In this appendix we gather together various mechanical dimensions relevant to the HRMA design and performance. Where possible, measured, as-built dimensions are provided; otherwise, the dimensions are obtained from the mechanical drawings, or from EKC technical notes. In some cases, the dimensions need to be built up from the component drawings.

E.1 HRMA Axial Datum Locations

The HRMA Central Aperture Plate (CAP) is the fundamental reference for HRMA buildup. High precision datums were machined at three locations on the paraboloid side (Datum -A-) and on the hyperboloid side (Datum -D-). These were to be machined to within 0.5 mil and the -A- and -D- Datums were to be parallel to within 1 mil. The design CAP -A- to -D- thickness is $1.968^{+.000}_{-.010}$ inches (drawing EK5010-001). The measured as-built CAP Datum -A- to Datum -D- thickness is 1.965 inches (Discher (1996)).

Working forward from the Center Aperture Plate (CAP), the major assemblies relevant to the axial positioning of the HRMA optics and the associated baffles are

- HRMA Outer Cylinder (attached to CAP; interfaces with the Forward HRMA Structure [FHS] and the Aft HRMA Structure [AHS]).
- Forward HRMA Structure (FHS); includes the Forward Heater Plate (FHP).
- Thermal Precollimator; interfaces to the FHS. The precollimator includes ten thermal baffles; the forwardmost baffle includes tantalum and is also a critical X-ray baffle.

Working aftward from the CAP, the major assemblies relevant to the axial positioning of the HRMA optics and the associated baffles and the Fiducial Transfer System Periscope are (see Figure E.1):

- HRMA Outer Cylinder (attached to CAP; interfaces with the FHS and the AHS).
- Aft HRMA Structure (AHS); interfaces to the HRMA Outer Cylinder and includes the Aft Heater Plate (AHP) and 5 thermal baffles.
- Fiducial Transfer System Periscope.

The axial datum locations are summarized in Figure E.1, adapted from Discher (1996). The dimensions have been recalculated, based on the as-measured dimensions, taking $X = 0$ at the CAP Datum -A- plane.

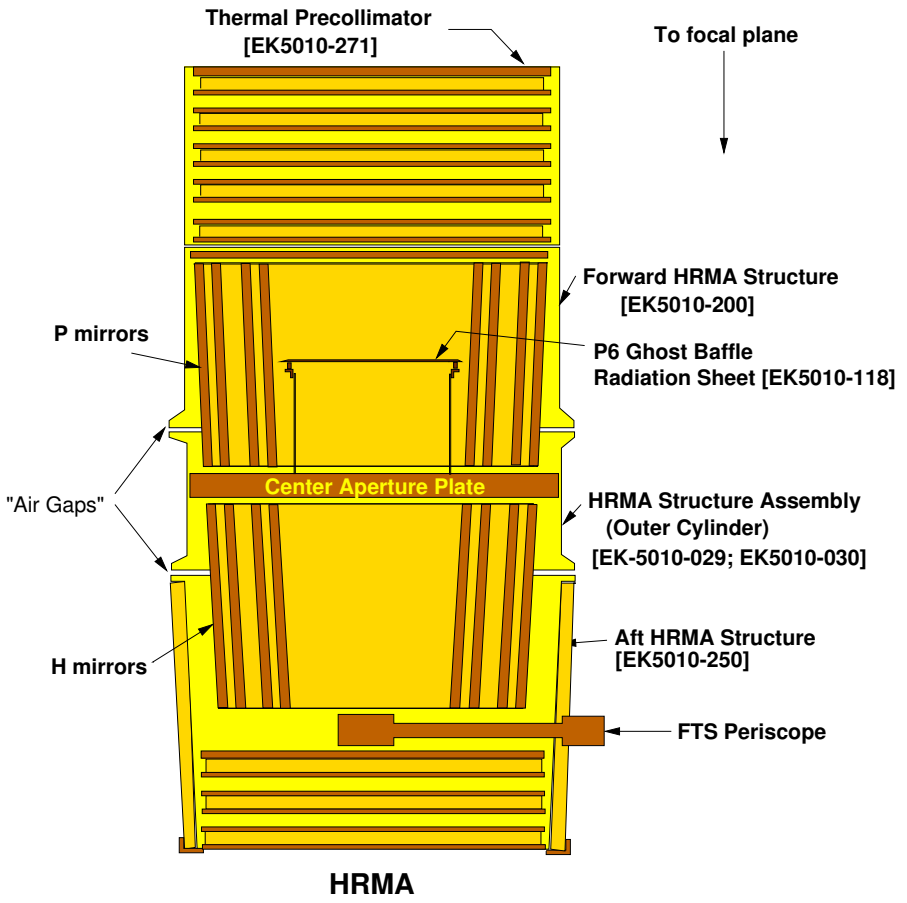

$Revision: 1.2 $ $Date: 1999/07/15 20:26:15 $

Figure E.1: Schematic of relevant HRMA assemblies

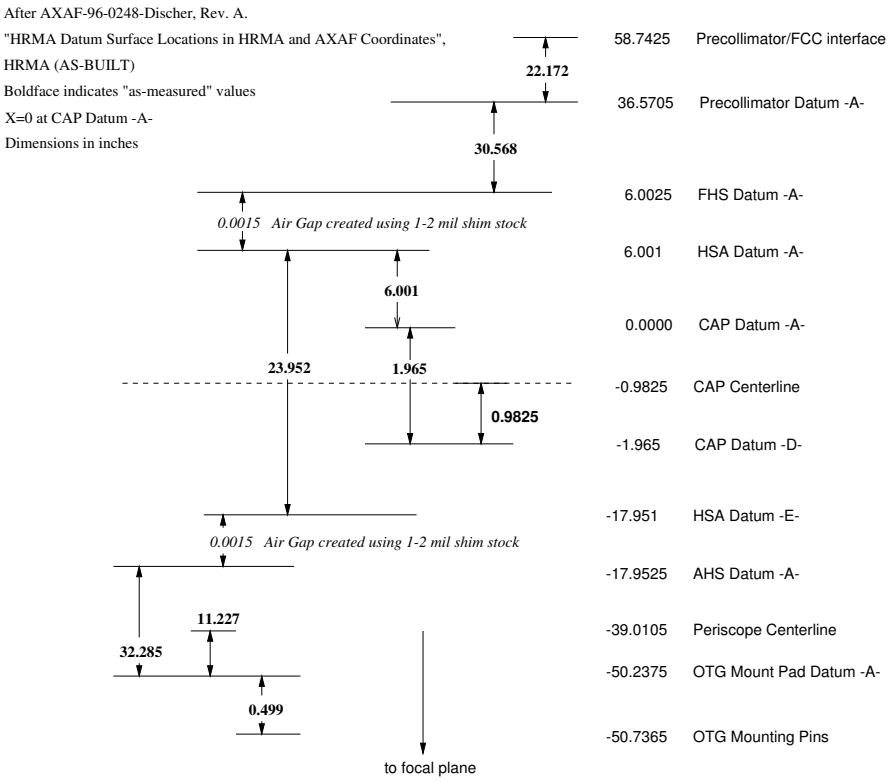

$Revision: 1.2 $ $Date: 1999/07/15 18:51:50 $

Figure E.2: HRMA Axial Datum Locations. After Discher (1996). Discher incorrectly swaps the labels for CAP Datum -A- and -D-; this has been corrected. Datum -A- is on the P-side of the CAP, and Datum -D- is on the H-side of the CAP.

E.1.1 HRMA Baffle Plates

The basic properties of the HRMA baffle plates are listed in Table E.1. These are all thermal baffles used in controlling the temperatures in the HRMA interior. Note that Precollimator Baffle Plate 1 also serves as a critical X-Ray baffle, and helps to determine the ghost imaging and vignetting properties of the HRMA.

Drawing	Precollimator & FHS plates	AHS plates	axial thickness (inches)	composition
EK5010-208	#1		0.105	GREP (T300) + Tantalum [1]
EK5010-221	#2–#8		0.075	GREP (T300)
EK5010-207	#9, #10	#2–#5	0.050	GREP (P75)
EK5010-209		#6	0.075	GREP (P75)
EK5010-210	FHP	AHP	0.250	GREP (P75)

[1] 0.05" GREP + 0.005" Ta + 0.05" GREP

Table E.1: Baffle plate information

E.1.2 P6 Ghost Baffle

In order to control the ghost imaging performance of the HRMA, an additional baffle is placed in the P6 interior space; Figure E.1.2 is a schematic drawing of the baffle. A 5 mil thick tantalum *radiation sheet* is attached to an aluminum support structure which in turn is mounted directly to the P side of the Center Aperture Plate.

E.1.3 HRMA Structure Assembly (HSA)

The HRMA Structure Assembly is detailed in drawings EK5010-029 (HRMA Outer Cylinder) and EK5010-030 (HRMA Structure Assembly). The primary axial datum is Datum -A- at the forward edge of the HSA; this mounts to the Forward HRMA Structure at FHS Datum -A-. The distance from HSA Datum -A- to the aft mounting points for the outer cylinder is nominally 23.950 ± 0.010 inches; the measured distance is 23.952 inches (EK5010-029 S/N#02; see Discher (1996)) The measured distance from CAP Datum -A- to HSA Datum -A- is 6.001 inches (Discher (1996); note that Discher labels CAP Datum -A- as -D- and *vice versa*).

E.1.4 Forward HRMA Structure (FHS)

Datum -A- for the Forward HRMA Structure (FHS) is at the aft mounting plane. The FHS Datum -A- plane is separated from the HSA Datum -A- plane by an air gap created using 1–2 mil shim stock; in the following we take the gap to be 1.5 mil.

The nominal axial length of the FHS from Datum -A- to the forward mounting points (where the FHS mounts to the thermal precollimator) is 30.565 inches (EK5010-200 sheet 1); the measured distance from FHS Datum -A- to Precollimator Datum -A- (aft of the Precollimator) is 30.568 inches (Discher (1996)).

The axial location of the Forward Heater Plate relative to FHS Datum -A- can be obtained from drawing EK5010-200; Figure E.1.4 is a schematic version of the drawing. The forward edge of the Forward Heater Plate (FHP) is 1.795 inches aft of the forward edge of the Forward HRMA Structure (Section H-H of drawing EK5010-200). The FHP is constructed from P75 Graphite Epoxy (GREP) and is 0.25 inches thick axially (EK5010-210). Using the HRMA datum surface

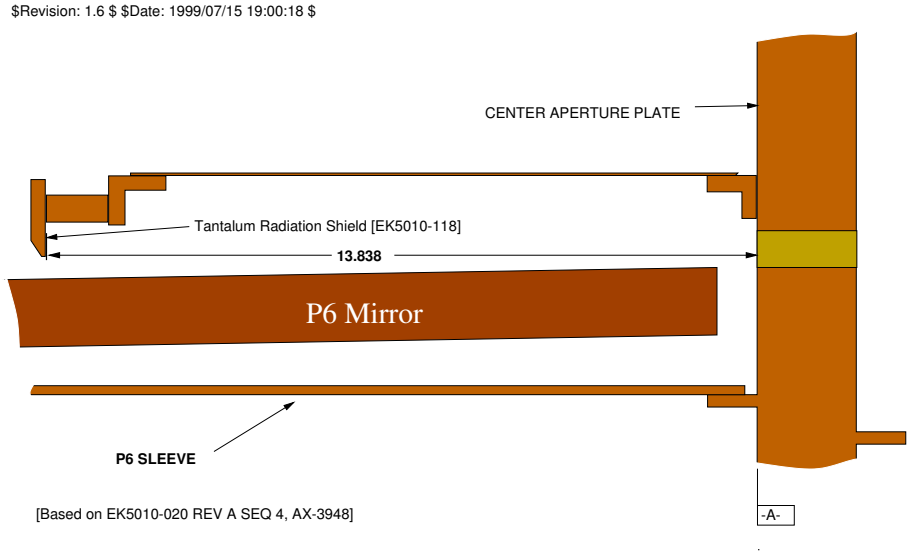

Figure E.3: Schematic of the P6 Ghost Baffle, based on drawing EK5010-020, Rev A, Seq 4. All dimensions are in inches.

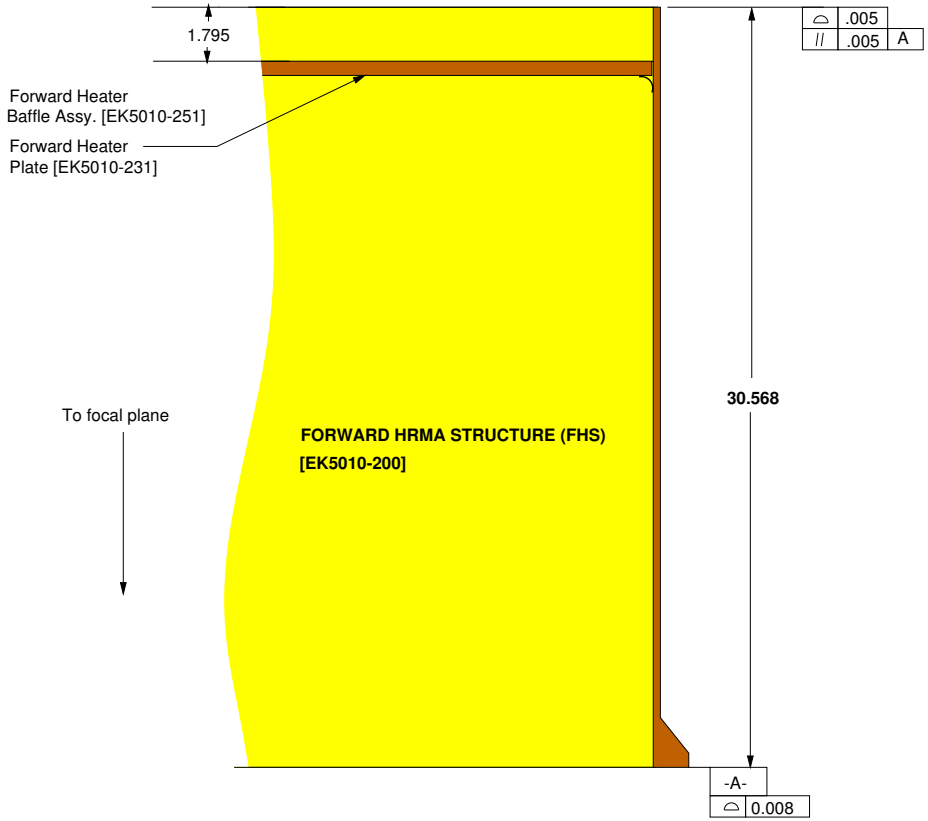

Figure E.4: Schematic of the Forward HRMA Structure (based on drawing EK5010-200) including dimensional information. All dimensions are in inches.

locations (Figure E.1) the axial location of the forward ($+X$) side of the Forward Heater plate is calculated in Table E.2; the position is compared against the design in Table E.3.

X_{fwd} [1] (inches)	Calculation (inches)	Baffle Plate
34.7755	36.5705 − 1.795	Forward Heater Plate

[1] Relative to CAP Datum -A-.

Table E.2: FHS baffle plate axial positions

Baffle Plate	X_{fwd} (inches)	$X^{[2]}_{fwd,corr}$ (inches)	X_{Casey} [3] (inches)	$X_{fwd,corr} - X_{Casey}$ (inches)
FHP	34.7755	35.758	35.745	+0.013

[1] Corrected for 1/2 CAP Datum -A- to -D- distance
[2] Design value (Casey (1994))

Table E.3: FHP as-built axial position *vs.* design.

E.1.5 Thermal Precollimator

The (thermal) Precollimator mounts to the forward edge of the Forward HRMA structure. The axial length of the Precollimator is 22.170 inches (EK5010-271); the measured distance from Precollimator Datum -A- to the Precollimator to Forward Contamination Cover interface is 22.172 inches (Discher (1996)).

The Precollimator includes ten baffle plates, the forwardmost one of which also serves as a critical X-ray baffle. Based on Section G–G of drawing EK5010-271, the distances from Precollimator Datum -A- to the aft side of of the plates in baffle assemblies #4, #6, #8, and #10 are 14.855, 10.045, 5.235, and 0.475 inches, respectively. In addition, the distance from the foward edge of one plate to the aft edge of the next (forward) plate is 2.320 ± 0.010 inches. Figure E.1.5 is a schematic version of drawing EK5010-271. From these dimensions, using the HRMA datum surface locations (Figure E.1) together with the plate thickness information (Table E.1) we can reconstruct the locations of the forward ($+X$) faces of the Precollimator baffles; see Table E.4. These axial positions are compared to those in the original design (Casey (1994)) in Table E.5.

E.1.6 Aft HRMA Structure (AHS)

Datum -A- for the Aft HRMA Structure (AHS) is at its forward mounting plane; it attaches to the HRMA Structure Assembly at the HSA Datum -E- plane. The AHS Datum -E- plane is separated from the AHS Datum -A- plane by an air gap created using 1–2 mil shim stock; in the following we take the gap to be 1.5 mil.

The Aft HRMA Structure contains six baffle plates, labeled AHP (Aft Heater Plate), 2, 3, 4, 5, and 6. The axial locations of the AHS baffle plates can be obtained from drawing EK5010-250; Figure E.1.6 is a schematic version of the drawing. The basic dimensions are summarized in Table E.6; these can be combined with HRMA datum surface locations (Figure E.1) and baffle plate thicknesses (Table E.1) to get the axial positions of the forward ($+X$) faces of the AHS baffle plates (Table E.7); in Table E.8, these values are compared against the design values.

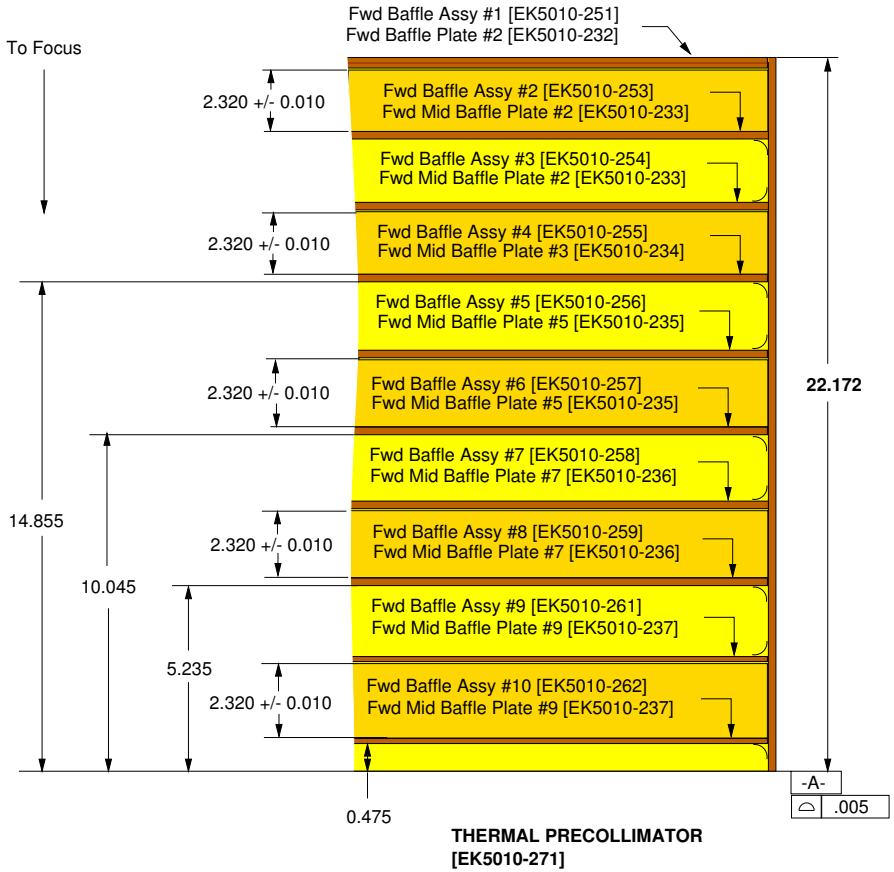

Figure E.5: Schematic of the Thermal Precollimator (based on drawing EK5010-271, the Baffle Assembly drawings EK5010-252–259, EK5010-261–262, and Discher (1996)). All dimensions are in inches. See Table E.14 for the baffle nomenclature.

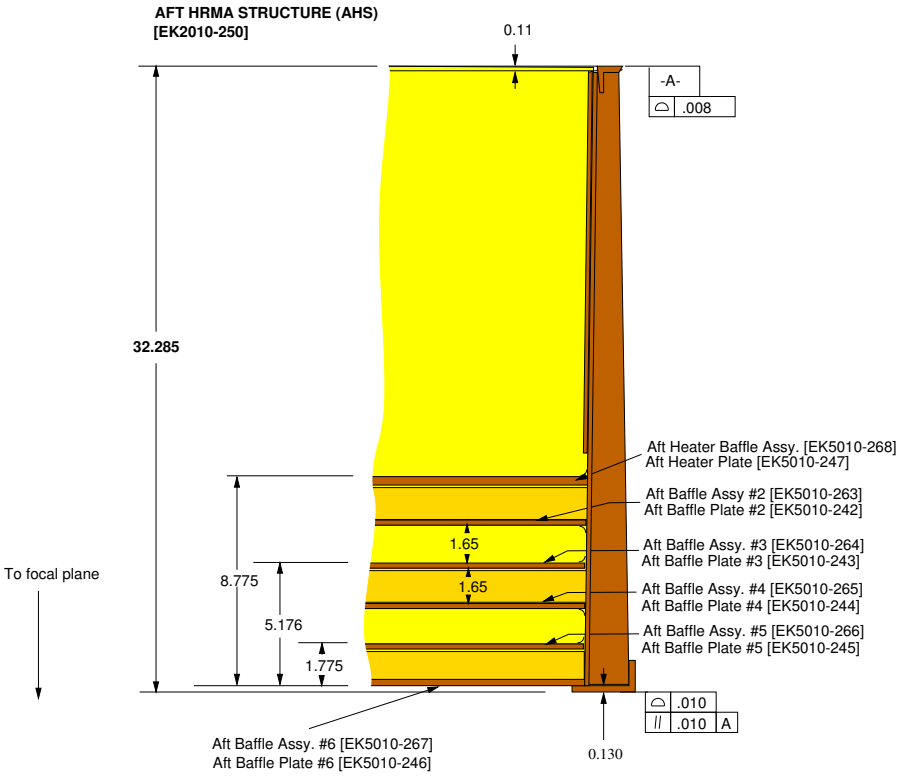

$Revision: 1.4 $ $Date: 1999/07/15 20:18:59 $

Figure E.6: Schematic of the Aft HRMA Structure (based on drawing EK5010-250 sheet 5) including dimensional information. All dimensions are in inches. See Table E.14 for the baffle nomenclature.

X_{fwd} [1] (inches)	Calculation (inches)	Baffle Plate[2]
58.7425	36.5705 + 22.172	Precollimator plate #1
37.0955	36.5705 + 0.475 + 0.050	Precollimator plate #10
41.8805	36.5705 + 5.235 + 0.075	Precollimator plate #8
46.6905	36.5705 + 10.045 + 0.075	Precollimator plate #6
51.5005	36.5705 + 14.855 + 0.075	Precollimator plate #4
39.4655	37.0955 + 2.320 + 0.050	Precollimator plate #9
44.2755	41.8805 + 2.320 + 0.075	Precollimator plate #7
49.0855	46.6905 + 2.320 + 0.075	Precollimator plate #5
53.8955	51.5005 + 2.320 + 0.075	Precollimator plate #3
56.3175	58.7425 − 2.320 − 0.105	Precollimator plate #2

[1] Relative to CAP Datum -A-.

[2] See Table E.14 for the baffle nomenclature.

Table E.4: Precollimator baffle plate axial positions

E.2 HRMA Mirror Spacing

A critical aspect of the HRMA design is the positioning of the mirrors relative to the CAP datums. The P to H optic separation controls the influence of symmetric errors, and the relative P to H positioning for different shells controls the axial parfocalization. The mirror axial positions were measured during HRMA assembly and alignment by gauging from CAP reference Datum -A- (in the case of the P optics) and Datum -D- (in the case of the H optics). Figure E.7 is a schematic of the mirror positioning relative to the CAP, and Table E.9 summarizes the measurements.

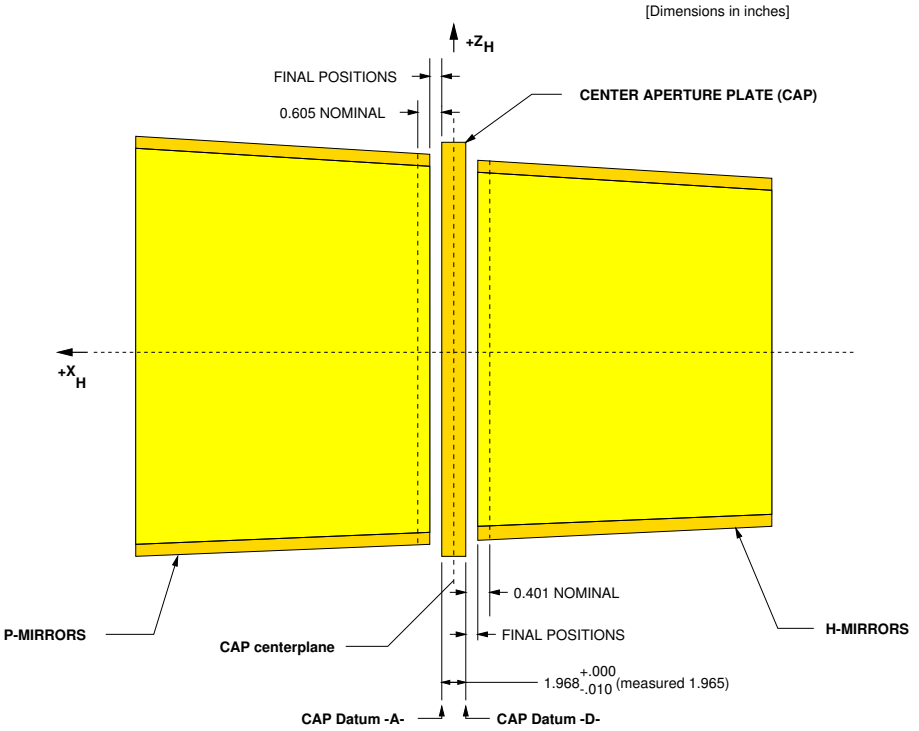

Figure E.7: Schematic of HRMA mirror positions. Adapted from a K. A. Havey (EKC) schematic."

Baffle Plate[1]	X_{fwd} (inches)	$X^{[2]}_{fwd,corr}$ (inches)	X_{Casey} [3] (inches)	$X_{fwd,corr} - X_{Casey}$ (inches)
#1	58.7425	59.725	59.710	+0.015
#2	56.3175	57.300	57.280	+0.020
#3	53.8955	54.878	54.875	+0.003
#4	51.5005	52.483	52.470	+0.013
#5	49.0855	50.068	50.065	+0.003
#6	46.6905	47.673	47.660	+0.013
#7	44.2755	45.258	45.255	+0.003
#8	41.8805	42.863	42.850	+0.013
#9	39.4655	40.448	40.445	+0.003
#10	37.0955	38.078	38.065	+0.013

[1]See Table E.14 for the baffle nomenclature.
[2]Corrected for 1/2 CAP Datum -A- to -D- distance
[3]Design value (Casey (1994)); baffle thickness ignored.

Table E.5: Precollimator as-built baffle plate axial positions *vs.* design.

X_{fwd} (inches)	Calculation (inches)	Aft HRMA Structure distances[1]
32.100	$32.285 - 0.11 - 0.075$	AHS Datum -A- to fwd edge of plate #6
32.175	$32.285 - 0.11$	AHS Datum -A- to aft edge of plate #6
1.775		aft edge plate #6 to fwd edge plate #5
5.175		aft edge plate #6 to fwd edge plate #3
8.775		aft edge plate #6 to fwd edge Aft Heater Plate (AHP)
1.65		aft edge plate #3 to fwd edge plate #4
1.65		fwd edge plate #3 to aft edge plate #2

[1]See Table E.14 for the baffle nomenclature.

Table E.6: AHS baffle plate axial information

X [1] (inches)	Calculation (inches)	Baffle Plate[2]
−50.0525	$-17.9525 - 32.100$	Aft HRMA Structure plate #6 (fwd)
−50.1275	$-17.9525 - 32.175$	Aft HRMA Structure plate #6 (aft)
−41.3525	$-50.1275 + 8.775$	Aft Heater Plate (fwd)
−48.3525	$-50.1275 + 1.775$	Aft HRMA Structure plate #5 (fwd)
−44.9525	$-50.1275 + 5.175$	Aft HRMA Structure plate #3 (fwd)
−46.6525	$-44.9525 - 0.050 - 1.650$	Aft HRMA Structure plate #4 (fwd)
−43.2525	$-44.9525 + 0.050 + 1.650$	Aft HRMA Structure plate #2 (fwd)

[1]Relative to CAP Datum -A-.
[2]See Table E.14 for the baffle nomenclature.

Table E.7: AHS baffle plate axial positions

Baffle Plate[1]	X_{fwd} (inches)	$X^{[2]}_{fwd,corr}$ (inches)	X_{Casey} [3] (inches)	$X_{fwd,corr} - X_{Casey}$ (inches)
AHP	−41.3525	−40.370	−40.355	−0.015
#2	−43.2525	−42.270	−42.255	−0.015
#3	−44.9525	−43.970	−43.955	−0.015
#4	−46.6525	−45.670	−45.655	−0.015
#5	−48.3525	−47.370	−47.355	−0.015
#6	−50.0525	−49.070	−49.055	−0.015

[1] See Table E.14 for the baffle nomenclature.
[2] Corrected for 1/2 CAP Datum -A- to -D- distance
[3] Design value (Casey (1994))

Table E.8: Aft HRMA Structure as-built baffle plate axial positions *vs.* design.

Mirror	Measurements						Specs	
	A1 (inch)	A2 (inch)	A3 (inch)	Average (inch)	Average (mm)	final rel. to target[4]	Target[1] (inch)	Axial shift[2] (inch)	Nominal (target±shift)
P1	0.2165	0.214	0.215	0.2152	5.466	−0.0048	0.220[3]	0.385 closer to CAP[3]	0.605
P3	0.6147	0.6143	0.6145	0.6145	15.608	0.0005	0.614	0.009 away from CAP	0.605
P4	0.757	0.755	0.7555	0.7558	19.197	−0.0002	0.756	0.151 away from CAP	0.605
P6	0.944	0.943	0.9435	0.9435	23.965	0.0005	0.943	0.338 away from CAP	0.605
H1	0.407	0.407	0.4065	0.4068	10.333	−0.0002	0.407	0.006 away from CAP	0.401
H3	0.3918	0.3912	0.3904	0.3911	9.934	0.0001	0.391	0.010 closer to CAP	0.401
H4	0.3975	0.3975	0.3975	0.3975	10.097	0.0005	0.397	0.004 closer to CAP	0.401
H6	0.323	0.3235	0.323	0.3232	8.209	0.0002	0.323	0.079 closer to CAP	0.402

[1] Target is the spec value for "final installed position". Values are from mirror interface data drawings, numbers EK5003-101 Rev. A, EK5003-102, EK5003-103, EK5003-104, EK5003-105 Rev. A, EK5003-106, EK5003-107, EK5003-108
[2] Axial shift from nominal position as specified in the mirror interface data drawings, numbers EK5003-101 Rev. A, EK5003-102, EK5003-103, EK5003-104, EK5003-105 Rev. A, EK5003-106, EK5003-107, EK5003-108
[3] Value changed from 0.160" to 0.220" per DCO Rev A2 for EK5003-101. Axial shift was 0.605 - 0.160 = 0.445" Axial shift recalculated = 0.605" - 0.220" = 0.385"
[4] "+" value means further away from CAP than target; "−" means closer to CAP

Note: CAP required thickness: $1.968^{+0.000}_{-0.010}$ inches
CAP measured thickness: 1.965 inches (per EK5010-001 SN001 inspection report)

Table E.9: HRMA Mirrors: axial locations with respect to the CAP. (Adapted from K. A. Havey [EKC] spreadsheet.)

The data for the mirror length and end cuts are given in Table E.10. An attempt to perform a symmetric error correcting end cut was done for mirror pair P1/H1; the change in mirror figure following the end cut led to the remaining end cuts being performed at the nominal design location prior to final polishing.

Element	Dim K[1] (mm)	Dim L[2] (mm)	ΔZ[3] (mm)	Reference
P1	2.020	842.215±0.013	95.290	TE-E10-1455A
P3	1.977	842.208±0.018	74.223	TE-E10-1501
P4	2.002	842.208±0.023	74.198	TE-E10-1491
P6	2.007	842.209±0.023	74.190	TE-E10-1478
H1	1.998	842.192±0.014	77.818	TE-E10-1456B
H3	2.007	842.197±0.018	74.193	TE-E10-1506A
H4	2.015	842.225±0.023	74.185	TE-E10-1496C
H6	2.017	842.200±0.023	74.183	TE-E10-1485

[1]SECA location
[2]Mirror element length
[3]End cut location

Table E.10: AXAF element interface data, Reid (1997)

From the measurements in Table E.9 and the mirror lengths in Table E.10, the X coordinates (in mm) of key points used in the optical design can be calculated (see Table E.11 and Table E.12). The coordinate X is the nominal optical axis with $X = 0$ at the plane defined by the CAP Datum -A- points, and X increasing from the focal plane towards the HRMA. Note that in Table E.11 and Table E.12, the mirror lengths include the chamfers; according to the specification EQ7-002 (1994), the chamfer is 1.25 ± 0.75 mm *radially* at each end of the optic and at an angle of $45 \pm 5°$. The compliance matrices in HDOS DR:VR04 (1995) only note that the chamfer dimensions fall within this specification.

Mirror	length[1] (mm)	wide end (mm)	midpoint (mm)	narrow end (mm)	X(Datum -A-) (mm)
P1	842.215[2]	847.681	426.574	5.466	0.0
P3	842.208[3]	857.816	436.712	15.608	0.0
P4	842.208[4]	861.405	440.301	19.197	0.0
P6	842.209[5]	866.174	445.070	23.965	0.0

[1]Post endcut glass length; includes the chamfer at each end
[2]EK5003-101 Rev A, *P1 Mirror Interface Data*
[3]EK5003-102, *P3 Mirror Interface Data*
[4]EK5003-103, *P4 Mirror Interface Data*
[5]EK5003-104, *P6 Mirror Interface Data*

Table E.11: HRMA P Mirrors: key axial locations

Mirror	length[1] (mm)	X(Datum -D-) (mm)	wide end (mm)	midpoint (mm)	narrow end (mm)
H1	842.192[2]	−49.911	−60.244	−481.340	−902.436
H3	842.197[3]	−49.911	−59.845	−480.944	−902.042
H4	842.225[4]	−49.911	−60.008	−481.121	−902.233
H6	842.200[5]	−49.911	−58.120	−479.220	−900.320

[1]Post endcut glass length; includes the chamfer at each end
[2]EK5003-105 Rev A, *H1 Mirror Interface Data*
[3]EK5003-106, *H3 Mirror Interface Data*
[4]EK5003-107, *H4 Mirror Interface Data*
[5]EK5003-108, *H6 Mirror Interface Data*

Table E.12: HRMA H Mirrors: key axial locations

E.3 HRMA Baffles and Obstructions

The tables in the following sections were constructed directly from the `/rdb` data tables in the `/proj/axaf/simul/databases/apertures/data` directory at SAO. Table E.13 indicates the source `rdb` tables. The relation between the raytrace aperture nomenclature and the nomenclature of the EKC drawings is given in Table E.14

Baffle or Obstruction	Table	`/rdb file`
Precollimator and FHS	Tables E.15, E.16, E.17, and E.18	`precoll_rawdata_03.rdb`
Aft HRMA Structure	Tables E.19, E.20, E.21, and E.22	`postcoll_rawdata_02.rdb`
CAP Ghost Baffle	Table E.23	`cap_rawdata_02.rdb`
P6 Ghost Baffle	Table E.24	`ghostbaffle_rawdata_01.rdb`
FTS Periscope	Table E.25	`periscope_rawdata_01.rdb`

Table E.13: Baffle and Obstruction tables

Raytrace Nomenclature	EKC Assembly	EKC Baffle Plate
Precollimator Plate #1	Fwd Baffle Assy. #1 [EK5010-252]	Fwd Baffle Plate #1 [EK5010-232]
Precollimator Plate #2	Fwd Baffle Assy. #2 [EK5010-253]	Fwd Mid Baffle Plate #2 [EK5010-233]
Precollimator Plate #3	Fwd Baffle Assy. #3 [EK5010-254]	Fwd Mid Baffle Plate #2 [EK5010-233]
Precollimator Plate #4	Fwd Baffle Assy. #4 [EK5010-255]	Fwd Mid Baffle Plate #3 [EK5010-234]
Precollimator Plate #5	Fwd Baffle Assy. #5 [EK5010-256]	Fwd Mid Baffle Plate #5 [EK5010-235]
Precollimator Plate #6	Fwd Baffle Assy. #6 [EK5010-257]	Fwd Mid Baffle Plate #5 [EK5010-235]
Precollimator Plate #7	Fwd Baffle Assy. #7 [EK5010-258]	Fwd Mid Baffle Plate #7 [EK5010-236]
Precollimator Plate #8	Fwd Baffle Assy. #8 [EK5010-259]	Fwd Mid Baffle Plate #7 [EK5010-236]
Precollimator Plate #9	Fwd Baffle Assy. #9 [EK5010-261]	Fwd Mid Baffle Plate #9 [EK5010-237]
Precollimator Plate #10	Fwd Baffle Assy. #10 [EK5010-262]	Fwd Mid Baffle Plate #9 [EK5010-237]
Fwd Heater Plate (FHP)	Forward Heater Baffle Assy. [EK5010-251]	Fwd Baffle Plate #1 [EK5010-232]
Aft Heater Plate (AFP)	Aft Heater Baffle Assy. [EK5010-268]	Fwd Mid Baffle Plate #9 [EK5010-247]
Postcollimator Plate #2	Aft Baffle Assy. #2 [EK5010-263]	Mid Aft Baffle Plate #2 [EK5010-242]
Postcollimator Plate #3	Aft Baffle Assy. #3 [EK5010-264]	Mid Aft Baffle Plate #2 [EK5010-243]
Postcollimator Plate #4	Aft Baffle Assy. #4 [EK5010-265]	Mid Aft Baffle Plate #4 [EK5010-244]
Postcollimator Plate #5	Aft Baffle Assy. #5 [EK5010-266]	Mid Aft Baffle Plate #5 [EK5010-245]
Postcollimator Plate #6	Aft Baffle Assy. #6 [EK5010-267]	Top Aft Baffle Plate #6 [EK5010-246]

Table E.14: Raytrace and EKC baffle nomenclature

E.3.1 Thermal Precollimator and Forward HRMA Structure Baffles

The dimensions for the annular baffle openings were read from the "action copy" of each baffle drawing (see the *drawing* column in Tables E.15 to E.18). Note that plates 1 to 10 are installed in the Precollimator, while the FHP is installed in the Forward HRMA Structure. Table E.1 lists the plate thicknesses. Precollimator plate 1 also serves as a critical X-ray baffle; the tolerances on its radial dimensions are tighter than those for the other baffles, and it also includes a Tantalum layer. Plate 1 is a sandwich of a 5 mil Tantalum sheet between 50 mil GREP layers. Each baffle plate (including the FHP) includes twelve 0.5 inch radial support struts at intervals of 30 degrees from $+Y$.

shell	baffle	X_{fwd}[1] (in)	ΔX_{GREP} (in)	ΔX_{Ta} (in)	R_i (in)	R_o (in)	tol R_i[2] (in)	tol R_o[2] (in)	baffle plate drawing
1	1	58.7425	0.105	0.005	23.137	24.356	0.020	0.020	EK5010−232
1	2	56.3175	0.050	0.000	23.085	24.412	0.050	0.050	EK5010−233
1	3	53.8955	0.050	0.000	23.085	24.412	0.050	0.050	EK5010−233
1	4	51.5005	0.075	0.000	23.121	24.384	0.050	0.050	EK5010−234
1	5	49.0855	0.075	0.000	23.139	24.371	0.050	0.050	EK5010−235
1	6	46.6905	0.075	0.000	23.139	24.371	0.050	0.050	EK5010−235
1	7	44.2755	0.075	0.000	23.175	24.344	0.050	0.050	EK5010−236
1	8	41.8805	0.075	0.000	23.175	24.344	0.050	0.050	EK5010−236
1	9	39.4655	0.050	0.000	23.211	24.316	0.050	0.050	EK5010−237
1	10	37.0955	0.050	0.000	23.211	24.316	0.050	0.050	EK5010−237
1	FHP	34.7755	0.250	0.000	23.346	24.190	0.050	0.050	EK5010−231

[1] Table E.4, Table E.2,

[1] Casey (1994). Fabrication tolerance is ±9 mils.

Table E.15: Precollimator and Forward Hrma Structure Baffle Data; Shell 1.

shell	baffle	X_{fwd}[1] (in)	ΔX_{GREP} (in)	ΔX_{Ta} (in)	R_i (in)	R_o (in)	tol R_i[2] (in)	tol R_o[2] (in)	baffle plate drawing
3	1	58.7425	0.105	0.005	18.524	19.647	0.020	0.020	EK5010−232
3	2	56.3175	0.050	0.000	18.472	19.704	0.050	0.050	EK5010−233
3	3	53.8955	0.050	0.000	18.472	19.704	0.050	0.050	EK5010−233
3	4	51.5005	0.075	0.000	18.508	19.676	0.050	0.050	EK5010−234
3	5	49.0855	0.075	0.000	18.526	19.663	0.050	0.050	EK5010−235
3	6	46.6905	0.075	0.000	18.526	19.663	0.050	0.050	EK5010−235
3	7	44.2755	0.075	0.000	18.562	19.636	0.050	0.050	EK5010−236
3	8	41.8805	0.075	0.000	18.562	19.636	0.050	0.050	EK5010−236
3	9	39.4655	0.050	0.000	18.598	19.608	0.050	0.050	EK5010−237
3	10	37.0955	0.050	0.000	18.598	19.608	0.050	0.050	EK5010−237
3	FHP	34.7755	0.250	0.000	18.733	19.482	0.050	0.050	EK5010−231

[1] Table E.4, Table E.2,

[1] Casey (1994). Fabrication tolerance is ±9 mils.

Table E.16: Precollimator and Forward Hrma Structure Baffle Data; Shell 3.

shell	baffle	X_{fwd}[1] (in)	ΔX_{GREP} (in)	ΔX_{Ta} (in)	R_i (in)	R_o (in)	tol R_i[2] (in)	tol R_o[2] (in)	baffle plate drawing
4	1	58.7425	0.105	0.005	16.301	17.327	0.020	0.020	EK5010−232
4	2	56.3175	0.075	0.000	16.249	17.388	0.050	0.050	EK5010−233
4	3	53.8955	0.075	0.000	16.249	17.388	0.050	0.050	EK5010−233
4	4	51.5005	0.075	0.000	16.285	17.369	0.050	0.050	EK5010−234
4	5	49.0855	0.075	0.000	16.303	17.360	0.050	0.050	EK5010−235
4	6	46.6905	0.075	0.000	16.303	17.360	0.050	0.050	EK5010−235
4	7	44.2755	0.075	0.000	16.339	17.341	0.050	0.050	EK5010−236
4	8	41.8805	0.075	0.000	16.339	17.341	0.050	0.050	EK5010−236
4	9	39.4655	0.050	0.000	16.375	17.322	0.050	0.050	EK5010−237
4	10	37.0955	0.050	0.000	16.375	17.322	0.050	0.050	EK5010−237
4	FHP	34.7755	0.250	0.000	16.510	17.204	0.050	0.050	EK5010−231

[1] Table E.4, Table E.2,

[1] Casey (1994). Fabrication tolerance is ±9 mils.

Table E.17: Precollimator and Forward Hrma Structure Baffle Data; Shell 4.

shell	baffle	X_{fwd}[1] (in)	ΔX_{GREP} (in)	ΔX_{Ta} (in)	R_i (in)	R_o (in)	tol R_i[2] (in)	tol R_o[2] (in)	baffle plate drawing
6	1	58.7425	0.105	0.005	12.149	12.873	0.020	0.020	EK5010−232
6	2	56.3175	0.075	0.000	12.086	12.938	0.050	0.050	EK5010−233
6	3	53.8955	0.075	0.000	12.086	12.938	0.050	0.050	EK5010−233
6	4	51.5005	0.075	0.000	12.102	12.930	0.050	0.050	EK5010−234
6	5	49.0855	0.075	0.000	12.109	12.926	0.050	0.050	EK5010−235
6	6	46.6905	0.075	0.000	12.109	12.926	0.050	0.050	EK5010−235
6	7	44.2755	0.075	0.000	12.124	12.918	0.050	0.050	EK5010−236
6	8	41.8805	0.075	0.000	12.124	12.918	0.050	0.050	EK5010−236
6	9	39.4655	0.050	0.000	12.140	12.909	0.050	0.050	EK5010−237
6	10	37.0955	0.050	0.000	12.140	12.909	0.050	0.050	EK5010−237
6	FHP	34.7755	0.250	0.000	12.255	12.801	0.050	0.050	EK5010−231

[1] Table E.4, Table E.2,

[1] Casey (1994). Fabrication tolerance is ±9 mils.

Table E.18: Precollimator and Forward Hrma Structure Baffle Data; Shell 6.

E.3.2 Aft HRMA Structure Baffles

The dimensions for the annular baffle openings were read from the "action copy" of the baffle drawing (the *drawing* column in Tables E.19 to E.22). The forwardmost plate is the Aft Heater Plate (AHP) and it is thicker than the remaining AHS plates. The AHS baffle plates are made of GREP. Each baffle plate (including the AHP) includes twelve 0.5 inch radial support struts at intervals of 30 degrees from $+Y$.

shell	baffle	X_{fwd}[1] (in)	ΔX_{GREP} (in)	R_i (in)	R_o (in)	tol R_i[2] (in)	tol R_o[2] (in)	baffle plate drawing
1	AHP	−41.3525	0.250	21.028	21.809	0.050	0.050	EK5010−247
1	2	−43.2525	0.050	20.801	21.802	0.050	0.050	EK5010−242
1	3	−44.9525	0.050	20.687	21.706	0.050	0.050	EK5010−243
1	4	−46.6525	0.050	20.573	21.610	0.050	0.050	EK5010−244
1	5	−48.3525	0.050	20.459	21.515	0.050	0.050	EK5010−245
1	6	−50.0525	0.075	20.445	21.319	0.050	0.050	EK5010−246

[1] Table E.7

[2] Casey (1994). Fabrication tolerance is ±9 mils.

Table E.19: Aft Hrma Structure Baffle Data; Shell 1.

shell	baffle	X_{fwd}[1] (in)	ΔX_{GREP} (in)	R_i (in)	R_o (in)	tol R_i[2] (in)	tol R_o[2] (in)	baffle plate drawing
3	AHP	−41.3525	0.250	16.813	17.564	0.050	0.050	EK5010−247
3	2	−43.2525	0.050	16.604	17.580	0.050	0.050	EK5010−242
3	3	−44.9525	0.050	16.507	17.504	0.050	0.050	EK5010−243
3	4	−46.6525	0.050	16.409	17.429	0.050	0.050	EK5010−244
3	5	−48.3525	0.050	16.312	17.353	0.050	0.050	EK5010−245
3	6	−50.0525	0.075	16.314	17.178	0.050	0.050	EK5010−246

[1] Table E.7

[2] Casey (1994). Fabrication tolerance is ±9 mils.

Table E.20: Aft Hrma Structure Baffle Data; Shell 3.

shell	baffle	X_{fwd}[1] (in)	ΔX_{GREP} (in)	R_i (in)	R_o (in)	tol R_i[2] (in)	tol R_o[2] (in)	baffle plate drawing
4	AHP	−41.3525	0.250	14.763	15.513	0.050	0.050	EK5010−247
4	2	−43.2525	0.050	14.565	15.540	0.050	0.050	EK5010−242
4	3	−44.9525	0.050	14.477	15.474	0.050	0.050	EK5010−243
4	4	−46.6525	0.050	14.389	15.409	0.050	0.050	EK5010−244
4	5	−48.3525	0.050	14.302	15.343	0.050	0.050	EK5010−245
4	6	−50.0525	0.075	14.314	15.177	0.050	0.050	EK5010−246

[1] Table E.7

[2] Casey (1994). Fabrication tolerance is ±9 mils.

Table E.21: Aft Hrma Structure Baffle Data; Shell 4.

shell	baffle	X_{fwd}[1] (in)	ΔX_{GREP} (in)	R_i (in)	R_o (in)	tol R_i[2] (in)	tol R_o[2] (in)	baffle plate drawing
6	AHP	−41.3525	0.250	10.934	11.548	0.050	0.050	EK5010−247
6	2	−43.2525	0.050	10.760	11.596	0.050	0.050	EK5010−242
6	3	−44.9525	0.050	10.694	11.549	0.050	0.050	EK5010−243
6	4	−46.6525	0.050	10.628	11.502	0.050	0.050	EK5010−244
6	5	−48.3525	0.050	10.562	11.456	0.050	0.050	EK5010−245
6	6	−50.0525	0.075	10.596	11.309	0.050	0.050	EK5010−246

[1] Table E.7

[2] Casey (1994). Fabrication tolerance is ±9 mils.

Table E.22: Aft Hrma Structure Baffle Data; Shell 6.

E.3.3 CAP Ghost Baffles

The HRMA ghost baffle design includes Tantalum baffles located at the aft (H) side of the Center Aperture Plate. These baffles are mounted on thin aluminum support plates, and includes Tantalum *radiation sheets* which provides the critical X-ray baffle edge. Each shell has twelve CAP baffle pieces, one for each sector of the CAP. The radius of the ghost baffle was read from the Tantalum *radiation sheet* drawing listed in the *drawing* column in Table E.23. The outer radii listed in the table correspond to the edges of the annular slots machined into the CAP. Each shell is also obstructed by twelve CAP radial support struts (0.75 inches wide) spaced at 30° intervals from $+Y$.

shell	baffle	X_{fwd} (in)	R_i (in)	R_o (in)	tol R_i[1] (in)	tol R_o[1] (in)	radiation sheet drawing
1	CAP_D	−1.965	23.086	23.76	0.020	0.050	EK5010−097
3	CAP_D	−1.965	18.577	19.15	0.020	0.050	EK5010−114
4	CAP_D	−1.965	16.386	16.92	0.020	0.050	EK5010−096
6	CAP_D	−1.965	12.172	12.58	0.020	0.050	EK5010−098

[1] Casey (1994). Fabrication tolerance is ±9 mils.

Table E.23: CAP Ghost Baffle Data.

E.3.4 P6 Ghost Baffle

The outer radius of the P6 ghost baffle was read from the Tantalum *radiation sheet* drawing listed in the the *drawing* column in Table E.24. The ghost baffle is mounted on an aluminum annular plate attached to a cylindrical structure which mounts directly to the P-side of the CAP. Because only one critical edge is needed, this baffle has no radial support struts obstructing the clear aperture.

shell	baffle	X_{fwd} (in)	ΔX_{Ta} (in)	R_o (in)	tol R_o[1] (in)	radiation sheet drawing
6	P6 baffle	13.838	0.005	12.416	0.020	EK5010−118

[1] Casey (1994). Fabrication tolerance is ±9 mils.

Table E.24: P6 Ghost Baffle Data.

E.3.5 Fiducial Transfer System Periscope

The Fiducial Transfer System (FTS) periscope is an additional obstruction in the X-Ray path. It lies mostly in the shadow of a CAP radial strut (in the $[-Y, -Z]$ quadrant, 30° from $-Y$; a diagram of the Periscope is shown in Figure E.8, and the $Y-Z$ clocking of the Periscope is shown in Figure E.9.

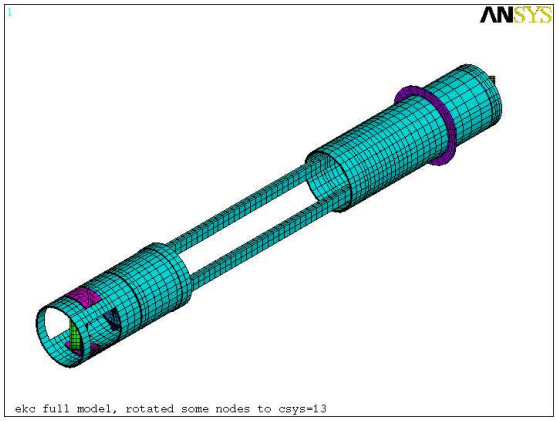

Figure E.8: EKC Solid Model of Fiducial Transfer System Periscope.

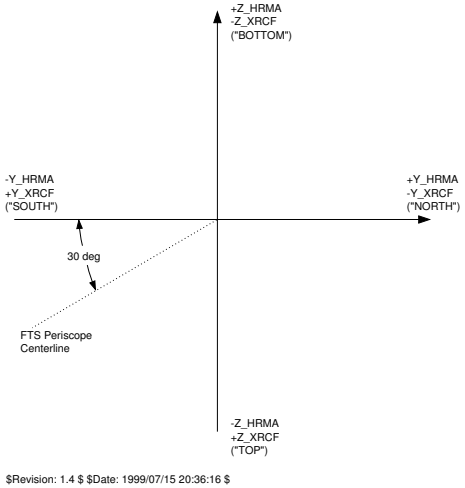

Figure E.9: Clocking angle for the FTS Periscope

The width of the periscope struts in the Y–Z plane is 0.72 inches, and the depth of each strut axially is 0.365 inches. The outside to outside dimensions of the struts (in the X direction) are 3.235 inches and the inside to inside dimensions are 2.505 inches; these dimensions were obtained from the 3D solid model from EKC. The critical dimensions for X-Ray obstruction are given in Table E.25.

baffle	X (in)	Width (in)	θ_C (°)
Periscope_Fwd	−37.393	0.72	150.0
Periscope_Aft	−40.628	0.72	150.0

Table E.25: FTS Periscope Data.

E.4 Relation between HDOS and Raytrace Coordinates

Several HDOS co-ordinate systems are relevant to both the scattering and the surface deformation maps. These are defined in the TRW mirror specification, EQ7-002 (Rev. E). The Telescope Ensemble (TE) coordinate system has its origin at the ideal focus and its Z azis positive (along the optical axis) from the ideal focal plane towards the HRMA. The ideal optical surface geometry with respect to the TE system is specified in EQ7-002.

The HDOS optical metrology data is specified in separate Mirror Element (ME) coordinate systems, one per optic. These ME coordinate systems are aligned with their Z axes along the TE Z axis, but with their zero point (in Z) offset such that $Z = 0$ in the ME system is coincident with the beginning of the *uncut* optic (each uncut optic was nominally 39 inches or 990.6 mm long). The X axes are aligned with the optic primary zero azimuth reference fiducial point.

The transformations between the TE system and the ME systems are:

$$Z_{ME} = Z_{TE} - 9103.6 \text{ mm} \quad \text{(for all H's)} \tag{E.1}$$

and

$$Z_{ME} = Z_{TE} - 10022.6 \text{ mm} \quad \text{(for all P's)} \tag{E.2}$$

The SAOsac raytrace system uses a body centered coordinate system (inherited from OSAC) for each optic; unfortunately, the sense of the raytrace Z axis is opposite that of the HDOS ME systems. The following series of operations is required to go from the HDOS ME coordinate system to the SAO raytrace coordinate system:

1. Translate the origin of the ME coordinate system to the center of the as-cut optic; the distance is: $(Z_{ec} + L/2)$ where Z_{ec} is the narrow end end cut value and L is as-cut optic length.

2. Rotate by 180° about the (translated) X axis (which reverses the sense of the Z axis). This leaves the new X axis aligned with the ME X axis but reverses the sense of the Y axis. Angles in the new system are measured in opposite direction (clocking) in the new system.

3. Rotate about the Z axis to move the X axis from the ME X to the desired SAOsac X, by an angle θ_C, the optic clocking angle. We have a choice of sign conventions here, and we have chosen to to define θ_C as the *positive* angular rotation about the SAOsac $+Z$ axis which is required to align the SAOsac X axis with the ME fiducial (X_{ME} axis).

Working in cylindrical coordinates, the relationships between the ME coordinate system and the SAOsac coordinate system are as follows:

$$Z_O = \left(Z_{ec} + \frac{L}{2}\right) - Z_{ME} \quad \text{(E.3)}$$

$$\theta_O = 2\pi - \theta_{ME} + \theta_C \quad \text{(E.4)}$$

$$R_O = R_{ME} \quad \text{(E.5)}$$

where Z_O and Z_{ME} are the Z coordinates in the SAOsac and ME systems, θ_O and θ_{ME} are the rotation angle measured from the corresponding X axis, positive with respect to the respective Z axes, and R_O and R_{ME} are the SAOsac and ME radial coordinates.

Based on the end cut data (Table E.10), the axial data are given in Table E.26. In this table, $Z_{ME,wide}$ and $Z_{ME,narrow}$ are the axial coordinates, in the ME system, of the wide and narrow ends of the optics.

Element	Z_{ec} (mm)	L (mm)	$Z_{ec} + L/2$ (mm)	ME Data Range $Z_{ME,wide}$ (mm)	ME Data Range $Z_{ME,narrow}$ (mm)
P1	95.290	842.215	516.397	95.290	937.050
P3	74.223	842.208	495.327	74.223	916.431
P4	74.198	842.208	495.302	74.198	916.406
P6	74.190	842.209	495.294	74.190	916.399
H1	77.818	842.192	498.914	77.818	920.010
H3	74.193	842.197	495.291	74.193	916.390
H4	74.185	842.225	495.297	74.185	916.410
H6	74.183	842.200	495.293	74.183	916.383

Table E.26: AXAF element axial data.

E.5 HRMA Optic Prescription

The HRMA optic prescription, adapted from the nominal prescription `ek05lvs` and adjusted for the end cuts, is given in Table E.27. The mirror conics are given by

$$\rho^2 = \rho_0^2 + 2\,K\,z - P\,z^2 \quad \text{(E.6)}$$

where ρ is the radius of the conic surface as measured from the optical axis, and z is distance along the optical axis measured from the *body center*, with z positive towards the narrow end of the optic. If L is the total length of the optic, then the forward (*wide end*) of the optic is at $-L/2$ and the aft (*narrow end*) of the optic is at $+L/2$.

Optic	P	k	ρ_0
h1	−1.7797716637950735E−03	−26.0506034413416841	579.89015840093919
h3	−1.1532395834759916E−03	−16.875942397594130	466.64379784205380
h4	−8.9864417477996457E−04	−13.150318066441841	411.91935912458604
h6	−4.9625995845653374E−04	−7.2620248152618760	306.09851668776219
p1	0.0	−8.9333113530131421	606.86080963697918
p3	0.0	−5.7939624154424676	488.46244215611011
p4	0.0	−4.5165799273846270	431.26225933154404
p6	0.0	−2.4957050467401789	320.56977725634789

Table E.27: HRMA Optic Prescription (including end cut) for ideal optics.

E.6 HRMA Optic Clocking Angles

The orientations of the HRMA, XRCF, and SAOsac coordinate systems are shown in Figure B.1; the convention for Kodak clocking angle on the MMIS is also indicated. The relations between the Kodak clocking convention and the SAOsac and double-pass SAOsac (DPSAOsac) clocking conventions are indicated in Figure E.10.

Optic	Kodak clocking (°)	SAOsac clocking (°)	DPSAOsac clocking (°)
P1	19.00[1]	109.00	251.00
P3	41.50[2]	130.50	229.50
P4	91.00[3]	181.00	179.00
P6	29.00[4]	119.00	241.00
H1	65.25[5]	155.25	204.75
H3	43.00[6]	132.00	228.00
H4	124.00[7]	214.00	146.00
H6	311.50[8]	41.50	318.50

[1]EK5003-101 Rev A, *P1 Mirror Interface Data*
[2]EK5003-102, *P3 Mirror Interface Data*
[3]EK5003-103, *P4 Mirror Interface Data*
[4]EK5003-104, *P6 Mirror Interface Data*
[5]EK5003-105 Rev A, *H1 Mirror Interface Data*
[6]EK5003-106, *H3 Mirror Interface Data*
[7]EK5003-107, *H4 Mirror Interface Data*
[8]EK5003-108, *H6 Mirror Interface Data*

Table E.28: Mirror clocking data.

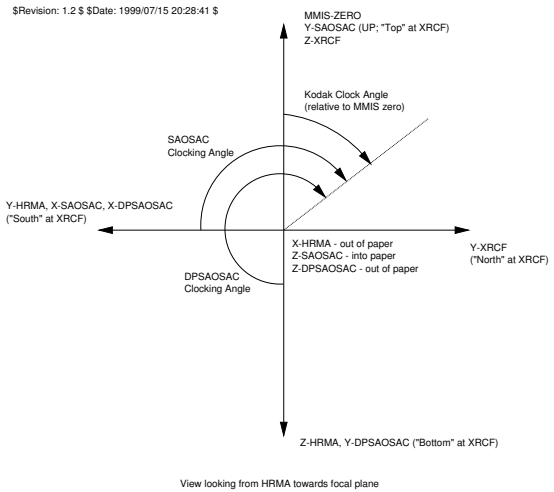

Figure E.10: EKC, SAOsac, and DPSAOsac optic clocking conventions.

Bibliography

Akima, H. 1978: *ACM Transactions on Mathematical Software* **4(2)**, 148

Algieri, A., Fischer, H. G., Holmgren, S.-O., and Szeptycka, M. 1994: *Nuclear Instruments and Methods in Physics Research A* **A338**, 348

Arnaud, K. 1996: in *Astronomical Data Analysis Software and Systems V, eds. Jacoby G. and Barnes J., ASP Conf. Series*, Vol. 101, p. 17, ASP

Auerhammer, J. M., Brandt, G., Scholze, F., Thornagel, R., Ulm, G., Wargelin, B. J., McDermott, W. C., Norton, T. J., Evans, I. N., and Kellogg, E. M. 1998: in *SPIE Proceedings*, Vol. 3444?, SPIE, San Diego

Austen, M. V. Z. G. K. and Torgenson, D. T. 1980: *High Resolution Mirror Assembly Optical Systems Stuch*, Interim Engineering Report SAO-AXAF-80-003, Feb. 1980, SAO

Beckmann, P. and Spizzichino, A. 1963: *The Scattering of Electromagnetic Waves from Rough Surfaces*, Pergamon Press, Oxford

Bevington, P. R. and Robinson, D. K. 1992: *Data Reduction and Error Analysis for the Physical Sciences*, McGraw-Hill Inc., New York, second edition

Casey, T. 1994: *HRMA Precollimator and Interior Baffle Dimensions*, Tech Note AXAF-94-0386-Casey, 7 Dec. 1994, Eastman Kodak Company

Cash, W. 1979: *Astrophysical Journal* **228**, 939

Chappell, J. H. and Murray, S. S. 1989: in *SPIE Proceedings*, Vol. 1149, p. 460, SPIE, San Diego

Cohen, L. 1995: *HXDS Flow Proportional Counter Window Analysis*, Memorandum, 25 Oct. 1995, Smithsonian Astrophysical Observatory

Cohen, L. M. 1997: *XRCF Measurement & Epoxy Strain*, Memorandum, Apr. 1997, Smithsonian Astrophysical Observatory

Discher, N. 1996: *HRMA Datum Suface Locations in HRMA and AXAF Coordinates*, Tech Note AXAF-96-0248-Discher, Rev. A, 18 Nov. 1996, Eastman Kodak Company

Edgar, R. J., Tsiang, E. Y., Tennant, A., Vitek, S., and Swartz, D. 1997: in *SPIE Proceedings*, Vol. 3113, p. 124, SPIE, San Diego

Elsner, R. F. and O'Dell, S. L. 1991: *Reflection and Transmission: Multilayers with Arbitrary Number of Layers*, 12 Dec. 1991

EQ7-002 1994: *Specification for the Finishing of the Advanced X-ray Astrophysics Facility (AXAF) Uncoated Mirror Elements*, Specification Document EQ7-002, Revision E, 7/18/94, 1994, TRW

Evans, I. N., Kellogg, E. M., McDermott, W. C., Ordway, M. P., Rosenberg, J. M., and Wargelin, B. J. 1997: in *SPIE Proceedings*, Vol. 3113, p. 18, SPIE, San Diego

Gaetz, T. J. 1993: *Final Report: AXAF-I Ghost Ray Study – On Orbit Case*, Technical Report SAO-AXAF-DR-93-053, 1993, Smithsonian Astrophysical Observatory

Gaetz, T. J., Podgorski, W. A., Cohen, L. M., Freeman, M. D., Edgar, R. J., Jerius, D., Van Speybroeck, L., and Zhao, P. 1997: in *SPIE Proceedings*, Vol. 3113, SPIE, San Diego

Goddard, R. 1994: *Critical Design Review of the HXDS*, Technical Report SAO-AXAF-DR-94-102, page REG.V.A.2c-13, 1994, Smithsonian Astrophysical Observatory

Graessle, D. E., Burek, A. J., Fitch, J. J., Harris, B., Schwartz, D. A., and Blake, R. L. 1997: in *SPIE Proceedings*, Vol. 3113, SPIE, San Diego

Griner, D. B., Zissa, D. E., and Korsch, D. 1985: *Test Method for Telescope Using a Point Source at a Finite Distance*, MSFC Center Director's Discretionary Fund Final Report, Project No. H20 Technical Memorandum TM-86523, Sept. 1985, NASA

HDOS DR:VR04 1995: *Advanced X-Ray Astrophysics Facility (AXAF) Ensemble Verification Report for P1/H1, P3/H3, P4/H4, P6/H6*, Technical Report DR:VR04, 1995, Hughes Danbury Optical Systems

Henke, L., Gullikson, E. M., and Davis, J. C. 1993: *Atomic Data and Nuclear Data Tables* **54**, 181, Additional data were taken from `http://www-cxro.lbl.gov/optical_constants/`

Jackson, J. D. 1962: *Classical Electrodynamics*, J. Wiley & Sons, New York, second edition

Jahoda, K. and McCammon, D. 1988: *Nuclear Instrumentation and Methods in Physics Research* **A272**, 800

Jenkins, R., Gould, R. W., and Gedge, D. 1981: *Quantitative X-Ray Spectrometry*, Marcel Dekker, Inc., New York

Jerius, D. 1997: *XRCF: Phase 1 Testing: Preliminary Results*, Technical Report SAO-AXAF-DR-97-282, 1997, Smithsonian Astrophysical Observatory

Kadyk, J. A. 1991: *Nuclear Instruments and Methods in Physics Research A* **A300**, 436

Knoll, G. F. 1989: *Radiation Detection and Measurement*, Wiley, New York, second edition

Kolodziejczak, J., Austin, R., Elsner, R., O'Dell, S., Sulkanen, M., Schwartz, D., Tennant, A., Weisskopf, M., Zirnstein, G., and McDermott, W. 1997: in *SPIE Proceedings*, Vol. 3113, p. 65, SPIE

Kraft, S., Scholze, F., Thornagel, R., Ulm, G., McDermott, W., and Kellogg, E. 1997: in *SPIE Proceedings*, Vol. 3114, p. 101, SPIE

Lederer, T., Rabus, H., Scholze, F., Thornagel, R., and Ulm, G. 1995: in *Proc. SPIE, X-Ray and Ultraviolet Sensors and Applications, Richard B. Hoover; Mark B. Williams; Eds.*, Vol. 2519, p. 92, SPIE

Lewis, T. S. 1993: *AXAF HRMA Alignment Test Analysis*, Tech Note XKR93-1831CD, 1993, Eastman Kodak Company

Matthews, G. 1997: *Encoder Values, IAP, and What It Means to Me*, Memorandum, 24 Mar. 1997, Eastman Kodak Company

Murray, S. S. et al. 1997: in *SPIE Proceedings*, Vol. 3114, p. 11, SPIE

Nousek, J. A. and Shue, D. R. 1989: *Astrophysical Journal* **342**, 1207

O'Dell, S., Elsner, R. F., Kolodziejeczak, J. J., Weisskopf, M. C., Hughes, J. P., and Speybroeck, L. P. V. 1992: in *Proc. SPIE, Multilayer and grazing incidence X-ray/EUV optics for astronomy and projection lithography; Proceedings of the Meeting, San Diego, CA*, Vol. 1742, pp 171–182, SPIE

Phillips, G. W. and Marlow, K. W. 1976: *Nuclear Instruments and Methods* **137**, 525

Reid, P. 1997: *AXAF element interface data*, Memorandum, 14 Feb. 1997, Smithsonian Astrophysical Observatory

SAO 1997: *HXDS Operation Instructions*, Technical Report SP-SAO-4004, 1997, Smithsonian Astrophysical Observatory

SAO 1998: *Contract End Item (CEI) Specification for the HRMA X-Ray Detection System HXDS*, Technical Report SAO-AXAF-DR-92-017, 1998, Smithsonian Astrophysical Observatory

Scholze, F. and Ulm, G. 1994: *Nuclear Instruments and Methods in Physics Research A* **A339**, 49

Texter, S. 1997: *IAP encoder Positions*, Memo, 1997, TRW

Tikkanen, T. 1997: *Radiat. Phys. Chem.* **50**, 527

Tsiang, E. Y. 1997: *JMKMOD: Models and Software for the Ground calibration of AXAF*, Technical Report SAO-AXAF-DR-97-276, 1997, Smithsonian Astrophysical Observatory

Tsiang, E. Y., Edgar, R. J., Vitek, S., and Tennant, A. 1997: in *SPIE Proceedings*, Vol. 3113, p. 132, SPIE, San Diego

Van Speybroeck, L. 1989a: *Mirror Prescription*, Memorandum, 20 Oct. 1989a, Smithsonian Astrophysical Observatory

Van Speybroeck, L. 1989b: *TMA II Performance Prediction*, Memorandum, 28 Apr. 1989b, Smithsonian Astrophysical Observatory

Waldman, M. 1995: *ARM Zone Diameters for HATS Software*, Tech Note AXAF-95-0209-WALDMAN, 1995, Eastman Kodak Company

Wargelin, B. J., Kellogg, E. M., McDermott, W. C., Evans, I. N., and Vitek, S. A. 1997: in *SPIE Proceedings*, Vol. 3113, p. 526, SPIE, San Diego

Weisskopf, M. C. and O'Dell, S. L. 1997: in *SPIE Proceedings*, Vol. 3113, p. 2, SPIE, San Diego

Zhao, P. 1995: *AXAF VETA-I Mirror X-ray Test Results (Cross Check with the HDOS Metrology Data)*, Technical Report SAO-AXAF-DR-95-146, 1995, Smithsonian Astrophysical Observatory

Zhao, P. 1996: *OSAC Parameters for AXAF Mirrors – Formulae and Precisions (Revised)*, Memorandum, 24 June 1996, Smithsonian Astrophysical Observatory

Zhao, P., Austin, R. A., Edgar, R. J., Elsner, R. F., Gaetz, T. J., Graessle, D. E., Jerius, D., Kolodziejczak, J. J., McDermott, W. C., O'Dell, S. L., Sulkanen, M. E., Schwartz, D. A., Swartz, D. A., Tennant, A. F., Speybroeck, L. P. V., Wargelin, B. J., Weisskopf, M. C., and Zirnstein, C. G. 1998: in *SPIE Proceedings*, Vol. 3444, p. 01, SPIE, Denver

Zhao, P., Cohen, L. M., and Spebroeck, L. P. V. 1997: in *SPIE Proceedings*, Vol. 3113, p. 106, SPIE, San Diego

Zhao, P., Freeman, M. D., Jerius, D., and Shao, Y. 1993: in *SPIE Proceedings*, Vol. 2011, p. 59, SPIE, San Diego

Zhao, P., Freeman, M. D., Kellogg, E. M., and Nguyen, D. 1992: in *SPIE Proceedings*, Vol. 1742, p. 75, SPIE, San Diego

Zissa, D. E. and Korsch, D. 1986: *Experimental Evaluation of the Ring Focus Test for X-ray Telescope Using AXAF's Technology Mirror Assembly*, MSFC Center Director's Discretionary Fund Final Report, Project No. H20 Technical Memorandum TM-86570, Oct. 1986, NASA